Ninth Symposium

NAVAL HYDRODYNAMICS

VOLUME 2

FRONTIER PROBLEMS

ACR-203

Office of Naval Research
Department of the Navy

Ninth Symposium

NAVAL HYDRODYNAMICS

VOLUME 2

FRONTIER PROBLEMS

sponsored by the

OFFICE OF NAVAL RESEARCH

the

MINISTERE D'ETAT CHARGE DE LA DEFENSE NATIONALE

and the

ASSOCIATION TECHNIQUE MARITIME ET AERONAUTIQUE

August 20-25, 1972

Paris, France

R. BRARD
A. CASTERA
Editors

ACR-203

OFFICE OF NAVAL RESEARCH—DEPARTMENT OF THE NAVY

Arlington, Va.

For sale by the Superintendent of Documents, U.S. Government Printing Office
Washington, D.C. 20402 - Price $13.55
Stock Number 0851-00063

PREVIOUS BOOKS IN THE NAVAL HYDRODYNAMICS SERIES

"First Symposium on Naval Hydrodynamics," National Academy of Sciences—National Research Council, Publication 515, 1957, Washington, D.C.; PB133732, paper copy $6.00, 335-mm microfilm $1.45.

"Second Symposium on Naval Hydrodynamics: Hydrodynamic Noise and Cavity Flow," Office of Naval Reserach, Department of the Navy, ACR-38, 1958; PB157668, paper copy $10.00, 35-mm microfilm $1.45.

"Third Symposium on Naval Hydrodynamics: High-Performance Ships," Office of Naval Research, Department of the Navy, ACR-65, 1960; AD430729, paper copy $6.00, 35-mm microfilm $1.45.

"Fourth Symposium on Naval Hydrodynamics: Propulsion and Hydroelasticity," Office of Naval Research, Department of the Navy, ACR-92, 1962; AD447732, paper copy $9.00, 35-mm microfilm $1.45.

"The Collected Papers of Sir Thomas Havelock on Hydrodynamics," Office of Naval Research, Department of the Navy, ACR-103, 1963; AD623589, paper copy $6.00, microfiche $1.45.

"Fifth Symposium on Naval Hydrodynamics: Ship Motions and Drag Reduction," Office of Naval Research, Department of the Navy, ACR-112, 1964; AD640539, paper copy $15.00, microfiche $1.45.

"Sixth Symposium on Naval Hydrodynamics: Physics of Fluids, Maneuverability and Ocean Platforms, Ocean Waves, and Ship-Generated Waves and Wave Resistance," Office of Naval Research, Department of the Navy, ACR-136, 1966; AD676079, paper copy $10.00, microfiche $1.45.

"Seventh Symposium on Naval Hydrodynamics: Unsteady Propeller Forces, Fundamental Hydrodynamics, Unconventional Propulsion," Office of Naval Research, Department of the Navy, DR-148, 1968: AD721180; Available from Superintendent of Documents, U.S. Government Printing Office, Washington, D.C. 20402, Clothbound, 1690 pages, illustrated (Catalog No. D 210.15:DR-148; Stock No. 0851-0049), $13.00; microfiche $1.45.

"Eighth Symposium on Naval Hydrodynamics: Hydrodynamics in the Ocean Environment," Office of Naval Research, Department of the Navy, ACR-179, 1970; AD748721; Available from Superintendent of Documents, U.S. Government Printing Office, Washington, D.C., 20404, Clothbound, 1185 pages, illustrated (Catalog No. D 210.15: ACR-179; Stock No. 0851-0056), $10.00; microfiche $1.45.

NOTE: The above books are available on microfilm and microfiche from the National Technical Information Service, U.S. Department of Commerce, Springfield, Virginia 22151. The first six books are also available from NTIS in paper copies. The catalog numbers and the prices for paper, clothbound, and microform copies are shown for each book.

PREFACE

The Ninth Symposium on Naval Hydrodynamics continues in all aspects the precedent, established by previous symposia in this series, of providing an international forum for the presentation and exchange of the most recent research results in selected fields of naval hydrodynamics. The Symposium was held in Paris, France on 20-25 August 1972 under the joint sponsorship of the Office of Naval Research, the Ministère d'Etat chargé de la Défense Nationale and the Association Technique Maritime et Aeroanutique.

The technical program of the Symposium was devoted to three subject areas of current naval and maritime interest. These subject areas are covered in the Proceedings in two volumes:

Volume 1 — The Hydrodynamics of Unconventional Ships
— Hydrodynamic Aspects of Ocean Engineering
Volume 2 — Frontier Problems in Hydrodynamics.

The planning, organization and management of a Symposium such as this is an undertaking of considerable magnitude, and many people have made invaluable contributions to the resolution of the myriad of large and small problems which invariably arise. The Office of Naval Research is acutely aware of the fact that the success of the Ninth Symposium is directly attributable to these people and wishes to take this opportunity to express its heartfelt gratitude to them. We are particularly indebted to Vice Admiral Raymond THIENNOT, Directeur Technique des Constructions Navales, Ministère d'Etat chargé de la Défense Nationale, to Professor Jean DUBOIS, Directeur des Recherches et Moyens d'Essais, Ministère d'Etat chargé de la Défense Nationale, and to Monsieur Jean MARIE, Président de l'Association Technique Maritime et Aeronautique, who provided the formal structure which made this joint undertaking possible. The detailed organization and management of the Ninth Symposium lay in the capable and competent hands of Vice Admiral Roger BRARD, Président de la Academie des Sciences, and Rear Admiral André CASTERA, Directeur du Bassin d'Essais des Carènes, who were most ably assisted in this endeavor by the charming Madame Jean TATON. Throughout the long days of planning and preparation the experienced and practical counsel of Mr. Stanley DOROFF of the Office of Naval Research provided continuous guidance which contributed in an immeasurable way to the success of the Ninth Symposium on Hydrodynamics.

Ralph D. Cooper

RALPH D. COOPER
Fluid Dynamics Program
Office of Naval Research

VOLUME 2

CONTENTS

FRONTIER PROBLEMS

FRONTIER PROBLEMS

Thursday, August 24, 1972

Morning Session

Chairman : Pr . J.V. Wehausen
University of California, Berkeley, U.S.A.

OPTIMUM SHAPES OF BODIES IN FREE SURFACE FLOWS

Th. Y. Wu
California Institute of Technology
Pasadena, California, U.S.A.

and

Arthur K. Whitney
Palo Alto Research Laboratory, Lockheed Aircraft Corp.
Palo Alto, California, U.S.A.

ABSTRACT

The general problem of optimum shapes arising in a wide variety of free-surface flows can be characterized mathematically by a new class of variational problems in which the Euler equation is a set of dual integral equations which are generally nonlinear, and singular, of the Cauchy type. Several approximate methods are discussed, including linearization of the integral equations, the Rayleigh-Ritz method, and the thin-wing type theory. These methods are applied here to consider the following physical problems :

(i) The optimum shape of a two-dimensional plate planing on the water surface, producing the maximum hydrodynamic lift ;

(ii) The two-dimensional body profile of minimum pressure drag in symmetric cavity flows ;

(iii) The cavitating hydrofoil having the minimum drag for prescribed lift.

Approximate solutions of these problems are discussed under a set of additional isoperimetric constraints and some physically desirable end conditions.

I. INTRODUCTION

The general problem of optimum shapes of bodies in free-surface flows is of practical as well as theoretical interest. In applications of naval hydrodynamics these problems often arise when attempts are made to improve the hydromechanical efficiency and performance of lifting and propulsive devices, or to achieve higher speeds of operation of certain vehicles. Some examples of problems that fall under this general class are illustrated in Figure 1. The first example is to evaluate the optimum profile of a two-dimensional plate planing on a water surface without spray formation, and producing the maximum hydrodynamic lift under the isoperimetric constraints of fixed chord length ℓ and fixed wetted arc-length S of the plate. The second example depicts the problem of determining the shape of a symmetric two-dimensional plate so that the pressure drag of this plate in an infinite cavity flow is a minimum, again with fixed base-chord ℓ and wetted arc-length S . The third is an example concerning the general lifting cavity flow past an optimum hydrofoil having the minimum drag for prescribed lift, incidence angle α , chord length ℓ and the wetted arc-length S. In these problems the gravitational and viscous effects may be neglected as a first approximation for operations at high Froude numbers. Physically, there is no definite rule for choosing the side constraints and isoperimetric conditions, but the existence and the characteristic behavior of the solution can depend decisively on what constraints and conditions are chosen. Mathematically, it has been observed in a series of recent studies that the determination of the optimum hydromechanical shape of a body in these free-surface flows invariably results in a new class of variational problems. Only a very few special cases from this general class of problems have been solved, the optimum-lifting-line solution of Prandtl being an outstanding example.

There are several essential differences between the classical theory and this new class of variational problems. First of all, the unknown argument functions of the functional under extremization are related, not by differential equations as in the classical calculus of variations, but by a singular integral equation of the Cauchy type. Consequently, the "Euler equation" which results from the consideration of the first variation of the functional in this new class is also a singular integral equation which is, in general, nonlinear. This is in sharp contrast to the Euler differential equation in classical theory. Another characteristic feature of these new problems is that while regular behavior of solution at the limits of the integral equation may be required on physical grounds, the mathematical conditions which insure such behavior generally involve functional equations which are

difficult, and sometimes just impossible, to satisfy.

Because of these difficulties and the fact that no general techniques are known for solving nonlinear singular integral equations, development of this new class of variational problems seems to require a strong effort. Attempts are made here to present some general results of the current study. Some necessary conditions for the existence of an optimum solution are derived from a consideration of the first and second variations of the functional in question. To solve the resulting nonlinear, singular integral equation several approximate methods are discussed. One method is by linearization of the integral equation, giving a final set of dual singular integral equations of the Cauchy type. When the variable coefficients of this system of integral equations satisfy a certain relationship, this set of dual integral equations can be solved analytically in a closed form ; the results of this special case provide analytical expressions which can be extensively investigated to determine the behavior of a solution near the end points. Another approximate method is the Rayleigh-Ritz expansion ; it has the advantages of retaining the nonlinear effects to a certain extent, of incorporating the required behavior of the solution near the end points into the discretized expansion of the solution, but the method is generally not convergent. A third approach depends on a thin wing type theory to describe the flow at the very beginning, a variational calculation is then made on an approximate expression of the physical quantities of interest. These mathematical methods will be discussed and then applied to three problems described earlier. While the results to be presented should be considered as still preliminary, since exact solutions to these problems have not yet been found, it is hoped that this paper will succeed in stimulating further interest in the development of the general theory, and, in turn, aid in the resolution of many hydromechanic problems of great importance.

II. GENERAL MATHEMATICAL THEORY

To present a unified discussion of the general class of optimum hydromechanical shapes of bodies in plane free-surface flows, including the three examples (i) - (iii) depicted in Figure 1, we assume the flow to be inviscid, irrotational, and incompressible, taking as known that the physical plane $z = x + iy$ and the potential plane $f = \varphi + i\psi$ correspond conformally to the upper half of the parametric $\zeta = \xi + i\eta$ plane by the mapping that can be signified symbolically as

$$f = \varphi + i\psi = \nu(\zeta; c_1, \ldots c_n), \qquad (1)$$

where ν is an analytic function of ζ and may involve geometric parameters $c_1, \ldots c_n$, so that the wetted body surface corresponds to $\eta = 0^+$, $|\xi| < 1$, and the free surface, to $\eta = 0^+$, $|\xi| > 1$. Specific forms of the function $\nu(\zeta)$ will be given later, but our purpose at this time is merely to illustrate the type of nonlinear variational problem that arises.

Description of the flow is effected by giving the parametric expressions $f = f(\zeta)$ and $\omega = \omega(\zeta)$,

$$\omega(\zeta) = -\log(df/dz) = \tau + i\theta \qquad (2)$$

being the logarithmic hodograph. The boundary conditions for ω may be specified either as a Dirichlet problem, by giving

$$\tau^+ = \mathrm{Re}\ \omega(\xi + i0) = \begin{cases} \Gamma(\xi) & (\text{given for } |\xi| < 1), \\ 0 & (|\xi| > 1), \end{cases} \qquad (3)$$

or as a Riemann-Hilbert problem,

$$\theta^+ = \mathrm{Im}\ \omega(\xi + i0) = \beta(\xi) \qquad (|\xi| < 1), \qquad (4a)$$

$$\tau^+ = \mathrm{Re}\ \omega(\xi + i0) = 0 \qquad (|\xi| > 1). \qquad (4b)$$

The formulation of the ω problem is completed by specifying a condition at the point of infinity, say

$$\omega \to 0, \qquad (|z| \to \infty), \qquad (5)$$

and by prescribing a set of end conditions, which are generally on $\Gamma(\xi)$, as

$$\Gamma(\pm 1) = 0, \qquad (6)$$

or similar ones. The end conditions are usually required on physical grounds in order that the fluid pressure is well behaved at the end points $\xi = \pm 1$, at which the free boundary meets the wetted body surface.

The solution to the Dirichlet problem (3), (5), (6), i. e.

$$\omega(\zeta) = \frac{1}{i\pi} \int_{-1}^{1} \frac{\Gamma(t)dt}{t-\zeta}, \qquad \Gamma(\pm 1) = 0, \tag{7}$$

and the solution to the Riemann-Hilbert problem (4), (5), (6), given by

$$\omega(\zeta) = \frac{1}{i\pi} (\zeta^2 - 1)^{1/2} \int_{-1}^{1} \frac{\beta(t)dt}{(1-t^2)^{1/2}(t-\zeta)}, \tag{8a}$$

with

$$\int_{-1}^{1} \frac{\beta(t)dt}{(1-t^2)^{1/2}} = 0, \tag{8b}$$

are equivalent to each other, as can be readily shown. Here, the function $(\zeta^2 - 1)^{1/2}$ is one-valued in the ζ -plane cut from $\zeta = -1$ to $\zeta = 1$. On the body surface, we deduce from (7), by applying the Plemelj formulas, that

$$\beta(\xi) = -\frac{1}{\pi} \oint_{-1}^{1} \frac{\Gamma(t)dt}{t-\xi} \equiv -H_{\xi}[\Gamma] \quad (|\xi| < 1), \tag{9}$$

where the integral with symbol C signifies its Cauchy principal value, and also defines the finite Hilbert transform of $\Gamma(t)$, as denoted by $H_\xi[\Gamma]$.

From this parametric description of the flow we derive the physical plane by quadrature

$$z(\zeta) = \int_{-1}^{\zeta} e^{-\omega(\zeta)} \frac{df}{d\zeta} \, d\zeta \quad . \tag{10}$$

With the solution (7) - (10) in hand, we see that the chord ℓ, wetted arc-length S, angle of attack α, as well as the drag D, lift L, etc. can all be expressed as integral functionals with argument functions $\Gamma(\xi)$ and $\beta(\xi)$, which are further related by (9).

III. THE VARIATIONAL CALCULATION

The general optimum problem considered here is the minimization of a physical quantity which may be expressed as a functional of the form

$$I_o[\Gamma, \beta; c_1, \ldots c_n] = \int_{-1}^{1} F_o(\Gamma(\xi), \beta(\xi), \xi; c_1 .. c_n) \, d\xi \tag{11}$$

under M isoperimetric constraints

$$I_\ell[\Gamma, \beta; c_1, \ldots c_n] = \int_{-1}^{1} F_\ell(\Gamma, \beta, \xi; c_1, \ldots c_n) \, d\xi = A_\ell \tag{12}$$

where A_ℓ's are constants, $\ell = 1, 2, \ldots M$.

The original problem is equivalent to the minimization of a new functional

$$I\ [\Gamma, \beta\ ; c_1, \ \ldots\ c_n] \ = I_o - \ \sum_{\ell = 1}^{M} \lambda_\ell (I_\ell \ - A_\ell)\ , \qquad (13)$$

where λ_ℓ 's are undetermined Lagrange multipliers.

We next seek the necessary conditions of optimality. Let $\Gamma(\xi)$ denote the required optimal function which, together with its conjugate function $\beta(\xi)$ given by (9), minimizes $I[\Gamma, \beta]$. We further let $\delta\Gamma(\xi)$ denote an admissible variation of $\Gamma(\xi)$, which is Hölder continuous, satisfies the isoperimetric constraints (12) and the end conditions (6). The corresponding variation in $\beta(\xi)$ is found from (9) as

$$\delta\beta(\xi) \ = \ - H_\xi[\delta\Gamma] \qquad (\ |\xi| < 1)\ . \qquad (14)$$

The variation of the functional I due to the variations $\delta\Gamma$ and $\delta\beta$ is

$$\Delta I \ = \ I[\ \Gamma + \ \delta\Gamma\ ,\ \ \beta + \delta\beta\ ;\ c_n + \delta c_n] \ - \ I[\Gamma\ ,\ \beta\ ;\ c_n] \qquad (15)$$

where δc_n's are variations of parameters c_n. For sufficiently small $|\delta\Gamma|$, $|\delta\beta|$ and $|\delta c_n|$, expansion of the above integrand in Taylors'series yields

$$\Delta I \ = \ \delta I \ + \frac{1}{2\ !} \ \ \delta^2 I \ + \frac{1}{3\ !} \ \ \delta^3 I \ + \ldots\ , \qquad (16)$$

where the first variation δI and the second variation $\delta^2 I$ are

$$\delta I \ = \ \int_{-1}^{1} [F_\Gamma \ \ \delta\Gamma \ + F_\beta \ \delta\beta\ ]\, d\xi \ + \delta c_n \ \int_{-1}^{1} (\ \partial F / \ \partial c_n)\, d\xi\ , \qquad (17)$$

$$\delta^2 I = \int_{-1}^{1} \left[F_{\Gamma\Gamma} \ (\delta\Gamma)^2 + 2F_{\Gamma\beta}\,\delta\Gamma\,\delta\beta \ + F_{\beta\beta}\,(\delta\beta)^2 \right] d\xi \ + \ \delta c_n \, \delta c_m$$

$$\int_{-1}^{1} \frac{\partial^2 F}{\partial c_n \ \partial c_m} \, d\xi \qquad (18)$$

+ cross product term between δc_n and $\delta\Gamma$ or $\delta\beta$,

in which the subindices denote partial differentiation. The variations δI, $\delta^2 I \ldots$ depend on $\delta\Gamma$ as well as on Γ. For I to be minimum, we must have

$$\delta I \left[\ \Gamma \, , \, \delta\Gamma \ \right] \ = \ 0 \ , \qquad (19)$$

$$\delta^2 I \left[\ \Gamma \, , \, \delta\Gamma \ \right] \ \geq \ 0 \ , \qquad (20)$$

in which β and $\delta\beta$ are understood to be related to Γ and $\delta\Gamma$ by (9) and (14). Relation (19) assures I to be extremal, and with the inequality (20), I is therefore a minimum.

Now, substituting (14) in (17) reduces it to

$$\delta I \ = \ \int_{-1}^{1} \left\{ F_{\Gamma} \ + H_{\xi} \left[F_{\beta} \ \right] \right\} \delta\Gamma \, (\, \xi \,) d\xi \ + \ \delta c_n \int_{1}^{1} \partial F / \partial c_n d\xi \qquad (17)'$$

after inter-changing the order of integration, which is permissible under certain integrability conditions (see Tricomi 1957, § 4.3) which will be tacitly assumed to hold. Since the variations $\delta\Gamma \, (\, \xi \,)$

and δc_n are independent and arbitrary, the last integral in (17)' and the factor in the parenthesis of the first integrand must all vanish, hence

$$\int_{-1}^{1} \partial F\left(\Gamma(\xi),\ \beta(\xi),\ \xi; c_1 \ldots c_n\right) / \partial c_j d\xi = 0 \quad (j = 1, \ldots n), \tag{21}$$

$$F_\Gamma\left(\Gamma(\xi),\ \beta(\xi);\ \xi\right) = -H_\xi\left[F_\beta\right] = -\frac{1}{\pi}\int_{-1}^{1} \frac{F_\beta\left(\Gamma(t),\ \beta(t),\ t\right)}{t-\xi} dt . \tag{22}$$

The nonlinear integral equation (22) combines with (9) to give a pair of singular integral equations for the extremal solutions. This is one necessary condition for $I[\Gamma]$ to be extremal ; it is analogous to the Euler differential equation in the classical theory. Presumably, calculation of the extremal solution $\Gamma(\xi)$ from (22) and (9) can be carried out with $\lambda_1, \ldots \lambda_M$ regarded as parameters, which are determined in turn by applying the M constraint equations (12). While we recognize the lack of a general technique for solving the system of nonlinear integral equations (9) and (22), we also notice the difficulty of satisfying the end conditions (6), as has been experienced in many different problems investigated recently. The last difficulty may be attributed to the known behavior of a Cauchy integral near its end points which severely limits the type of analytic properties that can be possessed by an admissible function $\Gamma(\xi)$ and its conjugate function $\beta(\xi)$.

Supposing that these equations can be solved for $\Gamma(\xi; c_1, c_2, \ldots c_n)$, we proceed to ascertain the condition under which this extremal solution actually provides a minimum of $I[\Gamma]$. From the second variation $\delta^2 I$ we find it is necessary to have

$$\int_{-1}^{1} \left(\partial^2 F / \partial c_j^2\right) d\xi \geq 0 , \tag{23}$$

$$\int_{-1}^{1} \left[F_{\Gamma\Gamma} \ (\delta\Gamma)^2 + 2F_{\Gamma\beta}\ \delta\Gamma\,\delta\beta + F_{\beta\beta}(\delta\beta)^2 \right] d\xi \geq 0 . \qquad (24a)$$

By substituting (14) in (24a), interchanging the order of integration according to the Poincaré-Bertrand formula (Muskhelishvili, 1953) wherever applicable, it can be shown that (24a) can also be written as

$$\int_{-1}^{1} g(\xi)\,(\delta\Gamma)^2 \ d\xi \quad + \frac{1}{\pi} \int_{-1}^{1} \int_{-1}^{1} \frac{h(t) - h(\xi)}{t - \xi}\ \delta\Gamma(t)\ \delta\Gamma(\xi)dt \ d\xi \geq 0 \qquad (24b)$$

where

$$g(\xi) = F_{\Gamma\Gamma} + F_{\beta\beta} , \quad h(\xi) = F_{\Gamma\beta} + H_{\xi}\left[F_{\Gamma\beta}\right] .$$

If we suppose that $F_{\Gamma\Gamma}$, $F_{\Gamma\beta}$, $F_{\beta\beta}$ are Hölder continuous, and consider a special choice of $\delta\Gamma$ which vanishes for $|\xi - \xi_o| > \epsilon$, bounded ($|\delta\Gamma| \leq B$) and is of one sign for $|\xi - \xi_o| < \epsilon$, where ξ_o is any interior point of $(-1, 1)$, then it can be shown that the first term on the left side of (24b) predominates, hence a necessary condition for (24 b) to hold true is the inequality $g(\xi) \geq 0$, or

$$F_{\Gamma\Gamma} + F_{\beta\beta} \geq 0 \qquad (|\xi| < 1) . \qquad (24c)$$

This condition is analogous to the Legendre condition in the classical theory.

The preceding illustrates the method of solution of the extremum problem by singular integral equations. We should reiterate that the integral equations are nonlinear unless F is quadratic in Γ

and β . No general methods have been developed for the exact solution of nonlinear singular integral equations. Further, it may not always be possible to satisfy the condition $\Gamma(\pm 1) = 0$, which are required on physical grounds. With these difficulties in mind, we proceed to discuss some approximate methods of solution.

IV. LINEARIZED SINGULAR INTEGRAL EQUATION

The least difficult case of the extremal problems in this general class is when the fundamental function $F[\Gamma, \beta]$ is quadratic in Γ and β , that is

$$F(\Gamma, \beta, \xi; c_j) = a\Gamma^2 + 2b\Gamma\beta + c\beta^2 + 2p\Gamma + 2q\beta , \quad (25)$$

in which the coefficients $a, b, \ldots q$ are known functions of ξ and may depend on the parameters $c_1, \ldots c_n$. It should be stressed that the above quadratic form of F can generally be used as a first approximation of an originally nonlinear problem in which F is transcendental or contains higher order terms than the quadratic. With this approximation the integral equation (22) is then linear in Γ and β , and reads

$$a\Gamma + b\beta + p = -H_\xi [b\Gamma + c\beta + q] \quad (|\xi| < 1), \quad (26)$$

which combines with (9) to provide a set ot two linear integral equations, both of the Cauchy type. The necessary condition (24c), obtained from the consideration of the second variation, now becomes

$$a(\xi) + c(\xi) \geq 0 \qquad (|\xi| < 1) . \quad (27)$$

For the present linear problem (regarding the integral equations) two powerful analytical methods become immediately useful. First, the coupled linear integral equations (9) and (26) can always be reduced to a single Fredholm integral equation of the second kind. When the coefficients $a(\xi)$, $b(\xi)$ and $c(\xi)$ of the quadratic terms satisfy a certain relationship, the method of singular integral equations can be effected to yield an analytical solution in a closed form.

(i) Fredholm integral equation

By substituting (9) in (26), we readily obtain

$$a(\xi)\,\Gamma(\xi) - b(\xi)H_\xi[\Gamma] + H_\xi[b\Gamma] - H_\xi[c(t)H_t[\Gamma]] = \\ = -H_\xi[q] - p(\xi) .$$

Upon using the Poincaré-Bertrand formula (with appropriate assumptions) for the last term on the left side of the above equation, there results

$$\{a(\xi) + c(\xi)\}\,\Gamma(\xi) + \int_{-1}^{1} K(t, \xi)\,\Gamma(t)\,dt = -H_\xi[q] - p(\xi) , \tag{28a}$$

where

$$K(t, \xi) = \frac{1}{\pi}\,\frac{b(t) - b(\xi)}{t - \xi} + \frac{1}{\pi^2}\,\oint_{-1}^{1} \frac{c(s)\,ds}{(s-t)(s-\xi)} . \tag{28b}$$

This is a Fredholm integral equation of the second kind, with a regular symmetric kernel, for which a well-developed theory is available.

(ii) Singular integral equation method

When the coefficients $a, b, c,$ satisfy the following relationship

$$a(\xi) + c(\xi) > 0 , \quad b(\xi) = b_o \pm (ac)^{1/2}, \quad b_o = \text{const} , \tag{29}$$

the system of equations (26) and (9) can be reduced in succession to a single integral equation, each time for a single variable, and these equations are of the Carleman type, which can be solved by known methods (see Muskhelishvili 1953), yielding the final solution in a closed form.

In the first step we multiply (9) by b_o, and subtracting it

from (26), giving

$$a^{1/2} \quad \Phi_{\pm}(\xi) = H_{\xi}\left[\pm c^{1/2}\Phi_{\pm}\right] + \Psi(\xi) \qquad (30a)$$

$$(\ |\xi| < 1)\ ,$$

where

$$\Phi_{\pm}(\xi) = a^{1/2}\ \Gamma \pm c^{1/2}\beta \quad , \quad \Psi(\xi) = -H_{\xi}[q] - p(\xi)\ . \qquad (30b)$$

After this Carleman equation for $\Phi_{\pm}$ is solved, a second Carleman equation results immediately upon elimination of β between the expression for $\Phi_{\pm}$ and (9). The details of this analysis are given by Wu and Whitney (1971). These analytical solutions are of great interest, since in their construction there are definite, but generally very limited degrees of freedom for choosing the strength of the singularity, or the order of zero, of the solution $\Gamma(\xi)$ and $\beta(\xi)$ at the end points $\xi = \pm 1$. It is in this manner that the analytical behavior of the solution $\Gamma(\xi)$ and $\beta(\xi)$ can be explicitly and thoroughly examined. This procedure will be demonstrated later by examples.

V. THE RAYLEIGH-RITZ METHOD

The central idea of this method, as in classical theory, consists in expansion of $\Gamma(\xi)$ and $\beta(\xi)$ in a finite Fourier series

$$\Gamma_m(\xi) = \sum_{k=1}^{m} \gamma_k \sin k\theta\ , \quad (\ \xi = \cos\theta\ ,\ 0 \leqslant \theta \leqslant \pi\ ) \qquad (31a)$$

$$\beta_m(\xi) = \sum_{k=1}^{m} \gamma_k \cos k\theta\ . \qquad (31b)$$

This expansion is noted to satisfy (9) automatically. The functional

$I[\ \Gamma\ ,\ \beta\ ]$ is now an ordinary function of the Fourier coefficients γ_k ,

$$I\ [\Gamma\ ,\ \beta\ ;\ c_1,\ \ldots\ c_n] \ =\ \int_o^{\pi} F(\Gamma_m,\ \beta_m,\ \cos\theta\ ;\ c_1\ \ldots\ c_n)\sin\theta\ d\theta$$

$$= I(\gamma_1,\ \ldots\ \gamma_m;\ c_1,\ \ldots\ c_n)\ . \qquad (32)$$

For I to be extremum, we require that

$$\partial I/\ \partial\gamma_k\ =\ 0 \qquad (k\ =\ 1,\ \ldots\ m)\ , \qquad (33)$$

and

$$\partial I\ /\ \partial c_j\ =\ 0 \qquad (j\ =\ 1,\ \ldots\ n)\ . \qquad (34)$$

These $(m + n)$ equations together with M constraint equations (12) determine the m coefficients γ_1 , ... γ_m, n parameters c_1, ... c_n, and M multipliers λ_1 , ... $_M$. It should be pointed out, however, that the coefficients γ_k's and parameters c_j's generally appear in the expression for $I(\gamma_k, c_j)$ in a nonlinear or transcendental form, making their determination, by algebraic, numerical means or otherwise, extremely difficult even when their number is moderately small, such as three or more.

The preceding general theory will be further discussed and clarified with several specific examples in the presentation of this study.

ACKNOWLEDGMENT

This work was sponsored in an early stage by the Naval Ship System Command General Hydrodynamics Research Program, administered by the Naval Ship Research and Development Center under Contract Nonr-220(51), and partially by the Office of Naval Research, under Contract N00014-67-A-0094-0012.

REFERENCES

[1] MUSKHELISHVILI, N. I., 1953, "Singular Integral Equations", Groningen, Holland, Noordhoff.

[2] TRICOMI, F. G., 1957, "Integral Equation", New York, Interscience Publ.

[3] WU, Th. Y. & WHITNEY, A. K., 1971, "Theory of optimum Shapes in Free-Surface Flows", Rept. No E 132 F. 1, Calif. Inst. Tech. Pasadena, California.

* * *

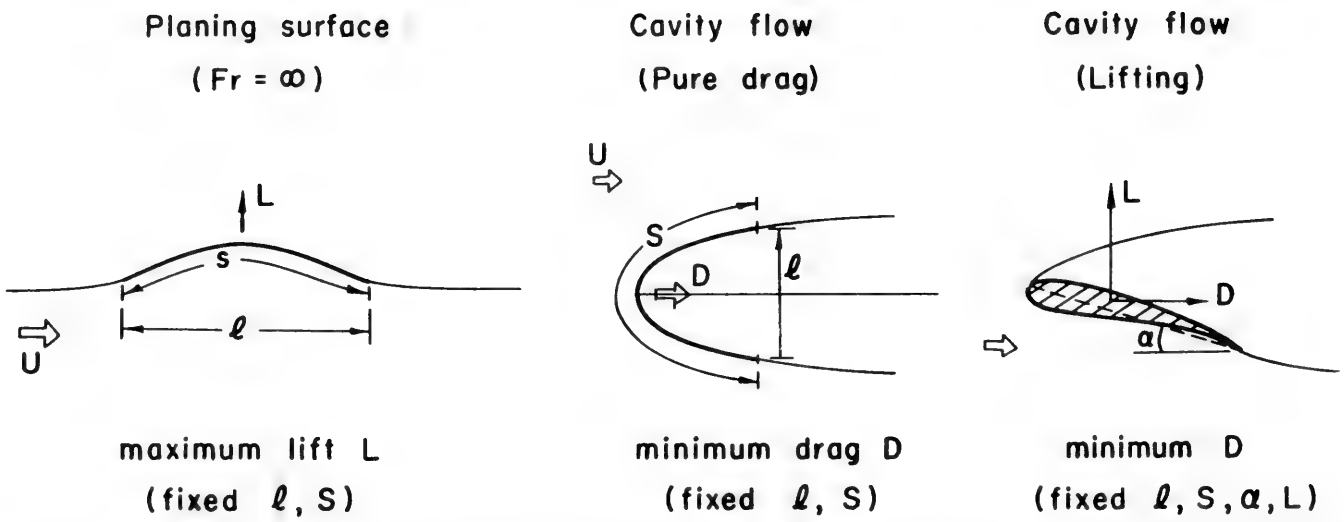

Figure 1 – Examples of Physical Problems (2-Dimensional)

DISCUSSION

Ernest O. Tuck
University of Adelaide
Adelaide, Australia

At a meeting like this it might seem strange to ask about existence and uniqueness solutions to mathematical problems but I think it is possibly relevant here. I wondered if the authors know in their examples whether they can expect a solution, on either physical or mathematical grounds ?

REPLY TO DISCUSSION

Arthur K. Whitney
Palo Alto Research Laboratory, Lockheed Aircraft Corp.
Palo Alto, California, U.S.A.

That is one of the unresolved questions in this minimisation technique, we simply do not know the answer at this point. If it turns out that solutions to the exact nonlinear equations do not exist, this still does not invalidate solutions by the approximate methods. It may mean, however, that as we take more and more terms in the approximate solutions, these solutions do not converge. An existence proof, especially a constructive existence proof, would be very much desirable.

DISCUSSION

William B. Morgan
Naval Ship Research and Development Center
Bethesda, Maryland, U.S.A.

In connection with your third examples, how do you plan to determine the point of separation on the suction side of the foil when the leading edge is blunt ?

REPLY TO DISCUSSION

Arthur K. Whitney
Palo Alto Research Laboratory, Lockheed Aircraft Corp.
Palo Alto, California, U.S.A.

These problems are formulated as inverse problems, so you know the point of separation in all cases. That is, if $\Gamma(\xi)$ is given as the dependent variable, the hodograph variable is then determined and the physical plane, including the shape of the wetted foil surface, is given by a quadrature.

REPLY TO DISCUSSION

Theodore Y. Wu
California Institute of Technology
Pasadena, California, U.S.A.

May I add a few comments to Dr. Morgan's question ? For the lifting problem, I think we can also impose two conditions as isoperimetric constraints for a fixed chord and a fixed arc-length. These constraints may provide a good method to overcome the difficulty due

to unknown position of the separation points. Suppose we start with $K = 0$ (K being defined as the ratio of the wetted arc-length to the chord length minus 1, or $K = S/\ell - 1$), then we know that at $K = 0$, the two end points of the cavity boundary would be of the type of fixed detachment, at which point the curvature of the free streamline is singular. As K is increased by giving more arc-length to the body profile, we hope the profile can be expanded in such a way as to arrive at the required optimum shape. When K reaches a certain positive value, one of the end points of the optimum profile would firts reach the state of smooth detachment (in the sense that the local curvature of the free streamline will be equal to that of the body at the detachment). Near this critical point ($K = K_c$ say) and from then on ($K > K_c$) I think other physical quantities such as the viscous effects and the physical condition,that the pressure on the body remains nowhere less than the cavity pressure, must be thoroughly examined from the final results predicted by the theory. This proposed procedure is to be carried out in the future study. Would this answer Dr. Morgan's question ?

DISCUSSION

Vsevolod V. Rogdestvensky
Shipbuilding Institute
Leningrad, U.S.S.R.

I think you have done very interesting work, but there are many questions in this problem. In order to decide the problem in general, it is necessary to make good tests. I should like to ask, have you any comparison with experience ? Have you any experimental data ?

REPLY TO DISCUSSION

Arthur K. Whitney
Palo Alto Research Laboratory, Lockheed Aircraft Corp.
Palo Alto, California, U.S.A.

No, we have not tested any of these optimum shapes experimentally.

* * *

HYDRODYNAMIC CAVITATION AND SOME CONSIDERATIONS OF THE INFLUENCE OF FREE GAS CONTENT

Frank B. Peterson
Naval Ship Research and Development Center
Bethesda, Maryland, U.S.A.

ABSTRACT

Hydrodynamic cavitation inception on an axisymmetric body with a 5-cm diameter was measured in a standard water tunnel. Particulate matter and free-gas bubble size distributions were directly measured immediately upstream of the bodies with a high-speed holographic technique and related to calculated bubble trajectories. Discrimination between particulate matter and gas bubbles was possible for diameters larger than 0.0025 cm. Inception was measured acoustically and high-speed movies at 10,000 frames per second were taken to verify the type of cavitation present. The influence of headform surface chemistry was studied using plastic, copper, and gold-plated bodies with and without various types of colloidal silica coatings. Physical surface characteristics were checked with scanning electron microscopy.

All cavities observed in the water tunnel tests were approximately hemispherical in shape and translated along the headform surface. When the results were compared with previously reported tests in a high-speed towing basin, it was concluded that the measured free stream gas bubbles in these standard test facilities did not significantly contribute to the nucleation of cavitation when acoustic detection was used. Other recent research is summarized that describes the de novo production of stable hydrophobic particulate in water through the mechanism of aera-

tion. These particulate are felt to have a major role in the cavity nucleation process.

INTRODUCTION

Over the years there has been continued discussion about the role of the air content in water on the cavitation inception process. Typical recent surveys on the subject have been by Eisenberg [1]*, Holl [2] , Knapp [3] , Plesset [4] , and van der Walle [5] . Much of the discussion has been concerned with the determination of the nature of the "nuclei" that are attributed to the onset of a vapor cavity. At the present time, no conclusive results have been reported that fully explain the relative importance of the free stream gas bubbles, the unwetted (hydrophobic) solid particles and the gas trapped in crevices on the test body. Presumably, each of these postulated nuclei sources will contribute to the formation of cavitation, with various degrees of relative importance. The actual importance of each during any given test will be dependent on the fluid and body characteristics and the pressure and velocity fields.

What is presently needed is a series of definitive tests that would elucidate the role of the various types of nuclei as a function of the various controlling parameters. Before this series of tests can be performed, an adequate physical understanding must be developed to recognize and plan a definitive experiment. It is the aim of this paper to assist in extending the presently available knowledge on the cavity nucleation process in hydrodynamic cavitation. Since the available literature on cavity nucleation has been surveyed by many writers, the contribution of the present paper will be concerned principally with the recent work performed at the Naval Ship Research and Development Center (NSRDC). The results of other investigators will be considered and compared to the extent that their work has a bearing on the interpretation of the observed phenomena.

The recent cavitation research at NSRDC has been concerned with developing a better understanding of the role of the free and dissolved gas content on hydrodynamic cavitation. The emphasis of the work reported here will be concerned with the importance of gas bubbles in the free stream for the type of cavitation occurring on one headform shape at one velocity in a water tunnel. By restricting the test conditions in this manner, changes in parameters such as the

---

* References are listed on page 1156.

free stream turbulence, body boundary layer characteristics, and body pressure distribution are minimized. Specific studies were performed to evaluate the importance of headform surface nucleation sources. Surface treatment procedures were designed to reduce the surface nucleation capability of the body. In this way the role of free stream nuclei could be more clearly defined. The actual gas bubbles and solid particles just ahead of the headform were recorded by high speed holography. The path and stability of the bubbles as they passed over the body were determined analytically. These calculations were necessary to determine through what cross-sectional area upstream of the body all bubbles must pass if they are to contribute to the visually observed cavities on the body. The inception condition was measured acoustically and high speed movies were taken to verify the type of cavitation present. The headforms tested consisted of several bodies each of plastic (Delrin)* and metal (copper and gold plated copper) materials. Cavitation tests on several bodies of the same material gives a check on the surface machining accuracy and the material variety assists in evaluating the role of surface originating nuclei. The results of these water tunnel tests were compared with previous tests of the same bodies in the high speed towing basin. The significant aspects of the towing basin are that essentially no free gas bubbles are present and the turbulence levels are very low. From all of these studies the importance of free gas bubbles on acoustically measured cavitation inception can be evaluated for at least the headforms tested.

In the interest of introducing into the cavitation literature recent research results from other disciplines pertinent to cavity nucleation, a review of this work will also be given. Specifically, these results demonstrate a mechanism by which stable hydrophobic particles can be produced in water by the process of aeration.

EXPERIMENTAL FACILITIES, INSTRUMENTATION, AND PROCEDURE

All of the experimental studies were carried out in the standard test facilities at NSRDC [6]. The cavitation inception studies to be reported here were performed in the 12-inch water tunnel using normal tap water filtered to remove particles larger than 25 μm. Deaeration was accomplished by passing the water through a standard design pac-

* Delrin, Acetal Resin, manufactured by E. I. Dupont de Nemours and Co., Wilmington, Delaware.

ked column desorber. The test body used throughout the work was from the series tested by Rouse and McNown [7]. This is the same series from which the headform used for the ITTC comparative tests was selected [8]. The bodies tested had a minimum pressure coefficient, $C_{P_{min}}$, equal to 0.82, a diameter of 5 cm, and were installed in the water tunnel as shown in Figure 1. An axisymmetric headform was selected as the test body for several reasons. First, inception measurements are relatively straight-forward, because the body is stationary and it is easy to manufacture with a high degree of accuracy. Secondly, vortex cavitation is not present.

Cavitation inception was detected acoustically for all of the results presented here. The measurements were made by locating a hydrophone inside the headform on its axis. Details of the equipment and operational characteristics can be found in references [9] and [10]. The noise level of the facility was determined for a tunnel pressure slightly above that corresponding to a cavitation inception number, σ_i, equal to $-C_{P_{min}}$. The associated electronics were then adjusted so that all cavitation noise exceeding the tunnel background level would be indicated. The cavitation inception number σ_i, is defined as

$$\sigma_i = \frac{P_\infty - P_V}{\frac{1}{2}\rho V_\infty^2}$$

where P_∞ and V_∞, are the upstream pressure and velocity respectively, ρ is the density, and P_V the water vapor pressure. The criteria for the actual inception was selected to be one acoustic event per second. The technique of acoustic detection of inception will be considered in more detail later in this paper.

The test procedure used in the water tunnel studies was to install the headform and then deaerate the water to the desired total dissolved gas content. This dissolved gas content was measured with a standard van Slyke apparatus. All tests were run at a free stream velocity of 9.1 meters per second. The test section pressure was adjusted in stages to produce a range of cavitation conditions as measured acoustically. When the cavitation inception pressure was reached, a series of holograms were made of the bubbles and solid particles in the water just upstream of the body. High speed photography at 10,000 frames per second and 20 microsecond exposure time were also taken for selected runs at the inception conditions.

BUBBLE TRAJECTORY ANALYSIS

Implicit in all discussions on the role of free stream gas bubbles in the cavity nucleation process is that they will be transported into a sufficiently low pressure region to be available to nucleate the cavity. The mere existence of gas bubbles in water is not in itself sufficient to conclude a knowledge of their importance. For this reason the bubble trajectory and its radial dynamics must be evaluated. When this information is combined with the bubble size and population information, then a better understanding of the importance of these bubbles can be developed.

The trajectory of a bubble in a flow field with large pressure gradients has been considered by Johnson and Hsieh [11] , Hsieh [12] , and Schrage and Perkins [13] . The governing equations derived by these authors can be reduced to essentially the same form and contain the following assumptions:

1. The flow field is axisymmetric.
2. The bubble remains a sphere throughout its trajectory.
3. The fluid is assumed to be inviscid for the purpose of the flow velocities and pressures.
4. The bubble is assumed to be sufficiently small so that the flow field is not affected by the presence of the bubble.
5. The fluid is not taken to be inviscid with respect to the bubble, i.e., the bubble experiences a drag dependent on the relative velocity between bubble and fluid (see ref. 14).
6. Diffusion of gas and heat transfer through the bubble wall are negligible.

The equation for the dynamics of bubble radius, r_b , can be shown to be

$$r_b \frac{d^2 r_b}{dt^2} + \frac{3}{2}\left(\frac{dr_b}{dt}\right)^2 = \frac{1}{\rho}\left[P_V + (P_r - P_V + \frac{2\delta}{r_{bo}})\frac{r_{bo}^3}{r_b^3} - \frac{2\delta}{r_b} - P(x,y)\right] \quad (1)$$

where

t is time,

ρ is the fluid density,

P_V is the vapor pressure of the fluid,

o a subscript denoting a value at the initial bubble position,

δ is the surface tension of the fluid,

$P(x, y)$ is the external pressure of the fluid at (x, y),

(x, y) refers to the location of the bubble in Cartesian coordinates.

The vector equation of motion for the bubble moving in an axisymmetric flow field, can be written as

$$\rho \frac{2}{3} \pi r_b^3 \frac{d\vec{u}}{dt} = \frac{1}{2} \rho \quad C_D \quad \pi r_b^2 (\vec{v}-\vec{u}) \left|\vec{v}-\vec{u}\right| \qquad (2)$$

$$- 2\pi r_b^3 \nabla P_f \; - \frac{4}{3} \pi r_b^3 \nabla P_g \; + \; 2\pi\rho \, r_b^2 \frac{dr_b}{dt} (\vec{v}-\vec{u})$$

where $\vec{u}$ is the vector velocity of the bubble

$$\vec{u} = \frac{dx}{dt} \; \hat{i} + \frac{dy}{dt} \; \hat{j} \; ,$$

$\hat{i}, \hat{j}$ are unit vectors in the x, y directions, respectively,

$\vec{v}$ is the fluid velocity vector $= v_x \hat{i} + v_y \hat{j}$,

C_D is the drag coefficient, (see reference [14]),

P_f is the pressure due to flow, and

P_g is the pressure due to gravity.

Using these equations, Schrage and Perkins [13] compared their analytical prediction of the bubble path with experiments in both rotating water and glycerin and obtained excellent agreement.

A numerical study was carried out at NSRDC where the potential flow field around the headform was combined with equations 1 and 2 to determine the trajectory and radial dynamics of a free stream gas bubble. The description of the pressure and velocity field around the body was determined through the use of a computer program for potential flow around an axisymmetric body [15] .

The most important aspect of these calculations was the deter-

mination of the region upstream of the body in which the bubbles would have to be located in order to produce cavitation. The results of the numerical calculations are shown in Figures 2 - 4 as the local pressure coefficient, C_p , experienced by the bubbles along the bubble trajectory. Figures 2 and 3 show the situation for a typical cavitation inception condition experienced in the 12 inch water tunnel with a metallic body. The bubble screening effect is easily seen. The 25 μm diameter bubble does not experience as low a local pressure as the 50 μm diameter bubble when they both start at the same point upstream. Correspondingly, the 25 μm bubble does not pass as close to the body as the 50 μm bubble and does not strike the body as soon.

Figures 5 and 6 show the variation in bubble diameter for some of the bubble sizes considered. None of the bubbles experienced extremely rapid growth rates. For the range of bubble trajectories considered, all the bubble wall velocities were less than 0.1 meter per second. Once a bubble touched the body, the numerical method is of course not valid. However, it appears reasonable to assume that when the bubble touches the body, its translational velocity may decrease sufficiently to permit further volume increase. On this basis it was concluded from Figures 2, 3, 5, and 6, that all bubbles would have to be initially within the cross-sectional area of radius 3.75 mm upstream from the 5 cm diameter headform for them to produce cavitation. For the purposes of further discussion, the bubbles outside this area are assumed not to contribute to the cavitation on the body.

The question still to be resolved is whether the bubbles that strike the body will in fact actually produce a vaporous cavity. Before discussing this aspect of the problem, the numerical calculations of the bubble trajectories over the same body with the same inception coefficient, σ_i , but at a pressure approximately 3.4 times higher, should be considered. Figures 4 and 7 represent a typical inception condition when the same headform was tested in the high speed towing basin [16] . The experimental results from the basin were essentially the same as those obtained in the water tunnel and therefore the same σ_i was used in the calculations. The interesting result is that for the higher speeds in the basin, the bubble trajectories are slightly further from the headform and therefore the bubble diameters are correspondingly smaller. If the bubble strikes the headform, it strikes further downstream. From this result it can be concluded that if given identical bubble size distributions, then the rate at which bubbles produced cavities should be directly proportional to the velocity of the body in the basin or conversely, the up-

stream velocity in the water tunnel. This conclusion assumes that the viscous effects, such as boundary layer separation, do not influence inception. Further discussion on boundary layer separation will be deferred until later. Following the same reasoning, if the body size had been changed, then the number of freestream bubbles cavitating per unit time would vary directly with the square of the ratio of the body diameters.

The key to all of the preceding discussion on bubble screening is whether in fact the free stream gas bubbles are responsible for cavitation. The remainder of this paper will be concerned with experiments specifically planned to extend our understanding of the role of gas content in water.

VARIATION OF FREE GAS CONTENT AND BODY SURFACE QUALITY

A. Criteria for Cavitation inception

The commonly accepted criteria for the onset of vaporous cavitation is when a cavity grows "explosively", with the local pressure less than or equal to the vapor pressure (e.g. [17]) and is generally considered the only true cavitation. On the other hand, gaseous cavitation can occur at pressures either greater or lower than vapor pressure, with gas diffusion into the bubble possibly important and the growth rate of the bubble considered something less than "explosive". However, these definitions are not specific enough for the purposes of the discussion here to delineate when in fact a cavity is growing "explosively". This problem was apparent to Hsieh [12] when he calculated bubble dynamics in the bubble trajectory. None of the bubbles he considered had what could be considered "explosive" growth, but in fact had a bounded maximum size. Therefore Hsieh arbitrarily defined a bubble to be cavitating when its diameter reached a certain minimum "visible"size.

On the basis of the trajectory and bubble diameter calculations in the previous section for the NSRDC headform, it is felt that only bubbles actually striking the body could nucleate a vaporous cavity. This assumption is based on the observation through high speed photography that the cavities appeared hemispherical in shape from the time of their first observation and translated along the body surface during both the growth and collapse. The "visible" size criteria is not applicable here since once a bubble strikes a body, the calculations are no longer valid and in fact the visually observed cavity growth could correspond to gaseous cavitation. Since all of the cavities observed in these studies were observed to be translating along

the surface, it is particularly important to have some means of discriminating between vaporous and gaseous cavities. If the cavity is truly vaporous, and grows "explosively", then the collapse should also be far from equilibrium with the local pressure field and should produce noise. This definition has been used by innumerable investigators. For headform studies, Saint Anthony Falls Hydraulic Laboratory (SAFHL) [18] , [19] and NSRDC have regularly been using the acoustic radiation as the criteria for inception.

It can be shown that the velocity of cavity collapse for nominally hemispherical cavities scales approximately as the square root of the pressure difference across the cavity wall [20] , [21] . Thus, if one assumes that the shape of the cavity during collapse is essentially the same for slight changes in this pressure difference, then the collapse velocities also would only experience slight changes. On this basis it will be assumed in this paper that the noise produced by the collapsing cavities will not be significantly affected by small changes in the pressure of the water tunnel.

When the acoustic impedence between the water and the headform material is changed, then the amplitude of the noise detected by the hydrophone will be affected. As one would expect, the peak noise amplitude will vary over a finite range. This has been experimentally shown by Brockett [10] for a headform made of Delrin which is a good impedence match to water. When the headform material is a metal, such as copper, then there is a poor acoustic impedence match and one would expect to detect a lower peak noise amplitude from the collapsing cavity. This material influence cannot be entirely cancelled out by adjusting the detection threshold of the electronics on the basis of background noise. Therefore, it is expected that the DELRIN headforms will indicate cavitation at a somewhat higher water tunnel pressure than for a metal headform. This aspect is not of significant concern here because direct comparison of the cavitation inception number, σ_i, for the two types of materials is not intended. The most important concern is to determine how variations in the free gas bubble distributions affect the inception on a headform of the same material.

B. Free Stream Bubble Size and Distribution Measurements

The microscopic gas bubbles immediately upstream of the headform at inception conditions have been measured with a high speed holographic technique. This technique was selected because it appeared to be unique in its ability to (1) make direct measurements with no calibration required, (2) discriminate between bubbles

and solid particles, and (3) record both bubble size and spatial distribution in a large liquid volume instantaneously. A mathematical analysis of the complete holographic process for bubbles and solid particles is given in Appendix A. The schematic representation of the holographic equipment at the water tunnel is shown in Figure 8. The resulting holograms obtained in these studies recorded the bubbles and solid particles contained within a liquid volume 5 cm in diameter and 15 cm long. A small magnified view of a hologram for 2-25 μm diameter wires and many bubbles and solid particles, is shown in Figure 9. As shown in Figure 10, typical exposure duration was 10 nanoseconds. The hologram is then used to produce the 3-dimensional image of the contents of the original volume. This volume was scanned with a traveling microscope and the size and location of the bubbles and solid particles recorded. Figures 11 and 12 show the appearance of a bubble and a solid particle as the microscope is moved away from the focussed position. For the optics used in these studies, it was determined both analytically and experimentally that 25 μm diameter was the smallest bubble size that could be reliably distinguished from a solid particle for the optical configuration used. Smaller bubbles could have been distinguished if different optics had been used but a sacrifice in the fluid volume recorded would have been necessary. The smallest size possible would have been approximately 10 μm diameter because of the nature of this type of holographic process. Conclusions to be made later in this paper will show that the additional effort to measure smaller sizes was not merited. Typical bubble and solid particle size distributions are shown in Figure 13.

A comparison can be made between the number of measured bubbles calculated to strike the body and the total dissolved gas content of the water. This is shown in Figure 14 along with the corresponding σ_i and the headform material. High speed photography has shown that for a dissolved gas content referred to test section pressure, α/α_{TS}, of 1.45 and $\sigma_i = 0.61$, approximately 1000 transient hemispherical cavities per second were visible on the headform. However, when $\alpha/\alpha_{TS} = 0.22$ and $\sigma_i = 0.48$ and there were only on the order of 10 visible hemispherical cavities per second on the headform. These observations are in general agreement with the calculated number of bubbles that would strike the body. The most significant result apparent in Figure 14 is that for changes in α/α_{TS} around the saturation condition, very large changes in free gas content will occur with very little change in σ_i . It appears that although σ_i is less than $|C_{Pmin}|$, the visible cavities do not produce a significant amount of noise when they collapse. The small difference noted between metallic and plastic bodies is attributed to the

large difference in acoustic impedence between the materials as previously discussed in Section A. Brockett [9] , [10] has also observed, during studies with the same shape headform, that not all visible cavities produce noise. It should again be noted that the estimated rate at which bubbles struck the headform did not include bubbles less than 25 μm in diameter. Therefore, the estimates are to be considered low. In any event, it certainly appears that there were a sufficient number of bubbles available to account for the number of visible cavities observed photographically. When the dissolved gas content of the water was reduced, some filtering of the water also occurred. However, it can be seen from the particle size distributions in Figure 13 that when the gas bubble content of the water was reduced by over a factor of 10, little change occurred in the number of solid particles present. At this point no conclusions can be made concerning the effect of the presence of the solid particles in the water on the nucleation process. If they have a density greater than that of water, then they may have a trajectory which tends to direct them away from the low pressure region of the body. If their density is approximately that of water, then one would expect that these solid particles would have trajectories corresponding to the streamlines. In any event, it is clear that a large number of solid particles were always present and for the sake of completeness their size distributions are presented here.

When the dissolved gas content, α/α_{TS} , was reduced below approximately 0.6, the number of gas bubbles were so few it became impractical to manually scan the image volume with a microscope. However, inception measurements were made and these are given in Table 1. The results indicate that the addition of new water into the tunnel may have had some effect, but the statistics are inadequate to verify this point. From the data one can also see that the typical decrease in cavitation inception number, σ_i , occurs as the dissolved gas content is reduced. Based on the previous discussion, however, it is not readily apparent what type of nuclei are most affected by this change and further discussion of this result must also be deferred.

C. Modifications to the Surface Characteristics of the Headforms

Nuclei originating from gas trapped in crevices on the body surface have been postulated as one source of cavitation nuclei. There is sufficient experimental data available to show that under certain circumstances this type of nucleus can be a significant factor in cavity formation on a body [1] , [2] , [22] . Therefore, the possibility exists that this nucleus source may have been a factor in the experiments reported here. Studies were carried out to evaluate this factor in two ways. First, headforms were plated with gold to minimize sur-

face irregularities and corrosion. Second, an attempt was made to increase the wettability of the solid in order to promote wetting of microscopic crevices by the water.

Electron probe microanalysis of the gold plated copper headforms was carried out. In the secondary electron mode of operation no copper x-rays were found that would have indicated a pore in the plating. Although resolution was limited to 1 μm, experience with gold plated materials of this type leads us to suspect that no pores of smaller size were present.

A scanning electron microscope was used to study the surface features of both the plastic (DELRIN) and metallic (gold plated) bodies. The most significant surface feature on the gold surface was the scratch shown in Figure 15. All surface scratches were less than 0.5 μm across and shallow. All protuberances appeared to be less than 0.2 μm. The plastic surface shown in Figure 16 can best be characterized as consisting of a series of shallow scratches, the width of which are larger than the typical surface roughness element. High speed photography gave no macroscopic indication that cavities repetitively occurred from any single location.

The gold plated bodies were coated with 1% colloidal silica and the plastic headform surface coated with a positive sol also of 1% concentration. This procedure is described in detail in Appendix B.

The results of studies on various surface treatments can be summarized as follows :

a. Gold plating a copper headform to give a smoother surface did not change σ_i ,

b. Colloidal silica coating on the gold plated surface did not change σ_i ,

c. Use of a positive sol on the plastic headform did not change σ_i ,

It is concluded from these studies that cavity nucleation was not significantly affected by roughness elements or from gas trapped in hydrophobic crevices on the solid surface of the headforms.

D. Boundary Layer Separation

Separation of the boundary layer could have a strong influence on the local velocity and pressure distribution of the headform. As is

well known, separation can occur in both laminar and turbulent boundary layers. In both cases, the separation will take place downstream of the minimum pressure point on the surface in the region of a positive pressure gradient. A relatively crude experiment was performed using a fluorescent oil film on the headform surface [9] , [16] . The result indicated that separation occurred at an X/D = 0.5, for velocities below 4.2 meters per second and a water temperature of 10°C. This is in agreement with tests performed at the California Institute of Technology with a hemispherical nose headform [23] . There, laminar boundary layer separation was also found to occur downstream from the minimum pressure point. From the high speed movies of the headform in the 12 inch water tunnel it was found that many bubbles were already visible at the minimum pressure point. This same result was apparent in the experiments run in the high speed basin and reported earlier [16] . On the basis of this discussion it is felt that boundary layer separation, if present, occurred sufficiently downstream to be of negligible influence on the inception observed in the experiments.

E. Comparison Between Water Tunnel and High Speed Towing Basin Cavitation Studies

In order to clarify the role of the free stream gas bubble in the cavitation nucleation process occurring in the water tunnel tests, it is worth while to compare results with those obtained in the high speed towing basin at NSRDC. As previously reported [16] , these same headforms were mounted on a strut and tested in the towing basin. The prodedure was to wait at the end of the basin for 45 minutes prior to each run. In this period of time the basin water became very smooth and high speed photography was possible through its surface. It was found that the incipient cavitation number varied between 0.6 and 0.8. The higher values were again typical of the plastic (DELRIN) headforms and this is attributed to the difference in acoustic impedence between the metal and plastic. In the towing basin the inception velocity was also determined with a hydrophone inside the body. Unlike the water tunnel tests, these acoustic results were found to agree with the high speed photography.

From the data on the buoyant rise of bubbles in water [14] , it can be estimated that a bubble 4 μm in diameter will rise 270 mm in the 45 minute period. Larger bubbles will rise correspondingly faster. By any one of a number of theories for gas bubbles in water (e.g., [24] , [25]) it can be shown that bubbles smaller than 4 μm in diameter should have dissolved completely in a matter of minutes. This is supported by the experimental evidence of Liebermann [26] .

Thus it appears that the probability of bubbles existing in the towing basin water immediately prior to a run, is extremely remote.

Now, if in fact free stream bubbles are necessary for cavitation inception, then a dichotomy exists between the basin and the water tunnel studies. The measured free stream bubbles in the water tunnel can account for the visually observed cavities but not the acoustic determination of cavitation inception. The towing basin acoustic determination of inception agreed with the basin high speed movies and the water tunnel acoustic inception determination. As already pointed out, the probability of free gas bubbles existing in the basin water is extremely remote although the dissolved gas content was approximately 100 percent saturated.

On the basis of these studies, it appears that the free stream bubbles contributed to the production of the visibly observed cavities on the headforms but were not necessary for the generation of those cavities that produced acoustic radiation during collapse. Just as numerable investigators have concluded before, the results of the studies reported here can also best be explained by the existence of a hydrophobic particle with gas trapped within a crevice ([27] - [29]). There has been a considerable amount of research performed by investigators in other research disciplines that has significantly increased the plausibility of this postulated nucleation mechanism. Within the cavitation literature available to this writer, it appears that these new related research results have not been discussed. Therefore, the next section will deal specifically with this related research.

STABLE HYDROPHOBIC PARTICLES IN THE WATER

The concept of cavity nucleation by a hydrophobic particle in water has long been the subject of considerable discussion. The basic hypothesis is that a small quantity of gas is trapped in a crevice of a particle and stabilized by the surface tension of the water because the particle itself is hydrophobic. This theory was first advanced by Harvey, et al [27, 28, 29] and has most recently been reviewed by Apfel [30] . A number of recent experiments have been carried out that indicate the hydrophobic particle may play an important role in the cavity nucleation process in water [30 - 33] . In keeping with the nature of this paper, a survey of the literature on this subject will not be attempted but rather only those references most pertinent to the discussion will be considered. One of the most detailed experiments was carried out by Greenspan and Tschiegg [32] with an acoustically excited cylindrical resonator. They found that the cavitation threshold for unfiltered

water increased significantly as the dissolved gas content was reduced. However, after filtering the water through an 0.2 μm filter, the threshold was then essentially independent of the air content for undersaturated water. For organic liquids, the threshold was high and was not affected by filtering. Hayward [31] used a "tension manometer" to produce a tension in the liquid of 0.15 bar. Various liquids were tested by measuring the number of bars prepressurization a sample would have to be subjected before it could withstand the 0.15 bar tension in the device. Nine organic fluids, including a water-in-oil emulsion, were tested and all were found to withstand the test tension with no prepressurization required. Of the liquids tested, only water was affected by the prepressurization and Hayward concluded that only water contained cavitation nuclei capable of stabilization. A further result was that distilled water (of unstated quality) and polluted river water both required approximately the same level of prepressurization. These experimental results are considered typical of the efforts directed toward understanding the role of the particulate in the cavity nucleation process.

In the case of hydrodynamic cavitation where the body is moving in a stationary fluid or conversely, a fluid is moving past a stationary body, an important consideration is how these hydrophobic particles are produced and why they remain suspended in the water. As has been pointed out by Plesset [4], if the solid particles have densities in the range of 2-3 gm/cm^3, then their radius must be on the order of 0.01 μm to remain suspended in quiescent water. On the other hand, unwetted particles of this size would require a tension on the order of approximately 100 bar to nucleate cavities.

Before this subject of the Harvey model of cavitation nuclei is pursued further, some recent oceanographic research pertinent to this subject should be considered. Sutcliffe, et al [34] have found that aeration of filtered sea water will produce a suspension of insoluble organic particles. Some of these particles eventually settled out after aeration but most always remained in suspension. A significant amount of this particulate was larger than the 0.43 μm pore size of the filter. It was found that large surface-active organic molecules adsorb at the air/water interface of the bubble to produce a monomolecular layer. This layer can be aggregated into insoluble organic particles by folding into polymolecular layers to form colloidal micellae or by collapsing into fibers. Coalescence of these colloidal particles then produce a semistable suspension of organic material. Riley [35] has confirmed the Sutcliffe, et al, work by also producing through aeration insoluble particulates from the dissolved organic matter in the sea. He also found that the aggregates will in-

crease in size by coalescence or further adsorption and eventually become indistinguishable from natural aggregates. The longest dimension of typical newly formed aggregates was on the order of 25 μm.

Wallace and Wilson [36] have shown the effectiveness of concentrating dissolved organic compounds as particulates through aeration. They found that for their test protein solution of 5 parts per billion, aeration gave almost 100 percent recovery of the compound in the form of particulate.

This is typical of the concentration of dissolved organic compounds in seawater. The sum of these compounds, however, can reach the part per million range.

Similar results have been found by other investigators not specifically studying the de novo particulate production in water. For example, Liebermann [26] found in the course of studies on the solubility of air bubbles in water that the contamination at the interfacial boundary between the air and water had no effect on the diffusion of air into the water. After the addition of many organic compounds and surfactants to the water, he stated that ... "no laboratory condition could be found in which the rate of bubble diffusion was significantly altered." Lieberman also showed that when a bubble in multiple distilled water collapsed on a chemically clean surface, a microscopic amount of residue remained. When the pressure was reduced to 1/4 bar, the residue quite frequently nucleated another bubble.

In another series of experiments on the diffusion of gas out of a bubble, Manley [37] found results similar to Liebermann. In this work, also, bubbles collapsing in distilled water left a small deposit of impurity.

From the above discussion, it is apparent that in the typical cavitation test facilities, there should be no difficulty in producing particulate capable of cavitation nucleation. These can remain suspended in quiescent water and can readily be produced whenever at least some degree of aeration of the water takes place.

CONCLUSIONS

The general objective of this work was to develop a better understanding of the role of the free and dissolved gas content in water on the nucleation of hydrodynamic cavitation. The means by which this was accomplished was to use only one type of body, a headform,

in the natural existing environment of standard test facilities with emphasis on the measurement of flow conditions and the control of headform surface condition. This simple body produced only discrete cavities translating along the surface. From these results and a comparison with the pertinent literature certain conclusions can be inferred.

The results substantiate what other investigators have found in that a very precise definition of inception is necessary. When noise is used as an inception criteria, then it was shown that free gas bubbles were not specifically needed for the nucleation of the noise producing transient cavities under discussion in this paper. Hydrophobic particles can function as an adequate source of nuclei.

The dissolved gas is important because it can affect, through the mechanism of diffusion, the amount of gas trapped in hydrophobic particles for a given pressure history of the water. Conversely for a given dissolved gas content, changes in the normal pressure history of the water will also affect the ability of these hydrophobic particles to nucleate cavities. For the experiments reported here, body surface nucleation of cavitation was not considered a significant influence. If a material such as teflon is used which is hydrophobic and known to be porous on a microscopic scale, then surface nuclei could in fact be the controlling source.

New stable nuclei can be generated in the typical test facility water whenever a gas/water interface is produced because of local adsorption at the interface of dissolved organic material. In a water tunnel this could occur during the filling process, by the introduction of locally supersaturated water or even during the deaeration process. In both water tunnels and towing basins this could occur during the actual tests where bubbles of one form or another are produced. In any event, the persistance of these hydrophobic particles can be expected unless very special water treatment procedures are followed.

If either 2- or 3- dimensional boundary layer separation occurs, σ_i may be affected but the type of cavity nucleus initially responsible may not be important if an attached cavity eventually forms.

For flow fields to cavitate when nuclei mobility across streamlines is required - such as a vortex - then the free gas content of the water can be expected to be of prime importance. But here again, care must be taken to specifically define whether cavitation is based on visual or acoustic observations.

If scaling of cavitation inception from a model to a prototype is required, then the detailed properties of the flow field must be considered in conjunction with a consideration of the type of nuclei controlling the inception process.

The essential aspect of these conclusions are of course not original in this paper, but it was the attempt of this paper to add additional physical basis for their validity.

ACKNOWLEDGMENTS

Many individuals at the Naval Ship Research and Development Center have assisted in obtaining the results reported in this paper. Specific recognition should be given to Dr. H. Wang and Mr. C. Dawson for their contribution in developing the computer program used in the bubble trajectory analysis. This work was authorized and funded by the Naval Ship Systems Command under its General Hydromechanics Research Program, Task SR 023 0101.

APPENDIX A

ANALYTICAL EVALUATION OF THE HOLOGRAPHIC PROCESS FOR A BUBBLE

When a light beam is incident on a bubble, some of the light is reflected at the first surface. However, a significant amount of light is refracted at the first surface and eventually passes out through the bubble. In Figure A1, several rays are shown. As shown by Davis [38], ray 2 gives the largest contribution to the transmitted energy for $0° < \theta < 40°$. This information will be used to represent the light passing through the bubble in the following calculations.

In order to differentiate between a bubble image and an opaque spherical particle image, the light transmitted through the bubble must be observed. Thus, the holographic process must be evaluated to determine how the transmitted light can be expected to influence the holographic reconstruction of the bubble image. The general method will be an extension of the method used by DeVelis et al., for solid particles [39].

The wave equation in vector form

$$\nabla^2 V(\vec{x}, t) = \frac{1}{C^2} \frac{\partial^2 V(\vec{x}, t)}{\partial t^2} \tag{1A}$$

describes the propagation of optical monochromatic radiation, where

$$V(\vec{x}, t) = \Psi(\vec{x}) e^{-i\omega t}$$

and $\Psi(\vec{x})$ is the complex amplitude.

Physically, the wave amplitude will vary as

$$\mathrm{Re}\left\{\Psi(\vec{x}) e^{-i\omega t}\right\} .$$

If the operations on $V(\vec{x}, t)$ are linear and only the long time average is required, then the physical quantity is the real part of the final expression. Thus, for our application, the wave equation can be transformed to the Helmoltz equation

$$(\nabla^2 + k^2)\, \Psi(\vec{x}) = 0 \tag{2A}$$

where the wave number $k = \frac{2\pi}{\lambda} = \frac{\omega}{C}$. Here we have applied the restriction that the radiation is essentially monochromatic. The solution of equation (2A) can be written in integral form with $G(\vec{\xi} : \vec{x})$ the appropriate Green's function,

$$\Psi(\vec{x}) = \iint_s g(\vec{\xi}) \frac{\partial}{\partial n} \left[G(\vec{\xi} : \vec{x}) \right] d\vec{\xi} \tag{3A}$$

where $\Psi(\vec{\xi}) = g(\vec{\xi})$ on the surface s , and
$\vec{\xi} = \xi\hat{i} + \eta\hat{j}$, $\vec{x} = x\hat{i} + y\hat{j}$

with $\hat{i}$ and $\hat{j}$ unit normal vectors.
S is a plane perpendicular to the Z axis and its outer normal is in the direction of negative Z . The Green's function for this case is

$$G(\vec{\xi} : \vec{x}) = \frac{e^{ikr}}{4\pi r}$$

where $r = \sqrt{Z^2 + |\vec{\xi} - \vec{x}|^2}$.

Using the paraxial approximations, $Z \gg |\vec{\xi}-\vec{x}|$, and the Fraunhofer (i.e., far field) approximation $\frac{k|\xi|^2}{2Z} \approx 0$, then it can be shown that

$$\Psi(\vec{x}) = \frac{-ik}{4\pi Z} e^{ikz} e^{ik|\vec{x}|^2/2Z} \iint_{\vec{\xi}} g(\vec{\xi})\, e^{-i\frac{k}{z}\vec{\xi}\cdot\vec{x}}\, d\vec{\xi} \quad (4A)$$

The boundary conditions, $g(\vec{\xi})$, selected to represent the bubble are

$$g(\vec{\xi}) = g_1(\vec{\xi}) + g_2(\vec{\xi}) + g_3(\vec{\xi})$$

$$g(\vec{\xi}) = 1 - D(\vec{\xi}) + \alpha e^{ik|\vec{\xi}|^2/2f} e^{-a|\vec{\xi}|^2}$$

where
$$D(\vec{\xi}) \begin{cases} = 1, & |\vec{\xi}| \le |\vec{\xi}_o| \\ = 0, & |\vec{\xi}| > |\vec{\xi}_o| \end{cases} \quad (5A)$$

The first 2 terms of (5A) represent an opaque object and the 3rd term is an equivalent to a lens with a negative focal length f, attenuation factor α , and Gaussian transmittance distribution. The use of a negative lens is an approximation to ray 2 of Figure 1A. It is assumed here that a uniform plane wave is incident on the object plane $(\vec{\xi})$.

Substituting $g_1(\vec{\xi})$ in equation 4A gives

$$\Psi_1(\vec{x}) = e^{ikz} , \quad (6A)$$

i.e., a plane wave.

The second integral gives $\Psi_2(\vec{x})$ when $g_2(\vec{\xi})$ is substituted into 4A. For a circular disc of radius $|\vec{\xi}_o| = \ell_o$,

$$\Psi_2(\vec{x}) = \frac{i\ell_o}{\rho} e^{ikz} e^{ik\rho^2/2Z} J_1(k\rho\ell_o/Z) \quad (7A)$$

where $\rho = |\vec{x}|$

The third integral $\Psi_3(\vec{x})$ can be shown to be

$$\Psi_3(\vec{x}) = -ic_1 e^{ikz} e^{ik\rho^2/2Z} e^{-c_2\rho^2} e^{-ic_3} e^{ic_4\rho^2} . \quad (8A)$$

By combining terms,

$$\Psi_3(\vec{x}) = -ic_1 e^{ikz} e^{-c_2\rho^2} e^{-ic_3} e^{ic_5\rho^2} \tag{9A}$$

where

$$\begin{aligned} c_1 &= \frac{\alpha k}{2Z\sqrt{a^2 + (k/2f)^2}} \\ c_2 &= \frac{a}{a^2 + (k/2f)^2} (k/2Z)^2 \\ c_3 &= \tan^{-1} (k/2fa) \\ c_4 &= \frac{k}{2f\left[a^2 + (k/2f)^2\right]} (k/2Z)^2 \\ c_5 &= \frac{k}{2Z} + c_4 \end{aligned} \tag{10A}$$

It should be noted that equation (8A) was evaluated with the assistance of reference [40] . Thus the complete wave amplitude distribution in the $\vec{x}$ plane, a distance Z away from the object plane, $\vec{\xi}$, is

$$\Psi(\vec{x}) = e^{ikz}\left[1 + \frac{i\ell_o}{\rho} e^{ik\rho^2/2Z} J_1(k\rho\ell_o/Z) - ic_1 e^{-c_2\rho^2} e^{-ic_3} e^{ic_5\rho^2}\right] \tag{11A}$$

Since both photographic emulsions and the human eye are square law detectors, the quantity actually measured is $\Psi(\vec{x})\,\Psi(\vec{x})^*$, the intensity.

$$\begin{aligned} \Psi\Psi^* = 1 &- \frac{2\ell_o}{\rho} \sin(k\rho^2/2Z)\, J_1(k\rho\ell_o/Z) + (\ell_o/\rho)^2 J_1^2(k\rho\ell_o/Z) \\ &- 2c_1 e^{-c_2\rho^2} \sin(c_3 - c_5\rho^2) \\ &- \frac{2\ell_o}{\rho} c_1 J_1(k\rho\ell_o/Z) e^{-c_2\rho^2} \cos(k\rho^2/2Z + c_3 - c_5\rho^2) \\ &+ c_1^2 e^{-2c_2\rho^2} \end{aligned} \tag{12A}$$

For photographic emulsions it has been found that after proper exposure and processing the emulsion density will vary linearly as follows,

$$D = \delta \log_{10} I_i$$

$$D = \log_{10} (I_i / I_t),$$

where δ = constant

I_i = incident intensity

I_t = transmitted intensity

Now, since wave amplitude varies as $\Psi \sim (I)^{\frac{1}{2}}$

then $(I_i)^{\frac{1}{2}} = (I_i / I_t)^{\frac{1}{2}} = \Psi_i / \Psi_t$

and for a unit amplitude incident wave, $\Psi_t = I_i^{-\delta/2}$

If δ is positive a photographic "negative" is produced. Conversely, if δ is negative a photographic "positive" is produced.

The holographic process has been analytically described for the production of the hologram. If on the hologram a plane wave is incident, then we have the same analytical situation previously described. The new boundary condition is the variation in amplitude of the incident radiation.

$$A - \left[\Psi(\vec{x})\Psi(\vec{x})^*\right]^{-\delta/2}$$

where $\Psi\Psi^*$ is given by equation (12A) and A is the plane wave amplitude outside the hologram diffraction pattern. $(\Psi\Psi^*)^{-\delta/2}$ has the form $(1-X)^q$ and if $|X| < 1$ and sufficiently small, taking only the first 2 terms of a series expansion gives

$$A - (\Psi\Psi^*)^{-\delta/2} \simeq A - 1 - \frac{\delta}{2} X \qquad (14A)$$

Thus, the use of the integral solution to the Helmholtz equation, (4A) with the boundary condition given in (14A), will result in an image of the original object.

From equation (4A) it is apparent that the wave amplitude in the hologram plane is essentially a Fourier transform of the wave amplitude distribution in the object plane. With appropriate change of sign, the process of going from the hologram plane to the image plane is just an inverse Fourier transform.

The evaluation of the image intensity distribution has been performed numerically. Thus, by the use of a computer program, the influence of hologram size, emulsion signal to noise ratio, and many other factors can be studied analytically. The effects of either the holographic process or the test facility can be estimated prior to the actual physical measurement. The following constants were used in the calculations for Figures A2 - A4.

Z_1 = 100.00 mm

k = 9045/mm

ℓ_o = 0.03 mm

α = 1.0

ρ = 7 (i.e., the limit of integration)

f = - 0.3 mm

a = 1080

δ = 4

A = 4

As the image focusing distance, Z_2 , is changed from 99.7 mm to 100.0 mm and then to 100.3 mm, it can be seen in Figures A2 through A4 respectively, the focusing property of the hologram. When Z_2 equals 100.0 mm, then the bubble and opaque sphere shape are in focus. The light passing through the bubble produces an interference pattern within the bubble outline. For Z_2 equal to 100.3 mm, the bubble shape is no longer in focus, but the apparent point source of the light passing through the bubble is in focus. This is the distinguishing property of a bubble image in contrast to that of an opaque sphere.

APPENDIX B

APPLICATION OF COATINGS TO THE HEADFORM

As a result of a previous study at NSRDC, [22] , it was concluded that through the use of the principles of surface chemistry, the number of cavity nucleation sites on the solid surface could be significantly reduced. In order to assist in evaluating the role of free stream originating nuclei, it was necessary to determine whether or not surface nucleation sites were contributing to acoustically measured cavitation inception on the headform.

The underlying objective of the surface coating procedure was to enhance the wettability of the solid on a microscopic scale. The coating selected was one formed by the application of colloidal silica. As is well known, [41] , amorphous silica has a very low interfacial surface energy in contact with water. This is basically because the atomic structure of water is quite similar to silica. When silica dissolves in water, the process involves simultaneous hydration of the SiO_2 surface and depolymerization. This leads to the formation of monosilicic acid.

$$(SiO_2)_m + 2m\,(H_2O) = m\ Si(OH)_4$$

From monosilicic acid colloidal particles of silica can be produced. On the surface of each particle a monolayer of water is chemisorbed that can only be removed by heating a dried surface to 600°C. It is also known that these particles will have a negative charge in an alkaline medium.

The concept of the coating process is to utilize this negative charge and the colloidal particle dimensions to microscopically coat a solid surface. The surface selected was gold that was recently plated on the headform. The headform was flushed with spectroscopically pure acetone and then cleaned in a special chamber with steam produced from a potassium permanganate solution. Following cleaning, a 1 percent solution of colloidal silica* was put in the chamber and a positive potential applied to the headform. The head-

* Ludox SM, Colloidal Silica, manufactured by E.I. Dupont de Nemours and Co., Wilmington, Delaware.

form was dried in the chamber and then removed. When a small quantity of water was applied to the surface, it immediately spread and then appeared to dry as a film. Later applications of water also spread over the surface.

Plastic bodies made of Delrin were also coated with colloidal silica. However, since the plastic has a weak negative charge naturally occuring on the surface, a special positively charged colloidal silica** was used. After cleaning the surface and applying the positive sol, the water also spread over the solid surface and appeared to dry as a film.

Both the plastic and the gold plated bodies were then immersed in a container of water distilled from a potassium permanganate solution to minimize organic surfactant material from contaminating the coatings. The bodies were installed underwater while still in the pure water of the container. The test results comparing the coated with the uncoated bodies are given in Table 1.

* * *

** Positive Sol 130M, manufactured by E.I. Dupont de Nemours and Co., Wilmington, Delaware.

REFERENCES

[1] EISENBERG, P., "Environmental and Body Conditions Governing the Inception and Development of Natural and Ventilated Cavities." Appendix I, Report of Cavitation Committee, Proceedings, 12th International Towing Tank Conference, Rome, 1969, pp. 346-350.

[2] HOLL, J.W., "Nuclei and Cavitation", Journal of Basic Engineering, Trans. ASME, Series D, vol. 92, No 4, 1970, pp. 681-688.

[3] KNAPP, R.T., "Cavitation and Nuclei", Trans. ASME, Vol. 80, 1958, pp. 1315-1324.

[4] PLESSET, M.S., "The Tensile Strength of Liquids", pp. 15-25, Cavitation State of Knowledge, ed. J.M. ROBERTSON and G.F. WISLICENUS, ASME, 1969, New-York.

[5] van der WALLE, F., "On the Growth of Nuclei and the Related Scaling Factors in Cavitation Inception", Netherlands Ship Model Basin, Laboratory Memorandum No. V2, Wageningen (1963). See also International Shipbuilding Progress, Vol. 10, No. 106, 1963, pp. 195-204.

[6] VINCENT, da C., "The Naval Ship Research and Development Center", Naval Ship Research and Development Center Report 3039, June 1969.

[7] ROUSE, H. and McNOWN, J.S., "Cavitation and Pressure Distribution, Headforms at Zero Angle of Yaw", State University of Iowa Studies in Engineering, Bulletin 32, 1948.

[8] JOHNSSON, C-A., "Cavitation Inception on Head Forms. Further Tests", Appendix V, Report of Cavitation Committee, Proceedings, 12th International Towing Tank Conference, Rome, 1969, pp. 381-392.

[9] BROCKETT, T., "Some Environmental Effects on Headform Cavitation Inception", Naval Ship Research and Development Center Report 3974 (in review).

[10] BROCKETT, T., "Cavitation Occurrence Counting - Comparison of Photographic and Recorded Data", ASME Cavitation Forum, Evanston, Illinois, June 1969, pp. 22-23.

[11] JOHNSON, V.E., Jr and HSIEH, T., "The Influence of the Trajectories of Gas Nuclei on Cavitation Inception", 6th Symposium on Naval Hydrodynamics, October 1966, Washington, D.C., pp. 163-182.

[12] HSIEH, T., "The influence of the Trajectories and Radial Dynamics of Entrained Gas Bubbles on Cavitation Inception", Hydronautics, Inc. Report 707-1, October 1967.

[13] SCHRAGE, D.L., and PERKINS, H.C., Jr, " Isothermal Bubble Motion Through a Rotating Liquid", Journal of Basic Engineering, Trans. ASME, Series D, Vol. 94, no. 1, 1972, pp. 187-192.

[14] HABERMAN, W.L. and MORTON, R.K., "An Experimental Investigation of the Drag and Shape of Air Bubbles Rising in Various Liquids", David Taylor Model Basin Report 802, September 1953.

[15] HESS, J.L., and SMITH, A.M.O., "Calculation of Potential Flow About Artitrary Bodies", Progress in Aeronautical Sciences, Vol. 8, 1967.

[16] PETERSON, F.B., "Water Tunnel, High Speed Basin Cavitation Inception Comparisons", 12th International Towing Tank Conference, Proceedings, Rome, 1969, pp. 519-523.

[17] EISENBERG, P., "Cavitation Dictionary", Appendix VI, Report of Cavitation Committee, 13 th International Towing Tank Conference, Berlin/Hamburg, September 1972.

[18] SCHIEBE, F.R., "The influence of Gas Nuclei Size Distribution on Transient Cavitation Near Inception", Project Report No. 107, St. Anthony Fall Hydraulic Laboratory, University of Minnesota, May 1969.

[19] SCHIEBE, F.R., "Cavitation Occurrence Counting - A New Technique in Inception Research", ASME Cavitation Forum, New York, November 1966.

[20] CHAPMAN, R.B., and PLESSET, M.S., "Nonlinear Effects in the Collapse of a Nearly Spherical Cavity in a Liquid", Journal of Basic Engineering, Trans. ASME, Series D, Vol. 94, No. 1, March 1972, pp. 142-146.

[21] NAUDE, C.F. and ELLIS, A.T., "On the Mechanism of Cavitation Damage by Nonhemispherical Cavities Collapsing in Contact with a Solid Body", Journal of Basic Engineering, Trans, ASME, Series D, Vol. 83, No. 4, December 1961, pp. 648-656.

[22] PETERSON, F.B., "Cavitation Originating at Liquid-Solid Interfaces", Naval Ship Research and Development Center Report 2799, September 1968.

[23] ARAKERI, V., "Water Tunnel Observations of Laminar Boundary Layer Separation Using Schlieren Technique", ASME Cavitation Forum, San Francisco 1972, pp. 29-30.

[24] EPSTEIN, P.S., and PLESSET, M.S., "On the Stability of Gas Bubbles in Liquid-Gas Solutions", Journal of Chemical Physics, Vol. 18, 1950, pp. 1505-1509.

[25] WARD, C.A., "On the Stability of Gas-Vapour Bubbles in Liquid-Gas Solutions", University of Toronto, Department of Mechanical Engineering Report TP-7105, May 1971.

[26] LIEBERMANN, L., "Air Bubbles in Water", Journal of Applied Physics, Vol. 28, No. 2, 1957, pp. 205-211.

[27] HARVEY, E.N. et al., "On cavity Formation in Water", Journal of Applied Physics, Vol. 18, 1947, pp. 162-172.

[28] HARVEY, E.N., et al., "Removal of Gas Nuclei from Liquids and Surfaces", Journal fo American Chemical Society, Vol. 67, No. 1, 1945, pp. 156-157.

[29] HARVEY, E.N., et al., "Bubble Formation in Animals; Physical Factors", Journal of Cellular and Comparative Physiology, Vol. 24, 1944, pp. 1-22.

[30] APFEL, R.E., "The Role of Impurities in Cavitation-Threshold Determination", Journal of Acoustical Society of America, Vol. 48, No. 5, (part 2), 1970, pp. 1179-1186.

[31] HAYWARD, A.T.J., "The Role of Stabilized Gas Nuclei in Hydrodynamic Cavitation Inception", National Engineering Laboratory Report 452, May 1970.

[32] GREENSPAN, M. and TSCHIEGG, C., "Radiation-Induced Acoustic Cavitation; Apparatus and Some Results", Journal of Research National Bureau of Standards, 71C, No. 4, 1967, pp. 299-312.

[33] MESSINO, C.D., SETTE, D., and WANDERLINGH, F., "Effects of Solid Impurities on Cavitation Nuclei in Water", Journal of Acoustical Society of America, Vol. 41, No. 3, 1967, pp. 573-583.

[34] SUTCLIFFE, W.H., Jr., BAYLOR, E.R., and MENZEL, D.W. "Sea Surface Chemistry and Langmuir Circulation", Deep-Sea Research, Vol. 10, no. 3, 1963, pp. 233-243.

[35] RILEY, G.A., "Organic Aggregates in Sea Water and the Dynamics of Their Formation and Utilization", Limnology and Oceanography, Vol. 8, No. 4, 1963, pp. 372-381.

[36] WALLACE, G.T., Jr., and WILSON, D.F., "Foam Separation as a Tool in Chemical Oceanography", Naval Research Laboratory Report 6958, November 1969.

[37] MANLEY, D.M.J.P., "Change of Size of Air Bubbles in Water Containing a Small Dissolved Air Content", British Journal of Applied Physics, Vol. 11, January 1960, pp. 38-42.

[38] DAVIS, G.E., "Scattering of Light by an Air Bubble in Water", Journal of the Optical Society of America, Vol. 45, No. 7, 1955, pp. 572-581.

[39] DeVELIS, J.B., PARRENT, G.B., and THOMPSON, B.J., "Image Reconstruction with Fraunhofer Holograms", Journal of the Optical Society of America, Vol. 56, No. 4, 1966, pp. 423-427.

[40] GRADSHTEYN, I.S. and RYZHIK, I.M., Table of Integrals, Series and Products, Academic Press, New-York, 1965, p. 485.

[41] ILER, R.K., The Colloidal Chemistry of Silica and Silicates, Cornell University Press, Ithaca, 1955.

* * *

TABLE 1. ACOUSTIC INCEPTION ON HEADFORMS

(V = 9.1 meters per second; Acoustic event rate = 1 per second)

RUN	HEADFORM	COATED	a/a_{TS} x100	σ_i	REMARKS
1	CU	NO	132	.66	NEW TUNNEL WATER
2	CU	NO	63	.62	SAME TUNNEL WATER AS RUN 1
3	CU	NO	34	.61	SAME TUNNEL WATER AS RUN 1
4	CU	NO	34	.57	SAME TUNNEL WATER AS RUN 1
5	CU	NO	8.5	.54	SAME TUNNEL WATER AS RUN 1
6	CU	NO	22	.48	NEW TUNNEL WATER
7	AU	NO	149	.65	NEW TUNNEL WATER
8	AU	YES	149	.64	SAME TUNNEL WATER AS RUN 7
9	AU	YES	220	.60	NEW TUNNEL WATER
10	AU	YES	49	.55	SAME TUNNEL WATER AS RUN 9
11	AU	YES	145	.61	SAME TUNNEL WATER AS RUN 9
12	AU	NO	159	.59	NEW TUNNEL WATER
13	DELRIN	NO	166	.70	NEW TUNNEL WATER
14	DELRIN	NO	88	.69	SAME TUNNEL WATER AS RUN 13
15	DELRIN	NO	162	.71	SAME TUNNEL WATER AS RUN 13
16	DELRIN	NO	21	.65	NEW TUNNEL WATER
17	DELRIN	NO	44	.64	SAME TUNNEL WATER AS RUN 15
18	DELRIN	NO	152	.73	SAME TUNNEL WATER AS RUN 15
19	DELRIN	NO	81	.68	SAME TUNNEL WATER AS RUN 15
20	DELRIN	YES	118	.72	SAME TUNNEL WATER AS RUN 15
21	DELRIN	YES	91	.70	SAME TUNNEL WATER AS RUN 15
22	DELRIN	YES	42	.66	SAME TUNNEL WATER AS RUN 15
23	DELRIN	YES	34	.58	SAME TUNNEL WATER AS RUN 15

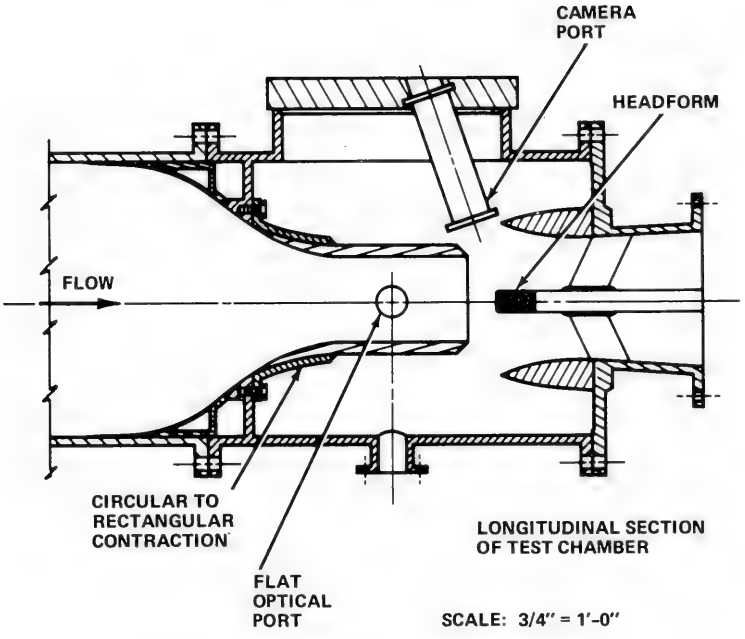

FIGURE 1. MODIFIED 12" WATER TUNNEL

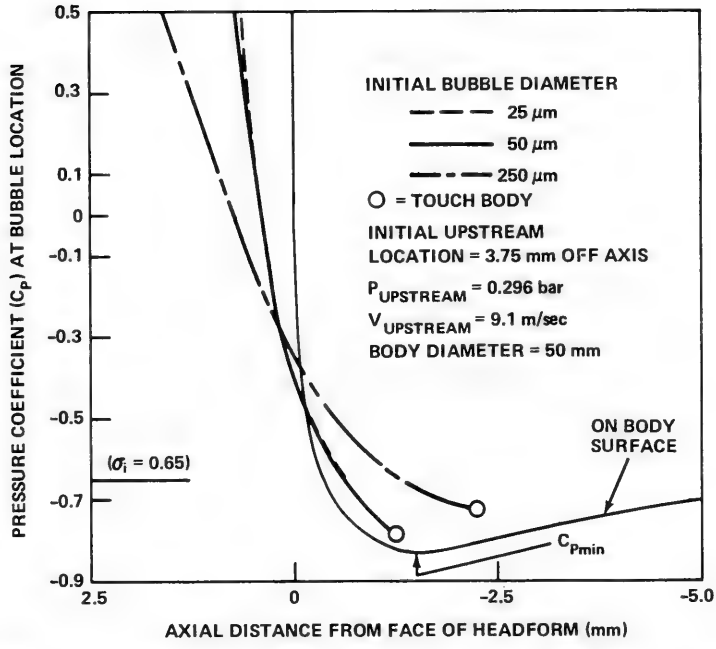

FIGURE 2. BUBBLE DIAMETER ALONG BUBBLE TRAJECTORY: INITIAL UPSTREAM LOCATION OF 3.75 MM OFF AXIS; $V_{UPSTREAM}$ = 9.1 M/SEC

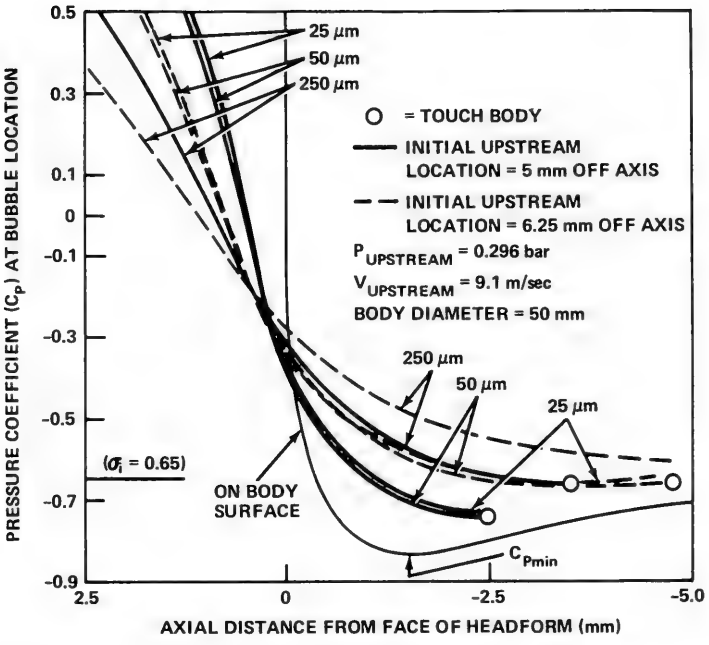

FIGURE 3. PRESSURE COEFFICIENT VARIATION ALONG BUBBLE TRAJECTORY: INITIAL UPSTREAM LOCATION OF 5.0 MM, 6.25 MM; $V_{UPSTREAM}$ = 9.1 M/SEC

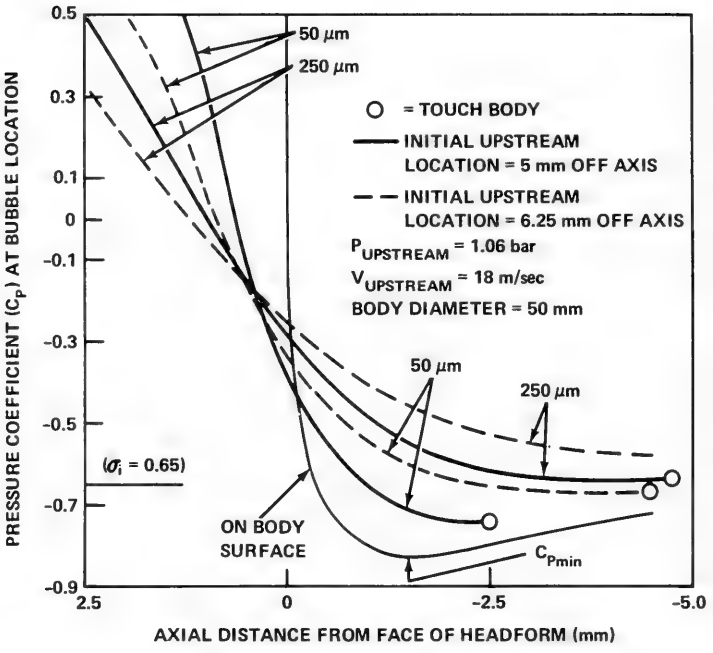

FIGURE 4. PRESSURE COEFFICIENT VARIATION ALONG BUBBLE TRAJECTORY: INITIAL UPSTREAM LOCATION OF 5.0 MM, 6.25 MM; $V_{UPSTREAM}$ = 18 M/SEC

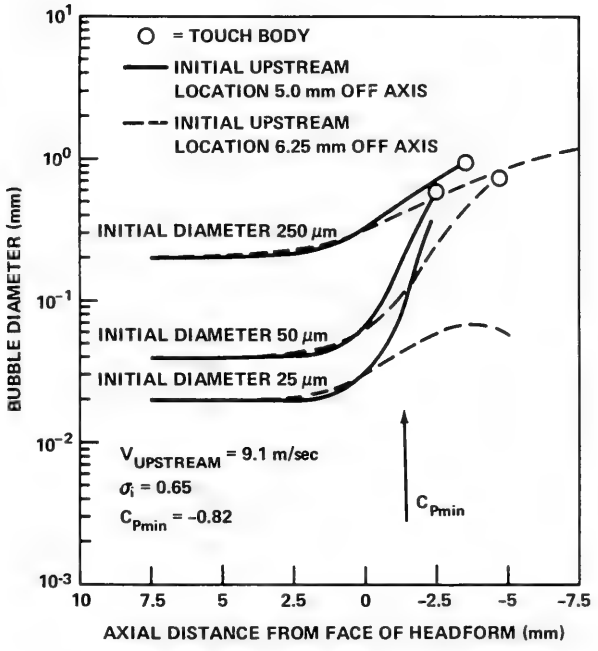

FIGURE 5. BUBBLE DIAMETER ALONG BUBBLE TRAJECTORY: INITIAL UPSTREAM LOCATION OF 5.0 MM, 6.25 MM OFF AXIS; $V_{UPSTREAM}$ = 9.1 M/SEC

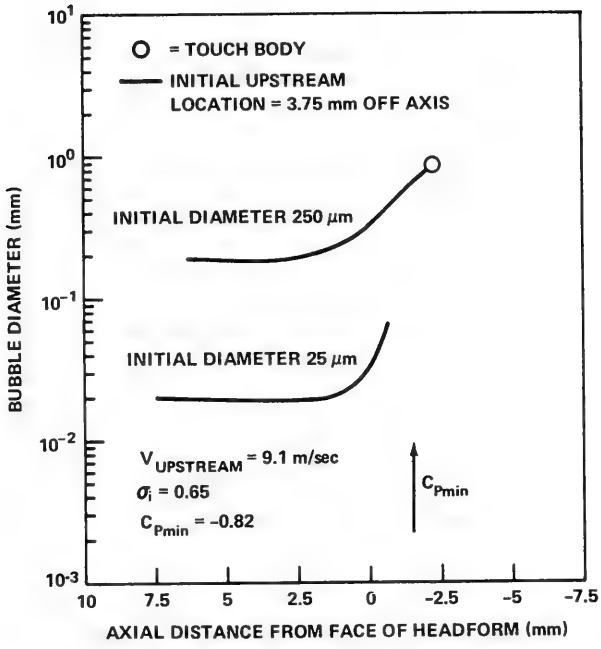

FIGURE 6. PRESSURE COEFFICIENT VARIATION ALONG BUBBLE TRAJECTORY: INITIAL UPSTREAM LOCATION 3.75 MM; $V_{UPSTREAM}$ = 9.1 M/SEC

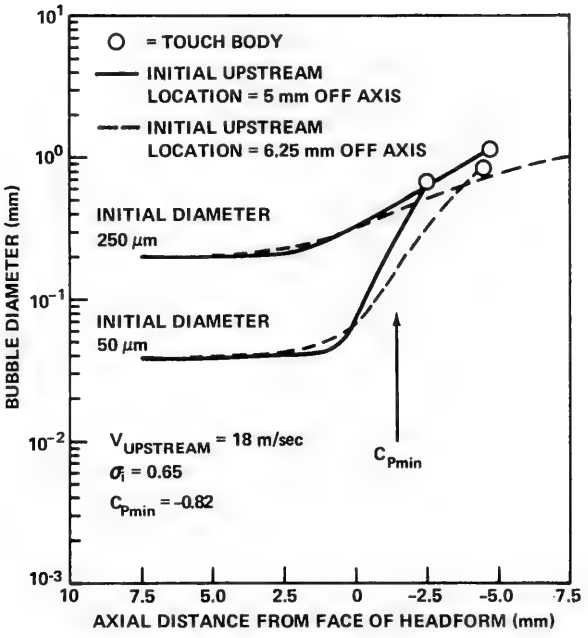

FIGURE 7. BUBBLE DIAMETER ALONG BUBBLE TRAJECTORY: INITIAL UPSTREAM LOCATION OF 5.0 MM, 6.25 MM OFF AXIS; $V_{UPSTREAM}$ = 18 M/SEC

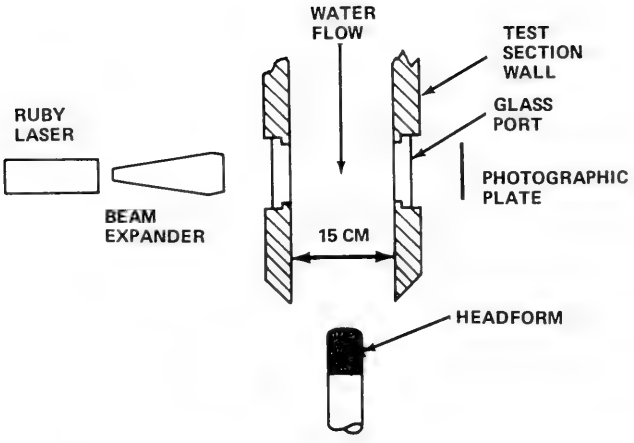

FIGURE 8. BASIC SCHEMATIC FOR BUBBLE MEASUREMENT WITH FRAUNHOFER HOLOGRAPHY

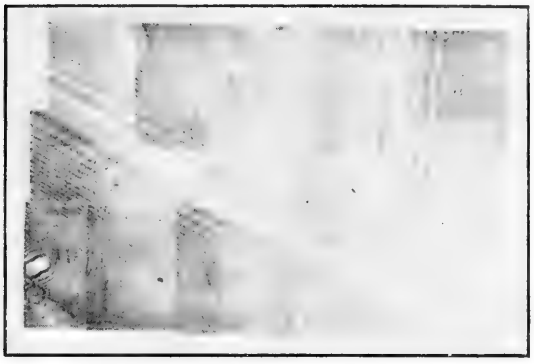

FIGURE 9
MAGNIFIED VIEW OF A HOLOGRAM FOR TWO 25μm WIRES, BUBBLES, AND PARTICULATE

NSRDC

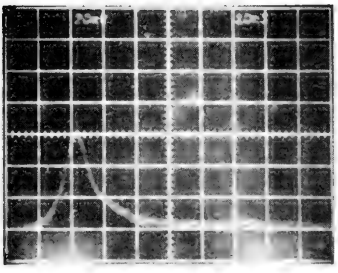

FIGURE 10
RUBY LASER PULSE SHAPE

NSRDC

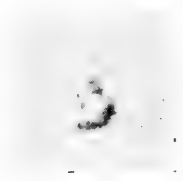

60 μm Diameter
Focussed

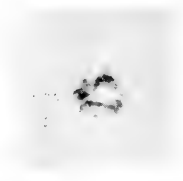

Defocussed 0.3 mm.

FIGURE 11 - BUBBLE IMAGE

70 μm Diameter
Focussed

Defocussed 0.3 mm

FIGURE 12 - SOLID PARTICLE IMAGE

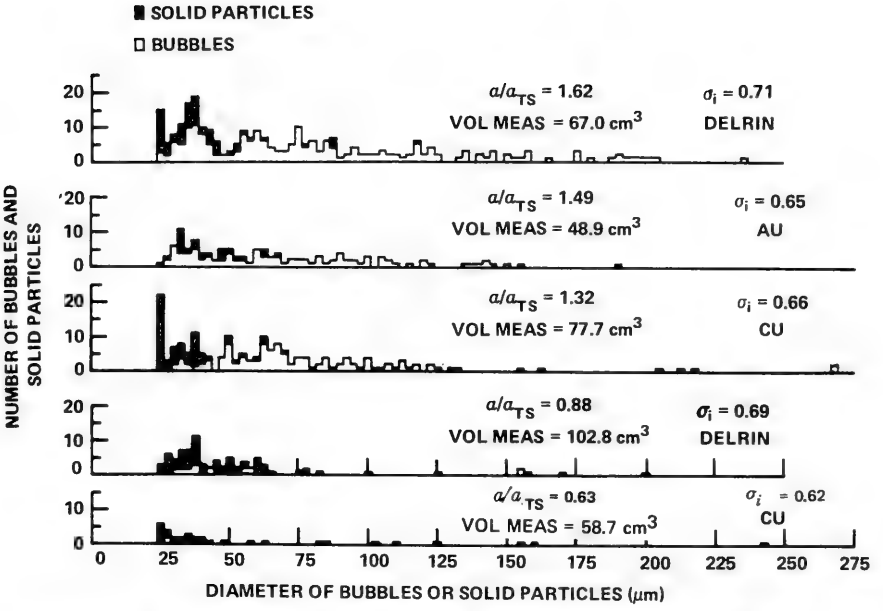

FIGURE 13. BUBBLE AND SOLID PARTICLE DISTRIBUTIONS

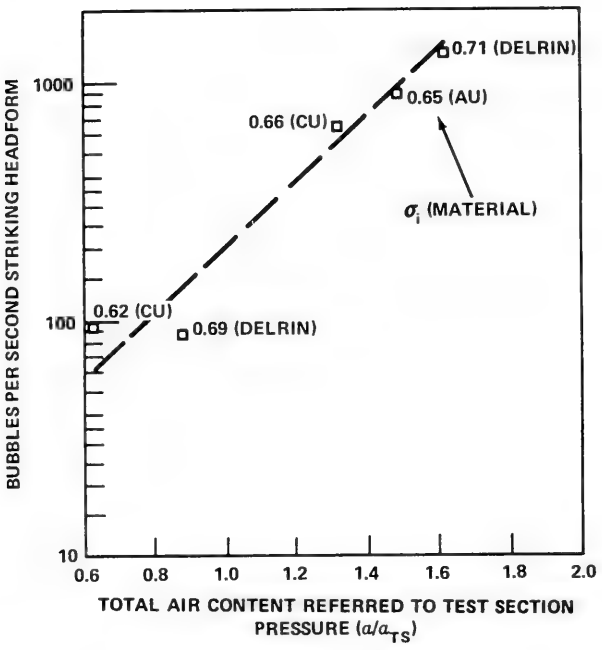

FIGURE 14. NUMBER OF BUBBLES $\geq$ 25 μM DIAMETER STRIKING HEADFORM FOR VARIOUS (α/α_{TS})

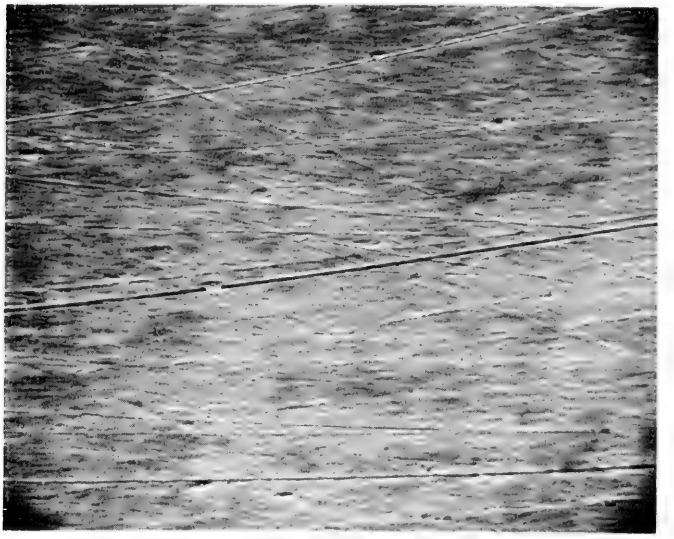

10μm

Typical Sem Photograph of Gold Plated Body

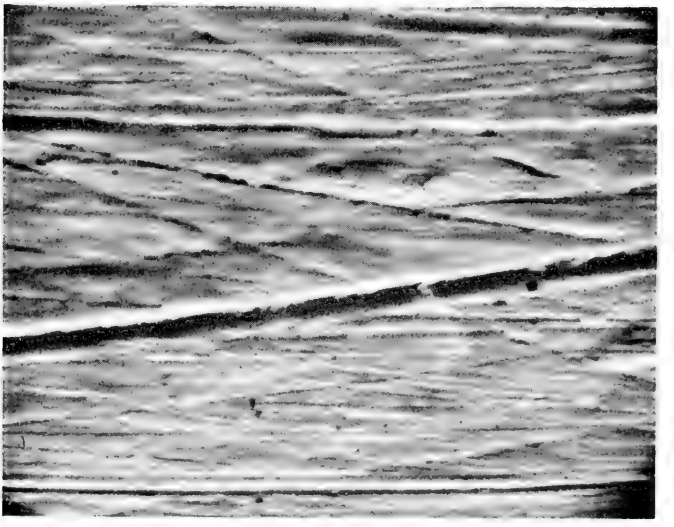

2μm

FIGURE 15
TYPICAL SEM PHOTOGRAPH OF GOLD PLATED BODY

50μm

Typical Sem Photograph of Delrin Headform

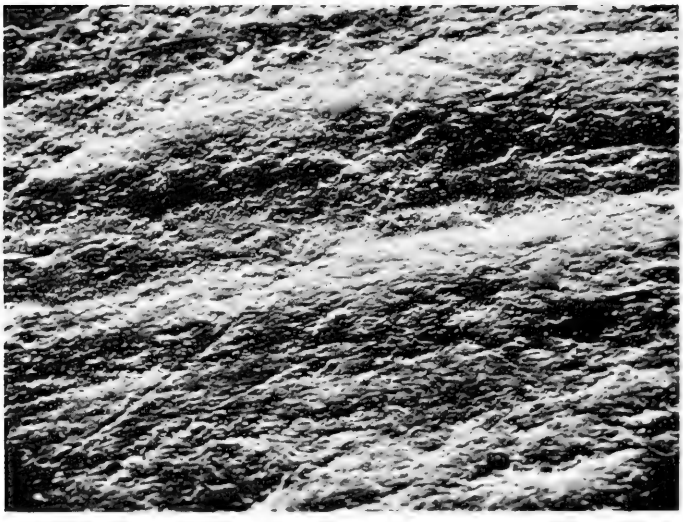

10μm

FIGURE 16
TYPICAL SEM PHOTOGRAPH OF DELRIN HEADFORM

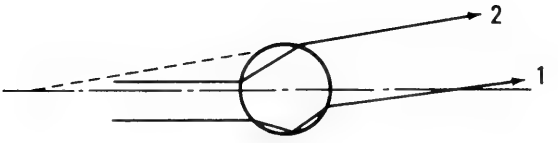

FIGURE A-1. LIGHT THROUGH A BUBBLE – TWO MOST IMPORTANT CASES

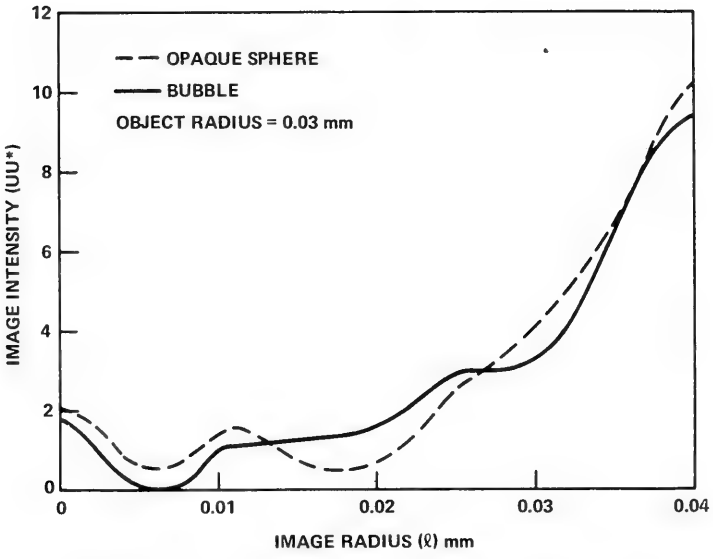

FIGURE A-2. LIGHT INTENSITY VS IMAGE RADIUS
Z_2 = 99.7 MM

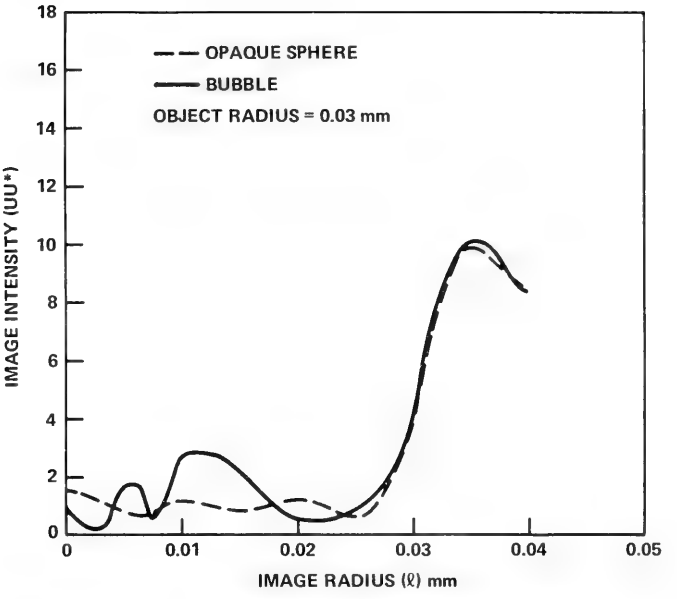

FIGURE A-3. LIGHT INTENSITY VS IMAGE RADIUS
$Z_2 = 100.00$ MM

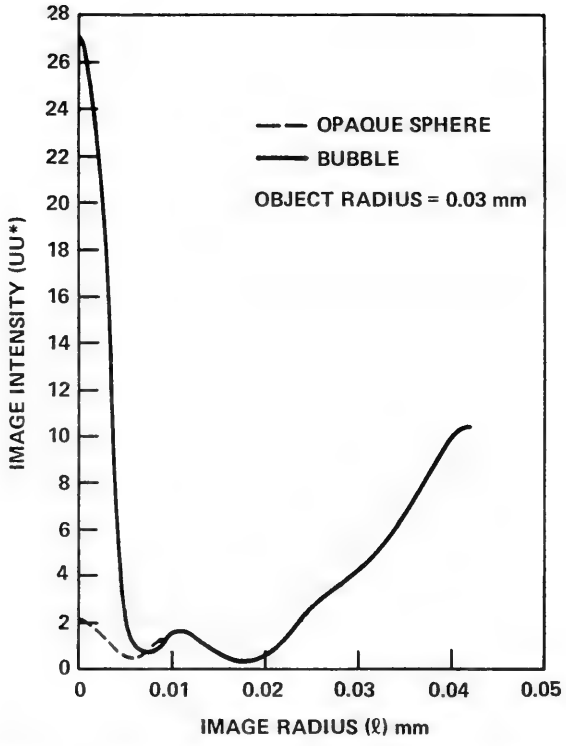

FIGURE A-4. LIGHT INTENSITY VS IMAGE RADIUS
Z_2 = 100.3 MM

DISCUSSION

Carl-Anders Johnsson
Statens Skeppsprovningsanstalt
Göteborg, Sweden

In this very interesting paper the author discusses the different mechanisms proposed throughout the years as responsible for cavitation inception. One of his conclusions seems to be that, for the type of experiments referred to, nuclei trapped in crevices of hydrophobic particles could play the main role in the nucleation process leading to cavitation inception.

A consequence of this reasoning would be that the role of free stream nuclei is not so important as has been assumed during the last years. The dissolved gas content is important however as it can affect the amount of gas trapped in the hydrophobic particles.

I will show a slide, which may give some support to this conclusion. The slide shows photographs of the free bubbles in the test sections of the two tunnels at SSPA during tests similar to those described in the paper.

The same body was tested in the two cases and can be used for estimating the bubbles sizes. The test conditions are the same in the two cases :

$$\text{water speed } 7.5 \text{ m/s}, \qquad \sigma = 0.3, \qquad \alpha/\alpha_s = 0.1$$

and the water taken from the same storage tank. The upper photograph shows the test section of the new large tunnel ; the lower that of the smaller tunnel. The difference in bubble spectrum is quite large and is of course due to the large difference in the pressure history for the water entering the test section in the two cases.

The point is that the same inception cavitation number of $\sigma_i = 0.45$ was observed visually in the two cases. This might indicate that the influence of the free bubbles is not important.

* * *

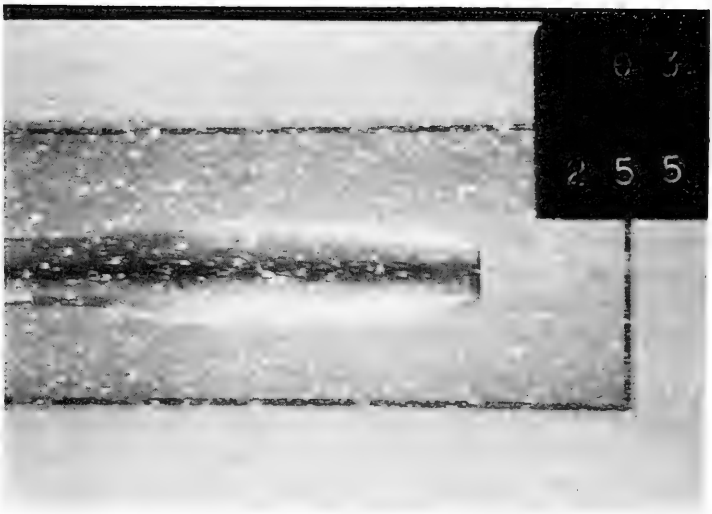

a) test in the large tunnel

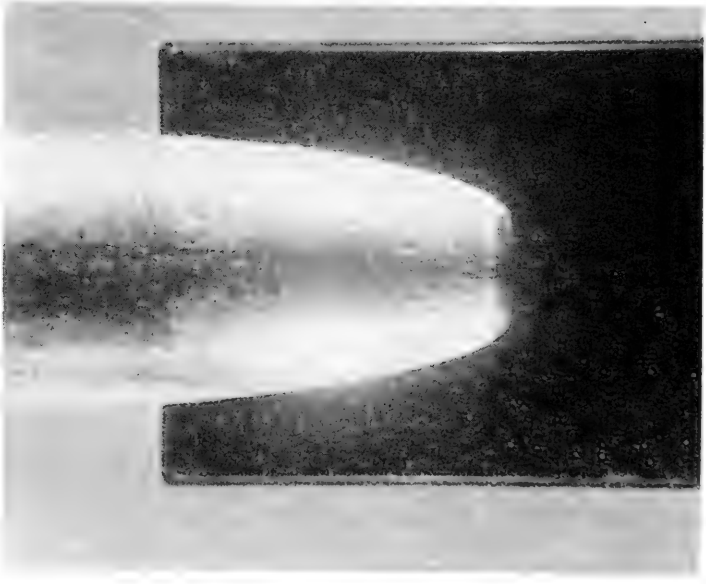

b) test in the small tunnel

Comparative tests of the same body at the same σ in the two tunnels of SSPA

DISCUSSION

Edward Silberman
St. Anthony Falls Hydraulic Laboratory
Minneapolis, Minnesota, U.S.A.

I want to comment on two points. I would agree that the free stream nuclei, which are very important, need not be gas bubbles in the usual sense that we may think of them as having uncontaminated interfaces between gas and water. I made observations about 25 years ago (1), using a microscope, of bubbles being dissolved under pressure in a rotating apparatus. This was in connection with resorption problems that we were working on at that time to get rid of bubbles in water tunnels. I was measuring time rate of change of diameter of single bubbles generated by cavitation. In watching these bubbles I found that a relatively small number of those generated would not disappear but instead would collapse on a thin, wrinkled, opaque skin. I recorded this fact in the reference paper, although at that time it did not seem important. When the pressure was reduced again these bubbles would expand just like normal gas bubbles. I think this is pertinent to what Peterson said, and enables us to treat nuclei as though they are gas bubbles. I believe that what is left in the water could be these bubbles with skins on them.

It should be mentioned that these bubbles in the rotating apparatus, when they appeared to be pure gas bubbles would be near the center of rotation, but when they collapsed on a skin, their diameters remained constant, and they would wander around in the centrifugal pressure field without regard to the pressures indicating mean bubble densities near that of water. Such bubbles could sustain themselves in a towing tank for a long time - maybe indefinitely.

My second point refers to the implications in the paper that it is necessary for the nuclei to touch the body in order to produce cavitation. I do not believe that this is correct. If you think about what I

---

(1) SILBERMAN, E., "Air Bubble Resorption", Tech. Paper No. 1, Series B, St. Anthony Falls Hydraulic Laboratory, 1949.

said avout the possibility of the bubbles being of almost neutral density, perhaps it is then very likely that such nuclei follow the streamlines or very close to them. It is our belief from work that we have done more recently at our laboratory that bubbles following these streamlines merely have to enter the low-pressure field of the headform in order to produce cavitation (1). Of course, more bubbles will cavitate near the body than farther from it.

DISCUSSION

Serge Bindel
Délégation Générale à la Recherche Scientifique et Technique
Paris, France

(Translated from French)

I read with a great interest the paper presented by Dr. Peterson and I must say firstly that I do not agree completely with its last conclusion. When Dr. Peterson tells us that his paper is a contribution among others about cavitation and that there is nothing original in its conclusion, I frankly believe that he is too modest. In fact this contribution seems to be very important in several respects. First due to the nature itself of program, and to the quality of the measurements. In particular, it seems to me that for the first time the bubble spectrum in front of the test body has been measured, not only the spectrum of free bubbles but also that of the solid particles by means of an unquestionable method, here the holographic one. That leads to estimate that the author's conclusions are based on serious data and consequently that this paper is by no means negligible.

This point being reminded, I would like to make for my part two series of remarks ; first on the analytical calculation of the trajectories. It has to be pointed out what are the limits of such a calculation ; it is based on some simplifying hypotheses, which are not original, but these hypotheses are not completely valid, even far from the body. As was shown for example by Foissey in a recent paper

(1) SCHIEBE, F. R., "Measurement of the Cavitation Susceptibility of Water Using Standard Bodies", Proj. Rpt. No. 118, St. Anthony Falls Hydraulic Laboratory, 1971.

presented to Association Technique Maritime et Aeronautique (x), using a singular perturbation method, the solution of the problem cannot be reduced at not order to Stokes solution. Foissey showed in particular that some terms, which are currently put in the equations are not in fact correct, even far from the walls ; a fortiori close to the body, in particular inside the boundary layer, since it would be necessary to take into account the rotation of the bubbles and their deformation. But the analytical calculation may have a qualitative interest, namely to show the screening effect. Concerning this effect it seems that there exists some discrepancy between the present results and those obtained by Johnson and Hsieh from the same hypotheses. For Johnsson and Hsieh, if my memory is good, the bubbles are kept away from the solid body and only the smallest ones starting from the axis of the body can reach it. On the contrary, Dr. Peterson tells us that bubbles starting away from the axis can reach the body and cavitate on it. I would like this point to be cleared.

My second series of remarks are relative to the respective influence of the stream free bubbles and of the hydrophobic particles as cavitation nuclei. When the air content in the water of the tunnel is decreased, it is noted that the free bubbles are decreased in number and diameter but that the noise remains constant, and from this it is concluded that hydrophobic particles are responsible for cavitation, at least for cavitation noise. I believe that this conclusion may be true but that it is perhaps premature. It is indeed possible that the bubbles which can be observed when the air content is high are not cavitation bubbles but gaseous bubbles or pseudo-cavitation bubbles, that is bubbles filled with a great quantity of air, and leading to visual but not noisy phenomena. The noise could be perhaps produced by smaller free bubbles i. e. by true cavitation bubbles and not necessarily by hydrophobic particles.

I believe that these considerations bring us back, as ever, to that difficulty of defining incipient cavitation. This can be only defined by its effects, either bubble growth, that is a visible phenomenon, with the difficulty of making the distinction between cavitation and gaseous bubbles, or an acoustical phenomenon that presents difficulty for an analytical treatment. In the ITTC Cavitation Committee, we have had serious discussion before reaching an agreement on the definition of

(x) FOISSEY, C., "Application d'une méthode de perturbation singulière à l'étude de la cavitation naissante." Association Technique Maritime et Aeronautique, session 1972.

the term "cavitation" itself, and now Dr. Peterson seems to question it in his paper. That means that there is yet much work to be done. For my part I am convinced that studies like that which was presented here can bring a new light on this problem, and I hope that they will pursued.

DISCUSSION

Luis Mazarredo
Escuela T.S. de Ingenieros Navales
Associacion de Investigacion de la Construccion Naval
Madrid, Spain

I want to thank Dr. Peterson for showing the results of his very accurate experiments. Tests like these may give a real experimental basis and avoid the contradictory results we sometimes found. This is for instance the case with the no influence of the surface state which has been shown. Though this might be predicted, since conditions in its crevices are permanent and there is no input (which would not be the case in a central propeller or in boiling) such a confirmation is wellcomed. Since positive results are still more interesting, may I ask Mr. Peterson wether he intends to perform tests, in the future, to check the magnitude of the influence of speed on this transient phenomenon ?

REPLY TO DISCUSSION

Frank B. Peterson
Naval Ship Research and Development Center
Bethesda, Maryland, U.S.A.

In response to Mr. Johnsson's comments about his photographic bubble measurements, all I can say is that in our work we tried to differentiate between the visual and the acoustic measurements. If we had in fact used the observations taken in high-speed photography then we would have said that inception had occurred earlier when there were more bubbles in the water. I think that might have been shown on one of the slides I presented. But in spite of that we still, appa-

rently, came up with the same general conclusion as to the bubble distribution importance.

I should like to thank Professor Silberman for pointing out a paper of his which was unknown to me. It is unfortunate since the Navy Department apparently funded that work and I was remiss in not seeing it in the literature.

I would like to say that all of this work can be considered a conservative estimate in that I emphasised free gas bubbles must touch the surface. If I gave looser bounds to the calculations and said that the bubbles did not have to touch the surface but only had to reach within a certain distance from the surface, in fact it would make the case I was presenting even stronger. As you may have noticed, the actual bubble distribution was not even used in this work. All we took were the total number of bubbles observed. We did not even discriminate between bubbles that had an order of magnitude difference in size because we felt it was not necessary to make the point.

On Mr. Bindel's comments, I should like to point out that we could only discriminate between bubbles and solid particles larger than 25 micrometres and the conclusion that bubbles were not important at all was drawn by inference from the studies that we made in the high-speed basin. The analytical calculations of the trajectory by Foissey are not familiar to me but I think a comparison would be interesting between the methods of calculation. I might say that the paper pointed out that the calculations that I have used were compared with experimental measurements of bubbles in pressure gradients in water and in glycerine and there was quite good agreement, so I suspect that there may be a close agreement between the work of Foissey and the calculation methods that we used. This work does agree with the work of Hsieh. The equations used were essentially the same. Perhaps it is unfortunate, but in the slide that I showed I did not show that some bubbles would be drawn away from the body, but given a pressure distribution on the surface - and in my case it was different from that of Hsieh and Johnson - and given different bubble sizes, some bubbles would by the pressure gradients be forced away from the surface. I should like to reference the work of Dr. Brockett at the Naval Ship Research and Development Center. He has in a report correlated the noise produced by the collapse of the cavity and the visual observation through high-speed photography of the collapse of the cavity on the surface. It has been shown that basically in the work on this body the cavitation that occurred on the surface produced the noise and to the best of our information the cavities that were further from the surface and did not touch the surface, did not produce noise within the significant range of this work.

It is very possible that for the pressures that we had in these tests, the bubbles that were off the surface never really reached, or very few of them reached, the region at the vapour pressure of the water.

I am not sure of the extent of the work that will be carried out, Professor Mazarredo, as far as the influence of speed is concerned. The work requires a lot of effort and making detailed measurements at various speeds in water tunnels could be significant, but it is possible that the towing basin work which was done at a speed twice as high may, at least for the time being, serve our purposes of analysis.

I appreciate all of discussion and I'd like to thank all of you for giving the pertinent and valuable comments.

* * *

VORTEX THEORY FOR BODIES MOVING IN WATER

Roger BRARD
Bassin d'Essais des Carènes
Paris, France

ABSTRACT

This paper presents in a synthesized form old and new results about the vortex theory for bodies moving in water. It is shown that the hydrodynamic forces exerted on such a body can be derived from the knowledge of a vortex distribution kinematically equivalent to the body. A method is proposed for determining both the bound vortices and the free vortices when the bound vortex distribution is chosen to be adherent to the hull surface. The total vortex distribution is divided into two parts. The first one consists of a volume distribution inside the hull and of a vortex sheet on the hull surface. The volume distribution is identical with the vortex distribution due to the angular velocity of the body. The sheet is determined by the condition that this first part of the total distribution induces outside the hull a velocity null everywhere at every time. This first part may be calculated once for all. The second part consists of the free vortex sheets shed by the body and of a bound vortex sheet on the hull. It is equivalent to a normal dipole distribution whose density is the solution of a Volterra equation. The determination of the hydrodynamic forces exerted on the body is derived from the dynamical equilibrium of the fluid outside the body, of the fluid inside the body and of the total bound vortex on the hull. This system can be subdivided into three systems : the quasi-steady system, the system due to the added masses and the system depending on the history of the motion.

This paper has been written to suscitate new researches in the field of the maneuverability and control of marine vehicles.

INTRODUCTION

The vortex theory in incompressible, inviscid and homogeneous fluids plays a role of importance in many chapters of Ship Hydrodynamics. However it is not systematically applied to all the problems where it should be especially useful. This is the case of those related to maneuverability and control of bodies which behave as rather poor lifting surfaces because of their large displacement/length ratios. The research reported in the present paper has thus been undertaken with the purpose of determining how much help one can expect from the theory when dealing with such bodies in any given steady or unsteady motion.

Indeed the question was not to draw up a new vortex theory, but rather to extend known results relevant to fluid kinematics and dynamics and to increase their generality and effectiveness.

The joined table of contents suffices to show the writer's line of thought.

The startpoint is Poincaré's formula which permits to determine the velocity in a closed domain when the vorticity inside that domain and the velocity on its boundary are known. This leads to a mathematical model where the hull surface is replaced by a fluid surface moving without alteration of its shape. There exists an infinite class of vortex distributions kinematically equivalent to the body. They only depend on the choice of the vorticity distribution inside the hull. The most interesting one is that which permits the exterior fluid to be adherent to the hull. Inside the hull the absolute fictitious fluid motion coincides with that of the body. From the point of view of kinematics, one of the features of the theory is that the total vortex distribution can be divided into two families almost independent of each other. One consists of a volume distribution inside the hull and of a vortex sheet over the hull, it is so calculated as to induce outside the body a velocity which is null everywhere. It only depends on the angular velocity of the body and can be determined once for all for any given hull. The second family is the union of a vortex sheet distributed over the hull and of the free vortices shed by the hull. It is determined by the condition that the fluid inside the

hull be at rest with respect to the body and by a complementary condition expressing that the pressure is continuous through the line of shedding of the free vortices.

Only the second vortex family has a physical meaning. But both are necessary for determining the hydrodynamic pressure on the hull. This is not really surprising since both the fluid inside the hull and the bound vortex sheet over the hull must be in dynamical equilibrium. A consequence is that the classical expression for the force exerted by the flow on an arc of vortex filament which does not move with the fluid cannot be readily extended to the case when this arc belongs to the bound vortex sheet adherent to the hull. The hydrodynamic pressure on the hull is expressed in terms which only depend on the total vortex distribution. The dynamical problem is thus completely solved for any given hull in any given motion whatever the incident flow may be.

The theory developed in the present paper is quite general. Its application to practical ends does not seem to lead to insuperable difficulties provided that reasonable assumptions can be made concerning the position of the free vortex sheets with respect to the body and the possible variation of that position with time. In any case, it is shown in the last section that an older and less complete vortex theory is still useful in maneuvering. Thus it is hoped that the present one can guide the experimental and theoretical researches which are to-day urgently needed.

I. A BRIEF SURVEY ON VORTEX THEORY

The vortex theory can be divided into four parts.

(i) The first part is, in fact, a chapter of Vectorial Analysis. The vector $\vec{V}$ is the velocity of the fluid points in a certain fluid motion at a fixed instant t and the vorticity $\vec{\omega}$ is defined as

$$\vec{\omega} = \text{curl } \vec{V} = \nabla \wedge \vec{V}. \tag{1.1}$$

The starting point is the Stokes Theorem, according to which the flux of $\vec{\omega}$ through an open surface is equal to the circulation of $\vec{V}$ in the closed circuit consisting of the edge of the surface. A consequence is that no vortex filament can begin or end in the fluid. A vortex filament is therefore a closed ring or its ends are located on the boundary of the fluid domain, or at infinity. A consequence is that the intensity of a vortex tube is a constant along the tube. The

intensity of a flat tube or of a tube whose all transverse dimensions are null can be finite. This is the case of the vortex tubes on a vortex sheet and of the isolated concentrated vortex filaments.

Equation (1.1) can be solved with respect to $\vec{V}$. Poincaré's formula gives $\vec{V}$ when the vorticity is known. A particular case is the Biot and Savart formula which expresses the velocity "induced" by an isolated vortex filament. A consequence of Poincaré's formula is that the perturbation flow due to a body moving in an inviscid fluid can be regarded as generated by a vortex sheet distributed over the hull of the body and fulfilling the condition that the fluid adheres to the hull. There is a kinematical equivalence between the body and the vortex sheet.

(ii) The second part deals with the evolution of the vorticity with time under the assumptions that the fluid is inviscid and that the exterior force per unit mass is the gradient of a certain potential. The basic theorems are due to Cauchy and Helmholtz. The intensity of every vortex filament is independent of time and the vortex filaments move with the fluid. This means that every vortex filament is composed of an invariable set of fluid points. Lagrange's theorem follows according to which the fluid motion is irrotational if its starts from rest under the effect of forces continuous with respect to time (shock-free motions). This theorem seems to be contradicted by the possible existence of vorticity in the motion of an inviscid fluid, but the difficulty can be overcome by considering such a motion as the limit of the motion of a real fluid when the viscosity goes to zero. Although the second part of the theory is based on the Euler equation, it only deals with fluid kinematics.

(iii) The third part of the theory concerns the dynamical interaction between flow and vorticity. If the set of fluid points belonging to an arc of vortex filament does not move with the fluid, this interaction cannot be null. The concept of force exerted by the flow on every bound arc of a vortex filament is now classical. Conversely, the set of fluid points belonging to this arc exerts a force equal and opposite on the adjacent sets of fluid points which proceed with the general flow.

As it has been shown by Maurice Roy [1], the system of forces exerted by a steady flow on a body in a uniform motion can be obtained in this way. This led to an important generalization of the Kutta-Joukowski theorem. Later von Karman and Sears have successfully solved the problem for wing profiles in a quasi-rectilinear non uniform motion [2]. The pressure distribution on such profiles has been calculated by the present writer [3]. There exist now

powerful methods of computing the pressure distribution on a wing of finite aspect ratio in the same kind of motion (see, for instance [4]).

The case of bodies of high displacement/length ratio in an unsteady motion is sensibly more intricate than the case of the usual lifting surfaces and there was a need for a general theory. Poincaré's formula gives means for determining such a vortex distribution on the hull and inside the hull that the fluid adhere to the hull. This vortex distribution is kinematically equivalent to the body. But it is not the only vortex distribution with this property. Furthermore if the motion of the fluid about the body is unsteady, any vortex distribution kinematically equivalent to the body varies with time. Lastly the theory would be without practical interest if it were not capable to take into account the effect of the free vortices shed by the body and that of an arbitrarily given incident flow. This paper gives an answer to the problems arising from the afore-mentioned needs.

(iv) The fourth part of the theory concerns vorticity in viscous fluid motions, but it does not fall within the scope of the paper.

II. POINCARE'S FORMULA

VORTEX SHEET

Let $\sum$ be a part of a certain surface. The two sides $\sum_i$, $\sum_e$ of $\sum$ are distinguished from each other. The unit vector $\vec{n}$ normal to $\sum$ is uniquely defined at every point P of $\sum$ and in the direction from $\sum_e$ towards $\sum_i$. We put $\overrightarrow{PP_i} = \vec{n}_P(0+)$, $\overrightarrow{PP_e} = -\vec{n}_P(0+)$, P_i and P_e being the intersections of $\vec{n}_P$ with $\sum_i$ and $\sum_e$ respectively. (Figure 1 and 2).

Let $\sum_i'$, $\sum_e'$ denote the surfaces described by the points P_i', P_e' such that $\overrightarrow{PP_i'} = \frac{\epsilon}{2}\vec{n}_P$, $\overrightarrow{PP_e'} = -\frac{\epsilon}{2}\vec{n}_P$, respectively. We suppose that a vortex $\vec{\omega}$ is continuously distributed between $\sum_i$ and $\sum_e$. $\vec{\omega}(M)$ is normal to $\vec{n}_P$ at every point M of each segment $P_i' P_e'$. When $\epsilon \downarrow 0$, $\epsilon\vec{\omega}(M)$ has a finite limit $\vec{T}(P)$ tangent to $\sum$. Let $\vec{\theta}_P$, $\vec{\tau}_P$ denote two unit vectors tangent to $\sum$ at P, such that the directions $(\vec{n}_P, \vec{\theta}_P, \vec{\tau}_P)$ make a right-handed system, with $\vec{\tau}_P$ in the direction of $\vec{T}_P$. A line $\mathcal{L}$ tangent to $\vec{\tau}$ at each of its points is a vortex filament of the limiting distribution. Let $\mathcal{L}$, $\mathcal{L}_1$ be two lines $\mathcal{L}$ close to each other. Let $\mathcal{C}$ be a line orthogonal to the $\mathcal{L}$'s and containing P. It intersects $\mathcal{L}_1$ at P_1. We may put $\overrightarrow{PP_1} = d\sigma\,\vec{\theta}_P$. For the limiting distribution, $\vec{T}\,\vec{\tau}_P\,d\sigma$ is the flux of the vortex through the area of the infinitely

flat rectangle $P_i P_e P_{e1} P_{i1}$ and is therefore equal to the circulation $d\Gamma$ of the velocity $\vec{V}$ in the closed contour of this rectangle.

Consequently

$$\left[\vec{V}(P_i) - \vec{V}(P_e)\right] \cdot \vec{\theta}_P \, d\sigma = \vec{T}(P) \cdot \vec{\tau}_P \, d\sigma = d\Gamma \quad (2.1)$$

or equivalently :

$$\vec{V}(P_i) - \vec{V}(P_e) = \vec{T}(P) \wedge \vec{n}_P \quad (2.2)$$

Conversely, if the velocity $\vec{V}$ is discontinuous through a surface $\sum$, and if the jump is tangent to $\sum$, then the above formula defines a vortex sheet $\left(\sum, \frac{\vec{T}}{\epsilon}\right)$ with $\vec{T}_P = \vec{n}_P \wedge \left[\vec{V}(P_i) - \vec{V}(P_e)\right]$.

The expression (2.1) is the local intensity of the "vortex ribbon" located between $\mathcal{L}$ and $\mathcal{L}_1$. It is a constant along the ribbon if no vorticity $\vec{\omega}'$ coming from the regions outside $\sum$ joins the distribution $\frac{\vec{T}}{\epsilon}$ over $\sum$. We will see in the next Section that the opposite case is frequent.

POINCARE'S FORMULA

We consider in the fluid a closed surface S with a tangent plane at every point. Let D_i, D_e be the interior and the exterior of S. The unit vector $\vec{n}$ normal to S is in the inward direction. The interior side S_i of S is considered as included in D_i, and the exterior side S_e as included in D_e.

The time t is fixed.

The velocity $\vec{V}$ is supposed continuous and twice continuously differentiable within D_i. Let $\vec{A}$ be a vector function of its origin M and defined by

$$\vec{A}(M) = \frac{1}{4\pi} \iiint_{D_i} \frac{\vec{V}(M')}{MM'} dD_i(M') .$$

We use the classical formula

$$\text{curl curl } \vec{A} = \nabla \operatorname{div} \vec{A} - \Delta \vec{A},$$

where Δ is the Laplace operator : $\Delta = \nabla^2 = \sum_j \frac{\partial^2}{\partial x_j^2}$, and ∇ the operator $\frac{\partial}{\partial x_1}, \frac{\partial}{\partial x_2}, \frac{\partial}{\partial x_3}$, the system of rectangular axes $O(x_1, x_2, x_3)$ being right-handed. By Poisson's formula :

$$\Delta \vec{A}(M) = \begin{cases} -\vec{V}(M) & \text{if } M \in D_i, \\ 0 & \text{if } M \in D_e . \end{cases}$$

Furthermore it is easily seen that

$$\text{curl } \vec{A} = \left[\frac{1}{4\pi} \iint_S \frac{(\vec{n} \wedge \vec{V})_{M'_i}}{MM'} dS(M') + \frac{1}{4\pi} \iiint_{D_i} \frac{\vec{\omega}(M')}{MM'} dD_i(M') \right],$$

$$\operatorname{div} \vec{A} = \left[\frac{1}{4\pi} \iint_S \frac{(\vec{n}.\vec{V})_{M'_i}}{MM'} dS(M') + \frac{1}{4\pi} \iiint_{D_i} \frac{(\operatorname{div} \vec{V})_{M'}}{MM'} dD_i(M') \right].$$

Consequently :

$$\text{curl} \left[\frac{1}{4\pi} \iint_S \frac{(\vec{n} \wedge \vec{V})_{M'_i}}{MM'} dS(M') + \frac{1}{4\pi} \iiint_{D_i} \frac{\vec{\omega}(M')}{MM'} dD_i(M') \right]$$

$$+ \text{grad} \left[\frac{-1}{4\pi} \iint_S \frac{(\vec{n}.\vec{V})_{M'_i}}{MM'} dS(M') + \frac{-1}{4\pi} \iiint_{D_i} \frac{(\operatorname{div} \vec{V})_{M'}}{MM'} dD_i(M') \right] = \tag{2.3}$$

$$= \begin{cases} \vec{V}(M) & \text{if } M \in D_i \\ 0 & \text{if } M \in D_e \end{cases}$$

This is the Poincaré formula.

Let us suppose that the fluid is incompressible. The triple integral in the second term is not necessarily null for sources with a density $\sigma = \text{div } \vec{V}$ could be distributed through D_i. The double integral in the second term represents a source distribution over S with the density $\sigma = (\vec{n} \cdot \vec{V})_{Mi}$. There is a jump of $\vec{V}$ through S. Its normal component $\vec{n}(\vec{V}_e - \vec{V}_i) = -(\vec{n}\vec{V})_{M_i}$. According to (2.2) its tangential jump from $\sum_e$ to $\sum_i$ is that due to a vortex sheet over S, with the vorticity $\frac{1}{\epsilon}(\vec{n} \wedge \vec{V})_{Mi}$.

Poincaré's formula solves the equation

$$\vec{\omega} = \nabla \wedge \vec{V}$$

with respect to $\vec{V}$, when the vorticity $\vec{\omega}$ and div $\vec{V}$ are known inside D_i, if, furthermore, $\vec{V}$ is known on $\sum_i$.

Biot's and Savart's formula - (Figure 3)

Let us suppose that all the points of S are at infinity, that $\text{div } \vec{V} \equiv 0$ and that $\vec{\omega}$ is null everywhere except in a very thin tube $\mathscr{C}_{\delta\sum}$ with a transverse area $\delta\sum$. Let us suppose that the measure of $\mathscr{C}_{\delta\sum}$ goes to zero, while $\vec{\omega}\delta\sum \to \vec{\Gamma}$. The vorticity reduces to a vortex filament $\mathscr{L}$ with the intensity $\vec{\Gamma}$ tangent to $\mathscr{L}$. Let ds denote the element of arc of $\mathscr{L}$.

Then Poincaré's formula gives

$$\vec{V}(M) = \text{curl}\frac{1}{4\pi}\int_{\mathscr{L}}\frac{\vec{\Gamma}(M')}{MM'}ds(M') = \text{curl}\frac{\Gamma}{4\pi}\int_{\mathscr{L}}\frac{\vec{ds}(M')}{MM'}. \qquad (2.4)$$

This is the Biot and Savart formula which gives the velocity induced at M by the vortex filament $\mathscr{L}$ the intensity of which is $\vec{\Gamma}$.

As $\vec{\omega} \equiv 0$ except on $\mathscr{L}$, there is a velocity potential Φ except on $\mathscr{L}$. Let $\sum$ be an open surface whose edge coincides with $\mathscr{L}$ and $\vec{n}$ the unit vector normal to $\sum$, oriented in the positive direction with respect to the arc $\vec{ds}$ of $\mathscr{L}$. One has

$$\vec{V} = \nabla\Phi \text{ with } \Phi = \frac{-\Gamma}{4\pi}\iint_{\sum}\frac{\partial}{\partial n_{M'}}\frac{1}{MM'}\,d\sum(M'), \qquad (2.5)$$

Φ is therefore generated by a distribution of normal dipoles over $\sum$, with the constant density Γ. Of course, Φ is not single-valued. If C is a closed circuit intersecting $\sum$ at P and surrounding $\mathcal{L}$ one time, then the circulation of $\vec{V}$ in that circuit is

$$\int_C \vec{V}\ \vec{ds} = \Gamma\ (C) = \Phi\ (P_i) - \Phi\ (P_e) = \Gamma \ . \qquad (2.6)$$

Application to vortex sheets

Let us consider the part $\delta \sum$ of a vortex sheet. The contribution of $\delta \sum$ to the velocity $\vec{V}$ is given by

$$\delta \vec{V} = \text{curl} \frac{1}{4\pi} \iint_{\delta\Sigma} \frac{\vec{T}(M')}{MM'} d\sum (M') \qquad (2.7)$$

III. VORTEX DISTRIBUTIONS KINEMATICALLY EQUIVALENT TO A HULL SURFACE

Let $\sum$ denote the hull surface of a solid body completely submerged in an unbounded, incompressible fluid at rest at infinity. Let $\vec{V}_E$ denote the velocity of the body and $\vec{\Omega}_E$ its angular velocity. One has

$$\vec{\omega}_E = \text{curl}\ \vec{V}_E = 2\ \vec{\Omega}_E$$

Let D_i - resp. D_e - be the interior - resp. the exterior - of $\sum$, and $\sum_i$, $\sum_e$ the two sides of $\sum$. For convenience, $\sum_i \subset D_i$ and $\sum_e \subset D_e$. The unit vector normal to $\sum$ is in the inward direction. Let $\vec{V}$ denote the velocity of the fluid inside D_e. One has

$$\vec{n}\ \vec{V}_E \equiv \vec{n}\ \vec{V} \text{ on } \sum_e \ . \qquad (3.1)$$

Poincaré's formula applied to $\vec{V}_E$ inside D_e gives :

$$\operatorname{curl}\left[\frac{1}{4\pi}\iint_{\sum/}\frac{(\vec{n}\wedge\vec{V}_E)_{M'_i}}{MM'}\,d\sum(M')+\frac{1}{4\pi}\iiint_{D_i}\frac{\vec{\omega}_E(M')}{MM'}\,dD_i(M')\right]$$

$$+\ \overrightarrow{\operatorname{grad}}\left[\frac{-1}{4\pi}\iint_{\sum}\frac{(\vec{n}\,.\,\vec{V}_E)_{M'_i}}{MM'}\,d\sum(M')\right]\ =\ \begin{cases}\vec{V}_E & \text{if } M\in D_i\,,\\ 0 & \text{if } M\in D_e\,.\end{cases}$$

The same formula applied to $\vec{V}$ inside D_e gives :

$$\operatorname{curl}\left[\frac{-1}{4\pi}\iint_{\sum}\frac{(\vec{n}\wedge\vec{V})_{M'_e}}{MM'}\,d\sum(M')\right]\ +\ \overrightarrow{\operatorname{grad}}\,\frac{1}{4\pi}\iint_{\sum}\frac{(\vec{n}\,.\,\vec{V})_{M'_e}}{MM'}\,d\sum(M')\ =$$

$$=\ \begin{cases}0 & \text{if } M\in D_i\\ \vec{V}(M) & \text{if } M\in D_e\end{cases}$$

Adding these two equations and taking into account the boundary condition (3.1), we get

$$\vec{V}'\ =\ \operatorname{curl}\left[\frac{1}{4\pi}\iint_{\sum}\frac{\vec{T}(M')}{MM'}\,d\sum(M')+\frac{1}{4\pi}\iiint_{D_i}\frac{\vec{\omega}_E(M')}{MM'}\,dD_i(M')\right]\ =$$

$$=\ \begin{cases}\vec{V}_E(M) & \text{if } M\in D_e\\ \vec{V}(M) & \text{if } M\in D_i\,,\end{cases}\qquad(3.2)$$

where

$$\vec{T}(M')\ =\ -\vec{n}_{M'}\ \wedge\left[\vec{V}(M'_e)-\vec{V}_E(M')\right]\ \text{on}\ \sum\ .\qquad(3.3)$$

This shows that the vorticity distribution

$$(\sum, \frac{\vec{T}}{\epsilon}) + (D_i, \vec{\omega}_E), \quad (\epsilon = 0+), \tag{3.4}$$

is kinematically equivalent to the body inside D_e and generates inside D_i a fictitious motion identical with the motion of the body. The relative velocity $\vec{V}_R = \vec{V} - \vec{V}'$ fulfils the condition

$$\vec{V}_R \equiv 0 \text{ on } \sum_i . \tag{3.5}$$

Therefore, the vortex sheet $(\sum, \frac{\vec{T}}{\epsilon})$ allows the fluid to be adherent to the solid wall $\sum_i$ of the body. This gives the image of a very thin boundary layer which the real boundary layer would reduce to if the fluid viscosity μ were going to zero.

It is easily seen that curl $\vec{V} = 0$ inside D_e, so that

$$\vec{V} = \nabla . \Phi \text{ inside } D_e ,$$

Φ being the unique solution of the Neumann problem with the boundary condition

$$\frac{\partial \Phi}{\partial n} = \vec{n}.\vec{V}_E \text{ on } \sum_e .$$

For the sake of brevity, let us put :

$$\vec{J}(M) = \frac{1}{4\pi}\iint_{\sum} \frac{\vec{T}(M')}{MM'} d\sum(M'), \quad \vec{J}_E(M) = \frac{1}{4\pi}\iiint_{D_i} \frac{\vec{\omega}_E(M')}{MM'} dD_i(M'). \tag{3.6}$$

The components of $\vec{J}_E$ are continuous and continuously differentiable inside $D_i + D_e$ (and harmonic within D_e). Those of $\vec{J}$ and of curl $\vec{J}$ are discontinuous through $\sum$ because

$$\left.\begin{matrix} \frac{\partial}{\partial n}\vec{J}(M_i) \\ \frac{\partial}{\partial n}\vec{J}(M_e) \end{matrix}\right\} = \mp\frac{1}{2}\vec{T}(M) + \frac{1}{4\pi}\iint_{\sum}\vec{T}(M')\ \frac{\partial}{\partial n_M}\frac{1}{MM'}\ d\sum(M') .$$

It follows that

$$\left.\begin{matrix} \text{curl}\ \vec{J}(M_i) \\ \text{curl}\ \vec{J}(M_e) \end{matrix}\right\} = \mp\frac{1}{2}(\vec{n}\wedge\vec{T})_M + \frac{1}{4\pi}\iint_{\sum}\text{curl}_M\ \frac{\vec{T}(M')}{MM'}\ d\sum(M') \qquad (3.7)$$

Equation (3.2) expresses that

$$\text{curl}\ \vec{J}(M) = \vec{V}_E(M) - \text{curl}\ \vec{J}_E(M) \quad \text{when M describes } D_i , \qquad (3.8)$$

and therefore entails

$$-\frac{1}{2}(\vec{n}\wedge\vec{T})_M + \frac{1}{4\pi}\iint_{\sum}\text{curl}_M\frac{\vec{T}(M')}{MM'}\,d\sum(M') = \vec{V}_E(M) - \text{curl}\ \vec{J}_E(M), \quad \underline{M\in\sum} \qquad (3.9)$$

As

$$\text{curl}\left[\vec{V}_E(M) - \text{curl}\ \vec{J}_E(M)\right] \equiv 0 \ \text{ within } D_i ,$$

$$\text{div}\left[\vec{V}_E(M) - \text{curl}\ \vec{J}_E(M)\right] \equiv 0 \ \text{ within } D_i ,$$

the difference $\vec{V}_E$ - curl $\vec{J}_E$ is within D_i the gradient of a harmonic potential, and, for (3.8) to be satisfied everywhere inside D_i, it suffices that it be satisfied on $\sum_i$. Thus :

$$(3.8) \Longleftrightarrow (3.9)$$

Consequently, $\vec{T}$ has to be determined by (3. 9) and the complementary condition

$$\vec{n}\,\vec{T} \equiv 0 \quad \text{on} \sum . \tag{3. 9'}$$

Equation (3. 9) is a vectorial Fredholm equation of the 2nd kind. It is singular since $\vec{T} = \lambda\,\vec{n}$, λ being a constant, is a solution of the homogeneous equation

$$-\frac{1}{2}(\vec{n} \wedge \vec{T})_M + \frac{1}{4\pi}\iint_{\sum} \operatorname{curl}_M \frac{\vec{T}(M')}{MM'}\, d\sum(M') = 0 .$$

For (3. 9) to have solutions, it is necessary and sufficient that its right side - say $\vec{B}$ (M) - be orthogonal to $\vec{n}$ on $\sum$:

$$\iint_{\sum} \vec{n}.\vec{B}\, d\sum = 0 \tag{3. 10}$$

This requirement is fulfilled because $\vec{V}_E$ and $\operatorname{curl}\vec{J}_E$ are divergenceless inside D_i. Hence, if $\vec{T}'$ is a particular solution of the complete equation (3. 9), the general solution is

$$\vec{T} = \vec{T}' + \lambda\,\vec{n} .$$

But $\vec{n}\,\vec{T}'$ = const. = m on $\sum$, and therefore

$$\boxed{\vec{T} = \vec{T}' - m\,\vec{n}} \tag{3. 11}$$

is the only solution which fulfils both (3. 9) and (3. 9') [1]

(1) The proof that (3. 10) is sufficient and that $\vec{n}.\vec{T}'$ = const. on $\sum$ has been omitted because it is possible to substitute for (3. 9) a scalar equation which does give rise to no difficulty (see Ch. VI, eq. (6. 6'). An equation similar to (3. 9) has been considered by J. Delsarte [5] in the case of a fluid motion inside a closed vessel. In Ch. V, we will deal with an equation (5. 7) analogous to (3. 9) and (6. 6').

$\vec{T}$ being determined in that manner, the velocity $\vec{V}'$ generated by the vortex distribution $\frac{\vec{T}}{\epsilon}$ on $\sum$ and $\vec{\omega} = \vec{\omega}_E$ inside D_i, is equal to $\vec{V}_E$ within D_i. Therefore, as the jump of $\vec{V}'$ through $\sum$ is purely tangential, one has $\vec{n}\,\vec{V}' = \vec{n}\,\vec{V}_E$ on $\sum_e$ and $\vec{V}'$ evidently coincides with the velocity $\vec{V}$ of the irrotational fluid motion inside D_e.

The above results can be extended to the case when there exists inside D_e some incident flow of velocity $\vec{V}_o$. It suffices to replace $\vec{V}_E$ by $\vec{V}_E - \vec{V}_o$ into the right side of (3.9). The resulting velocity is

$$\vec{V}' + \vec{V}_o = \begin{cases} \vec{V}_E & \text{inside } D_i \,, \\ \vec{V} & \text{inside } D_e \,. \end{cases}$$

If D_e were bounded by solid walls and (or) a free surface, one would have to add singularities distributed beyond the boundaries. These singularities would be linear functionals of $\vec{T}$ and therefore $\vec{T}$ would be found on the right side of (3.9) too.

Furthermore, it is seen that the incident flow $\vec{V}_o$ could be due totally or partly to free vortices shed by the hull itself. In such cases, the right side of (3.9) would depend upon the history of the motion of the body.

Various remarks

(i) It is to be noted that the vorticity inside D_i could be chosen arbitrarily. $\vec{J}_E$ should be replaced by $\vec{J}_1 = \frac{1}{4\pi} \iiint_{D_i} \frac{\vec{\omega}_1(M)}{MM'}\, dD_i(M')$ The possibility condition (3.10) would still be fulfilled. And, for the same reasons as above, $\vec{T}$ would still be determined uniquely by (3.9) and (3.9'). But, inside D_i, the resulting velocity could no longer be identical with $\vec{V}_E$.

In all the cases, the resulting velocity $\vec{V}$ on $\sum$ - i.e. between $\sum_i$ and $\sum_e$ - is given by

$$\vec{V}(M) = \frac{1}{2}\left[\vec{V}(M_e) + \vec{V}(M_i)\right] \qquad (3.12)$$

(ii) When $\vec{T}$ is determined so that $\vec{V}(M_i) = \vec{V}_E(M_i)$, the jump of $\vec{V} - \vec{V}_E$ through $\sum$ is equal to $\vec{V}_R(M_e)$, and

$$\vec{V}_R(M) = \frac{1}{2}\vec{V}_R(M_e) \text{ on } \sum .$$

$\vec{T}$ is perpendicular to $\vec{V}_R$ on $\sum$ and the edges of the vortex-ribbons on $\sum$ are orthogonal to the streamlines $\mathcal{C}$ of the relative motion over $\sum_e$.

If, furthermore, no free vortices are shed by the hull, these edges make closed rings $\mathcal{L}$ on $\sum$. (Figure 4). Let $d\sigma$ be the element of arc of a particular streamline $\mathcal{C}$. The intensity of the vortex ribbon between two rings $\mathcal{L}$, $\mathcal{L}'$ close to each other is

$$d\Gamma(M) = V_R(M_e)\, d\sigma(M_e) . \tag{3.13}$$

(iii) If $\vec{\omega} \equiv 0$ inside D_i, then, $d\Gamma$ is a constant when M describes $\mathcal{L}$, and the fluid motion inside D_e and inside D_i depends on the velocity potential

$$\Phi(M) = \frac{-1}{4\pi}\iint_{\sum} \Gamma(M')\, \frac{\partial}{\partial n_{M'}}\, \frac{1}{R}\, d\sum(M'), \quad (R = MM')$$

This potential is generated by a normal dipole distributions. Γ is determined up to an additive constant.

If $\vec{\omega} \not\equiv 0$ inside D_i, then, $d\Gamma$ is no longer a constant between $\mathcal{L}$ and $\mathcal{L}'$; ds being the element of arc of $\mathcal{L}$, one has

$$\frac{\partial^2 \Gamma}{\partial\sigma\partial s}\, d\sigma\, ds = -\vec{\omega}\,\vec{n}\, d\sigma\, ds$$

The same phenomenon happens in the case of the vortex distributions $(D_i,\ 2\vec{\omega}_E) + (\sum, \frac{\vec{T}}{\epsilon})$ - see Section V, Figure 5.1.

IV. FREE AND BOUND PARTS OF A VORTEX SHEET

EULER'S EQUATION IN A MOVING SYSTEM OF AXES

The fluid is assumed to be inviscid, incompressible and homogeneous. Consequently, its mass density ρ is independent of position and time.

Let $\sum$ be the hull surface of a body moving in the fluid.

Let S' , S denote two right-handed systems of axes. S' is at rest and the fluid motion with respect to S' is said the "absolute" motion of the fluid. S moves with the body and the motion with respect to S is said the "relative" motion. The subscript R refers to the relative motion. $\vec{F}$ is the absolute exterior force ; $\vec{V}$, $\vec{\omega}$ = curl $\vec{V}$ and $\vec{\gamma} = \frac{d\vec{V}}{dt}$ are the absolute velocity, vorticity and acceleration. The instantaneous motion of S with respect to S' is termed the "entrainment" motion. It consists of the addition of a rotation about a certain axis $\vec{\Delta}$ and of a translation parallel to $\vec{\Delta}$. If O and M are two points of S , the entrainment velocity $\vec{V}_E(M)$ of M can be expressed as

$$\vec{V}_E(M) = \vec{V}_E(O) + \vec{\Omega}_E \wedge \overrightarrow{OM} ,$$

where $\vec{\Omega}_E$ is the angular entrainment velocity.

The relative velocity of a fluid point P located at M at the instant t is

$$\vec{V}_R(P) = \vec{V}(P) - \vec{V}_E(M) .$$

One has

$$\vec{\gamma}(P) = (\vec{\gamma}_R + \vec{\gamma}_E + 2\vec{\Omega}_E \wedge \vec{V}_R)_P$$

$$\vec{\omega}_R = \text{curl } \vec{V}_R = \vec{\omega} - 2\vec{\Omega}_E$$

and the exterior force $\vec{F}_R$ per unit mass in the relative motion is

given by

$$\vec{F}_R = \vec{F} - \vec{\gamma}_E - 2\vec{\Omega}_E \wedge \vec{V}_R$$

Let p be the pressure. The Euler equation in the system S can be written in the form :

$$\frac{1}{\rho}\nabla p = \vec{F}_R - \frac{d\vec{V}_R}{dt} = (\vec{F} - \vec{\gamma}_E - 2\vec{\Omega}_E \wedge \vec{V}_R) -$$

$$- \left[\frac{\partial \vec{V}_R}{\partial t} + \vec{\omega}_R \wedge \vec{V}_R + \nabla\left(\frac{1}{2}V_R^2\right)\right] =$$

$$= \vec{F} - \frac{\partial \vec{V}}{\partial t} - \vec{\omega} \wedge \vec{V}_R - \nabla\left(\frac{1}{2}V_R^2\right) + \frac{1}{2}\nabla\left(\Omega_E^2 r^2\right), \quad (4.1)$$

where r is the distance from the axis $\vec{\Delta}$.

We suppose that $\vec{F} = \nabla \mathcal{U}$, and put

$$p_d = p - \rho \mathcal{U} \quad , \quad p_s = \rho \mathcal{U} \qquad (4.2)$$

p_s and p_d are the hydrostatic pressure and the hydrodynamic pressure respectively. Equation (4.1) becomes

$$\frac{1}{\rho}\nabla p_d = -\frac{\partial \vec{V}}{\partial t} - \vec{\omega} \wedge \vec{V}_R - \nabla\left(\frac{1}{2}V_R^2\right) + \nabla\left(\frac{1}{2}\Omega_E^2 r^2\right). \quad (4.1')$$

FREE AND BOUND VORTICES

From the Euler equation in the system S' of axes, namely :

$$\frac{1}{\rho}\nabla p_d = -\frac{d\vec{V}}{dt} = -\frac{\partial \vec{V}}{\partial t} - \vec{\omega} \wedge \vec{V} - \nabla\left(\frac{1}{2}V^2\right)$$

it follows that

$$\text{curl}\ \left(\frac{\partial \vec{V}}{\partial t} + \vec{\omega} \wedge \vec{V}\right) \equiv 0 .$$

Taking into account the continuity equation, one obtains the basic Helmholtz equation

$$\frac{d}{dt}\left(\frac{\vec{\omega}}{\rho}\right) = \left(\frac{\vec{\omega}}{\rho} . \nabla\right) \vec{V} \quad (1) \qquad (4.3.)$$

This equation entails the following consequences :

(i) If $\vec{F}$ and the boundary conditions are continuous with respect to time, and if the fluid starts from rest, then

$$\vec{\omega} \equiv 0 \quad \text{everywhere at every} \quad t .$$

(ii) Every vortex filament is made of an invariable set of fluid points.

(iii) The circulation of the velocity in any closed fluid circuit is time-invariant.

According to consequence (i), the absolute fluid motion should be irrotational everywhere. This explains why the concept of velocity potential is of importance in the motions of inviscid fluids. However, this consequence does not hold if there exist regions where $\vec{F}$ is not the gradient of a potential $\mathcal{U}$. This is obviously the case when the fluid is submitted to the condition of adherence to solid walls.

For this reason, the vortices existing in the motion of an inviscid fluid about a set of solid bodies have to be considered as originating on the surfaces of these bodies. Thus every vortex filament is made of two sets of fluid points : one of these two sets is at rest with respect to the surface of a solid body, the second one is free and moves with the fluid.

---

(1) This equation holds if the fluid is not incompressible, provided that

$$\rho = \frac{1}{h\,(p)}$$

BEHAVIOR OF THE FREE PART OF A VORTEX SHEET

Let dE be the set of fluid points belonging to an element $d\sum$ of a vortex sheet. The sheet begins or ends on the surface $\sum$ of a body moving in the fluid. Its bound part is located between the interior side $\sum_i$ and the exterior side $\sum_e$ of $\sum$ and the relative velocity $\vec{V}_R$ of every fluid set belonging to this bound part is null. On the contrary if dE belongs to the free part $\sum_f$ of the vortex sheet, it moves with the relative velocity $\vec{V}_R$ inside the sheet. Let $\sum_{fi}$, $\sum_{fe}$ denote the two sides of $\sum_f$, $\vec{n}$ be the unit vector normal to $\sum_f$ in the direction from $\sum_{fe}$ towards $\sum_{fi}$, and let ϵ be the infinitely small thickness of the sheet. The vorticity inside the sheet is $\vec{\omega}_f = \frac{\vec{T}_f}{\epsilon}$ with

$$\vec{T}_f(M) = -\vec{n}_M \wedge \left[\vec{V}_R(M_e) - \vec{V}_R(M_i)\right] ,$$

$$M \in \sum_f , \quad \overrightarrow{MM_i} = \vec{n}_M \cdot \frac{\epsilon}{2} ; \quad \overrightarrow{M_e M} = \vec{n}_M \cdot \frac{\epsilon}{2} ,$$

and the relative velocity of the fluid point located at M is

$$\vec{V}_R(M) = \frac{1}{2}\left[\vec{V}_R(M_e) + \vec{V}_R(M_i)\right] .$$

Since there is no exchange of matter between the sheet and the adjacent fluid sets

$$\vec{n}_M \cdot \vec{V}_R(M_e) = \vec{n}_M \cdot \vec{V}_R(M_i) = \vec{n}_M \cdot \vec{V}_R(M) = 0 . \quad (4.4)$$

Let $\vec{I}_R(dE)$ be the momentum of dE in the relative motion. We have

$$\frac{d}{dt}\vec{I}_R(dE) = \rho \frac{\partial \vec{V}_R}{\partial t} \epsilon \, d\sum_f + \rho \left\{ \left[\vec{n}_M \cdot \vec{V}_R(M_i)\right] \cdot \vec{V}_R(M_i) - \left[\vec{n}_M \cdot \vec{V}_R(M_e)\right] \cdot \vec{V}_R(M_e) \right\} d\sum_f \quad (4.5)$$

Furthermore, as the pressure does not depend on the axes, we have, by the momentum theorem

$$\frac{d}{dt}\,\vec{I}_R\,(dE) = \vec{n}_M\left[p_d\,(M_e) - p_d\,(M_i)\right] d\Sigma_f\,(M)\,.$$

This quantity is null because of (4.4) and $\epsilon = +0$. Consequently

$$p_d\,(M_e) = p_d\,(M_i)\,. \tag{4.6}$$

Hence the pressure is continuous through the free vortex sheet.

For the sake of simplicity, let us suppose that we deal with only one moving body.

We also assume that we deal with one vortex sheet only. The vorticity generated by the body is thus concentrated inside that vortex sheet.

The absolute velocity $\vec{V}$ in the domain D'_e really occupied by the fluid can be divided into three components:

- the velocity $\vec{V}_d$ induced by the vortex distribution $(D_i\,,\ 2\vec{\Omega}_E) + (\Sigma, \frac{1}{\epsilon}\vec{T})$ which permits the fluid located between Σ_i and Σ_e to be at rest with respect to the hull;
- the velocity $\vec{V}_o$ of some incident flow,
- the velocity $\vec{V}_f$ due to the free vortex sheet shed by the body.

According to Section III, we have

$$\vec{V}_d + \vec{V}_f = \operatorname{curl}\left[\frac{1}{4\pi}\iint_{\Sigma}\frac{\vec{T}(M')}{MM'}\,d\Sigma(M') + \frac{1}{4\pi}\iiint_{D_i}\frac{2\vec{\Omega}_E(M')}{MM'}\,dD_i(M')\right.$$
$$\left. + \frac{1}{4\pi}\iint_{\Sigma_f}\frac{\vec{T}_f(M')}{MM'}\,d\Sigma_f\,(M')\right] \tag{4.7}$$

with the boundary conditions

$$\begin{cases} \vec{V}_d\,(M_i) \equiv \vec{V}_E\,(M_i) - \vec{V}_o\,(M_i) - \vec{V}_f\,(M_i) \text{ on } \sum_i \\ \vec{n}_M \cdot \vec{T}\,(M) \equiv 0 \text{ on } \sum . \end{cases} \tag{4.8}$$

$\vec{V}_o$ is due to causes located outside $\sum_e$ and one may consider that there exists a velocity potential Φ_o such that

$$\vec{V}_o = \nabla \Phi_o$$

at least in the region of D'_e close to $\sum_e$ and inside $D_i + \sum$.

$\vec{V}_d + \vec{V}_f$ is irrotational outside $\sum + \sum_f$. Therefore, M_e and M_i being given on $\sum_{f_e}$ and $\sum_{f_i}$, respectively - with $\overrightarrow{M_e M_i} = \vec{n}_M\,(0+)$, one can find a path starting from M_i and arriving at M_e so that $\vec{V}$ be irrotational everywhere along this path. Putting

$$\vec{V} = \nabla \Phi , \tag{4.9}$$

we obtain, by integrating (4.1) along the path :

$$p_d\,(M_e) - p_d\,(M_i) = -\rho \left(\frac{\partial \Phi}{\partial t}\right)_{M_i}^{M_e} - \frac{1}{2}\rho \left(V_R^2\right)_{M_i}^{M_e}$$

Hence (4.6) gives :

$$\boxed{\left(\frac{\partial \Phi}{\partial t}\right)_{M_i}^{M_e} + \frac{1}{2}\left[V_R^2\,(M_e) - V_R^2\,(M_i)\right] = 0} \tag{4.10}$$

One has

$$\vec{T}_f\,(M) = -\vec{n}_M \wedge \left[\vec{V}_R\,(M_e) - \vec{V}_R\,(M_i)\right]$$

Consequently

$$\vec{T}_f(M) \wedge \vec{V}_R(M) = \vec{V}_R(M) \wedge \left\{ \vec{n}_M \wedge \left[\vec{V}_R(M_e) - \vec{V}_R(M_i) \right] \right\}$$

$$= \frac{1}{2} \vec{n}_M \left[V_R^2(M_e) - V_R^2(M_i) \right] \qquad (4.11)$$

Thus, when the relative motion is steady, $\vec{T}_f(M)$ and $\vec{V}_R(M)$ are colinear, and both are in the direction of the bissectrix of the angle $(\vec{V}_R(M_e), \vec{V}_R(M_i))$.

If the relative motion is unsteady, $|V_R(M_e)|$ and $|V_R(M_i)|$ are no longer equal to each other and therefore the direction of $\vec{T}(M)$ is no longer that of the bissectrix.

Equation (4.10) expresses the dynamical equilibrium of any part of a free vortex sheet.

DEFINITION OF THE FORCE EXERTED BY THE FLOW ON AN ELEMENT OF THE BOUND VORTEX SHEET ADHERING TO A MOVING BODY

Let us consider now a set dE of fluid points belonging to the element $d\sum$ of the bound vortex sheet.

We have

$$\vec{V}_R(M_i) = 0 , \qquad \text{and} \qquad \frac{d}{dt}\vec{I}(dE) = 0 .$$

But the expression for $\frac{d}{dt}\vec{I}(dE)$ does not reduce to $\left[p_d(M_e) - p_d(M_i)\right] \vec{n}_M \, d\sum$, for, because of the adherence of the fluid to $\sum_i$, a force $-d\vec{\mathcal{F}}_T$ is exerted by the element $d\sum$ of the hull surface on dE. The equilibrium of dE requires :

$$0 = \frac{d}{dt}\vec{I}(dE) = -\overrightarrow{d\mathcal{F}_T} + \left[p_d(M_e) - p_d(M_i) \right] \vec{n}_M \, d\sum \qquad (4.12)$$

Conversely, the equation

$$\overrightarrow{d\mathscr{F}_T} = \left[p_d (M_e) - p_d (M_i) \right] \vec{n}_M \, d\Sigma (M) \qquad (4.13)$$

shows that the fluid sets adjacent to dE exert the force $\overrightarrow{d\mathscr{F}_T}$ on the set dE.

V. THE STRUCTURE OF THE VORTEX SHEETS GENERATED BY A MOVING BODY

Two cases will be studied in the present Section.

(i) One free vortex sheet only is shed by the body,

(ii) Two vortex sheets are shed by the body.

In the first case the fluid motion is irrotational everywhere outside the body, except through the free vortex sheet Σ_f. In the second case, if the fluid motion is unsteady, vorticity is necessarily distributed in a certain volume downstream from the body.

A - STEADY MOTION IN THE CASE OF A UNIQUE FREE VORTEX SHEET

We can define on Σ such a vortex $\frac{\vec{T}'}{\epsilon}$ that each of the two vortex distributions

$$\mathscr{D}_1 = (D_i , 2\vec{\Omega}_E) + (\Sigma, \frac{\vec{T}'}{\epsilon}) \qquad (5.1)$$

$$\mathscr{D}_2 = (\Sigma , \frac{\vec{T}-\vec{T}'}{\epsilon}) + (\Sigma_f , \frac{\vec{T}_f}{\epsilon}) \qquad (5.2)$$

be complete and that they sum up to the total vortex distribution

$$\mathscr{D} = (D_i , 2\vec{\Omega}_E) + (\Sigma , \frac{\vec{T}}{\epsilon}) + (\Sigma_f , \frac{\vec{T}_f}{\epsilon}) \qquad (5.3)$$

The vortex family $(D_i , 2\vec{\Omega}_E) + (\Sigma , \frac{\vec{T'}}{\epsilon})$

The new vortex distribution (5. 1) will be chosen so that the velocity

$$\vec{V}'(M) = \operatorname{curl} \frac{1}{4\pi} \iint_{\Sigma} \frac{\vec{T}'(M')}{MM'} d\Sigma(M') + \operatorname{curl} \frac{1}{4\pi} \iiint_{D_i} \frac{2\vec{\Omega}_E(M')}{MM'} dD_i(M') \tag{5.4}$$

be identically null inside D_e . Inside D_i , $\vec{V}'$ is the velocity of a fictitious fluid motion due to a certain force $\vec{F} + \vec{F}'$ per unit mass (determined in Section VI). One has :

$$\operatorname{curl} \vec{V}' \equiv 2\vec{\Omega}_E \quad \text{inside} \quad D_i . \tag{5.5}$$

The condition

$$\vec{V}'(M) \equiv 0 \quad \text{if} \quad M \in D_e \tag{5.6}$$

is obviously equivalent to the condition

$$\vec{V}'(M_e) \equiv 0 \quad \text{on} \quad \Sigma_e . \tag{5.6'}$$

The fictitious fluid motion defined by $\vec{V}'$ is one of the fluid motions which could exist inside the vessel bounded by Σ_i if the body were at rest.

(5. 6') means that

$$\operatorname{curl} \frac{1}{4\pi} \iint_{\Sigma} \frac{\vec{T}'(M')}{M'M_e} d\Sigma(M') \equiv - \operatorname{curl} \frac{1}{4\pi} \iiint_{D_i} \frac{2\vec{\Omega}_E(M')}{M_eM'} dD_i(M') \text{ on } \Sigma_e$$

Because of the discontinuity of the left-hand side through Σ , this equation can be written in the form :

$$\frac{1}{2}\vec{n}_M \wedge \vec{T}'(M) + \text{curl}\frac{1}{4\pi}\iint_{\Sigma}\frac{\vec{T}'(M')}{M'M}\,d\Sigma(M') =$$

$$-\text{curl}\frac{1}{4\pi}\iiint_{D_i}\frac{2\vec{\Omega}_E(M')}{M_eM'}\,dD_i(M') \,. \qquad (5.7)$$

where M is located on Σ .

This is a Fredholm vectorial equation of the 2nd kind which is quite analogous to (3. 9) in spite of the fact that the condition to be verified concerns the side Σ_e of Σ instead of the side Σ_i.

First one observes that this equation is singular, since the left hand side vanishes when $\vec{T}'(M) = \lambda\vec{n}_M$, λ being a constant. The right-hand side must therefore satisfy a possibility condition.

As

$$\iint_{\Sigma}\vec{n}(M_e)\,.\,\left[\text{curl}\frac{1}{4\pi}\iint_{\Sigma}\frac{\vec{T}'(M')}{M_eM'}\,d\Sigma(M')\right]\,d\Sigma(M_e)$$

$$=\iiint_{D_e}\text{div curl}\left[\frac{1}{4\pi}\iint_{\Sigma}\frac{T'(M')}{MM'}\,d\Sigma(M')\right]\,dD_e(M) = 0 \,,$$

one must have

$$\iint_{\Sigma}\vec{n}(M_e)\,.\,\left[\text{curl}\frac{1}{4\pi}\iiint_{D_i}\frac{2\vec{\Omega}_E(M')}{M_eM'}\,dD_i(M')\right]\,d\Sigma(M_e) = 0 \,. \qquad (5.8)$$

This condition is obviously fulfilled since the latter expression is equal to

$$\iiint_{D_e} \operatorname{div}\ \operatorname{curl}\left[\frac{1}{4\pi}\iiint_{D_i}\frac{2\vec{\Omega}_E(M')}{MM'}d\Sigma(M')\right]dD_e(M) = 0 .$$

It follows, as in the case of (3.9), that the solutions of (5.7) are

$$\vec{T}'(M) = \vec{T}'_1(M) + \lambda\vec{n}_M$$
$$\text{with} \qquad \vec{n}\ \vec{T}'_1 = \text{constant on } \Sigma \qquad (5.9)$$

and therefore that there exists one, and only one, vortex $\frac{\vec{T}'}{\epsilon}$ which is tangent to Σ and satisfies (5.7).

One has

$$\vec{T}'(M) = -\vec{n}_M \wedge\left[\vec{V}'(M_e) - \vec{V}'(M_i)\right] = \vec{n}_M \wedge\vec{V}'(M_i) \text{ on } \Sigma . \qquad (5.10)$$

At each point M on Σ, $(\vec{n}_M, \vec{\theta}_M, \vec{\tau}_M)$ are three unit vectors making a right-handed system ; $\vec{n}$ is normal to Σ in the inward direction, and $\vec{\tau}$ is in the direction of $\vec{T}'$. The lines $\mathcal{C}'$ tangent to $\vec{\theta}'$ and the lines $\mathcal{L}'$ tangent to $\vec{\tau}'$ determine on Σ two systems of orthogonal curvilinear coordinates, the arcs σ' on $\mathcal{C}'$ and s' on $\mathcal{L}'$ being oriented in the direction of $\vec{\theta}'$ and $\vec{\tau}'$ respectively.

Let us consider (Figure 5.1) two lines $\mathcal{L}'(\sigma_1)$ and $\mathcal{L}'(\sigma'_2)$ close to each other and two lines $\mathcal{C}'(s'_1)$, $\mathcal{C}'(s'_1 + ds')$. The flux $d\Gamma'$ of the vortex $\frac{\vec{T}}{\epsilon}$ through the area $M_{e_1} M_{e_2} M_{i_2} M_{i_1}$ is equal to $\vec{V}'(M_i)\vec{\theta}'_M\, d\sigma'$ (where $d\sigma' = \sigma_2' - \sigma_1'$). Through the area $M'_{e_1} M'_{e_2} M'_{i_2} M'_{i_1}$, it is equal to $\vec{V}'(M'_i)\vec{\theta}_{M'}\, d\sigma' = d\Gamma' - \vec{\omega}\vec{n}\, d\sigma'\, ds'$ with $ds' = s'_2 - s'_1$. Hence $\frac{\partial^2}{\partial s'\,\partial\sigma}\Gamma'(s,\theta) = -\vec{\omega}.\vec{n} = -2\vec{\Omega}_E . \vec{n}$. This results from the fact that the vortex ribbon whose edges are $\mathcal{L}'(\sigma'_1)$ and $\mathcal{L}'(\sigma'_2)$ loses, between $\mathcal{C}'(s'_1)$ and $\mathcal{C}'(s'_2)$, vortex filaments entering D_i.

The $\mathcal{L}'_s$ are closed rings, since the ends of any segment of

a vortex filament $2\vec{\Omega}_E$ interior to D_i necessarily belong to the same line $\mathcal{L}'$.

The vortex family $\left(\sum, \frac{\vec{T} - \vec{T}'}{\epsilon}\right) + \left(\sum_f, \frac{\vec{T}_f}{\epsilon}\right)$.

The velocity $\vec{V}''$ induced by this vortex distribution is given by

$$\vec{V}''(M) = \operatorname{curl}\left[\frac{1}{4\pi}\iint_{\sum} \frac{(\vec{T} - \vec{T}')_{M'}}{MM'} d\sum(M') + \frac{1}{4\pi}\iint_{\sum_f} \frac{\vec{T}_f(M')}{MM'} d\sum_f(M')\right]. \tag{5.11}$$

$\vec{V}''$ is irrotational everywhere except on $\sum$ and on $\sum_f$. On $\sum_e$, one has $\vec{V}''(M_e) = (\vec{V} - \vec{V}_o)_{M_e}$ and, on $\sum_i$, $\vec{V}''(M_i) = (\vec{V}_E - \vec{V}' - \vec{V}_o)_{M_i}$ Accordingly :

$$\vec{V}''(M_e) - \vec{V}''(M_i) = \vec{V}_R(M_e) + \vec{V}'(M_i). \tag{5.12}$$

Let $\vec{\tau}$, $\vec{\theta}$ denote two unit vectors on $\sum$, $\vec{\tau}$ (M) being in the direction of $(\vec{T} - \vec{T}')_{M'}$, so that the three directions $(-\vec{n}, \vec{\theta}, \vec{\tau})$ make a right-handed system. It follows that $\vec{\theta}$ (M) is in the direction of $\vec{V}_R(M_e) + \vec{V}'(M_i)$. The curves $\mathcal{C}$ tangent everywhere at $\vec{\theta}$ and the vortex filaments $\mathcal{L}$ on $\sum$ define a system of orthogonal coordinates (σ , s) increasing in the directions of $\vec{\theta}$ and $\vec{\tau}$, respectively.

We may consider $\vec{V}''$ as generated by a normal dipole distribution on $\sum + \sum_f$. Let μ and μ_f denote the density of the distributions on $\sum$ and $\sum_f$, respectively. We have :

$$\vec{V}'' = \nabla\Phi'', \quad \Phi'' = \Phi_d + \Phi_f, \quad \vec{V}_d = \nabla\Phi_d, \quad \vec{V}_f = \nabla\Phi_f,$$

$$\Phi_d(M) = \frac{-1}{4\pi}\iint_{\sum} \mu(M') \frac{\partial}{\partial n_{M'}} \frac{1}{MM'} d\sum(M')$$

$$\Phi_f(M) = \frac{-1}{4\pi}\iint_{\sum_f} \mu_f(M') \frac{\partial}{\partial n_{M'}} \frac{1}{MM'} d\sum(M') \tag{5.13}$$

Let $\sum_{f_1}$, $\sum_{f_2}$, denote the two sides of $\sum_f$, $\vec{n}_f$ on $\sum_f$ being in the direction from $\sum_{f_2}$ towards $\sum_{f_1}$. One has

$$\mu(M) = \Phi_d(M_e) - \Phi_d(M_i) \ , \ \mu_f(M_f) = \Phi_f(M_{f_2}) - \Phi_f(M_{f_1}) \ ;$$

$$\frac{\partial \mu}{\partial \sigma} = \frac{\partial \Gamma}{\partial \sigma} \text{ with } d\Gamma = \left[\vec{V}_R(M_e) + \vec{V}'(M_i)\right] \cdot \vec{\theta}(M)\, d\sigma \ ;$$

$$\frac{\partial \mu_f}{\partial \sigma_f} = \frac{\partial \Gamma_f}{\partial \sigma_f} \text{ with } d\Gamma_f = \left[\vec{V}(M_{f_2}) - \vec{V}(M_{f_1})\right] \cdot \vec{\theta}_f(M)\, d\sigma_f =$$

$$= \left[\vec{V}_R(M_{f_2}) - \vec{V}_R(M_{f_1})\right] \vec{\theta}_f(M)\, d\sigma_f . \qquad (5.14)$$

Let $\mathcal{B}$ denote (Figure 5.2) the intersection of $\sum$ with $\sum_f$. Two parts $\sum_1$ and $\sum_2$ of $\sum$ are adjacent to each other along $\mathcal{B}$. The part $\sum_1$ corresponds to $\sum_{f_1}$ and the part $\sum_2$ to $\sum_{f_2}$. Let μ_1, μ_2 be the determination of μ on $\sum_1$ and $\sum_2$ respectively. Let $\mathcal{L}_f$, $\mathcal{L}_1^\circ$, $\mathcal{L}_2^\circ$ be three vortex filaments intersecting $\mathcal{B}$ at the same point B° and located on $\sum_f$, $\sum_1$, $\sum_2$, respectively.

Similarly, $\mathcal{L}_f$, $\mathcal{L}_1$, $\mathcal{L}_2$ intersect $\mathcal{B}$ at the same point B and $\mathcal{L}'_f$, $\mathcal{L}'_1$, $\mathcal{L}'_2$ intersect $\mathcal{B}$ at B'. The points B and B' are chosen in opposite directions with respect to B°. Thus $\mathcal{L}_f^\circ$ belongs to the vortex ribbon L_f, the edges of which are $\mathcal{L}_f$, $\mathcal{L}'_f$. Similarly $\mathcal{L}_1^\circ$ belongs to the vortex ribbon L_1 and $\mathcal{L}_2^\circ$ to the vortex ribbon L_2, the edges of L_1 being $\mathcal{L}_1$, $\mathcal{L}'_1$, while those of L_2 are $\mathcal{L}_2$, $\mathcal{L}'_2$. Let M_f, M'_f be the intersection points with $\mathcal{L}_f$, $\mathcal{L}'_f$ of the curve $\mathcal{C}_f$ intersecting $\mathcal{L}_f^\circ$ at M_f°. Let us define in a similar manner the points M_1 and M'_1 on $\mathcal{L}_1$ and $\mathcal{L}'_1$, and the points M_2, M'_2 on $\mathcal{L}_2$ and $\mathcal{L}'_2$.

We now suppose that M_f°, M_1° and M_2° are chosen so that

$$M_f^\circ B^\circ = O(\eta) \ , \ M_1^\circ B^\circ = O(\eta) \ , \ M_2^\circ B_2^\circ = O(\eta) \ , \qquad (5.15)$$

η being a small length that we shall finally equate to zero.

Let $\Gamma''(C)$ be the circulation of $\vec{V}''$ in some closed circuit C.

We consider the following circuits :

$$C^\circ : \quad M^\circ_{e_2} \quad M^\circ_{f_2} \quad M^\circ_{f_1} \quad M^\circ_{e_1} \quad M^\circ_{i_1} \quad M^\circ_{i_2} \quad M^\circ_{e_2} \quad ,$$

$$C_1 : \quad M_{e_1} \quad M'_{e_1} \quad M'_{f_1} \quad M_{f_1} \quad M_{e_1} \quad ,$$

$$C_2 : \quad M'_{e_2} \quad M_{e_2} \quad M_{f_2} \quad M'_{f_2} \quad M'_{e_2} \quad ,$$

$$C_i : \quad M_{i_1} \quad M'_{i_1} \quad M'_{i_2} \quad M_{i_2} \quad M_{i_1} \quad ,$$

$$C_f : \quad M_{f_1} \quad M'_{f_1} \quad M'_{f_2} \quad M_{f_2} \quad M_{f_1} \quad ,$$

$$C_e : \quad M_{e_1} \quad M'_{e_1} \quad M'_{e_2} \quad M_{e_2} \quad M_{e_1} \quad .$$

We have

$$\Gamma''(C^\circ) = 0 , \quad \Gamma''(C_1) = 0 , \quad \Gamma''(C_2) = 0 , \quad \Gamma''(C_i) = 0. \tag{5.16}$$

The first equality gives

$$\left[\Phi_d(M^\circ_{e_2}) - \Phi_d(M^\circ_{i_2})\right] + \left[\Phi_f(M^\circ_{f_1}) - \Phi_f(M^\circ_{f_2})\right] + \left[\Phi_d(M^\circ_{i_1}) - \Phi_d(M^\circ_{e_1})\right] = O(\eta)$$

or, equivalently

$$\boxed{\mu_f(M^\circ_f) = \mu_2(M^\circ_2) - \mu_1(M^\circ_1) + O(\eta)} \tag{5.17}$$

The other three equalities (5.16) give :

$$\vec{V}''(M^{\circ}_{e_1})\ \overrightarrow{M_1M'_1} + \vec{V}''(M^{\circ}_{f_1})\ \overrightarrow{M'_fM_f} = O(\eta),$$

$$\vec{V}''(M^{\circ}_{e_2})\ \overrightarrow{M'_2M_2} + V''(M^{\circ}_{f_2})\ \overrightarrow{M_fM'_f} = O(\eta),$$

$$-\vec{V}''(M^{\circ}_{i_1})\ \overrightarrow{M_1M'_1} - V''(M^{\circ}_{i_2})\ \overrightarrow{M'_2M_2} = O(\eta),$$

By adding these new equalities, we obtain after (5.12) :

$$\left[\vec{V}_R(M^{\circ}_{e_1}) + \vec{V}'(M^{\circ}_{i_1})\right] \cdot \overrightarrow{M_1M'_1} + \left[\vec{V}_R(M^{\circ}_{e_2}) + \vec{V}'(M^{\circ}_{i_2})\right] \overrightarrow{M'_2M_2} =$$

$$= \Gamma''(C_f) + O(\eta)$$

The left member is equal to $\Gamma''(C_e) + O(\eta)$; we have thus :

$$\Gamma''(C_e) = \Gamma''(C_f) + O(\eta). \tag{5.18}$$

But $\Gamma''(C_e)$ is equal to the flux of $\frac{\vec{T} - \vec{T}'}{\epsilon}$ through any open surface S_e the edge of which is C_e. We may take

$$S_e = \text{rectangle } M_{e_1} M'_{e_1} M'_{i_1} M_{i_1} + S_1$$

$$+ \text{rectangle } M'_{e_2} M_{e_2} M_{i_2} M'_{i_2} \tag{5.19}$$

where S_1 is any open surface the edge of which is the contour

$$C_i : M'_{i_1} \; M'_{i_2} \; M_{i_2} \; M_{i_1} \; M'_{i_1} \; .$$

We can take for S_1 a surface entirely located within D_i. Therefore the flux of $\frac{\vec{T} - \vec{T}'}{\epsilon}$ through S_1 is null. Let $\vec{\nu}_1$ be the unit vector normal to the first rectangle so that the three directions $\overrightarrow{M_{e_1} M'_{e_1}}$, $\vec{n}_1$, $\vec{\nu}_1$ make a right-handed system and let $\vec{\nu}_2$ be the unit vector normal to the second rectangle such that the three directions $\overrightarrow{M'_{e_2} M_{e_2}}$, $\vec{n}_2$ $\vec{\nu}_2$ also make a right-handed system. The vectors $\vec{\nu}_1$, $\vec{\nu}_2$ are tangent to $\mathcal{L}_1{}^\circ$ at M_1° and to $\mathcal{L}_2{}^\circ$ at M_2°, respectively, and both are in the direction towards B°. Hence :

$$\Gamma''(C_e) = \left[\text{area } M_{e_1} \; M'_{e_1} \; M'_{i_1} \; M_{i_1}\right] \cdot \vec{\nu}_1 \cdot \left(\frac{\vec{T} - \vec{T}'}{\epsilon}\right)_{M_1^\circ} \cdot$$

$$+ \left[\text{area } M'_{e_2} \; M_{e_2} \; M_{i_2} \; M'_{i_2}\right] \cdot \vec{\nu}_2 \cdot \left(\frac{\vec{T} - \vec{T}'}{\epsilon}\right)_{M_2^\circ} \cdot$$

The intensities $d\Gamma_1$ of the vortex ribbon L_1 and $d\Gamma_2$ of the vortex ribbon L_2 are given by

$$d\Gamma_1 = \left[\text{area } M_{e_1} \; M'_{e_1} \; M'_{i_1} \; M_{i_1}\right] \cdot \vec{\tau}_1 \left(\frac{\vec{T} - \vec{T}'}{\epsilon}\right)_{M_1^\circ} ,$$

$$d\Gamma_2 = \left[\text{area } M'_{e_2} \; M_{e_2} \; M_{i_2} \; M'_{i_2}\right] \cdot \vec{\tau}_2 \left(\frac{\vec{T} - \vec{T}'}{\epsilon}\right)_{M_2^\circ} ,$$

respectively.

Hence

$$\Gamma''(C_e) = d\Gamma_1 \cdot (\vec{\nu}_1 \cdot \vec{\tau}_1) + d\Gamma_2 \cdot (\vec{\nu}_2 \cdot \vec{\tau}_2) .$$

Similarly, $\vec{\nu}_f$ being the unit vector normal to the rectangle $M_{f_1} \; M'_{f_1} \; M'_{f_2} \; M_{f_2}$ and such that the three directions $\overrightarrow{M'_{f_2} M_{f_2}}$, $\vec{n}_f$, $\vec{\nu}_f$ make a right-handed system, we have :

$$\Gamma''(C_f) = \left[\text{area } M_{f_1} M_{f_2} M'_{f_2} M'_{f_1}\right] \cdot \vec{\nu}_f \cdot \left(\frac{\vec{T} - \vec{T}'}{\epsilon}\right) M^{\circ}_{f_2} \cdot$$

We have thus :

$$\Gamma''(C_f) = d\Gamma_f \cdot (\vec{\nu}_f \cdot \vec{\tau}_f)$$

where $d\Gamma_f$ is the intensity of the vortex ribbon L_f.

According to (5.18), it is seen that

$$d\Gamma_1 \cdot (\vec{\nu}_1 \cdot \vec{\tau}_1) + d\Gamma_2 \cdot (\vec{\nu}_2 \cdot \vec{\tau}_2) = d\Gamma_f \cdot (\vec{\nu}_f \cdot \vec{\tau}_f). \quad (5.20)$$

Let $B^{\circ}_{f_1}$, $B'^{\circ}_{f_1}$ be the points derived from B, B' by the translation $+\frac{\epsilon}{2}\vec{n}_f(B)$ and $B^{\circ}_{f_2}$, $B'^{\circ}_{f_2}$ those derived from B, B' by the translation $-\frac{\epsilon}{2}\vec{n}_f(B)$. Let $\sum'_1$ denote the surface whose edge is the contour $B^{\circ}_{f_1} M_{f_1} M'_{f_1} B'^{\circ}_{f_1}$ and $\sum'_2$ the surface whose edge is the contour $B^{\circ}_{f_2} B'^{\circ}_{f_2} M'_{f_2} M_{f_2}$. Similarly let $\sum'_{e_1}$ be the surface bounded by the contour $M_{e_1} M'_{e_1} B'^{\circ}_{f_1} B^{\circ}_{f_1}$ and $\sum'_{e_2}$ the surface bounded by the contour $M_{e_2} M'_{e_2} B'^{\circ}_{f_2} B^{\circ}_{f_2}$, S_f the surface bounded by the contour C_f and S_e the surface bounded by the contour C_e. The surface

$$S_e + \sum'_{e_1} + \sum'_1 + S_f + \sum'_2 + \sum'_{e_2}$$

is closed and the flux of $\frac{\vec{T} - \vec{T}'}{\epsilon}$ through this surface is null. As it is equal to $+ (d\Gamma_1 + d\Gamma_2 - d\Gamma_f)$ if $\vec{\nu}_f \vec{\tau}_f = +1$ and to $- (d\Gamma_1 + d\Gamma_2 - d\Gamma_f)$ if $\vec{\nu}_f \vec{\tau}_f = -1$, we have

$$d\Gamma_1 + d\Gamma_2 = d\Gamma_f \quad (5.21)$$

By comparing with (5.20), we obtain

$$\vec{\nu}_1 \cdot \vec{\tau}_1 = \vec{\nu}_2 \cdot \vec{\tau}_2 = \vec{\nu}_f \cdot \vec{\tau}_f \quad (5.22)$$

This shows that :

$$\begin{cases} \text{If } L_f \text{ starts from } BB', \text{ then both } L_1 \text{ and } L_2 \text{ end at } BB'; \\ \text{If } L_f \text{ ends at } BB', \text{ then both } L_1 \text{ and } L_2 \text{ start from } BB'. \end{cases}$$

Consequently, every vortex filament $\mathcal{L}_f^\circ$ can be considered as the union of two free vortex filaments $\mathcal{L}_{f_1}^\circ$ and $\mathcal{L}_{f_2}^\circ$, $\mathcal{L}_1^\circ$ and $\mathcal{L}_{f_1}^\circ$ being two complementary arcs of the same vortex filament $\mathcal{L}_1$; similarly $\mathcal{L}_2^\circ$ and $\mathcal{L}_{f_2}^\circ$ belong to the same vortex filament $\mathcal{L}_2$. $\mathcal{L}_1$ and $\mathcal{L}_2$ are closed.

When η goes to zero, (5.17) becomes

$$\mu_f(B^\circ) = \mu_2(B^\circ) - \mu_1(B^\circ) . \tag{5.23}$$

According to (5.22), if $\vec{\nu}_f \cdot \vec{\tau}_f = +1$, then $\vec{\theta}_1$ is in the direction from $\mathcal{L}_1'$ towards $\mathcal{L}_1$, $\vec{\theta}_2$ in the direction from $\mathcal{L}_2$ towards $\mathcal{L}_2'$ and $\vec{\theta}_f$ in the direction from $\mathcal{L}_f$ towards $\mathcal{L}_f'$. If $\vec{\nu}_f \cdot \vec{\tau}_f = -1$, the directions of $\vec{\theta}_1$, $\vec{\theta}_2$ and θ_f are opposite to the preceding ones. Thus, from B to B', the variations of Γ_1, Γ_2 and Γ_f are

$$\left.\begin{aligned} d\Gamma_1 &= \Gamma_1(\mathcal{L}'_1) - \Gamma_1(\mathcal{L}_1) = \mp\left[\mu_1(\mathcal{L}'_1) - \mu_1(\mathcal{L}_1)\right] = \mp\, d\mu_1 \\ d\Gamma_2 &= \Gamma_2(\mathcal{L}'_2) - \Gamma_2(\mathcal{L}_2) = \mp\left[\mu_2(\mathcal{L}'_2) - \mu_2(\mathcal{L}_2)\right] = \pm\, d\mu_2 \\ d\Gamma_f &= \Gamma_f(\mathcal{L}'_f) - \Gamma_f(\mathcal{L}_f) = \pm\left[\mu_f(\mathcal{L}'_f) - \mu_f(\mathcal{L}_f)\right] = \pm\, d\mu_f \end{aligned}\right\} \begin{array}{l}(\text{upper sign if} \\ \vec{\nu}_f \cdot \vec{\tau}_f = +1 \\ \text{lower sign if} \\ \vec{\nu}_f \cdot \vec{\tau}_f = -1)\end{array}$$

As it was to be expected, (5.21) and (5.23) are therefore equivalent.

Fig. 5.3 sketches the configuration of a vortex ribbon when there exists only one free vortex sheet.

This case is that of a wing with a finite aspect ratio. $\mathcal{B}$ is the trailing edge of the wing.

Let us suppose that the wing is in a uniform motion of translation and that the relative motion is steady. Figure 5.3 shows the general configuration of the vortex distribution. The free parts of the vortices are closed at infinity downstream from the wing. (In the figure the concentration of the free vortices around the edges of the free vortex sheet is neglected). The second frontier between $\sum_1$ and $\sum_2$ consists of the bound part of the vortex filament shed at the junction of the leading edge with the trailing edge. The sum $\sum_1 + \sum_2$ does not cover entirely the wing surface $\sum$. The vortices located on $\sum_3 = \sum - (\sum_1 + \sum_2)$ contain no free arc ; they make closed rings entirely located on $\sum_3$.

Let $\mathcal{B}_{e_1}$ denote the intersection of $\sum_{f_1}$ with $\sum_{e_1}$ and $\mathcal{B}_{e_2}$ that of $\sum_{f_2}$ with $\sum_{e_2}$. These two curves are infinitively close to $\mathcal{B}$. The relative velocity $\vec{V}_R$ is tangent to $\mathcal{B}_{e_1}$ at every point $B^\circ_{e_1}$ and to $\mathcal{B}_{e_2}$ at every point $B^\circ_{e_2}$. These two points can be considered as belonging to $\sum_{f_1}$ and to $\sum_{f_2}$ respectively. Thus $\vec{V}_R(B^\circ_{e_1}) - \vec{V}_R(B^\circ)$ and $\vec{V}_R(B^\circ) - \vec{V}_R(B^\circ_{e_2})$ are equal and orthogonal to $\mathcal{L}^\circ_f$. But $|\vec{V}_R(B^\circ_e)| = |\vec{V}_R(B^\circ_{e_2})|$ because the pressure is continuous through the free vortex sheet as shown in Section 4. Consequently $\vec{V}_R(B^\circ) = 0$. Hence $\mathcal{L}^\circ_f$ is orthogonal to $\mathcal{B}$. $\mathcal{L}^\circ_1$ and $\mathcal{L}^\circ_2$ also are orthogonal to $\mathcal{B}$ since they are orthogonal to $\vec{V}_R$ on $\sum_1$ and on $\sum_2$ respectively. Furthermore the intensities $d\Gamma_1 = \vec{V}_R(B^\circ_{e_1})\ \vec{BB'}$ and $d\Gamma_2 = -\vec{V}_R(B_{e_2})\ \vec{BB'}$ are equal. Hence, as shown by Maurice Roy.

$$d\Gamma_1 = d\Gamma_2 = \frac{1}{2}\, d\Gamma_f \tag{5.24}$$

Of course, this relationship does no longer hold when the motion is unsteady.

B - STEADY MOTION IN THE CASE OF SEVERAL SHEDDING VORTEX LINES

One case of several free vortex sheets is sketched in Fig. 5.4 which represents the lower half of a double model the two halves of which are the images of each other with respect to the (X, Y) - plane. The (Z, X) - plane is the longitudinal plane of symmetry of the hull. The fluid is unbounded. The body is in a uniform motion of translation in the positive x-direction and the fluid motion is supposed to be steady. The drift angle α = (Ox, OX) is positive, so that the starboard side is the pressure side and the port side is the

suction side. The transverse cuts of the hull are V or U - shaped, the radius of curvature of the U's is small.

Experiments show that, if α is not too great, then the relative streamlines on the port side $\sum_1$ are less inclined on the (X, Y) plane than those located on the starboard side $\sum_2$. Let E_1, E_2, ... be a sequence of points on the lower half-stem. On $\sum_1$, the relative streamlines coming from the E_n's leave the hull at points S'_n located either on the lower half-stern-post or on the keel, in the (Z, X) - plane. On $\sum_2$, the relative streamlines leave the hull at points S''_n also located either on the lower half-stern-post or on the keel. But the points S''_n located on the stern-post are below the points S'_n, and the points S''_n located on the keel are upstream of the points S'_n. Consequently, the two streamlines arriving at a point B on the keel (or on the stern-post) come from two different points E. The relative velocities on these two streamlines are equal at B, but their directions differ. This entails the shedding of a free vortex filament from B.

Thus there exist three surfaces $\sum_f$. One, denoted $\sum_{f_o}$, is generated by the free vortices shed along the keel ; the second one, denoted $\sum_{f_1}$ is the mirror image of $\sum_f$; the third surface, denoted $\sum'_f$ is generated by the free vortices shed along the stern-post $\sum'_f$ is its own image (Figure 5.5).

Let $\mathcal{B}'$ denote the complete stern-post $S_o SS_1$ and $\mathcal{B}_o$, $\mathcal{B}_1$ the keel and its image, respectively. Every free vortex filament $\mathcal{L}_f$ starts either from the upper half of $\mathcal{B}'$ or from $\mathcal{B}_1$ and goes at infinity downstream from the body. Because of the steadiness of the motion, $\mathcal{L}_f$ coincides with a relative streamline. Consequently, $\sum_{f_1}$ is nearly parallel to the (X, Y) - plane. So does the upper edge of $\sum'_f$. The said vortex filament $\mathcal{L}_f$ comes back from infinity towards the body and reaches it either on the lower half of $\mathcal{B}'$ or on $\mathcal{B}_o$.

The start point B_1 of $\mathcal{L}_f$ and its end B_o are mirror images. Let $\mathcal{L}_1$ be the bound vortex $B_o B_1$ on $\sum_1$ and $\mathcal{L}_2$ the bound vortex $B_1 B_o$ on $\sum_2$. As the relative velocity on $\sum_{e_1}$ is greater than on $\sum_{e_2}$, the intensity $d\Gamma_f$ of the free vortex ribbon starting from the body between two points B_1, B'_1 and arriving on $B_o B'_o$ is equal to the difference $d\Gamma_1 - d\Gamma_2$, $d\Gamma_1$ being the intensity of the bound vortex ribbon L_1 on $\sum_1$ starting from $B_o B'_o$ and arriving at $B_1 B'_1$, while $d\Gamma_2$ is that of the bound vortex ribbon L_2 on $\sum_2$ starting from $B_o B'_o$ and arriving at $B_1 B'_1$

$$d\Gamma_f = d\Gamma_1 - d\Gamma_2 \tag{5.25}$$

Hence (5.24) does not hold.

Let C denote a closed contour around the stern post. Let $\sum'_{f_1}$ denote the port side of $\sum_f$ and $\sum_{f_2}$ its starboard side. C intersects $\sum_f$ at M_f, $\sum_1$ at M_1 and $\sum_2$ at M_2. The circulation of the fluid velocity $\vec{V}$ in that circuit is null. Hence, if all the points of C are close to the stern-post

$$0 = \left[\Phi''(M_{f_1}) - \Phi''(M_{f_2})\right] + \left[\Phi''(M_{i_1}) - \Phi''(M_{e_1})\right] + \Phi''(M_{e_2}) - \Phi''(M_{i_2})$$

where

$$\Phi'' = \frac{-1}{4\pi}\iint_{\sum_{f_1}+\sum_{f_o}} \mu_f(M') \frac{\partial}{\partial n_{M'}} \frac{1}{MM'} \, d\sum_f(M')$$

$$+ \frac{-1}{4\pi}\iint_{\sum'_f} \mu_f(M') \frac{\partial}{\partial n_{M'}} \frac{1}{MM'} \, d\sum(M')$$

$$+ \frac{-1}{4\pi}\iint_{\sum_1+\sum_2} \mu(M') \frac{\partial}{\partial n_{M'}} \frac{1}{MM'} \, d\sum(M') \qquad (5.26)$$

If the normal to $\sum'_f$ is in the direction from $\sum'_{f_2}$ to $\sum'_{f_1}$, we obtain

$$\mu'_f(B) = \mu_2(B) - \mu_1(B), \qquad (5.27)$$

μ_1 being the determination of μ on $\sum_1$, while μ_2 is its determination on $\sum_2$.

Similarly, by taking $\vec{n}$, on $\sum_{f_1}$, in the positive z-di-

rection and, on $\sum_{f_o}$ in the negative z-direction, it is easily found that

$$\mu_f(B) = \mu_2(B) - \mu_1(B) \begin{cases} \text{for B on } \mathcal{B}_o \\ \text{for B on } \mathcal{B}_1 \end{cases} \tag{5.28}$$

Equation (5.23) holds in all the cases.

Let us consider two values α_1 , α_2 of α , with $\alpha > \alpha$. The dissymmetry of the flow is more strongly marked for $\alpha_2 \geq \alpha_1$. The part of free vortices coming from $\mathcal{B}_1$ and arriving on $\mathcal{B}_o$ is greater in the second case than in the first one, while the part of those coming from the upper part of $\mathcal{B}'$ and arriving on the lower part is smaller. This entails a rapid variation with α of the position of the lift, that is of the y-component of the hydrodynamic force exerted on the body.

It has been assumed that the line $\mathcal{B}$ is in the (Z, X) plane, In fact, if the bottom is flat, the line $\mathcal{B}$ becomes a curve with positive values of Y . However this phenomenon cannot alter seriously the velocity induced on the hull by the vortex distribution.

One among the advantages due to the substitution of a normal dipole distribution for the vortex distribution is that one needs not know exactly the direction of the free vortex filaments.

When α is too large, the relative streamlines on $\sum_2$ tend to pass from $\sum_2$ to $\sum_1$ and separation occurs on the suction side. In such case, the above considerations do not hold.

C - UNSTEADY MOTIONS IN THE CASE OF A UNIQUE FREE VORTEX SHEET

Let us consider a point M_f on $\sum_f$ at time t , and let $\mathcal{B}_{t'}$ denote the position of $\mathcal{B}$ at $t' < t$. Let P be the fluid point located at M_f at t . The condition

$$\overrightarrow{B_f(t')\, M_f} = \int_{t'}^{t} \vec{V}_R(P, \tau)\, d\tau \tag{5.29}$$

with $B_f(t')$ infinitely close to a point $B \in \mathcal{B}_t$, determines the time t' at which P has left $\mathcal{B}$. It may happen that the position of B on $\mathcal{B}$ depends on t'. In that case, B can be defined by its abscissa σ_B on $\mathcal{B}$. During the time interval $(t', t' + dt')$ a free vortex filament of density $d_{t'} d_\sigma \Gamma$ is lying on a closed contour $B'_f B_f C_f C'_f B'_f$, with $B_f B'_f = d_\sigma(B)$ and $\overrightarrow{B_f C_f} = \vec{V}_R(B_f, t')\, dt'$. At t, this vortex filament is lying on the closed contour $M'_f M_f N_f N'_f M'_f$, where

$$\overrightarrow{B'_f M'_f} = \int_{t'}^{t} \vec{V}_R(P', \tau)\, d\tau \quad , \quad \overrightarrow{M_f N_f} = \vec{V}_R(M_f, t)\, dt'.$$

We have therefore

$$d\Gamma_f(M_f, t) = \int_{t'}^{t} \frac{\partial}{\partial \tau}\, d_\sigma \Gamma_f(\sigma_B(\tau), \tau)\, d\tau \tag{5.30}$$

or equivalently,

$$d\mu_f(M_f, t) = \int_{t'}^{t} \frac{\partial}{\partial \tau}\, d_\sigma\, (\mu_2 - \mu_1)_{\sigma_B(\tau), \tau}\, d\tau \tag{5.31}$$

If B is independent of t', then we obtain by integrating from one of the edges of $\sum_f$:

$$\mu_f(M_f, t) = (\mu_2 - \mu_1)_{B, t} - (\mu_2 - \mu_1)_{B(t')},$$

$$\text{with} \quad \overrightarrow{B(t')\, M_f} = \int_{t'}^{t} \vec{V}_R(P, \tau)\, d\tau \tag{5.32}$$

In the latter case, the support of the vortex sheet is generated by the relative trajectories of the fluid points leaving $\mathcal{B}$ at $t' < t$.

D - UNSTEADY MOTIONS WITH SEVERAL VORTEX SHEETS

As shown in Subsection B, a double model in a uniform motion of translation in a direction $\vec{V}_E$ parallel to the (X, Y) - plane of symmetry, sheds three free vortex sheets starting from the keel $\mathscr{B}_o$, from its image $\mathscr{B}_1$, and from the stern-post, respectively.

We consider below a body which could not be necessarily a double model. Its stern-post is denoted $S_1 S S_o$; its stem is the arc $E_1 E E_o$; the segments $E_1 S_1$ and $E_o S_o$ are parts of straight-lines. The origin O of the axes O X Y Z moving with the body is in the middle section, the X-axis containing the points S and E, and the Z-axis being in the longitudinal plane of symmetry of the body (See Fig. 5.6).

At a given instant t', there are between two points $B_o B'_o$ on the keel $E_o S_o$ (or on the lower stern-post), two bound vortex ribbons, one on the port side $\sum_1$, with the intensity $dX \frac{\partial \Gamma_1}{\partial X}(B_o, t')$ and the other one on the starboard side $\sum_2$, with the intensity $dX \frac{\partial \Gamma_2}{\partial x}(B_o, t')$. These two vortex ribbons end along the same arc $B_{1,t'} B'_{1,t'}$ on the upper keel $E_1 S_1$ (or on the stern). The position of $B_{1,t'}$ depends on B_o, hence on the abscissa X of B_o, and possibly on t'.

In the interval (t', t' + dt'), the increments of the intensities of the two bound vortex ribbons are $dt'\, dX \left(\frac{\partial^2 \Gamma_1}{\partial t' \partial x}\right)_{B,t'}$, $dt'\, dX \left(\frac{\partial^2 \Gamma_2}{\partial t' \partial x}\right)_{B,t'}$. If they are not equal to each other a free vortex ribbon is shed. It begins on the segment $B_{1e,t'} B'_{1e,t'}$ and ends at $B_{oe}\, B'_{oe}$; the points with subscript e are infinitely close to $B_{1,t'}$, $B'_{1,t'}$, B_o, B'_o. For the sake of brevity, we consider this free vortex ribbon as an arc of free vortex filament $B_{1e,t'}\, B_{oe'}$ with the intensity

$$dt'\, dX \frac{\partial^2}{\partial t'\, \partial X} (\Gamma_1 - \Gamma_2)_{B_o, t'} .$$

The fluid point P which was at $B_{1e,t'}$ at time t', is a time t at a position $J_{X,t'}$. In the system of axes moving with the body

$$\overrightarrow{B_{1e,t'}\, J_{X,t'}} = \int_{t'}^{t} \vec{V}_R (P, t'')\, dt'' . \qquad (5.33)$$

Similarly, the fluid point P which was at B_{o_e} at t' is at t at a point $I_{X,t'}$, and

$$\overrightarrow{B_{o_e} I_{X,t'}} = \int_{t'}^{t} \vec{V}_R (P, t'')\, dt'' . \qquad (5.34)$$

The fluid points which were at t' on the arc $B_{o_e} B_{1_{e,t'}}$ infinitely close to $B_o B_{1,t'}$ are at t on an arc $J_{X,t'} I_{X,t'}$. Let t_o be the time of the beginning of the unsteady motion. We suppose that the y-component of $\vec{V}_R$ has on the arc $B_{o_e} B_{1_{e,t'}}$ a constant sign (positive) during the time interval $[t_o, t)$ (Fig. 5.6). But it might occur that this sign changes at times t_1, t_2, ... We also suppose that this sign does not depend on the abscissa X of B_o. The most general case is still more complicated and will not be examined in this paper.

The points $I_{X,t'}$ describe a line starting from I_{X,t_o} and ending at B_{o_e}. Similarly the points $J_{X,t'}$ describe a line starting from J_{X,t_o} and ending at $B_{1_{e,t}}$. These lines generate a surface $\sum_{f_o}$ and a surface $\sum_{f_1}$, respectively. The arc $J_{X,t'} I_{X,t'}$ generates a surface S_X beginning at $J_{X,t_o} I_{X,t_o}$ and ending on the arc $B_{o_e} B_{1_{e,t}}$. The arc $I_{\frac{L}{2},t_o} S_{o_e}$ is one of the edges of $\sum_{f_o}$ and the arc $J_{\frac{L}{2},t_o} S_{o_e}$ is one of the edges of $\sum_{f_1}$. The fluid points which were at t' on $S_{o_e} S_{1_e}$ describe a surface $\sum'_f$ when t' varies from t_o to t. On $\sum$, at t', we had on the port side $\sum_1$ a bound vortex filament of intensity $d_X \Gamma_1 (X, t')$ on the arc $B_o B_{1,t'}$, and on the starboard side $\sum_2$ a bound vortex filament of intensity $d_X \Gamma_2 (X, t')$ with the support $B_{1,t'} B_o$. During the interval (t', t' + dt') the variations of these two intensities are $d_{t'} d_X \Gamma_1 (X, t')$ and $d_{t'} d_X \Gamma_2 (X, t')$. It is because they are not equal to each other that a free vortex is shed. At t' the support of this free vortex is $B_{1_{e,t'}} B_{o_e}$ and its intensity in the direction from $B_{1_{e,t'}}$ to B_{o_e} is equal to $d_{t'} d_X \left[\Gamma_1 (X, t') - \Gamma_2 (X, t')\right]$. Because the intensity of a free vortex is time-invariant, the intensity of the free vortex filament whose support is $J_{X,t'} I_{X,t'}$ is at t also equal to $d_{t'} d_X \left[\Gamma_1 (X, t') - \Gamma_2 (X, t')\right]$. The closed contour $B_{o_e} B_{1_{e,t}} J_{X,t'} I_{X,t'} B_{o_e}$ is thus the support of a free vortex filament of intensity $d_{t'} d_X \left[\Gamma_1 (X, t') - \Gamma_2 (X, t')\right]$.

Let $\mathscr{L}_X(t')$ denote this free vortex filament. On the arc $B_{1_{e,t'}}\, J_{X,t'}$ we find the union of the vortex filaments $\mathscr{L}_X(\tau)$ shed during the interval $\left[t_o\ ,\ t'\right)$. The total intensity of that union on $J_{X,t'}\, J_{X,t_o}\, B_{1_{e,t}}$ thus varies with $J_{X,t'}$. At $J_{X,t'}$ it is equal to $\int_{t_o}^{t'} d_{t'}\, d_X\left[\Gamma_1(X,t') - \Gamma_2(X,t')\right] = d_X\left[\Gamma_1(X,t') - \Gamma_2(X,t')\right]$ and it is in the direction towards J_{X,t_o}. Similarly we have a union of vortex filaments on the arc $I_{X,t_o}\, B_{o_e}$; its intensity at $I_{X,t'}$ is equal to $d_X\left[\Gamma_1(X,t') - \Gamma_2(X,t')\right]$ and it is in the direction towards B_{o_e}.

Let us consider a point M_{f_o} on $\sum_{f_o}$. It is one of the points $I_{X,t'}$. It belongs to the trajectory of a fluid point P which was at an anterior time t' at a certain point B_{o_e}. Hence, M_{f_o} being given, B_{o_e} and t' may be considered as determined functions of M_{f_o} and t. The same is true for any point M_{f_1} on $\sum_{f_1}$ and any point M'_f on $\sum'_f$, and also for any point M which is at t on a vortex filament $\mathscr{L}_X(t')$.

We have supposed that the arc $B_{o_e}\, B_{1_{e,t}}$ is infinitely close to the arc $B_o B_{1,t}$ on port side $\sum_1$ and nevertheless that $\vec{V}_R$ on the arc $B_{o_e}\, B_{1_{e,t}}$ is not tangent to $\sum_1$. This implies a contradiction of the same nature as that encountered in the scheme relative to a steady flow about a wing of finite thickness. We have seen in the latter case that the relative velocity on the wing is tangent to its trailing edge and we however assumed that the free vortices leave the wing in a direction orthogonal to this edge. In the present case, the distance of the arc $B_{o_e}\, B_{1_{e,t}}$ from the arc $B_o B_{1,t}$ is not really null, for the boundary layer is not infinitely thin. The contradiction seems to be an ineluctable consequence from the assumption that the fluid is almost inviscid.

We now drop the subscript e and consider that the support of the vortex filament $\mathscr{L}_X(t')$ at time t is the closed contour $B_o B_{1,t}\, J_{X,t'}\, I_{X,t'}\, B_o$. The arc $B_o B_{1,t}$ is bound while the three others are free. The intensity of this vortex filament previously determined is $d_{t'}\, d_X\left[\Gamma_1(X,t') - \Gamma_2(X,t')\right]$. The quantity $d_X\left[\Gamma_1(X,t') - \Gamma_2(X,t')\right]$ is positive for the free vortex to be shed from port, but its variation with t' may be positive or negative.

To make easier the drawing, the angles between $B_o\, J_{X,t'}$ and the longitudinal plane of symmetry has been considerably magnified in Fig. 5.6. Furthermore, one observes that, if the minimum value of X on the keel is necessarily equal to $-\frac{X}{2}$ (for $S_o S_1$ plays the role of the ordinary trailing edge of a wing), its maximum value

can be less than $\frac{L}{2}$.

At time t, the surface S_X generates a volume W_t when X increases from $-\frac{L}{2}$ to its maximum value. We therefore deal with a three-dimensional wake W_t, which was not the case in the preceding sections A, B or C. Within W_t a vorticity $\vec{\omega}_f$ is continuously distributed. The vector $\vec{\omega}_f(M)$ is tangent to the arc $J_{X,t'} I_{X,t'}$ which passes through M.

The total velocity $\vec{V}_f$ induced by the vortex filaments $\mathscr{L}_X(t')$ at a point M located inside or outside W_t is given by Poincaré's or Biot-Savart's formula :

$$\vec{V}_f(M) = \operatorname{curl}\left\{\frac{1}{4\pi}\iint_{\Sigma_1}{}' \frac{\vec{T}'_1(P)}{PM}\, d\Sigma'_1(P) + \frac{1}{4\pi}\iint_{\Sigma f_o} \frac{\vec{T}_{f_o}(P)}{PM}\, d\Sigma_{f_o}(P) + \frac{1}{4\pi}\iint_{\Sigma_f}{}' \frac{\vec{T}_f(P)}{PM}\, d\Sigma'_f(P) + \frac{1}{4\pi}\iiint_{W_t} \frac{\vec{\omega}_f(P)}{PM}\, dW_t(P)\right\} \qquad (5.35)$$

The velocity $\vec{V}_f$ is irrotational outside (W_t + its boundaries). It is, in particular, irrotational within D_i. The other vortex distributions to be considered are the distributions

$$\begin{cases} \mathscr{D}_1 = (\Sigma, \frac{\vec{T}'}{\epsilon}) + (D_i, 2\vec{\Omega}_E), \\ \mathscr{D}_2 = (\Sigma, \frac{\vec{T}_2}{\epsilon}) \quad . \end{cases} \qquad (5.36)$$

The velocity $\vec{V}'$ induced by $\mathscr{D}_1$ is null outside the hull, and

$$\operatorname{curl} \vec{V}' = 2\vec{\Omega}_E \text{ within } D_i \quad . \qquad (5.37)$$

The vortex distribution $\mathscr{D}_2$ consists of ring vortices on Σ. Each ring is made of two arcs $B_o B_{1,t}$ on Σ_1 and $B_{1,t} B_o$ on Σ_2. The intensity of the ring is a constant $d_X \Gamma_2(X,t)$ along the ring. On an arc $B_o B_{1,t}$ located on the part Σ'_1 of Σ_1, there exists the vortex filament of intensity $d_X \Gamma_1(X,t)$ already considered in formula (5.35) - see integral extended to Σ'_1. The vortex distribution $\mathscr{D}_2$ is equivalent to a normal dipole distribution $(\Sigma, \mu_2 \vec{n})$. It generates a velocity $\vec{V}_2$, and one has

$$\vec{V}_2 = (\vec{V}_E - \vec{V}') - \vec{V}_f - \vec{V}_o \text{ within } D_i \, , \qquad (5.38)$$

where $\vec{V}_o$ is due to some incident flow on the body. Outside the body, the total velocity is

$$\vec{V}(M) = \vec{V}_f(M) + \vec{V}_2(M) + \vec{V}_o(M) \, . \qquad (5.39)$$

Let us put $\vec{V}_f = \nabla \Phi_f$ (outside W_t + its boundaries) (5.40)

To calculate Φ_f, one can observe that a vortex filament $\mathscr{L}_X(t')$ is equivalent to a uniform dipole distribution on any open surface the edge of which coincides with $\mathscr{L}_X(t')$. For that surface we may take the surface $S_{X,t'}$ consisting of the five following parts :

(i) The part $\Sigma_1^{\pi}(X)$ of Σ_1 behind the arc $B_o B_{1,t}$;

(ii) The part of Σ_{f_o} interior to the contour $S_o I_{-\frac{L}{2},t'} I_{X,t'} B_o S_o$;

(iii) The part of Σ_{f_1} interior to the contour $S_1 J_{-\frac{L}{2},t'} J_{X,t'} B_{1,t} S_1$;

(iv) The part of Σ_f' interior to the contour $I_{-\frac{L}{2},t'} S_o S_1 J_{-\frac{L}{2},t'} I_{-\frac{L}{2},t'}$;

(v) The part of the surface $S_{t'}$ generated by the arc $J_{X,t'} I_{X,t'}$ when X varies from $-\frac{L}{2}$ to the value X defining the vortex filament $\mathscr{L}_X(t')$.

(5.41)

On this surface let us select a unit vector $\vec{\nu}$ normal to it ; for instance, $\vec{\nu}$ is on Σ_1' in the outward direction with respect to the hull. On the fifth part of $S_{X,t'}$ $\vec{\nu}$ is thus directed toward Σ_1', etc. Let M^+, M^- be two points infinitely close to each other, M^+ being on one side of the surface and M^- on the other one so that M^-M^+ is in the direction of $\vec{\nu}$. The circulation of the velocity induced by $\mathscr{L}_X(t')$ in a circuit starting from M^+, turning around $\mathscr{L}_X(t')$ and ending at M^- is equal to the intensity of $\mathscr{L}_{X,t'}$ and equal to the density of the normal dipole distribution on the surface. Hence the velocity potential due to the dipole distribution is

$$d_{t'} d_X \varphi_{X,t'}(M) = \frac{-1}{4\pi} d_{t'} d_X \left[\Gamma_1(X,t') - \Gamma_2(X,t')\right] \iint_{S_{X,t'}} \frac{\partial}{\partial \nu_{M'}} \frac{1}{MM'} dS(M'). \quad (5.42$$

The total potential outside W_t and its boundary is

$$\Phi_f(M) = \int_{t_o}^{t} \int_{-\frac{L}{2}}^{\max X} d_{t'} d_X \varphi_{X,t'}(M) . \quad (5.43)$$

According to (5.41) the contribution from Σ_1' is

$$-\frac{1}{4\pi} \iint_{\Sigma_1'} \left[\Gamma_1(X,t) - \Gamma_2(X,t)\right]_{M'} \frac{-\partial}{\partial n_{M'}} \frac{1}{M'M} d\Sigma_1'(M') \; ; \quad (5.44)$$

this notation recalls that any point M' on $\sum'_1$ belongs to an arc $B_o B_{1,t}$, the abscissa X of B_o being at t a function of M.

Let us consider a point M_{f_o}, M_{f_1} or M'_f on $\sum_{f_o}$, $\sum_{f_1}$ or $\sum'_f$. For instance M_{f_o} determines a pair (X, t') and it belongs only to the vortex filaments $\mathscr{L}_X(\tau)$ for $\tau < t'(M_{f_o})$. The contribution from $\sum_{f_o}$ is thus :

$$\iint_{\sum_{f_o}} (\Gamma_1 - \Gamma_2)_{X(M_{f_o}),\, t'(M_{f_o})} \frac{\partial}{\partial \nu_{M_{f_o}}} \frac{1}{M_{f_o} M} \, dS(M_{f_o}). \quad (5.45)$$

The contributions from $\sum_{f_1}$ and $\sum'_f$ have analogous expressions. Lastly the contribution from the fifth part of $S_{X,t'}$ is given by

$$\int_{t_o}^{t} d_{t'} \iint_{S_{t'}} \frac{\partial}{\partial t'} (\Gamma_1 - \Gamma_2)_{X(M',t')} \frac{\partial}{\partial \nu_{M'}} \frac{1}{M'M} dS(M') \quad (5.46)$$

Remark -

- The considerations of the present Subsection involve the implicit assumption that the positions of the lines $\mathscr{B}$, $\mathscr{B}_o$ on the hull are independent of time. This may be untrue if the amplitude of the unsteady motions is great, and also if a strong separation occurs.

- It is also to be pointed out that several free vortex sheets can exist without a rotational wake W_t. This is, for instance, the case of biplanes. Each of the two wings gives rise to one vortex sheet and one deals with horseshoe free vortex filaments on each vortex sheet.

VI - EQUATIONS DETERMINING THE TWO VORTEX FAMILIES (1)

The fluid motion about the given body depends on the hull geometry, on the own motion of the body and on the incident flow on the body. The hull geometry is referred to a system S of axes moving with the body. The fluid motion is referred to a system S' of axes fixed in space.

(1) See foot note on the following page.

S' is chosen as to coincide with S at a certain time t_o . As t_o is arbitrary, it is possible to express the fluid motion in term of the hull geometry.

The theory of chapter V.A, applies at any time t. The fluid velocity $\vec{V}$ is defined in the whole space. We have :

$$\vec{V}(M',t) = \begin{cases} \nabla\left[\Phi_d(M',t)+\Phi_f(M',t)\right]+\vec{V}_o(M',t) & \text{if } M\in D_e \\ \nabla\left[\Phi_d(M',t)+\Phi_f(M',t)\right]+\vec{V}_o(M',t)+\vec{V}'(M',t) & \\ \qquad = \vec{V}_E(M',t) \text{ if } M\in D_i \ . & \end{cases} \tag{6.1}$$

In this formula $\vec{V}_o$ is the velocity of the incident flow. We have :

$$\vec{V}_o = \nabla\Phi_o \quad \text{on } \Sigma_e \text{ and inside } \Sigma_e : \tag{6.2}$$

$$\begin{cases} \vec{V}'(M',t) = \operatorname{curl} \dfrac{1}{4\pi}\displaystyle\iint_{\Sigma}\frac{\vec{T}'(P',t)}{M'P'}\,d\Sigma(P') + \frac{1}{4\pi}\iiint_{D_i}\frac{2\vec{\Omega}_E(t)}{M'P'}\,dD_i(P') \\ \text{with } \vec{V}'(M',t) = 0 \text{ if } M'\in D_e \ , \ \vec{n}'\,\vec{V}' = 0 \text{ on } \Sigma_i : \end{cases} \tag{6.3}$$

$$\begin{cases} \vec{V}_d(M',t) = \nabla\Phi_d(M',t) \ , \quad \vec{V}_f(M',t) = \nabla\Phi_f(M',t), \\ \Phi_d(M',t) = \displaystyle\iint_{\Sigma}\mu(P',t)\frac{\partial}{\partial n_{P'}}\frac{1}{M'P'}\,d\Sigma(P'), \\ \Phi_f(M',t) = \displaystyle\iint_{\Sigma_f}\mu_f(P',t)\frac{\partial}{\partial n_{P'}}\frac{1}{M'P'}\,d\Sigma_f(P'). \end{cases} \tag{6.4}$$

---

(1) For the sake of simplicity, it will be assumed in this Section and also in Section VII either that there exists only one free vortex sheet.

Within D_i , curl $\vec{V}' = \text{curl}\ \vec{V}_E$. There exists therefore a velocity potential Φ_1 , such that

$$\vec{V}_E - \vec{V}' = \nabla\Phi_1 \quad , \quad \text{with} \quad \frac{\partial\Phi_1}{\partial n} = \vec{n}.\vec{V}_E \quad \text{on} \quad \Sigma_i \tag{6.5}$$

since $\vec{n}.\vec{T}' = 0$ and $\vec{T}' = -\vec{n}\wedge\left[V'(M'_e) - \vec{V}'(M'_i)\right] = (\vec{n}.\vec{V}')_{M_i}$ on Σ_i.

This potential is then the solution of a Neumann interior problem. We can put

$$\Phi_1(M', t) = \frac{-1}{4\pi}\iint_{\Sigma}\frac{\sigma(P', t)}{P'M'}\, d\Sigma(P', t) \tag{6.6}$$

with

$$\frac{1}{2}\sigma(M', t) - \frac{1}{4\pi}\iint_{\Sigma}\sigma(P', t)\ \frac{\partial}{\partial n_{M'}}\ \frac{1}{P'M'}\, d\Sigma(P', t) = (\vec{n}.\vec{V}_E)_{M', t} \tag{6.6'}$$

Eq. (6.6') is singular, but the condition $\iint_{\Sigma}\vec{n}.\vec{V}_E\, d\Sigma = 0$ is satisfied at every t and Φ_1 is determined up to an additive constant within D_i . Eq. (6.6') replaces Eq. (5.7), and it is much simpler.

Let u_1 , u_2 , u_3 denote the components on the moving axes S of the velocity $\vec{V}_E(0)$ of their origin O and u_4 , u_5 , u_6 those of their angular velocity $\vec{\Omega}_E$. According to (6.6) and (6.6'), we may write :

$$\Phi_1(M', t_o) = \sum_{j=1}^{6}\Phi_{1j}(M)\, u_j(t_o) . \tag{6.7}$$

In this formula, M is the point moving with the body which coincides with M' at $t = t_o$. The Φ_{1j}'s only depend on the hull geometry and on the position of the system of axes S with respect to the body.

Furthermore, it follows from the second equation (6.1) that

$$\Phi_d(M'_i, t_o) = \Phi_1(M'_i, t_o) - \Phi_o(M', t_o) - \Phi_f(M', t_o) ,$$

with $M' \in \Sigma$ and $\overrightarrow{M'M'_i} = \vec{n}_M(0+)$. (6.8)

Consequently, the density μ of the normal dipole distribution on Σ which generates Φ_d is the solution of the regular integral equation :

$$-\frac{1}{2}\mu(M', t_o) - \frac{1}{4\pi}\iint_{\Sigma}\mu(P', t_o)\,\frac{\partial}{\partial n_{P'}}\,\frac{1}{M'P'}\,d\Sigma(P') \qquad (6.9)$$

$$= \Phi_1(M_i', t_o) - \Phi_o(M', t_o) - \Phi_f(M', t_o).$$

Let us consider the following three particular cases :

Case a - $\vec{V}_o \equiv 0$; no free vortex is shed by the body.

According to (6.7) and (6.9) we obviously obtain :

$$\mu(M', t_o) = \sum_j \mu_j(M)\, u_j(t_o). \qquad (6.10)_a$$

Case b - $\vec{V}_o \equiv 0$; $\vec{\Omega}_E(t) = 0$, $\vec{V}_E(0) =$ constant ;

the fluid motion is steady with respect to the body. Hence, the support of the free vortex sheet is close to the surface generated by half straight lines starting from the curve $\mathscr{B}$ in the direction of $-\vec{V}_E(0)$. At P fixed with respect to the body and located on the generatrix starting from B , we have

$$\mu_f(P) = (\mu_2 - \mu_1)_B , \qquad (6.10)_b$$

μ_1 and μ_2 being the values of μ in the vicinity of $\mathscr{B}$ on the parts Σ_1 , Σ_2 of Σ adjacent to each other along $\mathscr{B}$. To determine μ on Σ a complementary condition is needed. Since the pressure p is necessarily continuous through the free vortex sheet Σ_f , this condition expresses that p is continuous on Σ_e through $\mathscr{B}_e$.

Case c - $\vec{V}_o \equiv 0$; the motion of the body consists of a translation nearly uniform with small variations of $\vec{V}_E(0)$ and $\vec{\Omega}_E$.

In that case, the support of the free vortex sheet $\sum_f$ is practically the same as in case b. This case will be studied in some details in the next Section.

VII - HYDRODYNAMIC FORCES EXERTED ON THE BODY

The case a previously defined (Section VI) can be subdivided into two cases, a_1 , a_2 according as the motion of the body is uniform or not.

Case a_1 - The body is in uniform motion

Since $\vec{V}_o$ is null inside D_e and no free vortex is shed by the body, the fluid motion is steady with respect to the system of axes S. Hence $\frac{\partial \vec{V}_R}{\partial t} \equiv 0$ inside D_e , and in this domain, Euler's equation

$$\frac{1}{\rho} \nabla p = \vec{F}_R - \frac{d\vec{V}_R}{dt}$$

reduces to

$$\frac{1}{\rho} \nabla p_d = - \vec{\gamma}_E - \vec{\omega} \wedge \vec{V}_R - \nabla \left(\frac{1}{2} V_R^2\right)$$

$$= \nabla \left(\frac{1}{2} \Omega_E^2 r^2 - \frac{1}{2} V_R^2\right) \text{ inside } D_e$$

We have therefore

$$\frac{1}{\rho} p_d(M_e) = \frac{1}{2} \Omega_E^2 r^2(M_e) - \frac{1}{2} V_R^2(M_e) + \text{constant on } \sum_e \quad (7.1)_{a1}$$

The system $\mathscr{S}_d$ of hydrodynamic forces exerted on the body consists

of the elementary forces $\left[p_d(M_e)\,\vec{n}_M\,d\Sigma(M)\right]$. This may be written in the form :

$$\mathscr{S}_d = \left[\left(\frac{1}{2}\rho\,\Omega_E^2\;r^2(M_e)\,\vec{n}_M - \rho\,\vec{T}(M)\wedge\vec{V}_R(M)\right)d\Sigma(M)\right] \qquad (7.2)_{al}$$

where

$$\vec{V}_R(M) = \frac{1}{2}\left[\vec{V}_R(M_e) + \vec{V}_R(M_i)\right] = \frac{1}{2}\,\vec{V}_R(M_e)\ , \qquad (7.3)$$

This relative velocity is calculated <u>inside</u> the bound vortex sheet by using the vortex distribution ; it can be considered as the <u>incident</u> velocity on the element of bound vortex filament $\frac{T}{\epsilon}(\epsilon\,d\Sigma)$ which is at rest with respect to the body.

The equilibrium of the set E of fluid points located inside D_i requires

$$\frac{1}{\rho}\nabla\,p_d = -\,\vec{\gamma}_E = \nabla\left(\frac{1}{2}\,\Omega_E^2\;r^2\right). \qquad (7.4)_{al}$$

This gives

$$p_d(M_i) = \frac{1}{2}\,\Omega_E^2\;r^2(M_i) + \text{constant on } \Sigma_i \qquad (7.4')_{al}$$

The system of forces exerted on the set E' of fluid points belonging to the bound vortex sheet is thus

$$\mathscr{S}_T = \left[\left(p(M_e)\,\vec{n}_M - p(M_i)\,\vec{n}_M\right)d\Sigma(M)\right] = \left[-\,\rho\,\vec{T}(M)\wedge\vec{V}_R(M)\,d\Sigma(M)\right] \qquad (7.5)_{al}$$

Finally we have :

$$\mathscr{S}_d = \mathscr{S}_T - \vec{F}_C \qquad (7.6)_{al}$$

where

$$\vec{F}_C = m\ \Omega_E^2\ \vec{r}\ (C)\ ; \qquad (7.7)_{a_1}$$

m being the mass of E, and $\vec{r}(C)$ the vector orthogonal to the axis $\vec{\Delta}$ of the helicoidal motion of the body with its origin on $\vec{\Delta}$ and its end at the center C of the domain D_i. $\vec{F}_C$ is thus the centrifugal force exerted on the set E of fluid points, i.e. the centrifugal force acting on the fluid mass "displaced" by the body.

Case a_2-

This case differs from case a_1 in that $\vec{V}_E(0)$ and (or) $\vec{\Omega}_E$ may depend on time.

$(7.4)_{a_1}$ does no longer apply if $\frac{d\vec{\Omega}_E}{dt} \neq 0$ for

$$\text{curl}\ \vec{\gamma}_E = 2\frac{d\vec{\Omega}_E}{dt}\ , \qquad (7.8)_{a_2}$$

and $-\vec{\gamma}_E$ cannot be identified with $\frac{1}{\rho}\nabla p_d$. The equilibrium of the set E of fluid points therefore requires that the expressions for the absolute force per unit mass be different inside D_e and inside D_i. If $\vec{F} = \nabla \mathscr{U}$ denotes the expression of that force inside D_e, its expression inside D_i is $\vec{F} + \vec{F}'$, and we must have

$$\begin{cases} \frac{1}{\rho}\nabla p_d(M', t_o) = \vec{F}'(M', t_o) - \frac{d}{dt}\vec{V}_E(M', t_o), \quad \text{with} \\ \\ \text{curl}\ \vec{F}'(M', t_o) = 2\frac{d\vec{\Omega}_t}{dt} = \text{curl}\frac{d\vec{V}_E}{dt}(M', t_o) = \text{curl}\frac{\partial\vec{V}_E}{\partial t}(M', t_o) \\ \qquad\qquad\qquad\qquad\qquad\qquad\qquad\qquad\qquad\qquad \text{inside}\ D_i \end{cases} \qquad (7.9)_a$$

Since

$$\vec{V}'(M', t) - \vec{V}_E(M', t) = -\nabla\ \Phi_1(M', t)\ ,$$

we have

$$\vec{F}' = \frac{\partial\vec{V}'}{\partial t}(M', t_o) + \nabla\Psi_1(M', t_o)$$

and

$$\frac{1}{\rho}\nabla p_d(M', t_o) = -\nabla\frac{\partial \Phi_1}{\partial t}(M', t_o) + \left(\frac{\partial}{\partial t} - \frac{d}{dt}\right)\vec{V}_E(M', t_o) + \nabla\Psi_1(M', t_o) \qquad (7.10)_{a_2}$$

or

$$\frac{1}{\rho} p_d(M_i', t_o) = -\frac{\partial}{\partial t}\Phi_1(M_i', t_o) + \frac{1}{2}\left(\Omega_E^2 r^2\right)_{M', t_o} + \Psi_1(M_i', t_o) \text{ on } \sum_i \qquad (7.10')_{a_2}$$

The unknown function Ψ_1 has to be determined by the condition that

$$\frac{1}{\rho} p_d(M_i', t_o) \text{ reduce to } \nabla\frac{1}{2}\left(\Omega_E^2 r^2\right), \qquad (7.11)_{a_2}$$

when case a_2 reduces to case a_1

This implies that Ψ_1 is harmonic inside D_i.

Since

$$\Phi_1(M_i', t_o) = \sum_j u_j(t_o)\ \Phi_{1j}(M_i),$$

the derivative $-\frac{\partial}{\partial t}\Phi(M_i', t_o)$ contains two kinds of terms. The terms of the first kind are those due to the variations of the u_j's when the rotation of the system S of axes is ignored. Let us denote

$$\sum_j \dot{u}_j(t_o)\ \Phi_{1j}(M)$$

the sum of the terms of the first kind. The terms of the second kind are due to the fact that M_i is fixed on $\sum_i$, while M_i' is fixed in the space referred to the fixed axes S'. Consequently they sum up to

$$-\vec{V}_E(M_i', t_o) \cdot \nabla\Phi_1(M_i', t_o).$$

We thus obtain :

$$\Psi_1 (M_i', t_o) = \vec{V}_E (M_i', t_o) . \nabla\Phi_1 (M_i', t_o) , \qquad (7.12)_{a_2 \& a_1}$$

This expression takes the same values in both cases a_2 and a_1 provided that in the uniform motion of the body corresponding to case a_1, $\vec{V}_E(0)$ and $\vec{\Omega}_E$ be identical at t_o with those of the real non-uniform motion. Since Ψ_1 is harmonic within D_i, it is uniquely determined in that domain by (7.12). We have

$$\frac{1}{\rho} p_d(M_i', t_o) = - \sum_j \dot{u}_j(t_o) \Phi_{1j}(M_i) + \frac{1}{2} \Omega^2_E(t_o) r^2(M_i, t_o) \text{ on } \Sigma_i \qquad (7.13)_{a_2}$$

Now, let us consider the velocity potential Φ inside D_e. Euler's equation gives, after (4.1'),

$$\frac{1}{\rho} p_d(M_e', t_o) = \frac{\partial\Phi}{\partial t}(M_e', t_o) + \frac{1}{2} \Omega^2_E(t_o) r^2(M_e', t_o) - \frac{1}{2} V^2_R(M_e', t_o) \text{ on } \Sigma_e \qquad (7.14)_{a_2}$$

By comparing with $(7.1)_{a_1}$, we obtain

$$\frac{\partial\Phi}{\partial t}(M_e', t_o) = 0 \quad \text{on } \Sigma_e \quad \underline{\text{in case } a_1} . \qquad (7.15)_{a_1}$$

In cases a_1 and a_2, we have

$$\Phi = \Phi_d \quad \text{inside } D_e , \qquad (7.16)_a$$

and according to (6.7) and $(6.10)_a$:

$$\Phi_d(M'_e, t_o) = \Phi_d(M'_i, t_o) + \mu(M', t_o) = \sum_j u_j(t_o) \left[\Phi_{1j}(M_i) + \mu_j(M) \right] \text{ on } \sum_e \qquad (7.17)_a$$

Hence, with the above notation, we have :

$$\frac{\partial}{\partial t} \Phi_d(M'_e, t_o) = \sum_j \dot{u}_j(t_o) \left[\Phi_{1_j}(M_i) + \mu_j(M) \right]_{t_o} - \vec{V}_E(M'_e, t_o) . \nabla \Phi_d(M'_e, t_o)$$

The second term on the right side only depends on the instantaneous velocities. It is the same in cases a_2 and a_1 for equal velocities $\vec{V}_E(0)$ and $\vec{\Omega}_E$. But, in case a_1, the first term on the right side is null ; the term on the left side is null also by virtue of $(7.15)_{a_1}$ Hence we obtain :

$$\frac{\partial}{\partial t} \Phi_d(M'_e, t_o) = \sum_j \dot{u}_j(t_o) \left[\Phi_{1j}(M_i) + \mu_j(M) \right] \qquad (7.18)_a$$

Let us put

$$d\vec{F}'_T = - \rho \vec{T}(M) \wedge \vec{V}_R(M) \, d\sum(M) \qquad (7.19)$$

The system of forces exerted on the bound vortex sheet is that of the elementary forces

$$\left[d\vec{F}_T \right] = \left[(p_d(M'_e, t_o) - p_d(M'_i, t_o)) \vec{n}_{M'} \, d\sum(M') \right]$$
$$= \left[- \rho \sum_j \dot{u}_j(t_o) \mu_j(M) \vec{n}_M \, d\sum(M) \right] + \left[d\vec{F}'_T \right] . \qquad (7.20)_a$$

The system of forces exerted on the set E of fluid points is that of the elementary forces

$$\left[p_d(M_i', t_o)\,\vec{n}_{M'}\,d\Sigma(M')\right] = \left[-\rho \left(\sum_j \dot{u}_j(t_o)\,\Phi_{lj}(M_i)\,\vec{n}_M + \frac{1}{2}\,\Omega_E^2\, r^2(M)\,\vec{n}_M \right) d\Sigma(M) \right] \qquad (7.21)_a$$

$$= -\vec{F}_C + \left[-\rho \sum_j \dot{u}_j(t_o)\,\Phi_{lj}(M_i)\,\vec{n}_M\,d\Sigma(M) \right] .$$

Putting

$$\begin{cases} \mathcal{S}_{q.s.} = \left[d\vec{F}'_T\right] - \vec{F}_C , \\ \mathcal{S}_a = \left[-\rho \sum_{j=1}^{6} \dot{u}_j(t_o)\,(\Phi_{lj}(M_i) + \mu_j(M))\,\vec{n}_M\,d\Sigma(M) \right] , \end{cases} \qquad (7.22)_a$$

we see that the final expression for the system of hydrodynamic forces exerted on the body is as follows :

$$\boxed{\mathcal{S}_d = \mathcal{S}_{q.s.} + \mathcal{S}_a} \quad ; \qquad (7.23)_a$$

q. s. is the "quasi-steady" system of forces and $\mathcal{S}_a$ is that due to the so called "added masses".

Case b -

This case is a limiting one, involving the assumption that the motion of translation of the body became uniform at a time t considerably anterior to the present time t_o. Since $\vec{\Omega}_E = 0$, one has

$$\mathcal{S}_d = \mathcal{S}_T \qquad (7.24)_b$$

But $\mathcal{S}_d$ cannot reduce to a torque because of the effect of the free vortex sheet.

Case c -

The x'-axis is taken in the direction opposite to the mean velocity $\vec{V}'_E$ of the origin of the system of axes moving with the body. Let u'_E be the absolute value of the x'-component of $\vec{V}'_E$. The support of the vortex sheet may be considered as generated by half straight lines starting in the positive x'-direction from a certain line $\mathscr{B}$ on $\sum$. Let P'_f and B'_f denote two points on the same generatrix, B'_f being infinitely close to $\mathscr{B}$. We put $\xi = |B'_f P'_f|$. Let $\Theta = -\infty$ be the time of the beginning of the motion of the body and t_o the present time.

If the fluid motion were steady as in case b, one would have $\mu_f(P'_f, t_o) = \mu_f(B'_f, t_o)$. Because it is unsteady, one has

$$\mu_f(P'_f, t_o) = \mu_f(B'_f, t_o) - \int_{-\infty}^{t_o - \frac{\xi}{u'_E}} \frac{\partial}{\partial \tau} \mu_f(B'_f, \tau)\, d\tau \quad . \qquad (7.25)_c$$

For reasons which will be elucidated later, we put

$$\begin{cases} \mu_f(P'_f, t_o; 0+) = \mu_f(B'_f, t_o) - \delta\mu_f(P'_f, t_o; 0+) \\ \mu_f(P'_f, t_o; t_o - t') = \mu_f(B'_f, t_o) - \delta\mu_f(P', t_o; t_o - t'), \text{ with} \qquad (7.26)_c \\ \delta\mu_f(P'_f, t_o; t_o - t') = \begin{cases} 0 \text{ if } \xi < u'_E(t_o - t') \\ \displaystyle\int_{-\infty}^{t_o - t' - \frac{\xi}{u'_E}} \frac{\partial}{\partial \tau} \mu_f(B'_f, \tau)\, d\tau \text{ if } \xi > u'_E(t_o - t') \end{cases} \end{cases}$$

One sees that, if $\mu_f(B_f, t)$ is a constant in the time interval (t', t_o), then $\mu_f(P'_f, t_o ; t_o - t')$ is equal to that constant at t_o, provided $\xi < u'_E(t_o - t')$. For $\xi > u'_E(t_o - t')$, then μ_f at P'_f still depends at time t_o on the variations of $\mu_f(B'_f, t)$ for $t < t'$. In particular, the

fluid motion would be steady at t_o if $\mu_f(B_f, t)$ were constant during the infinitely large interval $(-\infty, t_o)$.

One may write

$$\Phi_f(M', t_o ; 0+) = \frac{-1}{4\pi} \iint_{\Sigma_f} \mu_f(P'_f, t_o ; 0+) \frac{\partial}{\partial n_{P'_f}} \frac{1}{M'P'_f} d\Sigma(P'_f). \quad (7.27)_c$$

This expression is the velocity potential due to the normal dipole distribution on Σ_f.

The expression

$$\delta\Phi_f(M', t_o ; t_o - t') = \frac{1}{4\pi} \iint_{\Sigma_f} \delta\mu_f(P'_f, t_o ; t_o - t') \frac{\partial}{\partial n_{P'_f}} \frac{1}{M'P'_f} d\Sigma_f(P'_f) \quad (7.28)_c$$

is the difference between the true expression of $\Phi_f(M', t_o ; 0+)$ given by $(7.27)_c$ and that which would be reached at t_o if the motion of the body had been uniform in the interval (t', t_o), the velocities $\vec{V}_E(0)$ and $\vec{\Omega}_E$ during this interval being constant and equal to those of the real motion at t_o.

Obviously :

$$\delta\Phi_f(M', t_o ; t_o - t') \longrightarrow 0 \text{ when } t_o - t' \longrightarrow +\infty ; \quad (7.29)_c$$

$\Phi_f(M', t_o ; +\infty)$ is the limit reached when $t' \longrightarrow -\infty$. This limit defines the steady case b when $\vec{V}_E(0)$ and $\vec{\Omega}_E$ are constant (since $t' \ll t_o$) and equal to the velocities which determine $\mu_f(B'_f, t_o)$ and $\mu_f(P'_f, t_o) = \mu_f(B'_f, t_o)$ for every $\xi > 0$.

The difference

$$\delta\Phi_f(M', t_o ; +\infty) = \Phi_f(M', t_o ; +\infty) - \Phi_f(M', t_o ; 0+) \quad (7.30)_c$$

is the deficiency of Φ_f, that is the difference between the Φ_f determined in the steady case for the present velocities $\vec{V}_E(0, t_o)$ and $\vec{\Omega}_E(t_o)$ at t_o and the true Φ_f in the real motion at t_o.

Let B'_{e_1} and B'_{e_2} denote two points infinitely close to B'_f, but located on $\sum_{e_1}$ and $\sum_{e_2}$, respectively. We have

$$\mu_f(B'_f, t_o) = \mu(B'_{e_2}, t_o) - \mu(B'_{e_1}, t_o) ; \qquad (7.31)_c$$

μ is the solution of the integral equation

$$-\frac{1}{2}\mu(M', t_o) - \frac{1}{4\pi}\iint_{\sum} \mu(P', t_o) \frac{\partial}{\partial n_{P'}} \frac{1}{M'P'} \, d\sum(P')$$

$$= \Phi_1(M'_i, t_o) - \Phi_f(M', t_o ; 0+) , \quad M' \text{ being on } \sum. \qquad (7.32)_c$$

We have

$$\mu(M', t_o) = \sum_{j=1}^{6} u_j(t_o) \mu_j(M) - \mathcal{G}(\Phi_f(M', t_o ; 0+)) \qquad (7.33)_c$$

$\mathcal{G}$ being a linear and homogeneous functional the argument of which is the function $\Phi_f(M', t_o ; 0+)$: it may be written in the form

$$\mathcal{G}(M', t_o ; 0+) = \iint_{\sum} K(M', P') \Phi_f(P', t_o ; 0+) \, d\sum(P').^{(1)} \qquad (7.33')_c$$

Let us substitute $(7.27)_c$ into $(7.33)_c$ and take into account (7.26) and also the condition

(1) K is the resolvent kernel of equation $(7.32)_c$.

$$p\,(B'_{e_1}\,,\ t_o) \;=\; p\,(B'_{e_2}\,,\ t_o)\,. \qquad (7.34)_c$$

Then we obtain for determining $\mu_f(B'_f\,,\ t_o\,;\ 0+)$ a Volterra integral equation. This shows that the fluid motion at time t_o does depend not only on the present velocities $\vec{V}_E(0, t_o)$ and $\vec{\Omega}_E(t_o)$, but also on the history on the motion during the whole interval $t < t_o$.

Let us consider now the system $\mathscr{S}_d$ of hydrodynamic forces exerted on the body. We readily obtain

$$\mathscr{S}_d \;=\; \mathscr{S}_T' \;-\; \vec{F}_C \;+\; \mathscr{S}_a \;+\; \mathscr{S}_a'\,, \qquad (7.35)_c$$

where

$$\mathscr{S}_T' \;=\; \left[d\vec{F}'_T\right] \;=\left[\;-\;\rho\,\vec{T}(M)\ \wedge\vec{V}_R(M)\,d\Sigma\,(M)\right],$$

$$-\,\vec{F}_C \;=\; \left[-\,\rho\,\Omega_E^2\ \vec{r}\,dD_i\right] \;=\; \left[\rho\frac{1}{2}\,\Omega_E^2(t_o)\ r^2(M, t_o)\,\vec{n}_M d\Sigma(M)\right],$$

$$\mathscr{S}_a \;=\; \left[-\,\rho\sum_j \dot{u}_j(t_o)\,(\,\Phi_{1j}(M_i) + \mu_j(M)\,)\,\vec{n}_M\,d\Sigma\,(M)\right],$$

$$\mathscr{S}_a' \;=\; \left[-\,\rho\mathscr{G}\left(\frac{\partial}{\partial t}\ \ \Phi_f(M', t_o\,;\,0+)\right)\vec{n}_{M'}\,d\Sigma\,(M')\right]. \qquad (7.36)_c$$

The definition of $\left[d\vec{F}'_T\right]$ and of $\mathscr{S}_a$ are exactly the same as in formulas $(7.20)_a$ and $(7.22)_a$, respectively. But the system of forces $\left[d\vec{F}'_T\right]$ does not coincide with that defined in case a. This is due to the effect of potential Φ_f on potential Φ_d. On the contrary, the systems of forces $\mathscr{S}_d$ coincide in both cases if the systems of the six accelerations $\dot{u}_j(t_o)$ are identical.

Let $\mathscr{S}''_T$ denote the system of forces $\mathscr{S}'_T$ evaluated at t_o under the assumption that $\vec{V}_E(0)$ and $\vec{\Omega}_E$ coincide with $\vec{V}_E\,(0, t_o)$ and $\vec{\Omega}_E(t_o)$ in the time interval (t', t_o), with $t' \ll t_o$. Then the difference

$$\delta \underline{\mathscr{S}}_T = \mathscr{S}''_T - \mathscr{S}'_T = \left[d\vec{F}''_T\right] - \left[dF'_T\right] \qquad (7.37)_c$$

is the deficiency of $\mathscr{S}'_T$ due to the deficiency $\mathscr{S}_f$ defined in $(7.30)_c$.

For the sake of simplicity, the true system $\delta\Phi_d$ of hydrodynamic forces acting on the body is very often replaced by the estimate

$$\mathscr{S}'_d = \underline{\mathscr{S}}''_T - \vec{F}_C + \mathscr{S}_a . \qquad (7.38)_c$$

The system $\mathscr{S}''_T - \vec{F}_C$ is called the quasi-steady system of forces :

$$\mathscr{S}_{q.s.} = \mathscr{S}''_T - \vec{F}_C . \qquad (7.39)_c$$

The error involved in the substitution of $\mathscr{S}'_d$ for $\mathscr{S}_d$ is

$$\mathscr{S}_d - \mathscr{S}'_d = - \delta\mathscr{S}'_T + \mathscr{S}'_a . \qquad (7.40)_c$$

Like $\mathscr{S}_a$, $\mathscr{S}'_a$ represents an inertial effect, but due to the free vortex sheet only.

Let us assume, for example, that a jump of $\vec{V}_E(0)$ and $\vec{\Omega}_E$ occur in the infinitely small interval $(t_o - 0, t_o)$, and that these two velocities remain constant for $t > t_o$. It follows from the third equation $(7.26)_c$ that

$$\delta\mu_f(P'_f, t_o ; 0+) = 0 \quad \text{for every } \xi . \qquad (7.41)_c$$

Hence the free vortex sheet is not immediately altered. But, one has :

$$\frac{\partial}{\partial t}\Phi_f(M', t_o\ ;\ 0+) = \frac{1}{4\pi}\iint_{\Sigma}\frac{\partial}{\partial t}\mu_f(B'_f, t_o)\ \frac{\partial}{\partial n_{M'}}\frac{1}{M'P'_f}\,d\Sigma_f(P'_f) \quad (7.42)_c$$

$\mathscr{S}'_T$ at t_o has the same components as at $t_o - 0$. $\mathscr{S}_a$ is null at t_o, but the system of forces necessary for creating the jump is infinite. Furthermore, at $t_o + 0$, $\mathscr{S}'_a$ is generally finite. Of course, when $t \longrightarrow +\infty$, the deficiency $\delta\mathscr{S}'_T$ calculated by taking into consideration the new velocities $\vec{V}_E(0)$ and $\vec{\Omega}_E$ tends to zero ; $\mathscr{S}'_a$ also tends to zero and

$$\text{limit}\ \mathscr{S}_d - \mathscr{S}'_T \longrightarrow 0. \quad (7.43)_c$$

The effect of $\mathscr{S}'_a$ may be considerable. For instance, it has been shown that the jump of the lift of a wing with an infinite aspect ratio is at $t_o + 0$ equal to half the difference between its final value and its value at $t_o - 0$ (See [2] , [3]) .

THE ORIGIN OF THE FORCES EXERTED BY THE FLOW ON A BOUND VORTEX DISTRIBUTION

The above considerations started from the idea that a dynamical relationship necessarily exists between the hull of a moving body and the vortex distribution satisfying the adherence condition on the hull surface.

Another viewpoint is that any vortex filament which does not move with the fluid is necessarily submitted to forces exerted by the adjacent sets of fluid points.

The proof is classical. It is sufficient to summarize it.

Let $\mathscr{L}$ be a vortex filament, $\mathscr{L}_1$ its bound part, ds_1 an arc of $\mathscr{L}_1$. Let 0 denote the middle of the arc ds_1 , 0z an axis in the direction of $\vec{ds}_1$, and r , θ , z a system of semi-polar coordinates. Let D' denote the domain

$$D' = \left[\ r, \theta, z :\ 0 < r \leqq R\ ,\quad 0 \leqq \theta < 2\pi\ ,\ |z| < \frac{1}{2}ds_1\right].$$

Hence D' does not include the arc ds_1 . We consider the relative motion of the fluid with respect to the system of axes just defined. The velocity may be written in the form

$$\vec{V}_R = \vec{V}_o + (\vec{V}' - \delta V') + \delta V' ,$$

where $\vec{V}_o$ defines some incident flow, $\vec{V}'$ is the velocity induced by $\mathscr{L}$ and $\delta \vec{V}'$ that induced by the part ds_1 of $\mathscr{L}$. Let dE' be the set of fluid points inside D', and dE_1 the set of fluid points belonging to ds_1 . One easily sees that the momentum $\vec{I}(dE_1)$ is null, and, therefore, that, $\vec{I}(dE')$ being the momentum of dE' ,

$$\frac{d}{dt}\vec{I}(dE') = \frac{d}{dt} I\,(dE' + dE_1) = \iint_{S'} \rho\, \vec{V}_R\, (\vec{n}\vec{V}_R)\, dS' ;$$

($\vec{n}$ is in the outward direction , and S' is the boundary of (D' + ds)).

One readily obtains :

$$\lim_{R\to 0} \frac{d}{dt}\vec{I}(dE') = \frac{1}{2}\rho\, \vec{\Gamma} \wedge \vec{V}_i\, ds_1 , \qquad (7.44)$$

where Γ is the intensity of $\mathscr{L}$: $\Gamma = \vec{\Gamma}.\ \vec{i}_{s1}$, $\vec{i}_s$ being the unit vector tangent to $\vec{ds}_1$ and $\vec{V}_i$ the finite incident velocity on the arc ds_1 :

$$\vec{V}_i = \vec{V}_o + \vec{V}' - \delta\vec{V}' .$$

On the other hand, by the momentum theorem, one has

$$\frac{d}{dt}\vec{I}(dE') = - d\vec{F}'_T + \iint_{S'} - p\,\vec{n}\, dS' ,$$

where $-d\vec{F}'_T$ is the force exerted on dE' by dE_1. From Euler's equation (4.1), we have inside D' :

$$\frac{1}{\rho}\nabla p_d = -\frac{\partial \vec{V}_i}{\partial t} - (\operatorname{curl} \vec{V}_o) \wedge (\vec{V}_i + \delta\vec{V}') - \nabla\left[\frac{1}{2}(\vec{V}_o + \delta\vec{V}')^2\right].$$

This gives, when $R \longrightarrow 0$, $p_d = -\rho \vec{V}_i \cdot \delta\vec{V}'$ + constant on S, and

$$\lim_{R\to 0} \frac{d}{dt}\vec{I}(dE') = -d\vec{F}'_T - \frac{1}{2}\rho\vec{\Gamma} \wedge \vec{V}_i\, ds_1 \qquad (7.45)$$

By comparing (7.44) and (7.45), one finally obtains

$$\boxed{d\vec{F}'_T = -\rho\vec{\Gamma} \wedge \vec{V}_i\, ds_1} \qquad (7.46)$$

$d\vec{F}'_T$ is the force exerted on the arc ds_1 of the bound part $\mathcal{L}_1$ of $\mathcal{L}$ by the adjacent sets of fluid points. The force vanishes with $\vec{V}_i$, that is when the arc ds_1 moves with the fluid.

Formula (7.46) is of practical interest when the vortex distribution equivalent to the hull is replaced by a unique concentrated vortex and a suitable distribution of sources or normal dipoles on the hull surface.

This formula does not imply that the fluid motion around the bound arc of the vortex filament is steady. If Γ varies with time, one has to consider that another vortex filament $\mathcal{L}'$, of intensity $d\Gamma$, appears in the time interval $(t, t + dt)$. $\mathcal{L}'$ is distinct from $\mathcal{L}$ although their supports have a common part ; the free part of $\mathcal{L}'$ does not coincide with the free part of $\mathcal{L}$.

Let us consider now a flat vortex tube inside the bound vortex sheet over a hull $\sum$. This tube has a thickness ϵ , a width $d\sigma$ Let ds_1 be the element of arc of the tube. Applying (7.46), we have

$$d\vec{F}'_T = -\rho\,\vec{\Gamma}\wedge\vec{V}_i\,ds_{1M} = -\rho\left[\vec{T}(M).\,d\sigma_M\right]\wedge\vec{V}_R(M)ds_{1_M} =$$

$$= -\rho\,(\vec{T}\wedge\vec{V}_R)_M\,d\Sigma(M) \qquad (7.47)$$

because

$$\vec{V}_R(M) = \lim_{d\sigma\downarrow 0}\vec{V}_i(M)\,.$$

We know that, if the motion is unsteady, $d\vec{F}'_T$ must be replaced by $d\vec{F}_T$. However there exists no contradiction. The term $-\rho\frac{\partial\mu}{\partial t} = -\rho\frac{\partial\Gamma}{\partial t}$ which appears when the vortex tubes belong to a sheet comes from the integration of $-\rho\frac{\partial\vec{V}}{\partial t}$ through the sheet. When the vortex tube is isolated, there is no discontinuity of $\vec{V}$ on the surface S' and the contribution of the term $\rho\frac{\partial\vec{V}}{\partial t}$ in the integration of $\rho\nabla p$ on S' is $0(R'\,ds_1)$, thus negligibly small. This is not the case when one deals with a sheet.(1)

CASE OF A HULL EQUIPPED WITH MOVABLE APPENDAGES

The treatment of the problem arising from the presence of such appendages obviously depends upon their position with respect to the hull. When the axis of the rudder coincides with the edge of the stern, this rudder may be regarded as a part of the hull. The shape of the hull varies with time. At each instant t there is however a vortex sheet adhering to this hull. The method of Section VI therefore applies in principle. But separation may occur at the leading edge of the rudder because of lack of continuity. Furthermore the effect of the viscous boundary layer is never negligible in this region.

When the rudder (or diving plane) is at some distance from the hull, the rudder behaves as a lifting surface with a small aspect ratio. Because of the thinness of the rudder, the concept of the "interior" of the rudder becomes meaningless and the thin wing theory is to be used.

(1) By using (7.46) one can simplify the expression of the fictitious force F' inside D_i when $\frac{d\Omega E}{dt} \neq 0$ - See [13] Chapter III, B, art. 9.

VIII - THE APPLICATION FIELD OF VORTEX THEORY IN SHIP HYDRODYNAMICS

GENERAL -

It has been seen in the preceding Sections that the vortex theory applies to any body moving in water whatever its motion may be. The methods to be used in practice may considerably vary with the shape of the hull, the motion of the body, the boundaries of the fluid domain. To perform the calculations, it may be advantageous to substitute normal doublet distributions for vortex distributions because a regular scalar Fredholm equation then replaces a vectorial singular Fredholm equation. This is why the vortex distribution kinematically equivalent to the body has been divided in Sections V and VI into two parts, one of them being equivalent to a normal dipole distribution. When the motion of the body consists of a pure translation, the vortex theory leads to computations which are not more complicated than those involved when source distributions are used ; they are even simpler when the distribution of the pressure over the hull is needed. This can be of interest when there exists an incident unsteady flow. The theory extends to the case when there exists a free surface, at least when the condition on the free surface is linearized. Nevertheless, some difficulties are to be expected when the hull pearces the free surface. It is necessary to close the vortex filaments by their mirror images with respect to the plane of the free surface at rest. This can lead to difficulties analogous to those encountered in the case of the Zero-Froude number approximation when the hull is replaced by a normal dipole distribution [6, 7] .

One of the main features of the theory developed in the present paper is that it includes the case of bodies which are neither thin, flat nor slender. However, to the knowledge of the writer, the vortex theory is still used only in cases of thin lifting surfaces. There is thus a need for more general methods and one of the purposes of this paper is to give means to extend the field of applications.

In this Section the present field of application is briefly outlined. Yet the problem of maneuverability and control of marine vehicles is examined in a more detailed manner, for progresses in that domain seem to be strongly needed.

D'ALEMBERT'S PARADOX

There exist many proofs of this theorem. The following one may be of interest,for it clearly explains the physical meaning of the

hypothesis required for its validity.

The body moves with a constant speed $\vec{V}_E$ in an unbounded, inviscid fluid at rest at infinity. One supposes that no separation occurs and that no vortex sheet is shed by the body. Let $(\sum, \frac{\vec{I}}{\epsilon})$ be the vortex sheet which allows the fluid to adhere to the side $\sum_i$ of the hull. The vortex filaments $\mathcal{L}$ are closed rings on $\sum$. They are orthogonal to the relative streamlines $\mathcal{C}$. Let $\vec{i}_s$ be the unit vector tangent to a line $\mathcal{L}$ in the direction of $\vec{T}$, and $\vec{i}_\sigma$ the unit vector tangent to a line $\mathcal{C}$ in the direction opposite to the relative velocity $\vec{V}_R$. A vortex filament $\mathcal{L}$ is defined by the curvilinear abscissa σ_o of its intersection with a line $\mathcal{C}_o$ chosen once for all. The intensity $d\Gamma$ of the vortex ribbon located between two vortex filaments $\mathcal{L}(\sigma_o)$ and $\mathcal{L}(\sigma_o + d\sigma_o)$ is a constant. One has:

$$d\Gamma = \vec{T} \cdot \vec{i}_s \, d\sigma = \gamma(\sigma) \, d\sigma = \gamma(\sigma_o) \, d\sigma_o , \qquad (8.1)$$

and the absolute velocity of the fluid is

$$\vec{V}(M) = \operatorname{curl} \frac{1}{4\pi} \iint_{\sum} \frac{\vec{T}(M')}{MM'} \, d\sum(M') =$$

$$= \operatorname{curl} \frac{1}{4\pi} \int_{\text{stern}}^{\text{bow}} \gamma(\sigma_o) d\sigma_o \int_{\mathcal{L}(\sigma_o)} \frac{\vec{ds}(M')}{MM'} . \qquad (8.2)$$

The relative velocity is $\vec{V}_R = \vec{V} - \vec{V}_E$. Thus the hydrodynamic force on the part $(d\sum, \frac{\vec{I}}{\epsilon})$ of the vortex distribution is

$$\overrightarrow{dF_T} = \overrightarrow{d\mathcal{F}_{T_1}} + \overrightarrow{d\mathcal{F}_{T_2}} , \quad \text{with}$$

$$\overrightarrow{d\mathcal{F}_{T_1}} = - \rho \vec{T}(M) \wedge (-\vec{V}_E) \, d\sum(M) ,$$

$$\overrightarrow{d\mathcal{F}_{T_2}} = - \rho \vec{T}(M) \wedge \vec{V}(M) \, d\sum(M) .$$

The system of forces $\overrightarrow{d\mathcal{F}_{T_2}}$ is that of the forces exerted by the vortex distribution on itself and is therefore equivalent to zero. Also the systems of forces $\mathcal{S}_a$, $\mathcal{S}'_a$ of the general theory are equivalent to zero. Consequently the system of the hydrodynamic forces exerted on the body reduces to that of the forces $\overrightarrow{d\mathcal{F}_{T_1}}$. This gives the general resultant

$$\vec{\mathcal{R}}_d = \rho \iint_{\Sigma} \vec{T}(M) \wedge \vec{V}_E \, d\Sigma(M)$$

and the resulting moment with respect to a given point 0 :

$$\vec{\mathcal{M}}_d = \rho \iint_{\Sigma} \overrightarrow{OM} \wedge \left[\vec{T}(M) \wedge \vec{V}_E(M) \right] d\Sigma(M) .$$

Since $\int_{\mathcal{L}(\sigma_o)} \vec{ds}(M) = 0$, one has :

$$\vec{\mathcal{R}}_d = \rho \int_{\text{stern}}^{\text{bow}} \vec{V}_E \, \gamma(\sigma_o) \, d\sigma_o \int_{\mathcal{L}(\sigma_o)} \vec{ds}(M) = 0 \qquad (8.3)$$

Furthermore :

$$\vec{\mathcal{M}}_d = \rho \iint_{\Sigma} \left\{ \vec{T}(M) \left[\vec{V}_E \cdot \overrightarrow{OM} \right] - \vec{V}_E \left[\overrightarrow{OM} \cdot \vec{T}(M) \right] \right\} d\Sigma(M)$$

$$= -\rho \vec{V}_E \int_{\text{stern}}^{\text{bow}} \gamma(\sigma_o) \, d\sigma_o \int_{\mathcal{L}(\sigma_o)} \overrightarrow{OM} \cdot \vec{ds}(M)$$

$$+ \rho \int_{\text{stern}}^{\text{bow}} \gamma(\sigma_o) \, d\sigma_o \int_{\mathcal{L}(\sigma_o)} (\vec{V}_E \cdot \overrightarrow{OM}) \, \vec{ds}(M) .$$

$$= \rho \int_{\text{stern}}^{\text{bow}} \gamma(\sigma_o) \, d\sigma_o \int_{\mathcal{L}(\sigma_o)} (\vec{V}_E \cdot \overrightarrow{OM}) \, \vec{ds}(M) . \qquad (8.4)$$

This term is not null, at least in general.

Equation (8.3) expresses the d'Alembert paradox. If free vortices are shed by the body, then (8.3) is no longer verified. $\mathcal{R}_d$ has two components ; one of them is a lift and the other one is the "induced resistance".

KUTTA-JOUKOWSKI'S THEOREM -

The first version of this theorem concerned wing profiles in a uniform motion of translation, with $\vec{V}_o = 0$. The wing is an infinite cylinder and its profile $\mathcal{C}$ is its intersection by a plane normal to the generatrices. The problem can be considered as the limiting case of that of a wing, when the aspect ratio of which tends to infinity. When the aspect ratio is finite, the relative velocities on the two sides Σ_{1_e} , Σ_{2_e} of the wing near the trailing edge are equal and opposite. This follows from the continuity of the flow between Σ_{1_e} and Σ_{f_1} and between Σ_{2_e} and Σ_{f_2} . Hence, in the case of a wing profile, one must have $\vec{V}_{R_E} = 0$ at the trailing edge B . This is the Kutta condition which determines the density of the vortex sheet on Σ , that is the ratio $\frac{d\Gamma}{d\sigma}$ on the contour $\mathcal{C}$ of the profile.

The Kutta condition holds when the motion is unsteady.

The theory developed in the preceding Sections applies to wing profiles. But because one deals with two-dimensional motions, the concept of complex velocity potential can be used and leads to considerable simplifications. In particular, one can associate a vortex distribution and a source distribution on the skeletton of the hull to obtain the desired profile shape (1) .

(1) The determination of the exact distribution of the velocity at the leading edge requires some care [8] .

WING PROFILE IN A QUASI-RECTILINEAR, NON-UNIFORM MOTION

This problem has been considered by many authors and finally solved by von Karman and Sears in 1938 [2] . These authors gave the correct form of the Volterra integral equation for the total circulation Γ around the profile. They showed, in particular, how the circulation behaves following a perturbation in form of a step function occurring at time t_o . The response time is long and approximately corresponds to a path equal to 15 times the chord, but the effect of the total virtual masses is considerable and the lift at time $t_o + 0$ is half its final value. In [3] the writer has completed the calculation in order to obtain the pressure distribution on the profile.

UNSTEADY THREE-DIMENSIONAL MOTION OF A WING WITH A FINITE ASPECT RATIO

There now exist methods for solving the previous problem in the case of a thin wing of finite aspect ratio when the amplitudes of the deviations from a uniform motion of translation are small. Dat and Malfois [4] have given a linearized theory using an acceleration potential $\Psi = \psi e^{ist}$ with

$$\psi = - V_E \frac{\partial \varphi}{\partial x} + is\,\varphi \quad \text{for} \quad \Phi = \varphi e^{ist} \quad ,$$

V_E being here in the negative x-direction. The pressure P is given by

$$p = - \rho \psi \quad , \quad P = p\, e^{ist}$$

The component in the vertical direction of the velocity is

$$W = w\, e^{ist} \quad \text{with} \quad w = \frac{1}{4 \pi \rho V_E} \iint_{\text{wing}} K(x - \xi,\ y - \eta)\, \delta p(\xi, \eta)\, d\xi d\eta \ ,$$

where δp is the pressure difference between the two sides of the wing. The difficulties due to the singularity of the kernel have been overcome by the authors who obtained a very good agreement between calculated and measured values of δp for harmonic motions.

PROPELLER THEORY

The determination of the steady and unsteady forces acting on a propeller is a problem of importance (efficiency, risk of cavitation, vibrations, noise, etc...). We just mention it for it is beyond the purpose of the present paper.

SHIP MANEUVERABILITY THEORY

A first step in the mathematical maneuverability theory consists of the determination of the bound vortices when the relative motion is steady. This problem has been considered by P. Casal in his Thesis dissertation for a ship at a constant drift angle in the horizontal plane and for a ship in a forced turning motion in the same plane(1). Several drastic simplifications were made :

(i) The waves generated by the ship are neglected. Thus one deals with the Zero-Froude-number approximation.

(ii) The ship is assumed to be infinitely thin ; the heel angle is ignored.

(iii) The free vortex sheets are attached to the hull along the keel and its mirror image with respect to the plane of the free surface at rest.

(iv) The free vortex filaments start in the direction of the bissectrix of the angle between the local velocity of the body on the keel and the keel line.

In fact, because of the errors due to the first three assumptions, the fourth one is essentially used for the determination of the

(1) Casal's Thesis was written 20 years ago when the author was staying as scientist at the Bassin d'Essais des Carènes (Report Bassin d'Essais des Carènes - 1951) and published much later [9] .

behavior of the curves giving the density of the bound vortices in the plane of symmetry of the ship ($y = 0$). Let ξ denote the reduced abscissa $\frac{x}{L/2}$, the origin of the moving axes being at the center of the plane $y = 0$.

The integral equation of the problem expresses that the velocity induced by the total vortex distribution is tangent to the plane $y = 0$. We give below the density $f(\xi)$ of the circulation. In the case of an oblique translation, one has :

$$f(\xi) = \frac{\pi V L}{2} \epsilon \tan \alpha \quad \varphi_1(\xi) \quad \text{with}$$

$\frac{\epsilon}{2}$ = draft/length ratio, α = drift angle, and

$$\varphi_1 = \delta(1 - \xi) + 0.4e^{0.4(1 - \xi)}, \quad \delta = \text{Dirac function}$$

In the case of a gyration of radius R about an axis whose orthogonal projection on the plane $y = 0$ is at the abscissa $\xi_J = \frac{2R}{L} \sin \alpha$, one has :

$$f(\xi) = \frac{\pi V L}{2} \epsilon \frac{L}{2R} \varphi(\xi),$$

$$\varphi(\xi) = (1 - \xi_J)\,\delta(1 - \xi) - 1.$$

Figures 8.2 and 8.3 show the graphs of φ in the first case and in the second case respectively.

The force Y and the moment N with respect to the z-axis (vertical upwards) are

$$Y = \frac{1}{2} SV^2 \pi\epsilon \cos\alpha \left[A \sin\alpha + B \frac{L}{2R} + C \frac{L}{2R} \left|\frac{L}{2R}\right|\right], \quad C = C(\xi_j)$$

$$N = \frac{L}{2} \cdot \frac{1}{2} \rho SV^2 \pi \cos\alpha \left[A_1 \sin\alpha - B_1 \frac{L}{2R} - C_1 \frac{L}{2R} \left|\frac{L}{2R}\right|\right], \quad C_1 = C(\xi_j)$$

A , B , A_1 , B_1 are constants relatively close to unity, and C , C_1 are functions of ξ_j . As ξ_j is practically invariable, C and C_1 may also be considered as constants.

In fact all the coefficients depend on the hull shape and must be experimentally determined. Let $-\Phi$, $\frac{L}{2}\Phi$ be the y-component and the moment of the hydrodynamic force exerted on the rudder, M_o the added mass for the double model calculated by neglecting the free vortices effect for a non-uniform motion in the y-direction, and I_o the similar inertial moment in a non-uniform rotation about the z-axis. We put :

$$\begin{cases} M = \frac{1}{2}\rho S \frac{L}{2} \pi\epsilon \quad k , \quad M_o = \frac{1}{2}\rho S \frac{L}{2} \pi\epsilon \quad k_o , \quad k_1 = k + k_o \\ I + I_o = (M + M_o)\left(\frac{L}{2}\right)^2 \quad \frac{h}{k_1} \end{cases}$$

Furthermore, because the circulation can never take immediately its asymptotic value corresponding to the steady motion defined by the present values of α and $\frac{L}{2R}$, the present value of Y is not given by the above expression, but by $Y - Y_2$. Similarly the hydrodynamic moment is not N, but $N - N_2$. Y_2 and N_2 are the deficiencies due to the history of the motion.

Finally the equations of the unsteady motion are as follows :

$$k \frac{L}{2R} - k_1 \frac{L}{2V} \frac{d\alpha}{dt} = A\alpha + B \frac{L}{2R} + C \frac{L}{2R} \left|\frac{L}{2R}\right| - \frac{\Phi + Y_2}{\frac{1}{2}\rho SV^2 \pi\epsilon}$$

$$\frac{L}{2V} h \frac{d}{dt}\left(\frac{L}{2R}\right) = A_1 \alpha - B_1 \frac{L}{2R} - C_1 \left|\frac{L}{2R}\right| \frac{L}{2R} + \frac{\Phi + \frac{N_2}{L/2}}{\frac{1}{2}\rho SV^2 \pi\epsilon} .$$

Let

$$S = A_1 B + A B_1 - A_1 k .$$

One sees that in a steady motion, the ratio $\frac{L}{2R}$ is given by

$$(A + A_1)\frac{\Phi}{\frac{1}{2}\rho SV^2 \pi\epsilon} = S \frac{L}{2R} + (A_1 C + A C_1) \frac{L}{2R} \left|\frac{L}{2R}\right| .$$

If $S > 0$, this equation has one and only one root. If $S < 0$, there exist three roots for small values of $\frac{\Phi}{\frac{1}{2}\rho S V^2 \pi \epsilon}$, and, in particular, for $\Phi = 0$. Let $(\frac{L}{2R})_1$, $(\frac{L}{2R})_2$ and $(\frac{L}{2R})_3$ be the three roots with $(\frac{L}{2R})_1 < (\frac{L}{2R})_2 < (\frac{L}{2R})_3$. It is to be expected that the steady motion $(\frac{L}{2R})_2$ is unstable.

This is confirmed by the study of the equations of the unsteady motion when Y_2 and N_2 are neglected. After a perturbation, the stable steady motion is reached again without oscillation.

When one takes into account Y_2 and N_2, that is the terms depending on the history of the motion, one sees that, if $S > 0$, the steady motion is still stable, but, after a perturbation, it may occur that the transient motion be oscillating. It may even occur that no straight motion be possible for Φ equal to zero ; the head is constant in the mean, but it is continuously oscillating.

Oscillating motions in calm water are therefore a consequence of the delayed circulation around the ship. They appear when the ship has to proceed a long path before the circulation becomes close to its asymptotical value.

In spite of the rather rough assumptions involved in Casal's theory, it appears that this theory is qualitatively in good agreement with experiments, except for what concerns the position of the resultant force in the oblique translations. According to the above expressions for Y and N when R = , this force should intersect the plane of symmetry at a point practically invariable and located inside the ship. Experiments on models show, on the contrary, that this point can be located ahead of the bow for very small angles of attack. Then,when the angle of attack increases, the ξ of this point rapidly decreases and, finally, takes a value rather close to that assigned by the theory.

The explanation of that discrepancy seems to be that the free vortices are shed along the stern-post and not along the keel line when α is very small. Because self-sway motions are very undesirable, attention is to be paid to this point. That is also for this reason that we have indicated above the existence near the bow of a very strong vortex represented, in a first approximation, by a δ-function.

In the past, the wanted maneuvering qualities mainly concerned the characteristics of the motions at large rudder angles.

Some cases of course unstability had been stated, but regarded as rather exceptional and the behavior of the ship in transient motions was not a prior matter of concern. The situation became quite a different one with submarines achieving very high speeds. A dynamic stability in the vertical and horizontal planes of motion are required, and an automatic pilot system is used for performing combined maneuvers in both planes.

Surface vessels such as big tankers also need remarkable maneuvering qualities ant to that end, they are also equipped with automatic steering systems.

Nevertheless, the automatic control of the ship does not solve all the difficulties involved in maneuvering. One can even say that, from a certain point of view, it gives rise to new problems.

The writer has described some years ago some among the methods used at the Bassin d'Essais des Carènes for studying experimentally the case of submerged bodies, determining the coefficients of the equations of the motion and predicting the real motion of the full scale vehicle [10]. In a recent paper [11], M. Gertler developed analogous views on the purpose of this type of matched experimental and mathematical researches.

However powerful this way may be, it leads to the introduction in the equations of motion of much too many coefficients and perhaps in an unappropriate manner. This situation does not favour the progress of the knowledge of the fundamentals in maneuverability. In [12], the writer drew the attention to the time response to a maneuver and the risk of erroneous interpretation of experimental results. The writer is of the opinion that new purely theoretical researches are needed. Casal's thesis has been given as an example to base this opinion. The present paper has been inspired by the same line of thought.

CONCLUSION

Although the Vortex Theory plays an important role in many Chapters of Ship Hydrodynamics, it does not seem to be used in all the cases where it could really be fruitful. It is so when one deals with the Ship herself.

Several explanations of the rather reluctant attitude of the Naval Architects with respect to the application of vortex theory to

ship hulls could probably be found. A fact is that an arc of vortex filament does not generate a velocity potential and in practice the representation of the hull by a source distribution can be simpler than its representation by a vortex distribution. However the vortex theory, which allows the fluid to satisfy the physically meaningful condition of adherence to the hull, certainly offers mathematical models closer to the reality than those drawn from the other types of hull representation. Furthermore, it leads more rapidly to the determination of the distribution of the pressure and of the velocity on the hull surface.

The present paper is therefore an attempt to explain the fundamentals of the vortex theory and of its application to the kinematics and dynamics of bodies moving in water.

After a brief survey on the various aspects of the vortex theory in inviscid fluids (Section I), one will find in Section II the Poincaré formula which permits the calculation of the velocity in a fluid domain when the vorticity inside the domain and the velocity on its boundary are known, and in Section III the application of Poincaré's formula to the determination of vortex distributions kinematically equivalent to any given ship hull. The class of these distributions is infinite. Each consists of a volume distribution inside the hull and of a surface distribution over the hull. The volume distribution can be chosen arbitrarily. The surface distribution associated with it is determined by means of a singular vectorial Fredholm equation of the second kind.

Section IV gathers material to be used later to solve the dynamical problem.

Section V is devoted to the study of the structure of the vortex distribution which permits the fluid to adhere to the hull surface. The surface distribution is the sum of infinitely flat vortex tubes called here "vortex ribbons". The vorticity inside the hull is twice the angular velocity of the body. Thus, if the angular velocity is not null, the intensity of each vortex ribbon is not a constant along its length. Furthermore, if free vortices are shed by the hull, some of the vortex ribbons do not close on the hull. To overcome the difficulties arising from these circumstances, the vortex distribution generated by the body is divided into two distinct families almost independent of each other. One consists of the volume distribution and of the surface distribution associated with it so that the velocity induced by this first family outside the hull be null. The second family consists of a vortex sheet entirely located over the hull when no free vortex-sheet is shed by the hull. In the opposite case, it includes the free vortex-sheets.

As shown in Subsection D, it may also include a volume vortex distribution in the wake when the motion is unsteady.

Section VI deals with the integral equations determining the two families of the total vortex distribution. The singular vectorial integral equation related to the first family can be replaced by a singular scalar Fredholm equation for a Neumann interior problem. It can be solved once for all whatever the body motion may be. The integral equation for the second family reduces to the scalar regular Fredholm equation of the second kind for a certain Dirichlet interior problem when the fluid is unbounded and at rest at infinity. In the most general case it becomes a Volterra equation expressing the solution in terms depending on the history of the motion.

Section VII is devoted to the study of the system $\mathscr{S}_d$ of hydrodynamic forces exerted on the body. As stated before the total vortex distribution determines inside the hull a fluid fictitious motion which coincides with the absolute motion of the body. For this kinematical condition to be compatible with the dynamical equilibrium of the fluid, it is necessary to introduce a certain system of fictitious forces per unit mass inside the hull.

The system $\mathscr{S}_d$ of hydrodyhamic forces exerted on the body at t_o can be written in the form

$$\mathscr{S}_d = \mathscr{S}_{q.s.} + \mathscr{S}_a - \delta\mathscr{S}_T + \mathscr{S}_a$$

where $\mathscr{S}_{q.s.}$ is the quasi-steady system of forces, that is the system to which $\mathscr{S}_d$ would reduce if the motion of the body were uniform in a large interval (t', t_o). $\mathscr{S}_a$ is the system due to the so-called added masses ; it is independent of the free vortices shed by the body. There exists a difference between the structure of the free vortices at t_o and at $t = +\infty$, the latter being evaluated under the assumption that the motion of the body is uniform to $t > t_o$. This difference affects both the bound vortex distribution on the hull and the incident velocity on it. It entails the term $-\delta\mathscr{S}_T$. The last term $\mathscr{S}'_a$ is an inertial effect due to the partial derivative $\frac{\partial}{\partial t}$, at t_o, of the bound vortex sheet. $\mathscr{S}_d$ reduces at $t_o + 0$ to $\mathscr{S}_{q.s.}(t_o - 0) + \mathscr{S}'_a(t_o + 0)$ if the body motion is uniform for $-\infty < t_o - 0$ and for $t > t_o + 0$, but discontinuous between $t_o - 0$ and t_o.

Section VIII consists of a brief synopsis of the present applications of the vortex theory to ship hydrodynamics with somewhat greater emphasis on ship maneuverability. Attention is drawn to Casal's thesis about this problem. Casal's theory certainly involves too drastic simplifications and some among the conclusions are unacceptable. First, a ship cannot be considered as infinitely thin, and even if such an assumption could be accepted in a first approximation, it would be necessary to satisfy the boundary condition on the whole surface of the longitudinal plane of symmetry of the ship. It is still necessary to resort the empirical or semi-empirical methods. But, in the writer's opinion the part devoted to theory is really unsufficient.

The purpose of this paper was to prompt researches in that direction.

REFERENCES

[1] ROY, M., "Aérodynamique des ailes sustentatrices et des hélices", Gauthier Villars, Paris, 1928.

[2] Von KARMAN, Th. and SEARS, W.R., "Airfoil theory for non-uniform motion", Journal of the Aeronautical Sciences, vol. 5, No 10, August 1938.

[3] BRARD, R., "Mouvements plans non permanents d'un profil déformable.", Association Technique Maritime et Aéronautique, No 63, 1963.

[4] DAT, R., and MALFOIS, J-P., "Sur le calcul du noyau de l'équation intégrale de la surface portante en écoulement subsonique instationnaire", La Recherche Aérospatiale, No 1970-5, September-October 1970.

[5] DELSARTE, J., "Included in "Leçons sur les tourbillons" by H. VILLAT, Gauthier Villars, Paris, 1930.

[6] KOTIK, J., and MORGAN, R., 'The uniqueness problem for wave resistance calculated from singularity distributions which are exact at Zero Froude Number", Journal of Ship Research, vol. 13, No 1, march 1969.

[7] BRARD, R., "The representation of a given ship form by singularity distributions when the boundary condition on the free surface is linearized", Journal of Ship Research, vol. 16, No 1, march 1972.

[8] DARROZES, J-S., "On the uniformly valid approximate solutions of Laplace equation for an inviscid fluid flow past a three-dimensional thin body", ONERA Report.

[9] CASAL, P., "Théorie de l'aile portante de très faible envergure", Publications Scientifiques et Techniques du Ministère de l'Air, No 384, Paris, 1962.

[10] BRARD, R., BINDEL, S., LECOEUR, G. and CHAVEREBIERE de SAL, A., "Le modèle libre de sous-marin du Bassin d'Essais des Carènes", Association Technique Maritime et Aéronautique, No 68, 1968.

[11] GERTLER, M., "Some recent advances in dynamic stability and control of submerged vehicles", International Symposium on Directional Stability and Control fo Bodies moving in Water. The Institution of Mechanical Engineers, London, 1972.

[12] BRARD, R., "A vortex theory for the manoeuvring ship with respect to the history of her motion", 5th Symposium on Naval Hydrodynamics, Bergen, 1964.

[13] BRARD, R., "A Mathematical Introduction to Ship Manoeuverability (2nd Series, David Taylor Lectures , NSRDC - Washington, (in the Press), Sept. 1973.

* * *

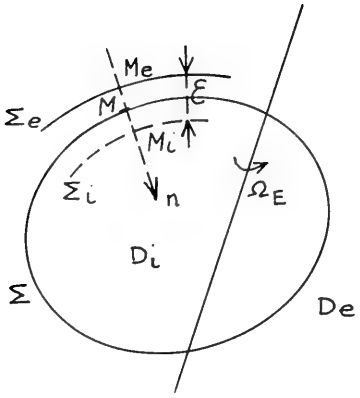

Figure 1

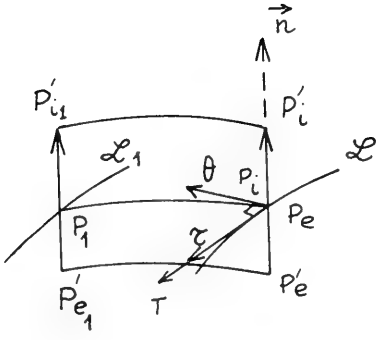

Figure 2

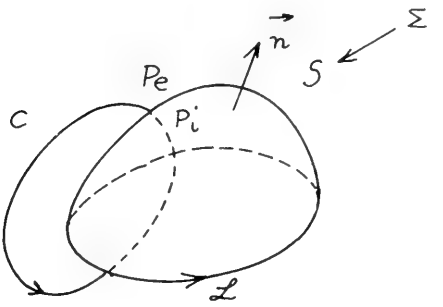

Figure 3

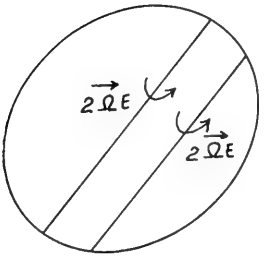

Figure 4

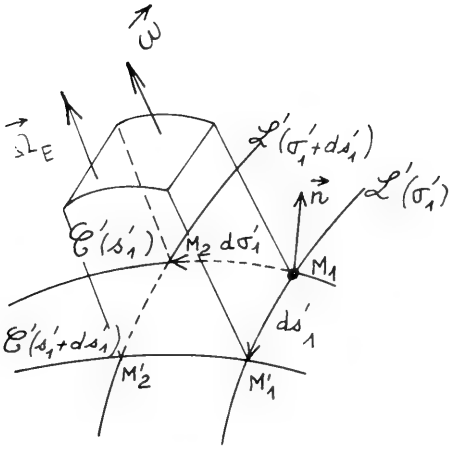

Figure 5.1

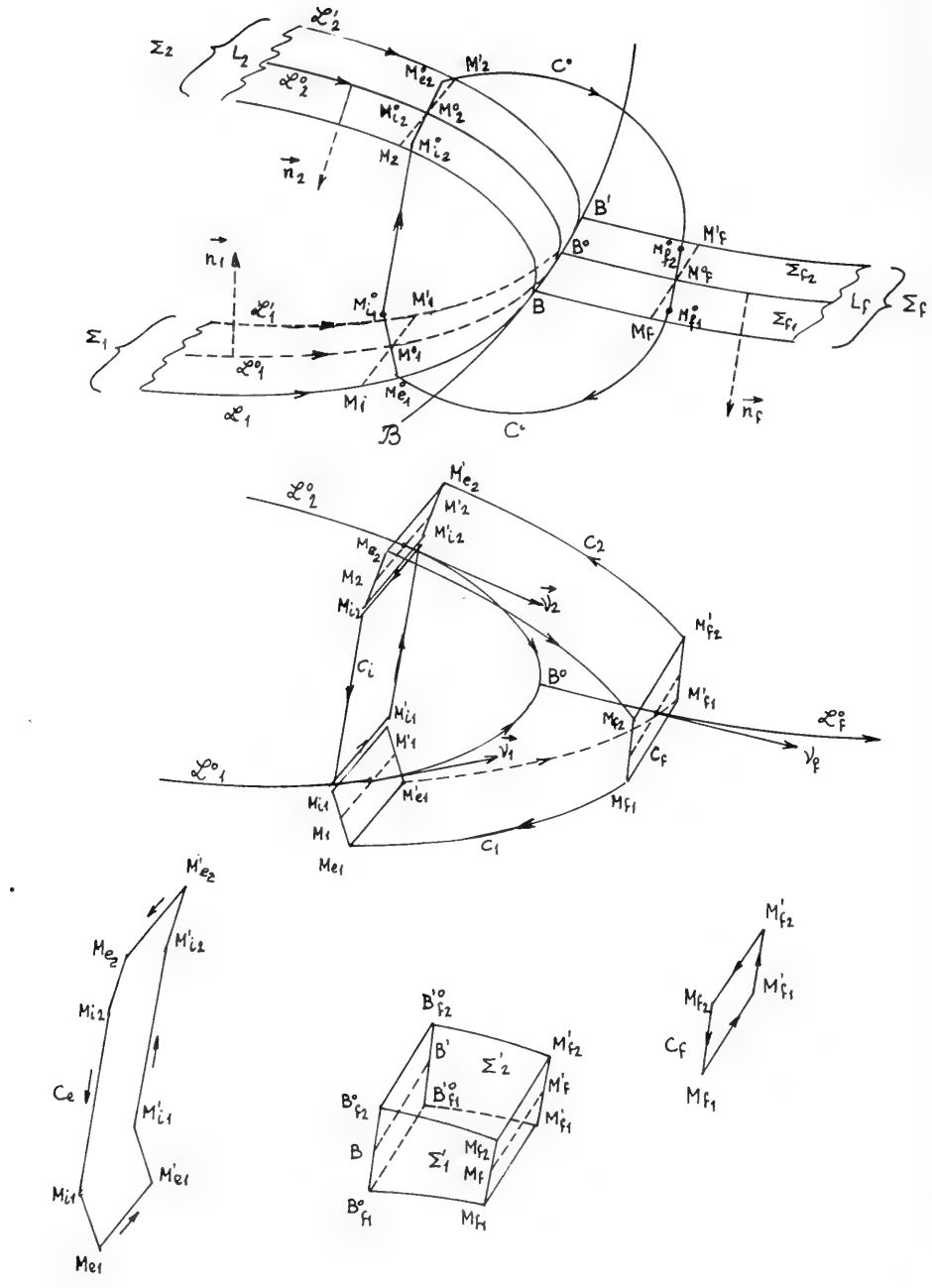
Σ2
L2
M'2
C°
B'
B°
M'f
Σf2
Lf
Σf
B
MF
Σf1
Σ1
M'1
M1
C°
B
C2
Ci
B°
Cf
C1
Ce
Mi2
Mi1
Me2
Me1
M'i2
M'i1
M'e2
M'e1
M'f2
M'f1
Mf2
Mf1
Cf
B'f2
B'f1
B'f1
B'
Σ'2
Σ'1
Mf2
Mf
Mf1

Figure 5.2

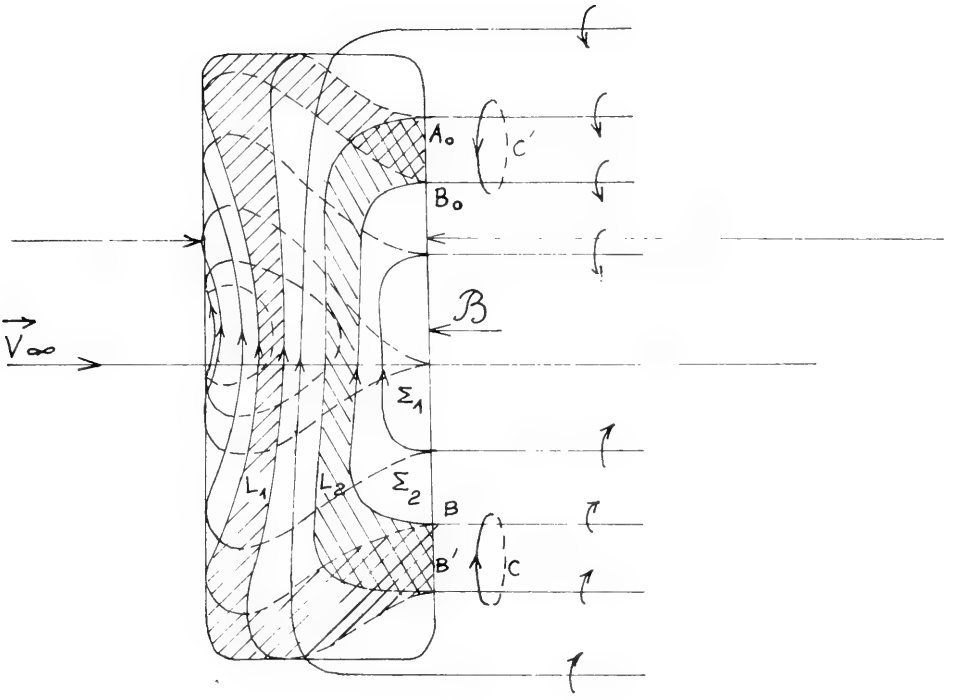

Figure 5.3

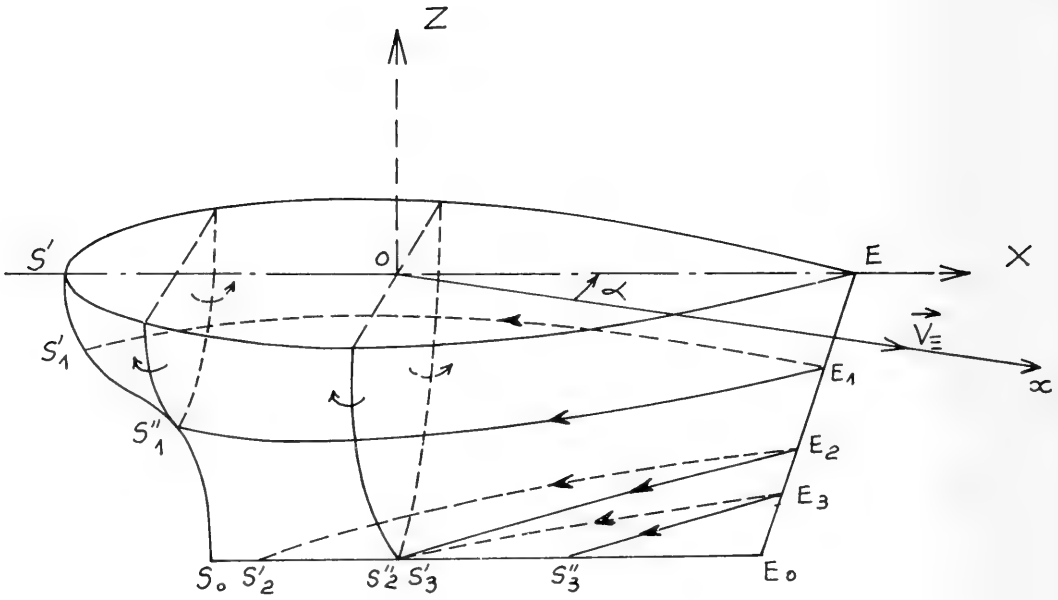

Figure 5.4 - Half-model in oblique translation (positive drift, permanent motion).

The streamlines of the relative motion are more inclined towards starboard than towards port. The lines ending on a same point of the longitudinal contour SS_oE_o do not have the same direction, hence the shedding of free vortices along SS_oE .

E_n streamlines starting points on the stem,

S'_n end point of the starboard streamlines,

S''_n end point of the port streamlines.

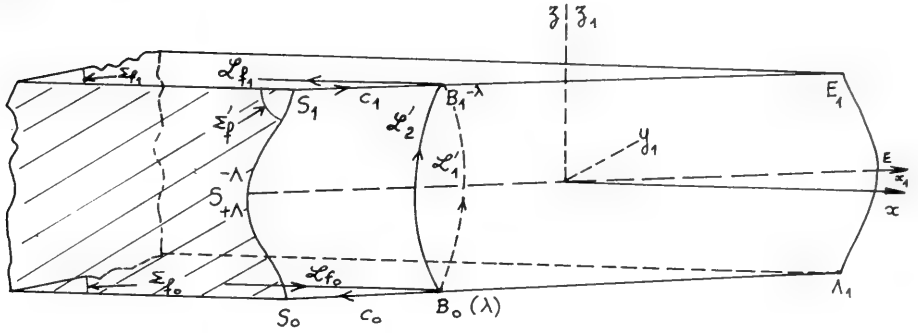

Figure 5.5. a

$\Sigma_{f_0}(\lambda)$ part of Σ_{f_o} on the rear of $\mathcal{L}_{f_o}$,

$\Sigma_{f_1}(\lambda)$ Σ_{f_1} $\mathcal{L}_{f_1}$,

$\Sigma_1(\lambda)$ Σ_1 $\mathcal{L}_1$, $\Sigma_f(\lambda) =$

$= \Sigma_{f_o}(\lambda) + \Sigma'_f + \Sigma_{f_1}(\lambda)$.

$\Sigma_2(\lambda)$ Σ_2 $\mathcal{L}_2$,

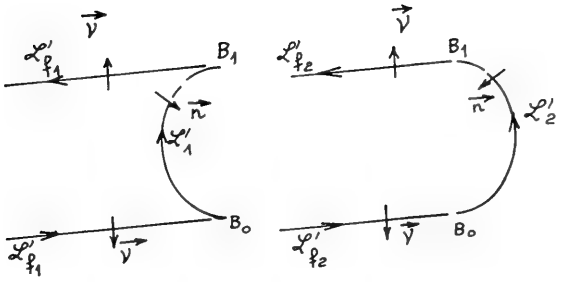

Figure 5.5. b

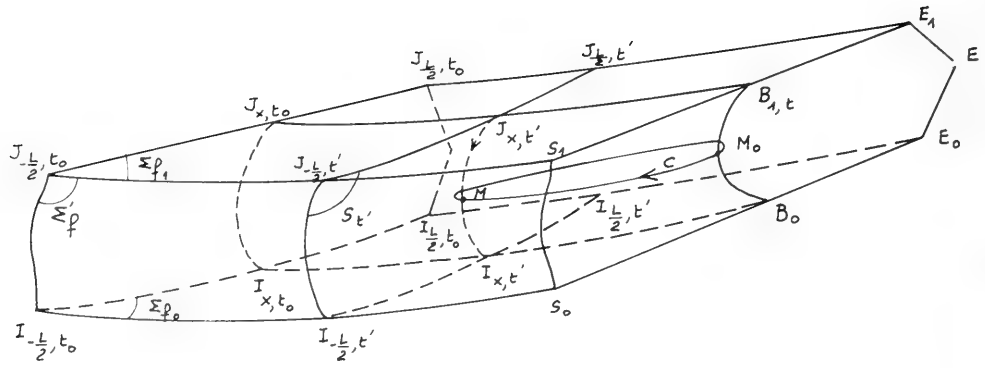

Figure 5.6

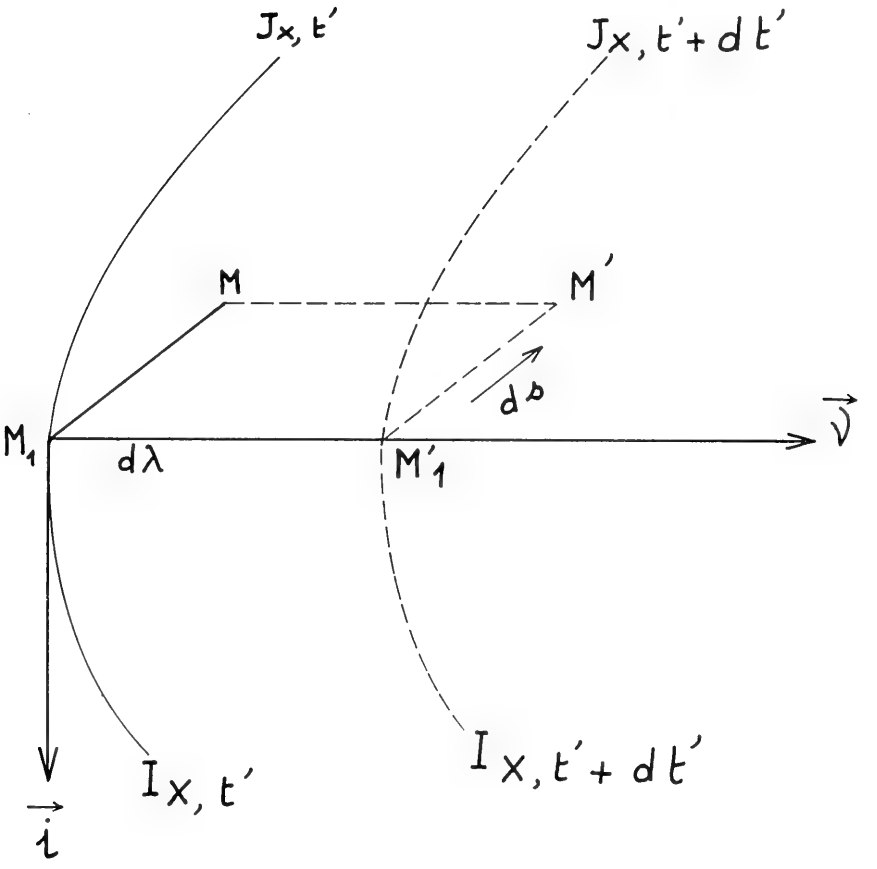

Figure 5.7

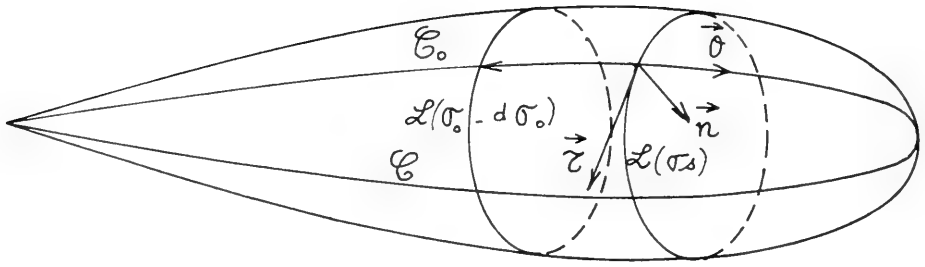
$\mathcal{C}_0$
$\vec{v}$
$\mathcal{L}(\sigma_0 - d\sigma_0)$
$\vec{n}$
$\mathcal{C}$
$\vec{\tau}$
$\mathcal{L}(\sigma_s)$

Figure 8. 1

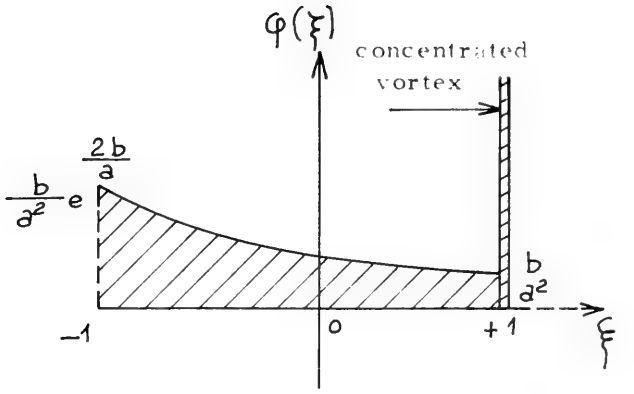

Figure 8.2

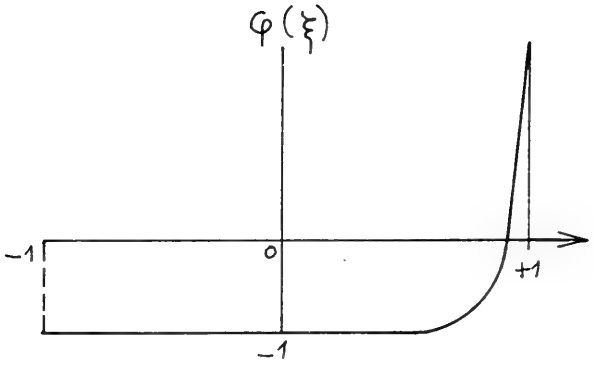

Figure 8.3

NOMENCLATURE

1. OPERATORS

∇ $= \left(\frac{\partial}{\partial x_1}, \frac{\partial}{\partial x_2}, \frac{\partial}{\partial x_3}\right)$, (the axes x_1, x_2, x_3 make a right-handed system).

Δ $= \nabla^2$ Laplacian operator

$\wedge$ Symbol of vectorial multiplication.

2. VORTEX FILAMENTS AND VORTEX SHEETS

$\mathscr{L}$ Vortex filament

$d\Sigma$ Element of area of a vortex sheet

Σ_e, Σ_i The two sides of Σ

ϵ Infinitely small thickness of the vortex sheet

$\vec{n}$ Unit vector normal to the sheet in the direction from Σ_e towards Σ_i

$\vec{V}$ Velocity of a fluid point

$\vec{\omega}$ Curl of $\vec{V}$

$\vec{T}$ Limit of $\epsilon \vec{\omega}$ when $\epsilon \longrightarrow 0$; $\vec{T} = (\vec{T} - \vec{T}') + \vec{T}'$ in sections V, VI, VII.

$\vec{\tau}$ Unit vector tangent to Σ in the direction of $\vec{T}$

$\vec{V}(P_i) - \vec{V}(P_e)$, (or $\vec{V}(M_i) - \vec{V}(M_e)$) : jump of $\vec{V}$ through Σ from P_e to P_i (or from M_e to M_i), P_e (or M_e), P_i (or M_i) belonging to Σ_e, Σ_i, respectively.

$$\vec{T} = -n \wedge \left[\vec{V}(M_e) - \vec{V}(M_i)\right]$$

$\mathscr{C}$ Line on Σ orthogonal to the $\mathscr{L}$'s

Γ Circulation of $\vec{V}$ in a closed circuit

$d\Gamma$ Intensity of a flat vortex tube on Σ, the width of the tube being $d\sigma$.

$\overrightarrow{d\Gamma} = d\Gamma \cdot \vec{\tau}$

3. GEOMETRY AND KINEMATICS

Σ Hull surface

D_i, D_e Interior, exterior of Σ respectively

D'_e Domain occupied by the real fluide : $D'_e \subset D_e$

$\vec{V}$ Absolute velocity of a fluid point

$\vec{V}_R$ Relative velocity of a fluid point : velocity with respect to axes moving with Σ

$\vec{V}_E$ Velocity of a point fixed with respect to the moving axes

Ω_E Angular velocity of the moving axes

Σ_f Surface supporting a free vortex sheet

$\vec{V}_o$ Incident velocity on Σ

Φ, Φ_o Velocity potentials : $\vec{V} = \nabla\Phi$ if curl $\vec{V} = 0$, $\vec{V}_o = \nabla\Phi_o$

$\vec{\omega}$ = curl $\vec{V}$

$\vec{\omega}_R$ = curl $\vec{V}_R$

$\mathscr{B}$ (with or without accents) : line on Σ along which Σ_f is attached to Σ

$\vec{V}_d$ Velocity induced by the bound vortices

$\vec{V}_f$ Velocity induced by the free vortices

$\vec{T}_f$ Vector $\vec{T}$ on Σ_f

$d\Gamma_f$ $d\Gamma$ on Σ_f

μ Density of a normal doublet distribution over the hull surface Σ

μ_f Density of a normal doublet distribution over the free vortex sheet $\sum_f$

$\mathscr{L}_f$ Vortex filament on $\sum_f$

Φ_d , Φ_f Velocity potentials generated by the normal doublet distribution on $\sum$, $\sum_f$ respectively

$\vec{V}'$ Velocity induced inside D_i by the vortex family $(D_i , 2\vec{\Omega}_E)$ + $(\sum, \frac{\vec{T} - \vec{T}'}{\epsilon})$ in Sections V, VI and VII.

Φ_i Velocity potential defined inside D_i such that $\vec{V}_E - \vec{V}' = \nabla\Phi_i$ (Sections VI and VII)

4. DYNAMICS

ρ Mass density of the fluid

$\vec{F}$ Exterior force per unit mass : $\vec{F} = \nabla\mathcal{U}$

$\vec{F}'$ Additional exterior force inside D_i if $\frac{d\vec{\Omega}_E}{dt} \neq 0$; $F' = \frac{\partial\vec{V}'}{\partial t}$

p_d Hydrodynamic pressure

$\overrightarrow{d\mathcal{F}_T}$ Hydrodynamic force exerted by the flow on an element $d\sum$ of a bound vortex sheet or on an element of arc of a vortex filament which does not move with the fluid

$\mathscr{S}_T$ System of hydrodynamic forces exerted on the vortex sheet $(\sum , \frac{\vec{T}}{\epsilon})$

$\mathscr{S}_d$ System of hydrodynamic forces exerted on the hull

$\mathscr{S}_i$ System of inertial forces inside D_i

$\mathscr{S}'_i$ System of complementary forces $\rho\vec{F}'\, dD_i$ inside D_i

$\mathscr{S}_d$ System of forces $-\rho(\frac{\partial\Phi}{\partial t})_{M_e} \vec{n}\, d\sum(M)$ on $\sum_e$

$\mathscr{S}'$ System of forces $-\rho\vec{T}(M)\ \vec{V}_R(M)\, d\sum(M)$

$\mathscr{S}_{a_o}$ System of forces due to the added masses when there exists no vortex sheet

$\mathscr{S}'_{q.s.}$ Estimate of $\mathscr{S}'$ when the deficiency affecting Φ_f is neglected

$\mathscr{S}_{d_o} = \mathscr{S}_{a_o} + \mathscr{S}'_{q.s.}$ Estimate of $\mathscr{S}_d$ when the deficiencies affecting Φ_d and Φ_f are neglected

DISCUSSION

Peter T. Fink
University of New South Wales
Kensington, Australia

The principal message of Admiral Brard's paper is that we should take bound vorticity more seriously, and although I like the vortex ribbons I cannot make up my mind about them before trying some examples. I want to make a contribution concerned with the problem of modelling shed vorticity, particularly when there are sharp edges fixing separation at known positions. Figure 1 is an example of a laboratory simulation of a section of a ship heaving at its moorings, with no forward speed. A student, Mr. W. K. Soh, and myself are devoting ourselves to potential flow modelling of (in this case) bilge keel separations and I think there is something of more general interest in this which I should like to speak about.

In two-dimensional flow such problems can, of course, be transformed to the case of a flat plate moving normal to itself in arbitrary unsteady motion. For practical calculations it is usually necessary to replace the vortex sheet by discrete vortices and one might expect the calculation to be straightforward, using Kutta conditions at the edges, the Kelvin Theorem to ensure that the total circulation remains constant and the condition of zero force on each vortex in the standard classical way. This certainly works quite satisfactorily for lifting aerofoils with unsteady motion in two dimensions. However, for a blade moving normal to itself the circulation is always zero, so that the Kelvin theorem does not help and a degree of arbitrariness has to be injected. The arbitrariness is required because the Kutta condition will not give both the strength and the position of the first of the vortices one is going to put in. Figure 2 is an example which shows a plate of unit length moving towards the left, in this case five seconds after an implusive start, that is, when the motion is still largely inertial. Fresh discrete vortices have to be added to give the picture shown here and in one of the earlier attempts they were added at constant intervals of time ; and not long after a degree of zigzagging developed, as shown. My attention was drawn to the fact that Professor Birkhoff had issued a warning about this sort of procedure over ten years ago.

Figure 3 shows the improvement when the time intervals are

not equal but are chosen so as to make the distance travelled by the nth shed vortex equal to the separation of the first vortex from the edge, but there is still some zigzagging. The real problem of this kind of discretisation is that when the discrete vortices are spaced too closely, when they get close to each other, they indulge in a planetary motion about each other ; and if they are spaced too far apart you will not get the velocity field right and the shape of the sheet will not develop properly.

Figure 4 shows our current recipe for this sort of situation, and that is that after each step of the calculation one moves the vortices to approximately equidistant positions while maintaining the centre of vorticity of the whole lot in the correct position.

Figure 5 shows a comparison with the only exact solution known to myself, von Wedemayer's. The circles on that graph, using the equispacing recipe, seem to give excellent agreement for the development of circulation with time for the vorticity shed from one of the edges. The total circulation shed into the stream is, of course, zero, and that is one of the big troubles in this game.

Figure 6 shows what can be done with this method. Here a plate has completed one half cycle of oscillatory motion normal to itself and Figure 7 shows the disposition of the vorticity after a complete cycle. I will not bother you with estimates of force associated with this kind of thing or conformal transformations, but I would like to pass to the last example.

This shows the case of a plate, Figure 8, a bit like the earlier one, growing in length vertically while moving normal to itself. We have applied that solution to slender lifting surfaces of arbitrary platform (arbitrary, that is, while still remaining slender) and camber and we seem to get rather better results for that type of lift surfaces with leading edge vortex separation than the results obtained over the years, first by Legendre here and then by Brown and Michael and others. So we are not completely put off by Birkhoff's warning and I would recommend our particular recipe for calculating the development of vortex sheets, although we have not, naturally, got anything on uniqueness for the results.

We are now working on a number of configurations of interest where there are sharp edges to fix the separation, such as that shown in the first picture, and also on others, where non-linear lift phenomena occur.

REPLY TO DISCUSSION

Roger Brard
Bassin d'Essais des Carènes
Paris, France

Professor Fink has presented a number of examples of great interest, but, in general, not connected at least directly with ship manoeuvrability problems, that is with the main purpose of my paper. For instance, the first case mentioned by Professor Fink is essentially related to the damping effect of a bilge keel on the rolling motion of a ship at zero speed.

The concept of vortex sheet does not apply in two-dimensional motions except in some cases like that of a flat wing in an unsteady motion of small amplitude in the direction perpendicular to the velocity of the incident flow at infinity (Kármán-Sears problem). Vortex theory in inviscid fluid does not permit to predict the growing and the shedding of vortices in the vicinity of the edge of a flat plat moving in a direction perpendicular to its plane. This phenomenon is dependent on the viscosity. The theory however applies provided complementary conditions be added to precise the mathematical model. The considerations developed by Professor Fink could have been the subject of a separated paper to this Symposium.

The case of a lifting surface with separation at the leading edge seems to be similar to that of the Δ wings. I suggest to Professor Fink to compare his method to those used at present by the Office National d'Etudes et de Recherches Aérospatiales (ONERA). An ONERA-report is quoted in the list of references joint to my paper.

DISCUSSION

V.N. Treshchevsky
Kryloff Research Institute
Leningrad, U.S.S.R.

Professor Brard has presented a very interesting paper here. I think it is very important and relevant, especially in cases where non-stationary hydrodynamic characteristics are discussed for ship constructions for instance, which are very difficult for calculation. From the other side the experimental data in this case is connected with insticable errors, so mutual correction with theoretical and experimental data seems to be necessary.

I must say that work in this direction has been carried out in the USSR under the connection of professors Fedayevsky and Polyakoff. The analysis of investigations shows that the choice of a proper scheme for decision ground equations, is very important because the initial equations for vortex density are singular.

In this connection my first question is, what methods of practical calculations were used and, particularly, whether the decision corresponds to a definite class of functions, and if so what kind of class is used here ?

Another question concerns the structure of the vortex sheet behind and near the body. I want to ask whether in case of a wing the mentioned structure supposed in the sheet will correspond to Sears or Birnbaum representations or is it an original one ?

REPLY TO DISCUSSION

Roger Brard
Bassin d'Essais des Carènes
Paris, France

In reply to Dr. Treshchevsky's comments, I would like to draw his attention to the fact that the equation giving the vortex distribution on the hull is not singular when the motion of the body consists of a pure translation. If no free vortices are shed, the vortex distribution on the hull is equivalent to a normal dipole distribution. The density of the latter distribution is yielded by a regular Fredholm equation expressing that the interior determination of the velocity potential coincides with cx + constant, if the body moves in the x-direction with the speed c. Hence one deals with the Fredholm equation for the Dirichlet interior problem.

If the angular velocity of the body is not null, then the total vortex distribution on the hull is the sum of two distributions. The equation giving one of them is regular. The other one is singular. But it is possible to show that the irregular vectorial equation is equivalent to a scalar Fredholm equation for an interior Neumann problem. The solution of this equation is much simpler. This point has been omitted in the preprint of my paper, but it will be included in its final version.

When free vortices are shed, a point of importance is to determine the position of the shedding line. It may occur that several shedding lines exist simultaneously. The problem would be underdetermined if no account were taken for the condition concerning the continuity of the pressure on the hull through each of the shedding lines.

It is also to be pointed out that, if the shedding line is unique, then the vortex distribution on the hull given by the regular Fredholm equation and the free vortex distribution can be combined in such a way that they can be replaced by normal dipole distributions. This probably leads to important simplifications.

When one deals with a wing of finite thickness, the method using the acceleration potential does not apply in a simple manner, except, perhaps, if one can combine source and vortex distribution.

DISCUSSION

John P. Breslin
Stevens Institute of Technology
Hoboken, New Jersey, U.S.A.

Admiral Brard has certainly given us an exhaustive treatment of vortex representations, and I think he has made an excellent point that this approach to ship problems has been largely neglected. I just wanted to make a point here of an intuitive character.

He points out on page 1255, regarding Casal's theory - which, as I recall, is a vortex theory for the lateral force and moment on a ship, which is considered to be quite thin, that while the lift force obtained from this theory is quite reasonable, (and I believe was in agreement with low aspect ratio theory if one takes twice the draft divided by the length as the aspect ratio of an equivalent wing) there is a disappointment in that the position of this lateral force does not coincide with the observations obtained when one measures the lateral force and static yawing moments on ship models. In that case, when one divides the moment by the force the result is a lever arm which is greater than the half length of the ship. In any event, this so-called point of application of the lateral forces is often off the ship. It seems to me, most of us are aware that if you take a body revolution - the spheroid is the classic example - it has a zero lateral force in an inviscid fluid but it has a very definite moment, say, about its midlength called the Munk moment. It is my feeling that ships may be neither fish nor fowl, they are neither bodies of revolution, nor are they flat lifting surfaces to which the lifting vortex theory could be expected to apply in all respects. In particular, if we think of the ship as a modification of a body revolution, that is that the central portion looking at it side on, together with its zero Froude number reflection on the water plane, can be described as a body of revolution plus flat surfaces fitted into the bow and stern representing the sharp bow and the sky in the region of the stern, then we should expect that it would be necessary to account for the combined effect of these fin areas or to treat the body as a body revolution with fins fore and aft. This problem, then, has to be solved theoretically. This, I should think, would then exhibit some of the body revolution characteristics in its moment and without disturbing particularly the rather excellent agreement that one obtains from small angles with the vortex theory.

REPLY TO DISCUSSION

Roger Brard
Bassin d'Essais des Carènes
Paris, France

I agree with Dr. Breslin that a real ship is not reducible to part of a vertical plane and that, for this reason, Casal's model does not give the exact features of the flow about a ship.

I think, however, that many points of Casal's approximate solution are of interest. The existence of a concentrated bound vortex near the stem seems to me in qualitative agreement with experiments. The fact that, in the case of a ship in translatory motion at small angle of attack, the lateral force is often located ahead of the stem could be explained by the velocity induced on the stern by the strong vortex filament to which the said concentrated bound vortex belongs.

One of the drawbacks of Casal's model is that the boundary condition on the hull is satisfied only on a horizontal segment at equal distance from the two horizontal edges of the longitudinal plane of symmetry. Furthermore the solution does not fulfill the pressure continuity condition through the free vortex sheets in the vicinity of the shedding lines.

I am not so optimistic as Dr. Breslin about thin wing theory with an aspect ratio of .2. One of the advantages of Casal's theory is that it is an approach for taking into account the fact that the so-called trailing edge is a very short part of the true shedding line (often less than 20%).

In conclusion I would like to thank warmly the discussors. Their valuable remarks will give me the opportunity to improve in some places the initial version of my paper.

ON THE VALIDITY OF A GENERAL SIMILARITY HYPOTHESIS FOR JET AND WAKE FLOWS*

Leo Fink and Eduard Naudascher
University of Karlsruhe
Karlsruhe, Germany

ABSTRACT

The validity of a new analytical approach by which the development of any free-turbulence shear flow in an incompressible fluid is predicted through the use of a general similarity hypothesis, has been tested by applying it to laminar jets in uniform unconfined streams. Because of the lack of experimental data, the analytical solutions derived for plane and axisymmetric jets in coaxial parallel flow were compared to corresponding solutions based on coordinate-type perturbation expansions. The satisfactory agreement obtained in all cases suggests strongly that the new similarity analysis is a valid approach which, if used with suitable turbulence hypotheses, will also predict successfully the characteristics of any turbulent jet and wake flows.

INTRODUCTION

Jets and wakes are the most common examples of free shear flows. Since the foundation of the boundary-layer theory by Prandtl in 1904, they have been the subject of numerous investigations both analytical and experimental. Nevertheless, reliable solutions are restricted so far to simple cases like free jets in stagnant fluids or small-deficit wakes. On the other hand, it is just the more complex flows like jets in external streams which are of special interest with respect to applications in fields ranging from Aerodynamics to Civil and Chemical Engineering. The reasons why there are no common

*) This work is part of a project sponsored by the Sonderforschungsbereich 80 «Ausbreitungs- und Transportvorgänge in Strömungen» at the University of Karlsruhe, Federal Republic of Germany.

solutions are twofold. First, there is the closure problem in the equations of motion, if the flow is turbulent. And second, even if one of the widespread effective-viscosity assumptions has been introduced to describe the structure of turbulence, there is the difficulty in handling the partial differential equations.

In the following, we shall deal solely with methods designed to overcome the latter difficulty. There are several well-established methods to solve the parabolic partial differential equations of the boundary-layer type. In the last decade, some powerful methods for numerical treatment of the governing equations were put forward (e.g., see Ref. [1]). Further, the application of the generalized Galerkin-Ritz Method (i.e., the G-K-D method) has proven to be very useful [2], although this method has not yet reached perfection.

In this paper, we shall use the well-known integral method combined with suitable similarity transformations as initially proposed by von Kármán. The advantage of this method lies in the relatively simple, closed-form deduction of approximate solutions, which in most cases are good enough for engineering purposes. Moreover, the method is very helpful when applying numerical procedures to flow situations complicated by special boundary conditions or by density stratification etc., because it allows to predetermine special features of the solutions like e.g., the behavior in the asymptotic ranges.

A disadvantage of integral methods, if used in combination with the conventional similarity assumptions and the corresponding simplifications, is the fact that they can rarely be extended to flow configurations which differ from those for which the assumptions and simplifications were designed. This may partly explain why not much progress has been achieved in this field since the classical works of Tollmien (1931, small deficit wake [3]) and Schlichting (1933, free jet in stagnant surrounding [4]).

There exists a close relationship between the flows treated by Tollmien and Schlichting and the laminar free jet in a uniform stream to be treated in this paper : in that part of the field where the velocity in the jet is an order of magnitude larger than the free stream velocity, the flow can be treated approximately like a free jet in otherwise quiescent fluid. On the other hand, at some distance downstream from the flow origin, the excess velocity along the center-line becomes small in comparison with the velocity of the external flow, irrespective of the initial strength of the jet, because the excess-momentum flux is distributed over an ever-increasing diffusion zone ; in this region the same approximations as in wake flows should hold true.

Since with the classical similarity assumptions, these approximations lead to different equations, predictions for general free-jet problems can be obtained in the asymptotic ranges at best. To overcome these deficiencies, different suggestions have been made. For example, Wygnanski and Fiedler [5] succeeded in solving the equation of motion with the help of the conventional similarity assumptions for the special case of a general laminar free jet with tailored pressure gradient in the outer stream. Unfortunately, the solutions are mainly of academic interest, because such special cases are seldom realized in practice.

To obtain solutions for the development of any free-turbulence shear flow in an incompressible fluid, the senior author has derived a new, more general similarity analysis [6] . Through the formulation of similarity functions based on three dynamic scales, mean flow as well as turbulence characteristics were shown to have a strong tendency toward self-preserving profiles even for such flows as the turbulent wake of a self-propelled body and turbulent jets in moving coaxial and cross streams. All solutions were satisfactorily verified by comparison with experimental data [7, 8] .

The key part of the new similarity analysis is the replacement of the conventional velocity-type representation of the mean flow field by a momentum-type description. It is the main purpose of this paper to provide further evidence of the validity of this assumption. In order to achieve this, the new approach is applied to flows, for which the similarity assumption suffices to produce solutions without the introduction of unreliable hypotheses concerning the structure of turbulence. As flows to be described we have chosen laminar jets in uniform unconfined streams. In this way, we are not only able to perform a crucial test of the key assumption of the new theory ; at the same time, we can obtain more reliable predictions for the case of unconfined laminar free-jet flow, and this not only in the asymptotic ranges but in the transition region as well, which is of most practical interest.

THEORETICAL ANALYSIS

From the observation of a jet developing in a uniform coflowing stream, one is led to accept that the flow can be separated in an irrotational outer flow (potential flow) and a shear zone extending only slowly in the lateral direction. Since this narrow zone, which is dominated by large lateral velocity gradients, is characterized by a boundary-layer type of flow, the governing Navier-Stokes equations can be approximated for large Reynolds numbers by the boundary-layer equations given by Prandtl. The same simplifications hold also for all other pertinent transport equations. This procedure has been repeatedly verified

by experiments for related flow configurations, so that it can be assumed valid in this case as well.

If the local Reynolds number $IR = \frac{U^* \ell}{\nu}$ is large* , but not exceeding the critical one, the stationary flow of an incompressible, isothermal fluid which is not affected by external forces is represented by following set of equations :

$$\frac{\partial(uy^j)}{\partial x} + \frac{\partial(vy^j)}{\partial y} = 0 \tag{1}$$

$$u\frac{\partial u}{\partial x} + v\frac{\partial u}{\partial y} = -\frac{1}{\rho}\frac{\partial p}{\partial x} + y^{-j}\frac{\partial (y^j \tau/\rho)}{\partial y} \quad \text{with} \quad \tau/\rho = \nu\frac{\partial u}{\partial y} \tag{2a}$$

$$-\frac{1}{\rho}\frac{\partial p}{\partial y} = 0 \tag{2b}$$

$\tau = 0$, $v = 0$ at $y = 0$ and

$\tau = 0$, $u = U_\infty$, $U_\infty \frac{dU_\infty}{dx} = -\frac{1}{\rho}\frac{dp}{dx}$ for $y \geq y_0$

where x and y are Cartesian coordinates (x in the direction of flow, measured from the geometrical origin of the flow) and u and v are the velocity components in the x and y directions, respectively. For plane symmetry, $j = 0$, and for axisymmetric conditions, $j = 1.0$ (see Figure 1).

Integration of Eq. 2a first over a lateral distance y_0 and then with respect to x between the boundaries x' and x in conjunction with the boundary conditions

$\tau = 0$, $v = 0$ at $y = 0$ and

$\tau = 0$, $u = U_\infty$, $U_\infty \frac{dU_\infty}{dx} = -\frac{1}{\rho}\frac{dp}{dx}$ for $y \geq y_0$

---

* For definition of symbols, see Nomenclature.

and the continuity equation yields

$$\int_0^{y_0} (u^2 - U_\infty u) y^j dy + \int_{x'}^{x} \frac{dU_\infty}{dx} \left(\int_0^{y_0} u y^j dy - U_\infty \int_0^{y_0} y^j dy \right) dx = H \text{ const} \quad (3)$$

provided the flow origin is excluded from this control volume. With $u = U_\infty + u_d$ one obtains for unconfined flow $(dU_\infty/dx = 0)$

$$\int_0^{y_0} (u_d^2 + u_d U_\infty) y^j dy = H \quad (4)$$

This partial differential equation can be reduced to an ordinary differential equation by substituting the following similarity transformation

$$(u_d^2 + u_d U_\infty) / (U^{*2}(x) + U^*(x) U_\infty) = f(\eta), \quad \text{with} \quad \eta = y/\ell(x), \quad U^* = U^*(x) \quad (5)$$

which was introduced by Naudascher [6].

Some algebraic manipulations yield the condition

$$(U^{*2} + U^* U_\infty) \ell^{j-1} = \frac{H}{I_1} \quad \text{with} \quad I_1 = \int_0^{\eta_0} f \eta^j d\eta = \text{const} \quad (6)$$

It should be remarked that in deriving Eq. 6, the momentum equation does not require further simplifications or restrictions as long as the special form of similarity expressed by Eq. 5 is adopted.

To solve for the velocity and length scales $U^*(x)$ and $\ell(x)$ one must look for an additional information. The energy equation is chosen here, following the example of Wieghardt [9] and Liepmann and Laufer [10]. After substituting the same boundary-layer approximations as in the equation of motion, the energy equation becomes

$$u^2 \frac{\partial u}{\partial x} + uv \frac{\partial u}{\partial y} = -u \frac{1}{\rho} \frac{\partial p}{\partial x} + uy^{-j} \frac{\partial (y^j \tau/\rho)}{\partial y} \quad (7)$$

Integration over a lateral distance y_0 yields with $u = U_\infty + u_d$

$$\frac{d}{dx}\left[\int_0^{y_0} U_\infty(u_d^2 + u_d U_\infty)\, y^j dy + \frac{1}{2}\int_0^{y_0} u_d(u_d^2 + u_d U_\infty)\, y^j dy\right] + \nu\int_0^{y_0}\left(\frac{\partial u_d}{\partial y}\right)^2 y^j dy = 0 \tag{8}$$

As was done with Eq. 4, this integral relationship can be reduced by substituting the similarity transformation (Eq. 5). In regard to the integration to follow, it is useful to rewrite the governing differential equations in dimensionless form :

from momentum equation :

$$\left(\frac{\ell}{\Theta_j}\right)^{j+1} I_1 = \frac{V^2}{1+V} \tag{9}$$

from energy equation :

$$\frac{d}{d(x/\Theta_j)}\left[\left(\frac{\ell}{\Theta_j}\right)^{j+1} \frac{1+V}{V^2}\int_0^{\eta_0} f\sqrt{1+4f\frac{1+V}{V^2}}\,\eta^j d\eta\right] + \frac{4\nu}{U_\infty\Theta_j}\left(\frac{\ell}{\Theta_j}\right)^{j-1}\int_0^{\eta_0}\frac{(df/d\eta)^2}{1+4f\frac{1+V}{V^2}}\,\eta^j d\eta = 0 \tag{10}$$

$$\text{with} \quad V = \frac{U_\infty}{U^*} \quad \text{and} \quad \Theta_j = \left(\frac{H}{U_\infty^2}\right)^{\frac{1}{j+1}}$$

Combining Eq. 9 with Eq. 10 leads to the ordinary differential equation

$$\frac{d}{d(x/\Theta_j)}\int_0^{\eta_0} f\sqrt{1+4f\frac{1+V}{V^2}}\,\eta^j d\eta = -4\frac{\nu I_1}{U_\infty\Theta_j}\left(\frac{1+V}{V^2}\right)^{3-j}\int_0^{\eta_0}\frac{(df/d\eta)^2}{1+4f\frac{1+V}{V^2}}\,\eta^j d\eta \tag{11}$$

which, because of the structure

$$dV/d(x/\Theta_j) = \text{fkt}\left[V\ ,\ \int_0^{\eta_0} f_1(\eta)\ F(V)\,d\eta\right]$$

involves elliptical integrals and therefore cannot be solved in closed form. The main difficulties arise from the substituted terms for u_d and $\partial u_d/\partial y$ in Eq. 8. In order to get at least an approximate solution of the problem, it seems reasonable to replace these terms by some less complicated expressions.*

By inspecting Eq. 5, one can easily realize that there are two asymptotic cases included in the new similarity transformation, namely $\partial U_\infty/U^* \ll 1.0$ (strong jet flow) and $U^*/U_\infty \ll 1.0$ (weak jet flow of the wake type). For these asymptotic cases, the postulated similarity of momentum reduces to mere similarity of defect velocity.

$$\frac{u_d}{U^*} = g(\eta) \qquad \text{with} \qquad \eta = y/\ell \tag{12}$$

which is equivalent to the conventional similarity assumption. If this expression is used along with Eq. 5, Eq. 8 becomes

$$\frac{I_2}{I_3 I_1}\cdot\frac{dV}{d(x/\Theta_j)} = \frac{\nu\Theta_j U_\infty}{H}\left(\frac{\ell}{\Theta_j}\right)^{j-1} \qquad \text{with} \begin{cases} I_2 = \dfrac{1}{2}\displaystyle\int_0^{\eta_0} f g \eta^j d\eta \\ I_3 = \displaystyle\int_0^{\eta_0}\left(\frac{dg}{d\eta}\right)^2 \eta^j d\eta \end{cases} \tag{13}$$

If solved simultaneously with Eq. 9, this equation yields the general solutions

---

* While this paper was prepared, Eq. 11 was solved by a Runge-Kutta-procedure for various forms of the similarity function $f(\eta)$. It was found that no inconsistencies arise from the introduction of the new similarity transformation (Eq. 5 in the integral form of the energy equation. Thus it can be concluded that Eq. 5 is fully compatible with the governing equations. The numerical solutions display the same features as do the closed-form solutions, which are described in this paper. Full details will be given in a subsequent report.

$$\ell n(1+\frac{U_\infty}{U^*}) - \frac{U_\infty}{U^*} + \frac{1}{2}(\frac{U_\infty}{U^*})^2 = \frac{I_1^2 \cdot I_3}{I_2} \cdot \frac{\nu U_\infty}{H} \frac{x - x_0}{\theta_0} \quad (14)$$

and

$$\frac{U_\infty}{U^*} = \frac{I_3 \cdot I_1}{I_2} \cdot \frac{\nu}{H^{1/2}} \cdot \frac{x - x_0}{\theta_1} \quad (15)$$

for plane flow (j = 0) and axisymmetric flow (j = 1), respectively. The constant of integration was obtained from the boundary condition $x/\theta_j \longrightarrow x_0/\theta_j$; $U_\infty /U^* \longrightarrow 0$, which defines the virtual kinematic origin. The value of x_0/θ_j must be determined from experiments.

Now the growth of the length scale ℓ (x) can be determined from the momentum equation (Eq. 9) and Eqs. 14 and 15 after elimination of the parameter $V = U_\infty /U^*$.

All analytical solutions are presented graphically in Figures 2 to 7. They show the following general characteristics:

a) For small distances from the flow origin, one obtains the verified asymptotic laws for the free jet in otherwise stagnant fluid, that is

$$\left.\begin{aligned} \frac{U_\infty}{U^*} &\propto (\frac{x}{\theta_0})^{1/3} \\ \frac{\ell}{\theta_0} &\propto (\frac{x}{\theta_0})^{2/3} \end{aligned}\right\} \text{ for } j = 0 \quad \text{and} \quad \left.\begin{aligned} \frac{U_\infty}{U^*} &\propto (\frac{x}{\theta_1})^{1} \\ \frac{\ell}{\theta_1} &\propto (\frac{x}{\theta_1})^{1} \end{aligned}\right\} \text{for } j = 1$$

b) Far downstream, the solutions converge toward the well-known power laws of the respective wake flows, that is

$$\left.\begin{aligned} \frac{U_\infty}{U^*} &\propto \left(\frac{x}{\theta_0}\right)^{1/2} \\ \frac{\ell}{\theta_0} &\propto \left(\frac{x}{\theta_0}\right)^{1/2} \end{aligned}\right\} \text{ for } j = 0 \quad \text{and} \quad \left.\begin{aligned} \frac{U_\infty}{U^*} &\propto \left(\frac{x}{\theta_1}\right)^{1} \\ \frac{\ell}{\theta_1} &\propto \left(\frac{x}{\theta_1}\right)^{1/2} \end{aligned}\right\} \text{ for } j = 1$$

This twofold asymptotic behavior suggests the conclusion that the presented solutions render also reliable predictions in the transition region. In any case they are superior to the conventional similarity solutions, which display correct behavior only at one limit.

Unfortunately, there are no data available to check the validity of the derived solutions by experiments. However, a comparison is possible with the analytical investigation of laminar coaxial jet flows by Wygnanski [10, 11] . Wygnanski starts with the same governing equations (Eqs. 1 and 2). But instead of a similarity assumption, he uses a coordinate-type perturbation expansion for the plane- and axisymmetric jets in still surroundings (Figures 6 and 7). A comparison of Figures 2 and 6 reveals that the two solutions can be made identical by mere translation. This fact allows one to establish a correlation between the definitions of streamwise coordinates used in this paper and by Wygnanski. The difference for intermediate distances x between the solutions in Figures 4 and 7 arise mainly because of the fact that the integrals I_1 , I_2 , I_3 are not constants but take different values at the two asymptotes "free jet in stagnant fluid" and "small-deficit wake".

CONCLUSIONS

Approximate solutions have been derived for the decay of the maximum axial excess velocity and the growth of the characteristic length scale of laminar plane- and axisymmetric jets in uniform infinite streams. In contrast to the conventional notion that there exist no similarity solutions for free shear flows with more complicated boundary conditions, the laminar coaxial jet was successfully treated by a new similarity assumption, for which the conventional velocity-type representation of the flow-field is replaced by a momentum-type description. The solutions derived with the aid of the momentum and energy equations, both simplified by the boundary-layer approximations, were found to apply over practically the whole range of axial distances, excluding only the immediate proximity of the flow origin.

This satisfactory agreement suggests strongly that the physical approach involved is sound. One is thus led to the conclusion that the momentum-type similarity characteristic is a more significant parameter for flow description than the classical mean-velocity types, and that the corresponding new approach should prove promising in the analysis of turbulent flows as well. There is no reason to abandon the powerful tool of integral methods as long as they are combined with suitable similarity assumptions. Indeed, as was shown in Refs. [6] and [8], this method yields satisfactory results for a variety of non-elementary free-turbulence shear flows even though the turbulence hypotheses used in these cases were far from being elaborate.

NOMENCLATURE

f, g	similarity functions
H	value of excess momentum flux
I_1, I_2, I_3	definite integrals of the similarity functions
j	exponent (equal to zero for plane flows and equal to unity for axisymmetric flows)
ℓ	length scale characteristic of the width of the shear zone
p	pressure
lR	local Reynolds number $lR = \frac{U^*\ell}{\nu}$
u, v	axial, lateral velocity
U_∞	velocity in the outer stream
u_d	excess velocity $u_d = u - U_\infty$
U^*	velocity scale, chosen as maximum excess velocity
V	ratio U_∞ / U^*
x, y	Cartesian coordinates

x_0	virtual kinematic origin
y_0	lateral distance, greater or equal to the width of the shear zone
ϵ_s	small perturbation parameter
η_0	transformed lateral distance $\eta_0 = y_0/\ell$
θ_j	momentum thickness $\theta_j = \left(\frac{H}{U_\infty{}^2}\right)^{\frac{1}{j+1}}$
ν	kinematic viscosity
ρ	density of fluid
τ	shear stress

REFERENCES

[1] PATANKAR, S. V., and SPALDING, D. B., "Heat and Mass Transfer in Boundary Layers, A General Calculation Procedure", Intertext Books, London, 2nd Edition, 1970.

[2] ABBOTT, D. E., and BETHEL, H. E., "Application of the Galerkin-Kantorovich-Dorodnitsyn Method of Integral Relations to the Solution of Steady Laminar Boundary Layers", Ingenieur-Archiv, XXXVII. Band, 1968.

[3] TOLLMIEN, W., "Grenzschichten", Handbuch der Experimentalphysik IV, Teil I, p. 241-287, 1931.

[4] SCHLITING, H., "Laminare Strahlausbreitung", Zeitschrift für Angewandte Mathematik und Mechanik, 13, p. 260-263, 1933.

[5] WYGNANSKI, I. and FIEDLER, H. E., "Jets and Wakes in Tailored Pressure Gradient", The Physics of Fluids, Vol. 11, No. 12, 1968.

[6] NAUDASCHER, E., "On a General Similarity Analysis for Turbulent Jet and Wake Flows", Iowa Institute of Hydraulic Research, Rep. No. 106, 1967.

[7] NAUDASCHER, E., "Flow in the Wake of Self-Propelled Bodies and Related Sources of Turbulence", Journal of Fluid Mechanics, Vol. 22, part 4, 1965.

[8] NAUDASCHER, E., "On the Distribution and Development of Mean-Flow and Turbulence Characteristics in Jet and Wake Flows", Iowa Institute of Hydraulic Research, Rep. No. 110, 1968.

[9] WIEGHARDT, K., "Uber einen Energiesatz zur Berechnung laminarer Grenzschichten", Ingenieur-Archiv 16, p. 231-242, 1948.

[10] LIEPMAN, H.W. and Laufer, J., "Investigations on Free Turbulent Mixing", NACA Techn. Note No. 1527, 1947.

[11] WYGNANSKI, I., "The Two-Dimensional Laminar Jet in Parallel Streaming Flow", Journal of Fluid Mechanics, Vol. 27, part 3, 1967.

[12] WYGNANSKI, I., "The Axisymmetric Laminar Jet in an Infinite Stream", Chemical Engineering Science, Vol. 24, 1969.

[13] ANDRADE, E.N. and TSIEN, L.C., "The Velocity-Distribution in a Liquid-Into-Liquid Jet", Proceedings, Physical Society, Vol. 49, pt. 4, July 1937.

[14] SYMONS, E.P. and LABUS, Th. L., "Experimental Investigation of an Axisymmetric Fully Developed Laminar Free Jet", NASA Techn. Note D-6304, April 1971.

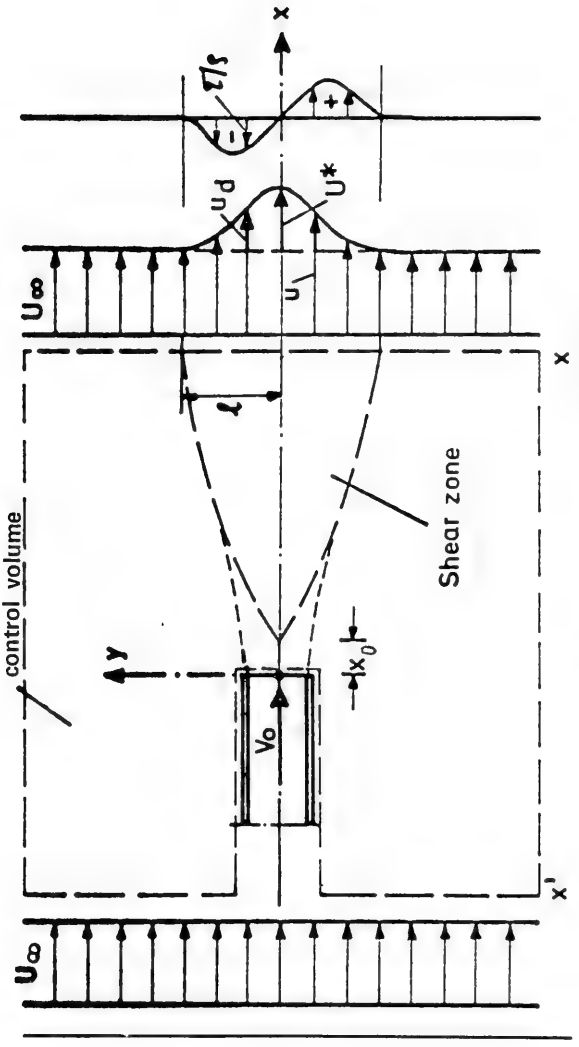

Figure 1. Definition sketch

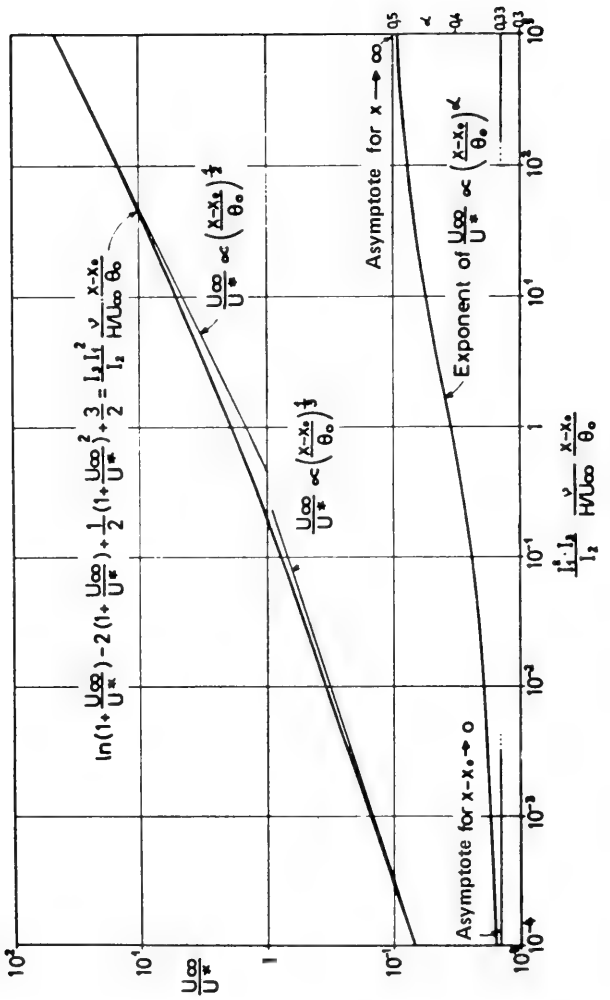

Figure 2 Axial variation of the jet excess velocity of a plane laminar free-jet

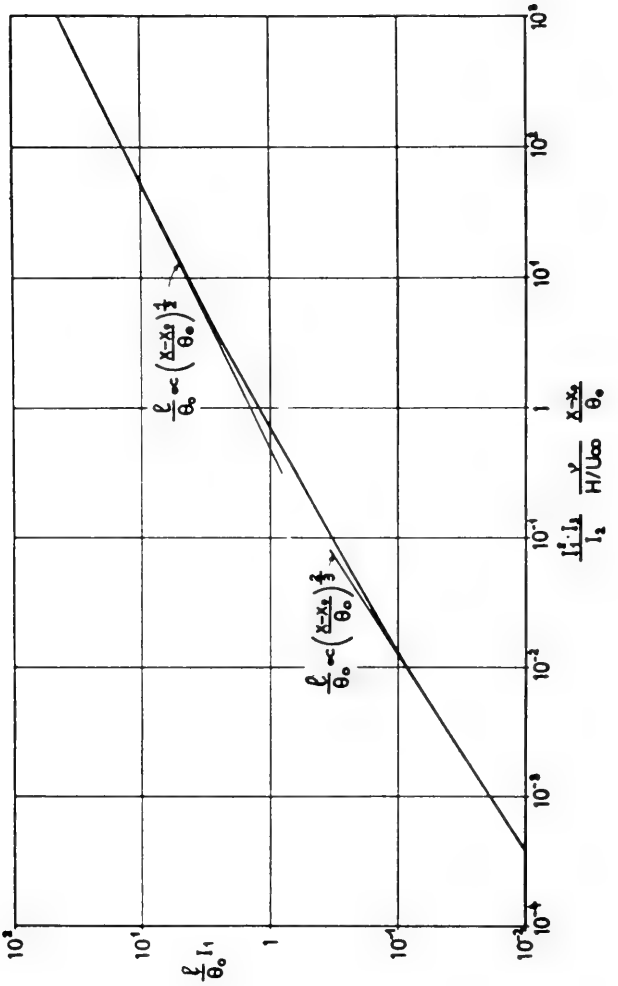

Figure 3 Axial variation of the effective width of the shear zone of a plane laminar free-jet

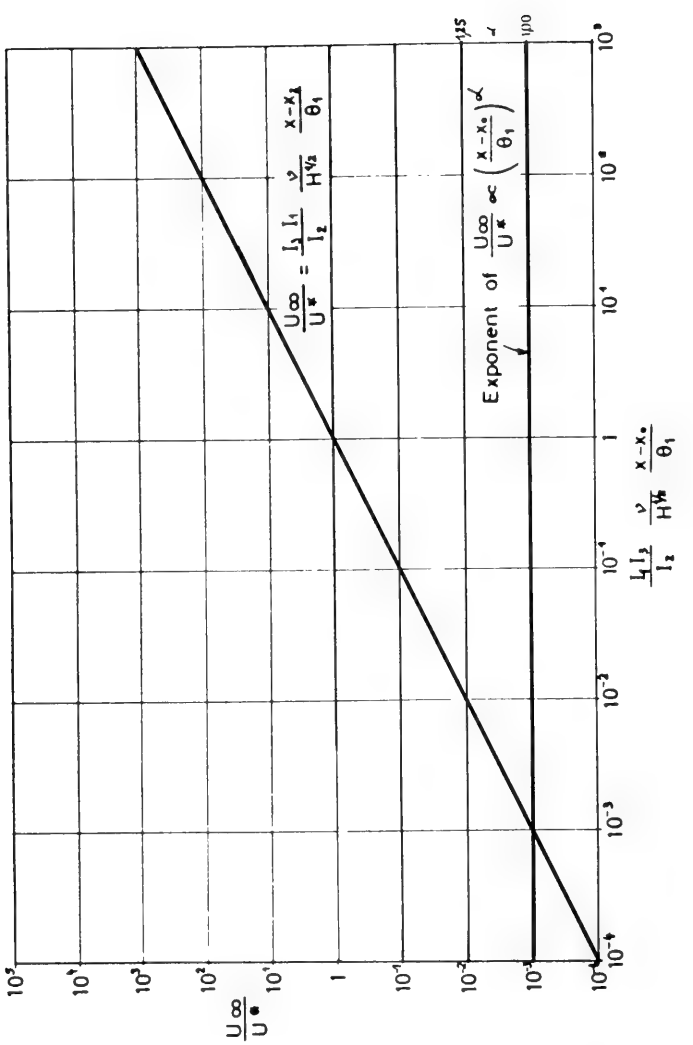

Figure 4 Axial variation of the jet excess velocity of a round laminar free-jet

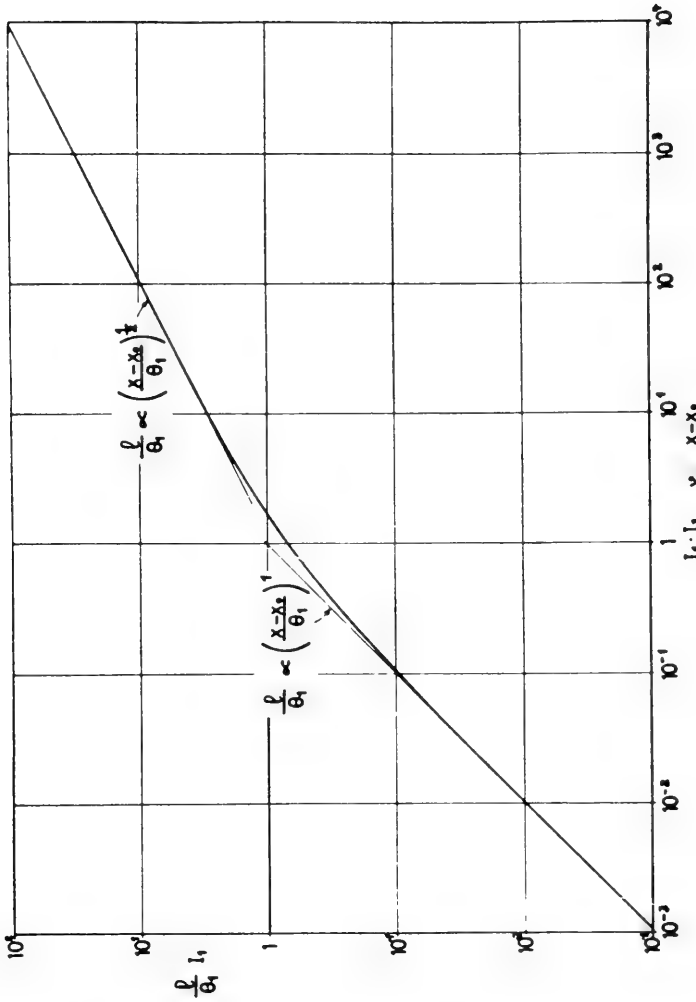

Figure 5 Axial variation of the effective width of the shear zone of a round laminar free-jet

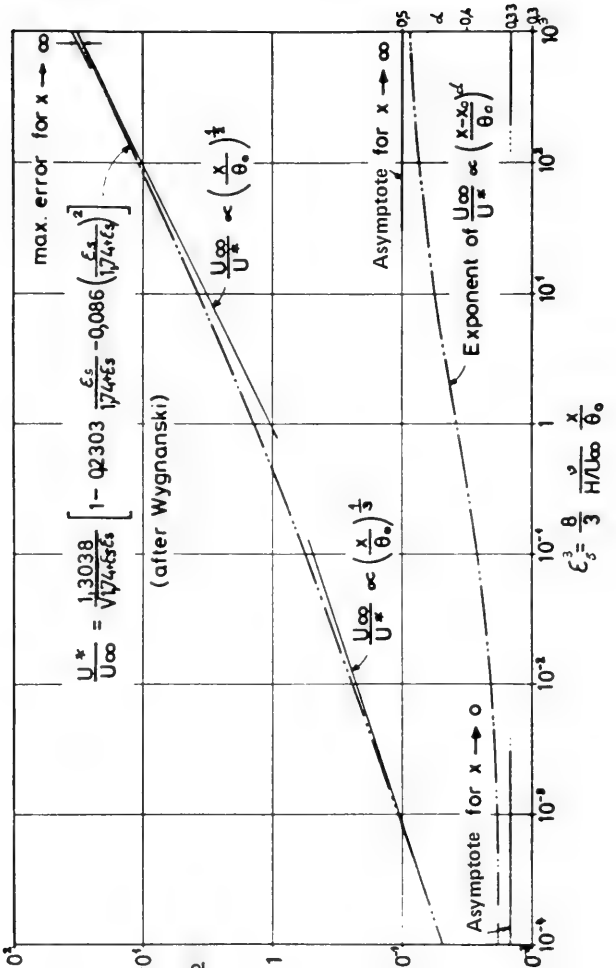

Figure 6 Axial variation of the jet excess velocity of a plane laminar free-jet

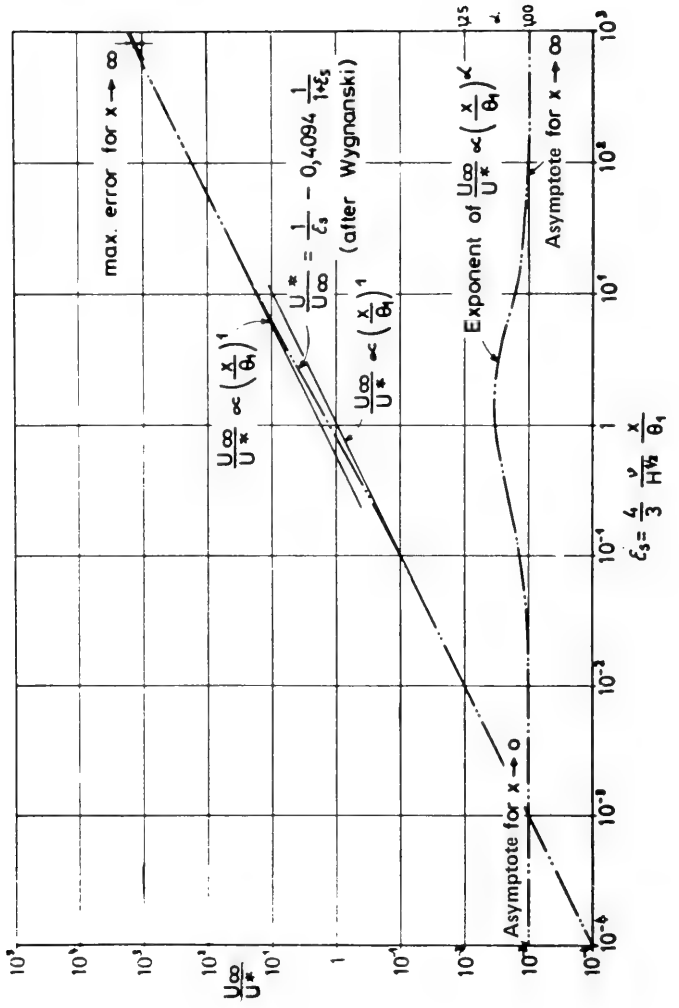

Figure 7 Axial variation of the jet excess velocity of a round laminar free-jet

DISCUSSION

Paul Lieber
University of California
Berkeley, California

How do you account physically for the superiority of the momentum similarity law as compared to the velocity similarity law, if I understood your statement ?

REPLY TO DISCUSSION

Leo Fink
University of Karlsruhe
Karlsruhe, Germany

If you substitute the conventional hypothesis in the differential form of the boundary-layer equation, you obtain a contradiction, and if you substitute the new hypothesis into this equation, you will not find any incompatibilities. This is perhaps the explanation why this new hypothesis works better than the old one. One other reason you can put forward is that these types of flow are mainly governed by the momentum equation because the momentum flux is a constant in these cases. Therefore, if the momentum equation is not violated by any of your assumptions, you have described the flow better than if you used the conventional hypothesis.

VELOCITY DISTRIBUTION AND FRICTION FACTORS IN FLOWS WITH DRAG REDUCTION

Michael Poreh and Yona Dimant
Technion - Israel Institute of Technology
Haifa, Israel

ABSTRACT

A simple descriptive model, based on van Driest's mixing length $\ell = ky\ [1 - \exp(-y^+/A^+)]$ with a variable damping parameter A^+, is proposed to represent the effect of linear macromolecules in dilute solutions on the wall region in boundary layer flows. Measurements used to support an elastic sublayer model for drag reduction are shown to be in better agreement with the proposed model. A relation between A^+ and parameters of the polymer solution and the flow identified by Virk (1971), is derived for the range where Virk's correlations are valid. The maximum drag reduction appears to be associated with an asymptotic value of A^+.

INTRODUCTION

The ability of minute quantities of high molecular weight polymers to reduce the turbulent skin friction and thus to decrease the drag of underwater bodies, has excited many investigations of the phenomenon of drag reduction. Theoretical efforts to explain the mechanism of drag reduction have not been very successful, probably because drag reduction is affected by an interaction between the molecules and the time-dependent, non-linear turbulent flow near the edge of the viscous sublayer. On the other-hand, experimental and semi-empirical studies have succeeded in documenting many features of simple drag reduction flows and describing them in approximate phenomenological models.

The earlier descriptions of such flows employed a two-layer model to describe the mean velocity profile (Meyer 1966, Elata et al

1966); a viscous sublayer where $u^+ = y^+$ (1)

and a log region where

$$u^+ = A_n \log y^+ + B_n + \Delta u^+ \quad (2)$$

where $A_n \simeq 5.75$, $B_n \simeq 5.5$., $u^+ = u/V^*$, $y^+ = yV^*/\nu$ and V^* is the shear velocity. The term Δu^+, which describes the upward shift of the log profile in the conventional law of the wall representation, was empirically related to the shear velocity and polymer characteristics by the equations

$$\Delta u^+ = \alpha \log (V^*/V^*_{cr}) \; ; \; V^* > V^*_{cr} \quad (3a)$$

$$\Delta u^+ = 0 \; ; \; V^* < V^*_{cr} \quad (3b)$$

where V^*_{cr} is the shear velocity at the onset of drag reduction and α is a concentration dependent parameter.

Virk and Merril (1969) correlated measurements of the onset of drag reduction in "thin" solvents by the semi-empirical relation

$$(Ref^{1/2})_{cr} = 2\sqrt{2}\,\Omega \cdot (R/R_g) \quad (4)$$

where R_g is the polymer radius of gyration in dilute solutions, Ω a non-dimensional constant characteristic to the polymer species-solvent combination, R is the radius of the pipe, Re the Reynolds number based on the mean velocity and diameter, and f Fanning's friction coefficient.

Integration of u^+ over the area of the pipe yields an expression for the friction coefficient f. At high Reynolds numbers and small to moderate values of Δu^+, the contribution of the sublayer to the integral of u^+ is negligible, yielding for $V^* > V^*_{cr}$ the equation

$$1/f^{1/2} = a_n \log (Ref^{1/2}) - b_n + \alpha \log (V^*/V^*_{cr})/\sqrt{2} \quad (5)$$

Where $a_n \simeq 4.0$ and $b_n \simeq 0.4$. Plotted on Prandtl coordinates, $f^{-1/2}$ versus $Ref^{1/2}$, Eq. (5) gives straight lines which intersect the Newtonian line ($\alpha = 0$) at $(Ref^{1/2})_{cr}$, where $V^* = V^*_{cr}$. This result has been supported by numerous independent pressure-loss measurements at large Reynolds numbers for small values of Δu^+. The data deviates from Eq. (5) at large values of Δu^+, where Δu^+ seems to reach a maximum value (Seyer and Metzner 1969, Whittist et al 1968)

as well as near $(\mathrm{Re}f^{1/2})_{cr}$, where a smooth transition from the Newtonian curve to the polymer solution curve is observed.

The effect of the transition region between the viscous sublayer and the log region, was first considered by Poreh and Paz(1968) The velocity in this zone was approximated by the following log law

$$u^+ = y_1^+ \ln (y^+/y_1^+) + y_1^+ \tag{6}$$

where y_1^+, the "thickness" of the viscous sublayer, was assumed to be proportional to the "thickness" y_j^+ in the two-layer model

$$y_1^+ = 0.43\, y_j^+ \tag{7}$$

and the value of y_j^+ was determined by the intersection of Eqs. (1) and (2). When $\Delta u^+ = 0$ and $y_j^+ = 11.6$ Eq. (6) reduces to

$$u^+ = 5.0 \ln y^+ - 3.05 \tag{8}$$

which had been used by von Karman to describe the buffer zone in Newtonian flows. The model has been used successfully to relate heat transfer characteristics to friction losses in dilute polymer solutions. The effect of the buffer zone on the friction coefficient was found, however, to be negligible.

Recently, Virk (1971) proposed a new 3-layer model to describe the velocity distribution in drag reducing fluids. He termed the transition between the viscous sublayer and the log region - elastic sublayer and proposed to describe it by a universal logarithmic law

$$u^+ = A_m \ln y^+ + B_m \tag{9}$$

where $A_m \simeq 11.7$ and $B_m \simeq -17.0$. The "edge" of the viscous sublayer y_v^+ is given by the intersection of Eqs. (1) and (9). The "edge" of the elastic sublayer, is given by the intersection of Eqs. (9) and (2). The relation between Δu^+ and the thickness of the elastic layer is given by

$$\Delta u^+ = \left(A_m - \frac{A_n}{2.3}\right) \ln (y_e^+/y_v^+) \tag{10}$$

Thus, when Δu^+ becomes small the elastic sublayer deminishes.

Except for small values of $R^+ (R^+ = RV^*/\nu)$ and large values of Δu^+, the contributions of both the viscous and elastic layers to the integral of u^+ are small (see table 3, Virk (1971)). In these cases, the details of the sublayer are insignificant and Virk's model gives the same friction coefficient as the model of Meyer and Elata. Virk termed this case - the polymeric regime. (Note that the last term in Virk's friction factor relation for this regime, Eq. (12) in Virk (1971), is identical to Δu^+ in Eq. (10).

In the other extreme case where the elastic sublayer becomes large and the contribution of the log region to the integral of u^+ is negligible, the friction coefficient is described by a universal law obtained by integration of (9),

$$1/f^{1/2} = 19.0 \log (Ref^{1/2}) - 32.4 \qquad (11)$$

Equation (11), termed the maximum drag reduction asymptote, describes reasonably well the maximum values of drag reduction obtained in many investigations at small values of R^+.

A very similar, but slightly more complicated 3-layer model, has been offered independently by Tomita (1970).

Virk's analysis of data in the polymeric regime has yielded an additional contribution. He has correlated semi-empirically the dependence of the slope of the straight lines in Prandtl's coordinates, which are described by Eq. (5), to identifiable polymeric parameters. Defining a fractional slope increment Δ in Prandtl's coordinate system, which is proportional to α in Eq. (2),

$$\Delta = (S_p - S_s) / S_s = \alpha / \sqrt{2S_s^2} \qquad (12)$$

Where S_p is the slope with polymers and $S_s = A_n = 4.0$ is the Newtonian slope, Virk showed that

$$\Delta \simeq \alpha / \sqrt{32} = K (\mathcal{N} C/M)^{1/2} N^{3/2} \qquad (13)$$

where $\mathcal{N}$ is Avogadro's number 6.02×10^{23}, C concentration as a weight fraction, M molecular weight, N number of backbone chain links and K a characteristic constant of the species-solvent combination. The parameter Δ appears as well in an expression which Virk derived theoretically for the turbulent strain energy of the macromolecules.

Virk's correlations describe a large volume of the data in the polymeric regime and in the maximum drag reduction regime. It should be noted, however, that the correlations proposed for the two regimes are not related. The equations proposed for the polymeric regime are unaffected by the details of the elastic sublayer, whereas Eqs. (9) and (11) proposed for the maximum drag reduction regime, are independent of the polymer properties. Thus, it appears to the authors that the correlations do not prove the existence of an elastic sublayer, which is described by a universal law and is fundamentally different in character from the corresponding layer in a Newtonian fluid. We shall show that this transitional zone in dilute polymer solutions is similar to the conventional buffer zone in a Newtonian fluid by deriving the entire velocity profile in the wall region for both cases using van Driest's mixing length model.

$$\ell = ky \quad [1 - \exp(-y^+ / A^+)] \tag{14}$$

letting A^+ be a function of the polymer-solvent properties and the shear. The model which gives a continuous velocity distribution can be easily applied to other boundary layer flows and to problems of heat transfer and diffusion.

A MODEL FOR CALCULATING THE MEAN VELOCITY DISTRIBUTION

In analogy to the damping of harmonic oscillations near a wall, van Driest (1958) proposed that the turbulent mixing length near a wall be described by Eq. (14) where $A^+ = 26$ is a dimensionless universal constant for smooth boundaries and $k = 2.3/A_n = 0.4$. There is some doubt whether A_n and B_n are truly Reynolds number independent. Coles (1954) for instance, suggests that A_n slightly increases at low Reynolds numbers. Accordingly, the shear stress in a turbulent pipe flow, given by $\tau = \rho (\nu + \ell^2 |du/dy|) du/dy$, can be described by the equation

$$\tau^+ = \left\{ 1 + k^2 y^{+2} |du^+/dy^+| [1 - \exp(-y^+/A^+)]^2 \right\} du^+/dy^+ \tag{15}$$

where $\tau^+ = \tau / \tau_w$ and $\tau_w = \rho V^{*2}$. Equation (15) may also be written as

$$\frac{du^+}{dy^+} = \frac{2\tau^+}{1 + \sqrt{1 + 4k^2 y^{+2} [1 - \exp(-y^+/A^+)]^2 \tau^+}} \tag{16}$$

In order to find the mean velocity profile, van Driest used the constant

shear approximation, namely $\tau = \tau_w$, or $\tau^+ = 1$. Denoting the velocity obtained in this manner by u_0^+, one can write that

$$\frac{du_0^+}{dy^+} = \frac{2}{1 + \sqrt{1 + 4k^2 y^{+2}[1 - \exp(-y^+/A^+)]^2}} \qquad (17)$$

Integration of Eq. (17) gives for large values of y^+ the log law $u_0 = k^{-1} \ln y^+ + B$ (Eq. 2) where the value of B is a function of A^+. Very close to the wall, where $\exp(-y^+/A^+) \simeq 1$, the solution of Eq. (17) is $u_0^+ = y^+$ (Eq. 1). A comparison with measurements in Newtonian fluids (van Driest 1958) shows that the velocity profile obtained from Eq. (17) is in good agreement with measurements in the sublayer, buffer zone and the log region in zero pressure gradient boundary layers and pipe flows. A deviation of the data from the log law is observed in the outer region of the flows.

We have already seen that the effect of drag reducing additives is to change the value of B in the log law. It is therefore natural to examine the possibility of describing the velocity distribution in such flows by the integral of Eq. (17) with values of A^+ larger than 26. We have also seen that the contribution of the velocities in the viscous sublayer and the buffer zone to the calculation of the friction or drag coefficient in the polymeric regime is small. Thus the proposed model would be useful only if it can describe the velocity distribution near and in the maximum drag reduction regime. Now, the maximum drag reduction regime corresponds to large values of A^+ and small values of R^+, and one sees from Eq. (17) that its asymptotic solution for small values of R^+/A^+ is given by $u^+ = y^+$. Since we do not expect the velocity at any point in the pipe to exceed the velocity given by the parabolic distribution in a laminar flow,

$$u^+ = y^+(1 - y^+/2R^+), \qquad (18)$$

one has to disqualify this solution. The reason for the failure of this solution is of course the assumption $\tau = \tau_w$ which is valid only close to the wall. We shall show later that although the error introduced by this assumption in Newtonian flows is small, it is large for small values of R^+/A^+. In view of this difficulty, we shall modify van Driest's solution by taking into account the variation of the shear stress in the pipe as well as the different character of the flow near the center of the pipe.

The proposed model for drag reducing flows in pipes assumes that the velocity distribution is composed of two parts

$$u^+ = u_1^+ + u_2^+ \tag{19}$$

The first part, describing the law of the wall, is given by the solution of Eq. (16) with $\tau^+ = 1 - y^+/R^+$, namely

$$\frac{du_1^+}{dy^+} = \frac{2\,(1 - y^+/R^+)}{1 + \sqrt{1 + 4k^2 y^{+2}[1 - \exp(-y^+/A^+)]^2(1 - y^+/R^+)}} \tag{20}$$

It is easy to see that the limit of Eq. (20) for small values of R^+/A^+ is

$$du_1^+ / dy^+ = 1 - y^+/R^+ \tag{21}$$

which describes the parabolic velocity distribution (18). This result implies that u_2^+, which is zero near the wall, has to vanish identically for small values of R^+/A^+. In other words, the deviation from the law of the wall has to decrease as the region where the damping is effective increases. This condition is satisfied by the following equation proposed for u_2^+.

$$u_2^+ = \frac{\Pi}{2K}\left[1 - \cos(\pi y^+/R^+)\right]\left[1 - \exp(-2R^+/A^+)\right] \tag{22}$$

where $\Pi = 0.67$ is a universal constant for pipe flows. The value of Π has been determined so that the Newtonian friction factor at $Re = 5.10^5$ would satisfy Eq. (5) with $\alpha = 0$, $a_n = 4.0$ and $b_n = 0.4$. Note that for large values of R^+/A^+, which is always the case if $A^+ = 26$, the exponential term in Eq. (22) vanishes and u_2^+ becomes identical to Coles' Wake Function.

Undoubtedly, many other schemes can be used to describe the deviation of the velocity profile near the center of the pipe from u_1^+ and its dependence on A^+. As we shall see later the relative contribution of u_2^+ is very small and thus any consistent model which complies with the boundary conditions would be satisfactory. The choice of Coles'Wake Function is justified mainly for convenience in future applications of the model to boundary layer flows.

DISCUSSION AND COMPARISON WITH EXPERIMENTAL DATA

A clear distinction between the new model and the constant shear approximation used by van Driest, is the dependence of the velocity profile on R^+. Both u_1^+ and u_2^+ are functions of R^+ and

it is not possible to describe u^+ as a function of y^+ and A^+ alone. We have plotted in Fig. 1 numerically computed distributions of u_1^+, u^+ and u_0^+ for $A^+ = 26$ and $A^+ = 300$*. We see that the various velocity distribution curves for $R^+ = 10.000$ are practically the same at small values of y^+/R^+. The maximum difference between u^+ and u_1^+ is about 5% for $A = 26$ at the center of the pipe and only half of it for $A^+ = 300$. This indicates of course that the contribution of the u_2^+ is relatively small. Another interesting observation is that the differences at this value of R^+, between u^+ and u_0^+ can be hardly noticed. They are better distinguished in Fig. 2 where velocity defects $u^+_{max} - u^+$, $u^+_{max} - u_1^+$ and $u^+_{max} - u_0^+$ are plotted. Note that at center of the pipe $du^+/dy^+ = 0$ whereas $du_0^+/dy^+ \neq 0$.

We have also shown in Fig. 1 the distribution of u^+ for $R^+ = 1000$ and $R^+ = 100$. We see that the differences between the velocity profiles for $R^+ = 10.000$ and $R^+ = 1000$ are small. Practically the same profile is also obtained in the Newtonian case for $R^+ = 100$; however, the velocity distribution for $R^+ = 100$ and $A^+ = 300$ does not coincide any more with the other profiles which have larger values of R^+/A^+. The velocity distributions according to the various models for $R^+ = 100$ are plotted separately in Fig. 3. We see from this figure that the difference between u^+ and u_0^+ for $A^+ = 300$, is large. Note that the velocity u^+ near the wall merges with the parabolic equation $u^+ = y^+(1 - y^+/2R^+)$ whereas u_0^+ is tangent to the $u^+ = y^+$ curve and goes above the parabolic profile. We have also plotted in this figure Virk's ultimate profile (Eq. 9). Virk's profile is quite close to u^+ but it also gives at one region slightly larger velocities than in a laminar pipe flow.

Measured velocity distributions are compared with the calculated profiles of u^+ in Figs. 4 - 7. The values of A^+ were chosen arbitrarily (The data is taken from Virk (1971), Fig. 3, using the same symbols to denote the various entries.) The agreement with the data is very good. In particular the velocity profiles in the maximum drag reduction regime, Figs. 6 and 7, describe the measurements much better than the velocity profiles proposed by Virk's elastic sublayer model.

---

* A computer program for the calculations of u^+ and f is available on request from the authors.

FRICTION FACTORS AND RELATION TO POLYMERIC PROPERTIES

The dependence of the friction factor $f^{-1/2}$ on $Re_f^{1/2}$ as a function of A^+, has been obtained numerically and plotted in Fig. 8. One sees that at large values of $Re_f^{1/2}$ the variation of $f^{-1/2}$ for constant values of A^+ is described by a logarithmic law. The Newtonian case $A^+ = 26$ coincides with the line describing the equation $f^{-1/2} = 4.0 \log Re_f^{1/2} - 0.4$. Integration of the theoretical limit of Eq. (19) for small values of R^+/A^+ gives the laminar friction law.

$$f = 16 / Re \tag{23}$$

Several data points appearing in Fig. 1 of Virk (1971), near $Re_f^{1/2} = 200 (R^+ = 70)$, are quite close to Eq. (23). However, the available data at larger values of $Re_f^{1/2}$ indicate that the values of A^+ obtained so far in dilute polymer solutions are bound by $A^+ = 350$.

At the polymeric regime, as defined by Virk, an approximate relation between A^+ and the polymeric properties can be found using Virk's correlations. At large values of $Re_f^{1/2}$, where the friction factor curves for different values of A^+ are described by parallel lines, Δu^+ is uniquely related to A^+. From Fig. 8 it was found that at this range

$$\Delta u^+ / \sqrt{2} \simeq 40 \log (A^+/A_n^+ + 4) - 28 \tag{24}$$

At small values of $Re_f^{1/2}$ the relation between Δu^+ and A^+ depends on the values of $Re_f^{1/2}$, however, if $\Delta u^+ (A^+)$ is measured along straight lines originating at $Re_f^{1/2} > 1000$ and having slopes which do not exceed the slopes recorded in actual measurements, the deviation from Eq. (24) is less than 5%.

The relation between A^+ and the shear stress can now be obtained from Eq. (3). This equation is composed of two expressions ; for $V^* < V_{cr}^*$ and for $V^* > V_{cr}^*$. It is suggested that a better description of the variation of Δu^+ is obtained by the single equation

$$\Delta u^+ = (\alpha/4) \log \left[1 + (V^*/V_{cr}^*)^4\right] . \tag{25}$$

Equation (25) deviates from Eq. (3a) at $V^* > 2V_{cr}^*$ by less than 3% and is practically zero for $V^* < V_{cr}^*/2$. The values of V_{cr}^* according to Eq. (25) should be determined by the intersection of the straight

line (3a) with the Newtonian profile, which is exactly the procedure used by Virk. It follows from Eqs. (24) and (25) that

$$A^+/A_n^+ = 5\left[1 + V^*/V^*_{cr})^4\right]^{\alpha/160\sqrt{2}} - 4 \qquad (26)$$

where α is related to the polymer properties by Eq. (13).

We have used Eqs. (26) and (12) to calculate the variation of $f^{-1/2}$ versus $Ref^{1/2}$ for solutions of the polymers AP-30 and Guar Gum. (Estimated values of the critical shear and molecular properties are given by Whitistt et al (1968) and Virk (1971), table 5). The calculated curves for the three solutions, and curves for constant values of A^+ are compared with the measurements of Whitistt et al (1968) in Figs. 9 - 12. At small and moderate values of V^*/V^*_{cr} the agreement between the data and the theoretical calculations (solid lines) seems to be satisfactory even for small values of $Ref^{1/2}$. The agreement is not surprising as it merely reflects the adequacy of Virk's correlations and the slight improvement due to the use of the continuous equation (25) rather than equations (3a) and (3b). The phenomenon of maximum drag reduction, however, appears now in a different light. One sees that when V^*/V^*_{cr} becomes large, the data deviates from Eq. (26) and seem to be correlated with curves of constant A^+. The measurements in the concentrated polyox solutions and the smaller pipe-diameters seem to be bound by the curve $A^+ = 350$, which is close to Virk's maximum drag reduction asymptote in the range $Ref^{1/2} < 1000$. However, the deviation from the lines which are calculated using Virk's polymeric regime correlations, and the approach to the maximum value of A^+, do not occur only near the maximum drag reduction asymptote. It appears that for each solution, there exists a maximum value of A^+ (or Δu^+) approximately independent of the pipe diameter. Only when R^+ is small the curves coincide in a limited region with Virk's maximum drag reduction asymptote (11). This evidence is not manifested in Virk's model which predicts drag reduction values of the order of 90% for very large shear rates. It is also interesting to note that the measurements of drag reduction with aluminium distearate in an organic solvent shown in Fig. 12 (McMillan et al, 1971) exceed the maximum drag reduction curve and appear to reach values of $A^+ = 600$.

In the absence of a theoretical model for drag reduction mechanism there is no way at present to determine whether the asymptotic value of A^+ is determined by properties of the particular polymers used, experimental limitations, a dependence of drag reduction on the existence of a minimum level of turbulence necessary to deform the macromolecules in solution, degradation or other causes.

CONCLUSIONS

It has been shown that the effect of linear macromolecules in dilute solutions on the flow in the wall region, can be described by van Driest's mixing length model with a variable damping parameter A^+. If the Reynolds number of the flow R^+ is large, the constant shear approximation used by van Driest can be used. When R^+/A^+ is not large, it is necessary to take into consideration the variation of the shear stress with the distance from the wall. The velocity distribution in the outer region is modified in this case using Coles' Wake Function multiplied by a factor. The factor decreases as the damping action of the molecules increases. Although the model does not explain the damping mechanism it suggests a similarity between flows with and without polymers, which is not present in the elastic sublayer model. The model does not explain the nature of the maximum drag reduction asymptote either, however, it is pointed out that the maximum drag reduction curves for a given polymer might be associated with a maximum value of the damping parameter A^+.

REFERENCES

[1] COLES, D. J., of Appl. Math. & Physics. (ZAMP), Vol. 5 No. 3, 1954.

[2] ELATA, C., LEHRER, J. & KAHANOVITZ, 1966, ISRAEL, J. Tech. 4, 87.

[3] McMILLAN, M. L., HERSHEY, H. C. & BAXTER, R. A., 1971, "Drag reduction", Chem. Eng. Prog. Symposium Series, 111, 67, 27.

[4] MEYER, W. A., 1966, A. I. Ch. E. J. 12, 522.

[5] POREH, M. & PAZ, U. 1968, Inter. J. Heat Mass Transfer, 11, 805.

[6] TOMITA, Y., 1970, Bull. J. S. M. E. 13, 935.

[7] VAN DRIEST, E. R., 1965, J. Aero. Sci. 23, 1007.

[8] VIRK, P.S. & MERRILL, E.M., 1969, Viscous Drag reduction (Ed. C.S. Wells) Plenum Press.

[9] VIRK, P.S., 1971, J. Fluid Mech. 45, 417.

[10] WHITISTT, N.F., HARRINGTON, L.J. & CRAWFORD, H.R., 1968, Clearing House AD 677467.

* * *

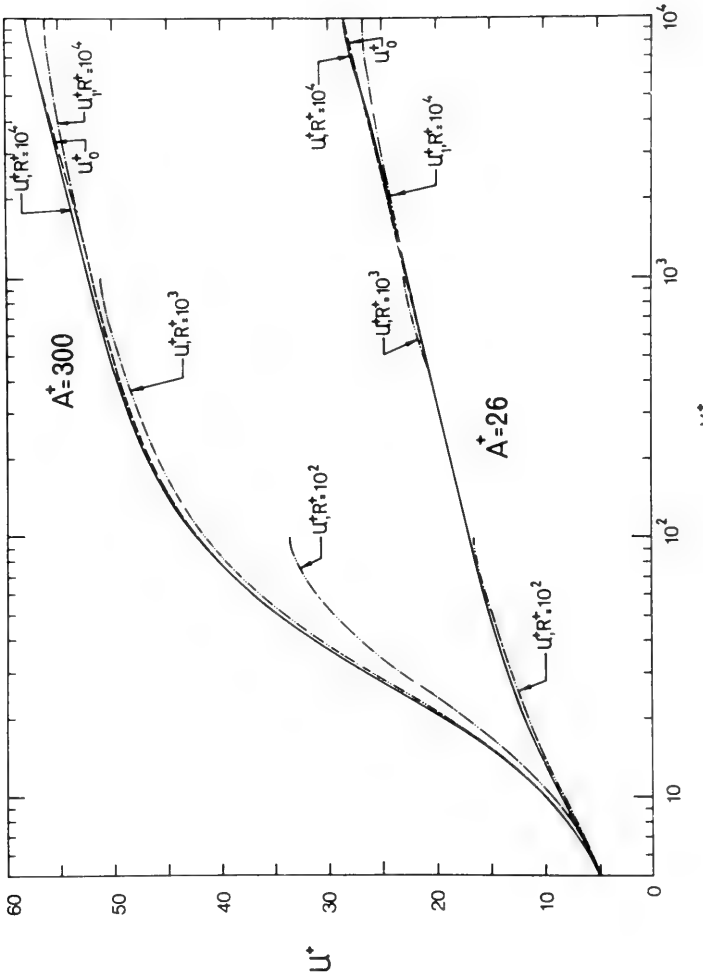

Fig. 1 Velocity distributions according to the various models ($A^+ = 26$, $A^+ = 300$).

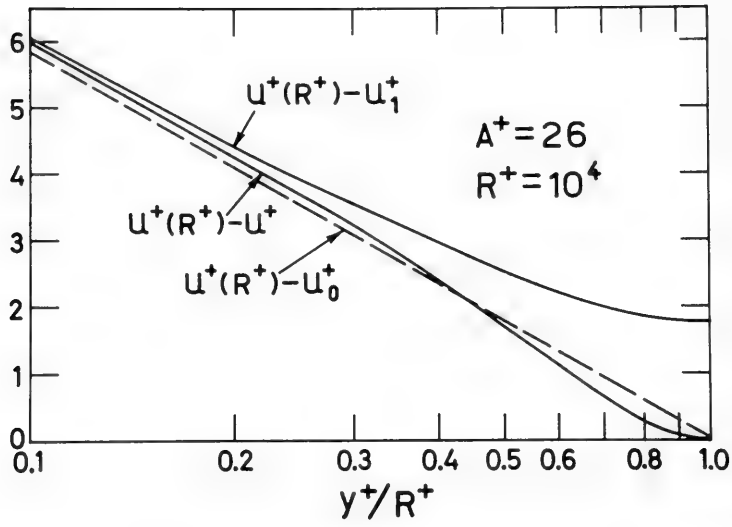

Fig. 2 Defect velocities in the various models ($R^+ = 10000$, $A^+ = 26$).

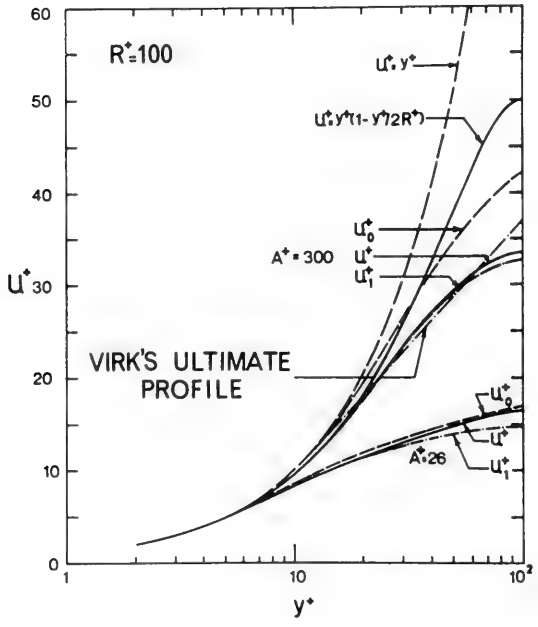

Fig. 3 Velocity distributions for $R^+ = 100$. ($A^+ = 26$, $A^+ = 300$).

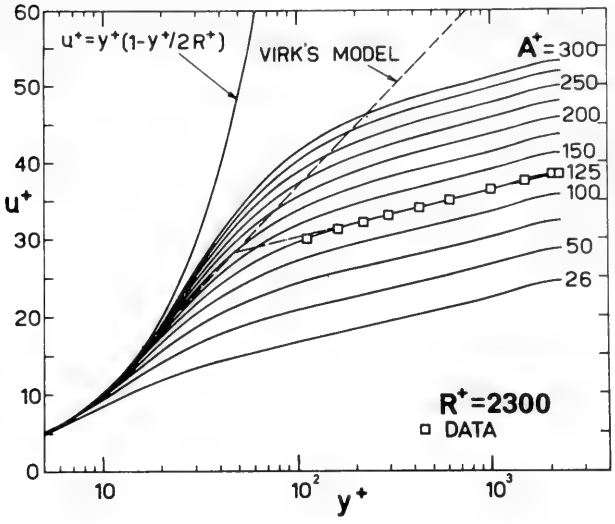

Fig. 4 Velocity distributions for $R^+ = 2300$.

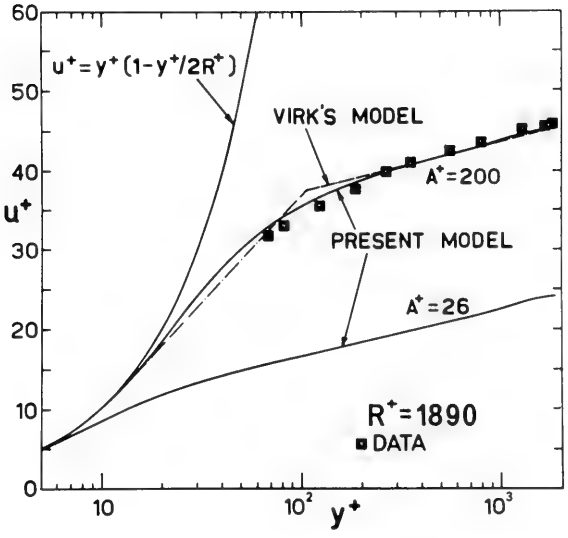

Fig. 5 Velocity distributions for $R^+ = 1890$.

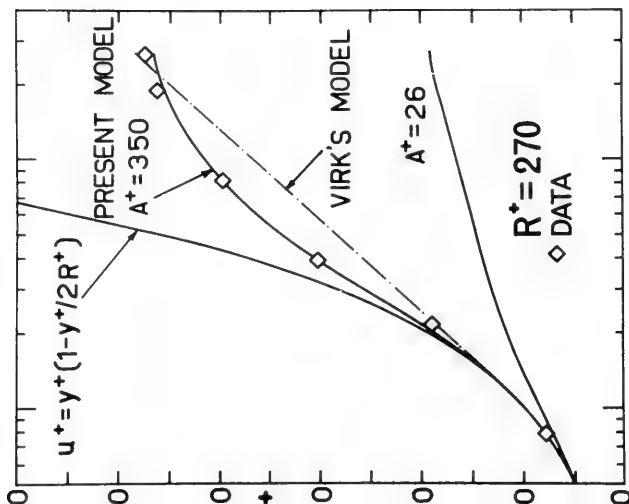

Fig. 7 Velocity distributions for $R^+ = 270$.

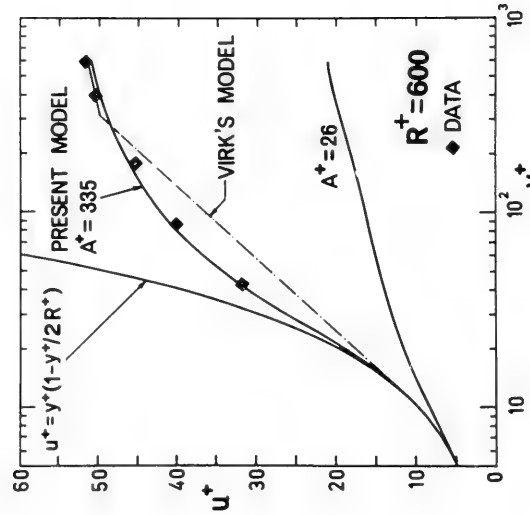

Fig. 6 Velocity distributions for $R^+ = 600$.

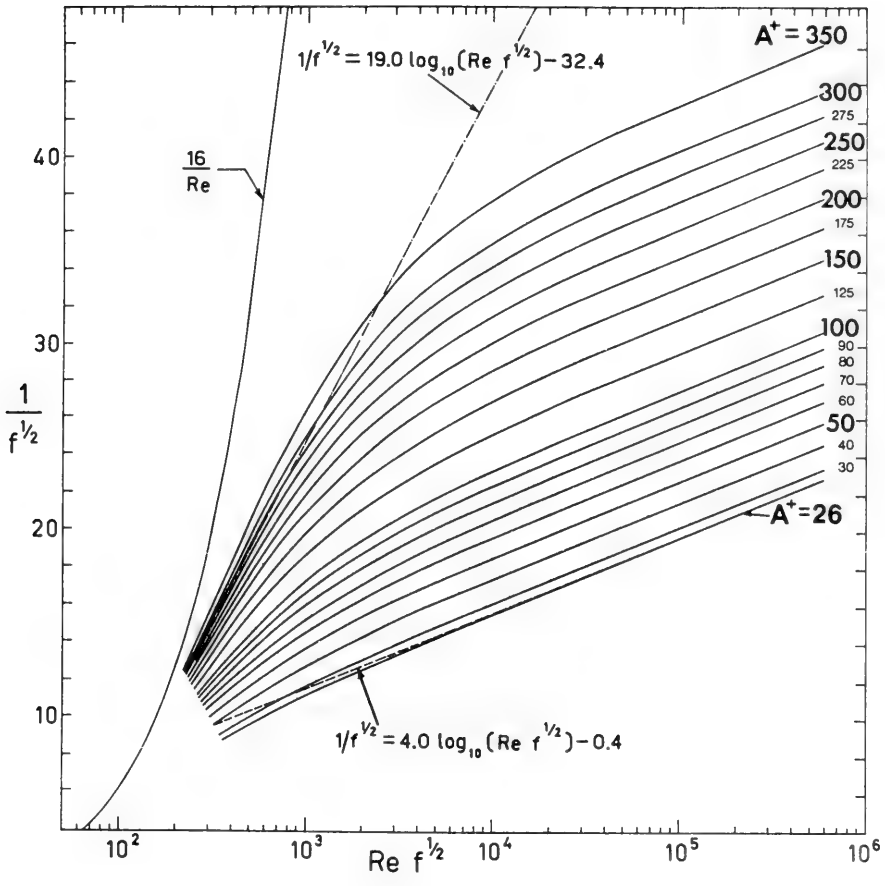

Fig. 8 Friction factor curves as a function of A^+.

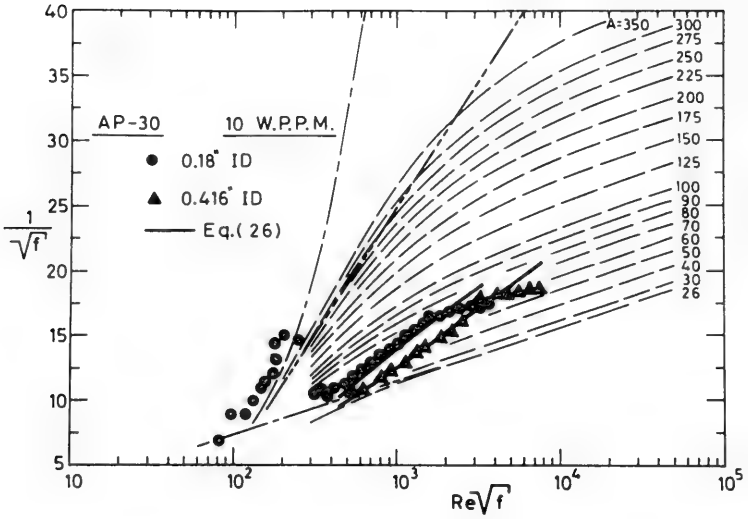

Fig. 9 Measurements of friction coefficients.

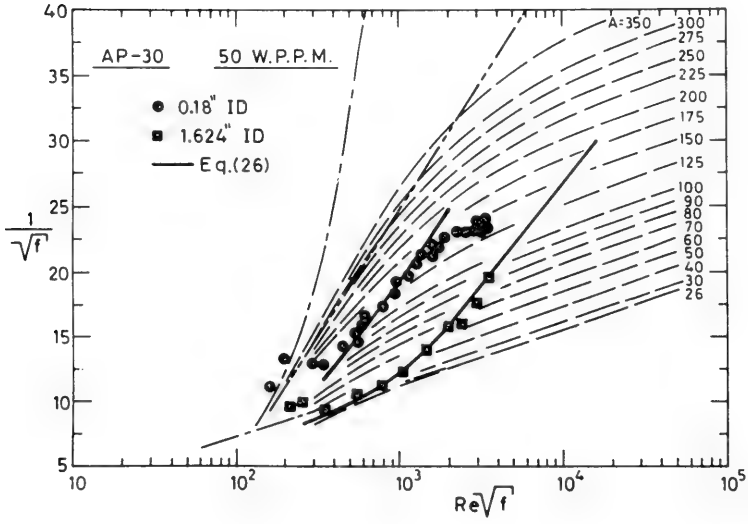

Fig. 10 Measurements of friction coefficients.

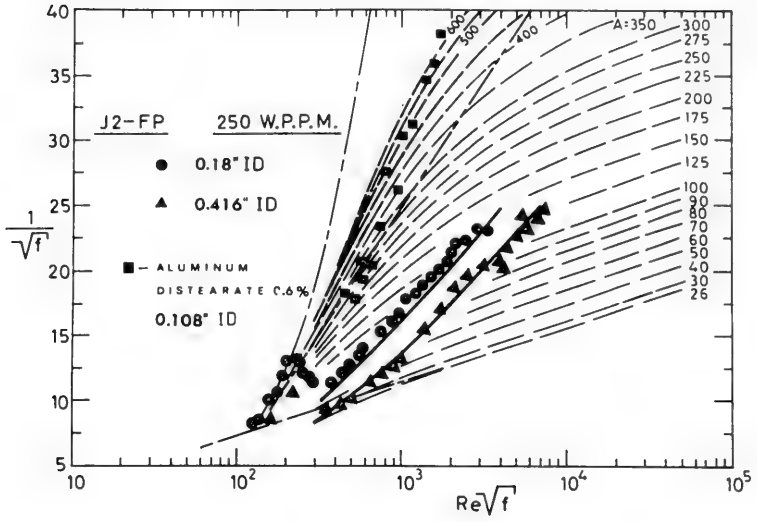

Fig. 11 Measurements of friction coefficients.

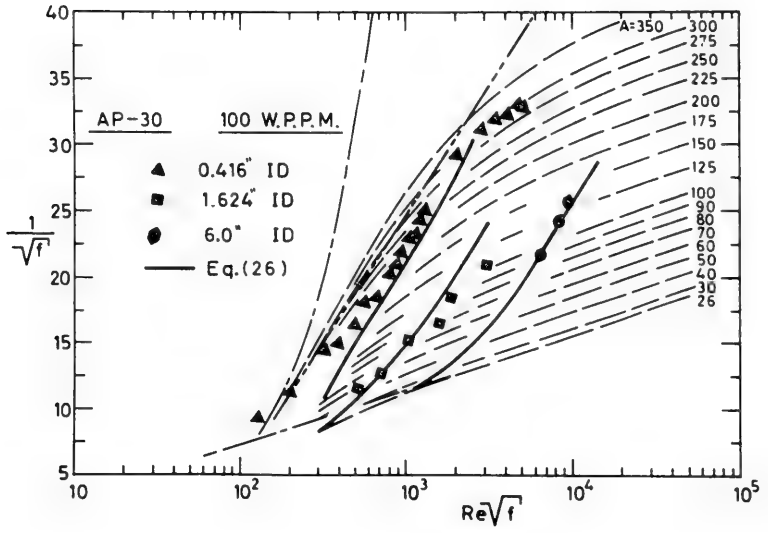

Fig. 12 Measurements of friction coefficients.

DISCUSSION

Thomas T. Huang
Naval Ship Research and Development Center
Bethesda, Maryland, U.S.A.

The authors are to be congratulated on providing a most detailed velocity-profile model for the turbulent flows with drag reduction. However, the empirical fundamental equations (equations (3) and (4) are applicable to poor drag reducers, for example guar gum, at certain concentration and shear ranges. It would be more appropriate to put down the limitations of these equations and to indicate that the results derived here are valid only within these limitations. I have three other comments of a minor nature.

The maximum drag reduction asymptote stated in equation (3) and used to compare with the experimental result is not in good agreement with our experimentation. The Virk first formula agrees better with our data and if you use the Virk first formula (JFM 1967) there is very little difference between the Virk model and the present model, i.e. within the accuracy of experiments.

Second, the optimal concentration to reach the maximum drag reduction is found by us to be a function of shear stress and thickness of boundary layer divided by kinematic viscosity. The effect of the scale does play an important role in this respect. Once drag reduction reaches this maximum value the results arrived at here are no longer valid. This limitation is suggested to be stated in the paper.

The present model does not offer any advantage for predicting drag reduction. Nevertheless, it may be more suitable for diffusion and heat transfer prediction, as authors stated. In this application, more definite experimental results would serve the field more than empirical calculation based on bold assumptions.

DISCUSSION

Jaroslav J. Voitkounsky
Shipbuilding Institute
Leningrad U.S.S.R.

The problem being discussed is of great interest, of course, but it is very difficult for us. It is important to describe the phenomena in the turbulent flow and in my opinion it is especially useful to try to apply for it Prandtl's ideas about the "Mischungsweg" (mixing lengths). Such a method was used by the author and some years ago it was used in the Soviet Union too. In particular the van Driest idea about the construction of formulae for the mixing length was used. I think it is a very useful method and the results obtained by the authors are also very interesting.

I should be grateful if the author who presented the paper could answer one question. What, in his opinion, is the prospect of applying that method to the case of the rough surfaces because from the application point of view it is a very interesting problem. Some years ago in England these natural experiments were carried out with a natural ship and it is clear that the roughness of the surface of that ship was of a high degree, and it would be very interesting to apply this theory to a description of that phenomena.

DISCUSSION

Edmund V. Telfer
R.I.N.A.
Ewell, Surrey, U.K.

This is quite a fascinating paper and whilst it has many diverse applications I would like to ask the author for his opinion on only one point. We have all been attracted by the possibilities of drag reduction, but I would like to suggest that there are also immense advantages to be got by going in the opposite direction so far as ship model experiments are concerned. When one considers the terrific

wealth which has been wasted in all the experiment tanks in the world by the intrusion of laminar flow affecting the accuracy of their results, I wonder whether the question of doping the tank water with something which will have entirely the opposite effect from that of the drag reducing polymers should be considered. In other words, is there a dope which could go into the tank water which would make the occurence of drag reduction or laminar flow quite impossible ? If that could be found, a lot of the quite arbitrary and, to many people, unacceptable devices currently in use to eliminate turbulent flow would be avoided. I offer this thought sincerely to the author of this paper, and would like to congratulate him on the way the paper was delivered and on its content.

REPLY TO DISCUSSION

Michael Poreh
Technion Israel Institute of Technology
Haifa, Israel

The concern of Pr. Telfer is well understood. The presence of drag reducing agents in the towing tanks is favorable from the modeling point of view. Dr. J. Hoyt has published an excellent review paper in the Journal of Basic Engineering (June 1972) in which he discussed this problem. The uncertainty of the data which has been accumulated in the past is due to the fact that the drag reduction was not controlled or recorded. Pr. Telfer suggests, if I have understood correctly, to eliminate the effect altogether. I believe that this can be done by adding chemicals which will inhibit the growth of algae and drag reducing bacteria as well as creating unfavorable conditions for the stretching of the molecules. However, the more difficult task of maintaining a controled standard level of drag reduction in towing tanks seems more attractive as it enables one to improve the similarity in modeling ship motion.

The interest of Pr. Voitkounsky in the effect of roughness is natural. I have published a paper in the Journal of Hydronautics* in which I proposed an approximate model for describing this effect. The work in the Soviet Union in this area is not known to me and I'll appreciate if Pr. Voitkounsky will help me in receiving the papers he has mentioned.

* (Jour. of Hydronautics, 4, 4, Oct. 1970)

As to the remarks of Dr. Huang I would like to stress that the model proposed is not based on Virk's data. In particular it is not based on Virk's maximum drag reduction curves. The opposite, our model suggests that one should not look for a universal maximum drag reduction curve. Equations (3) and (4) are not the starting point of the analysis and have only been used to obtain the correlation between A^+ and the polymer properties at the end of the paper. If Dr. Huang feels that better correlations exist he can use them instead, and the only equation that will have to be modified is Equation 26. Thus, his conclusions as to the validity of the model are not accepted.

* * *

FRONTIER PROBLEMS

Thursday, August 24, 1972

Afternoon Session

Chairman : J. Dieudonné
Institut de Recherches de la Construction Navale, Paris, France

OCEAN WAVE SPECTRA AND SHIP APPLICATIONS

Ming-Shun Chang
Naval Ship Research and Development Center
Bethesda, Maryland, U.S.A.

ABSTRACT

This paper presents the results of two studies : one dealing with the analytical representation of unidirectional wave spectra, and the other dealing with experimental determination of directional wave spectra.

(1) A two-parameter wave-spectrum formulation for determining the seakeeping qualities of ships was evaluated by application to hindcast data for the North Atlantic Ocean. Computations indicate that the two-parameter representation does not properly distribute wave energy over the full range of wave frequencies.

(2) An experiment was conducted in a large seakeeping basin to assess techniques for determining directional wave spectra from wave elevation measurements obtained with sonic probe arrays. The measurements were found to be sufficiently accurate for analysis of the wave directions, when the directional spectra are approximated by a ninth-order Fourier series.

INTRODUCTION

In order to describe the properties of ocean waves, one considers the seaway as a random process having a spectral representation. The spectrum of ocean waves is two-dimensional, and thus it is a function of both wave frequency and wave direction. It is difficult to obtain a directional wave spectrum, and in many applications the

spectrum is considered to be a function of wave frequency only with its direction arbitrarily specified. A commonly used representation of ocean waves is the Pierson-Moskowitz spectrum [1]. This spectrum is a special case of a form suggested earlier by Bretschneider [2], The International Towing Tank Conference (ITTC) in 1969 [3] recommended a two-parameter idealized spectrum of the Bretschneider form whenever statistical information on the characteristic wave period and height was available and recommended the Pierson-Moskowitz spectrum whenever such information was not available. Because of the lack of confidence in wave period and height data, the Pierson-Moskowitz spectrum has been widely employed as the basis for evaluating ship performance in a seaway and in the design of marine structures.

For the study of long-term ship performance, Cummins [4] suggested the use of the two-parameter idealized spectrum of the Bretschneider form. This spectrum recommended by the ITTC has been recently applied to North Atlantic hindcast wave data [5], and the results obtained were considered to be less than completely satisfactory. These results showed that in the idealized spectra the wave energy was not properly distributed with respect to frequency. This could result in serious errors in the prediction of ship motions. The same conclusion is substantiated by more recent measurements of ocean wave spectra [6].

In modern ocean engineering, the need for knowledge of directional wave spectra is especially important. Several techniques have been developed to determine the wave directions in the ocean. Examples are the stereo-photographic method developed at New York University [7], the floating buoy method developed by Longuet - Higgins at the National Institute of Oceanography [8], and the array method suggested by Barber and Pierson [9]. Despite these efforts only a few measured [7],[8],[10] directional-wave spectra for the ocean are available. Moreover, the accuracies of the measurements are not known.

In an attempt to better assess the problem of determining directional wave spectra, it was decided to measure and analyse wave data under controlled conditions. An experiment was conducted in the Naval Ship Research and Development Center's seakeeping basin to study the angular resolution associated with measured wave spectra.

---

* References are listed on page 1347

The water surface elevation was measured by an array of sonic probes and the directions of the waves were then estimated from those measurements. The results indicate that the measurements obtained by the probes are indeed suitable for analyzing directional spectra. However, the technique used in estimating the cross spectra between different probes was not sufficiently accurate for determining the wave directions in the case where a regular wave train and an irregular wave train are propagating at 90 degrees to each other.

This paper reports on the experimentally determined directional wave spectra and a study of the application of the two-parameter wave spectrum model.

UNIDIRECTIONAL WAVE SPECTRA

One is aware of the variety of the ocean spectra, yet one must establish some order in this chaos for practical application. For estimating the seakeeping qualities of ships, Cummins [4] proposed a technique which makes use of a two-parameter wave spectrum of the general Bretschneider form. This two-parameter spectral formulation was studied by applying it to North Atlantic hindcast wave data [5]. The analysis procedure and results are given below.

Let $x(t; T_1, H_{1/3})$ be the response of a ship in a seaway which has average wave period T_1 and significant wave height $H_{1/3}$, where t is time. If x is linear, its variance $X(T_1, H_{1/3})$ is given by

$$X(T_1, H_{1/3}) = E\left[x^2(t; T_1, H_{1/3})\right] = \int_0^\infty Hx_\rho(\omega)\, S_\rho(\omega; T_1, H_{1/3})\, d\omega \tag{1.1}$$

where $E[a]$ represents the average value of a, $S_\rho(\omega)$ is the wave spectrum, $H_{x\rho}$ is the frequency response function of the ship and ω is the wave frequency. By the use of the wave spectrum form recommended by ITTC [3], that is

$$S_\rho(\omega) = S_\rho^I(\omega) = \frac{173\, H_{1/3}^2}{T_1^4\, \omega^5}\, e^{-691(T_1\omega)^{-4}} \tag{1.2}$$

where $S_\rho^I(\omega)$ is the idealized two-parameter spectrum. The statistics of the response $X(T_1, H_{1/3})$ are completely determined by the statistics of T_1 and $H_{1/3}$ if $H_{x\rho}$ is a deterministic function. The

long-term variance of response is

$$E\left[X(T_1, H_{1/3})\right] = \int_0^\infty \int_0^\infty X(T_1, H_{1/3})\ p(T_1, H_{1/3})\, dT_1\, dH_{1/3} \quad (1.3)$$

where $p(T_1\ H_{1/3})$ is the joint probability density function of T_1 and $H_{1/3}$.

Substituting equations (1.1) and (1.2) into (1.3), one has

$$E\left[X(T_1, H_{1/3})\right] = \int_0^\infty Hx\rho(\omega)\, S_\rho^*(\omega)\, d\omega \quad (1.4)$$

where

$$S_\rho^*(\omega) = \int_0^\infty \int_0^\infty S_\rho^I(\omega; T_1, H_{1/3}) p(T_1, H_{1/3}) dT_1 dH_{1/3} \quad (1.5)$$

S_ρ^* is the averaged idealized spectrum by definition.

It is seen from equation (1.4) that the long-term averaged variance of the response $X(T_1, H_{1/3})$ is the integral with respect to frequency of the product of the frequency response function and the averaged idealized spectrum, S_ρ^*. The averaged idealized spectrum of the environment determines the long-term averaged variance of the response for a given frequency response function of a ship. In addition to the convenience in calculating the averaged long-term ship responses, the two-parameter spectrum approach provides a rapid method for estimation of the probability of short term average ship response and its higher moments. If a probability diagram of T_1 and $H_{1/3}$ is constructed such that

$$z = P(T_1 \leqslant a)$$

and

$$y = P(H_{1/3} \leqslant b; T_1)$$

where z and y are the two coordinates of the diagram and the P's are the probability functions, then from (1.1) the probability distribution of short-term ship response, $P(X \leqslant a)$, is given by

$$P(X \leqslant a) = \int_0^{\infty} \int_0^{g(T_1, H_{1/3}) = a} p(T_1, H_{1/3})\, dH_{1/3}\, dT_1$$

$$= \int_0^{\infty} \int_0^{g(T_1, H_{1/3}) = a} p(H_{1/3}; T_1)\, p(T_1)\, dH_{1/3}\, dT_1$$

$$= \int_0^{1} \int_0^{g(T_1(z), H_{1/3}(z, y))} dy\, dz$$

where

$$g(T_1, H_{1/3}) = \int_0^{\infty} Hx\rho(\omega)\, S_{\rho}^{I}(\omega; T_1, H_{1/3})\, d\omega$$

$P(X \leqslant a)$ is simply enclosed by the two coordinate axes and the curve of

$$g(T_1, H_{1/3}) = \int_0^{\infty} Hx\rho(\omega)\, S_{\rho}^{I}(\omega; T_1, H_{1/3}) d\omega = a$$

The use of this diagram will be illustrated below.

North Atlantic hindcast wave data which contains spectra hindcast at 519 points in the North Atlantic every six hours for a period of one year, was selected to study the two-parameter spectral model. Spectra at 16 grid points were selected for this study. A total of $16 \times 365 \times 4 = 23,360$ spectra were analyzed. T_1 and $H_{1/3}$ were calculated for each spectrum by the use of the following formulas, which have been proposed by the ITTC[3]

$$T_1 = \frac{24.17}{26.84} \frac{\int_0^\infty \frac{1}{\omega} S(\omega)\, d\omega}{\int_0^\infty S(\omega)\, d\omega} \tag{1.6}$$

$$H_{1/3} = 4\sqrt{\int_0^\infty S(\omega)\, d\omega} \tag{1.7}$$

The statistics of T_1 and $H_{1/3}$, $p(T_1, H_{1/3})$, are then constructed from these calculated values with equal weights. The averaged idealized spectrum was calculated from equations (1.5), (1.2), and $p(T_1, H_{1/3})$.

The resulting averaged idealized spectrum was compared with the averaged hindcast spectrum $S_A(\omega)$ of those 23,360 spectra ; that is

$$S_A(\omega) = \frac{1}{23,360} \sum_{i=1}^{23,360} S_{\rho i}(\omega)$$

where $S_{\rho i}(\omega)$ are the hindcast spectra. As seen in Figure 1, the comparisons do not agree very well. In comparison to the averaged hindcast spectrum, the idealized spectrum does not contain enough energy over both the high frequency and very low frequency range, and is high for the middle frequency band. Figure 2 shows the probability diagram constructed from the statistics of T_1 and $H_{1/3}$ of the hindcast wave data. For illustration purposes, Figures 3 and 4 show the corresponding purely imaginary family of responses which result from assuming that

$$g(T_1, H_{1/3}) = \frac{C}{100} H_{1/3}^2 (T_1/T_1^*)^2 \exp(-2T_1/T_1^*)$$

where C and T_1^* are constants. The curves of response for a = 0.1C and 0.4C are shown in the figures. With T_1^* = 10 sec the probability that the response would exceed 0.4C and 0.1C was estimated as 1 percent and 17 percent, respectively, by measuring the areas. The

probabilities were higher for the case of $T_1^* = 15$ sec. These were ~ 1.5 percent and ~ 21 percent for $a = 0.4C$ and $0.1C$, respectively.

Recently, Webb Institute analyzed a group of wave records measured at weather station I [6]. Preliminary unpublished results from these newly analyzed data indicate that the idealized two-parameter spectral form does not agree well with the measured spectra.

Figure 5 illustrates how the wave energy is improperly distributed over the frequencies in the idealized spectrum when it is compared against the measured wave spectrum. The solid curve in the figure is the average measured spectrum calculated from some of the recently analyzed spectra[6] . The other curves are the corresponding average idealized spectra calculated from three different definitions of T_1 as follows

$$T_1 = \frac{2\pi \int_0^\infty S_\rho(\omega)\, d\omega}{\int_0^\infty \omega S_\rho(\omega)\, d\omega} \equiv T_1(1) \quad ,$$

$$T_1 = \frac{2\pi \int_0^\infty \frac{1}{\omega} S_\rho(\omega)\, d\omega}{\int_0^\infty S_\rho(\omega)\, d} \times \frac{24.171}{26.847} = T_1(-1)$$

$$T_1 = 2\pi \left[\frac{\int_0^\infty S_\rho(\omega)\, d\omega}{\int_0^\infty \omega^2 S_\rho(\omega)\, d\omega} \right]^{1/2} \times \frac{24.171}{22.248} = T_1(2)$$

For an idealized spectrum, $T_1(1)$, $T(-1)$, and $T_1(2)$ are the same by their definition. However, for a measured ocean spectrum the various T_1's can be different. The differences reflect the departure of

a measured spectrum from an idealized spectrum. By use of the different definitions of T_1 one will thus obtain the different corresponding idealized spectra. The use of T_1 (1) is recommended by ITTC[3].

Figure 5 indicates that all of the idealized spectra underestimate the wave energy for the high and low frequency band by a factor of 1/2 and overpredict the wave energy for the middle frequency band. The use of different definitions of T_1 has not altered the result significantly , calculation base on T(-1) is slightly better than that of the others, but is not significantly better. The probability diagram was not constructed for measured spectra because of the small number of the samples.

These differences in the energy distribution of the idealized spectra and that of the measured spectra are consistent with the differences found between the energy distribution of the idealized spectra and the average hindcast spectrum shown in Figure 1. In both cases the energy in the high and low frequency bands is underestimated by the idealized spectra, and in the middle frequency range it is overestimated. This leads one to suspect the usefulness of the two-parameter spectrum for approximating the ocean environment, especially in studying the motions of platforms and buoys.

In spite of the bias described above, the parameterized spectrum approach has simplified the prodedured in calculating the statistical properties of the ship responses. The probability diagram representation is a good tool to engineers, if the idealized spectrum form is improved and the statistical bias is tolerable.

DIRECTIONAL WAVE SPECTRA

The motion of a ship in a seaway depends not only on the frequencies of the waves, but also on the directions of the component waves. The unidirectional spectrum discussed previously has little use when the ocean waves do not propagate in a dominant direction. Unlike the unidirectional wave spectrum, a directional wave spectrum can not be obtained from a continuous record of wave elevation at a single location on the sea surface. It requires knowledge of wave elevations over an area of the sea. Due to this requirement only a few measured directional ocean wave spectra are available [7][8][10].

The rapid growth of techniques for seakeeping analysis requires a more accurate description of a ship's environment. In order to make meaningful comparisons between the analytic results, basin experiments, and full scale trials one has to establish the capability

of measuring the directions of the ocean waves and generating directional waves in a seakeeping basin. In this section the result of preliminary work on basin-generated directional wave spectra is presented.

The elevation of the sea surface η is considered to be a stationary and homogeneous random process in time t and space $\vec{x}$, respectively. In the linear theory the spectral representation of η is given by

$$\eta(t,\vec{x}) = \mathrm{Re}\int\int_{-\infty}^{\infty} e^{i(\vec{k}\cdot\vec{x}-\omega t)}\, d\xi(\vec{k}) \qquad (2.1)$$

where $\vec{x}(x_1, x_2)$ is the position vector, with x_1 and x_2 the two surface coordinates ; $\vec{k} = (k\cos\theta,\ k\sin\theta) = (k_1, k_2)$ is the wave number vector, with $k = (k_1^2 + k_2^2)^{1/2}$ and $\theta = \tan^{-1} k_2/k_1$ the wave number and wave direction, respectively ; k_1 and k_2 are respectively the wave-number components in the x_1 and x_2 directions ; and $d\xi(\vec{k})$ is the random variable. According to linear theory the wave frequency, ω, is given by $\omega^2 = g(k_1^2 + k_2^2)^{1/2}$ in deep water.

In applications, one assumes that $d\xi(\vec{k})$ satisfies the following expected value condition

$$\frac{1}{2} E\left[d\xi(\vec{k})\,\overline{d\xi(\vec{k}')}\right] = \begin{cases} \bar{S}(\vec{k})\, d\vec{k} & \text{if } \vec{k} = \vec{k}' \\ 0 & \text{if } \vec{k} \neq \vec{k}' \end{cases} \qquad (2.2)$$

where a bar denotes the complex conjugate.

In the above expression $\bar{S}(\vec{k})$ is the directional wave spectrum. $\bar{S}(\vec{k})\, d\vec{k}$ can be interpreted as the mean-square value of η arising from wave elements which lie in the infinitesimal range of wave number components $(k_1, k_1 + dk_1)$ and $(k_2, k_2 + dk_2)$. Knowing the directional wave spectrum, $\bar{S}(\vec{k})$, of the sea determines the composition of waves in all directions.

In applications it is usually necessary to parameterize $\bar{S}(\vec{k})$. A general representation of $\bar{S}(\vec{k})$ is given by its Fourier series. By decomposing the directional wave spectrum $\bar{S}(\vec{k}; \omega_o)$ at a given frequency ω_o into a Fourier series with respect to direction θ, Longuet-Higgins[8] was able to relate the Fourier coefficients to the

cross spectra of the surface elevation and its space derivatives. The floating buoy built at the National Institute of Oceanography was designed for this approach. Barber[8] related the Fourier coefficients to the cross spectra of the surface elevations measured at several points in space. However, in the latter case the relations become more complicated and the lower order harmonic coefficients can not be determined without assumptions regarding the higher order harmonic coefficients.

From the Fourier representation of $\bar{S}(\vec{k};\omega_o)$ with respect to the wave-number component k_1, Barber and Pierson[9] have shown that $\bar{S}(\vec{k};\omega_o)$ can be approximated directly from an array of probes which lies in a direction parallel to the x_1 coordinate. The Fourier coefficients obtained from this approach have a one-to-one correspondence with the cross spectra of measurements having space separations of $\vec{r} = (nD, 0)$, $n = 1, 2, \ldots N$; where $\vec{r}$ is the separation vector and D is the fundamental separation of the probes. Thus, from an array of probes which has separations $D, 2D, \ldots ND$, one is able to approximate the directional spectrum up to the N^{th} harmonic. The derivation of this is given below.

By multiplying equation (2.1) by the corresponding equation for $\eta(t+\tau, \vec{x}+\vec{r})$ and taking the expected value, one has

$$E\left[\eta(t,\vec{x})\ \eta(t+\tau,\vec{x}+\vec{r})\right] = \frac{1}{2}\iiint_{-\infty}^{\infty} e^{i\left[(\vec{k}\cdot\vec{x}-\omega t)-i\left[\vec{k}'\cdot(\vec{x}+\vec{r})-\omega(t+\tau)\right]\right.} \cdot E\left[d\xi(\vec{k})\,\overline{d\xi}(\vec{k}')\right] = \iint_{-\infty}^{\infty} e^{i(\omega\tau-\vec{k}\cdot\vec{r})}\bar{S}(\vec{k})\,d\vec{k} \tag{2.3}$$

where τ is the time lag. Since the wave field is assumed stationary as well as homogeneous, the correlation function $E\left[\eta(t,\vec{x})\,\eta(t+\tau,\vec{x}+\vec{r})\right]$ in the above equation is a function of τ and $\vec{r}$ only; it is independent of t and $\vec{x}$. If the correlation function is denoted by $R(\tau,\vec{r})$, equation (2.3) can be written as

$$R(\tau,\vec{r}) = \iint_{-\infty}^{\infty} e^{i(\omega\tau-\vec{k}\cdot\vec{r})}\bar{S}(\vec{k})\,d\vec{k} \tag{2.4}$$

$$= \int_{-\infty}^{\infty} \left[\int_{-\frac{\omega^2}{g}}^{\frac{\omega^2}{g}} e^{-i\vec{k} \cdot \vec{r}} S(k_1; \omega)\, dk_1 \right] e^{i\omega\tau}\, d\omega \tag{2.4}$$

where $S(k_1; \omega) dk_1\, d\omega = \bar{S}(\vec{k})\, d\vec{k}$. The dependence of $\bar{S}$ on k_1 and k_2 is replaced here by dependence on k_1 and ω, making use of the dispersion relation between k_1, k_2, and ω. Equation (2.4) relates the directional wave spectrum $\bar{S}(\vec{k})$ to the correlation function $R(\tau, \vec{r})$. In the above equation

$$\int_{-\omega^2/g}^{\omega^2/g} S(k_1; \omega)\, e^{-i\vec{k} \cdot \vec{r}}\, dk_1$$ is the

Fourier transform of $R(\tau, \vec{r})$ with respect to τ and is called the cross spectrum, which is denoted by $Co(\omega) - iQ(\omega)$. Thus,

$$R(\tau, \vec{r}) = \int_{-\infty}^{\infty} \left[Co(\omega; \vec{r}) - iQ(\omega; \vec{r}) \right] e^{i\omega\tau}\, d\omega \tag{2.5}$$

where

$$\int_{-\omega^2/g}^{\omega^2/g} S(k_1; \omega)\, e^{-i\vec{k} \cdot \vec{r}}\, dk_1 \equiv Co(\omega; \vec{r}) - iQ(\omega; \vec{r}) \tag{2.6}$$

Thus, if one represents the directional wave spectrum $S(k_1, \omega)$ in a Fourier series with respect to $k_1 D$, where D satisfies $\frac{\omega^2}{g} D \leqslant \pi$, one can obtain the Fourier coefficients directly from equation (2.6) by their definitions. That is

$$S(k_1, \omega) = A_0 + \sum_{n=1}^{\infty} (A_n \cos nk_1 D + B_n \sin nk_1 D) \tag{2.7}$$

where

$$A_0 = \frac{D}{2\pi} Co(\omega; \vec{r} = (0, 0)) \tag{2.8}$$

$$A_n = \frac{D}{\pi} Co(\omega;\vec{r} = (nD, 0)) \qquad n = 1, 2, \ldots$$

$$B_n = \frac{D}{\pi} Q(\omega;\vec{r} = (nD, 0)) \qquad (2.8)$$

By arranging the probes to measure wave elevations such that one can calculate the Co's and Q's up to $\vec{r} = (ND, 0)$, the coefficients A_0, A_1, B_1, ... A_N, B_N can be readily obtained from (2.8). The relations in equation (2.8) are simple and they form the basis for the experiments described below.

The accuracy of the approximation of equation (2.7) is dependent on both the order N and the non-dimensional parameter $\omega^2 D/g$. For given N and D the angular resolution, θ_r, is defined as $\theta_r = \sin^{-1}(\frac{\pi}{ND\omega^2/g})$. Physically this is a measure of the width of the angle over which a narrow band wave-spectrum is spread. θ_r increases with decreasing ω; that is the angular resolution increases with increasing wave length. On the other hand if N and ω are given, then θ_r increases with decreasing probe separation, D. For a specific experimental setup, D can be adjusted for optimum results.

As an example consider a narrow band directional wave spectrum which satisfies

$$\int_{k_i - \Delta k_1}^{k_i + \Delta k_1} S(k_1;\omega)dk_1 = C(\omega) \quad \text{if} \quad k_i = k_0 \qquad (2.9)$$

$$= 0 \qquad \text{Otherwise}$$

where $C(\omega)$ is an arbitrary function of frequency ω and $2\Delta k_1$ is the band width of the wave number k_1. The directional spectrum can then be represented by a delta function, δ, and its Fourier representation is given by

$$S(k_1;\omega) = C(\omega) D\delta(k_1 D - k_0 D)$$

$$= \frac{C(\omega) D}{\pi}\left[\frac{1}{2} + \sum_{n=1}^{\infty} \cos n(k_1 - k_0)D\right] \qquad (2.10)$$

where $n = 1, 2, \ldots$ The N^{th} order approximation gives

$$S(k_1;\omega) \cong \frac{C(\omega)\,D}{\pi}\left[\frac{1}{2} + \sum_{n=1}^{N} \cos n(k_1 - k_0)\,D\right] \qquad (2.11)$$

At $k_1 = k_0$ the approximation $S(k_1;\omega)$ has its maximum value of $\frac{C(\omega)\,D}{\pi}(\frac{1}{2} + N)$. At $k_1 - k_0 = \frac{\pi}{ND}$ one has $S(k_1;\omega) \cong \frac{C(\omega)D}{\pi}(-\frac{1}{2})$ It is a factor of $-1/(1+2N)$ smaller than the maximum value. The approximation of equation (2.8) to the narrow band directional spectrum, equation (2.9) of $k_0 = 0$, is shown in Figure 6. From this figure, one sees how a narrow-band directional wave-spectrum is directionally spread out as a function of $\frac{\omega^2}{g} D$ in this approach. The loss of accuracy, i.e., increase of spreading, with decreasing $\frac{\omega^2}{g} D$, which has been discussed previously, is clearly shown in the figure.

EXPERIMENT

The basic approach described in the previous section was applied to the measurement of the directional spectrum of waves generated in NSRDC's seakeeping basin. Wave measurements were taken with sonic probes, using three separate array configurations, which are shown in Figure 7. For the linear arrays, the fundamental distance between the probes was 2.5 feet and the total array length was 32.5 feet. This arrangement enables one to approximate the Fourier series of the directional wave spectrum up to the ninth harmonic. This configuration was suggested by Pierson[11]. The reason this arrangement was used rather than the optimum array suggested by Barber[12],[13] is that in Barber's configuration the total array length would have been only 22.5 feet; a greater length was preferred. The linear array was arranged in two orientations relative to the wave generators. In the first case the array was mounted parallel to the West bank of the basin and at a distance of 100 feet from the bank, as shown in Figure 3. In the second case the same array was rotated 45 degrees clock-wise to the North. The third array consisted of a pentagon arrangement, and employed six probes: one in the center and five outside forming an equilateral pentagon. The sides were designed to be 10 feet long. The orientation is shown in Figure 3.

The seakeeping basin has wave generators along both the West and North banks and the wave generators on the two banks are operated independently. During the study three kinds of directional wave fields were generated. These were: wave coming from West bank, waves

coming from the North bank and waves coming simultaneously from both banks. Both regular and irregular waves were generated. The periods of the regular waves were 1.6, 2.0, 2.5, and 3.0 seconds. These wave periods correspond to waves with angular resolution of less than 10 degrees up to 90 degrees. The irregular waves were generated from available random seaway tapes. These wave trains had average wave periods ranging from 1.6 to 3.0 seconds.

Sonic probes operating at a frequency of 200 KH were mounted approximately 20 inches above the still water surface. These devices can measure the instantaneous water surface elevations with great accuracy. From the digitized records, cross spectra were calculated for all irregular waves. Wave amplitudes and wave phases were calculated for the regular waves by means of Fourier transforms. The directional wave spectra were then obtained by the use of Equation (2.8).

Some resulting directional wave spectra measured from the linear array are shown in Figures 8 through 16. Figures 8 through 11 are for regular waves and Figures 12 through 16 are for irregular waves. The curves for regular waves represent the directional spectra obtained under several different conditions such as different wave-maker dome air pressures, which are indicated in terms of blower rpm, different directions, which are designated by N or W for waves generated at the North and West banks, respectively, and different wave combinations. The coordinates of the figures are the normalized wave vector components in the direction parallel to the array, and the normalized spectrum density

$$S^*(k_1;\omega) = \frac{S(k_1;\omega)}{S_A(\omega)}$$

where $S_A(\omega)$ is the average of the one-dimensional spectrum densities obtained by the five probes. Since $S(k_1;\omega)$ is approximated by a ninth order Fourier series, the normalized spectrum density $S^*(k_1;\omega)$ should be less than 9.5 as previously discussed. The theoretical maximum value of $S^*(k_1;\omega)$ depends on the wave conditions. If a wave of a given frequency were generated at only one bank, $S^*(k_1;\omega)$ should have a maximum value of 9.5 in the direction in which it was generated. For other directions, it will be less than 9.5. The actual value depends on the combination of the wave amplitudes generated at the two banks. The regular wave results as shown in the figures agree with this theoretical value very well regardless of the wave frequencies, wave amplitudes and the presence of

waves coming from other directions. Figure 11 shows how the angular resolutions varied with the frequencies of the waves. As discussed previously, the angular resolution increases with increasing wave period and the theoretical value of $S^*(k_1, \omega)$ is -0.5 at direction θ_r, $(k_1 - k_0) = \frac{\pi}{ND}$; The measured angular resolution agrees fairly well with the theoretical value. However, away from the peaks, $S^*(k_1; \omega)$ oscillated with a much higher value than one would expect, especially for the wave periods of 2.5 and 3 seconds. The irregular wave results do not agree as well with the tehoretical value. Figure 12 shows the resulting directional wave spectra of irregular wave trains generated at the North bank. It indicates that the waves were all coming from the North bank and the peak values of the spectra are between 6.5 and 8 . In comparison with the regular wave measurements of Figure 7, the peak value is decreased. However, as the tail value also decreases, one concludes that the mixture of the frequencies in the same direction does not affect the angular spreading significantly.

Figure 13 shows the measured directional spectra under a different wave condition. From it is concluded that there were long waves of period 2.5 to 3 seconds coming from the West and short waves of period 1.6 seconds propagating to the South. The directional distribution of the 2.0 second period wave is meaningless. However, the actual wave field was different from the one pictured above. An irregular wave train was generated at the North bank and a regular wave of period 2.5 seconds was generated at the West bank. The loss of accuracies of the wave directions for the waves with wave frequencies near that of the regular wave is clear. Figure 14 illustrates the same phenomena. For this case the period of the regular wave was 2.0 seconds and the amplitude was smaller in comparison with the previous case. The loss of information on the wave directions in this case was not as serious as in the previous case. The presence of the 2.0 second period wave reduced the peak value of the 2.4 second period wave but increased that of the 1.6 second period wave. Figure 15 shows the measured directional wave spectra for the case of two low-amplitude irregular wave trains propagating at 90 degrees to each other. The directional distribution of the wave is reasonable.

By examining the calculated cross-spectra we found that the method used in estimating the cross spectrum was responsible for the errors which appear in Figures 13 and 14. Special care is necessary when analyzing the directional wave fields in these cases. By the use of a narrower frequency band-width, the result was improved ; it is shown in Figure 16.

The directional spectra obtained from the pentagonal arrangement were not good and are not shown here. The measured phase lags between the probes had the same accuracies as those obtained by the linear array. However, as previously mentioned, the relations between the Fourier coefficients and cross spectra are more complicated and thus, the results were not as good as those obtained from the linear array method.

DISCUSSION

The result of the study on the idealized unidirectional spectrum indicates the need for improvements in recommended spectral forms in order to obtain a better prediction of long term ship motions. The two-parameter spectral form underestimates the wave energy for both high and low frequencies and overestimates the wave energy over the wave frequency range of 0.1 cycle/sec. to 0.14 cycle/sec. This has been illustrated in Figures 1 and 5.

For applications, one has not only to be aware of this limitation associated with the idealized spectrum but also the varieties of ocean wave spectra. For a better representation of the ocean environment, one needs to know not only the averaged wave period and wave height but also other parameters. With more measured spectra a data bank of wave spectra can be established on a digital computer and stored on tapes for direct access. Such a data bank would eventually make idealized spectra obsolete. It would certainly be more accurate than the idealized spectra and would contain samples of all of the various ocean wave spectra.

The experiment on the directional waves suggests that the accuracy of a measured directional spectrum depends more on the directional compositions of a wave field than on frequency compositions of the waves. This is demonstrated in Figures 11, 12 and 13. In order to accurately measure the spectrum of a swell and wind waves combined sea, one has to use a technique which can estimate a sharp peaked cross-spectrum accurately, such as the narrow band process or the time shift process[14] . However, it will require much longer records of surface elevation.

The linear array is a better probe arrangement than a pentagon arrangement for the wave fields generated for this paper. However, a linear array does not allow one to separate the waves propagating in the direction left of the array from those of the right. Two linear arrays may be needed for the measuring of an actual wave field in which waves propagate in an angle of more than 90 degrees .

The angular resolution illustrated previously can be improved if one applies a weighting function to the Fourier coefficients. The choice of the weighting function depends on one's taste, as has been discussed by Longuet-Higgins[8]

The separation D was 2.5 feet in the present experiment. This separation can be adjusted to improve the long-wave angular resolution. The choice of the D depends on the wave frequency range in which one is interested. If one is only interested in the long waves then one can chose a suitably large D such that $\frac{\omega^2}{g} D \leqslant \pi$ for all frequencies in which one is interested. But in this case, the total array length will certainly be increased, and the increase in the array length can complicate the operations of the detectors. This has to be considered in the choice of an optimum D . By moving the probes opposite to the direction of the waves, one can also improve the angular resolution significantly[11] . It is applicable in an open sea where the waves are considerably homogenious over a large area. It may not be suitable for a model basin unless the basin is large and the waves are very homogenious with respect to space.

The length of the wave records used for the above irregular wave calculations are approximately one minute long. The accuracy might have been improved if longer wave records had been used.

ACKNOWLEDGMENTS

The author is indebt to Dr. Wm. E. Cummins for his suggestion of the subject and the guidance given during the course of the work. Also, the author wishes to thank Mr. Daniel Huminik for his assistance with the experiments and many others who helped on the manuscript.

REFERENCES

[1] PIERSON, J. W. and MOSKOWITZ, L., "A Proposed Spectral Form for Fully Developed Wind Seas Based on the Similarity Theory of S. S. Kitaigorodskii", J. Geophys. Res., Vol. 69, No. 24, 1964.

[2] BRETSCHNEIDER, "Wave Variability and Wave Spectra for Wave Generated Gravity Waves", Technical Memorandum, No. 118, Corps of Engineers, Department of the Army, 1959.

[3] Proceedings of the 12th Internat. Towing Tank Conference, 1969.

[4] CUMMINS, W. E., "A Proposal on the Use of Multiparameter Stand Spectra", Proceedings of the 12th ITTC, 1969.

[5] PIERSON, W. J. and TICK, L. J., "Wave Spectra Hindcasts and Forecasts and Their Potential Uses in Military Oceanography", The U. S. Navy Symposium on Military Oceanography, 1965.

[6] MILES, M., "Wave Spectra Estimated from a Stratified Sample of 323 North Atlantic Wave Records", NRC Report LTR-SH-118, October 1971. (Unpublished)

[7] CHASE, J., et al, "The Directional Spectrum of a Wind-Generated Sea as Determined from Data Obtained by the Stereo Wave Observation Project", New York University, College of Engineering Report, July 1957.

[8] "Ocean Wave Spectra, Proceedings of a Conference", Prentice Hall, New York, 1963.

[9] BARBER, W. F. and PIERSON, W. J., "Review of Methods of Finding the Directional Spectra in a Towing Tank", New York University, College of Engineering Report, 1963.

[10] EWING, J. S., "Some Measurements of the Directional Wave Spectrum", Journal of Marine Research, Vol. 27, No. 2, 1969.

[11] PIERSON, W. J., "The Estimation of Vector Wave Number Spectra by Means of Data Obtained from a Rapidly Moving Hydrofoil Vehicle", Techn. Report No. 68-56, Oceanics, 1968.

[12] BARBER, N. F., "Optimum Arrays for Direction Finding", N. Z. J. Science 1 (1), 1958.

[13] CUMMINS, W. E., "The Determination of Directional Wave Spectra in the TMB Maneuvering-Seakeeping Basin", DTMB Report 1362, 1959.

[14] PIERSON, W. J. and DALZELL, J. F., "The Apparent Loss of Coherency in Vector Gaussian Processes Due to Computational Procedures with Application to Ship Motions and Random Seas", College of Engineering, Research Division, New York University, 1960.

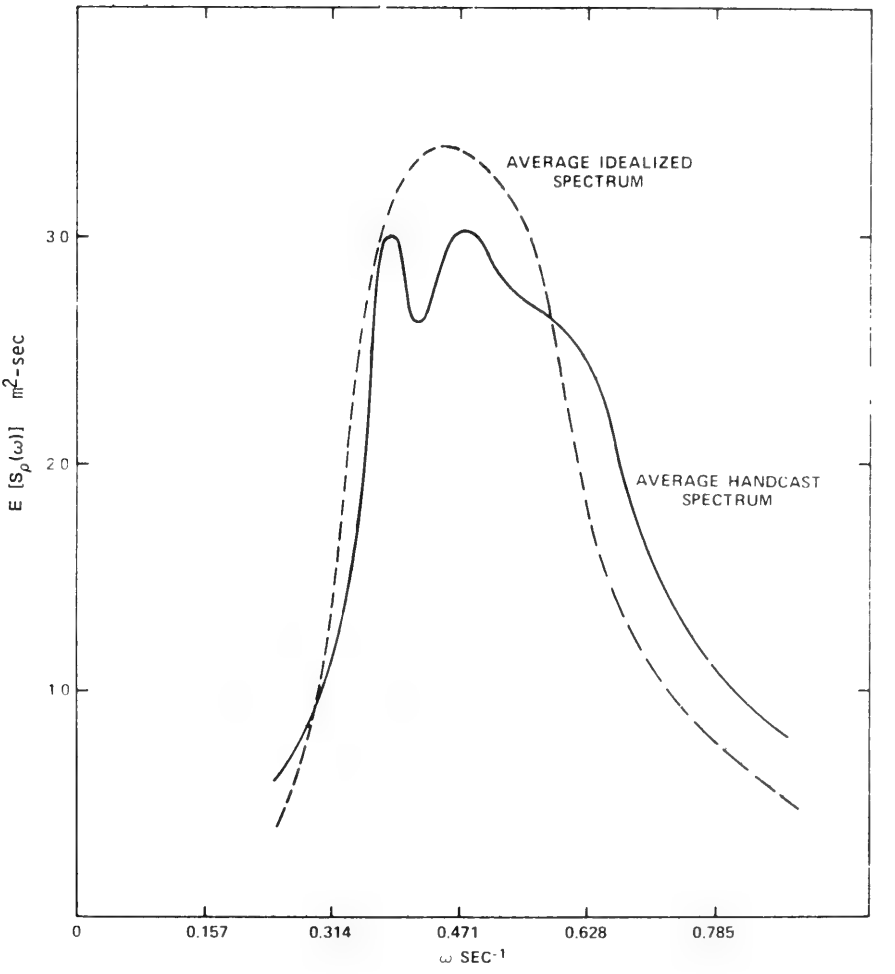

Figure 1 Average hindcast, wave spectra calculated at station near station India

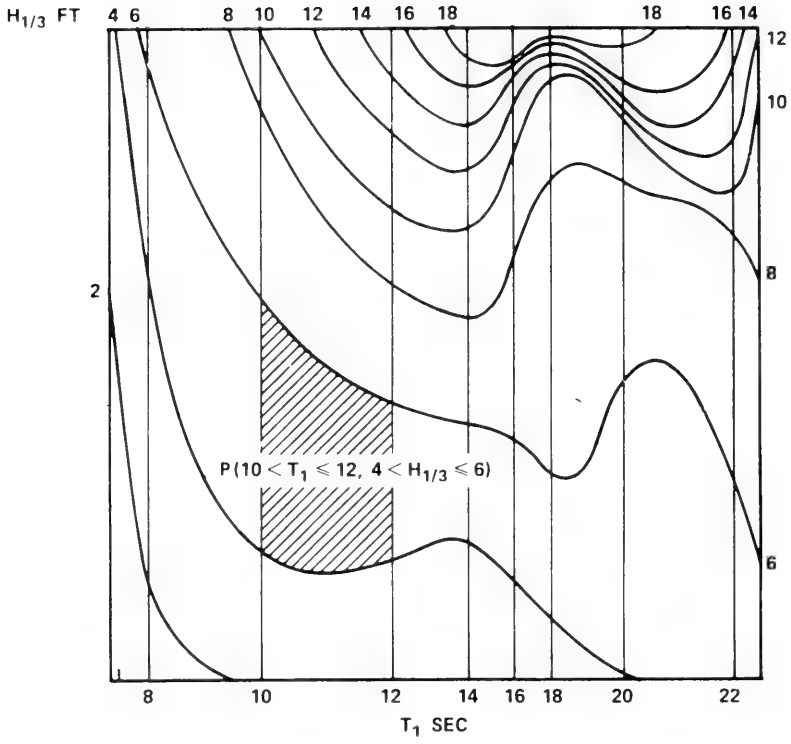

Figure 2 Probability diagram of T_1 and $H_{1/3}$ based on hindcast wave data

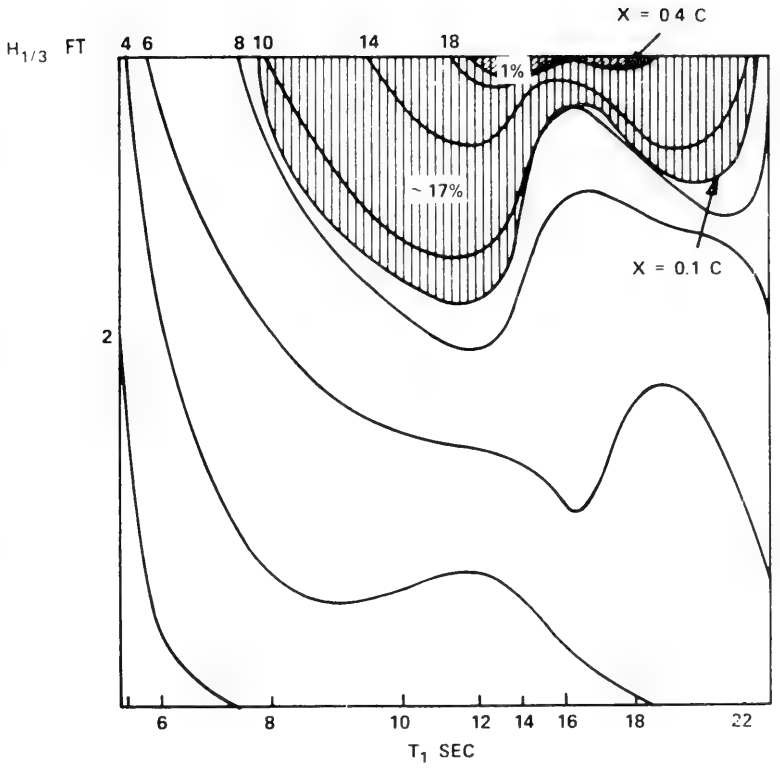

Figure 3 Probability distribution of the imaginary family of ship responses with $T_1^* = 10$ sec.

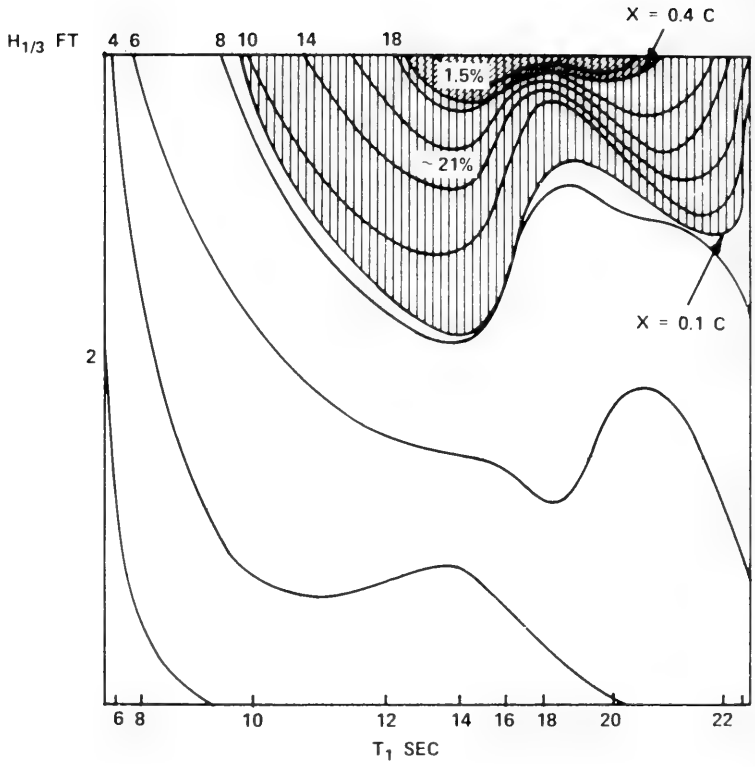

Figure 4 Probability distribution of the imaginary family of ship responses with $T_1^* = 15$ sec.

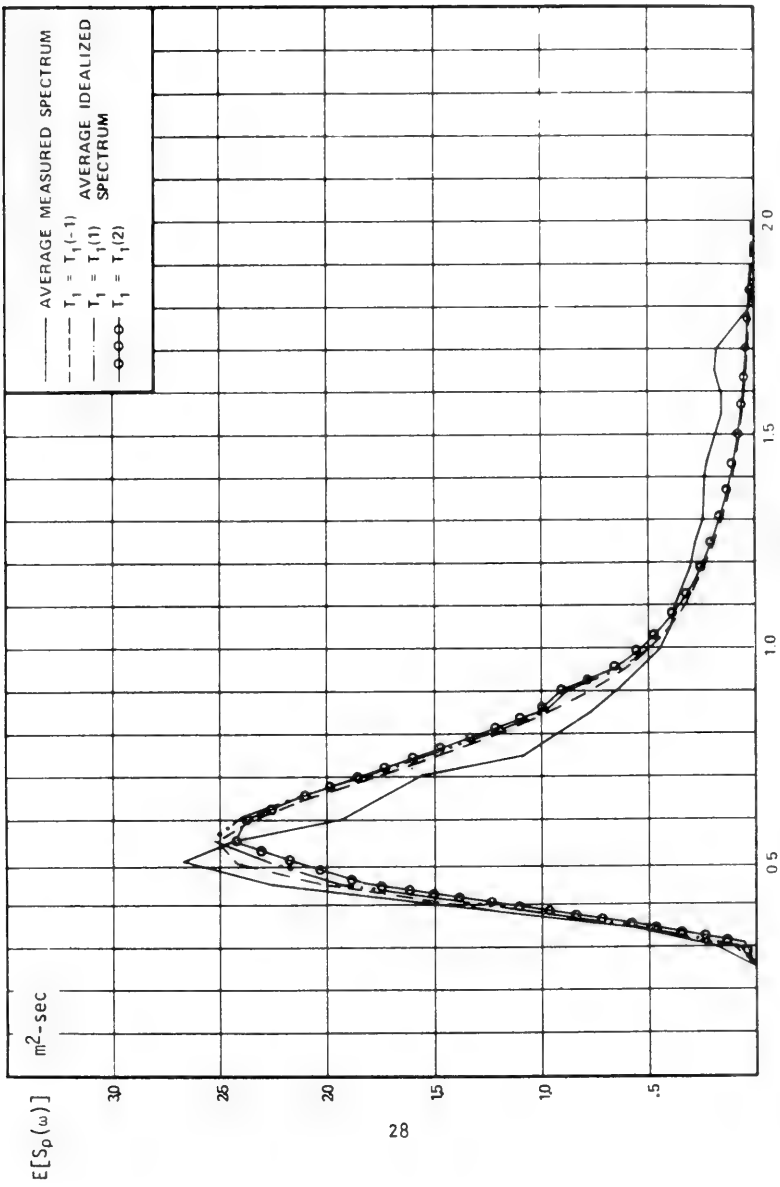

Figure 5 Average measured spectra

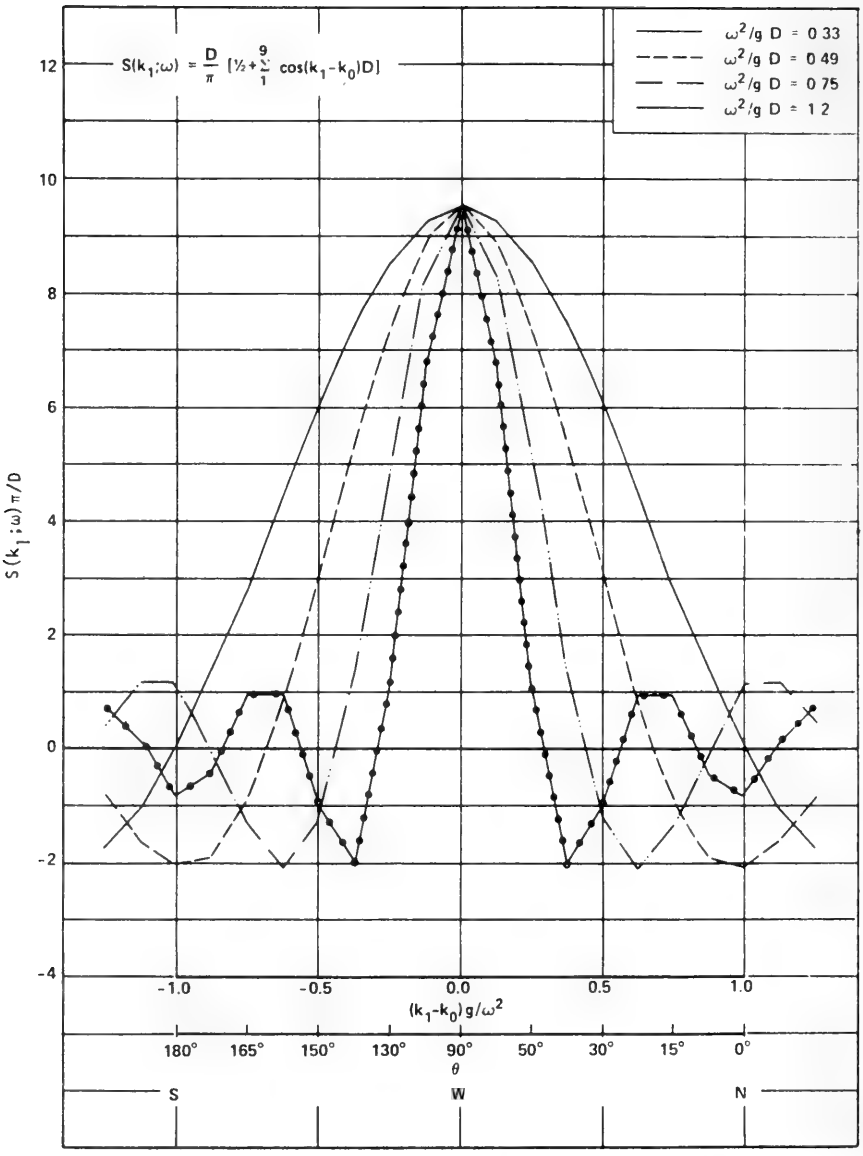

Figure 6 The ninth order harmonic representation of the narrow band directional spectra

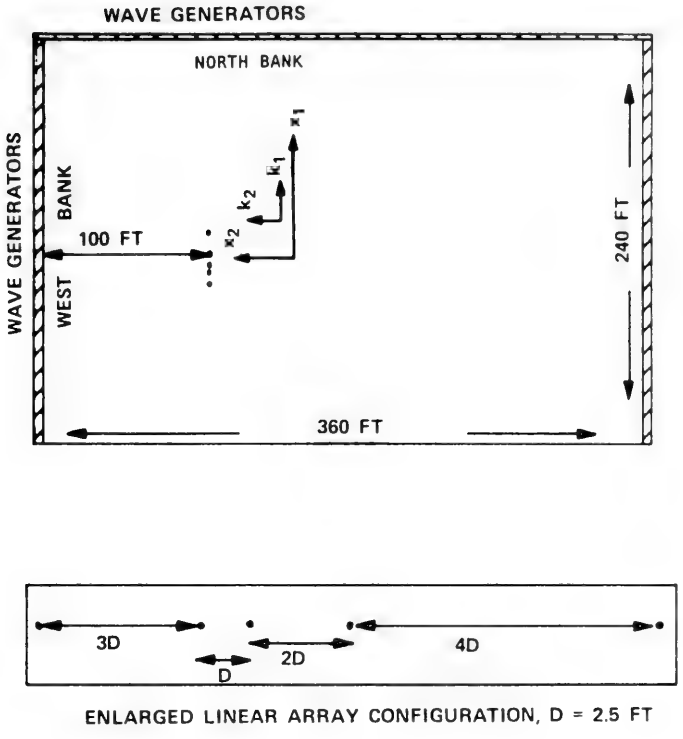

Figure 7 Wave-height probe configurations

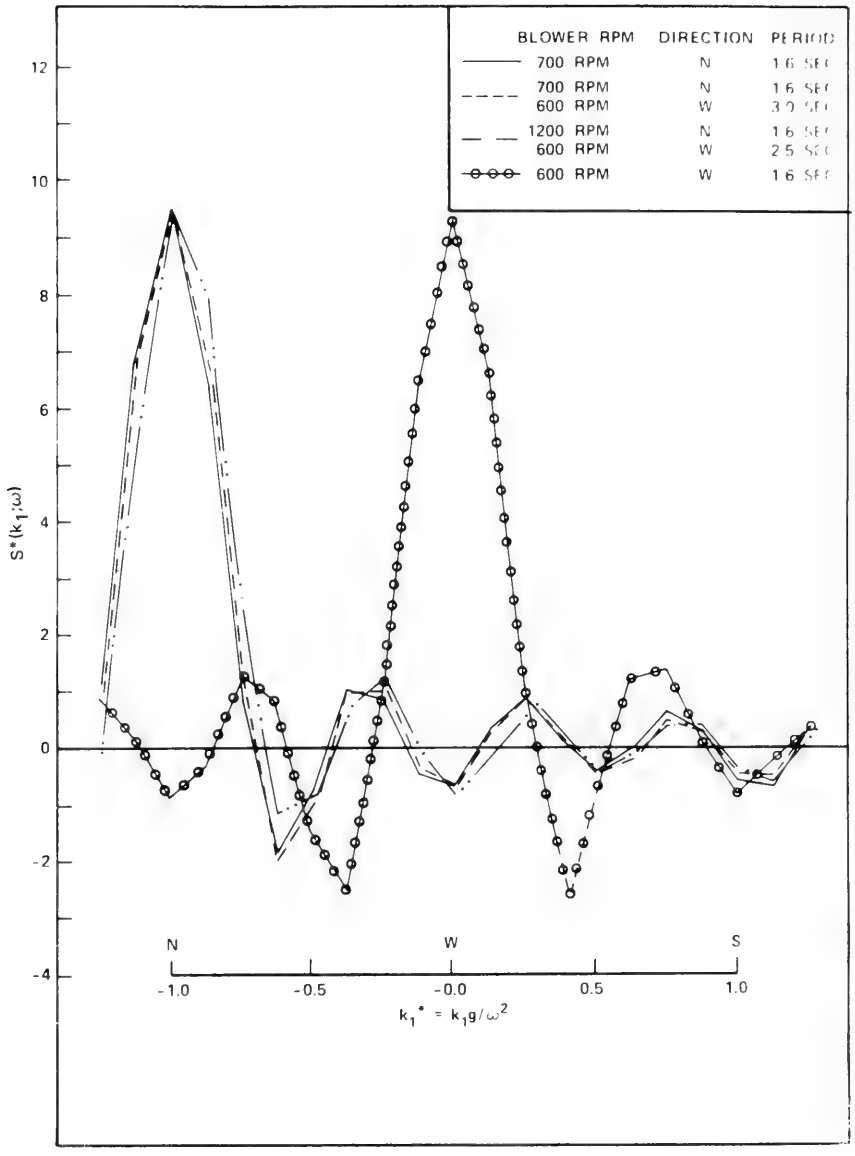

Figure 8 Measured directional spectra of 1.6 sec. period waves only, with array parallel to West bank

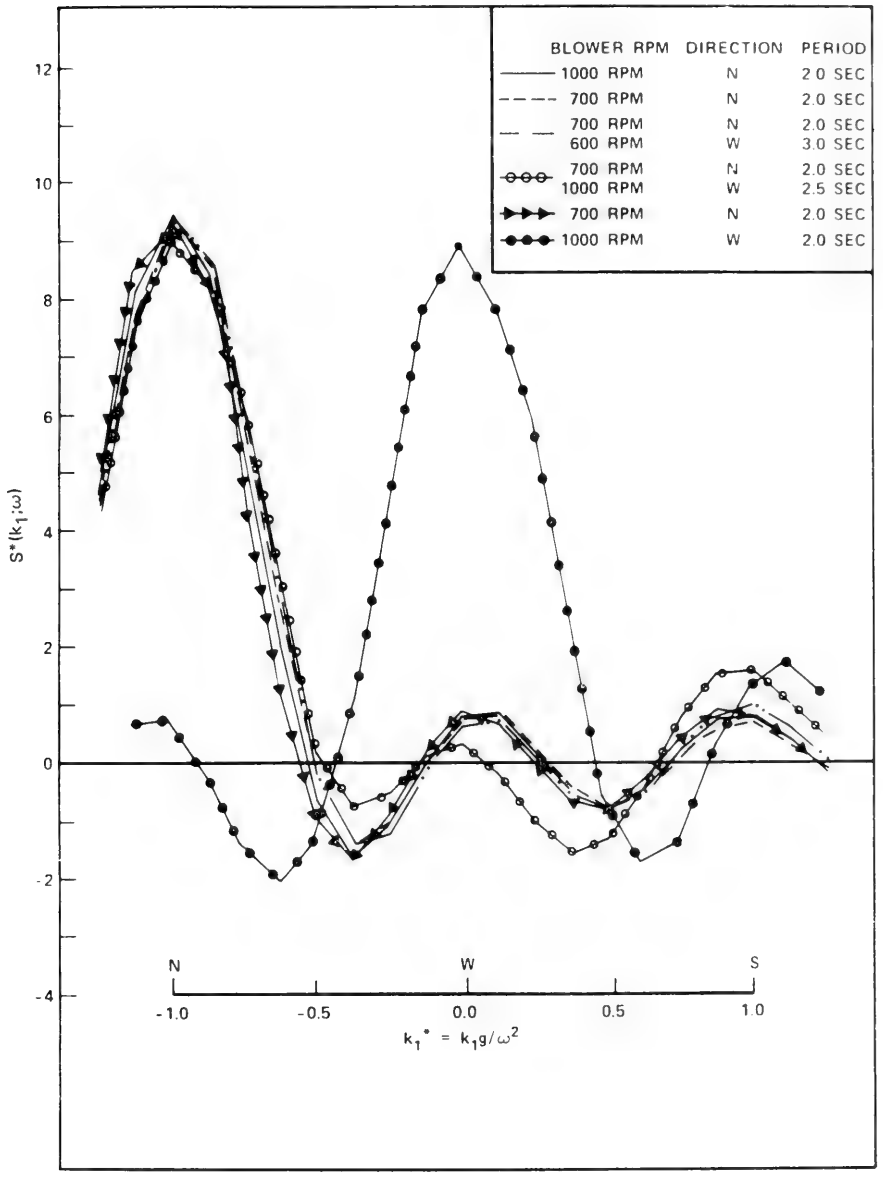

Figure 9 Measured directional spectra of 2.0 sec. period waves only, with array parallel to West bank

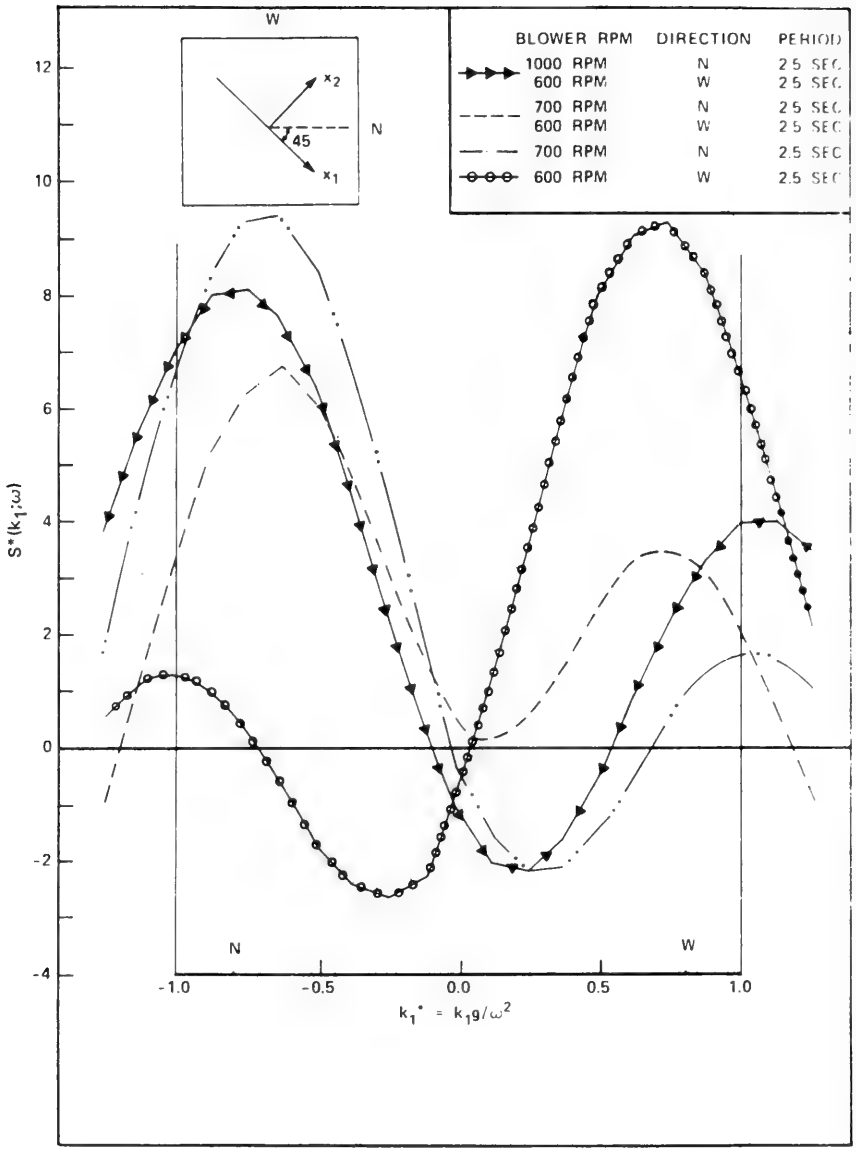

Figure 10 Measured directional spectra of 2.5 sec. period waves only, with array 45° to West bank

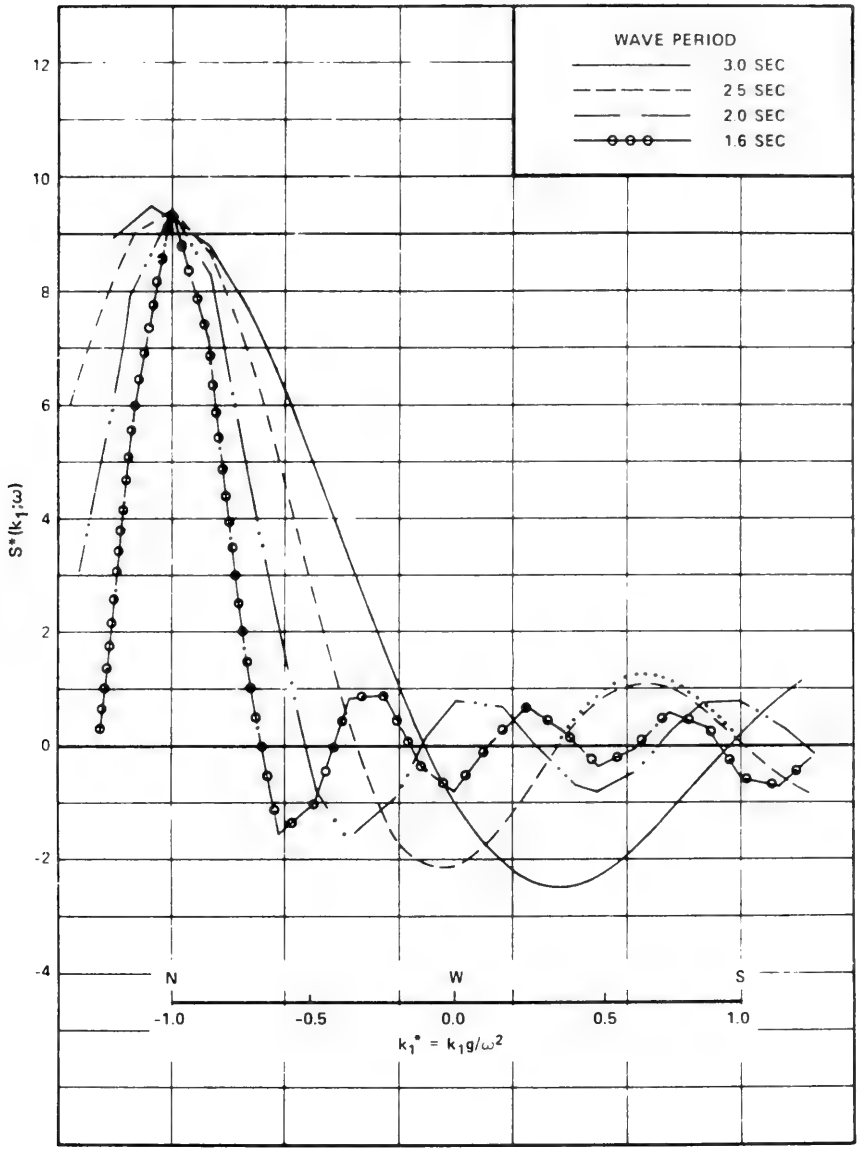

Figure 11 Dependence of angular resolution on wave period for wave generated at North bank and array parallel to West bank

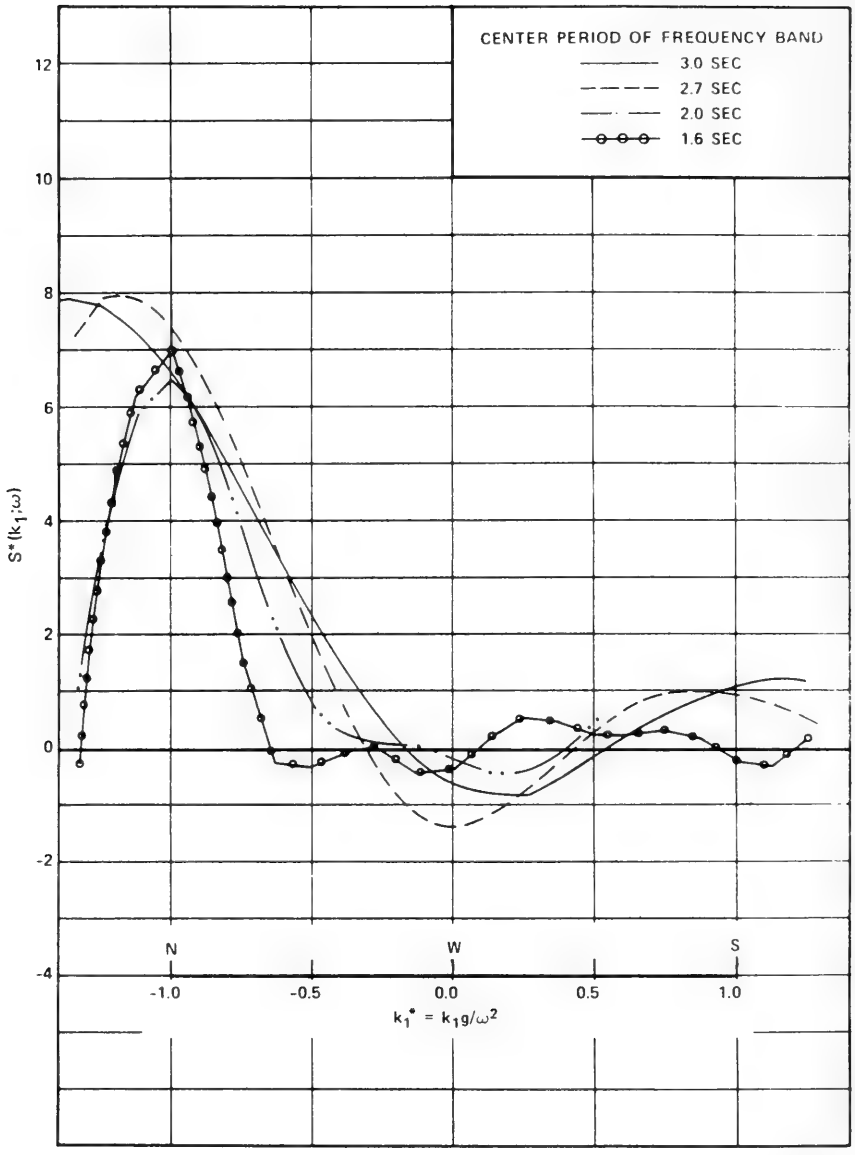

Figure 12 Measured directional spectrum of irregular waves generated at North bank

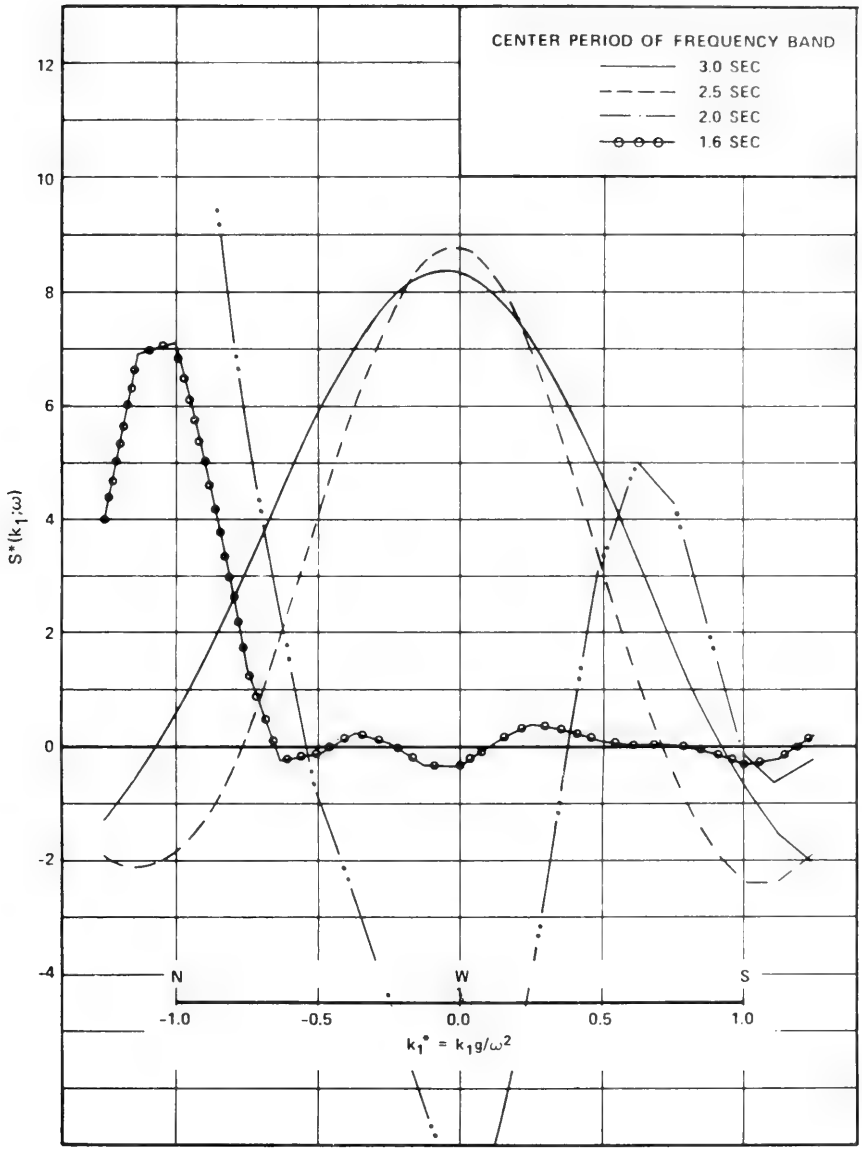

Figure 13 Measured directional spectrum of an irregular wave train with a high amplitude regular wave train of 2.5 sec. period

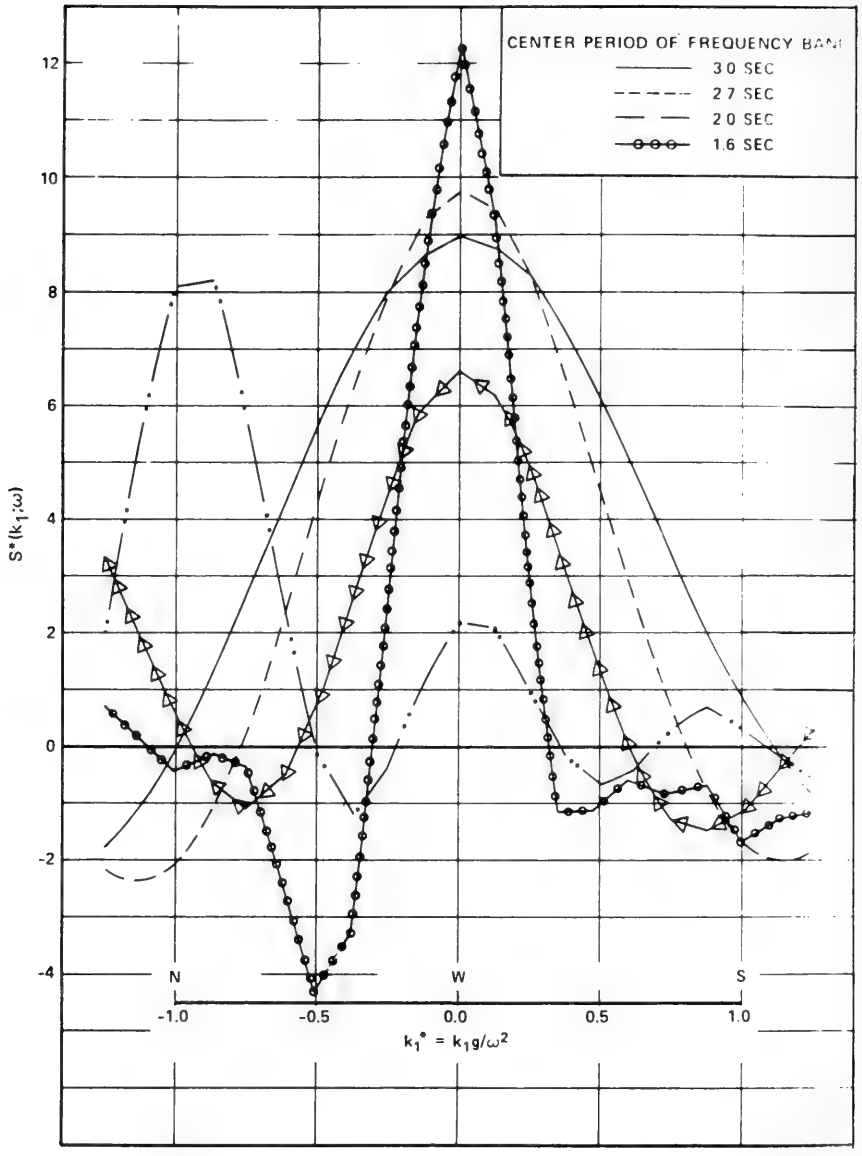

Figure 14 Measured directional spectrum of an irregular wave train with a low amplitude regular wave train of 2.0 sec. period

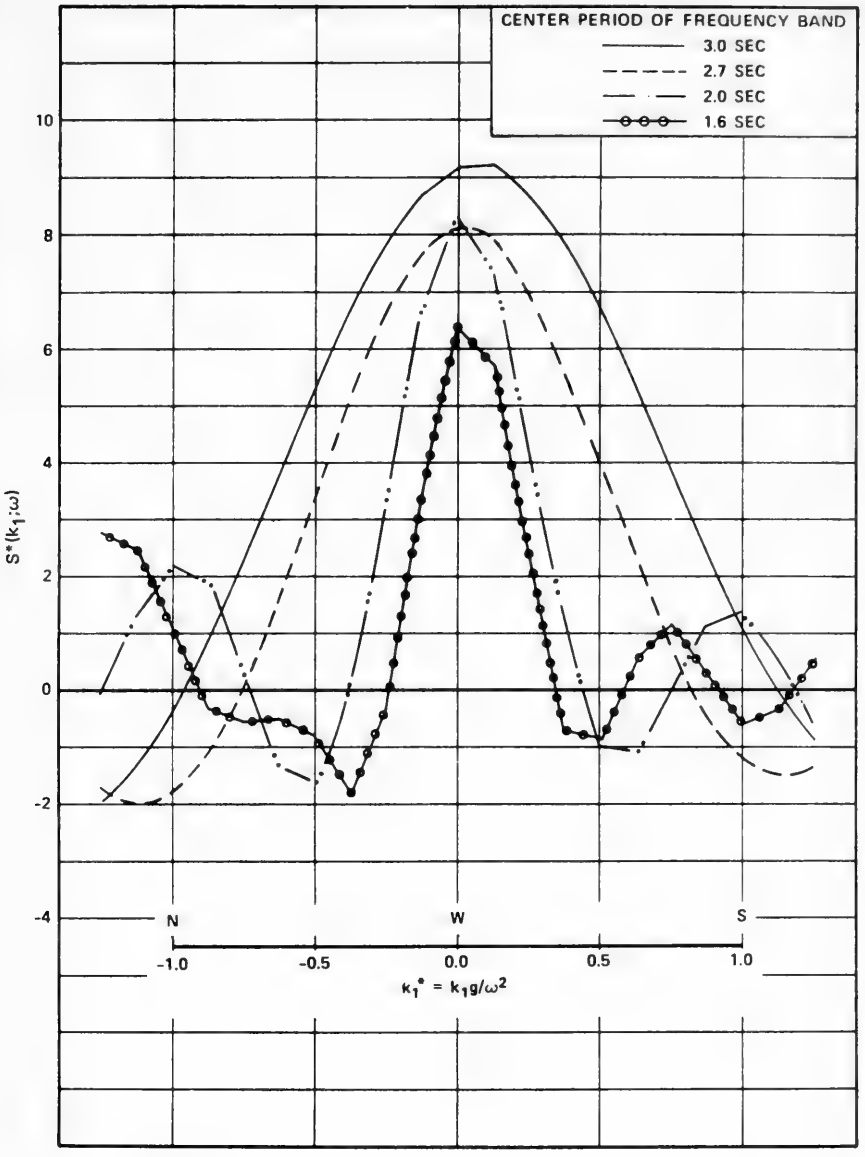

Figure 15 Measured directional spectrum of two irregular wave trains

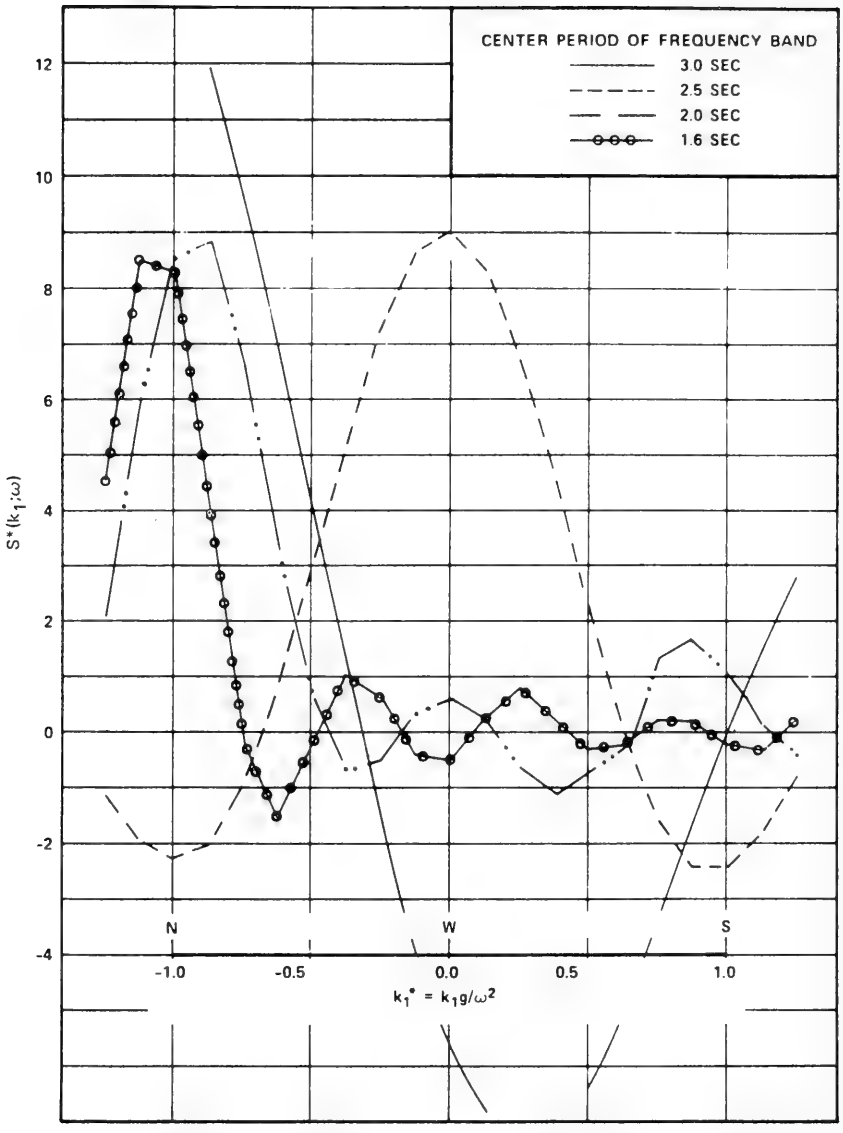

Figure 16 Directional spectrum of Figure 12 with a narrow frequency bandwidth

DISCUSSION

William E. Cummins
Naval Ship Research and Development Center
Bethesda, Maryland, U.S.A.

As originally scheduled, I was to be a co-author of this Paper and I should to offer a word of explanation. Because of high pressures in the Navy Department it was not possible for me to contribute to this to the extent that would justify my name being on the cover. All the work and most of the good ideas are Dr. Chang's. I will not dissociate myself from any bad ideas, although I do not admit that there are any in the Paper. Fortunately Dr. Chang was able to do an excellent job without me. She has started work in a very difficult field which we have all neglected, and which we must not neglect much longer.

I shall say a few words about the first part of her paper on the problem of standard spectra, which is something we have been fighting over in the ITTC now for some six years. I expect there will be a good deal of concern with it next month in Germany as well.

The more we learn the more we realise that we are in trouble. We are using sea spectra in the United States Navy and we find that we do not know enough to use them well. I would like to offer a word of explanation on some of the troubles that Dr. Chang showed where there were discrepancies at the two ends of the "average" spectrum. The average which was based on the fully developed spectrum tended to underestimate the ends, and in the middle it tended to overestimate. I remember Bill Pierson warning us many times that when he and Neumann and Moskovitz and the others who worked on the fully developed spectrum, they based their theories on only 15 percent of the measured spectra available to them, 85 percent could not be considered fully developed. So the naval architects who have been using them, against this advice of the oceanographers, have been concentrating on something that occurs about one time out of seven.

If you have been to sea and looked with your eyes open you

will realise that almost invariably what you see is a local wind sea with a swell underneath. The wind sea tends to be of relatively short wave length. The swell comes from some distant storm ; it has been through the filtering effect of distance, so it is a narrow band. Even when you cannot see it with your eye the ship usually does see it. The local wind sea is usually doing one of two things : it is either growing or falling. So what you have is really a dumb-bell spectrum. You have a swell here from somewhere else and a wind sea developed locally. These are not taken account of in the fully developed spectra on which we have been basing much of our work, yet they are very important for the naval architect ; we cannot ignore them.

I was on a ship just two months ago. It was not a normal ship but nevertheless it is an interesting case. The average wave height on one day was about four feet. There was a swell about 300 feet long for our 250 foot ship. We here heading into it. It was a quiet day. The surface even glassy. The local wind sea was virtually zero - and we slammed about 55 times per hour by count. The next day we had a local wind sea about the same height ; a few white caps, not much ; a lovely day. The waves were much shorter. It was an absolutely wonderful day, because the ship was just alive in the water. The ship behaved completely differently.

Over and over again we have used the fully developed spectrum for characterising response when it is just plain wrong. We have to look at all of the seas that the ships encounter.

DISCUSSION

Michel Huther
Bureau Veritas
Paris, France

I first thank the authors for the very interesting Paper they present.

As the authors noted it, for ship behaviour calculations sea states representation by spectra is nowaday commonly used. The main problem for naval architects remains the question of the multi-directionality of the sea. I shall be pleased to know the opinion of the authors upon the two commonly used representations, i.e. the cosine

of the angle incidence spacial repartition of the energy from the main direction, and the concept of the superposition of different unidirectional spectra coming from different directions.

DISCUSSION

Manley Saint-Denis
University of Hawai
Honolulu, U.S.A.

The spectral theory of waves is a difficult subject to discuss with clarity and cohesion because the subject, even today, is in great turmoil and no matter how much or how well is said about it, even more remains in doubt. At the present state of the art, a point can be strongly developed only by disregarding a plethora of other points which, however, remain to haunt one like ghosts demanding to be heard in the night.

Miss Chang's Paper is a welcome and well-written exposition on a point of keen interest, namely, do the idealisations made in the effort to obtain a working description of the sea yield disfigurations of reality ? Miss Chang believes that the correspondence between model and reality is unsatisfactory, yet I suspect this is only a question of standards and that hers are somewhat higher than those of us who, being older, have learnt that nature, no matter how well-behaved, cannot be very well fitted by simple formulae, no matter how well they may be conceived. For me, the fit of measured and idealised spectra in Figure 5 of the text seems to be very good.

Miss Chang suspects the usefulness of the two-parameter spectrum and suggests a data bank. Such an idea would have been frightening a few years ago but now that computers with abundant memory are available, the suggested solution is feasible, yet for all the merit of the idea I should like to enter a plea for elegance - that is, for minimum effort, that is, for simple formulations instead of quasi-infinities of numbers, the designer will be happier ; for, having been brought up over the past century to depend on a length over 20 wave, he would appreciate something almost quite so simple. Whether the simple formula can be fitted to the vagaries of the sea wave depends, in my opinion, on how representative the probability distributions of Figures 2 and 4 in the text are, i.e. upon whether the

probability distributions really represent the sea behaviour, and to this end, I urge Miss Chang to explain, if possible, the double dip in the curves. After long meditation on the subject I have succeeded only in convincing myself that I do not understand the plot and am in somewhat of a dilemma as to whether the explanation underlying the double dip is a physical or a statistical inaccuracy. At all events, the orderly presentation is a pleasant reward for the reader who seeks insight into this fascinating subject of how to describe the wind-driven sea and leaves him with a stimulating thought for further work. From a single Paper written by a young lady one cannot possibly ask for more.

REPLY TO DISCUSSION

Ming-Shun Chang
Naval Ship Research and Development Center
Bethesda, Maryland, U.S.A.

My thanks to Dr. Cummins and Dr. Saint-Denis for their kind comments.

On the question of how well the linear supposition of the directional waves can be applied to the ship applications, I do not yet know the answer. This is one of the reasons for doing the directional waves experiment in the basin.

The cosine power law spreading in the wave directions has been observed by a few experimental studies such as SWOP and the floating buoy of N.I.O. However, these data were taken with respect to wind generated waves. For a large percent of the time, the waves in the ocean are a combination of swell and wind waves ; thus, one should not expect this power law to hold in general. The Atlantic hindcast data could give a preliminary picture on this subject.

As to Dr. Saint-Denis' comment on the use of two parameter spectral formulation, I certainly agree that it is dependent on the types of problems one is studying. I do not believe it will be very good for studying optimum design and its associated problems because the shifting period may introduce a large error in probability at the large response end.

About Dr. Saint-Denis' question on the probability diagram

and the dip in it, I have as yet not studied it very carefully. However I believe the dip is due to the combination of swell and wind waves. This combination depends on the distribution of the wind field over the area under study. I would say that you will find the answer in the wind statistics.

* * *

THE ROLE OF THE DOMINANT WAVE IN THE SPECTRUM OF WIND-GENERATED WATER SURFACE WAVES

E. J. Plate
University of Karlsruhe
Karlsruhe, Germany

ABSTRACT

In an appendix to a paper on the structure of wind generated waves Plate et. al. (1969) have shown that the - 5 power law of Phillips is not necessarily an indication of a gravitational subrange but could be a consequence of the dominance of a train of significant waves. These waves are similar in shape but not necessarily sinusoidal. The consequences of these observations were exploited in developing modeling laws for wind generated waves, by Plate and Nath (1970), and interpreting the shape of the spectrum of wind generated waves (Plate. 1971). Although these concepts serve well to explain a number of previously unexplained phenomena - such as the "overshoot phenomenon" of Barnett and Sutherland (1968) _ there appear certain features in observed field data which are not in accord with the results. For example, many ocean wave measurements reveal a broader spectrum than that of the similarity hypothesis, and non-constancy of the coefficient in Phillips - 5 power law. It is the purpose of the paper to explain at least qualitatively the development of the ocean wave spectrum in terms of modifications to the similarity concept and to assess the consequences of these modifications for the laboratory simulation of ocean waves.

I. INTRODUCTION

There exist two different methods of describing the state of the sea surface : the method of the dominant wave and the method of the spectrum. The former has recently been replaced in many labora-

tory and theoretical studies by the latter. In this paper, it will be shown that the two concepts are not mutually exclusive but complement each other. It will be shown that the dominant wave concept may have some important advantages for an understanding of the physical processes involved in the energy transfer from the wind to the water surface. In particular, it will be shown that the equilibrium spectrum constant β of Phillips can be associated with the slope of the dominant wave. Consequences of this relationship between the dominant wave and the spectrum will be pointed out.

II. THE EQUILIBRIUM SPECTRUM

In calculations of forces exerted by wind-generated waves on off-shore structures two different views of the wave field have been held. The engineer of older days has used what is called the "design wave" for his structures : starting from the observation that for a long duration wind there arises a wave field in which similar waves of approximately equal lengths and frequency but of variable height dominate the motion of the water surface, he defined an average wave from the largest third or so of the observed waves and used the corresponding height or length for his design. Such concepts lead to the representation of the design waves in the form of a fetch graph (see Wiegel (1970) for the latest version of this graph). We shall call henceforth this wave the "dominant wave".

This essentially physical view of the ocean surface is contrasted by the more recent, essentially mathematical representation of the water surface at a point as a random time series as used by many modern writers. This time function has some interesting properties which were determined experimentally. It was found, for example, that the elevations of the surface at a point constitute, after a long duration wind, a stationary sample of a Gaussian distributed ensemble (Longuet-Higgins (1953), Hess et. al. (1969)) with Rayleigh distributed extrema, with a variance that can be decomposed into a variance spectrum. Physics enters into this latter concept through the spectrum. As sinusoidal waves satisfy the linear equations governing surface waves, the spectrum was thought to represent a superposition of very many "component waves", that is, linear waves of very small amplitude who by superposition form the large waves. Empirically, it was found soon enough that the spectra of the water surface at many different points in many different regions of the oceans had a somewhat similar shape, and attemps were made - which are by now classical - to empirically associate a functional form with the spectrum, whose parameters were empirically correlated with local independent parameters, such as wind speed and fetch.

It might well be said that this development found its culmination in Phillips' (1958) derivation of the - 5 - power law for the high frequency end of the spectrum. From reasoning that all component waves shorter than some limiting, longest component are at equilibrium in a state of breaking, he deduced the equation for the high frequency end of the spectrum :

$$S(\omega) = \beta g^2 \omega^{-5} \qquad \text{for } \omega \gg \omega_{max} \tag{1}$$

where $S(\omega)$ is the spectral density, g the acceleration of gravity and ω the angular frequency which has a value ω_m where the maximum $S(\omega_m)$ in the spectral density occurs. How well the - 5 - power law equation 1 fits the experimental data is illustrated in figure 1a (from Hess et. al. (1969)). The data are from many different sources and range from short fetch laboratory data to long fetch ocean data obtained at winds near Hurricane conditions. A separate set of data, by Mitsuyasu (1969) is shown in figure 1b. Through both sets, a curve is drawn according to equation 1 with $\beta = 1.48 \cdot 10^{-2}$.

Unsatisfactory in equation 1 is the fact that β is an empirical constant. An analytical model that overcomes this defect by relating β to the energy input into the wave field from the wind was suggested by Longuet-Higgins (1969). Assuming the rate of energy lost to turbulence by wave breaking to be proportional to the wave energy contained in the wave field, and equating this to the work done by the wind on the waves, he was able to show that if all wave components at frequencies above ω_m are in the state of breaking the coefficient β can be related to the drag coefficient C for the wind through :

$$\beta = - \frac{0,125}{\log 1600\, C^{3/2}\, \rho_a / \rho_w} \tag{2}$$

where $C = \tau_w / \rho_a u_h^2$, τ_w is the water surface stress exerted by the wind, ρ is the density, and u_h is the wind velocity at height h, while the subscripts a and w refer to air and water, respectively. A drag coefficient of $C = 1.5 \times 10^{-3}$ leads to a value of $\beta = 1.3 \times 10^{-2}$ in reasonable agreement with observed values, and since it is empirically observed that the drag coefficient decreases with fetch, or with duration, the theory is even capable of predicting a slight decrease in β as has indeed been reported.

III. THE SIMILARITY SPECTRUM

The model of Phillips and Longuet-Higgins for the high frequency end of the spectrum appears to neatly solve the difficult problem of describing the water surface spectrum by means of physical concepts, thus closing the gap between the purely mathematical description of the surface and the physics of the generation process. Yet, there are a number of observed phenomena which do not fit into this model. There is, for example, practically no observed spectrum which does not possess "humps", or small oscillations, of the high frequency end of the spectrum about the best fitting - 5 - power law. These humps appear regularly in the neighbourhood of higher harmonics of ω_m and are more pronounced in the laboratory data (for example, Hidy and Plate (1966)) than in field data (for example, Moskovitz et. al. (1962), or Liu (1971)). There is, also, no observational evidence of a water surface on which waves of all wave lenghts or frequencies are breaking simultaneously. In fact, it appears unreasonable to expect that small waves and large waves should be affected by the wind in the same way, because larger waves are always exposed to the wind, while smaller waves either are exposed or sheltered, depending on where they are located with respect to the crests of the large waves.

Add to this the strange phenomenon of the "overshoot". Both in the laboratory and in the field, if for identical wind conditions a plot is made of the spectral density at one particular frequency as a function of fetch it is observed that the spectral density first increases very rapidly with fetch, then reaches a maximum (for that fetch at which the component coincided with the peak of the local spectrum), and with longer fetches decreased and developed into an oscillatory curve. An example of an overshoot plot is shown in figure 2 which is taken from a paper by Barnett and Sutherland (19).

The experimental evidence and the theoretical models can be reconciled through the concept of the similarity spectrum, of which Phillips' law equation 1 is a special case. Similarity spectra are derived on the basis of the idea that by a proper non-dimensionalization of the frequency scale and the spectral density scale all observed spectra can be made to collapse upon a single curve. In the literature, one finds a number of different representations of a similarity spectrum which differ in the functional form of the spectral density distribution, as well as in the parameters by which the measured quantities are non-dimensionalized. Well known is the similarity spectrum of Kitaigorodski (1962), but other forms are perhaps

more useful.

I think that G. Hidy and I were the first (Hidy and Plate (1965)) to suggest a method for avoiding the problem of determining the proper functional form of the scale parameters. To normalize the spectral density we used the fact that the integral over the spectrum had to equal the variance σ^2 of the sea surface, and we used the frequency ω_m to scale the frequency. In this manner, a similarity spectrum of the form :

$$S_s\left(\frac{\omega}{\omega_m}\right) = S(\omega)\ \frac{\omega_m}{\sigma^2} \qquad (3)$$

is obtained, where the non-dimensional spectrum S_s is a universal function of ω/ω_m. We did not specify the functional form of equation 3. But we pointed out that the high frequency end could be represented by the - 5 - power law. Many later writers have adopted the same procedure and represented their spectra in the form of equation 3. Examples are shown in figure 3, in which three different results for the similarity spectrum are given. The solid curve is a "best fit" equation through non-dimensional data obtained on Lake Michigan by Liu (1971). - This curve has a maximum at $\omega/\omega_m = 1$ of 1.5. Superimposed are the curves of Hidy and Plate (1965) and of Mitsuyasu (1969). The curve of Hidy and Plate was derived from laboratory data. It has been corrected here for a scale factor of ten by which the vertical scale had been distorted in the original paper. Thus, the maximum of the peak is found to be at about 5 rather than 0.5 (as has been used, for example, by Plate and Nath (1969)). At a first glance, one may attribute the difference in the shapes of this and Liu's curve to the difference in the conditions at which the data were taken and one may conclude that there exist different spectral forms for laboratory and field. Older analytical spectra for sea waves are found to have dimensionless peaks close to the one given by Liu. Mitsuyasu (1969) has shown that the maximum values obtained from the spectra of Pierson and Maskovitz (1965) and Neumann (1952) are equal to 1.43 and 1.15, respectively.

But there is evidence that there must be a different reason for the difference in the peak values of Hidy and Plate (1965) and Liu (1971). There are the spectra for laboratory and field waves, as presented by Mitsuyasu (1969). For both conditions he finds almost identical spectral shapes, with a maximum dimensionless density at $\omega/\omega_m = 1$ which is equal to 2.74. One may therefore suspect that the difference in the three results may be due to the data analysis

technique employed, and that a similarity spectrum which is the same in field and laboratory is a physical possibility (see also Plate and Nath (1969)). For the discussion in this and the following section, an equilibrium spectrum of universal shape and in the form given by Mitsuyasu is assumed to exist.

The spectral shapes shown in Fig. 3 are averaged in the sense that the "humps" in the experimental spectra have been removed by drawing a smooth curve through them. There is no requirement that a similarity spectrum must be a monotonous function, and the multiple peaks observed in the experimental spectra will, since they occur at multiples of ω_m, occur again in the similarity spectrum. I have shown in a recent paper (Plate (1971)) that the concept of such a similarity spectrum leads naturally to an explanation of the overshoot phenomenon. But the significance of the similarity spectrum goes much further. For if the spectra are similar at all frequencies, then the measurement of the properties at one particular frequency suffices to fully specify the spectrum. This is an important conclusion, for it permits to reconcile the spectrum approach with the older dominant wave approach. If a single wave component suffices to describe the spectrum, why not use the dominant wave for this component ?

This proposition is almost obvious, and yet, there is a very fundamental objection to it. For it is in general not permissible to identify component waves and physical waves. A physical wave is a water surface contour, while the component wave is a Fourier component. Consequently the former arises from a superposition of many of the latter. Fortunately, the sharp peak in the spectrum indicates that component waves of appreciable magnitudes are clustered around ω_m, and as a consequence are only weakly affected by components at higher or lower frequencies. This is of course reflected in the observed wave pattern. Since the dominant waves are waves that belong into a narrow band of components with frequency near ω_m, it follows that the dominant wave, the component wave at ω_m, and the higher maxima of the time series correspond to very nearly the same thing. In particular, one can assume that the highest n out of m waves below some number $n < n_o$ all are dominant waves with frequency ω_m.

Civil Engineers and Oceanographers are accustomed to use the average height of the highest one-third of observed waves as a measure of the wave height of the dominant wave. This usage reflects the observation that these waves remain well defined and do not vary greatly in length or period or progression speed. One therefore can

put n_o equal to 0.333 . m. The water surface maxima are Rayleigh distributed, and thus the water surface variance σ^2 is related to the average height $H^{1/3}$ of the highest one third waves through the relation (Longuet-Higgins (1953)) :

$$\sigma^2 = \frac{1}{16} (H^{1/3})^2 \tag{4}$$

where the wave height is defined in the usual manner as the distance between trough and crest of a wave. Equation 4 is remarkable because it connects the physical concept of a wave with the mathematical description of the surface, and through this with the spectrum.

Equation 4 is not sufficient to define the magnitude of the spectral density at ω_m. We must find an additional condition which puts bounds on the growth of the individual wave. This condition is imposed by the breaking of the dominant wave, much as in the concept on which Phillips model is based. But unlike the breaking of all component waves, the similarity spectrum presupposes a limiting growth pattern imposed on the whole spectrum by the dominant wave. An equilibrium spectrum exists also for the similarity spectrum, but in a different sense than that used by Phillips. The physically unrealistic condition of breaking is no longer imposed on each of the mathematical component waves. But there is no doubt that a limiting form of a spectrum exists. It is well known that at given fetch and with constant wind velocity, there is found (at least in the laboratory), a condition at which the time function representing the water surface elevation becomes truly stationary. Every spectrum that is determined from this time function is a sample from the same ensemble. There is also sufficient evidence to suggest that even in the duration-limited case of water wave generation - that is, in a case where a wind of constant u has started to blow over a water surface which was initially at rest -, there exist only such waves on the water surface which have grown to the maximum possible heights. Only in those instances when the wind had calmed after generating equilibrium waves, or when wind starts blowing over non-equilibrium waves that have entered from another storm area in the form of swell, or when wind blows over waves that are left from a previous storm, there will be spectra that are not of the equilibrium type. These spectra are likely to have a shape that cannot be described by the similarity law. We conclude that the similarity shape is always valid for the maximum possible waves, and thus the spectrum of the water surface at equilibrium contains the maximum spectral densities, i.e. the equilibrium spectrum is the envelope to all possible wave spectra at any one fetch and wind speed.

If the spectrum can be described through the dominant wave, then the breaking of the dominant wave affects the spectrum everywhere and sets the scale of the maximum level that the energy of the water surface can attain. Breaking of the wave occurs when the maximum acceleration a_m of the wave, that is, the acceleration of the crest of the wave, reaches some limiting value determined by the acceleration of gravity g, such that

$$a_m = \alpha . g \tag{5}$$

where α in the case of a breaking Stokes wave is equal to 0.5 (Longuet-Higgins (1969)). Plate et. al. (1969) (see also Plate and Nath (1969)) have shown that the assumption equation 5 leads to a relation for the spectral peak given to :

$$S(\omega_m) = \beta_1 g^2 \omega_m^{-5} \tag{6}$$

with $\beta_1 = \frac{S_s(1)\,\alpha^2}{4}$. We note that there exists a constant value of β_1 if α is a constant. The assumption $\beta \approx \beta_1$ then leads to a value for α . By putting $S_s(1) = 2.74$ (using Mitsuyasu's value as an average) and $\beta = 1.5 \cdot 10^{-2}$ (as given by Mitsuyasu for the field) one obtains $\alpha \approx 0.15$, which is of the same order, but considerably smaller than the upper limit 0.5.

A constant α or β , and a similarity spectrum whose shape does not depend on the size of the dominant wave, has a very important consequence for modeling of the ocean surface in a laboratory tank. As Plate and Nath (1969) have shown, it implies that wind-generated waves can be used in the laboratory to exactly duplicate in shape and reduced magnitude the wave spectra of the ocean surface, provided that the Froude Fr number

$$Fr = \frac{\omega_m \cdot \sigma}{\sqrt{gL}} \tag{7}$$

is the same in model and prototype. The condition equation 7 can be satisfied in the laboratory, and thus it is possible to perform model studies of vibrating non-linear structures subjected to wind waves. Unfortunately, the exact correspondence of the field-and laboratory is not quite assured, as will be discussed in the remainder of the paper.

IV. THE EQUILIBRIUM RANGE CONSTANTS β AND β_1

One reason for a difference in laboratory and field spectra is found in the behaviour of α. We know that α should be less than 0.5, and a numerical value for α was obtained in section 3 from the condition of wave breaking. We note that if β is not constant, then α will also vary. Thus, if we take Mitsuyasu's laboratory data, we find $\beta = 0.08$, about 6 times larger than the field value, and with this an α value of 0.148. $\sqrt{6} = 0.36$ - very close to the maximum theoretical value of 0.5. There exists also the possibility of inferring α from the maximum observed wave slope. Observations of dominant waves from different sources have been reviewed by Deardorff (1967) who finds that the wave slope $H^{1/3}/L$ is approximately constant, at least for smaller ocean waves, and equal to about 0.08. As the wave is approximately sinusoidal with wave number $k_m = 2\pi/L$, where L is the wave length, with frequency ω_m, and with wave height $H^{1/3}$ one can infer a value of $\alpha = 0.25$ from the maximum acceleration α_{max} of the sinusoidal wave on deep water : $\alpha_{max} = \frac{1}{2}$ Hgk. For laboratory waves, the slope can be steeper. Chang et. al. (1971) report a value of $H^{1/5}/L \approx 0.1$, and thus $\alpha \approx 0.30$. For larger ocean waves, the slope appears to decrease further, and consequently the observed α decreases. As a result, we would expect to find a β_1 value which is not quite constant but decreases with increase of wave lenght. This is in agreement with the observations of measured β values. One should realize that β is likely to be smaller than β_1 in the laboratory because the drop-off of the laboratory spectra near the peak of the spectrum is more rapid than the - 5 law of Phillips. In the field, it is the other way round, β is larger than β_1. As the values of β_1 are not reported from field data, we shall use β to approximate β_1, as we have done above.

A close inspection of figure 1a reveals that the - 5 power law does not quite connect the peaks of the spectra. At low frequencies, the experimental spectra have peaks which constantly fall below, while at high frequencies they lie above the average curve. In figure 1b, the spectra have slightly different β and β_1 values. The same observation applies to the high frequency end of the spectrum. Longuet-Higgins (1969) has given a summary of observed β values which were plotted as a function of the fetch parameter gx/u^2 by Mitsuyasu (1969) and Liu (1971), from whose paper figure 4 is taken. In defining the fetch parameter, x is the distance from the point of observation to the nearest upwind shore, or to the storm center, and u is the shear velocity $u = (\tau_w/\rho_a)^{1/2}$. The curve of Liu (1971) through the data may not be a final result, because it is based on da-

ta which might not be applicable. The data at small fetch parameters are all by Mitsuyasu, and do not agree with the data of Hidy and Plate (1966) reproduced in figure 1 and which allow at most the conclusion that $\beta \approx 3 \cdot 10^{-2}$ for small values of the fetch parameter. Also, as Liu states, the value at the largest fetch parameter is a result pertaining to a spectrum not in equilibrium, because the wave pattern has not yet adjusted to the decrease in wind speed which had taken place. While one may debate if the rate of change of β is properly expressed by the curve shown in figure 4, it appears conclusive that β as well as β_1 decrease with increase of fetch parameter, or more exactly with decrease of ω_m. But is it proper to associate this decrease with the decrease of the drag coefficient, as the model of Longuet-Higgins and equation 2 implies? I think that while the conclusion might be correct, - as one cannot disprove at this time, - the model is certainly oversimplified, in more than one respect. To begin with Longuet-Higgins' model neglects the part of the wind energy that is transmitted to the drift current. It would differ by a constant factor if this was a constant percentage of the total, but all indications are that this partition depends on the "wave age" c/u_* where c is the phase-speed of the dominant wave. It is at present not clear, which fraction of the work done by the wind goes into the waves, and which fraction increases the energy of the drift current. Opinions on this differ, from assumptions like those of Longuet-Higgins to those of Manton (1971) according to whose model a maximum of only 52% of the total shear goes directly into wave motion.

A second aspect not considered in the model of Longuet-Higgins is that wave growth changes with fetch. Consequently, some of the energy fed into the waves is convected further downwind rather than being dissipated through the wave breaking, a feature that must be considered in energy balance models. It is the reason for the existence of the fetch graph. In fact, by assuming zero wave breaking and a wave shape which remains one of constant maximum slope at all fetches Deardorff (1967) was able to quite adequately predict the fetch graph, without however being able to provide an explanation on how a wave of this sort can exist. We must therefore point to this effect, although a mathematically and physically accepted model for the wave development with fetch appears at present not to be available.

V. THE DOMINANT WAVE AND THE SPECTRUM

Apart from the properties of the wave acceleration limit α there exists an important difference of laboratory and field data in the shape of the dominant wave itself. It was already mentioned that

the wave spectrum has those significant "humps" at harmonics of the frequency of the dominant wave ω_m. I have pointed out in a previous paper (Plate (1971)) that these humps indicate not so much a general behaviour of the spectrum, but could be the energy densities associated with the higher harmonics of the dominant waves, that is with the fact that the dominant wave is not a true sinusoid.

For an illustration of this point, figure 5 is reproduced. It shows the average shape of the highest 20 out of 100 waves observed on the surface of a laboratory channel by Chang (Chang et. al. (1971)). One notices that this curve is skewed and decidedly non-sinusoidal. The skewness can be attributed to the pressure pattern that must exist for this case. As the streamline pattern shown in figure 5 indicates, the air flow separates from the air crest and reattaches at some distance upslope of the next wave. The result must be a non-symmetric pressure distribution with pressure at the wave backs and suction at the wave fronts. Separation is also responsable for a streamline pattern above the dominant wave which is remarkably unaffected by the waves : all vertical velocities induced by the wave motion are smoothed out because the streamline formed by the wave and the upper limit of the separation bubble is pretty much a straight line. In the laboratory one therefore finds under these conditions that the air flow at some short distance above the water waves resembles that observed in the turbulent boundary layer along a rough surface.

The spectral shape associated with the wave of Chang et. al. can be inferred from the Fourier components of the wave of figure 5. The spectral density must be proportional to the square of the amplitude of the phase-shifted harmonic component at any frequency $n\omega_m$, with n = 1, 2, 3, ..., divided by the bandwidth $\frac{2\pi}{P}$ where P is the period of the wave. These are plotted in figure 6 against n. It is seen that the envelope to the Fourier component energies is remarkably close to a - 5 power law. As spectral analysis is not capable of providing filters that are so sharp as to prevent any side lobe leakage, it is not unlikely that the similarity spectrum is basically the smeared out energy spectrum of the dominant wave, in particular since dominant waves do not move as a periodic wave train but in groups which are phase-shifted with respect to each other. Such a behaviour explains the peaky structure of the spectrum. But it also may explain the difference in the peaks of the similarity spectra of the waves of Mitsuyasu (1969) and Hidy and Plate (1965) which are so evident in figure 3. If the spectrum is essentially that of a pure sinusoid, then the energy density at the peak is the energy of the sinusoid spread over the chosen bandwidth (the resolution bandwidth of spectral analysis). A very narrow resolution bandwidth leads to a very large density

at the peak and rapid drop off of the sinusoid's energy in the neighbourhood of the peak, while a wide resolution bandwidth has the tendency of spreading the wave over a broader part of the spectrum. It follows that very sharply peaked spectra can be compared only if the resolution bandwidth for all spectra is defined as $m \cdot \omega_m$, where ω_m is the frequency of the peak and m is a constant for all spectra. For such an analysis, proportional bandwidth filters are very suitable, which is one reason why a former student of mine, Mr. P. Su (1970) has developed in his MS Thesis a new filtering technique for the analysis of water surface data. It is one of the purposes of this paper to plead to future authors that they should present their wave spectra with all the information on resolution bandwidth, spacing of the data, and methods used for their spectral analysis.

A second important consequency of the dominant wave not being purely sinusoidal is that there exists only one phase velocity for all harmonics of the dominant frequency. Instead of a phase velocity of the component waves given to $c^2 = g/k$, where k is the wave number of the particular component wave, all components travel at the speed of the component at the spectral peak. As in the case of the Stokes wave in finite amplitude wave theory, this speed is larger than that calculated from $c^2 = g/k_m$. To prove that this is indeed so, Su (1970) has determined the phase speed of component waves filtered out of a wave record. He determined the wave records at two wave gages which were placed closely behind one another in a wind wave tank. For both records simultaneously, one particular wave component was filtered out and the cross correlation of the two filtered records was determined. The distance between the wave gages divided by the time lag between the maximum correlation and zero yielded the phase velocity. Figure 7 shows a representative record. The filtering produces very high correlations even at long time lags (according to the uncertainty theorem of Fourier analysis) due to the narrowness of the filter, and the wave nature causes oscillation of the cross correlation function. These features are not important for the present purpose. Important is that the envelope to the cross correlation function shows a maximum at the same time lag for all harmonics of ω_m and Su has shown that this time lag implies a phase speed of all components equal to that observed directly for the dominant wave.

Waves on the sea surface and on laboratory channels may show important differences. This may be inferred from the average wave of Konda et. al. (1971) reproduced in figure 8. This wave also is nonsinusoidal, but in contrast to laboratory waves it appears to be much less skewed. Unfortunately, Konda et. al. do not give a wave

spectrum corresponding to the observed wave. It can therefore not be ruled out that the wave pattern is not of the equilibrium type, and thus the wave could be of less than maximum possible height. But it is not unreasonable to expect that separation, if in this case it occurs at all, does not cause pressure pattern which differs as much at the upstream and downstream faces of the wave as the laboratory case. Some observational evidence for this comes from the fact that Konda et. al. have found a very significant vertical velocity component in the air which was related to the period of the waves. A velocity profile of the vertical velocity above the wave is shown in the figure. The velocity is measured with a probe that was fixed on a tower at a constant distance above an undisturbed water surface.

The spectrum corresponding to the wave in Fig. 8 is also shown in Fig. 6. In this case the spectrum of the average wave drops off faster than the spectrum of the average laboratory wave, and its shape is much more like that of a Stokes wave, whose energy spectrum has also been drawn into Fig. 6. We conclude from this that the dominant wave of the laboratory may differ in form from the dominant wave of the ocean.

How then is it possible that the similarity spectra of the ocean and the laboratory are so much alike? A tentative explanation may be as follows. As we saw, the laboratory wave has, by accident or for a reason which is at present not known, a shape that yields a spectrum whose high frequency end obeys approximately a - 5-power law. The spectral analysis techniques currently practised tend to smear this energy of the waves over a broader spectrum, thus obscuring gaps which might be in the laboratory spectrum. In contrast to the laboratory situation, the ocean waves are less skewed and tend to have lower energies associated with higher harmonics. But the air flow can follow the contours of the large waves and finds only little resistance on them. Therefore, there might be generated on the large waves smaller waves which show the same characteristics as the laboratory waves. These then might "flesh out" the high frequency end of the spectrum, the result being that the spectra in field and laboratory become similar in shape.

VII. CONCLUSIONS

I have shown in this paper that the model of Phillips and Longuet-Higgins of a water surface covered by waves of all possible frequencies above some lower cut-off value which are in the state of breaking, and for which the work done on the waves by the wind is equal to the energy dissipated by breaking, does not agree with the

reality of the physical situation. Instead, the spectra of the water surface might be determined fully or at least to a large extend by the dominant wave. Further progress in understanding ocean waves must then be expected to come from a study of the energy balance of the dominant waves. In pursuit of this model one can relate the equilibrium range "constant" β to the accerelation and thus to the slope of the dominant wave, and one can explain the spectrum as essentially that of the dominant wave alone which has been distorted and shaped into a continuous spectrum by the randomness of the generation process and by the analysis methods by which the spectra have been determined. Of the essential correctness of this model I am so convinced that I recommend to future workers on ocean waves to direct their attention to the characteristics of the dominant waves and to develop statistical techniques, such as the ones used by Chang et. al. (1971) or Konda et. al. (1971) to isolate the dominant wave and the associated wind pattern from the records of measured ocean surface waves, and to analyse their behaviour as function of space, time, and wind field.

The results of such studies will find important applications in modeling forces on structures, which are caused by wind-generated water surface waves. Most of the conclusions concerning modeling the similarity spectrum as arrived at by Plate and Nath (1969) apply equally well to the modeling of dominant waves, with the important distinction that now the frequency of the dominant wave must be matched with the structural eigenfrequencies.

* * *

LITERATURE

1 T. P. Barnett and A. J. Sutherland 1968 " A note on an overshoot effect in wind-generated waves" J. Geophys. Res. Vol. 73, p. 6879

2 T. Brooke Benjamin and J. E. Feir 1967 "The disintegration of wave trains on deep water. Part I" JFM (1967) Vol. 27, Part 3, pp. 417-430

3 P. C. Chang, E. J. Plate and G. M. Hidy 1971 "Turbulent air flow over the dominant component of wind-generated water waves" J. Fluid Mech. Vol. 47, pp. 183-208

4 J. Deardorff 1967 "Aerodynamic theory of wave growth with constant wave steepness" Journal Ocean. Society, Japan, Vol. 23, pp. 278-297

5 G. D. Hess, G. M. Hidy and E. J. Plate 1969 "Comparison between wind waves at sea and in the laboratory" J. Marine Res., Vol. 27, p. 216

6 G. M. Hidy and E. J. Plate 1965 "Frequency spectrum of wind-generated waves" Phys. of Fluids, Vol. 8, p. 1387

7 G. M. Hidy and E. J. Plate 1966 "Wind action on water standing in a laboratory channel" J. Fluid Mech., Vol. 26 pp 651-687

8 S. A. Kitaigorodskij 1961 "Applications of the theory of similarity to the analysis of wind-generated wave motion as a stochastic process" Izv. Geophys. Ser., Acad. Sci. USSR Vol. 1, p. 105

9 J. Konda, Y. Fujinawa and G. Naito 1972 "Wave induced wind fluctuation over the sea" J. Fluid Mech., Vol. 51, pp. 751-771

10 P. C. Liu 1971 "Normalized and equilibrium spectra of wind waves in Lake Michigan" J. Physical Oceanography, Vol. 1, pp. 249-257

11 M. S. Longuet-Higgins 1952 "On the statistical distribution of the heights of sea waves" Journal of Marine Research Vol. 11, p. 245

12 M.S. Longuet-Higgins 1963 "The generation of capillary waves by steep gravity waves" Journal of Fluid Mechanics Vol. 16, pp. 138-159

13 M.S. Longuet-Higgins 1969 "On the wave breaking and the equilibrium spectrum of wind-generated waves" Proceedings, Royal Society of London, Series A., Vol. 310, pp. 151-159

14 M.J. Manton 1971 "Wave generation on the air-sea interface" Boundary Layer Meteorology, Vol. 1, pp. 152-159

15 H. Mitsuyasu 1969 "On the growth of the spectrum of wind-generated waves, II" Reports of Research Institute for Applied Mechanics Kyushu University, Fukuoka, Japan Vol. XVII, pp. 235-248

16 H. Mitsuyasu 1968 "On the growth of the spectrum of wind-generated waves, I" Report of Research Institute for Applied Mechanics, Kyushu University, Fukuoka, Japan Vol. XVI, pp. 459-482

17 L. Moskowitz, W.J. Pierson and E. Mehr 1962 "Wave spectra estimated from wave records obtained by the OWS Weather Explorer and the OWS Weather Reporter (I) " Tech. Rept. for the U.S. Naval Oceanographic Office, New York University, College of Engineering, Research Division

18 J.H. Nath and D.R.F. Harleman 1967 "The dynamics of fixed towers in deep water random waves" Presented at the "Civil Engineering in the Oceans" Conference ASCE held at San Francisco, California, p. 99

19 E.J. Plate, G.M. Hidy and P.C. Chang 1969 "Experiments on the generation of small water surface waves by wind" J. Fluid Mech. Vol. 35, pp 625-656

20 E.J. Plate and J.H. Nath 1969 "Modeling of structures subjected to wind waves" Proc. ASCE, Vol. 95, J. Waterways and Harbor Div., pp. 491-511

21 E.J. Plate 1971 "Limitations of spectral analysis in the study of wind-generated water surface waves" International

Symposium on Stochastic Hydraulics, Proceeding, pp. 522-539

22 K.S. Su 1969 "Design of digital band pass filter and its application to random water wave data" unpublished MS Thesis, Dept. of Civil Engineering, Colorado State University, Ft. Collins, Colo.

23 R.L. Wiegel 1970 "Ocean Dynamics" Chapter III in "Hydronautics", H.E. Sheets and W.T. Boatwright jr., editors, Academic Press, pp. 123-228

* * *

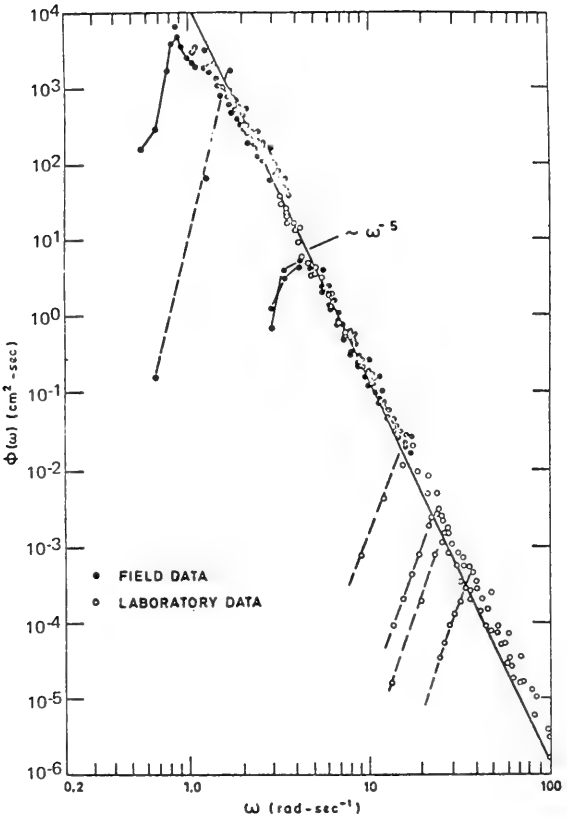

Figure 1a Windwave spectra. Data collection of Hess et. al. (1969)

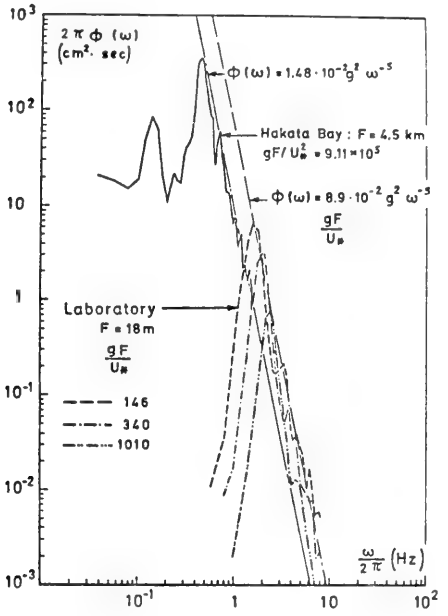

Figure 1b Wind wave spectra. Data of Mitsuyasu (1969)

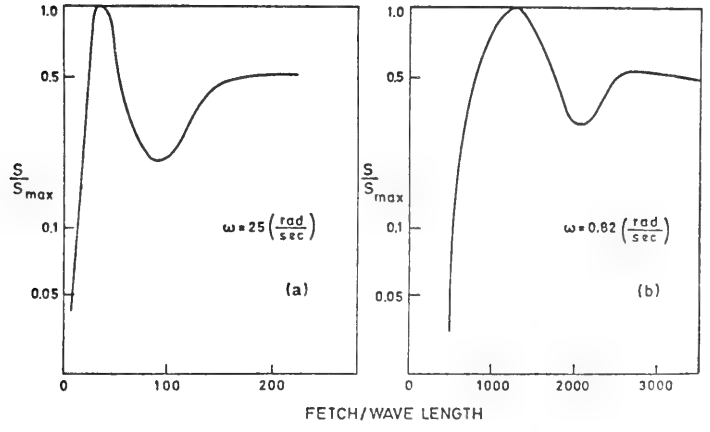

Figure 2 Measured overshoot curves (a) Laboratory, 25 rad/sec component, (b) Ocean 0.82 rad/sec component. (from Barnett and Sutherland, 1968)

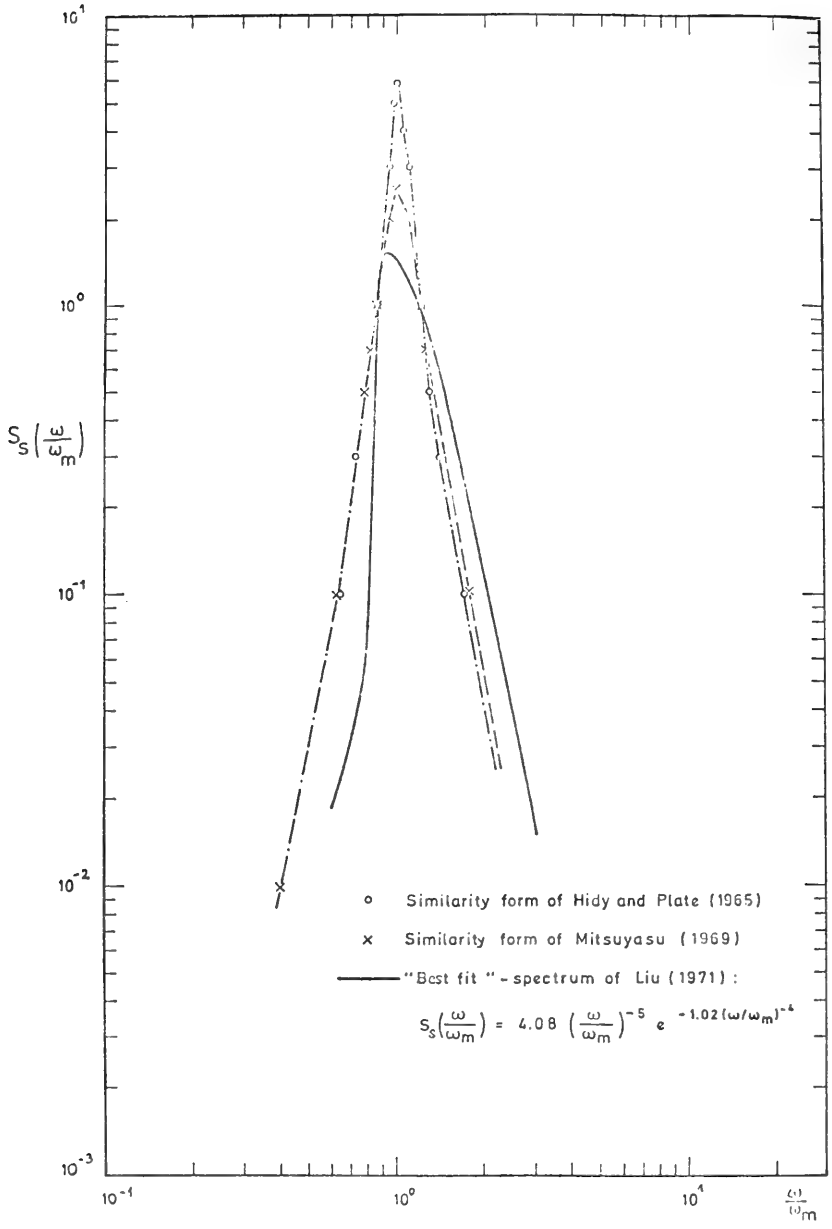

Figure 3 Similarity spectra from different sources.

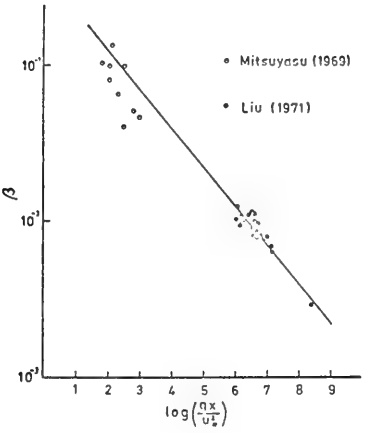

Figure 4 The equilibrium range constant β vs the dimentionless fetch parameter gF/u_*^2 . Data points from Mitsuyasu (1969) and Liu (1971)

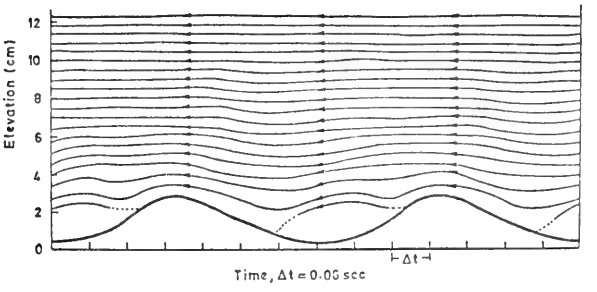

Figure 5 Streamline pattern and wind-generated waves. Laboratory data from Chang et. al. (1971)

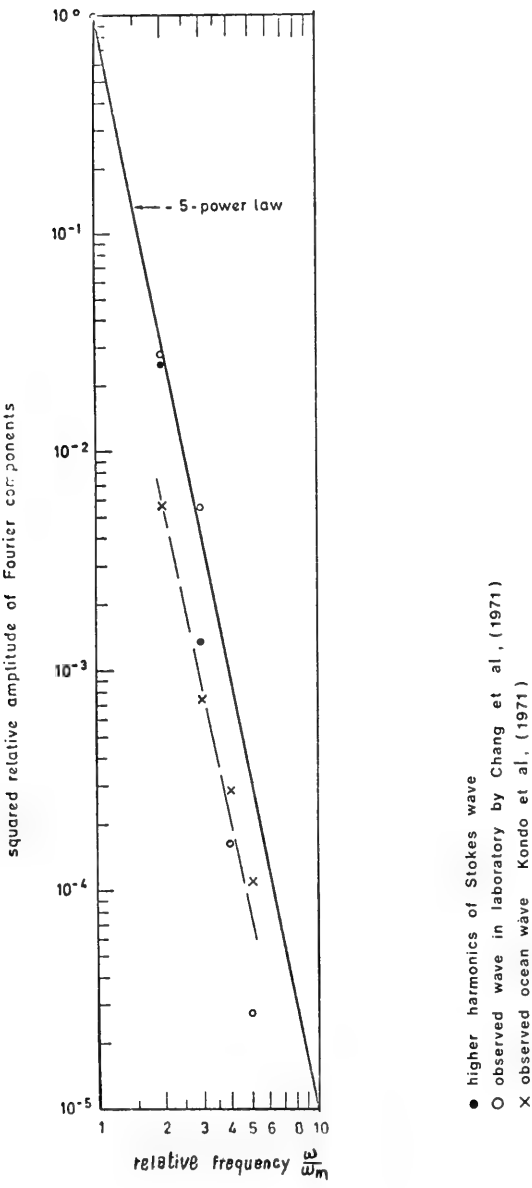

Figure 6 Energy line spectra of real waves

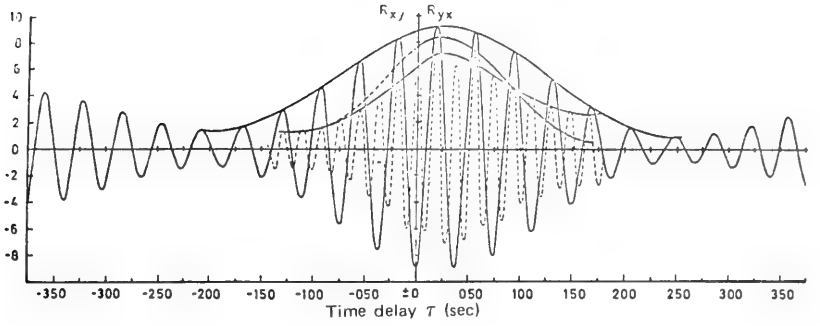

Figure 7 Filtered cross correlation for laboratory waves obtained from wave -gages placed 31.5 cm apart along the wind direction at a fetch of 9 m. From Su (1969)

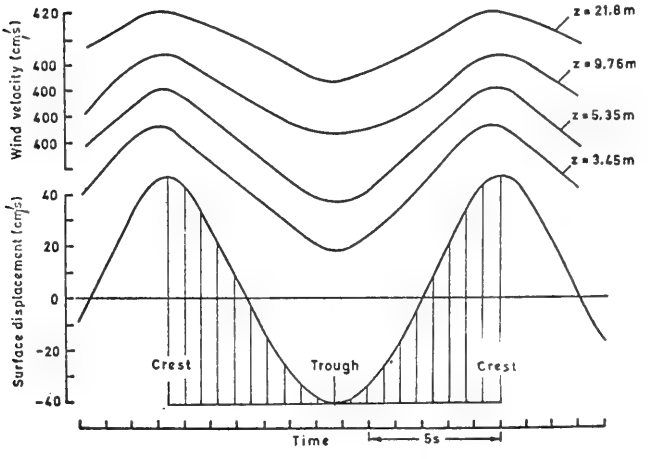

Figure 8 Average wave and horizontal wind component associated with it. Data by Kondo et. al. (1971)

DISCUSSION

M. Huther
Bureau Veritas
Paris, France

I first thank the author for the interesting paper he presents today.

In the calculation of springing of ships a good knowledge of the energies in the range of high frequencies (i.e. $\omega \simeq 1.50$ rad-s^{-1}) is necessary, so I shall be pleased to know the opinion of the author on the better sea state representation to be used in this case.

DISCUSSION

R. Tournan
Bureau Veritas
Paris, France

As described at a conference at the "ATMA 1972" "Sollicitations externes et internes des navires à la mer" (J.M. Planeix, M. Huther et R. Dubois), and in a paper in the International Shipbuilding Progress of August 1972. "Wave Loads - a correlation between calculations and measurements at sea" (J.M. Planeix Ph. D.), Bureau Veritas using classical spectral sea state representation has found a good correlation between calculated and measured ship behaviour.

So I ask to the author if such calculation and comparison had been done with dominant wave sea state representation?

REPLY TO DISCUSSION

E. J. Plate
University of Karlsruhe
Karlsruhe, Germany

I think the two questions amounted to about the same thing. I shall try to answer them indirectly by giving my opinion on how best to represent the sea state in a mathematical or laboratory model.

I must speak as a coastal engineer because we are usually concerned with structures that have very few degrees of freedom. In coastal engineering we can usually identify only one or at best a small number of degrees of freedom and of corresponding natural frequencies or eigen-frequencies of our structures. Therefore I would recommend that if one does laboratory studies of the vibrations of a structure one should always set the wave conditions for the laboratory in such a way that the most critical eigen-frequency of the structure corresponds to the peak in the spectrum of the wave, if this is at all possible. Of course, if this natural frequency is of the order of 25 Hz, it is pointless to try to get 25 Hz waves. But if it is, for example, of the order of 0.1 Hz, may be the most important design case arises when the frequencies of the dominant wave and the natural frequency of the structure match. This is somewhat different from present usage among coastal engineers.

I should like also to say a word against the necessity for using so-called random waves for modelling the sea state in a laboratory. You have probably all heard that it is becoming more and more fashionable to use a random wave generator instead of the older sinusoidal wave generator to model the forces on structure. In my opinion this is an ill-considered move for the simple reason that the random wave components you are generating are component waves - that is, each one of these waves is travelling at its own celerity. Therefore, these waves show interference pattern - that is, the small waves modulate the big waves, and vice versa, and you get a breaking of waves owing

to random modulation; you do not get a breaking of waves owing to the fact that they are real waves. Also, you do not find waves which are skewed like the ones I showed in my paper. And I think that you arrive at wrong conclusions, or no better conclusions, from this kind of study than those which you would get by just using a sequence of experiments with sinusoidal waves of increasing frequency and drew your response diagram in the usual manner, because you are basically trying to solve a non-linear wave surface problem by a linear superposition method. If you allow yourself to make this approximation, why not go all the way and just use sinusoidal generators, which would cost you a lot less money?

* * *

INTERNAL WAVES IN CHANNELS OF VARIABLE DEPTH

Chia-Shun Yih
University of Michigan
Ann Arbor, Michigan, U.S.A.

ABSTRACT

Internal waves in prismatic channels of variable depth propagating along the channel axis are studied. It has been shown that for whatever stratification of the fluid the frequency of the wave motion increases whereas the wave velocity decreases as the wave number increases. A general method of solution for an arbitrary channel is then presented in detail, which gives the wave velocity and the fluid motion for a given wave number and a given mode by successive approximations. Finally long waves are studied in some detail, a few specific examples of long waves are given, and the connection of the present theory with the classical shallow-water theory is shown.

I. INTRODUCTION

Known solutions of gravity waves in a prismatic channel of variable depth which have a degree of general applicability are of three categories. For very long waves (first category) the shallow-water theory (Lamb 1932, p. 273-274) gives $(gh)^{1/2}$ as the wave velocity, where g is the gravitational acceleration and h the average depth. For very short waves (second category) not confined to the edge region the variability of the depth is unimportant, since the motion is confined to the region near the free surface. The third category is the category of edge waves, which for short waves have an appreciable amplitude only near the shores (or the edges), and are therefore always affected by the geometry, specifically the slopes of the channel near the shore lines, however short the waves compared to

the maximum or average depth. The solution for edge waves (Stokes 1839, or Lamb 1932, p. 447) is exact if the region occupied by the water is semi-infinite, bounded only by the free surface and a plane of constant slope serving as the only solid boundary. If the channel is finite in both depth and width, Stokes' solution is nevertheless valid for each shore if the wave length (in the longitudinal direction) is very short, since the variability of the depth has then an important effect only near the shore lines.

Aside from these three categories, and interrelating them, are the exact solutions for water waves in a symmetrically placed triangular channel of vertex angle $\pi/2$ (Kelland 1839, or Lamb 1932, p. 447-449) or of vertex angle $2\pi/3$ (MacDonald 1894, or Lamb 1932, p. 449-450). These exact solutions are useful because they provide a check for any approximate theory.

In this paper internal waves in channels of variable depth are studied. The differential system governing the flow of a system of superposed layers of homogeneous fluids is formulated by first considering a single layer. Then for the layered system it is proved by the use of comparison theorems that the frequency σ of the waves increases but the wave velocity c decreases as the wave number k increases. Then the differential system governing the flow of a continuously stratified fluid is derived, and the increase of σ and decrease of c as k increases are again proved in general.

After giving a few solutions in closed form (under the restriction of the Boussinesq approximation), a general method of solution for wave motion in stratified fluids is given. In the form given the method is for application to continuously stratified fluids, but it can be adopted to deal with homogeneous fluids, and the manner of adoption is briefly indicated in the last paragraph of Section 7.

Finally we study long waves in some detail, and both continuously stratified fluids and layered systems are considered. A few examples are given, and the connection of the theory to the classical shallow-water theory for long waves in a single fluid is shown.

II. THE DIFFERENTIAL SYSTEM FOR THE CASE OF CONSTANT DENSITY

If viscous effects are neglected and the motion is supposed to have started from rest, and if the density of water is constant, the motion is irrotational and a velocity potential ϕ exists, the gradient of which is the velocity vector. We shall use the Cartesian coordinates (x, y, z), with z measured longitudinally, y measured vertically,

and x measured across the channel. If the velocity components in the directions of increasing x, y and z are denoted by u, v and w, respectively, we have

$$u = \frac{\partial \phi}{\partial x}, \quad v = \frac{\partial \phi}{\partial y}, \quad w = \frac{\partial \phi}{\partial z}. \tag{1}$$

The equation of continuity then becomes

$$\left(\frac{\partial^2}{\partial x^2} + \frac{\partial^2}{\partial y^2} + \frac{\partial^2}{\partial z^2} \right) \phi = 0, \tag{2}$$

which is the equation to be solved.

At solid boundaries the normal velocity component vanishes, so that

$$\frac{\partial \phi}{\partial n} = 0, \tag{3}$$

where n is measured in a direction normal to the solid boundaries. At the free surface the pressure is constant, so that, with the square of the velocity neglected and with η denoting the displacement of the water surface from its equilibrium position, the Bernoulli equation is

$$\frac{\partial \phi}{\partial t} + g\eta = \text{constant}, \tag{4}$$

in which t is the time. Since

$$v = \frac{\partial \eta}{\partial t},$$

(4) can be written as

$$\frac{\partial^2 \phi}{\partial t^2} + g \frac{\partial \phi}{\partial y} = 0 , \tag{5}$$

which is the free-surface condition.

We shall assume

$$\phi = f(x, y) \exp i(kz - \sigma t) , \tag{6}$$

in which k is the wave number and $\sigma / 2\pi$ is the frequency. Then (2) becomes

$$f_{xx} + f_{yy} - k^2 f = 0 , \tag{7}$$

(3) becomes

$$\frac{\partial f}{\partial n} = 0 , \tag{8}$$

and (5) becomes

$$\sigma^2 f = g f_y \quad \text{at the free surface} , \tag{9}$$

with subscripts indicating partial differentiation. Equations (7), (8), and (9) constitute an eigenvalue problem, of which, k^2 being given, σ^2 is the eigenvalue to be found.

III. THE DIFFERENTIAL SYSTEM FOR SUPERPOSED LAYERS

If the fluid system consists of superposed layers, each of which is homogeneous, the differential equation for each layer is still (2), the boundary condition (3) still holds. The interfacial condition at each surface of discontinuity can be derived in a way similar to the way in which (5) is derived. The result is

$$\frac{\partial^2}{\partial t^2}\left[(\rho\phi)_\ell - (\rho\phi)_u\right] + g(\rho_\ell - \rho_u)\,\phi_y = 0\,, \qquad (10)$$

in which the subscript ℓ indicates the lower fluid and the subscript u the upper fluid and $(\phi_y)_\ell = (\phi_y)_u = \phi_y$. If there is a free surface, $\rho_u = 0$ there, and (10) reduces to (5). With the form of ϕ (for any layer) given by (6), we can write (10) as

$$\sigma^2\left[(\rho f)_\ell - (\rho f)_u\right] = g(\rho_\ell - \rho_u)\,f_y\,, \qquad (11)$$

The differential system consists of (7) for each layer, (8), and (11) for each interface.

IV. VARIATION OF σ^2 OR c^2 WITH k^2 FOR CONSTANT OR STEPWISE DENSITY

We can show that σ^2 increases and c^2 decreases as k^2 increases, in a very general manner, whether or not the fluid is stratified. Consider first the case ρ = constant, and let k^2 have two values, k_1^2 and k_2^2. The corresponding eigenvalues will be denoted by σ_1^2 and σ_2^2, and the corresponding eigenfunctions by f_1 and f_2. Then

$$\nabla^2 f_1 - k_1^2 f_1 = 0\,, \qquad \nabla^2 = \frac{\partial^2}{\partial x^2} + \frac{\partial^2}{\partial y^2}\,, \qquad (12)$$

$$\nabla f_2 - k_2^2 f_2 = 0\,, \qquad (13)$$

and the free surface conditions are

$$\sigma_1^2 f_1 = g\,\frac{\partial f_1}{\partial y} \qquad (14)$$

$$\sigma_2^2 f_2 = g \frac{\partial f_2}{\partial y} \tag{15}$$

Multiplying (12) by f_2 and (13) by f_1, integrating over the domain occupied by water, utilizing (8), (14), and (15) whenever necessary, and applying the well-known Green Theorem, we obtain

$$\frac{\sigma_1^2}{g} J_m = I_{m1} + k_1^2 I_{m0} , \tag{16}$$

$$\frac{\sigma_2^2}{g} J_m = I_{m1} + k_2^2 I_{m0} , \tag{17}$$

with

$$\left.\begin{aligned} I_{m0} &= \iint f_1 f_2 \, dA , \quad I_{m1} = \iint (f_{1x} f_{2x} + f_{1y} f_{2y}) \, dA , \\ J_m &= \int_a^{a+b} f_1 f_2 \, dx , \end{aligned}\right\} \tag{18}$$

where a and $a + b$ are the values of x at the shore lines, so that b is the width of the free surface. The difference of (17) and (16) is

$$\frac{1}{g}(\sigma_2^2 - \sigma_1^2) J_m = (k_2^2 - k_1^2) I_{m0} , \tag{19}$$

so that in the limit (as k_1 approaches k_2)

$$\frac{d\sigma}{dk}^2 = \frac{gI_0}{J} > 0 , \tag{20}$$

where

$$I_0 = \iint f^2 \, dA , \quad J = \int_a^{a+b} f^2 dx . \tag{21}$$

One consequence of (20) is that the group velocity c_g is always of the same sign as the wave velocity c, since

$$c = \frac{\sigma}{k} , \quad c_g = \frac{d\sigma}{dk} , \tag{22}$$

so that

$$cc_g = \frac{d\sigma}{dk}^2 > 0 . \tag{23}$$

Now we wish to see how c^2 varies with k^2. Rewriting (19) as

$$\frac{1}{g} k_1^2 (c_2^2 - c_1^2) J_m = (k_2^2 - k_1^2) (I_{m0} - \frac{c_2}{g}^2 J_m) , \tag{24}$$

and going to the limit, we have

$$\frac{1}{g} k^2 \frac{dc}{dk}^2 J = I_0 - \frac{c^2}{g} J . \tag{25}$$

But from (16), on making $k_2 = k_1$, we have

$$\frac{c^2}{g} J = I_0 + k^{-2} I_1 ,$$

so that the right-hand side of (25) is negative, and we have

$$\frac{dc^2}{dk^2} < 0 . \tag{26}$$

Since

$$c_g = c + k\frac{dc}{dk} ,$$

from (23) and (26) we have

$$0 < cc_g < c^2 , \tag{27}$$

which means that the magnitude of c_g is always less than the magnitude of c, whether or not c is positive.

For superposed layers, each of which is homogeneous within itself, (23) and (26) are obtained in much the same way. All we need to do is to apply the same procedure to each of the layers, and then apply the interfacial condition (11) at each interface.

IV. THE DIFFERENTIAL SYSTEM FOR A CONTINUOUSLY STRATIFIED FLUID

If the fluid is continuously stratified, we shall denote the density of the fluid when it is undisturbed by ρ_0, which is a function of y alone. The density perturbation will be denoted by ρ, so that the total density is $\rho_0 + \rho$. The mean pressure p_0 is related to ρ_0 by the hydrostatic equation

$$\frac{dp_0}{dy} = - g\rho_0 \ . \tag{28}$$

Then the linearized equations of motion are

$$\rho_0 \frac{\partial}{\partial t}(u, v, w) = - \left(\frac{\partial}{\partial x}, \frac{\partial}{\partial y}, \frac{\partial}{\partial z} \right) p + (0, - g\rho, 0) \ , \tag{29}$$

where p is the pressure perturbation. The linearized equation of incompressibility is

$$\frac{\partial \rho}{\partial t} + v\rho_0' = 0 \ , \tag{30}$$

with the accent indicating differentiation with respect to y. The equation of continuity is

$$\frac{\partial u}{\partial x} + \frac{\partial v}{\partial y} + \frac{\partial w}{\partial z} = 0 \ . \tag{31}$$

Cross differentiation of the first and third equation in (29) gives

$$\frac{\partial}{\partial t} \left(\frac{\partial (\rho_0 u)}{\partial z} - \frac{\partial (\rho_0 w)}{\partial x} \right) = 0 \ . \tag{32}$$

Since dependent variables will all be assumed to have the time factor $e^{-i\sigma t}$, (32) gives

$$\frac{\partial (\rho_0 u)}{\partial z} - \frac{\partial (\rho_0 w)}{\partial x} = 0 \ , \tag{33}$$

from which we have

$$\rho_0 u = \frac{\partial \phi}{\partial x} , \quad \rho_0 w = \frac{\partial \phi}{\partial z} , \tag{34}$$

ϕ being a velocity potential for u and w.

Let F be a function of x, y, z and t defined by

$$F = \frac{\partial}{\partial t}(\rho_0 v) + g\rho \quad . \tag{35}$$

Then the second equation in (29) can be written as

$$F = - \frac{\partial p}{\partial y} \quad . \tag{36}$$

In view of (34) and the third equation in (29), differentiation of (36) gives

$$\frac{\partial F}{\partial z} = \phi_{tyz} \quad . \tag{37}$$

Assuming for all dependent variables the factor $\exp i(kz - \sigma t)$, we can write (37) as

$$F = \phi_{ty} \quad . \tag{38}$$

The subscripts in (37) and (38) indicate partial differentiation. Recalling that the first and third equations in (29) are

$$\phi_{tx} = - p_x , \quad \phi_{tz} = - p_z ,$$

and combining (36) and (38) into

With v given by (43), (40) becomes (remembering the factor exp i(kz - σt))

$$\frac{\partial^2 \phi}{\partial x^2} - k^2 \phi + \sigma^2 \rho_0 \frac{\partial}{\partial y}\left(\frac{\phi_y}{\sigma^2 \rho_0 + g\rho_0'}\right) = 0 . \tag{44}$$

The boundary condition at the solid boundary is

$$n_1 u + n_2 v = 0 , \tag{45}$$

where u and v are given by (34) and (43), and n_1, n_2 and n_3 (=0) are the direction cosines of the normal to the solid boundary. The Bernoulli equation is still valid in the free surface (if there is one). In fact, the Bernoulli equation obtained by integrating (29) is simply (39). But we must recall that p is the pressure perturbation only. If we require the total pressure $p + p_0$ to be zero on the free surface, and use (28), we have (with the new definition for ϕ)

$$\frac{1}{\rho_0} \frac{\partial \phi}{\partial t} + g\eta = \text{constant (at the free surface)} , \tag{46}$$

which gives, upon idfferentiation with respect to t,

$$\phi = \frac{g \rho_0 \phi_y}{\sigma^2 \rho_0 + g \rho_0'} . \tag{47}$$

V. VARIATION OF σ^2 AND c^2 WITH k^2

For the purpose of establishing the comparison theorems, we shall write (44) as

$$\frac{I}{\rho_0}\frac{\partial^2\phi}{\partial x^2} - \frac{k^2}{\rho_0}\phi + \sigma^2\frac{\partial}{\partial y}\left(\frac{\phi_y}{\sigma^2\rho_0 + g\rho_0'}\right) = 0 , \qquad (48)$$

and we recognize that this is really the same as the equation of continuity (31). We also recognize that (47) can be written in the much simpler form

$$\frac{\sigma^2\phi}{\rho_0} = gv . \qquad (47a)$$

We now consider two wave numbers k_1^2 and k_2^2, with the corresponding eigenvalues σ_1^2 and σ_2^2, and the corresponding eigenfunctions ϕ_1 and ϕ_2. The velocity components (u_1, v_1, w_1) and (u_2, v_2, w_2) satisfy

$$\frac{\partial u_1}{\partial x} + \frac{\partial v_1}{\partial y} + \frac{\partial w_1}{\partial z} = 0 , \qquad (49)$$

$$\frac{\partial u_2}{\partial x} + \frac{\partial v_2}{\partial y} + \frac{\partial w_2}{\partial z} = 0 . \qquad (50)$$

Multiplying (49) by ϕ_2 and integrating over the fluid domain, and utilizing the Green's Theorem and the boundary conditions (45) and (47a) for $\sigma = \sigma_1$, $\phi = \phi_1$, $v = v_1$, we have

$$I_{1m} + k_1^2 I_{0m} + \sigma_1^2 (J_{1m} - H_m) = 0 , \qquad (51)$$

in which

$$I_{1m} = \iint \frac{1}{\rho_0}\phi_{1x}\phi_{2x}\,dA , \qquad I_{0m} = \iint \frac{1}{\rho_0}\phi_1\phi_2\,dA ,$$

$$J_{1m} = \iint \frac{\phi_{1y}\,\phi_{2y}}{\sigma_1^2\,\rho_0 + g\rho_0'}\,dA\ , \qquad H_m = \int_a^{a+b} \frac{1}{g\rho_0}\,\phi_1\,\phi_2\,dx\ ,$$

where a and a + b are the abscissae of the shore lines. Similarly, on multiplying (50) and integrating, we have

$$I_{1m} + k_2^2 I_{0m} + \sigma_2^2 (J_{2m} - H_m) = 0\ , \tag{52}$$

where

$$J_{2m} = \iint \frac{\phi_{1y}\,\phi_{2y}}{\sigma_2^2\,\rho_0 + g\rho_0'}\,dA\ . \tag{53}$$

The difference between (52) and (51) is

$$(k_2^2 - k_1^2)\, I_{0m} = (\sigma_2^2 - \sigma_1^2)\,(H_m + K_m)\ , \tag{54}$$

where

$$K_m = -\iint \frac{g\rho_0'\ \phi_{1y}\ \phi_{2y}}{(\sigma_2^2\,\rho_0 + g\rho_0')(\sigma_1^2\,\rho_0 + g\rho_0')}\,dA\ . \tag{55}$$

From (54) we have

$$\frac{d\sigma^2}{dk^2} = \frac{I_0}{H+K}\ , \tag{56}$$

where I_0, H and K are respectively the value of I_{0m}, H_m and K_m when $K_1 = K_2$ and are obviously positive. Hence

$$\frac{d\sigma^2}{dk^2} > 0 \quad . \tag{57}$$

We can write (54) as

$$(k_2^2 - k_1^2)\left[I_{0m} - c_1^2(H_m + K_m) \right] = k_2^2(c_2^2 - c_1^2)(H_m + K_m) \quad ,$$

which gives

$$\frac{dc^2}{dk^2} = \frac{I_0 - c^2(H + K)}{k^2 (H + K)} \quad . \tag{58}$$

It is a simple matter to show that

$$J + K > 0 \quad ,$$

where J is the value of J_{1m} (or J_{2m}) when $k_1 = k_2$ and $\sigma_1 = \sigma_2$. From (51), on making $k_1 = k_2$, we have

$$I_0 + c^2 (J - H) < 0 \quad .$$

Hence

$$I_0 - c^2 H - c^2 K = (I_0 - c^2 H + c^2 J) - c^2 (J+K) < 0 \quad ,$$

and (58) gives

$$\frac{dc^2}{dk^2} < 0 \quad , \tag{59}$$

As before (57) and (59) imply, respectively,

$$cc_g > 0 \qquad \text{and} \qquad 0 < cc_g < c^2 \quad . \tag{60}$$

VI. SOME SOLUTIONS FOR ARBITRARY WAVE NUMBERS

If the density stratification is exponential, and if the inertial effect of density variation is neglected (i. e., if the Boussinesq approximation is used), it is possible to obtain solutions in closed form for waves in a symmetric triangular channel, whatever the wave number may be, provided there is a free surface.

Let

$$\rho_0 = \rho_0(0)\, e^{-\beta y} \quad , \tag{61}$$

where y is measured from the vertex of the triangular channel, and let the sides of the channel be given by

$$y = \pm mx \quad . \tag{62}$$

With ρ_0 given by (61), (44) becomes

$$\phi_{xx} + \lambda^2 (\phi_{yy} + \beta\phi_y) - k^2\phi = 0 \quad , \tag{63}$$

in which

$$\lambda^2 = \frac{\sigma^2}{\sigma^2 - \beta g} \tag{64}$$

If the inertial effect of density variation is neglected, (63) becomes

$$\phi_{xx} + \lambda^2 \phi_{yy} - k^2 \phi = 0 \ . \tag{65}$$

The boundary conditions at the sides are, in accordance with (45) and (62) and with u and v given by (34) and (43) ,

$$\phi_x \mp \frac{\lambda^2}{m} \phi_y = 0 \tag{66}$$

for the two sides given by (45), respectively.

The solutions for symmetric modes have the form

$$\phi = A \cosh \alpha x \cosh \gamma y \cos k(z - \hat{c}t + \epsilon) \ , \tag{67}$$

provided

$$\alpha^2 + \lambda^2 \gamma^2 = k^2 \ . \tag{68}$$

The ϵ in (67) is an arbitrary constant. Since the channel is symmetric and (67) is symmetric with respect to x , it is necessary to consider only the boundary.

$$y = mx \tag{62a}$$

where

$$\phi_x = \frac{\lambda^2}{m} \phi_y \ . \tag{66a}$$

Substituting (67) into (66a) and using (62a), we obtain

$$\frac{\alpha m}{\gamma \lambda^2} \tanh \alpha x \coth \gamma m x = 1$$

which demands

$$\alpha = \gamma m \quad . \quad \frac{\alpha m}{\gamma \lambda^2} = 1 \quad . \tag{69}$$

Thus

$$\lambda^2 = m^2 \quad . \tag{70}$$

Since m is real, λ^2 must be positive. Equations (68), (69) and (70) give

$$2m^2 \gamma^2 = k^2$$

so that

$$\gamma = \frac{k}{\sqrt{2m}} \qquad \text{and} \qquad \alpha = \frac{k}{\sqrt{2}} \tag{71}$$

The dispersion relation is given by the free-surface condition (47), which in this case can be written as

$$\sigma^2 \phi = g \lambda^2 \phi_y \quad . \tag{72}$$

Substitution of (67) and (70) into (72) gives

$$\sigma^2 = \frac{gkm}{\sqrt{2}} \tanh \frac{kd}{\sqrt{2m}} \quad , \tag{73}$$

where d is the maximum depth. Given β and m, σ^2 is known, and (73) gives k. We can also write (73) as

$$\sigma^2 = \frac{gk\lambda}{\sqrt{2}} \tanh \frac{kd}{\sqrt{2\lambda}} \quad . \tag{74}$$

With λ^2 given by (64), given β and k we can find σ from (74). Then λ^2 is known and hence m^2 is known.

Evidently there is also an antisymmetric mode, given by

$$\phi = A \sinh \alpha x \sinh \gamma y \cos k(z-ct+\epsilon) \quad .$$

Then (69), (70), and (71) still stand but the dispersion formula is now

$$\sigma^2 = \frac{gkm}{\sqrt{2}} \coth \frac{kd}{\sqrt{2m}} \quad , \tag{75}$$

or

$$\sigma^2 = \frac{gk\lambda}{\sqrt{2}} \coth \frac{kd}{\sqrt{2\lambda}} \tag{76}$$

It can be easily shown from (65) that if there is no free surface λ^2 must be negative. The solutions given above all correspond to positive λ^2. Hence the presence of the free surface is essential for the existence of these solutions. The waves these solutions represent are therefore largely free-surface waves rather than internal waves, and the density stratification has only a minor effect - that of affecting the value of the slope m. For this reason these solutions are not very interesting. We note that if $\beta = 0$ we have $m^2 = 1$, and (73) becomes

$$\sigma^2 = \frac{gk}{\sqrt{2}} \tanh \frac{kd}{\sqrt{2}} , \qquad (77)$$

which is just the solution of Kelland (1839).

We shall now proceed to study truly internal waves.

VII. A GENERAL METHOD OF SOLUTION

Given a density stratification ρ_0 and a channel cross section, our task is to find the relation between σ^2 and k^2 determined by (44) and (45), supplemented by (47) if there is a free surface. Since σ^2 appears in the denominator of the third term in (44) and as a multiplier of that term, (44) is inconvenient to use as it stands. We shall transform it into an equation in v. Differentiating (44) with respect to y, and using (43), we have

$$\left(\rho_0 + \frac{g\rho'_0}{\sigma^2} \right) \left(\frac{\partial^2}{\partial x^2} v - k^2 v \right) + \left(\rho_0 v' \right)' = 0 . \qquad (78)$$

with the accent on ρ_0 and on v indicating differentiation with respect to y .

The boundary condition (45) has to be written in terms of v alone. Since u is given by (34) and v by (43), we can write

$$\rho_0 u = \frac{\partial}{\partial x} \left[\int_0^y \left(\rho_0 + \frac{g\rho'_0}{\sigma^2} \right) v\,dy + f_1(x) \right] , \qquad (79)$$

where $f_1(x)$ is an arbitrary function of x. It will be shown later that the boundary condition (45) demands that $f_1(x)$ be a constant. Hence

$$\rho_0 u = \frac{\partial}{\partial x} \int_0^y \left(\rho_0 + \frac{g \rho'_0}{\sigma^2} \right) v dy \quad . \tag{80}$$

Multiplying (45) by ρ_0 and using (80), we have

$$n_1 \frac{\partial}{\partial x} \int_0^y \left(\rho_0 + \frac{g \rho'_0}{\sigma^2} \right) v dy + n_2 \rho_0 v = 0 \quad , \tag{81}$$

in which the boundary geometry not only determines n_1 and n_2, but will play a role after v has been differentiated with respect to x in the first term. We shall show later that the integral form of (81) can be changed to a differential form.

If there is a free surface the condition there is (47), which again must be expressed in terms of v. By virtue of (43), (47) can be written as

$$\sigma^2 \phi = g \rho_0 v .$$

Applying the operator ∇^2 on this and using (40), we have

$$v' = -\frac{g}{\sigma^2} \left(\frac{\partial^2 v}{\partial x^2} - k^2 v \right) . \tag{82}$$

Equations (78), (81), and (82) constitute the differential system defining the eigenvalue problem.

We shall now impose two restrictions on our study : (i) we shall assume that the channel is symmetric, and (ii) we shall exclude sloshing modes (with motion in the x-y plane only) from consideration. Asymmetric channels can be similarly treated without any substantial additional difficulties, and sloshing modes need a separate treatment. We shall describe the boundary of the symmetric channel by

$$x^2 = \left[f(y) \right]^2 ,$$

and consider only the branch

$$x = f(y) . \tag{83}$$

Then the direction numbers $(n_1 , n_2 , 0)$ of the normal to the boundary are

$$n_1 = 1, \; n_2 = - f'(y), \; n_3 = 0 . \tag{84}$$

Restriction (ii) enables us to use the following expansions :

$$\begin{aligned} v = {} & v_{00}(y) + k^2 v_{02}(y) + k^4 v_{04}(y) + \ldots \\ & + k^2 x^2 \left[v_{20}(y) + k^2 v_{22}(y) + k^4 v_{24}(y) + \ldots \right] \\ & + k^4 x^4 \left[v_{40}(y) + k^2 v_{42}(y) + k^4 v_{44}(y) + \ldots \right] \\ & + \ldots \end{aligned} \tag{85}$$

and

$$\frac{1}{c^2} = \lambda_0 + k^2 \lambda_2 + k^4 \lambda_4 + \ldots \tag{86}$$

where

$$c^2 = \left(\frac{\sigma}{k}\right)^2 . \tag{87}$$

Substituting (85) and (86) into (78), and extracting the terms of zeroth order in k, we have (ρ'_0 assumed never to vanish)

$$2\lambda_0 g\rho'_0 v_{20} - g\rho'_0 \lambda_0 v_{00} + (\rho_0 v'_{00})' = 0 , \tag{88}$$

which gives v_{20} in terms of v_{00} .

If terms of zero order in k in (81) are taken, that equation becomes, with n_1 and n_2 given by (84),

$$2x\int_0^y \lambda_0 g\rho'_0 v_{20}\, dy - f'(y)\,\rho_0 v_{00} = 0 .$$

With x equal to f(y), this becomes

$$2\int_0^y \lambda_0 g\rho'_0 v_{20}\, dy - \frac{f'}{f}\,\rho_0 v_{00} = 0 . \tag{89}$$

This equation is valid for all y. Hence we can differentiate it with respect to y and obtain

$$2\lambda_0 g\rho'_0 v_{20} - (f'f^{-1}\rho_0 v_{00})' = 0 . \tag{90}$$

Eliminating v_{20} between (88) and (90), we have

$$(\rho_0 v'_{00})' + (f'f^{-1}\rho_0 v_{00})' - \lambda_0 g \rho'_0 v_{00} = 0 . \tag{91}$$

or

$$Lv_{00} \equiv (\rho_0 f v'_{00})' + f\left[(\rho_0 f'f^{-1})' - \lambda_0 g \rho'_0\right] v_{00} = 0 \tag{91a}$$

The boundary condition* at $y = 0$ is

$$v_{00}(0) = 0 . \tag{92}$$

If the upper surface is fixed, the boundary condition there is

$$v_{00}(d) = 0 . \tag{93}$$

If there is no flat upper surface, and the conduit is full of fluid, (93) can simply be applied at the highest point. On the other hand, if the upper surface is free, the boundary condition (82) can be written as

$$v'_{00}(d) = -\lambda_0 g \left[2v_{20}(d) - v_{00}(d)\right] . \tag{94}$$

Integrating (90) in the Stieltjes sense over a vanishingly thin layer at the free surface, we obtain

$$2\lambda_0 g v_{20}(d) = \frac{f'(d)}{f(d)} v_{00}(d) .$$

Substituting this into (24), we obtain

$$v'_{00}(d) = \left[\lambda_0 g - \frac{f'(d)}{f(d)}\right] v_{00}(d) , \tag{95}$$

---

* If there is a flat rigid upper surface the boundary condition there for v_{20} is $v_{20}(d) = 0$, which can be satisfied only if $f'(d) = 0$. The present analysis for symmetric channels is therefore valid only if the channel boundary has no flat rigid part.

which could have been obtained by integrating (91) across the free surface in the Stieltjes sense.

If $f(y)$ is a constant, (91) becomes

$$(\rho_0 v'_{00})' - \lambda_0 g \rho'_0 v_{00} = 0 ,$$

which agrees with the equation governing wave motion (Yih 1965, p. 29) in a stratified fluid for $k = 0$. Furthermore, (95) becomes

$$v'_{00}(d) = \lambda_0 g v_{00}(d) ,$$

Which is the free-surface boundary condition for a rectangular channel, and which agrees with (82) when v is independent of x and when $k = 0$ (for which $\lambda = \lambda_0$). The conditions (92) and (93) remain unchanged if $f(y)$ is constant. Hence the differential system consisting of (91), (92) and (93), or (91), (92) and (95), agrees, as it should, with that for a rectangular channel when $f(y)$ is taken to be a constant.

From the system (91), (92) and (93) or (91), (92) and (95) we can determine λ_0 and $v_{00}(y)$. Then $v_{20}(y)$ is known from (90).

We shall describe the next stage of approximation. The procedure of successive paaroximation will then be clear. Taking terms of order k^2 in (78), we have

$$(\rho_0 v_{02})' + (\rho_0 + g\rho'_0 \lambda_2)(2v_{20} - v_{00}) + g\rho'_0 \lambda_0 (2v_{22} - v_{02})$$

$$+ x^2 \left[(\rho_0 v'_{20})' + g\rho'_0 \lambda_0 (12 v_{40} - v_{20}) \right] = 0 . \qquad (96)$$

The equation corresponding to (89) is now, for terms of order k^2 and free from x,

$$2\int_0^y (\lambda_0 g\rho'_0 v_{22} + \lambda_2 g\rho'_0 v_{20} + \rho_0 v_{20})\,dy + I$$

$$-\frac{f'}{f}\rho_0\left[v_{02}(y) + f^2 v_{20}(y)\right] = 0\,, \tag{97}$$

where

$$I = 4f^2\int_0^y \lambda_0 g\rho'_0 v_{40}\,dy\,.$$

Differentiation of (97) gives

$$2(\lambda_0 g\rho'_0 v_{22} + \rho_0 v_{20} + \lambda_2 g\rho'_0 v_{20}) = \left(\frac{f'\rho_0}{f} v_{02}\right)' + (ff'\rho_0 v_{20})' - I'\,. \tag{98}$$

Elimination of v_{22} between (96) and (98) gives, after multiplication by f,

$$L\,v_{02} = f\left[-(ff'\rho_0 v_{20})' + (\rho_0 + \lambda_2 g\rho'_0)v_{00} + I'\right]\,, \tag{99}$$

in which L is the operator on v_{00} in (91a). We see from the terms* of order x^2 in (96) that v_{40} can be expressed in terms of v_{20}, and is therefore known. Thus I in (98) is known.

---

* Equating terms of $0(x^2)$ in (96) to zero also guarantees the satisfaction of the free surface boundary condition for terms of $0(k^2x^2)$, as can be seen from a Stieltjes integration of those terms at the free surface and from (82).

The boundary conditions* are, if there is no free surface,

$$v_{02}(0) = 0 = v_{02}(d) . \tag{100}$$

If we now multiply (91) by v_{02} and (99) by v_{00}, and integrate the resulting equations, by parts if necessary, and using (92), (93), and (100) whenever possible, we obtain two equations the left-hand sides of which are identical. Taking the difference of these two equations, we have

$$\int_0^d f \left[(ff' \rho_0 v_{20})' - (\rho_0 + \lambda_2 g \rho'_0) v_{00} - I' \right] dy = 0 , \tag{101}$$

which determines λ_2, since v_{20} and v_{00} are known. Then (99) can be integrated by the method of the variation of parameters to give v_{02}. Then v_{22} is known. Further approximations follow the same pattern.

If the upper surface is free, the free-surface boundary condition can be found by integrating (99) in the Stieltjes sense, and an equation similar to (101) can be found. In fact, to obtain it one need only add the terms

$$- f^2 f' \rho_0(d) v_{20}(d) + \lambda_2 f g \rho_0(d) v_{00}(d) + 4 f^2 \lambda_0 g \rho_0(d) v_{40}(d)$$

to the left-hand side of (101).

It remains to show that the $f_1(x)$ in (79) can be taken to be a constant. The argument is as follows. We have obtained successive approximations to the eigenvalue and the eigenfunction, at each stage satisfying all the boundary conditions. If $f_1(x)$ is not a constant, it is an additional term for the potential ϕ in (34), which gives rise to an additional velocity whose y component is zero. That velocity

---

* Recall that a flat rigid upper surface is ruled out, and at the highest point of the symmetric channel $x = 0$, so that $v_{40}(d)$ does not have to vanish.

therefore cannot possibly satisfy (45) unless its x-component is zero - or unless $f_1(x)$ is a constant.

In the next section we shall study long waves. But before we leave this section we shall make two comments : (i) The method of expansion can be slightly modified to deal with unsymmetric channels. (ii) If the fluid is not stratified, ρ_0 is constant, and from (90) one deduces that v_{00} vanishes and with it v_{20} also vanishes, according to (88). However, for the second approximation, in which terms of $0(k^2)$ are considered, it is found that v_{02} is governed by the equation

$$v''_{02} - (f'f^{-1} v_{02})' = 0 , \tag{102}$$

which is what (99) becomes. The boundary condition on v_{02} is identical with (95) :

$$v'_{02}(d) = \left[\lambda_0 g - \frac{f'(d)}{f(d)} \right] v_{02}(d) . \tag{103}$$

Equation (102) is easily integrated, giving the result

$$v'_{02} - f'f^{-1} v_{02} = C , \tag{104}$$

and

$$\frac{v_{02}}{f} = C \int_0^y f dy . \tag{105}$$

Substitution of (104) and (105) into (103) gives

$$c_0^2 = g \frac{\int_0^d f\,dy}{f(d)} = gh , \tag{106}$$

where h is the average depth. Equation (106) agrees with the result of the classical shallow-water theory for long waves. Thus every comparison we have made indicates the correctness of our procedure.

VIII. LONG WAVES

We shall give some specific examples of the speeds of long internal waves, and shall consider two special classes of density stratification.

(i) Exponential density distribution. If the density distribution is given by (61), we can work directly with (44), which in this case becomes (63), with λ^2 defined by (64). If we expand ϕ in a power series in k^2, we have

$$\begin{aligned} \phi = {} & \phi_{00}(y) + k^2 \phi_{02}(y) + k^4 \phi_{04}(y) + \dots \\ & + k^2 x^2 \left[\phi_{20}(y) + k^2 \phi_{22}(y) + \dots \right] \\ & + k^4 x^4 \left[\phi_{40}(y) + k^2 \phi_{42}(y) + \dots \right] + \dots \end{aligned} \tag{107}$$

Since we expect λ^2 to be negative for internal waves (i.e., waves that do not owe their existence primarily to the free surface), and since λ^2 contains the factor σ^2, which contains the factor k^2, we shall write

$$\lambda^2 = a_2 k^2 + a_4 k^4 + \dots , \tag{108}$$

in which

$$a_2 = -\frac{1}{\gamma^2} . \tag{109}$$

We shall endeavor to determine γ for a given channel cross-section and a given β in (61).

Substituting (107) and (108) into (63) and taking terms of order k^2, we obtain

$$2\phi_{20} - \gamma^{-2}(\phi''_{00} + \beta\phi'_{00}) - \phi_{00} = 0 . \tag{110}$$

Let the channel boundary be given by (62). Then the condition there is, from (34), (43), (45), and the definition of λ^2 given by (64),

$$m\phi_x - \lambda^2\phi_y = 0 . \tag{111}$$

The terms containing k^2 in (111) are

$$2mx\phi_{20}(y) + \gamma^{-2}\phi'_{00}(y) = 0 , \tag{112}$$

or

$$2y\phi_{20}(y) + \gamma^{-2}\phi'_{00}(y) = 0 , \tag{113}$$

after substitution of y for mx (it being sufficient to consider one half of the symmetric boundary).

Combination of (110) and (113) gives

$$\phi''_{00} + \left(\beta + \frac{1}{y}\right)\phi'_{00} + \gamma^2\phi_{00} = 0 . \tag{114}$$

If the inertial effect of the density variation is neglected (Boussinesq approximation), this equation becomes

$$\phi'_{00} + \frac{1}{y}\phi'_{00} + \gamma^2\phi_{00} = 0 \quad , \tag{115}$$

the solution of which satisfying the boundary condition at $y = 0$ is $J_0(\gamma y)$, where J_0 is the Bessel function of the zeroth order.

If the upper surface is free, then (47) gives the condition

$$-\beta\phi_{00}(d) = \phi'_{00}(d) \quad , \tag{116}$$

so that (116) is replaced by

$$\beta J_0(\gamma d) = \gamma J_1(\gamma d) \quad . \tag{117}$$

which gives γ. Once γ is known, the long-wave speed c_0 is calculated from

$$\frac{k^2 c_0^2}{-\beta g} = -\frac{k^2}{\gamma^2} \quad , \quad \text{or} \quad c_0^2 = \frac{\beta g}{\gamma^2} \quad . \tag{118}$$

It is important to note that the roots of (116) or of (117) are for internal waves only. The speed of waves due predominantly to the presence of the free surface is found in the following way. First of all, differentiation of (46) with respect to t gives directly

$$\sigma^2\phi = \frac{g\rho_0\sigma^2\phi_y}{\sigma^2\rho_0 + g\rho'_0} \quad . \tag{119}$$

We see that there are no terms free of k in (63) and (119). Hence any solution of (114), which automatically satisfies condition (45) at the channel boundary, is an acceptable solution. But at this stage we cannot determine c_0. Proceeding to the second approximation, whether or not the Boussinesq approximation is used, we reach a nonhomogeneous differential equation in $\phi_{02}(y)$, the solution of which together with the boundary conditions then determines γ or c_0. The c_0 so determined is not proportional to $\sqrt{\beta}$, but is much larger, and the corresponding waves are predominantly surface waves, the density stratification merely causing a minor correction if β is small.

Because of the convenience afforded by the exponential density stratification, we have used the differential equation in ϕ instead of (78). Remembering (61), (86),

$$f = x = m^{-1} y \ ,$$

and

$$\lambda_0 = \frac{1}{c_0^2} = \frac{\gamma^2}{\beta g} \ ,$$

one can readily show that (114) is equivalent to (91). In fact, $\phi'_{00}(y)$ is proportional to $\rho_0 v_{00}(y)$.

(ii) Superposed homogeneous layers. If the fluid is composed of superposed layers, in each layer the governing equation is (2) or (7). The boundary conditions are (8) for the rigid channel boundary, (11) for the interfaces, and (9) for the free surface. Of course, (9) is a special case of (11). Note that the f in (7) is not the f in (83).

The solution is now not restricted to symmetric channels. Suppose there are n layers. We shal use the expansion

$$f_m(x,y) = f_{m0} + k^2 f_{m2} + k^4 f_{m4} + \ldots \tag{120}$$

for the mth layern counting from the bottom up. Furthermore, we shall write

$$\sigma^2 = \sigma_0^2 + k^2 \sigma_2^2 + k^4 \sigma_4^2 + \ldots \tag{121}$$

Substituting (120) and (121) into (7) and taking only terms free from k, we see that the solution is

$$f_{m0} = C_m \ , \quad \sigma_0 = 0 \ , \tag{122}$$

which satisfy all the boundary conditions if only terms free from k are taken.

For the second approximation we have to solve the equations

$$\left(\frac{\partial^2}{\partial x^2} + \frac{\partial^2}{\partial y^2}\right) f_{m2} = C_m \quad \text{for} \quad m = 1, 2, \ldots n, \tag{123}$$

together with the boundary conditions. Now (123) is just the equation for potential flow with uniformly distributed sources of strength C_m. If (8) is satisfied (with f now identified with f_{m2}), and if d_m is the height of the mth interface,

$$\int_0^{b_1} f'_{12}(x, d_i)\, dx = A_1 C_1 ,$$

$$\int_0^{b_2} f'_{22}(x, d_z)\, dx = A_1 C_1 + A_2 C_2 , \qquad (124)$$

$$\int_0^{b_n} f'_{n2}(x, d_n)\, dx = \sum_{m=1}^{n} A_m C_m ,$$

by virtue of continuity. In (124) b_m is the width of the mth interface, and A_m the cross-sectional area of the mth layer. (See Figure 1). Integrating (11) across b_m, layer by layer, we have

$$c_0^2 b_1 (\rho_1 C_1 - \rho_2 C_2) = g(\rho_1 - \rho_2) A_1 C_1 ,$$

$$c_0^2 b_2 (\rho_2 C_2 - \rho_3 C_3) = g(\rho_2 - \rho_3)(A_1 C_1 + A_2 C_2) , \qquad (125)$$

$$\cdots\cdots\cdots\cdots\cdots\cdots$$

$$c_0^2 b_n \rho_n C_n = g \rho_n \sum_{m=1}^{n} A_m C_m .$$

There are n unknowns C_m, not all of which are zero. Hence we obtain a determinant which must vanish. Its vanishing gives n values for c_0. The last of the equations in (125) corresponds to a free surface. If the upper surface* is rigid, it is to be replaced by [since

* Now a rigid flat upper surface is not excluded.

f'_{n2} must vanish at $y=d_n$ being the height of the upper surface measured from the lowest point of the channel]

$$\sum_{m=1}^{n} A_m C_m = 0 .$$

Indeed, the theory given here is a natural generalisation of the classical shallow-water theory for a single fluid of constant density. If there is only one single fluid, and if it has a free surface, the last equation in (125) gives, with $n = 1$, $b = b_1$, and $A = A_1$,

$$c_0^2 b = gA , \quad \text{or} \quad c_0^2 = gh ,$$

h being the average depth. This is a classical result.

ACKNOWLEDGMENT

This work has been sponsored by the Office of Naval Research, under Grant NR-062-448 to the University of Michigan.

REFERENCES

1 KELLAND, P., 1839, "On Waves," Trans. R.S. Edin., Vol. 14.

2 LAMB, H., 1932, "Hydrodynamics", Cambridge Univ. Press and The MacMillan Co., Sixth Edition.

3 MacDONALD, H. M., 1894, "Waves in canals", Proc. Lond. Math. Soc., Vol. 25, p. 101.

4 STOKES, G.G., 1839, "Report on recent researches in Hydrodynamics, Brit. Assoc. Rep., 1846.

5 YIH, C.-S., 1965, "Dynamics of nonhomogeneous fluids", The MacMillan Co., New York.

Figure Caption

Figure 1. Definition sketch

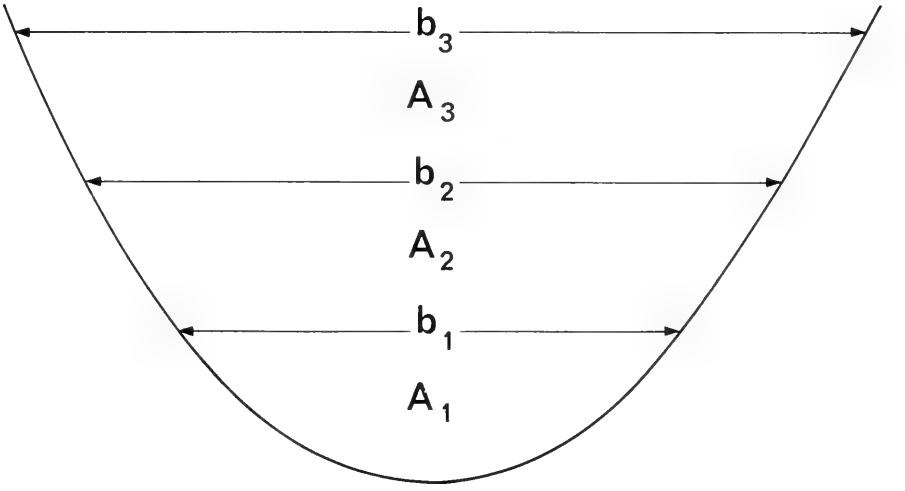

DISCUSSION

Michael N. Yachnis
Naval Facilities Engineering Command
Washington D.C. , U.S.A.

It seems to me that "boundary waves" or "inter-face waves" are more suitable terms for two or three layers of fluid that the term "internal waves". I have four basic questions associated with the application of Professor Yih's Paper, especially on actual ocean internal waves :

1. Possibility of short internal waves and breaking phenomena.

2. Interaction between surface waves and internal waves.

3. Effects of internal waves on fixed or moving structures.

4. Influence of earthquake or disturbances of the bottom of the channel on internal waves.

REPLY TO DISCUSSION

C.S. Yih
University of Michigan,
Ann Arbor, Michigan, U.S.A.

I have been asked by Dr. Yachnis to comment on four matters. This is a great compliment. I do not know that much, but I shall try.

I am glad he mentioned short internal waves. I forgot to mention short internal waves propagating along a channel of variable depth in the direction of the axis. If you do not have stratification, very short waves are not terribly interesting, for this reason : if the den-

sity is uniform the motion is concentrated in a region near the free surface and the fluid does not "feel" the nonuniformity of the depth. But for internal waves, especially if the modes are high, that is to say if there are many internal zeros, then even for short waves the entire fluid participates in the motion. This has not been studied very much. My expansion scheme is not suitable at all for large wave numbers. One can do an asymptotic study of the differential equation to deal with that case, and I do not think it would be terribly difficult to do so. As to breaking, I should think that breaking is probably more severe for long waves. In fact, we know that long internal waves in a system of two layers indeed very often break. Although there are a lot of other solutions for non breaking waves (cnoidal waves, solitary waves and so on), if you make a laboratory test, pushing a plate against a layered system you will see that indeed the interface breaks. Mathematical studies of the breaking of internal waves are even more difficult than the studies of the breaking of ordinary waves in one single fluid, and I certainly do not know the mathematical theory. You surely remember the last picture shown by Pr. Plate. If a wave goes that far I would keep well away, both physically and intellectually.

Secondly, about the interaction between surface waves and internal waves, that too has not been studied a great deal. We all know that after a storm there are internal waves created in the sea. How is the surface disturbance created and how are the messages transmitted from the surface down to the depths of the sea ? Not much is known about that. I think, however, that the interaction between surface waves and internal waves can be considered in this way : if the surface waves already created have a frequency very far away from that of any of the internal waves, there is no chance for the resonance phenomenon to happen. However, if short surface waves have the same frequency as some longer internal waves, the surface waves can excite internal waves, especially if the amplitude is not small. If the amplitude is small we do not need to worry about excitation.

As for the effect of internal waves on moving structures, I do not have much to say about that. Naturally there would be an internal-wave drag for moving submerged structures.

The last question concerns the creation of internal waves by earthquake disturbances. I think that as far as the linear theory goes it is really just a matter of Fourier analysis. If one knows the details fo an earthquake, you can obtain the spectrum of internal waves created. Indeed, the linear theory should be quite simple.

* * *

MODELING AND MEASUREMENTS OF MICROSCOPIC STRUCTURES OF WIND WAVES

Jin Wu

Hydronautics Inc.
Laurel, Maryland, U.S.A.

ABSTRACT

The microstructure of the wind-disturbed water surface, characterized by surface-slope and surface-curvature distributions, is measured in a laboratory tank under various wind and wave conditions. The relative frequencies of occurrence of various slopes generally follow a normal distribution. At low wind velocities, the formation of parasitic waves causes a skewed slope distribution; at high wind velocities, the wave breaking causes a peaked slope distribution. It is also shown that the mean-square slope rises suddenly at about the wind velocity where the airflow boundary layer becomes turbulent. The curvature distribution of the wind disturbed water surface observed from different angles is generally skewed with greater radius of curvature at steeper viewing angles from the normal to the mean water surface. As the wind velocity increases, the average radius of curvature decreases rapidly at low wind velocities when waves are effectively excited by wind, and gradually at high wind velocities when waves approach saturated state. The present measurements of surface curvatures are the only set of data of its kind. The mean-square surface slopes are compared favorably with those determined in the field; and both sets of data are consistent with the equilibrium wind-wave spectra.

I. INTRODUCTION

The wind-disturbed water surface consists of waves of various lengths moving at various speeds. There has been ever-increasing interest in determining the statistical properties of the microstructure (wavelets) of such a surface. From a fluid-mechanics point of view, these wavelets are involved in the inception of wind waves and are believed to be related to the dissipation of the wave energy. From an oceanographic point of view, the quantitative measurement of the mean square surface slope provides the best determination of the coefficient involved in the equilibrium wind-wave spectrum for describing the directional energy-density distribution of ocean waves. From a meteorological point of view, the microstructure plays a major role on the radiation of thermal energy from the sea surface. Finally, from the remote-sensing point of view, ripples are important for interpreting reflection and back scattering of electromagnetic waves from the ocean surface.

A few optical methods have been adopted in the past for determining the microstructure of the wind disturbed water surface; these include the photographic method of Schooley (1954, 1955), and of Cox and Munk (1956), and the light refraction method of Cox (1958). However, the photographic method so far developed involves rather tedious data analysis and, moreover, is not completely apt for laboratory application. Owing to the limited fetch, the water surface structure in the laboratory wind-wave tank lacks spatial homogeneity, which is required for the photographic method. In the light refraction method, the apparatus consists of submerged parts which offer obstruction to waves and are rather difficult to construct; in addition, the under tank illumination required is inconvenient for a deep wind wave tank which is appropriate to simulate the air-sea interface for more advanced studies. The present instrument, utilizing a light reflection principle, is capable of determining not only the surface slope but also surface curvature with high resolution.

In the present study, the microstructure of the wind-disturbed water surface, characterized by surface-slope and surface-curvature distributions, is measured in a laboratory tank under various wind and wave conditions. The features of these distributions are discussed, along with their variations with structures of dominant waves and the growth of slope and curvature statistics with the wind. The present measurement of surface curvatures is the only set of data of its kind. The mean-square sea-surface slope obtained by Cox and Munk (1956) are reanalyzed and compared with the present results. These two sets of data are shown in good agreement and to be complementary to the equilibrium wind-wave spectra. Finally,

some discussion is included on mechanism of wave generation by wind through comparing the cutoff wavelength of the slope data with the calculated neutrally stable wavelength.

II. EQUIPMENT AND EXPERIMENTAL PROCEDURE

II. 1 Wind-wave tank and general instruments

The wind-wave tank has a 1.5 × 1.55-m cross section and is 14 m long; see Figure 1a. The top of the tank is covered for 5.5m, up to the test section. Mounted at the upstream end of the tank is an axial-flow fan, and a permeable-type wave absorber is installed at the downstream end. The maximum obtainable wind velocity with a 0.35-m-deep air passage above 1.2-m-deep water is 14 m/sec.

The wind-velocity profile in the tunnel is determined by the vertical traverse of a pitot-static tube. The drift current is measured by timing the motion of floats of various sizes. The surface drift current is determined by extrapolating the measured current-distribution curve to the water surface. The results of surface drift currents and of wind velocities are used together to obtain the wind velocity relative to the water surface.

Two types of instruments have been used simultaneously for wave measurements: a conductivity probe for recording gravity-wave profiles, and an optical instrument for surface-slope and surface-curvature measurements. The conductivity probe, a wave-height gauge, does not provide enough resolution for measuring wavelets that ride on top of gravity waves and have amplitudes only small fractions of the latter. A detailed description of the wave tank and its associated instruments has been given elsewhere (Wu 1968, 1971a)

II. 2 Optical instrument

The optical instrument, shown in figure 1b, consists of a light source, a telescope, and a photomultiplier unit. Supported over the wave tank, the instrument can be set at any desired inclination from the water surface. The photomultiplier receives reflected light only when the water surface is normal to the plane containing the light beam and the telescopic axis. The cross section of the light beam is rectangular, with a length-to-width ratio of 20 to 1. The short side of the beam is aligned with the direction of the wind. Therefore, the angular sensitivity of the instrument in the traverse (cross-wind) direction is about 1/20 times that in the longitudinal (wind) direction. The angular tolerance of the instrument to the water-surface slope

in the longitudinal direction is about 1°; see figure 2.

The focal spot of the telescope on the water surface is circular, with 0.7-mm diameter. This spot is completely bright when the water surface is relatively flat and is partially bright when the curved water surface reflects part of the impinging light away from the telescope. Simple calculations have been made along with a calibration test consisting of passing cylinders, with the same kind of reflecting surface but with various radii, under the instrument. The longitudinal axis of the cylinder is always parallel with the same axis of the lamp. From the geometry in figure 3a, the following relationships can be obtained for a curved surface with radius of curvature R :

$$2\alpha = \cot^{-1}\left[\frac{L_\ell - R\cos\alpha}{w/2 + R\sin\alpha}\right] - \cot^{-1}\left[\frac{L_t - R\cos\alpha}{d/2 + R\sin\alpha}\right] \qquad (1)$$

for a convex surface, and

$$2\alpha = \cot^{-1}\left[\frac{L_\ell + R\cos\alpha}{w/2 + R\sin\alpha}\right] + \cot^{-1}\left[\frac{L_t + R\cos\alpha}{d/2 + R\sin\alpha}\right] \qquad (2)$$

for a concave surface, where d is the diameter of the pinhole located in front of the photomultiplier, w is the effective width of the plano-convex cylindrical lens for focusing the light, and L_t and L_ℓ are the distances from the telescope and the light box lens to the mean water surface, respectively. Only single reflections are considered.

By choosing the size of the pinhole to be much smaller than the beamwidth of the light and by putting the instrument away from the surface (for the present setup, $w/d \doteqdot 400$ and $L_t/w \doteqdot L_\ell/w \doteqdot 50$), we can show that the second term on the right of (1) and (2) is much smaller than the first term in each respective equation. In other words, by the proper setting of the distance between the instrument and the water surface ($L_\ell >> R$), both (1) and (2) can be approximated by

$$\alpha = \frac{1}{2}\cot^{-1}\left[L_\ell / (w/2)\right] \qquad (3)$$

Hence, the response of the instrument to surface curvature is essentially the same for both concave and convex surfaces.

If we designate r as the radius of the focal spot of the telescope on the water surface, the degree of saturation of the light signal (s = 1 for saturated signal) can be shown as

$$s = 1 - \frac{2}{\pi}\left\{\cos^{-1}\left(\frac{h}{r}\right) - \frac{h}{r}\left[1 - (h/r)^2\right]^{\frac{1}{2}}\right\} \qquad (4)$$

where

$$h = R \sin \alpha$$

is the half-width of the bright portion of the water surface image (see figure 3a). Of course, the radius of the focal spot of the telescope on the water surface, r, depends upon the diameter of the pinhole, d, as well as on the characteristics of the telescope lens. The calibrated response for the present setup, as well as those obtained directly from (3) and (4), is plotted in figure 3b. The scattering of the calibration points is believed to be the result of local deflects on the calibration cylinder.

In summary, the light signal is continuous and saturated to a prescribed level, insensitive to the change of curvature, as long as the angular change of the wavy water surface from the downwind face to the upwind face is less than the acceptance width of the instrument (about 1°). As the angular change increases beyond that, or if the surface curvature increases further, the signal becomes discontinuous. The signal is essentially a light pulse. The intensity of the signal, i.e., the pulse height, is related to the surface curvature; the period of the signal, or the pulse width, is the time required for a detectable slope to pass completely under the instrument.

The distribution of the surface slopes is determined by accumulating the numbers of light pulses for each inclination of the instrument for a constant period (10 min). To determine the distribution of surface curvatures, each series of light pulses is sorted according to their intensity into 50 channels of the pulse-height analyzer, with preset intensity bands. The output from the analyzer, the height distribution of light pulses for a given instrument inclination, is first traced on a x-y plotter and later digitized.

The block diagram of the apparatus is shown in figure 4a. The light source is a 1500 W incandescent lamp, approximately 18 cm long. The photomultiplier tube is a nine stage, side-on unit with S-4 spectral response. The high voltage power supply is adjustable so that adequate sensitivity with minimum dark current noise can be obtained. The output of the electrometer is comprised of irregularly

shaped pulses, varying from 0 to 10 V in amplitude and having durations of a few milliseconds. However, the pulse height analyzer (ND-110 128- channel analyzer manufactured by Nuclear Data, Inc.) requires pulses of much shorter periods and places very stringent requirements on the risetime. The pulse conditioning circuit shown in figure 4a is thus required.

The pulse conditioner is capable of analyzing both pulse height and pulse width (pulse period). In both modes, the signal activates the Schmitt trigger. This in turn sets the binary and opens electronic switch N° 1. In the height mode, the track hold amplifier output is compared with the incoming signal. When the input drops, the amplifier is put in hold. In other words, the amplifier tracks the signal to its maximum value and holds this value until it is reset. On the other hand, when the signal drops below the threshold of the Schmitt trigger monostable τ_1 is started. This closes electronic switch N° 2 for 5 μ sec. During this time the amplitude of the track hold amplifier is gated to the pulse height analyzer as a pulse with a suitable width and risetime. At the end of this time, τ_2 is started again to reset the binary and to close electronic switch N° 1. By doing so the track hold amplifier is reset until a new pulse is received.

In the time mode, the operation is identical except that the Schmitt trigger controls a ramp generator, which is tracked to convert time to amplitude. Consequently, the amplitude gated to the pulse height analyzer is proportional to the signal pulse duration. The pulse described above, from the signal to the pulse height analyzer, are shown in figure 4b. The widths of τ_1 and τ_2 are exaggerated for clarity.

III. EXPERIMENTAL CONDITIONS

III. 1 Wind conditions

The wind-velocity profiles were found to follow essentially the logarithmic law near but not too close to the water surface (Wu 1968). The shear velocities, obtained at different wind velocities, are presented in figure 5. Lines shown in the same figure are the shear velocity for a laminar boundary layer.

$$u_* = \left(\frac{1}{2} \cdot \frac{0.664}{R_n^{\frac{1}{2}}}\right)^{\frac{1}{2}} \cdot U_o \qquad (5)$$

and for a turbulent boundary layer in the aerodynamically smooth

flow regime,

$$u_* = \left(\frac{1}{2} \cdot \frac{0.059}{R_n^{1/5}} \right)^{\frac{1}{2}} \cdot U_o \qquad (6)$$

wherein the Reynolds number ($R_n = U_o \cdot L/\nu$) is defined in terms of the free-stream air velocity, U_o, the distance between the fan and the test section, L, and the kinematic viscosity of air, ν .

Judging from the trends of the data shown in figure 5, we see that

a) the air-flow boundary layer seems to be in the pretransition region for $U_o < 1.9$ m/sec. Because the air was sucked into the wind-wave tank by an axial fan and through guiding vanes, which were arranged to straighten the flow but not to diminish the high turbulence level, the latter arrangement was helpful to increase the effective lenght of the wind fetch.

b) the effective transition region of the boundary layer from laminar to turbulent is very narrow, at wind velocities between 1.9 and 2.4 m/sec.

c) once the boundary layer becomes turbulent, $U_o > 2.4$ m/sec, the transition from smooth to rough boundary layer takes place and this process is completed at $U_o = 3.5$ m/sec, the aerodynamically smooth flow regime is rather narrow.

d) for the aerodynamically rough flow regime, the two groups of data are separated physically by the transfer of the governing mechanism of wind-wave interaction from surface tension to gravity (Wu 1968, 1969); this separation occurs at $U_o = 9$ m/sec.

It should be emphasized here that because of the difference of scales (such as wind fetch) between the ocean and laboratory conditions and of differences of the wind structures (such as turbulence levels) between various wind-wave tanks, the shear velocity rather than the wind velocity should be adopted to characterize the wind conditions (Wu 1968). By use of the shear velocity, data obtained in the present experiment may readily be correlated with results of other investigations.

III.2 Wave conditions

From the continuous wave-profile recording, the periods of more than 100 basic waves for each wind velocity are obtained (Wu

1968). The average values of the wavelength, calculated from the measured period by using the dispersion relation for small-amplitude deep-water waves, are shown in figure 6. A general observation is that small-amplitude capillary waves are generated at very low wind velocities (U_o < 2 m/sec). Rhombic wave cells are observed before the wind boundary layer becomes fully rough (2 m/sec < U_o < 3 m/sec); the waves forming cells are short gravity waves. As the wind velocity further increases, the propagation of waves becomes more and more along the direction of the wind. Parasitic capillaries are formed in front of the gravity wave crests immediately following the transition of the wind boundary layer from smooth to rough ($U_o \doteqdot$ 3 m/sec), the water surface is generally smooth elsewhere. As the wind velocity increases passing 9 m/sec, ripples are seen covering the water surface and breaking is observed along the wave crests, which span transversely across the tank. Various stages of wave growth with the wind velocity are indicated in figure 6.

IV . SURFACE SLOPES

IV. 1 Distribution of surface slopes

For each wind velocity, the number of light pulses in 10-second intervals is counted electrically with the optical instrument set at various angles of inclination. Each light pulse represents the occurrence of a particular water-surface slope, whose inclination from the horizontal is the same as that of the instrument from the vertical. More than 30 sets of readings are recorded for each inclination, of which the average value as well as the standard deviation from the average are plotted versus the angle of inclination in figure 7. As shown in the lower right corner of figure 7, slopes with their normals pointing up-wind are considered to be negative, whereas those pointing down-wind are positive. A short vertical line accompanying each data point indicates the value of the standard deviation of the data from the average. The reliability of the data is indicated by the small values of the standard deviations.

The data points shown in figure 7 are seen to follow essentially a gaussian distribution. The area defined by the data points is first integrated by means of Simpson's rule to determine the median value. Around this median value, the data points for each wind velocity are then normalized. The normal distribution curve, found on the basis of least-square curve fitting, is drawn as the continuous line shown in figure 7. It is now seen that the nearly normally distributed data are skewed (maximum and median values at angles other than 0°) at medium wind velocity and peaked (maximum values beyond the gaussian curve) at

high wind velocity.

IV.2 Inception of high-frequency components of wind waves

The standard deviations of the slope-distribution curves, shown in figure 7, are equivalent to rms water-surface slopes and are shown in figure 8. The trend of the slope variations shows that the rms water-surface slope is only a fraction of a degree at very low wind velocities, $U_o < 1.9$ m/sec. A sudden rise of the water-surface slope is observed in the wind-velocity range between 2 and 3.5 m/sec. Beyond this range, the slope shows a steady but gradual increase with wind velocity. Figure 8 shows that the slope seems to reach a saturated value of 17.3°, when the wave growth with wind velocity ceases, and whitecaps appear at virtually every wave crest.

As is shown in figure 2, the slope resolution of the present optical instrument is 1°. It is conceivable that increasing the slope resolution of the instrument (narrowing the slope-response curve shown in figure 2), would shift the lower end of the sudden slope rise (with slopes less than or near 1°) toward lower wind velocities, but the major rising portion (with slopes greater than 1°) will stay in the same wind-velocity range, shown in figure 8.

The boundary-layer regimes of the wind are superimposed on the velocity scale in figure 8. It is very interesting to see that as soon as the effective transition of air flow from laminar to turbulent occurs, the surface slope rises suddenly. This rapid change indicates, therefore, very efficient inception of waves as soon as the wind boundary layer becomes turbulent, as suggested earlier by Phillips (1958b). These rapid changes soon slow down but the waves have already been created and have grown to a considerable size.

A similar sudden rise of the water-surface slope was reported by Cox (1958); see the comparison between the present and Cox's results in figure 9. It is seen that these two sets of data behave similarly with regard to the sudden slope rise corresponding to the inception of wind waves, as demonstrated in figure 8. The sudden slope rise obtained in the present study has been related to the initiation of the turbulent boundary layer of the wind. No wind-structure survey was provided by Cox; the close agreement between Cox's and the present data at the wave-inception stage suggests, however, that the sudden rise of the water-surface slope in his experiment is also related to the transition of the airflow boundary layer, as first suggested by Phillips (1958b).

Following the sudden slope rise, the present data seem to show three stages of development : gradual change, rapid change, and approaching saturation, as marked successively in figure 9 by three segments of lines. The rapid change begins when waves start to break occasionally and ends when wave breaking was observed at most wave crests. Cox's data display only two stages of development. The shorter wind fetch and the lower turbulence level are believed to be the reasons for causing the general shift of Cox's results. The wave regime in Cox's tank may not have passed the occasional breaking stage; wave breaking was not reported by Cox.

IV. 3 Features of slope-distribution curves

The slope-distribution curves, shown in figure 7, are skewed toward the down-wind direction at medium wind velocities. The skewness disappears at high wind velocities and peakedness follows. The skewnesses of slope distributions, a measure of the asymmetry of wind-generated water waves, are shown in figure 10a.

In order to understand the skewness features, an experiment was done by placing the wave-height gauge 3 mm transversely from the telescope focal spot at the water-surface. The outputs of the optical instrument, set in the vertical plane, were recorded simultaneously with those of the wave height gauge. The location of the light pulse relative to the wave-height profile, shown on the records, corresponds physically to the relative position of the capillary waves distributed along the basic wave profile.

The distribution of the capillary waves on the down-wind and up-wind faces of the basic wave profile is plotted in figure 10b. At medium velocity, the pulses (wavelets) at the down-wind face very much outnumber those at the up-wind face. This is the velocity range at which the maximum skewness of the surface-slope distribution occurs. As the wind velocity increases, the pulses (wavelets) become more and more evenly distributed over the up-wind and down-wind faces, and the slope-distribution curve thus becomes less and less skewed.

The distribution of wavelets along basic wave profiles, presented in figure 10b, is also interesting in two other ways. This distribution indicates the presence of one of the equilibrium regimes, the formation of parasitic capillaries in the front face of the basic wave profile. This distribution may cause different backscattering of electromagnetic waves from the leeward (down-wind) and from the windward (up-wind) faces of the basic wave profile.

The skewness of the slope distribution is shown to be related to an excess of wavelets riding on the down-wind face of the basic wave profile. Because the down-wind face is sloped, the skewness results. On the other hand, wave breaking introduces a local excess of wavelets near the crests of the basic waves, and consequently, peakedness results at high wind velocities.

V. SURFACE CURVATURE

V.1 Distribution of surface curvature observed from vertical

The surface-curvature distribution for each wind velocity was determined by setting the optical instrument in the vertical plane and sorting the light pulses according to their intensities. During a portion of the experiment, only two channels were available; the total number of pulses was counted in one channel and the pulses with intensities within the preset intensity range were counted in the other channel. The frequency of occurrence of light pulses within a particular range can thus be determined. This process is repeated by changing the band settings to obtain the surface-curvature distribution, as shown in figure 11. The short vertical line is once again used to indicate the standard deviation of the data from the average, which is generally less than 5 percent.

The lower cutoff radius of curvature of the present optical instrument is 0.067 cm. This cutoff, marked by a long vertical line shown on the left in each block of figure 11, is set just above the maximum instrument noise, which is about 5 percent of the maximum signal intensity and about 1.7 percent of the maximum detectable radius of curvature. The upper cutoff (the maximum detectable radius of curvature) is 4 cm. Below the lower cutoff, no signal can be picked up by the instrument. Any wave that has a radius of curvature greater than the upper cutoff is registered as having a 4-cm radius of curvature. Except at very low wind velocities, less than 2 m/sec, the radius of curvature of the water surface seldom reaches the upper cutoff value.

V.2 Angular distributions of surface curvatures

This portion of the experiment was conducted with the pulse analyzer described in previous sections. For each wind velocity, the optical instrument is set at various angles of inclination. The signals are directed, according to their intensity, to proper channels of the analyzer and are counted there. Each channel is assigned a certain range of signal intensity, between zero and the saturation voltage.

A typical trace of a series of automatic sorting and counting for one instrument inclination is shown in figure 12a. Channel 10 represents the lower cutoff, below which the intensity of signal is comparable with noise; such light pulses are not counted. The upper bound of channel 50 is set just above the saturation voltage, so that the saturated signals can be counted. From the digitized data, the total number of signals for each angle can be obtained. A gaussian curve, fitted on the basis of the least-square principle, is shown in figure 13 to represent the distribution of water-surface slope for each wind velocity. (For clarity, the data points are not shown in figure 13).

The data shown in figure 12a are first replotted in figure 12b, where the horizontal axis is transformed from channel number (or voltage) into radius of curvature. The lower cutoff radius of curvature of the present optical instrument is marked by a long vertical line shown on the left in figure 12b. The centroid is then determined of the area, shown in figure 12b, enclosed by the measured distribution curve, the horizontal axis and the lower cutoff radius of curvature. The centroid, indicated in the same figure, is the average absolute radius of curvature. The average (absolute) radii of curvature, viewed from different angles for various wind velocities, are presented in figure 13.

V.3 Features of surface-curvature measurements.

The typical distribution of radii of curvature is shown in figure 12b, of which the shape is in rough agreement with that obtained analytically by Longuet-Higgins (1959) for a gaussian surface. A complete distribution of radii of curvature, extending to very small radii of curvature, was not obtained. The present measurements, however, are sufficient for determining the average radius of curvature. Any uncertainty on the lower end of the data, the righ-hand side of figure 12b, would not affect the determination of the centroid of the area under the distribution curve.

The average radius of curvature is seen in figure 13 to have its minimum value at a small but positive viewing angle. The average radius generally increases when the observation changes continuously from zero to negative viewing angles and reaches a rather high value at a steep negative viewing angle. On the other hand, the average radius of curvature first decreases to the minimum value, then increases when the observation angle increases, and finally reaches a high value at a steep positive viewing angle. A continuous curve was drawn to indicate the trend of the data, which is believed to be the first set of radii of curvature of wind-disturbed water surfaces measured from various viewing angles and at different wind velocities.

The angular distribution of average radius of curvature, shown in figure 13, is normalized with respect to the slope distribution and replotted in figure 14. The normalization involves only dividing the observation angle by the standard deviation of the slope-distribution curve. Such a step, relating the average radius of curvature to the relative frequency of occurrence, is helpful for comparing results obtained at various wind velocities. The relative frequency of occurrence for the converted scale, on the basis of the standard deviation, is given by the error function.

V. 4 Skewed angular distribution of surface curvatures

The angular distribution of average radius of surface curvature, shown in figure 14, displays three different shapes corresponding approximately with the occurence of three types of carrier-wave patterns discussed in an earlier section. At the lowest wind velocity, a very skewed, bell-shaped distribution curve is related to rhombic waves, although it is not clear at this stage what is the reason for this correlation.

At medium wind velocities ($3 < U_o < 9$ m/sec), the steep-faced parasitic capillaries, riding on the forward face of the carrier waves, undoubtedly cause a skewed angular distribution of the average radius of curvature. The observation angle with the minimum radius of curvature is about the same as the forward-face slope (from the horizon) of the carrier wave. This regime with highly skewed surface-curvature distributions, however, probably exists only in laboratory tanks (Wu 1970)

At high wind velocity ($U_o > 9.5$ m/sec), the carrier wave is covered rather evenly by ripples. This is the gravity-governing regime. The case with the wind velocity of 9.3 m/sec is in the transition region between the surface-tension regime at low wind velocities and the gravity-governing regime at high wind velocities. The microstructures of disturbed water surface for the three highest wind velocities are very similar to oceanic conditions; nonlinear interaction between short and long waves is believed to be active in this regime.

The horizontal contraction of the water surface near the crest of the long wave was stated by Longuet-Higgins and Stewart (1960) to shorten the lengths and to increase the amplitudes of short waves (ripples). When these ripples are saturated, further shortening will cause their breaking. Phillips (1963) then showed analytically that the energy loss by short waves near the crests of long waves is partially supplied by the long wave, and, therefore, causes the attenuation of

long gravity waves. Later, slow moving short waves are considered (Longuet-Higgins 1969) to be swept through by fast-moving long waves and to lose their energy to the long waves at a rate proportional to the orbital velocity in the long waves. More recently, Hasselmann (1972) found that the work done on the long waves through the sweeping is balanced by the loss of potential energy due to taking mass of high potential energy from the crests of long waves and returning it at a lower potential level in the troughs. The dynamics of nonlinear interaction of oceanic waves is therefore rather confused. However, all of these models are based on one common phenomenon : long waves sweeping through short waves and causing short waves to break on the forward faces of the longwave crests. Some physical evidence substantiating this basic phenomenon has been obtained through photographs of glitter patterns (Wu 1971b).

Figure 13 shows that the minimum radius of curvature is observed at a positive angle for all of the wind velocities. The minimum radius of curvature is undoubtedly produced by crests and troughs of the shortest waves. The present results therefore seem to confirm earlier observations and conclusions that waves with the smallest radii of curvature, very likely produced by nonlinear wave-wave interaction, ride on the forward faces of long carrier waves having positive slopes. In other words, the skewed shape of the angular distribution of average radius of curvature is probably due to the nonlinear wave-wave interaction.

V. 5 Low and high grazing angles for back scattering.

The reflection and back scattering of electromagnetic waves impinging on the air-sea interface depend on the sizes of the specular areas. The latter can be described statistically by the average radius of curvature. The distribution of the size of the specular areas was considered by Schooley (1955) to be substantially the same for all slopes. The results, obtained here and shown in figures 13 and 14 suggest that this earlier consideration may be approximately true for the ocean surface and at limited angles near the normal to the horizon. As discussed in the previous section, the skewed angular distribution of surface curvature seems to be as expected as a result of parasitic capillaries at medium wind velocities and of nonlinear wave-wave interaction at high wind velocities.

The measurements for the three highest wind velocities are most interesting for practical application, because the surface structures for these three cases are believed to be very similar to the air-sea interface. As shown in figures 13 and 14, and stated in the pre-

vious paragraph, the microstructure may be considered nearly isotropic for viewing angles very close to the normal to the mean water surface, say, less than the root-mean-square slope. Beyond this region, the sizes of specular areas, represented by the average radius of curvature, increases rather rapidly with the angle from the normal. No data were obtained at very steep angles, where the situation is further complicated by possible shadowing effect.

Judging from the data shown in figure 14, the backscattering measurement is ideally made at small angles from the normal, where the sea surface is nearly isotropic. A small error of the angular measurement at large angles would introduce serious change of the results because the sea surface in this case is highly nonisotropic.

V. 6 Growth of high-frequency wind waves.

In order to find the over-all average radius of curvature of the disturbed water surface for each wind velocity, the cross product of the smooth data shown in figure 13, is found. One curve shows the angular distribution of average surface curvature and the other curve shows the relative frequency of occurrence of the particular curvature. Consequently, the cross product represents the overall average of surface curvature obtained at a given wind velocity.

The overall average radius of surface curvature are shown in figure 15. The data indicate a rapid decrease of the radius of surface curvature with increasing wind-shear velocity is observed at low wind velocities and a steady but gradual decrease at high wind velocities. Figure 15 shows that the radius of curvature seems to reach a saturated value of 1/4 cm, when the wave growth with wind ceases.

VI . SEA-SURFACE SLOPE AND EQUILIBRIUM WAVE SPECTRA

VI. 1 Equilibrium wind-wave spectra.

The directional wind-wave spectra $\Psi(\overline{k})$ in the equilibrium range was proposed by Phillips (1958a, 1966):

$$\text{Gravity waves}: \Psi(\overline{k}) = \frac{B}{\pi} f(\theta) k^{-4}, \quad k_\gamma > k > k_o$$
$$\text{Capillary waves}: \Psi(\overline{k}) = \frac{B'}{\pi} f(\theta) k^{-4}, \quad k_\nu > k > k_\gamma \qquad (7)$$

where $\overline{k}$ and k are the wave-number vector and scalar, respectively;

k_o is the wave-number at the spectral maximum; k_γ is the maximum wave-number where the influence of surface tension is negligible; k_ν is the neutrally stable wave-number, B and B' are the spectral coefficients for the gravity and the capillary ranges, respectively; finally, $f(\theta)$ is a dimensionless function specifying the directional distribution of wave components (Schule et al. 1971) where $\theta = 0$ indicates the wind direction. The wave-number k_γ can be expressed as

$$k_\gamma = (\rho g/T)^{\frac{1}{2}} \tag{8}$$

wherein ρ is the density of water, g is the gravitational acceleration and T is the surface tension. The neutrally stable wave-number corresponds to the wavelength at which the energy input from the wind is balanced by the energy dissipation through viscosity. This specific wavelength was expressed by Miles (1962) as a function of the wind shear velocity.

It is considered for the equilibrium wave spectra that high-frequency wave components spread isotropically. In this case $f(\theta)$ equals to unity and the one-dimensional spectra, identical in all directions, becomes

$$\Psi(k) = (B/2\pi)k^{-3} \quad \text{and} \quad \Psi(k) = (B'/2\pi)k^{-3} \tag{9}$$

In laboratories, owing to narrowness of the tank the waves propagate predominantly in the direction of the wind. The spectra may be considered to be unidirectional and may be described by (9) in the direction of the wind.

The mean square slope of the wind-disturbed water surface, $\overline{s^2}$, can be obtained from the directional wave-number spectrum $\Psi(\bar{k})$, or

$$\overline{s^2} = \int_o^\infty k^2 \Psi(\bar{k})\, d\bar{k} \tag{10}$$

The integration should cover the possible range of the wave-number. Substituting (7) into (10), we have (Phillips 1966)

$$\overline{s^2} = B\, \ell_\eta\, (k_\gamma/k_o) + B'\, \ell_\eta\, (k_\nu/k_\gamma) \tag{11}$$

The first term on the right-hand side of (11) represents the contribution of gravity waves to the mean-square surface slope, and the second term on the right-hand side represents the contribution of capillary waves.

It is noted that the longitudinal (upwind-downwind) component is about one half of the total mean-square sea-surface slope, as short ocean waves propagate nearly isotropically. In the laboratory tank, the longitudinal component is about the same as the total mean-square surface slope, as waves propagate nearly unidirectionally. Needless to say, these ratios can only be approximations, because the propagation of wind waves can neither be exactly isotropical nor be exactly unidirectional.

VI. 2 Sea-surface slope and spectral coefficients.

Cox and Munk (1956) deduced slopes of the sea-surface from the brightness distribution of photographs of sun glitter of the sea-surface. The wind velocity at the time of taking sun glitter pictures was recorded at two heights, 9 and 41 ft. from the mean sea level. The lower height may be too close to the water surface to be free from the wave-induced air motion, especially at higher wind velocities. Therefore, the wind velocity measured at the upper height was used along with the wind-stress coefficient (C_{10}) formula (Wu 1969),

$$C_{10} = 0.5\ U_{10}^{\frac{1}{2}} \times 10^{-3} \qquad (12)$$

to determine from the logarithmic wind profile the corresponding wind velocity U_{10} at the standard anemometer height. It may be worthwhile to note, however, that this correction is very small and that the wind velocities U_{10} obtained from both methods are about the same. The results of the mean-square surface slope of a clean surface $\overline{s^2}$ versus U_{10} are plotted in a semilogarithmic form in figure 16. Various boundary layer regimes of the wind (Wu 1968) are shown in the same figure. The results of mean-square slopes obtained from the interior of an artificial slick are not included in this figure.

It is very obvious from figure 16 that the data are divided into two groups : one in the hydrodynamically smooth flow regime and the transition region ($U_{10} < 7$ m/sec), and the other in the hydrodynamically rough flow regime ($U_{10} > 7$ m/sec). A straightline can fit the results in each group rather well. The data are scattered at low wind velocities where the wind condition is less stable in the transition region, scattering of the data seems to be inevitable. An excellent correlation of the mean-square slope with the wind velocity is seen in figure 16.

Most of the results of Cox and Munk were obtained from a

clean sea surface, where capillary waves were undoubtedly present and should contribute to the mean-square surface slope. On the other hand, some of their observations were taken in the interior of a dense artificial slick, where waves shorter than 30.5 cm (1 ft) were reported by Cox and Munk to be absent. For the latter case, the maximum wavenumber for existing waves, designated as k_s (with the minimum wavelength γ_s), is certainly well outside the capillary range, or in other words k_s smaller than k_γ . Therefore, for this portion of the data obtained in the interior of artificial slicks. Equation (11) can be rewritten as

$$\overline{s^2} = B \ell_\eta \left[(U_{10}^2 / g) k_s \right. \tag{13}$$

in which the wavenumber k_o is substituted with g/U_{10}^2 (Phillips 1966). It is now obvious, if we replot the mean-square slope data in the semilogarithmic form and fit the replotted data with a straight-line, we can determine both B and k_s independently. The k_s so determined can then be compared with the observed k_s .

Replotted in figure 17 in the proposed form and fitted with straightlines by means of the least-square principle are the data of three different groups : (a) clean sea surface with the airflow in the hydrodynamically smooth regime and the transition region, (b) clean sea surface with the airflow in the hydrodynamically rough regime, and (c) sea surface covered with slicks. For the last group, the values of B and k_s , determined from the slope and the intercept of the fitted straightline, are

$$B = 4.6 \times 10^{-3}, \quad \lambda_s = 38 \text{ cm} \tag{14}$$

The value of B is identical to that obtained earlier by Phillips (1966). Taking into account the scattering of the data and the rather crude visual observations of the minimum wavelength in dense slicks, the λ_s can be considered in rather close agreement with the observed value of 1 ft. This agreement also supports the technique used here to determine the spectral constant.

For a clean sea surface, the contribution of the capillary waves to the mean-square surface slope, the second term on the right-hand side of (11), cannot be neglected. Relative to the data obtained in the slick, those obtained in the hydrodynamically smooth regime of clean water surface are seen in figure 17 to be shifted almost parallel upward and twoward the left. Referring to (11) and (13) the upward and nearly parallel shift of the data indicates that the

contribution to mean-square slope from wave components having their wavenumbers greater than k_s are about the same for all wind velocities in the smooth regime. This trend is along the lines of Phillips concept (Phillips 1958a) of the development of the wave spectrum, in which the higher-frequency waves reach the saturated state earlier. The shift toward the left of the clean-surface data or the shift toward the right of the slick data is also very interesting. This clearly indicates that the wind boundary-layer transition from smooth to rough regime is delayed by the presence of the slick. It **is expected** that the ocean surface becomes smoother when it is covered by a dense oil slick.

The difference of mean-square slope between the clean and the contaminated sea surfaces at low wind velocity is about 0.0115. This difference is the contribution to the mean-square surface slope from wave components having their wavenumbers greater than k_s. Accepting this argument we can estimate from the slope difference the cutoff wavenumber k_c at low wind velocities provided that k_c is smaller than k_γ. From (13) and (14) we have

$$0.0046 \ell_\eta (k_c / k_s) = 0.0115 \qquad k_c = 2.5 \text{ cm}^{-1} \qquad (15)$$

This value is indeed smaller than k_γ which is about 3.6 cm^{-1}. The closeness of these two values indicates that the straightline fitted through the clean surface data at low wind velocities may be the upper bound of the contribution from waves in the gravity range. In other words, the contribution to the mean-square slope at higher wind velocities shown in figure 17 above the extension of this straight line must come from waves in the capillary range. At first look, this consideration may seem rather arbitrary. Actually, since B is very small, the choice of a slightly different cutoff wavenumber k_c has an insignificant effect on the results. On the other hand, the coefficient B' to be shown later, is much greater than B, so that wave components in the capillary range contribute much more effectively to the mean-square sea surface slope than those in the gravity range. Consequently, once the integration of the wave spectrum extends into the capillary range, a change in the trend of the data, such as that shown in figures 16 and 17, is expected. More studies are needed to see whether it is just a coincidence that this separation of slope behavior coincides with the change of the regimes of the wind boundary layer.

An excellent correlation of data between $\overline{s^2}$ and U_{10}^2 / g is shown in the hydrodynamically rough regime of wind. This trend indicates two possibilities : the contribution to mean-square slope

from waves of capillary range is independent of the wind velocity and the coefficient B has a different value for the hydrodynamically rough flow regime; or k_ν is proportional to U_{10}^2. The former cannot be true, because any downward shift of the slope data shown in figure 17, in order to get rid of the contribution from waves in the capillary range, would mean that the contribution from gravity wave components to the slope at the lower portion of high wind velocities is lower than that at the upper portion of low wind velocities. Furthermore, referring to (13), the cutoff wavenumber obtained from the intercept of the straight line fitted to the data at high wind velocities is simply too great to be reasonable.

In summary, the data seem to indicate that the mean-square slope is contributed by wave components from only the gravity range at low wind velocities ($U_{10} < 7$ m/ sec), and from both gravity and capillary ranges at high wind velocities. In addition, the cutoff wavenumber, or as considered by Phillips (1966), the neutrally stable wavenumber is proportional to U_{10}^2, the square of the wind velocity measured at he standard anemometer height. Following this consideration, we now plot U_{10}^2 versus the difference between the slope measured at high wind velocities and that contributed by gravity wave components, and rewrite (11) as

$$s^2 - B \ell_\eta (k_\gamma U_{10}^2 / g) = B' \ell_\eta (k_\nu / k_\gamma) \qquad (16)$$

Therefore, the straight line fitted through the replotted data shown in figure 18 allows an independent determination of the spectral coefficient B' and the dependency of k_γ on U_{10}. It is noted that the trend of the data shown here provides a good verification of the form of the Phillips' capillary-wave spectrum, which has not previously been verified by observations.

The value of B' is found to be

$$B' = 3.15 \times 10^{-2}$$

which is about the value 1.5×10^{-2} offered by Phillips (1966). Comparing the curves, fitted by the spectral coefficients shown in figures 17 and 18 with those shown in figure 4.17 of Phillips (1966), one is inclined to believe that the former may be more accurate than the latter. Moreover, Phillips adopted Miles (1962) calculation of the neutrally stable wavenumber as the cutoff wavenumber of the slope data in his process to obtain B' , while the present technique allows an independent determination of B' and the cutoff wavenumber. The

latter technique is desirable especially when Miles' calculation has not been verified experimentally.

VII . COMPARISON OF LABORATORY AND OCEANIC RESULTS

The average wavelengths obtained at various wind velocities are replotted in figure 19a. As the wind velocity increases, the waves, as described previously, passing the following stages of development : (A) infinitesimal capillary waves, (B) rhombic wave cells, (C) long waves accompanied by parasitic capillaries, and (D) breaking long waves. The mean-square surface slope determined at various wind velocities are replotted in figure 19b. Taking together the results presented in figure 19a, b, we see that capillary waves with infinitesimal amplitudes are the sole contributor to mean-square slope in stage (A), gravity waves are the sole contributor in stage (B), and both contributors in stage (C) and (D)

Because of the great difference between wind fetches existing in the wind-wave tank and the field, the shear velocity rather than the wind velocity should provide a basis for comparison of slope data. The upwind-downwind components of Cox and Munk's data and our laboratory results of the same components are replotted in figure 20a. This comparison is made possible on the basis (Phillips 1958b) that high-frequency wind waves, the principal contributor to surface slopes, reach equilibrium states at very short fetches. Such a concept is further illustrated by Cox's (1958) measurements of mean-square slopes, which reach equilibrium states, ceasing to grow spatially, at a fetch slightly greater than 3 m. The wind fetch for the present experiment is about 6 m.

It has been shown that oceanic slope data are divided into two groups : gravity waves are the sole contributor to sea-surface slope at low wind velocities and both gravity and capillary waves contribute to sea-surface slope at high wind velocities. The portion of the oceanic data fitted by a straightline in figure 20a is the second group. A straightline is also drawn to fit the laboratory data in figure 20a. It is interesting to see that the fitted line for the laboratory data which contributions from both gravity and capillary waves is parallel with the line fitted through the oceanic data which the same contributors; see figure 19.

The same trend of variation between the oceanic and the laboratory data further confirms our earlier discussion : the separation of oceanic slope data into two groups is indeed due to the fact that capillary waves contribute to mean-square sea-surface slope

only at high wind velocities. Moreover, since the slope of the fitted straightline for the oceanic data is related to the spectral coefficients in the equilibrium range, the same slope of the fitted lines shown here for laboratory and oceanic data indicates that the spectral coefficients are universal constants independent of wind fetches. Consequently, the present results also verify the concept on developing the equilibrium wind-wave spectrum : high-frequency wind waves saturate at short fetches.

The cross-wind slope has not been measured in the present tank. However, the fetch for the growth of resonance waves is about half the width of the tank, or 0.5 m, because the slope measurement was made at the center of the tank. According to Cox (1958), the mean-square slope should not rise until the fetch is greater than 1m. Therefore, the cross-wind slope should be negligible in the present tank. Consequently, the upwind-downwind component of the present measurement should be nearly the total slope.

The upwind-downwind components of the laboratory results are plotted along with the mean-square slopes of the sea surface in figure 20b. Excellent agreement is seen between the oceanic data and the laboratory results except at low wind velocities, where the wind boundary layer in the laboratory tank is not even turbulent. The boundary layer in the present tank becomes fully turbulent when the wind-shear velocity is greater than 12 cm/sec. The agreement of oceanic and laboratory data further substantiates some previous considerations the spectral coefficients are indeed universal; the spreading of wave-number vectors is nearly isotropic for the sea and is nearly unidirectional in the laboratory.

The comparison shown in figure 20b explains the discrepancy between the oceanic (Cox and Munk 1956) and the laboratory (Cox 1958, Wu 1971) results. Furthermore, the agreement on one hand implies that short waves are directly generated by the wind and the wind-shear velocity is therefore the appropriate parameter for correlating results obtained at different fetches. On the other hand, the agreement indicates the possibility of modeling microstructures at the sea surface in a laboratory tank.

VIII . CONCLUSION

In the present study, the microstructure of the wind-disturbed water surface, characterized by surface-slope and surface-curvature distributions, is measured in a laboratory tank under various wind and wave conditions. It is shown that wind waves arise at about the

time when the airflow boundary layer becomes turbulent. The relative frequencies of occurrence of various slopes generally follow a normal distribution. At lower wind velocities, the formation of parasitic waves causes a skewed slope distribution; at high wind velocities, the wave breaking causes a peaked slope distribution. The skewed slope distribution may produce different back scattering of electromagnetic waves from the leeward and from windward faces of the basic wave profile.

The curvature distribution of the wind-disturbed water surface observed from different angles is generally skewed with greater radius of curvature at steeper viewing angles from the normal to the mean water surface. As the wind velocity increases, the average radius of curvature decreases; rapidly at low wind velocities when waves are effectively excited by wind, and gradually at high wind velocities when waves approach saturated state. The skewness is caused by the presence of parasitic capillaries at low wind velocities and by nonlinear wave-wave interaction at high wind velocities. The back scattering measurement is ideally made at small angles from the normal, where the sea surface is nearly isotropic.

The present measurements of surface curvatures are the only set of data of its kind. The mean-square surface slopes are compared with those determined in the field, and the difference is explained as a result of various directional distribution of wave components. Equilibrium energy spectra of wind waves was first established for the gravity range and later extended to the capillary range. The verification of the latter extension and the determination of the spectral coefficients for both ranges are discussed on the basis of the experimental results for mean-square slopes. Good agreement between present and oceanic results indicate a possible modeling of the microstructure of the air-sea interface in a laboratory tank.

ACKNOWLEDGEMENT

This is a summary report of our work on measurements and modeling of microstructures of the air-sea interface. This program is under the direction of Mr. M. P. Tulin, who also suggested the design of the optical instrument, and of Dr. S. G. Reed, Jr., who also reviewed this report. Portions of this report have been published elsewhere. This work was supported by the Office of Naval Research under Contracts N° N00014-70-C-0345, NR 220-016 and N° N00014-72-C-0509, NR 062-472.

REFERENCES

COX, C.S., and MUNK, W.H., 1956, "Slopes of the Sea Surface Deduced from Photographs of Sun Glitter," 6, No. 9, Scripps Institution of Oceanography.

COX, C.S., 1958, "Measurements of Slopes of High-Frequency Wind Waves," J. Mar. Res. 16, 199-225.

HASSELMANN, K., 1971, "On the Mass and Momentum Transfer Between Short Gravity Waves and Large-Scale Motions," J. Fluid Mech. 50, 189-205.

LONGUET-HIGGINS, M.S., 1959, "The Distribution of the Sizes of Images Reflected in a Random Surface," Proc. Cambridge Phil. Soc. 55, 91-100.

LONGUET-HIGGINS, M.S., 1969, "A Nonlinear Mechanism for the Generation of Sea Waves," Proc. Roy. Soc. A 311, 371-89.

LONGUET-HIGGINS, M.S., and STEWART, R.W., 1960, "Changes in the Form of Short Gravity Waves on Long Waves and Tidal Currents," J. Fluid Mech. 8, 565-83.

MILES, J.W., 1962, "On the Generation of Surface Waves by Shear Flows," J. Fluid Mech. 13, 433-48.

PHILLIPS, O.M., 1958a, "The Equilibrium Range in the Spectrum of Wind-Generated Waves," J. Fluid Mech. 4, 426-34.

PHILLIPS, O.M., 1958b, "Comment on a Paper by Dr. Cox," J. Mar. Res. 16, 226-30.

PHILLIPS, O.M., 1963, "On the Attenuation of Long Gravity Waves by Short Breaking Waves," J. Fluid Mech. 16, 321-32.

PHILLIPS, O.M., 1966, "The Dynamics of the Upper Ocean," Cambridge University Press.

SCHLICHTING, H., 1968, "Boundary-Layer Theory," 6th Ed., McGraw-Hill Book Company, New York.

SCHOOLEY, A.H., 1954, "A Simple Optical Method for Measuring the Statistical Distribution of Water Surface Slopes," J. Opt. Soc. Am. 44, 37-40.

SCHOOLEY, A.H., 1955, "Curvature Distribution of Wind-Created Water Waves," Trans. Am. Geophys. Union 36, 273-78.

SCHULE, J.J., Jr., LLOYD, S.S., and DeLEONIBUS, P.S., 1971, "A Study of Fetch-Limited Wave Spectra with an Airborne Laser," J. Geophys. Res. 76, 4160-71.

WU, JIN, 1968, "Laboratory Studies of Wind-Wave Interactions," J. Fluid Mech. 34, 91-112.

WU, JIN, 1970, "Wind-Wave Interactions," Phys Fluid 13, 1926-1930.

WU, JIN, 1971a, "Slope and Curvature Distributions of Wind-Disturbed Water Surface," J. Opt. Soc. Am. 61, 852-58.

WU, JIN, 1971b, "Observations on Long Waves Sweeping Through Short Waves," Tellus 23, 364-70.

WU, JIN, 1972, "Surface Curvature of Wind Waves Observed from Different Angles," J. Opt. Soc. Am. 62, 395-400.

WU, JIN, 1972, "Sea-Surface Slope and Equilibrium Wind-Wave Spectra," Phys. Fluids 15, 741-47.

WU, JIN, LAWRENCE, J.M., TEBAY, E.S., and TULIN, M.P., 1969, "A Multiple Purpose Optical Instrument for Studies of Short Steep Water Waves," Review of Scientific Instruments 40, 1209-13.

* * *

(a) General View of Wind-Wave Tank

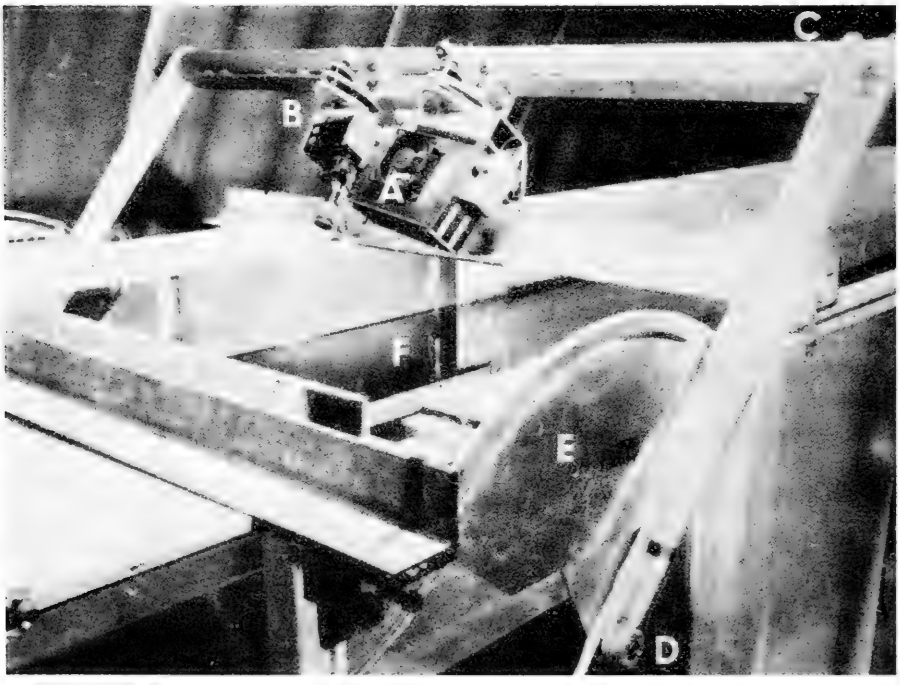

A = Light Source and Adjustment Assembly; B = Light-Signal Receiver and Adjustment Assembly
C = Cross-Beam and Arm Unit; D = Hinge-Joint Support; E = Angle Indicator; F = Water Surface

(b) Optical Instrument

FIGURE 1 - WIND-WAVE TANK AND INSTRUMENTS

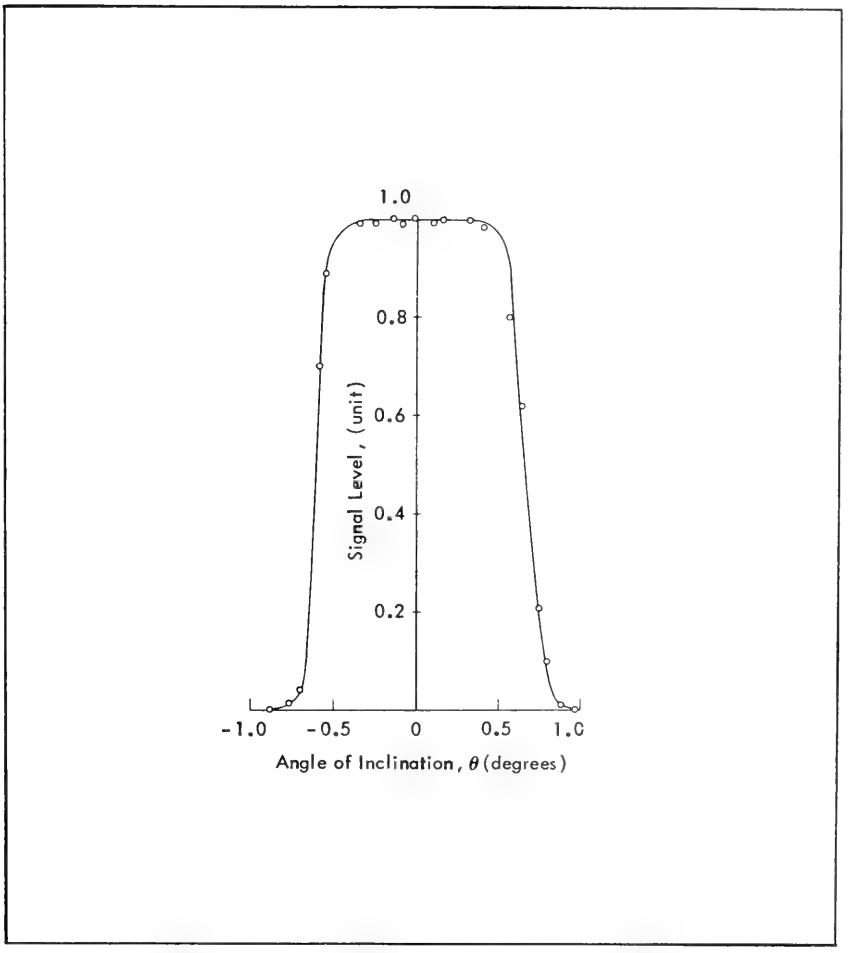

FIGURE 2 - ANGULAR RESPONSE OF OPTICAL INSTRUMENT.

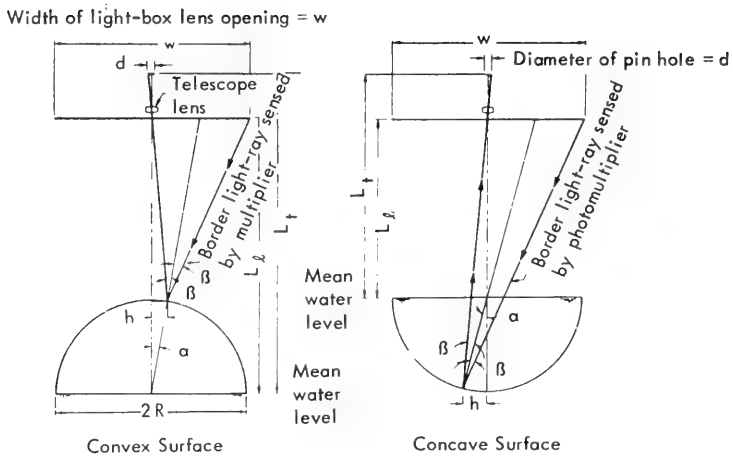

(a) Geometry

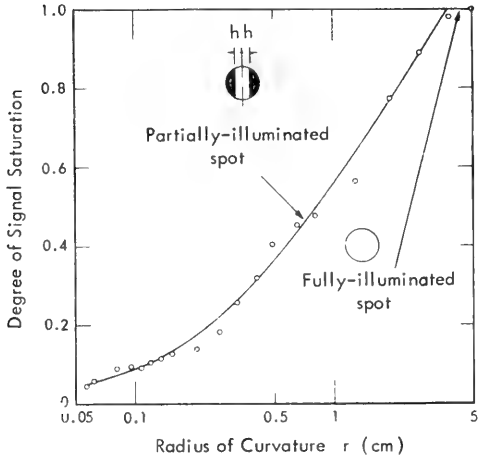

(b) Calibration

FIGURE 3 - CURVATURE RESPONSE OF OPTICAL INSTRUMENT.

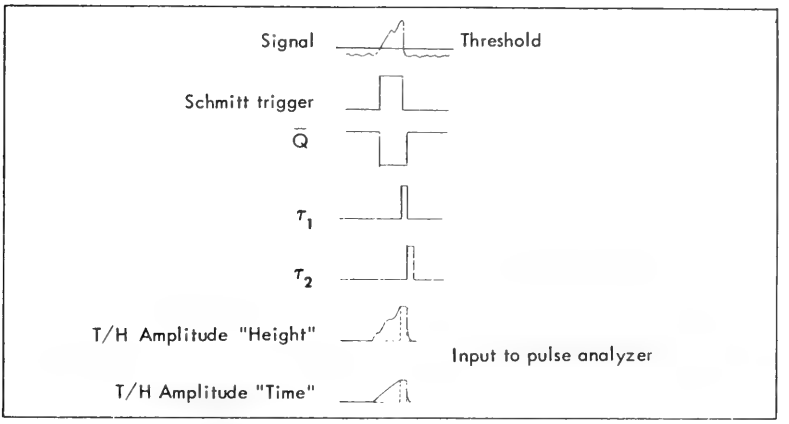

(a) Pulse Shape and Timing Diagram of Pulses Passing Various Stages of Pulse Conditioner

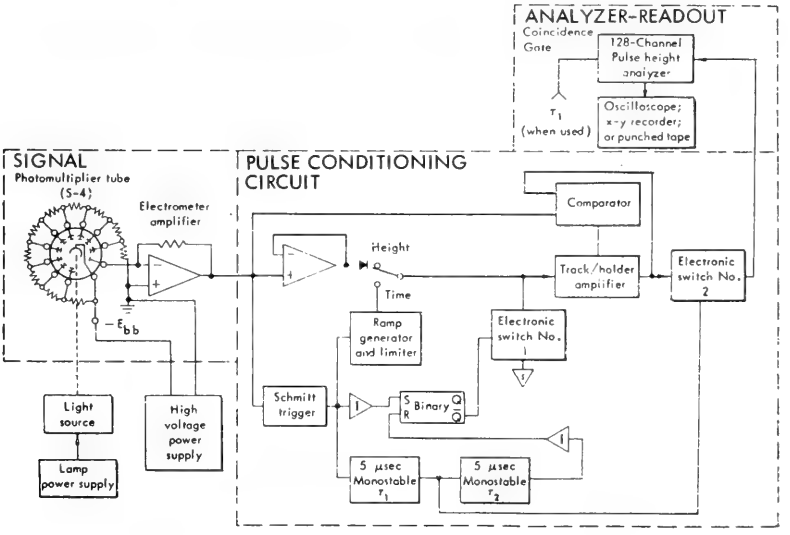

(b) Block Diagram of Optical Instrument

FIGURE 4 - ELECTRONICS OF OPTICAL INSTRUMENT.

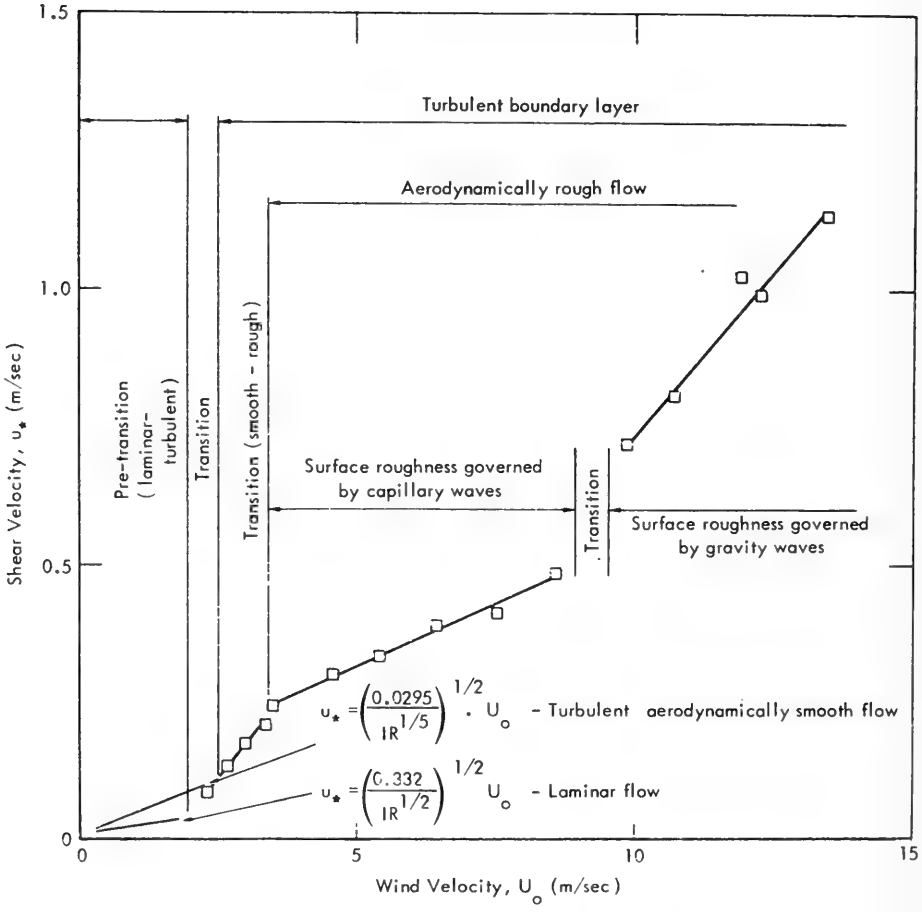

FIGURE 5 - WIND-SHEAR VELOCITY AND BOUNDARY-LAYER REGIMES

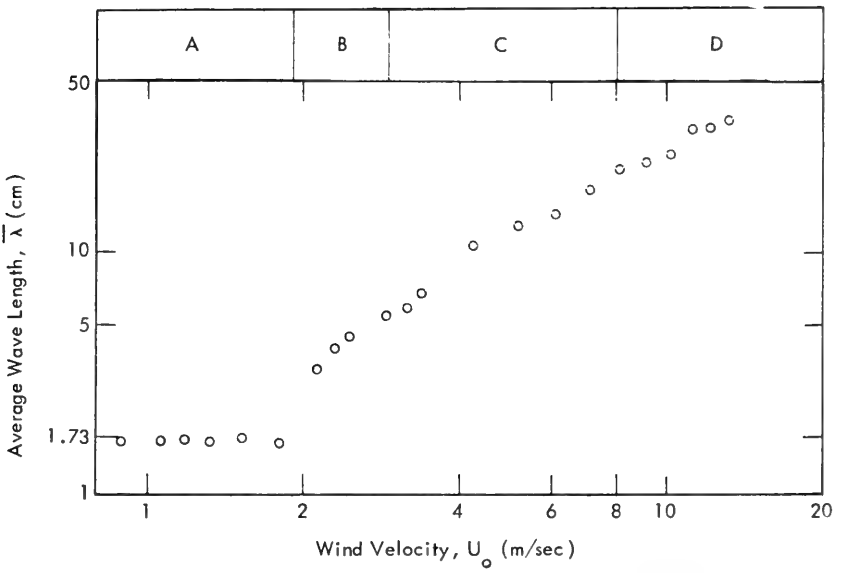

FIGURE 6 - GROWTH OF WIND-WAVES. Stages of wave growth with wind velocity: (A) Capillary waves; (B) Rhombic, short gravity; (C) Gravity waves with parasitic capillaries; (D) Breaking gravity waves.

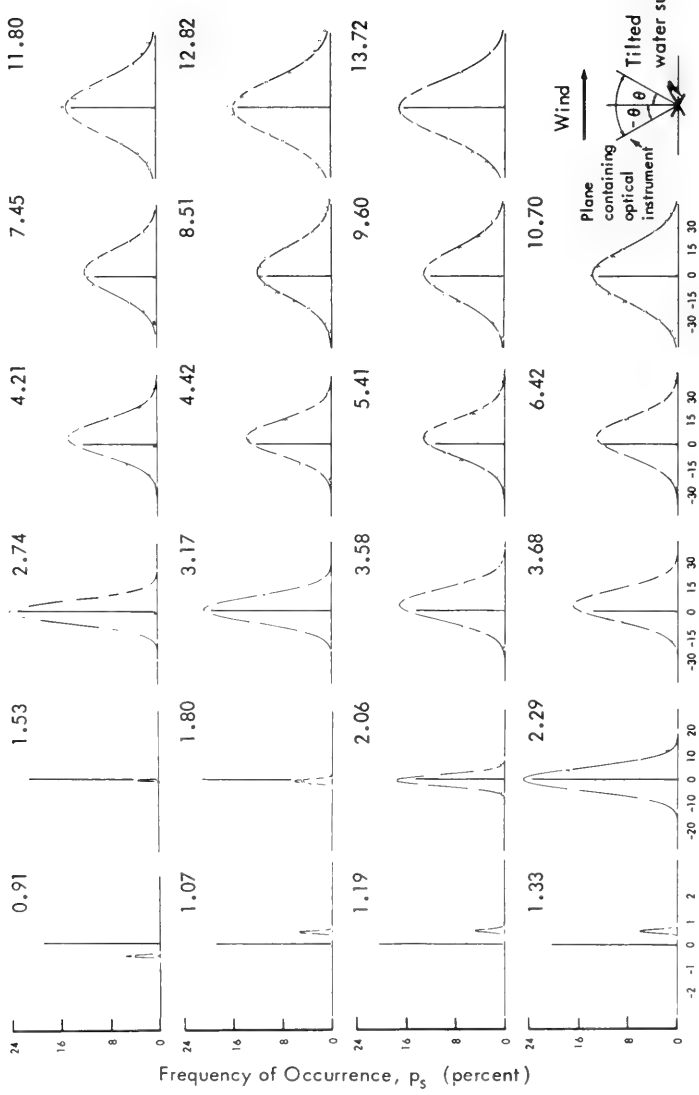

FIGURE 7 – SURFACE SLOPE DISTRIBUTIONS.

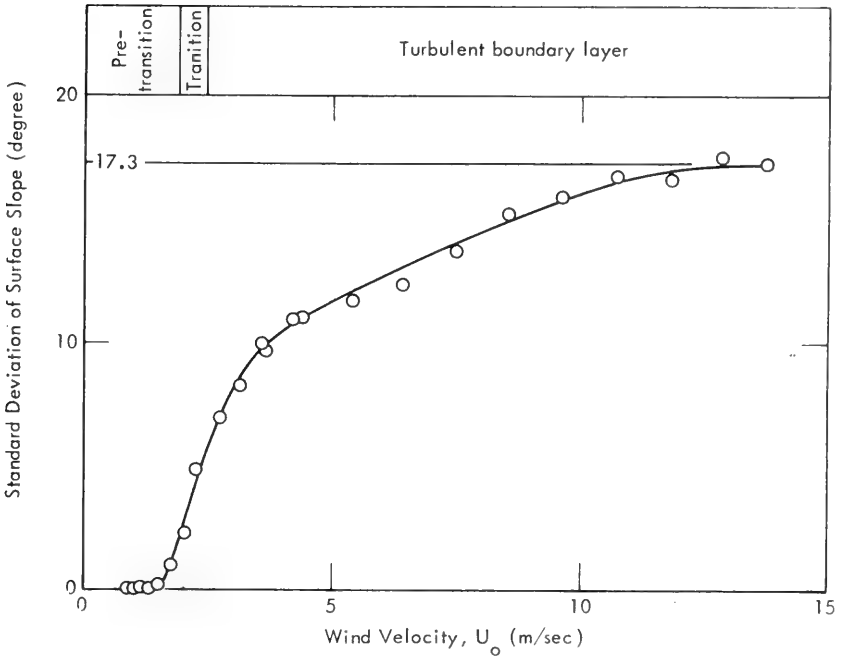

FIGURE 8 - INCEPTION OF HIGH-FREQUENCY COMPONENTS OF WIND WAVES.

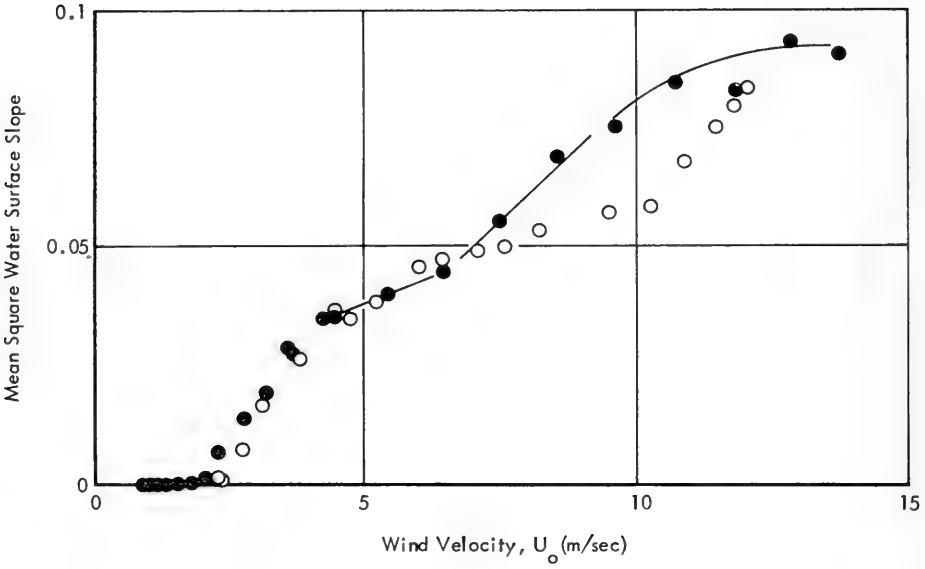

FIGURE 9 - COMPARISON OF PRESENT RESULTS (●) WITH THOSE OBTAINED BY COX (O)

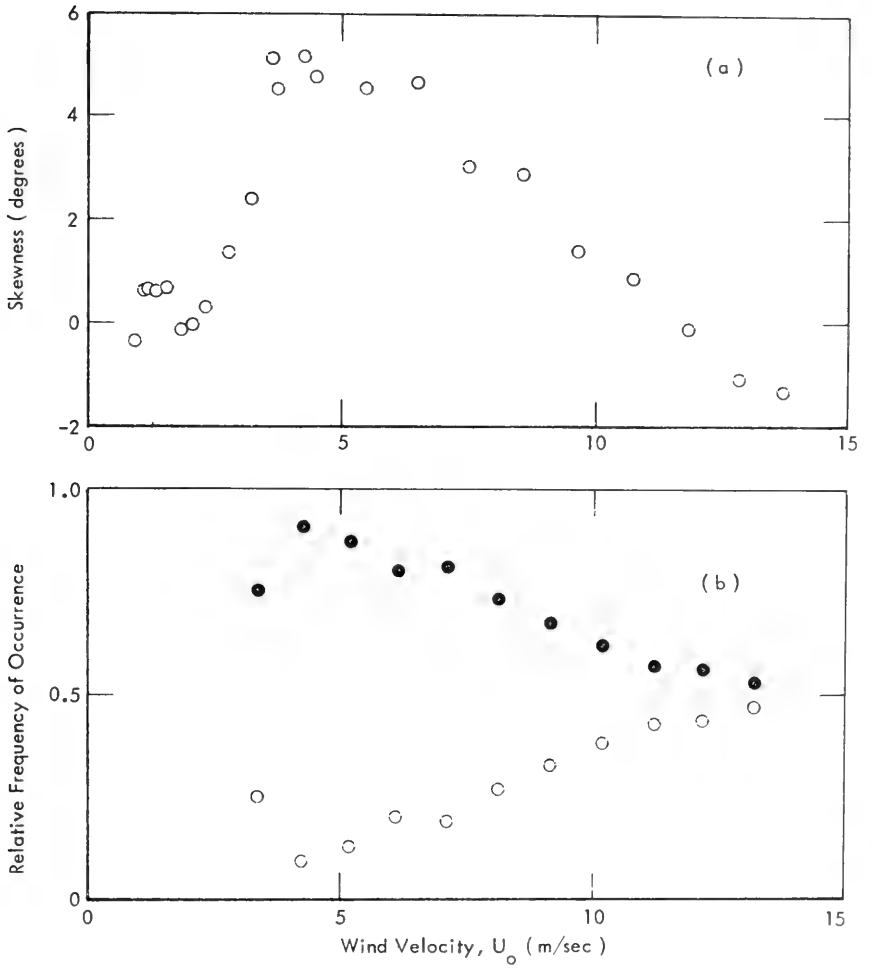

FIGURE 10 - SKEWNESS OF WATER-SURFACE SLOPES AT VARIOUS WIND VELOCITIES
(a) Skewness of Slope-distribution curves;
(b) Relative Frequency of Occurrence of Capillary Waves at Upwind (O) and Downwind (●) Faces of Gravity Waves

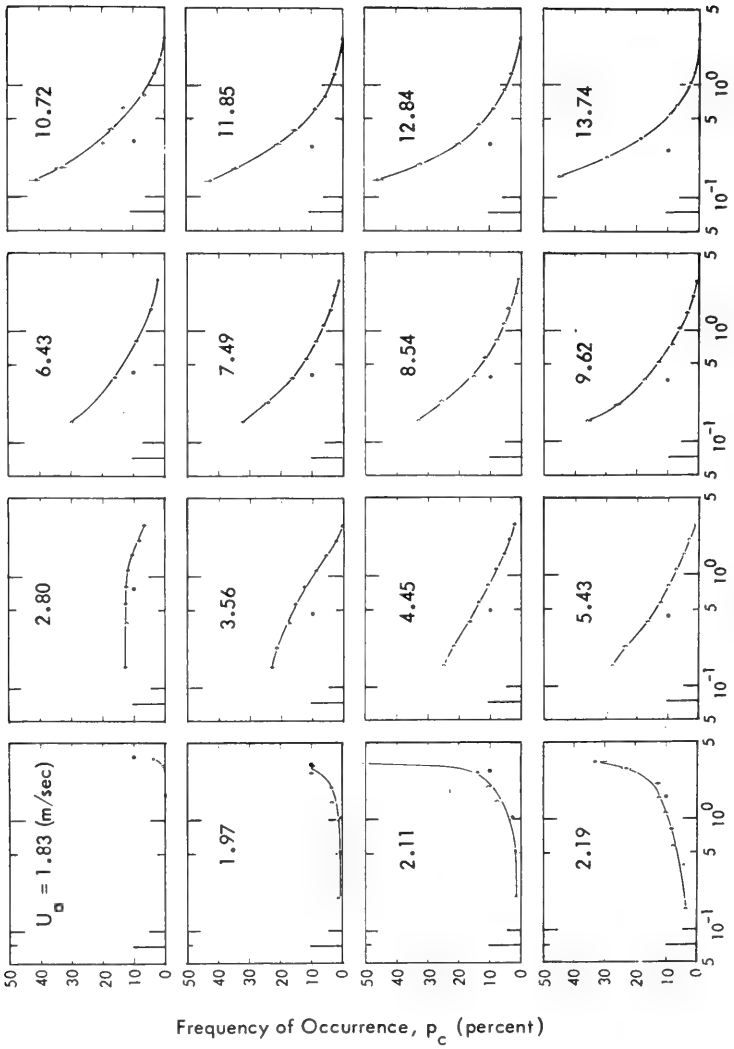

FIGURE 11 – SURFACE CURVATURE DISTRIBUTION

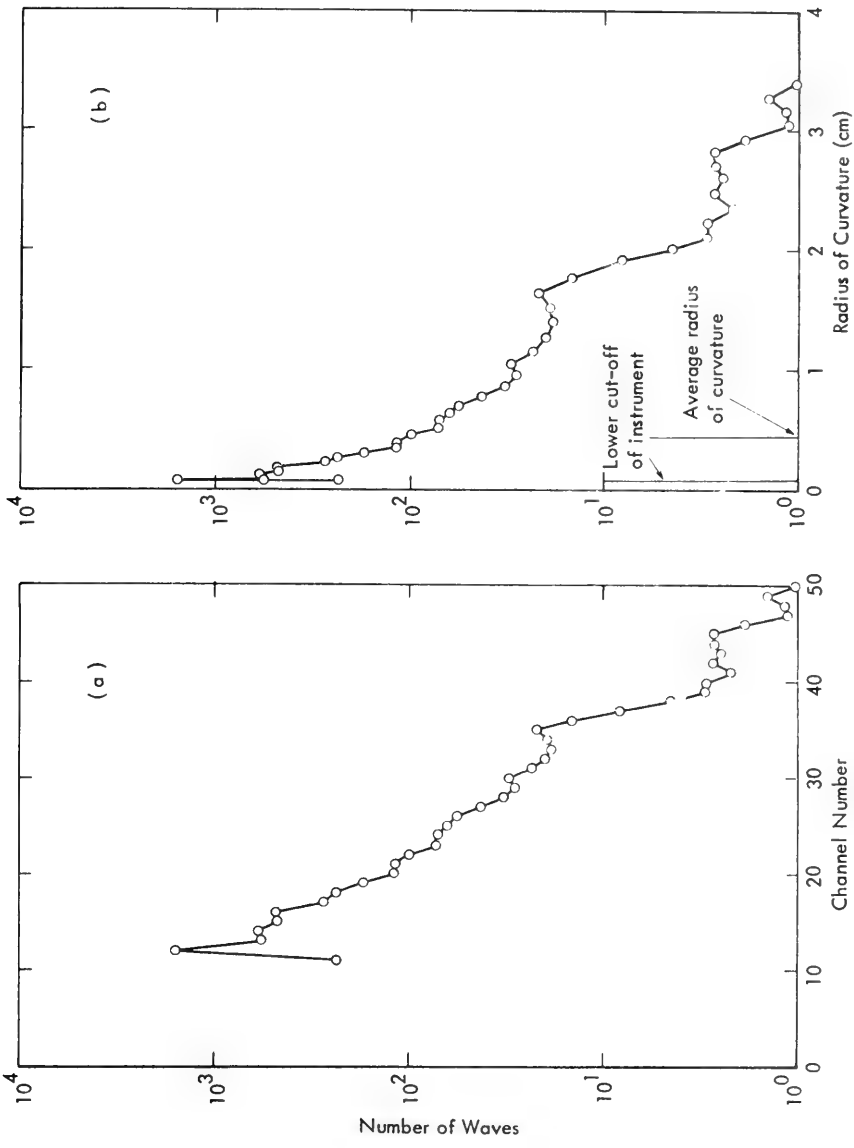

FIGURE 12 - TYPICAL DATA

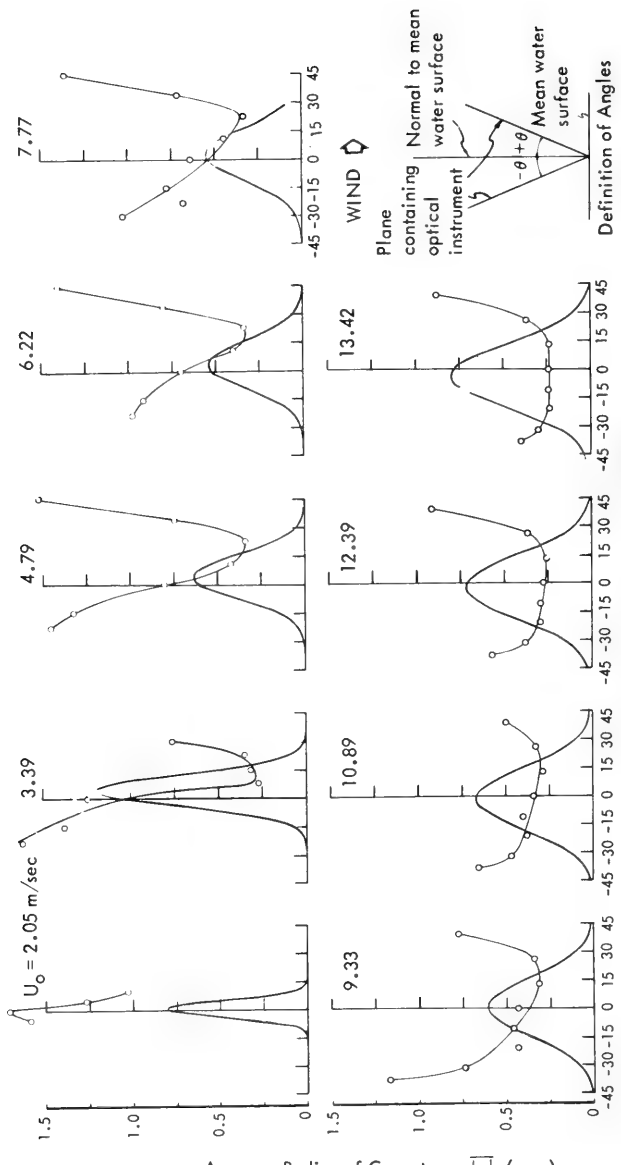

FIGURE 13 - ANGULAR DISTRIBUTION OF AVERAGE RADIUS OF CURVATURE UNDER VARIOUS WIND CONDITIONS

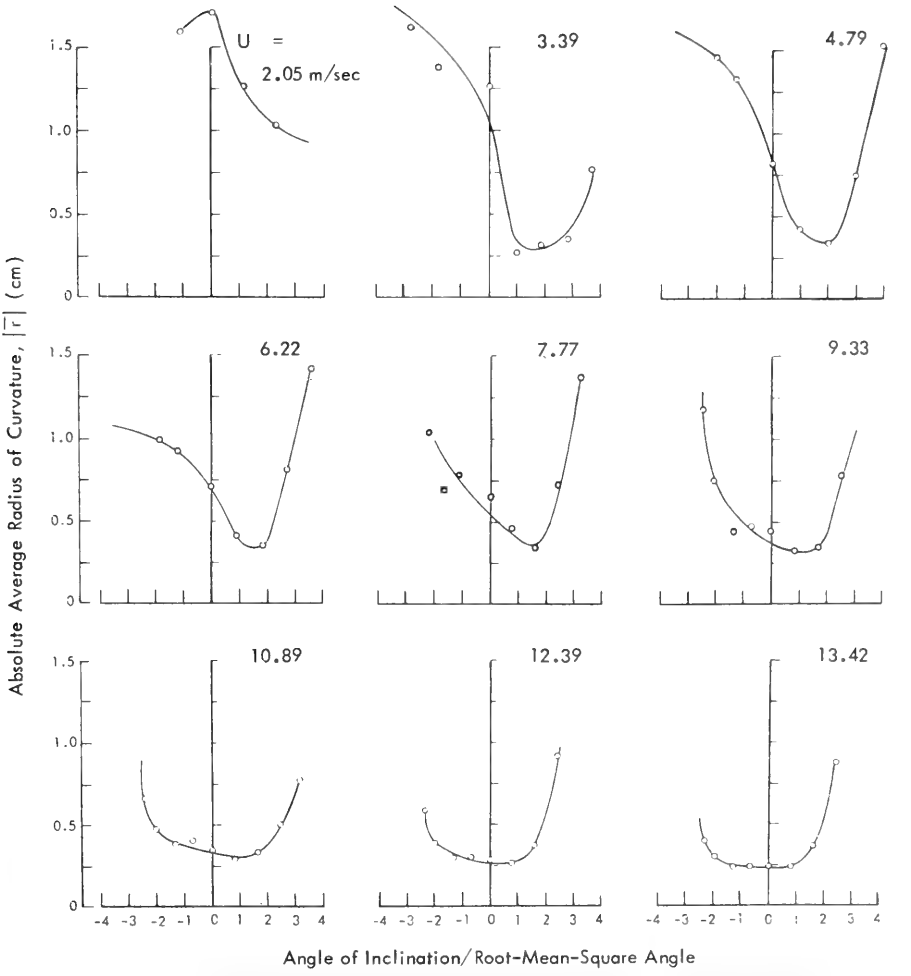

FIGURE 14 - ANGULAR DISTRIBUTION OF RADIUS OF CURVATURE NORMALIZED WITH RESPECT TO ROOT-MEAN-SQUARE SLOPE.

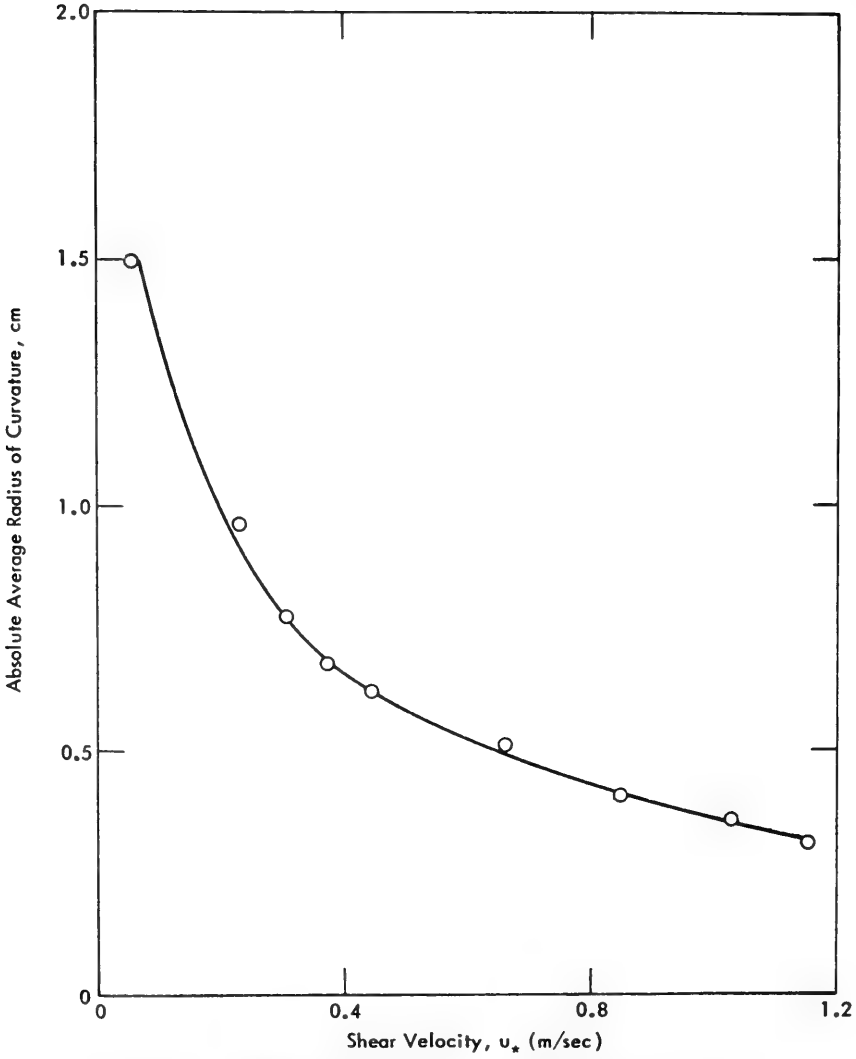

FIGURE 15 - VARIATION OF RADIUS OF CURVATURE WITH WIND SHEAR VELOCITY

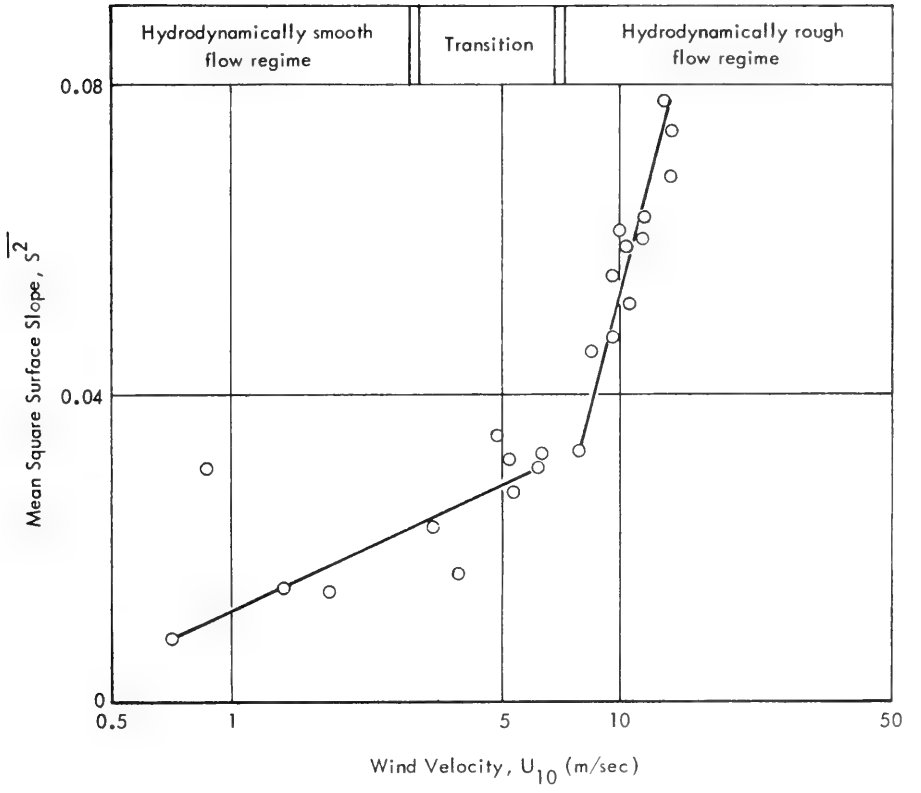

FIGURE 16 - MEAN-SQUARE SEA SURFACE SLOPE IN DIFFERENT BOUNDARY-LAYER REGIMES OF WIND

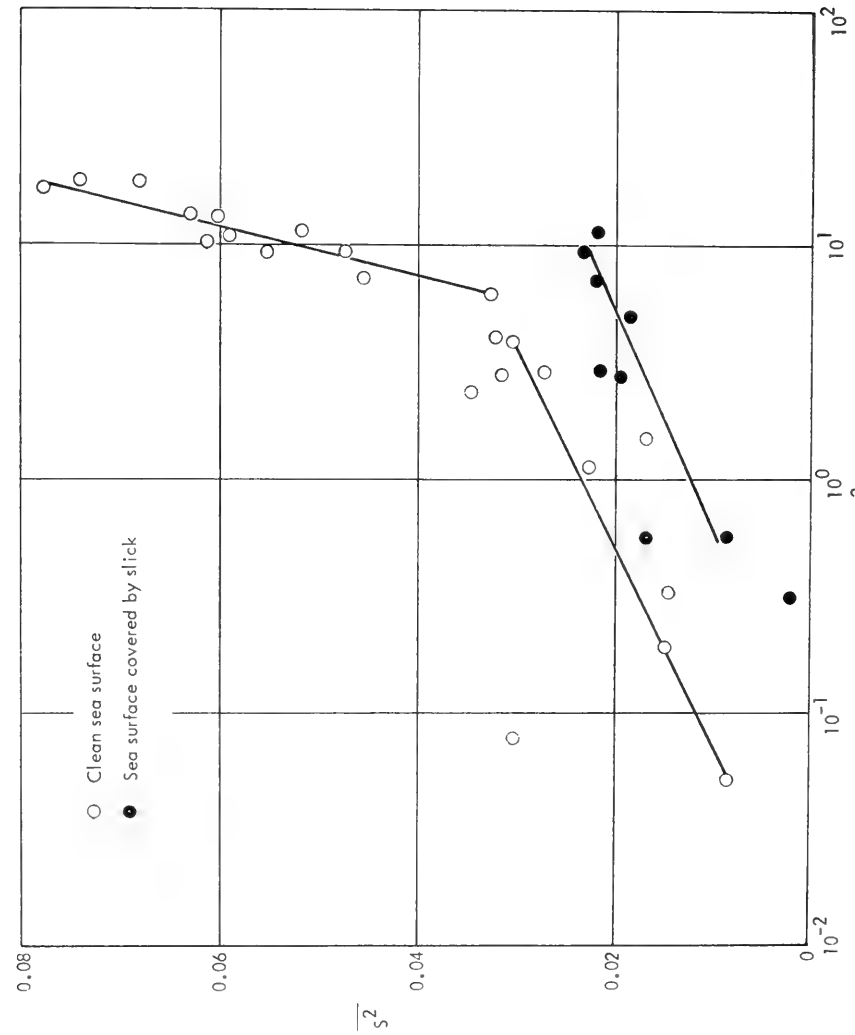

FIGURE 17 - DETERMINATION OF SPECTRAL CONSTANTS FROM RESULTS OF MEAN-SQUARE SURFACE SLOPES.

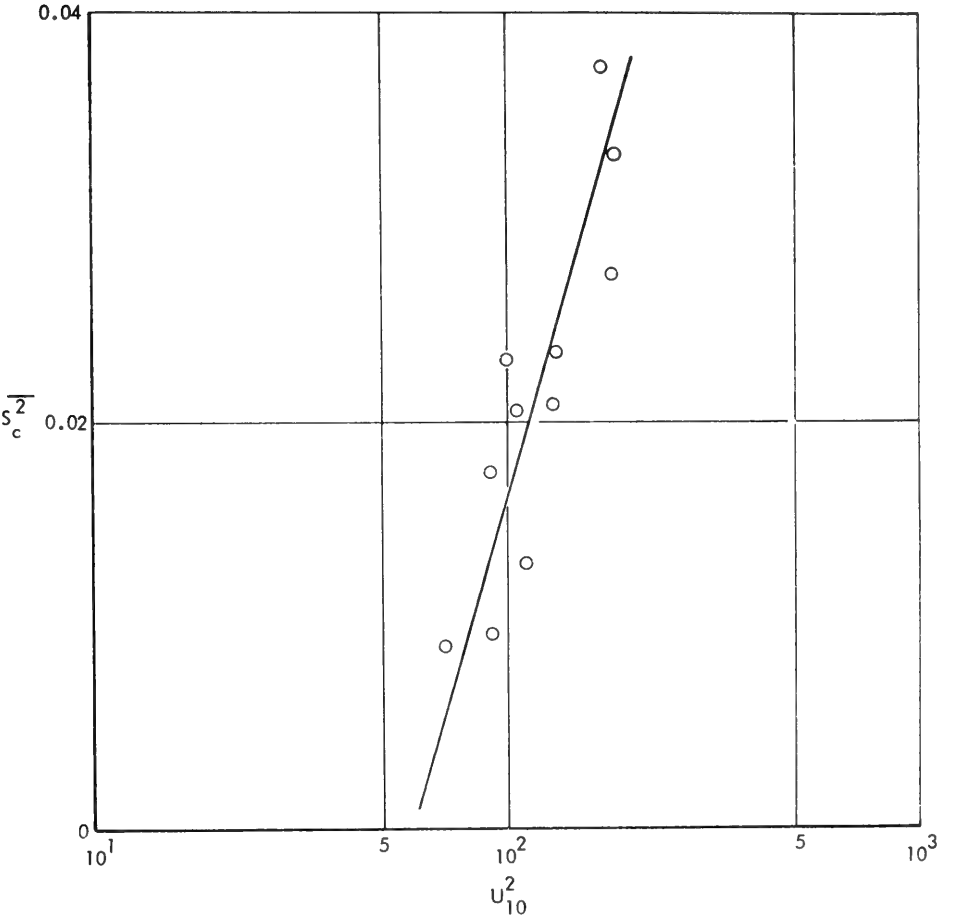

FIGURE 18 - CONTRIBUTION OF CAPILLARY WAVES TO MEAN-SQUARE SURFACE SLOPE.

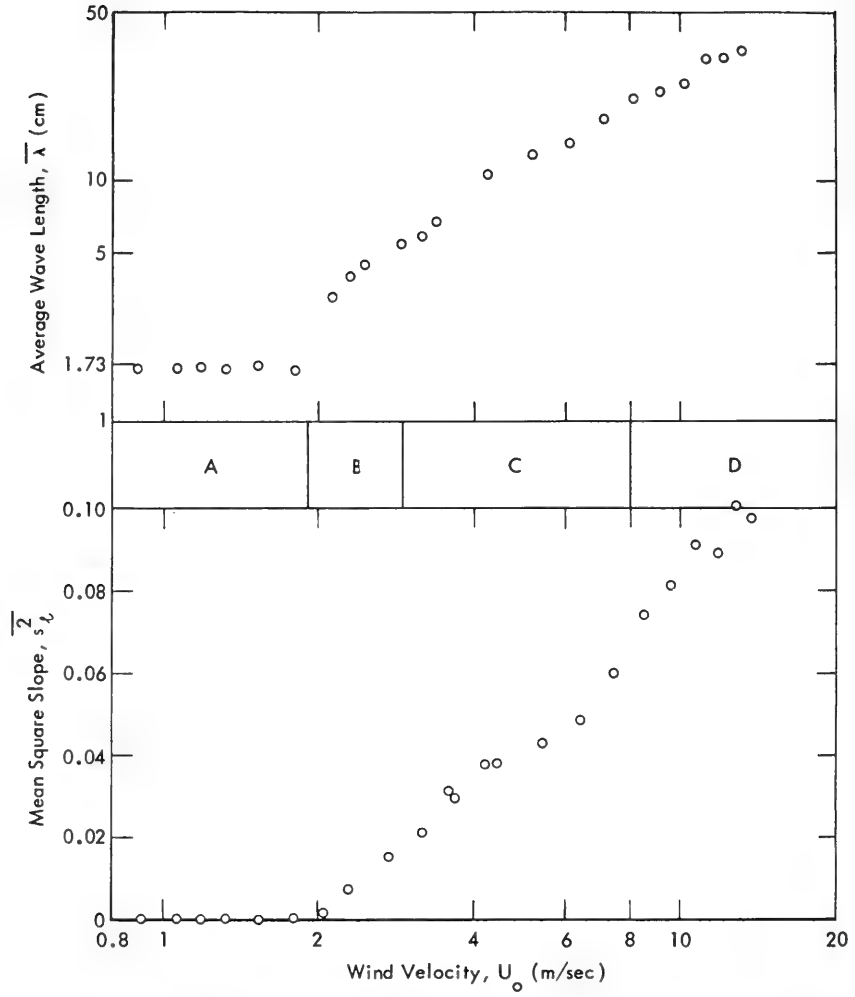

FIGURE 19 - LABORATORY MEASUREMENTS OF DOMINANT-WAVE LENGTH AND MEAN SQUARE SURFACE SLPOE. Stages of wave growth with wind velocity: (A) Capillary waves; (B) Rhombic, short gravity waves; (C) Gravity waves with parasitic capillaries; (D) Breaking gravity waves.

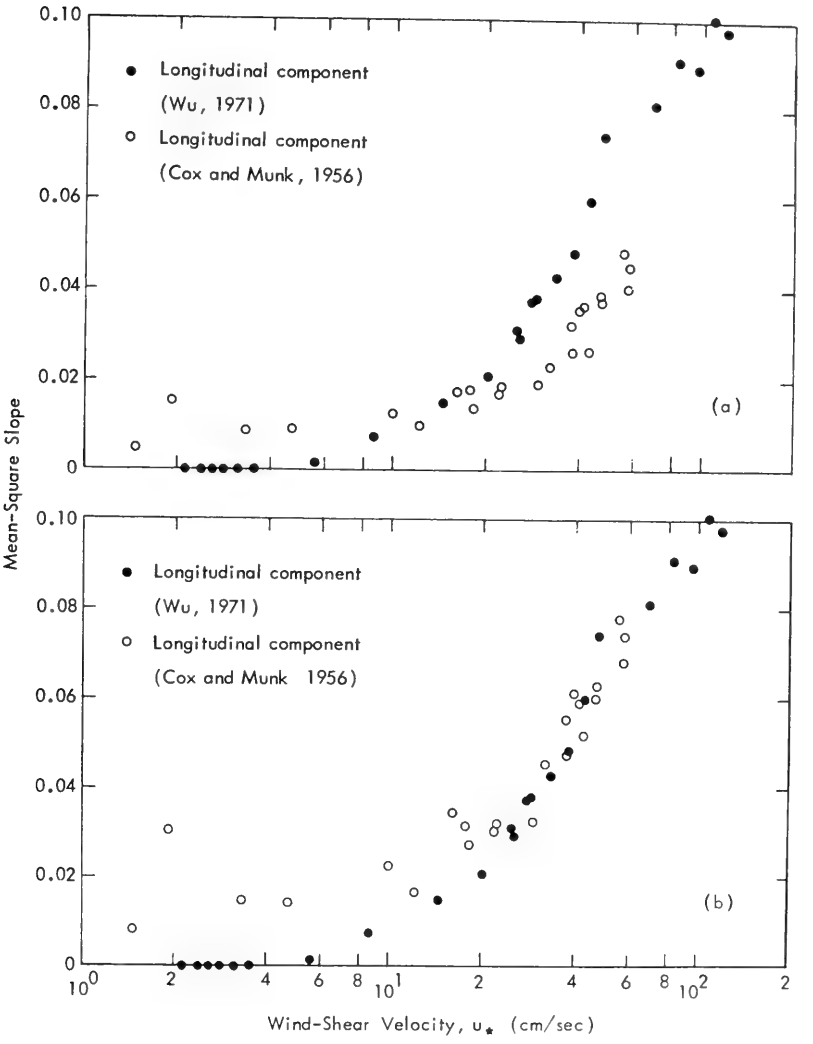

FIGURE 20 - COMPARISON OF OCEANIC AND LABORATORY SLOPE MEASUREMENTS

FRONTIER PROBLEMS

Friday, August 25, 1972

Morning Session

Chairman : Dr. W.E. Cummins
Naval Ship Research and Development Center,
Bethesda, U.S.A.

THE WAVE GENERATED BY A FINE SHIP BOW

T. Francis Ogilvie
University of Michigan
Ann Arbor, Michigan, U.S.A.

ABSTRACT

The flow field near the bow of a ship has some characteristics of a high-Froude-number problem, even if ship speed is moderate. Some of these features can be predicted by slender-body theory if the usual assumptions of that theory are modified in the bow region to allow for the occurrence of longitudinal rates of change greater than normally assumed. Analytical results are derived for the case of a fine wedge-shaped bow, in which case a universal curve can be drawn for the shape of the bow wave on the hull, regardless of speed, draft, or entrance angle (all within limits, of course). The lengths must be nondimensionalized by the quantity $(HU^2/g)^{1/2}$, where H is the draft, U is ship speed, and g is the gravitation constant. It is shown how this mathematical model matches with the usual slender-body model and how it eliminates certain of the objectionable features of the latter, with only minor complications. Some experimental results are shown which generally confirm the predictions.

I. INTRODUCTION

The Froude number can be taken as a rough measure of the relative magnitude of inertial forces with respect to gravitational forces in the interior of a fluid region. In the usual problem of ship hydrodynamics, neither of these forces dominates the other in the overall picture, and this fact is recognized in the custom of treating Froude number as a quantity which is $O(1)$ as $\epsilon \to 0$, where ϵ is the small parameter that provides the reference for ordering all quantities

in the problem. If we take as the Froude number $F = U/\sqrt{gL}$, where U is the forward speed, L is ship length, and g is the gravitational acceleration, then the statement that $F = O(1)$ means that there is a characteristic length U^2/g which is comparable with ship length and which is unrelated to the small parameter, ϵ.

In a strict sense, this should always be the case. Suppose that ϵ is a measure of ship thinness or of ship slenderness. As $\epsilon \to 0$, there is no reason to expect that U^2/g should become either very large or very small; one should certainly be able to specify the forward speed independently of ship thinness or slenderness, and g does not vary significantly in any case.

But there are a couple of reasons sometimes not to accept this apparently natural assumption: a) When we develop an asymptotic analysis, we expect it to be more and more nearly valid as the small parameter becomes infinitesimally small. But we usually obtain just one or two terms in our expansions, and we try to use those expansions for computations when the small parameter is quite finite. We may actually obtain more accurate formulas if we assume an unnatural relationship between ϵ and the length U^2/g. For example, if the latter is actually comparable to ship beam in the cases of practical interest, we may be better off in assuming that $U^2/g = O(\epsilon)$ when we formulate the boundary value problem. b) The implication about the ratio of inertial and gravitational forces may be locally invalid. That is, in some regions, one of these forces may dominate the other to the extent that the asymptotic solution gives grossly wrong predictions in those regions.

The first of these two points I have discussed at length in a previous paper [1]*. In fact, the idea was not original there; it was used many years earlier by Vossers [2] and also by Joosen [3], for example.

The second point is already implicit in slender-ship theory, for one assumes there that rates of change in the transverse directions are very great compared with rates of change in the longitudinal direction, at least in a region near the ship. This means that accelerations (and thus forces) are greater in one direction than another, and the ratio between them depends on ϵ. Thus, to the extent that

---

* Numbers in square brackets denote references listed at the end of the paper.

we accept slender-ship theory, we have already recognized that the overall Froude number does not characterize the ratio of inertial and gravitational forces uniquely throughout the fluid region.

This idea was also discussed in the earlier work [1] already mentioned. There I pointed out that special order-of-magnitude consideration should be given to conditions near the ship bow. Because of the presence of the free surface, the fluid particles just a very short distance ahead of the bow are quite unaffected by the oncoming ship, until -suddenly ! - those particles are in the region of highly accelerated flow around the ship bow. The effects of water displacement by the moving ship are much greater than the effects of gravity, which normally hold the water surface horizontal, and so the presence of the free surface is momentarily simply equivalent to a pressure-relief surface. All of this can be implied by saying that the flow near the ship bow is a high-Froude-number flow.

Thus we come to the concept that the bow flow is a high-Froude-number problem, even if the ship speed is moderate. The previous argument then suggests that we try to relate the Froude-number aspect of the bow flow to the slenderness parameter. In this paper, I have done this in a very pragmatic way :

In the usual slender-body theory, we assume, in a symbolic notation, that $\partial/\partial x = O(1)$ but that $\partial/\partial y$ and $\partial/\partial z = O(1/\epsilon)$, where x is the longitudinal coordinate. This means that rates of change in the longitudinal direction are smaller than rates of change in the transverse direction by an order of magnitude ϵ . (It is this very gradual variation in the longitudinal direction that leads to the typical feature of the slender-ship near field, namely, that the free surface acts as a rigid wall. Rates of change are so gradual that gravity dominates and holds the free surface horizontal.) This intuitive picture is formalized in the mathematics by stretching coordinates in the transverse directions by a factor $1/\epsilon$.

Now we suppose that, near the bow, rates of change of the flow variables should be greater than those usually assumed in slender-body theory. We may expect to introduce such a notion formally by stretching the x coordinate from the bow sternward. But what should be the degree of stretching ? Let us define a new longitudinal coordinate, $X = x/\epsilon^n$, with x and X both measured from the bow in the downstream direction. If $n = 0$, we have the usual slender-body theory, and if $n = 1$ we have the original problem in three dimensions. (In the latter case the stretching is isotropic.) Therefore we seek a value of n such that $0<n<1$. It turns out that a nontrivial problem

arises only if $n = 1/2$, and so I make such an assumption in this paper.

The resulting theory is still a slender-body theory, in that the first approximation involves a Laplace equation in the two transverse dimensions only. The rates of change in the near field are much greater in the transverse direction than in the longitudinal direction, but the difference in order of magnitude between them is less than in the usual slender-body theory.

One can describe the theory as being valid (presumably) in a region just behind the bow in which $x = O(\epsilon^{1/2})$, where x is measured in units such that ship length is $O(1)$. It will be convenient sometimes to speak of a "bow near field", by which I shall mean an asymptotically defined region in which $x = O(\epsilon^{1/2})$ and $r = (y^2+z^2)^{1/2} = O(\epsilon)$. In the "usual near field", we assume that $x = O(1)$ and $r = O(\epsilon)$, whereas in the far field all variables are $O(1)$ (which means simply that we can fix our attention on a point in the fluid and the point is not supposed to move as $\epsilon \to 0$).

Some interesting things happen in the bow near field. We no longer have the rigid-wall free-surface condition which is typical of the usual near field. Instead, we find exactly the same linear free-surface conditions that are familiar from classical thin-ship theory, for example. But the partial differential equation is the Laplace equation in two dimensions, as in ordinary slender-body theory. This means that we must solve an equation in the variables y and z, with boundary conditions involving derivatives with respect to x.

The explicit solution of this problem is presented for the case of a thin, wedge-shaped bow. The shape of the wave along the side of the body has been computed, and experiments were conducted for comparison with the predictions. The results are in fair agreement.

From the analysis, it can be concluded that an appropriate length for purposes of nondimensionalization is the geometric mean of two lengths, the draft and the characteristic length, $\lambda/2\pi = U^2/g$. That is, we refer all lengths to $(HU^2/g)^{1/2}$, where H is the draft of the forebody. The extent to which the experimental data then collapse into simple curves is quite remarkable. Even in cases of very low forward speed, in which the analysis fails completely, the same data collapse still appears to occur.

The conditions to be satisfied in the bow near field automatically match with the conditions in the usual near field of slender-body theory. So it is not surprising that the solutions also match auto-

matically, in the sense of the method of matched asymptotic expansions. We can say that the new analysis actually encompasses the usual slender-ship theory, in that the formulas and equations of the new analysis include all of the terms in the corresponding expressions, plus some extra terms that would be considered as of higher order, in the usual theory.

It is quite striking how the solution of the bow-near-field problem goes over into the solution for the usual slender-body near field : In a region extremely close to the bow, the flow has the character expected of a high-Froude-number flow, i. e., the fluid velocity is mostly perpendicular to the plane of the undisturbed free surface. However, as $x/\epsilon^{1/2} \equiv X \to \infty$, the fluid velocity at the plane of the undisturbed free surface becomes approximately parallel to that plane. The wave elevation alongside the body changes order of magnitude in this transition : Wave elevation is $O(\epsilon^{3/2})$ in the bow near field, but it is $O(\epsilon^2)$ in the usual slender-ship near field ; the present analysis shows how this change takes place.

Finally, it should be mentioned that this analysis probably contains no information that is not inherent in a thin-ship analysis. However, the information which is available from the present analysis is quite easily obtainable, in contrast to the usual situation with thin-ship calculations. For example, the calculation of wave profile along the side of the ship was carried out in a few hours with a desk calculator ! Also, there are other possible applications of the ideas contained herein, applications which would probably not be feasible with thin-ship theory as a starting point. For example, Hirata [4] has treated the case of a cambered thin ship (actually with zero thickness) and Baba [5] has analyzed a flat ship by this basic method. The latter problem was partly anticipated by Maruo [6] .

II. THE BOW-FLOW PROBLEM

Let the ship be travelling in the negative x direction, the origin of coordinates being fixed to the bow. The z axis points upwards. The ship geometry is defined by the formula

$$y = \pm b(x, z) ,$$

where the non-negative function $b(x, z)$ is the hull offset corresponding to the point $(x, 0, z)$ on the ship centerplane. The free surface shape is given by the formula

$$z = \zeta(x, y) ,$$

defined for $|y| > b(x, 0)$.

It is assumed that the ship is "slender", which means that there is a small parameter, ϵ , characterizing the smallness of beam/length and draft/length ratios. As $\epsilon \to 0$, the ship shrinks down to a line, the part of the x axis between the origin and $x = L$, L being the ship length at the waterline. But "slenderness" means more than this. It implies also that the size and shape of hull cross-sections change gradually in the longitudinal direction. In particular, we shall require that

$$\frac{\partial b}{\partial x} = O(\epsilon) , \quad 0 < x < L ,$$

even in the bow near field.

The "bow near field" is defined as the region in which

$$x = O(\epsilon^{1/2}) , \quad r = (y^2 + z^2)^{1/2} = O(\epsilon) .$$

It is assumed that, in the bow near field, the flow variables are changed in order of magnitude when they are differentiated, according to the following symbolic rules

$$\frac{\partial}{\partial x} = O(\epsilon^{-1/2}) ; \frac{\partial}{\partial r} , \frac{\partial}{\partial y} , \frac{\partial}{\partial z} = O(\epsilon^{-1}) .$$

These effects could be brought about formally through the introduction of new variables, $x = X\epsilon^{1/2}$, $y = Y\epsilon$, $z = Z\epsilon$, after which we would require that differentiation with respect to X , Y , and Z have no effect on orders of magnitude. However, the rules will simply be carried along implicitly, the introduction of such new variables being quite unnecessary.

Note that there is one exception to the above procedure : We have already required that $b(x, z) = O(\epsilon)$ and $\partial b(x, z)/\partial x = O(\epsilon)$. This is simply a condition on hull geometry. It has nothing to do with the nature (or existence) of a flow around the ship.

We assume everything that is necessary for the existence of a velocity potential, which we write in the following form

$$Ux + \phi(x, y, z) \quad .$$

As usual, the potential satisfies the Laplace equation in the fluid domain :

$$[L] \qquad 0 = \phi_{xx} + \phi_{yy} + \phi_{zz} \quad .$$

$$[\phi/\epsilon] \quad [\phi/\epsilon^2] [\phi/\epsilon^2]$$

The expressions in square brackets give the orders of magnitude in the bow near field of the terms immediately above. Although we do not yet know the order of magnitude of ϕ , it is already clear that we can ignore the term ϕ_{xx} in finding the first approximation to the solution in the bow near field.

The boundary condition on the hull can be written

$$0 = \pm U b_x \pm \phi_x b_x - \phi_y \pm \phi_z b_z \qquad \text{on} \qquad y = \pm b(x, z) \quad .$$

$$[\epsilon] \quad [\phi\epsilon^{1/2}] \quad [\phi/\epsilon] \quad [\phi/\epsilon]$$

Dropping the one term which is clearly of negligible order of magnitude, we can rewrite this condition

$$[H] \qquad \frac{\partial \phi}{\partial n} \sim \frac{\pm \phi_y - b_z \phi_z}{\sqrt{1 + b_z^2}} \sim \frac{U b_x}{\sqrt{1 + b_z^2}} = O(\epsilon) \quad .$$

Since the operator $\partial/\partial n$ is similar to, say, $\partial/\partial r$ with respect to its effect on orders of magnitudes, we can now conclude that either $\phi = O(\epsilon^2)$ or the first approximation to ϕ satisfies a homogeneous boundary condition on the hull. Let us suppose that the former is true. If this is wrong, we shall discover that fact when we consider the other conditions on ϕ .

There are the usual two boundary conditions to be satisfied on the free surface

$$\left.\begin{aligned} [A] \qquad 0 &= g\zeta + U\phi_x + \frac{1}{2}[\phi_x^2 + \phi_y^2 + \phi_z^2] \,, \\ &\quad [\zeta] \quad [\epsilon^{3/2}] \qquad [\epsilon^3] \quad [\epsilon^2] \quad [\epsilon^2] \\ [B] \qquad 0 &= U\zeta_x + \phi_x\zeta_x + \phi_y\zeta_y - \phi_z \,, \\ &\quad [\zeta/\epsilon^{1/2}] \quad [\epsilon\,\zeta] \qquad [\zeta] \qquad [\epsilon] \end{aligned}\right\} \quad \text{on} \quad z = \zeta(x, y) \,.$$

The orders of magnitude involving ϕ have been noted, but of course we have not yet reached any conclusions, even tentatively, about the order of magnitude of ζ. In condition [A] we can clearly neglect all of the quadratic terms, and in condition [B] the second and third terms on the right side can be neglected. Thus we have reduced the number of terms to the following

$$\left.\begin{aligned} [A] \qquad 0 &= g\zeta + U\phi_x \,, \\ [B] \qquad 0 &= U\zeta_x - \phi_z \,, \end{aligned}\right\} \quad \text{on} \quad z = 0 \,.$$

In [A], the first term cannot be lower order than the second, because we would then have the meaningless result: $\zeta \equiv 0$. Thus, either the two terms are the same order of magnitude or the first term is higher order than the second. If the latter is the case, the first term in [B] is higher order than the second term in [B], and this leads to an ill-posed potential problem. Therefore we must conclude that $\zeta = O(\epsilon^{3/2})$, and the two conditions are consistent in orders of magnitude. Note that this order-of-magnitude estimate for ζ allows us to impose the boundary conditions at $z = 0$ with negligible error.

Finally, we can combine the two conditions above into the following

$$[F] \qquad 0 = \phi_{xx} + K\phi_z \,, \qquad \text{on} \qquad z = 0 \,,$$

where $K = g/U^2$.

In finding the first approximation to ϕ , we have a boundary-value problem to solve in the y-z plane. That is, we have a partial differential equation involving only the transverse rates of change. The body boundary condition is a simple Neumann condition, but the free-surface condition involves derivatives with respect to x , and so a 3-D aspect is introduced through this condition. The problem in the cross plane is illustrated in Figure 1(a).

For the moment, we shall confine our attention to a special case of this problem, namely, to narrow bodies which can be generated approximately by a distribution of sources on the centerplane, $y = 0$. This special case is depicted in Figure 1(b). A modification of our method of solution has been worked out for more general cases, but we shall not consider such cases further in the present paper ; they would only distract us from the simple ideas which are being developed.

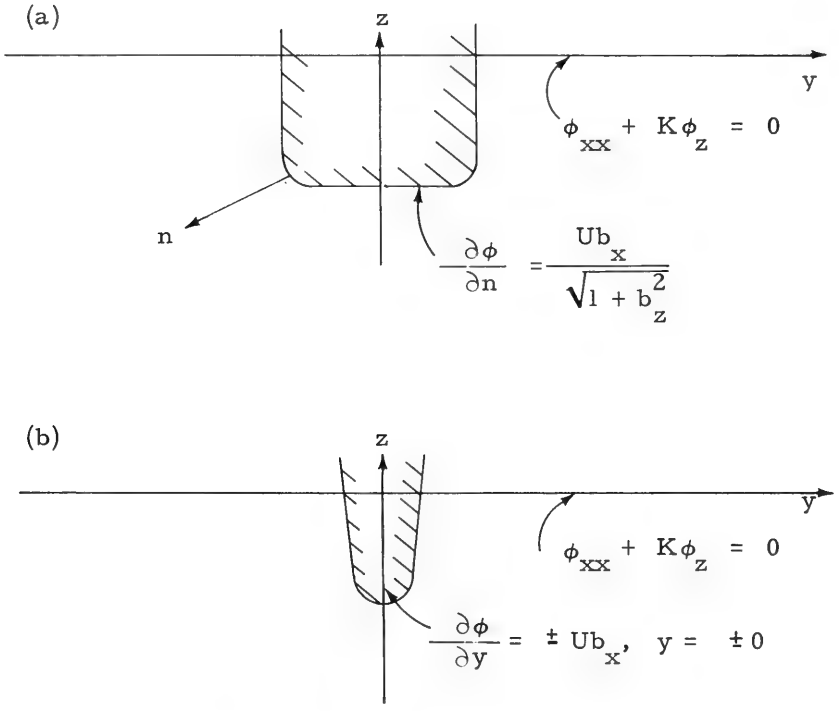

Figure 1 Problem for the First Approximation
(a) General body. (b) Thin body.
In both cases, the potential satisfies : $\phi_{yy} + \phi_{zz} = 0$.

For the thin bodies being considered, we shall suppose that the body boundary condition can be expressed

$$\frac{\partial \phi}{\partial n} \simeq \pm \frac{\partial \phi}{\partial y} \simeq U b_x \qquad \text{on} \quad y = \pm 0 \ , \quad \text{for} \quad z > -H(x) \ .$$

The following 2-D potential function satisfies this body boundary condition

$$\text{Re} \left\{ -\frac{U}{\pi} \int_{-H(x)}^{0} d\zeta \ b_x(x, \zeta) \ \log (y + iz - i\zeta) \right\} \ .$$

In fact, if we let v and w respectively denote the corresponding velocity components in the y and z directions, we find easily that

$$v - iw = \frac{U}{\pi} \int_{-H(x)}^{0} \frac{d\zeta}{i\zeta - (y + iz)} b_x(x, \zeta) \ .$$

For $y = \pm 0$, this can be evaluated through use of the Plemelj formula

$$(v - iw)_{y = \pm 0} = \pm U b_x(x, z) + \frac{U}{i\pi} \int_{-H(x)}^{0} \frac{d\zeta \, b_x(x, \zeta)}{\zeta - z} \ .$$

Thus,

$$v(x, \pm 0, z) = \pm U b_x(x, z) \ ,$$

as required.

The above potential function satisfies the partial differential equation and the body boundary condition. To that potential, we can add the potential for any other source distribution which induces no net normal velocity component on $y = 0$, $-H(x) < z < 0$. We choose to write $\phi(x, y, z)$ in the following fashion

$$\phi(x, y, z) = \mathrm{Re}\left\{ +\frac{U}{\pi} \int_{-H(x)}^{0} d\zeta \; b_x(x, \zeta) \; \log (y + iz - i\zeta) \right.$$

$$-\frac{U}{\pi} \int_{0}^{H(x)} d\zeta \; b_x(x, -\zeta) \; \log (y + iz - i\zeta)$$

$$\left. -\frac{1}{\pi i} \int_{-\infty}^{\infty} \frac{d\eta \; \psi(x, \eta)}{\eta - (y + iz)} \right\} \qquad (1)$$

The quantity in braces is a function of the complex variable $(y + iz)$. The y and z components of velocity are obtained easily

$$\phi_y - i\phi_z = -\frac{U}{\pi} \int_{-H(x)}^{0} \frac{d\zeta \; b_x(x, \zeta)}{i\zeta - (y+iz)} + \frac{U}{\pi} \int_{0}^{H(x)} \frac{d\zeta \; b_x(x, -\zeta)}{i\zeta - (y+iz)}$$

$$- \frac{1}{\pi i} \int_{-\infty}^{\infty} \frac{d\eta \; \psi_\eta(x, \eta)}{\eta - (y + iz)} \quad .$$

If we require only that

$$\psi(x, y) = \psi(x, -y) \; ,$$

the boundary condition on $y = \pm 0$ is satisfied, for the last term above is purely imaginary on $y = 0$, and the next-to-last term represents a source distribution on the centerplane above $z = 0$. Furthermore, if we approach the plane of the undisturbed free surface from below, we find that

$$\lim_{z \uparrow 0} \phi(x, y, z) = \psi(x, z) \; , \qquad (2)$$

which will be an important fact in the analysis ahead.

The first two integrals in (1) represent the flow due to a line of 2-D sources on the negative z axis and a line of sinks symmetrically located on the positive z axis. Together they cause only a vertical flow at the plane of the undisturbed free surface, $z = 0$. The third integral in (1) can represent a flow with both vertical and horizontal components at the plane $z = 0$.

We now substitute the above potential function into the free-surface condition, [F]

$$0 = \phi_{xx} + K\phi_z$$

$$= \psi_{xx} - \frac{2UK}{\pi} \int_{-H(x)}^{0} \frac{d\zeta\, \zeta\, b_x(x,\zeta)}{\zeta^2 + y^2} - \frac{K}{\pi} \int_{-\infty}^{\infty} \frac{d\eta\, \psi_\eta(x,\eta)}{\eta - y}$$

Rewritten slightly, this is an integro-differential equation for $\psi(x, y)$

$$\psi_{xx} - \frac{K}{\pi} \int_{-\infty}^{\infty} \frac{d\eta\, \psi_\eta(x,\eta)}{\eta - y} = \frac{2UK}{\pi} \int_{-H(x)}^{0} \frac{d\zeta\, \zeta\, b_x(x,\zeta)}{\zeta^2 + y^2} . \qquad (3)$$

The next task is to solve this equation for $\psi(x, y)$. When that has been done, we can use (1) to express $\phi(x, y, z)$.

The above equation applies to thin bodies of rather general shape ; there is not much restriction on the function $b(x, z)$. Rather than try immediately to solve this general problem, I have decided that it was more important to determine first the degree of validity of the fundamental assumptions that were made. For this reason, I shall next concentrate on one special case, for which the solution is easily obtained. We can then compare the predictions of this analysis with the results of experiments and determine wether it is worthwhile to solve Equation (3) for more general shapes.

III. SOLUTION FOR A SPECIAL CASE : A WEDGE-SHAPED BOW

We now restrict our attention to wedgelike bodies. In the bow near field, in which $x = O(\epsilon^{1/2})$, we assume that the body shape is given by

$$y = \pm b(x) \quad , \qquad -H < z < 0 .$$

As before, we assume that $b = O(\epsilon)$ and also that $b'(x) = db/dx = O(\epsilon)$. A consequence is that in the bow near field we have

$$b(x) = b(0) + x\,b'(0) + \frac{1}{2}x^2\,b''(0) + \ldots \quad .$$

$$[\epsilon^{3/2}] \qquad [\epsilon^2]$$

For a wedgelike entrance, $b(0) = 0$, and so we have, approximately,

$$y = \pm x\alpha\,[1 + o(1)], \qquad -H < z < 0 , \tag{4}$$

as the description of the body, where $\alpha = b'(0)$, the wedge half-angle. This argument might have been used previously to justify the thin-body approximation, although one might question whether it would be more convincing than the simple statement of assumption made previously. However, now it serves a much more practical purpose : we can simplify the right-hand side of Equation (3). In the bow near field, the integro-differential equation becomes

$$\psi_{xx} - \frac{K}{\pi}\int_{-\infty}^{\infty}\frac{d\eta\ \psi_\eta(x,\eta)}{\eta - y} = -\frac{KU\alpha}{\pi}\log\frac{H^2 + y^2}{y^2} \quad . \tag{5}$$

At first sight, this equation appears rather formidable. But the integral can be considered as a convolution integral, a fact which suggests the use of Fourier transforms to eliminate the y dependence. In what follows, we manipulate some transforms which are nonsense in a classical analysis ; whenever necessary, integrals should be interpreted in the sense of generalized functions. We follow Lighthill [7] in such respects.

Let the Fourier transform be defined as follows

$$F\left\{f(y)\right\} = f^*(\ell) = \int_{-\infty}^{\infty} dy\, e^{-i\ell y}\, f(y) \quad ;$$

$$F^{-1}\left\{f^*(\ell)\right\} = f(y) = \frac{1}{2\pi}\int_{-\infty}^{\infty} d\ell\, e^{i\ell y}\, f^*(\ell) \quad .$$

The transform of the right-hand side of Equation (5) can be computed as follows

$$\int_{-\infty}^{\infty} dy\, e^{-i\ell y} \log \frac{H^2 + y^2}{y^2} = \int_{-\infty}^{\infty} dy\, e^{-i\ell y} \left[\log (y-iH) + \log (y+iH) - 2 \log |y|\right]$$

$$= \frac{1}{i\ell} \int_{-\infty}^{\infty} dy\, e^{-i\ell y} \left(\frac{1}{y - iH} + \frac{1}{y + iH}\right) + 2\pi i \frac{\operatorname{sgn} \ell}{i\ell}$$

$$= \frac{2\pi}{|\ell|} \left[1 - e^{-H|\ell|}\right] \quad .$$

The integral term in Equation (5) can be treated as an ordinary convolution integral, with the result that

$$\int_{-\infty}^{\infty} dy\, e^{-i\ell y} \left(-\frac{K}{\pi} \int_{-\infty}^{\infty} \frac{d\eta\ \psi_\eta\ (x,\eta)}{\eta - y}\right)$$

$$= -\frac{K}{\pi} \left[i\ell \psi^*(x;\ell)\right] \left[\pi i \operatorname{sgn} \ell\right] = K|\ell| \psi^*(x;\ell) \quad .$$

The integro-differential equation now becomes an ordinary differential equation with respect to x

$$\psi^*_{xx}(x;\ell) + K|\ell|\psi^*(x;\ell) = -\frac{2KU\alpha}{|\ell|} \left\{1 - e^{-H|\ell|}\right\} \quad . \qquad (6)$$

The solution of this equation is now readily obtained. A particular solution is the following

$$\psi^*(x;\ell) = -\frac{2U\alpha}{\ell^2} \left\{1 - e^{-H|\ell|}\right\} \left\{1 - \cos\sqrt{K|\ell|}\ x\right\}$$

$$= \phi^*(x;\ell;0) \qquad \text{(by Equation (2))} . \qquad (7)$$

In principle, we should include the complementary solution, and this would be easy enough to do. However, the above solution appears to suffice for all that follows.

There seems to be little point in writing out the corresponding expression for $\phi\ (x, y, z)$, which could be done through use of Equation (1). In fact, we shall not even bother at this point to write out the inverse transform of the expression in (7), although we note that the latter can be expressed in terms of Fresnel integrals. It is worthwhile to write at least the transforms of two related quantities, namely, $\phi^*_z(x;\ell;0)$ and $\phi^*_x(x;\ell;0)$:

$$\phi^*_z(x;\ell;0) = \frac{2U\alpha}{|\ell|}\left(1 - e^{-H|\ell|}\right)\cos\sqrt{K|\ell|}\,x \quad ; \tag{8}$$

$$\phi^*_x(x;\ell;0) = -\frac{2U\alpha}{\ell^2}\sqrt{K|\ell|}\left(1 - e^{-H|\ell|}\right)\sin\sqrt{K|\ell|}\,x \quad . \tag{9}$$

The behavior of ϕ^*_z at large distance from the bow will be interesting to note presently, and ϕ^*_x is essentially the transform of the wave height, which can be seen from the dynamic free-surface condition [A] .

IV. LIMIT BEHAVIOR OF THE SOLUTION FOR THE WEDGE BOW

Behavior as $|y| \to \infty$. Since the potential and its derivatives on the plane $z = 0$ are all given in terms of Fourier transforms with respect to y , it is nearly a trivial matter to determine how the inverse transforms act when $y \to \pm\infty$. We need only to examine the behavior of the transforms near their singularities. The only singularities occur at $\ell = 0$. For example, $\phi^*_z(x;\ell;0)$ can be expressed

$$\phi_z(x;\ell;0) = 2U\alpha\left\{H - \frac{1}{2}H^2|\ell| + \ldots\right\}\left\{1 - \frac{1}{2}K|\ell|x^2 + \ldots\right\}$$

$$= 2U\alpha H\left[1 - |\ell|\left\{\frac{H}{2} + \frac{1}{2}Kx^2\right\} + \ldots\right] \quad .$$

Treating this transform as a generalized function, we can obtain the limit behavior of its inverse transform by using the methods described by Lighthill [7] . We find that

$$\phi^*_z(x, y, 0) = \frac{U\alpha H(H + Kx^2)}{\pi y^2} + \ldots \qquad \text{as} \quad y \to \infty \ .$$

This shows that, far off to the sides, the disturbance appears to be caused by a vertical dipole distribution. Such a result should not be

too surprising, since the body boundary condition was satisfied by distributing sources over the underwater part of the centerplane, to which we added a distribution of opposite sinks on the abovewater image of the centerplane. These two distributions alone would certainly lead to the dipole-like behavior far off to both sides. Apparently, the third term in the expression for ϕ , as given in [1] , has negligible influence in this sideways limit.

Actually, we guaranteed such a result by choosing the complementary solution as we did in [7] . Effectively, we have implied that there are no waves upstream of the bow, even in the bow near field. In the final section, we shall return to this point ; it requires much more study in the future.

The transform of the wave deformation function can be expressed

$$\zeta^*(x;\ell) = -\frac{U}{g}\,\phi_x^*(x;\ell;0) \quad ,$$

and, from (9) , this quantity has the following behavior near $\ell = 0$

$$\begin{aligned}\zeta^*(x;\ell) &= \frac{2\alpha}{|\ell|\sqrt{K|\ell|}}\left(1 - e^{-H|\ell|}\right)\sin\sqrt{K\,|\ell|}\;x \\ &= 2\alpha Hx\left\{1 - |\ell|\left[\frac{H}{2} + \frac{Kx^2}{6}\right] + \ldots\right\} \quad .\end{aligned} \tag{10}$$

The inverse transform then must have the behavior

$$\zeta(x,y) = \frac{\alpha Hx}{\pi y^2}\left[H + \frac{Kx^2}{3}\right] + \ldots \quad \text{as} \quad |y| \to \infty \quad .$$

It can be shown that the potential itself drops off inversely with y^2 , but this does not seem to provide any special insight into the results.

Behavior as $x \to \infty$. This is an important limit; for it provides the connection to the usual slender-body solution. Let us recall that $x = O(\epsilon^{1/2})$ in the bow near field region. Our solution, when we let $x \to \infty$, should match the solution of the usual slender-body problem if we let $x \to 0$ in the latter.

In order to obtain these limits, we manipulate the inverse transforms into forms so that the generalized-function procedures can again be used. For the vertical component of velocity, for example, we go through the following steps

$$\phi_z(x,y,0) = \frac{1}{2\pi}\int_{-\infty}^{\infty} d\ell\, e^{i\ell y}\left\{\frac{2U\alpha}{|\ell|}\left(1 - e^{-H|\ell|}\right)\cos\sqrt{K\,|\ell|}\,x\right\}$$

$$= \frac{2U}{\pi}\int_0^{\infty} d\ell\cos\ell y\left(\frac{1 - e^{-H\ell}}{\ell}\right)\cos\sqrt{K\ell}\,x$$

$$= \frac{4U\alpha}{\pi}\int_0^{\infty} d\lambda\cos\lambda x\,\cos\frac{y\lambda^2}{K}\left(\frac{1 - e^{-H\lambda^2/K}}{\lambda}\right)$$

$$= \frac{2U\alpha}{\pi}\int_{-\infty}^{\infty} d\lambda\, e^{i\lambda x}\,\cos\frac{y\lambda^2}{K}\left(\frac{1 - e^{-H\lambda^2/K}}{|\lambda|}\right)$$

$$\sim -\frac{4U\alpha H}{\pi K x^2} \qquad \text{as} \qquad x \to \infty \ . \tag{11}$$

The interpretation of this result is of some interest. The quantities α and H are each of order ϵ. In addition, $x = O(\epsilon^{1/2})$ in the bow near field. Thus, $\phi_z = O(\epsilon)$ in the bow near field. Now, we have already commented that the solution in the bow near field must match the solution given by the usual slender-body theory. In fact, the near field of the usual slender-body theory is a far field with respect to the bow region; $x = O(1)$ in the usual theory. From this point of view, the expressions obtained above for ϕ_z represent a one-term inner expansion, and the final formula above is the one-term outer expansion of the one-term inner expansion. In matching it with the corresponding "far field", we must reinterpret the variables as far-field variables and re-order the expansion. In the present case, this means only that we revise our estimate by considering x to be $O(1)$, in which case we observe that $\phi_z = O(\epsilon^2)$ on the plane $z = 0$ as $x \to \infty$. This agrees with the well-known result of the usual slender-body theory. We shall say more about this presently.

What is most remarkable about the above result is the manner in which the flow completely changes its character in the downstream direction. Very close to the bow, the flow appears to have been caused by a distribution of vertical dipoles, and so the flow at the plane $z = 0$ is almost completely normal to the plane. However,

as $x \to \infty$, we find that the normal component of velocity on the plane $z = 0$ vanishes and the flow becomes parallel to the plane.

We also examine how the wave elevation varies asymptotically in the downstream direction. We proceed as with ϕ_z : We write ζ as the inverse transform of the expression in (10) and then manipulate it so that it appears formally to be a transform with respect to x . We obtain in this way

$$\zeta(x, y) = \frac{2\alpha}{\pi i} \int_{-\infty}^{\infty} d\lambda \, e^{i\lambda x} \, \mathrm{sgn}\lambda \, \cos\frac{y\lambda^2}{K} \left(\frac{1 - e^{-H\lambda^2/K}}{\lambda^2} \right)$$

$$\sim \frac{2\alpha H}{\pi i K} \int_{-\infty}^{\infty} d\lambda \, e^{i\lambda x} \, \mathrm{sgn}\lambda \left[1 - \frac{H\lambda^2}{2K} + \ldots \right]$$

$$\sim \frac{4\alpha H}{\pi K x} + O(1/x^5) \qquad \text{as} \qquad x \to \infty \qquad . \tag{12}$$

It is worth noting that the y dependence enters only in the term which drops off inversely with x^5. We also observe that $\zeta = O(\epsilon^{3/2})$ in the bow near field, where we assume that $x = O(\epsilon^{1/2})$, but when we reinterpret x as being $O(1)$ we must conclude that $\zeta = O(\epsilon^2)$. This is in agreement with the well-known results of the usual slender-body theory.

Finally, we obtain an estimate for $\phi(x, y, 0)$ as $x \to \infty$. The transform of this quantity was given in Equation (7). It is clear that we cannot follow exactly the same procedure as we did for estimating ϕ_z of ζ , since there is a part of the expression in (7) which does not even depend on x . However, we can proceed in two steps :

a) First we consider the part of the transform in (7) that does not depend on x , namely, the quantity

$$-\frac{2U\alpha}{\ell^2} \left(1 - e^{-H|\ell|} \right) \qquad .$$

We shall find that this is the transform of

$$\mathrm{Re}\left\{ \frac{U\alpha}{\pi} \int_{-H}^{H} d\zeta \, \log(y + iz - i\zeta) \right\} \Bigg|_{z = 0} \qquad . \tag{13}$$

The interpretation of this result will be discussed after we prove that it is true. By elementary means, we obtain the following result

$$\mathrm{Re}\left\{\frac{U\alpha}{\pi}\int_{-H}^{H} d\zeta \log (y + iz - i\zeta)\right\}\Bigg|_{z=0}$$

$$= \frac{U\alpha}{2\pi}\int_{-H}^{H} d\zeta \log (y^2+\zeta^2)$$

$$= \frac{U\alpha}{\pi}\left[H \log (H^2+y^2)/y^2 + H \log y^2 + 2\left[y \cot^{-1}(y/H) - H\right]\right].$$

The last expression is now broken into several pieces, for each of which we obtain the generalized Fourier transform. For the first piece, the transform exists even in the classical sense

$$\int_{-\infty}^{\infty} dy\, e^{-i\ell y} \log \frac{H^2 + y^2}{y^2} = 2\int_{0}^{\infty} dy \cos \ell y \log \frac{H^2 + y^2}{y^2}$$

$$= \frac{2\pi}{|\ell|}\left(1 - e^{-H|\ell|}\right) \quad .$$

From the point of view of generalized functions, we have the following result

$$\int_{-\infty}^{\infty} dy\, e^{-i\ell y} \log y^2 = -\frac{2\pi}{\ell} \operatorname{sgn} \ell = -\frac{2\pi}{|\ell|} \quad .$$

One more integral can be computed readily

$$\int_{-\infty}^{\infty} dy\, e^{-i\ell y}\left[y \cot^{-1}(y/H) - H\right] = 2\int_{0}^{\infty} dy \cos \ell y \left[y \cot^{-1}(y/H) - H\right]$$

$$= -\frac{2}{\ell}\int_{0}^{\infty} dy \sin \ell y \left(\cot^{-1}\frac{y}{H} - \frac{yH}{y^2 + H^2}\right)$$

$$= -\frac{\pi}{\ell^2} + \frac{\pi}{\ell^2} e^{-H|\ell|}\left[1 + H|\ell|\right] \quad .$$

These three transforms can now be combined to yield the result stated above, that is,

$$-\frac{2U\alpha}{\ell^2}\left(1 - e^{-H|\ell|}\right) = \frac{U\alpha}{\pi}\int_{-\infty}^{\infty} dy\, e^{-i\ell y}\left[H \log(H^2+y^2) + 2\left[y \cot^{-1}(y/H) - H\right]\right].$$

The expression in (13) is the potential for the flow caused by a line distribution of sources on the centerplane and on the above-water image of the centerplane, the potential having been evaluated on $z = 0$. We recall that we started constructing our solution, in Equation (1), by assuming that there was a distribution of sources on the submerged part of the centerplane and a distribution of opposite sinks on the image of the centerplane. We now discover the interesting fact that one part of the potential, when evaluated on the plane of the undisturbed free surface, represents a symmetrical distribution of singularities, rather than an antisymmetrical distribution. The symmetrical distribution would have been a logical starting point in the ordinary slender-body theory, in which a rigid-wall free-surface condition must be satisfied. It appears in the present analysis as a natural consequence in the region downstream of the bow region, although we started with quite a different picture of the flow around the bow.

b) The remaining part of the expression in (7) is oscillatory with respect to x, and so we use the procedure that worked well in estimating the downstream behavior of ϕ_z and ζ. We go through the following steps

$$\frac{1}{2\pi}\int_{-\infty}^{\infty} d\ell\, e^{i\ell y}\,\frac{2U\alpha}{\ell^2}\left(1 - e^{-H|\ell|}\right)\cos\sqrt{K|\ell|}\,x$$

$$= \frac{2U\alpha}{\pi}\int_0^{\infty} d\ell \cos\ell y\left[\frac{(1 - e^{-H|\ell|})\cos\sqrt{K\ell}\,x}{\ell^2}\right]$$

$$= \frac{2U\alpha K}{\pi}\int_{-\infty}^{\infty}\frac{d\lambda}{\lambda^3} e^{-i\lambda x}\,\operatorname{sgn}\lambda\,\cos\frac{y\lambda^2}{K}\left[1 - e^{-H\lambda^2/K}\right]$$

$$\sim -\frac{4U\alpha H}{\pi} \log Cx + O(1/x^2) \qquad \text{as} \qquad x \to \infty ,$$

where C is a constant which cannot be determined from this analysis.

From the two-part analysis above, we obtain our desired result, the estimate of the potential on $z = 0$ as $x \to \infty$:

$$\phi(x, y, 0) \sim \mathrm{Re}\left\{\frac{U\alpha}{\pi}\int_{-H}^{H} d\zeta \log (y - i\zeta)\right\} - \frac{4U\alpha H}{\pi} \log Cx + O(1/x^2)$$
$$\text{as} \quad x \to \infty \quad . \tag{14}$$

Thus, we see that the potential represents the source distribution already discussed, in addition to which there is a term which becomes infinite logarithmically when x goes to infinity. These results will both appear in a proper perspective when we consider what the usual slender-body theory predicts near the bow. Both of the explicit terms above are $O(\epsilon^2 \log \epsilon)$ in the bow near field.

The appearance of the constant, C, in the above result is an unfortunate consequence of our use of generalized-function theory. In general, the value of the constant may even have to change as the formulas are manipulated. From a strict mathematical point of view, it is quite improper to leave a final formula in such a shape that it can be interpreted only in terms of generalized functions, especially when it is supposed to have direct physical significance. Fortunately, this is not so much of a problem for us here as might be supposed. The quantities with real physical significance are ϕ_z and ζ, and their estimates are not at all murky.

V. THE USUAL SLENDER-BODY SOLUTION

If one stretches coordinates near the body in such a way that

$$x = X \ , \quad y = \epsilon Y \ , \quad z = \epsilon Z$$

and then treats derivatives with respect to the new variables as if they had no effect on orders of magnitude, one obtains the usual problem and solution of slender-body theory. Without going through the formalism of such changes of variables, we write down directly the boundary-value problem that results for the wedge-like body that we are considering in this paper. The first approximation to the near-field pertur-

bation potential satisfies the following

$$[L] \qquad \phi_{yy} + \phi_{zz} = 0 \ ;$$

$$[H] \qquad \begin{cases} \dfrac{\partial \phi}{\partial y} = \pm U b'(x) & \text{on} \quad y = \pm b(x) \ , \\ \dfrac{\partial \phi}{\partial z} = 0 & \text{on} \quad z = -H \ ; \end{cases}$$

$$\left.\begin{aligned} [A] \qquad & g\zeta + U\phi_x + \frac{1}{2}\phi_y^2 = 0 \\ [B] \qquad & \phi_z = 0 \end{aligned}\right\} \quad \text{on} \quad z = 0 \ .$$

The last condition, [B] , is of course the rigid-wall condition which replaces the free-surface condition. The dynamic boundary condition on the free surface, [A] , serves only for the determination of the free-surface shape, ζ , after the potential problem is solved. In the body boundary condition, we have stated a separate condition for the bottom of the wedge, for we do not need or want to restrict ourselves to a "thin" slender-body over the entire body length.

The above problem can be solved precisely, by mapping, for example. We do not need that complete solution, however. Let $\Phi(x, y, z)$ be the solution of this 2-D problem which has the property

$$\Phi(x, y, z) \sim \frac{2UHb'(x)}{\pi} \log \left| y^2 + x^2 \right|^{1/2} \quad \text{as} \quad \left| y^2 + z^2 \right|^{1/2} \to \infty .$$

Then the perturbation potential, $\phi(x, y, z)$, is given by

$$\phi(x, y, z) = \Phi(x, y, z) + F(x) \ ,$$

where $F(x)$ is given by [8]

$$F(x) = \frac{U}{2\pi} \int_{-\infty}^{\infty} d\xi \ s''(\xi) \left\{ \operatorname{sgn}(x-\xi) \log 2|x-\xi| + \frac{\pi}{2} \mathbf{H}_0(K(x-\xi)) + (2 + \operatorname{sgn}(x-\xi)) \frac{\pi}{2} Y_0(K|x-\xi|) \right\} \ ,$$

where $s(x)$ is the area of the immersed part of the cross-section at x, Y_0 is the Bessel function of the second kind, and $\mathbf{H}_0$ is a Struve function. (Notation is the same as in [9].) Near the bow, we note that

$$s(x) = \begin{cases} 0 & x < 0 , \\ 2\alpha H x + \ldots & 0 < x , \end{cases}$$

where the "..." denotes some smooth function of x. The first and second derivatives of $s(x)$ can then be expressed as follows

$$s'(x) = \begin{cases} 0 & x < 0 , \\ 2\alpha H + \ldots & 0 < x ; \end{cases}$$

$$s''(x) = 2\alpha H \delta(x) + \ldots ,$$

where $\delta(x)$ is the Dirac delta function.

The function $F(x)$ represents the effects of interactions between the various cross-sections. For a body in an infinite fluid, we would have just the first term in the integrand, and one can show easily that it represents the flow on the x axis caused by a distribution of sources both upstream and downstream of the point under consideration. The other two terms represent the effects of the free-surface, and they combine with the logarithm term in such a way as to cancel any flow upstream of a source. Tuck [8] has shown this explicitly. The integrand of the $F(x)$ expression has a wavelike nature for $\xi < x$ but not for $\xi > x$.

We are interested in how the above solution behaves as $x \to 0$. In fact, the easiest procedure for determining this behavior is to treat x as being $O(\epsilon^{1/2})$ and re-order all quantities accordingly. When we do this (after much algebra, expanding of the Bessel functions, etc.), we find that

$$F(x) \sim -\frac{4UH\alpha}{\pi}\left[\log x + \frac{1}{4}\log\frac{K^3}{4} + \frac{3}{4}\gamma\right], \quad \text{for} \quad x = O(\epsilon^{1/2}) ,$$

where γ is Euler's constant. The problem for Φ becomes, for $x = O(\epsilon^{1/2})$, a wedge-flow problem, with a rigid wall in place of the free surface ; its solution is

$$\Phi(x, y, z) = \mathrm{Re}\left\{\frac{U\alpha}{\pi}\int_{-H}^{H} d\zeta \log (y + iz - i\zeta)\right\} \quad . \tag{15}$$

When we combine the two results above, we obtain a one-term expansion of the potential, to be matched with the bow-near-field expansion

$$\Phi(x, y, z) \sim \mathrm{Re}\left\{\frac{U\alpha}{\pi}\int_{-H}^{H} d\zeta \log (y + iz - i\zeta)\right\} - \frac{4U\alpha H}{\pi}\log Cx \ ,$$

where

$$\log C = -\frac{1}{4}\log\frac{K^3}{4} + \frac{3}{4}\gamma \quad .$$

This result should be compared with that in (14) : the matching is perfect, with the previously unknown constant C now fixed. The interpretation is, of course, different. In (14) , the potential was approaching infinity logarithmically as $x \to \infty$; here, the potential is approaching infinity logarithmically as $x \to 0$.

The kinematic free-surface condition, [B] , does not mean that ϕ_z is precisely equal to zero on the plane $z = 0$; it means only that $\phi_z|_{z=0} = 0$ for the leading-order term in the solution for ϕ . The first approximation to ϕ is $O(\epsilon^2)$ and the first approximation to ϕ_z is $O(\epsilon)$. Thus, the statement that $\phi_z|_{z=0} = 0$ really means that $\phi_z|_{z=0} = o(\epsilon)$. This remains true even as $x \to 0$. Thus, the first-order term in ϕ_z automatically has the correct behavior for matching with (11), which gave the behavior of ϕ_z in the bow near field, under the condition that $x \to \infty$.

Finally, we consider once more the wave-shape function, $\zeta(x, y)$. From the dynamic boundary condition, [A] , combined with what we have found above concerning the slender-body potential for this problem, we can express ζ in the following way

$$\zeta(x, y) = -\frac{U}{g}\Phi_x - \frac{U}{g}F'(x) - \frac{1}{2g}\Phi_y^2 \ , \quad \text{on} \quad z = 0 \ .$$

For the wedge-shaped bow, with constant draft, we can find immediately that $\Phi_x \simeq 0$. (See (15)) For x very small, we also find easily

that

$$F'(x) = -\frac{4UH\alpha}{\pi x}$$

The final term needed is the one involving Φ_y, this quantity being

$$\Phi_y = \mathrm{Re}\left\{\frac{U\alpha}{\pi}\int_{-H}^{H}\frac{d\zeta}{i\zeta - (y+iz)}\right\} + \cdots ,$$

the remainder being a quantity which goes to zero at the bow. We need to evaluate this quantity only on $z = 0$, for which we find

$$\Phi_y \simeq \frac{2U\alpha}{\pi}(\mathrm{sgn}\ y)\tan^{-1}\frac{H}{|y|} .$$

We now have the following representation for the wave shape

$$\zeta(x,y) \sim -\frac{4H\alpha}{\pi Kx} - \frac{2\alpha^2}{\pi^2 K}\left[\tan^{-1}\frac{H}{|y|}\right]^2 = O(\epsilon) .$$

The last estimate of order of magnitude is still valid in the usual near field, where $x = O(1)$. In order to match this result with the bow-near-field formula, we must reinterpret the order of magnitude of x, that is, consider that $x = O(\epsilon^{1/2})$, and re-order the expansion. When we do this and keep just one term, we have only

$$\zeta(x,y) \sim -\frac{4H\alpha}{\pi Kx} = O(\epsilon^{3/2}) .$$

We now observe that this matches precisely with the expression in (12).

V. COMPARISON OF RESULTS WITH EXPERIMENTS

From Equation (10), we can compute the shape of the free-surface disturbance :

$$\zeta(x, y) = \frac{\alpha}{\pi}\int_{-\infty}^{\infty} d\ell\, e^{i\ell y}\left(\frac{1 - e^{-H|\ell|}}{|\ell|}\right)\left(\frac{\sin\left(\sqrt{K|\ell|}\ x\right)}{\sqrt{K|\ell|}}\right)$$

$$= \frac{2\alpha}{\pi}\int_{0}^{\infty} d\ell\, \cos\ell y\left(\frac{1 - e^{-H\ell}}{\ell}\right)\left(\frac{\sin\sqrt{K\ell}\, x}{\sqrt{K\ell}}\right) . \qquad (16)$$

For $y = 0$, this simplifies further

$$\zeta(x, 0) = \frac{2\alpha}{\pi}\int_{0}^{\infty} d\ell\left(\frac{1 - e^{-H\ell}}{\ell}\right)\left(\frac{\sin\sqrt{K\ell}\, x}{\sqrt{K\ell}}\right) \qquad (16')$$

We obtain our simplest form when we make the following changes of variables

$$X = x\sqrt{K/H} \quad , \qquad Z(X) = \frac{\pi}{2\alpha}\sqrt{\frac{K}{H}}\ \zeta(x, 0) \quad . \qquad (17)$$

Equation (16') now collapses into the following

$$Z(X) = \int_{0}^{\infty} d\mu\left(\frac{1 - e^{-\mu}}{\mu}\right)\left(\frac{\sin\sqrt{\mu}\ X}{\sqrt{\mu}}\right) \quad . \qquad (18)$$

Thus, the wave along the side of the wedge can be nondimensionalized in such a way that we have a single universal curve, a function of just one variable, which purports to describe the wave shape for any speed, any draft, and any wedge angle. Of course, we have not yet considered the range of validity of these results, but it is clear that they are very simple results.

It is worthwhile to notice the manner in which the length scales are made nondimensional : The reference length is $(H/K)^{1/2} = (HU^2/g)^{1/2}$. This is the geometric mean of two lengths, the draft H and characteristic free-surface length U^2/g.

Also, the wedge half-angle enters in a very simple way : The non-dimensional wave height, Z , must be multiplied by the ratio,

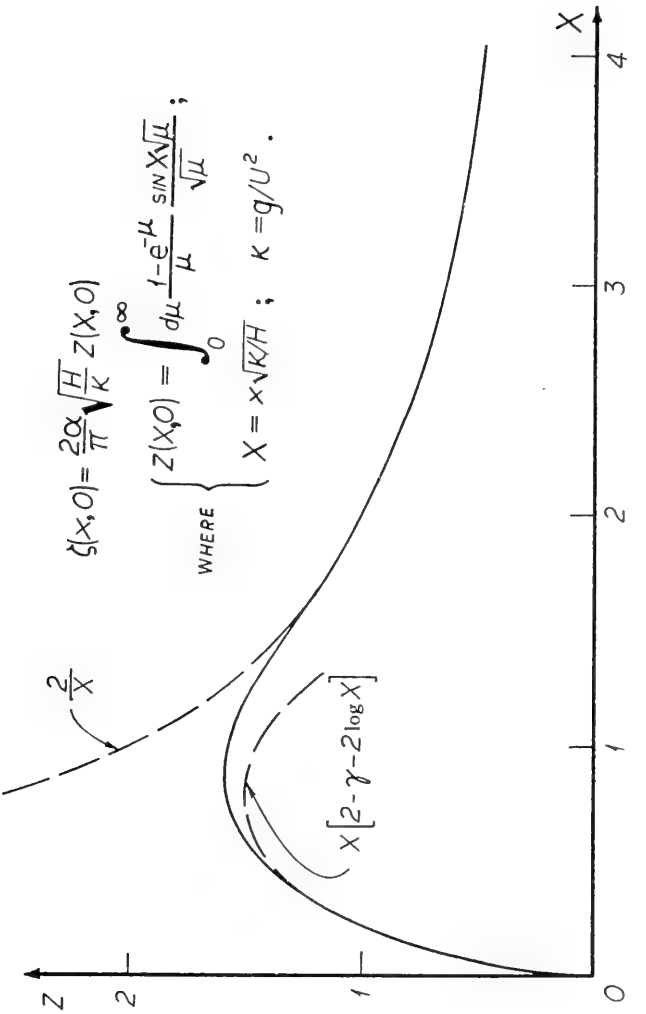

Figure 2. Predicted bow-wave shape on symmetrical wedge

$\alpha/(\pi/2)$ (in addition to being made dimensional on the scale of $(H/K)^{1/2}$). Thus, the theory predicts that wave height along the side of the wedge will be proportional to the wedge angle.

Calculation of $Z(X)$ has been carried out, with the results shown in Figure 2. In addition, the integral in (18) has very simple asymptotic approximations which are valid as $X \to 0$ or $X \to \infty$, and these are shown by the broken curves in Figure 2.

In order to determine whether this result was even approximately valid, we conducted some experiments with a very simple model. The planform of the model was that of an unsymmetrical diamond ; at one end, the model was a wedge with a half-angle of 7.5°, and at the other end the half-angle was 15°. Tests were conducted at speeds up to about 15 ft./sec., with drafts from 4 in. to 16 in. A grid had been inscribed on the model so that wave shapes could be measured from photographs of the bow wave.

In Figures 3 and 4, two selected series of tests are shown. In both figures, the model is being tested at a draft of 12 in.

There are several qualitative features in these photographs that are worth noting :

(i) The model speed in Figure 3(a) is 1.64 ft./sec., which is only about twice the minimum speed at which waves can travel on a water/air interface. (Minimum speed is about 23.2 cm./sec.) In fact, capillary waves are quite evident in this picture, as well as in several of the higher-speed test pictures. Whether these ripples can actually be seen apparently depends more on the lighting than on anything else. The existence of a sharp edge on the model presumably accentuated the amplitude of the ripples in all of our tests.

(ii) In (b) - (e) of Figure 3, the water level at the bow edge is about 1 in. above still-water level. (The white mark at the bow is at the 18 in. draft mark, and the squares are 1 in. on a side.) This rise of water level ahead of the bow is, of course, not predicted in the analysis. We fully expected to observe such a rise, and we recognized that it would represent a source of error in the predictions. What we did not anticipate was that the rise is quite insensitive to forward speed. From a speed of about 5 ft./sec. (Figure 3(b)) to a speed in excess of 15 ft./sec. (Figure 3(e)), this rise increases from about 0.8 in. to about 1.2 in.

(iii) The corresponding rise in water level at the bow is greater for the wider-angle bow, but even in this case the level seems to

U = 1.64 ft./sec.

U = 4.95 ft./sec.

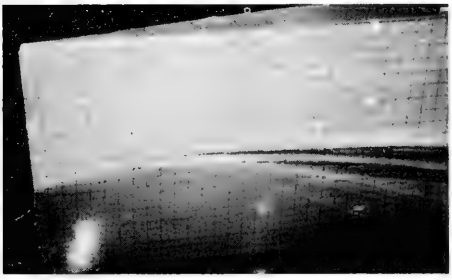

U = 8.22 ft./sec.

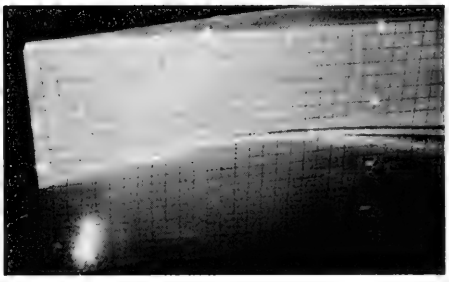

U = 11.52 ft./sec.

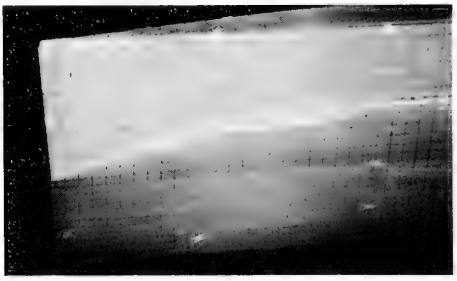

U = 15.17 ft./sec.

Figure 3. Bow wave on a wedge

Draft = 12 in.

Half angle = 7.5°

U = 3.64 ft./sec.

U = 4.98 ft./sec.

U = 7.64 ft./sec.

U = 9.80 ft./sec.

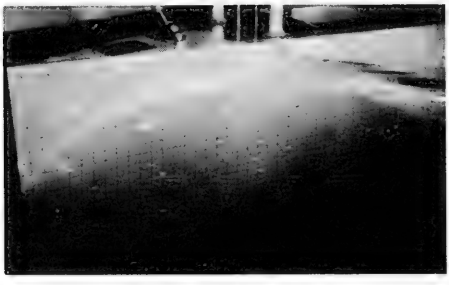

U = 11.46 ft./sec.

Figure 4. Bow wave on a wedge

Draft = 12 in. Half angle = 15°

stabilize at about 1.7 in. See Figure 4, parts (b) to (e), in which the rise varies between about 1.5 and 1.9 in. while the speed increases from 5.0 to 11.5 ft./sec. (Note : the white mark on the bow here is at the 16 in. draft.)

(iv) The region in which the bow wave dominates the picture increases steadily with forward speed. (The analysis predicts that the peak of the bow wave moves aft in proportion to U, the speed.) In the lowest-speed tests, there is a clear wave-trough behind the bow wave. See, for example, Figure 4, parts (a) and (b) : The lowest visible white marks are on the still-water waterline. The trough is not predicted in the present analysis, and so we see that there are non-negligible waves at low speed which simply are not evident under the assumptions which have been made here. We cannot say whether the same kind of troughs occur at the higher speeds, because the model length was not great enough to observe the phenomenon.

From Figure 2, it was clear that we have a "universal" bow-wave curve which is supposed to apply to all wedges at all speeds at all drafts - within some unknown limits. To check this conclusion quantitatively, we measured just the amplitude and longitudinal position of the peak of the bow wave. For the finer wedge, the results for the wave amplitude are shown in dimensional form in Figure 5 ; the corresponding data for the longitudinal position of the peak are shown in Figure 6. These dimensional data are shown only to provide the reader with an impression of the scale of what was observed. The nondimensional wave-peak data are shown in Figure 7 ; according to the analysis, the nondimensional amplitude, Z_{max}, should always have the same value, approximately 1.6. Figure 7 shows clearly that this is only roughly substantiated in the experiments. In fact, there are two ways in which the analysis is obviously deficient :

1) The assumption that made our analysis distinct from the usual slender-body theory was that the bow flow is essentially a "high-Froude-number" problem, in some sense. The depth-Froude-number is the only reasonable Froude number to consider in the bow region, and one can hardly expect the analysis to give good answers when $F_H \to 0$. In fact, it gives terrible answers then !

2) At the higher Froude numbers, the wave peak occurs at a considerable distance from the bow, at a place where the "thin-ship" representation of the body is probably quite invalid. We used the "thinness" twice, first in satisfying the body boundary condition approximately, then in evaluating the wave height on the body. (We simply set $y = 0$ in passing from (16) to (16').) The worse agreement for the wider wedge suggests that this "thinness" assumption

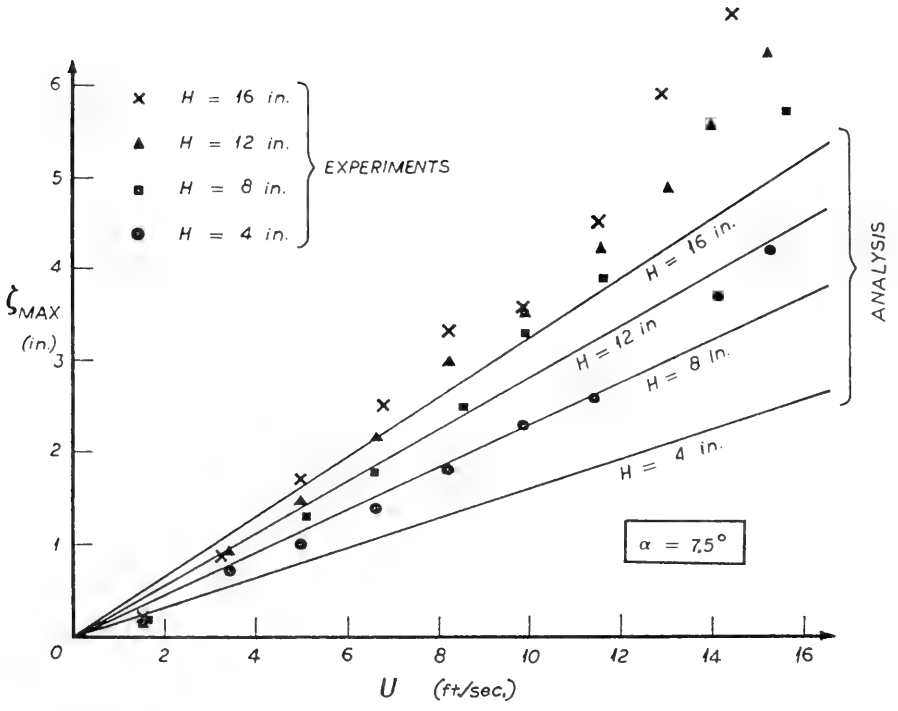

Figure 5. Bow wave amplitude on wedge

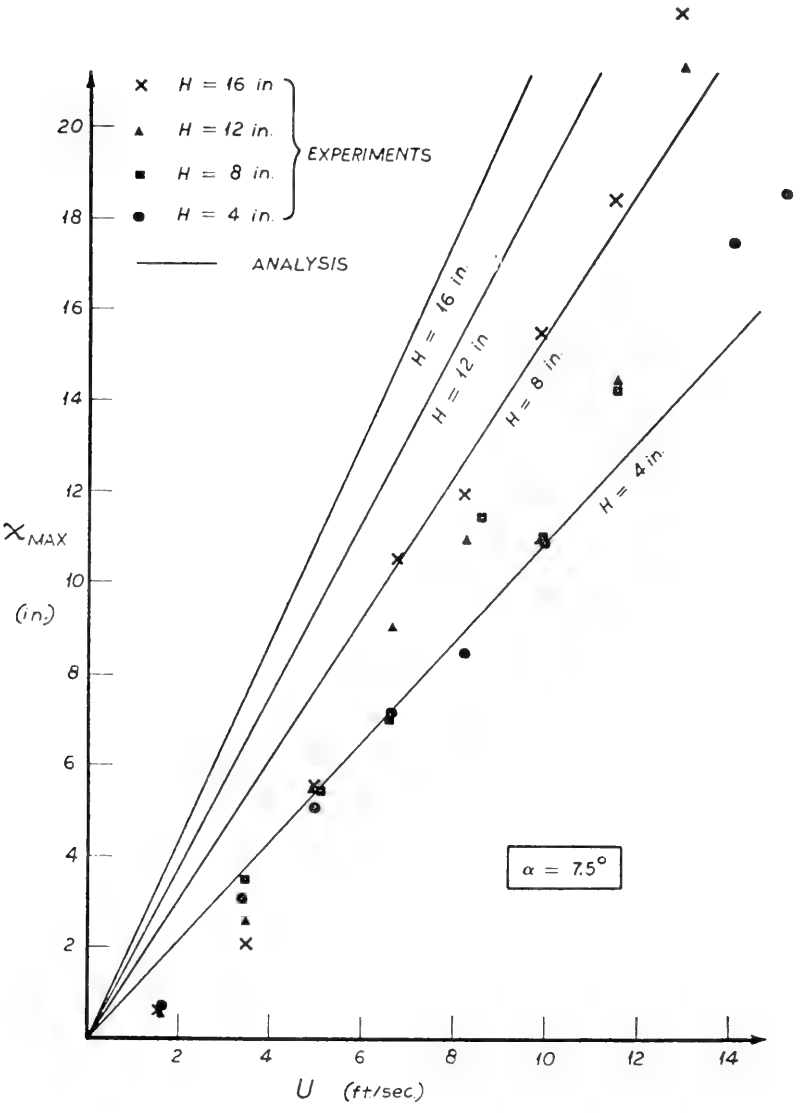

Figure 6. Longitudinal position of wave peak

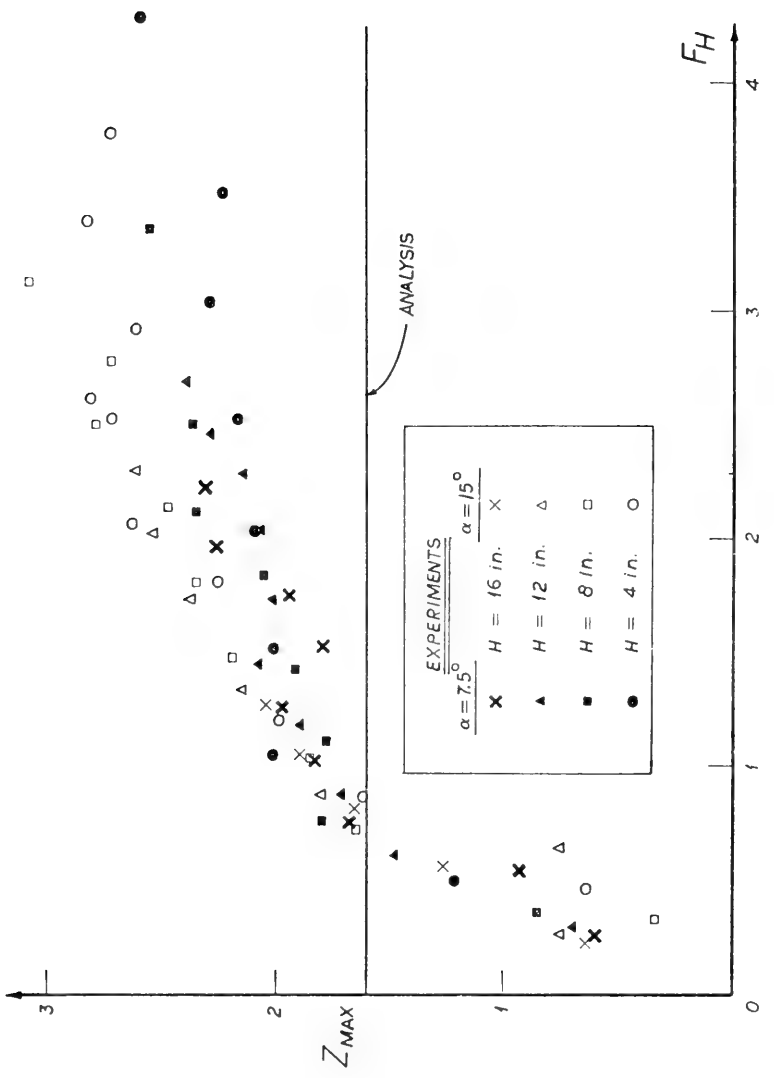

Figure 7. Bow wave amplitude (in nondimensional form)

may well be the cause of the increasing error at high Froude number.

If F_H is below some moderate value, it can be seen from Figure 7 that our method of nondimensionalizing the data seems to be still valid even when the Froude number drops below the level at which the analysis is valid. The reason for this is not clear, but the fact may be useful in reducing experimental data, even in cases in which the present analysis is obviously invalid.

The inaccuracy of the wave height predictions at high Froude numbers can probably be ameliorated if not completely removed by the introduction of a more precise method of solution of the problem. In principle, it appears to be possible to solve the bow-flow problem without introducing the thinness assumption, and some efforts have already been made to do just this. At the moment, however, we have no results to show for this effort.

VI. CRITIQUE OF THE ANALYSIS

Intuitively, we visualize a "slender body" as a body of which the length is much greater that the transverse dimensions. In addition, if we want to be a bit more precise, we require that there be no sudden changes in cross-section size or shape.

For such bodies, slender-body theory is likely to lead to reasonable predictions concerning a fluid flow around the body - provided we do not examine too closely what is happening near the ends of the body. The last qualification is necessary because slender-body theory is based on one major assumption which is usually violated near the body ends : It is assumed that the rates of change of all flow variables are much greater in the transverse directions than in the longitudinal direction. For a body with cusped ends, this assumption is valid even in the region near the ends, but the assumption is not valid near the body ends for most bodies of practical interest. The result is that slender-body theory typically predicts some kind of singular flow near the body ends.

Such a result is not necessarily unacceptable. If the singularities are integrable in some appropriate fashion and if the solution is approximately correct in most of the flow region, the presence of singularities in the mathematical solution may not even be serious. If one is very careful in obtaining the singularity strengths, one can even make some reasonable calculations concerning the flow around a blunt body in an infinite fluid. At cross-sections not too near the ends, the presence of singularities in the solution for the body end regions manifests itself as a perturbation of the longitudinal velocity compo-

nent ; this effect is rather minor over most of the body surface, and its precise evaluation is carried out by matching the near-field and far-field solutions.

In the free-surface problem, this procedure leads to an essential difficulty : In the far-field problem, the disturbance caused by the presence of the body appears actually to be caused by a line distribution of sources along the x axis, this axis lying in the plane of the undisturbed free surface. A concentrated source in the plane of the free surface is completely intolerable, because it causes much more than just local problems. (For example, the wave resistance of such a source is infinite.) Therefore we cannot hope to represent end effects in the simple way that is sometimes so successful for bodies in an infinite fluid. In particular, we note the following important fact : No matter how nonlinear the local flow around the bow of the body may be, it cannot appear from afar as if it had been caused by a concentrated source.

In fact, an even stronger statement is possible : If, in the far field, the disturbance appears to have been caused by a line distribution of sources, the distribution must have a density which varies continuously. For the wedgelike body considered in this paper, slender-body theory predicts that the source density in the far-field expansion should have a jump at the bow. Actually, there may be a steep rise in the curve of source density, but there can be no jump in value. Otherwise the whole far-field solution has little meaning. The far-field solution must be less singular at the bow than one might expect from infinite-fluid slender-body theory.

There is another point of view which also encourages some optimism for treating the free-surface problem. The local behavior at the nose of a body in an infinite fluid appears to be intrinsically a three-dimensional problem. The presence of the body must have a fairly significant upstream influence. However, the additional presence of a free surface should reduce such upstream influences. Moreover, the isobaric property of the free surface may tend to smooth out variations in the longitudinal direction. Thus, one may be greatly encouraged to attempt to analyze the ship problem by slender-body theory.

These rationalizations have come, for the most part, after the preceding analysis had been developed and found to compare fairly well with experiments. Originally the motivation had been more like that described in the Introduction. In any case, we have found fair agreement between the analysis and our experiments, and so we should proceed to investigate further the internal consistency of the

analysis, while we also investigate possible modifications and check them against experiments.

In the analysis as presented here, one may observe that the solution in the "bow near field" was never matched directly with the usual far-field solution of slender-ship theory. As Hirata [4] discovered, this is no small task. I have not yet carried out this matching, but I assume that it would lead only to a modification of the far-field source density in the neighborhood of the ship bow. Presumably, the source density curve would be rounded over in a region of length $O(\epsilon^{1/2})$ near the bow. Thus it would be possible to compute the wave resistance of this shape of ship. (We have no assurance that the value computed would be accurate, but it would be a big improvement over ordinary slender-ship theory, which would give an infinite value of wave resistance for the ship with wedgelike bow !)

We have made only a few crude attempts to predict what happens just ahead of the edge of the wedge, and these attempts have not been described. Using a very heuristic mathematical mode, I concluded at one time that the rise in water level ahead of the bow should be independent of forward speed (for a given wedge angle), and it was this tentative conclusion that led us to examine our photographs carefully, after which we came to a conclusion that there must be some truth in the crude analysis, since the water rise is in fact quite insensitive to forward speed.

The fact that the analysis is linear is, of course, a great help in obtaining a solution, but the most casual observation of the physical situation (as in Figures 3 and 4) suggests that linearisation may be a great over-simplification. In defense of the linearization in this analysis, I offer just two comments :

(i) It always seems reasonable to try a linear analysis of any problem. One must in any case trust experimental evidence for the justification of an analysis. In the present problem, it is evident that the linear analysis is not grossly wrong.

(ii) In many mathematical analyses of fluid mechanics problems, apparently unacceptable singular solutions often become very useful when they are properly interpreted. I have already mentioned the appearance in slender-body theory of flow singularities which result from the invalidity of the assumptions in the regions near the body ends. Perhaps an even more interesting situation arises in some problems in which we find that the solution to a linearized problem represents approximately the correct flow patterns - but in slightly wrong places. Our bow-flow solution, for example, is not so singular

as that which results from the usual slender-body theory, but it is still singular. It is interesting to note that the experimental data in Figure 6 would have a more orderly appearance if the ordinate scale had started at about $x_{max} \simeq -2$. In other words, the predictions in Figure 6 are considerably improved if we arbitrarily assume that the rise in water level should have been measured from a point about 2 in. ahead of the bow. To this extent, our linearized results follow the pattern mentioned above : They are approximately correct, but in the wrong place.*

The form chosen for the solution in (1) is not an essential part of the analysis presented in this paper. It was an easy way to arrive quickly at a solution for a particular case. It has already been mentioned that this simplification may be at least partly responsible for the discrepancy between analysis and experiments at the higher Froude numbers. Having now determined that we have found some general agreement between analysis and experiments, we shall next try to obtain more precise solutions for these and similar problems. For example, the body cross-section shown in Figure 1 (either (a) or (b)) can be mapped into an auxilliary plane in which body and free surface together make up the horizontal axis. The free-surface condition must be transformed, of course, and then an integro-differential equation comparable to (3) can be obtained. This procedure can also be followed for bodies which are not symmetrical or for bodies which have an angle of attack. No solutions have been obtained yet except for that described by Hirata [4] for the case of a plate of zero thickness with an angle of attack. I hope that we shall be able to obtain solutions for several more realistic situations - for which comparisons with experimental data will provide more definitive evaluations of the fundamental approach described in the present paper.

* * *

---

* A more careful study of Figure 6 shows that the predicted curves have the correct slopes if the origin is placed on a sliding scale, with essentially no shift for the case of small draft, up to a shift of about 5 in. for the maximum draft case. I do not want to try to read too much quantitative significance into this result, however.

ACKNOWLEDGEMENTS

The analysis described in this paper developed during and out of discussions that I had in the spring of 1971 with several students in the Department of Naval Architecture and Marine Engineering at the University of Michigan : Eiichi Baba, Odd M. Faltinsen, Miguel H. Hirata, Arthur M. Reed, and William S. Vorus. It was a unique experience for me to have these students together, working as a group, analyzing problems without inhibitions even while criticizing one another. Each of them contributed in some way to this paper, and I dedicate it to them, scattered as they now are over four continents.

This research was carried out under the Naval Ship Systems Command General Hydromechanics Research Program, Subproject SR 009 01 01, administered by the Naval Ship Research and Development Center (Contract No. N00014-67-A-0181-0033).

NOTATION

$b(x, z)$	hull offset (half-width)
$b(x)$	special case of $b(x, z)$ (the wedge problem)
g	gravitation constant
$H(x)$	draft of the section at x
H	special case of $H(x)$ (the wedge problem)
ℓ	transform variable
L	ship length
r	$(y^2 + z^2)^{1/2}$
U	forward speed
x, y, z	coordinates
X	$x\sqrt{K/H}$
α	$b'(0)$, half-angle of the wedge
ϵ	slenderness parameter
$\zeta(x, y)$	free-surface elevation
$Z(X)$	nondimensional $\zeta(x, 0)$; see Equation (17)
K	g/U^2
ϕ	perturbation velocity potential
$\psi(x, y)$	$\phi(x, y, 0)$

REFERENCES

[1] OGILVIE, T.F., "Nonlinear High-Froude-Number Free-Surface Problems", Jour. Engin. Math., 1 (1967) 215-235.

[2] VOSSERS, G., "Some Applications of the Slender Body Theory in Ship Hydrodynamics", Ph. D. thesis, 1960, Technical University of Delft.

[3] JOOSEN, W.P.A., "Slender Body Theory for an Oscillating Ship at Forward Speed", Fifth Symposium on Naval Hydrodynamics, ACR-112, 1964, pp. 167-183, Office of Naval Research, Washington, D.C.

[4] HIRATA, M.H., "On the Steady Turn of a Ship", Ph. D. thesis, 1972, The University of Michigan.

[5] BABA, E., unpublished manuscript, 1971.

[6] MARUO, H., "High- and Low-Aspect-Ratio Approximation of Planing Surfaces", Schiffstechnik, 14 (1967) 57-64.

[7] LIGHTHILL, M.J., "Fourier Analysis and Generalised Functions", 1959, Cambridge University Press, Cambridge.

[8] TUCK, E.O., "A Systematic Asymptotic Expansion Procedure for Slender Ships", Jour. Ship Research, 8:1 (1964) 15-23.

[9] ABRAMOWITZ, M. and STEGUN, I.A., Ed., "Handbook of Mathematical Functions", Applied Mathematics Series - 55, National Bureau of Standards, 1964, Washington, D.C.

DISCUSSION

Reinier Timman
Delft Institute of Technology
Delft, Netherlands

I do not have many questions to ask. The only thing I want to do is congratulate Professor Ogilvie on his paper. Slender body theory for years has been stagnating because we all knew that it did not work well at the bow region. Professor Ogilvie has apparently opened a way to get good results even there. It could be asked, though, what would happen with a blunt body, but that is rather trivial. The only thing you know is that this does not work for a blunt body but it gives a result with this wedge shaped body which is really very good and his way of looking at it opens up a new way of attacking several other problems. So there is hope of making real progress in connection with many questions in this field. I am very happy that this paper has been presented here and I hope that it will open the way for new progress.

REPLY TO DISCUSSION

T. Francis Ogilvie
University of Michigan
Ann Arbor, Michigan, U.S.A.

I just want to say one word besides, obviously, thank you. This same analysis has also been applied to a rather blunt, flat ship by Baba. I am sorry that I have not been able to read it yet although I have a copy, but it is in Japanese. He also claims some rather remarkable success so perhaps there is something there for blunt ships.

DISCUSSION

Ernest O. Tuck
University of Adelaide
Adelaide, Australia

I have just one very small comment. The nature of the two-dimensional problem that Professor Ogilvie is solving is, in fact, that of a Cauchy-Poisson problem. The co-ordinate x appears as a parametric co-ordinate, since it does not enter the governing field equation, so that it plays a role which is identical to the role played by time in a two-dimensional Cauchy-Poisson problem. In fact, with that interpretation the problem solved by Professor Ogilvie here actually corresponds to a growing wedge in a Cauchy-Poisson two-dimensional problem and presumably the Baba problem is the equivalent of a pressure distribution on a free surface which is growing laterally as well as increasing with time.

REPLY TO DISCUSSION

T. Francis Ogilvie
University of Michigan
Ann Arbor, Michigan, U.S.A.

I should have recognized that. Of course, Wagner recognized that many years ago when he put these two problems together in one paper.

DISCUSSION

Gedeon Dagan
Technion and Hydronautics Ltd.
Haifa, Israël

I should like to ask if nevertheless you have tried to compare the experiments with thin ship computation, and I will go farther than that. I think that the slender body theory can be shown to be a kind of particular case of the thin body theory if you let the draft go down to zero, and I wonder if your theory also can be derived as a particular case of the ship approximation.

REPLY TO DISCUSSION

T. Francis Ogilvie
University of Michigan
Ann Arbor, Michigan, U.S.A.

In fact I have a comment somewhere in the paper on that. If you think back to the boundary value problem that I solved, I had the same free surface condition which everybody uses in thin ship theory and I had the same body boundary condition which everybody uses in thin ship theory. The only difference was that I dropped one term from the Laplace equation. So to the extent that that term is small then they ought to give identical results. Of course, that term is probably not small and that is part of the reason I am looking at it. So I am not quite sure what the difference would be.

* * *

TRANSCRITICAL FLOW PAST SLENDER SHIPS

G. K. Lea
National Science Foundation
Washington, D. C. U.S.A.

J. P. Feldman
Naval Ship Research and Development Center
Washington, D. C. U.S.A.

ABSTRACT

The transcritical shallow water flow past slender ships is analyzed using the method of matched asymptotic expansions. A consistent first order approximation was derived which is analogous to the non-linear transonic equation with the Froude and Mach numbers playing similar roles. Solutions are obtained for sinkage and trim in the transcritical region and are compared with experimental results. An important result is that both sinkage and trim are functions of Froude number as well as beam to length ratio in the region where Froude number based on undisturbed depth is close to unity.

INTRODUCTION

In a series of papers Tuck [1] [2] developed a systematic expansion procedure for the approximate solution to the shallow water flow past slender ships. It was pointed out that a close analogy exists between this problem and the inviscid slender body aerodynamics problem. In fact, Tuck's solution contains the same type of singularity that is encountered in aerodynamic theory and we present here an attempt to remove the singularity which occurs in the transcritical region. Thus the shallow water problem that will be examined is concerned only with steady translational motion of a slender ship and the associated surface waves so that viscous and compressibility effects are neglected.

The Froude number ($F_h = U_\infty / \sqrt{gh}$, where U_∞ is the free stream speed, g is the acceleration of gravity, h is the undisturbed

depth) can be interpreted as the ratio of a characteristic speed to the propagation speed of small disturbances on the water surface in shallow water theory. On the other hand in aerodynamic theory, the Mach number ($M_\infty = U_\infty / a_\infty$, where U_∞ is the free stream speed and a_∞ is the isentropic speed of sound) is the ratio of the characteristic speed to the propagation speed of acoustic signals in the gas. Thus we see that Froude and Mach numbers play similar roles and this is reflected in the mathematical formulation of the two problems. For example, Tuck[2] gave for the first approximation a hyperbolic equation for supercritical flow $F_h > 1$ and an elliptic equation for subcritical flow $F_h < 1$. We find the same situation in inviscid compressible flow past slender bodies for supersonic $M_\infty > 1$ and subsonic $M_\infty < 1$ flows. His results for vertical force, trim moment as well as drag contains integrals which relates the source sink distribution to the local hull area and multiplied by the following factor :

$$\rho U_\infty^2 \; / \; h\sqrt{1 - F_h^2} \qquad \text{for subcritical flow and}$$

$$\rho U_\infty^2 \; / \; h\sqrt{F_h^2 - 1} \qquad \text{for supercritical flow}$$

This factor seem to indicate catastrophic failure at critical flow $F_h = 1$. However, it should be pointed out that aside from the transcritical region, where $| F_h^2 - 1 |$ is small, Tuck's results appears to be more than adequate for most engineering purposes.

We shall seek a singular perturbation solution to the problem of shallow water flow past a slender ship with the requirement that the solution must be valid within the transcritical region. This approach is that followed by Tuck[1][2] and is well documented in books by Cole[3] and Van Dyke [4] . The important difference between what follows and the works of Tuck is that two small parameters appear in the formulation, slenderness ratio and Froude number parameter $| F_h^2 - 1 |$, instead of only the slenderness ratio. Appearence of an additional parameter drastically alters the mathematical representation of the problem and the nonlinear effects suggested by Tuck[2] are indeed present.

I. EXACT STATEMENT OF THE INVISCID PROBLEM

Consider a ship immersed in a steady stream of inviscid, incompressible stream with free stream velocity of $U_\infty \hat{e}_x$. A cartesian coordinate system is afixed to the ship with its origin at the bow and at the undisturbed waterline. The positive x-axis is directed toward the stern of the ship and z-axis is directed vertically upward.

The total velocity in the flow field is given by :

$$\vec{q} = U_\infty \hat{e}_x + \text{grad } \varphi$$

where φ is the disturbance potential due to the presence of the ship. The dimensional governing equations are the Laplace equation, free surface kinematic and pressure equations, bottom condition and hull tangency condition. These are as follows :

$$\varphi_{xx} + \varphi_{yy} + \varphi_{zz} = 0 \qquad (1\text{-a})$$

$$\varphi_z = (1 + \varphi_x)\,\zeta_x + \varphi_y \zeta_y \qquad (1\text{-b})$$

$$2\zeta g/U_\infty^2 = -(2\varphi_x + \varphi_x^2 + \varphi_y^2 + \varphi_z^2)_{z=\zeta(x,y)} \qquad (1\text{-c})$$

$$(\varphi_z)_{z=-H} = 0 \qquad (1\text{-d})$$

$$\varphi_y = (1 + \varphi_x) A_x + \varphi_z A_z \qquad (1\text{-e})$$

where $\zeta(x, y)$ is the unknown free surface and $A(x, z)$ is the given surface of the ship hull. If we are to proceed in a systematic fashion the relative orders of magnitude of the various terms must be established. One way of accomplishing this is by selecting proper scales for all the dependent as well as independent variables and thereby introduce non-dimensional variables of order unity. This does not mean that all quantities will have its maximum of one, but rather that if we choose the correct scale the maximum value could be large as ten units but not one thousand units. We take U_∞ as the velocity scale and the undisturbed depth, H, as the vertical length scale. The selection of a horizontal length scale is a bit more involved as it must reflect the shallow water approximation include the transcritical nonlinearities produced by a slender hull.

Now, shallow water theory assumes as a first approximation that the vertical pressure variation is purely hydrostatic or that vertical accelerations are negligible compare to horizontal accelerations. This can be derived in a systematic manner assuming that the depth to characteristic wave length ($H / L_w << 1$) is small and utilize L_w as the length scale in x and y directions and expand φ as a power series in H / L_w . We note that shallow water theory is not necessarily linearization and the latter results from restrictions that we place on the type of "wave maker" present in the problem. Furthermore, we note that the surface wave system generated by a ship at critical

speed is a single wave of translation perpendicular to the free stream. In the absence of viscous dissipation this wave extend to infinity so that the disturbance in the lateral, y, direction is greater than in the axial, x, direction. Thus it seems logical that we should have $x=0(1)$ and $y=0(\varepsilon^{-n})$ at large distances from the ship where ε is a small parameter related to the "shallowness" of the water.

Shallowness implies that depth is small relative wave length ($H / L_w << 1$) and slenderness implies that the wave maker, the ship, must be longer than it is either wide or deep. If we define B as the maximum beam, T as the maximum draft, then slenderness means

$$B / L << 1 , \quad T / L << 1$$

where L is the length of the ship. In order to proceed in an orderly manner some estimates must be placed on the relative orders of magnitude between L_w and L . We note that the dispersion relationship for steady progressive free waves in two-dimensions is

$$\tanh (2\pi H / L_w) / (2\pi H / L_w) = U_\infty^2 / gH \qquad (2)$$

which can be approximated by the following expression after making use of the long wave assumption ($H / L_w << 1$)

$$H / L_w \cong \sqrt{(3 / 2\pi) (1 - F_H^2)}, \quad F_H^2 = U_\infty^2 / gh \qquad (3)$$

The behaviour of this expression in the transcritical region is estimated as

$$H / L_w = 0 (\sqrt{1 - F_H^2}) \qquad (4)$$

Furthermore, if we take the depth to ship length ratio H / L as gauged by the slenderness of the hull, i. e. $H / L = 0 (\varepsilon)$, then

$$L_w / L = 0 (\varepsilon / \sqrt{1 - F_H^2}) \qquad (5)$$

As the ship approaches the critical flow condition, the characteristic wave length of the surface wave decreases so that in order to retain the transcritical effects and at the same time impose slenderness assumption we take

$$L_w / L = 0 (\varepsilon / \sqrt{1 - F_H^2}) = 0 (1)$$

We note that in Tuck's analysis[2] it was assumed that as the ship

approaches a line ($\varepsilon \to 0$) that $|1 - F_H^2|$ remains fixed and of order unity which implies that $L_w \,|_L = 0(\varepsilon) \ll 1$ and is equivalent to the condition $F_L = U_\infty / \sqrt{gL} = 0(\sqrt{\varepsilon})$. Thus outside the transcritical region the proper scale length in any horizontal plane is the length of the hull L. However, the situation within the transcritical region is $L = 0(L_w)$ so that we can choose either L or L_w as a horizontal characteristic length with the restriction $\varepsilon / \sqrt{|1 - F_H^2|} = 0(1)$ or

$$F_H^2 = 1 + \varepsilon K \tag{6}$$

where K is some similarity constant which is of order unity. The particular form chosen here is guided by the transonic aerodynamics analysis of the slender airfoil theory since we anticipate a close analogy between it and the present shallow water problem. It should be noted that in aerodynamic theory K is not uniquely determined by any analytical approach but depends on the correlation of experimental data.

II. FAR FIELD APPROXIMATION

Singular perturbation solution is a systematic procedure by which successive estimates to the solutions can be made in the various regions of the domain of solution. If properly applied, the dominate features of each of these regions will be magnified and secondary features suppressed by scaling of variables. We expect that in the far field details of the ship hull will be lost and that the dominate feature of the problem is that of the surface wave system. As noted in the previous section $L_{wave} / L_{ship} = 0(1)$ in transcritical region so that for scaling purposes either one would be appropriate and we shall refer to it as simply the characteristic length L. The shallowness parameter ε and the slenderness parameter δ are given by

$$\varepsilon = H / L$$

$$\delta = B/L,\ T/L$$

We shall restrict our attention to that class of problems in which the hull must be more slender than the water is shallow, i. e. the maximum draft be less than the depth, thus

$$\lim_{\varepsilon \to 0} (\delta / \varepsilon) = 0$$

A simple relation which satisfies this condition is

$$\varepsilon = \delta^m \quad , \quad 0 < m < 1$$

where m is a constant which will be determined by the matching of far field solution to near field solution. It must be remembered that this restriction placed on ε and δ does not imply the existence of a functional relationship between slenderness of hull and depth of free stream. We have chosen the shallowness parameter, ε, as a convenient gauge function* and use it as a standard for order of magnitude comparisons.

The following non-dimensional and scaled variables are introduced :

$$\overline{x} = x L \, , \; \overline{y} = y L \varepsilon^{-p} \, , \; \overline{z} = z L \varepsilon \, , \; \overline{\zeta} = \zeta L \varepsilon$$

and the non-dimensional variables

$$\overline{q} = q U_{\infty} \, , \; \overline{\varphi} = U_{\infty} L \varphi \, , \; F_H^2 = 1 + \varepsilon K \, , \; K = 0(1)$$

The full inviscid equations become :

Potential Equation

$$\varphi_{zz} + \varepsilon^2 \varphi_{xx} + \varepsilon^{2+2p} \varphi_{yy} = 0 \tag{7-a}$$

Bottom Tangency

$$\varphi_z (x, y, -1) = 0 \tag{7-b}$$

Free Surface Kinematic

$$\varphi_z = \varepsilon^2 (1 + \varphi_x) \zeta_x + \varepsilon^{2+2p} \varphi_y \zeta_y \quad \text{on } z = \zeta(x, y) \tag{7-c}$$

Free Surface Pressure

$$2 \varepsilon^2 \zeta / 1 + \varepsilon K = -(\varphi_z)^2 - \varepsilon^2 [2\varphi_x + (\varphi_x)^2 + \varepsilon^{2p} (\varphi_y)^2]$$

$$\text{on } z = \zeta(x, y) \tag{7-d}$$

We assume the following far field expansions for the disturbance potential and the free surface elevation

$$\varphi \sim \sum_{n=1} \varepsilon^n \varphi_n (x, y, z) \, , \quad \zeta \sim \sum_{n=1} \varepsilon^n \zeta_n (x, y) \tag{8}$$

Substituting these expansions into the full inviscid equations and equating like powers of ε results gives the following :

* See Van Dyke (4), pages 23-28

Disturbance Potential :

$$\varphi \sim f_1(x,y)\,\varepsilon + f_2(x,y)\,\varepsilon^2 + \left[f_3(x,y) - (z+1/2)^2 f_{1xx}\right]\varepsilon^3 \ldots$$
$$+ \varepsilon^4\left[f_4(x,y) - (z+1/2)^2 (f_{2xx} + f_{1yy})\right] + 0(\varepsilon^5) \qquad (9\text{-a})$$

Free Surface Kinematic :

$$(\zeta_{1x} + f_{1xx})\varepsilon^3 + (\zeta_{2x} + f_{2xx} + \zeta_{1x} f_{1x} + \zeta_1 f_{1xx} + f_{1yy})\varepsilon^4 \ldots$$
$$+ 0(\varepsilon^5) = 0 \qquad (9\text{-b})$$

Free Surface Pressure :

$$(\zeta_1 + f_{1x})\varepsilon^3 + (2\zeta_2 + 2f_{2x} + f_{1x}^2 + 2Kf_{1x})\varepsilon^4 + 0(\varepsilon^5) = 0 \qquad (9\text{-c})$$

The bottom tangency condition is satisfied to $0(\varepsilon^4)$ and the "stretch" in the y-coordinate is taken as $\bar{y} = yL/\varepsilon^p = yL/\sqrt{\varepsilon}$ or $p = 1/2$. This is determined by the observation that if $p<1/2$, then the expansions should proceed as fractional powers of ε which cannot be matched to the near field solution. On the other hand, if $p > 1/2$, then the term f_{1yy} would not appear to $0(\varepsilon^4)$ and a degenerate case results. Thus the choice of $p = 1/2$ results in a "distinguished limit process" as $\varepsilon \longrightarrow 0$.* The governing equation for the first approximation to the disturbance potential ($\varphi_1 = f_1(x,y)$ is obtained by elimination of second order variables (f_2 and ζ_2) between the free surface kinematic and pressure conditions to $0(\varepsilon^4)$ and is

$$(K + 3f_{1x})\,f_{1xx} - f_{1yy} = 0 \qquad (10)$$

The mathematical structure of this equation could change locally in the domain of solution depending on the algebraic sign of the term $(K + 3f_{1x})$. This equation can describe locally subcritical flow (elliptic equation) when $(K + 3f_{1x}) < 0$, supercritical flow (hyperbolic equation) when $(K + 3f_{1x}) > 0$ and the local characteristics have the slope

$$(dy/dx) = \pm\left[K + 3f_{1x}\right]^{-1/2} \qquad (11)$$

The expansion for the disturbance potential (φ) given by equation (9-a) is similar to Tuck's outer expansion; however, it must be noted that our small parameter is based on depth ($\varepsilon = H/L$) while Tuck's parameter is the slenderness ratio ($\delta = B/L$). We

* See Cole (3), page 46

note that the Laplacian operator in the horizontal plane does not occur to $0(\varepsilon^4)$ thus in this respect the present expansion for the disturbance potential is simpler than the linear theory. On the other hand, the free surface kinematic and pressure conditions for φ_1 are derived from higher order approximation which lead directly to the nonlinearity in the problem. It would appear that in the transcritical region the nonlinear free surface conditions are dominate and the potential nature of the flow is only secondary. In passing we note that equation (10) is mathematically identical to the equation governing transonic flow past two dimensional airfoils.

We can now define the relative orders of magnitude between the shallow water parameter (ε) and the slender body parameter (δ) by examination of the behavior of the far field solution on the body surface. While this can actually be done by the formal matching process, we choose to do it here to simplify the algebra. Substituting the far field variables and expansion into the hull tangency condition, we obtain for the leading terms

$$\varepsilon^{3/2} f_{1y}(x, \delta A) + \varepsilon^{5/2} f_{2y}(x, \delta A) = \delta A_x + \varepsilon\delta\left[f_{1x}(x, \delta A) A_x \cdots - (z+1) f_{1xx}(x, \delta A) A_z\right] \quad (12)$$

where the "slenderness" of the ship hull is exhibited explicitly through δA with $A = 0(1)$. Guided by the two-dimensional aerodynamic slender air foil theory, we take $\varepsilon^{3/2} = \delta$ which satisfies our earlier requirement that $\lim_{\varepsilon \to 0} (\delta/\varepsilon) = 0$. Thus it seems to imply that the shallow water problem is analogus to high aspect ratio airfoil problem while the deepwater problem is analogus to the low aspect ratio problem.

III. NEAR FIELD APPROXIMATION

The nonlinear effects are not expected to be important in the near field region where the basic flow pattern is strongly influenced by the hull form. As a result, one would expect that the near field expansion would yield a series of Neumann problems in the (y-z) cross flow plane similar to those derived by Tuck [2] . The following non-dimensional and scaled variables are introduced :

$$\bar{x} = XL\,,\ \bar{y} = \varepsilon LY\,,\ \bar{z} = \varepsilon LZ, \bar{\zeta} = \varepsilon L\zeta,\ \bar{N} = \varepsilon LN$$

All the remaining variables are as in the case of far field approximation. An additional variable $\bar{N}$ is introduced such that the unit vector $\hat{e}_N$ in the N direction is normal to $\hat{e}_x$ and the hull contour $(\delta A(Y, Z))$

at any given cross section. We assume the following expansions for the disturbance potential and the free surface elevation

$$\varphi \sim \sum_{n=1} \alpha_n(\varepsilon)\, \sigma_n \quad , \qquad \zeta \sim \sum_{n=1} \beta_n(\varepsilon)\, \zeta_n \quad . \tag{13}$$

Following the same procedure as for the far field solution, we obtain a consistant approximation in the near field to $0\ (\varepsilon^{5/2})$ given by

$$\alpha_1(\varepsilon) = \varepsilon^{3/2} \ , \ \alpha_2(\varepsilon) = \varepsilon^{5/2} \ , \ \beta_1(\varepsilon) = \varepsilon$$

$$\nabla^2_{(Y,Z)} \sigma_n = 0 \qquad (n = 1, 2) \tag{14-a}$$

$$\sigma_{nZ}(X\ Y, -1) = 0 \qquad (\text{all n's}) \tag{14-b}$$

$$\sigma_{nZ}(X, Y, 0) = 0 \qquad (n = 1, 2) \tag{14-c}$$

$$\sigma_{nN}(X, A) = \sigma_n \ , \ \sigma_1 = 0, \ \sigma_2 = A_X/\sqrt{1+A_Z^2} \tag{14-d}$$

To the second approximation (n = 2), the boundary value problems derived are identical to those of Tuck[2] as well as the order of magnitude estimate placed on the disturbance potential.* However, we note there is a difference in the estimate placed on the elevation of the free surface and is

$$\overline{\zeta}_{\text{Tuck}} \sim 0(\varepsilon^2_{\text{Tuck}}) = 0\,(\delta^2_{\text{present}}) = 0\,(\varepsilon^{6/2}_{\text{present}})$$

$$\overline{\zeta}_{\text{present}} \sim 0(\varepsilon^2_{\text{present}}) = 0(\delta^{4/3}_{\text{present}}) = 0(\varepsilon^{4/3}_{\text{Tuck}})$$

Thus we see that the surface disturbance is stronger here than in the linear case.

Since the Neumann problems defined by equations (14) have already discussed in detailed by Tuck[1][2] , we shall make use of his results and using the restricted matching technique of Van Dyke [4] to match one term far field to the two terms near field approximation. The important result is the hull tangency condition for the far field equation on a equivalent body and gives

$$f_{1Y}(x, 0^+) = S'(x) / 2 \tag{15}$$

---

* We note here the difference in notation $\varepsilon_{\text{Tuck}} = \delta_{\text{pres.}} = \varepsilon^{3/2}_{\text{pres.}}$

where S(x) is the cross sectional area of the ship hull immersed in the water.

IV . RESULTS AND DISCUSSION

The resulting nonlinear problem, for the first approximation, can be solved numerically or solved approximately using methods of local linearization developed in transonic aerodynamic literature[5] [6] . We have taken the latter approach due to limitations on computer time and the details of which are given by Feldman[7]. Here, we shall present some results for the sinkage and trim of a semi-submerged spheroidal hull. The cross sectional area of the hull is

$$R = B_{max} (x / L - x^2 / L^2)^{1/2},$$

where B_{max} is the maximum beam. The trim and sinkage are computed at the bow with units of trim measured in terms of ship length and slenderness ratio of 1:10. The results are presented in figure 1 where the Froude number is based on the undisturbed depth. In figure 2, we have presented the same curves but using a different scale so that the linear results computed from Tuck's[2] solution can be viewed simultaneously for comparison.

The apparent discontinuity in slope at $F_h = 1.0$ and $F_h = 1.09$ is due to the method of solution and not the model equation. We note that these solutions do indicate the overshoot as well as undershoot of sinkage and trim respectively through the transcritical region which have been measured in experiments such as the works of Graff, Kracht and Weinblum[8] as well as the more recent work of Graff and Binek[9]. Sinkage as well as trim data have been computed for more realistic hulls and these will be reported else-where*. However, one particular case with experimental results of Graff[8] et al is given here for comparison. The hull chosen is Model A3 of D. W. Taylor's Standard Series and the flow condition is exactly critical ($F_h = 1$). For computational purposes, the cylindrical hull is approximated by a fourth degree polynomial-arc, we have

Experiment (Graff et al)

$\text{Trim}_{bow} = 2.0$, $\text{Sinkage/Length}_{bow} = -.015$

Theory

$\text{Trim}_{bow} = 2.09$, $\text{Sinkage/Length}_{bow} = -.0123$

at $F_h = 1.0$

---

* Paper to appear in the proceedings of the 13th ITTC Conference by Feldman and Lea.

The theory appears to be in fair agreement with experiment and indicates that this direction or research should be fruitful.

V. ACKNOWLEDGMENT

We are greatly indebted to Professors Th. Y. Wu and J.N. Newman who encouraged us and nudged us along the path to a possible solution. One of us (G.K.L.) wishes to express his sincere thanks to Mrs. Lea who typed and retyped this manuscript expertly and willingly.

REFERENCES

1 TUCK, E.O., "A Systematic Asymptotic Expansion Procedure for Slender Ships", Journal Ship Research, 1964.

2 TUCK, E.O., "Shallow-Water Flows Past Slender Bodies" Journal of Fluid Mechanics, Vol. 26, Part I, 1966.

3 COLE, J.D., "Perturbation Methods in Applied Mathematics" Blaisdell Publishing Company, Waltham, Massachusetts, 1968.

4 VAN DYKE, M.D., "Perturbation Methods in Fluid Mechanics" Academic Press, New-York, 1964.

5 SPREITER, J.R. and ALKSNE, A.Y. "Thin Airfoil Theory Based on Approximate Solution of the Transonic Flow equation" NACA Technical Report 1359, 1958.

6 HOSKAWA, I. "A Simplified Analysis for Transonic Flows Around Thin Bodies" Symposium Transsonicum, Aachen, September 3-7, 1962, Springer-Verlag, Berlin, 1964.

7 FELDMAN, J.P. "Transcritical Shallow Water Flow Past Slender Ships", Ph. D. Dissertation, The George Washington University, Washington, D.C., 1971.

8 GRAFF, W., KRACHT, A. and WEINBLUM, G., "Some Extensions of D.W. Taylor's Standard Series", Transactions of the Society of Naval Architects and Marine Engineer, Vol. 72, 1964.

9 GRAFF, W. and BINEK, H., "Untersuchung des Modelltankeinflusses an einem Flachwasserschiff" Forschungsberichte des Landes Nordrhin-Westfalen, Nr 1986, Westdeutscherverlag, 1971.

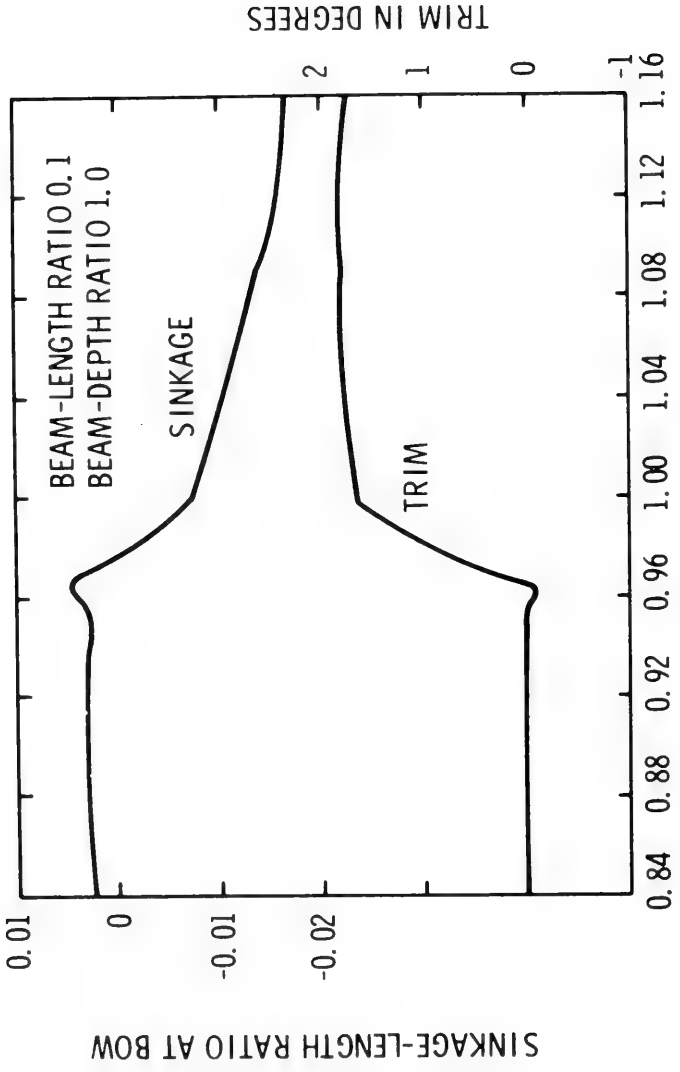

Figure 1 Semi-submerged spheroidal hull

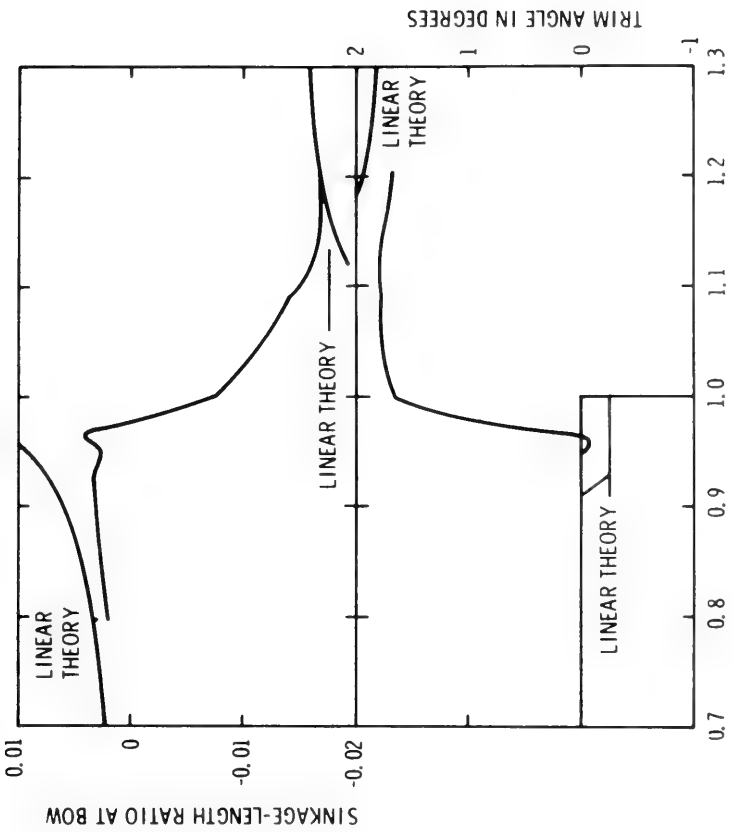

Figure 2 Comparison between the linear and transcritical theories for a semi-submerged spheroidal hull of beam-length ratio of 0.1 and beam-depth ratio of unity

DISCUSSION

Ernest O. Tuck
University of Adelaïde
Adelaïde, Australia

I am very please to see this done. One thing that bothers me is the condition that delta is order epsilon to the three halves. It seems very surprising that the theory should depend upon such a restriction. In my original linear theory, delta and epsilon were identical, and it seems unreasonable of a theory to demand such a geometrical constraint a priori.

REPLY TO DISCUSSION

George K. Lea
National Science Foundation
Washington D.C., U.S.A.

The odd power of 3/2 appears is due directly to the critical flow parameter $\sqrt{F_H^2-1}$. You must remember that the relation between ϵ and δ is an artificial one. Their relative orders of magnitude are established through matching, with the a priori requirement that a reasonable solution can be obtained as $F_H \rightarrow 1$. This type of proceedure must always be followed when more than one small parameter appears in the problem. The difference between this and your linear result is the difference between non-linear and linear approximations.

DISCUSSION

Ian W. Dand
National Physical Laboratory
Feltham, England

We have obtained some measurements of sinkage and trim on tanker forms in sub-critical flow, but, using self-propelled and towed models. These showed that the effect of the propeller when the model was self-propelled was such as to modify appreciably the measured trim. I have two questions as a result.

1. Were the model results, used as a comparison in this paper, obtained with self-propelled or towed models ?

2. As the effect of self-propulsion on trim seems to be quite marked in our experience, is it possible to take account of this theoretically ?

REPLY TO DISCUSSION

George K. Lea
National Science Foundation
Washington D.C., U.S.A.

We did not run any model tests ourselves and all comparisons were made with the data of Professor Weinblum and others given in the list of references. Test were towed tests.

Self-propelled models may be under additional moments due to the onboard thruster which could cause an initial trim even at zero Froude number. The result is that the water plane area could be different and this can be accounted for by changing the area distribution, S(x), in our computations. I would expect the differences between towed and self-propelled models to be the least for trim when you are dealing with full-forms like tankers.

* * *

COMPUTATION OF SHALLOW WATER SHIP MOTIONS

R. F. Beck and E. O. Tuck
University of Adelaide
Adelaide, Australia

ABSTRACT

In previous papers by Tuck (Journal of Ship Research, 1970) and Tuck and Taylor (8th Symposium on Naval Hydrodynamics, 1970), a framework was set up for a complete theory of ship motions in shallow water, in all 6 degrees of freedom. The present paper continues this work by presenting actual computed motions for a full form hull, both restrained and unrestrained, in long waves of various headings.

I. INTRODUCTION

In this paper we present computed results and/or discussion of motions in all six degrees of freedom of a Series 60, block coefficient 0.80 ship, at zero speed of advance in shallow water. These motions are supposed to be induced by incident plane sinusoidal waves of various headings.

The shallow water theory of Tuck (1970) (see also Tuck and Taylor, 1970, and Beck and Tuck, 1971) is used to provide the coefficients in the equations of motion. This theory requires that the wavelength be much greater than the depth of the water, which restricts attention to long waves and low frequencies. Such long waves are important for large ships, since they have the greatest potential for motions excitation, even though the low frequency assumption rules out resonance in heave, pitch or roll.

In Section 2 we discuss some general analytical features of the equations of motion of a ship in shallow water, and consider the relative importance for each mode of motion in turn of various types of inertial, hydrostatic, and hydrodynamic forces. The force balances

which dictate the ultimate motions are complicated, but in most cases there are pairs of forces which contribute most to this balance, other forces being formally of a smaller order of magnitude with respect to a small parameter such as beam/length ratio.

For instance, in heave and pitch the dominant force balance is between hydrostatic restoring force and the pressure of the incident wave (so-called Froude-Krylov exciting force). Inertia, both natural and hydrodynamic (added mass), damping, and diffraction of the incident wave are all effects of lesser significance in the range of wave periods considered. Indeed, remarkably in shallow water the natural inertia or mass of the ship has the least influence of all these forces. Similar simplifications can be made to the other modes of motion, leading to "first-order) theories involving only the dominant forces.

However, the computations presented in Section 3 for coupled surge, heave and pitch do include all forces, not only those of first order. The first order computations are verified as numerically reasonable, and information is obtained about the most significant second order effects. For example, the diffraction exciting force (unfortunately neglected by Beck and Tuck, 1971, in making similar comparisons) appears to be the most significant second-order contribution to heave, whereas pitch is affected more by added hydrodynamic inertia than by diffraction effects.

In the case of surge the first order balance is between natural inertia and Froude-Krylov exciting force, and this first order result appears to be remarkably accurate. In particular, there appears little need to worry about coupling with the other modes. Some mooring force considerations are discussed in Section 4, the conclusion being that for large ships only surge is likely to be affected, and then perhaps only marginally. The general theory of surging of moored ships has been thoroughly treated in the Civil Engineering literature (see Wilson, 1967, for a bibliography), and perhaps the only new contribution we can make here concerns the correct evaluation of the surge exciting force as a function of hull geometry. This question is given some attention in Section 3 and Appendix III.

In Section 5 we continue the theoretical treatment of the very difficult problem of horizontal plane motions, clearing up most but not all of the loose ends left by Tuck (1970) for sway, roll and yaw. The appropriate integral equations which determine the hydrodynamic coefficients in these modes have been set up, but the roll equations have not yet been solved.

Finally in Section 6 we present computed sway and yaw motions, neglecting coupling with roll. This is justifiable, as discussed in Section 2, if the metacentric height is sufficient to remove the roll resonance period from the range of wave periods of interest, a situation which is not unlikely in shallow water. The resulting motions agree well with simple approximate and limiting results, which may be used for estimates in lieu of the very complicated computation procedure needed in the general case. As indicated by Tuck and Taylor (1970), the detailed computations are, however, of importance if swaying is to be in any way resisted, by moorings, fenders, etc.

In no case have the present results been experimentally verified. The apparent lack of systematic (as distinct from ad hoc) experimental measurements of ship motions in shallow water in the published literature is deplorable in view of the importance of this subject today, and it is to be hoped that this situation will be remedied as soon as possible.

II. THE EQUATIONS OF MOTION IN GENERAL

The equations of motion for any ship moving sinusoidally with complex amplitude ζ_j at radian frequency σ in the jth mode of motion, the time-dependent displacement being

$$n_j(t) = \Re \{ \zeta_j e^{-i\sigma t} \}, \tag{2.1}$$

are (Salvesen, Tuck & Faltinsen 1970, Tuck 1970)

$$\sum_{j=1}^{6} (-\sigma^2 M_{ij} - T_{ij} + C_{ij}) \zeta_j = F_i , \quad i = 1, 2, \ldots 6 \tag{2.2}$$

Here M_{ij} is a generalized mass matrix, i.e.

$$[M_{ij}] = \begin{bmatrix} M & 0 & 0 & 0 & Mz_G & 0 \\ 0 & M & 0 & -Mz_G & 0 & Mx_G \\ 0 & 0 & M & 0 & -Mx_G & 0 \\ 0 & -Mz_G & 0 & Mk_4^2 & 0 & -I_{46} \\ Mz_G & 0 & -Mx_G & 0 & Mk_5^2 & 0 \\ 0 & Mx_G & 0 & -I_{46} & 0 & Mk_6^2 \end{bmatrix} \tag{2.3}$$

where M = ship mass

$(x_G, 0, z_G)$ = coordinates of centre of gravity

k_4 = roll radius of gyration

k_5 = pitch radius of gyration

$k_6 \simeq k_5$ = yaw radius of gyration

I_{46} = roll-yaw product of inertia (small).

C_{ij} is a matrix of restoring force coefficients, including all hydrostatic effects and mooring forces, if any, but no hydrodynamic effects. The hydrostatic contributions to C_{ij} are zero except for

$$\left.\begin{aligned} C_{33} &= \rho g A_{WL} \\ C_{35} = C_{53} &= -\rho g x_F A_{WL} \\ C_{55} &= \rho g k_F^2 A_{WL} \\ C_{44} &= Mg(z_M - z_G) \end{aligned}\right] \qquad (2.4)$$

where

A_{WL} = waterplane area

x_F = x coordinate of centre of flotation (centroid of A_{WL})

k_F = radius of gyration of A_{WL}

z_M = z co-ordinate of meta-centre .

Possible mooring force contributions to C_{ij} are discussed in Section 4.

The remaining terms in the equations of motion are hydrodynamic in nature, consisting of the hydrodynamic forces involving T_{ij} and exciting forces of amplitude F_i . T_{ij} is a complex-valued transfer function equal to the hydrodynamic force in the ith mode due to a unit amplitude movement of the ship in the jth mode, and can be written (Tuck 1970) in the form

$$T_{ij} = \sigma^2 a_{ij} + i\sigma b_{ij} \qquad (2.5)$$

where $a_{ij}(\sigma)$ is a real added mass and $b_{ij}(\sigma)$ a real damping coefficient, both frequency-dependent.

F_i is the force in the ith mode due to the incident wave. If the latter is a pure sine wave of amplitude ζ_o at an angle β to the x axis, i.e. has equation

$$z = \zeta_o e^{ik(x \cos \beta + y \sin \beta) - i\sigma t} \tag{2.6}$$

where $k = 2\pi/\text{wavelength}$, we can write (Tuck, 1970)

$$F_i = (T_{io} + T_{i7}) \zeta_o \tag{2.7}$$

where T_{io} is the Froude-Krylov force per unit wave amplitude i.e. that obtained by integrating the incident pressure field over the equilibrium hull position, and T_{i7} is the correction due to diffraction of the incident wave around the (fixed) hull. This notation for the exciting forces is convenient in allowing us to display all hydrodynamic effects in the form of a 6×8 matrix $[T_{ij}]$, $i = 1, 2, \ldots 6$, $j = 0, 1, 2, \ldots 7$.

The foregoing applies to a very general class of ship motion problems, and in particular is not yet subject to restrictions on the nature of the sea floor. However, bottom topography determines the dispersion relationship between k and σ, and in the present work we assume the shallow water approximation in uniform depth h, namely

$$\sigma^2 = ghk^2, \tag{2.8}$$

which is valid only so long as $kh \ll 1$, a very restrictive condition, as we shall see.

In addition, of course, the bottom topography has a profound effect on the numerical values of the frequency-dependent transfer functions T_{ij}. The whole difficulty in any ship motions calculation is in the computation of T_{ij}, since once these quantities are known, (2.1) is trivially solvable. In following sections of this paper we discuss in detail various specifications of T_{ij} and solve some of the resulting motions problems.

First, however, it is of interest to provide a general summary

of the orders of magnitude of various terms in the equations of motion. We find that not all terms are of equal importance, and some may be neglected to an acceptable order of accuracy. This is a conclusion which may be arrived at formally by asymptotic expansion with respect to a small parameter $\epsilon \ll 1$ such that the beam and draft of the ship and the depth of the water are all small $0(\epsilon)$ quantities relative to both the length of the ship and the wavelength of the incident waves. In some cases in addition we provide in later sections direct confirmation of the smallness of the numerical effect on motions of terms which are asymptotically small.

The orders of magnitude of T_{ij} with respect to ϵ are

$$0(T_{ij}) = \begin{bmatrix} \epsilon^2 & \epsilon^4 & 0 & \epsilon^3 & 0 & \epsilon^3 & 0 & \epsilon^3 \\ \epsilon^2 & 0 & \epsilon^3 & 0 & \epsilon^4 & 0 & \epsilon^3 & \epsilon^2 \\ \epsilon & \epsilon^3 & 0 & \epsilon^2 & 0 & \epsilon^2 & 0 & \epsilon^2 \\ \epsilon^3 & 0 & \epsilon^4 & 0 & \epsilon^5 & 0 & \epsilon^4 & \epsilon^3 \\ \epsilon & \epsilon^3 & 0 & \epsilon^2 & 0 & \epsilon^2 & 0 & \epsilon^2 \\ \epsilon^2 & 0 & \epsilon^3 & 0 & \epsilon^4 & 0 & \epsilon^3 & \epsilon^2 \end{bmatrix} \qquad (2.9)$$

Recall that the first column gives Froude-Krylov exciting forces, the last column diffraction exciting forces, and the remainder of the matrix added inertia and damping forces. The above orders of magnitude are quite difficult to estimate, and the following observations are by way of explanation.

Lateral symmetry of the ship provides the zero entries, decoupling horizontal and vertical modes, and also affects some exciting force orders of magnitude. For example, if the ship did not possess lateral symmetry there would be an $0(\epsilon)$ contribution to the Froude-Krylov force $T_{2\,0}$ in sway.

The water depth h, assumed $0(\epsilon)$, has a significant effect on these orders of magnitude, especially in the vertical modes. Whereas in infinite depth of water a unit magnitude vertical motion of a slender ship produces a small $0(\epsilon)$ motion of the water in cross-flow planes, such a ship motion produces a significant $0(1)$ lateral motion of water of $0(\epsilon)$ depth. Thus the surge, heave and pitch self and diffraction forces are all one order of magnitude larger than the corresponding estimates (Newman & Tuck 1964) for infinite depth.

In horizontal modes (sway, roll and yaw) the assumption has

been made above that the clearance (water depth minus ship draft) is not small compared with the water depth. In the case of small clearances, the order of magnitude of the horizontal self and diffraction forces is increased above that shown, in the ratio "water depth/clearance".

We now consider the effect of these order of magnitude estimates on the equations of motion (2.2), supplementing the hydrodynamic estimates (2.9) with the information

$$\left.\begin{array}{ll} \sigma^2 & = 0(\epsilon) \\ M & = 0(\epsilon^2) \\ z_G, k_4 & = 0(\epsilon) \\ I_{46} & = 0(\epsilon^3) \\ C_{33}, C_{35}, C_{53}, C_{55} & = 0(\epsilon) \\ C_{44} & = 0(\epsilon^3) \end{array}\right\} \qquad (2.10)$$

Note that (2.8) requires $\sigma^2 = 0(\epsilon)$, restricting attention to low frequencies or long waves, and at least in principle ruling out resonance in any mode. The order of magnitude of C_{44} is an upper bound, on the basis that the metacentric height is at most $0(\epsilon)$; in fact it becomes a crucial question for roll to assess correctly the minimum order of magnitude of C_{44}.

The significance of the various forces in the equations of motion (2.2) may now be summarized for each mode in turn as follows.

SURGE, $0(\epsilon^{-1})$ motion

Important Forces, $0(\epsilon^2)$: natural inertia, F-K exciting force.

Small Forces, $0(\epsilon^3)$: added inertia and damping, coupling from heave and pitch, diffraction exciting force.

HEAVE-PITCH, $0(1)$ motion

Important Forces, $0(\epsilon)$: hydrostatics, F-K exciting force.

Small Forces, $0(\epsilon^2)$: added inertia and damping, coupling from surge, diffraction exciting force.

Very Small Forces, $0(\epsilon^3)$: natural inertia.

SWAY-YAW, $0(\epsilon^{-1})$ motion

Important Forces, $0(\epsilon^2)$: natural inertia, added inertia and damping, F-K and diffraction exciting forces.

Very Small Forces, $0(\epsilon^4)$: coupling from roll.

ROLL, $0(1)$ motion

Important Forces, $0(\epsilon^3)$: hydrostatics, coupling from sway and yaw, F-K and diffraction exciting forces.

Very Small Forces, $0(\epsilon^5)$: natural inertia, added inertia and damping.

Several features of the above table are at first sight surprising. Firstly we should note that the conclusion that surge, sway and yaw involve large $0(\epsilon^{-1})$ motions, while heave and pitch involves only $0(1)$ motions (i.e. of the order of the wave amplitude) is reasonable, in that the ship moves more or less as does a water particle and the horizontal particle motions in a shallow water wave are much greater by a factor of order wavelength/water depth than the vertical particle motions. Roll is rather special, and its $0(1)$ magnitude is due to the assumed sufficiently large order of the metacentric height.

Forced surging is an extremely inefficient method of creating hydrodynamic disturbance, so that all hydrodynamic effects on surge are small. Note however, that the added inertia is only one order of magnitude smaller than the natural inertia, whereas in infinite depth it becomes two orders of magnitude smaller.

Heave, pitch and roll are the only modes to involve hydrostatics, and the hydrostatic contribution is necessarily dominant for these

modes. The main force balance in heave and pitch is between hydrostatics and Froude-Krylov exciting forces, exactly as in infinite depth (Newman & Tuck 1964) . Remarkably however, in shallow water the added inertia dominates the natural inertia. This conclusion is only valid so long as $\sigma^2 = 0(\epsilon)$, i. e. for reasonably low frequencies, certainly well below resonance. This question is discussed further in Section 3.

In sway and yaw most forces are comparable in magnitude so long as the clearance is not small, the only negligible effect being roll coupling. The latter is only significant if the roll magnitude is $0(\epsilon^{-2})$, two orders of magnitude higher than that predicted. If the clearance is small, the added inertia dominates the natural inertia by an extra factor of depth/clearance.

Finally, the amplitude of roll is profoundly affected by the order of magnitude of the metacentric height. The orders given correspond to $z_M - z_G = 0(\epsilon)$, but broadly similar conclusions apply for (say) $z_M - z_G = 0(\epsilon^2)$. Only if $z_M - z_G = 0(\epsilon^3)$ does the roll amplitude become large enough for roll to affect sway and yaw, or for roll inertia to be important.

Another way of looking at this effect is to observe that the roll resonance frequency is roughly given by

$$\sigma_R^2 \simeq \frac{g(z_M - z_G)}{k_4^2}$$

Since $k_4 = 0(\epsilon)$, the frequencies of interest such that $\sigma^2 = 0\ (\epsilon)$ are necessarily far below resonance in roll, unless the metacentric height is as little as $0(\epsilon^3)$.

A final rather more intuitive argument for neglect of roll is that the shallow water assumption requires that the incident wave pressure be uniform with depth. Thus the resultant force on a vertical wall (modelling a ship with a very small clearance in shallow water, beam seas) acts through the mid-point of the wall. One should anticipate a pure swaying motion of the ship section due to such a uniform distribution of pressure. In terms of a roll angle measured about an axis in the waterplane, this amounts to the conclusion that the sway coupling term from M_{24} in (2. 3) cancels out the net incident pressure moment about the waterline.

III. COUPLED SURGE, HEAVE AND PITCH MOTIONS

The formulae for the transfer functions T_{33} , T_{53} were derived by Tuck (1970), and in a similar manner we may obtain the following results, valid for all $i = 1, 3, 5$ and all $j = 1, 3, 5, 7$,

$$T_{io} = \rho g \int_{-\ell}^{\ell} dx e^{ikx \cos\beta} A_i(x) \qquad (3.1)$$

$$T_{ij} = \frac{i\rho\sigma^2}{4h} \int_{-\ell}^{\ell} dx d\xi \, A_i(x) A_j(\xi) H_o^{(1)}(k|x-\xi|), \qquad (3.2)$$

where

$$A_1(x) = S'(x) \qquad (3.3)$$

$$A_3(x) = B(x) \qquad (3.4)$$

$$A_5(x) = -xB(x) \qquad (3.5)$$

$$A_7(x) = \left[-B(x) + \frac{S(x)\cos^2\beta}{h} - \frac{iS'(x)\cos\beta}{kh}\right] e^{ikx\cos\beta}. \qquad (3.6)$$

Here $B(x)$ is the full waterline width and $S(x)$ the section area at station x , while $H_o^{(1)}$ is an Hankel function (Abramowitz and Stegun 1964, p. 358).

A brief derivation of the above results is given in Appendix I. The physical plausibility of these results, especially the rather complicated formula (3.6) for the diffraction exciting force, may be exhibited by considering the direct effect on the equations of motion.

For instance, in heave, $i = 3$, the equations of motion (2.2) state

$$-\sigma^2 M\zeta_3 + C_{33}\zeta_3 + C_{35}\zeta_5 - T_{30}\zeta_0 = T_{31}\zeta_1 + T_{33}\zeta_3 + T_{35}\zeta_5 + T_{37}\zeta_0$$

$$= \frac{i\rho\sigma^2}{4h} \int_{-\ell}^{\ell} dx B(x) \int_{-\ell}^{\ell} d\xi \left[B(\xi)(\zeta_3 - \xi\zeta_5 - \zeta_0 e^{ik\xi\cos\beta}\right) \qquad (3.8)$$

$$+\frac{d}{d\xi}S(\xi)\left(\zeta_1 - \frac{i\zeta_o\cos\beta}{kh}e^{ik\xi\cos\beta}\right)\Big] \cdot H_o^{(1)}(k|x-\xi|) \tag{3.8}$$

The terms on the left of (3.8) constitute natural inertia, hydrostatics, and Froude-Krylov exciting forces, all hydrodynamic effects being on the right. The expression

$$\zeta_3 - \xi\zeta_5 - \zeta_o e^{ik\xi\cos\beta} \tag{3.9}$$

is the relative vertical displacement between ship and wave at station ξ, whereas the term

$$\zeta_1 - \frac{i\zeta_o\cos\beta}{kh}e^{ik\xi\cos\beta} \tag{3.10}$$

is the relative horizontal displacement between the (surging) ship and the water particles in the wave.

This display of the equation of motion is similar to that given by Newman and Tuck (1964) for infinite depth, except that in infinite depth the horizontal motion terms do not appear. It should be noted that the surge motion ζ_1 and the horizontal fluid particle motions are large in shallow water, of $0(\epsilon^{-1})$, which is the reason why the relative horizontal motion is now potentially as important as the relative vertical motion in determining hydrodynamic effects.

The first step to actual solution for the motions is numerical evaluation of the coefficients T_{ij}. This is a moderately difficult task, especially as regards the double integrals in (3.2). This task is carried out indirectly, by Fourier transform techniques as described in Appendix II.

An apparently trivial but actually significant point about the numerical computations is the fact that we may wish to avoid numerical differentiation of the section area curve $S(x)$ to give $S'(x)$ in (3.3) and (3.6). In fact a simple integration by parts avoids this difficulty, but raises another question. If the section area $S(x)$ does not vanish at the ends $x = \pm\ell$ (e.g. with transom sterns), what do we do about the "integrated part" after integration by parts ? This is a classical end-effect problem in slender body theory, since at least in principle slender body theory is inapplicable to such blunt ships.

This question is examined further in Appendix III, where it is argued that, at least in so far as the surge exciting force T_{10} is concerned, the theory remains valid for "blunt" ships, provided we discard the terms arising from integration by parts. It seems likely that a similar consideration applies to all expressions involving $S'(x)$. Of course in the absence of transoms etc., i.e. when $S(\pm\ell) = 0$, this difficulty of interpretation does not arise, and this is true of the computations to be presented here for the Series 60, block 0.80 hull.

Figures 3.1 - 3.3 show vertical motions computations in all 3 modes for head seas ($\beta = 180°$). The horizontal scale chosen is ship length divided by wavelength, while the vertical scales represent linear displacement amplitudes divided by wave amplitudes. In pitch this is equivalent to vertical bow motion due to pitching alone. The results are given for depths of 1.0 and 2.5 times the draft of the ship (0.062 and 0.15 times the ship length). A depth equal to the draft is of course not safely achievable, but no difficulty arises theoretically in this case for vertical modes (not so for horizontal modes) and this case may be viewed as a limiting one in practice.

The motions shown are those resulting from use of all available information about terms in the equations of motion. In spite of the imbalance in orders of magnitude as indicated in the previous section, no terms have been neglected, and all couplings between all three modes have been included.

For comparison purposes however, the first-order results are also shown, these being balances between hydrostatic and Froude-Krylov forces only in heave and pitch, and between natural inertia and Froude-Krylov forces only in surge. In heave and pitch the first-order result is independent of depth at fixed wave-length, whereas the first-order surge varies inversely as the depth.

The effects of the second (and third) order terms are quite varied, but some general comments can be made. The main difference between the first order and full heave results in Figure 3.1 is due to the diffraction exciting force. This is particularly true near the minimum of the first order heave (about $L/\lambda = 1.2$), where the heave is substantially increased by diffraction effects.

The general trend of the heave results is remarkably similar to those of Newman and Tuck (1964) for infinite depth. The first order heave minimum at about $L/\lambda = 1.2$ appears in both cases to be shifted by second order effects, especially diffraction, to about $L/\lambda = 1.4$. This is not too surprising numerically in view of the similarity between (3.8) and the equation of motion in infinite depth.

Pitch is almost unaffected by diffraction effects, the substantial increases shown in Figure 3.2 over the first-order theory at about the pitch maximum ($L/\lambda = 0.8$) being instead largely due to inertia, especially added inertia. A rough explanation of the numerical smallness of the pitch diffraction force is that the first term of (3.6) involving $B(x)$ is a nearly even function for a nearly fore-and-aft symmetric ship ; for reasonably low values of k (thus low L/λ) the corresponding value of T_{57} is small because $A_5 = -xB$ is nearly an odd function of x. The terms of (3.6) involving $S(x)$ correspond broadly to surge motion, and lead to small effects when the surging is small, as it is at these wavelengths.

All second order effects on surge appear to be small, the first-order balance between natural inertia and Froude-Krylov exciting force being (Figure 3.3) remarkably close to the full result. The magnitude of the surge motion is, as expected, quite large for the longer waves, $L/\lambda < 0.8$, say, for which the horizontal particle motion in the wave is large. At fixed L/λ , the first-order surge varies exactly inversely with depth, and the full equations give a similar trend except at high frequencies where surging is in any case quite small.

Computations have also been carried out in oblique seas, i.e. for values of β other than $180°$. In general, effects of reasonable heading angle on vertical plane motions are mostly accounted for by use of head seas results, but with the effective wavelength $\lambda \sec\beta$ instead of λ in the horizontal scale.

This is exactly true for the first-order results in heave and pitch, and nearly so when second and higher order terms are included. In surge this effect is combined with a "$\cos^2\beta$" factor, tending to reduce surging. However, since the effective wavelength is longer than the true wavelength and surge is greatest in longest waves, we should anticipate increased surging, were it not for the $\cos^2\beta$ factor. The net effect at fixed (true) wavelength is a "$\cos\beta$" reduction factor on surge.

Since the computed results agree well with the above qualitative discussion, we omit presenting computations for bow seas ($\beta = 135°$) . Note however, that the "stretching out" of the head seas curves due to the $\sec\beta$ factor means that heave and pitch are both increased at values of L/λ (true) of about $1.2 - 1.6$, where the head seas responses were small. In this important range bow seas produce significantly greater net vertical bow motions than do head seas (see Beck and Tuck, 1971).

One interesting feature of the heave equation of motion in beam seas ($\beta = 90°$) for a fore-and-aft symmetric ship is that all second order terms disappear, so that were it not for the third-order mass terms the heave would exactly equal the wave amplitude. Thus at $\beta = 90°$, (3.6) gives $A_7(x) = -B(x) = -A_3(x)$, and we have $T_{37} = -T_{33}$. But also $T_{30} = C_{33}$, hence assuming fore-and-aft symmetry the heave equation of motion is

$$-\sigma^2 M\zeta_3 + (C_{33} - T_{33})(\zeta_3 - \zeta_0) = 0 . \tag{3.11}$$

Hence

$$\begin{aligned} \zeta_3 &= \zeta_0 \Big/ \left[1 - \frac{\sigma^2 M}{C_{33} - T_{33}} \right] \\ &= \zeta_0 (1 + 0(\epsilon^2)) \end{aligned} \tag{3.12}$$

Similarly, if we do neglect all second and third order effects, the first order theory predicts zero surge and pitch, and heave $\zeta_3 = \zeta_0$ even in the absence of fore-and-aft symmetry.

Figures 3.4 - 3.5 show computed heave and pitch motions in beam seas. There is a substantial (60%) increase in heave over the first-order value $\zeta_3 = \zeta_0$ as the depth increases, especially at about $L/\lambda = 1.5$. The pitch (in bow motion) remains below 25% of the wave amplitude, however, and surge is quite negligible, never more than 2% of the wave amplitude at any frequency.

IV. MOORING FORCES

As an example of the type of analysis required in order to account for the effect of mooring lines on motions (and perhaps more importantly, vice versa !), we give below a simple discussion of the effect of a single linear bow mooring line on vertical plane motions. More realistic and complicated types of mooring systems can be studied with similar procedures and conclusions. The general conclusion is that of Wilson and Yarbaccio (1969), who find that "the spring is quite weak compared to the mass, and the ship can be considered to be floating unrestrained except for restraint against continuous drifting".

If we consider only linear effects of mooring lines, the appropriate modifications to the equation of motion simply require contributions to the restoring force coefficients C_{ij} in equation (2.2).

Consider for example a linear elastic cable of spring constant k and length R, attached to the bow and initially nearly parallel to the calm water line and nearly lying in the centre plane of the ship. Small angular deviations from this equilibrium configuration have no effect on the restoring coefficients. We suppose there is a mean cable tension T_0 at equilibrium due to wind, wave (mean stress) and current effects.

The displacements of the bow as a result of small vertical plane motions are ζ_1 longitudinally and $\zeta_3 - \ell\zeta_5$ upwards, and from Figure 4.1 we see that the new cable length is

$$\begin{aligned} R' &= \sqrt{R^2 - 2\zeta_1 R + \zeta_1^2 + (\zeta_3 - \ell\zeta_5)^2} \\ &\simeq R - \zeta_1 \end{aligned} \tag{4.1}$$

if all $\zeta_j \ll R$, and the new cable tension is thus

$$\begin{aligned} T &= T_0 + k(R' - R) \\ &= T_0 - k\zeta_1 \end{aligned} \tag{4.2}$$

Thus heave and pitch have no effect on cable tension in this case. However, this does not mean that there is no vertical restoring force in these modes.

In fact the surge restoring force due to the mooring is

$$\begin{aligned} F_1 &= (T - T_0)\cos\theta \\ &\simeq T - T_0 \\ &= -k\zeta_1 , \end{aligned} \tag{4.3}$$

the heave restoring force is

$$\begin{aligned} F_3 &= -T\sin\theta \\ &\simeq -T_0(\zeta_3 - \ell\zeta_5) \end{aligned} \tag{4.4}$$

and the pitch moment is

$$F_5 = -\ell F_3 \ . \tag{4.5}$$

Thus the restoring force coefficients due to this mooring are

$$C_{11} = k \tag{4.6}$$

and

$$C_{33} = \frac{T_0}{R}, \quad C_{35} = -\frac{\ell T_0}{R}, \quad C_{55} = \frac{\ell^2 T_0}{R}, \tag{4.7}$$

all other C_{ij} being zero. The total restoring force coefficient C_{ij} for use in equation (2.2) is the sum of the hydrostatic contributions given in equations (2.4) and the mooring contributions given in (4.6), (4.7) above.

Equation (4.7) show that there is a small additional contribution to the restoring forces in heave and pitch from the equilibrium tension in the mooring line, independent of its elasticity. Since these modes already possess very large hydrostatic restoring forces, it is very difficult to conceive of equilibrium cable tensions sufficient to produce significant effects on heave and pitch.

For example, if we use $T = 37$ tons and $R = 100$ feet, the former being computed from Taylor's air resistance formula

$$T = 0.00218\ B^2 V^2 \tag{4.8}$$

where B is beam and V wind speed (assumed 40 knots), we obtain less than one tenth of a percent change in the computed heave and pitch motions of a 200000 ton ship. For this type of mooring or any combination of such moorings, the equilibrium tension would have to be quite unrealistically large* for any significant change to occur in the heave and pitch motions.

---

* For a single cable the figure of 37 tons is of course already in this category !

Surge is rather different, in that the mooring provides the only restoring force (4.6). If we assume, as is clear from the results of the previous section, that all hydrodynamic effects on surge are negligible, we can analyse linear surging as a simple one-degree-of-freedom undamped spring-mass system, with the result that the surging amplitude is

$$\zeta_1 = \frac{F_1}{k - M\sigma^2} \tag{4.9}$$

or (neglecting diffraction)

$$\zeta_1 / \zeta_0 = \frac{T_{10}}{k - M\sigma^2} \tag{4.10}$$

where $T_{10} = T_{10}(\sigma)$ is obtained from (AIII.5).

In fact the surging amplitude in the presence of a mooring is simply equal to the factor

$$\left| \frac{\sigma^2}{M\sigma^2 - k} \right| = \left| \frac{1}{1 - \sigma_R^2/\sigma^2} \right| \tag{4.11}$$

times the free surging amplitude, where $\sigma_R = \sqrt{k/M}$ is the resonant frequency. Figure 4.2 shows this factor as a function of frequency σ. Note that unless the wave frequency is less than 70% of the resonant frequency $\sigma_R = \sqrt{k/M}$, the effect of the mooring is to increase the motions. For large ships, conceivable values of σ_R correspond to periods of minutes or more, so that typical sea or swell gives frequencies well above resonance; however (Wilson 1959) long period range action in harbors can produce resonance, with disastrous effects. The condition $\sigma < 70\%\ \sigma_R$ is in general met only by tides and currents, and indeed the purpose of the moorings must be to overcome these very low frequency excitations.

On the other hand if $\sigma \gg \sigma_R$, it is clear that the mooring is having very little effect on the surge motion of the ship, which moves as if free. The force exerted on the mooring by the ship is then of prime interest, and this may simply be computed by assuming given free ship motions. This also applies of course to motions in other modes (e.g. sway), so long as the wave frequency is again well above

the resonant frequency of the mooring.

The actual variable tension in the cable resists only a small fraction of the exciting force under these circumstances, which is just as well, since these exciting forces on large ships are generally enormous. The ratio between the amplitude of variation of the cable tension and the exciting force is

$$\left| \frac{k\zeta_1}{F_1} \right| = \left| \frac{k}{k - M\sigma^2} \right| = \left| \frac{1}{1 - \sigma^2/\sigma_R^2} \right| \tag{4.12}$$

which is also shown in Figure 4.2 . For example, if $\sigma > 5\sigma_R$ (i.e. the wave period is less than one fifth of the mooring resonant period), the mooring bears less than 4% of the exciting force, and the motions are not more than 4% higher than the free motions.

V. THEORETICAL CONSIDERATIONS ON HORIZONTAL PLANE MOTIONS

The developments of the theory of Tuck (1970) and Tuck and Taylor (1970) on horizontal plane motions were confined in effect to computation of the sway exciting force. The resulting formula for the total exciting force is

$$T_{i0} - T_{0i} = i\rho ghk \sin\beta \int_{-\ell}^{\ell} dx e^{ikx \cos\beta} \Delta\phi_i(x) \tag{5.1}$$

where $\Delta\phi_i$ is a "potential jump" across the ship section, computable from purely near-field considerations. Although (5.1) was only derived for $i = 2$ (sway) it is also valid for $i = 4$ (roll) and $i = 6$ (yaw). In the case of yaw, there is no need to obtain $\Delta\phi_6$ separately, since $\Delta\phi_6 = x\,\Delta\phi_2$. The computation of $\Delta\phi_2$ and $\Delta\phi_4$ will be discussed later.

Tuck (1970) also suggested a connection between the integral (5.1) at $\beta = 0$ and the added mass and damping coefficients. For instance we have

$$T_{22} = -\rho\sigma^2 \int_S n_2 \phi_2 \, dS \tag{5.2}$$

$$= -\rho\sigma^2 \int_{-\ell}^{\ell} dx \int_H \frac{\partial y}{\partial n} \phi_2 d\ell \tag{5.2}$$

where H is the section at station x , and $\underset{\sim}{n}$ is outward from the hull (into the fluid). Now the contour integral can be evaluated entirely in the near field region as follows.

$$\int_H \frac{\partial y}{\partial n} \phi_2 d\ell = \int_H \left[\frac{\partial y}{\partial n}\phi_2 - y \frac{\partial \phi_2}{\partial n}\right] d\ell + \int_H y \frac{\partial \phi_2}{\partial n} d\ell$$

$$= \int_{H+F+B+R_\infty+L_\infty} \left[\frac{\partial y}{\partial n}\phi_2 - y\frac{\partial \phi_2}{\partial n}\right] d\ell - \int_{F+B+R_\infty+L_\infty} \left[\frac{\partial y}{\partial n}\phi_2 - y\frac{\partial \phi_2}{\partial n}\right] d\ell$$

$$+ \int_H y n_2 d\ell \tag{5.3}$$

where F denotes the free surface, B the bottom, R_∞ and L_∞ vertical lines at $y = +\infty$ and $y = -\infty$ respectively in the inner (y, z) plane, as shown in Figure 5.1 .

The first integral above vanishes by Green's theorem and there is no contribution from F or B in the second integral since both $\frac{\partial \phi_2}{\partial n}$ and $\frac{\partial y}{\partial n}$ vanish on F and B . On L_∞ , $d\ell \frac{\partial}{\partial n} = dz \frac{\partial}{\partial y}$, whereas on R_∞ , $d\ell \frac{\partial}{\partial n} = -dz \frac{\partial}{\partial y}$. Hence (using also (A. 1. 9))

$$\int_H \frac{\partial y}{\partial n} \phi_2 d\ell = -\int_{-h}^{0} dz \left[\phi_2 - y \frac{\partial \phi_2}{\partial y}\right]_{y=-\infty}^{y=+\infty} + S(x) . \tag{5.4}$$

But the boundary condition for the inner potential ϕ_2 is (Tuck 1970)

$$\phi_2 \longrightarrow yV_2 \underset{-}{+} 1/2\, \Delta\phi_2 \quad \text{as} \quad y \longrightarrow \underset{-}{+}\infty \tag{5.5}$$

Hence

$$\phi_2 - y\,\frac{\partial \phi_2}{\partial y} \longrightarrow \pm\ 1/2\,\Delta\phi_2 \qquad \text{as} \qquad y \longrightarrow \pm\,\infty \ ,$$

i.e.
$$\left[\phi_2 - y\,\frac{\partial \phi_2}{\partial y}\right]_{-\infty}^{\infty} = \Delta\phi_2 \ , \tag{5.6}$$

and we have
$$\int_H \frac{\partial y}{\partial n}\,\phi_2\, d\ell = h\Delta\phi_2(x) + S(x) \tag{5.7}$$

Thus finally

$$T_{22} = -\rho\sigma^2 \int_{-\ell}^{\ell} dx \left[h\Delta\phi_2(x) + S(x)\right]$$

$$= -\rho\sigma^2 h \int_{-\ell}^{\ell} dx\,\Delta\phi_2(x) - \sigma^2 M \tag{5.8}$$

where
$$M = \rho \int_{-\ell}^{\ell} dx S(x) \tag{5.9}$$

is the mass of the ship. Note that the term involving the mass M was erroneously omitted by Tuck (1970). The new result indicates that the virtual or total inertia, not just the added inertia, is proportional to the real part of the exciting force integral (5.1) at $\beta = 0$.

The above analysis may now be repeated for T_{ij}, for all $i, j = 2, 4, 6$ except for the roll self-force term T_{44}. For example

$$T_{26} = T_{62} = -\rho\sigma^2 h \int_{-\ell}^{\ell} dx x \Delta\phi_2(x) - \rho\sigma^2 \int_{-\ell}^{\ell} dx x S(x) \tag{5.10}$$

$$T_{66} = -\rho\sigma^2 h \int_{-\ell}^{\ell} dx x^2 \Delta\phi_2(x) - \rho\sigma^2 \int_{-\ell}^{\ell} dx x^2 S(x) \tag{5.11}$$

$$T_{24} = T_{42} = -\rho\sigma^2 h \int_{-\ell}^{\ell} dx \Delta\phi_4(x) + \rho\sigma^2 \int_{-\ell}^{\ell} dx\left[S(x)z_c(x) + \frac{1}{12}B^3(x)\right] \tag{5.12}$$

where $z_c(x)$ is the z-co-ordinate of the centroid of the section at x. Unfortunately if $i = 4$, the element $n_4 = yn_3 - zn_2$ cannot be written as the normal derivative of a harmonic function, so that the two-dimensional Green's theorem cannot be used, as in the above derivation. It would appear that we must leave the formula for T_{44} in the form

$$T_{44} = -\rho\sigma^2 \int_{-\ell}^{\ell} dx \int_H n_4 \phi_4 d\ell \tag{5.13}$$

and evaluate the contour integral explicitly.

Computation of all quantities (apart from T_{44}) in the horizontal equations of motion now proceeds via preliminary computation of the potential jumps $\Delta\phi_i(x)$. These are related to the inner streaming velocity $V_i(x)$ by (Tuck 1970, Equation (54))

$$V_i(x) = \frac{i}{4}\left[\frac{d^2}{dx^2} + k^2\right] \int_{-\ell}^{\ell} \Delta\phi_i(\xi) H_0^{(1)}(k|x - \xi|)\, d\xi \tag{5.14}$$

which comes from the outer expansion, and

$$\phi_i \longrightarrow yV_i(x) \pm 1/2\, \Delta\phi_i(x) \quad \text{as} \quad y \longrightarrow \pm\infty \tag{5.15}$$

which is the inner boundary condition. Solving the inner flow problem leads to a connection between V_i and $\Delta\phi_i$, which in combination with (5.14) gives an integro-differential equation for $\Delta\phi_i(x)$.

For example, if we solve the canonical problems indicated by Figure 5.2, $i = 2, 4$, we have

$$\phi_2 = V_2 y + (V_2 - 1)\psi_2 \tag{5.16}$$

and

$$\phi_4 = V_4(y+\psi_2) - \psi_4 , \tag{5.17}$$

from which follows *

$$\Delta\phi_2 = 2C_2(V_2 - 1) \tag{5.18}$$

and

$$\Delta\phi_4 = 2C_2(V_4 - C_4 / C_2) . \tag{5.19}$$

Thus we have the integro-differential equations

$$\frac{i}{4}\left[\frac{d^2}{dx^2} + k^2\right] \int_{-\ell}^{\ell} d\xi\, \Delta\phi_i(\xi) H_0^{(1)}(k|x-\xi|) - \frac{\Delta\phi_i(x)}{2C_2(x)} = \frac{C_i(x)}{C_2(x)} \tag{5.20}$$

which can be converted into integral equations of the form

$$\begin{aligned} \frac{i}{4} \int_{-\ell}^{\ell} d\xi\, \Delta\phi_i(\xi) H_0^{(1)}(k|x-\xi|) - \frac{1}{k}\int_0^x d\xi\, \frac{\Delta\phi_i(\xi)}{2C_2(\xi)} \sin k(x-\xi) \\ = A_i \cos kx + B_i \sin kx + \frac{1}{k}\int_0^x d\xi\, \frac{C_i(\xi)}{C_2(\xi)} \sin k(x-\xi) . \end{aligned} \tag{5.21}$$

where A_i , B_i are constants to be determined by the end conditions $\Delta\phi_i(\pm\ell) = 0$. Although the left side of (5.21) contains the same kernel for $i = 4$ as for $i = 2$, the parameter $C_4(x)$ which appears on the right has not yet been evaluated numerically, so that in the following section results are given only for sway and yaw.

VI. COUPLED SWAY AND YAW

As discussed in Section 1., there are indications that roll is not a significant mode of motion in shallow water, and that in particular its coupling with sway and yaw is small. Therefore we present here computed free motions of the Series 60, block 0.80 , ship in

* The quantity C_2 corresponds to $C(x)$ as in Tuck (1970) .

sway and yaw, with complete neglect of roll coupling. The equations to be solved can be written

$$-T_{22}^{*}\ \zeta_2 - T_{26}^{*}\ \zeta_6 = F_2 \tag{6.1}$$

$$-T_{62}^{*}\ \zeta_2 - T_{66}^{*}\ \zeta_6 = F_6 \tag{6.2}$$

where

$$T_{22}^{*} = -\rho\sigma^2 h \int_{-\ell}^{\ell} dx\, \Delta\phi_2(x) \tag{6.3}$$

$$T_{26}^{*} = T_{62}^{*} = -\rho\sigma^2 h \int_{-\ell}^{\ell} dx\, x\, \Delta\phi_2(x) \tag{6.4}$$

$$T_{66}^{*} = -\rho\sigma^2 h \int_{-\ell}^{\ell} dx\, x^2 \Delta\phi_2(x) - \sigma^2 \int_{-\ell}^{\ell} dx\, x^2 (\rho S(x) - W(x)) \tag{6.5}$$

$$F_2 = \zeta_0 ik\rho g h \sin\beta \int_{\ell}^{\ell} dx\, \Delta\phi_2(x)\, e^{ikx\cos\beta} \tag{6.6}$$

$$F_6 = \zeta_0 ik\rho g h \sin\beta \int_{\ell}^{\ell} dx\, x\, \Delta\phi_2(x)\, e^{ikx\cos\beta}. \tag{6.7}$$

Here starred quantities represent natural inertia plus hydrodynamic effects. Note that natural inertia cancels out corresponding terms in the equations (5.8), (5.10) for the unstarred quantities T_{22}, T_{62} and T_{26}, assuming the unexcited ship is in equilibrium. However there is a contribution to T_{66}^{*} if the longitudinal radius of gyration of the displacement of the ship does not equal that of its actual mass distribution, expressed in (6.5) as $W(x)$ per unit length. This extra term in (6.5) is quite small in practice, but has been included in the computed results.

The quantity $\Delta\phi_2(x)$ is obtained numerically by solving the integral equation (5.21), which for $i = 2$ reduces to

$$\frac{i}{4}\int_{-\ell}^{\ell} d\xi \Delta\phi_2(\xi) H_0^{(1)}(k\,x-\xi) - \frac{1}{k}\int_0^x d\xi \frac{\Delta\phi_2(\xi)}{C_2(\xi)} \sin k(x-\xi) \qquad (6.8)$$

$$= \frac{1}{k^2} + A_2 \cos kx + B_2 \sin kx \ . \qquad (6.8)$$

Numerical procedures for obtaining $C_2(x)$ and hence by solving (6.8), $\Delta\phi_2(x)$, are discussed by Taylor (1971) and summarized by Tuck and Taylor (1970).

Figures 6.1 and 6.2 show the resulting solutions for the sway and yaw amplitudes respectively. At high frequencies, the motions tend to zero rapidly. On the other hand, as the frequency tends to zero (wavelength to infinity) the sway motion tends to infinity, as in the case of surge, because the ship is then following the horizontal fluid particle motions.

For a fore-and-aft symmetric ship ($T_{26}^* = 0$) in beam seas ($\beta = 90°$), the sway equation of motion simplifies to

$$\zeta_2 \cdot \rho\sigma^2 h \int_{-\ell}^{\ell} dx \Delta\phi_2(x) = \zeta_0 \cdot ik\rho gh \int_{-\ell}^{\ell} dx \Delta\phi_2(x)$$

i.e. the integral containing the potential jump $\Delta\phi_2(x)$ cancels out, leaving simply

$$\zeta_2 = \frac{-i\zeta_0}{kh} \ . \qquad (6.9)$$

This remarkable result shows that in this case the sway motion equals the horizontal fluid particle motion at all frequencies, not just as the frequency tends to zero. The small amount of asymmetry in the Series 60 ship does not prevent (6.9) from giving quite close agreement with the curve of Figure 6.1 for $\beta = 90°$. Note that (6.9) predicts that sway varies in direct proportion to wavelength (or period), and inversely as the water depth. These qualitative properties are also confirmed by the full computations.

Clearly the geometry of the ship, which in general influences $C_2(x)$, hence $\Delta\phi_2(x)$, has little effect on the free sway amplitude in

beam seas, since the integrals involving $\Delta\phi_2(x)$ tend to cancel out. We may expect a similar conclusion for other headings, and for yaw motions. On the other hand, as indicated by Tuck and Taylor (1970), if the swaying motion is to be restrained, by moorings, fenders, etc. a knowledge of $C(x)$ and hence $\Delta\phi_2(x)$ is vital for computation of the required restraining forces.

The yaw motion is plotted in Figure 6.2 as horizontal bow motion, analogously to pitch. Note that yaw vanishes identically in both head and beam seas, irrespective of fore-and-aft symmetry, so that maximum yaw occurs at some intermediate heading angle.

As the frequency tends to zero, the yaw motion tends to a finite limiting value which may be estimated for a fore-and-aft symmetric ship as follows. We also assume that we can neglect the second term of (6.5), which is true if the radii of gyration of displacement and mass are nearly equal. Then as $k \longrightarrow 0$, we have

$$\zeta_6 \cdot \rho\sigma^2 h \int_{-\ell}^{\ell} dx x^2 \Delta\phi_2(x) = \zeta_0 ik\rho gh \sin\beta \int_{-\ell}^{\ell} dx x \Delta\phi_2(x)[1+ikx\cos\beta+\ldots]$$

$$= -\zeta_0 k^2 \rho gh \sin\beta \cos\beta \int_{-\ell}^{\ell} dx x^2 \Delta\phi_2(x) .$$

Again the integrals involving $\Delta\phi_2(x)$ cancel out, leaving

$$\zeta_6 \simeq \frac{\zeta_0 \sin\beta \cos\beta}{h} . \qquad (6.10)$$

However, this result is of much more limited validity than (6.9), in particular being valid only for low frequency. Note again an inverse dependence on depth, and a maximum at 45° heading.

VII. CONCLUSION

In the present age of offshore mooring facilities for supertankers and giant ore carriers, the usefulness of a shallow water ship motion theory is obvious. However, the results presented in this paper are purely theoretical. To the author's knowledge there is very little experimental verification available. Until there are experiments with which to compare the theory, we are forced to rely on the good

agreement between experiments and deep water theories to give us confidence in the present shallow water theory.

In the case of heave and pitch, the theory presented in this paper (but with neglect of diffraction exciting forces) has been compared to Kim's (1968) shallow water strip theory by Beck and Tuck (1971). As expected, the present slender body theory seems to give more acceptable results in the very low frequency range, while the strip theory should be more accurate for high frequencies. In the intermediate frequency range, both theories give similar predictions of heave and pitch motions.

This work was supported by the Australian Research Grants Committee.

APPENDIX I

DERIVATION OF T_{ij} FOR VERTICAL MODES

The definition of T_{ij} is $(i, j = 0, 1, .., 7)$

$$T_{ij} = -\rho\sigma^2 \int n_i \phi_j \, dS \qquad (A.1.1)$$

where

$$\phi_0 = \frac{g}{\sigma^2} e^{ikx \cos\beta} \cdot \frac{\cosh k(z+h)}{\cosh kh} e^{iky \sin\beta} \qquad (A.1.2)$$

$$= \frac{g}{\sigma^2} e^{ikx \cos\beta} (1 + iky \sin\beta + 0(\epsilon^2)) \qquad (A.1.3)$$

and the result of Tuck (1970) is that for $j = 1, 3, 5$

$$\phi_j = \frac{i}{4h} \int_{-\ell}^{\ell} A_j(\xi) H_0^{(1)}(k|x-\xi|) \, d\xi \qquad (A.1.4)$$

$$= \phi_j(x)$$

where

$$-A_j(x) = \int_H n_j \, d\ell \qquad (A.1.5)$$

is the flux across the section H at station x in the jth mode. The results (3.1), (3.2) for T_{i0} and T_{ij}, $i,j = 1,3,5$ now follow directly from (A.1.1), while that for $j = 7$ follows after using symmetry, $T_{i7} = T_{7i}$.

It remains to evaluate the quantities $A_j(x)$ in terms of hull geometry, an easy task for $j = 1,3,5$ using the elementary results

$$\int_H n_1 d\ell = -S'(x) \tag{A.1.6}$$

and*

$$\int_H n_3 d\ell = -B(x) \tag{A.1.7}$$

with $n_5 = -xn_3$. For $j = 7$ we have

$$\begin{aligned} n_7 &= -n_0 = -\frac{\partial \phi_0}{\partial n} \\ &= -\left[n_1 \frac{\partial \phi_0}{\partial x} + n_2 \frac{\partial \phi_0}{\partial y} + n_3 \frac{\partial \phi_0}{\partial z}\right] \end{aligned} \tag{A.1.8}$$

Carrying out the differentiations of (A.1.2) and integrating we obtain

$$A_7(x) = e^{ikx\cos\beta} \int_H \left[n_1\left[\frac{i\cos\beta}{kh}\right] + n_2\left[-\frac{y\sin^2\beta}{h}\right] + n_3\left[1 + \frac{z}{h}\right]\right] d\ell$$

which leads to (3.6), using the further elementary results

$$\int_H y n_2 d\ell = \int_H z n_3 d\ell = S(x) . \tag{A.1.9}$$

---

* The corresponding result in Tuck (1970) has a sign error which occurs twice and therefore does not affect the final answer for T_{33}!

APPENDIX II

COMPUTATION PROCEDURE FOR VERTICAL PLANE INTEGRALS

The task of evaluating the integrals (3.2) is simplified by re-casting them in a Fourier transform manner. Thus

$$T_{ij} = \frac{i\rho\sigma^2}{2\pi h} \int_0^\infty \frac{d\lambda}{\sqrt{1-\lambda^2}} A_i^*(k\lambda)\, \overline{A_j^*}(k\lambda) \qquad \text{(AII. 1)}$$

where

$$A_i^*(\lambda) = \int_{-\ell}^{\ell} dx A_i(x)\, e^{i\lambda x} , \qquad \text{(AII. 2)}$$

a bar denotes a complex conjugate, and we adopt the convention that for $\lambda > 1$, $\sqrt{1-\lambda^2} = i\sqrt{\lambda^2 - 1}$. The result (AII. 1) follows from the integrals

$$J_0(z) = \frac{2}{\pi} \int_0^1 \frac{d\lambda}{\sqrt{1-\lambda^2}} \cos \lambda z$$

and

$$Y_0(z) = -\frac{2}{\pi} \int_1^\infty \frac{d\lambda}{\sqrt{\lambda^2 - 1}} \cos \lambda z ,$$

with $H_0^{(1)} = J_0 + iY_0$.

The Fourier transforms A_i^* (which are incidentally also required for the Froude-Krylov forces T_{i0} in (3.1)) are obtained by a modification of Filon's quadrature (Tuck, 1967). Data concerning $A_i(x)$ (i.e. beam $B(x)$ and section area $S(x)$) is supplied at given (not necessarily equally spaced) values of x. Data actually used was read directly from the table for the Series 60, block 0.80 parent form (Todd, 1963) at 25 stations. The Filon quadrature maintains uniform accuracy as the parameter λ increases.

The integration with respect to λ in (AII. 1) is carried out separately for $0 < \lambda < 1$ and $1 < \lambda < \infty$. In both cases there is a

square root singularity at $\lambda = 1$, removed by the changes of variables $\lambda = 1 \mp u^2$, respectively. The integrals are then evaluated by the trapezoidal rule, with a fixed given interval in u. In practice an interval 20-30 points per unit of λ have been found sufficient. The infinite range of the integral is accounted for by testing for convergence after integrating through about one unit of λ at a time, stopping when the answer changes by less than 0.1% .

The program is accurate but inefficient and expensive to run, taking about one minute (CDC 6400) for a run at a single depth and a single heading angle, each run including 8 frequencies. This time is at least half due to diffraction force computations, which doubles the number of Fourier transforms to be evaluated because of the factor $e^{ikx \cos\beta}$ in (3.6). Also, were it not for the diffraction force, the integrals (3.2) would be independent of depth and heading angle, enabling more information to be obtained cheaply for each run. Clearly much can be done to improve the efficiency of this integration procedure.

APPENDIX III

END-EFFECTS IN SURGE FOR TRANSOM STERNS

In evaluating the surge exciting force T_{10} we appear to require the derivative $S'(x)$ of the section area curve. To avoid numerical differentiation, we can integrate (3.1) by parts in this case, obtaining

$$T_{10} = \rho g \left[S(x)\, e^{ikx \cos\beta} \right]_{-\ell}^{\ell} - \rho g i k \cos\beta \int_{-\ell}^{\ell} dx S(x)\, e^{ikx \cos\beta} \qquad \text{(AIII. 1)}$$

If $S(\pm \ell) \neq 0$, the question arises as to whether retention of the integrated part in (AIII. 1) is correct. This question is not easy to answer, in view of the fact that such extreme bluntness of the ends of the ship ought to be precluded on slender body grounds.

However, it is clear by considering the following special case that a decision on this matter can be made. Suppose the ship is a rectangular box, with $S(x) = S_0 = \text{constant}$, $|x| < \ell$. Then clearly the Froude-Krylov exciting force arises solely from pressure differences between the two flat ends of the ship. That is, the force amplitude per unit wave amplitude is

$$T_{10} = S_0 \left[P(-\ell) - P(\ell) \right] \qquad \text{(AIII. 2)}$$

where $P(x)$ is the amplitude of the pressure in a unit amplitude incident wave i. e.

$$P(x) = \rho g e^{ikx \cos\beta} \tag{AIII. 3}$$

Equation (AIII. 3) neglects pressure variations with y and z over the "end plates", consistent with the slender body assumption. Thus

$$T_{10} = -2i\rho g S_0 \sin(k\ell \cos\beta) \tag{AIII. 4}$$

On the other hand, the original formula (3. 1) leads to the ridiculous result $T_{10} = 0$, since $S'(x) = 0$ for $|x| < \ell$ with this ship. This is reflected in the modified formula (AIII. 1) by the fact that the integrated part cancels the integral exactly. In fact if we "neglect" the integral part in (AIII. 1), leading to

$$T_{10} \doteq -\rho g i k \cos\beta \int_{-\ell}^{\ell} dx\, S(x)\, e^{ikx \cos\beta}, \tag{AIII. 5}$$

we obtain the correct result (AIII. 4) for the special case $S(x) = S_0 =$ constant !

Thus it would seem that the correct procedure is to disregard integrated parts on integrating $S'(x)$ by parts. This is equivalent to saying that all ships actually have zero area at their ends, so that a transom is replaced by a very rapid decrease to zero area. If the ship in fact has no transom this question does not arise, of course, and the only example used in the present paper comes into this category.

Although the justification is far from obvious, we have used the same procedure in <u>all</u> integrals involving $S'(x)$. For instance, the Fourier transform A_1^* required in (AII. 1) is actually evaluated as

$$A_1^*(\lambda) = -i\lambda \int_{-\ell}^{\ell} dx\, S(x)\, e^{i\lambda x}. \tag{AIII. 6}$$

REFERENCES

1 ABRAMOWITZ, M. and STEGUN, L.A., (eds), "Handbook of Mathematical Functions", National Bureau of Standards, Applied Mathematics Series No. 55, Washington, D.C., 1964.

2 BECK, R.F. and TUCK, E.O., "Heave and Pitch of Ships in Shallow Water", 4th Australasian Conference on Hydraulics and Fluid Mechanics, pp. 272-279, Monash University, Melbourne November 1971.

3 KIM, C.H., 'The Influence of Water Depth on the Heaving and Pitching Motions of a Ship Moving in Longitudinal Regular Head Waves", Schiffstechnik, Vol. 15, pp. 127-132, 1968.

4 NEWMAN, J.N., and TUCK, E.O., "Current Progress in the Slender Body Theory for Ship Motions", 5th Symposium on Naval Hydrodynamics, Bergen, 1964.

5 SALVESEN, N., TUCK, E.O., and FALTINSEN, O., "Ship Motions and Sea Loads", Trans. Soc. Nav. Architects & Mar. Engrs., Vol. 78, pp. 250-287, 1970.

6 TAYLOR, P.J., "The effect of beam seas on a stationary ship in shallow water", Ph. D. thesis, University of Adelaide, 1971. (See also : Journal of Ship Research, Vol. 17, pp. 97-105, 1973).

7 TODD, F.H., "Series 60 - Methodical Experiments with Models of Single Screw Merchant Ships", Naval Ship Research & Development Center, Report No. 1712, July 1963.

8 TUCK, E.O., "A Simple 'Filon-Trapezoidal' Rule ", Math. of Computation, Vol. 21, pp. 239-241, 1967.

9 TUCK, E.O., " Ship Motions in Shallow Water", Journal of Ship Research, Vol. 14, pp. 317-328, 1970.

10 TUCK, E.O., and TAYLOR, P.J., "Shallow Water Problems in Ship Hydrodynamics", 8th Symposium on Naval Hydrodynamics, Pasadena, 1970.

11 WILSON, B.W., "A Case of Critical Surging of a Moored Ship", J. Waterways & Harbors Div. A.S.C.E., Vol. 85, pp. 157-176, 1959.

12 WILSON, B.W., "Elastic Characteristics of Moorings", J. Waterways & Harbors Div. A.S.C.E., Vol. 93, pp. 27-56, 1967.

13 WILSON, B.W. and YARBACCIO, D.H., "Dynamics of Ship Anchor Lines in Wave and Current", J. Waterways & Harbors Div. A.S.C.E., Vol. 95, pp. 449-465, 1969.

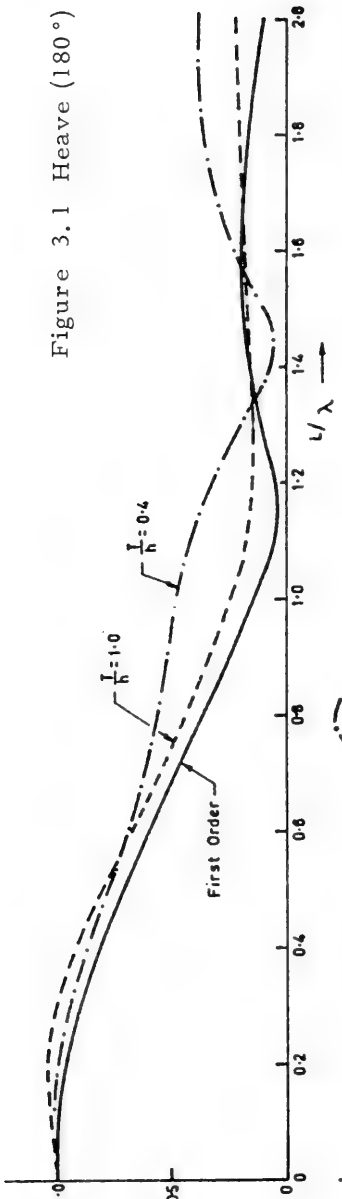

Figure 3.1 Heave (180°)

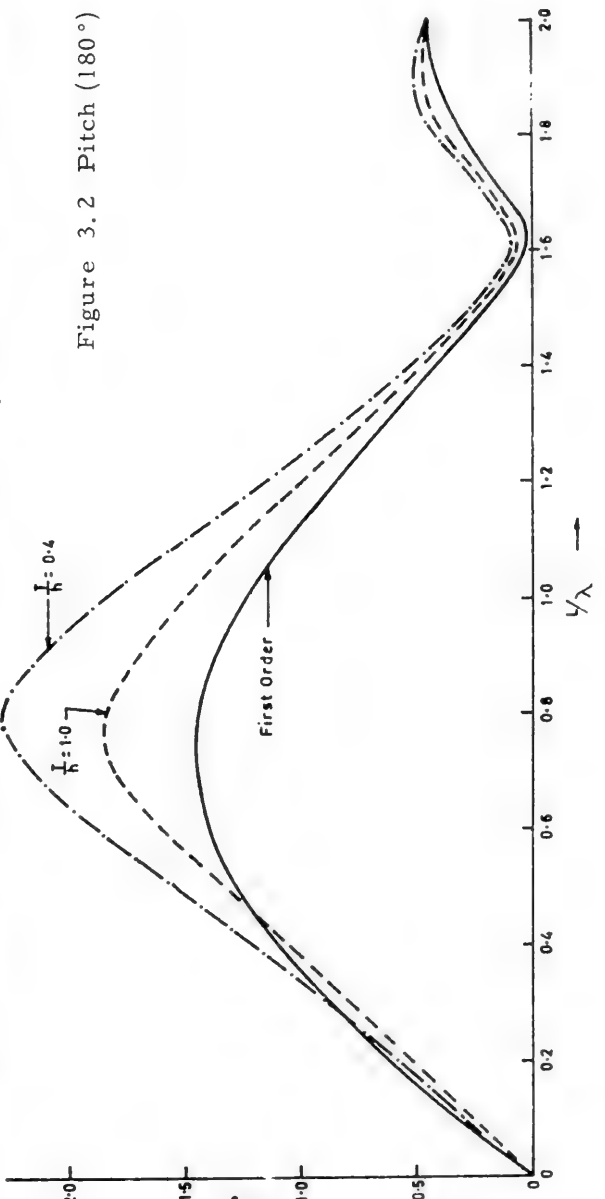

Figure 3.2 Pitch (180°)

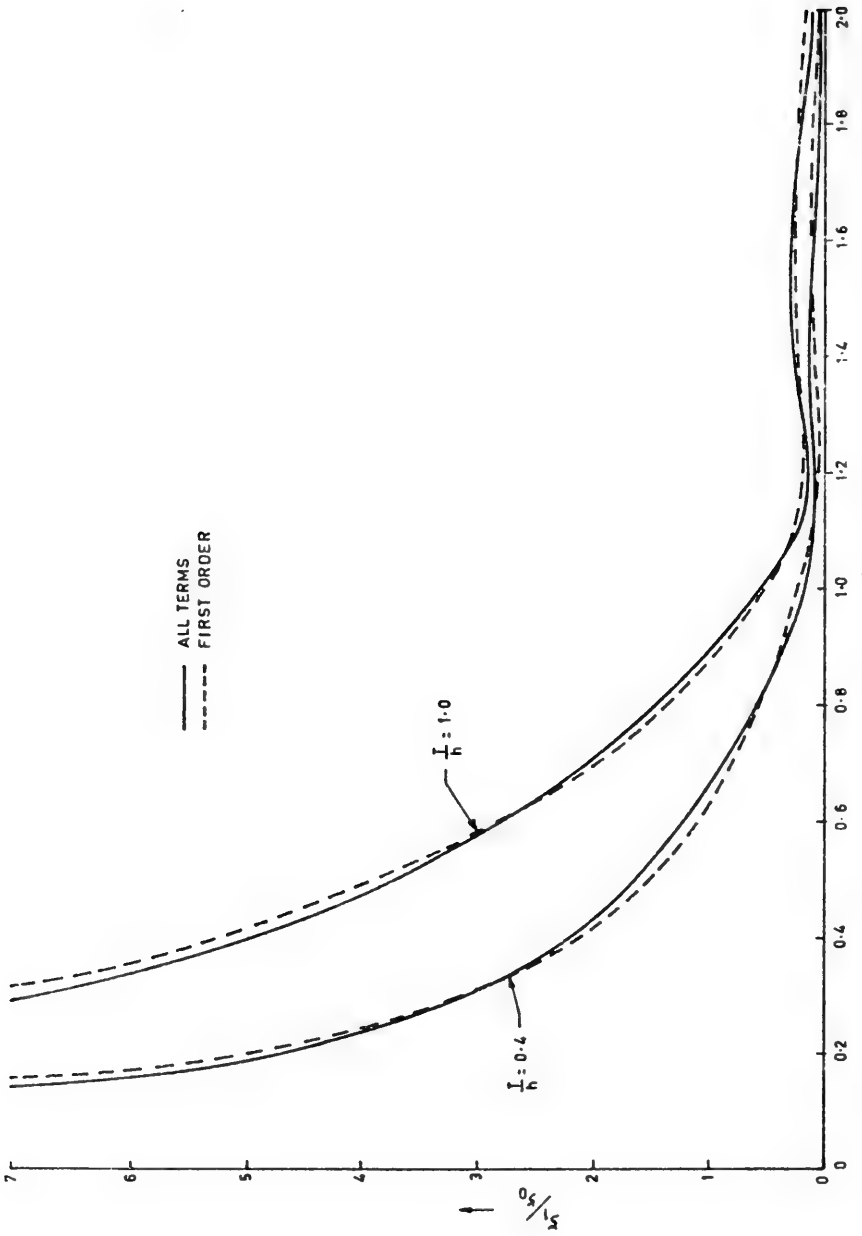

Figure 3.3 Surge (180°)

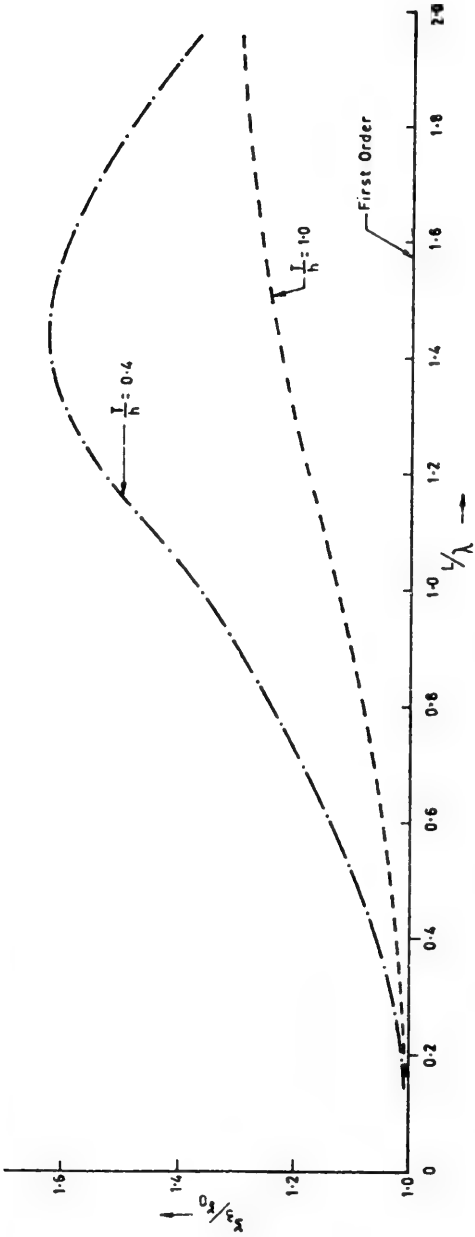

Figure 3.4 Heave (90°)

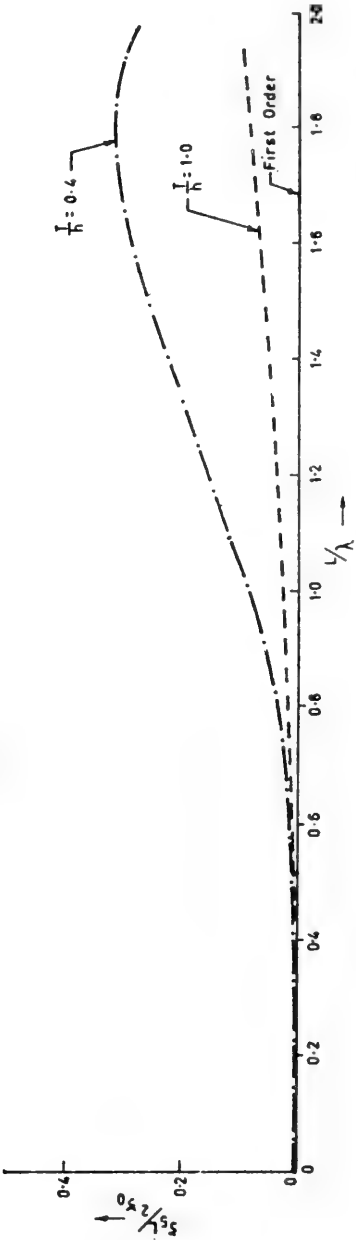

Figure 3.5 Pitch (90°)

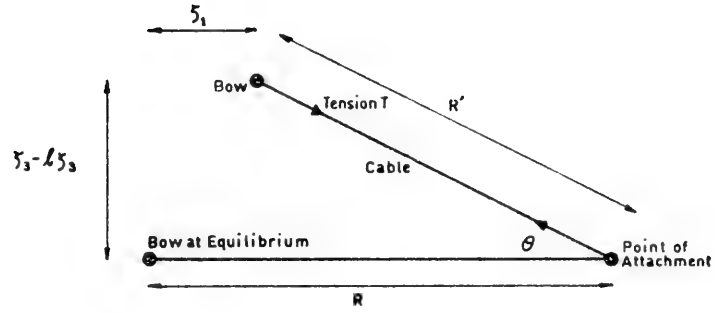

Figure 4.1

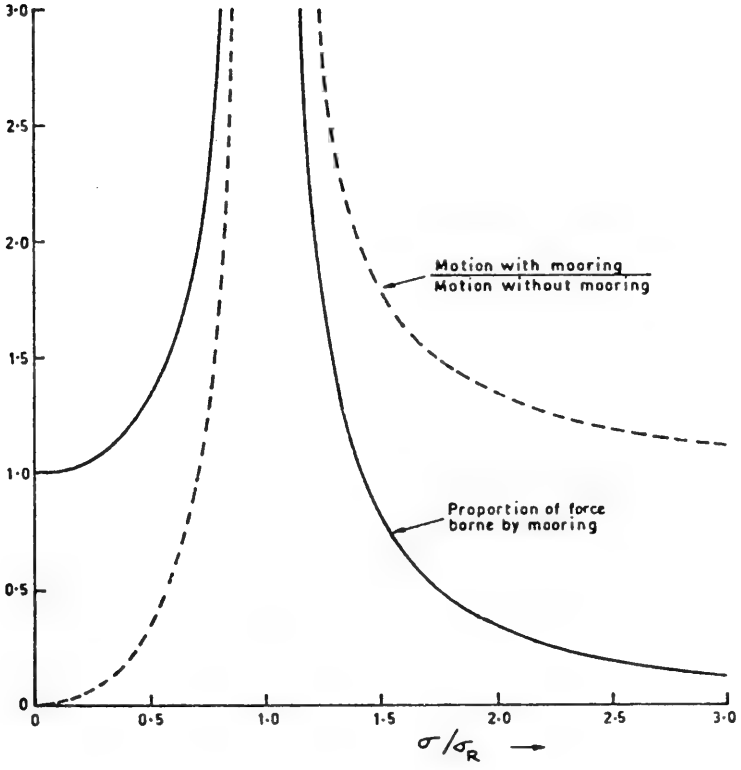

Figure 4.2

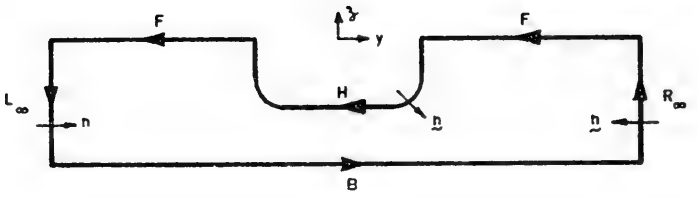

Figure 5.1

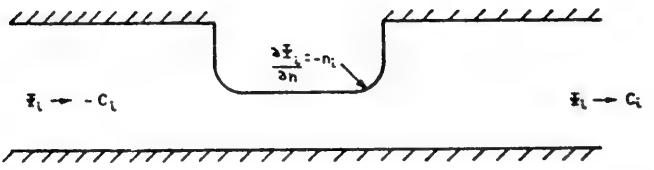

Figure 5.2

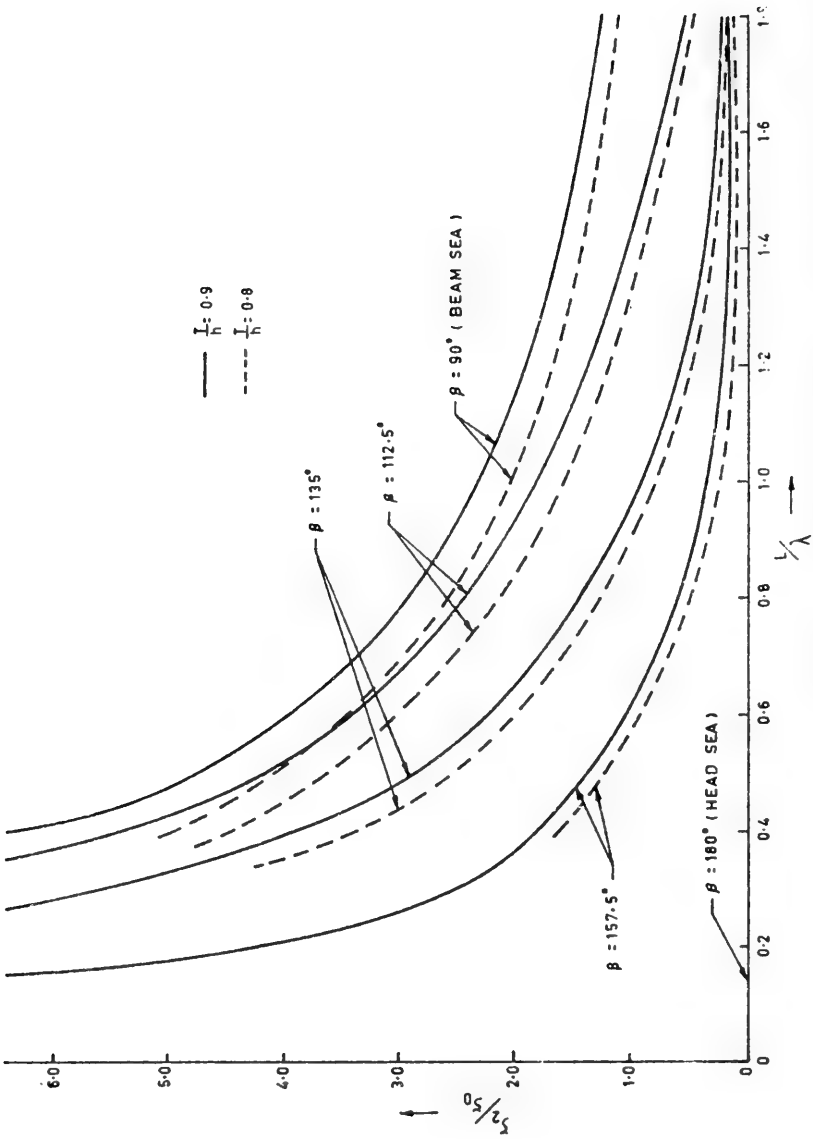

Figure 6.1 Sway

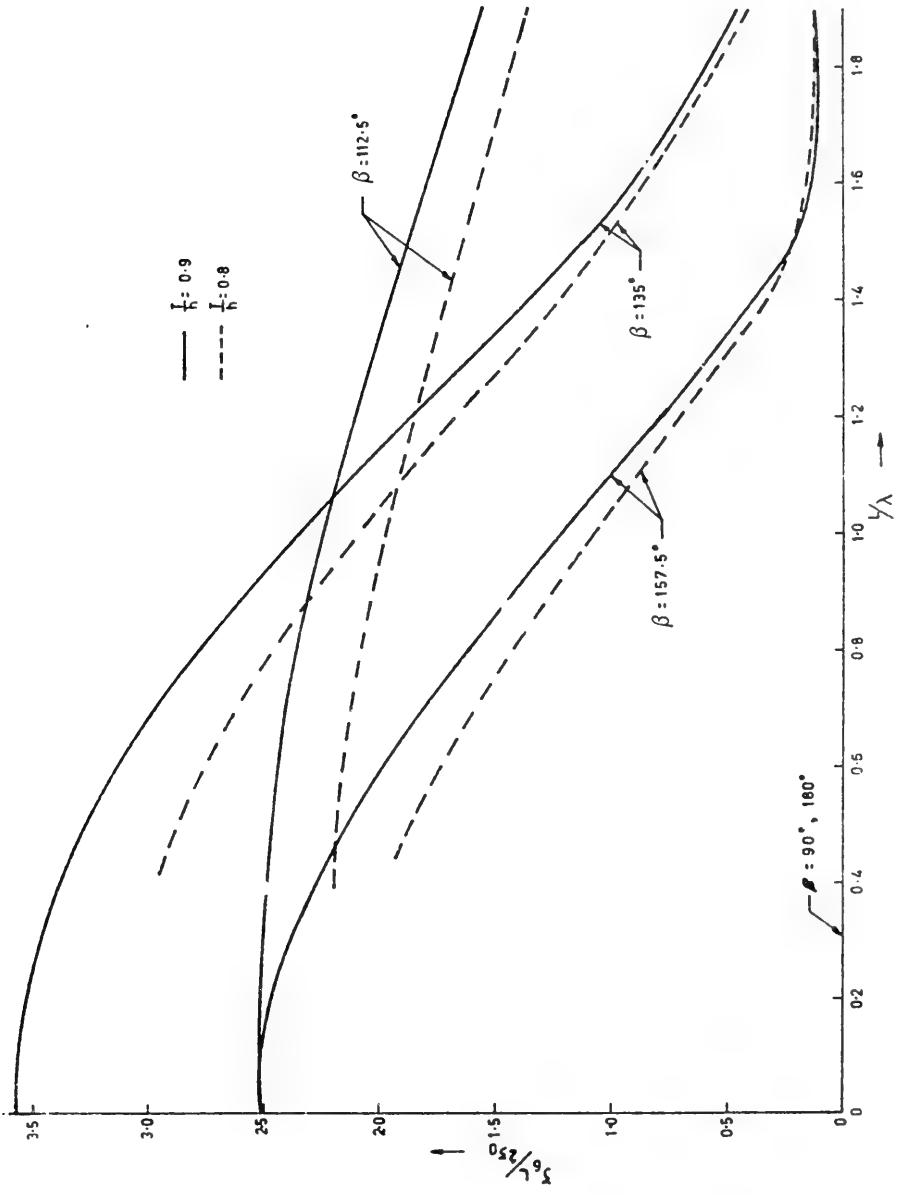

Figure 6.2 Yaw

DISCUSSION

Valter Kostilainen
Ship Hydrodynamics Laboratory
University of Technology, Helsinki, Finland

We all know that we cannot use the results obtained in studying ship motions in deep water to compute ship motion in shallow water. For instance, most of the ships sailing in Finnish fair-ways should, according to this shallow-water theory, touch the bottom quite frequently. We do have some groundings now and then but not quite so often. The importance of research on ship motion in shallow water has been recognised and the present paper is an important step forward in the study of this topic. In our laboratory we try to approach the problem experimentally and one of the most important things from our point of view is the effect of viscosity. If the ship is moving in shallow water the thickness of the boundary layer is of the same order as the clearance between the bottom of the ship and the bottom of the sea. This introduces some scaling problems in model testing and I should like to ask the authors, first, if they have taken account of viscous effects in their computation in zero speed and, secondly, wether they are, as I hope, planning any further investigation for non-zero speed and how they are then going to take account of viscous effect.

REPLY TO DISCUSSION

Robert F. Beck
University of Michigan
Ann Arbor, Michigan, U.S.A.

This theory was derived for zero forward speed and an ideal fluid. Thus, no account was taken of viscous effects. At this time I do not know if we will include forward speed in the theory or not. At zero forward speed, I am not sure what the effect of viscosity will be.

With appendages like bilge keels, it will certainly be important in such terms as the roll damping. As for the problem of the boundary layer under the ship, I do not know how important it would be for zero forward speed.

DISCUSSION

Cheung-Hun C. Kim
Stevens Institute of Technology
Hoboken, New-Jersey, U.S.A.

I recently calculated the motion of the same model ship moving in head seas. Perhaps Dr. Tuck and Dr. Beck have made a comparison with these results in forward zero speed : for h/T, the depth draft ratio = 2.5 and 1.5 . If so have you found any difference between your calculation and my own ?

REPLY TO DISCUSSION

Robert F. Beck
University of Michigan
Ann Arbor, Michigan, U.S.A.

Dr. Kim has computed the results of finite depth ship motions using a strip theory as opposed to a slender body theory. We compared our computed results with his in the Melbourne paper which we have referenced. It may be a good idea to repeat this comparison at this time.

In Figures 1 and 2 the results for heave and pitch are shown. These results are for head seas only, for a Series 60 ship with a block coefficient of .70 . In Figures 1 and 2 the dashed line is the first-order theory mentioned in the present paper. The chain dotted line is for a so-called "second order" theory ; it is the first-order theory with, in addition, just the mass of the ship taken into account, and is not, in fact, a consistant approach, since there is no added mass or

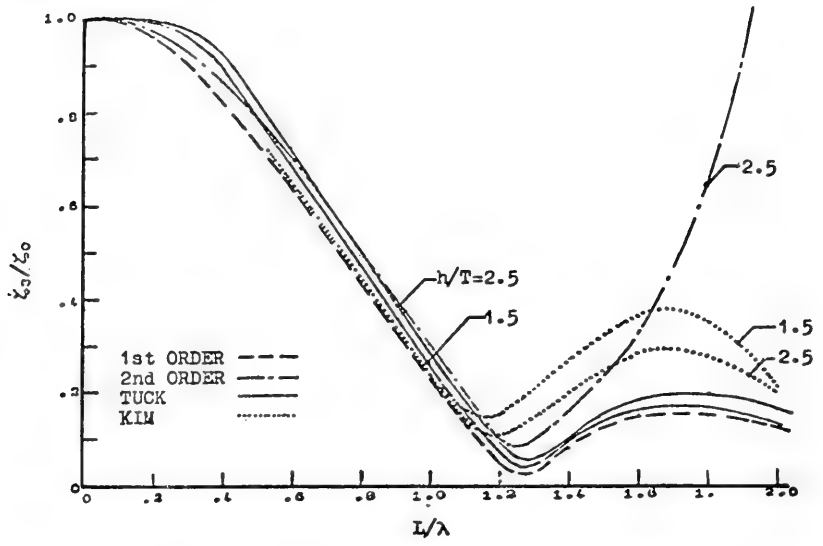

Figure 1 Heave motion in head seas

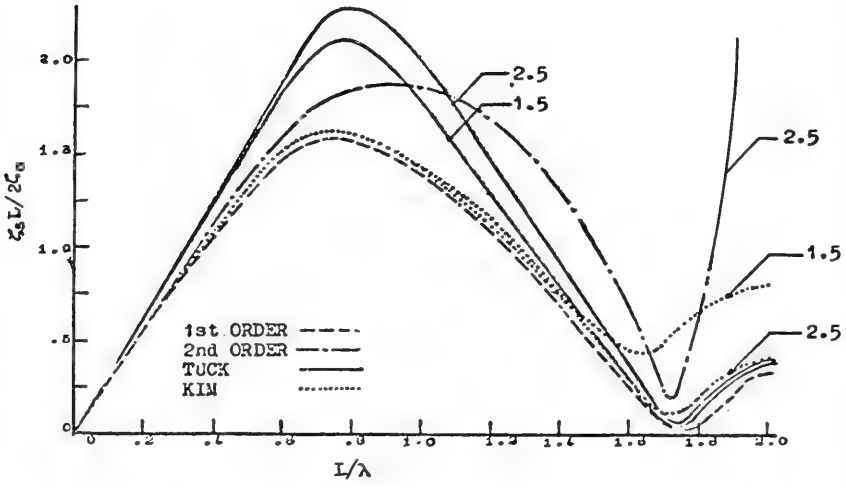

Figure 2 Pitch motion in head seas

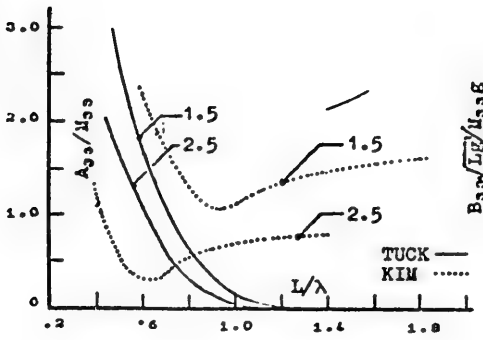

Figure 3 Heave added mass

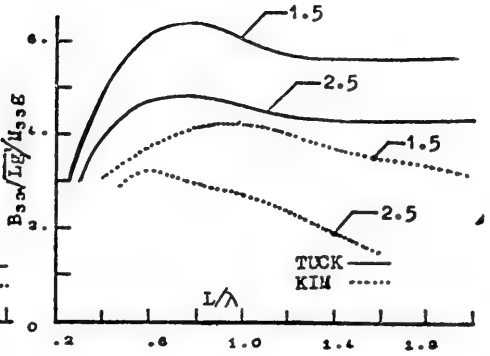

Figure 4 Heave damping

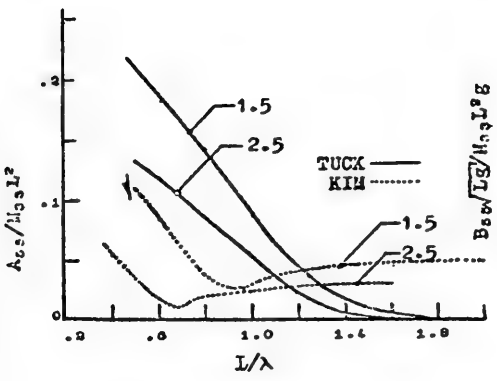

Figure 5 Pitch added inertia

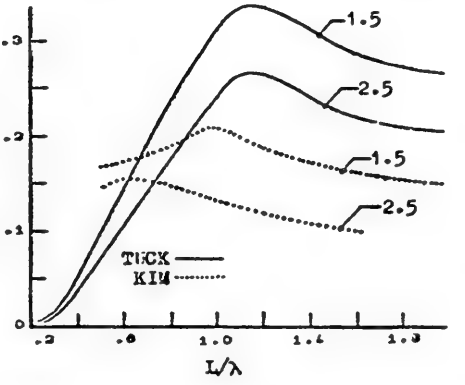

Figure 6 Pitch damping

damping. Thus, you can see the infinite motion at resonance in both pitch and heave, just as you would expect. Finally, the solid lines (labelled "Tuck") are from the present theory without diffraction effects, and the dotted lines are the results of Kim. The differences between the two are very interesting because slender body theory is a theory which is inherently good for very long wavelengths, and strip theory, on the other hand, was developed for a higher frequency where the wave length is the order of the beam. What you can see in Figures 1 and 2 is that at the low frequency end, Tuck's results gave larger motions and at the high frequency end, Kim's results are larger. In the region of short wave lengths we would not expect our theory to give particularly good results since it was derived for very long waves. In this region strip theory would be expected to produce the more accurate results.

Notice that the results in both Figures 1 and 2 are reasonably close to the first order theory. This is because of the dominance of the hydrostatic terms and the Froude-Krylov exciting force. The pitch results for slender body theory do show a marked increase over the first-order theory at around L/λ of .8. This is due primarily to the increase in added moment of inertia. We can actually see this in Figures 3, 4, 5 and 6. In addition, the reasons for the differences between slender body theory and strip theory can be obtained from these figures.

In Figures 3 and 4 are the heave, added mass and damping for head seas. In Figures 5 and 6 are the pitch added inertia and damping. The solid lines are the results of slender body theory. At low frequencies, we can see that the pitch added inertia of slender body theory is much higher than computed by strip theory. This accounts for the larger pitch motion in this region. In the higher frequency region, the damping of both heave and pitch computed by slender body theory are much larger than the strip theory results. This accounts for the fact that in this region, where there is resonance, the motions we compute are much smaller than Kim's. In this region Kim's results are no doubt more accurate.

In the low frequency range, we know that theoretically the damping curve has to go to zero with zero slope at zero frequency. The slender body theory correctly predicts this, whereas the strip theory results, which are not strictly valid in this region, asymptote to zero at a slope other than zero.

In the high frequency region, the heave added mass and pitch added inertia as computed by slender body theory go to zero. However, we know that they should asymptote to a finite value obtainable

by replacing the free surface by a plane of symmetry. The strip theory results seem to be headed in the right direction. Thus, as state before, we would not expect our results to be good in this region.

DISCUSSION

Cheung-Hun C. Kim
Stevens Institute of Technology
Hoboken, New-Jersey, U.S.A.

Thank you. May I ask you another question ? You used the Froude-Krylov forces, why did not you calculate the diffracted wave exciting force in your calculation ?

REPLY TO DISCUSSION

Robert F. Beck
University of Michigan
Ann Arbor, Michigan, U.S.A.

Unfortunately, we overlooked those terms at the time. However, I do not think the results will change very much. The curves would just be shifted slightly in the high frequency region.

SEAKEEPING CONSIDERATIONS IN A TOTAL DESIGN METHODOLOGY

Chryssostomos Chryssostomidis
Massachusetts Institute of Technology
Cambridge, Massachusetts, U.S.A.

ABSTRACT

A procedure leading to the prediction of seakeeping qualities of monohulls in a seaway is briefly reviewed. The two parameter conformal representation of hull sections is described and compared with the close-fit representations.

A proposal for incorporating seakeeping considerations into a total ship design methodology with particular emphasis on the identification of the problem areas and design indices associated with seakeeping is made. The advantages and limitations of the two parameter representation are discussed. The optimization criterion, constraints, and optimization scheme used in conjunction with the proposed design methodology are discussed and illustrated by an example.

I - INTRODUCTION

Attempts to improve the methodology for designing large ocean based systems such as ships have recently appeared in literature, e.g. References 1 and 2. The approach proposed in both these references has retained the iterative nature of the traditional solution method but it has attempted to introduce most of the factors that can influence the overall configuration of the ship as early in the design cycle as possible.

In order to do so the proposed approach requires that the largest possible number of alternatives be examined at the outset of

the study and that all considerations that can affect the final decision be introduced at that time. To be able to do so within the time and resource limitations imposed in all real life problems the proposed approach requires the development of suitable mathematical models that can be used at the different iteration cycles. The mathematical model to be used in the first iteration must be quick (speed is gained by sacrificing the degree of detail) but of sufficient detail to permit the decision maker to select correctly from among the large number of alternatives that are being investigated. This selection usually involves elimination of all infeasible alternatives. The mathematical model to be used in the second iteration must be sufficiently detailed and relatively quick to permit the decision maker to select from the alternatives that were not eliminated in the first iteration. This selection usually involves the elimination of all clearly inferior alternatives. The mathematical model to be used in the final iteration must be fully detailed in order to provide all the information necessary that will permit the decision maker to make the correct final decision. Fig. 1 shows all the steps involved in the proposed design methodology.

Seakeeping is a consideration that can affect the final decision because it can affect the system's cost (profit) and feasibility to perform its mission. Therefore according to the method proposed above seakeeping considerations should be incorporated as early as possible in the design cycle.

A procedure for incorporating seakeeping considerations in the design cycle is proposed in this study and is described in some detail in the sequel.

II - FIRST ITERATION

The mathematical model describing the system under investigation during the first iteration of the proposed design methodology must have at least the following two attributes. First, it must be quick to enable its user to investigate the large number of alternatives called for by the proposed methodology and second, it must be accurate enough to allow its user to draw the correct conclusions from its results. The method that will permit us to construct the seakeeping part of the mathematical model to be used in the first iteration of the proposed design methodology is given in Reference 3.

The highlights of this method are described below.

II. 1. Method

The notion of using standard series, see for example Ref. 4

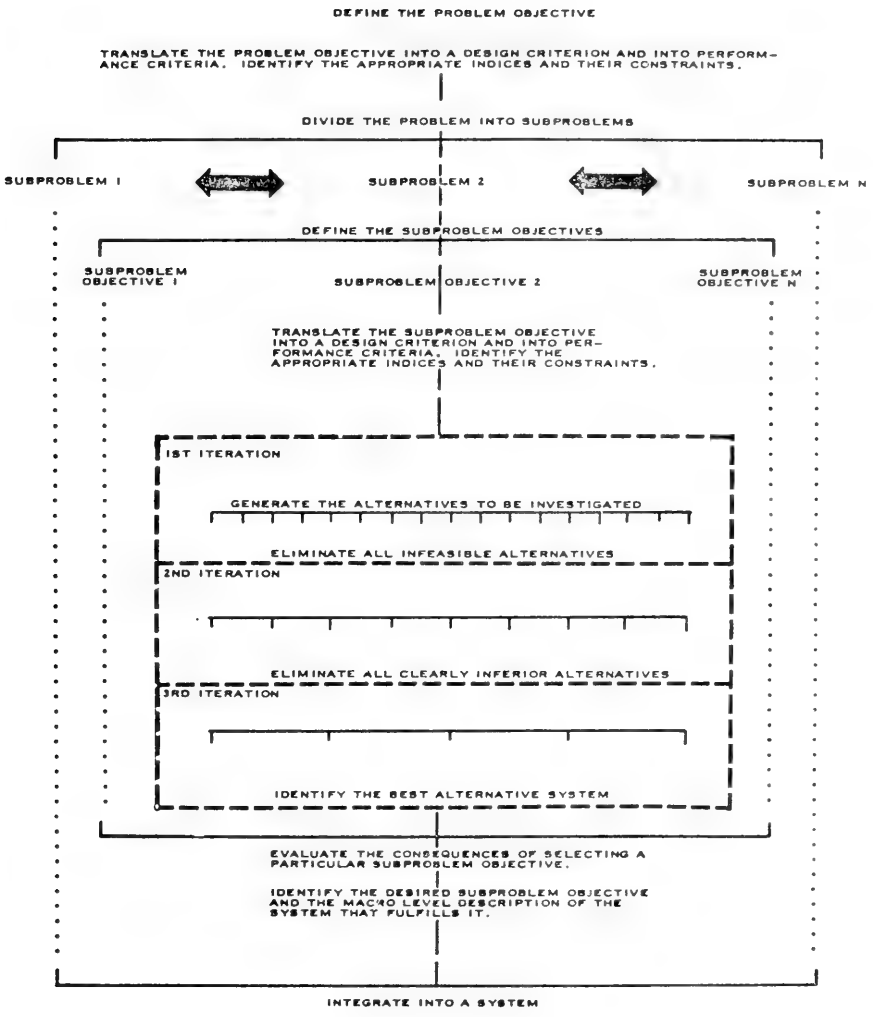

Figure 1 Exploration phase flow diagram

for the determination of the calm water resistance of a given ship is extended to permit the determination of the seakeeping qualities of a ship operating in a seaway. The preliminary results of such an effort are given in Reference 3 where the results for heave amidships, pitch, wave bending moment amidships, added resistance, acceleration at stations 0, 5, 10, 15 and 20 and relative motion and velocity at stations 1, 2, 3, 4 and 20 of a ship operating in long-crested head seas can be found tabulated. The results are given as a function of :

Froude No.	0.10 (0.05) 0.30
$H^{1/3}/LBP$	0.015, 0.020, 0.025, 0.030, 0.040, 0.050, 0.075 and 0.100
LBP/B	5.50 (1.50) 8.50
B/T	2.00 (1.00) 4.00 and
CB	0.55 (0.05) 0.90

and are applicable for cruiser stern type ships.

The 72 hull forms, the six Froude Numbers and the eight non-dimensional sea states ($H^{1/3}/LBP$) defined above form a grid which allows the user to predict the seakeeping qualities of his ship by interpolation (extrapolation) with all the accuracy called for in the first iteration of the proposed design methodology. A sample table from Reference [3] is included in Appendix I of this study for the reader's convenience.

II. 2. Mathematical Model

The following describes the method employed in the present study to determine the values of independent variables of the system that will best satisfy an owner's given set of requirements.

a) Assign different combinations of values to the independent variables.

b) Evaluate the mathematical equations describing the system under investigation for each combination of values of the independent variables (each evaluation constitutes a sampling cycle of the optimization procedure).

c) Eliminate all infeasible designs.

d) Evaluate the optimization criterion for all feasible designs, and

e) Select the alternative that is feasible and satisfies the problem objective.

The part of the mathematical model that is directly related to the seakeeping considerations will now be described in some detail. The other elements of the mathematical model can be found described in the literature dealing with the subject of preliminary ship design optimization, see for example Reference [5], and therefore will not be repeated here.

Description of the Environment

The environment in which the system under investigation is to operate must be described in order to permit the evaluation of the system's seakeeping qualities. Given the route of operation such a description can be obtained from the information given in Reference [6]. The complete environment description would require the construction of a frequency histogram as a function of significant wave height, average period, direction,time and geographical location.

For the present study the environment description was simplified to a frequency histogram which is a function of the significant wave height and geographical location only, and the spectrum describing such seaways (fully developed, long crested) is given by :

$$\Phi^{+}_{\zeta\zeta}(\omega) = \alpha \omega^{-5} \exp(-\beta \omega^{-4})$$

where $\alpha = 0.0081\, g^2 \quad [ft^2/sec^4]$

and $\beta = 0.0324\, g^2/(H^{1/3})^2 \quad [sec^{-4}]$

In addition only head seas were considered in this study.

The simplifications adopted in this study are not considered unrealistic. In the route chosen for investigation (New York-Rotterdam) head seas were predominantly encountered at least 50% of the time

spent at sea, see Reference 6 . In addition the seasonal variation is not significant as can be seen from the tables presented in Ref. 6 , and fully developed seas are the predominant seas encountered in the North Atlantic as can be seen from the results of Reference 7 .

The frequency histogram obtained from Reference 6 for the area of interest is given in Table 1. Table 1 also gives the simplified histogram used in this study. The author did not have access to a computer during the study and had to keep computations to a minimum, resulting in this further simplification. However attention was paid to retain enough detail in the environment description. Therefore valid conclusions can be drawn from the results of the present study.

TABLE 1

Significant Wave Height Histogram
for the New York-Rotterdam Route

Histogram from Reference 6		Histogram used in this Study	
Significant Wave Height	Percentage	Significant Wave Height	Percentage
ft	%	ft	%
4.76	4.16	7.94	48.25
5.48	6.81	10.58	26.14
6.92	17.32	13.23	13.47
8.37	19.96	15.87	7.87
9.81	14.90	21.16	2.38
11.25	11.24	26.45	1.89
12.70	7.70		
14.14	5.77		
15.58	3.82		
17.03	3.44		
18.47	0.61		
19.91	0.59		
21.36	0.90		
22.80	0.89		
24.25	0.37		
25.69	0.44		
27.20	0.34		
28.58	0.22		
30.02	0.17		
31.46	0.34		
35.79-44.46	0.01		

E. H. P. Calculations

The Effective Horse Power (EHP) of a ship operating in the seaway is computed in the following manner.

First, the bare hull calm water Effective Horse Power is computed as a function of ship speed from Reference 4 . This estimate is then augmented by 3% to account for the presence of appendages. Second, the Effective Horse Power necessary to overcome the increased resistance because of fouling is computed. It is assumed that the ship is dry docked every year. From the results reported in Reference 8 it is found that increasing the value of ΔCF by 0.00015 would account, on the average, for the yearly increase of resistance due to fouling. Therefore :

$$EHP_{fouling} = \frac{0.00015 * \rho * V^3 * (1.6889)^3 * \text{wetted surface}}{2 * 550}$$

where V = ship's speed in knots

and ρ = sea water density in slugs/ft.^{3}

Third, the wind resistance is computed as a function of the ship speed and sea state ($H^{1/3}$). From Reference 9 the Effective Horse Power necessary to overcome the wind resistance is given by

$$EHP_{wind} = \frac{0.00435 * B^2 * VR^2 * V}{2 * 325.66}$$

where B = ship's beam in ft.
VR = wind velocity relative to the ship in knots.

The wind velocity relative to the ship, VR, is computed by adding the wind speed corresponding to each sea state to the ship's speed V. The wind speed as a function of sea state ($H^{1/3}$) is determined from Fig. 2.

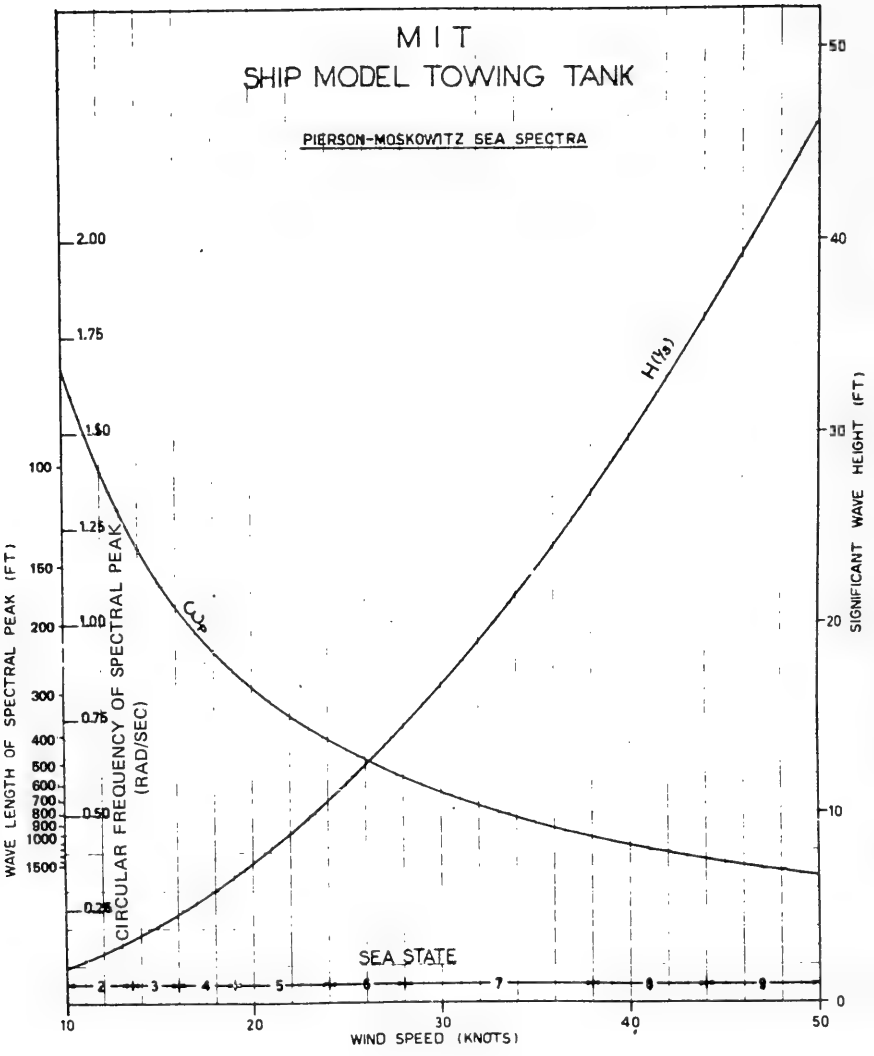

Figure 2 Principal parameters for fully developed seaways

Fourth, the Effective Horse Power necessary to overcome the mean added resistance in waves as a function of ship speed and sea state ($H^{1/3}$) is computed using the appropriate Seakeeping Tables from Reference 3. Finally, the Effective Horse Power of a ship operating in a seaway is obtained by adding the bare hull calm water EHP (augmented by the appendage allowance) and the EHP necessary to overcome the increased resistance due to fouling, the wind resistance and the mean added resistance in waves. The results of such a computation can be found in Figures 3 and 4.

Speed Calculations without Motion Considerations

Given the EHP curves as a function of ship speed and sea state it is possible to compute the average ship speed (assuming no limitations due to motion) for a prespecified engine output, SHP_a, in the following manner.

First, a family of propellers is selected. For the present study the Wageningen B-Screw Series, see Reference 10, is selected. The propeller type used in the present study is the B.4.55 propeller. It is of interest to note that ships similar to the ones investigated in this study operate using propellers with characteristics similar to the B.4.55 propeller.

Next the curve of K_T/J^2 is computed and plotted on the propeller diagram to allow the selection of the most efficient propeller for operation in a prespecified sea state. In the present study it was decided to optimize for the sea state characterized by $H^{1/3} = 7.94$ ft. because according to information given in Table 1 it is the sea state that occurs most frequently. In the computation of

$$\frac{K_T}{J^2} = \frac{EHP * 325.66}{\rho * d^2 * V^3 * (1.6889)^3 * (1-w)^2 * (1-t)}$$

the EHP and ship speed V was determined from the EHP vs V and $H^{1/3}$ curves developed in the previous section, the propeller diameter d was taken as in Reference 4, i.e. $d \approx 0.70\ T$, and the values for w and t were determined from Reference 4 from the calm water data. These values were assumed to apply to the propeller operating in the seaway. Unfortunately the effect of this assumption cannot be estimated as very little is published on the subject. However the results obtained from the calculations using this assumption appear to be in agreement with published results and it is there-

fore concluded that this assumption is not unrealistic.

Once the open water efficiency η_O is computed the propulsive efficiency η_P, is then calculated

$$\eta_P = \eta_O \quad \eta_H \quad \eta_R \quad \eta_S$$

where η_H = $(1-t) / (1-w)$

η_R = relative rotative efficiency

(Reference 9 suggests a value of 1.026 which was adopted for all sea states)

η_S = shaft transmission efficiency

(Reference 9 suggests a value of 0.98 for machinery aft, which was adopted in the present study)

This allows to compute, SHP_r, the power required to operate a given ship at a given speed and sea state from the following equation

$$SHP_r = EHP / \eta_P.$$

The above calculations are repeated by selecting pairs of values for EHP and V until $SHP_r = SHP_a$.

This procedure is then repeated using pairs of EHP and V values from the EHP curves corresponding to the other sea states of interest. In these calculations of course the propeller selected for the sea state characterized by $H^{1/3} = 7.94$ ft. is always used. Once the speed that can be achieved in all the sea states of interest for a given SHP_a, the average speed, V_a, can be obtained from the following equation

$$V_a = \frac{1}{100} \sum_{i=1}^{N} F_i V_i$$

where

F_i is the frequency of occurrence of the ith sea state $(H^{1/3})$ obtained from Table 1.

V_i is the ship speed in the ith sea state (no motion considerations)

and N is the number of sea states $(H^{1/3})$ used to describe the environment ($N = 6$ for this study).

The results of such a computation can be found in Figures 5 and 6.

At this stage it is important to point out that in the present study SHP_a is an independent variable because the calculations are not done for an assumed average condition, as was the case with Reference 5, but rather for the actual operating environment.

Speed Calculations with Motion Considerations

The ship speed as a function of sea state $(H^{1/3})$ determined from the previous analysis must now be modified to account for possible further reductions due to motion considerations.

The criteria used to determine whether a given ship is motion limited or not are the following

a) For the safety of the crew the RMS vertical acceleration at station 15 is not to exceed the value of 0.125 g. This value is determined from Reference 11 .

b) For the safety of the cargo

(i) the average 1/10 highest values of vertical acceleration must not exceed one **g** anywhere along the ship's length. From Reference 12

$$H^{1/10} = 1.800 \sqrt{8m_o(1-\epsilon^2/2)}$$

where $\sqrt{m_o}$ is the RMS of the response of interest

and ϵ is the broadness factor assumed to equal 0.60 for the present study.

In order to satisfy the requirement that the 1/10 highest values of vertical acceleration does not exceed one g anywhere along the ship's length the inequality $\sqrt{m_o} \leq 0.217$ must be satisfied.

(ii) the probability P_w that the amplitude of relative motion at station 1 will exceed the freeboard at station 1 (f_w) be less than 0.01.
From Reference 12

$$P_w = \exp(-f_w^2/A_{rm}^2)$$

where $$A_{rm}^2 = 2(1-\epsilon^2/2)m_o$$

c) For the safety of the ship the probability, P_s of slamming at station 2 should not exceed 0.01.

$$P_s = \exp\left[-(f_s^2/A_{rm}^2 + V_{cr}^2/A_{rv}^2)\right]$$

where f_s is the draft at station 2

V_{cr} is the threshold critical velocity assumed to equal 12 ft/sec for a 500 ft. ship and scaled according to Froude for other ship lengths

and $A_{rv}^2 = 2(1-\epsilon^2/2)m_o$.

Once the motion indices are calculated the speed determined from resistance considerations is reduced (if necessary) until the motion criteria are satisfied. If the speed is reduced to 3.5 knots (speed assumed to be necessary for the maintainance of a prespecified course) and the motion criteria are not satisfied, no further speed

reduction is allowed in the model proposed in the present study. When this occurs it is advisable to augment the optimization criterion by outputing the seakeeping qualities of the ship at this reduced speed in order to provide the decision maker with all the information necessary for the selection of the "best" ship.

In the present analysis since only head seas are considered it is only meaningful to satisfy the motion limitations by speed reductions. This is not always what happens in actual operation where in heavy seas the operator might elect to change course. It is actually common practice to take heavy seas at 30°-35° off the bow in order to ease the pitching motion. However this limitation in the model is not considered important because in other headings the speed increases, see Reference 13 , which partly compensates for the lost time due to extra distance traveled.

The average ship speed in a seaway can be computed using the same formula given in the previous section the only difference being that now V_i is the ship speed in the ith sea states including motion considerations. The results of such a computation can be found in Figure 5.

Fuel Consumption

Steam Turbine is the main propulsion unit adopted in this study. The specific fuel consumption at powers other than 100% power can be obtained from

$$SFC_{x\%} = \frac{SFC_{100\%} \quad \eta_{100\%}}{\eta_{x\%}}$$

Typical values for power, RPM and efficiency η are given in Table 2.

It is also assumed that for a given power setting if the value of RPM is less than the one shown in Table 2, it will not affect the efficiency of the steam turbine. This is a reasonable assumption since steam turbines are constant power machines.

TABLE 2

RPM - Power - Efficiency Curves for a Typical Steam Turbine

RPM [fraction of design RPM]	Power [fraction of full Power]	Efficiency
0.60	0.216	0.766
0.65	0.275	0.807
0.70	0.343	0.845
0.75	0.432	0.881
0.80	0.512	0.913
0.85	0.614	0.941
0.90	0.729	0.965
0.92	0.779	0.973
0.94	0.831	0.979
0.96	0.885	0.984
0.98	0.941	0.988
1.00	1.000	0.990

TABLE 3

Ship and Propeller Principal Characteristics

	CASE A	CASE B
LBP [ft.]	529.00	666.50
LWL [ft.]	538.15	678.03
B [ft.]	75.57	95.21
T [ft.]	25.19	31.74
D at Amidships [ft.]	45.00	56.70
D at Station 1 [ft.]	55.50	69.94
CB	0.650	0.650
CP	0.661	0.661
Δ [long tons]	18700	37400
Wetted Surface [sq. ft.]	48510	77000
d [ft.]	17.50	22.50
Pitch/d	1.00	1.00

II. 3. Example

The two ships and propellers whose characteristics are given in Table 3 are the two cases analysed in the present study. Ships A and B are geometrically similar and ship B has twice the displacement of ship A. The calculations performed in this section are the calculations that the designer would have to perform in a typical sampling cycle of the solution of a problem where the unknowns are the vessel size and speed of a fleet of ships that will satisfy a prespecified transport capability and optimization criterion.

Figures 3 and 4 give the EHP vs. speed and sea state curves for ships A and B. The EHP vs. speed curve with the traditional 25% allowance is also shown dashed for comparison purposes. It is of interest to note that in the speed range of practical interest the EHP curve with the 25% allowance is almost identical with the EHP curve for $H^{1/3} = 7.94$ ft.

The SHP_a assumed for this study is determined from the value of EHP with 25% margin using a propulsive efficiency equal to 0.75 as suggested in Reference 5. This was done in order to be able to compare the results of the present study with the results that would have been obtained if seakeeping considerations were not included in the analysis. The values of SHP_a used in the present study were 18000 for ship A and 37400 for ship B, both of which correspond to a speed of 20 knots. The results of the speed calculations are shown in Figures 5 and 6.

From resistance considerations alone, the average speed for ship A is 18.85 and for ship B is 18.81 knots. When motion considerations are included the average speed of ship A is reduced to 18.62 knots while the speed of ship B remains unaffected.

The speed reduction for ship A was primarily due to the wetness criterion. Slamming considerations yielded restrictions which were slightly less binding than wetness while vertical acceleration considerations were not binding. For ship B the motion considerations were not at all binding and if the ship had more power available it could go at a higher speed.

The ship speed at the low sea states was computed to be lower than 20 knots even though the EHP value computed with the method suggested in the previous section is about the same as the value of EHP computed using the method suggested in Reference 5. This is due to the fact that the propulsive efficiency computed in the

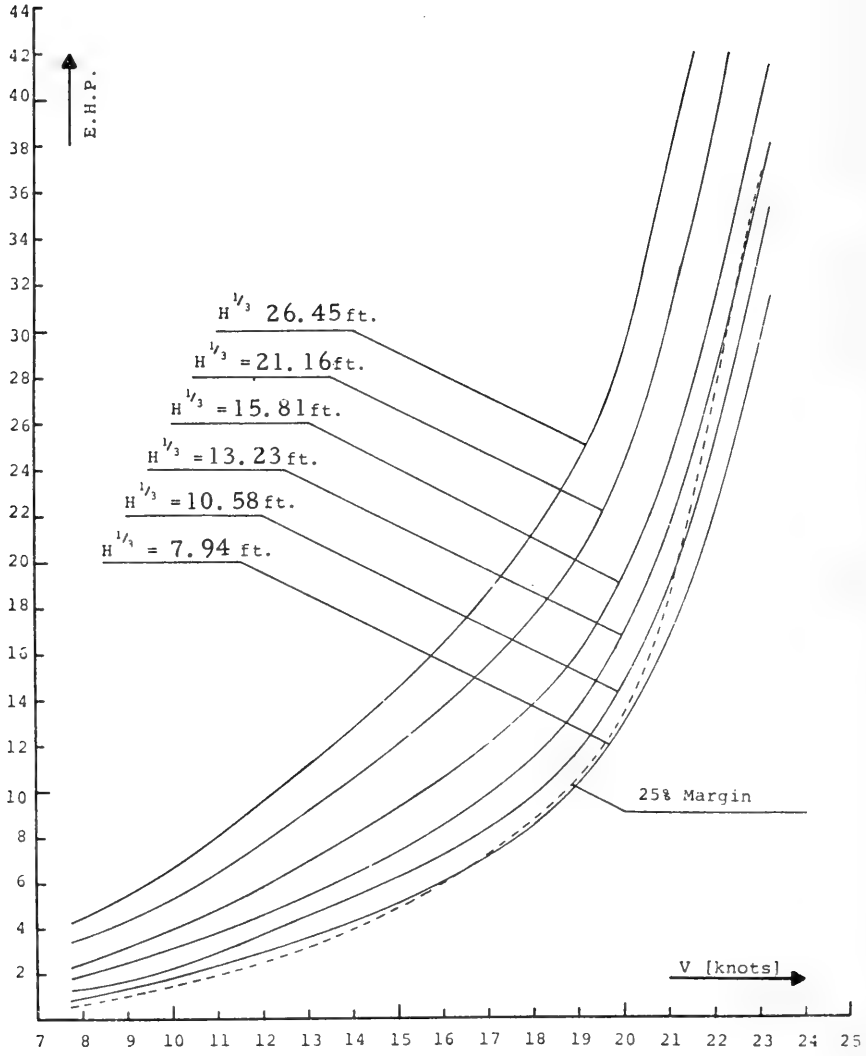

Figure 3 EHP curves for ship A

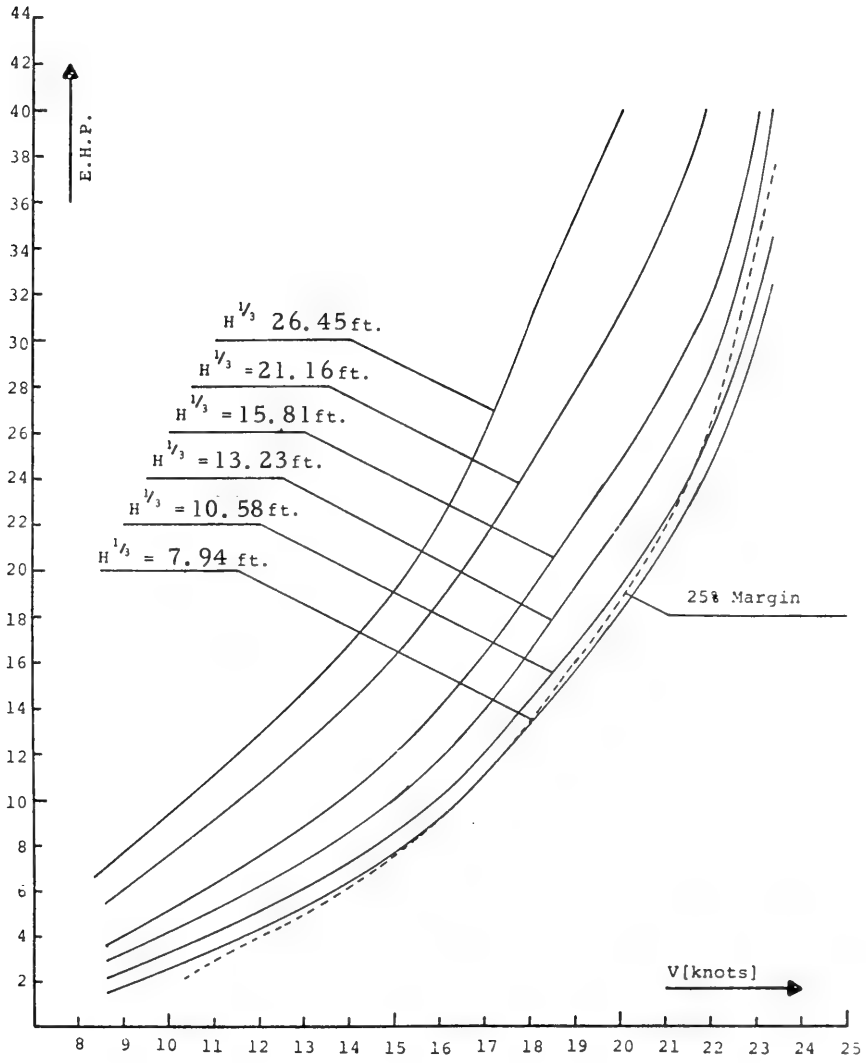

Figure 4 EHP curves for ship B

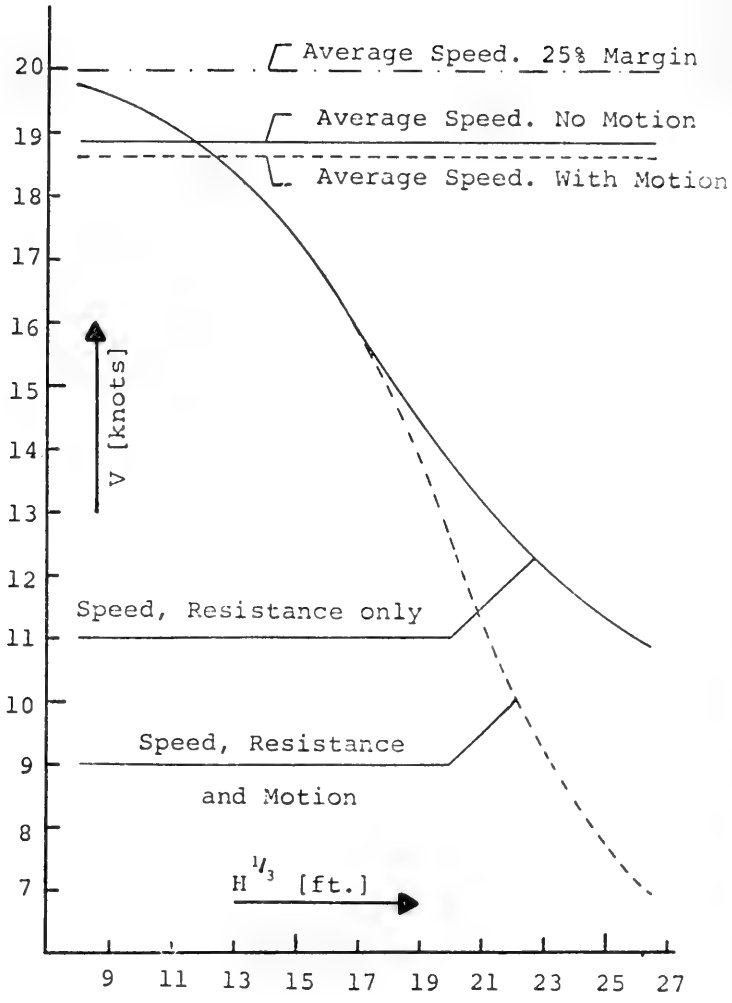

Figure 5 Speed curves for ship A

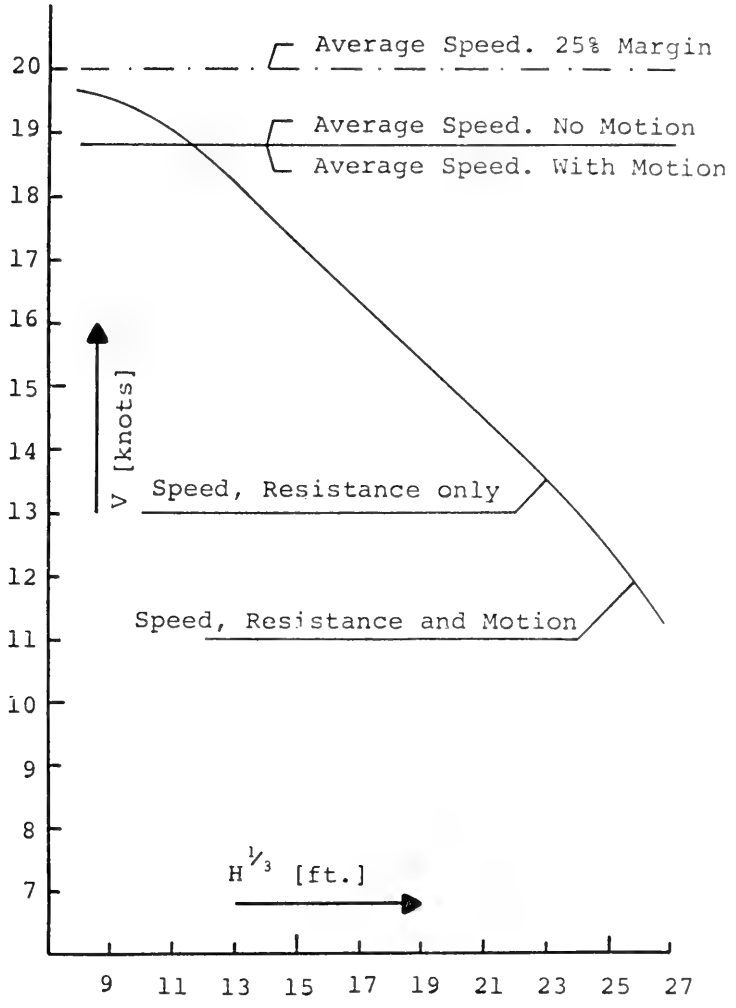

Figure 6 Speed curves for ship B

present study is lower (0.69 vs. 0.75) than the one suggested in Reference 5 . The reason is that in the present analysis the design point for the propeller corresponds to a heavier load condition than the one used in Reference 5 . It is also of interest to point out that because the design point of both propellers of this study is well to the left of the peak of the efficiency curve, there was no need to make any special provisions to assure efficient operation in light loads as this is achieved automatically.

II.4. Analysis of the Results. Conclusions and Recommendations

From the results of the previous section it can be seen that seakeeping considerations should be incorporated in preliminary design as they affect the ship's speed and hence its profit earning capability and/or ability to perform its mission. It is recommended that seakeeping considerations be included when speed (SHP_a) is a variable in the optimization scheme. This is not so much because of the variation of added resistance with speed for a given ship but because of the importance of motion limitations above a certain speed. It is also recommended that seakeeping considerations be incorporated in preliminary design optimization schemes when large differences exist among the alternatives investigated, as is the case with ships A and B of the previous section, because their seakeeping performance is different.

The results also suggest that when optimization does not involve large changes in the principal characteristics of the different alternatives considered, as in the case of ships with constant payload. then seakeeping considerations should not be included in the optimization scheme because they are not expected to influence the final decision. It should be emphasized however, that this is not to be interpreted that seakeeping considerations are not to be included in preliminary design of such ships. On the contrary they should be included because it is only then that the designer can predict with confidence the speed (and hence profit) of his ship in the actual operating environment.

The optimization criterion to be used in conjunction with the model proposed in the present study must include profit considerations. This is so because speed and payload are variable and therefore minimum cost solutions are not necessarily synonymous with the "best" solution.

Comparison with published results show that the speed reduction from motion considerations is underpredicted, see Ref. 14 . This is not because unrealistic motion indices were adopted but rather

because wave added resistance is overpredicted. Since preliminary ship design decisions are primarily based on ship speed it is recommended that research effort be directed to improving the prediction of wave added resistance. Research should also be directed in the area of propeller operation in the seaway in order to permit a better prediction of the propulsive efficiency as it also affects our ability to predict correctly the ship's speed. Finally the establishment of some ship motion criteria that are widely accepted is also recommended.

As a continuation of the present work the author suggests computerization of the mathematical model described in the previous section in order to permit a complete investigation of the effect of seakeeping in preliminary ship design. In addition such a model will help to direct seakeeping research by examining the importance of its contribution in ship design. It is suggested that the computer program recommended for development employ a more detailed description for the environment that the one used in the present analysis. It is also suggested to extend the model to include ballast condition considerations. Finally it is recommended to extend the coverage of the Seakeeping Tables of Reference 3 to include transom stern ships as these types of ships are extensively used in certain trades such as container transportation.

III - SECOND AND THIRD ITERATION

III. 1. Second Iteration

The model recommended for the second iteration of the proposed design methodology for the prediction of the seakeeping qualities of the different alternatives under investigation, is in the form of detailed seakeeping computer programs. The description of typical examples of such computer programs can be found in References 12, 15 and 16 .

With the aid of these computer programs it is possible to analyse the effect of variations in the value of LCB-LCF separation, for example, for which average values were assumed in the first iteration. However unless the designer is willing to investigate large changes in these parameters the effect in the seakeeping qualities of the ship is not expected to be appreciable.

Recently the Classification Societies, e.g. Lloyds, ABS, etc., started to recommend the use of seakeeping theory for the prediction of wave bending moment. For the application of such information in ship design the reader is directed to Reference 17 .

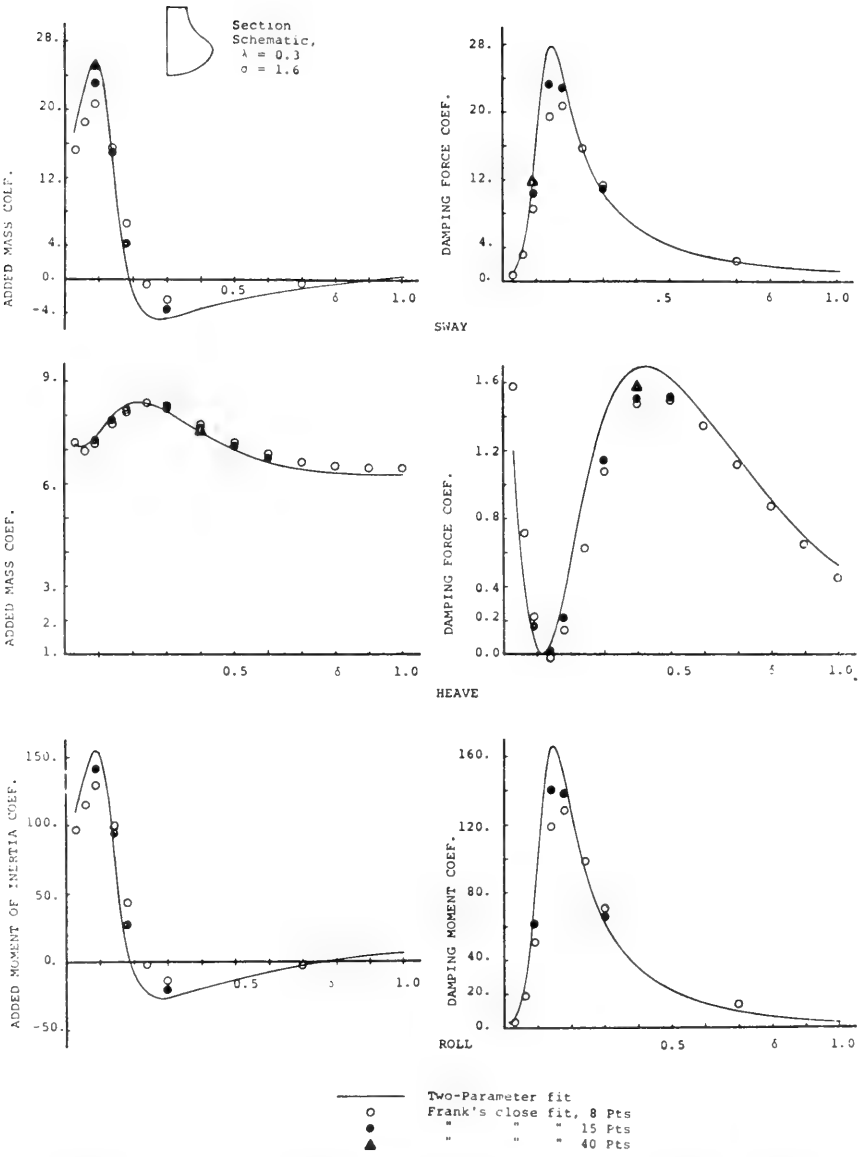

Figure 7 Hydrodynamic coefficients of a bulbous section

The computer programs described in References 12 and 15 employ a two parameter conformal representation for the hull sections. This has been found to be very satisfactory when compared to the close fit representation. Figure 7 from Reference 18 shows that the close fit representation approaches the results of the two parameter representation when the number of points employed in the close fit representation is increased (i. e. its accuracy is increased). However as the number of points is increased in the close fit representation the expense also increases and for 40 points it is prohibitive. The limitation of the two parameter fit is that all calculations are performed with the transformed sections and not with the original sections. This however is not considered important because good two parameter description of regular sections and of sections with moderate bulbs is presently available. In addition moderate geometrical changes in the section shape do not affect the seakeeping results. In any case if a section is to be described accurately in the close fit representation, especially bulb sections, a large number of points is necessary which make it prohibitively expensive.

The expense for the use of seakeeping programs can be considerable especially if a complete investigation is to be made. In an attempt to overcome this limitation the authors of Reference 3 are extending the notion developed therein and are currently working on a scheme in which the Hydrodynamic properties of a section is stored in a matrix as a function of the two parameters describing the section, λ and σ, and the non-dimensional frequency δ. Although the work is still underway, it is expected that a sparsely populated matrix will provide all the accuracy necessary in the second iteration of the proposed design methodology. This will permit the designer to perform the analysis suggested above at almost no cost at all.

Before concluding this discussion the author wishes to take this opportunity to suggest research in the area of viscous roll damping under speed and with bilge keels because the state of the art in this area is not satisfactory.

III. 2. Third Iteration

In the final iteration the author suggests the use of seakeeping experiments for the selection of these parameters whose effect cannot be predicted by either models described above such as for example the above water hull shape. In addition these experiments can serve as a confirmation of the prediction made with the seakeeping computer programs especially in the areas where the theory is weak, for example in the prediction of power. The author recognises that seakeeping experiments are time consuming and expensive and there-

fore in designs where previous experience has demonstrated that seakeeping performance is satisfactory seakeeping experiments should be omitted. However where no previous experience is available, as in the case of a novel design, such experiments are highly recommended.

IV - CONCLUSIONS

From the results presented in the previous sections the author has concluded that it is advantageous to incorporate seakeeping considerations in preliminary ship design optimization programs because of the potential payoff. However seakeeping considerations should only be included where it is meaningful to do so for example when the speed and size of ships are variable. They should not be included when only small changes in the principal characteristics of the ship are contemplated as they will not affect the final outcome.

Special attention was drawn to the case of novel designs where seakeeping can be the controlling factor in the feasibility of the system. In this case seakeeping must be considered at the outset of the study.

Although the state of the art permits the incorporation of seakeeping considerations in the design of monohulls improvement in the theory in certain areas will be worthwile as it will permit a better analysis. In particular, improvement in the theory to permit better predictions for added resistance, propulsive efficiency and viscous roll damping is considered worthwhile. In addition a better definition of the motion indices is necessary.

NOMENCLATURE

B	beam
CB	block coefficient
EHP	effective horse power
Fn	Froude number
g	acceleration of gravity
$H^{1/3}$	significant wave height
J	advance coefficient
K_T	thrust coefficient

LBP	length between perpendiculars
LWL	lenght on designed waterline
RMS	root mean square value
SHP_a	available shaft horse power
SHP_r	required shaft horse power
T	draft
V	ship speed
δ	non dimensional frequency ($\delta = \omega^2 B / 2g$)
ΔCF	correlation allowance ($\Delta CF = 0.0004$)
ϵ	broadness factor
λ	half bean to draft ratio for each section
ρ	specific density of salt water
σ	sectional area coefficient for each section
ω	circular frequency

REFERENCES

1 MANDEL. P. and CHRYSSOSTOMIDIS, C., "A Design Methodology for Ship and Other Complex Systems", London, England, Royal Society, 1972.

2 SNAITH, G. R. and PARKER, M. N., "Ship Design with Computer Aids", Transactions of the North East Coast Institution of Engineers and Shipbuilders, vol. 88, 1972, p. 151-72.

3 LOUKAKIS, T. and CHRYSSOSTOMIDIS, C., "The Seakeeping Performance of an Extended Series 60" , to be published as a Report by the U. S. Maritime Administration.

4 TODD, F. H., "Series 60 : Methodical Experiments with Models of Single-Screw Merchant Ships", David Taylor Model Basin, Report No. 1712, Washington, D. C. : U. S. Government Printing Office, 1963.

5 MANDEL, P. and LEOPOLD, R., "Optimization Methods Applied to Ship Design", Transactions of the Society of Naval Architects and Marine Engineers, vol. 74, 1966, p. 477-521.

6 HOGBEN, N. and LUMB, F. E., "Ocean Wave Statistics", Ministry of Technology National Physical Laboratory, Her Majesty's Stationary Office, London, England, 1967.

7 LOFFT, R. F., "I. T. T. C. Wave Spectrum - Slope Parameter", Proceedings of the 12th International Towing Tank Conference, Rome, 1969, p. 779-80.

8 HADLER, J. B., WILSON, C. J. and BEAL, A. L., "Ship Standardization Trial Performance and Correlation with Model Predictions", Transactions of the Society of Naval Architects and Marine Engineering, vol. 70, 1962, p. 749-807.

9 "Principles of Naval Architecture", 2nd Edition, Edited by J. P. Comstock, Society of Naval Architects and Marine Engineers, New York, New York, 1967.

10 VAN LAMMEREN, W. P. A., VAN MANEN, J. D. and OOSTERVELD, M. W. C., "The Wageningen B-Screw Series", Transactions of the Society of Naval Architects and Marine Engineers, vol. 77, 1969, p. 269-317.

11 DREWRY, J. T., "Vertical Acceleration of Ships in Irregular Waves and Associated Motion Sickness", S. M. Thesis Massachusetts Institute of Technology, Cambridge, Mass., 1966.

12 LOUKAKIS, T. A., "Computer Aided Prediction of Seakeeping Performance in Ship Design", Cambridge, Mass. : Massachusetts Institute of Thechnology, Department of Naval Architecture and Marine Engineering, Report No. 70-3, 1970.

13 MARKS, W. et al., "An Automated System for Optimum Ship Routing", Transactions of the Society of Naval Architects and Marine Engineers, Vol. 76, 1968, p. 22-55.

14 ZUBALY, R. B., "Causes and Extent of Lost Time at Sea for Dry Cargo Ships", Technical and Research Report No. R-10 of the Society of Naval Architects and Marine Engineers.

15 CHRYSSOSTOMIDIS, C. and LOUKAKIS, T. A., "The Seakeeping Performance of a Ship in a Seaway", To be published as a report by the U. S. Maritime Administration.

16 SALVESEN, N., TUCK, E. O. and FALTINSEN, O., "Ship Motions and Seal Loads", Transactions of the Society of Naval Architects and Marine Engineers, vol. 78, 1970, p. 250-287.

17 MANSOUR, A., "Methods of Computing the Probability of Failure Under Extreme Values of Bending Moment", Journal of Ship Research, vol. 16, number 2, 1972, p. 113-23.

18 LOUKAKIS, T. and CHOO, K. Y., "A Reappraisal of Two Parameter Representation of Ship Sections for Seakeeping Calculations", Report to be published by the Massachusetts Institute of Technology, Department of Ocean Engineering.

* * *

APPENDIX I. SAMPLE SEAKEEPING TABLE

Definitions of the quantities that appear in the sample Seakeeping Table.

Froude No.	Ship Speed/ $\sqrt{g(LWL)}$
Non-dimensional Sea State	Significant Wave Height/LBP
Heaving Motion	RMS Heave Amidships/LBP
Pitching Motion	RMS Pitch in Degrees
Bending Moment	$\frac{(\text{RMS Bending Moment Amidships})\ 10^3}{\rho g\ (LBP)^4}$
Added Resistance	(Mean Added Resistance) $10^3/\rho g(LBP)^3$
Acceleration	RMS Acceleration/g
Relative Motion	RMS Relative Motion/LBP
Relative Velocity	RMS Relative Velocity/ $\sqrt{g(LBP)}$

* * *

EXTENDED SERIES 50 CB=0.650 L/B=7.00 B/T=3.00 LCB= 0.50%

FROUDE NO	0.10	0.15	0.20	0.25	0.30
HEAVING MOTION					
N 0.015	0.0007	0.0008	0.0008	0.0008	0.0008
O 0.020	0.0015	0.0019	0.0023	0.0025	0.0025
N 0.025	0.0025	0.0031	0.0038	0.0043	0.0046
0.030	0.0036	0.0044	0.0054	0.0061	0.0067
D 0.040	0.0060	0.0069	0.0081	0.0093	0.0104
I 0.050	0.0085	0.0095	0.0108	0.0122	0.0136
M 0.075	0.0151	0.0161	0.0174	0.0189	0.0204
E 0.100	0.0217	0.0226	0.0238	0.0253	0.0268
N S I **PITCHING MOTION**					
O 0.015	0.32	0.31	0.28	0.23	0.21
N 0.020	0.67	0.68	0.67	0.64	0.60
A 0.025	1.01	1.06	1.07	1.06	1.03
L 0.030	1.31	1.40	1.44	1.45	1.44
0.040	1.84	1.96	2.03	2.08	2.11
S 0.050	2.26	2.41	2.51	2.57	2.63
E 0.075	3.00	3.18	3.32	3.42	3.50
A 0.100	3.50	3.69	3.84	3.95	4.06
S T **PENDING MOMENT**					
A 0.015	0.0058	0.0059	0.0057	0.0055	0.0055
T 0.020	0.0102	0.0108	0.0110	0.0111	0.0110
E 0.025	0.0139	0.0151	0.0159	0.0163	0.0166
0.030	0.0170	0.0185	0.0199	0.0208	0.0215
0.040	0.0216	0.0236	0.0256	0.0275	0.0291
0.050	0.0247	0.0272	0.0296	0.0320	0.0343
0.075	0.0290	0.0319	0.0351	0.0383	0.0414
0.100	0.0313	0.0343	0.0377	0.0413	0.0449
ADDED RESISTANCE					
0.015	0.0010	0.0009	0.0008	0.0007	0.0005
0.020	0.0026	0.0027	0.0028	0.0027	0.0027
0.025	0.0047	0.0052	0.0057	0.0060	0.0064
0.030	0.0068	0.0079	0.0090	0.0100	0.0111
0.040	0.0110	0.0129	0.0148	0.0176	0.0204
0.050	0.0139	0.0171	0.0203	0.0246	0.0288
0.075	0.0179	0.0243	0.0307	0.0376	0.0446
0.100	0.0204	0.0300	0.0397	0.0487	0.0577

FROUDE NO	0.10	0.15	0.20	0.25	0.30
ACCELERATION STA 0					
N 0.015	0.040	0.044	0.042	0.039	0.036
O 0.020	0.074	0.084	0.087	0.094	0.097
N 0.025	0.102	0.125	0.142	0.152	0.158
0.030	0.124	0.156	0.182	0.200	0.213
D 0.040	0.157	0.199	0.235	0.267	0.293
I 0.050	0.179	0.229	0.274	0.312	0.347
M 0.075	0.208	0.268	0.323	0.374	0.420
E 0.100	0.223	0.286	0.346	0.403	0.456
N S I **ACCELERATION STA 5**					
O 0.015	0.023	0.025	0.024	0.022	0.021
N 0.020	0.043	0.052	0.057	0.059	0.059
A 0.025	0.059	0.075	0.087	0.094	0.098
L 0.030	0.072	0.094	0.112	0.125	0.135
0.040	0.093	0.120	0.146	0.169	0.189
S 0.050	0.107	0.140	0.171	0.199	0.226
E 0.075	0.126	0.165	0.204	0.241	0.276
A 0.100	0.137	0.178	0.221	0.262	0.302
S T **ACCELERATION STA 10**					
A 0.015	0.009	0.011	0.012	0.012	0.013
T 0.020	0.016	0.023	0.030	0.035	0.038
E 0.025	0.023	0.033	0.046	0.056	0.064
0.030	0.029	0.043	0.060	0.075	0.088
0.040	0.039	0.057	0.079	0.103	0.124
0.050	0.048	0.069	0.095	0.122	0.150
0.075	0.063	0.087	0.117	0.150	0.185
0.100	0.074	0.098	0.130	0.167	0.205
ACCELERATION STA 15					
0.015	0.016	0.019	0.022	0.022	0.022
0.020	0.027	0.034	0.044	0.052	0.058
0.025	0.036	0.048	0.063	0.078	0.090
0.030	0.045	0.059	0.079	0.101	0.119
0.040	0.059	0.077	0.101	0.130	0.155
0.050	0.070	0.090	0.119	0.151	0.181
0.075	0.087	0.110	0.143	0.182	0.225
0.100	0.098	0.122	0.156	0.198	0.246
ACCELERATION STA 20					
0.015	0.032	0.036	0.039	0.038	0.038
0.020	0.057	0.068	0.079	0.089	0.096
0.025	0.077	0.095	0.114	0.133	0.148
0.030	0.095	0.117	0.143	0.171	0.193
0.040	0.120	0.150	0.182	0.218	0.255
0.050	0.138	0.172	0.211	0.253	0.298
0.075	0.164	0.202	0.248	0.300	0.354
0.100	0.177	0.218	0.266	0.322	0.383

SEAKEEPING TABLE

EXTENDED SERIES 60 CB=0.650 L/B=7.00 B/T=3.00 LCB= 0.50%

FROUDE NO	0.10	0.15	0.20	0.25	0.30	FROUDE NO	0.10	0.15	0.20	0.25	0.30
		RELATIVE MOTION STA 1						RELATIVE VELOCITY STA 1			
0.015	0.0055	0.0053	0.0049	0.0046	0.0045	0.015	0.028	0.032	0.035	0.039	0.043
0.020	0.0092	0.0094	0.0093	0.0089	0.0085	0.020	0.037	0.042	0.046	0.049	0.052
0.025	0.0124	0.0132	0.0136	0.0135	0.0132	0.025	0.045	0.052	0.057	0.060	0.063
0.030	0.0150	0.0164	0.0173	0.0176	0.0176	0.030	0.052	0.060	0.066	0.071	0.075
0.040	0.0189	0.0209	0.0225	0.0236	0.0243	0.040	0.061	0.071	0.079	0.086	0.092
0.050	0.0215	0.0241	0.0261	0.0276	0.0289	0.050	0.066	0.078	0.088	0.097	0.104
0.075	0.0249	0.0282	0.0310	0.0333	0.0352	0.075	0.072	0.086	0.099	0.109	0.118
0.100	0.0266	0.0301	0.0333	0.0350	0.0383	0.100	0.074	0.089	0.102	0.114	0.124
		RELATIVE MOTION STA 2						RELATIVE VELOCITY STA 2			
0.015	0.0053	0.0052	0.0049	0.0046	0.0044	0.015	0.028	0.032	0.035	0.039	0.043
0.020	0.0085	0.0088	0.0088	0.0085	0.0081	0.020	0.036	0.041	0.044	0.048	0.051
0.025	0.0112	0.0121	0.0125	0.0126	0.0123	0.025	0.042	0.049	0.054	0.058	0.061
0.030	0.0133	0.0148	0.0158	0.0162	0.0163	0.030	0.047	0.055	0.062	0.067	0.071
0.040	0.0165	0.0186	0.0202	0.0214	0.0222	0.040	0.055	0.065	0.073	0.080	0.086
0.050	0.0186	0.0212	0.0233	0.0249	0.0262	0.050	0.059	0.070	0.080	0.088	0.096
0.075	0.0212	0.0245	0.0274	0.0297	0.0316	0.075	0.063	0.076	0.088	0.099	0.107
0.100	0.0225	0.0260	0.0292	0.0319	0.0342	0.100	0.064	0.078	0.091	0.102	0.112
		RELATIVE MOTION STA 3						RELATIVE VELOCITY STA 3			
0.015	0.0050	0.0050	0.0047	0.0045	0.0044	0.015	0.027	0.031	0.035	0.039	0.043
0.020	0.0077	0.0081	0.0082	0.0080	0.0077	0.020	0.034	0.039	0.043	0.046	0.050
0.025	0.0098	0.0109	0.0114	0.0116	0.0115	0.025	0.039	0.045	0.051	0.055	0.058
0.030	0.0115	0.0131	0.0142	0.0147	0.0149	0.030	0.043	0.051	0.057	0.062	0.067
0.040	0.0140	0.0162	0.0179	0.0192	0.0201	0.040	0.048	0.058	0.066	0.073	0.079
0.050	0.0156	0.0183	0.0205	0.0221	0.0235	0.050	0.051	0.062	0.072	0.080	0.087
0.075	0.0176	0.0209	0.0238	0.0261	0.0282	0.075	0.053	0.066	0.078	0.088	0.096
0.100	0.0185	0.0220	0.0252	0.0280	0.0303	0.100	0.054	0.067	0.080	0.090	0.100
		RELATIVE MOTION STA 4						RELATIVE VELOCITY STA 4			
0.015	0.0046	0.0047	0.0045	0.0043	0.0042	0.015	0.026	0.031	0.034	0.038	0.042
0.020	0.0067	0.0073	0.0075	0.0075	0.0073	0.020	0.031	0.036	0.041	0.045	0.048
0.025	0.0084	0.0095	0.0102	0.0105	0.0105	0.025	0.035	0.042	0.047	0.051	0.055
0.030	0.0097	0.0113	0.0125	0.0132	0.0136	0.030	0.037	0.045	0.052	0.058	0.062
0.040	0.0115	0.0138	0.0155	0.0169	0.0180	0.040	0.041	0.051	0.059	0.066	0.072
0.050	0.0126	0.0154	0.0176	0.0194	0.0209	0.050	0.043	0.054	0.063	0.071	0.078
0.075	0.0140	0.0173	0.0202	0.0227	0.0248	0.075	0.044	0.056	0.067	0.077	0.085
0.100	0.0146	0.0181	0.0213	0.0241	0.0266	0.100	0.044	0.056	0.068	0.079	0.088
		RELATIVE MOTION STA 20						RELATIVE VELOCITY STA 20			
0.015	0.0037	0.0036	0.0035	0.0036	0.0037	0.015	0.023	0.028	0.032	0.037	0.041
0.020	0.0056	0.0052	0.0051	0.0053	0.0055	0.020	0.027	0.030	0.034	0.039	0.044
0.025	0.0074	0.0070	0.0068	0.0071	0.0076	0.025	0.030	0.033	0.037	0.042	0.048
0.030	0.0090	0.0085	0.0085	0.0088	0.0096	0.030	0.033	0.035	0.039	0.044	0.051
0.040	0.0116	0.0110	0.0108	0.0115	0.0127	0.040	0.037	0.038	0.042	0.048	0.056
0.050	0.0134	0.0128	0.0128	0.0134	0.0150	0.050	0.039	0.041	0.044	0.050	0.059
0.075	0.0160	0.0155	0.0155	0.0164	0.0181	0.075	0.042	0.043	0.046	0.052	0.062
0.100	0.0173	0.0169	0.0169	0.0179	0.0198	0.100	0.043	0.043	0.046	0.052	0.063

SEAKEEPING TABLE (cont.)

DISCUSSION

Manley Saint-Denis
University of Hawaî
Honolulu, U.S.A.

I should like to suggest that the paper does not live up to its title. The problem of seakeeping is both one of tremendous scope and the preeminent hydrodynamic one facing the ship designer, but the reduction of such a problem to the determination of the speed lost in head seas of the Pierson-Moskowitz type, having a height of roughly 8 ft., is, I think, something too brutal. To try to predict the seakeeping characteristics of the ship in such a manner is like trying to predict the behaviour of all ladies (and some non-ladies) by that of one's own wife. I should like to think that one might be in for some surprises.

To develop the proper perspective note that for over a century the ship designer has equated seakeeping to transverse metrocentric height. It is obvious that one parameter is insufficient to cover all the sins and virtues of a ship, but one cannot overlook the experience of past years, which indicates that of all the aspects that of roll is by far the most important. The greatest motion is that of roll, and the greatest danger comes in roll. But the only time the author mentions the work roll is when he speaks of recommendations on viscous roll damping research, and even that recommendation is unsupported by anything in the text. This I find to be a disturbing omission.

Of the three iterations, only one is developed, and that one partially, and the other two are only hinted at. The first iteration is simply a recommendation that the seakeeping behaviour of a ship is assessed in some approximate manner by how a series 60 ship behaves when fitted with a Wageningen B. 4. 55. propeller. The series 60 was designed to find out how resistance varied with pertinent parameters. But the tests undertaken certainly did not cover adequately the parameters of form that are important for seakeeping. In fact, Dr. Todd and his collaborators did not even think about seakeeping in those days. But that I mean to say that series 60 good as it is for estimating the resistance of ships of normal form, it is not necessarily relevant to determining the seakeeping characteristics of any ship that a designer might have in mind ; and indeed the relevance of series 60 is not a point to be assumed but a point to be approved, if anything, and I do

not think this can be done, or done very easily. To remain with series 60, the work of Vosser on the motions of this series is totally ignored. In fact, if I study the references I find something strange : a preponderance of them are from authors at M. I. T. Now I am an alumnus of M. I. T. and am very proud of the work that is being done there but I think that the paper is a bit parochial and I have the feeling that it is essentially an advertising brochure for the work done there.

DISCUSSION

Raymond Vermter
Naval Ship Research and Development Center
Bethesda, Maryland, U.S.A.

This interesting paper represents a rather ambitious extension of our normal ship design process and I should like to discuss several points made by the author and to advise some caution in the use of the procedure. First, the author states that for the particular example given in the paper, fully developed long crested sea spectra are used and that this simplification is not considered unrealistic. It would appear from some of yesterday's discussion regarding sea spectra, however, that this assumption is unrealistic, that the fully risen case is rarely realised and that swell forms an important component of most seaway forcing functions. That the consideration of swell is an important factor for the successful accomplishment of naval missions has been painfully demonstrated to us at the Naval Ship Research and Development Center several times in the recent past and it is never accounted for through the use of standard spectra. It is suggested that multi parameter direction spectral considerations are necessary for a valid design study of this type.

One might also question the suggested number of iterations concerning the establishment of an EHP value for propeller selection and, even more generally, the real importance of power limitations as regards ship operation in a seaway. It has been our experience that naval ships are never power limited, but that power is voluntarily limited from a fear on the part of the captain that he will cause either personnel injury or structural damage if he drives his ship harder. Propeller design considerations for the Naval ship case involve proper blade stressing and vibration considerations for maximum power and cavitation free operations to as high a speed as possible, trading

these factors off against the propeller efficiency.

So it would seem that improper assumptions have been made in this paper regarding propeller selection.

Even in the case of the merchant ship design it is hard to conceive of a ship being power limited in a seaway prior to arriving at the voluntary limitation point. Here in propeller design we again consider stress and vibration characteristics for full power, but design for maximum efficiency at 80 percent power. While 80 percent is an arbitrary number arrived at through experience, it is a design point of some significance to the ship owner. It represents a real value around which full scale propeller performance can be evaluated and indicates whether the propeller is on or off design. This performance determines payment or financial penalty for the designer. It appears that the proposed procedure may tend to shroud this well defined design point in statistical vagueness.

REPLY TO DISCUSSION

Chryssostomos Chryssostomidis
Massachusetts Institute of Technology
Cambridge, Massachusetts, U.S.A.

Answering Dr. Saint-Denis first. The thesis of my paper is that in the first iteration of the proposed methodology, once the user decided to adopt a cruiser stern monohull as the solution to his problem, Series 60 ships form as good a basis as any other standard series or for that matter as any other realistic point designs to provide the information needed to make the decisions called for in the first iteration of the proposed methodology. The small variations between the final design and whatever standard form was used do not influence the outcome of the first iteration and their effect need only be considered as it is suggested in the paper, in the subsequent iterations of the proposed design methodology.

Roll was not included in the present study, as it was stated in the paper, not because it was considered unimportant but because the state of the art is such that does not permit theoretical prediction of roll with any reliability and therefore a creation of a theoretical derived standard series for roll was considered unwise.

Finally answering the comment about the optimization criterion. I do not believe that my considerations were limited to an environment having a wave height of roughly 8 ft.

In answer to Dr. Wermter, I recognise that the environment description adopted in the present study was rather limiting. What is of importance is to recognise that the proposed procedure can accommodate other standard environment descriptions which are considered to be more suitable. I believe, however, that in the first iteration the environment description must be kept as simple as possible, as long as it is realistic, in order to allow the user to investigate the large number of alternatives called for by the proposed methodology and that the appropriate place to use the exact environment description is in the second iteration.

Answering the question about power. The proposed methodology treats the available power as an independent variable and permits the user to determine the "optimum" power that one must install in a ship operating in the "actual" environment taking into account both voluntary and non-voluntary speed reductions.

Answering the question about detailed propeller design. This, in the proposed methodology, is treated in a subsequent iteration. In the first iteration it is necessary to accept a standard but realistic propeller design, in order to be able to examine as early as possible the influence of seakeeping considerations in the decision making process.

DISCUSSION

Reuven Leopold
U.S. Navy. Naval Ship Engineering Center
Hyattsville, Maryland, U.S.A.

When I saw the title of the paper, "Seakeeping considerations in a total design methodology", I was looking forward with great interest to the paper itself, which I must admit is rather disappointing. There are several reasons for my disappointment. The first is because I read with great interest and enthusiasm reference 1 "A design methodology for ship and other complex systems" by Professor Chryssostomidis and Professor Mandel in London earlier this year, which I feel

laid a very good foundation and framework for a sophisticated ship design methodology, which we badly need, and I thought this might be a second instalment in that direction.

The second reason for my disappointment is because I had made repeated attempts to incorporate seakeeping considerations into early design decisions, as this paper repeatedly points out by referring to reference 5 and while I feel that in reference 5 Professor Mandel and myself have described the principles of such a step, we found that it did not influence those early decisions.

The third reason is that because of the latter experience I thought that maybe this paper would show how seakeeping considerations can influence early gross design decisions. Unfortunately, the paper does not achieve this objective. In fact, in the conclusions chapter it is even stated : "The results also suggest that when optimization does not involve large changes in the principal characteristics of the different alternatives considered, as in the case of ship with constant payload, then seakeeping considerations should not be included in the optimization scheme because they are not expected to influence the final decision".

But after all, the normal ship design problem is posed in such a way as : "Transport or carry a certain payload (say with some future growth and convertibility for a warship) with a certain maximum speed and endurance optimized against some criterion". Therefore to say what the author has stated in the conclusions part of the paper, which I quoted earlier, seems to me to cut out the majority of design situations. Thus accounting for seakeeping indices, such as acceleration in certains locations along the ship, slamming, wetness and added powering in waves versus not accounting for them in the normal ship design case will not have a significant effect on the gross ship dimensions.

I am obviously not referring to a whole host of ship hull characteristics such as LCB-LCF locations, sheer and freeboard, the detailed design of the hull form itself and the selection of various stabilization systems. What I am referring to, is this : given the mathematical model and superimposed optimization technique, reference 5 , the existence of a subroutine for seakeeping indices considerations would not result in, say, a 10-20 percent change in gross ships characteristics of a conventional monohull design.

There is a big difference between being able to predict the performance of a vessel, which is important, versus changing the significant gross ship characteristics as a result of considering or not con-

sidering seakeeping characteristics.

REPLY TO DISCUSSION

Chryssostomos Chryssostomidis
Massachusetts Institute of Technology
Cambridge, Massachusetts, U.S.A.

Thank you, Mr. Leopold ; I fully agree with your conclusions in the case of conventional ships with conventional missions. If there are not going to be large changes in the owner's requirements I do not believe it is profitable to include seakeeping considerations in the optimization scheme of the first iteration of the proposed methodology. For unconventional ships however, I believe seakeeping considerations should be introduced as early as possible in the decision making process because they might determine feasibility. We have a recent example of this in the form of a small catamaran vessel. I also believe that in unconventional missions even with conventional ships one must introduce seakeeping considerations as early as possible in the decision making process because they might influence the final solution. Recently I was involved in the design of a deep ocean mining ship where seakeeping considerations forced me to accept as "optimum" a much larger ship than I would have accepted if no seakeeping considerations were introduced in the investigation.

DISCUSSION

Michel K. Ochi
Naval Ship Research and Development Center
Bethesda, Maryland, U.S.A.

The author has brought up an important subject in the first iteration of the proposed design methodology, namely, the speed reduction due to ship motion. As part of the criteria to estimate the speed reduction due to ship motion, the author considers the probability of occurrence of deck wetness at Station 1 and the probability of

slamming at station 2. It is understood that these two probabilities are considered to be independent in the author's mathematical model. I would like to point out that these two probabilities are both a function of relative motion at stations 1 and 2, respectively. Since these two relative motions are highly correlated, the two probabilities cannot be treated as independent. The correlation coefficient for relative motions at any two forward locations on the ship is usually of the order of 0.7 to 0.8 depending on ship speed. I would like to suggest that the evaluation should be based on the joint probability function of the two relative motions taking into account the correlation between them.

REPLY TO DISCUSSION

Chryssostomos Chryssostomidis
Massachusetts Institute of Technology
Cambridge, Massachusetts, U.S.A.

Thank you, Dr. Ochi, for your recommendation. I will look into this.

DISCUSSION

Edmund V. Telfer
R.I.N.A.
Ewell, Surrey, U.K.

In my very early professional life this was a subject to which I devoted probably far too much of my time but I now find it rather sad, that although most of that work was probably published before the author was born, it has had practically no influence upon his thinking. I do not mind this, but I do regret that the author makes no reference to the work of Professor Aertssen, and I think anybody attempting a thesis of this nature who has not carefully studied, and profited, I hope, by the work of Aertssen - and still earlier the work of Kent - will not see the many issues involved as clearly as he ought to in 1972 AD.

It is by no means necessary to go into the esoteric detail that the author does. Very much simpler and reliable information can be obtained by straightforward consideration of the problem as the owner himself sees it, and I would recommend the author, if he has time, to look at some of the earlier work that has been published in the subject. Personnally, I find it quite tragic, looking over the references to many papers in this symposium, to find that very little of the work goes back more than five years. I do stress to my younger colleagues that quite a lot of good work was done before five years ago, and nobody will hold it against them if they refer to and see good in the work done 30, 40, 50 or even a hundred years ago.

I still hope, however, despite this criticism, that the author will continue with his subject, gain perspective and, by so doing, add to professional information on the subject.

REPLY TO DISCUSSION

Chryssostomos Chryssostomidis
Massachusetts Institute of Technology
Cambridge, Massachusetts, U.S.A.

Thank you Dr. Telfer. The list of references included in my paper is not a complete list of all the material consulted.

DISCUSSION

Edmund Lover
Admiralty Experiment Works
Haslar, Gosport, Hants, U.K.

For some time it has become apparent that a systems analysis including seakeeping considerations is necessary for modern ship design, we should be grateful to the author for demonstrating how these might be taken into account.

Such an analysis does however require a quantification of performance parameters that are very difficult to quantify. The author has bravely stocked this problem but I wonder whether his assumptions concerning the effects of overall size on hull efficiency elements are not oversimplified. Also for instance SHP_r is not always equal to EHP/η_D - a paradox that is discussed at length within the I. T. T. C. and elsewhere.

The example given is particularly interesting, not only as a demonstration of the method, but also for the result obtained. In this case, the ship with twice the displacement is shown to be better able to maintain speed in a seaway. This result is not surprising. What is surprising however is that the difference appears to be so slight.

Here is an example of two vessels, designed for the same speed but with one having twice the displacement, and hence twice the payload of the other. A comparative through costing of performance would therefore need to compare the profitability of one ship versus two and would involve an assessment of profound differences of deployment, availability, and manning, as well as first cost.

I suggest that these outweigh the seakeeping speed and fuel effects to an extent that one can conclude that these may be ignored when determining the overall size of a large merchant ship design, even when large changes are possible. In other words, the first iteration is redundant in such a case and efforts should be concentrated on evolving detailed design improvements - incorporation of adequate freeboard, suitable bow sections to avoid slamming and so on.

I am not however suggesting that a systems approach including seakeeping is always unnecessary. Such an approach is appropriate for smaller vessels and is indeed vitally necessary for the design of small warships, where other considerations of crew operation and weapon deployment become dominant.

REPLY TO DISCUSSION

Chryssostomos Chryssostomidis
Massachusetts Institute of Technology
Cambridge, Massachusetts, U.S.A.

Thank you Dr. Lover. I agree with all your conclusions.

THE APPLICATION OF SYSTEM IDENTIFICATION TO DYNAMICS OF NAVAL CRAFT

Paul Kaplan, Theodore P. Sargent
and Theodore R. Goodman
Oceanics, Inc
Plainview, New York

ABSTRACT

An important problem associated with establishing a mathematical model that adequately represents the motions of a naval vessel is the question of the proper form of the equations, as well as the values of the various parameters entering the equation system. A technique for determining the ability of a particular mathematical form to represent the motions of such a vehicle, together with the determination of the numerical values of various parameters (such as stability derivatives, etc.) is carried out by application of the technique known as system identification. The method of system identification is used in this context for the means to determine the unknown parameters in a dynamical system representation from measurements of the time histories of the vehicle trajectories. Different techniques are used for application to problems that are of transient nature, following a sudden disturbance or control deflection in a smooth seaway, and for those problems associated with the motions of a vehicle in a disturbed seaway where the motion is continuously forced in a random manner. In addition the influence of noise in its generalized effect as a source of measurement error is also considered in this work. These techniques have been successfully applied to the determination of the stability derivatives (and nonlinear function coefficients) of a conventional surface ship, a hydrofoil craft, and an SES (surface effect ship) craft.

These applications have included vehicle trajectories obtained from computer-generated data, as well as full scale data. The utility of the techniques is demonstrated by the results obtained for these applications, together with a discussion of limitations in different towing tanks throughout the world for this purpose, ranging from multi-component balances for static force and moment measurement,rotating arms, horizontal and vertical planar motion oscillator mechanisms, etc. (see [1] - [2]). Considering the computational and data reduction equipment required as ancillary elements of the measurement devices, as well as the time and expense required to obtain the required parameter values by these means, other methods that may reduce the effort required for determination of hydrodynamic coefficients then become attractive(especially to laboratories or organizations that do not have such involved instrumentation).

A particular approach to determine the values of various parameters in a mathematical representation of the dynamics of an arbitrary system (whether it is a vehicle, a chemical process, control system, etc.) has been developed recently as part of modern control theory. This procedure is known as "system identification", which in the present case is a means of determining the numerical values of the coefficients that enter into a set of mathematical equations that are assumed to represent the dynamic motions of a particular vehicle or system (in addition the procedure can also determine the suitability of a particular mathematical model form as well as the sensitivity of different modes of motion to particular coefficients, as will be demonstrated herein). These values are considered to be the appropriate values representing the system dynamics when they are obtained with the same values from a number of different trajectories of the vehicle motion, thereby insuring their uniqueness. The extent of realism inherent in the coefficient values is related to the capability of the mathematical equation model to represent the vehicle motions, since the results of captive model tests in wind tunnels, water tunnels, towing tanks, etc. are aimed at measuring such coefficients experimentally, where the coefficient structure is based

upon the form of the equations that will be or are assumed for representing the motion of the system. Therefore the basic foundation underliying system identification as a means of representing the vehicle dynamics has (at least) the same degree of validity as any method of dynamic analysis that is presently used as a model of vehicle behavior.

What is done in this technique is to obtain responses of a vehicle by measuring "trajectories"(such as vehicle linear and angular displacements, velocities accelerations, etc.) following different types of disturbances. With the formulated mathematical model, values for the unknown parameters are then sought so that the solutions to the dynamic equations give a best fit to the data, where this best fit is defined by minimizing the mean square error between the solution of the equations using these coefficients and the actual data record itself. The procedure can be applied to data from both full scale and model scale trajectory observations, thereby increasing its utility for correlation and validation purposes of particular mathematical simulations of naval vehicles .

Obtaining stability derivatives from full scale trajectories has been standard practice in the aircraft industry from its inception, and this has ordinarily been done by various means of data analysis that are primarily based upon the assumption that the equations are linear. In addition to considerations of nonlinearity which are important for certain naval craft the sensitivity of some modes of motion of particular craft (such as hydrofoils, SES craft, etc.) to surface wave disturbances requires consideration of the influence of random forcing functions, sensor errors and other "noisy" disturbances applied to the system and its measured motion responses. These different effects then require particular techniques for their analysis, and the present paper will provide a description of the analysis methods as well as the results obtained when the methods are applied to different representative naval craft.

The work described in this paper was carried out under the support of different agencies in the course

of various study contracts, viz. the Office of Naval Research, the Naval Ship Research and Development Center, and the Surface Effect Ships Project Office.

INTRODUCTION

In order to predict the dynamic performance of various naval vessels, different methods of simulation are often employed. The general term "dynamic performance" used here refers to the determination of dynamic stability, maneuvering and turning properties, response to control input commands, motions in wave systems, etc; the term "simulation" includes both free model trajectory tests as well as the use of computer solutions based on a mathematical model that is assumed to represent the craft motions. Considering the basic limits of free model testing, which are associated with limitations in the size of models and/or test facilities (or inherent limits such as in the case of submarine maneuvers), propulsion and control modeling errors, time constant differences, etc., the major emphasis for motion prediction is the use of computer simulation using mathematical models.

When considering prediction and simulation studies of ship dynamics with the use of a mathematical model, a vital aspect is establishment of the proper form of the equations as well as the appropriate numerical values of the various parameters (coefficients, stability derivatives, etc.) entering the equation system. At the present time the main method of determining the various hydrodynamic force and moment coefficients in a desired mathematical model for a particular type of marine craft is by means of captive model tests in a towing tank, together with the associated mathematical analysis of the experimental data in order to provide the required coefficients. Various special purpose apparatus exist.

GENERAL DESCRIPTION OF ANALYTICAL TECHNIQUES

When considering a vehicle in an undisturbed smooth water environment, transient responses of the craft are excited by means of different initial conditions or excitation inputs (such as a rapid rudder deflection or other impulsive disturbance). The measured outputs (i.e. vehicle motions) are recorded and operated upon by a technique that is essentially a generalization of a Newtonian iteration procedure [3]. The differential equations of motion of the vehicle, whether it is linear or nonlinear, are used together with additional

variables that represent the unknown coefficients in these equations. The coefficients themselves are the actual variables that are sought in this system identification procedure, and different techniques are used within the course of the analysis with the understanding that the variables desired are the coefficients in the equations. Solutions are necessary for all the variables starting with estimated initial conditions, where the variables include the state variables of the system as well as the coefficients themselves. Errors between the calculated state variables and the actual measured trajectory data itself are determined, and then modifications of the unknown coefficients are obtained in this procedure. These new values are then inserted again, solutions obtained, modified coefficient values found, and these are inserted again with the method repeated, i. e. an iterative procedure.

The main features of this method are the fact that the basic dynamic system itself can be nonlinear (in terms of the state variables) and it is not necessary to measure every response variable in order to obtain the values for the coefficients. Even in the case of a linear system, if each and every response variable, including displacements, velocities, and accelerations of all degrees of freedom are measured, then the only unknowns are the coefficients themselves which can be obtained from solution of a set of linear algebraic equations. However it is often difficult, if not impossible, to measure every variable, derivative, etc., as well as the fact that often such measurements are not very accurate due to instrument limitations. The technique applied here requires selecting just those variables that are easiest to measure and which are available, but nevertheless a certain number of variables must be measured since in a coupled system more than one mode of motion applies; e. g. as an illustration, it is necessary to obtain measured data on yaw and roll responses since measuring a single mode such as yaw alone would not yield sufficient data to obtain information on roll coefficients, and vice-versa.

The original derivations in [3] presented a method for determining unknown parameters in an otherwise known dynamic system using only measurements of the time history of just one state variable. However, practical experience with large systems containing a number of degrees of freedom and many parameters led to a generalization of the procedure involving the use of an increased number of measured trajectory records, (as mentioned above), and this improved procedure overcame many difficulties in regard to convergence and uniqueness of the results. A number of applications were made to different vehicles, including aircraft, a surface ship, and a hydrofoil craft, and the results obtained are described in [4] and [5] . A description of the mathematical procedures, and a discussion of results obtained

by use of this method, are given in following sections of this paper.

When considering the case of a craft in waves, the effect of continuous random forcing functions (due to the waves) is present. Therefore another technique different from the one used in the previous work described above, which is based on transient responses with no "noisy" measurements or random forcing functions, must be used. The method proposed for application to this problem is based on developments in recent literature of modern control theory (maximum principle, two-points boundary value problems, invariant imbedding, and sequential estimation) which are described in [6] and [7] . The basic technique is applied to problems that are generally nonlinear, with the possibility of measurement observation errors and with unknown random inputs. Using continuous time histories of the observed output measurements, the task is then to obtain optimal estimates of the state variables and also various parameters in the equations (such as coefficients and other unknown magnitude mathematical forms) by a procedure that is based on minimizing an integral of the sum of weighted squares of residual errors. The errors are the difference between the observed data and the actual desired system outputs (i. e. eliminating the measurement noise), and also the difference between the nominal trajectory of the system and the assumed form of the equation representation (i. e. eliminating the noisy input excitation and achieving a proper representation of the basic system dynamics). In this case, the unknown parameters are also added as additional variables in the complete dynamic representation.

The equations that result for the estimates of the system state and also for the parameters provide an on-line filtering procedure together with a sequential estimation technique, which does not require repeating all calculations after additional observations or measurements are made, as in classical estimation schemes. The resulting equations are of a form that is somewhat similar to that of the Kalman filter [8] , but they are applicable to nonlinear systems. In addition the terms entering the equations are not dependent upon a knowledge of the statistical characteristics of the input disturbances or the measurement errors, thereby allowing consideration of vehicles in arbitrary seaway conditions and hence increasing the generality of the approach.

The equations developed for this system identification procedure use the continuous measurements of the actual system outputs as observed, and those signals are operated on and processed with the special estimator equations. As time evolves the combined fil-

tering action and identification allows the evaluation of the desired parameters to exhibit themselves as functions of time and arrive at their final steady value. Similarly the estimation of state variables with random disturbances present also evolves as a function of time, and the ability of the estimated state variables to "track" the measured trajectories when using the estimated parameter values in the representative system equations is directly exhibited in this procedure.

Applications of this technique that allows for the presence of "noise" in the system response have been made for the case of a surface effect ship (SES craft) as well as for a hydrofoil craft (see [9] and [10]). The mathematical procedures underlying this particular technique, as well as the results obtained in practical applications to different seagoing craft, are described in later sections of this paper.

MATHEMATICAL PROCEDURES - ITERATION METHOD

The iterative technique used for system identification of dynamic systems for which transient response data is available is described by the following. The dynamical equations representing the system are assumed to be given in the form

$$\dot{Y}_i = g_i (Y_1, \ldots Y_n, \quad \alpha, t), \; Y_i (0) = c_i \qquad (1)$$

where the dot denotes differentiation with respect to time t, α denotes the unknown parameter vector and c denotes the initial value of the solution vector Y and may or may not be totally known. Measurements b_{1m} , b_{2m} , ... of the state variables Y_1 , Y_2 ... at times t_m are available, and it is required to find an initial vector c together with a parameter vector α which minimize the sum of the squares of the deviations :

$$\epsilon = \frac{1}{M} \left\{ w_1 \sum_{m=1}^{M} \left[Y_1 (t_m) - b_{1m} \right]^2 + \right.$$

$$w_2 \sum_{m=1}^{M} \left[Y_2 (t_m) - b_{2m} \right] + \ldots \Bigg\} \tag{2}$$

where the weighting factors w are chosen to make each sum non-dimensional and of the same order of magnitude. Thus, the solution of (1) is sought which is in best agreement with the measurements in a least square sense. The parameter vector, α, is suppressed in (1) by considering its components to be additional state variables subject to the equation

$$\dot{\alpha} = 0 \tag{3}$$

The number n is thereby increased to include the additional state variables and the extended c vector includes the unknown parameter vector in addition to the state variable initial conditions.

The parameters of the system are determined in the following way : the initial vector is estimated and (1) is integrated. The estimated initial vector is denoted by c^* and the resulting solution of (1) by Y^*. The deviation can then be calculated and its value denoted by ϵ^*. Assuming the initial vector to be changed by an increment δc, this would cause the solution vector to be changed by an increment δY and the deviation by an increment $\delta \epsilon$. From (2) it is seen that

$$\frac{M}{2} \delta \epsilon = w_1 \sum_{m=1}^{M} \left[Y_1 (t_m) - b_{1m} \right] \delta Y_1 (t_m) + \ldots \tag{4}$$

The equations which the incremental solution vector safisfies are called the equations of differential corrections and are obtained by expanding (1) in a Taylor series and retaining only linear terms :

$$\delta Y_1 (t) = \sum_{j=1}^{n} \left(\frac{\partial g_i}{\partial Y_j} \right)^* \delta Y_j \tag{5}$$

(the asterisk means that the coefficients are calculated using solution Y^*). Equation (5) is now integrated n times; the jth time the integration is performed the initial conditions are that $\delta Y_j(0) = 1$ and all the other $\delta Y_i(0)$'s vanish. This special solution is denoted by δY_{ij}, and the general solution can then be written, by superposition, as

$$\delta Y_i = \sum_{j=1}^{n} \delta c_j \, \delta Y_{ij}(t) \tag{6}$$

This incremental solution vector is used to express δY_1, δY_2, ... in terms of δc, and upon substituting into (4) and interchanging the order of summation the variation of the deviation becomes

$$\frac{M}{2}\delta\epsilon = \delta c_j \left\{ w_1 \sum_{m=1}^{M} \left[Y_1(t_m) - b_{1m} \right] \delta Y_{1j}(t_m) + \ldots \right\} \tag{7}$$

where the repeated suffix implies summation on j from 1 to n. The variation of the deviation has thus been expressed directly in terms of the variation of each of the initial conditions. In order for ϵ to be minimum $\delta\epsilon$ must vanish for an arbitrary variation in the initial conditions. This means that if U_j is defined to be

$$U_j = w_1 \sum_{m=1}^{M} \left[Y_1(t_m) - b_{1m} \right] \delta Y_{1j}(t_m) + \ldots \tag{8}$$

then the error will be minimized with respect to the c_j's whenever.

$$U_j = 0, \quad j = 1, \ldots n \tag{9}$$

In general, using the estimated vector c^* and the resulting solution vector y^*, the values of U_J will not vanish. Denoting the value of U_j, as calculated in this way by U_j^*, the objective is

to make the U_j vanish by an iteration procedure. Considering the increment in U_j caused by the increment in Y_j, from (8) there is obtained

$$\delta U_i = w_1 \sum_{m=1}^{M} \delta Y_1(t_m) \quad \delta Y_{1j}(t_m) + \ldots \tag{10}$$

in order for each U_j and hence $\delta\epsilon$ to vanish the condition

$$\delta U_j = -U_j^* \tag{11}$$

must be imposed. Upon substituting (6) into (10) and interchanging the order of summations there is finally obtained

$$U_i = \delta c_j \left\{ w_1 \sum_{m=1}^{M} \delta Y_{1j}(t_m) \quad \delta Y_{1i}(t_m) + \ldots \right\} \tag{12}$$

Equations (8) with $Y = Y^*$, together with Equations (11) and (12), constitute n simultaneous linear algebraic equations for the n unknowns δc_i. Upon adding the incremental values to the estimated values of c_i^*, improved estimates of the c_i are obtained, and the procedure is then repeated until convergence is achieved.

A modification of the above algorithm which at times is found to be useful is to introduce some or all of the b's into the right hand sides of Equations (1) and (6) in place of the respective y*'s.

A digital computer program for the above procedure was established, and various guidelines evolved for its effective use. One of the problems associated with an iterative procedure is to achieve convergence, and this depends upon the compatibility between the mathematical model and the actual physical system as well as the "quality" of the initial guess of the unknown parameters. Even when these conditions are satisfied there are often cases where convergence does not readily follow, and different strategies are used.

Among these are using measurements of additional state variables, applying a gain on the δc vector (to inhibit any over-correction), and to vary the length of the record in steps (from a short record to longer records, using the converged outputs of each step as the initial guess for the next longer record length until the entire record is processed).

Another problem is that of the proper values of the parameters, even if they produce trajectories that match the measured values quite well. Sometimes a parameter that has only a small influence on the particular motion data being analyzed is sought by the system identification technique. In that case very little information related to that parameter is contained in the data, and the value determined by this procedure is spurious (and could also sometimes "contaminate" other parameter values). Various means of increasing confidence have been developed as a result of experience. Among these are using as many state variable measurements as possible, as well as monitoring the change in the estimates of the converged c^* values as the record length is increased. Since lengthening the record introduces more information, the c^* values should begin to settle at some value (i.e. to stabilize), after which no further record lengthening is necessary. Another means of establishing confidence in the results is to vary the weighting factors. When a change in the weighting factors produces no apparent effect on the results, confidence in these results is increased.

APPLICATIONS OF THE ITERATION TECHNIQUE

The iteration technique described above was applied to a number of dynamic systems for which transient motion response data was available. The naval craft of interest that were treated by this method are a surface ship and a hydrofoil craft. For the case of the surface ship, the nonlinear three degree of freedom system of equations describing the steering and maneuvering of that ship are

$$\begin{aligned}
\dot{u} &= f(u) + C_1 v^2 + C_2 r^2 + C_3 u^2 \delta^2 \\
\dot{v} &= C_4 uv + C_5 ur + C_6 \frac{rv^2}{u} + C_7 u^2 \delta \\
\dot{r} &= C_8 uv + C_9 ur + C_{10} \frac{rv^2}{u} + C_{11} u^2 \delta
\end{aligned} \tag{13}$$

where u = surge velocity,

v = sway velocity,

r = yaw rate,

δ = rudder deflection,

$f(u)$ = known function of u that represents the difference between thrust and resistance,

C_i = coefficients to be determined.

These equations were obtained from (11), and the "measured" input to the system identification program is provided by a maneuver generated on the computer with known parameters typical of a conventional cargo ship, as obtained from [11] . The maneuver chosen is a turning circle initiated by commanding a 35 degree rudder angle.

Difficulty in converging to the known set of eleven coefficients was encountered with the basic computer algorithm even though the predicted time histories of u, v and r themselves became indistinguishable from their respective input records. Efforts to improve the results by sampling at a higher rate or by taking a longer record proved fruitless, and only by retaining an inordinate number of significant digits in the input data did the converged coefficients agree with their known values. However, the accuracy of data measured by real sensors is limited, and, the difficulty in obtaining good coefficients was eliminated by applying the modification to the technique which used the measured state variables instead of the predicted values in the operations of Equations (1) and (6). Using this modification, the effect of varying the sampling period, length of record, number of records, and accuracy of the data was investigated to indicate the measuring requirements for the identification of a real ship (or model) from a maneuver. It was found that a sampling period of from one to two seconds and a record length of from one-half to one minute was adequate for successful identification of a full scale ship. However, it was found necessary to have measured all three variables, namely u, v and r, to identify the eleven coefficients in Equation (13).

Using the computer generated data of u, v and r accurate to four significant digits, which was sampled every second for one minute, the identification by this iterative technique was carried out. The resulting C-coefficients are shown in Table 1 together with their time values, where reasonably close values were found. The identification process converged very rapidly, as only two iterations were required.

Table 1

Results of System Identification of Surface Ship

	True Values	4 Dig. Digit Data	2% Noise	5% Noise	Analog Data
$C_1 \times 10^2$	-. 203	-.202	-.071	-.127	
$C_2 \times 10^{-2}$	. 113	.109	-.589	-1.64	
$C_3 \times 10^3$	-. 214	-.213	-.164	-.091	
$C_4 \times 10^2$	-. 146	-.149	-.185	-.231	-.143
C_5	-. 334	-.337	-.370	-.415	-.342
$C_6 \times 10^{-1}$	. 958	.942	.796	.611	
$C_7 \times 10^3$	. 323	. 322	.321	.318	
$C_8 \times 10^4$	-. 122	-.114	-.072	-.012	-.119
$C_9 \times 10^2$	-. 397	-.391	-.360	-.315	-.399
C_{10}	-. 120	-.116	-.097	-.070	
$C_{11} \times 10^5$	-. 584	-.583	-.586	-.591	

In order to assess the accuracy requirements, the input was contaminated by adding Gaussian noise of 2 and 5% error magnitudes, where this error is based on the indicated percentage of the maximum value of the variable. The results of identification with these inputs are also shown in Table 1. It is seen that as the noise level is increased some coefficients remain close to their true values while others drift away and still others lose all significance. The coefficients C_1 and C_2 are seen to deteriorate the most rapidly. These coefficients have been shown in [11] to be of minor importance, and the present results support the relative ordering given in [11] .

Ship trajectory data was also generated on an analog computer, using only linear equations in v and r while assuming a constant forward speed. The equations in that case were given arbitrary initial conditions and then allowed to seek equilibrium. The v and r analog signals were sampled every two seconds by A/D convertors to provide the input to the system identification program. The results using the data supplied from the analog experiment are also included in Table I and in that case, even though the data can at best be considered to be 1% accurate, better values for the four coefficients considered as unknowns are obtained than that predicted using the noisy digitally generated data. This is ascribed to the fact that more accurate values of unknown coefficients can be predicted for a simpler system than for a system with a larger number of unknown coefficients. It is also possible that real "noise" from the analog computer output, which is closer to true processed experimental data, may not be as severe as the artifically generated digital noisy data.

For the case of a hydrofoil craft, the nonlinear longitudinal equations of motion for a typical hydrofoil craft under autopilot control are :

Normal Force Equation

$$\ddot{h} = 32.17 - \frac{L_F}{m} - \frac{L_R}{m} - C_1 \dot{w}_F - C_2 \dot{w}_R \qquad (14)$$

Pitching Moment Equation

$$\theta = \gamma_1 \left(\frac{L_F}{m} + C_1 \dot{w}_F \right) - \gamma_2 \left(\frac{L_R}{m} + C_2 \dot{w}_R \right) \qquad (15)$$

The lift on the forward foil is

$$\frac{L_F}{m} = -\gamma_3 \left\{ \left[\frac{w_F}{V} + C_3 \delta_e + \gamma_4 \right] \left[\frac{\gamma_5 + C_5 \zeta_F}{\gamma_6 + C_6 \zeta_F} \right] + C_9 \left(\frac{w_F}{V} \right)^2 \right\} \qquad (16)$$

where

$$w_F = \dot{h} + V\theta - \ell_f \dot{\theta}$$
$$\zeta_F = \zeta_{F_o} + h - \ell_f \theta \tag{17}$$

Similar expressions are given for the lift L_R on the rearward foil, where the unknown parameters C_3, C_5, C_6, C_9 are replaced by C_4, C_7, C_8 and C_{10}.

Autopilot Transfer Functions

$$\delta_{e_{command}} = \left[\frac{\gamma_{11}}{(\tau s + 1)} + \gamma_{12}\right] \dot{w}_f - \gamma_{13}\left[\frac{\tau s}{\tau s + 1}\right]\theta + \frac{\gamma_{14}}{(\tau_1 s + 1)} \quad (h_{command} - \zeta_{HS}), \tag{18}$$

in terms of the Laplace transform operator s,

$$\delta_{f_{command}} = \gamma_{15} \dot{w}_R + \gamma_{16} \dot{\theta} \tag{19}$$
$$\zeta_{HS} = \zeta_{HSO} - h + \ell_{HS} \theta$$

Flap Actuation System Transfer Functions

$$\delta_e = \left(\frac{1}{\tau_2 s + 1}\right) \delta_{e_{command}}, \quad \delta_f = \left(\frac{1}{\tau_3 s + 1}\right) \delta_{f_{command}} \tag{20}$$

where

h = heave,

θ = pitch angle,

V = craft velocity (assumed constant),

$\ell_F, \ell_R, \ell_{HS}$ = lengths from c. g. to forward foil, real foil and height sensor,

γ, τ = given constants,

ζ_{HSO} = vertical distance from height sensor to undisturbed water surface at design foilborne condition,

s = Laplace transform operator,

C_i = unknown parameters.

To demonstrate the feasibility of using system identification to estimate the C's from full-scale tests, computer generated trajectories were first used as trial inputs. The sponsoring agency supplied the computer generated trajectories but withheld the values of the C's used in the generation until the results of system identification became known. Three sets of trajectories for each of the three different configurations, termed A, B, and C (i.e., for three different sets of C's) were supplied. A run in each case consisted of a step change in the commanded height after the craft had reached equilibrium. Altogether, there were 9 sets of trajectories supplied.

Even though there was no prior information given as to the proper values for the C's other than the crudest order of magnitude estimates, no difficulty was encountered by the system identification program in converging to a set of C's for each configuration and run. Confidence in the converged results was investigated by varying the record length as described previously, and also by comparing the results from different runs of the same configuration. In all cases high confidence in the results were indicated. The estimates from system identification are given in Table 2, together with the true values.

Table 2

Hydrofoil System Identification Results

	Configuration True (Estimated)		
	A	B	C
C_1	.0450(.0439)	.0450(.0439)	.0950(.0942)
C_2	.131 (.131)	.131 (.129)	.131 (.129)
C_3	.1794(.179)	.1794(.179)	.1906(.190)

C_4	.3276(.327)	.4446(.445)	.4446(.445)
C_5	1.912(1.97)	1.912(1.97)	2.114(2.18)
C_6	.5097(.53)	.5097(.53)	.5579(.58)
C_7	2.668(2.67)	2.053(2.06)	1.886(1.87)
C_8	.4427(.45)	.4427(.45)	.5126(.51)
C_9	0 (0(.2))	10.0 (10.3)	0 (0(.2))
C_{10}	0 (0(.1))	0 (0(.2))	0 (0(.1))

The parameters C_9 and C_{10} represent coefficients of nonlinear lift. Nonlinear lift appeared to play an insignificant role in almost all the trajectories, making it impossible to obtain firm estimates of these parameters. It was only possible to estimate the order of magnitude of these parameters. This has been indicated in the table by use of an order symbol (as an example, the entry $0(.2)$ is to be interpreted to mean that the value of the parameter is no greater than $\pm .2$). In the case of C_9 for configuration B, the nonlinear lift term had been artifically increased so that it played a more significant role in the trajectory, and was therefore detectable. The comparison with the true values in Table 2 shows a remarkable agreement between the values estimated by system identification and their respective true values.

More detailed information concerning the results obtained for the case of a surface ship and a hydrofoil craft by means of this particular system identification method is given in [4] and [5]. In addition to consideration of these particular naval craft, results of application of this technique to the case of a V/STOL aircraft using experimental trajectory data from a dynamic free-flight test facility (for vertical plane motion) and also a full scale airplane using flight test data (three lateral modes of motion), are also presented in [5]. For those cases the agreement with other techniques of data analysis, or by virtue of matching measured trajectories, also provide vertification of the present technique and its ability to successfully identify many unknown parameters in large dynamical systems from measurements of time histories of state variables (a total of eleven stability derivative parameters were determined for the full scale aircraft case).

When considering the utility of system identification techniques for analyzing data from full scale maneuvers or from towing tank tests for naval craft, there are various ways in which it could be most efficiently used for such analyses. This is especially true in the case of model testing where the ability to constrain motions enables selected coefficients to be sought independently from the others. The system identification program has the ability to identify simpler constrained maneuvers first and then incorporate the resultant or otherwise known coefficients into the more complete model when a complex maneuver is analyzed. This might also relax the indicated measuring requirements as less demand would be placed on the system identification program. In the case of full scale sea trials, where the motions are naturally unconstrained, system identification techniques offer a useful method of directly analyzing ship motions when seeking knowledge of a large number of unknown coefficients simultaneously.

Another possible use of system identification for surface ship problems is an application to the case of a ship in a restricted waterway, such as a canal, when applied to model testing. Various static force and moment derivatives and related hydrodynamic data can be obtained from captive model tests in a towing tank with specially configured restrictions simulating the canal. However the important dynamic derivatives due to angular velocity, and angular velocity effects combined with lateral velocity and forward velocity, cannot be obtained with ease or without serious questions as to data validity (for oscillator experiments) with ordinary towing tank test techniques. In that case the use of system identification applied to trajectory data from model experiments would allow determination of basic stability derivatives by that method, when normal test procedures have basic limitations. Thus it serves as an adjunct to model testing that would allow more complete determination of pertinent parameters, thereby resulting in more reliable prediction of full scale ship performance.

The major problem exhibited in the application of this method is demonstrated when noise is artificially added to the observed data, as illustrated in the case of the surface ship. However, the low level noise associated with analog computer output data, for a lower order equation system, did not seem to influence the results. Similarly the full scale data of the aircraft analyzed in [5] also contained some noise in the records, and the influence of this noise was reduced by means of simple smoothing operations applied to each data point (obtaining average values in terms of data points on either side of a particular data point at each instant of time). While the generated

noise in the surface ship case may have been more severe than noise that would be experienced with actual recorded data on a full scale ship, or in the case of model test trajectories, the indications are that the influence of noise tends to degrade the estimated parameter values given by this technique of system identification. This behavior might be anticipated to some extent in view of the fact that the basic analysis method makes no allowance for the presence of noise in the recorded data, or noise present as a result of an arbitrary (unknown) random excitation. The only requirement is that the resulting differences between observed and predicted trajectories satisfy the minimum mean square error criterion, and that may not be sufficient without other ancillary conditions that would allow for the presence of such noise influences. More extensive investigations of the influence of noise on the prediction capabilities of this method of system identification must be obtained in order to determine its limits when applied to such realistic cases. A discussion of the application of this iteration technique to a full scale case where significant noise disturbances were present is given in a later section of this paper, when considering techniques applicable to noisy systems. A description of the mathematical techniques and the results of application to different naval craft where noise has a significant influence is presented in the following sections.

MATHEMATICAL PROCEDURES - SEQUENTIAL ESTIMATION TECHNIQUE

When considering the use of system identification for cases where the observed data is contaminated by noise or if the system is excited by a random input, the method that is used is based upon a sequential estimation procedure that is derived as illustrated below. The basic problem underlying this system identification technique is that of estimating the state variables and the parameters in a noisy nonlinear dynamical system, and this problem is treated in [7], which is an extension of the simpler problem where only observation errors occur [6]. Considering the scalar case (i.e. a single state variable), the system is represented by

$$\dot{x} = g(x, t) + k(x, t)\ u(t) \tag{21}$$

where $u(t)$ is the unknown disturbance input. The measurements or observations of the output are

$$y(t) = h(x, t) + (\text{Measurement errors}) \tag{22}$$

No assumptions regarding the statistics of the unknown input functions or the measurements error is made. With measurements of the output $y(t)$, for $0 \leq t \leq T$, it is required to estimate $x(T)$ on the basis of minimizing with respect to $\bar{x}(t)$ (a nominal trajectory) the functional

$$J = \int_0^T \left| e_1^2(t) + w(\bar{x}, t)\, e_2^2(t) \right| dt, \qquad (23)$$

where $w(\bar{x}, t)$ is a positive weighting factor, and the errors e_1 and e_2 are defined by

$$e_1(t) = y(t) - h(\bar{x}, t) \qquad (24)$$

$$e_2(t) = \dot{\bar{x}} - g(x, t) \qquad (25)$$

The least squares estimate of $x(T)$, denoted as $\hat{x}(T)$, is obtained from minimizing the integral of the (weighted) mean square errors, where the error $e_2(t)$ represents the difference between a nominal trajectory and the assumed form of its equation representation.

The minimization problem is then a problem in variational calculus, which leads to the associated Euler-Lagrange equations that contain an unknown Lagrange multiplier. The boundary conditions for this Lagrange multiplier are known at the ends of the interval, i.e. 0 and T, but there is no information about the value of $x(T)$, and hence the problem reduces to a two point boundary value problem (TPBVP) that yields the optimal estimate $\hat{x}(T)$. With the variable T now considered as a running time variable, the problem is treated as a family of problems with different final points, T, and the problem becomes one of sequential estimation, i.e. the TPBVP must be continuously solved for all values of T (the running time variable).

The problem is solved by application of the concept of invariant imbedding [12], which is used to convert a TPBVP into an initial value problem that can be easily solved. The missing "initial condition" is represented in a general manner for different values of T, thereby establishing a family of problems. On the basis that neighboring processes (i.e. system responses) are related to each other, the missing condition is found by examining the relationships between such neighboring processes. The procedure leads to a

partial differential equation that is solved by an expansion of the solution about the desired reference condition, which in the present case is the estimate $\hat{x}(T)$ (see [71]). The result of this invariant imbedding approach is a sequential estimator, which is such that previous data points do not have to be repeated whenever new observations are added, and hence the estimation operation can be carried out at a fast computational rate.

The estimator equations for the scalar case are

$$\frac{d\hat{x}}{dT} = g(\hat{x}, T) + 2P(T)\, h_{\hat{x}}(\hat{x}, T) \left[Y(T) - h(\hat{x}, T) \right] \tag{26}$$

$$\frac{dP}{dT} = 2P(T) g_{\hat{x}}(\hat{x}, T) + 2P \frac{\partial}{\partial \hat{x}} \left\{ h_{\hat{x}}(\hat{x}, T) \left[Y(T) - h(\hat{x}, T) \right] \right\} P + \frac{1}{2w(\hat{x}, T)} \tag{27}$$

where

$$h_x = \frac{\partial h(\hat{x}, T)}{\partial \hat{x}}, \quad g_{\hat{x}} = \frac{\partial g(\hat{x}, T)}{\partial \hat{x}} \tag{28}$$

The above results are somewhat similar to, and represent a generalization of the results of linear Kalman filtering [8]. The weighting function $P(T)$ is found from a Riccati-type equation, and the two equations are solved when given the initial conditions. The initial value $\hat{x}(0)$ represents the best estimate of the system state at $t = 0$, which is based on available a priori information, and the initial value $P(0)$ reflects the confidence in the initial value of $\hat{x}$ and the observed signal $y(t)$.

The estimator equations for the vector case are derived in [7] and are given below as

$$\frac{d\hat{x}}{dT} = g(\hat{x}, T) + 2P(T)\, H(\hat{x}, T)\, Q \left\{ Y(T) - h(\hat{x}, T) \right\} \tag{29}$$

$$\frac{dP}{dT} = g_{\hat{x}}(\hat{x}, T)\, P + P g_{\hat{x}}(\hat{x}, T)' + 2P \left[HQ \left\{ Y(T) - h(\hat{x}, T) \right\} \right]_{\hat{x}} P + \frac{1}{2} k(\hat{x}, T) V^{-1}(\hat{x}, T) k'(\hat{x}, T) \tag{30}$$

where

$$H(\hat{x}, T) = \left[\frac{\partial h(x, T)}{\partial \hat{x}}\right]' \tag{31}$$

(' symbol represents transpose of matrix), Q is a normalizing matrix used to weight the observation errors in the minimization procedure, the function $k(\hat{x}, T)$ is a coefficient of the unknown input forcing function (as in Equation (21), but for the vector case , and the function $V(\hat{x}, T)$ is defined by

$$V(\hat{x}, T) = k'(\hat{x}, T)\, W(\hat{x}, T)\, k(\hat{x}, T) \tag{32}$$

with W the weighting matrix for the errors in the basic equations due to the input disturbances. In the estimator equations the term $\left[HQ\left\{Y(T) - h(x, T)\right\}\right]_{\hat{x}}$ is an nxn matrix with i^{th} column given by

$$\frac{\partial}{\partial \hat{x}_i}\left[HQ\left\{Y(T) - h(\hat{x}, T)\right\}\right] \tag{33}$$

The basic equations of the system and its observations are similar to those of Equations (21) and (22) but generalized to the vector case. With x and n-vector, P(T) is an nxn matrix, so that the number of equations required to be solved are $n^2 + n$ which can become a large computational task. Some possible simplification could occur in some cases where the P-matrix has symmetry for the off-diagonal terms, depending on the form of the functions H, Q, etc., thereby leading to a reduction of the number of equations to be solved.

In the case where identification of parameters is considered, the constant (but unknown) parameters, denoted as a vector a (with m elements), satisfy the differential equation

$$\frac{da}{dt} = 0 \tag{34}$$

and the m elements of a can be considered as additional elements in the state vector, i.e. they are adjoined to the state vector elements (ℓ elements) so that $n = \ell + m$ is the total number of elements in the state variable $\hat{x}$, which also includes the estimates of the m

unknown parameters in a. The equation given in Equation (34) is easily absorbed into the total system representation in establishing the g-matrix, and the remaining equations for P readily follow. The only problem resulting from the introduction of the additional elements is the increase in the total number of equations to be solved which increases the computational complexities. Illustrations of the results obtained by application of the equations presented above are given in the following sections of this paper.

APPLICATIONS OF SEQUENTIAL ESTIMATION TECHNIQUE

The digital computer program established for solution of the coupled estimator and gain equations is structured to carry out the solution of the equations as a group of coupled first order ordinary differential equations. These equations are nonlinear and time-varying, in general, and the technique for solution is based upon use of a Runge-Kutta fourth order integration scheme. The integration step size is not arbitrary, since there is a maximum basic frequency of the vehicle motion modes for any particular craft, and hence sampling of any data would have to be made at twice the rate of the largest frequency manifested in the system response in accordance with the requirements of the sampling theorem [13] . The integration time step can be less than this amount, and the values to be used would depend upon requirements of stability, total time of solution, bandwidth properties, etc. All of the computer operations for a general equation system are carried out in matrix form, as indicated by the representation of the equations given in the preceding section, and various subroutines to make use of matrix manipulations are employed, which are standard procedures associated with digital computer operations. The results of application of these equations for various illustrative, cases and for different naval craft are provided below.

In order to illustrate the capabilities of the basic method of analysis, a series of computational experiments were carried out on simple systems with known parameter values. The first problem considered is that of a second order system, where it is required to find the two unknown parameters, and the second problem is to obtain one of the coefficients in a third order system. The test cases are selected with no external forcing function, thereby being transient response trajectory data as input information. These particular problems are similar to test problems solved using analog computers in [14] , with noisy forcing functions there, and serve to validate the digital computer program and procedures.

The first problem is represented by the differential equa-

tion

$$\ddot{y} + a\dot{y} + by = 0 \tag{35}$$

and it is required to estimate the coefficients a and b, assuming that measurements are made of the time histories of $\dot{y}$ and y. Solutions were obtained on the digital computer for Equation (35) with known coefficients having the values $a = 0.1$ and $b = 0.4$, and these were the input information to the estimator and gain equations. The output time histories of the estimated and observed trajectories of $\dot{y}$ and y are shown in Figure 1, showing the rapid convergence of the estimated values to the observed data and the "tracking" of these estimates to the true values. The coefficient estimate were started with initial conditions (or "guess" values) at $a = 0.6$ and $b = 10$, and the rapid convergence to the true values is exhibited in Figure 2.

The second problem is represented by the equation

$$\dddot{y} + a_1\ddot{y} + a_2\dot{y} + a_3 y = 0 \tag{36}$$

and it is required to find the value of the coefficient a_2 when the other coefficients are known (the values chosen are $a_1 = 0.05$, $a_2 = 0.3$, $a_3 = 0.01$). Defining the four state variables

$$x_1 = y, \quad x_2 = \dot{y}, \quad x_3 = \ddot{y}, \quad x_4 = a_2 \tag{37}$$

the system equations are

$$\begin{aligned} \dot{x}_1 &= x_2 \\ \dot{x}_2 &= x_3 \\ \dot{x}_3 &= -0.05x_3 - x_4x_2 - 0.01x_1 \\ \dot{x}_4 &= 0 \end{aligned} \tag{38}$$

and the observed variable is y or x_2, with the observations given by the solution of Equation (36) with all the known coefficient values. The results obtained from the digital computer solution of this system (4 state variables, 16 P_{ij} equations) are shown in Figure 3, where the error signal $\epsilon = x_2 - \hat{x}_2$ and the coefficient estimate $\hat{x}_4$ are given. The initial condition for x_2 (the actual system response) is

$\hat{x}_2(0) = 1$, and the estimated initial condition for x_2 and x_4 are

$$\hat{x}_2(0) = 0, \quad \hat{x}_4(0) = 0 \tag{39}$$

The rapid convergence of $\hat{x}_2 \rightarrow x_2$, and the value of $\hat{x}_4$ to the true value of $a_2 = 0.3$, in a time period of about 10 sec., shows an effective technique for this simple case.

The results obtained here indicate that the technique applied to these test cases can provide valid parameter estimates in a relatively short computation time, and that performance is working properly. Similar performance using analog computers for the same type of problems, including noisy forcing functions, was shown by the results in [14], and hence the present system identification technique is applicable to the case of naval craft in waves.

No noisy forcing functions were applied in these test cases for the exercise of a digital computer program because of the extensive effort required to produce a forcing function (by digital means) within a prescribed bandwidth for the representative test systems. This is an important requirement for system identification, i.e. a proper input signal that would excite the system adequately, and that is obviously related to the effective response bandwidth of the system. In order to gain some insight into the effect of the forcing function bandwidth, some experiments were made with the simple second order system given by Equation (35) that was treated above. The forcing function in that case was obtained from a random number generator. With the sampling and integration step at every 0.01 seconds, it was found that the identification would not be achieved in that case. The system never settled toward a convergent situation, and this was ascribed to the relatively high frequency of the forcing function relative to the system bandwidth. Thus it appears that, in any identification procedure, the excitation should not be unrealistic in comparison to the expected range of frequencies of the forcing functions for the system to be identified. This is a general guideline for all identification studies, and should be considered for various simulation procedures in generating actual data. Since the occurrences in nature for various systems often have natural limits consistent with system behavior, there does not appear to be a severe problem in that (more realistic) case.

For the case of an SES craft, the basic linearized mathematical model for vertical plane motion is given by

$$m\ddot{z} = Z_{\dot{z}}\dot{z} + Z_z z + Z_{\dot{\theta}}\dot{\theta} + Z_\theta \theta - A\Delta p + Z_{waves} \quad (40)$$

$$I_Y\ddot{\theta} = M_{\dot{\theta}}\dot{\theta} + M_\theta \theta + M_{\dot{z}}\dot{z} + M_z z + M_{waves} \quad (41)$$

where Z_{waves} and M_{waves} are the wave-induced vertical force and pitch moment, respectively, which are random forcing functions. The quantities m, I_Y and A (plenum area) are known constants, and the unknown coefficients are $Z_{\dot{z}}$, Z_z, $Z_{\dot{\theta}}$, Z_θ, $M_{\dot{\theta}}$, M_θ, $M_{\dot{z}}$ and M_z. For these equations there is also appended a relation involving the pressure, leakage rate, fan characteristics, etc. which is derived on the basis of consideration of mass in the air cushion.

In the representation given by Equations (40) and (41) it is assumed that the center of pressure of the bubble volume is at the CG, and the mathematical model only represents the vehicle motion, with no consideration of any seal motion or even of a direct presence of any seals. Similarly there is no direct dynamic force influence of the seals embodied in the mathematical relations above, except for the possible influence of the seal forces in determining the total hydrodynamic stability derivatives in the equations.

Mathematical experiments were carried out with these equations, using computer generated data. In these experiments on the application of the system identification method, it is assumed that the pressure is a precisely known function, which is still a random function in general, and that this pressure variation is obtained from measurements. Thus the problem is reduced to treating only the two degrees of freedom of heave and pitch, and 8 coefficients have to be determined. The basic procedures were applied to this problem, which contained 4 state variables and 8 unknown coefficients, leading to a requirement for 156 equations for this case. Various difficulties in regard to long computation time and small movement of the coefficients were found, and other approaches were considered.

Instead of using a noisy input function to excite the system, which was attempted with the use of a random number generator in the digital computer, it was decided to make use of trajectory data that was generated using the large digital computer simulation program for rigid sidewall SES craft. This particular simulation also included a complete representation of seal dynamics, which allowed for seal motions nnd the generation of water contact forces that would be transmitted to the craft. The type of wave system exciting

the motions was appropriate to a sea state that was generated by a summation of separate regular sinusoidal waves.

The method of analysis used in the identification procedure is based upon assuming that the pressure is a known measured quantity, which is the actual real case, and it is also assumed that continuous time histories of $\dot{z}$, z, $\dot{\theta}$ and θ are available. On that basis it is then possible to analyze the equations for heave and pitch separately, so that only 4 coefficients are required in each case, i.e. the derivative $Z_{\dot{z}}$, Z_z, $Z_{\dot{\theta}}$, Z_θ can be obtained from a model based on Equation (40), while values of $M_{\dot{\theta}}$, M_θ, $M_{\dot{z}}$, and M_z are obtained from a model using Equation (41). Computations were carried out for the pitch motion case primarily, since the heave motion is mainly due to the effects of pressure and both hydrostatic and hydrodynamic force terms have only a small influence for that particular motion.

For the heave motion case the hydrostatic terms are the only contributions from the sidewalls, while there is a hydrodynamic term in addition that contributes to M_θ, as well as a small destabilizing effect due to the bubble pressure. It is expected that the hydrostatic term is the predominant effect for M_θ in this case. However, there is also some influence of the seals, on the moment derivatives, and that may be difficult to estimate accurately since the seals are not "statically" maintained in the water but partake of their own motion, and hence are a complicated element in this entire representation. The values found from the identification procedures are essentially the hydrodynamic stability derivatives divided by the particular inertia term in the equation, i.e. the mass m for the stability derivatives in the heave motion and the moment of inertia I_Y for the pitch stability derivatives.

Computations were made for the heave equations initially, with pressure as an input that is precisely known and using the values of $\dot{z}$, z, $\dot{\theta}$ and θ as obtained from the simulated trajectory outputs. Values of the coefficients in the heave equation were found, and an examination made of the results. In a number of simulations it was found that the signs of certain terms changed, and in addition values of some coefficients were found to have signs that were different than would be ordinarily expected. When such "unrealistic" values are produced in a number of different identification studies, this is an indication that the parameter may not have a significant influence on the resulting motions of the craft. The terms that did not appear to have a particular influence on the heave motion were the derivatives $Z_{\dot{\theta}}$ and Z_θ, and special studies were made to

determine whether they had any influence or could be discarded for further consideration. It was suspected that these terms would have little effect, based on the fact that the heave motion is primarily influenced by pressure effects and the only hydrodynamic or hydrostatic terms that would influence the heave motion would be those terms involving heave motions per se. Previous simulation studies of similar SES craft have demonstrated that the coupling of pitch motion into heave had little effect, and the results obtained for heave motion responses with these pitch derivative terms deleted were almost the same as when they were included. Thus they were neglected in the identification experiments.

A similar treatment in the case of pitch motion was made where the 4 pitch stability derivatives associated with Equation (41) were estimated. Computations made with all motions ($\dot{\theta}$, θ, $\dot{z}$ and z) assumed to be measured and available produced values for these particular derivatives, with different magnitudes resulting for the coupling coefficients M_z and $M_{\dot{z}}$ that could not be reconciled with simple estimates based on hydrostatic computations, for example, in the case of the derivative M_z. Similarly the change in sign of $M_{\dot{z}}$ in different runs also indicated that this particular variable had a small influence on the resulting pitch motion, and in accordance with the procedure applied in the case of heave motion these quantities were also neglected. The results obtained for the derivatives $M_{\dot{\theta}}$ and M_{θ}, with all motions measured including the effect of $M_{\dot{z}}$ and M_z, are shown in Figure 4, while those obtained with the assumption that $M_z = M_{\dot{z}} = 0$ are shown in Figure 5, which uses only measurements of θ and $\dot{\theta}$. These results are sufficiently close so that it can be assumed that there is no significant influence of these variables, just as in the case of the coupling coefficients for heave motion, and hence they can be ignored in future system identification work.

An interesting result was obtained when it was assumed that only measurements of the pitch angle were available, and in that case the stability derivatives are shown in Figure 6, which indicates a well converged solution that does not deviate much from the initial guess values. In order to determine if these coefficients are really appropriate to this particular motion, the pitch angle trajectory is shown in Figure 7, together with the estimated trajectory using these values. It is seen that very good tracking of the observed pitch trajectory is indicated by these values and hence they can be used as the appropriate estimates from system identification. This is indicated by a comparison of values given in Figure 6 with those in Figures 4 and 5, showing only a small difference in M_{θ} while there is some difference of the order of 25-30% for the derivative $M_{\dot{\theta}}$.

Since the hydrodynamic contributions to M_θ by the sidewalls are known to be small (from other analytical studies), and there is also a small influence of the destabilizing moment due to pressure, these two quantities generally negate each other leaving mainly the hydrostatic term. This result appears to be sufficient, since the estimate of M_θ given by Figures 4-6 is close to the value of -9.0 (for M_θ / I_Y) obtained from hydrostatics, and can then be considered to be a good estimate of this particular parameter.

The magnitude of $M_{\dot{\theta}}$ determined by this technique was somewhat different from the values estimated by theory due to the influence of the sidewalls. The predominant contribution to this stability derivative is due to the rigid stern seal hydrodynamic forces, which depend upon the seal wetted length. Since it is difficult to determine this contribution due to the seals, and the simplified equation system does not include any representation of seal dynamics, the procedure only gives a measure of the overall seal contribution to the resulting vehicle dynamics in this case.

It would appear on the basis of these results that the presence of the seals has an important influence on the values of effective stability derivatives in the linearized equations representing SES craft motions. Since they are not statically fixed, and transmit their forces directly to the craft, some other representation would be necessary to adequately model an SES craft together with the seals and their influence on the craft dynamics. This would certainly require some representation of the seal motion as a separate degree of freedom, together with measurements of the seal motions in order to characterize the seal parameters adequately. Since this was not done in a way that would provide useful information in the full scale measurements, no mathematical modeling was carried out for the seals (i.e. for coupling the seal motions with the vehicle motions) in the case of simulation studies used for the application of system identification to such a system. One possible influence of the seals that has not been included in the determination of various stability derivatives is the fact that the seal forces due to the varying seal and bubble pressure have an effect on the seal as well, which in turn influences the resulting dynamics of the craft. Since only limited treatment of the hydrodynamic forces on the seal has been included, that may be one reason why there is poor matching between the theoretical prediction of the damping-type stability derivatives that included the seal terms, as compared to the estimates obtained from system identification. A much more precise match of measured data and quantities that must be modeled in the mathematical representation has to be made in order to carry out successful system identi-

fication for vertical plane motions of SES craft.

Although there has only been a somewhat limited degree of success in identifying (i. e. , finding correct numerical values) the various important stability derivatives for heave and pitch motions using the trajectory data obtained from simulation studies with a complete mathematical model, important insight into the requirements for achieving improved results was obtained. The importance of seal dynamics and forces ; the lack of significant influence of certain coupling coefficients ; the effect of measurement of more state variables ; and the influence of sampling time and integration step size on stability and convergence of the solutions, are examples of the various conclusions obtained from these particular studies. In order to obtain more understanding of methods for treating full scale data, which is the ultimate objective, the methods were applied to some full scale data.

This data was recorded on magnetic tape, in digital form, with the "important" information necessary for dynamic analysis provided by samples at the rate of 100 cps. The data useful for the present analysis was CG heave acceleration (z), bubble pressure (p), and pitch angle (θ). Pitch rate data ($\dot{\theta}$) was recorded at a much slower rate (10 cps) and hence was not compatible with the pitch angle data, as well as possibly losing important information due to improper sampling at too low a frequency (the Nyquist sampling rate for the present SES craft corresponds to 20 cps, or sampling every 0. 05 sec.). No information on the heave motion except heave acceleration was available and hence $\dot{z}$ and z would have to be found by integration operations, which have more stringent sampling and time increment requirements. In addition, the actual data measured during the full scale tests suffered from telemetry errors that result in sudden "drop-out" of data. This caused "spikes" in the resulting data, above and beyond the generally spike-like appearance of much of the data, especially for bubble pressure and accelerations, and this data was specially treated by filtering and interpolation procedures to assure a relatively continuous and "smooth" data output. Thus the measured data itself may have certain inherent defects from the point of view of its applicability as a source of trajectory data for system identification, while it is still perfectly good for its original purpose of providing information on vehicle response characteristics (e. g. level of accelerations, maximum and average pitch angles-bubble pressure variations, etc).

The experience in applying this method of system identification to full scale data obtained from tests of the SES craft in irregular waves provided valuable guidelines for future applications.

Various procedures were used to carry out the required integrations of heave acceleration to obtain velocity and displacement records, and the sampling times, integration time step, and numerical integration techniques used had to satisfy certain requirements for use in system identification work. Similarly it was found necessary to have proper accelerometers that provided data relative to a "true" vertical, rather than with reference to the craft body axes, which requires a properly aligned accelerometer system, i.e. a "stable table". In addition, accurate data on the craft weight, CG location, moment of inertia, etc. appropriate to the actual test condition in full scale must be available so that the precision of system identification can be fully realized using the representative mathematical model.

As a result of the analyses illustrated here, it appears to be possible to determine the numerical values of certain stability derivative coefficients in a simple linear mathematical model characterizing vertical plane motions of SES craft. Some coefficients have been shown to have negligible influence on different modes of motion as a result of the identification analyses, thereby verifying similar indications from separate simulation studies. While the more simple hydrostatic-type stability derivatives have been found with consistent values close to those from theoretical predictions, the damping-type terms are shown to be affected by force contributions that probably arise from the seals. It is thus necessary to include additionel degrees of freedom in the mathematical model for vertical plane motion to represent seal motion and seal forces that are transmitted to the craft.

Other requirements for successful system identification are that the data should be sampled, for use in digital processing, at a rate equal to 10 times as fast as the highest frequency of interest in the expected vehicle response, and possibly faster depending upon the number of integration stages to be applied for determining state variable trajectories. On this basis, and with the proper mathematical model (including seal dynamics) it can be anticipated that successful estimation of the important stability derivatives for SES craft vertical motion can be achieved using measured data obtained during tests in a random seaway.

Another application of this particular technique was made to the case of a hydrofoil craft, using data generated on a digital computer. In that case the equations were exactly those given by Equations (14) - (20), with the addition of random forcing functions on the right hand side of Equations (14) and (15), which were

supposed to represent the wave-induced vertical force and pitch moment due to waves. In addition to the excitations due to random waves, various step changes in commanded height were made at different times in the trajectory records.

For the present application, the elevator and flap angles were generated in accordance with the transfer function relations given in Equations (18) - (20) but their time histories were assumed to be known (i.e. as measured input) and hence inserted into the identification equation system. This procedure is sensible, and also serves to reduce the order of the equations to be treated by a significant amount, thereby reducing the required computation time. In the present hydrofoil case the magnitude of the "noisy" excitation, which was generated by filtering the output of digital random number generators, was very small as supplied by the sponsoring agency who provided such trajectory data. Thus there was little to "drive" the system by means of this noise and the identification depended upon use of the larger disturbances provided by the commanded step changes due to the controls.

The generated trajectory data used in the identification was that of pitch angle θ, pitch rate $\dot{\theta}$, and the CG heave displacement h which was obtained from combining signals involving the height sensor, pitch angle, etc. As mentioned above, the elevator and flap deflection δ_e and δ_f were also used as known input data, and all of this trajectory information was sampled every 0.05 sec. for use in the identification equations. With 10 unknown coefficients and 4 state variable equations, a total of 210 differential equations must be solved for this problem (by use of symmetry considerations in the P_{ij} matrix elements, this can be reduced to 119 equations). Different runs were made for the trajectories representing the same craft, starting with an initial guess for each of the 10 unknown parameters. Typical outputs illustrate the manner in which the various coefficients evolve as functions of time, as shown in Figure 8. Those values that appear to approach a limit after a period of time are then used as initial values for another run with the recorded trajectory data (since the continuous "noisy" forcing functions were not sufficiently large to excite the main dynamic responses), and a comparison of the predicted trajectory (using the estimated coefficients in the equations) with the recorded (i.e. generated) trajectory illustrates how well the estimated parameters produce adequate "tracking" of the actual system responses. An illustration of these results, where the final values of the estimated parameters are established since they do not change significantly throughout the time period of the experiment, is shown in

Figure 9. The good agreement between the observed motion responses and the predicted trajectories is exhibited in this graph, and the final estimated parameters are listed below together with the actual (true) value used in the computer simulation that generated the observed data.

Table 3

Hydrofoil Estimated Parameters From Noisy Data

Parameter	Estimate	Actual Value
$m_f = mC_1$	300-350	375
$m_r = mC_2$	900	892
C_3	.50	.491
C_4	.16	.167
C_5	2.2	2.053
C_6	.57	.521
C_7	2.13	1.829
C_8	.55	.457
C_9	.18	0
C_{10}	.18	0

In this particular case the values of mC_1 and mC_2 (where m is the craft mass) did not change at all, throughout the total time of computation from the original initial guess value. The good estimates of the added masses, together with the probable small influence of the differences in values of added mass on the motions, resulted in satisfactory trajectory tracking with these values. Similarly the nonlinear lift terms, represented by C_9 and C_{10}, did not appear to have much influence either since the motions (and angles) were small, so that the data itself did not allow an adequate estimate of these values, just as in the case with the iteration method discussed previously. While there were some small differences in the estimated values of C_5, C_6, C_7 and C_8 as compared to the actual values,

the ratios C_5/C_6 and C_7/C_8, which is the form in which these coefficients are determined, are about the same from the estimates and the true values. In general the values shown in Table 3 are sufficiently close to represent a successful identification of the system parameters, as is also indicated by the trajectory matching in Figure 9.

Full scale responses of a hydrofoil craft (essentially the same craft treated above using simulated responses) were provided as a means to test the techniques developed herein for system identification. This data was supposed to be obtained as a result of imposing various commands to the craft controls (i.e. elevator and flaps) in an ostensibly smooth seaway, i.e. they were expected to represent transient responses of the craft. The basic equations representing the craft motions included the additional degree of freedom due to surge; the craft propulsive thrust force was represented in the equations as a function of propeller rpm, and drag forces (which included quadratic terms in resulting angle of attack) were also present in their influence on surge and also the pitch moment (see [10] for a more detailed discussion of these equations). The initial intent was to apply the iteration method for transient responses that was discussed previously, and this approach was attempted. The equations were simplified to eliminate the surge degree of freedom (since the speed was almost constant during these particular maneuvers) and the iteration method was applied. The results showed a lack of convergence and/or stabilization throughout many attempts, and further simplification was made to eliminate the drag forces from consideration since the motions were generally small.

For the more simplified representation of the craft dynamics success was still not achieved due to lack of convergence and/or stabilization of the parameter estimates, although for some portion of time the estimated trajectories seemed to be in fair coincidence with the measured data. The experimental trajectory data, which included the pitch angle, pitch rate, and the height sensor time histories, did exhibit fairly large "noise" superposed on the main craft responses due to the commanded control deflections. A typical illustration of the control deflections experienced in the full scale tests is shown in Figure 10, and similar types of noise were present in all of the recorded data (the observed data from the tests was presented in digital form every .05 sec., as a result of digitizing the measured craft motion tape records). The record for the flap deflection really represents the average of starboard and port aileron deflections, which was the chosen method of representing this control action in the analysis of this trail data. Simple smoothing operations

applied to the data still did not allow proper identification of the required parameters by the iteration method, and hence the sequential estimation technique was applied.

The equations representing the hydrofoil craft motion for the full scale case were simplified to represent only heave and pitch, as previously considered for the computer generated data. However nonlinear lift terms were still retained while the added mass terms were kept fixed (assumed known) at the values 350 slugs forward and 950 slugs for the rear foil. The equations contain expressions for the lift forces on the forward and rear foil, which are represented in terms of the lift coefficients as :

$$C_{L_F} = \left(\frac{w_F}{V} + K_e \delta_e + \gamma'\right) F_1 + K_1 \left(\frac{w_F}{V}\right)^2 \qquad (42)$$

where

$$F_1 = \frac{A_1 + B_1 \zeta_F}{C_1 + \zeta_F} , \qquad (43)$$

and similarly

$$C_{L_R} = \left(\frac{w_R}{V} + K_f \delta_f + \gamma''\right) F_2 + K_2 \left(\frac{w_R}{V}\right)^2 \qquad (44)$$

$$F_2 = \frac{A_2 + B_2 \zeta_R}{C_2 + \zeta_R} \qquad (45)$$

The 10 unknown parameters are K_e , K_1 , A_1 , B_1 , C_1 , K_f , K_2 , A_2 , B_2 , C which are similar to the coefficients previously represented ; i.e. $K_e = C_3$, $K_f = C_4$, $K_1 = C_9$, $K_2 = C_{10}$. The representation of F_1 and F_2 in Equations (43) and (45) was proposed as the required form for the depth effect on lift by the sponsoring agency, who supplied the proposed mathematical model.

The analysis of the full scale data was applied to the first maneuver (Experiment 1) in the vertical plane, with the initial guess of the coefficients taken from the results of the computer generated data analysis discussed above, and the initial values of the coefficients in the depth terms F_1 , and F_2 were taken as 1.0. A 10 sec. data portion was analyzed twice, with the parameter es-

timates obtained from the first "pass" used as the initial guess for the second pass. The results are shown in Figure 11 for the manner in which the parameter values change as functions of time. It is seen that all of the parameter values stabilized except for K_f which tended to fall off toward the end of the maneuver. Examination of the various motion and deflection time histories showed erratic fluctuations in δ_f in this region , so that the value of K_f before the fall-off was retained. These coefficient values obtained from Experiment 1 were then used as the initial guess values from analysis of another maneuver of the craft, denoted as Experiment 4 (the control deflection for that case is shown in Figure 10).

In the analysis of Experiment 4 the initial value of K_e was inadvertently taken as .05 instead of .50. However the estimate of K_e rapidly moved back to a reasonable value as time increased in the first pass. All of the other parameters did not show much change from their initial values, which were taken from the results of Experiment 1 and from the first pass for the second pass case. An illustration of the variation of the parameters during the analysis of Experiment 4 is given in Figure 12. A tabulation of the values obtained from analysis of the full scale hydrofoil data is given below in Table 4.

Table 4

Hydrofoil Parameters-System Identification Using Full Scale Data

Parameter	Estimated Value
K_e	.32
K_f	.33
K_1	.07
K_2	.14
$\frac{1}{C_1}$	.10
$\frac{A_1}{C_1}$	.97
$\frac{B_1}{C_1}$	1.30

Parameter	Estimated Value
$\frac{1}{C_2}$	.085
$\frac{A_2}{C_2}$	.965
$\frac{B_2}{C_2}$	1.42

With the parameter values established by this procedure, the resulting trajectories of the craft are presented in comparison with the measured full scale data (from Experiment 4) in Figure 13. The time histories of CG heave h, pitch angle θ, and pitch rate $\dot{\theta}$ are compared in Figure 13, and it can be seen that there is generally good agreement using the estimated coefficients obtained from this system identification procedure. Some of the small differences can be explained, since the heave motion is obtained by combining various measured signals, including that from the height sensor which will contain "noise" due to local ambient waves as well as waves generated by the craft motions themselves. The lack of more precise agreement in the final values of the pitch angle is due to the inability of the present mathematical model (a simplified quasi-linear model, with reduced degrees of freedom, and neglecting drag and thrust influences, etc.) to provide a very accurate measure of trim condition near or at equilibrium. The deviations in pitch rate are actually quite small in magnitude as can be seen from the scale in Figure 13, so that the "tracking" by the predicted $\dot{\theta}$ trajectory is better represented by the ability to change sign and generally follow the measured data, which is done sufficiently well.

Examination of Figure 12 shows that the representation of the parameter values associated with the depth variation expression is exhibited in terms of $\frac{1}{C_1}$, $\frac{A_1}{C_1}$, $\frac{B_1}{C_1}$, etc. The values of $\frac{1}{C_1}$ and $\frac{1}{C_2}$ for these functions seem to approach zero, so that the resulting values of F and F behave in an almost linear variation with $\zeta_{F,R}$ while these F_1 and F_2 functions approach an almost constant value as $\zeta_{F,R}$ vary for the representation used in the case of the computer generated data model. This is shown by the curves in Figures 14 and 15. A means of judging the effect of this difference is to compare the values of the products $K_e F_1$ and $K_f F_2$ obtained from the full scale tests with the values used in the computer simulation mathematical model, since these terms represent the lift effectiveness of

the controls. The product $K_e F_1$, which varies slightly throughout the depth range covered in the full scale tests and the simulation data, is found to compare very well using the respective parameter values obtained in each case. This indicates the same lift effectiveness being manifested by the forward foil elevator control.

The values of the product $K_f F_2$, representing the rear foil flap effectiveness were quite different, ranging up to about 3-4 times as large in the case of the full scale data value when compared to the mathematical simulation model value. This result indicates a possible difference in the flap areas (or other dimensional changes) between the values assumed for the mathematical model exercise and the actual craft flap characteristics, or it may also imply a defect in the form of mathematical representation used, as given in Equation (44). Still another possibility is that since there were separate port and starboard flap deflections, the use of an average value may not be proper for the present application test of system identification ; there may be some rolling motion developed by the different flap deflections that causes different relative immersions on each side of the craft ; etc.

With regard to the question concerning the basic mathematical model given in Equation (44), as well as the representation in Equation (42), the quantity F_2 (or F_1) represents the foil lift coefficient rate C_{L_α} for the particular foil. The depth dependence inherent in this type of representation appears to be appropriate, as exhibited in Figure 14, which was the basis for its selection in the mathematical model. However that functional form of F_1 and F_2 implies that the same depth dependence is present for the control elements of the foil as is the case for a total foil angle of attack change. This does not appear to be a reasonable assumption, in view of the small sizes of the control element chords relative to the craft foil submergences. It would appear to be more appropriate to assume a realistic depth dependence, with known values similar to the variation exhibited in Figure 14, for the terms associated with the angle of attack variables in Equations (42) - (44). The unknown functional form of F_1 and F_2 , which would just be associated with the unknown elevator and flap parameters K_e and K_f , would then be sought by means of the present system identification technique to determine the appropriate parameter values and check the resulting trajectory tracking. Thus the results of system identification provide a means of judging the general validity of particular mathematical model representations that are assumed to represent vehicle dynamics.

The results demonstrated here show that the present sequential estimation technique can provide accurate estimates of parameters as a means of system identification for cases where random-noise interference or excitation is present. For the case where the data was generated on a computer, and the mathematical model was precisely known, quite good agreement between estimated parameter values and the true ones were demonstrated for the hydrofoil case. The analysis of the full scale case was partially successful, in that generally reasonable parameter values were found that yielded good tracking of observed trajectories when using well stabilized values of the parameter estimates. There is a question concerning the proper form of the equations to represent the depth dependence influence on the effectiveness of the controls, as well as a possible influence on the nature of the measured input data on the results, when examining the results of this system identification procedure. These questions aid in the development of more rational mathematical model representations as well as on the nature of data acquisition for use in this type of analysis.

There are a number of features of this particular sequential estimation technique that have been observed in the present work. These features are concerned with methods used to obtain convergence and useful solutions, as well as information on computation time requirements. It is easily seen that the computation time generally increases as the number of variables (including unknown parameters) is increased. A general rule is that the time increases as n^3 , where n = sum of number of state variables in equations and the number of unknown parameters. For the present case of the hydrofoil problem, with $n = 14$, the computation time was 22 times longer that the "real time" extent of the observed data, and this is for the case of a sequential estimation technique that would minimize computation time as compared to the classical nonsequential estimation schemes (with the problems being run on a very fast large computer, the CDC 6600). This time could be reduced by about 50% by applying symmetry considerations to the P_{ij} elements, thereby reducing the number of equations to be solved, as mentioned previously. Another possibility is to separate the equations into separate sets of a smaller number of equations, by means of partitioning, which could then reduce the time significantly depending on the number of partitioned elements. These particular computational modifications were not carried out in this work due to the increased programming effort required, and the fact that the main objective of the work was to develop the capability of system identification per se. These approaches to reduce computer time remain as a further step in providing a more "computa-

tionally" efficient method for system identification purposes.

Various techniques for reducing the time (i. e. real time of the observed data) for convergence of the parameters, which would then also reduce total computer time, were also found. Thus an improved convergence time is found when the constant matrix elements on the right hand side of the gain equations (i. e. the P-equations, as shown in Equation (30)) are made larger, but that improvement does not show significant gains for larger equation systems. The most useful approach is to vary the magnitudes of the elements in the weighting Q-matrix that appears in Equations (29) and (30) in order to reflect the importance of measured state variable data that are well known. Thus larger values of the matrix elements are used for particular variables that are known to be measured accurately and directly, rather than data that is not directly observable or has a lower degree of accuracy due to instrumentation difficulties. Thus these particular strategies are useful means of achieving more rapid convergence for this type of system identification technique.

CONCLUSIONS

The present paper has demonstrated the feasibility of using different system identification techniques to determine the values of major parameters and coefficients in a mathematical model representing the motion of different naval craft. This was demonstrated by application to a number of diverse vehicles, such as a surface ship, a hydrofoil craft, and an SES craft, using data that was generated on a computer (with known coefficients and a known mathematical model) as well as from full scale tests. Different techniques are used, in accordance to the extent of the influence of noise on the system (and its measured responses), and their limitations as well as capabilities are described in the paper. Certain virtues of the two different methods used are quite important, such as having a means of determining a level of confidence for different converged parameters while carrying out the identification, as well as an indication that a particular mathematical model is not fully appropriate for representing certain features of the craft motions. The two techniques demonstrated here are generally applicable to a number of different stability and control problems of naval craft, for both full scale and model scale data and analyses. Depending upon the degree of accuracy and the procedures used for data acquisition, these methods can be applied to determine stability derivatives, nonlinear coefficients, etc. in a structured mathematical model representation, from data taken in model tanks. Such data would only involve motion trajectory measurements of free models and could

provide a simpler means of determining the required dynamic data without recourse to complicated special purpose test apparatus. More opportunities to apply these methods for this purpose will provide a final demonstration of its utility and practicality.

REFERENCES

1 Symposium on Towing Tank Facilities, Instrumentation and Measuring Technique, Zagreb, Sept. 1959.

2 Proceedings, Twelfth International Towing Tank Conference, Rome, Sept. 1969.

3 GOODMAN, Théodore R., "System Identification and Prediction - An Algorithm Using a Newtonian Iteration Procedure", Quarterly of Applied Mathematics, Vol. XXIV, No. 3, Oct. 1966.

4 SARGENT, Théodore P., and KAPLAN, P., "System Identification of Surface Ship Dynamics", Oceanics, Inc. Rpt. no. 70-72, March 1970.

5 GOODMAN, Théodore R., and SARGENT, Théodore P., " A Method for Identifying Nonlinear Systems with Applications to Vehicle Dynamics and Chemical Kinetics", presented at the 1971 Joint Automatic Control Conference, Washington Univ., St Louis, Mo., Aug. 1971.

6 BELLMAN, R.E., KAGIWADE, H.H., KALABA, R.E., and STRIDHAR, R., "Invariant Imbedding and Nonlinear Filtering Theory", Rand Corp., Memorandum RM-4374-PR, Dec. 1964.

7 DETCHMENDY, D.M., and SRIDHAR, R., " Sequential Estimation of States and Parameters in Noisy Nonlinear Dynamic Systems", J. of Basic Engineering, ASME, June 1966.

8 KALMAN, R.E. and BUCY, R.S., "New Results in Linear Filtering and Prediction Theory", J. Basic Engineering, Vol. 83, No. 95, 1961.

9 KAPLAN, P., and SARGENT, Théodore P., " A study of Surface Effect Ship (SES) Craft Loads and Motions, Part IV - System Identification of SES Dynamics and Parameters", Oceanics, inc. Rpt. No. 71-84D, Aug. 1971.

10 KAPLAN, P., and SARGENT, Théodore P., "Determination of Stability Derivatives of Hydrofoil Craft via System Identification", Oceanics, Inc. Rpt in preparation.

11 STROM-TEJSEN, J., "A Digital Computer Technique for Prediction of Standard Maneuvers of Surface Ships", David Taylor, Model Basin, Rpt. 2130, Dec. 1965.

12 LEE, E., STANLEY, Quasilinearization and Invariant Imbedding With Applications to Chemical Engineering and Adaptive Control, Academic Press, 1968.

13 HAMMING, R. W., Numerical Methods for Scientists and Engineers, McGraw-Hill Book Company, 1962.

14 Unpublished work at Oceanics, Inc. on system identification for human operator dynamics.

* * *

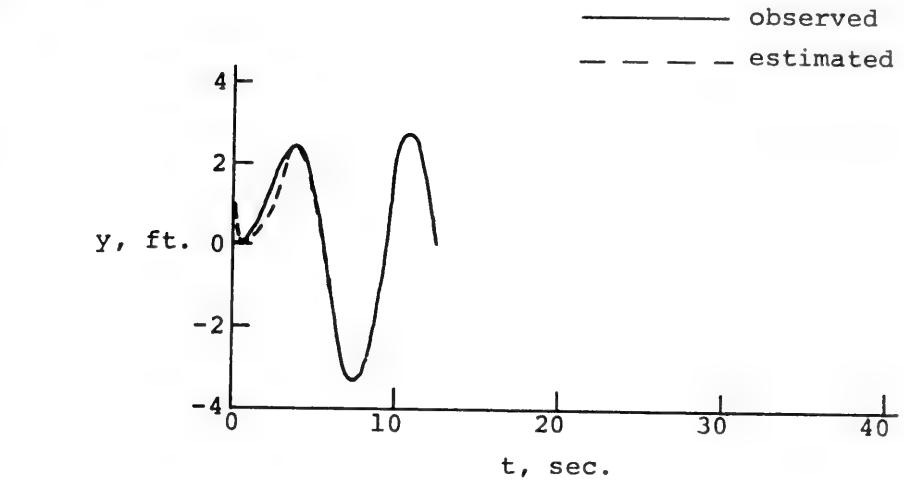

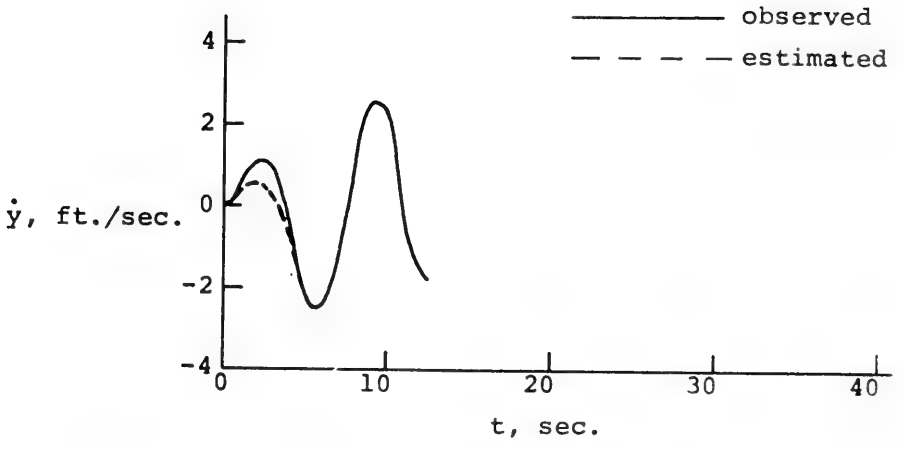

Figure 1. Estimation of states for second order system, transient response.

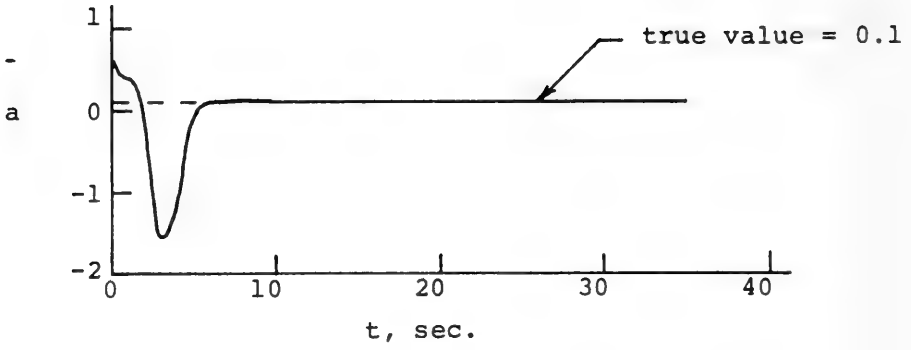

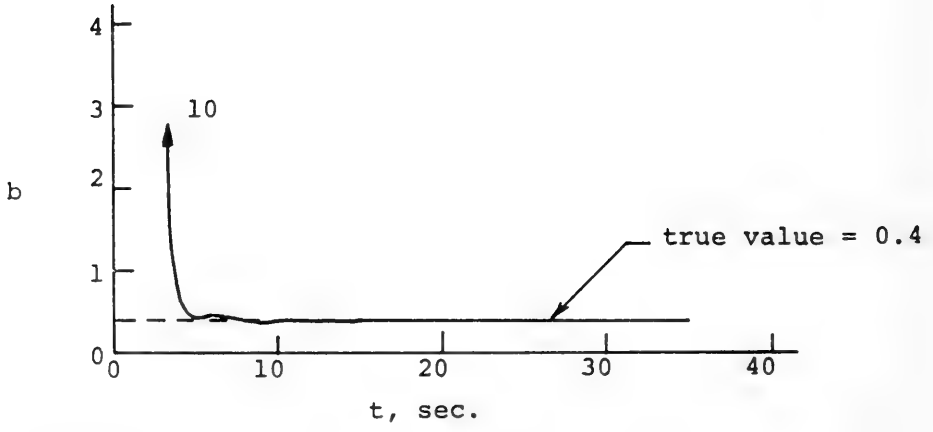

Figure 2. Estimation of parameters in second order system, transient response.

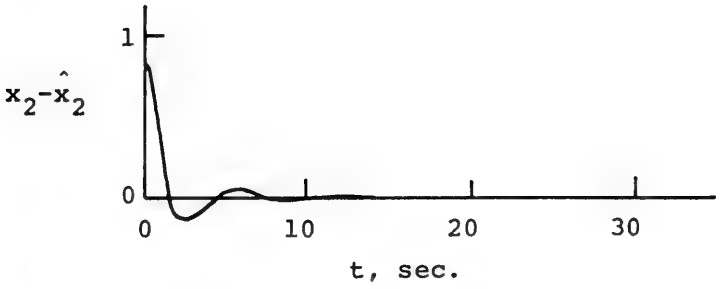

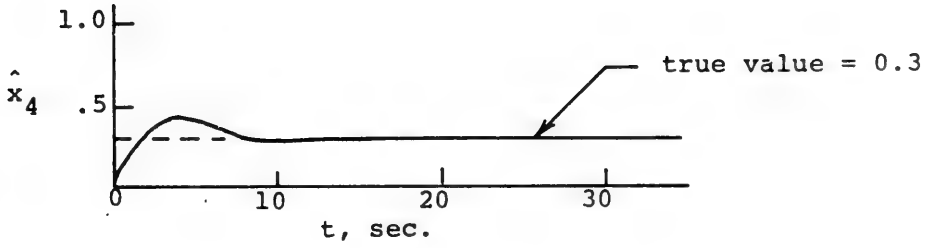

Figure 3. Estimation of state and unknown parameter for third order system, transient response.

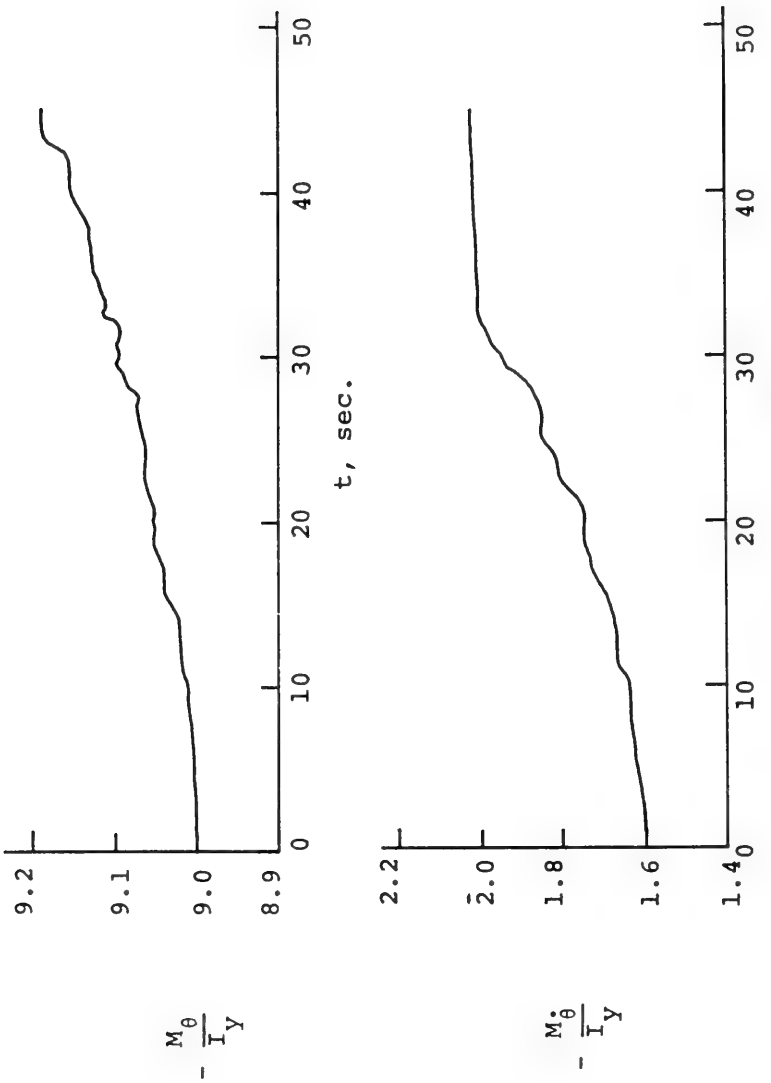

Figure 4 Estimates of stability derivatives for pitch motion for SES craft ; $\dot\theta$ θ z , z measured.

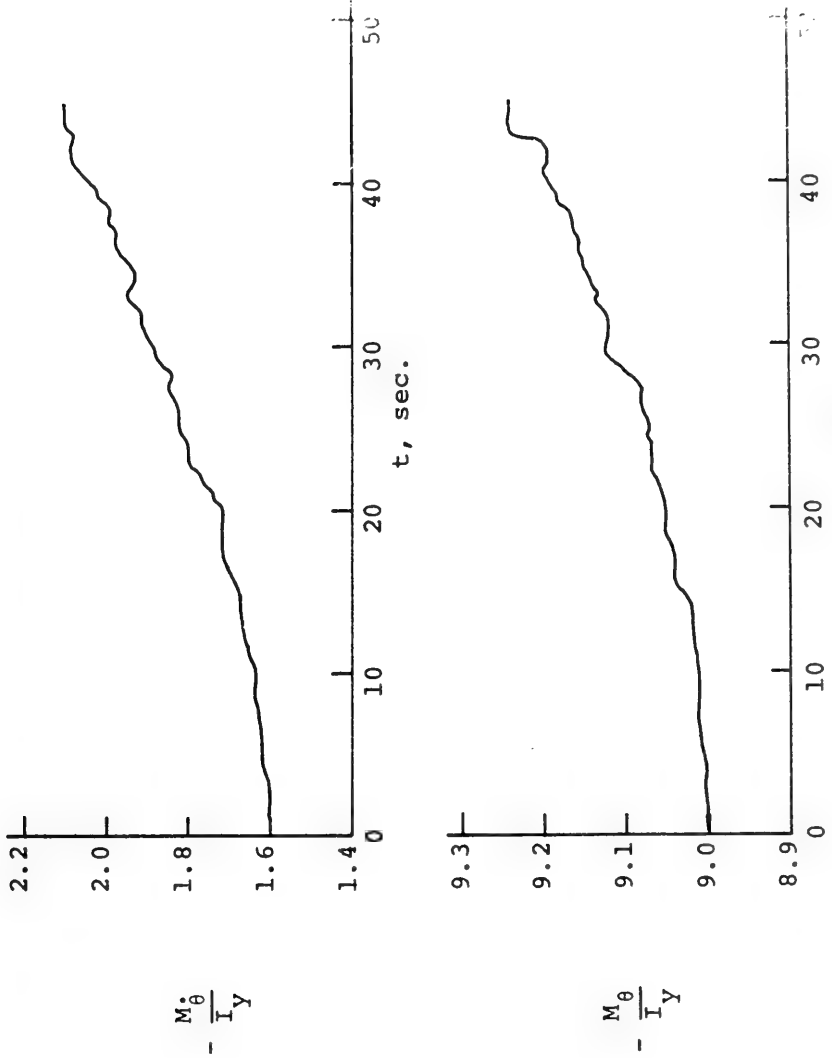

Figure 5. Estimates of stability derivatives for pitch motion for SES craft ; $\dot{\theta}$ and θ measured ; $M_z = M_{\dot{z}} = 0$.

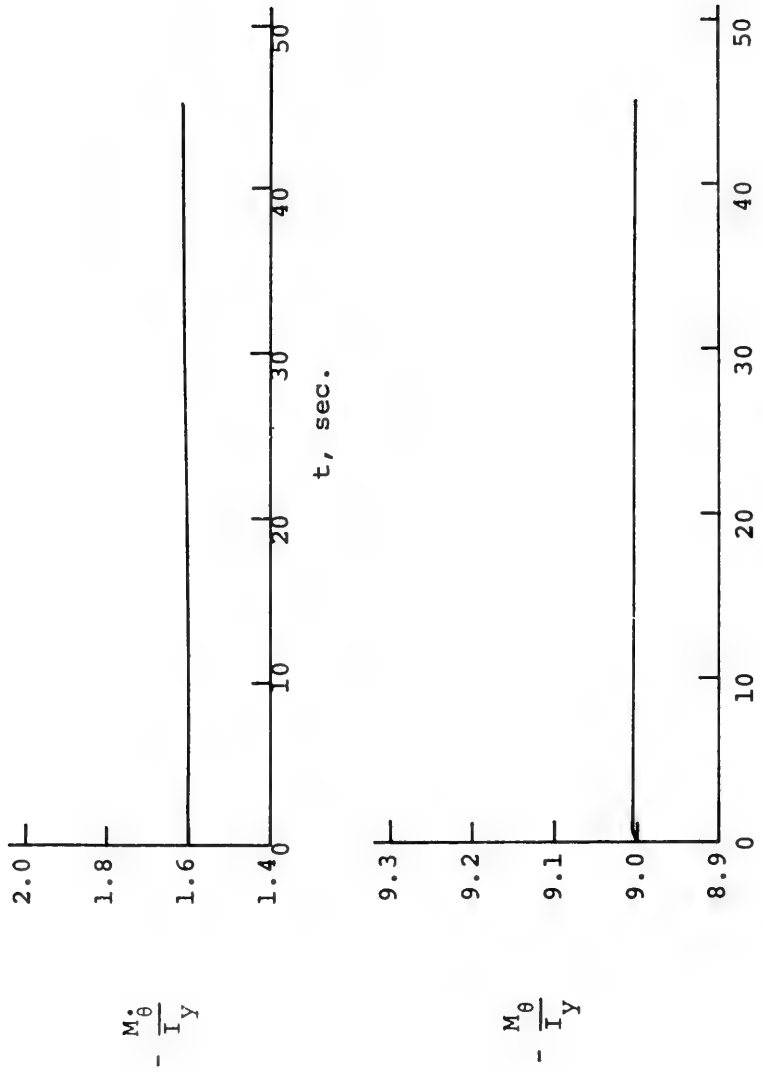

Figure 6 Estimates of stability derivatives for pitch motion for SES craft, θ measured ; $M_z = M_{\dot{z}} = 0$.

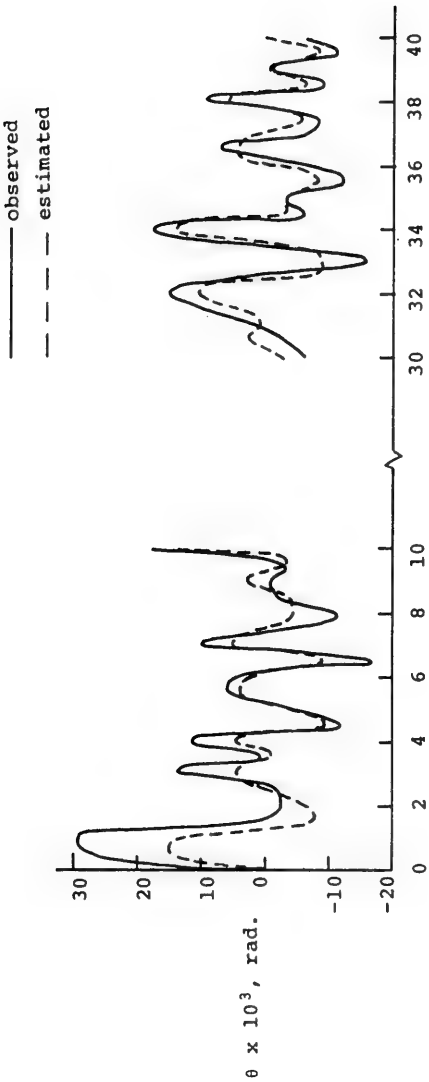

Figure 7 Estimation of pitch angle trajectory for SES craft, using stability derivatives corresponding to conditions in Fig. 6.

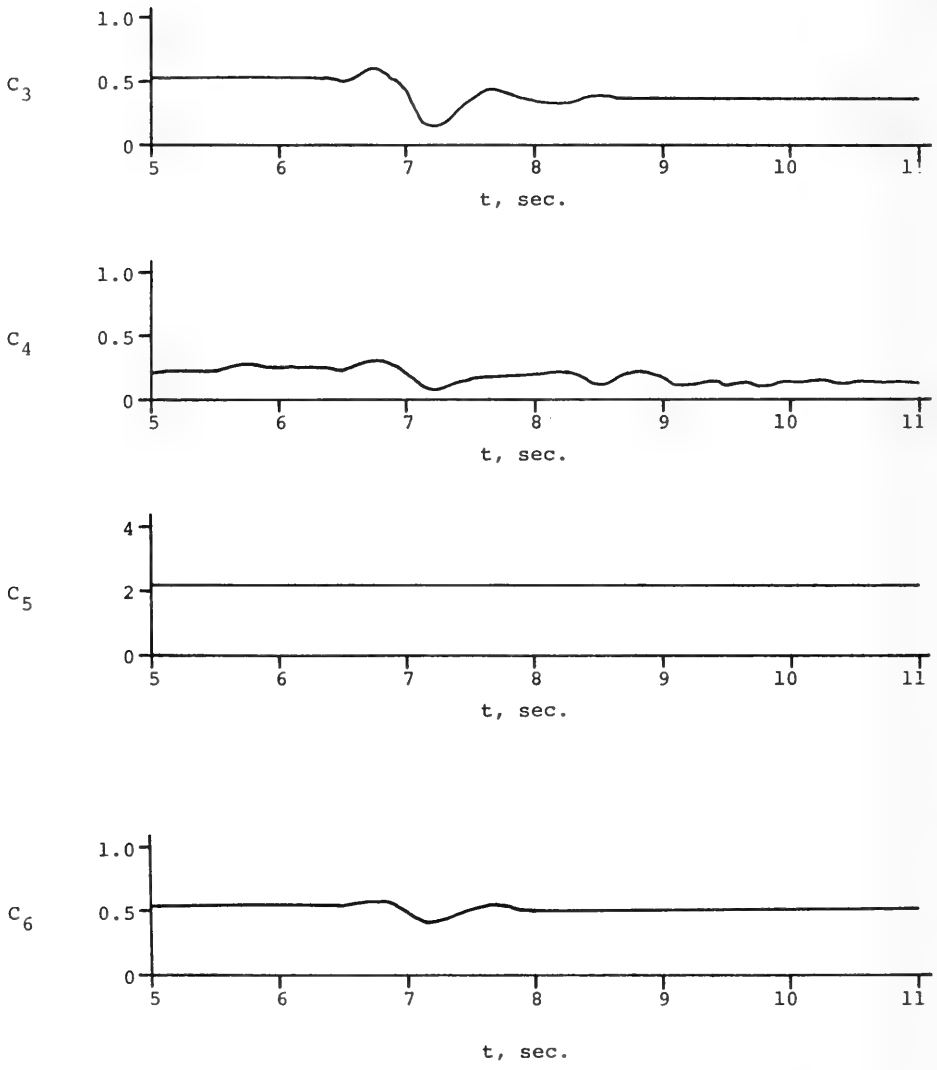

Figure 8 Variation of hydrofoil craft parameter values (as a function of time) from computer generated data.

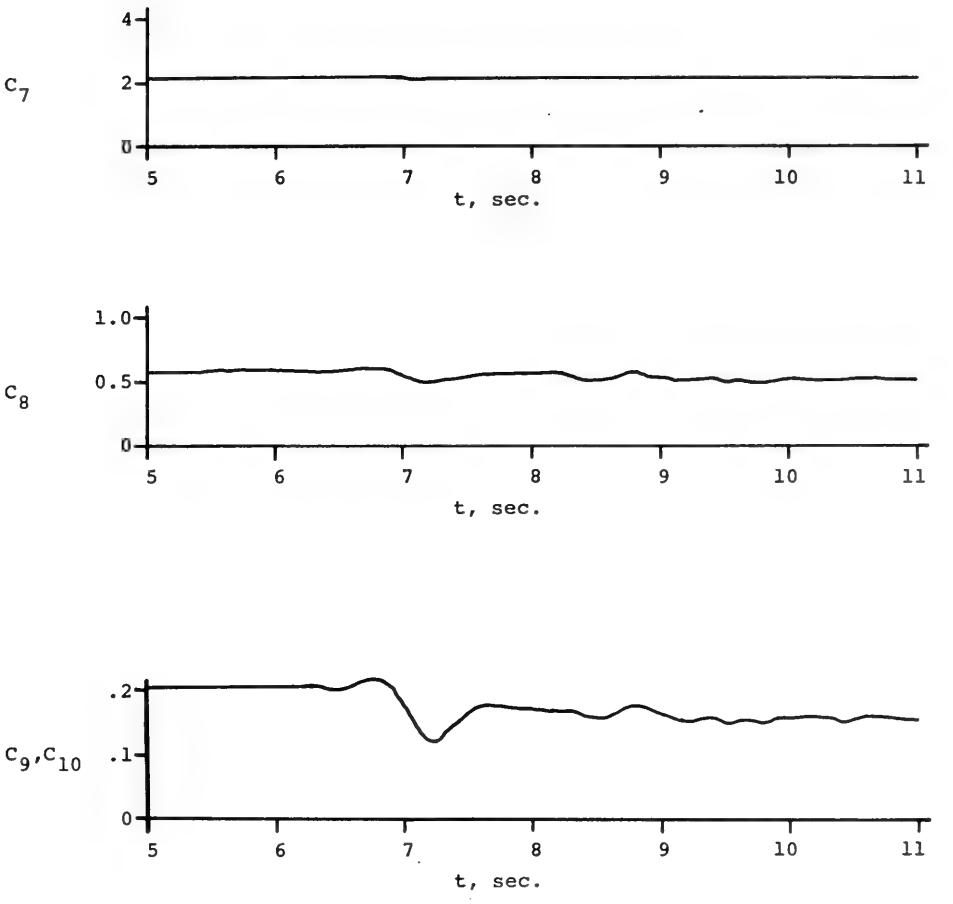

Figure 8 (continued)

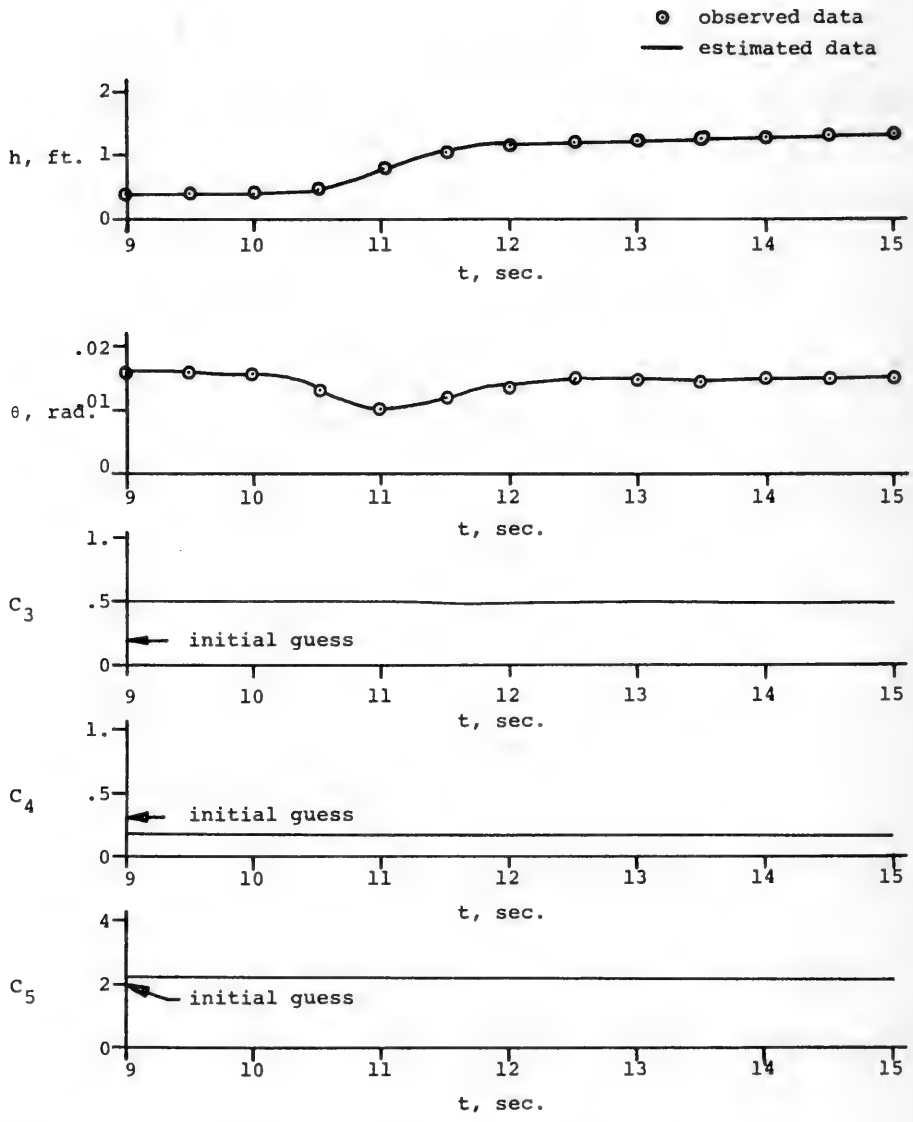

Figure 9 Comparison of trajectories (observed and estimated) and parameters of hydrofoil craft, computer generated data.

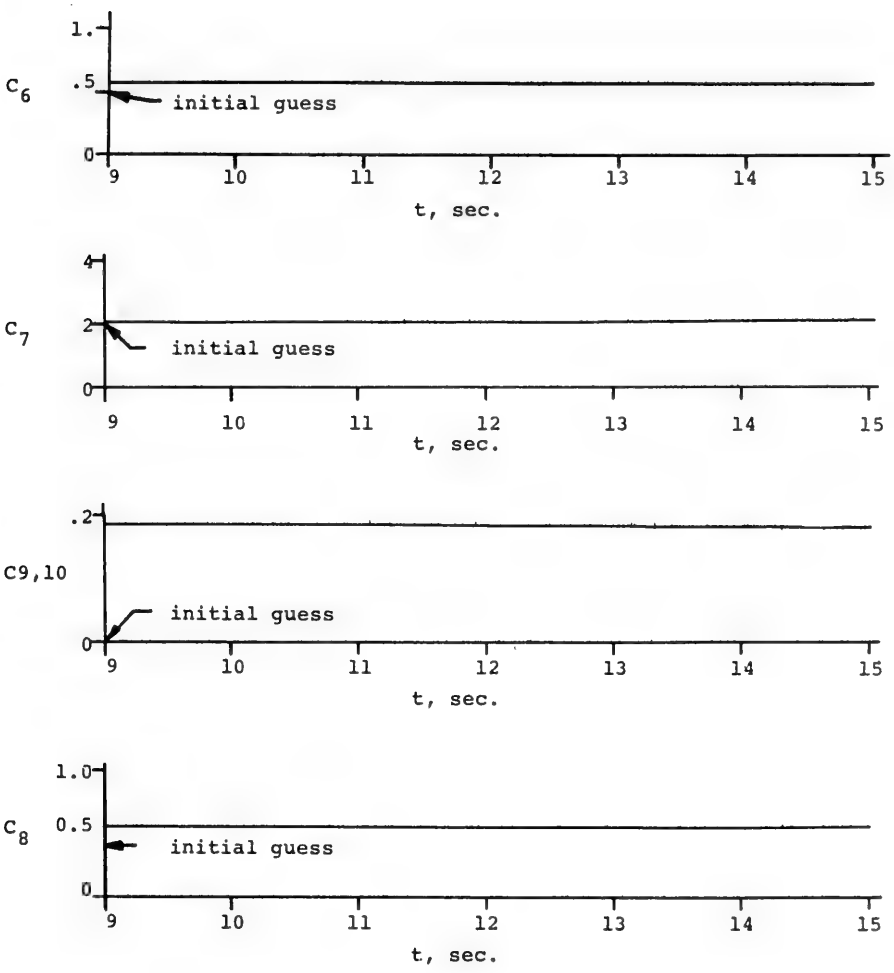

Figure 9 (continued)

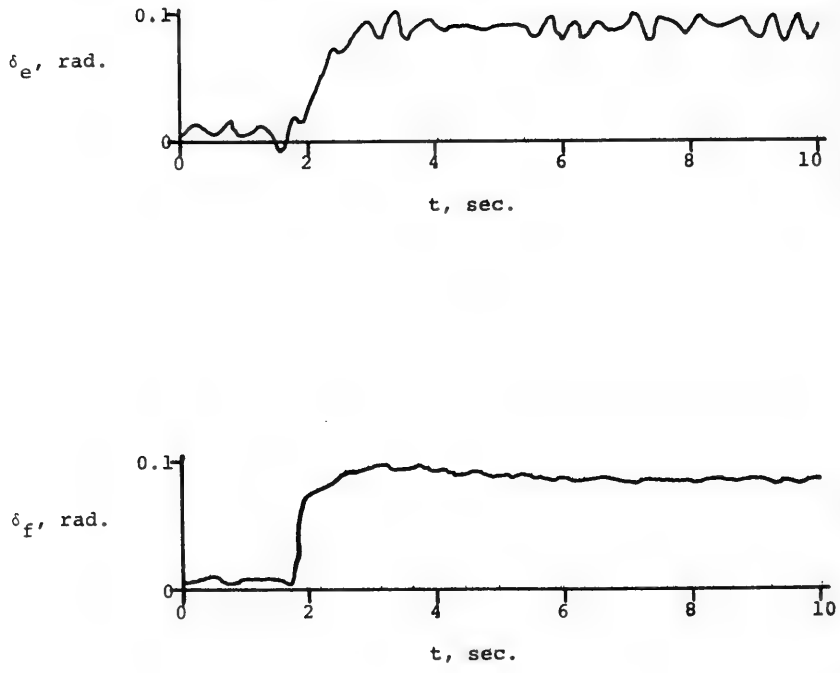

Figure 10 Time histories of hydrofoil control deflections, full scale data.

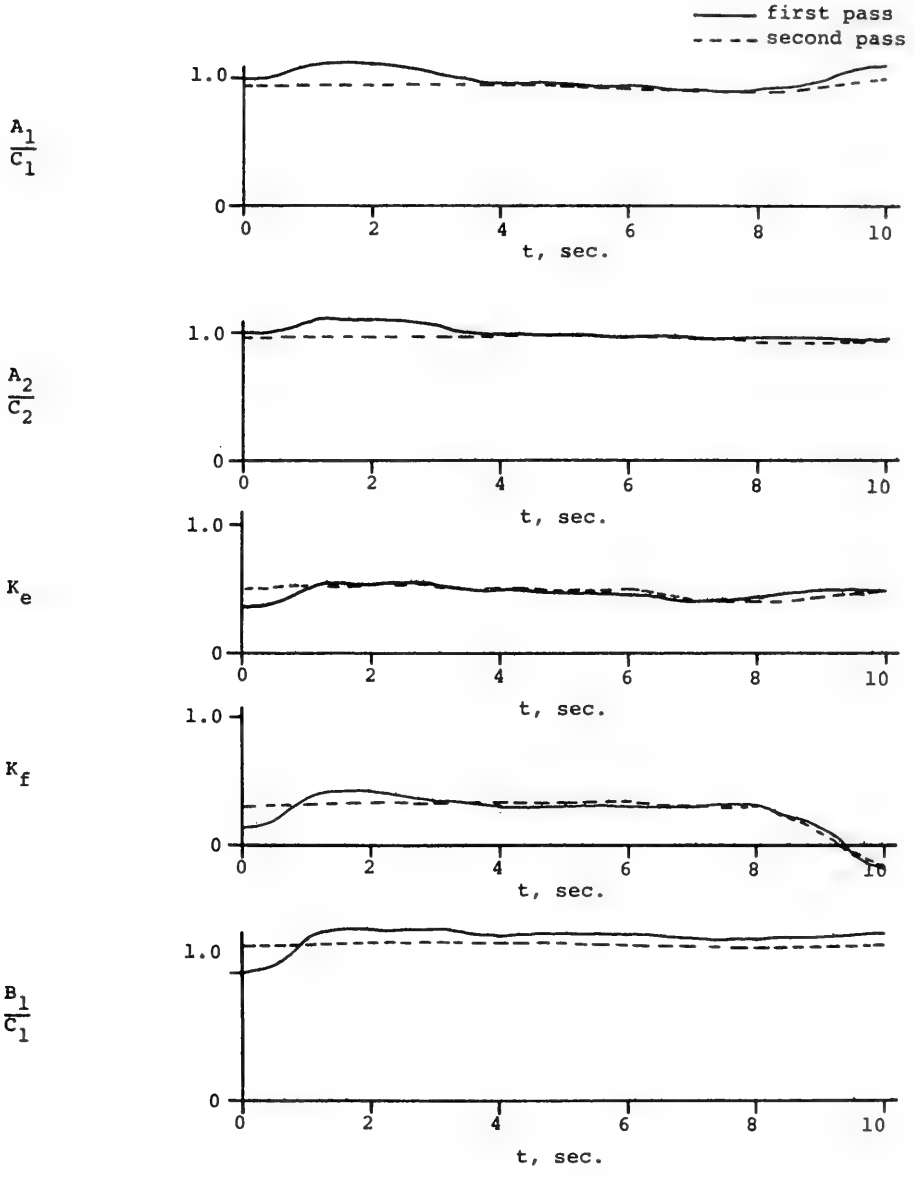

Figure 11 Variation of hydrofoil craft parameters from full scale data, Experiment 1.

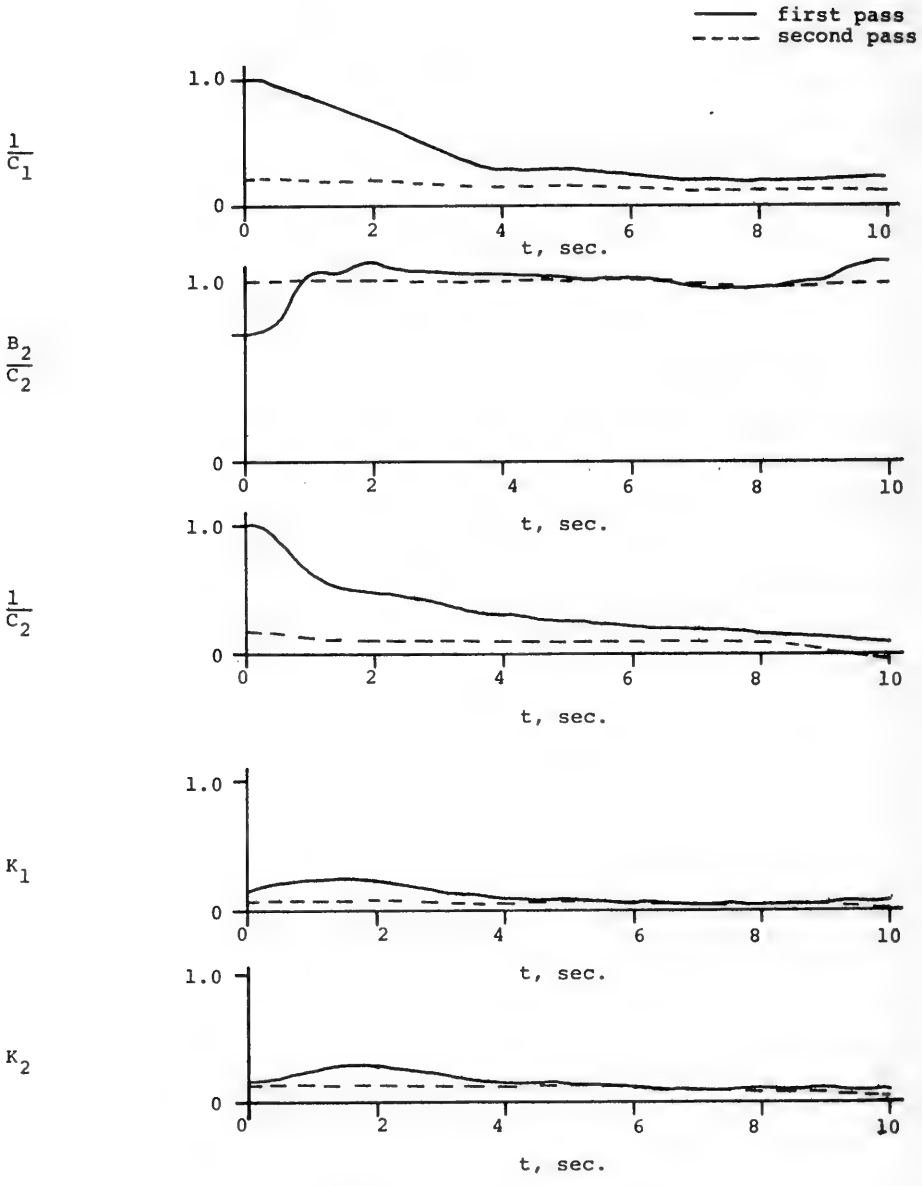

Figure 11 (continued)

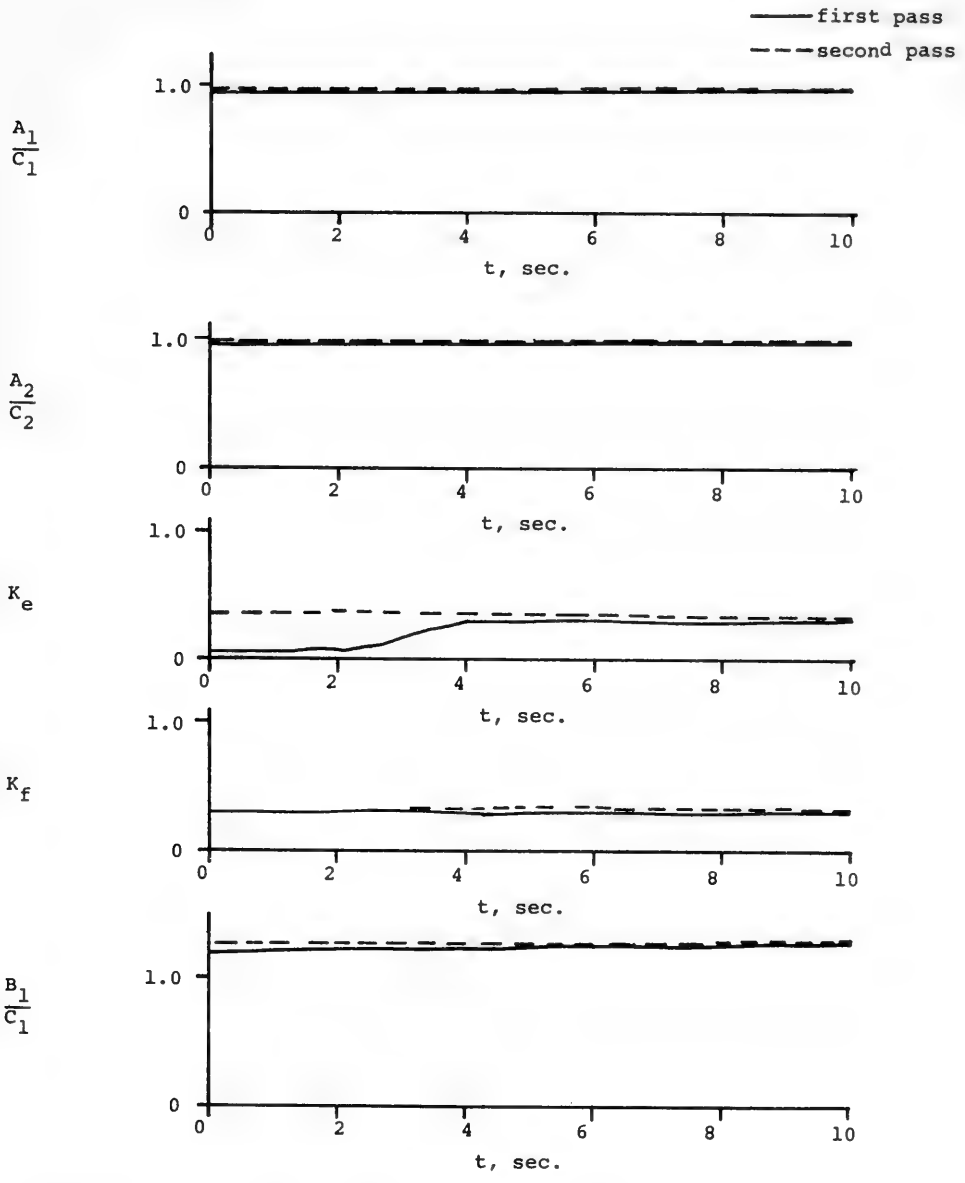

Figure 12 Variation of hydrofoil craft parameters from full scale data, Experiment 4.

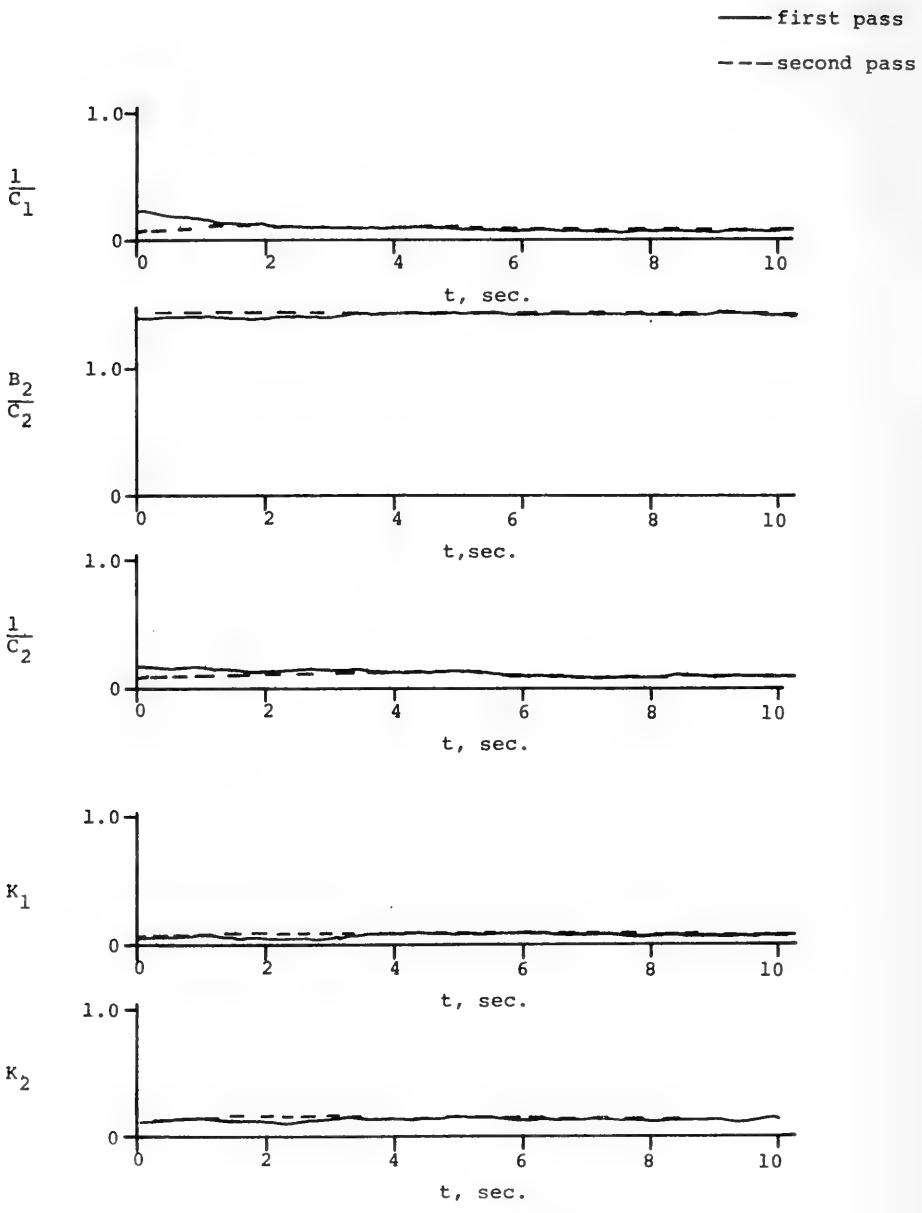

Figure 12 (continued)

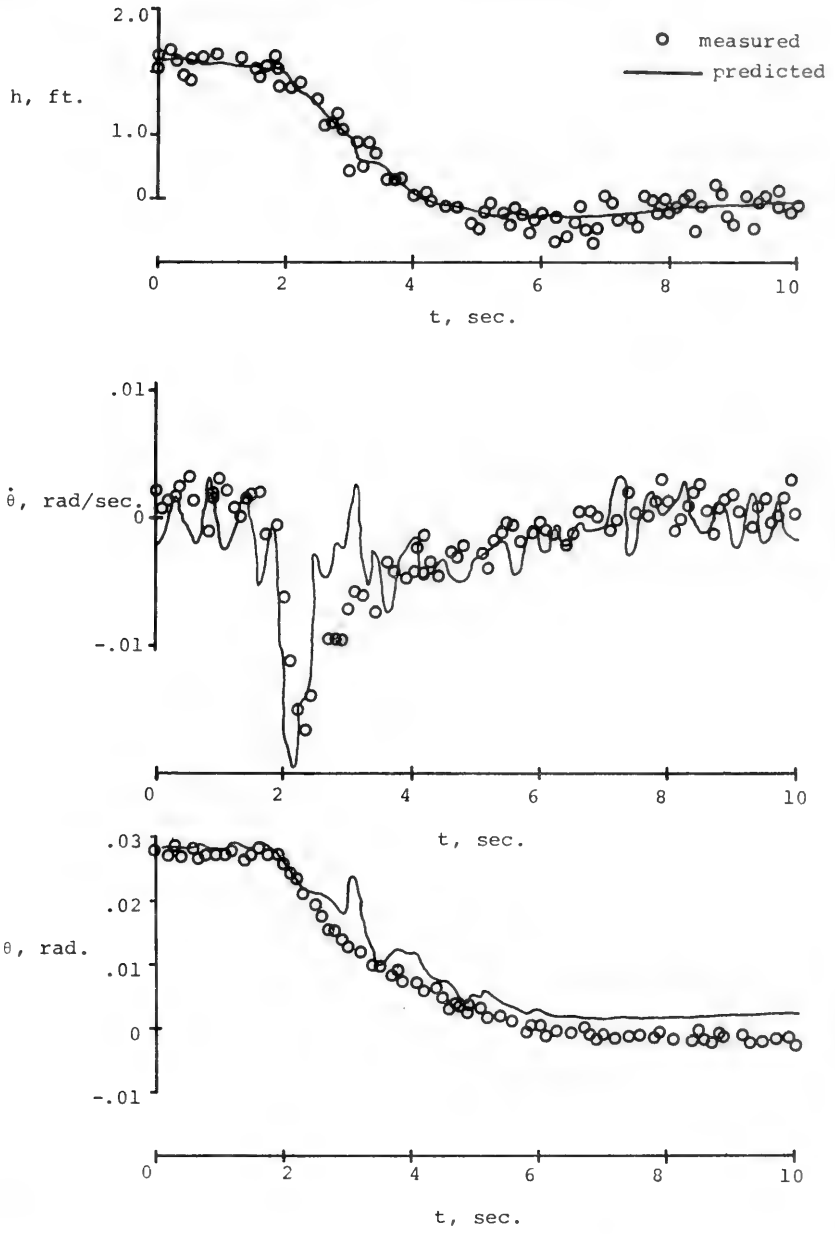

Figure 13 Comparison of measured and predicted trajectories using estimated parameters for hydrofoil craft, full scale data, Experiment 4.

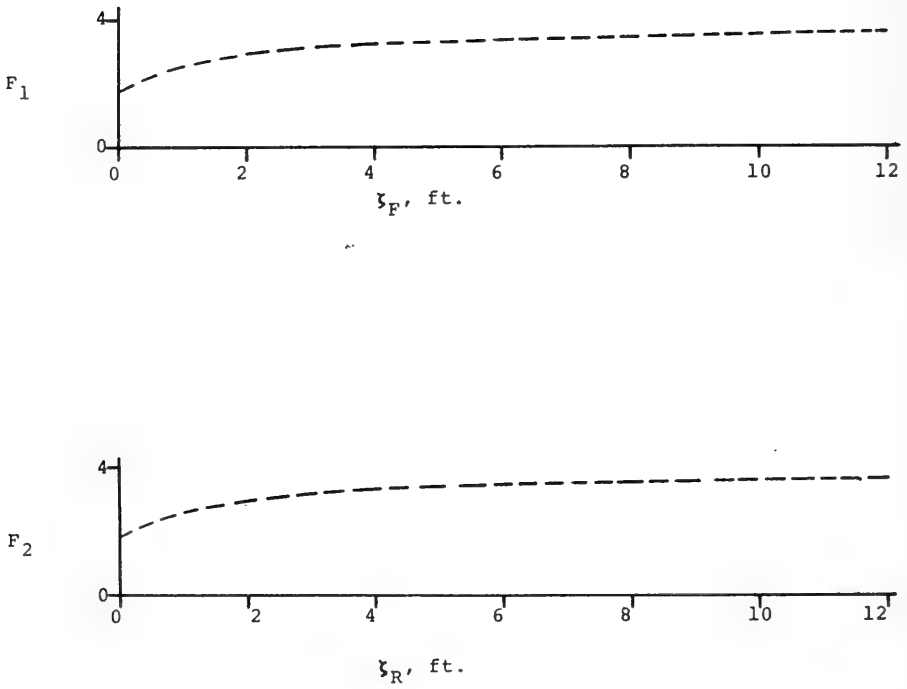

Figure 14 Depth dependence functions for hydrofoil craft lift forces identified from computer generated data.

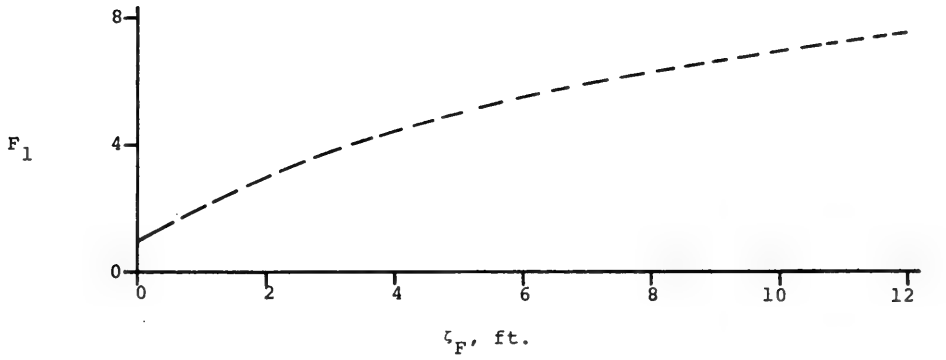

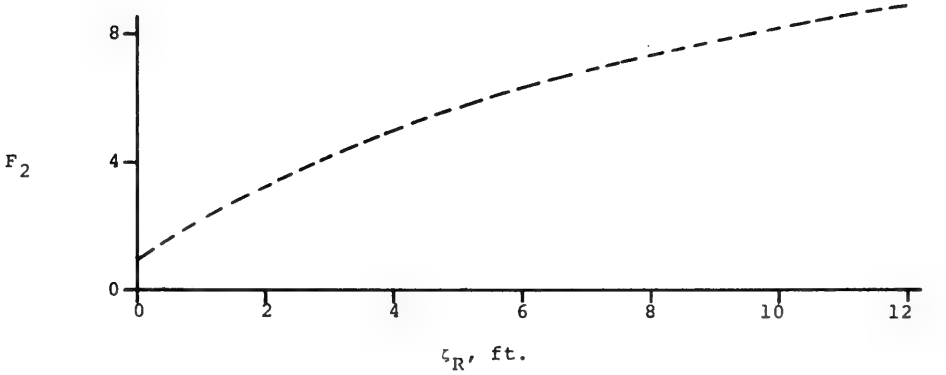

Figure 15 Depth dependence functions for hydrofoil craft lift forces identified from full scale data.

DISCUSSION

D.S. Blacklock
Hydrofin
West Chiltington, Sussex, U.K.

Mr. Christopher Hook, the inventor of the hydrofin had to leave two days ago for England, but he has two friends in this gathering, Professor Weinblum and Dr. Saint-Denis and I think another gentleman was to have come here, Dr. Todd. They all helped Mr. Hook in 1951 after he had shown the Red Bug hydrofoil at New York Boat Show. Hook believes in trying to learn through the seat of his pants : ever since 1944 when he converted a scrap cockpit he has been risking his life on hydrofoils with stability devices, and for this he deserves a great deal of credit. It is now thirty years since his 3-ft hydrofin was tested in the sea near Simonstown Naval Base but with the growing importance of Oceanology there is still time for the superiority of his design to be recognised and for large-scale construction to be undertaken by France, America and ourselves.

The paper which we have just been listening to could be entitled "Out of the test-tank and into the computer". I wonder whether we are better off. Perhaps what we tend to do is to be so dazzled that we fail to notice the paramount criterion, parameter or coefficient, viz. "low-g stability". The other eleven factors discovered by the authors (or nine factors for their hydrofoil) are irrelevant. What we are trying to design is a stabilising homeostatic device, something that is stable in spite of speed. If now we invert the criterion of stability we have one of the two components of a sensible unit for costing sea-transport, K/G for "knots over g-rating". What we hope to provide is a service, say ton-miles, where one ton provides space for three passengers, but people pay not only for a service to get across the Channel, la Manche, but also for speed, and speed in rough weather, and comfort in rough weather. Garbage IN, garbage OUT and we cannot afford to build surface-skimmers on bad criteria. Criteria and costing are very important, if you are trying to be commercial. Yet another criterion is the smallness of the craft.

This brings to mind the fact that although the Tucumcari gunboat which has just returned from Vietnam is a wonderful device and the films are absolutely superlative, it was so costly and big that there is no commercial hydrofoil in the United States at the present time

(footnote A). There are a dozen surface-piercing foil craft at Hong Kong, mainly made by the Japanese, but no country has a hydrofin for commerce (footnote B).

I realize that my remarks are disjointed and I apologize to the very able Oceanics team. I am myself a statistician and I am enormously impressed by the precision of the authors' predictions. C'est magnifique, but is it what we want ? I am reminded of a paper read to the Royal Statistical Society Journal twenty years ago - and this should should please Professor Telfer - by Barnet Wolf on multi-factor regression analysis. He called it the add-a-variant system for he added a factor at a time and tested for significance. Does the added factor improve your predicting of the criterion you are really interested in-namely, stability at speed ? If not, and if you carry on this testing of possible factors, you will end up with a sensible regression equation, having 5 or 6 inputs. Another method is to confine attention to a single factor with a sequence of observed values over time. We cannot afford to have clutter. We just simplify the problem and predict, whether by multi-factor regression or by auto-regression (footnote C).

If I may have one more minute I should like to say that after I had used my firm, Plasticol, Ltd., to exhibit the hydrofin in London in January 1969 our Centre of Industrial Innovation at Strathclyde University decided to do a computer study as advocated by the Oceanics Team. The report ran to 66 pages and cost £ 10,000, but it did not produce the low-cost sea-transport. There was no man willing to risk his money in producing hydrofoils for the British Navy or for anyone else. So we turned in desperation to the Daily Express, whose

---

A. The authors do not name their hydrofoil, but Mr Kaplan told me it was the (naval) Plainview of Grumman-Lockheed ; this craft has now joined the costly ladder-type hydrofoils of the Canadian Navy in retirement.

B. My prepared comments had been handed to the Chairman, but they did refer to the re-designing of hydrofin by Cox & Gibbs in 1952, with sonic sensers, for the US Navy. Mr Hook has been asked to describe the system at the January 1972 Symposium of the Aero-Space Corporation, Los Angeles.

C. Auto-regression includes the Box Jenkins formula and my own, Orthodiction, with its freedom from swings with runs of errors in prediction sharing the same sign.

reporter is here, and they found a school in Devon with 20 boys and for the sum of £ 500 they have built a 24-foot sailing hydrofin which in my opinion will win the £ 2,000 race next month financed by Player's cigarettes (footnote D). I am sorry if I have been advertising and I realize now that I have. Would you please edit my remarks before they appear in the Journal.

DISCUSSION

Peter T. Fink
University of New South Wales
Australia

It is, of course, marvellous to have a transfer of an advanced control technology concept into this field and obviously a lot of success has been achieved. What we are dealing with seems to be a very sophisticated kind of curve fitting and I wonder if Mr Kaplan is aware of one thing that was mentioned at the IUTAM meeting on manoeuvrability and control in London in April. After a discussion of a very impressive Ph.D. thesis from MIT by Lt. Hayes of the United States Navy, in which he was adapting similar concepts to the evaluation of a vast number of coefficients describing a deep submergence rescue vehicle, and I think pretty successfully, the discussion after that by Mr Nils Norbin of Sweden revealed something which I found very disturbing and which I think must have a bearing on this sort of game as well. He was discussing the question of what sort of law to fit to a yaw rate rudder response curve, say y as a function of x and he took first of all the sum of a linear term, with an x modulus x^2 term. Then he did it again taking a linear term with a different coefficient, plus an $x3$ term. He achieved very nice coincidence of the experimental points with both of these curves, but in one case the linear coefficient was 50 per cent different from that obtained for the other case! So it looks to me as if a very great deal depended on just how you chose these powers, and when you get to much more sophisticated systems like those Mr Kaplan deals with, it must be much harder to

---

D. I was wrong but only because the British entrepreneur had to make do with existing moulds for the floats. The British climate is inimicable to the private entrepreneur.

make the intelligent engineering decisions that he is calling for. It would be interesting to have his comments on that.

REPLY TO DISCUSSION

Paul Kaplan
Oceanics Inc.
New York, U.S.A.

A number of points are raised by Mr Blacklock. With regard to the particular case of a hydrofoil craft, the design of a control system for such a craft is a function of the basic dynamics of that craft, which differs from that for a surface ship, a submarine or an SES craft. This difference is manifested by finding what are the basic dynamics of the vehicle and then using that information to guide the application of particular sensor outputs to provide commands to the control. This is most often done nowadays for very complex systems by means of computer simulation, and certainly well before actual experiments with the vehicle at sea.

The procedure in this paper is not in any way to be considered as statistical. What we are doing here is applying something that is independent of actual statistics but functions within the domain of randomness, which represents the real situation. We are finding values of the coefficients that are supposed to be invariant for a vehicle throughout the whole range of maneuvers or motions that it will experience. This is a way of dealing with full scale dynamics, which is really another method of replacing getting data from a towing tank under controlled tests. When you go to sea how is one to find out what the numerical values of the coefficients are ? All you have is a resulting trajectory for which there are a lot of possible ways that one can "fit" some representation to. However there is something that is unique and invariant which must be close to what is being measured in the tank in order to allow an analyst to structure a representation of the original system. That is a feature of this method, since it brings you to that point of comparison with model test data as well as the effective values of the coefficients representing the full scale craft dynamics.

The next point is in regard to Dr Fink's comments. There are a number of features of the work of Lt Hayes that are somewhat si-

milar to our own results, although the particular cases considered for illustration are different in each paper. There is a problem which has not been mentioned and emphasized in any evaluation of coefficients using system identification. This is concerned with the time required for obtaining convergent values of the coefficients, which in the case of the hydrofoil craft required computation time 22 times as long as real time (of the trajectory time history) in order to determine these values. We had 14 state variables, including the coefficients, and since computation time increases as the cube of the number of state variables in your system, too many coefficients in a representation will involve a tremendous computational effort. Thus the simplest possible representation of a dynamic system is necessary when carrying out system identification, as well as any simulation work, as long as the major features of the craft dynamics are adequately represented.

With regard to the aspect of fitting the curve that Mr Norrbin presented, I am fully aware of the paper wherein he presented these results, since I have seen it and also looked into the same question. The real issue of importance is not the value of the linear coefficient that is obtained by using different representations (for the nonlinear portion of the force) in the mathematical form used to express the force. The major point is how well the overall representation fits the total measurement of the force, and most important of all how well whatever mathematical formulation you use for the hydrodynamic forces and moments results in matching the trajectory of the vehicle under varied motions and maneuvers. Thus it is easy to see that there is more than one mathematical form that can represent any set of data, with different coefficients associated with different powers of the variables, and the particular choice may be dictated by considerations of formulation, ease of manipulation and subsequent evaluation, etc. I hope that this answers your question.

* * *

FRONTIER PROBLEMS

Friday, August 25, 1972

Afternoon Session

Chairman : Dr. P.G. Maioli
Vasca Navale, Roma, Italy

NON-LINEAR SHIP WAVE THEORY

Gedeon Dagan
Technion Haifa, and Hydronautics Ltd
Rechovoth, Israel

ABSTRACT

Systematic attempts to extend ship wave theory into the non-linear range are described. The basic derivations are carried out for two-dimensional flows and the bearing of the results on corresponding ship wavemaking problems is discussed. The main topics are : (i) the derivation of the second order wave resistance for a body generated by an arbitrary distribution of sources, (ii) the wave resistance at low Froude numbers. A uniform solution, valid at low speeds, is for the first time presented and (iii) a few preliminary experimental results on the bow breaking wave.

I - INTRODUCTION

The linearization of the problem of free surface gravity flow past a ship body has (unlike the equivalent aerodynamical problem) a two-fold effect : not only the body boundary condition is simplified, but also the free surface boundary condition is linearized. Although these two simplifications are associated with the same first order term in a perturbation expansion in which the uniform flow is the zero order leading term, the mathematical difficulties associated with the nonlinearity of each one are quite different. It is relatively easy with the present large computers to derive a solution which satisfies the boundary condition of zero normal velocity on the hull body. It is extremely difficult, if not impossible, to satisfy the non-linear free surface condition, even by numerical approaches. It is no wonder, therefore, that effort has been spent in the last years for solving the flow past ship like bodies, while keeping the free surface condition in its linearized version (the so called Neumann - Kelvin problem). The aim of such studies was to determine the range of

validity of the usual linearized solutions and to improve them, when necessary. This way it was hoped that a better agreement between theory and experiment could be achieved.

The present work is dedicated mainly to the influence of the nonlinearity of the free-surface conditions on the wave resistance. Since at this stage we are interested in elucidating problems of principle and basic concepts, we have carried out the derivations for two-dimensional flows. Two-dimensional solutions are obtained much easier than the three-dimensional ones due to the use of the powerful tool of analytical functions. They permit to find in a simple way quick answers for problems which in three dimensions need a tedious numerical treatment. It is realized, however, that the final conclusions about the applicability of the results derived here to flow past ships could be drawn only after their extension to three dimensions. We consider, nevertheless, at each stage of the present study, the implications of the results to associated ship problems.

II - THIN BODY EXPANSION.

II . 1 - General.

We consider an inviscid two-dimensional flow past a submerged body (fig. 5a). Let $z' = x' + iy'$ be a complex variable, $f' = \phi' + i\psi'$ the complex potential and $w' = u' - iv' = df'/dz'$ the complex velocity. We limit our considerations to a symmetrical body parallel to the unperturbed free surface : h'_c is its submergence depth, $2L'$ its length and $2T'$ the maximum thickness. With U' the velocity of uniform flow far upstream, we make variables dimensionless as follows :

$$x = x'/L' \quad , \quad y = y'/L' \quad , \quad z = z'/L' \quad , \quad w = u - iv = w'/U' \quad , \eta = \eta'/L'$$

$$f = \phi + i\psi = f'/U'L' \quad , \quad h = h'_c/L' \quad , \quad \epsilon = T'/L' \quad , \quad F = U'/(gL')^{1/2}$$

$$F_n = U'/(2gL')^{1/2} \qquad (1)$$

η' being the free surface elevation above $y' = 0$.

The exact boundary conditions satisfied by $w(z)$, which is analytical in the flow domain $y \leqslant \eta(x)$, given here for convenience of reference, are as follows

$$\left.\begin{aligned} &\mathrm{Im}\left[iF^2\,(\bar{w})^2\,\frac{dw}{dz} - w\right] = 0 \\ &\mathrm{Im}\,\bar{w}dz = 0 \end{aligned}\right\} \quad (y = \eta) \qquad (2),\ (3)$$

$$u \to 1 \qquad (x \to -\infty) \qquad (4)$$

$$\mathrm{Im}\,\bar{w}dz = 0 \qquad (|x|<1,\ y = \pm\epsilon t(x)) \qquad (5)$$

where $t(x) = t' / T'$ is the dimensionless thickness distribution and $\bar{w} = u + iv$.

For a given body shape w depends on z, ϵ, h and F. We consider now a "thin body expansion", i.e. an expansion of w for $\epsilon = o(1)$ and F, $h = 0(1)$. This is the basic linearization procedure used in ship wave resitance theory.

Hence, with

$$w(z, \epsilon, F, h) = 1 + \epsilon w_1(z, F, h) + \epsilon^2 w_2(z, F, h) + \ldots$$

$$f(z, \epsilon, F, h) = z + \epsilon f_1(z, F, h) + \epsilon^2 f_2(z, F, h) + \ldots$$

$$\eta(x, \epsilon, F, h) = \epsilon \eta_1(x, F, h) + \epsilon^2 \eta_2(x, F, h) + \ldots \qquad (6)$$

the free surface (2), (3), radiation (4) and body boundary condition (5) become at first and second order

$$\left.\begin{aligned} &\mathrm{Im}\left(iF^2\,\frac{df_1}{dz} - f_1\right) = p_1(x) = 0 \qquad (7) \\ &\eta_1 = -\psi_1 \qquad (8) \end{aligned}\right\} \quad (y = 0)$$

$$f_1 \to 0 \qquad (x \to -\infty) \qquad (9)$$

$$\psi_1 = \pm t \qquad (|x|<1,\ y = -h \pm 0) \qquad (10)$$

$$\left.\begin{aligned} &\mathrm{Im}\left(iF^2\,\frac{df_2}{dz} - f_2\right) = p_2(x) = -\frac{F^2}{2}\left[3(u_1)^2 + (v_1)^2\right] + u_1 v_{1,x} \qquad (11) \\ &\eta_2 = \frac{1}{F^2}(\eta_1)^2 - \psi_2 \qquad (12) \end{aligned}\right\} \quad (y=0)$$

$$f_2 \to 0 \qquad (x \to -\infty) \tag{13}$$

$$\psi_2 = \pm u_1 t \qquad (|x| < 1,\ y = -h \pm 0) \tag{14}$$

Equations (7) - (14) have been written, after a simple integration, in terms of f_1 , f_2 rather than w_1 , w_2 (the derivation may be found, for instance, in Wehausen & Laitone, 1965).

The main purpose of this section is to derive the second order solution f_2 , and the associated wave resistance, with application to a few particular shapes.

Such computations have been carried out previously by Tuck (1964) for a submerged cylinder and Salvesen (1969) for a submerged hydrofoil. The subsequent developments in this section are a continuation of their work. The cylinder is an extremely blunt shape whose three dimensional counterpart is a sphere. In the case of the hydrofoil it was found that a major nonlinear contribution comes from the vorticity associated with the Kutta-Joukovsky condition. We have been interested to extend the previous computations to the case of elongated two-dimensional bodies ressembling ships and we have also considered only the contribution of thickness, since the trailing edge condition has no direct counterpart in three dimensions. In contrast with the previous works, we have been able to derive f_2 in a closed analytical form and we are inclined to believe that the method employed here may be efficiently used in three dimensional cases.

To obtain simple results we replace the body by a distribution of an arbitrary number n of discrete sources of strength q'_j , located at $z'_j = x'_j - ih'$ $(j = 1, \ldots, n)$ (fig. 1). Under this scheme the two boundary conditions (10) and (14) become

$$f = z + \epsilon \left[\frac{\epsilon_j}{2\pi} \ln(z - z_j) \right] + 0(\epsilon^3) \qquad |z - z_j| = \epsilon \epsilon_j \tag{15}$$

where $\epsilon_j = q'_j / U'T' = 2 \Delta t'_j / T' = 2 \Delta t_j$ is the change of the relative thickness at z_j . Obviously, by (15) the actual body is replaced by one undergoing abrupt thickness changes at each source, but by taking the spacing $x_{j+1} - x_j$ sufficiently small in the portions of steep variation of t , we can achieve any desired accuracy. Again, in view of our interest in three dimensional applications, we do not take into account the trailing edge Kutta-Joukovsky condition. Our problem reduces, therefore, in determining f_1 and f_2 , subject to (7), (9), (11), (13) and (15). The profile of the far free waves is

obtained subsequently from (8) and (12) with x

II . 2 - Solution for two Sources.

We derive now f_1^{jk} and f_2^{jk} , the potentials related to the flow past two sources of strengh ϵ_j , ϵ_K at $z_j = x_j - ih$, $z_K = x_K - ih$ respectively. The advantage of the body discretization is the easy extension of the solution for $n = 2$ to any other n . The first order solution is given (Wehausen and Laitone 1965) by

$$f_{1,jk} = \frac{\epsilon_j}{2\pi} \ln (z - z_j) + \frac{\epsilon_k}{2\pi} \ln (z - z_k) - \frac{\epsilon_j}{2\pi} \ln (z - z_j - 2ih) +$$

$$+ \frac{\epsilon_k}{2\pi} \ln (z - z_k - 2ih) - \frac{\epsilon_j}{2} \omega\left(\frac{z - z_j - 2ih}{F^2}\right) -$$

$$- \frac{\epsilon_k}{2\pi} \omega\left(\frac{z - z_k - 2ih}{F^2}\right) \qquad (16)$$

The function $\omega(\zeta)$ is defined as

$$\omega(\zeta) = \alpha + i\beta = e^{-i\zeta} \; \overline{Ei}(i\zeta) = e^{-i\zeta} \int_{-\infty}^{\zeta} (e^{i\lambda}/\lambda) \, d\lambda \qquad (17)$$

where the λ plane is cut along the real negative axis and the integration is carried out below the cut, such that (9) is satified.

The equation of the far downstream wave is obtained from the ω terms of (16), by the residue in (17), as follows

$$\eta_{1,jk} = -\psi_{1,jk}(x, 0) = 2 e^{-h/F^2} \cdot$$

$$\cdot \left[\left(\epsilon_j \cos \frac{x_j}{F^2} + \epsilon_k \cos \frac{x_k}{F^2} \right) \cos \frac{x}{F^2} + \right.$$

$$\left. + \left(\epsilon_j \sin \frac{x_j}{F^2} + \epsilon_k \sin \frac{x_k}{F^2} \right) \sin \frac{x}{F^2} \right] \qquad (x \to \infty) \qquad (18)$$

The second order potential is now split into two parts $f_{2,jk} = f^b_{2,jk} + f^s_{2,jk}$ where $f^b_{2,jk}$ is the body correction with the free surface condition kept in its homogeneous form (7) and $f^s_{2,jk}$ is the free surface correction related to the linearized pressure $p_{2,jk}$ of (11) in the absence of the body.

We begin with the body correction. To satisfy (15) we have to cancel arround the source j, on $|z - z_j| = \epsilon\epsilon_j$, the velocities induced at z_j by the first order terms of (16), excepting the first term representing the source itself. In other words we require $w^*_j = (df_{1,jk}/dz) - [\epsilon_j \ln(z - z_j)/2\pi] \to 0$ for $|z - z_j| = \epsilon\epsilon_j$. To satisfy this requirement at second order we have to superimpose a source of strength $\epsilon^2 \epsilon_j u^*_j(x_j, -h)$ to the original source of strength $\epsilon\epsilon_j$ and also a vertical doublet of strength $-\epsilon^3 \epsilon_j v^*_j(x_j, -h)$. Since we consider only second order terms, we disregard the vertical doublets which contribute only at third order. Adding the appropriate sources at z_j and z_k and carrying out the computations (for details see Dagan, 1972a) we obtain finally, for the second order streamfunction far downstream, the following expression

$$\psi^b_{2,jk}(x, 0) = \mathrm{Im}\, e^{-ix/F^2} \{(\epsilon_j^2 e^{ix_j/F^2} + \epsilon_k^2 e^{ix_k/F^2}) iB^b + \epsilon_j \epsilon_k [(e^{ix_j/F^2} - e^{ix_k/F^2}) i E^b_{jk} + e^{ix_k/F^2} i I^b_{jk}]\} \qquad (x \to \infty) \qquad (19)$$

where

$$B^b = 2e^{-3h/F^2}$$

$$E^b_{jk} = \frac{e^{-h/F^2}}{\pi} \left[\frac{4h^2}{\ell_{jk}(F^2\ell^2_{jk} + 4h^2)} + 2\beta\left(-\ell_{jk} - \frac{2h}{F^2}\right)\right]$$

$$I^b_{jk} = 4e^{-3h/F^2} \cos\ell_{jk} \qquad (20)$$

In deriving (19) and (20) we have assumed that $k > j$, $x_k > x_j$ and $\ell_{jk} = (x_k - x_j)/F^2 > 0$.

We consider now, the second order free surface correction which results from the linearized pressure $p_2(x)$ in (11), acting on the free surface. In the case of a pair of sources p_2 can be written as follows

$$p_{2,jk} = \frac{\epsilon_j^2}{4\pi^2} \tilde{p}_{jj} + \frac{\epsilon_k^2}{4\pi^2} \tilde{p}_{kk} + \frac{\epsilon_j \epsilon_k}{4\pi^2} \tilde{p}_{jk} \qquad (21)$$

the different terms resulting from the substitution of the real and imaginary parts of $df_{1,jk}/dz$ into the last term of (11). The complex potential of the flow generated by $\tilde{p}_{jk}$, for instance, is (Wehausen and Laitone, 1965)

$$\tilde{f}_{jk} = -\frac{i}{\pi F^2}\int_{-\infty}^{\infty} \tilde{p}_{jk}(s; x_j, x_k, h, F^2)\ \omega\left(\frac{z-s}{F^2}\right) ds \qquad (22)$$

$\tilde{f}_{jj}$ and $\tilde{f}_{kk}$, corresponding to $\tilde{p}_{jj}$ and $\tilde{p}_{kk}$ of (20), respectively, are obtained from $\tilde{f}_{jk}$ by letting $x_j \to x_k$

Carrying out the detailed computations (see Dagan, 1972a) yields for the streamfunction far downstream

$$\psi_{2,jk}(x, 0) = \mathrm{Im}\, e^{-ix/F^2}\{(\epsilon_j^2 e^{ix_j/F^2} + \epsilon_k^2 e^{ix_k/F^2})(A^s + iB^s) +$$

$$+ \epsilon_j \epsilon_k [(e^{ix_j/F^2} + e^{ix_k/F^2}) C^s_{jk} +$$

$$+ (e^{ix_j/F^2} - e^{ix_k/F^2}) iE^s_{jk} + e^{ixk_i}(I^s_{jk} + iK^s_{jk})]\} +$$

$$+ (\epsilon_j^2 + \epsilon_k^2) G^s + \epsilon_j \epsilon_k G^s \cos \ell_j k \qquad (x \to \infty) \quad (23)$$

where

$$A^s = \frac{2}{\pi} e^{-h/F^2}\left[\ell n(2h/F^2) + 0.8272 - 2\alpha(0, -\frac{2h}{F^2}) + \frac{F^2}{4h}\right]$$

$$B^s = 2e^{-h/F^2}(1 + 2e^{-h/F^2})$$

$$C^s_{jk} = \frac{2}{\pi} e^{-h/F^2}\left[\frac{1}{2}\ell n(1+\frac{4h^2}{\ell_{jk}^2}) + \alpha(-\ell_{jk}\ 0) - 2\alpha(-\ell_{jk}\ -\frac{2h}{F^2}) +\right.$$

$$\left. + \frac{h}{\ell_{jk}^2 + 4h^2}\right.$$

$$E^s_{jk} = \frac{2}{\pi} e^{-h} \left[-\tan \frac{2h}{\ell_{jk}} + \beta(-\ell_{jk}, 0) + 2\beta\left(-\ell_{jk}, -\frac{2h}{F^2}\right) + \right.$$

$$\left. + \frac{2h^2}{\ell_{jk}(\ell^2_{jk} + 4h^2)} \right]$$

$$I^s_{jk} = 4\, e^{-h/F^2} (1 + 2e^{-2h}) \cos \ell_{jk}$$

$$K^s_{jk} = 4\, e^{-h/F^2} (-1 + 2e^{-h}) \sin \ell_{jk}$$

$$G^s = -2e^{-2h/F^2} \qquad (24)$$

II . 3 - The Wave Resistance of n Sources.

In the case of n sources (fig. 1) the streamfunction far downstream is obtained from the solution for two sources as a finite sum. If we write for n sources

$$\psi_1 (x, 0) = \psi_1^{cos} \cos x + \psi_1^{sin} \sin x \qquad (x \to \infty)$$

$$\psi_2 (x, 0) = \psi_2^{cos} \cos x + \psi_2^{sin} \sin x + \psi_2^{const} \qquad (x \to \infty) \qquad (25)$$

where ψ_2^{const} results from the last two terms of (23), then the wave resistance at second order (Salvesen, 1969) is given by

$$D = \epsilon^2 D_1 + \epsilon^3 D_2 \qquad (26)$$

with

$$D_1 = \frac{1}{4} \left[(\psi_1^{cos})^2 + (\psi_1^{sin})^2 \right]$$

$$D_2 = \frac{1}{2} \left(\psi_1^{cos} \psi_2^{cos} + \psi_1^{sin} \psi_2^{sin} \right) \qquad (27)$$

where $D = D' / \rho g L'^2$ and D' is the wave drag.

By using the results for two sources, D_1 and D_2 for n sources are found after some manipulations (Dagan, 1972a) as

$$D_1 = e^{-2h/F^2} \sum_{j=1}^{n} \sum_{k=1}^{n} \epsilon_j \epsilon_k \cos \ell_{jk} \tag{28}$$

$$D_2 = D_2^b + D_2^s = -e^{-h/F^2} \{ \sum_{j=1}^{n} \sum_{k=1}^{n} \epsilon_j \epsilon_k^2 [A^s \sin \ell_{jk} + (B^b + B^s) \cos \ell_{jk}] +$$

$$+ \sum_{m=1}^{n} \sum_{j=1}^{n-1} \sum_{k=j+1}^{n} \epsilon_m \epsilon_j \epsilon_k [C_{jk}^s (\sin \ell_{mj} + \sin \ell_{mk}) +$$

$$+ (E_{jk}^b + E_{jk}^s) (\cos \ell_{mj} - \cos \ell_{mk}) + (I_{jk}^b + I_{jk}^s) \cos \ell_{mk} -$$

$$- K_{jk}^s \sin \ell_{mk}] \} \tag{29}$$

D_2^b and D_2^s are obtained in (29) by the selection of the coefficients with the appropriate upper index. All the coefficients are given in an analytical closed form in (20) and (24). (29) permit the computation of the nonlinear wave resistance of a body of arbitrary thickness distribution at any desired accuracy. The function α and β (18) may be taken from the tables in Abramowitz and Stegun (1964), taking into account that $\omega(\zeta) = e^{i\zeta} [2\pi i - E_1(-i\zeta)]$, or may be easily calculated by using the appropriate power series of $Ei(i\zeta)$.

I.4 - Application to Bodies of Different Shapes.

We consider first the simplest conceivable case, i.e. the wave resistance of an isolated source. We immediately obtain from (28) and (29) with $n = 1$, $\epsilon_1 = 2$

$$D_1 = 4e^{-2h/F^2}$$

$$D_2^b = -16e^{-4h/F^2} / F^2$$

$$D_2^s = -16e^{-2h/F^2}\,(1 + 2e^{-2h/F^2}) / F^2 \qquad (30)$$

The wave resitance (30), of a blunt semi-infinite body in our approximation (fig. 2a), is represented in fig. 2c. We have used there the more common drag coefficient $C_D = D' / \rho U'^2 T' = D / \epsilon F^2$. With $C_D = \epsilon\ C_{D1} + \epsilon^2\ (C_{D2}^b + C_{D2}^s)$ we have $C_{D1} = D_1 / F^2$, $C_{D2} = D_2 / F^2$. We have also taken in this case $L' = h'$, i.e. $h = 1$, $F^2 = U'^2 / gh'$ and $\epsilon = T' / h'$.

On the same fig. 2c we have represented the coefficient of wave resistance for a semi-infinite body having a fine leading edge of a wedge shape (fig. 2b), created by distributing ten sources of equal strength at constant spacing. This way we could estimate the influence of the fineness of the bow on the nonlinear wave resistance. In fig. 2c we have represented C_{D1} as well as the ratios C_{D2}^s / C_{D2}^b and C_{D2} / C_{D1}. The first ratio is a measure of the relative importance of the free surface correction versus the body correction. The second ratio represents the relative magnitude of the second order correction.

In these examples there are no interference effects because the bodies are of semi-infinite length. The next case considered was of a closed body generated by a source and a sink of equal strength (fig. 3a and 4a). With $n = 2$ and $\epsilon_1 = -\epsilon_2 = 2$ in (28) and (29) we obtain in this case

$$D_1 = 8e^{-h/F^2}\ [1 - \cos(2 / F^2)]$$

$$D_2 = -8\,(e^{-h/F^2}/F^2)\ \{(2A^s - 2C_{12}^s + K_{12}^s)\sin(2/F^2) +$$

$$+ (-2E_{12}^b + I_{12}^b - 2E_{12}^s + I_{12}^s)\ [1 - \cos(2 / F^2)]\} \qquad (31)$$

where all the coefficients are given by (20) and (24).

Again, we have represented the wave resistance in figs. 3 and 4 in terms of the more common coefficient $C_D = D'/2\rho U'^2 L' = D/2F^2$. Hence with $C_D = \epsilon^2 C_{D1} + \epsilon^3 C_{D2}$ we have this time $C_{D1} = D_1 / 2F^2$ and $C_{D2} = D_2 / 2F^2$. In fig. 3b C_{D1}, $C_D 2$

and C_{D2}^{b} are represented as functions of the Froude number for a body of length submergence ratio $2L' / h' = 20$. In fig. 4b the same curves are represented for the case $2L' / h' = 10$. It is emphasized that the scales of the various quantities are different in figs. 3b and 4b.

II . 5 - Discussion of Results and Conclusions.

Fig. 2 permits to draw a few conclusions on the effect of the bow shape on the nonlinear wave resistance. First, it is seen that the free surface correction C_{D2}^{s} is larger than the body correction C_{D2}^{b} by a factor of three at sufficiently large $F = U' / (gh')^{1/2}$. When F decreases this ratio begins to increase in a very steep manner. Hence, any conclusion regarding nonlinear effects which is based on the body correction solely is completely misleading, particularly at small Froude numbers. The total nonlinear correction C_{D2} is a small part of C_{D1} at large F . Again, the nonlinear correction becomes unboundedly large as $F \to 0$. In fact, from (30) we have $C_{D2} / C_{D1} \sim - 16 / F^2$ as $F \to \infty$ and $C_{D2} / C_{D1} \sim C_{D2}^{s} / C_{D1} \sim - 4 / F^2$ as $F \to 0$. The influence on the nonlinear wave resistance of making the bow fine is manifest in the medium range of F values, when the bow length and the wave length are of the same order of magnitude. In that range, for a fine bow C_{D2}/C_{D1} is almost constant over a large stretch of Froude numbers and is smaller than C_{D2} / C_{D1} of a blunt bow. At small and very large F the behavior is similar to that of an isolated sources. Finally the second order effect is always negative, i. e. it diminishes the wave resistance. Moreover, if ϵ is not sufficiently small $C_D = \epsilon C_{D1} + \epsilon^2 C_{D2}$ (figs. 3 and 4) may become negative, which is obviously an absurdity.

Figs. 3 and 4 display clearly the interference effects. The nonlinear effect is very large for the large length submergence ratio of fig. 3 ($2L' / h' = 20$) and becomes significantly smaller for $2L' / h' = 10$ (fig. 4). Obviously, these large ratios have been selected in order to emphasize the nonlinear effect. To render it relatively small, the body has to be exceeedingly thin or not so blunt. Again the body correction C_{D2}^{b} is generally smaller than C_{D2}^{s} , especially at small F. The nonlinear term C_{D2} tends to sharpen the peaks of the resistance cuve and to widen its hollows. The nonlinear effect becomes very large in comparison to the first order wave resistance for small F . Again, we may arrive at negative wave resistance near the zeros of C_{D1} if ϵ is not sufficiently small.

One of the stricking results of our computations, which has

been observed previously by Salvesen (1969) is the singular behavior of the waves amplitude and wave resistance at small Froude numbers. If ϵ is kept constant, and no matter how small, the second order wave resistance becomes unboundedly large in comparison with the first order wave resistance as $F \to 0$. Hence the linear theory, as well as the second order correction, become inadequate at small Froude number, although both C_{D1} and C_{D2} tend to zero as $F \to 0$. This effect is called subsequently "the second small Froude number paradox".

Finally, we believe that our method of computing the wave resistance of n sources by starting with the solution for two sources offers a possible efficient way of attacking three-dimensional problems.

III - SMALL FROUDE NUMBERS PARADOXES.

III . 1 - Introduction.

We have seen before that the computation of the wave resistance by the thin body expansion, which is the method universally used at present as far as the free surface condition is concerned, becomes doubtful at small Froude numbers. This could be observed only after evaluating the second order terms. Experiments also support the conclusion that the linearized theory fails to predict correctly the wave resistance at low speeds. The aim of Chaps. III and IV is to elucidate this problem The same subject has been considered previously by Ogilvie (1968). Some of his ideas are validated by the present study, but his solution is shown to be incomplete.

III . 2 - Solutions in the Potential Plane.

As long as we seek solutions of two-dimensional flows it is more convenient to operate in the potential plane $f = \phi + i\psi$, as the plane of the independent variable, rather than the physical plane $z = x + iy$, in order to derive results of principle. The advantage stems from the fact that the free surface is kept at the fixed and known location $\psi = 0$. Hence, we consider now the solution of $w(f)$ (fig. 5b) analytical in the half plane $\psi \leqslant 0$ cut along $|\phi| < 1$, $\psi = -h \pm 0$ satisfying the following condition, equivalent to (2), (3) and (4)

$$\mathrm{Im}\left[iF^2 \left(\overline{w}\right)^2 w \frac{dw}{df} - w\right] = 0 \qquad (\psi = 0) \qquad (32)$$

$$u \to 1 \qquad (\phi \to -\infty) \tag{33}$$

Here, the variables are made dimensionless with respect to U' and L' (fig. 5b) and h is defined as h'_s / L'

The physical plane is mapped on f with the aid of

$$z = \int \frac{df}{w} \tag{34}$$

which leads to an unwieldy integral equation replacing the boundary condition (5). We shall see, however, that in different approximations the body boundary condition becomes quite simple.

We consider now two basic types of perturbation expansions of $w(f; \epsilon, F, h)$ aimed to linearize (32) :

(i) the thin body expansion, considered in Chap. II,

$$w(f; \epsilon, F, h) = 1 + \epsilon w_1 (f; F, h) + \epsilon^2 w_2 (f; F, h) + \ldots \tag{35}$$

for $\epsilon = o(1)$, $F = 0(1)$ and

(ii) the naive small Froude expansion

$$w(f; \epsilon, F, h) = w^0 (f; \epsilon, h) + F^2 w^1 (f; \epsilon, h) + \ldots \tag{36}$$

for $F = o(1)$, $\epsilon = 0(1)$.

Our aim to study the solutions obtained for different limits $\epsilon \to 0$, $F \to 0$.

III . 3 - The Thin Body Expansion.

The thin body expansion in the potential plane yields results similar to those obtained in the physical plane. The mapping (34) becomes

$$z = f + \epsilon z_1 + \epsilon^2 z_2 + \ldots \tag{37}$$

where

$$z_1 = -\int w_1 df, \qquad z_2 = -\int [w_2 - (w_1)^2 / 2] \, df \ \ldots$$

Using these relationships we obtain the following set of equations for w_1 and w_2, similar to (7)-(14)

$$\mathrm{Im}\left(iF^2 \frac{dw_1}{df} - w_1\right) = 0 \qquad (\psi = 0) \tag{38}$$

$$w_1 \to 0 \qquad (\phi \to -\infty) \tag{39}$$

$$\mathrm{Im}\, w_1 = \pm \tau(\phi) \qquad (|\phi| < 1, \quad \psi = -h \pm 0) \tag{40}$$

$$\mathrm{Im}\left(iF^2 \frac{dw_2}{df} - w_2\right) = -\frac{F^2}{2} \frac{\partial}{\partial \phi}\left[3(u_1)^2 + (v_1)^2\right] \quad (\psi = 0) \tag{41}$$

$$w_2 \to 0 \qquad (\phi \to -\infty) \tag{42}$$

$$\mathrm{Im}\, w_2 = \pm\left(u_1 + x_1 \frac{d\tau}{d\phi}\right) \qquad (|\phi| < 1, \quad \phi = -h \pm 0) \tag{43}$$

where $\tau = dt\,|dx|_{x=\phi}$ is the slope of the body contour and under the linearization process $L' = L' + o(L')$, $h_s' = h_c' + o(h_c')$ such that h, ϵ and F retain their meaning of (1). Equations similar to (38)-(43) may be written for higher order terms.

Due to the similarity between (38)-(40) and (7)-(10) the solution for w_1 may be written at once as

$$w_1 = \frac{1}{\pi}\int_{-1}^{1} \frac{\tau(s)}{f + ih - s}\, ds - \frac{1}{\pi}\int_{-1}^{1} \frac{\tau(s)}{f - ih - s}\, ds + \frac{2i}{\pi F^2}\int_{-1}^{1} \tau(s)\, \omega\left(\frac{f - ih - s}{F^2}\right) ds \tag{44}$$

where ω is defined by (17) (for details see Dagan, 1972b).

w_2, obeying (41)-(43) may be again found like in Chap. II by a discrete source distribution. It will display the same singular behavior for small F as $w_2(z)$.

Let us consider now a small Froude number limit of w_1 (44), i. e. an expansion of the type

$$w_1 = w_1^0 + F^2 w_1^1 + \ldots \tag{45}$$

for $F^2 = o(1)$. To carry out the expansion of (44) we have to find the asymptotic expansion of ω for large arguments.

It can be shown that the function $\omega(\zeta) = e^{i\zeta} E_1^-(i\zeta)$ has the following asymptotic expansion for large ζ

$$\omega(\zeta) = \sum_{k=0}^{\infty} \frac{k!}{(i\zeta)^{k+1}} \qquad (-\pi \leqslant \arg\zeta \leqslant -\delta)$$

$$\omega(\zeta) = \sum_{k=0}^{\infty} \frac{k!}{(i\zeta)^{k+1}} + 2\pi i e^{-i\zeta} \qquad (-\delta < \arg\zeta \leqslant \pi) \tag{46}$$

where δ is an arbitrarily small angle (see Erdely, 1956).

Hence, by using (46) we find that w_1 has the following expressions

$$w_1^0 = \frac{1}{\pi} \int_{-1}^{1} \tau(s) \left(\frac{1}{f + ih - s} + \frac{1}{f - ih - s}\right) ds$$

$$(-\pi \leqslant \arg(f - ih + 1) \leqslant \delta) \tag{47}$$

and

$$w_1^0 = \frac{1}{\pi} \int_{-1}^{1} \tau(s) \left(\frac{1}{f + ih - s} + \frac{1}{f - ih - s}\right) ds - \frac{4}{F^2} e^{-h/F^2} e^{-if/F^2} \int_{-1}^{1} \tau(s) e^{is/F^2} ds$$

$$(-\delta < \arg(f - ih + 1) \leqslant \pi) \tag{48}$$

Hence (47) is valid in the f lower half plane, excepting a "wake" attached to the image of the body across the free-surface (fig. 6). In this wake we have to add the last "wavy" term of (48) to (47). In particular (47) is not uniform along any line parallel to $\psi = 0$ and below $\psi = h$. In other words, no matter how small is F, it is always possible to find, for $\psi \leqslant h$, a sufficiently large ϕ such that the wavy term of (48) becomes arbitrarily larger in comparison with the first term. In fact (48) is a uniform asymptotic expansion in the

region $-\pi + \delta \leqslant \arg(f - ih + 1) \leqslant \pi$

The far free waves associated with w_1 (44) or w_1^0 (48) are given by z_1 (37) as

$$z_1 = A_1 e^{-if/F^2} = \left[4ie^{-h/F^2} \int_{-1}^{1} \tau(s) e^{is/F^2} ds\right] e^{-f/F^2} \qquad (49)$$

and the coefficient of wave resistance is

$$C_{D1} = |A_1|^2 / 8F^2 \qquad (50)$$

Again, these well known expressions continue to exist if $F \to 0$, in virtue of (48).

III . 4 - The Naive Small Froude Number Expansion

We turn now to (36), valid for a body of finite thickness moving at low speeds. Substituting (36) into (32) and (33) we obtain

$$\text{Im } w^0 = 0 \qquad (\psi = 0) \qquad (51)$$

$$\text{Re } w^0 = 1 \qquad (\phi \to -\infty) \qquad (52)$$

$$\text{Im } w^1 = -\frac{1}{4} \frac{\partial}{\partial \phi} (u^0)^4 \qquad (\psi = 0) \qquad (53)$$

$$w^1 \to 0 \qquad (\phi \to -\infty) \qquad (54)$$

w^0 is therefore the solution of uniform flow at infinity past the actual body beneath a rigid wall at $\psi = 0$, briefly "the rigid wall solution". w^1 described a flow generated by a source distribution along $\psi = 0$, (53) being a standard Neumann condition. It can be shown that the higher order approximations satisfy the same type of free-surface conditions (53). Moreover, it has been shown (Dagan and Tulin, 1972) that the total flux of the sources in (53) and higher order approximations is zero such that w^0, w^1, ... are $0(1/|f^2|)$ as $|f| \to \infty$ for a closed body (in the absence of circulation). In particular no free-waves are present and the wave resistance is identically zero.

We can now consider a thin body limit of w^0, i. e. an expansion of the type

$$w^0 = 1 + \epsilon w_1^0 + \dots \tag{55}$$

It is easy to show that

$$w_1 = w_1^{o,u} + w_1^{o,\ell} = \frac{1}{\pi}\int_{-1}^{1} \frac{\tau(s)}{f - ih - s}\, ds + \frac{1}{\pi}\int_{-1}^{1} \frac{\tau(s)}{f + ih - s}\, ds \tag{56}$$

(56) represents the rigid wall solution for the flow past the linearized body. It is easy to ascertain that $w_1^{o,u}(f) = \overline{w_1^{o,\ell}(\bar{f})}$.

We have arrived to what we call "the first small Froude number paradox" : the thin body limit ($\epsilon \to 0$) of the naive small Froude number solution w_1^0 (56) is not equal to the small Froude number limit of the thin body expansion w_1^0 (47, 48). The two solutions differe in the "wavy wake" of fig. 6.

III . 5 - Discussion of Results.

In the preceding sections we have defined the two small Froude number paradoxes occurring as $F \to 0$, in the solution of the problem which depends on the two small parameters ϵ and F . The nonuniform behavior of the solution may be related to the fact that in carrying out the naive small Froude number expansion (36) we have lowered the order of the boundary condition (32), the derivative disappearing in the l. h. s. of (51) and (53), similarly to well known boundary layer problems. This observation is strengthened by the inspection of the wavy term (49) : the function $e^{-1f/F2}$ changes its order by differentiation and the two terms of (38) become of the same order of magnitude no matter how small is F (this observation has underlain Ogilvie's (1968) study). The nonuniformity present in our problem is, however, different and more subtle than that of other singular expansions (Van Dyke, 1964; Cole, 1968) with a few respects (i) we cannot detect the nonuniformity of the solution from the naive small Froude number expansion which is well behaved in the entire flow domain. We cannot, therefore, rule out this solution at the present stage; (ii) for a submerged body the "wavy wake" is attached to the fictitious image of the body (fig. 6) rather than the body itself. It intersects the flow domain $\psi < 0$ only far behind the body and has an exponentially small effect upon the body itself; (iii) the wavy term $e^{-1f/F2} \sim e^{\psi/F2}\, e^{-1\phi/F2}$ has, for $F \to 0$, the character of an exponential boundary layer decay for $\psi < 0$ and a rapidly oscillating behavior in the ϕ direction. It displays, therefore, a complex pathological behavior as $F \to 0$.

It is also worthwhile to point out that only for $h \neq 0$ (submerged body) is the amplitude of the free waves decaying exponentially for $F \to 0$. Otherwise, for $h = 0$ the decay may be algebraic at best.

We are going to determine the origin of the small Froude number paradoxes and to derive uniform solutions for the wave resistance as $F = o(1)$ and $\epsilon = 0(1)$ or $\epsilon = o(1)$.

IV - WAVE RESISTANCE AT LOW SPEEDS.

IV .1 - The Model Problem.

Like in other nonlinear problems of hydrodynamics we seek a "model" problem which has the same features as the basic nonlinear problem, but can be solved exactly. We define our auxiliary problem as follows : determine the complex function $\omega(\zeta, \epsilon_1, \epsilon_2, h)$ of the complex variable $\zeta = \xi + i\chi$, analytical in the whole plane cut along $\chi = h$, $\xi < 1$ (fig. 7a), satisfying everywhere the differential equation

$$i\epsilon_2 \left[1 + \sigma(\zeta; \epsilon_1, \epsilon_2, h)\right] \frac{d\omega}{d\zeta} - \omega = \rho(\zeta; \epsilon_1, \epsilon_2, h) \qquad (57)$$

subject to the condition

$$\omega \to 0 \qquad (\xi \to -\infty, \chi < h) \qquad (58)$$

σ and ρ are given functions, holomorphic in the entire ζ plane excepting the slit $|\xi| < 1$, $\chi = h$ and $0(1/|\zeta|^2)$ as $|\zeta| \to \infty$ Moreover, σ and ρ are bounded along the slit and $1 + \sigma$ does not vanish there. To simplify matters we assume that σ and ρ admit expansions in power series in ϵ_1 and ϵ_2 of the type

$$\begin{aligned}
\sigma(\zeta; \epsilon_1, \epsilon_2, h) &= \sum_{k=1}^{\infty} \sum_{j=0}^{\infty} (\epsilon_1)^k (\epsilon_2)^j \sigma_k^j(\zeta; h) \\
\rho(\zeta; \epsilon_1, \epsilon_2, h) &= \sum_{j=0}^{\infty} (\epsilon_2)^j \rho^j(\zeta; \epsilon_1, h) \\
&= \sum_{j=0}^{\infty} \sum_{k=0}^{\infty} (\epsilon_2)^j (\epsilon_1)^k \rho_k^j(\zeta; h) \\
1/(1+\sigma) &= 1 + \sum_{j=0}^{\infty} (\epsilon_2)^j \mu^j(\zeta; \epsilon_1, h) \\
&= 1 + \sum_{j=0}^{\infty} \sum_{k=1}^{\infty} (\epsilon_2) (\epsilon_1)^k \mu_k^j(\zeta; h)
\end{aligned} \qquad (59)$$

uniform in the entire ζ plane cut along $\eta = h$, $|\xi| < 1$ and convergent for finite ϵ_1 and ϵ_2, not necessarily small.

The "model" problem is similar to our original flow problem, (57) being similar to (32), ϵ_2, ϵ_1, ω and ζ corresponding to F^2 ϵ, w and f, respectively, and ρ representing the body effect. Two major simplifications are present, however, in (57) : the coefficient of $d\omega / d\zeta$ is given, the equation being thus linearized, and equation (57), with analytical coefficients, is valid in the entire plane and not merely at $\psi = 0$. Due to these simplifications (57) admits an exact closed solution.

Our purpose is to establish, by using the exact solution, how can uniform expansions of ω for $\epsilon_2 = o(1)$ be obtained from the expansion of (57).

If we expand (57) for $\epsilon_1 = o(1)$, $\epsilon_2 = 0(1)$ (corresponding to the thin body expansion) with

$$\omega = \epsilon_1 \omega_1 + (\epsilon_1)^2 \omega_2 + \dots \tag{60}$$

we obtain for ω_1, ω_2 ... equations and solutions similar to (38), (39), (41), (42), (44). In particular, if we let subsequently $\epsilon \to 0$ into (60), i. e. $\omega_1 = \omega_1^0 + \epsilon_2 \omega_1^1 + \dots$, $\omega_2 = \omega_2^0 + \epsilon_2 \omega_2^1 + \dots$ we arrive at different asymptotic expansions in the two regions of the ζ plane (fig. 7a) exactly like in (47) and (48), "wavy" terms being present in the shaded region of fig. 7. If we start with an expansion of (57) for $\epsilon_2 = o(1)$, $\epsilon_1 = 0(1)$ (corresponding to finite thickness, naive small F expansion) with $\omega = \omega^0 + \epsilon_2 \omega^1 + \dots$ we obtain equations similar to (51)-(54) and solutions with no waves. Furthermore, if we let afterwards $\epsilon_1 \to 0$, i. e. $\omega^0 = \epsilon_1 \omega_1^0 + (\epsilon_1)^2 \omega_2^0 + \dots$, we obtain limits which are different from those of the preceeding expansion, in the shaded zone of fig. 7. Hence, our model problem leads to the same "paradoxes" as the prototype nonlinear problem.

Now, let us consider the exact solution for ω, satisfying (57) and (58), which can be written at once as

$$\omega(\zeta ; \epsilon_1, \epsilon_2, h) = -\frac{i}{\epsilon_2} \int_{-\infty}^{\zeta} \left\{ \frac{\rho(\lambda ; \epsilon_1, \epsilon_2, h)}{1 + \sigma(\lambda ; \epsilon_1, \epsilon_2, h)} \cdot \right. \tag{61}$$

$$\left. \cdot \exp\left[\frac{i}{\epsilon_2} \int_{\zeta}^{\lambda} \frac{d\nu}{1 + \sigma(\nu ; \epsilon_1, \epsilon_2, h)} \right] \right\} d\lambda$$

where the integrals are carried out below $\mathrm{Re}\,\lambda < 1$, $\mathrm{Im}\,\lambda = h$ and $\mathrm{Re}\,\nu < 1$, $\mathrm{Im}\,\nu = h$ in the λ and ν planes, respectively. We can use now the series (59) to rewrite (61) as follows

$$\omega = -\frac{i\epsilon_1}{\epsilon_2}\exp(-i\zeta/\epsilon_2)\int_{-\infty}^{\zeta}\Big[\rho_1^0 + \epsilon_1\mu_1^0\rho_1^0 + \epsilon_2\rho_1^1 + \ldots\Big]\exp(i\lambda/\epsilon_2)$$
$$\cdot\exp\frac{i\epsilon_2}{\epsilon_2}\int_{\zeta}^{\lambda}(\mu_1^0 + \epsilon_1\mu_2^0 + \epsilon_2\mu_1^1 + \epsilon_1\epsilon_2\mu_2^1 + \ldots)\,d\nu\Big]d\lambda \qquad (62)$$

valid for finite ϵ_1 , ϵ_2 . We are now in a position to expand (62) for small ϵ_1 and/or ϵ_2 . The detailed analysis may be found in Dagan (1972b). Herewith, the main results :

(i) the limit $\epsilon_1 = o(1)$, $\epsilon_2 = 0(1)$ of (62) yields the same results at first order, $\epsilon_1\omega_1$, as the solution obtained by expanding (57) if, and only if, $\epsilon_1/\epsilon_2 = o(1)$. This last condition stems from the existence of the ratio ϵ_1/ϵ_2 in the last exponential of (62);

(ii) the limit $\epsilon_2 = o(1)$, $\epsilon_1 = 0(1)$ of (62), ω_0 , does not coincide with that obtained by the naive expansion of (57). The uniform solution differs from the naive solution in the "wavy wake" and does comprise "waves". Moreover, to obtain a first order complete solution we have to retain in the last exponential of (62) all the written terms, up to $(\epsilon_2)^2$, in particular $\epsilon_2\mu_1^1$. The "far waves" are obtained by contour integration (fig. 7b) as follows

$$\omega^0_{\text{uniform}} = -\frac{i}{\epsilon_2}\exp(-i\zeta/\epsilon_2)\oint_S\Big[\rho^0(\lambda) + \rho^0(\lambda)\,\mu^0(\lambda)\Big]\cdot\exp(i\lambda/\epsilon_2)$$
$$\cdot\exp\Big\{\frac{i}{\epsilon_2}\int_{\zeta}^{\lambda}\Big[\mu^0(\nu) + \epsilon_2\,\mu^1(\nu)\Big]\,d\nu\Big\}\,d\lambda \quad (\mathrm{Re}\,\zeta\to\infty) \qquad (63)$$

Again, it is emphasized that in the last exponential $\epsilon_2\mu^1$ contributes at 0(1) because of the division with ϵ_2 . Going in reverse, the differential equation which yields the uniform first order solution, obtained by the appropriate expansion of (57), is

$$d\omega^0/d\zeta + (i/\epsilon_2)(1 + \mu^0 + \epsilon_2\mu^1)\,\omega^0 = (i/\epsilon_2)(\rho^0 + \rho^0\mu^0) \qquad (64)$$

where terms up to $(\epsilon_2)^2$ have been retained in $1/(1+\sigma)$, the coefficient of (59).

(iii) the limit $\epsilon_1 = o(1)$, $\epsilon_2 = o(1)$ of (62) is not defined unless we specify the order of ϵ_1 / ϵ_2. For $\epsilon_1 / \epsilon_2 = 0(1)$ we obtain again at first order a solution with a "wavy" term, the latter having the expression

$$\omega^0_{\text{uniform}} = \epsilon_1 \omega^0_{1,\text{uniform}} + \ldots = -\frac{i\epsilon_1}{\epsilon_2} \exp(-i\zeta/\epsilon_2) \int_S \rho_1^0(\lambda)$$

$$\cdot \exp(i\lambda/\epsilon_2) \cdot \exp\left[\frac{i\epsilon_1}{\epsilon_2} \int_\zeta^\lambda \mu_1^0(\nu)\, d\nu\right] d\lambda + 0(\epsilon_1^2/\epsilon_2)$$

$$(\text{Re}\ \zeta \to \infty) \tag{65}$$

This solution differs from that obtained by taking the limits $\epsilon_1 \to 0$ first and $\epsilon_2 \to 0$ afterwards in (57). Moreover (65) is obtained from the solution of the differential equation, derived from (57),

$$d\omega_1^0/d\zeta + (i/\epsilon_2)(1+\epsilon_1 \mu_1^0)\ \omega_1^0 = (i/\epsilon_2)\ \rho_1^0 \tag{66}$$

(iv) the limit $\epsilon_1 = o(1)$, $\epsilon_2 = o(1)$, $\epsilon_1/\epsilon_2 = o(1)$ yields by the expansion of

$$\exp\left[\frac{i\epsilon_1}{\epsilon_2} \int_\zeta^\lambda \zeta_1^0(\nu)\, d\nu\right] = 1 + \frac{i\epsilon_1}{\epsilon_2} \int_\zeta^\lambda \mu_1^0\, d\nu + \ldots \qquad \text{in (65)}$$

the usual linearized approximation

$$\omega_1^0 = -\frac{i\epsilon_1}{\epsilon_2} \exp(-i\zeta/\epsilon_2) \int_S \rho_1^0(\lambda) \exp(i\lambda/\epsilon_2)\, d\lambda \tag{67}$$

satisfying the differential equation

$$d\omega_1^0 + d\zeta + (i/\epsilon_2)\,\omega_1^0 = (i/\epsilon_2)\ \rho_1^0 \tag{68}$$

IV . 2 - Application of Results to the Nonlinear Problem (Potential Plane).

Due to the similarity between (32) and (57) the results obtained in the model problem can be extended to the hydrodynamical problem at once (for details see Dagan, 1972b). With $w = 1 + W$ the uniform solution, the key to obtaining first order uniform approximations W^0 (for $F^2 = o(1)$, $\epsilon = 0\ (1)$), ϵW_1 (for $\epsilon = o(1)$, $F^2 = 0(1)$) and ϵW_1^0($\epsilon = o(1)$, $F^2 = o(1)$, $\epsilon/F^2 = 0(1)$) is to expand the coefficient $(\bar{w})^2 w$ of dw/df in (32) in a naive small Froude number expansion and to retain the appropriate number of terms. By doing that we obtain the following uniform asymptotic approximations for W :

(i) $\epsilon = o(1)$, $F^2 = 0(1)$, i. e. $\epsilon/F^2 = o(1)$ (thin body, finite length Froude number, large thickness Froude number (U'^2/gT'), $W = \epsilon W_1 + \ldots . W_1$ coincides with (44), and the usual thin body approximation is, therefore, uniform.

(ii) $F^2 = o(1)$, $\epsilon = 0(1)$ (Small Froude number, finite thickness), $W = W^0 + \ldots . W^0$ satisfies the free-surface boundary condition (similar to 64)

$$\mathrm{Im}\left\{ iF^2 \left[(u^0)^3 + F^2(u^0)^2 (3u^1 + iv^1) + \ldots\right]\frac{dW^0}{df} - W^0\right\} = 0 \qquad (\psi = 0) \tag{69}$$

and along the body $1 + W^0 = w^0$, where w^0 (51, 52) is the naive small F solution. w^0 is not an uniform solution in the "wavy wake". The solution of W^0 subject to (69) is very difficult.

(iii) $F^2 = o(1)$, $\epsilon = o(1)$, $\epsilon/F^2 = 0(1)$ (small Froude number, thin body, thickness Froude number U'^2 / gT' of order one), $W = \epsilon W_1^0 + \ldots .$
W_1^0 satisfies the free-surface condition (similar to 66)

$$\mathrm{Im}\left[iF^2 (1 + 3\epsilon u_1^0) \frac{dW_1^0}{df} - W_1^0\right] = 0 \qquad (\psi = 0) \tag{70}$$

where $u_1^0 = \mathrm{Re}\, w_1^0$ is the naive linearized small F solution (56). Also, along the body skeleton S_ℓ (fig. 7) $W_1^0 = w_1^0$. By analytical continuation and integration by parts W_1^0 has been found in a close form as follows

$$W_1^0 = w_1^{o,\ell} - w_1^{o,u} + \frac{2i}{F^2} \exp(-if/F^2) \int_{-\infty}^{f} w_1^{o,u}(\lambda)$$

$$\cdot \exp(i\lambda/F^2) \cdot \exp\left[-\frac{3i\epsilon}{F^2} \int_{f}^{\lambda} w_1^0(\nu)\, d\nu \right] d\lambda \qquad (71)$$

For $F^2 \to 0$ $W_1^0 \to w_1^0 + o(F^2)$ excepting the "wavy wake". There, we obtain similarly to (67), by contour integration like in fig. 7b,

$$W = \epsilon W_1^0 + \ldots = \frac{2i\epsilon}{F^2} \exp\left[-i(f - ih)/F^2\right] \int_{-1}^{1} w_1^{o,u}(s + ih)$$

$$\cdot \exp(is/F^2) \cdot \exp\left[-\frac{3i\epsilon}{F^2} \int_{\infty}^{s+ih} w_1^0(\nu)\, d\nu \right] ds + \ldots$$

$$(\mathrm{Ref} \to \infty) \qquad (72)$$

where $w_1^{o,u}$ and $w_1^{o,\ell}$ are given by (56). w_1^o is obviously not a uniform solution.

Only, and if only, $\epsilon / F^2 = o(1)$ (72) degenerates into (47,48). The implications of the different limits are discussed in the following sections.

IV . 3 - Uniform Solutions in the Physical Plane.

It was advantageous to carry out the basic derivations in the potential plane. In applications it is convenient (and in three dimensions it is essential) to operate in the physical plane. It is easy to transfer the previous results to the physical plane. With $w(z ; \epsilon, F, h) = 1 + W(z; \epsilon, F^2, h)$ we have the following limits :

(i) $\epsilon = o(1)$, $F^2 = 0(1)$ (thin body, finite Froude number), $W = \epsilon W_1 + \epsilon^2 W_2 + \ldots$. W_1 , W_2 satisfy equations similar to (7) - (14). $W_1 = df_1 / dz$ is the usual thin body solution, $W_2 = df_2 / dz$ is the second order solution (see chap. II).

(ii) $F^2 = o(1)$, $\epsilon = 0(1)$ (Small Froude number, full body), $W = W^0 + F^2 W^1 + \ldots$. The complete first order term $W^0 = U^0 - iV^0$ satisfies the free-surface boundary condition

$$F^2 \left[(u^0)^2 + 2F^2 u^0 u^1 \right] \frac{\partial U^0}{\partial x} + 2F^4 u^0 v^1 \frac{\partial V^0}{\partial x} - V^0 = 0$$

$$(y = 0) \qquad (73)$$

on the unperturbed free-surface, similar to (64). $w^0 = u^0 - iv^0$ is the rigid wall solution for flow past the actual body and w^1 is the next term of the naive small Froude number solution.

(73) has a simple physical interpretation : it represents the equation satisfied by waves generated on a stream of variable speed $w^0 + F^2 w^1$, beneath $y = 0$. Ogilvie (1968) has retained only the first term in (73), i. e. has replaced (73) by

$$\mathrm{Im} \left[iF^2 (u^0)^2 \frac{dW}{dz} - W \right] = 0 \qquad (y = 0) \qquad (74)$$

He has based the derivation of (74) on the intuitive reasoning that at small F the wave length of the free waves becomes small compared to the body length scale (which governs the rigid wall solution) and, therefore, the waves are travelling on a basic stream of varying velocity. Although the argument valid in principle, (74) is not a uniform asymptotic approximation, as shown in the preceding section. To determine W^0, satisfying (73), is a difficult task which is not pursued here.

(iii) $\epsilon = o(1)$, $F^2 = o(1)$, $\epsilon / F^2 = 0(1)$ (thin body, small length Froude number, finite thickness Froude number), $W^0 = \epsilon W_1^0 + \ldots$ By analogy with (70) $W_1^0(z)$ satisfies the boundary condition

$$\mathrm{Im} \left[iF^2 (1 + 2\epsilon w_1^0) \frac{dW_1^0}{dz} - W_1^0 \right] = 0 \qquad (y = 0) \qquad (75)$$

the radiation condition

$$W_1^0 \to 0 \qquad (x \to \infty) \qquad (76)$$

and the body condition

$$W_1^0 = w_1^0 \qquad (|x| < 1, \; y = -h) \qquad (77)$$

along the skeleton of the body. w_1^0 the linearized rigid wall solution has the expression

$$w_1^0 = w_1^{o,u} + w_1^{o,\ell} = \frac{1}{\pi}\int_{-1}^{1} \frac{\tau(s)}{z - ih - s}\, ds + \frac{1}{\pi}\int_{-1}^{1} \frac{\tau(s)}{z + ih - s}\, ds \tag{78}$$

W_1^0 may be found by analytical continuation across $y = 0$. After some manipulations (Dagan, 1972b) the solution is found to be

$$W_1^0(z; h) = w_1^{o,\ell} - w_1^{o,u} + \frac{2i}{F^2}\, e^{-z/F^2} \cdot \int_{-\infty}^{z} w_1^{o,u}(\lambda) e^{i\lambda/F^2}\, e^{-2i\epsilon f_1(\lambda)/F^2}\, d\lambda \tag{79}$$

which is analogous to (71). The profile of the free waves $N = \epsilon N_1^0 +$ is derived from (79) as

$$N_1^0 = \mathrm{Im}\, A_1^0 e^{-ix/F^2} = \mathrm{Im}\Big[2\oint w_1^{o,u} e^{i\lambda/F^2} \cdot e^{-2i\epsilon f_1^0/F^2}\, d\lambda \Big] e^{-ix/F^2} \qquad (x \to \infty) \tag{80}$$

In (79) and (80), $f_1^0 = \int_{+\infty}^{\lambda} w_1^0(\nu)\, d\nu$ and S is the cut $|x| < 1$, $y = h \pm 0$ in the λ plane. Along S $w_1^{o,u} = u_1^{o,u} \pm i\tau$ and $f_1^0 = f_1^0 + \phi_1^{o,u} \pm it$. Hence, we can write for A_1^0 the following expression

$$A_1^0 = 4\int_{-1+ih}^{1+ih} e^{i\lambda/F^2}\, e^{-2i\epsilon (f_0^{1,} + \phi_0^{1,u})/F^2} \cdot \Big[u_o^{1,u} \sinh \frac{2\epsilon t}{F^2} + i\tau \cosh \frac{2\epsilon t}{F^2}\Big]\, d\lambda \tag{81}$$

The wave resistance coefficient C_D is given by

$$C_D = \epsilon^2 \left| A_1^0 \right|^2 / 8F^2 \tag{82}$$

(iv) $\epsilon = o(1)$, $F^2 = o(1)$, $\epsilon/F^2 = o(1)$ (thin body, small length Froude number, large thickness Froude number). This limit can be obtained in two ways : by expanding W_1 of (i) for $F^2 \to 0$ or

via (79) for $\epsilon \to 0$. Hence, the usual linearized approximation used in ship resistance theory may be extended in the range of small Froude numbers only if $\epsilon^2/F = gT'/U'^2$ is small. To keep ϵ fixed and to let $F^2 \to 0$ is tantamount to write in (80) $e^{-2i\epsilon f_1^0/F^2} \simeq 1 - 2i\epsilon f_1^0/F^2$ which is obviously illegitimate if ϵ/F^2 is not small. For this reason the second order approximation $2i\epsilon f_1^0/F^2$ may become large compared to unity and the expansion of (79) may diverge. For $\epsilon/F^2 = o(1)$ (81) leads to

$$A^0_{1,lin} = 4ie^{-h/F^2} \int_{-1}^{1} \tau(s)\, e^{is/F^2}\, ds \qquad (83)$$

i. e. the usual complex amplitude of linearized waves.

IV . 4 - Illustration of Results : Wave Resistance of a Biconvex Parabolical Body.

To illustrate the main features of the thin body small Froude number solution (79, 80, 81), presented here for the first time, we have computed the wave resistance for a parabolical body (fig. 8) with the thickness distribution $t = 1 - s^2$ ($|s| \leqslant 1$), $\tau = -2s$. The linearized rigid wall solution in this case is expressed by

$$f_1^0 = f_1^{o,\ell} + f_1^{o,u} = \frac{2}{\pi}\left\{2z - \frac{1}{2}\left[(z - ih)^2 - 1\right] ln \cdot \frac{z - ih + 1}{z - ih - 1} - \frac{1}{2}\left[(z + ih)^2 - 1\right] ln \frac{z + ih + 1}{z + ih - 1}\right\} \qquad (84)$$

and $w_1^0 = df_1^0/dz$. By using (81) we have computed C_D (82) by a simple Simpson integration, for $\epsilon = 0.05$ (Dagan, 1972b). C_D/ϵ^2 as function of $F_n = U'/(2gL')$ is represented in fig. 8. On the same figure we have represented $C_{D,lin}$, based on the usual linearized approximation (83). In addition we have represented $C_D/\epsilon^2 = C_{D,lin} + \epsilon C_{D2}$ based on an expansion up to ϵ^2 of (82), i. e. on an illegitimate expansion of the exponential in (80).

Our small Froude number thin body solution (81) differs from the usual one (83) with two respects : while (83) may be regarded as a summation of elementary waves $e^{-i(f-s)F2}$ generated by each element of thickness $dt = \tau\, ds$, in (81) the elementary waves $e^{-i(f-s)F2}$ have phase and amplitudes depending on λ in a complex manner. In particular waves are generated by the parallel part of the body ($\tau = 0$, $t = const$) and the amplitude changes if the direction of motion of an assymetrical body is reversed. The wave

resistance is always positive, while in an illegitimate expansion of $e^{-2i\epsilon f_1/F_2}$ in a truncated power series it may become negative. C_D is close to $C_{D\,lin}$ (fig. 8) at relatively high F_n (i.e. small ϵ^2/F), but shifted towards small F_n. The peaks of the resistance curve of the uniform solution are, excepting the highest peak, much smaller than those of the usual theory.

The disastrous effect of using the second order approximation of the thin body expansion in the region of small Froude numbers is illustrated clearly in fig. 8.

It is worthwhile to point out that the wave resistance (81) is integrable only if the leading (or trailing) edge singularity is like $w_1 \sim (z - ih + 1)^{-\alpha}$ where $\alpha < 1$. Hence, a parabolical nose ($\alpha = 0.5$) is acceptable, while a box like shape ($\alpha = 1$) is not integrable.

IV . 5 - Extension of Results to Three-dimensional Flows.

It is easy to proceed along the same lines and to derive the free-surface conditions satisfied by the various uniform approximations as $F \to 0$ in three dimensions. With u, v, w the velocity components and z a vertical coordinate the exact free-surface condition, counterpart of (2), may be written as follows

$$F^2 \left[u^2 u_{,x} + uv(v_{,x} + u_{,y}) + v^2 v_{,y} + uww_{,x} + uww_{,y}\right] + w = 0 \qquad (z = \eta) \tag{85}$$

The naive small Froude number expansion $(u, v, w) = (u^0, v^0, w^0) + F^2 (u^1, v^1, w^1) + \ldots, \eta = F^2 \eta^0 + \ldots$ leads to u^0, v^0, w^0 as a rigid wall solution for flow past the actual body. With ϵ a fineness or slenderness parameter, a further expansion of (u, v, w) yields $u^0 = 1 + \epsilon u_1^0 + \ldots, (v^0, w^0) = \epsilon (v_1^0, w_1^0) + \ldots$. The usual linearized approximations is obtained from (85), by expanding the velocity near the uniform flow $u = 1 + \epsilon u_1 + \ldots, (v, w, \eta) = \epsilon (v_1, w_1, \eta_1) + \ldots$, as follows

$$F^2 u_{1,x} + w_1 = 0 \qquad (z = 0) \tag{86}$$

Let now $1 + \nabla \Phi$ be a uniform small Froude number approximations. By analogy with (73), in the limit $F \to 0$, $\epsilon = 0(1)$ Φ^0 satisfies the following free-surface condition

$$F^2 \left\{ \left[(u^0)^2 + 2F^2 u^0 u^1 \right] \Phi^0_{,xx} + 2 \left[u^0 v^0 + F^2 (u^0 v^1 + u^1 v^0) \right] \Phi^0_{,xy} + \right.$$

$$\left. + \left[(v^0)^2 + 2F^2 v^0 v^1 \right] \Phi^0_{,yy} + F^2 u^0 w^1 \Phi^0_{,xz} + F^2 v^0 w^1 \Phi^0_{,yz} \right\} + \Phi^0_{,z} = 0$$

$$(z = 0) \qquad (87)$$

Φ^0 may be represented along the actual body surface by a distribution of singularities derived from the rigid wall solution. The rigid wall solution is asymptotic to Φ^0 as $F \to 0$ excepting a "wavy wake" which this time is generated by rays emanating from the body image across $z = 0$ towards $x \to \infty$ at an angle $-\delta$ (arbitrarily small) with the horizontal plane. To determine Φ^0, representing waves over a stream of variable velocity, is a very difficult task.

The simpler approximation of thin (slender) body $\epsilon = o(1)$ small Froude number $F = o(1)$, and finite beam (and draft) Froude number $\epsilon / F^2 = 0(1)$, is obtained from (87) like (75)

$$\Phi^0_{1,xx} + \frac{1 - 2\epsilon u^0_1}{F^2} \Phi^0_{1,z} = 0 \qquad (z = 0) \qquad (88)$$

Φ^0_1 may be represented by the source distribution of the rigid wall solution on the body skeleton (central plane, or axis). (88) is the extension of the usual linearized free-surface equation (86) (which is the basis of computation of ship wave resistance via Michell integral) into the range of small Froude numbers, where (86) becomes invalid. The solution of Φ^0_1 is the object of future studies.

IV . 6 - Discussion of Results and Conclusions.

The two small Froude number paradoxes have been explained with the aid of our model problem.

It was shown that the naive small Froude number expansion does not yield a uniform solution, the region of nonuniformity being the "wavy wake".

The elucidation of the second paradox has led to the important conclusion that the usual thin body first and higher order approximations are valid only for large thickness Froude numbers. For moderate values a new first order approximation has been derived : it results from taking in the free-surface condition a basic variable

speed, rather than a uniform flow, as an "unpurturbed" state. This new approximation is the natural extension of the thin body theory into the range of small Froude numbers.

The basic equations of flow past a body of finite thickness moving at low Froude number have been also derived. Again, to obtain a uniform solution one has to satisfy simultaneously the boundary condition on the full body and a free-surface condition in which a flow of varying velocity is taken as the basic state. This basic flow is derived by solving for the two terms of the naive small Froude number expansion (rigid wall and first order Neumann type problem).

To solve for flow past the actual body, while keeping the free-surface condition in its usual linearized form, may lead to erroneous results in the range of small Froude numbers.

V - PRELIMINARY EXPERIMENTS ON THE TWO DIMENSIONAL BREAKING WAVE.

An important free-surface nonlinear effect, present in the case of blunt bow ships, is related to the breaking wave. At the 8th Naval Hydrodynamics Symposium we have presented (Dagan & Tulin 1972) theoretical models of the breaking wave inception and of the bow jet. Recently, experiments have been conducted at Hydronautics Inc. under the supervision of Mr. M. Altman in order to visualise the two-dimensional breaking wave. The detailed results of these experiments will be reported elsewhere. Herewith a few preliminary observations.

A rectangular body has been towed at constant speed in the small Hydronautics towing tank. The water depth was 38 cm and the model has been submerged at (i) 2.5 cm and (ii) 1.25 cm beneath the unperturbed level, such that the effect of the bottom was negligible. The model has been towed at six different speeds in the range 0.61-1.46 m/sec. The model motion has been recorded through the channel glass wall on a 16 mm color film at 64 frames per second. Taking the pictures has started after 3.5 m of run (the tank total length is 24 m). In fig. 9 we have reproduced two pictures for the 2.5 cm model : at 0.61 m/sec and at 1.46 m/sec, the corresponding draft Froude numbers being 1.22 and 2.93, respectively.

The free-surface in front of the body had vertical pulsations which became more violent as the speed increased. This made quite difficult the definition of the average free-surface profile. It seems that the oscillations are related to gravity effects since the periods

for the two submergence depths were roughly in the same ratio as the square root of the drafts. Satisfactory Froude number similitude has been obtained for the free-surface elevation near the body for the two drafts.

The breaking wave inception apparently occurs at a Froude number somewhere between 1.20 and 1.50, which correlates quite well with our theoretical prediction of 1.50. Separation at the corner of the body profile, visible at high speeds, makes difficult the definition of the body shape for an inviscid flow calculation. We did not reach a "spray regime" in the range of considered speeds. The study of the complex flow pattern of a developed breaking wave is the object of future studies.

VI - GENERAL CONCLUSION.

We have discussed the pertinent conclusions at the end of each of the preceeding chapters. Here, we will try to discuss their bearing on ship wave resistance.

The usual thin (or slender) body first order linearized approximation, leading to the Michell integral, is valid for sufficiently large beam (and draft) Froude numbers. In its range of validity this approximation may be improved by taking into account the second order term. It seems that the contribution of the free-surface correction is of the same order of magnitude as that of the body correction in this second order term. As the shape becomes finer, the Froude number limiting from below the range of validity of the linearized approximation, as well as the second order correction, become smaller.

For moderate beam (and draft) Froude numbers and, henceforth, small length Froude numbers, the linearized solution is no more valid and the second order correction worsens the results, rather than improving them. To obtain a first order uniformly valid solution for a thin (or slender) body in this case, one has to take a variable velocity distribution, rather than a uniform, as the basic unperturbed distribution in the free-surface condition. This basic flow, as well as the singularity distribution along the center plane (or axis), may be computed by solving for a rigid wall flow pas the linearized body.

Linear free-surface conditions with variable coefficients have been derived also for the case of small length Froude number flow past the actual body (finite beam, or draft, length ratio). To

obtain a uniform solution, the basic nonuniform flow (on which the variable coefficients of the free-surface condition are based) has to include the rigid wall, as well as the next term, of a naive small Froude solution of flow past the actual body. The singularity distribution on the body surface may be taken from the rigid wall solution solely. This results suggests that solving for the actual body shape, but with a linearized free-surface condition with constant coefficients (the Neumann-Kelvin problem) does not yield a uniformly valid solution at small Froude numbers.

The above conclusions are based on the assumption that the results obtained in the two dimensional case may be extrapolated to the ship wave resistance problem, at least in principle. Only solving for actual three-dimensional flows will make the conclusions valid in both qualitative and quantitative terms. Such three-dimensional solutions pose, however, difficult mathematical problems which have not yet been touched.

The picture of the nonlinear ship wave resistance theory is not complete unless we refer to two components which are somehow related to viscous effects : the bow breaking wave and the wake. Only the first component has been considered in our studies.

ACKNOWLEDGMENT.

The present work has been supported by ONR under contract No. N00014-71-C-0080 BR 062-266 with hydronautics Inc. Most of the material is based on Hydronautics Rep. 7203-2 and 7203-3 (Dagan 1972a and 1972b in References). I wish to express my gratitude to M. P. Tulin for the stimulating discussions we had on the subject and for his collaboration in the different stages of the work.

* * *

LIST OF SYMBOLS.

Dotted variables have dimensions; undotted variables are dimensionless.

A	amplitude of free waves for downstream.
C_D	coef. of wave resistance.
D'	wave drag.
f'	complex potential
F	Froude number based on half length
F_n	Froude number based on length
h'_c, h'	submergence of body axis beneath unperturbed level.
h'_s	submergence of stagnation streamline far upstream.
q'_j	strength of source located at z'_j
$\ell_{jk} = (x'_k - x'_j)\, g/U'^2$	dimensionless distance between two sources
L'	body length
L'	length related to the body image in the potential plane
N	free-surface elevation in a uniform small F expansion
$t'(x')$	thickness distribution
T'	body maximum half thickness
u' , v'	velocity components
U'	unperturbed velocity
w'	complex velocity in two dimensions : vertical velocity component in 3d.
W	perturbation complex velocity in a uniform small F expansion
x'	horizontal coordinate positive in the direction of flow
y'	vertical upwards coord. in 2d, horizontal in 3d
z'	complex variable in 2d, vertical upwards coord. in 3d.
α , β	real and imaginary parts of ω
δ	angle arbitrarily small
ϵ	slenderness parameter

ϵ_1, ϵ_2 perturbation parameters.

ϕ velocity potential in two dimensions

Φ velocity potential of a uniform small F expansion in 3d.

ψ streamfunction in 2d.

$\omega(\zeta) = e^{-i\zeta}\ \overline{Ei}(i\zeta)$. $\overline{Ei}(\zeta)$ is the exponential integral

η' free-surface elevation above the unperturbed level

$\zeta, \xi, \chi, \lambda, \nu$ auxiliary variables

σ, ρ auxiliary functions

τ slope of body contour

REFERENCES

1 Abramowitz, M. & Stegun, I. A. Handbook of Mathematical Functions, Dover, 1964

2 Cole, J. D. Perturbation methods in applied mathematics, Blaisdell Publ. Comp. 1968

3 Dagan, G. Nonlinear effects for two-dimensional flow past submerged bodies moving at low Froude numbers, Hydronautics Inc. Tech. Rep. 7103-1, 45 p. 1971

4 Dagan, G. & Tulin, M. P. Two-dimensional gravity free-surface flow past blunt bodies, J. F. M., Vol. 51, p. 3; pp. 529-543, 1972

5 Dagan, G. A study of the nonlinear wave resistance of a two-dimensional source generated body, Hydronautics Inc. Tech. Rep. 7103-2, 1972a.

6 Dagan, G. Small Froude number paradoxes and wave resistance at low speeds, Hydronautics Inc. Tech. Rep. 7103-3, 1972b.

7 Erdely, A. Asymptotic expansions, Dover, N. Y., 1956

8 Ogilvie, T. F. Wave resistance : the low speed limit, Dept. of Naval Arch. & Mar. Eng. Univ. of Michigan, Rep. No. 002, 1968

9 Salvesen, N. On higher order wave theory for submerged two-dimensional bodies, J. F. M. Vol. 38, pt. 2, pp. 415-432, 1969

10 Tuck, E. O. The effect of non-linearity at the free-surface on flow past a submerged cylinder, J. F. M., Vol. 23, pt. 2 pp. 401-414, 1965

11 Van Dyke, M. Perturbation methods in fluid mechanics, Academic, 1964

12 Wehausen, J. V. & Laitone, E. V. Surface waves, in Encyclopedia of Physics, Vol. IX, pp. 446-779, Springer, 1960

* * *

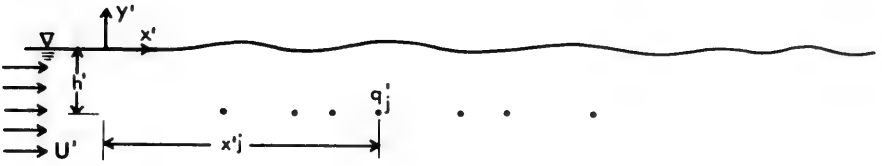

Fig. 1 A distribution of sources.

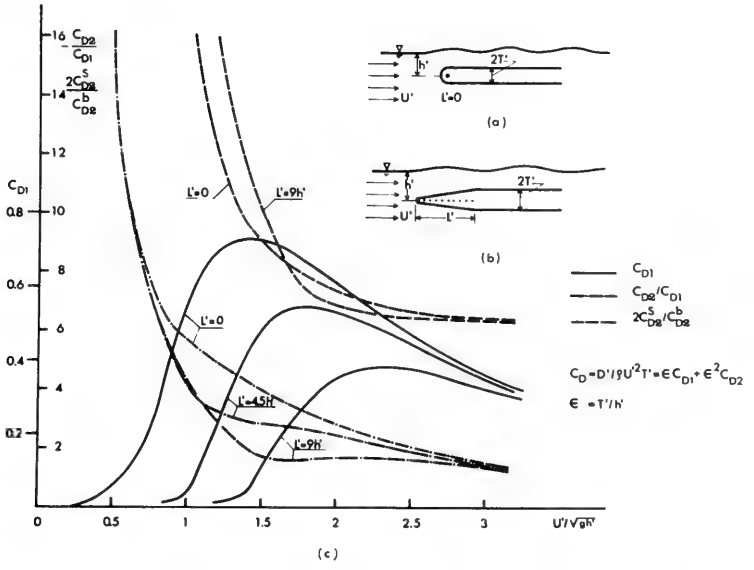

Fig. 2 Wave resistance of a body of semi-infinite length : (a) a source generated body, (b) wedge shape leading edge, and (c) wave resistance curves.

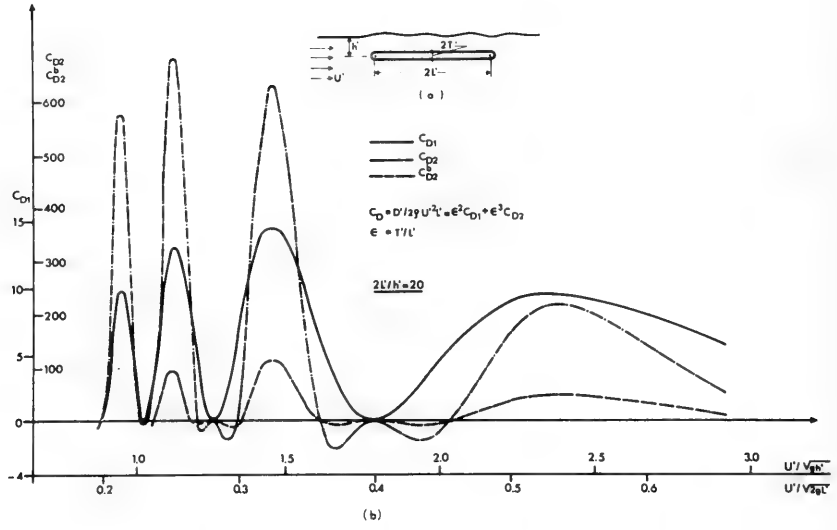

Fig. 3 Wave resistance of a source-sink body : (a) the body shape and (b) wave resistance curves for $2L' / h' = 20$

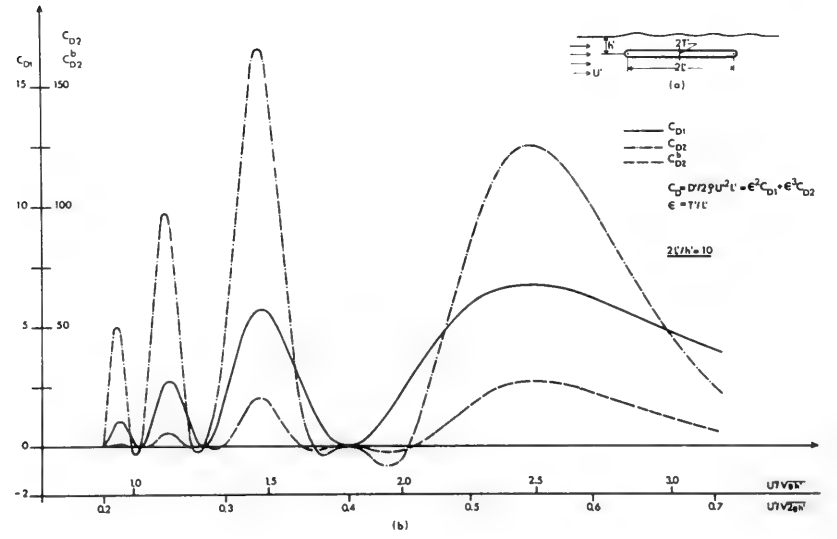

Fig. 4 Wave resistance of a source-sink body : (a) the body shape and (b) wave resistance curves for $2L' / h' = 10$

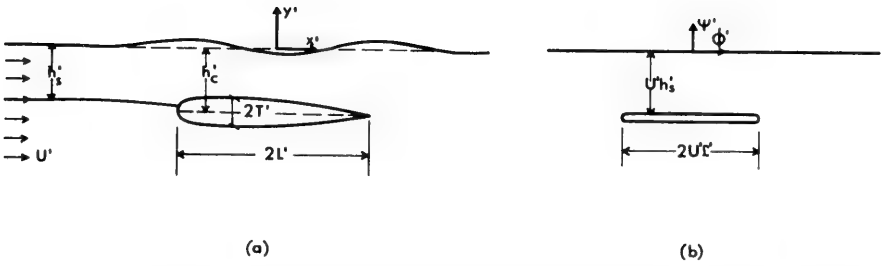

Fig. 5 Two-dimensional flow past a submerged body : (a) the physical plane and (b) the potential plane.

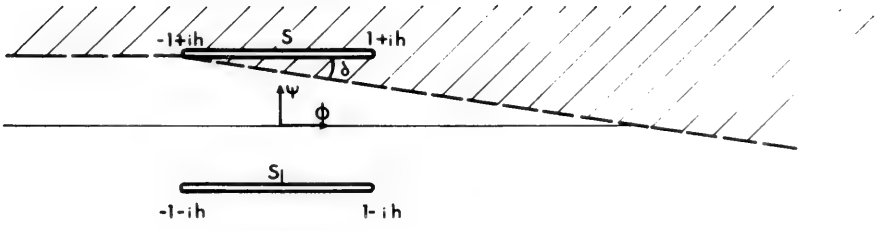

Fig. 6 Regions of uniformity of the small Froude number solutions.

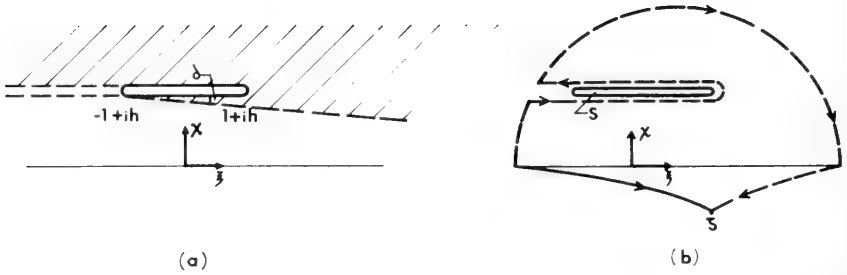

Fig. 7 (a) Regions of uniformity of small ϵ_2 solutions of the model problem and (b) integration path for large Re ζ

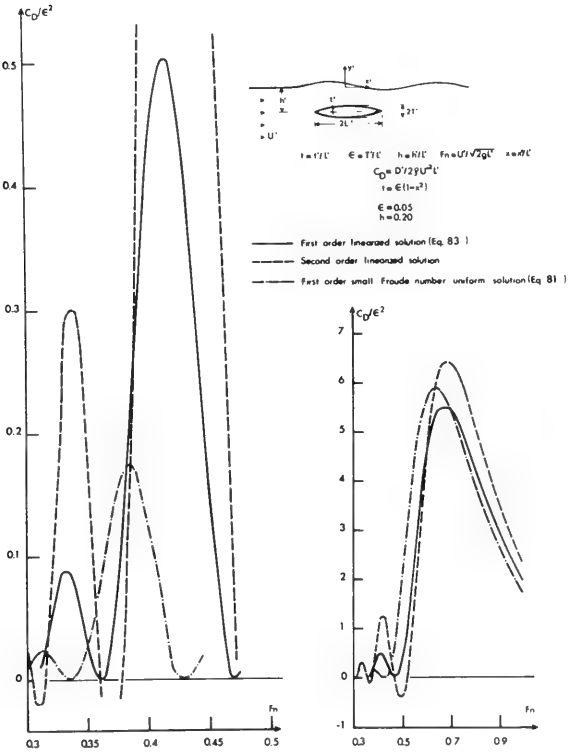

Fig. 8 Wave resistance of a biconvex parabolical body by different approximations.

(a) $U'/(gT')^{1/2} = 1.22$

(b) $U'/(gT')^{1/2} = 2.93$

Fig. 9 Flow in front of a rectangular body .

DISCUSSION

Ernest O. Tuck
University of Adelaide
Adelaide, Australia

In the first instance I want to pass on a comment that Dr. Salvesen asked me to make on his behalf because he could not be here today. Incidentally, I agree with his comment. The comment concerns neglect of the Kutta condition at the trailing edge of these two-dimensional bodies. In fact both Dr. Salvesen and I fell that our own original papers on these two-dimensional problems were deficient, in that we should have included the Kutta condition in the first order solutions. We are a little disappointed that in doing this problem again, Dr. Dagan has not seen fit to include the Kutta condition, for reasons which he has stated but with which we do not really agree.

My own comment is actually relevant to Dr. Salvesen's work, in that I feel that perhaps insufficient attention was paid to Dr. Salvesen's paper of a couple of years ago. Dr. Salvesen himself was aware of what Dr. Dagan has called the "second low Froude number paradox". He analysed this in some detail in this paper, and perhaps some direct reference could have been made to this work.

DISCUSSION

Edmund V. Telfer
R.I.N.A.
Ewell, Surrey, U.K.

I want to ask a very innocent question. Could the author tell me what he intends to be the significance of the word "naive" * in the

* According to the Oxford Dictionary the meaning of naive is " Characterised by unsophisticated or unconventional simplicity or artlessness.

description of the naive small Froude number? Is it an adjective, or should it correctly be an adverb, meaning "naively small" ? But how is anything naively small in the modern interpretation of the word "naive" ?

My second question is, would he care to hazard a guess as to how at very low speeds the wave-making resistance varies? Does it vary as the fourth power of the speed or does it vary as the sixth power of the speed? Could he just give an answer to that, because in a further paper to be discussed this afternoon this point will probably arise?

REPLY TO DISCUSSION

Gedeon Dagan
Technion Haifa, and Hydronautics Ltd
Rechovoth, Israel

Regarding the Kutta-Joukovsky condition, I have stated in the paper that I am not really interested in solving problems of two-dimensional flow, but only in using the two-dimensional computations as an instrument for understanding and opening the way for the more complex solution of three-dimensional ship problems. Since in the latter case only the thickness effect is generally taken into account, I did not consider the circulation. I agree that if one really wants to solve the problem of the hydrofoil (but I do not see the usefulness for small Froude numbers), the Kutta-Joukovsky condition has to be taken into consideration.

The paper of Dr.Salvesen has been amply quoted in the present work. I believe that my main contribution is the solution of the second paradox, and not its discovery.

The term "naive" as applied to a perturbation expansion has been borrowed from the applied mathematics literature. The word is used in the sense that one expands in an apparently natural way in a power series, without observing the nonuniformity of the expansion.

Since the present work is concerned with two-dimensional flow, no attempt has been made to correlate the resistance curve to the power of the Froude number.

ON THE UNIFORMLY VALID APPROXIMATE SOLUTIONS OF LAPLACE EQUATION FOR AN INVISCID FLUID FLOW PAST A THREE-DIMENSIONAL THIN BODY

J. S. Darrozes
Ecole Nationale Supérieure de Techniques Avancées
Paris France

ABSTRACT

The classical solution of the Laplace equation for an inviscid incompressible fluid flow past a three-dimensional thin body, is shown to be not uniformly valid in the vicinity of the planform edge (λ). In order to find a solution which is valid in the vicinity of (λ), the technique of "matched asymptotic expansions" is used. The inner solution in the neighbourhood of a rounded leading edge brings a shift correction to the classical outer solution. The inner solution in the vicinity of a sharp trailing edge gives the starting shape of the vortex sheet.

I. INTRODUCTION

The study of three-dimensional flows past arbitrary bodies gives rise to many problems of great interest in Naval Hydrodynamics. For an inviscid incompressible fluid, the velocity potential Φ is a solution of Laplace equation, and in the few last years, most of basic works have dealt with the numerical methods used to solve this problem. The greatest difficulty comes from the fact that there is no rigourous mathematical theory available for such a problem and numerical attempts may be handled only with addition of physical assumptions. A unique solution could be obtained, only after the difficult analysis of the corresponding high Reynolds number flow, in the limiting case of an evanescent viscosity. As it is not possible to do so, it is necessary to guess [1] some results in order to define a problem which has a unique solution. For instance, if the physical flow takes place with separation,

This work has been supported by the « Office National d'Etudes et de Recherches Aérospatiales »
29, Av. de la Division Leclerc – 92320 CHATILLON

we must give an a priori geometric description of the separated flow[2]. This is the reason why we will assume later on, that no separation occurs. With this condition, the Kutta-Joukowski theorem leads to a physically correct description, but, even with this requirement, one does not know the starting shape of the vortex sheet in a non-symmetric flow. So, the solution still depends upon an additive assumption[9].

One can go further, assuming that the body is very thin, because the flow is undisturbed in a first approximation, and the velocity potential Φ is formulated in the form of an asymptotic expansion. Unfortunately, new difficulties arise when the classical solution of this simpler problem is evaluated through a numerical analysis. The flow velocity is found to be infinite on the leading edge, the trailing edge and the vortex sheet edges. Up till now, theoretical investigations allow us to know the singular behaviour of the asymptotic expansion of the functions Φ , in the vicinity of the afore-mentioned lines, but they do not suffice to solve complety the problem[3] . The classical method is to consider an inner region in the neighbourhood of the singular lines in which we look for the velocity potential in the form of a new asymptotic expansion called the inner approximation. The technique of matched asymptotic expansions, which is the properway of investigation, has been successfully employed by M. J. Lighthill [4] and M. Van Dyke [5] , to solve the two-dimensional problem of a flow past a thin hydrofoil.

In this paper we apply the same technique for the three-dimensional case and it will be seen that the results depend strongly upon the wing geometry.

II. FORMULATION OF THE CLASSICAL OUTER PROBLEM

II. 1 - Basic equations

Figure 1 shows the body shape with the following assumptions and notations. The body is very closed to the plane $z = 0$, and the incident flow is supposed to have a uniform velocity at infinity, parallel to the plane xoy, in the x-direction. The planform (S) is the projection of the body on this plane, in the z-direction and its limiting curve (λ) is the projection of a curve (λ) drawn on the body. The curve (λ), which parametric equations are x(s), y(s) and ϵ z(s) separates the body surface into two parts.

- The upward surface S^+ has a given analytic expression :
  $z = \epsilon f^+(x, y)$
- The other part S^- is known in the same way :
  $z = \epsilon f^-(x, y)$

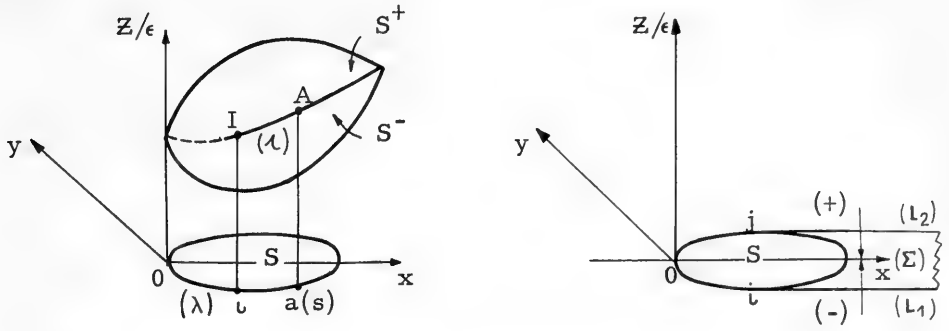

Figure I The Body shape

The straight lines (L_1) and (L_2), edges of the vortex sheet (Σ), are tangent to the planform at points i and j, projections of the points I and J belonging to the obstacle. In order to avoid separated flows, the rear part of (Λ) from I to J is assumed to be a sharp edge. The body is smooth at any other points. The vector $\vec{n}$ is a unit outward normal.

Written under its usual non-dimensional form, the problem to be solved for the velocity potential $\Phi(x, y, z, \epsilon)$ is the Laplace equation :

$$\Delta \Phi = 0$$

$$\vec{n} \cdot \vec{\nabla} \Phi = 0 \qquad \text{on } S^+(\epsilon) \cup S^-(\epsilon) \qquad (I)$$

$$\Phi \sim x \qquad \text{at infinity}$$

It is easily proved in any text-book, that the function Φ , may be approximated in term of an asymptotic expansion, the first step being the undisturbed uniform flow $\Phi^{(o)} \equiv x$

$$\Phi(x, y, z, \epsilon) = x + \epsilon \Phi^{(1)}(x, y, z) + \epsilon^2 \Phi^{(2)}(x, y, z) + O(\epsilon^3) \qquad (2)$$

At each step, we have to find an harmonic function, vanishing at infinity, and satisfying some boundary conditions, on both sides (+ and -) of planform S.

$$\left.\begin{array}{l} \Delta \Phi^{(i)} = 0 \\ \Phi^{(i)} \longrightarrow 0 \text{ at infinity} \end{array}\right\} \quad i = 1, 2, \ldots$$

$$\left.\begin{aligned} \frac{\partial \Phi^{(1)}}{\partial z} &= f'_x \Big|^{\pm} \\ \frac{\partial \Phi^{(2)}}{\partial z} &= f'_x \Big|^{\pm} \frac{\partial \Phi^{(1)}}{\partial x} + f'_z \Big|^{\pm} \frac{\partial \Phi^{(1)}}{\partial y} - f \Big|^{\pm} \frac{\partial^2 \Phi^{(1)}}{\partial z^2} \end{aligned}\right\} \begin{aligned} &z \longrightarrow 0^{\pm} \\ &(x, y) \in (S) \end{aligned}$$

We are going to consider now, the validity of the so-called "outer expansion" (2).
It could be plausible that some difficulties arise when looking for the behaviour of outer solutions $\Phi^{(i)}$ in the vicinity of the part (S) of the plane z = o, because the liquid cannot go through the body, and the first approximation seems to be a non uniform flow.

II. 2 - The region of uniform validity in the plane z = o

It is known that, any point in the xoy - plane is regular for the outer expansion (2), except the points located on the lines (λ) (L_1) and (L_2). This result is easily proved by introducing a new expansion in the following way.

Any function A (x, y, z) is written A (x, y, $\eta\tilde{z}$) = $\tilde{A}$ (x, y, $\tilde{z}$, η). The formal expansion of the function A , when z goes to zero, is identical to the expansion of the function $\tilde{A}$, when η goes to zero with a fixed value of $\tilde{z}$. The η -expansion must depend upon the cluster $\{\eta\ \tilde{z}\}$ since A does not depend upon η .

Inserting this formalism into the problem governing the ϵ - term $\tilde{\Phi}^{(1)}$ of the potential velocity, the behaviour of the solution for vanishing values of z is given by the corresponding η - expansion.

$$\tilde{\Phi}^{(1)}(x, y, \eta\tilde{z}) = \tilde{\Phi}^{(1)}(x, y, \tilde{z}, \eta) = \tilde{\Phi}_0^{(1)}(x, y) + \eta\, \tilde{\Phi}_1^{(1)}(x, y, \tilde{z}) + \ldots$$

$$\frac{\partial^2 \tilde{\Phi}^{(1)}}{\partial \tilde{z}^2} + \eta^2 \Delta_{xy} \tilde{\Phi}^{(1)} = o$$

$$\frac{\partial \tilde{\Phi}^{(1)}}{\partial \tilde{z}} = \eta\, f'_x \Big|^{\pm} \qquad \tilde{z} = o^{\pm} \quad , (x, y) \in (S).$$

The following result is obtained without any difficulty

$$\tilde{\Phi}^{(1)} = \tilde{\Phi}_0^{(1)} + \eta \tilde{z} f_x - \frac{1}{2}\eta^2 z^2 \Delta_{xy} \tilde{\Phi}_0^{(1)} - \frac{1}{6}\eta^3 \tilde{z}^3 \Delta_{xy} f'_x + \frac{1}{24}\eta^4 \tilde{z}^4 \Delta_{xy} \Delta_{xy} \tilde{\Phi}_0^{(1)} + o(\eta^5) \quad (3)$$

$\tilde{\Phi}_0^{(1)}(x,y)$ is an arbitrary function and Δ_{xy} stands for the operator

$$\frac{\partial^2}{\partial x^2} + \frac{\partial^2}{\partial y^2}$$

The same procedure is used to know the behaviour of the function $\Phi^{(2)}$

$$\frac{\partial \Phi}{\partial \tilde{z}} + \eta^2 \Delta_{xy} \tilde{\Phi}^{(2)} = 0$$

$$\frac{\partial \tilde{\Phi}^{(2)}}{\partial \tilde{z}} = \eta \left[f'^{\pm}_x \frac{\partial \tilde{\Phi}_0^{(1)}}{\partial x} + f'^{\pm}_y \frac{\partial \Phi_0^{(1)}}{\partial y} + f^{\pm} \Delta_{xy} \tilde{\Phi}_0^{(1)} \right] \tilde{z} = 0^{\pm}, \quad (x,y) \in (S)$$

The η -expansion in the vicinity of a point (x,y) on the planform (S) is

$$\tilde{\Phi}^{(2)} = \tilde{\Phi}_0^{(2)}(x,y) + \eta \tilde{z} \left[f'_x \frac{\partial \tilde{\Phi}_0^{(1)}}{\partial x} + f'_y \frac{\partial \tilde{\Phi}_0^{(1)}}{\partial y} + f \Delta_{xy} \tilde{\Phi}_0^{(1)} \right] - \frac{1}{2} \eta^2 \tilde{z}^2 \Delta_{xy} \tilde{\Phi}_0^{(2)} 0(\eta^3) \tag{4}$$

If we consider a point (x,y) on the vortex sheet (Σ), the Taylor behaviour of any function $\tilde{\Phi}^{(i)}$ is :

$$\tilde{\Phi}^{(i)\pm} = \tilde{\Phi}_0^{(i)\pm} + \eta \tilde{z} \tilde{\Phi}_1^{(i)\pm} + 0(\eta^2)$$

The pressure continuity across the sheet gives additive conditions such as

$$\frac{\partial \tilde{\Phi}_k^{(1)}}{\partial x} \Bigg|^{+} = \frac{\partial \tilde{\Phi}_k^{(1)}}{\partial x} \Bigg|^{-}$$

Outside $S \cup \Sigma$, $\tilde{\Phi}^{(i)} \equiv 0$. Consequently, $\tilde{\Phi}^{(i)}$ is a discontinuous function on the curves (λ), (L_1) and (L_2). At these points the flow velocity has no meaning and the outer expansion (2) is not valid. Elsewhere, this expansion is uniformly valid, as it can be shown easily in the following analysis corresponding to a point (x,y) located inside the planform (S).

If the approximation (2) is not valid in the neighbourhood of (S), it must be within a region of thickness $0(\epsilon)$, because, in such a layer, the boundary conditions must be written on the real body, and cannot be approximated by a condition on the plane $z = 0$. Replacing η by ϵ , the preceding results give the behaviour of the inner solution at infinity rewritten with the inner variable $\tilde{z}$, as indicated by the matching conditions.

$$\tilde{\Phi} = x + \epsilon \tilde{\Phi}_0^{(1)}(x,y) + \epsilon^2 \left[\tilde{\Phi}_0^{(2)} + z f'_x \right] + \qquad (5)$$

$$+ \epsilon^3 \tilde{\Phi}_0^{(3)} + z \left(f'_x \frac{\partial \tilde{\Phi}_0^{(1)}}{\partial x} + f'_y \frac{\partial \tilde{\Phi}_0^{(1)}}{\partial y} + f \Delta_{xy} \tilde{\Phi}_0^{(1)} \right) - \frac{\tilde{z}^2}{2} \Delta_{xy} \tilde{\Phi}_0^{(1)} \Big] + O(\epsilon^4)$$

The inner problem is formulated as follow :

$$\frac{\partial^2 \tilde{\Phi}}{\partial \tilde{z}^2} + \epsilon^2 \Delta_{xy} \tilde{\Phi} = 0$$

$$\frac{\partial \tilde{\Phi}}{\partial \tilde{z}} = \epsilon \left\{ f'_x \pm \frac{\partial \tilde{\Phi}}{\partial x} + f'_y \pm \frac{\partial \tilde{\Phi}}{\partial y} \right\} \quad \text{on } \tilde{z} = f^{\pm}(x,y)$$

+ Matching conditions at infinity.

The expansion (5) is shown to be the exact inner solution. Therefore, the inner region exhibits nothing more than the behaviour of the outer solution. This means that the outer expansion is regular at any point $(x, y) \in S$, and the inner region is not required.

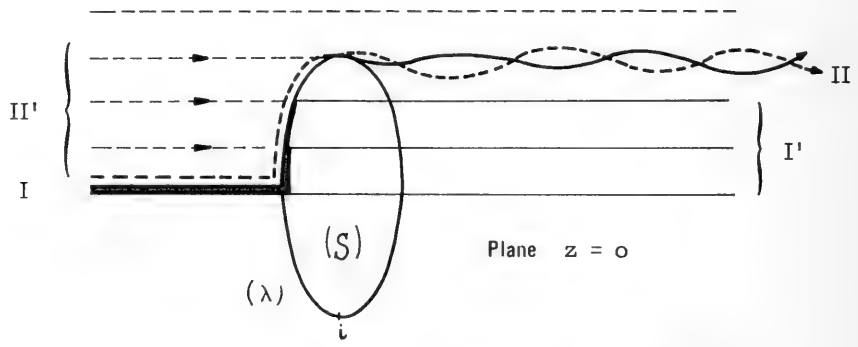

Figure 2 Sketch of the flow when ε goes to zero . The streamling I generates the streamlines I' from the leading edge. The streamlines II'gives only the streamline II.

Figure 2 shows the flow in the xoy-plane, when ε vanishes. There exist physical reasons to explain the singular behaviour of the outer solution on the lines (λ) and (L_1). On a round leading edge, the slope is infinite and the normal velocity $w = \partial\Phi/\partial z$ is o (1) instead of o (ε). At any point of the angular trailing edge, the Kutta- Joukowski condition requires a velocity tangent to the curve (λ), which contredicts the fact that there is a uniform flow in the first approximation. On the line (L_1) , the streamlines I' closed to the streamline II rolls up, and generates the apex vortex. At infinity downstream, any

streamline (I') goes to (L_1) and makes the vortex growing.

III. THE SINGULAR BEHAVIOUR OF THE OUTER SOLUTION ON THE PLANFORM EDGE (λ)

In this section, we look for the behaviour of the outer solutions $\Phi^{(1)}$ and $\Phi^{(2)}$, in the vicinity of a round leading edge, or a sharp trailing edge. To this end, a carefull description of the body geometry is required.

III. I The body geometry

Let us denote by $\vec{\nu}$ (s), the outward normal to (λ) in the plane z = o.

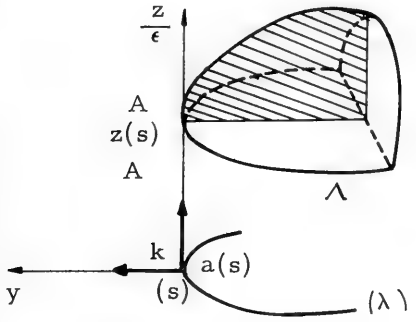

Figure 3 The leading edge geometry (upper surface).

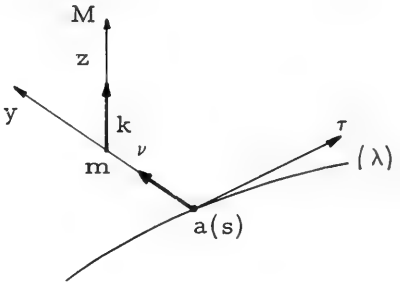

Figure 4 The local curvilinear coordinates.

We define a reference frame aXYZ, with aZ parallel to the z-axis, and the unit vector $\vec{\nu}$ in the Y-direction. Figure 4 shows the local curvilinear coordinates (s, Y, Z) :

$$\vec{OM} = \vec{Oa}\,(s) + Y\vec{\nu}\,(s) + Z\vec{k}$$
$$\vec{DM} = h_1\vec{\tau}\,ds + \vec{\nu}\,dY + \vec{k}\,dZ \qquad (6)$$
$$h_1 = 1 - Y\,C\,(s)$$

C (s) stands for the curvature of the planform edge (λ). If this quantity does not vanish for any value of s , the mapping (x, y, z) ⟷ (s, Y, Z) is a one to one transformation in a region of thickness less than $s^{inf}|C(s)|$, surrounding the curve (λ). In this region, the body equation may be written under the form :

$$\frac{Z}{\epsilon} = z_A(s) + H^{\pm}(s, Y) \qquad (7)$$

with the condition : $H^{\pm}(s, Y) \to o$ when $Y \to o$ for any s. The behaviour of functions $H^{\pm}$ when Y goes to zero is obtained using the reverse functions $G^{\pm} = H^{-1\pm}$. The identity : $Y \equiv G^{\pm}(s, H(s, Y))$ is expanded into Taylor series for small values of H :

$$Y \equiv a_1^{\pm} H^{\pm} + a_2^{\pm} H^{\pm 2}/2 + \ldots$$

The following results are found.

a) Round leading edge $a_1^{\pm} = o$, $a_2^{\pm} < o$

$$\frac{Z}{\epsilon} = z_A(s) + \sqrt{\frac{2Y}{a_2^{\pm}}} - \frac{a_3^{\pm} Y}{3(a_2^{\pm})^2} + O(Y^{2/3}) \qquad (8)$$

b) Sharp trailing edge $a_1^{\pm} \neq o$

$$\frac{Z}{\epsilon} = z_A(s) + \frac{Y}{a_1^{\pm}} - \frac{a_2^{\pm} y^2}{2(a_1^{\pm})^3} + \frac{1}{2(a_1^{\pm})^4}\left(\frac{(a_2^{\pm})}{a_1^{\pm}} - \frac{a_3^{\pm}}{3}\right) Y^3 + O(Y^4) \qquad (9)$$

c) The transitions point I and J. Assuming that $s(I) = o$, we must have $a_1(s) = o \quad s \leq o$; $a_1(s) \neq o \quad s > o$, and conversely for the other point J

When $s \to o^+$ we admit the following expansion

$$a_1(s) = \bar{a}_1 s^{\alpha} + o(s^{\alpha}) \qquad \alpha \geq 1$$

In that case the behaviour of the body equation in the vicinity of point I, depends upon the way in which s and Y goes to zero. In other words, the expansion (9) is not uniformly valid when s goes to zero. It is possible to write a uniformly valid approximation of the function $H(s, Y) = \frac{Z}{\epsilon} - z_A(s)$, for any limiting process ($s \to o$ and $Y \to o$)[7]. The corresponding description is given when Y and s go to zero simultaneously : $Y = \mu(s)\hat{Y}$, with $\mu(s) \to o$ when $s \to o$, and $\hat{Y}$ has a fixed value. The function $\mu(s)$ is determined by using the less degeneracy principle. Writting $H(s, Y) = H(s, \mu\hat{Y}) = \hat{H}(s, \hat{Y})$, we know that $\hat{H}(s, \hat{Y}) \to o$ when $s \to o$ for a fixed value of $\hat{Y}$, and

$$\hat{H}(s, \hat{Y}) = r(s)\left\{\hat{H}_o(\hat{Y}) + o(1)\right\}$$

Inserting these definitions in the equation

$$Y = a_1 H + \frac{a_2}{2} H^2 + \frac{a_3}{6} H^3 + \ldots$$

we obtain :

$$\mu(s)\hat{Y} = \bar{a}_1 s^{\alpha} r(s)\left\{\hat{H}_0 + \ldots\right\} + \frac{a_2}{2} r^2(s)\left\{\hat{H}_0 + \ldots\right\}^2 + \ldots$$

In order to take into account the greatest number of terms in the

first approximation, we must choose : $r(s) = s^{\alpha}$ and $\mu(s) = s^{2\alpha}$
Then

$$\frac{Z}{\epsilon} = z_A(s) - \frac{s^{\alpha}}{a_2^{\pm}}\left[\bar{a}_1^{\pm} - \sqrt{(\bar{a}_1^{\pm})^2 + 2a_2^{\pm}\hat{Y}}\right] + o(s^{\alpha}) \qquad (10)$$

This expansion is shown to be uniformly valid in a neighbourhood of the point I, after verifying that :
the limit $\hat{Y} \to \infty$ gives expression (8)
the limit $\hat{Y} \to 0$ gives expression (9)

III. 2 The vicinity of a round leading edge

This paragraph is devoted to the study of the singular behaviour of the outer solutions $\Phi^{(1)}$ and $\Phi^{(2)}$, in the vicinity of a point A belonging to a round leading edge. Let us start our investigation with the function $\Phi^{(1)}$, solution of the equation (11).

$$\Delta\,\Phi^{(1)} = o$$
$$\frac{\partial \Phi^{(1)}}{\partial z} = f'^{\pm}_{x} \qquad (x,y) \in S \qquad (11)$$

which is rewritten using the curvilinear coordinates :

$$\Delta_{YZ}\Phi^{(1)} - \frac{C(s)}{1 - YC(s)}\frac{\partial \Phi^{(1)}}{\partial Y} + (1 - YC(s))^{-2}\frac{\partial \Phi^{(4)}}{\partial s} + \frac{YC'(s)}{(1-YC)^3}\frac{\partial \Phi^{(1)}}{\partial s} = o$$

$$\frac{\partial \Phi^{(1)}}{\partial Z} = \frac{\cos\alpha(s)}{1 - YC(s)}\left(z'_A(s) + H'^{\pm}_s\right) - \sin\alpha(s)\,H'^{\pm}_y \quad (Z \to o^{\pm}) \qquad (12)$$

There are many solutions to this problem, due to the fact that we cannot take into account the condition at infinity, when looking for a beha - viour. Any solution of equation (12) is obtained from a particular one, after addition of a solution corresponding to the homogeneous problem $\left(\frac{\partial \Phi^{(1)}}{\partial \bar{Z}} = o \quad , \quad Z \to o\right)$

The homogeneous problem

In order to investigate the behaviour of the homogeneous solutions in the vicinity of A , we define the new variables

$$\tilde{Y} = Y/\eta\,; \qquad \tilde{Z} = \left(Z - \epsilon z_A(s)\right)/\eta$$

with $\eta \ll 1$

We look for an η - expansion of the function

$$\Phi^{(1)}\left(s,\ \eta\tilde{Y},\ \epsilon z_A(s) + \eta\tilde{Z}\right) = \tilde{\Phi}\ (s, \tilde{Y}, \tilde{Z})$$

solution of the homogeneous equation (13)

$$\Delta_{\tilde{Y}\tilde{X}} \Phi^{(1)} - \eta\, C(s)\, \frac{\partial \tilde{\Phi}^{(1)}}{\partial \tilde{Y}} + o(\eta^2) = o \qquad (13)$$

$$\frac{\partial \Phi^{(1)}}{\partial \tilde{Z}} = o \qquad \tilde{Z} = o \ , \quad \tilde{Y} < o$$

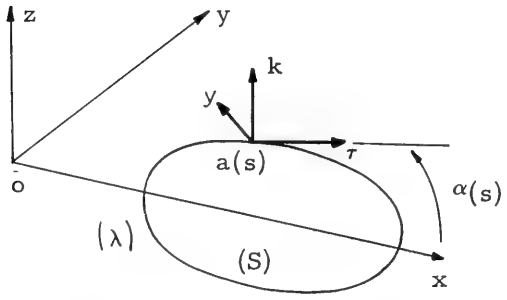

Geometry of the outer problem

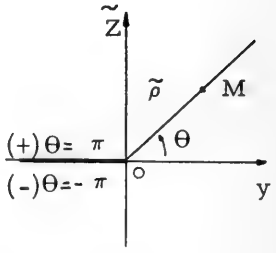

The complex variable

Figure 5

Using the complex variable $\tilde{z} = \tilde{\rho}\, e^{i\theta} = \tilde{Y} + i\, \tilde{Z}$, and its conjugated value $z_* = \tilde{Y} - i\, \tilde{Z}$, it is easily shown that the η - expansion of $\tilde{\Phi}^{(1)}$, must be written with the asymptotic sequence $\eta^{k/2}$ (k = 1, 2, ...)

$$\tilde{\Phi}^{(1)} = \Phi_0^{(1)} + \eta^{1/2} \tilde{\Phi}_1^{(1)} + \eta\, \tilde{\Phi}_2^{(1)} + O\left(\eta^{3/2}\right) \qquad (14)$$

Each term is obtained after resolution of a trivial Hilbert problem on the negative part of the real axis of the plane $\tilde{z}$. The final result is :

$$\tilde{\Phi}^{1} = c_0(s) + \eta^{1/2} d_1(s)\, \tilde{\rho}^{1/2} \sin\frac{\theta}{2} + \eta\, c_2(s)\, \tilde{\rho} \cos + \eta^{3/2} d_3(s)\, \tilde{\rho}^{3/2} \sin\frac{3\theta}{2} = O(\eta^{2})$$

$c_0(s)$, $d_1(s)$, $c_2(s)$ and $d_3(s)$ being arbitrary functions

The full problem

We are now looking for solutions of equation (16)

$$\Delta_{YZ} \tilde{\Phi}^{(1)} - \eta\, C(s)\, \frac{\partial \tilde{\Phi}^{(1)}}{\partial \tilde{Y}} + O(\eta^2) = o$$

$$\frac{\partial \tilde{\Phi}^{(1)}}{\partial \tilde{Z}} = \eta^{1/2} \frac{\delta_0^{\pm}(s)}{\tilde{\rho}^{1/2}} + \eta\, \delta_1^{\pm}(s) + \eta^{3/2} \delta_2^{\pm}(s) + 0(\eta^2) \qquad (16)$$

$$\tilde{Z} = o^{\pm} \ , \qquad \tilde{Y} \leqslant o$$

Using the previous result (15), it seems plausible to try an a priori expansion under the form :

$$\tilde{\Phi}^{(1)} = \eta^{1/2}\tilde{\Phi}_1^{(1)} + \eta\,\tilde{\Phi}_2^{(1)} + \eta^{3/2}\tilde{\Phi}_3^{(1)} + \dots \qquad (17)$$

It will be seen, later on, that expansion (17) is incomplete, because the asymptotic sequence must contain logarithmic terms.

Let us consider the problem to be solved in order to find $\tilde{\Phi}_1^{(1)}$

$$\Delta_{\tilde{Y}\tilde{Z}}\tilde{\Phi}_1^{(1)} = 0 \implies$$

$$\tilde{\Phi}_1^{(1)}(\tilde{z},\tilde{z}_*) = \left[A_1^{(1)}(\tilde{z}) + A_1^{(1)}(\tilde{z}_*)\right] + i\left[B_1^{(1)}(\tilde{z}) - B_1^{(1)}(\tilde{z}_*)\right]$$

where $A_1^{(1)}(\tilde{Y})$ and $B_1^{(1)}(\tilde{Y})$ are real functions on the positive part of the real axis. The holomorphic functions $A_1^{(1)}(\tilde{z})$ and $B_1^{(1)}(\tilde{z})$ are obtained after solving the Hilbert problems deduced from the boundary conditions

$$\frac{\partial\Phi_1^{(1)}}{\partial\tilde{Z}} = i\left(\frac{\partial A_1^{(1)}}{\partial\tilde{z}} - \frac{\partial A_1^{(1)}}{\partial\tilde{z}_*}\right) - \left(\frac{\partial B_1^{(1)}}{\partial\tilde{z}} + \frac{\partial B_1^{(1)}}{\partial\tilde{z}_*}\right) = \frac{\delta_0^{\pm}(s)}{\tilde{\rho}^{1/2}}$$

$$\tilde{Z} \longrightarrow 0^{\pm} \qquad \tilde{Y} < 0$$

$$\theta\to\pi \quad i\left(A_1'^{(1)+} - A_1'^{(1)-}\right) - \left(B_1'^{(1)+} + B_1'^{(1)-}\right) = \frac{\delta_0^{+}(s)}{\tilde{\rho}^{1/2}}$$

$$\theta\to\pi \quad i\left(A_1'^{(1)-} - A_1'^{(1)+}\right) - \left(B_1'^{(1)+} + B_1'^{(1)-}\right) = \frac{\delta_0^{-}(s)}{\tilde{\rho}^{1/2}}$$

$$A_1'^{(1)+} - A_1'^{(1)-} = -i\,\delta_0^{(e)}(s)/\tilde{\rho}^{1/2} \qquad (18)$$

$$B_1'^{(1)+} + B_1'^{(1)-} = -\delta_0^{(p)}(s)/\tilde{\rho}^{1/2} \qquad (19)$$

The following notations are used :

$$f'(\tilde{z}) = \frac{df}{dz} \quad ; \quad \delta_0^{(e)} = \frac{1}{2}\left(\delta_0^{\pm} - \delta_0^{-}\right) \quad ; \quad \delta_0^{(p)} = \frac{1}{2}\left(\delta_0^{+} + \delta_0^{-}\right)$$

The solution of equation (18) is : $A_1^{(1)} = \delta_0^{(e)}(s)\,\tilde{z}^{\frac{1}{2}}$ + homogeneous solution.

The solution of equation (19) is : $B_1^{(1)} = -\dfrac{\delta_0^{(p)}(s)}{\pi}\,z^{\frac{1}{2}}\log\tilde{z}$ + homogeneous solution.

Coming back to the previous variable $z = \eta\tilde{z} = Y + iZ$ we can see that $\eta^{\frac{1}{2}}\,\delta_0^{(e)}(s)\,\tilde{z}^{\frac{1}{2}} = \delta_0^{(e)}(s)\,z^{\frac{1}{2}}$ does not depend upon η . But the function

$$-\eta^{\frac{1}{2}}\frac{\delta_0^{(p)}(s)}{\pi}\,\tilde{z}^{\frac{1}{2}}\log\tilde{z} = -\frac{\delta_0^{(p)}(s)}{\pi}\,z^{\frac{1}{2}}\log z + \log\eta\,\frac{\delta_0^{(p)}}{\pi}\,z^{\frac{1}{2}}$$

still depends upon η .

It is easy to see that the logarithmic term is an homogeneous solution. Then, the expansion of the function $\tilde{\Phi}^{(1)}$ is :

$$\tilde{\Phi}^{(1)} = \eta^{1/2}\mathrm{Log}\,\eta\,\frac{2\delta_0^{(p)}}{\pi}\tilde{\rho}^{1/2}\sin\frac{\theta}{2} + \eta^{1/2}\tilde{\rho}^{1/2}\left[2\,\delta_0^{(e)}\cos\frac{\theta}{2} + \frac{2\delta_0^{(p)}}{\pi}\left(\mathrm{Log}\,\tilde{\rho}\sin\frac{\theta}{2} + \theta\cos\frac{\theta}{2}\right)\right] + O(\eta^{1/2})$$

The same procedure is used to evaluate the following terms, and after many computations, the final result is found to be :

$$\tilde{\Phi}^{(1)} =$$

$$+\eta^{1/2}\left[2\,\delta_0^{(e)}\tilde{\rho}^{1/2}\cos\frac{\theta}{2} + \frac{2\,\delta_0^{(p)}}{\pi}\tilde{\rho}^{1/2}\left(\log\tilde{\rho}\,\sin\frac{\theta}{2} + \theta\cos\frac{\theta}{2}\right)\right.$$

$$\left. + \eta\left[-\delta_1^{(p)}\tilde{\rho}\,\sin\theta - \frac{\delta_1^{(e)}}{\pi}\,\tilde{\rho}\left(\log\tilde{\rho}\,\cos\theta - \theta\sin\theta\right)\right.\right.$$

$$\left. - \eta^{3/2}\left\{\tilde{\rho}^{3/2}\cos\frac{3\theta}{2}\left[C(s)\,\delta_0^{(e)} - \frac{1}{3}\,\delta_2^{(e)}\right]\right.\right.$$

$$\left.\left. + \frac{2}{\pi}\,\tilde{\rho}^{3/2}\left(\sin\frac{3\theta}{2}\log\tilde{\rho} + \theta\cos\frac{3\theta}{2}\right)\left[C(s)\,\delta_0^{(p)} - \frac{1}{3}\,\delta_2^{(p)}\right]\right\}\right.$$

Particular solution of the non-homogeneous problem

$$\left. + C_0(s) + \eta^{1/2}\log\eta\,\frac{2\,\delta_0^{(p)}}{\pi}\tilde{\rho}^{1/2}\sin\frac{\theta}{2}\right.$$

$$\left. + d_1(s)\,\tilde{\rho}^{1/2}\sin\frac{\theta}{2}\right] - \eta\log\eta\,\frac{\delta_1^{(e)}}{\pi}\tilde{\rho}\cos\theta$$

$$\left. + C_2(s)\,\tilde{\rho}\cos\theta\right]$$

$$+\eta^{3/2}\log\eta\,\frac{2}{\pi}\sin\frac{3\theta}{2}\tilde{\rho}^{3/2}\left[C(s)\,\delta_0^{(p)} - \frac{1}{3}\,\delta_2^{(p)}\right]$$

$$+ d_3(s)\sin\frac{3\theta}{2} +$$

$$+ O\left(\eta^{5/2}\log\eta\right)$$

General solution of the homogeneous problem

Following the same argumentation, we investigate now the behaviour of the function $\Phi^{(2)}$ solution of the equation (21).

$$\Delta_{YZ}\Phi^{(2)} - \frac{C(s)}{1-YC(s)}\,\frac{\partial\Phi^{(2)}}{\partial Y} + (1-YC)^{-2}\,\frac{\partial^2\Phi^{(2)}}{\partial s^2} + \frac{YC'(s)}{(1-YC)^3}\,\frac{\partial\Phi^{(2)}}{\partial s} = o \qquad (21)$$

$$\frac{\partial\Phi^{(2)}}{\partial Z} = (1-YC)^{-2}\left(z_A'(s) + H_S^{\prime\pm}\right)\frac{\partial\Phi^{(1)}}{\partial s} + H_Y^{\prime\pm}\frac{\partial\Phi^{(1)}}{\partial Y} - H^{\pm}\frac{\partial\Phi^{(1)}}{\partial Z^2} \qquad Z \to o^{\pm},\ Y \leqslant o$$

With the new coordinates $\tilde{Y} = Y/\eta$ and $\tilde{Z} = (Z - \epsilon\, z_A(s))/\eta$, and using the known expansions

$$H^{\pm}(s,\ \eta\ \tilde{Y}) = \sqrt{\eta\,|\tilde{Y}|}\quad H_0^{\pm} + \eta\ \tilde{Y}\ H_1^{\pm} + \ldots$$

$$H_Y^{\prime\pm}(s,\ \eta\ \tilde{Y}) = \frac{1}{\sqrt{\eta\,|\tilde{Y}|}}\quad H_0^{\prime\pm} + \quad H_1^{\prime\pm} + \ldots$$

$$\frac{\partial\Phi^{(1)}}{\partial Y} = \frac{\log\eta}{\sqrt{\eta\,|\tilde{Y}|}}\quad \Phi_0^{\prime\pm} + \frac{1}{\sqrt{\eta\,|\tilde{Y}|}}\quad \Phi_1^{\prime\pm} + \log\eta\,\Phi_2^{\prime\pm} + \Phi_3^{\prime\pm} \quad + \ldots$$

$$\frac{\partial^2 \Phi^{(2)}}{\partial \tilde{Z}^2} = \frac{\log \eta}{(\eta |\tilde{Y}|)^{3/2}} \Phi_0^{\parallel \pm} + \frac{1}{(\eta |\tilde{Y}|)^{3/2}} \Phi_1^{\parallel \pm} + \frac{1}{\eta \tilde{Y}} \Phi_2^{\parallel \pm} + \dots$$

the equation (21) is rewritten below :

$$\Delta_{\tilde{Y}\tilde{Z}} \tilde{\Phi}^{(2)} - \eta C(s) \frac{\partial \tilde{\Phi}^{(2)}}{\partial \tilde{Y}} + o(\eta^2) = o$$

$$\frac{\partial \tilde{\Phi}^{(2)}}{\partial \tilde{Z}} = \frac{\text{Log } \eta}{\tilde{Y}} \left[- H_0^{\pm} \Phi_0^{\parallel \pm} + H_0^{\mid \pm} \Phi_0^{\mid \pm} \right] + \frac{1}{\tilde{Y}} \left[- H_0^{\pm} \Phi_1^{\parallel \pm} + H_0^{\mid \pm} \Phi_1^{\mid \pm} \right] +$$

$$+ \text{Log } \eta \sqrt{\frac{\eta}{|\tilde{Y}|}} \left[- H_1^{\pm} \Phi_0^{\parallel \pm} + H_0^{\mid \pm} \Phi_2^{\mid \pm} + H_1^{\mid \pm} \Phi_0^{\mid \pm} \right] +$$

$$+ \sqrt{\frac{\eta}{|\tilde{Y}|}} \left[- H_0^{\pm} \Phi_2^{\parallel \pm} + H_1^{\pm} \Phi_1^{\parallel \pm} + H_0^{\mid \pm} \Phi_3^{\mid \pm} + H_1^{\mid \pm} \Phi_1^{\mid \pm} \right]$$

$$+ \dots$$

$$\tilde{Z} \longrightarrow o \qquad \tilde{Y} < o$$

$$H_0 = \sqrt{\frac{2}{|a_2|}} \quad , \quad H_1 = - a_3 / 3 (a_2)^2 \quad , \quad H_0' = - 1 / \sqrt{2 |a_2|} \, ,$$

$$H_1' = - a_3 / 3 a_2^2$$

$$\Phi_0^{\mid \pm} = \mp \frac{\delta_0^{(p)}}{\pi}, \quad \Phi_1^{\mid \pm} = \pm d_1 \mp \frac{2 \delta_0^{(p)}}{\pi} \mp \frac{\delta_0^{(p)}}{\pi} \text{Log } |\tilde{Y}|, \quad \Phi_2^{\mid \pm} = - \frac{\delta_1^{(e)}}{\pi} \, ,$$

$$\Phi_3^{\mid \pm} = - \frac{\delta_1^{(e)}}{\pi} \text{Log } |\tilde{Y}| + 2 c_2 - \frac{\delta_1^{(e)}}{\pi}$$

$$\Phi_0^{\parallel \pm} = \pm \frac{\delta_0^{(p)}}{2 \pi} \, , \quad \Phi_1^{\parallel \pm} = + \frac{\delta_0^{(p)}}{2 \pi} \text{Log } |\tilde{Y}| \mp \frac{d_1}{2} \quad , \quad \Phi_2^{\parallel \pm} = - \frac{\delta_1^{(e)}}{\pi}$$

The expanded solution contains some terms $o (\text{Log } \eta)^2$ and $o \left(\eta^{1/2} (\text{Log } \eta)^2 \right)$ because the Hilbert problem :

$$\mu^+ - \mu^- = \text{Log } \tilde{\rho} \qquad \Theta = \pm \pi \qquad \tilde{\rho} = |\tilde{Y}|$$

has the particular solution $\mu (\tilde{z}) = \frac{1}{4 i \pi} (\text{Log } \tilde{z})^2$

After analytical calculations, the result is found to be :

$$\tilde{\Phi}^{(2)} = (\text{Log } \eta)^2 \tilde{\Phi}_0^{(2)} + \text{Log } \eta \, \tilde{\Phi}_1^{(2)} + \tilde{\Phi}_2^{(2)} + \eta^{1/2} (\text{Log } \eta)^2 \tilde{\Phi}_3^{(2)} + \eta^{1/2} \text{Log } \eta \tilde{\Phi}_4^{(2)} + \dots \quad (23)$$

$$\tilde{\Phi}_0^{(2)} = \frac{\delta_0^{(p)}}{2 \pi^2} \cdot \frac{H_0^+ + H_0^-}{2} \, , \quad \tilde{\Phi}_1^{(2)} = \frac{\delta_0^{(p)}}{\pi^2} \cdot \frac{H_0^+ + H_0^-}{2} \, ,$$

$$\tilde{\Phi}_2^{(2)} = \frac{\delta_0^{(p)}}{2\pi^2} \cdot \frac{H_0^+ + H_0^-}{2} \left[(\mathrm{Log}\,\tilde{\rho})^2 - \Theta^2 \right] - \frac{\Theta \delta_0^{(p)}}{\pi} \cdot \frac{H_0^+ - H_0^-}{2},$$

$$\tilde{\Phi}_3^{(2)} = -\frac{4}{\pi} \tilde{\rho}^{1/2} \sin\frac{\Theta}{2} \left[3\,\delta_0^{(p)} \frac{H_1^+ - H_1^-}{2} - \delta_1^{(e)} \frac{H_0^+ + H_0^-}{2} \right]$$

$$\tilde{\Phi}_4^{(2)} = -\frac{8}{\pi} \tilde{\rho}^{1/2} \left[3\delta_0^{(p)} \frac{H_1^+ - H_1^-}{2} - \frac{\delta_1^{(e)}}{2} \frac{H_0^+ + H_0^-}{2} \right] \left[(\mathrm{Log}\,\tilde{\rho} - 2)\sin\frac{\Theta}{2} + 2\Theta\cos\frac{\Theta}{2} \right] -$$
$$- \frac{2}{\pi} \tilde{\rho}^{1/2} \cos\frac{\Theta}{2} \left[3\,\delta_0^{(p)} \frac{H_1^+ + H_1^-}{2} - \frac{\delta_1^{(e)}}{2} \frac{H_0^+ - H_0^-}{2} \right]$$

III. 3 The vicinity of a sharp trailing edge

This paragraph is devoted to the study of the asymptotic behaviour of the flow velocity potential, in the neighbourhood of a sharp trailing edge. The function $\tilde{\Phi}^{(1)}(s, \tilde{Y}, \tilde{Z}, \eta)$ must fulfill the following equation :

$$\Delta_{\tilde{Y}\tilde{Z}} \tilde{\Phi}^{(1)} - \eta\, C(s) \frac{\partial \Phi^{(1)}}{\partial \tilde{Y}} + O(\eta^2) = o$$

$$\frac{\partial \tilde{\Phi}^{(1)}}{\partial \tilde{Z}} = \eta\, \delta_1^{\pm}(s) + \eta^2 \delta_2^{\pm}(s)\, \tilde{Y} + \ldots$$

$$\tilde{Z} \longrightarrow o^{\pm} \quad , \qquad \tilde{Y} < o \tag{24}$$

with the addition of the generalized Kutta-Joukowski condition :

$$\left| \frac{\partial \tilde{\Phi}^{(1)}}{\partial \tilde{Z}} \right| , \left| \frac{\partial \tilde{\Phi}^{(1)}}{\partial \tilde{Y}} \right| , \left| \frac{\partial \tilde{\Phi}^{(1)}}{\partial s} \right| \quad \text{bounded by } \tilde{\rho}^{-k} \text{ , when } \tilde{\rho} \longrightarrow o, \forall K > o \tag{25}$$

When $\tilde{Z} \longrightarrow o^{\pm}$ with a positive value of $\tilde{Y}$, the pressure must be a continuous function :

$$\tilde{p}^{(1)} = - \frac{\sin\alpha}{\eta} \frac{\partial \tilde{\Phi}^{(1)}}{\partial \tilde{Y}} + \cos\alpha \frac{\partial \tilde{\Phi}^{(1)}}{\partial s} \left[1 + \eta C \tilde{Y} + o(\eta^2) \right] \tag{26}$$

The symbols $\delta_1^{\pm}(s)$ and $\delta_2^{\pm}(s)$ have a new definition in this section (see (9))

$$\delta_1^{\pm} = \cos\alpha\, z_A'(s) - \sin\alpha / a_1^{\pm}(s)$$

$$\delta_2^{\pm} = -(a_2/a_1^3)^{\pm} \sin\alpha + C\cos\alpha\, z_A'(s) - \cos\alpha\,(a_1'/a_1^2)$$

Now, we proceed as in the last section, in the complexe plane $\tilde{z} = \tilde{Y} + i\,\tilde{Z}$

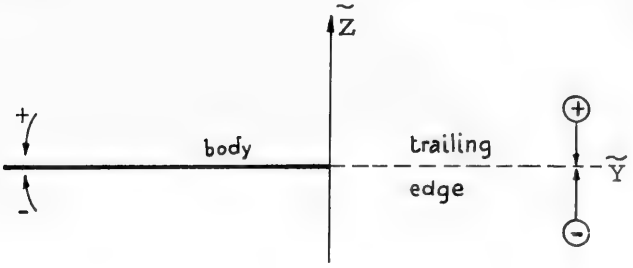

Figure 6

If the η-expansion of the velocity potential has a term o (1)

$$\tilde{\Phi}^{(1)} = \tilde{\Phi}_0^{(1)} + \ldots$$

the function $\tilde{\Phi}_0^{(1)}$ is a solution of the homogeneous problem

$$\Delta \tilde{\Phi}_0^{(1)} = o \Rightarrow \tilde{\Phi}_0^{(1)}(\tilde{z}, \tilde{z}_*) = A_0(\tilde{z}) + A_0(\tilde{z}_*) + i\left(B_0(\tilde{z}) - B_0(\tilde{z}_*)\right)$$

but $A_0(\tilde{z})$ and $B_0(\tilde{z})$ are holomorphic functions except on the real axis. For the negative values of $\tilde{Y}$, $A_0(\tilde{z})$ and $B_0(\tilde{z})$ are not defined when $\tilde{Z}$ goes to zero, and the limit functions are denoted $A_0^{\pm}(\tilde{Y})$ and $B_0^{\pm}(\tilde{Y})$.

In the same way, we denote by $A_0^{(\pm)}(\tilde{Y})$ and $B_0^{(\pm)}(\tilde{Y})$ the corresponding limits for $\tilde{Y} \geqslant o$. As an exemple, we solve the problem involving $A_0(\tilde{z})$.

$$A_0^{1+} = A_0^{1-} = k$$

$k = o$, because the function $A_0(\tilde{z})$ cannot contain $\tilde{z}$. Then $A_0(\tilde{z})$ is a constant, but this constant may have different values in the upper plane and in the lower plane ($\tilde{Z} < o$).

$$\begin{aligned} A_0(\tilde{z}) &= c_0^+(s) \qquad \tilde{Z} > o \\ A_0(\tilde{z}) &= c_0^-(s) \qquad \tilde{Z} < o \end{aligned} \tag{27}$$

It is easily proved that $B_0(\tilde{z}) = i e_0^{\pm}(s)$ so $\tilde{\Phi}_0^{(1)} = c_0(s) \pm e_0(s)$

The following term is the η-expansion of $\tilde{\Phi}^{(1)}$ is not of order $\eta^{1/2}$. In fact, if such a term $\eta^{1/2}\Phi_1^{(1)}$ does exist, with $\tilde{\Phi}_1^{(1)} = A_1(\tilde{z}) + A_1(\tilde{z}_*) + i\left[B_1(\tilde{z}) - B_1(\tilde{z}_*)\right]$ the pressure condition (26) shows that

$$A_1^{1\oplus} + A_1^{1\ominus} + i\left[B_1^{1\oplus} - B_1^{1\ominus}\right] = A_1^{1\ominus} + A_1^{1\oplus} + i\left[B_1^{1\ominus} - B_1^{1\oplus}\right] \tag{28}$$

This relation is fulfilled for any function $A_1(\tilde{z})$, and we must solve the Hilbert problem for a function $B_1(\tilde{z})$ holomorphic on the positive part of the real axis. This has been done in section III. 2, but the corresponding solution $\tilde{z}^{1/2}$, does not fulfill the Kutta-Joukowski condition (25).

Consequently : $\tilde{\Phi}^{(1)} = c_0(s) \pm \epsilon_0(s) + \eta \tilde{\Phi}_1^{(1)} + \ldots$

$$\Delta_{\tilde{Y}\tilde{Z}} \tilde{\Phi}_1^{(1)} = o \Longrightarrow \tilde{\Phi}_1^{(1)} = A_1(\tilde{z}) + A_1(\tilde{z}_*) + i\left[B_1(\tilde{z}) - B_1(z_*)\right]$$

$A_1(\tilde{z})$ and $B_1(\tilde{z})$ are sectionally holomorphic functions, satisfying the following relations

$$A_1^{I+} - A_1^{I-} = -i\,\delta_1^{(e)} \qquad \tilde{Z} = o \qquad \tilde{Y} < o \tag{29}$$

$$B_1^{I+} + B_1^{I-} = -\delta_1^{(p)} \qquad \tilde{Z} = o \qquad \tilde{Y} < o \tag{30}$$

$$B_1^{I\oplus} - B_1^{I\ominus} = -i \cot g\,\alpha\, e_0^{I}(s) \qquad \tilde{Z} = o\,, \quad \tilde{Y} > o \tag{31}$$

with $\delta_1^{(e)} = \frac{1}{2}(\delta_1^{+} - \delta_1^{-})$, $\delta_1^{(p)} = \frac{1}{2}(\delta_1^{+} + \delta_1^{-})$

The equation (29) has been solved in the preceding paragraph :

$$A_1(\tilde{z}) = -\frac{\delta_1^{(e)}}{2\pi}\,\tilde{z}\,\mathrm{Log}\,\tilde{z} + c_1^{\pm}(s)\,\tilde{z} \tag{32}$$

From equation (29)

$$B_1^{I}(\tilde{z}) = -\frac{1}{2}\delta_1^{(p)} + i\,e_1^{\pm}(s)$$

and using the relation (31), the solution is

$$B_1(\tilde{z}) = -\frac{1}{2}\tilde{z}\left[\delta_1^{(p)} \pm i \cot g\,\alpha\, e_0^{I}(s)\right] \tag{33}$$

From these results, the η - expansion of the flow velocity potential is written in the following form :

$$\tilde{\Phi}^{(1)} = c_0(s) \pm e_0(s) - \eta\,\mathrm{Log}\,\eta\,\frac{\delta_1^{(e)}}{\pi}\,\tilde{\rho}\cos\Theta + \eta\tilde{\rho}\left\{\frac{\delta_1^{(e)}}{\pi}\,(\Theta\sin\Theta - \mathrm{Log}\,\tilde{\rho}\cos\Theta)\right.$$
$$\left. + C_1(s)\cos\Theta + \delta^{(p)}\sin\Theta \pm e_0'(s)\cot g\,\alpha\cos\Theta\right\} + o(\eta^{3/2}) \tag{34}$$

In this expression, we have assumed that the vortex sheet has no thickness, so writing $\partial\tilde{\Phi}^{(1)}/\partial\tilde{Z}\,|^{\oplus} = \partial\tilde{\Phi}^{(1)}/\partial Z^{\ominus}$, we obtain $c_i^{+} = c_i^{-} = 2\,c_i$

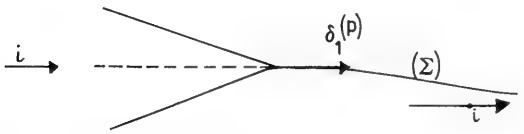

Figure 7 Outer description of the vortex sheet

The starting shape of the vortex sheet is given, in this outer solution by the value of $\partial \tilde{\Phi}^{(1)}/\partial \tilde{Z}$ when $\Theta = o$ or 2π. The figure 7 gives a sketch of this departure in a plane normal to the planform edge (λ). The slope is found to be $\delta_1^{(p)}$ as in the two-dimensional case of an hydrofoil without thickness.

We conclude the analysis of the outer problem, with the figures 8 and 9 which show the singular behaviour of $\tilde{\Phi}^{(1)}$ in the vicinity of a round leading edge (20) and a sharp trailing edge (34).

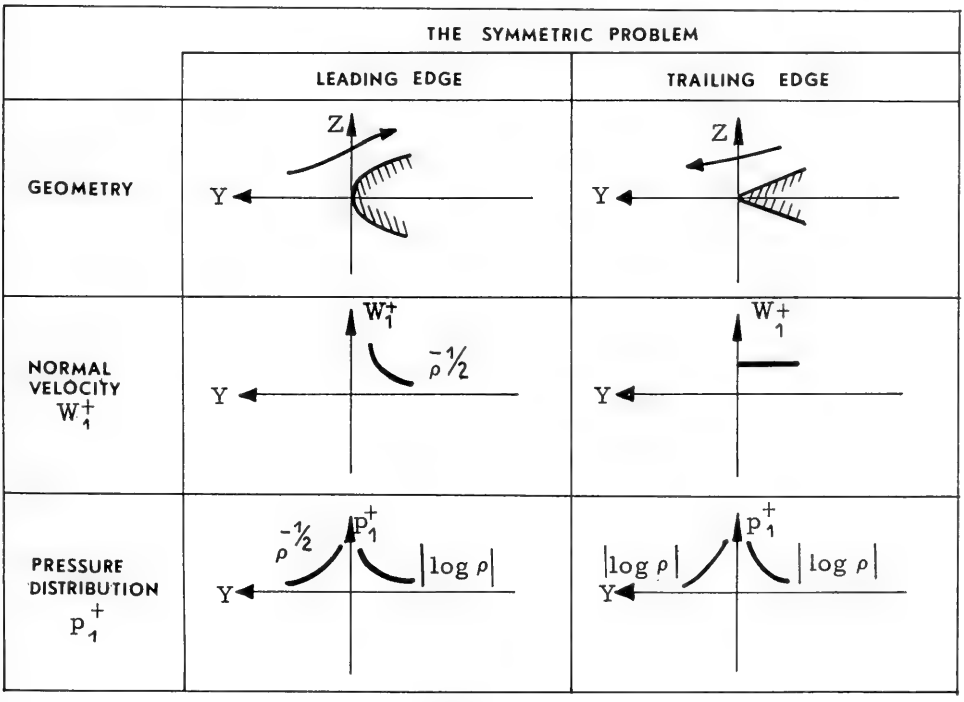

Figure 8

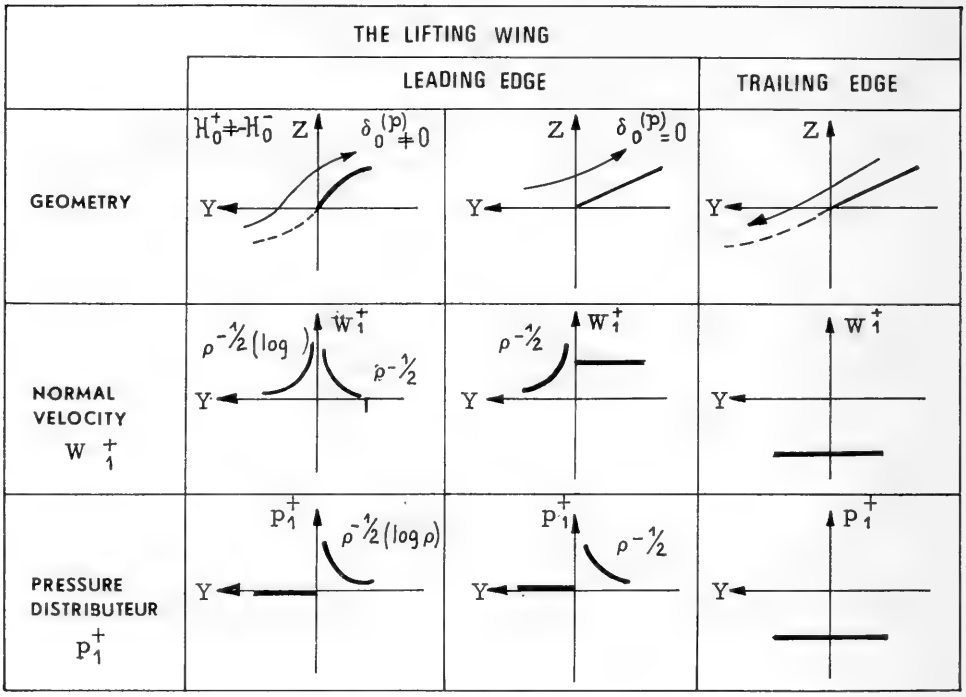

Figure 9 A discontinuity in the curvature of the leading edge increase the order of the singularity

IV. THE INNER SOLUTIONS

With the new variables $\tilde{Y} = Y / \eta$ and $\tilde{Z} = \frac{Z - \epsilon z_A}{\eta}$, the body equation is :

$$\tilde{Z} = \frac{\epsilon}{\eta^{1/2}} \sqrt{\frac{2\tilde{Y}}{a_2^{\pm}}} - \epsilon \frac{a_3^{\pm}}{3(a_2^2)^{\pm}} \tilde{Y} + \ldots$$

It is easily seen that, in an inner region of order $\eta = \epsilon^2$, the boundary conditions must not be written on $\tilde{Z} = o$, but on the exact body wall :

$$\tilde{Z} = \sqrt{\frac{2\tilde{Y}}{a_2^{\pm}}} + o(\epsilon)$$

Therefore, the study of the vicinity of a round leading edge requires the introduction of an inner layer with a thickness $0(\epsilon^2)$. The behaviour of the inner solution at infinity, for this region, is given by the outer solution (20) and (23).

$$\tilde{\Phi} = x(s) + \epsilon C_0(s) + (\epsilon \operatorname{Log} \epsilon)^2 \frac{2\,\delta_0^{(p)}}{\pi^2} \cdot \frac{H_0^+ + H_0^-}{2} + \epsilon^2 \operatorname{Log} \epsilon \frac{2\delta_0^{(p)}}{\pi} \left(\tilde{\rho}^{1/2} \sin\frac{\theta}{2} + \frac{H_0^+ + H_0^-}{2} \right) + \ldots$$

$$+ \epsilon^2 \left\{ - \tilde{Y} \sin\alpha(s) + \tilde{\rho}^{1/2} \left[2\,\delta_0^{(e)} \cos\frac{\theta}{2} + \frac{2\,\delta_0^{(p)}}{\pi} \left(\operatorname{Log} \tilde{\rho} \sin\frac{\theta}{2} + \cos\frac{\theta}{2} \right) + d_1(s) \sin\frac{\theta}{2} \right] + \right.$$

$$\left. + \frac{\delta_0^{(p)}}{2\pi^2} \frac{H_0^+ + H_0^-}{2} \left[(\operatorname{Log} \tilde{\rho})^2 - \theta^2 \right] - \frac{\theta \delta_0^{(p)}}{\pi} \frac{H_0^+ - H_0^-}{2} \right\} + o(\epsilon^3 \operatorname{Log} \epsilon) \qquad (35)$$

For the sharp trailing edge, the outer expansion is singular for the symmetric problem, as shown on figures 8 and 9

$$p \sim 1 - \epsilon \operatorname{Log} \rho \; \frac{\delta_1^{(e)}}{\pi} \qquad \rho = \eta \tilde{\rho} \to o$$

From this result, the study of the vicinity of a sharp trailing edge requires an inner region with thickness of order $\eta = o(e^{-1/\epsilon})$. The behaviour of the inner solution at infinity, for this layer, is given by the outer solution (34) :

$$\tilde{\Phi} = x(s) + \epsilon (c_0(s) \pm e_0(s)) + e^{-1/\epsilon} \left[\frac{\delta_1^{(e)}}{\pi} \tilde{\rho} - \tilde{\rho} \sin\alpha(s) \right] \cos\theta + o(\epsilon\, e^{-1/\epsilon}) \qquad (36)$$

IV.I The neighbourhood of a round leading edge

The full problem, to be solved in the general case of an unsymmetric nose is written below :

$$\Delta_{\tilde{Y}\tilde{Z}} \tilde{\Phi} - \epsilon^2 C(s) \frac{\partial \tilde{\Phi}}{\partial \tilde{Y}} + o(\epsilon^4) = o$$

-. $\vec{n} \cdot \vec{\nabla} \tilde{\Phi} = o$ on $\tilde{Y} = \frac{a_2^{\pm}}{2} \tilde{Z}^2 + o(\epsilon) \qquad (a_2 < o)$

-. Matching condition (35) at infinity

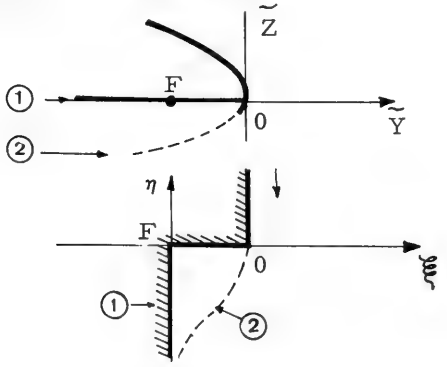

Figure IO The local problem for an unsymmetric leading edge

Taking into account the expansion (35) at infinity, the solution $\tilde{\Phi}$ is expanded under the form of an asymptotic approximation :

$$\tilde{\Phi} = \tilde{\Phi}_0 + \epsilon \tilde{\Phi}_1 + (\epsilon \text{Log } \epsilon)^2 \tilde{\Phi}_2 + \epsilon^2 \text{Log } \epsilon \tilde{\Phi}_3 + \ldots$$

We have obviously

$$\tilde{\Phi}_0 = x(s)$$

$$\tilde{\Phi}_1 = c_0(s)$$

$$\tilde{\Phi}_2 = \frac{2\delta_0^{(p)}}{\pi^2} \frac{H_0^+ + H_0^-}{2} \qquad \delta_0^{(p)} = \frac{\sin\alpha}{2} \cdot \frac{H_0^+ + H_0^-}{2} \qquad H_0^{\pm} = \pm \sqrt{\frac{2}{|a_2|^{\pm}}}$$

The function $\tilde{\Phi}_3$ is a solution of the following problem

$$\Delta_{\tilde{Y}\tilde{Z}} \tilde{\Phi}_3 = 0$$

$$\vec{n} \cdot \vec{\nabla} \tilde{\Phi}_3 = 0 \quad \text{on } \tilde{Y} = \frac{a_2^{\pm}}{2} \tilde{Z}^2 \; ; \text{ At } \infty \quad \tilde{\Phi}_3 \sim \frac{4\delta_0^{(p)}}{\pi} \sqrt{\rho} \sin\frac{\theta}{2} \tag{37}$$

In order to solve this problem, we must change the $\tilde{Z}$-axis and choose the focus of the upper parabola as a new origin

$$\bar{Y} = \tilde{Y} + \frac{1}{2|a_2|^+} \quad , \qquad \bar{Z} = \tilde{Z} \tag{38}$$

We define the conformal mapping $\bar{z} = \zeta^2$, with $\bar{z} = \bar{Y} + i\bar{Z}$ and $\zeta = \xi + i\eta$. In the ζ-plane, we have to determine a flow, with the uniform complex velocity $4i\delta_0^{(p)}/\pi$, along a step ① (when $a_2^- = 0$) or along a curvilinear wall in the general case ② (when $a_2^- \neq 0$). The solution, in the first case ① is easily obtained, but has no interest because the infinite velocity at the point O generates separation (except for the ideal angle of attack). The solution in the second case ② has not been obtained, but this solution does not present a great interest, because a slight change in the incidence remove this point of discontinuous curvature, from its present particular position. We restrict our study to the regular nose (i. e. discontinuous curvature). In that case $H_0^+ = -H_0^-$ and $\delta_0^{(p)} = 0$. From the expression (35), the behaviour of the inner solution at infinity is :

$$\Phi = x(s) + \epsilon c_0(s) + \epsilon^2 \left[-\tilde{Y}\sin\alpha + \sqrt{\tilde{\rho}}\,(2\delta_0^{(e)} \cos\frac{\theta}{2} + d_1(s)\sin\frac{\theta}{2}) + o(1) \right] + o(\epsilon^2)$$

and $\tilde{\Phi}$ is expanded under the form $\tilde{\Phi} = x(s) + \epsilon c_0(s) + \epsilon^2 \tilde{\Phi}_1 + o(\epsilon^2)$

With the new coordinates defined by (38), the function $\tilde{\Phi}_1$ is solution of

$$\Delta_{\bar{Y}\bar{Z}} \tilde{\Phi}_1 = 0$$

$$\overline{Y} = -\frac{1}{2a_2} + \frac{a_2}{2}\overline{Z}^2 \quad \text{is a stream line}$$

At infinity $\tilde{\Phi}_1 = R\left\{-\sin\alpha\,\overline{z}\right\}$

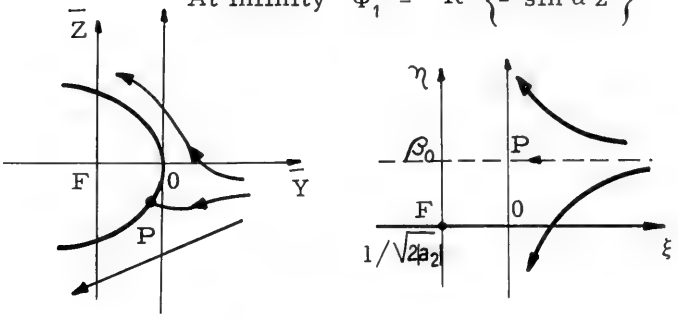

Figure 11 The local problem for a symmetric leading edge

Using the conformal mapping $\overline{z} = \zeta^2$, the given parabola is transformed into the straight line $\xi = 1/\sqrt{2\,|a_2|}$ and the corresponding complex potential is $f(\zeta) = \rho(\zeta) + i\,\psi(\rho)$

$$f(\zeta) = -\sin\alpha(\zeta - \zeta_0)^2 + \text{Cste}$$

with

$$\zeta_0 = \frac{1}{\sqrt{2\,|a_2|}} + i\beta_0$$

So, the solution we are looking for is :

$$\tilde{\Phi}_1 = -\sin\alpha\left[\overline{Y} - 2\overline{\rho}\left(\frac{1}{2\,|a_2|}\right)^{1/2}\cos\frac{\Theta}{2} + 2\overline{\rho}\beta_0\sin\frac{\Theta}{2} + K(s)\right]$$

and rewritting it, with the coordinates $\tilde{Y}$, $\tilde{Z}$:

$$\tilde{\Phi}_1 = R\left[-\sin\alpha\,\tilde{z} + 2\zeta_0\left(\tilde{z} + \frac{1}{2\,|a_2|}\right)^{1/2} + K(s)\right] \qquad (40)$$

The identification with the asymptotic behaviour (39) at infinity gives :

$\delta_0^{(e)} = \dfrac{\sin\alpha}{\sqrt{2\,|a_2|}}$ which is identically satisfied

$\beta_0 = d_1(s)/2$ which gives the position of the stagnation point P.

In the physical plane $\tilde{Y}$, $\tilde{Z}$, P is located at the point $(-d_1^2/4,\ d_1/\sqrt{2\,|a_2|})$

The arbitrary function $d_1(s)$ may be determined only after the resolution of the whole problem, the location of P depending upon the Kutta-Joukowski condition at the trailing edge. The matching condition is fulfilled up till $O(\epsilon^3)$.
The following term in the behaviour of the velocity potential at infinity, given by the matching conditions is :

$$-\epsilon^3 \mathrm{Log}\,\epsilon \frac{2\delta_1^{(e)}}{\pi}\rho\cos\theta + \epsilon^3 \mathrm{Log}\,\epsilon \frac{2\delta_1^{(e)}}{\pi}\frac{H_0^+ - H_0^-}{2}\tilde{\rho}^{1/2}\cos\frac{\theta}{2} =$$

$$\epsilon^3 \mathrm{Log}\,\epsilon \frac{2\delta_1^{(e)}}{\pi}\left[-\tilde{\rho}\cos\theta + \sqrt{\frac{2}{|a_2|}}\tilde{\rho}^{1/2}\cos\frac{\theta}{2}\right]$$

The expansion of $\tilde{\Phi}$ is then : $\tilde{\Phi} = x(s) + \epsilon c_0(s) + \epsilon^2\tilde{\Phi}_1 + \epsilon^3 \mathrm{Log}\,\epsilon\ \tilde{\Phi}_2 + o(\epsilon^3)$
$\tilde{\Phi}_2$ being a solution of the problem (41), written with the variables $\bar{Y}$ and $\bar{Z}$:

$$\Delta_{\bar{Y}\bar{Z}}\,\bar{\Phi}_2 = 0$$

$$\bar{Y} = -1/2a_2 + a_2\bar{Z}^2/2 \qquad \text{is a streamline} \qquad (41)$$

$$\text{at } \infty \quad \tilde{\Phi}_2 \sim \mathrm{R}\left(\frac{2\delta_1^{(e)}}{\pi}\ \bar{z}\right)$$

This solution is obtained as before :

$$\tilde{\Phi}_2 = \mathrm{Re}\left\{\frac{2\delta_1^{(e)}}{\pi}\left[-\tilde{\zeta} + 2\rho_1\left(\bar{z} + \frac{1}{2|a_2|}\right) + R(s)\right]\right\}$$

with

$$\zeta_1 = \frac{1}{\sqrt{2|a_2|}} + i\beta_1$$

The matching conditions show that $\beta_1 = 0$ and $\frac{2}{\sqrt{2|a_2|}} = \sqrt{\frac{2}{|a_2|}}$ which is identically fulfilled.

We can conclude by writting the composite expansion uniformly valid in the vicinity of the round leading edge. There is a shifting correction analogous to that found by M. Van Dyke in the 2-dimensional case [8].

$$\Phi = x(s) - Y\sin\alpha(s) + \epsilon\Phi^{(1)}(s, Y, Z) + \epsilon^2\Phi^{(2)}(s, Y, Z)$$
$$+\mathrm{R}\left\{\epsilon^2\left[\sqrt{\frac{2}{|a_2|}}(1 + \epsilon\mathrm{Log}\,\epsilon) + i\frac{d_1(s)}{2}\right]\left[\left(\frac{z}{\epsilon^2} + \frac{1}{2|a_2|}\right)^{1/2} - \frac{z}{\epsilon}\right]\right\} + o(\epsilon^3) \qquad (42)$$
$$z = Y + iZ$$

IV.2 The vicinity of a sharp trailing edge

The new problem that we investigate now is formulated as follows :

$$\tilde{\Phi} = x(s) + \epsilon \left(c_0(s) \pm e_0(s) \right) + e^{-1/\epsilon} \, \tilde{\tilde{\Phi}}(s, \tilde{Y}, \tilde{Z}, \epsilon)$$

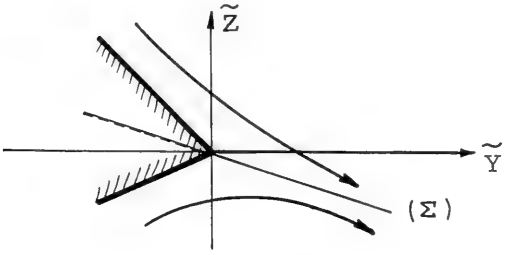

Figure I2

We must solve :

$$\Delta_{\tilde{Y}\tilde{Z}} \tilde{\tilde{\Phi}} + o(e^{-1/\epsilon}) = o$$

$$\vec{n} \cdot \vec{\nabla} \tilde{\tilde{\Phi}} = o \qquad \text{on} \qquad \tilde{Z} = \frac{\epsilon \tilde{Y}}{a_1^{\pm}(s)}$$

with the matching condition at infinity.

It is easy to see that the function

$$\tilde{\tilde{\Phi}}_0 = \mathcal{J} \left\{ U(\epsilon) e^{i\epsilon \frac{\delta_1^{(p)}}{\Phi \sin \alpha} Z \left(1 + \epsilon \frac{\delta_1^{(e)}}{\pi \sin \alpha} \right)} \right\} \tag{44}$$

is a particular solution of the two-dimensional problem, and the matching condition at infinity requires :

$$U(\epsilon) = e^{-\frac{\delta_1^{(e)}}{\pi \sin \alpha}} \left[-\sin \alpha + \epsilon \left(c_1 \pm e_0' \cot g \, \alpha \right) \right] \tag{45}$$

We did not prove the expected result :

$$\tilde{\tilde{\Phi}} = \tilde{\tilde{\Phi}}_0 + o(\epsilon^2)$$

Nevertheless, the departure of the vortex sheet, given by the expression (44) (see figure I2), is not in agreement with the results obtained by Mangler and Smith [6].

REFERENCES

[1] C. REHBACH, Etude numérique de l'influence de la forme de l'extrémité d'une aile sur l'enroulement de la nappe tourbillonnaire. Rech. Aérosp. n° 1971-6 (Nov-Déc).

[2] H. PORTNOY AND J. ROM, The flow near the tip and wake edge of a lifting wing with trailing-edge separation. T. A. E. Report n° 132.

[3] R. LEGENDRE, Calcul des ailes subsoniques. Rech. Aérosp. n° 112 (Mai-Juin 1966).

[4] M. VAN DYKE, a) Subsonic edges in thin-wing and slender-body theory NACA TN 3343,
b) Second-order subsonic airfoil-section theory and its practical application TN 3390.

[5] M. J. LIGHTHILL, A new approach to thin aerofoil theory. The aero-quaterly, Vol. III, Nov. 51, Part III.

[6] K. W. MANGLER et J. H. B. SMITH, Behaviour of the vortex sheet at the trailing edge of a lifting wing. The Aeronaut. Journ. of the Royal Aero. Soc. Nov. 70.

[7] J. S. DARROZES, The method of matched asymptotic expansions applied to problems involving two singular pertubation parameters Fluid dynamics transactions, Vol. 6, Part II.

[8] M. VAN DYKE, Perturbation methods in fluid mechanics. Applied Math. and Mech., Vol. 8, Acad. Press, New-York 1964.

[9] T. S. LUU, G. COULMY et J. SAGNARD, Calcul non linéaire de l'écoulement potentiel autour d'une aile d'envergure finie de forme arbitraire. Congrès de l'A. T. M. A., Session 1971.

WAVE FORCES ON A RESTRAINED SHIP IN HEAD-SEA WAVES

Odd Faltinsen
Det Norske Veritas
Oslo, Norway

ABSTRACT

The exact ideal-fluid boundary-value problem is formulated for the diffraction of head-sea regular waves by a restrained ship. The problem is then simplified by applying four restrictions: 1) the body must be slender; 2) the wave amplitude is small 3) the wave length of the incoming waves is of the order of magnitude of the transverse dimensions of the ship; 4) the forward speed is zero or it is the order of magnitude $\epsilon^{1/2-a}$; $0<a\leq 1/2$, where ϵ is the slenderness parameter.

The problem is solved by using matched asymptotic expansions. The result shows that the wave is attenuated as it propagates along the ship. The result is not expected to be valid near the bow or stern of the ship.

The experimental and theoretical pressure distribution along a prolate spheroid have been compared. The predicted attenuation of the peak pressure is very well confirmed by the experiments. In addition, theory and experiment agree that the peak pressure near the ship generally leads the Froude-Kriloff-pressure peak by 45°.

I. INTRODUCTION

There is a growing interest in finding the pressure distribution along a ship due to waves. Up to now one has mainly concentrated on finding motions, shear forces, bending moments and torsional moments along

the ship. But the development of the finite element technique in ship structure analysis has necessitated a more detailed information of the force distribution along the ship.

We are in this paper going to consider the regular wave case. But it is to day well accepted that we can apply the principle of linear superposition and statistical theories to sum up the responses in regular waves of different wave lengths and headings to predict the responses in irregular sea.

The solution of the regular wave problem is usually divided into two problems. One part is the case when the ship is forced to oscillate and there is no incoming waves. The other part is the problem when there is incoming regular waves and the ship is restrained from oscillating. Due to linearity the pressure, forces and moments obtained in those two problems can be superimposed to give the total pressure, forces and moments on a ship which oscillates in a steady-state condition in regular waves.

We will here consider the case when there is incoming regular waves on a ship which is restrained from oscillating. We will assume that the wave length is of the order of magnitude of the transverse dimensions of the ship, and that the waves are coming from ahead. Our goal is then to find the pressure distribution along the ship. The head-sea problem is up to now an unsolved problem. For the oblique-sea case Ursell (1968 b) found a solution but he was not able to find a solution for the head-sea case(Ursell (1968 a and b)).

Ogilvie and Tuck (1969) have considered the complementary problem, namely the forced heave and pitch oscillation of a ship when there are no incoming waves. For the zero-speed case the order of magnitude of the frequency of oscillation used in Ogilvie & Tuck (1969) is the same as the order of magnitude of the frequency of the waves assumed in this paper. In the forward-speed case, the assumptions in Ogilvie & Tuck (1969) and in this paper are different.

Ogilvie & Tuck got a strip theory result and it is well-known that strip theory gives good results for a wider range of wave lengths than Ogilvie & Tuck restricted themselves to (see Salvesen, Tuck & Faltinsen (1970)). So it is the hope that the theory presented in this paper also will cover a wider range of wave lengths. But it is only our experience that is going to tell us for how large wave lengths our theory is capable of predicting the pressure distribution along the ship. The theory predicts that head-sea waves of small wave length, are deformed as they propagate along the ship. Experiments seem to

indicate that this is true for a wave length which is half of the length of the ship, but that it is not true for a wave length which is three-fourths of the length of the ship.

By integrating the pressure in an appropriate way over the submerged part of the ship, we are able to predict the exciting force and moment on the ship. For the zero-speed case there is another way to obtain the exciting force and moment on a ship, namely to use the Khaskind relation (see Newman (1962)). The disadvantage of the Khaskind relation is that it cannot predict the pressure distribution along the ship. Further it is a formula derived on the basis of a general mathematical relationship, and so it does not give us much insight into the physical problem.

We are in this paper considering both the forward-speed and the zero-speed problem. They are separate problems and are handled as so. Both problems are solved by using the method of matched asymptotic expansions. We then introduce a farfield description which is valid in a distance of order one from the ship and a near-field description which is valid in a distance which is of order ϵ from the ship. Here ϵ is the usual slenderness parameter which is a measure of the transverse dimensions of the ship compared with the longitudinal dimensions of the ship. The ship is slender so ϵ is a small quantity. The length of the ship is a quantity of order one. It is the diffraction potential we solve for, and it is found that the far-field picture can be described by a line distribution of sources of density oscillating in the same way as the incoming waves and located on the x-axis between $-L/2$ and $L/2$ (see Figure 1). It is, however, the near-field solution that has the main interest. But the inner expansion of the far-field solution is giving us necessary boundary conditions on the near-field problem. It is found for both the zero-speed and the forward-speed problem that a first approximation to the diffraction potential in the near-field (not near the ends of the ship) is just minus the incident wave. So a first approximation to the total potential (incident + diffracted wave) will be given by the second approximation to the diffraction potential. Writing the total potential as

$$e^{i(\omega t - \nu x)}\psi$$

it is found that ψ satisfies the following equations in a cross-sectional plane of the ship.

(a) $$\frac{\partial^2 \psi}{\partial y^2} + \frac{\partial^2 \psi}{\partial z^2} - \nu^2 \psi = 0 \quad \text{in the fluid domain,}$$

(b) $$-\nu\psi + \frac{\partial \psi}{\partial z} = 0 \quad \text{on} \quad z = 0 \quad \text{outside the ship,}$$

(c) $$\frac{\partial \psi}{\partial n_{2D}} = 0 \quad \text{on the submerged part of the body,}$$

(d) condition to satisfy as $|y| \to \infty$.

For a definition of coordinates see Figure 1. Further ω is the frequency of encounter, t is the time variable, ν is the wave number, n_{2D} is a two-dimensional normal to the body in the cross-sectional plane.

Condition (d) is obtained by the matching procedure and it will be different for the zero-speed and the forward-speed problem. It should be noted that the longitudinal coordinate x will be a parameter in the solution of ψ .

Ursell (1968 a and b) set up a similar equation system as above. The very important difference is the condition (d). His mathematical solution to (a), (b) and (c) did not agree with his condition (d). But it will agree with our condition (d).

The solution to (a), (b), (c) and (d) can be written as

$$\psi = \sqrt{\frac{\omega + \nu U}{\omega_o}} \quad \psi_0$$

or

$$\psi = \frac{1}{\sqrt{x + L/2}} \quad \psi'(y, z; x)$$

Here ω_o is the frequency of the wave and U is the forward speed of the ship. $x = -\frac{L}{2}$ is the x-coordinate of the forward perpendicular. Positive x is in the direction of the after perpendicular.

We do not want to go into detail in this chapter about the mathematical expression for ψ_0 (or ψ'). For more details see the chapters about the zero-speed and the forward-speed problems. But we should note the following : ψ_0 is the solution to the zero-speed problem. So the solution at a certain forward speed U can simply be obtained from the solution of the zero-speed problem by multiplying with

$$\sqrt{\frac{\omega + U\nu}{\omega_o}}$$

Further ψ' will not vary with x if the submerged cross-sectional area of the ship is not varying. The second expression of ψ is then telling us that there is a decaying factor $(x + L/2)^{-1/2}$ as the wave propagates along the ship.

The presentation in this paper is divided into the following steps. First we set up a general formulation valid for both the zero-speed and the forward-speed problem. Then we study the zero-speed problem separately. We derive a far-field expansion for a source distribution located on the x-axis between -L/2 and L/2. We obtain an inner expansion of the far-field source solution and study then finally the near-field solution and the matching between the near-field and the far-field solution. Then we have a chapter for the forward-speed problem, which is presented in a similar way as the zero-speed problem. Finally we have a chapter about numerical calculations. A computer program has been developed for a ship having circular cross-sections, and comparisons between experiments and calculations have been done. The agreement is shown to be good.

II. GENERAL FORMULATION

We assume that the ship is moving with constant speed U in the direction of the negative x-axis. The z-axis is upwards, and the y-axis extends to starboard. The origin of coordinates is located in the undisturbed free surface at midship, so that the forward-speed effect appears as an incident, undisturbed flow with velocity U in the

direction of the positive x-axis.

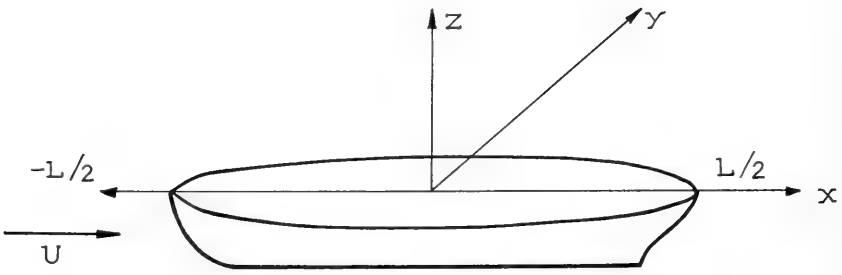

Figure 1 Coordinate system

The ship is slender and there is no other bodies in the fluid. The fluid has infinite depth. It is incompressible and the flow is irrotational, so that there exists a velocity potential ϕ which satisfies the Laplace equation.

$$\frac{\partial^2 \phi}{\partial x^2} + \frac{\partial^2 \phi}{\partial y^2} + \frac{\partial^2 \phi}{\partial z^2} = 0 \qquad (1)$$

in the fluid domain. The ship is restrained from performing any oscillatory motions, and so the boundary condition on the wetted surface of the ship will be

$$\frac{\partial \phi}{\partial n} = 0 \quad \text{on} \quad z = h(x, y) \quad . \qquad (2)$$

Here $z = h(x, y)$ is the mathematical description of the wetted surface of the ship. $\partial / \partial n$ denotes the derivative in the direction of the outwards normal on the surface of the ship.

The conditions on the free surface, $z = \zeta(x, y, t)$, are,

neglecting surface tension,

(A) the dynamic free surface condition

$$g\zeta + \phi_t + 1/2 \left[\phi_x^2 + \phi_y^2 + \phi_z^2\right] = 1/2\, U^2$$

$$\text{on} \quad z = \zeta(x, y, t) \tag{3}$$

(B) the kinematic free surface condition

$$\phi_x \zeta_x + \phi_y \zeta_y - \phi_z + \zeta_t = 0 \quad \text{on} \quad z = \zeta(x, y, t) \tag{4}$$

Here g is the acceleration of gravity.

ϕ must also satisfy a radiation condition, which will be discussed more later.

We will assume that there are incoming, regular gravity waves propagating along the positive x-axis. The wave amplitude is assumed to be small so that the classical linear free-surface theory is applicable. We will later linearize the problem with respect to the wave amplitude. The potential ϕ_I of the incoming waves will be given by

$$\phi_I = \underline{\text{Re}} \left[\frac{gh}{\omega_o} e^{\nu z} e^{i(\omega t - \nu x)}\right] \tag{5}$$

Re means the real part;* h is the wave amplitude of the incoming waves, ω_o is the wave frequency, ν is the wave number and t

* As is usual we are going to drop the notation Re . We will write the potential in complex form, and it should be understood that we should take the real part.

is the time variable. The wave number ν can be written as

$$\nu = \frac{2\pi}{\lambda} = \frac{\omega_o^2}{g} \tag{6}$$

where λ is the wave length. The frequency of encounter ω is related to ω_o, ν and U for the head-sea case by

$$\omega = \omega_o + \nu U \tag{7}$$

We are going to operate with a slenderness parameter ϵ. It is a measure of the transverse dimensions of the ship compared with the length of the ship. So ϵ is a small quantity. If we denote the x, y, z-components of the normal $\underline{n}$ on the wetted surface of the ship by n_1, n_2, n_3 respectively, then we can set

$$n_1 = 0(\epsilon), \quad n_2 = 0(1), \quad n_3 = 0(1) \tag{8}$$

We will assume that the frequency of the wave has the following asymptotic behaviour

$$\omega_o = 0(\epsilon^{-1/2}) \tag{9}$$

Using (6) this means that

$$\lambda = 0(\epsilon) \tag{10}$$

III. THE ZERO-SPEED PROBLEM

The frequency of encounter, ω, is the same as the frequency of the waves, ω_o, for the zero-speed case (see (7)). The time dependence of the incident wave is given by $e^{i\omega t}$ (see (5)). It is expected that the time dependence for the total potential is also given by $e^{i\omega t}$. We will use this fact and now write down the equations to

determine the velocity potential. From (1), (2), (3), (4) and the assumption about linearity it follows that ϕ satisfies

$$\frac{\partial^2 \phi}{\partial x^2} + \frac{\partial^2 \phi}{\partial y^2} + \frac{\partial^2 \phi}{\partial z^2} = 0 \quad \text{in the fluid domain} \tag{1}$$

$$\frac{\partial \phi}{\partial n} = 0 \quad \text{on} \quad z = h(x, y) \tag{2}$$

$$-\omega^2 \phi + g \frac{\partial \phi}{\partial z} = 0 \quad \text{on} \quad z = 0 \quad \text{outside the body} \tag{11}$$

In addition, the diffraction part of the potential must satisfy a radiation condition.

We will write ϕ as

$$\phi = \phi_I + \phi_D = \frac{gh}{\omega} e^{\nu z} e^{i(\omega t - \nu x)} + \phi_D \tag{12}$$

Here ϕ_D denotes the diffraction potential. To find ϕ_D we are going to use the method of matched asymptotic expansions (Van Dyke (1964), Ogilvie (1970)) and set up an asymptotic theory valid as $\epsilon \to 0$. As is usual, we introduce a far-field description and a near-field description. The far-field description is expected to be valid at distances which are $0(1)$ and larger from the ship. The near-field description is valid near the ship at distances which are $0(\epsilon)$, but not near the ends of the ship.

The steps we are going through is first to obtain a far-field description and then obtain an inner expansion of the far-field description. So finally we are studying the near-field solution and the matching between the near-field and the far-field solution.

III. 1. Far-field source solution and the inner expansion of the far-field source solution.

In the far-field description, we expect to have waves. In order to have waves, we must satisfy the condition (11). This means that the two terms in (11) must be of the same order of magnitude in

the far-field, and so $\partial/\partial z = 0(\epsilon^{-1})$. The existence of a surface wave implies that $\partial/\partial z$ and, say, $\partial/\partial s$ are the same order of magnitude, where s is measured normal to wave fronts. In the far-field, we cannot in general say that the normal to the wave fronts should be neither along the x-axis nor along the y-axis. This implies that $\partial/\partial x$ and $\partial/\partial y$ must also be of order ϵ^{-1} in the far-field.

From a far-field point of view, one cannot see the shape of the hull. As $\epsilon \to 0$ the disturbance from the hull to the far-field seems to emanate from a line of singularities located on the x-axis between $-L/2$ and $L/2$. The dominant far-away effect is expected to appear to be due to a line of sources. Since the incoming waves vary as $e^{i(\omega t - \nu x)}$, it is expected that the line of sources has a source density of the form

$$\sigma(x)\, e^{i(\omega t - \nu x)}$$

Due to the slenderness of the ship we assume $\frac{\partial \sigma}{\partial x} = 0(\sigma)$.

These physical arguments can be given a mathematical formulation. We can replace equation (1) by the Poisson equation

$$\frac{\partial^2 \phi_D}{\partial x^2} + \frac{\partial^2 \phi_D}{\partial y^2} + \frac{\partial^2 \phi_D}{\partial z^2} = \sigma(x)\, e^{i(\omega t - \nu x)}\, \delta(y)\, \delta(z - z_o). \quad (13)$$

Here δ is the Dirac-delta function, and initially we take $z_o < 0$. When the solution of ϕ_D is found, z_o will be set equal to zero. If we set $z_o = 0$ first, we would be in difficulties solving the problem.

We cannot expect that the far-field solution will satisfy the boundary condition on the hull given by (2), but it must satisfy a proper radiation condition. We must be sure that the diffraction potential ϕ_D does not contain an incoming wave. This is most easily taken care of by introducing the artificial Rayleigh viscosity μ (see for instance Ogilvie & Tuck (1969)). The free-surface condition (11) will then be modified to

$$(i\omega + \mu)^2 \phi_D + g \frac{\partial \phi_D}{\partial z} = 0 \quad \text{on} \quad z = 0 \tag{14}$$

At an appropriate later point, we will let μ go to zero.

The solution to (13) and (14) with $z_o = 0$ can for instance be found in Ogilvie & Tuck (1969) and is

$$\phi_D(x, y, z, t) = -\frac{1}{4\pi^2} e^{i\omega t} \int_{-\infty}^{\infty} dk\, e^{ikx} F\left\{\sigma(x) e^{-i\nu x}\right\}$$

$$\cdot \lim_{\mu \to 0} \int_{-\infty}^{\infty} \frac{d\ell\, e^{i\ell y + z\sqrt{k^2 + \ell^2}}}{\sqrt{k^2 + \ell^2} - \frac{1}{g}(\omega - i\mu)^2} \tag{15}$$

Here

$$F\left\{\sigma(x) e^{-i\nu x}\right\} = \int_{-\infty}^{\infty} dx e^{-ikx} \sigma(x) e^{-i\nu x} = \sigma^*(k + \nu)$$

Expression (15) can be rewritten in a form which is more convenient to handle for our purposes. The derivation is shown in Appendix A.

We can write

$$\phi_D(x, y, z, t) = \Phi(x, y, z) e^{i(\omega t - \nu x)} \tag{16}$$

where

$$\Phi(x,y,z) \simeq -\frac{\nu e^{\nu z}}{2\pi}\left[\int_{-\epsilon}^{0}\frac{dk\, e^{ikx - y\sqrt{k(k-2\nu)}}\,\sigma^*(k)}{\sqrt{k(k-2\nu)}}\right.$$

$$-i\int_{0}^{\epsilon^{-(1-\delta_1)}}\frac{dk\, e^{ikx - iy\sqrt{k(2\nu-k)}}\,\sigma^*(k)}{\sqrt{k(2\nu-k)}} \qquad (17)$$

$$-i\int_{\epsilon^{-(1-\delta_1)}-2\nu}^{0}\frac{du\, e^{iux + i2\nu x - iy\sqrt{(u+2\nu)(-u)}}\,\sigma^*(u+2\nu)}{\sqrt{(u+2\nu)(-u)}}$$

$$\left.+\int_{0}^{\epsilon^{-(1-\delta_1)}}\frac{du\, e^{iux + i2\nu x - y\sqrt{(u+2\nu)u}}\,\sigma^*(u+2\nu)}{\sqrt{(u+2\nu)u}}\right]$$

(17) is valid for $y = 0(1) > 0$. δ_1 in (17) is some very small positive number. It will be evident in Appendix B why it is convenient to have $\epsilon^{-(1-\delta_1)}$ as an integration limit in (17).

We will now find a two-term inner expansion of the far-field source solution. We then let y be of order ϵ, and we reorder the terms in (17). The procedure is shown in Appendix B. We get

$$\Phi(x,y,z) \sim -\nu e^{\nu z} e^{-i\pi/4}\int_{-L/2}^{x}\frac{d\xi\,\sigma(\xi)}{\sqrt{2\pi\nu\,|x-\xi|}} + \nu y e^{\nu z}\sigma(x) - e^{\nu z} e^{-i\pi/2}\frac{\sigma(x)}{2} \qquad (18)$$

Using (16) and the symmetry properties associated with sources, we can now write down a two-term inner expansion of the far-field source solution as

$$\phi_D(x,y,z,t) \sim e^{i(\omega t - \nu x)} e^{\nu z} \left[-\nu e^{-i\pi/4} \int_{-L/2}^{x} \frac{d\xi\, \sigma(\xi)}{\sqrt{2\pi\nu\,|x-\xi|}} + \nu|y|\,\sigma(x) - e^{-i\pi/2}\frac{\sigma(x)}{2} \right] \tag{19}$$

We note that this expression represents waves propagating along the ship in the same direction as the incoming wave. So to the lowest order it seems as if the disturbance created by the ship is carried along the ship in the direction of positive x-axis (see Fig. 1). Looking on what is happening at some cross-section x, we should therefore expect an integrated effect of what is happening at sections from the forward perpendicular ($x = -L/2$) up to the cross-section we consider. And this is what the lowest order term in (19) represents. The two last terms in (19) are the highest order terms. The last term represents an integrated effect from a given cross-section to the after end of the ship. This can be better understood from the mathematical expressions in Appendix B.

III. 2. The near-field problem and the matching.

We are now going to formulate the near-field problem and perform the matching between the near-field and the far-field solutions. A one-term far-field solution is found to be due to a line of sources with source density

$$\sigma_1(x)\, e^{i(\omega t - \nu x)}$$

spread along the line $y = z = 0$, $-L/2 \leq x \leq L/2$ (see Figure 1), and a one-term near-field solution will be found to be the negative of the incident wave. The matching between the lowest-order term in the near-field problem and the lowest-order term in the far-field

problem gives an integral equation for $\sigma_1(x)$ (see (32)). σ_1 is needed in the second order near-field solution. The two-term near-field solution is given by (48).

It should be noted that "Near-field" means the region near the body, where the distance from the body is $0(\epsilon)$. However, we do not expect the near-field approximations to be valid near the bow and stern.

We will express the potential of the diffracted wave as follows :

$$\phi_D = e^{i(\omega t - \nu x)} \psi(x, y, z) \quad . \tag{20}$$

By putting (20) into the Laplace equation, (1), we get

$$\frac{\partial 2\psi}{\partial y^2} + \frac{\partial^2 \psi}{\partial z^2} - \nu^2 \psi - 2i\nu \frac{\partial \psi}{\partial x} + \frac{\partial^2 \psi}{\partial x^2} = 0 \tag{21}$$

in the fluid region. The free-surface condition, (11), is :

$$\frac{\partial \psi}{\partial z} - \nu \psi = 0 \quad \text{on} \quad z = 0 \quad . \tag{22}$$

The body boundary condition, (2), together with (12), gives

$$\left[n_2 \frac{\partial \psi}{\partial y} + n_3 \frac{\partial \psi}{\partial z} - i\nu n_1 \psi + n_1 \frac{\partial \psi}{\partial x}\right] = \left[i\nu n_1 - \nu n_3\right] \frac{gh}{\omega} e^{\nu z} \tag{23}$$

$$\text{on} \quad z = h(x, y)$$

n_1 , n_2 , and n_3 have been explained before equation (8). A last condition on ψ is that it must match with the far-field solution.

We will assume that ψ varies very slowly in the x-direction compared with the variation of ψ in the transverse plane. We

assume that the rate of change of ψ in the transverse plane is governed by the order of magnitude of the transverse dimensions of the body and that the rate of change of ψ in the x-direction is governed by the order of magnitude of the longitudinal dimensions of the body.*

So in the ψ -problem we stretch the coordinates

$$y = \epsilon y \ , \qquad z = \epsilon z \ , \qquad n_{2D} = \epsilon N \ , \quad x = X \tag{24}$$

Here n_{2D} is the unit normal out of a cylinder with the same cross-section as the ship at a given section.

We will assume an asymptotic expansion of ψ of the form

$$\psi \sim \sum_{n=1}^{N} \psi_n (X, Y, Z, \epsilon) \tag{25}$$

where $\psi_{n+1} = o(\psi_n)$ as $\epsilon \to 0$ for fixed X, Y, Z.

We introduce

$$k = \nu \epsilon \tag{26}$$

and

$$C = \frac{gh}{\omega} \tag{27}$$

Since the problem is linear in C, we shall not be bothered with the order of magnitude of C.

---

* Note that the rate of change in the x-direction of the diffraction potential, ϕ_D, as given by (20) is of the same order of magnitude as the rate of change of ϕ_D in the transverse dimensions.

The lowest-order equations become

$$\left(\frac{\partial^2}{\partial Y^2} + \frac{\partial^2}{\partial Z^2} - k^2 \right) \psi_1 = 0 \; ; \tag{28}$$

$$\left(\frac{\partial}{\partial Z} - k \right) \psi_1 = 0 \quad \text{on} \quad Z = 0 \; ; \tag{29}$$

$$\frac{\partial}{\partial N}(\psi_1) = - Cn_3 k e^{kZ} \quad \text{on the body.} \tag{30}$$

In addition, ψ_1 must match with the far-field solution.

A one-term far-field solution is assumed to be the potential associated with a line distribution of sources of density

$$\sigma_1 (x) \; e^{i(\omega t - \nu x)}$$

spread along the line $y = z = 0$, $-L/2 \leq x \leq L/2$. That solution has been obtained in a previous chapter, and a one-term inner expansion of a one-term far-field solution can be found from (19). For any fixed x greater than $-L/2$, it is obvious that a one-term inner expansion is

$$e^{i (\omega t - \nu x)} \left[-\epsilon^{-1/2} \sqrt{\frac{k}{2\pi}} \; e^{kZ} \; e^{-i\pi/4} \int_{-L/2}^{x} \frac{d\xi \sigma_1(\xi)}{\sqrt{|x - \xi|}} \right] \tag{31}$$

and that the second-order term in the inner expansion is of order $\epsilon^{1/2}$ compared with the first-order term.

(31) should match with a one-term outer expansion of ψ_1 $e^{i(\omega t - \nu x)}$, as determined from (28), (29) and (30).

Ursell (1968 a) * has given a solution to that problem, but it does not appear to match with (31). However, if we say that the one-term near-field solution is just the negative of the incident wave (this is a special case of Ursell's solution), then (28), (29) and (30) are satisfied, and if we require that

$$\sqrt{\frac{k}{2\pi}}\ \epsilon^{-1/2}\ e^{kZ}\ e^{-i\pi/4} \int_{-L/2}^{x} \frac{d\xi\, \sigma_1(\xi)}{\sqrt{|x-\xi|}} = Ce^{kZ} \qquad (32)$$

then we see that a one-term outer expansion of the one-term near-field solution matches with a one-term inner expansion of a one-term far-field solution. So we have the solution

$$\psi_1(X, Y, Z, \epsilon) = -\epsilon^{-1/2} \sqrt{\frac{k}{2\pi}}\ e^{kZ}\ e^{-i\pi/4} \int_{-L/2}^{x} \frac{d\xi\, \sigma_1(\xi)}{\sqrt{|x-\xi|}} \qquad (33)$$

$$= -Ce^{kZ}$$

We solve (32) for $\sigma_1(x)$ formally by letting it be an equality for all $x \geq -L/2$. We recognize (32) as Abel's integral equation (see Dettman (1965)), which has the solution

$$\sigma_1(x) = \epsilon^{1/2} \sqrt{\frac{2}{\pi k(x + L/2)}}\ e^{i\pi/4} \cdot C \qquad (34)$$

This solution is singular at $x = -L/2$, which is a violation of the

---

* Ursell's solution will be needed in the second order term and will be discussed then.

assumptions made earlier. However, this is not a serious difficulty if we do not try to use our results very near the bow of the ship. The near-field expansion of which (33) gives the first term, is not uniformly valid near $x = -L/2$. In order to examine the solution precisely in the neighborhood of $x = -L/2$ we should construct a separate expansion for a region in which $x + L/2 = 0(\epsilon^{\gamma})$, for some $\gamma > 0$. One may expect then that $\sigma_1(x)$ is not given in that region by (34); rather, $\sigma_1(x)$ will decrease continuously to zero at $x = -L/2$, as physical considerations require that it must. Using (34) to express $\sigma_1(x)$ produces a higher-order, i.e., negligible, error in the velocity potential, provided that we restrict our attention to a region in which $\epsilon^{\gamma} = o(x + L/2)$.

We wish next to find ψ_2, but first we need to say some more about the far-field.

We expect that a two-term far-field expansion is obtained by a line distribution of sources of density

$$(\sigma_1(x) + \sigma_2(x))\, e^{i(\omega t - \nu x)} \tag{35}$$

spread along the line $y = z = 0$, $-L/2 \leq x \leq L/2$. It is assumed that

$$\sigma_2 = o(\sigma_1) \tag{36}$$

A two-term inner expansion of this two-term far-field expansion can be obtained from (19), and it is

$$e^{i(\omega t - \nu x)} \left[-\epsilon^{-1/2} \sqrt{\frac{k}{2\pi}}\, e^{kZ}\, e^{-i\pi/4} \int_{-L/2}^{x} \frac{d\xi\, \sigma_1(\xi)}{\sqrt{|x - \xi|}} \right.$$

$$-\epsilon^{-1/2} \sqrt{\frac{k}{2\pi}}\, e^{kZ}\, e^{-i\pi/4} \int_{-L/2}^{x} \frac{d\xi\, \sigma_2(\xi)}{\sqrt{|x - \xi|}}$$

$$\left. + e^{kZ}\, k\, |Y|\, \sigma_1(x) - e^{-i\pi/2}\, \frac{\sigma_1(x)}{2}\, e^{kZ} \right] \tag{37}$$

It is found that the near-field equations for ψ_2 is

$$\left(\frac{\partial^2}{\partial Y^2} + \frac{\partial^2}{\partial Z^2} - k^2 \right) \psi_2 = 0 \tag{38}$$

$$\left(\frac{\partial}{\partial Z} - k \right) \psi_2 = 0 \quad \text{on} \quad Z = 0 \tag{39}$$

$$\frac{\partial \psi_2}{\partial N} = 0 \qquad \text{on the body .} \tag{40}$$

In addition ψ_2 must match with the far-field solution.

Ursell (1968 a) has derived a solution of (38), (39) and (40). It can be written as

$$\psi_2 = A_2(x) \left[e^{kZ} + \int_{C(+)} k\mu(s;k) \cdot \left[G(kY, kZ; k\xi(s), k\eta(s)) + G(kY, kZ; -k\xi(s), k\eta(s)) \right] ds \right] \tag{41}$$

where

$$G(kY, kZ; k\xi, k\eta) = K_o \left[k \sqrt{(Y-\xi)^2 + (Z-\eta)^2} \right] + \frac{1}{4} \left[\int_{-\infty}^{\infty} + \int_{-\infty}^{\infty} \right] \frac{\cosh \mu + 1}{\cosh \mu - 1} \exp \left[ik(Y-\xi) \sinh \mu + k(Z+\eta) \cosh \mu \right] d\mu \tag{42}$$

The symbol $\int\!\!\!\!\!\!-$ denotes integration along a contour passing below the double pole at $\mu = 0$, with a corresponding meaning for $\int\!\!\!\!\!\!-\,.K_o$ is a modified Besselfunction of the second kind. In (41) $C(+)$ denotes the half of the boundary curve of the submerged cross-section at x for which $y > 0$; $Y = \xi(s)$, $Z = \eta(s)$ are the parametric equations of the curve $C(+)$. $\mu(s,k)$ is determined from satisfaction of the body boundary condition (40). It should be noted that (38), (39), and (40) will be satisfied for an arbitrary $A_2(x)$ in (41). $A_2(x)$ has to be determined by the matching procedure.

In order to match, we need an outer expansion of (41). Ursell (1968 a) has done that. The result is

$$A_2(x)\left[e^{kZ} - 4k^2\pi \frac{|y|}{\epsilon} e^{kZ} \int_{C(+)} \mu(s,k)\, e^{k\eta(s)}\, ds\right] \tag{43}$$

A three-term outer expansion of the two-term near-field solution,

$$(\psi_1 + \psi_2)\, e^{i(\omega t - \nu x)} \tag{44}$$

can now be written down. It is

$$e^{i(\omega t - \nu x)}\left[-\epsilon^{-1/2}\sqrt{\frac{k}{2\pi}}\, e^{kZ}\, e^{-i\pi/4} \int_{-L/2}^{x} \frac{d\xi\, \sigma_1(\xi)}{\sqrt{|x-\xi|}}\right.$$

$$\left. + A_2(x)\, e^{kZ} - A_2(x)\, 4k^2\pi \frac{|y|}{\epsilon} e^{kZ} \int_{C(+)} \mu(s,k)\, e^{k\eta(s)}\, ds\right] \tag{45}$$

The last term is the lowest-order term and the first term is the next lowest-order term. (45) should match with (37) and we see that it does if we set

$$A_2(x) = -\frac{\sigma_1(x)}{4k\pi \int_{C(+)} \mu(s,k)\, e^{k\eta(s)}\, ds} \tag{46}$$

$$= -\frac{\epsilon^{1/2} \sqrt{\frac{2}{\pi k (x + L/2)}}\, e^{i\pi/4}\, C}{4k\pi \int_{C(+)} \mu(s,k)\, e^{k\eta(s)}\, ds}$$

(σ_1 is given by (34)), and if also

$$-\epsilon^{-1/2} \sqrt{\frac{k}{2\pi}}\, e^{-i\pi/4} \int_{-L/2}^{x} \frac{d\xi\, \sigma_2(\xi)}{\sqrt{|x-\xi|}} = A_2(x) + e^{-i\pi/2}\, \frac{\sigma_1(x)}{2}$$

$$= \left[-\frac{1}{4k\pi \int_{C(+)} \mu(s,k)\, e^{k\eta(s)}\, ds} + \frac{e^{-i\pi/2}}{2} \right]$$

$$\epsilon^{1/2} \sqrt{\frac{2}{\pi k (x + L/2)}}\, e^{i\pi/4}\, C \tag{47}$$

which is a condition to be satisfied by σ_2 . Equation (47) gives us Abel's integral equation, and it can be solved in principle. It is to be noted that the term in the brackets is a function of x, which is determined in practice by numerical computation.

It is the near-field solution that has the primary interest. So let us summarize our result : A two-term near-field solution of the diffraction potential is given by

$$(\psi_1 + \psi_2)\, e^{i(\omega t - \nu x)} = e^{i(\omega t - \nu x)} \left[-Ce^{kZ} - \frac{\epsilon^{1/2} \sqrt{\frac{2}{\pi k(x+L/2)}}\, e^{i\pi/4} C}{4k\pi \int_{C(+)} \mu(s;k)\, e^{k\eta(s)}\, ds} \right.$$

$$\left. \cdot \left[e^{kZ} + \int_{C(+)} k\mu(s;k) \left[G(kY, kZ; k\xi(s), k\eta(s)) + G(kY, kZ; -k\xi(s), k\eta(s)) \right] ds \right] \right] \qquad (48)$$

where k and C are given by (26) and (27), and G is given by (42). The first term in (48) is just the negative of the incident wave and so (48) tells us that the total (incident-plus diffracted-wave) potential near the body (except near the bow and stern) will have a decay factor

$$(x + L/2)^{-1/2} \qquad (49)$$

in the x-direction. But note that μ in (48) is also a function of x, and so (49) does not give the total x-dependence. However, μ will be the same for similar cross-sections. So, if the cross-sections are not varying much in the x-direction, the potential will, roughly speaking, drop off with the factor $(x + L/2)^{-1/2}$ in the lengthwise direction. Note that we have assumed that the wave length is of the order of magnitude of the transverse dimensions of the ship.

THE FORWARD-SPEED PROBLEM

We write the total potential ϕ as follows

$$\phi(x, y, z, t) = Ux + U\phi_s(x, y, z) + \phi_T(x, y, t) \tag{50}$$

where $U\phi_s$ is the perturbation velocity potential in the steady motion problem. It can easily be shown that ϕ_T satisfies

$$\frac{\partial^2 \phi_T}{\partial x^2} + \frac{\partial^2 \phi_T}{\partial y^2} + \frac{\partial^2 \phi_T}{\partial z^2} = 0 \tag{51}$$

in the fluid domain and the body boundary condition

$$\frac{\partial \phi_T}{\partial n} = 0 \quad \text{on} \quad z = h(x, y) \tag{52}$$

By combining (3) and (4) and using the assumption about linearity, it can be shown that ϕ_T satisfies the free-surface condition

$$\left[\frac{\partial}{\partial t} + U\frac{\partial}{\partial x}\right]^2 \phi_T + g\frac{\partial \phi_T}{\partial z} = 0 \quad \text{on} \quad z = 0 \tag{53}$$

Since the time dependence of the incident wave is given by $e^{i\omega t}$ (see (5)), it is expected that the time dependence for the potential ϕ_T is also given by $e^{i\omega t}$. This implies that we can write equation (52) as

$$\left[i\omega + U\frac{\partial}{\partial x}\right]^2 \phi_T + g\frac{\partial \phi_T}{\partial z} = 0 \quad \text{on} \quad z = 0 \tag{54}$$

We will write ϕ_T as

$$\phi_T = \phi_I + \phi_D = \frac{gh}{\omega_o} e^{\nu z} e^{i(\omega t - \nu x)} + \phi_D \quad (55)$$

where ϕ_D denotes the diffraction potential. ϕ_D must satisfy a radiation condition. As in the zero-speed problem we are going to use the method of matched asymptotic expansions to find ϕ_D.

We will assume that the forward speed

$$U = 0(\epsilon^{1/2 - a}) \quad , \quad 0 < a \leq 1/2 \quad (56)$$

In the steady forward-motion problem we know that there is a length scale in the x-direction which is connected with the wave length $2\pi U^2/g$. So (56) implies that this length scale is large compared with the transverse dimensions of the ship, and that it can be of the same order of magnitude as the length of the ship. In some way, I expect this length scale will enter our diffraction problem and affect the rate of change of the variables in the x-direction. But it turns out that it will not have any influence on the first two approximations of the diffraction potential. The important length scale in the x-direction will be connected with the wave length of the incoming wave, in the same way as for the zero-speed problem. As we remember from equation (10), this wave length is assumed to be of order ϵ.

If, however, we had assumed that "a" were zero in (56), we would have been in difficulties finding the second approximation to the diffraction potential. The reason must be that there then are two important length scales of order ϵ in the x-direction, one connected with the wave length of the incoming wave and one connected with the forward speed, and it is difficult to separate out the effect of one of the length scales from the other.

Using (7) and (9), we can show that (56) implies that the order of magnitude of the frequency of encounter, ω will be

$$\omega = 0(\epsilon^{-1/2 - a}) \quad , \quad 0 < a \leq 1/2 \quad (57)$$

We then see that the order of magnitude of $\tau = \frac{\omega U}{g}$ is

$$\tau = \frac{\omega U}{g} = 0\left(\epsilon^{-2a}\right), \quad 0 < a \leq 1/2 \tag{58}$$

It is obvious that τ will be larger than $1/4$. This is important, because the solution will be singular when $\tau = 1/4$ (see Ogilvie and Tuck (1969)).

There are two parts in this chapter : (1) derivation of the far-field source solution due to a line of pulsating, translating sources located on the x-axis between $-L/2$ and $L/2$ (see Figure 1) and derivation of a two-term inner expansion of the far-field source solution ; (2) formulation of the near-field problem, and the matching of a two-term near-field solution with the far-field solution.

IV. 1. Far-field source solution and the inner expansion of the far-field source solution

In the far-field description we expect to have waves. It is difficult to say how differentiation changes order of magnitudes in the far-field. So, to be careful, we would rather keep too many terms in the far-field. But we have to be sure that we have a system of equations that describes a wave motion. Using arguments similar to those in the section "Far-field source solution and the inner expansion of the far-field source solution" in the chapter on the zero-speed problem, we can find that ϕ_D must satisfy the Poisson equation,

$$\frac{\partial^2 \phi_D}{\partial x^2} + \frac{\partial^2 \phi_D}{\partial y^2} + \frac{\partial^2 \phi_D}{\partial z^2} = \sigma(x)\, e^{i(\omega t - \nu x)}\, \delta(y)\, \delta(z - z_o)$$

where $z_o < 0$. We write the free-surface condition as follows :

$$\left(i\omega + U \frac{\partial}{\partial x} + \mu\right)^2 \phi_D + g \frac{\partial \phi_D}{\partial z} = 0 \qquad \text{on} \qquad z = 0$$

where μ is the artificial Rayleigh viscosity, which will approach

zero at a proper later point. This equation system does give waves.

The solution to the equation system with $z_o = 0$ can be found in Ogilvie & Tuck (1969). It is

$$\phi_D(x,y,z,t) = -\frac{1}{4\pi^2} e^{i\omega t} \int_{-\infty}^{\infty} dk\, e^{ikx}\, F\left\{\sigma(x)\, e^{-i\nu x}\right\} \tag{59}$$

$$\cdot \lim_{\mu \to 0} \int_{-\infty}^{\infty} \frac{d\ell\, e^{i\ell y + z\sqrt{k^2+\ell^2}}}{\sqrt{k^2+\ell^2} - \frac{1}{g}(\omega + Uk - i\mu)^2},$$

where

$$F\left\{\sigma(x)\, e^{-i\nu x}\right\} = \int_{-\infty}^{\infty} dx\, e^{-ikx}\, \sigma(x)\, e^{-i\nu x}$$

$$= \sigma^*(k+\nu).$$

We will rewrite (59) in a way similar to the way we did with (15) in the zero-speed problem. See Appendix C for more details.

We can write

$$\phi_D(x,y,z,t) = \Phi(x,y,z)\, e^{i(\omega t - \nu x)} \tag{60}$$

where $$\Phi(x,y,z) \simeq -\frac{i}{2\pi}\left[\int_{-\infty}^{k_2} + \int_{k_2}^{-\epsilon^{-(1-a-\beta)}} + \int_{-\epsilon}^{0} + \int_{0}^{\epsilon^{-(1-a-\beta)}} + \int_{\epsilon}^{\epsilon^{-(1-a+\delta_2)}}_{-(1-a-\beta)}\right] dk\, e^{ikx}\, \sigma^*(k) \left[1+\frac{Uk}{\omega_o}\right]^2 \frac{e^{i\ell_o y}\, e^{\nu z}\left[1+\frac{Uk}{\omega_o}\right]^2}{\ell_o/\nu} + I_{\alpha_1} + I_{\alpha_2} \tag{61}$$

In the first integral, $\ell_o = \sqrt{(\omega_o + Uk)^4/g^2 - (\nu - k)^2}$. In the second and third integrals, $\ell_o = i\sqrt{(\nu-k)^2 - (\omega_o+Uk)^4/g^2}$. In the fourth and fifth integrals, $\ell_o = -\sqrt{(\omega_o+Uk)^4/g^2 - (\nu-k)^2}$

Further

$$k_2 = -\frac{g}{U^2}(2\omega_o U/g + 1),$$

a the parameter introduced by (56), β and δ_2 some very small positive numbers and

$$I_{\alpha 1} = \frac{\nu e^{i\nu x}}{4\pi^2} \int_{\epsilon^{1-\delta_1}}^{0} d\alpha\, e^{-i\nu\alpha x}\, \sigma^*(\nu - \alpha\nu) \int_{\alpha}^{\infty} d\ell\, e^{-\nu y \ell} \tag{62}$$

$$\cdot\left[\frac{e^{i\nu z\sqrt{\ell^2-\alpha^2}}}{\sqrt{\ell^2-\alpha^2} + i\left[1+\frac{U\omega_o}{g}(1-\alpha)\right]^2} + \frac{e^{-i\nu z\sqrt{\ell^2-\alpha^2}}}{\sqrt{\ell^2-\alpha^2} - i\left[1+\frac{U\omega_o}{g}(1-\alpha)\right]^2}\right]$$

and

$$I_{\alpha 2} = -\frac{\nu e^{i\nu x}}{4\pi^2} \int_0^{\epsilon^{1-\delta_1}} d\alpha\, e^{i\nu\alpha x}\, \sigma^*(\nu+\nu\alpha) \int_\alpha^\infty d\ell\, e^{-\nu y \ell}$$

$$\cdot \left[\frac{e^{i\nu z\sqrt{\ell^2-\alpha^2}}}{\sqrt{\ell^2-\alpha^2} + i\left[1 + \frac{U\omega_o}{g}(1+\alpha)\right]^2} + \frac{e^{-i\nu z\sqrt{\ell^2-\alpha^2}}}{\sqrt{\ell^2-\alpha^2} - i\left[1 + \frac{U\omega_o}{g}(1+\alpha)\right]^2} \right] \tag{63}$$

Here, δ_1 is some very small positive number. (61) is valid for $y = 0(1) > 0$. We are now going to find a two-term inner expansion of the far-field source solution. We then let y be of order ϵ, and we reorder the terms in (61). The procedure is shown in Appendix D.

We get

$$\phi(x,y,z) = -\frac{e^{\nu z - i\pi/4}}{\sqrt{\pi}} \int_{-L/2}^{x} \frac{d\xi\, \sigma(\xi)}{\sqrt{\frac{2\omega + 2U\nu}{\nu\omega_o}\,|x-\xi|}}$$

$$+ \nu y e^{\nu z}\, \sigma(x) - \frac{e^{\nu z}\, \sigma(x)}{2\sqrt{2}} \tag{64}$$

Using (60) and the symmetry properties associated with sources, we can now write down a two-term inner expansion of the far-field source solution as

$$\phi_D(x, y, z, t) \sim e^{i(\omega t - \nu x)} \; e^{\nu z} \left[-\frac{e^{-i\pi/4}}{\sqrt{\pi}} \int_{-L/2}^{x} \frac{d\xi \, \sigma(\xi)}{\sqrt{\frac{2\omega + 2U\nu}{\nu\omega_o} |x - \xi|}} \right.$$

$$\left. + \nu |y| \, \sigma(x) - \frac{\sigma(x)}{2\sqrt{2}} \right] \tag{65}$$

As for the zero-speed problem we see that the two-term inner expansion represents waves propagating along the ship in the same direction as the incoming wave. Arguing as for the zero-speed problem we should therefore expect an integrated effect along the ship as the lowest order term in (65) represents.

We note that (65) does not reduce to (19) when $U = 0$. It should not be expected that (65) reduce to (19) when $U = 0$ since we have assumed $\tau = \frac{\omega U}{g} > 1/4$ and since this assumption has been an important part in our analysis. We should note that the last term in (65) represents a distrubance arising from upstream while the last term in (19) represents a disturbance arising from downstream.

IV. 2. The near-field problem and the matching

We now formulate the near-field problem and perform the matching between the near-field and the far-field solutions. A one-term far-field solution is found to be due to a line of sources with source density.

$$\sigma_1(x) \, e^{i(\omega t - \nu x)}$$

spread along the line $y = z = 0$, $-L/2 \leq x \leq L/2$. (See Figure 1). As in the zero-speed problem, a one-term near-field solution is found to be the negative of the incident wave. The matching of the far-field solution and the near-field solution determines $\sigma_1(x)$ in a similar

way for the zero-speed problem. The two-term near-field solution is given by (92).

It should be noted that "Near-field" means the region near the body where the distance from the body is $0(\epsilon)$. However, we do not expect the near-field approximations to be valid near the bow and stern.

We will express the potential of the diffracted wave as follows :

$$\phi_D = e^{i(\omega t - \nu x)} \psi(x, y, z) \tag{66}$$

Using (55), (51), (54), and the fact that the incident wave potential satisfies the Laplace equation and the free-surface condition (54), we get that ϕ_D will satisfy the Laplace equation and the free-surface condition (54).

Putting (66) into Laplace equation gives

$$\frac{\partial^2 \psi}{\partial y^2} + \frac{\partial^2 \psi}{\partial z^2} - \nu^2 \psi - 2i\nu \frac{\partial \psi}{\partial x} + \frac{\partial^2 \psi}{\partial x^2} = 0 \tag{67}$$

in the fluid region.

The free-surface condition is

$$(i\omega + U\frac{\partial}{\partial x})^2 \phi_D + g \frac{\partial \phi_D}{\partial z} = 0 \quad \text{on} \quad z = 0 \tag{68}$$

Putting (66) into (68) gives

$$-\omega_o^2 \psi + g \frac{\partial \psi}{\partial z} + 2iU\omega_o \frac{\partial \psi}{\partial x} + U^2 \frac{\partial^2 \psi}{\partial x^2} = 0 \tag{69}$$

$$\text{on} \quad z = 0$$

The body boundary condition (52) together with (55) gives

$$\left[n_2 \frac{\partial \psi}{\partial y} + n_3 \frac{\partial \psi}{\partial z} - i\nu n_1 \psi + n_1 \frac{\partial \psi}{\partial x}\right] = \left[i\nu n_1 - \nu n_3\right] \frac{gh}{\omega_o} e^{\nu z} \quad \text{on} \quad z = h(x, y) \tag{70}$$

A last condition on ψ is that it must match with the far-field solution.

As in the zero-speed problem, we stretch coordinates

$$y = \epsilon Y \ , \quad z = \epsilon Z \ , \quad n_{2D} = \epsilon N \ , \quad x = X \tag{71}$$

to express that ψ varies very slowly in the x-direction compared with the variation of ψ in the transverse plane.

We assume an asymptotic expansion of ψ of the form

$$\psi \sim \sum_{n=1}^{N} \psi_n(X, Y, Z; \epsilon) \tag{72}$$

where $\psi_{n+1} = o(\psi_n)$ as $\epsilon \to 0$ for fixed X, Y, Z.

As in the zero-speed problem we introduce

$$k = \nu \epsilon \tag{73}$$

and

$$C = \frac{gh}{\omega_o} \tag{74}$$

The lowest-order equations become

$$\left(\frac{\partial^2}{\partial Y^2} + \frac{\partial^2}{\partial Z^2} - k^2 \right) \psi_1 = 0 \qquad (75)$$

$$\left(\frac{\partial}{\partial Z} - k \right) \psi_1 = 0 \quad \text{on} \quad Z = 0 \qquad (76)$$

$$\frac{\partial}{\partial N} \psi_1 = - Cn_3 \, k e^{kZ} \quad \text{on} \quad Z = h(x, y) \qquad (77)$$

In addition ψ_1 must match with the far-field solution.

A one-term far-field solution is assumed to be the potential associated with a line distribution of sources of density

$$\sigma_1 (x) \, e^{i (\omega t - \nu x)}$$

spread along the line $y = z = 0$, $- L/2 \leq x \leq L/2$. That solution has been obtained in a previous section, and a one-term inner expansion of the far-field solution can be found from (65). For any fixed x greater that $- L/2$, a one-term inner expansion is

$$e^{i(\omega t - \nu x)} \left[- \frac{e^{\nu z - i \pi/4}}{\sqrt{\pi}} \int_{- L/2}^{x} \frac{d \xi \, \sigma_1 (\xi)}{\sqrt{\frac{2 \omega + 2 U \nu}{\nu \omega_o} |x - \xi|}} \right] \qquad (78)$$

In a similar way as for the zero-speed problem, one see that the only possibility for a solution satisfying (75), (76), (77), and matching (78) is by requiring that

$$\frac{e^{\nu z - i\pi/4}}{\sqrt{\pi}} \int_{-L/2}^{x} \frac{d\xi \sigma_1(\xi)}{\sqrt{\frac{2\omega + 2U\nu}{\nu\omega_o}|x - \xi|}} = Ce^{\nu z} \tag{79}$$

and letting a one-term near-field solution of the diffracted wave be the negative of the incident wave. So

$$\psi_1 = -Ce^{\nu z} \tag{80}$$

We solve (79) for $\sigma_1(x)$ formally by letting it be an equality for all $x \geq -L/2$. We get Abel's integral equation to solve (See Dettman (1965)). The solution is

$$\sigma_1(x) = \sqrt{\frac{2\omega + 2U\nu}{\pi\omega_o \nu(x + L/2)}} e^{i\pi/4} C \tag{81}$$

The discussion that followed the expression of $\sigma_1(x)$ for the zero-speed problem (see after equation (34)) can also be applied for the forward-speed problem. The conclusion was that we had to construct a separate expansion for a region in which $x + L/2 = 0(\epsilon^{\gamma})$, (γ some positive number), and that $\sigma_1(x)$ is not given in that region by (81).

We wish next to find ψ_2 , but first we need to say some more about the far-field.

We expect that a two-term far-field expansion is obtained by a line distribution of sources of density

$$\left(\sigma_1(x) + \sigma_2(x)\right) e^{i(\omega t - \nu x)} \tag{82}$$

spread along the line $y = z = 0$, $-L/2 \leq x \leq L/2$. A two-term inner expansion of this two-term far-field expansion can be obtained from (65).

It is

$$e^{i(\omega t - \nu x)} \left[-\frac{e^{\nu z}}{\sqrt{\pi}} e^{-i\pi/4} \int_{-L/2}^{x} \frac{d\xi \sigma_1(\xi)}{\sqrt{\frac{2\omega + 2U\nu}{\nu\omega_o}|x-\xi|}} - \right.$$

$$\left. -\frac{e^{\nu z}}{\sqrt{\pi}} e^{-i\pi/4} \int_{-L/2}^{x} \frac{d\xi \sigma_2(\xi)}{\sqrt{\frac{2\omega + 2U\nu}{\nu\omega_o}|x-\xi|}} + \nu|y| e^{\nu z} \sigma_1(x) - \frac{\sqrt{2}}{4} e^{\nu z} \sigma_1(x) \right] \tag{83}$$

In the same way as for the zero-speed problem we will find that ψ_2 satisfies

$$\left[\frac{\partial^2}{\partial Y^2} + \frac{\partial^2}{\partial Z^2} - k^2 \right] \psi_2 = 0 \tag{84}$$

$$\left[\frac{\partial}{\partial Z} - k \right] \psi_2 = 0 \quad \text{on} \quad Z = 0 \tag{85}$$

$$\frac{\partial \psi_2}{\partial N} = 0 \quad \text{on the submerged part of the body} \tag{86}$$

In addition ψ_2 must match with the far-field solution.

Ursell (1968 a) has derived a solution to (84), (85) and (86). It can be written as

$$\psi_2 = B_2(x)\left[e^{kZ} + \int_{C(+)} k\mu(s;k)\cdot\left[G(kY,kZ;k\xi(s),k\eta(s)) + G(kY,kZ;-k\xi(s),k\eta(s))\right] ds\right] \tag{87}$$

For an explanation of (87), see the discussion following equation (41) in the zero-speed problem. $B_2(x)$ in (87) is unknown at the moment now, but will be determined by matching.

The two-term near-field solution,

$$[\psi_1 + \psi_2]\ e^{i(\omega t - \nu x)} \tag{88}$$

has the following three-term outer expansion :*

$$e^{i(\omega t - \nu x)}\left[-\frac{e^{\nu z}}{\sqrt{\pi}}\ e^{-i\pi/4}\int_{-L/2}^{x}\frac{d\xi\,\sigma_1(\xi)}{\sqrt{\frac{2\omega + 2U\nu}{\nu\omega_o}|x-\xi|}} + B_2(x)\,e^{kZ} - B_2(x)\,4k^2\pi\,\frac{|Y|}{\epsilon}\,e^{kZ}\int_{C(+)}\mu(s,k)e^{k\eta(s)}\,ds\right] \tag{89}$$

* See (43) and the text in connection with (43)

We see that (89) matches with (83) if we set :

$$B_2(x) = -\frac{\sigma_1(x)}{4k\pi \int_{C(+)} \mu(s,k)\, e^{k\eta(s)}\, ds} \tag{90}$$

$$= -\frac{\sqrt{\frac{2\omega + 2U\nu}{\pi\nu\omega_o(x + L/2)}}\, e^{i\pi/4}\, C}{4k\pi \int_{C(+)} \mu(s,k)\, e^{k\eta(s)}\, ds}$$

and

$$-\frac{e^{-i\pi/4}}{\sqrt{\pi}} \int_{-L/2}^{x} \frac{d\xi\, \sigma_2(\xi)}{\sqrt{\frac{2\omega + 2U\nu}{\nu\omega_o}|x - \xi|}} = B_2(x) + \frac{\sqrt{2}}{4}\sigma_1(x) \tag{91}$$

Equation (91) gives us Abel's integral equation to solve. $B_2(x)$ on the right-hand side of (91) has to be numerically determined (see (90)). We are only interested in the fact that the near-field and far-field solutions match, and we are not going to find σ_2 .

It is the near-field solution that has the primary interest and we have found that a two-term near-field solution of the diffraction potential is

$$[\psi_1 + \psi_2]\, e^{i(\omega t - \nu x)} = e^{i(\omega t - \nu x)} \left[- Ce^{kZ} \right.$$

$$- \sqrt{\frac{2\omega + 2U\nu}{\pi \nu \omega_o (x + L/2)}} \cdot \frac{e^{i\pi/4}\, C}{4k\pi \int_{C(+)} \mu(s,k)\, e^{k\eta(s)}\, ds} \left[e^{kZ} \right.$$

$$\left. \left. + \int_{C(+)} k\mu(s;k) \left[G(kY, kZ; k\xi(s), k\eta(s) + G(kY, kZ; -k\xi(s), k\eta(s)) \right] ds \right] \right] \qquad (92)$$

V. NUMERICAL CALCULATIONS

V.1. Theoretical background

It would be time consuming to evaluate the solutions we have found (see (48) and (92)) for a ship with arbitrary cross-sections. But if the ship had circular cross-sections, there is a faster way to find the solutions. We can use the solution given by Ursell (1968 b) for a circular cross-section. Ursell has used a different coordinate system that we have used earlier, and I find it convenient using Ursell's coordinate system when talking about Ursell's solution. The coordinate system is shown in Figure 2.

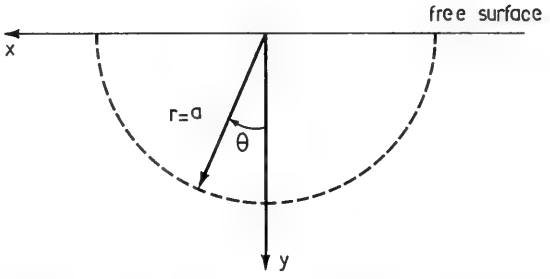

Figure 2 Ursell's coordinate system

The two-dimensional problem which Ursell solves is given by the Helmholtz equation

$$\left[\frac{\partial^2}{\partial x^2} + \frac{\partial^2}{\partial y^2} - \nu^2 \right] \phi = 0 \qquad (93)$$

in the fluid domain, and the boundary conditions

$$\nu \phi + \frac{\partial \phi}{\partial y} = 0 \quad \text{when} \quad y = 0, \quad |x| > a \tag{94}$$

and

$$\frac{\partial \phi}{\partial r} = 0 \quad \text{when} \quad r = a, \quad -\pi/2 < \theta < \pi/2 \tag{95}$$

He shows that a solution of (93), (94) and (95) can be written in the form

$$\phi = B_3 \left\{ A_o S_o(x, y) + \exp(-\nu y) + \sum_{m=1}^{\infty} A_m O_m(x, y) \right\} \tag{96}$$

The functions $S_o(x, y)$ and $O_m(x, y)$ will be discussed presently.

Ursell considered an infinitely long cylinder and there were no appropriate conditions for $x \longrightarrow \pm \infty$ that could determine the arbitrary constant B_3 in (96). But we consider a ship, and we have found a condition when $x \longrightarrow \pm \infty$ that will determine B_3. This is similar to what we did in finding the solutions (48) and (92). Then we used an integral equation approach to solve (93), (94) and (95). But for this special case with a circular cross-section it is more convenient to write the solution as (96). We will later come back to the determination of B after we have discussed the terms in (96) some more.

The source term S_o can be written as

$$S_o(x, y) = 1/2 \left[\int_{-\infty}^{\infty} + \int_{-\infty}^{\infty} \right] \frac{\cos h\, \mu}{\cos h\, \mu - 1} \exp(-\nu y \cos h\mu + i\nu x \sin h\mu)\, d\mu \tag{97}$$

The paths in the two integrals pass respectively below and above the double pole at $\mu = 0$.

We are going to rewrite (97) so that we can more easily evaluate it numerically. We introduce

$$\ell = \nu \sin h\mu$$

as a new integration variable.

We then introduce closed integration paths in the complex ℓ - plane properly indented at the branch points of the integrand.

By using the residue theorem, we can then write (97) as

$$S_o = 2 \int_0^\infty \frac{du\, u}{\sqrt{\nu^2 + u^2}} \left[\frac{u \cos(uy) - \nu \sin(uy)}{\nu^2 + u^2} \right] e^{-|x| \sqrt{\nu^2 + u^2}} - 2\pi\nu |x| e^{-\nu y} \tag{98}$$

The other unexplained terms in (96) are the wave-free potentials O_m. They are given by

$$O_m(x, y) = K_{2m-2}(\nu r) \cos(2m - 2)\theta + 2K_{2m-1}(\nu r) \cos(2m - 1) + K_{2m}(\nu r) \cos 2m\theta$$

$$m = 1, 2, 3, \ldots \tag{99}$$

(Ursell denoted these functions by $O_m^{(e)}$.)

K_n are modified Bessel functions as defined by Abramowitz and Stegun (1964).

The coefficients A_o and A_m in (96) are determined by satisfying the body boundary condition (95). This leads to an equation of the form

$$A_o \frac{\partial S_o}{\partial r} + \sum_{m=1} A_m \frac{\partial O_m}{\partial r} - \nu \cos\theta \, e^{-\nu r \cos\theta} = 0 \qquad \text{on } r = a \tag{100}$$

We have assumed here that we can differentiate the infinite series in (96) term by term, and we have used the fact that

$$x = r \sin\theta \quad , \qquad y = r \cos\theta \tag{101}$$

$\frac{\partial O_m}{\partial r}$ in (100) is obtained from (99) and by using 9.6.26 in Abramowitz and Stegun (1964). So

$$\frac{\partial O_m}{\partial r} = \left\{ - K_{2m-1}(\nu r) + \frac{2m-2}{\nu r} K_{2m-2}(\nu r) \right\} \nu \cos(2m-2)\theta$$

$$+ 2 \left\{ - K_{2m}(\nu r) + \frac{2m-1}{\nu r} K_{2m-1}(\nu r) \right\} \nu \cos(2m-1)\theta$$

$$+ \left\{ - K_{2m+1}(\nu r) + \frac{2m}{\nu r} K_{2m}(\nu r) \right\} \nu \cos 2m\theta$$

We will now describe in more detail how to solve (100) numerically and how numerically to evaluate S_o in (96) and $\frac{\partial S_o}{\partial r}$ in (100).

Equation (100) is solved by setting up a least-square condition. One assumes that the infinite sums in (96) and (100) converge sufficiently rapidly so that a finite number of terms in the infinite sums gives a satisfactory approximation. One calls this number M.

The least-square condition leads to the linear equation system

$$\sum_{m=0}^{M} A_m \left[\sum_{i=1}^{N} \frac{\partial O_m(r, \theta_i)}{\partial r} \frac{\partial O_n(r, \theta_i)}{\partial r} \right] = \tag{102}$$

$$= \nu \sum_{i=1}^{N} \cos\theta_i \, e^{-\nu a \cos\theta_i} \frac{\partial O_n(r, \theta_i)}{\partial r}$$

for $r = a$. n goes from zero to M. We have set $\frac{\partial S_o}{\partial r} = \frac{\partial 0_o}{\partial r}$ in (102).

N is chosen so that $N \geq 3/2\,(M + 1)$. It was found that $N = 10$ gives satisfactory results. θ_i have been chosen as

$$\theta_i = \frac{\pi}{4N} + \frac{\pi}{2N}(i - 1) \quad , \quad i = 1, 2, \ldots, N \tag{103}$$

(102) can be solved by standard methods. S_o in (96) are evaluated in the following way. We introduce (101) in (98) and write S_o as

$$S_o = -2\pi\nu r \sin\theta \; e^{-\nu r \cos\theta}$$

$$+ 2 \int_0^A \frac{du \; u^2}{(\nu^2 + u^2)^{3/2}} \cos(ur\cos\theta) \; e^{-r\sin\theta \sqrt{\nu^2 + u^2}}$$

$$- 2 \int_0^A \frac{du \; u\nu}{(\nu^2 + u^2)^{3/2}} \sin(ur\cos\theta) \; e^{-r\sin\theta \sqrt{\nu^2 + u^2}} \tag{104}$$

$$+ O(B_1) \qquad \text{for} \quad 0 < \theta < \pi/2$$

where $B_1 = \dfrac{e^{-r \sin\theta \sqrt{\nu^2 + A^2}}}{r \sin\theta}$.

A is chosen so that B_1 is sufficiently small. It was found that it was satisfactory to use $B_1 = 0.0001$.

Each integral in (104) was evaluated by first locating the zeroes for the integrand. For the first integrand the zeroes are easily found to be $u = 0$ and $u = \frac{\pi}{2r\cos\theta}(2m + 1)$, $m = 0, 1, 2, \ldots$ and for the second integrand the zeroes are $u = \frac{\pi}{r\cos\theta} m$, $m = 0, 1, 2 \ldots$ Between each zero in an integrand we then used Simpson's formula. As is seen above the length of the interval between each zero depends on θ, and so the number of points used in Simpson integration should depend on θ. When θ was close to $\pi/2$, as many as 50 points were needed in the Simpson integration. But when θ was close to 0, it was only necessary to use 8 points. If A was less than u at the second zero of an integrand, then Simpson's formula was only used between 0 and A.

$\frac{\partial S_o}{\partial r}$ was numerically evaluated in a way similar to that for S_o. We have now explained how to obtain numerically the terms in the brackets of (96). We will refer to these terms as "Ursell's solution" and denote them by ϕ_u. So

$$\phi = B_3 \phi_u \tag{105}$$

(See (96)). ϕ_u has been plotted in Figure 3 as a function of νr for different values of θ and in Figure 4 as a function of θ for different values of νr.

We now have to find B_3 in (105). B_3 will of course be determined in the same way as we did in the previous chapters where we solved the zero- and the forward-speed problem. We prefer now to use the coordinate system shown in Figure 1.

If we take an outer expansion of (105), the term which is linear in y will be

$$- B_3 A_o 2\pi\nu \left|y\right| \quad e^{\nu z} \tag{106}$$

(see (96) and (98)). In accordance with what has been done in the previous chapters, (106) should (for both the zero-speed and forward-speed cases) match with

$$\nu \left|y\right| \quad e^{\nu z} \quad \sigma_1(x) \quad e^{i(\omega t - \nu x)} \tag{107}$$

where $\sigma_1(x)$ can be written for both cases as

$$\sigma_1(x) = \sqrt{\frac{(2\omega + 2U\nu)}{\pi\omega_o \nu (x + L/2)}} \; e^{i\pi/4} \; \frac{gh}{\omega_o} \tag{108}$$

By equating (106) and (107) and putting the expression for B_3 into (105), we can write the potential

$$\phi = - \frac{e^{i\pi/4}}{2\pi A_o} \sqrt{\frac{2\omega + 2U\nu)}{\pi\omega_o \nu(x + L/2)}} \; \frac{gh}{\omega_o} \; e^{i(\omega t - \nu x)} \phi_u \tag{109}$$

Using Bernoulli's equation, it is now easy to find the pressure. To the leading order the pressure will be

$$\frac{p}{\rho gh} = \frac{e^{i3\pi/4}}{2\pi A_o} \sqrt{\frac{2\omega + 2U\nu}{\pi\omega_o \nu (x + L/2)}} \; \phi_u \quad e^{i(\omega t - \nu x)} \tag{110}$$

One should note the simple forward-speed dependence in (110). ϕ_u and A_o will only depend on the wave length. So for a

given wave length the amplitudes of the pressure, force and moment for a given forward speed can be obtained from the corresponding values at zero-speed by multiplying the zero-speed results by a constant factor.

V. 2. Comparison with Experiments

C. M. Lee has measured the pressure-distribution along a restrained, semi-submerged, prolate spheroid which was towed at a constant speed in regular head-sea waves. He used the experimental pressure values to calculate a longitudinal force distribution along the spheroid (C. M. Lee (1964)). He did not publish the data for the pressure distribution along the spheroid, but he was kind and gave us those data.

The surface of the prolate spheroid that C. M. Lee used can be described by the equation :

$$\frac{x^2}{\ell^2} + \frac{y^2 + z^2}{b_0^2} = 1,$$

where $\ell = 19.8''$ and $b_0 = 3.3''$. x, y, z are defined by Figure 1. He measured the pressure at cross-sections located at $x = -16''$ (called C_F), $x = -12.5''$ (called B_F), $x = -7''$ (called A_F), $x = 0$ (called ⊗), $x = 7''$ (called A_A), $x = 12.5''$ (called B_A), $x = 16''$ (called C_A). He did the experiments for $\lambda/L = 0.5,\ 0.75,\ 1.0,\ 1.25,\ 1.5$ and 2.0 where λ is the wave length and L is the length of the model. The Froude numbers of the model were $F_n = 0.082,\ 0.123,\ 0.164,\ 0.205,\ 0.246,\ 0.328$.

In our theory we have assumed that the wave length is of the order of magnitude of the transverse dimensions of the ship. But note that this does not necessarily mean that the theory is bad for larger wave lengths. One can refer to the strip theory which has shown to give good results for a wider range of wave lengths that one rationally has to restrict oneself to. The comparisons with the experiments by Lee seems to indicate that our theory is not good for wave lengths $\lambda/L = 0.75$ and larger. We will therefore only show the comparisons for $\lambda/L = 0.5$.

There were evidently some irregularities in the experiments

for $F_n = 0.328$, and so we did not compare experiments and theory for that Froude-number. We decided to present the comparisons between experiments and theory for Froude-numbers 0.082 and 0.205, but the agreement between theory and experiments was just as good for Froude-numbers 0.123, 0.164 and 0.246.

In Figures 5 through 10 are shown the comparisons of the pressure amplitudes for Froude-number 0.085. Figure 5 shows the longitudinal distribution of the pressure amplitude along the keel of the spheroid. It is seen that the experiments confirm the theoretically predicted longitudinal deformation of the wave along the ship. Figure 6 shows the pressure-variation along the cross-section B_F. (The index F indicates that the cross-section is on the forward part of the model.) The variable θ, the abscissa in the figure, is $\pi/2$ for a point in the undisturbed free-surface and 0 for a point located on the center plane of the model. It is seen that the agreement between theory and experiments is reasonably good. Similar comparisons are made for cross-section A_F in Figure 7, cross-section $\oslash$ in Figure 8, cross-section A_A in Figure 9, cross-section B_A in Figure 10. (The index A indicates that the cross-section is on the after part of the model.) It is seen that the agreement is good, especially for the after cross-sections.

In Figures 11 through 16 are shown the comparisons of the pressure amplitudes for Froude-number 0.205. Figure 11 shows the longitudinal distribution of the pressure along the keel of the spheroid. Figures 12-16 show the pressure variation on the cross-sections B_F, A_F, $\oslash$, A_A and B_A, respectively. It is seen that the agreement between experiments and theory is at least as good as in the case of the smaller Froude-number. Since the theory is not assumed to be valid near the bow or stern, no comparisons have been made for cross-sections C_F and C_A.

In Figure 17 is shown the comparison between theory and experiments for the longitudinal distribution of the phase angle of the pressure. The theory predicts that for all Froude-numbers the phase-angle of the pressure is $\pi/4$ before the phase-angle of the Froude-Kriloff pressure. For a given cross-section, the experimental value of the phase angle varied somewhat. So the presented data are averages. The variation is, roughly speaking, not more than $\pm 10°$. It is seen that the agreement between experiments and theory is good.

ACKNOWLEDGEMENT

This work is based on a doctoral thesis at The University of Michigan (Faltinsen (1971)). The author was then on leave from his position at the Research Department, Det norske Veritas, Oslo, Norway with a financial support from The Royal Norwegian Council for Scientific and Industrial Research (NTNF).

I want to thank the chairman of my doctoral committee, Professor T. Francis Ogilvie. Without his encouragement, helpful suggestions and contributions this work would never have been done.

I am also thankful to Professor R. Timman, Technical University of Delft. The discussions with him were a turning point in my work.

Further, I am thankful to Dr. Nils Salvesen, Naval Ship Research and Development Center, Washington DC., Dr. Choung Mook Lee, Naval Ship Research and Development Center, Washington DC. and Mr. Arthur M. Reed, University of Michigan for their contribution.

NOTATION

a		used in the description of the order of magnitude of the velocity U, $U = 0(\epsilon^{1/2-a})$, $0 < a \leq 1/2$.
C	$=$	$\frac{gh}{\omega_o}$
Fn	$=$	$U/\sqrt{Lg}$, Froude number.
g		acceleration of gravity.
$G(kY, kZ; k\xi, k\eta)$		wave source potential (see (42)).
h		wave amplitude of the incoming wave.
$h(x, y)$		function defining the wetted surface of the ship.
k		equal to $\nu \cdot \epsilon$ in the sections about the near-field problem and the matching. Otherwise integration variable in the Fourier transform.

k_1 = 0

k_2 = $-\frac{g}{U^2}(2\omega_o U/g + 1)$

L length of ship.

n coordinate-axis in the direction of the outward normal on the wetted surface of the ship.

N stretched coordinate (see (24)). (Can also mean a number.)

n_{2D} coordinate-axis normal to and out of a cylinder with the same cross-section as the ship at a given section.

n_i i = 1, 2, 3 : the x-, y-, z- component of the unit normal vector to the wetted surface of the ship.

r radial coordinate used in the chapter : "Numerical Calculations" (see Figure 2).

t time variable

T draft of the ship midships.

U forward speed of the ship.

x, y, z Cartesian coordinates (see Figure 1). (The ship moves in the direction of the negative x-axis, z is measured upwards, y to starboard).

X, Y, Z stretched coordinates (see (24) or (71)).

α = $\left|\frac{\nu - k}{\nu}\right|$ where k is an integration variable.

β very small positive number.

δ_1 very small positive number.

δ_2 very small positive number.

ϵ		slenderness parameter. It is a measure of the transverse dimensions of the ship compared with the longitudinal dimensions of the ship.
$\zeta(x, y, t)$		free-surface displacement
θ		angular coordinate used in the chapter : "Numerical Calculations"(see Figure 2). $\theta = 0$ is a point on the centerplane.
λ		wave length of the incoming wave.
μ		fictitious (Rayleigh) viscosity. (Note that μ (arg) has another meaning.)
ν	$=$	$\frac{\omega_o^2}{g} = \frac{2\pi}{\lambda}$
ρ		density of water (mass per unit volume).
$\sigma(x)e^{i(\omega t - \nu x)}$		source density per unit length in line distribution of sources.
$\sigma^*(k)$	$=$	$\int_{-\infty}^{\infty} dx e^{-ikx}\sigma(x)$ (the sign $*$ means here inverse Fourier transform).
τ	$=$	$\frac{\omega U}{g}$
$\phi(x, y, z, t)$		velocity potential in forward-speed problem and in zero-speed problem.*
$\phi_I(x, y, z, t)$		velocity potential of the incoming wave.
$\phi_D(x, y, z, t)$		velocity potential of the diffracted wave.
$\phi_s(x, y, z)$		$(1/U)$* perturbation-velocity potential in steady motion problem.

* Note, however, that in Chapter V "Numerical calculations", it means the time dependent part of the velocity potential.

$\phi_T(x, y, z, t)$	time-dependent part of velocity potential.
$\Phi(x, y, z)$	see (16) and (17) for zero-speed problem. See (60) and (61) for forward-speed problem.
$\psi(x, y, z)$	see (20) in zero-speed problem. See (66) in forward-speed problem.
ψ_i	$i = 1.2..... N, \psi \sim \sum_{i=1}^{N} \psi_i$
ω_o	wave frequency of the incoming wave.
ω	$\omega_o + \nu U$

REFERENCES

1 ABRAMOWITZ, M., and STEGUN, I.A., "Handbook of Mathematical Functions", National Bureau of Standards Mathematics Series, 55, Washington, DC. (1964).

2 DETTMAN, John W., "Applied Complex Variables", The Macmillan Company, New York - Collier - Macmillan Ltd, London (1965).

3 ERDELYI, A., "Asymptotic Expansions", Dover Publications, Inc., New York (1956).

4 FALTINSEN, O., "Wave Forces on a Restrained Ship in Head-Sea Waves", Ph. D. Thesis, The University of Michigan, Ann Arbor (1971).

5 JONES, D.S., "Generalized Functions", McGraw-Hill Book Co., New York (1966).

6 LEE, C.M., "Heaving Forces and Pitching Moments on a Semi-submerged and Restrained Prolate Spheroid Proceeding in Regular Head Waves", Report No. NA-64-2, Institute of Engineering Research, University of California, Berkeley, California, (1964).

7 LIGHTHILL, M. J., "Fourier Analysis and Generalized Functions", Cambridge University Press, Cambridge (1958).

8 NEWMAN, J. N., "The Exciting Forces on Fixed Bodies in Waves", Journal of Ship Research, 6:3 (1962) 10-17.

9 OGILVIE, T. F., Unpublished work (1969).

10 OGILVIE, T. F. and TUCK, E. O., "A Rational Strip Theory of Ship Motions : Part I", Department of Naval Architecture and Marine Engineering, College of Engineering, The University of Michigan, Ann Arbor, Michigan, Report No. 013, March 1969.

11 OGILVIE, T. F., "Singular Perturbation Problems in Ship Hydrodynamics", Department of Naval Architecture and Marine Engineering, College of Engineering, The University of Michigan, Ann Arbor, Michigan, Report No. 096, October 1970.

12 SALVESEN, N., TUCK, E. O., FALTINSEN, O., "Ship Motions and Sea Loads", SNAME Transactions, 78, (1970) 250-287.

13 URSELL, F., "On Head Seas Travelling Along a Horizontal Cylinder", J. Inst. Maths. Applics., 4 (1968 a) 414-427.

14 URSELL, F., "The Expansion of Water-Wave Potentials at Great Distances", Proc. Camb. Phil. Soc., 64, (1968 b), 811.

15 VAN DYKE, M., "Perturbation Methods in Fluid Mechanics", 1964, Academic Press, New York and London.

* * *

APPENDIX A

Simplification of the far-field expansion in the zero-speed problem

We will show how (15) can be rewritten into (16) and (17). The procedure is based on work by Ogilvie (1969).

We first introduce

$$k' = k + \nu$$

in (15). If we drop the primes we can write (15) as

$$\phi_D(x, y, z, t) = \Phi(x, y, z)\ e^{i(\omega t - \nu x)} \tag{A-1}$$

where

$$\Phi(x, y, z) = -\frac{1}{4\pi^2} \int_{-\infty}^{\infty} dk\ e^{ikx}\ \sigma^*(k)$$

$$\cdot \lim_{\mu \to 0} \int_{-\infty}^{\infty} \frac{d\ell\ e^{i\ell y + z\sqrt{\ell^2 + (\nu - k)^2}}}{\sqrt{\ell^2 + (\nu - k)^2} - (\nu - i\mu)} \tag{A-2}$$

We will let $y = 0(1)$ and we are going to assume that $y > 0$.

We define

$$I(k) = \lim_{\mu \to 0} \int_{-\infty}^{\infty} \frac{d\ell\ e^{i\ell y + z\sqrt{\ell^2 + (\nu - k)^2}}}{\sqrt{\ell^2 + (\nu - k)^2} - (\nu - i\mu)}. \tag{A-3}$$

The poles of the integrand are important in the evaluation of I(k). They are given in the limit $\mu \to 0$ by :

$$\ell^2 = (2\nu - k)\, k$$

Let us first study the case in which these singularities are imaginary, which means $k < 0$ or $k < 2\nu$. Then we study case II, in which $0 < k < 2\nu$.

Case I : $k < 0$ or $k < 2\nu$.

By introducing a closed curve in the complex ℓ -plane properly indented at the branchpoint $i\,|\nu - k|$ of the integrand of (A-3) and using the residue theorem, we will get

$$I(k) = \frac{2\pi\nu\, e^{\nu z - y\sqrt{k(k-2\nu)}}}{\sqrt{k(k-2\nu)}} + \int_{\alpha}^{\infty} d\ell \; e^{-\nu y \ell} \left[\frac{e^{i\nu z\sqrt{\ell^2 - \alpha^2}}}{\sqrt{\ell^2 - \alpha^2} + i} + \frac{e^{-i\nu z\sqrt{\ell^2 - \alpha^2}}}{\sqrt{\ell^2 - \alpha^2} - i} \right] \qquad \text{(A-4)}$$

Here $\alpha = \left| \frac{\nu - k}{\nu} \right|$. It can be shown that the integral term in (A-4) is exponentially small with respect to ϵ .

Case II : $0 < k < 2\nu$.

The poles of the integrand of (A-3) are now real. The Rayleigh viscosity is helping us to determine how to indent the integration path of I(k) around the poles. We get by using the residue theorem in the same way as for Case I that

$$I(k) = -\frac{2\pi i \nu e^{\nu z - iy\sqrt{k(2\nu - k)}}}{\sqrt{k(2\nu - k)}} \tag{A-5}$$

$$+ \int_{\alpha}^{\infty} d\ell\ e^{-\nu y \ell}\left[\frac{e^{i\nu z\sqrt{\ell^2 - \alpha^2}}}{\sqrt{\ell^2 - \alpha^2} + i} + \frac{e^{-i\nu z\sqrt{\ell^2 - \alpha^2}}}{\sqrt{\ell^2 - \alpha^2} - i}\right]$$

It can be shown that the integral term is $0(\epsilon)$ compared with the first term.

By using (A-2), (A-3), (A-4) and (A-5), we can now write

$$\Phi(x, y, z) = -\frac{\nu e^{\nu z}}{2\pi}\left[\int_{-\infty}^{0} \frac{dk\, e^{ikx - y\sqrt{k(k - 2\nu)}}\, \sigma^*(k)}{\sqrt{k(k - 2\nu)}}\right.$$

$$-i\int_{0}^{2\nu} \frac{dk\, e^{ikx - iy\sqrt{k(2\nu - k)}}\, \sigma^*(k)}{\sqrt{k(2\nu - k)}} \tag{A-6}$$

$$\left. + \int_{2\nu}^{\infty} \frac{dk\, e^{ikx - y\sqrt{k(k - 2\nu)}}\, \sigma^*(k)}{\sqrt{k(k - 2\nu)}}\right]$$

$$+ \text{higher order terms}$$

This expression can be rewritten as Eq. (17).

APPENDIX B

Inner expansion of far-field source solution for the zero-speed problem

We will show how a two-term inner expansion of (17) can be written as (18).

We let y be of order ϵ, and we reorder the terms in (17).

By expanding the integrands in (17) we obtain

$$\Phi(x,y,z) = \left[-\frac{\nu e^{\nu z}}{2\pi} \int_{-\epsilon}^{0} dk\, e^{ikx} \frac{\sigma^*(k)}{\sqrt{2\nu|k|}} \right.$$

$$\left. + \frac{\nu e^{\nu z}}{2\pi} i \int_{0}^{\epsilon-(1-\delta_1)} dk\, e^{ikx} \frac{\sigma^*(k)}{\sqrt{2\nu k}} \right]$$

$$+ \left[\frac{\nu e^{\nu z}}{2\pi} y \int_{-\epsilon}^{\epsilon-(1-\delta_1)} dk\, e^{ikx} \sigma^*(k) \right.$$

$$+ i \frac{\nu e^{\nu z}}{2\pi} e^{i2\nu x} \int_{-\epsilon}^{0} du\, e^{iux} \frac{\sigma^*(u+2\nu)}{\sqrt{2\nu|u|}}$$

$$\left. - \frac{\nu e^{\nu z}}{2\pi} e^{i2\nu x} \int_{0}^{\epsilon-(1-\delta_1)} du\, e^{iux} \frac{\sigma^*(u+2\nu)}{\sqrt{2\nu u}} \right]$$

(B-1)

$$+ \text{higher order terms}$$

The integration limits $\pm \epsilon^{-(1-\delta_1)}$ have played an important role in obtaining (B-1).

Note that the first brackets in (B-1) contain the lowest-order terms, the second brackets the next-lowest-order terms.

Because we want to apply Fourier-transform techniques, we want to set $\epsilon^{-(1-\delta_1)}$ equal to ∞. For the three higher-order terms in (B-1) we could do that ; the effect would be only to introduce higher-order, negligible effects. But we must be careful with the lower order terms. But assuming that $\sigma(x)$ and $\sigma'(x)$ are continuous in the interval $-L/2 \leq x \leq L/2$, it can be shown that $k^3\sigma^*(k)$ remains bounded as $k \to \pm\infty$. This enables us to replace $\epsilon^{-(1-\delta_1)}$ by in the first two integrals too.

Let us now define

$$F^*(k) = \begin{cases} \dfrac{1}{\sqrt{|k|}} & k < 0 \\ \dfrac{-i}{\sqrt{|k|}} & k > 0 \end{cases} \qquad \text{(B-2)}$$

$F^*(k)$ denote the Fourier transform of a function $F(x)$. So

$$F(x) = \frac{e^{-i\pi/4}}{\sqrt{\pi\,|x|}}\, H(x) \qquad \text{(B-3)}$$

where $H(x)$ is Heaviside step function.

We also define

$$G^*(u) = \begin{cases} -\dfrac{i}{\sqrt{|u|}} & u < 0 \\ \dfrac{1}{\sqrt{u}} & u > 0 \end{cases} \qquad \text{(B-4)}$$

So

$$G(x) = \frac{e^{-i\pi/4}}{\sqrt{\pi\,|x|}}\, H(-x) \qquad \text{(B-5)}$$

We can now write (B-1) as

$$\Phi(x,y,z) = -\frac{\nu e^{\nu z}}{2\pi\sqrt{2\nu}}\int_{-\infty}^{\infty} dk\, e^{ikx}\,\sigma^*(k)\,F^*(k) + \nu y e^{\nu z}\sigma(x)$$

$$-\frac{\nu e^{\nu z}\, e^{i2\nu x}}{2\pi\sqrt{2\nu}}\int_{-\infty}^{\infty} du\, e^{iux}\,\sigma^*(u+2\nu)\;G^*(u)\,. \qquad \text{(B-6)}$$

Using the convolution theorem we get

$$\Phi(x,y,z) = -\nu e^{\nu z}\, e^{-i\pi/4}\int_{-L/2}^{x}\frac{d\xi\,\sigma(\xi)}{\sqrt{2\pi\nu|x-\xi|}} + \nu y\, e^{\nu z}\sigma(x)$$

$$-\nu e^{\nu z}\, e^{i2\nu x}\, e^{-i\pi/4}\int_{x}^{L/2}\frac{d\xi\sigma(\xi)\, e^{-i2\nu\xi}}{\sqrt{2\,\nu\,|x-\xi|}}$$

By using an asymptotic expansion of the last integral (see Erdélyi (1956)), (B-7) can be written as Eq. (18).

APPENDIX C

Simplification of the far-field expansion in the forward-speed problem

We will show how (59) can be rewritten into (60) and (61).

We first introduce

$$k' = k +$$

in (59). If we drop the primes we can write (59) as

$$\phi_D(x,y,z,t) = \Phi(x,y,z)\, e^{i(\omega t - \nu x)} \qquad \text{(C-1)}$$

where

$$\Phi(x, y, z) = -\frac{1}{4\pi^2} \int_{-\infty}^{\infty} dk \; e^{ikx} \; \sigma^*(k)$$

(C-2)

$$\cdot \lim_{\mu \to 0} \int_{-\infty}^{\infty} \frac{d\ell \; e^{i\ell y + z\sqrt{(\nu - k)^2 + \ell^2}}}{\sqrt{(\nu - k)^2 + \ell^2} - \frac{1}{g}(\omega_o + Uk - i\mu)^2}$$

We will let $y = 0(1)$ and we are going to assume that $y > 0$.

We define

(C-3)

$$I(k) = \lim_{\mu \to 0} \int_{-\infty}^{\infty} \frac{d\ell \; e^{i\ell y + z\sqrt{\ell^2 + (\nu - k)^2}}}{\sqrt{\ell^2 + (\nu - k)^2} - \frac{1}{g}(\omega_o + Uk - i\mu)^2}$$

The poles of the integrand of (C-3) are important. They are given in the limit by

(C-4)

$$\ell = \pm \sqrt{\frac{1}{g^2}(\omega_o + Uk)^4 - (\nu - k)^2}$$

We have to study the sign of the radicand in order to determine the location of the poles in the complex ℓ-plane.

Let us define

$$k_1 = 0 , \tag{C-5}$$

$$k_2 = -\frac{g}{U^2}\left[\frac{2\omega_o U}{g} + 1\right] \tag{C-6}$$

It can be shown that when $k > k_1$ or $k < k_2$ the poles of the integrand of (C-3) are real and when $k_2 < k < 0$ the poles of the integrand of (C-3) are imaginary.

Let us now study I(k), given by (C-3), for different ranges of k :

Case I : $k_2 < k < k_1$

This is the case in which the poles are imaginary. We define

$$\ell_o = i\sqrt{(\nu - k)^2 - (\omega_o + Uk)^4 / g^2} \tag{C-7}$$

By introducing a closed curve in the complex ℓ-plane properly indented at the branch point $i|\nu - k|$ of the integrand of (C-3) and using the residue theorem, we will get

$$I(k) = \frac{2\pi i\nu \left[1 + \frac{Uk}{\omega_o}\right]^2 e^{i\ell_o y} e^{\nu z}}{\ell_o}$$

$$+ \int_\alpha^\infty d\ell \; e^{-\nu y \ell} \left[\frac{e^{i\nu z}\sqrt{\ell^2 - \alpha^2}}{\sqrt{\ell^2 - \alpha^2} + i\left[1 + \frac{Uk}{\omega_o}\right]^2} \right.$$

(cont.)

$$+ \frac{e^{-i\nu z\sqrt{\ell^2 - \alpha^2}}}{\sqrt{\ell^2 - \alpha^2} - i\left[1 + \frac{Uk}{\omega_o}\right]^2}\Bigg] , \tag{C-8}$$

Here $\alpha = \left|\frac{\nu - k}{\nu}\right|$. It can be shown that the integral terms in (C-8) are exponentially small with respect to ϵ .

Case II : $k > k_1$.

The poles of the integrand of (C-3) are now real. The Rayleigh viscosity μ is helping us to determine how to indent the integration path of I(k) around the poles. By using the residue theorem in the same way as for Case I, we will get a similar result as (C-8). In this case, however, we cannot say that the integral terms are exponentially small for all k. We can write

$$I(k) = \frac{2\pi i\nu\left[1 + \frac{Uk}{\omega_o}\right]^2 e^{i\ell_o y} e^{\nu z}\left[1 + \frac{Uk}{\omega_o}\right]^2}{\ell_o}$$

$$+ \text{ exponentially small terms}$$

for $0 < k < \epsilon^{-(1-a+\delta_2)}$. $I(k) = \int_\alpha^\infty d\ell e^{-\nu y\ell}\left[\frac{e^{i\nu z\sqrt{\ell^2 - \alpha^2}}}{\sqrt{\ell^2 - \alpha^2} + i\left[1 + \frac{Uk}{\omega_o}\right]^2}\right.$ (C-9) (cont)

$$+ \frac{e^{-i\nu z}\sqrt{\ell^2 - \alpha^2}}{\sqrt{\ell^2 - \alpha^2} - i\left[1 + \frac{Uk}{\omega_o}\right]^2}\Bigg]$$

+ exponentially small terms

$$\text{for} \quad \alpha = \left|\frac{\nu - k}{\nu}\right| < \epsilon^{(1 - \delta_1)}. \tag{C-9}$$

Here δ_1 and δ_2 are some very small positive numbers. "a" is defined by (56) and is restricted to $0 < a \leq 1/2$. ℓ_o is given by

$$\ell_o = -\sqrt{(\omega_o + Uk)^4/g^2 - (\nu - k)^2} \tag{C-10}$$

For all other values of k in Case II, I(k) will be exponentially small.

Case III : $k < k_2$.

We define

$$\ell_o = \sqrt{(\omega_o + Uk)^4/g^2 - (\nu - k)^2} \tag{C-11}$$

In this case the poles of the integrand of (C-3) are also real. The Rayleigh viscosity μ will tell us how to indent the integration path around the poles. By using the residue theorem in the same way as for case I, we will get a similar result as (C-8). It can be shown that the integral terms are exponentially small. We get

$$I(k) = \frac{2\pi i \nu \left[1 + \frac{Uk}{\omega_o}\right]^2 e^{i\ell_o y} e^{\nu z} \left[1 + \frac{Uk}{\omega_o}\right]^2}{\ell_o} \qquad \text{(C-12)}$$

$$+ \text{ exponentially small terms}$$

for $k < k_2$.

Using (C-2), (C-3), the different approximations we have obtained for I(k) and the fact that exponentially small terms in I(k) will give exponentially small terms in the expression for Φ , we can easily obtain (61).

APPENDIX D

Inner expansion of far-field source solution for the forward-speed problem.

We will show how a two-term inner expansion of (61) can be written as (64).

We let y be of order ϵ and we reorder the terms in (61).

We will assume as for the zero-speed problem (see Appendix B) that $\sigma(x)$ and $\sigma'(x)$ are continuous in the interval $-L/2 \leq x \leq L/2$. Outside $-L/2 \leq x \leq L/2$, $\sigma(x) \equiv 0$. It can then be shown (see Lighthill (1958)) that $k^3 \sigma^*(k)$ remains bounded as $k \to \pm\infty$. Using this it can be shown that the contribution from the inner expansion of $I_{\alpha 1}$, $I_{\alpha 2}$ and the fifth integral in (61) will be of higher order of magnitude than the terms we will retain in the inner expansion of (61).

In the third and fourth integral in (61) we make an expansion of the integrand. The integration limits $\pm \epsilon^{-(1-a-\beta)}$ will then play an important role. In the first two integrals in (61) we first introduce

the new variable

$$v = k - k_2$$

The next step is to change the integration limits so that the lower integration limit in the first integral is $-\epsilon^{-(1-a-\beta)}$ and the upper integration limit in the second integral is $\epsilon^{-(1-a-\beta)}$. Then we expand the integrands. We can then write a two-term inner expansion of (61) as

$$\Phi(x,y,z) \simeq -\frac{e^{\nu z}}{2\pi}\left[\int_{-\infty}^{0} \frac{dk\, e^{ikx}\, \sigma^*(k)}{\sqrt{\frac{2\omega + 2U\nu}{\nu\omega_o}|k|}} - i\int_{0}^{\infty} \frac{dk\, e^{ikx}\, \sigma^*(k)}{\sqrt{\frac{2\omega + 2U\nu}{\nu\omega_o}k}}\right]$$

$$+ \frac{\nu y e^{\nu z}}{2\pi}\int_{-\infty}^{\infty} dk\, e^{ikx}\, \sigma^*(k)$$

$$-\frac{e^{ik_2x + \nu z_i}}{2\pi}\left[\int_{-\infty}^{0} \frac{dv\, e^{ivx}\, \sigma^*(v + k_2)}{\sqrt{\frac{2\omega + 2U\nu}{\nu\omega_o}|v|}} - i\int_{0}^{\infty} \frac{dv\, e^{ivx}\, \sigma^*(v + k_2)}{\sqrt{\frac{2\omega + 2U\nu}{\nu\omega_o}v}}\right] \tag{D.1}$$

We should note that we have changed the integration limits from $\pm\epsilon^{-(1-a-\beta)}$ to $\pm\infty$. This can be justified for the two first integrals, which is the lowest order terms, by using the fact that $\sigma^*(k)\,k^3$ remains bounded as $k \to \pm\infty$. For the three last integrals, which is the highest order terms, it is obvious that we can change the integration limits from $\pm\epsilon^{-(1-a-\beta)}$ to $\pm\infty$.

By using (B-2), (B-3) and the convolution theorem we can now write

$$\Phi(x, y, z) \simeq -\frac{e^{\nu z - i\pi/4}}{\sqrt{\pi}} \int_{-L/2}^{x} \frac{d\xi\, \sigma(\xi)}{\sqrt{\frac{2\omega + 2U\nu}{\nu\omega_o}\,|x-\xi|}} + \nu y e^{\nu z}\, \sigma(x)$$

$$-\frac{e^{ik_2 x + \nu z + i\pi/4}}{\sqrt{\pi}} \int_{-L/2}^{x} \frac{d\xi\, \sigma(\xi)\, e^{-ik_2\xi}}{\sqrt{\frac{2\omega + 2U\nu}{\nu\omega_o}\,|x-\xi|}} \qquad \text{(D-2)}$$

By using an asymptotic expansion of the last integral (see Erdélyi (1956)), (D-2) can be written as (64).

* * *

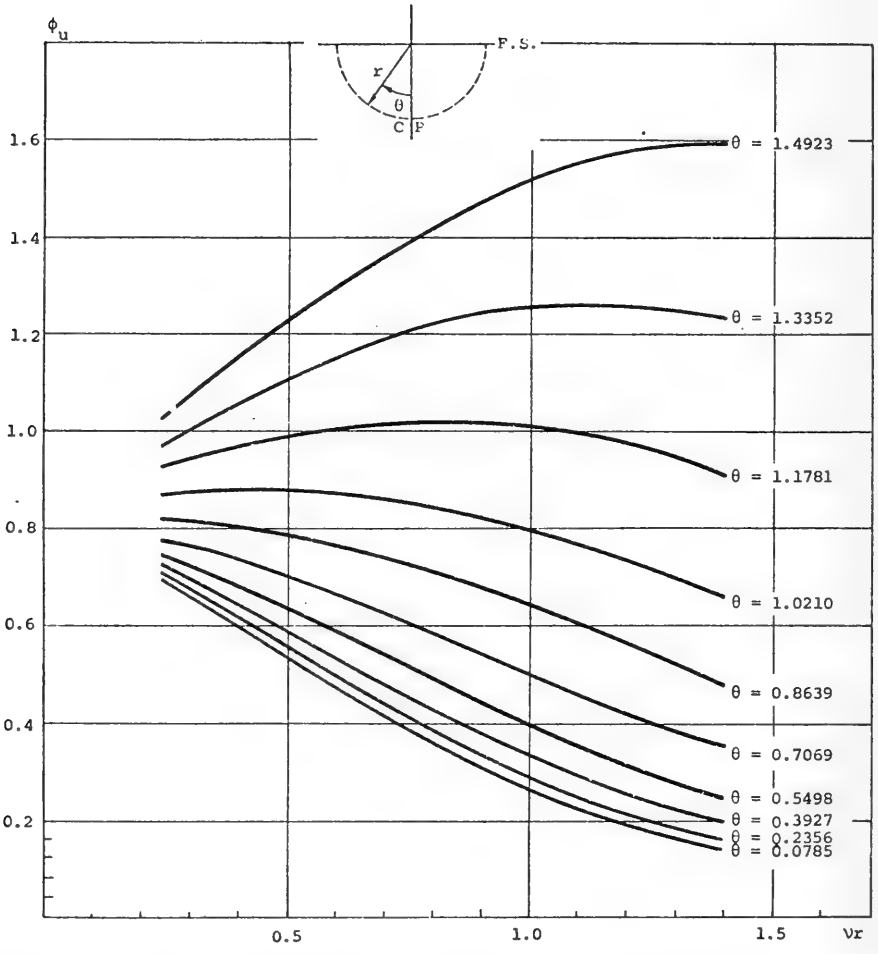

Figure 3 Ursell's solution as a function of νr for a given value of θ

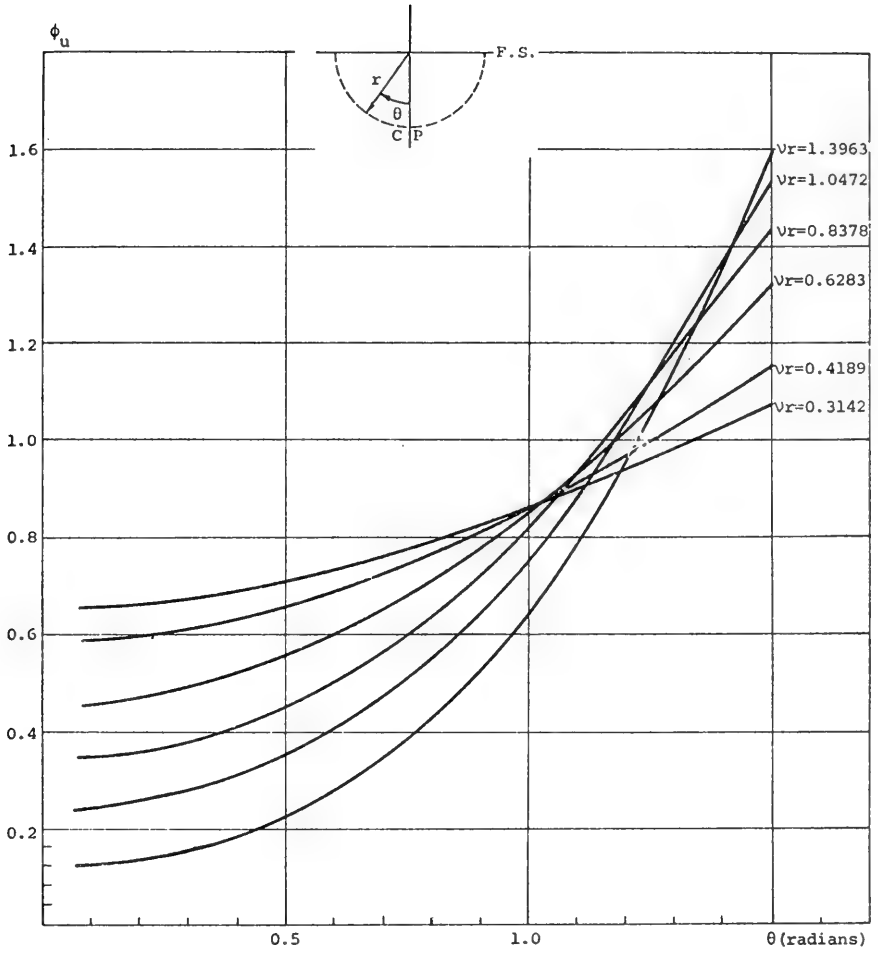

Figure 4 Ursell's solution as a function of θ for given value of νr

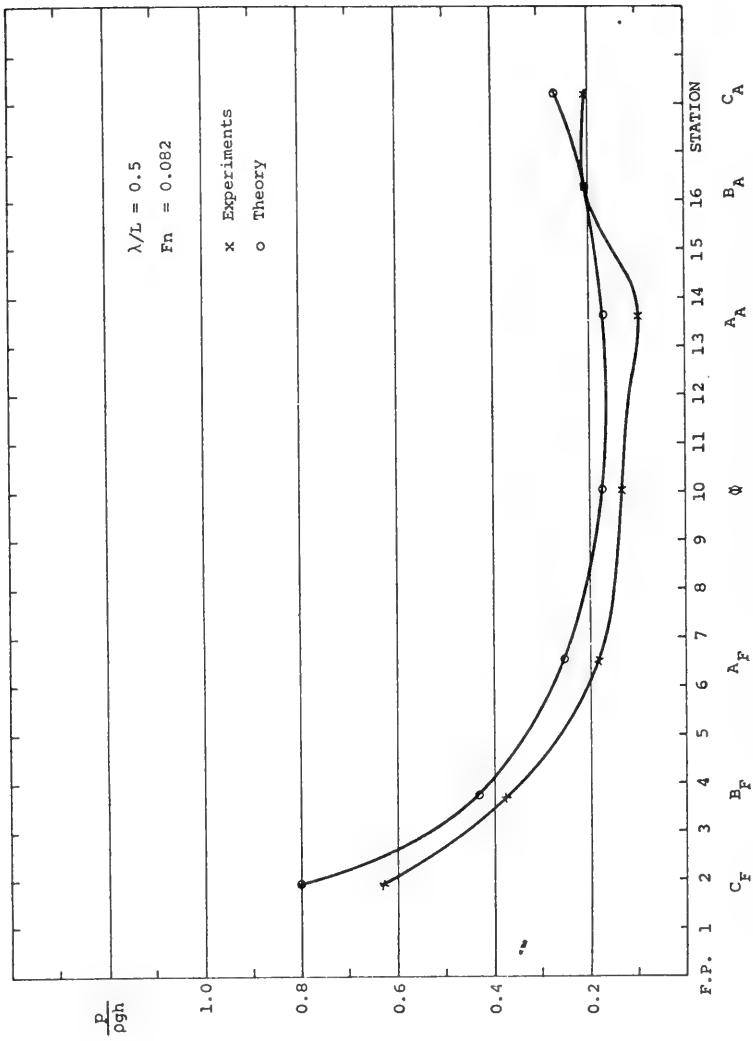

Figure 5 Longitudinal distribution of the pressure along the keel of the spheroid

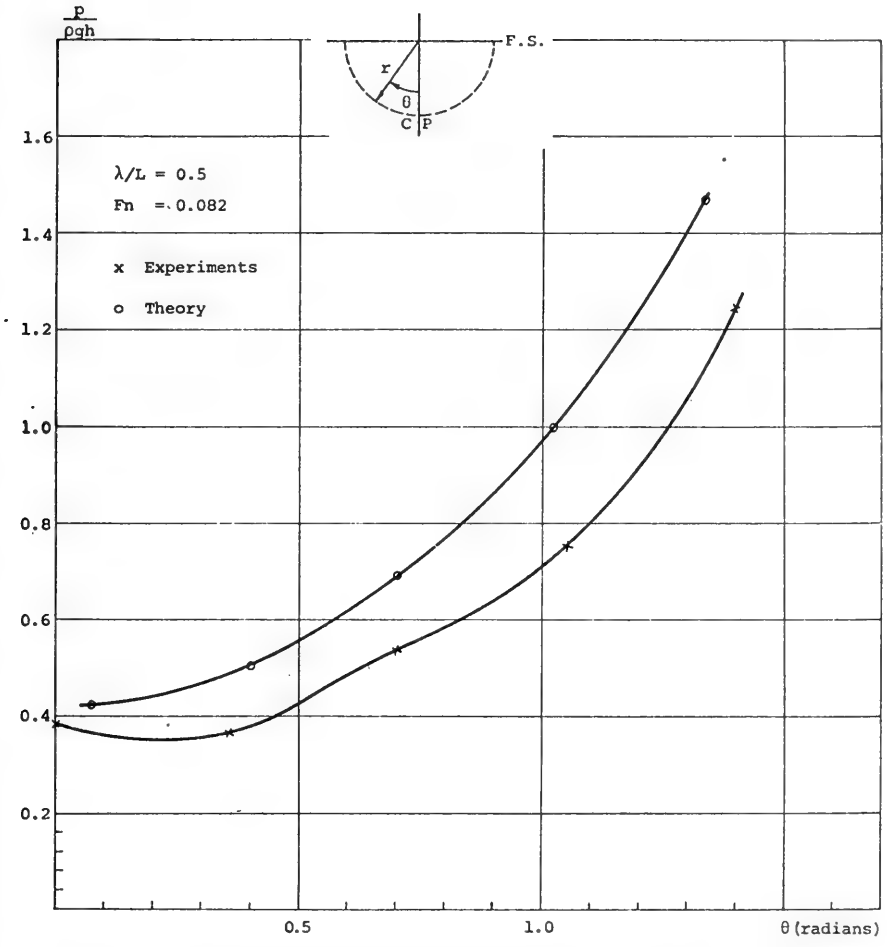

Figure 6 Pressure variation along the cross-section B_F

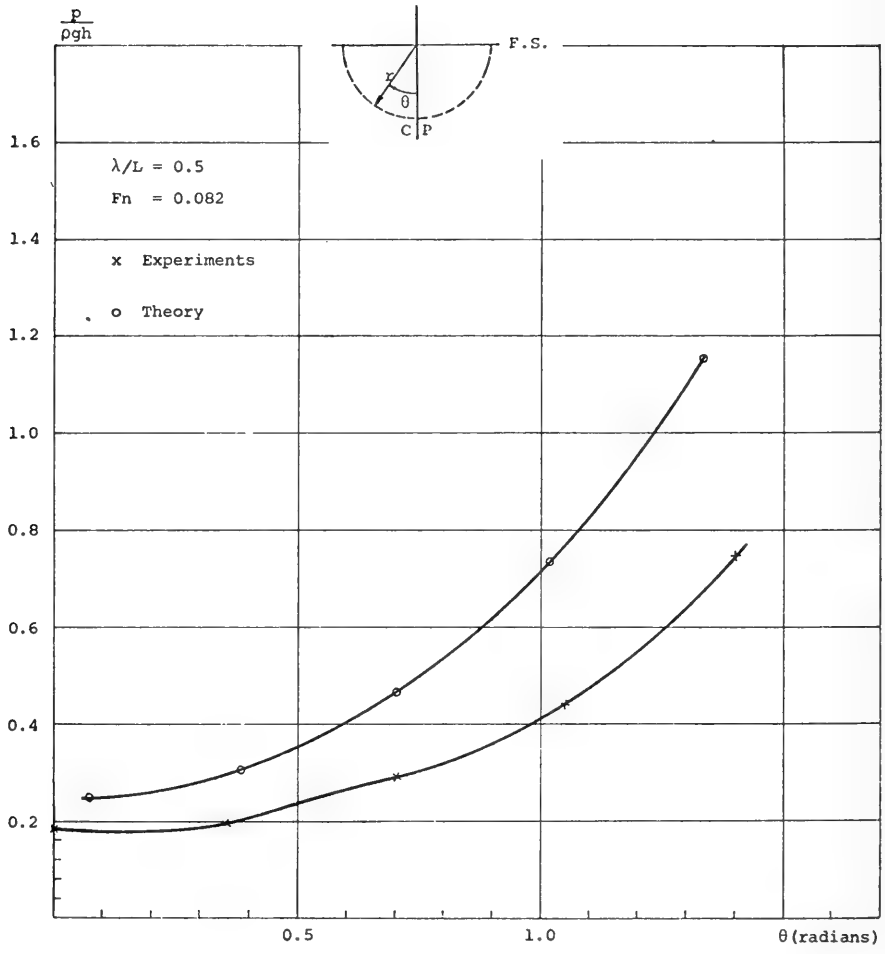

Figure 7 Pressure variation along the cross-section A_F

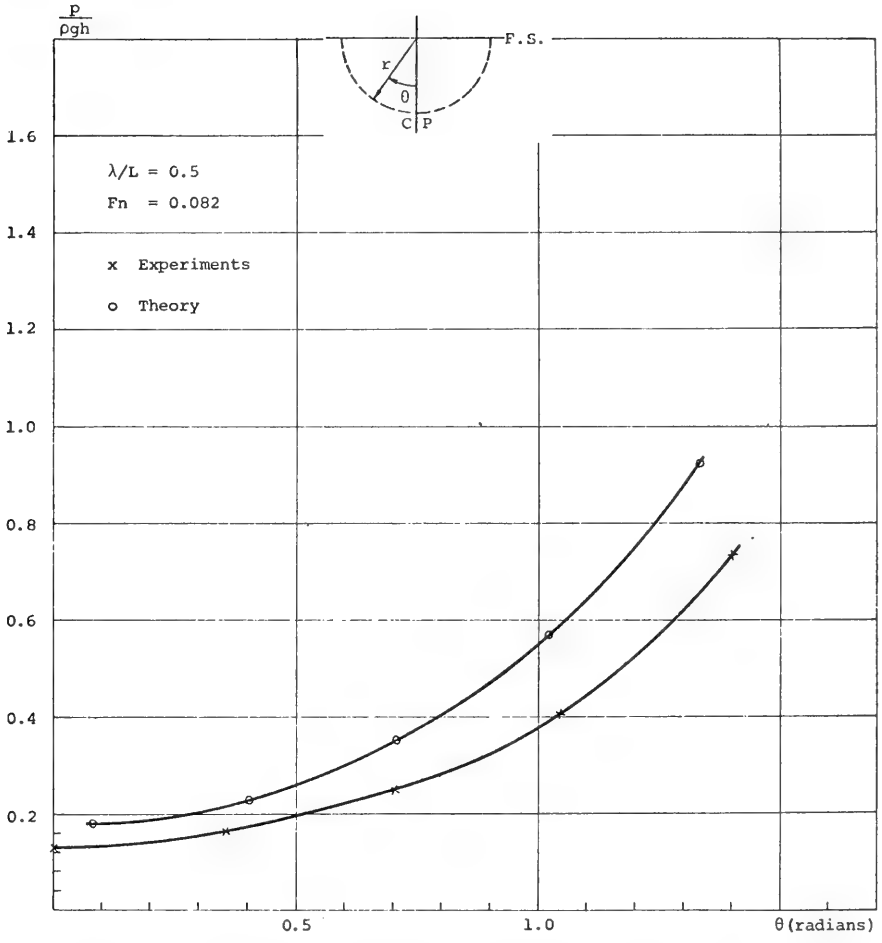

Figure 8 Pressure variation along the cross-section ⊄

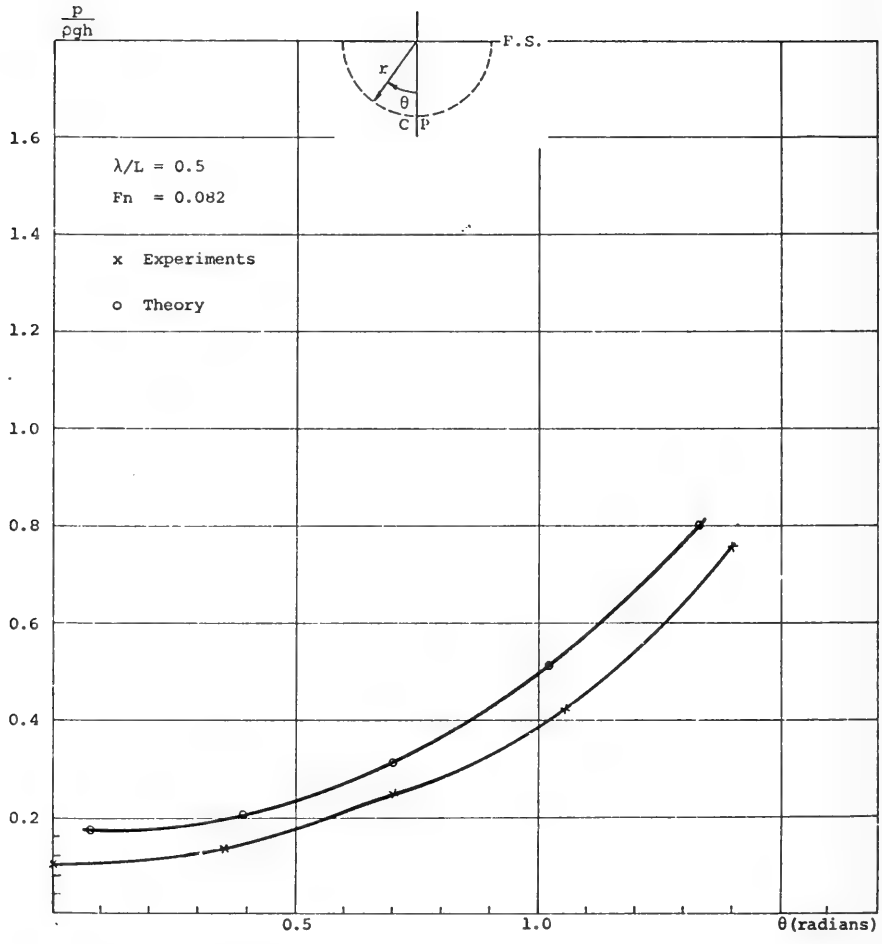

Figure 9 Pressure variation along the cross-section A_A

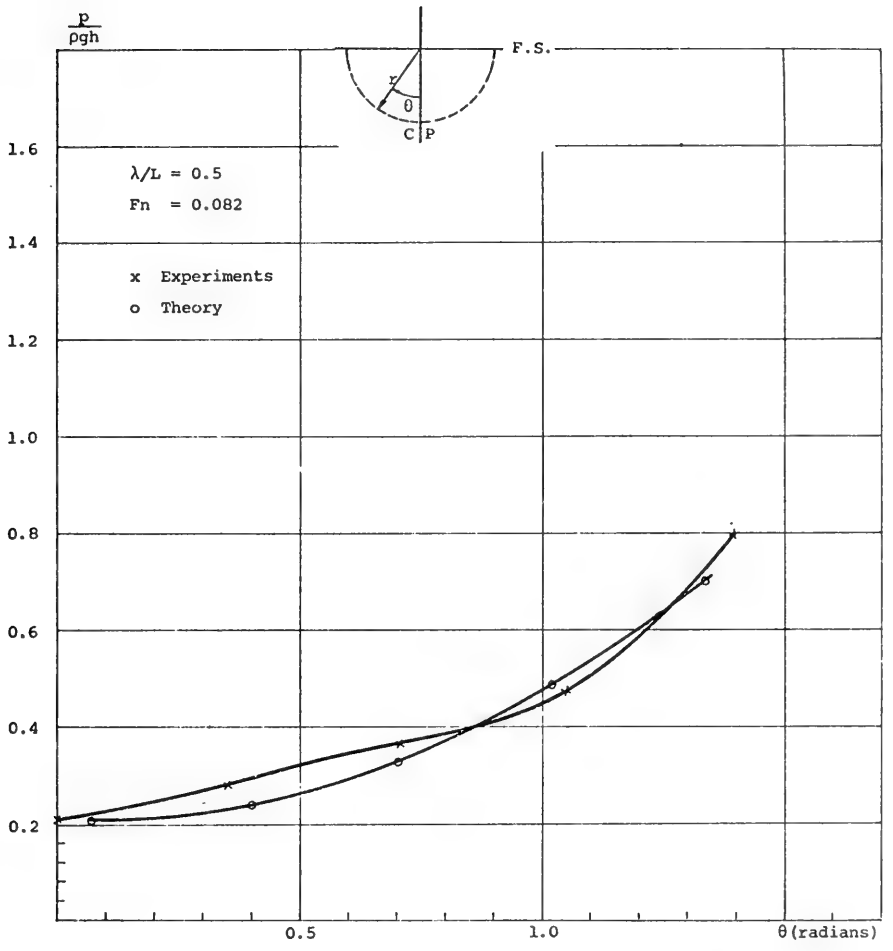

Figure 10 Pressure variation along the cross-section B_A

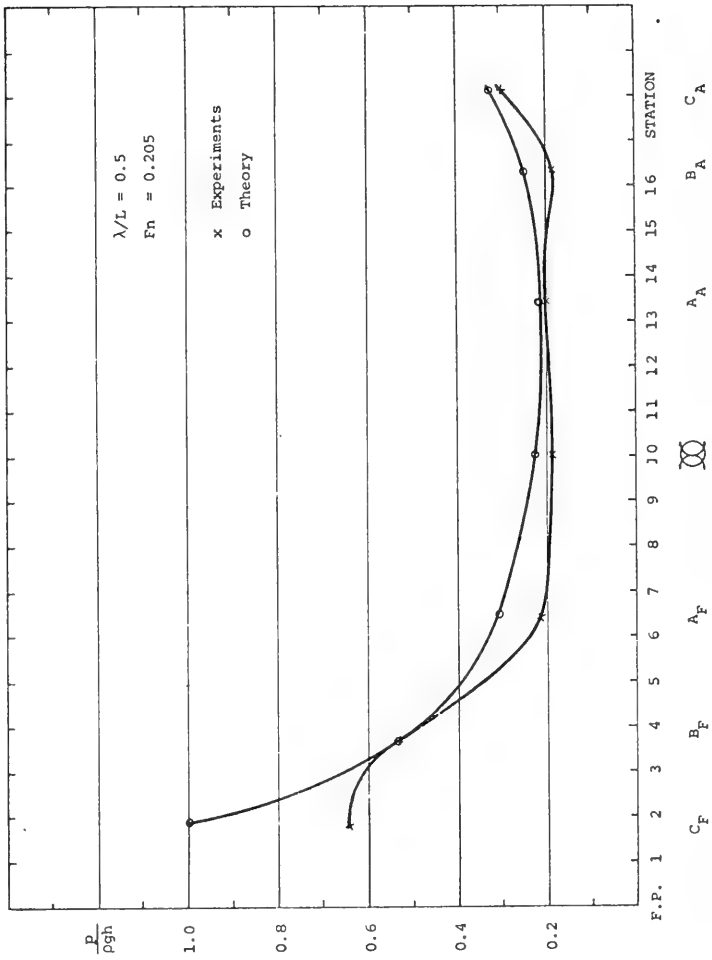

Figure 11 Longitudinal distribution of the pressure along the keel of the spheroid

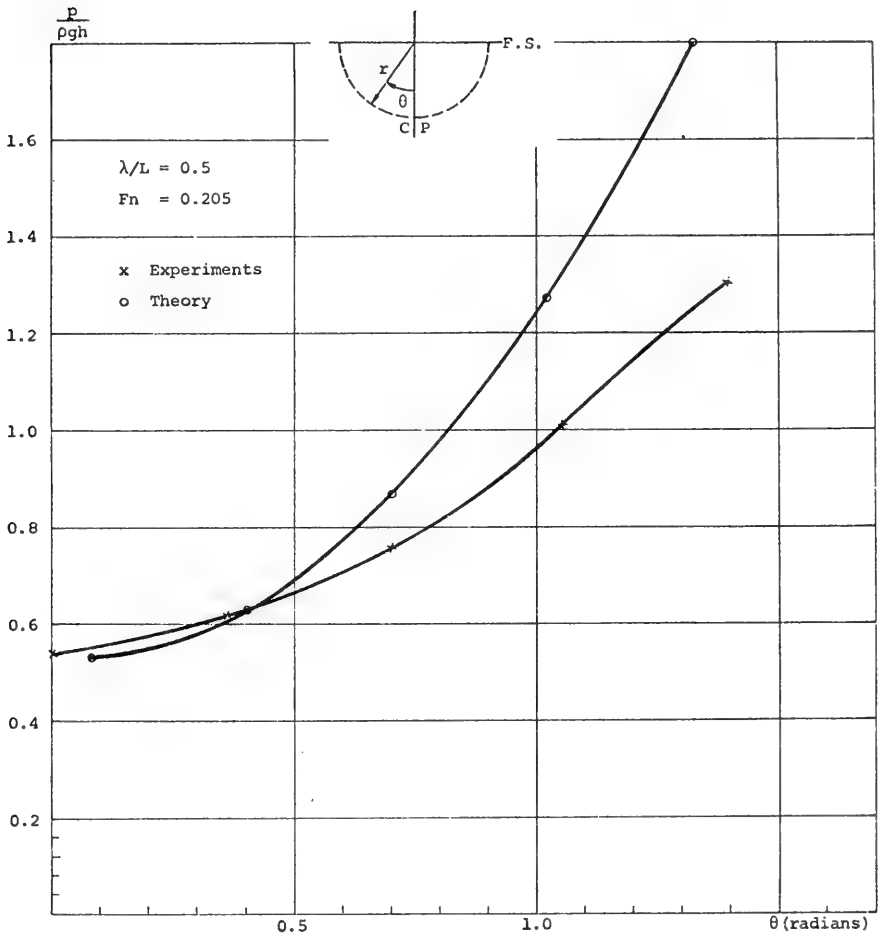

Figure 12 Pressure variation along the cross-section B_F

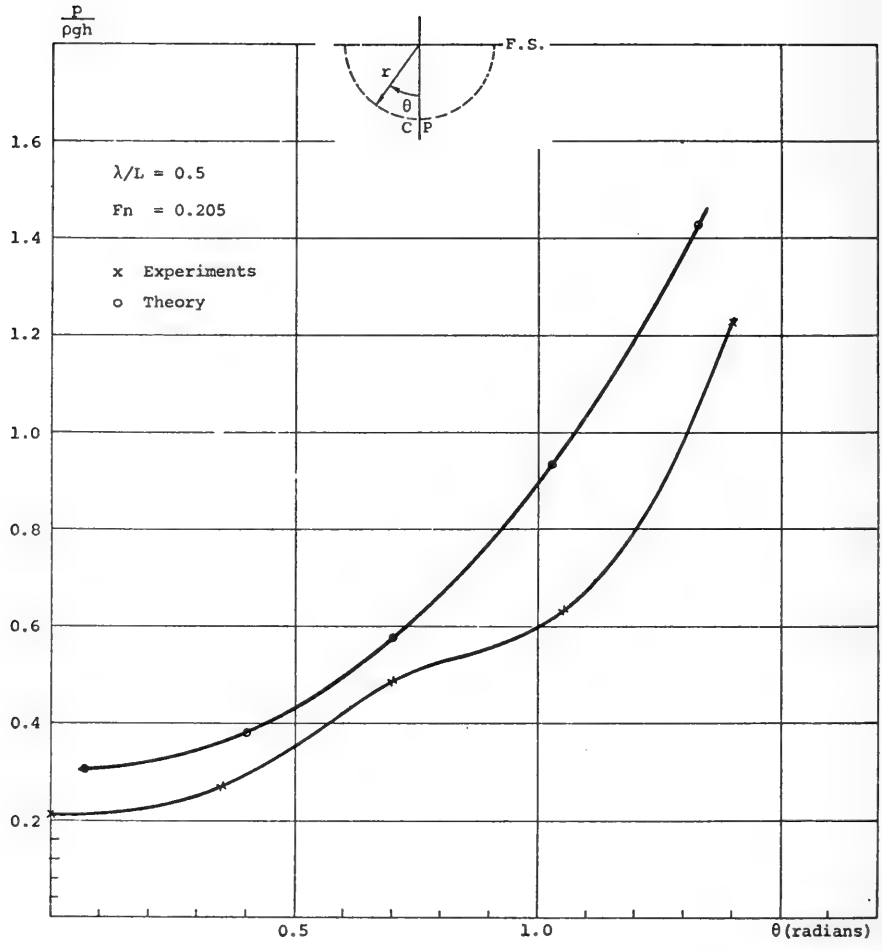

Figure 13 Pressure variation along the cross-section A_F

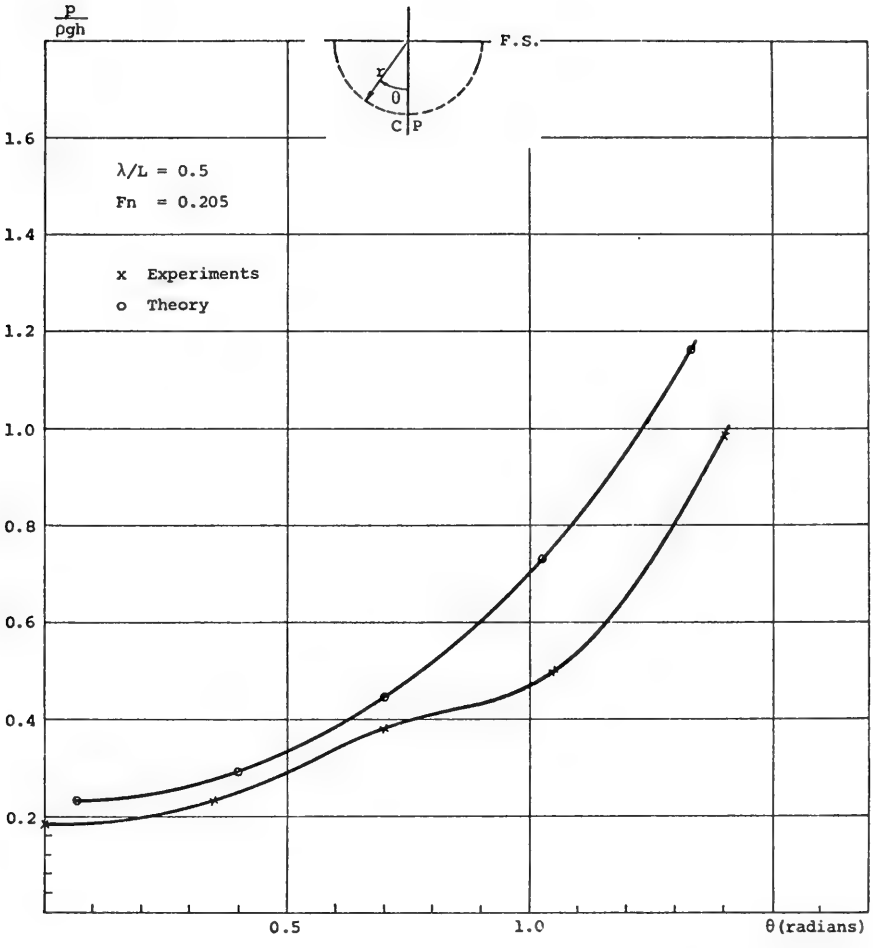

Figure 14 Pressure variation along the cross-section ⊗

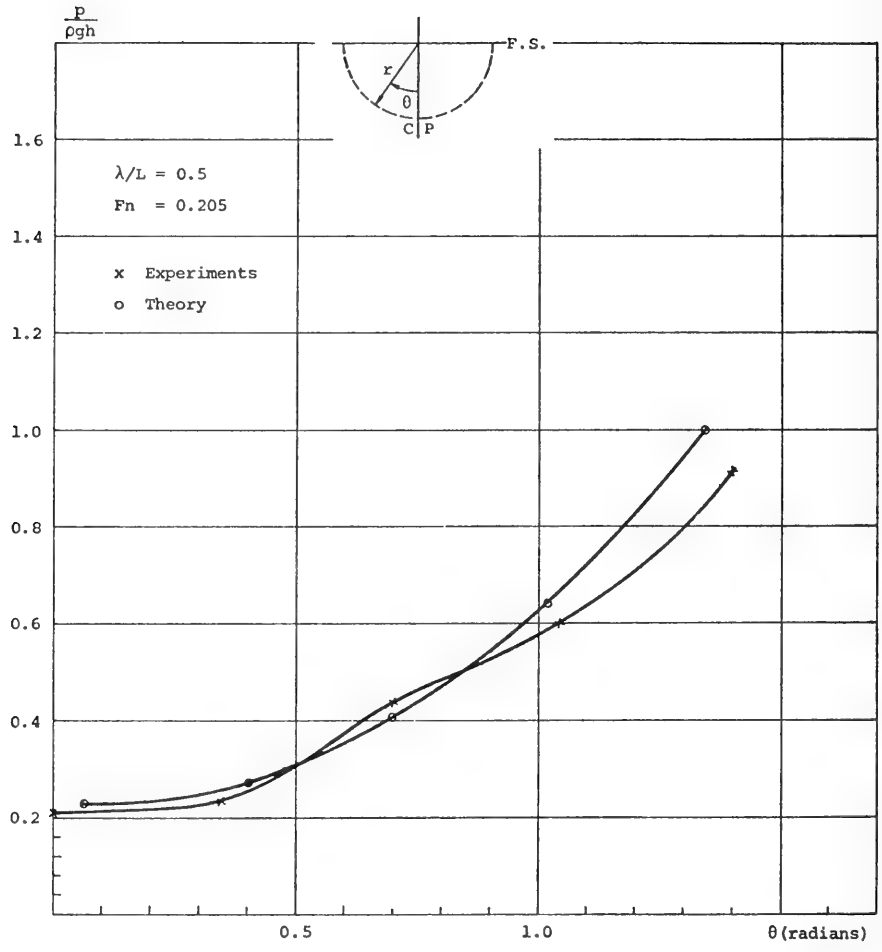

Figure 15 Pressure variation along the cross-section A_A

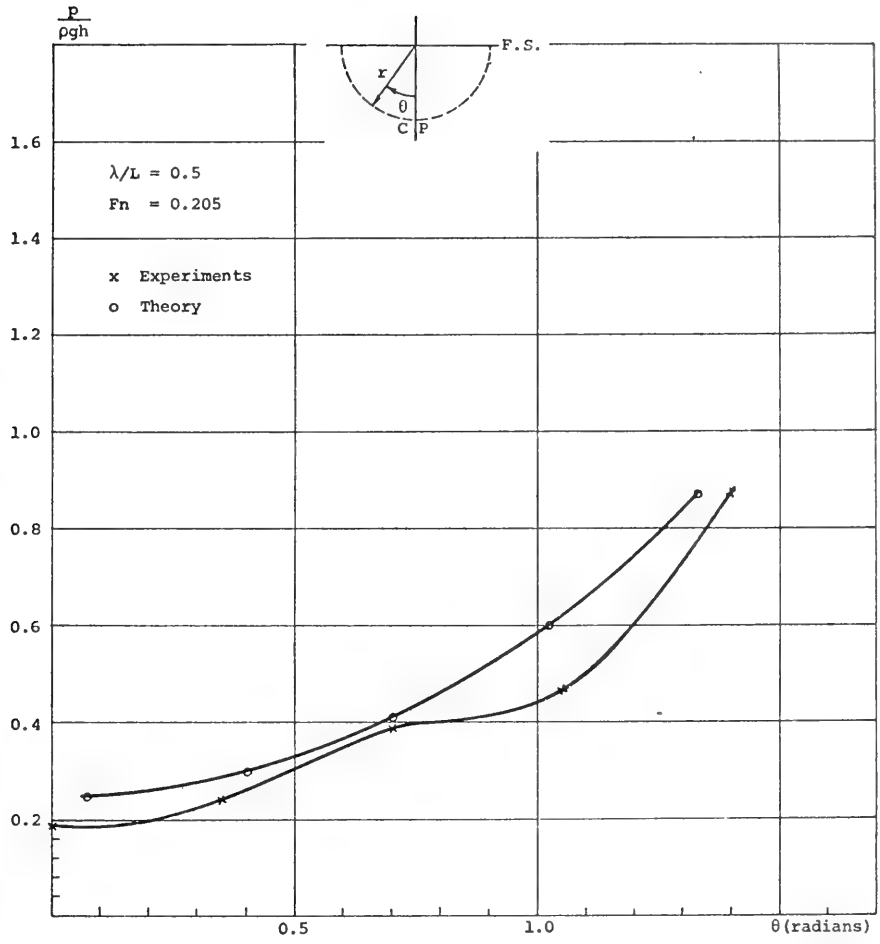

Figure 16 Pressure variation along the cross-section B_A

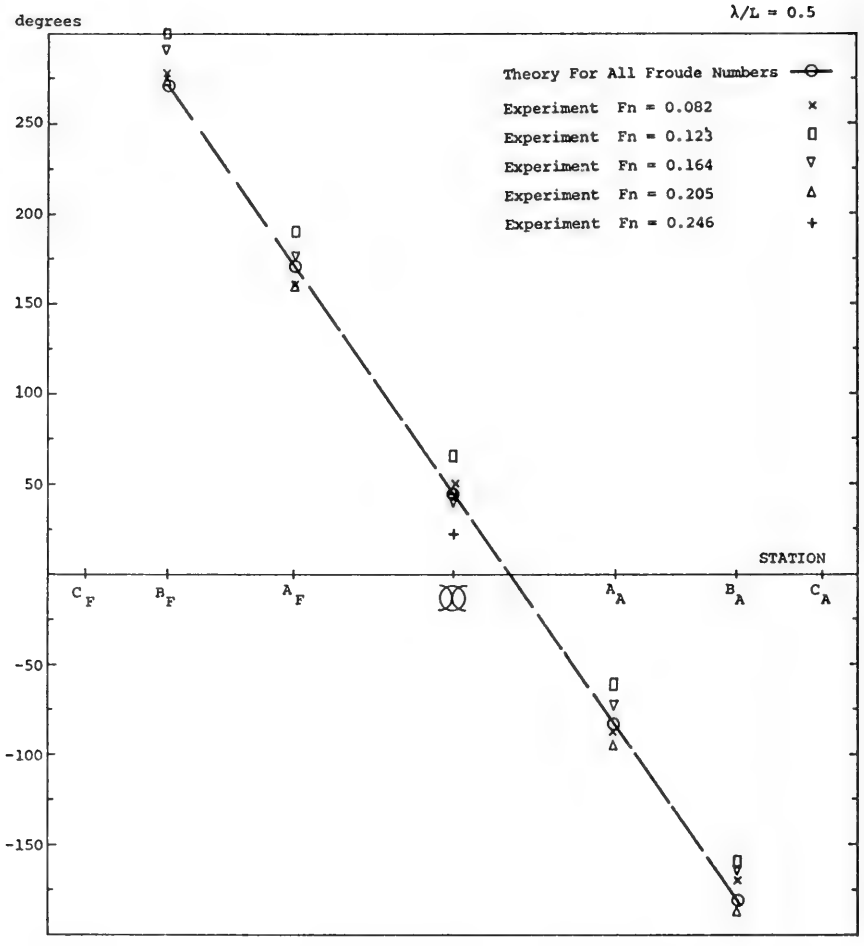

Figure 17 Longitudinal distribution of the phase angle of the pressure

DISCUSSION

Michel Huther
Bureau Veritas
Paris, France

I have been very interested by the presentation of the author, and I should be very pleased to know his opinion about the limitations and possible extensions of the method. I am interested to know the order of magnitude it is possible to use for the slenderness parameter. Also, have calculations been done with other section shapes as rectangular, for example, shapes more similar to the nowaday midship sections than the cylinder ?

The author writes that linear superposition can be used. I agree with this point of view for longitudinal motion such as pitching and heaving, but I should be pleased to know the author's opinion in the case of transverse motions such as rolling, where large amplitudes are to be considered.

DISCUSSION

Cheung-Hun C. Kim
Stevens Institute of Technology
Hoboken, New-Jersey, U.S.A.

Dr. Faltinsen proposes a method for improving the present strip method of evaluating the wave-exciting forces. His method is based on the slender body assumption and the comparison was made with the corresponding results of calculations based on the Froude-Krylov hypothesis. I would like to know why the comparison was not made with the corresponding results of calculations based on the strip-wise diffraction theory.

REPLY TO DISCUSSION

Odd Faltinsen
Det Norske Veritas
Oslo, Norway

The first limitation that I mentioned in my presentation was the small wave length assumption. I would guess that the upper limit for using the theory would be for a wave length divided by the length of the ship between 0.5 and 0.75. Another limitation is that the theory is not valid near the bow or the stern of the ship. Near the bow there is a singularity in the solution. For practical purposes I think one can use the Froude-Kriloff theory in the bow region.

The theory is not restricted to circular cross-sections and it is shown in the main text how to solve the problem for arbitrary cross-sections. But no calculations have been performed for arbitrary ship forms. Further it remains to test how slender the ship ought to be for the theory to be valid. But the slenderness assumption is not expected to be a great problem for conventional ship forms.

To get a similar theory for an arbitrary wave length does not seam easy. However, for the long wavelength range one can use the Froude-Kriloff theory to find the pressure.

I do not find the question about linear superposition to be appropriate in this context. But I agree that the linear superposition principle can be questionable in the case of roll. Further I did not hear good enough Dr. Kim's question about the strip method.

DISCUSSION

Cheung-Hun C. Kim
Stevens Institute of Technology
Hoboken, New-Jersey, U.S.A.

Dr Faltinsen evaluated the pressure distribution along the

keel line according to the method based on the Froude-Krylov hypothesis and for relatively short waves. It is well known that the Froude-Krylov assumption is valid only for very long waves. Would it not be better then to compare the results with calculations based on a strip method which evaluates rigorously the diffraction potential in the strip domain ?

REPLY TO DISCUSSION

Odd Faltinsen
Det Norske Veritas
Oslo, Norway

I see what you mean. I have not done that comparison. The reason why I showed a comparison with Froude-Kriloff pressure in the presentation of the paper, was to make clear that there is an order of magnitude between Froude-Kriloff pressure and pressure according to my theory in the low wave length range.

I do not agree with Dr Kim's last statement that the usual strip theory evaluates the diffraction potential rigorously in the strip domain. The usual strip method for zero speed is based on no interaction between different parts of the ship, and the two-dimensional Laplace equation is used to solve the problem. This can only be true for beam sea.

FREE - SURFACE EFFECTS IN HULL PROPELLER INTERACTION

Horst Nowacki
University of Michigan
Ann Arbor, Michigan, U.S.A.

Som D. Sharma
Hamburg Ship Model Basin
Hamburg, Germany

ABSTRACT

The quantitative role of wavemaking at the free surface in the phenomenon of hull propeller interaction is investigated by means of a general scheme devised to determine the potential, viscous and wave components of wake and thrust deduction. It requires the concerted application of various analytical tools such as the lifting line theory of propellers, the method of singularities for representing the hull and propeller by source distributions and the linearized free-surface theory of wavemaking, as well as model experiment techniques such as the conventional Froude analysis of propulsion factors, nominal wake measurements and wave profile measurements. The procedure is actually applied to the specific case of a thin mathematical hull form driven by a four-bladed propeller of simple geometry. It is found that the wave component is dominant in the wake and quite significant in the thrust deduction at Froude numbers around 0.3. Surprisingly, there seems to be an appreciable viscous component in the thrust deduction at practically all Froude numbers.

I. INTRODUCTION

The purpose of this research was to clarify by analysis, computation and experiment the quantitative role of wavemaking at the free surface in the phenomenon of hull propeller interaction and consequently its contribution to the hydrodynamic propulsive efficiency of the system hull and propeller.

Following Froude (1883), hull propeller interaction is conveniently studied in terms of three propulsion factors : wake, thrust deduction and relative rotative efficiency. The wake is caused by the presence of the hull and the free surface and is a simple measure of the change in propeller inflow as compared to an equivalent open-water condition (free running propeller in an infinite parallel stream). The thrust deduction is really an indirect expression of the fact that the force of resistance acting on the hull is modified (usually augmented as compared to the towed condition) as a result of propeller action. With the present state of our knowledge, only wake and thrust deduction are amenable to rational analysis, the relative rotative efficiency being an empirical catch-all for various unclarified effects of relatively insignificant magnitude.

Since the fundamental work of Dickmann (1938, 39), it has been customary to study hull propeller interaction as a superposition of three basic effects : "potential" effects due to an ideal displacement flow about a deeply submerged double body (the zero Froude number approximation), viscous effects due to the boundary layer and viscous wake, and wave effects due to the presence of the free surface. Using standard symbols w and t for wake and thrust deduction fractions respectively, one may write formally

$$w = w_p + w_v + w_w \tag{1}$$

$$t = t_p + t_v + t_w \tag{2}$$

where the subscripts p, v and w denote potential, viscous and wave respectively. By comprehensive theoretical analysis and careful experiments Dickmann demonstrated that the most significant components were w_p, t_p and w_v .

Among Dickmann's most impressive achievements were 1) a theoretical relation between potential wake and trust deduction involving the thrust loading coefficient, and 2) a reasonable explanation of the effect of the free surface on propulsive efficiency. His main analytical tools were a simple actuator disk model of the propeller

(momentum theory), the method of singularities (Lagally's theorem) for calculating forces on the hull and Havelock's method of images for a linearized treatment of the free surface.

In recent years considerable effort has been put into the investigation of potential and viscous effects in hull propeller interaction (see Bibliography). Especially in this country, Beveridge in a series of papers (1962, 63, 66, 68) has refined the technique of calculating the potential thrust deduction to a state of near perfection. At the same time, Hucho (1965, 68) in Germany has made significant contributions to our understanding of viscous effects. The wave effects, however, were persistently ignored for nearly thirty years since Dickmann(1939), until the fundamental treatise of Yamazaki (1967) revived interest in this subject and inspired the recent work of Nakatake (1967, 68) in Japan.

Still far from resolving the complex issues at stake, Nakatake's papers are just added evidence of the same conviction that underlies the present study(which, incidentally, was initiated without knowledge of the Japanese effort), namely that the time is now ripe to make a fresh attempt at the further clarification of this admittedly difficult problem. This is due mainly to the following reasons :

1) Major advances in the vortex theory of propellers now allow the use of a far more refined mathematical model of the propeller.

2) The recently developed technique of wave profile measurement and analysis enables us to verify by (almost) direct measurement the wave effects predicted by analytical theory.

3) The general availability of large electronic computers allows the use of more realistic singularity distributions for representing the hull, the propeller and their images in the free surface.

Beside the intrinsic interest of a fundamental problem in ship hydrodynamics, a recommendation by the Performance Committee of the International Towing Tank Conference 1966 for specific research in the basic problem area of hull propeller interaction - of which free surface effects are certainly the most intriguing aspect - as well as the prospect of practical application to modern high speed craft with propellers operating at shallow or even partial submergence were further motivations for undertaking this research.

II. GENERAL APPROACH

The originality of the present study lies not in the development of a novel method but in the concerted application of miscellaneous existing analytical, computational and experimental techniques to our specific purpose. Since these numerous tools have to be applied in a rather intricate sequence to get the information desired, it seems necessary in the interest of clarity to precede the account of work done by a brief schematic description of our general approach. The internal details of the individual techniques are only of indirect interest in the present context and will therefore be banished to appropriate appendices.

The basic aim is to determine for a given hull-propeller system the propulsion factors and their potential, viscous and wave components by all feasible analytical and experimental means. This dictates roughly the following set of operations.

First, a considerable amount of basic information can be gathered by a number of independent experiments and theoretical calculations which may be executed in any convenient sequence. On the experimental side we may deploy the following more or less routine model tests in the towing tank :

E 1) Hull resistance test,

E 2) Propeller open water test (at deep and shallow submergence),

E 3) Self-propulsion test with hull and propeller,

E 4) Nominal wake measurements behind the hull in forward and reverse motion, and

E 5) Wave profile measurements (e. g. longitudinal cuts) for the hull with and without propeller.

On the theoretical side only few calculations can be performed without resort to some empirical data ; these are :

T 1) Wavemaking resistance of the hull,

T 2) Wave wake induced by the hull in the propeller plane (both in forward and reverse motion), and

T 3) Potential wake induced by the hull in the propeller plane.

From here on the further analysis is of a semi-empirical nature and must be conducted in an essentially predetermined sequence because at each new step certain information from previous steps is required . It is helpful to list separately the pure hull analysis , the pure propeller analysis , and the interaction analysis .

The purpose of the hull analysis is to verify the mathematical representation of the hull as a source distribution and to establish the degree and range of validity of the linearized wave theory .

H 1) The total resistance measured in step E1 can be subjected to a simple form-factor analysis (based on a suitable plane friction formula) so as to yield the viscous and wavemaking components .

H 2) An alternative estimate of wavemaking resistance can be obtained from a Fourier analysis of the wave profiles measured in step E5 .

H 3) The experimental estimates of wavemaking resistance derived in the two preceding steps may now be compared with the theoretical calculations of step T1 .

H 4) For a more exacting test of the theory the experimental and theoretical free-wave spectra can be compared at each speed .

H 5) An additional test of the theory lies in comparing the sum of the calculated wave wake and potential wake from steps T 2 and T 3 to the measured wake in reverse motion from step E4 since the latter is essentially free of viscous effects .

H 6) If the mathematical model of the hull flow can be verified in the preceding steps then the calculated wave wake and potential wake may be subtracted from the measured total wake in forward motion to yield the important viscous wake component .

The purpose of the propeller analysis is to determine a vortex model of the propeller and to verify the validity of its alternative representation as a source distribution which is to serve as the basis for calculating thrust deduction and wave effects .

P 1) A computer program based on lifting line theory in conjunction with the Lerbs (1952) induction factor method may be used to calculate for any given propeller geometry and assumed foil characteristics the equivalent distribution of bound circulation over the radius and hence by Kutta-Joukowsky's theorem the thrust and torque coefficients as functions of the advance ratio .

P 2) The thrust and torque predictions of the previous step are compared with the actual performance as measured in step E 2 and the agreement is improved iteratively by adjusting the assumed foil characteristics. Again the crucial link in the algorithm is the circulation distribution.

P 3) Using the Hough and Ordway (1965) approximation, the circulation distribution is now translated into an equivalent source distribution over the propeller disk.

P 4) This source distribution is the basis for calculating the wavemaking due to the propeller by Havelock's (1932) theory. In particular, the axial velocities induced by the operation of the propeller near the free surface, in other words the self-induced free-surface wake of the propeller, can be calculated.

P 5) This self-induced wake is fed back into the propeller performance program based on lifting line theory to obtain predictions of thrust and torque with the propeller operating at shallow submergence.

P 6) A comparison of propeller performance predicted in step P 5 with actual measurements at the same submergence then provides a check on the correct accounting of free surface effects in the theoretical model.

After the mathematical representations of hull and propeller have been verified the actual interaction analysis can be executed as follows.

I 1) The Froude propulsion factors (mean effective wake, thrust deduction, relative rotative efficiency and propeller efficiency in the equivalent open water condition) are first determined from the results of tests E 1, E 2 and E 3 in the usual manner.

I 2) The radial distribution of nominal wake from step E 4 is adjusted to match the mean effective wake from step I 1 and fed into the propeller performance program. The output is the circulation distribution of the propeller in the behind ship condition at each Froude number.

I 3) Again the Hough and Ordway relation is used to translate the circulation distribution into a source representation of the propeller in the behind-ship self-propulsion condition.

I4) From the now known source representations of the hull and propeller free-wave spectrum and wavemaking resistance are calculated and compared with the corresponding results of the Fourier analysis of the wave profiles measured in step E 5. This provides a check on the principle of linear superposition of hull and propeller waves.

I5) The mutual flow patterns of hull and propeller can now be calculated and thence by Lagally's theorem the potential and wave thrust deduction.

I6) Finally the viscous component of thrust deduction can be estimated indirectly by subtracting the potential and wave components from the total thrust deduction of step I1.

III. DISCUSSION OF RESULTS

III. 1. Choice of Hull and Propeller

Since our work was to consist essentially of a single concrete example of the actual application of the sequence of operations outlined in the previous section it was rather important to choose as instructive and useful an example as possible. After considering various alternatives we finally selected the somewhat idealized hull propeller configuration of Figure 1 that has a sufficiently simple geometry for the ease of theoretical calculations and yet quite realistic proportions for the results to be of practical value. The arguments leading to this choice can be summarized as follows.

In order to keep the wavemaking calculations manageable it was decided to use a symmetric hull form with parabolic waterlines and frames. The wetted surface is then defined by the equation

$$y = \frac{B}{2}\left\{1 - (2x/L)^{2m}\right\}\left\{1 - (-z/T)^{n}\right\} \qquad (3)$$

The hull above water is a simple continuation of the underwater form with vertical sidewalls. The integer powers m, n and the form ratios L/B, B/T were chosen to satisfy the following requirements : 1) sufficiently thin hull for linearized theory to be valid, 2) sufficiently large angle of run to get measurable interaction with the propeller, and 3) realistic value of block coefficient.

This led to the following set of parameters :

$$
\begin{aligned}
m &= 2, \quad n = 4 \\
L/B &= 10, \quad B/T = 1.5 \\
C_M &= C_P = C_{WP} = 0.8 \\
C_B &= 0.64 \\
i_E &= i_R = \arctan 0.4 \approx 21.8^\circ
\end{aligned} \tag{4}
$$

The absolute size of the model for the towing experiments was dictated by the size of the tank and equipment available :

$$
\begin{aligned}
L &= 4.500 \text{ m} = 14.764 \text{ ft} \\
B &= 0.450 \text{ m} = 1.476 \text{ ft} \\
T &= 0.300 \text{ m} = 0.984 \text{ ft} \\
\nabla &= 0.3888 \text{ m}^3 = 13.731 \text{ ft}^3 \\
S &= 3.4962 \text{ m}^2 = 37.633 \text{ ft}^2
\end{aligned} \tag{5}
$$

The choice of propeller was governed mainly by considerations of availability and simplicity. Fortunately, it was possible to borrow a very suitable propeller from the Hamburg Ship Model Basin (HSVA), namely a 200mm diameter model of the Standard Propeller recommended by the ITTC Cavitation Committee in 1960 for comparative testing, see Burrill (1960). It has a simple geometry (constant pitch, no rake, no skew) with accurately defined offsets (Figure 2), and performance characteristics were already available from previous tests at the Hamburg and other tanks. Its two-dimensional foil characteristics, however, were not known. The center of the propeller was positioned at

$$
\begin{aligned}
x_p &= -0.51 \, L \\
y_p &= 0 \\
z_p &= -0.50 \, T
\end{aligned} \tag{6}
$$

in the coordinate system of Figure 1. This arrangement relative to hull ensured complete submergence (0.75 D at rest) at all speeds and a low axial clearance (0.225 D) with accordingly accentuated interaction effects.

III.2. Summary of Model Tests

In accordance with the scheme outlined in Section 2 the following model experiments were conducted :

E 1) Measurement of bare hull resistance over the entire feasible speed range of $0.1 \leq F_n \leq 0.45$.

E 2) Measurement of propeller performance in open water (thrust and torque as functions of speed of advance and rate of revolutions) over the range of advance coefficient $0 \leq J \leq 1.2$ at four depths of submergence : $h/R_P = 3.47,\ 2.00,\ 1.50$ and 1.00.

E 3) Propulsion tests with the propeller operating behind the hull (measurement of thrust, torque and residual towing force as functions of model speed and propeller rate of revolutions) at fourteen discrete speeds corresponding to $\gamma_o = 3.5$ step 0.5 until 8.0 step 1.0 until 11.0, and 12.5. At each speed the propeller revolutions were varied to obtain a sufficient range of loading usually covering both the model and the ship self-propulsion points (for an arbitrarily assumed model scale of 1:80).

E 4) Measurement of nominal wake in the propeller plane behind the hull ($x_p = -0.51$ L) in both forward and reverse motion at three selected speeds corresponding to $\gamma_o = 4.0,\ 7.0$ and 12.5. At each speed the circumferential average of the axial wake velocity was measured by means of calibrated wake wheels at ten different radii $R/R_P = 0.2$ step 0.1 until 1.1.

E 5) Measurement of longitudinal wave profiles at a fixed transverse distance ($y_o = 0.134$ L) from the model center plane in two conditions ; 1) model with propeller running at ship self propulsion point and 2) model with propeller replaced by a dummy hub, each at two selected speeds corresponding to $\gamma_o = 4.0$ and 7.0.

Revelant details of the test procedure are given in Appendix A.

III. 3. Hull Analysis

Figure 3 shows the measured total resistance of the bare hull as a function of speed in the usual nondimensional coefficient form : C_T versus F_n (or R_n). Also shown in the figure are the ITTC 1957 model-ship correlation line

$$C_F = 0.075 \,/\, (\log_{10} R_n - 2)^2 \qquad (7)$$

and the curve of estimated viscous resistance coefficient

$$C_V = (1+k)\, C_F \qquad (8)$$

The latter is based on the Hughes form factor concept and determined from the measured total resistance at low Froude numbers by the graphical method of Prohaska (1966). Assume

$$C_T = C_V + C_W \tag{9}$$

and further for $F_n \to 0$:

$$C_W = c_w F_n^4 \tag{10}$$

Then

$$C_T/C_F = (1+k) + c_w(F_n^4/C_F) \tag{11}$$

so the constants $(1+k)$ and c_w may be determined from a linear fit to the plot of C_T/C_F versus F_n^4/C_F for low Froude numbers. Figure 4 shows that the linear relation implied by Equation (11) applies reasonably well to our model up to Froude numbers up to 0.2. The numerical values of the viscous form factor $(1+k)$ and the coefficient c_w were found to be

$$(1+k) = 1.025 \qquad c_w = 0.73 \tag{12}$$

The coefficient of wavemaking resistance thus indirectly derived

$$C_W = C_T - (1+k) C_F \tag{13}$$

has been plotted in Figure 5 against the appropriate speed-length parameter γ_o and compared with the corresponding calculations based on linearized thin ship theory (see Appendix B, especially Eq. (B28)). Although there is a remarkable semblance between theory and experiment (e.g. the second, third and fourth humps can be clearly identified in the measured curve), it is disappointing to observe that even for our relatively thin ship (L/B = 10) reasonable quantitative agreement between theoretical predictions and experimental reality could be established only over a limited speed range of $2.5 \leq \gamma_o \leq 4.5$. At higher γ_o (i.e. lower Froude numbers) the experimental curve exhibits much less pronounced humps and hollows and its general level is only half as high as the theoretical curve. This suggests that the viscous boundary layer and separation probably made the stern quite ineffective in wavemaking.

In any case, the two speeds corresponding to $\gamma_o = 4 (F_n = 0.354)$ and $\gamma_o = 7 (F_n = 0.267)$ were singled out from Fig. 5 as the most promising for further investigation. At these speeds the wavemaking resistance was evaluated directly from measured wave profiles by the longitudinal cut method described in Appendix B.8. The result, as indicated by the two isolated spots in Fig. 5, showed that the wavemaking resistance associated with the wave pattern actually generated by the model was about 30 to 40 percent less than the theoretical prediction or the empirical estimate of Eq. (13). Further discussion of the results of wave profile analysis will follow in Section 3.5.

The next step in hull analysis was the evaluation of nominal wake, i.e. the flow perturbation created by the hull in the propeller plane in the absence of the propeller. In order to avoid the compli-

cations invariably caused by viscous effects behind the hull, we first compared the calculated and measured wake in reverse* motion, see Figure 6. The measured values were obtained from calibrated wake wheels directly as circumferential averages at ten discrete radii. The calculated values based on thin ship theory (see Appendix B5, especially Equation (B56)) were available pointwise in the propeller plane and were numerically averaged along the circumference at various radii for the ease of comparison with measurements. It is encouraging to observe in Figure 6 the fair agreement between theory and experiment, the discrepancy being nowhere larger than 0.03. In particular, both the mean effect of Froude number and the general variation with radius are correctly predicted by theory. However, the measured wake shows some erratic oscillations of unclarified origin at the outer radii.

Figure 7 shows an analogous comparison of calculated and measured wake in forward motion. Here we cannot expect direct agreement between experiment and theory since the former contains a substantial viscous component not included in the latter. However, if we subtract the calculated from the measured wake, we notice that the remainder is relatively insensitive to Froude number (see Fig. 7) as we would expect of the true viscous component. This may be interpreted as indirect evidence that wave effects actually present in the measured total wake are of the same order of magnitude as predicted by thin ship theory. This is quite encouraging, especially in view of the relatively poor agreement between calculated and measured values of wavemaking resistance.

For the sake of completeness the conventional "potential" or zero Froude number component of wake as calculated by theory (Appendix B.5, Equation (B54)) is also plotted in Figure 7. It is by definition independent of Froude number. In view of the foregoing, the trichotomy of nominal wake in potential, wave and viscous components as displayed in Figure 7 can be regarded as quite meaningful. Evidently, the wave effects are by no means negligible as commonly assumed.

---

* Incidentally, by virtue of the longitudinal symmetry of our hull the "stern" wake in the propeller plane $x = x_p$ in reverse motion is equivalent to the "bow" wake in the reflected propeller plane $x = -x_p$ in forward motion.

III. 4. Propeller Analysis

Measured propeller performance characteristics for three depths of submergence are plotted in Fig.8 in the usual nondimensional coefficient form. The largest depth ($h/R_P = 3.47$) was the maximum attainable with the propeller boat available for open water tests, and the smallest ($h/R_P = 1.50$) corresponds exactly to the immersion selected for self-propulsion tests ($z_P = -0.5T$) described later. Apart from verifying the measurements conducted previously at an even lager depth ($h/R_P = 4.0$) in the Hamburg Ship Model Basin (HSVA), the principal conclusion from these tests was that free-surface effects are negligibly small for depths $h/R_P \geq 1.50$.

At the shallowest depth investigated, however, with the propeller disk just touching the static water level ($h/R_P = 1.0$), pronounced free-surface effects were measured, see Fig.9. The observed loss of thrust and torque as compared to the deeply submerged condition, the steady accentuation of the effect with increasing loading (i.e. decreasing advance coefficient), and a slight drop in efficiency are to be naturally expected from the combined effects of ventilation and wave-making at the free surface. It is not intuitively obvious, however, why the thrust and torque should suddenly break down at some "critical" advance coefficient, here $J \approx 0.41$. Similar discontinuities have been measured by others, notably by Shiba (1953). Flow observations reveal that the discontinuity is accompanied by a sudden transition from partly ventilated to fully ventilated condition. A satisfactory theoretical explanation of this phenomenon would certainly require an intricate analysis of the stability of partly ventilated flow. It is also intriguing to note that the drop in thrust and torque is nearly proportionate so that the discontinuity is hardly perceptible in the curve of efficiency. This lends some credibility to Dickmann's (1939) simplified treatment of propeller ventilation as a mere reduction in the density of the medium due to a mixture of air with water!

For the sake of completeness it should be reported that ventilation also occured to some extent at two of the deeper immersions, namely $h/R_P = 1.5$ and 2.0, especially in the bollard condition and at the lowest advance coefficients. It was distinctly audible and often visible as a vortex from the free surface to the propeller tip, but its effect on thrust and torque was obviously too small to be measurable (see Fig.8).

The measured thrust and torque characteristics (in the deeply submerged condition) were transformed into an equivalent vortex model of the propeller by means of a computer program based on lifiting line theory and using assumed (or adjusted) two-dimensional foil characte-

ristics as the connecting link between propeller geometry and forces after taking account of the velocity perturbation induced by the trailing vortices . Without going into details , which are given in Appendix C , Fig. 10 is presented as evidence for the close fit finally achieved between calculations and measurement . Note that the results of two different calculations are displayed . The four sets of crosses mark the calculated performance of a series of hypothetical propellers individually designed at each respective advance coefficient so as to produce the known measured thrust with a minimum loss of energy (i.e. optimum distribution) . The exact agreement with the measured K_T values is therefore trivial , while the good agreement with the measured K_Q values proves that hydrodynamic losses were reasonably estimated in the calculation and that the actual performance of the propeller is nearly optimum over the range $0.6 \leq J \leq 0.9$. On the other hand , the four sets of squares in Fig. 10 mark at each respective advance coefficient the calculated performance of the given propeller with predetermined geometry . Hence , the perfect agreement with measured K_T and K_Q values is trivial only at the design point , assumed to be at $J = 0.8$, whereas at the three other points it demonstrates the usefulness of the scheme devised to calculate the off-design performance with the aid of assumed (or empirically adjusted) foil characteristics . In particular , it may be anticipated from the trend visible in Fig. 10 that a more elaborate off-design analysis (as compared to the simpler design point analysis) would probably pay off at higher loadings (lower J values) by producing a more accurate simulation of actual propeller performance .

The heart of the vortex model of the propeller used above is the calculated distribution of bound circulation along the blade . This is shown in a suitable nondimensional form in Fig. 11 for each of the four advance coefficients marked in Fig. 10 . It serves to illustrate the effect of loading and variation with radius , and is the basis of all further analysis . In passing we note that the two different calculations just discussed produced practically identical (within one percent) circulation distributions in the four cases considered here .

The vortex model of the propeller was in turn transformed into a sink disk model by means of the Hough and Ordway (1965) relation , and linearized wavemaking theory was applied to calculate its self-induced wake when operating near the free surface , see Appendix B , especially Equations (B 13) and (B 61) . The final results of four such calculations for a relatively shallow submergence of $h/R_P = 1.0$ are shown in Fig. 12 . It is a rather remarkable coincidence that although the calculated self-induced wake varied strongly over the disk , its circumferential averages came out almost independent of the radius .

The disk average $|w_f|$ increases steadily with loading (i. e. decreasing J) as one would naturally expect.

The next and final step in our propeller analysis was aimed at an indirect verification of the entire theoretical model by comparing the calculated performance at shallow submergence (based only on theory and the known performance at deep submergence) with actual measurements. For this purpose the calculated self-induced free-surface wake $w_f(R)$ was used in two ways. First, following Dickmann (1939), its disk average value w_f was used simply to define a virtual advance coefficient

$$J_f = (1-w_f)\, J \tag{14}$$

at which the thrust and torque values were read off from the known deep submergence characteristics (Figure 8) and replotted against J (see squares in Figure 13) as the predicted characteristics at shallow submergence. Second, the radial distribution $w_f(R)$ was fed into the computer program for off-design performance which then calculated the thrust and torque by vortex theory (see crosses in Figure 13). Since this program matched perfectly with the deep submergence characteristics (see Figure 10) and since $w_f(R)$ was practically constant over the radius (see Figure 12), the net effect was the same as in the first method, namely a loss of thrust and torque owing to the negative value of self-induced wake and increasing steadily with loading. The actually measured characteristics, replotted from Figure 9 as the dashed curves in Figure 13, indeed confirm that the calculated effect is in the right direction and of the right magnitude.

Encouraged by this success of the theory, we repeated the above calculation for the entire range of advance coefficients J = 0.10 step 0.05 until 1.10. However, for the sake of simplicity, we now estimated the source strength directly from the thrust coefficient by Dickmann's relation (i. e. substituting Equation (B10) instead of (B13) into (B61)) and applied only the simple method of virtual advance coefficient J_f explained above. The result is represented by the continuous curves in Figure 13. Although not as accurate as the previous calculations, which made use of vortex theory, even this simple approach leads to fairly reasonable predictions of the effect of wavemaking on propeller performance. Of course, at very high loadings, especially for advance coefficients below the "critical" value of 0.41, ventilation rather than wavemaking is the decisive factor, and hence wavemaking theory alone fails to predict the behavior found in the experiment.

As explained in Appendix B. 6, the wavemaking resistance of the propeller follows directly from its self-induced wake, see Equation (B62). Hence opportunity was taken to compare the three different source representations of the propeller, defined by Equations (B10), (B11) and (B13), by plotting for each the ratio of calculated wavemaking resistance to measured thrust as a function of advance coefficient, see Figure 14. Since the source disk is not a valid model for calculating forces acting on the propeller, the wavemaking resistance R_{WP} is not necessarily equal to the loss of thrust experienced by a propeller operating near the free-surface as compared to an equivalent deeply submerged condition. More appropriately, the ratio R_{WP}/T should be regarded as a measure of the loss of propeller efficiency due to the expenditure of energy for maintaining its steady wave pattern.

III. 5. Wave Analysis

It has already been stated that longitudinal wave profiles were measured at a fixed transverse distance (y_o = 0. 134 L) from the model center plane in two conditions : 1) model with propeller running at the ship self-propulsion point (for an arbitrarily assumed model scale of 1:80), and 2) model with propeller replaced by a dummy hub, each at two selected speeds corresponding to the two values of speed-length parameter γ_o = 7. 0 (F_n = 0. 267) and γ_o = 4. 0 (F_n = 0. 354). Two pairs of corresponding profiles are reproduced in suitable nondimensional form in Figures 15 and 16 respectively with the vertical scale magnified 100 times for the sake of clarity.

Evidently, the propeller exercised a measurable influence on the wave pattern of the model, the transverse wave amplitude behind the stern being higher with the propeller running in the cases shown. Even within the linearized wave theory two significantly different explanations can be offered for this effect. First, it might be a purely linear effect due to a superposition of the propeller wave on the hull wave. Second, it might be a pseudo-nonlinear effect due to a modification of the wavemaking properties of the hull itself as a result of propeller suction.

Another point of interest to note is the slight breaking of the bow wave clearly visible at the leading peaks in Figure 16. It shows that the wave pattern was in places steep enough to introduce truly nonlinear effects, at least locally. This should be kept in mind when making comparisons with the calculations based on strictly linearized theory.

The measured wave profiles were analysed by the Fourier transform method as explained in Appendix B.8 and the results compared with the corresponding theoretical calculations based on explicit source representations of the hull and the propeller .The measured and calculated nondimensional free-wave amplitude spectrum E , and its sine, cosine components F , G are plotted as functions of nondimensional transverse wave number u in Fig . 17 to 19 for $\gamma_o = 7.0$ and in Fig. 20 to 22 for $\gamma_o = 4.0$. The following remarks are added to avoid any ambiguities of interpretation . The bare hull calculations are based on Equation (B 23), the propeller calculations on Equation (B 27) in conjunction with (B 16) , and the total system hull-propeller on Equation (B 30) . The free-wave spectra of the propeller alone in Fig. 19 and 22 are referred to a coordinate system with its origin in the propeller plane , see Equation (B 73) , whereas all others refer to a coordinate system with its origin in the midship section of the hull (see Fig. 1).

Some obvious conclusions are in order here . First , the agreement between calculations and measurement is only qualitative at the lower speed , but quite good at the higher speed . Second , the discrepancy between theory and experiment for the bare hull is mostly in phase and not so much in the amplitude of the free-wave spectrum . This is consistent with previous results of similar comparisons , see Sharma (1969) . Third , the fair agreement between the "measured" free-wave spectrum of the propeller - it was actually derived from the principle of linear superposition , see Equation (B 72) - and the calculated spectrum shows that our theoretical model of propeller wavemaking is reasonable and that the pseudo-nonlinear effect of the propeller on the hull waves referred to above is at least not the predominant phenomenon .

Finally , the calculated and measured wavemaking resistance according to Equations (B 28, 29) and (B 74) respectively are compared in the following table .

Nondimensional coefficient $R_w g^2/\rho V^6$ as calculated (measured)		
Speed-length parameter	$\gamma_o = 7$ or $F_n = 0.267$	$\gamma_o = 4$ or $F_n = 0.354$
Hull alone	0.0650 (0.0380)	0.0354 (0.0245)
Propeller alone	0.0037 (0.0039)	0.0013 (0.0037)
Interaction term	0.0017 (0.0001)	0.0058 (0.0025)
System hull and propeller	0.0704 (0.0420)	0.0425 (0.0307)

As already noted in Section 3.3 (see Fig. 5), the measured values fall considerably short of the calculated ones, presumably due to viscous effects at the stern which reduce the wavemaking effectiveness of the afterbody. An interesting point to observe is that in one case the hull-propeller interaction term is found to be several times larger than the wave resistance of the propeller itself. This can be understood by reference to Equation (B 32) which shows that the order of magnitude of the interaction term is intermediate between that of hull wave resistance R_{WH} and propeller wave resistance R_{WP}. Since the wave resistance associated with the propeller is an indirect measure of the loss of efficiency, it follows that the effect of propeller waves on the propulsive efficiency of the system hull and propeller can be significantly larger than one would expect from the observed loss of open water propeller efficiency at the same submergence and loading.

III. 6. Interaction Analysis

III. 6. 1. Propulsive Efficiencies

The first step in hull-propeller interaction analysis was the empirical determination of the conventional Froude propulsion factors by an analysis of the self-propulsion tests in conjunction with the results of the hull resistance and propeller performance (open water) tests. Using standard definitions and symbols, the factors in question are: the hull efficiency η_H, the equivalent open water efficiency η_0 and the relative rotative efficiency η_R which combine to yield the propulsive efficiency η_D.

$$\eta_D = R_T V / 2\pi n Q_H$$

$$= \eta_H \eta_0 \eta_R \qquad (15)$$

In the present context, the factor of primary interest is the hull efficiency η_H which combines the effect of thrust deduction fraction t and the effective wake fraction w_E.

$$\eta_H = (1 - t) / (1 - w_E) \qquad (16)$$

Unfortunately, the breakdown of propulsive efficiency into various factors is not unique (except for the fraction t), but depends on the somewhat arbitrary definition of an "equivalent" open water propeller condition. The common alternatives are the thrust identity and the torque identity methods. In order not to prejudice our results by the

arbitrary choice of any one method , we carried out three complete analyses : one based on thrust identity (subscripts T) , one on torque identity (subscripts Q) , and one based on a mean (subscripts M) advance coefficient J_M defined as

$$J_M = (J_T + J_Q) / 2 \qquad (17)$$

where J_T and J_Q are the points of thrust and torque identity (between the behind hull condition and an equivalent open water condition of the propeller) respectively .

Our procedure for evaluating the propulsion factors can be briefly outlined as follows . Fig. 23 shows the typical result of a self-propulsion test at one Froude number , i.e. dimensionless coefficients of measured thrust T_H , torque Q_H , and residuary towing force F_D as functions of propeller advance coefficient J_H (based on hull speed) . Obviously , this presentation is suitable for determining the self-propulsion points . Thus the model self-propulsion point lies at $C_{FD} = 0$ and the ship self-propulsion point at

$$C_{FD} = C_{VM} - C_{VS}$$

$$= (1 + k) (C_{FM} - C_{FS}) \qquad (18)$$

if viscous resistance is estimated by the form-factor method and a surface roughness allowance is neglected for the sake of simplicity . Here C_{FM} and C_{FS} are the predetermined coefficients of friction at the model and ship Reynolds numbers respectively , see Equation (7) . For instance , the self-propulsion point of a smooth geosim 80 times as long as the model (and running in fresh water at a temperature of 15° C) is found to lie at $J_H = 0.733$. Leaving aside the self-propulsion point for the moment , at any value of J_H (representing a certain propeller loading) the propulsion factors are found as follows . Take from the resistance test (Fig. 3) the coefficient of total resistance C_T at the given Froude number and obtain the propulsive efficiency*

$$\eta_D = (R_T - F_D) V / 2 \pi n Q_H \qquad (19)$$

$$= (S/D^2) (C_T - C_{FD}) / 4 \pi K_{QH} J_H^3$$

* For a truly self-propelled system the towing force $F_D = 0$, and then Equation (19) agrees with Equation (15).

and the thrust deduction fraction

$$t = (T_H + F_D - R_T) / T_H$$

$$= 1 - (S/D^2)(C_T - C_{FD}) / 2K_{TH}J_H^2 \qquad (20)$$

Now read from the open water characteristics (Fig. 8) the advance coefficients J_T at thrust identity ($K_T = K_{TH}$) and J_Q at torque identity ($K_Q = K_{QH}$). Calculate J_M from Equation (17), and read the equivalent open water efficiencies η_{0T}, η_{0Q}, η_{0M} from Fig. 8 at J_T, J_Q, J_M respectively. Calculate effective wake fractions

$$w_T = 1 - J_T/J_H$$

$$w_Q = 1 - J_Q/J_H$$

$$w_M = 1 - J_M/J_H \qquad (21)$$

hull efficiencies

$$\eta_{HT} = (1-t) / (1-w_T)$$

$$\eta_{HQ} = (1-t) / (1-w_Q)$$

$$\eta_{HM} = (1-t) / (1-w_M) \qquad (22)$$

and relative rotative efficiencies

$$\eta_{RT} = \eta_D / \eta_{0T}\,\eta_{HT}$$

$$\eta_{RQ} = \eta_D / \eta_{0Q}\,\eta_{HQ}$$

$$\eta_{RM} = \eta_D / \eta_{0M}\,\eta_{HM} \qquad (23)$$

This completes the analysis.

The result of one such evaluation, out of fourteen actually carried out, is reproduced in Fig. 24. Since this is generally typical of all others, the following remarks are relevant. First, the thrust deduction fraction and relative rotative efficiency are relatively insensitive to changes in loading. Second, the equivalent open water efficiency decreases with increasing loading (decreasing J_H) as expected. Third the effective wake fraction, and consequently the hull efficiency decrease with increasing loading. This is in contradiction to the

theoretical behavior in potential flow (see Appendix D) . However, in a real flow the decrease in effective wake with increasing loading can be explained qualitatively by a supposed contraction of the viscous wake due to propeller suction as first pointed out by Dickmann (1939) , see also next section . Fourth , all propulsion factors vary slowly and almost monotonically with changes in loading, so that the arbitrary choice of one particular loading (e.g. that corresponding to the self-propulsion point of a ship of $\lambda = 80$) for further investigation is not liable to hide any important phenomena .

Fig. 25 shows the various propulsion factors as functions of Froude number over the range $3.5 \leq \gamma_0 \leq 12.5$, all evaluated at the self-propulsion point of a smooth ship of $\gamma = 80$. (This choice of scale ratio is arbitrary , but not crucial as just pointed out). The following features deserve special mention . First , all factors depicted exhibit a significant and oscillatory dependence on Froude number . Second , the self-propulsion point advance coefficient J_H , and consequently the equivalent open water efficiencies η_0 , depend mainly on hull resistance , and hence reveal humps and hollows in inverse phase to the coefficient of wave resistance (compare Fig. 5) as expected . Third , contrary to common belief , the thrust deduction and effective wake fractions vary significantly with Froude number , the most remarkable feature being the sudden drop around $\gamma_0 = 5$. The hull efficiency η_H merely shows their combined effect . Fourth , the relative rotative efficiency η_R is exceptionally low but approaches normal values at higher Froude numbers . Fifth , there is an unusually large discrepancy between thrust and torque identity points , but it tends to decrease with increasing Froude numbers . The last two effects are presumably due to strong nonuniformities in the viscous wake of the hull , which would also explain why they are relatively weaker at higher Froude numbers .

III. 6. 2. Wake

The next step in interaction analysis was an attempt to correlate by theory the measured wake and thrust deduction . This required first the generation of a mathematical model of the propeller in the behind hull condition . Again the computer program described in Appendix C was used . The inputs to the program were the advance coefficient J_M at the ship self-propulsion point , the corresponding thrust coefficient K_{TH} , the radial distribution of measured nominal wake $w(R)$, and the two-dimensional foil characteristics already established on the basis of open water characteristics (see Propeller Analysis) . In order to account for the difference between nominal and effective wake the program was allowed to determine by trial and error a wake corrector k_w , with which the nominal wake $w(R)$ was

multiplied, such that the calculated thrust coefficient equalled the measured K_{TH}. The primary output of the program was the distribution of bound circulation along the radius. In addition, it also furnished a calculated torque coefficient K_{QH} and a mean effective wake $\tilde{w}_T$ (based on thrust average rather than volume average) from which followed the equivalent open water advance coefficient J_T. This elaborate analysis was done only for three selected Froude numbers corresponding to $\gamma_o = 4.0$, 7.0 and 12.5. The results are shown in Fig. 26 and 27. The effect of wake on circulation distribution is quite evident in Fig. 26 where the circulation maxima have been shifted toward smaller radii as compared to the open water condition of Fig. 11. Turning now to Fig. 27, the good agreement between calculated and measured advance coefficient J_T is a confirmation of the realistic simulation of thrust generation in the theoretical model, while the lack of agreement between calculated and measured torque coefficient K_{QH} points up the shortcomings of the theoretical model, specially the total neglect of all circumferential nonuniformities and the associated lack of any simulation of the relative rotative efficiency. However, we would not expect these defects to have any serious effect on the intended calculation of thrust deduction.

Before passing on to the evaluation of thrust deduction we pause to consider briefly the issue of nominal wake versus effective wake. Conceptually, the distinction is clear : Nominal wake is the flow perturbation created by the hull in the propeller plane with the propeller removed, while effective wake is the flow perturbation due to the hull in the propeller plane with the propeller in place and operating. In practice, however, the relative magnitudes of these two wakes have been a topic of considerable controversy and confusion in the literature on hull propeller interaction. It is generally agreed that there are two fundamentally different reasons why these two wakes need not be identical. First, there is a genuine physical effect of the propeller on the flow perturbation caused by the hull. This has three partially counteracting components. a) The potential component, which may be understood as the additional flow induced by the image of the propeller in the hull, tends to increase the effective wake compared to the nominal wake, since this image consists predominantly of sinks in the afterbody. b) The viscous component, which results from a contraction of the viscous wake, is specially pronounced if the line of boundary layer separation is shifted rearward by propeller suction and generally tends to decrease the effective wake compared to the nominal wake by bringing more undisturbed flow into the propeller disk. c) The wave component, referred to as a pseudo-nonlinear effect of the propeller on the wavemaking properties of the hull in Section 3.5, can act in either direction depending upon Froude number. Second, there is a spurious computational effect due to dif-

ferent methods of averaging. The measured nominal wake is conventionally averaged over the disk on a volume flux basis, while the mean effective wake is measured by the propeller as a calibrated thrust (or torque) generating device which tends to put maximum weight near the radii where the circulation is a maximum. The following table, a by-product of our calculations, is likely to shed some light on the relative importance of these two effects.

Speed-length parameter		Measured nominal wake		Wake corrector	Corrected nominal wake		Effective wake	
							Simulated	Measured
γ_o	F_n	w	$w(.7R_P)$	k_w	$k_w w$	$k_w w(.7R_P)$	$\tilde{w}_T$	w_T
4.0	0.354	0.208	0.230	0.704	0.146	0.162	0.153	0.145
7.0	0.267	0.291	0.322	0.892	0.259	0.287	0.291	0.285
12.5	0.200	0.304	0.370	0.933	0.284	0.346	0.377	0.360

First, note that the wake corrector k_w is a measure of the true physical difference between nominal and effective wake since, as explained earlier, it was determined by trial and error as the required multiplier of the measured nominal wake in the computer program to ensure that the simulated and measured thrusts were equal. This difference is here seen to vary from -7% at the lowest Froude number to -30% at the highest. That it is strongly negative, suggests that the viscous effect mentioned above was probably dominant in this case. Second, the residual difference (up to +33%) between the corrected volume average wake $k_w w$ and the thrust average wake $\tilde{w}_T$ must be attributed to the difference in the methods of averaging. Note that this spurious effect is greatest at the lowest Froude number where the concentration of bound circulation over the inner radii was also the most pronounced. Third, the good agreement between the computer simulated and the experimentally measured mean effective wake is rather encouraging. Fourth, note that the effective wake is much better approximated by the corrected nominal wake at 0.7 radius, $k_w w(.7R_P)$, than by its disk average, $k_w w$. This observation has direct relevance to the design of wake-adapted propellers. Finally, as a word of caution, it should be noted that the relative magnitudes of the nominal and effective wakes as well as the quantitative rankings of the different effects found here may be peculiar to this model and therefore should not necessarily be generalized.

To complete the discussion of wake, Fig. 28 shows the measured versus calculated wake as a function of Froude number. The following quantities are plotted : 1) The disk average of the measured

nominal wake w. This was available at three speeds only (compare Fig. 7). 2) The disk average of the potential wake w_p calculated by thin ship theory, see Appendix B.5, especially Equation (B 54). This is a zero Froude number approximation. 3) The disk average of the sum of potential and wave wakes $(w_p + w_w)$ also calculated by thin ship theory, see Appendix B.5, especially Equation (B 53). 4) The quantity $(w_T - w_p - w_w)$ as an approximate estimate of the viscous component w_v, see Equation (1). The striking correlation between the measured effective wakes and the calculated wave wake certainly suggests that the observed oscillations of wake with Froude number are indeed free-surface effects and that the thin ship wavemaking theory despite all its weaknesses does give a reasonable estimate of this phenomenon. Even the quantity $(w_T - w_p - w_w)$, which as the difference of a measured effective wake and calculated nominal wake components must be regarded with due caution, gives a credible impression of the magnitude of viscous wake w_v. However, one cannot put much faith in its observed oscillations.

III. 6. 3. Thrust Deduction

We now turn to our final goal of calculating the thrust deduction fraction and its components. This was done to two different degrees of approximation. At the three selected Froude numbers, where the calculated circulation distribution was available (see Fig. 26), the Hough and Ordway relation, Equation (B 16) in conjunction with the simulated effective wake $k_w w(R)$, was applied to generate the equivalent sink disks. At all other Froude numbers we had to be content with Dickmann's approximate relation between thrust coefficient and source strength, Equation (B 15) in conjunction with the measured effective wake w_T. The numerical difference between these two approximations is illustrated in Fig. 29. Evidently, the Hough and Ordway approximation yields slightly higher mean values and, in accordance with the distribution of bound circulation, effects a concentration of sink strength toward the inner radii. It is believed to be more accurate than Dickmann's uniform sink disk since the vortex model yields a more realistic flow pattern than the simple momentum theory.

In either event, the sink disk was used to calculate first the wavemaking resistance of the propeller alone and of the system hull and propeller as explained in Appendix B. The wavemaking resistance (and free-wave spectrum) of the propeller in the behind hull condition calculated in this way were found to be in reasonable agreement with the corresponding results of measured wave profile analysis at two Froude numbers as already discussed in Section 3.5. Given the wavemaking resistances of the hull R_{WH}, propeller R_{WP}, and total system R_{WT}, only one additional quantity $\delta_H R_{WP}$, see Eq. (B 64),

was needed for calculating the combined potential and wave thrust deduction force $\delta_P R_{WH}$, see Equation (B 65), from which followed the thrust deduction fraction $(t_p + t_w)$ by Equation (B 66). The potential component t_p alone was obtained from a simple degenerate case (zero Froude number wake) of this calculation, see remark following Equation (B 67). The final results of this calculation are shown in Fig. 30 in comparison to the measured total thrust deduction t replotted from Fig. 25.

Let us try to interpret the salient features of Fig. 30. First, the wave component of thrust deduction t_w is small, but not negligible compared to the potential component t_p. Second, the oscillations in calculated thrust deduction are not due to t_w, but are already present in t_p. This can be understood by reference to Equation (B 63) which defines thrust deduction as the Lagally force on the hull sources due to the axial flow induced by the propeller sources. Since our hull sources were assumed independent of Froude number and since the flow induced by a source upstream of itself is almost monotonic with Froude number, the observed oscillations of calculated thrust deduction can only be due to variations of propeller source strength with Froude number. This is indeed the case, for by Equation (B 15) the source strength depends on loading and wake, which were both found to oscillate with Froude number. As a result the calculated thrust deduction t_p (as well as t_w) correlates strongly with advance coefficient J_H and effective wake w_T (compare Fig. 25). Third, the oscillations in the measured thrust deduction t are much stronger than in the calculated $(t_p + t_w)$. This means that either the residual viscous component of thrust deduction t_v, see Equation (2), oscillates appreciably with Froude number or that our assumption of the hull sources being independent of Froude number was invalid. This point cannot be decided at the moment. But in any case it points to a significant interaction of viscous and wave effects at the stern, presumably intensified by propeller suction. For instance, if the line of boundary layer separation is pulled rearward by the propeller, the result would be a negative viscous thrust deduction as well as a relative increase in the effective sink strength of the afterbody. Fourth, specifically the steep variation of measured thrust deduction around $\gamma_o = 5$ cannot presently be explained, except as a possible viscous effect, i. e. a reduction in the extent of boundary layer separation under the combined influence of a negative wave wake (Fig. 28) and a high propeller loading (Fig. 25). Fifth, the thrust deductions calculated from the Hough and Ordway sink disk are significantly higher than those calculated from the Dickmann sink disk and are in better agreement with measurements. This is a direct consequence of the significant difference between the two sink disks, both in average intensity and in its relative distribution over propeller radius, see Fig. 29.

IV. CONCLUDING REMARKS

It has been demonstrated by practical application to a specific example that our conceptual scheme for determining the potential, viscous and wave components of wake and thrust deduction is indeed workable. It has required the concerted application of miscellaneous analytical, computational and experimental techniques. The varying degrees of success achieved with the individual techniques have been discussed in detail in the appropriate sections and need not be repeated here. Several results were obtained by more than one method, for instance by independent calculation and measurement, and in most cases there was fair agreement, at least there were no striking contradictions except perhaps in the calculated and measured wavemaking resistance at low Froude numbers, which came as no surprise.

It would be rash to try to derive general conclusions concerning the quantitative role of wavemaking at the free surface in the phenomenon of hull propeller interaction on the basis of one single example. However, two salient results do seem to have a broader significance. First, it was found that contrary to common belief the wave component can be dominant in the wake and quite significant in the thrust deduction at Froude numbers around $F_n = 0.3$. Second, there seemed to be an appreciable viscous component in the thrust deduction at practically all Froude numbers. Moreover, the undulating variation of this component with Froude number points to a complicated interaction of viscous boundary layer, hull wave pattern and propeller suction near the stern.

These two effects are of direct relevance to the hydrodynamic design of fast ships and also to the methods of extrapolating propulsive performance from model to full-scale.

It is recommended that further studies of this nature be undertaken to resolve the remaining issues and to collect systematic design data on the effect of wavemaking on the propulsive performance of ships.

V. ACKNOWLEDGMENTS

We want to sincerely thank the following individuals and organisations for their valuable contributions to this project :

Mr. J.L. Beveridge and Dr. W.B. Morgan of the Naval Ship Research and Development Center for crucial consultations in the planning stage of this work,

Mr. W.S. Vorus, Ph. D. candidate at the University of Michigan, for a major share of the computer programming and test evaluation,

Dr. C. Östergaard, visiting scientist at the University of Michigan, for the computer program for propeller design originated at the Technical University of Berlin and extended at the University of Michigan to cover the off design performance,

Mr. A.M. Reed, graduate student at the University of Michigan, for the computer programs for wave profile analysis and theoretical wavemaking resistance,

Mr. B. Hutchison and Miss S. Pian, students at the University of Michigan, for their assistance in writing the computer program for hull wave flow calculations by thin ship theory,

Mr. E. Snyder of the Ship Hydrodynamics Laboratory, University of Michigan, for his expert execution of the model test program,

Messrs. T. Little, A. Toro, and B.L. Young, students at the University of Michigan, for their enthusiastic help in conducting the model tests,

The staff of the Ship Hydrodynamics Laboratory, University of Michigan, for their careful and patient handling of all jobs pertaining to the model tests,

The Hamburg Ship Model Basin (HSVA), Hamburg, Germany, for lending a model propeller for our experiments, and

The Naval Ship Research and Development Center, Carderock, Maryland, for providing copies of computer programs for propeller design (Lerbs induction factor program) and potential flow calculations (Hess and Smith program).

* * *

LIST OF SYMBOLS

Note : - The standard symbols recommended by the ITTC Presentation Committee have been used wherever possible . See also Section B.1 for the special notation used in Appendix B .

B	Beam of hull
C_B	Block coefficient of hull form
C_D	Drag coefficient of propeller blade section
C_{DD}	Value of C_D at design point J_D
C_F	Coefficient of friction , Equation (7)
C_{FD}	Coefficient of residual towing force = $2F_D/\rho SV^2$
C_{FM}	Value of C_F at model Reynolds number
C_{FS}	Value of C_F at ship Reynolds number
C_L	Lift coefficient of propeller blade section
C_{LD}	Value of C_L at design point J_D
C_M	Midship section area coefficient
C_P	Longitudinal prismatic coefficient
C_T	Coefficient of total resistance = $2R_T/\rho SV^2$
C_{Th}	Thrust loading coefficient , Equation (B15)
C_V	Coefficient of viscous resistance = $2R_V/\rho SV^2$
C_{VM}	Value of C_V at model Reynolds number
C_{VS}	Value of C_V at ship Reynolds number
C_W	Coefficient of wave resistance = $2R_W/\rho SV^2$
C_{WP}	Waterplane area coefficient
C, S	Fourier cosine , sine transforms, Equation (B50)
C^*, S^*	Modified Fourier cosine , sine transforms , Eqn. (B70)
D	Diameter of propeller
$E(u)$	Free-wave amplitude spectrum
$E_H(u)$	$E(u)$ of hull alone
$E_P(u)$	$E(u)$ of propeller alone

$E_T(u)$	E (u) of total system hull and propeller
$E_{i,j}$	Special function , Equation (B39)
F (u)	Sine component of free-wave spectrum
	Subscripts H, P, T apply as to E (u)
F_D	Residual towing force in self-propulsion test
F_n	Froude number = $V / \sqrt{gL}$
F_{nh}	Submergence Froude number = $V/\sqrt{gh}$
$F^{(N)}$	N = 1, 2, 3 ; Special functions , Equation (B24)
$\tilde{F}_P, \tilde{G}_P$	Free-wave spectrum of propeller in a coordinate system with origin in the propeller plane , Eqn. (B73)
G	Non dimensional bound circulation = $\Gamma / \pi DV$
G	Green's function of point source , Equation (B33), (B57)
G_x	Partial derivative of G , Equation (B58)
G (u)	Cosine component of free-wave spectrum Subscripts H, P, T apply as to E (u)
$G^{(N)}$	N = 1, 2, 3 : Special functions , Equation (B47)
Im	Imaginary part of
I_o	Modified Bessel function of zero order
J	Advance coefficient of propeller = V / nD for free-running propeller = V_A/nD for propeller operating behind hull
J_D	Value of J at the design (optimum) point
J_f	Virtual advance coefficient of propeller operating near the free surface , Equation (14)
J_H	Advance coefficient of propeller based on hull speed = V/nD
J_M	Mean of J_Q and J_T
J_Q	Value of J at torque identity $K_Q = K_{QH}$
J_T	Value of J at thrust identity $K_T = K_{TH}$
K_Q	Torque coefficient of free-running propeller = $Q/\rho n^2 D^5$
K_{QH}	Torque coefficient of propeller behind hull = $Q_H/\rho n^2 D^5$

K_T	Thrust coefficient of free-running propeller = $T/\rho n^2 D^4$
K_{TH}	Thrust coefficient of propeller behind hull = $T_H/\rho n^2 D^4$
L	Length of hull
Oxyz	Coordinate system, see Figure 1
P	Pitch of propeller
Q	Propeller torque in open water
Q_H	Propeller torque behind hull
Re	Real part of
R_H	Propeller hub radius
R_n	Reynolds number of hull = VL/ν
R_P	Propeller tip radius
R_T	Total resistance of hull
R_V	Viscous resistance of hull
R_W	Wavemaking resistance
R_{WH}	R_W of hull alone
R_{WP}	R_W of propeller alone
R_{WT}	R_W of total system hull and propeller
R, θ	Polar coordinates in propeller plane, Equation (B9)
R', θ'	Coordinates of source point in propeller plane
S	Wetted surface area
T	Draft of hull
T	Propeller thrust in open water
T_H	Propeller thrust behind hull
V	Speed of advance of hull
V	Speed of advance of free-running propeller
V_A	Speed of advance of propeller relative to wake in the behind hull condition
V_m	Speed of model
Z	Number of blades of propeller

a_1, a_2	Empirical constants defining propeller foil characteristics , Equation (C13)
b	Half beam of hull = B/2
c	Chord length of propeller blade section
c_w	Empirical constant , Equation (10)
dD	Drag generated by blade element, Equation (C10)
dL	Lift generated by blade element , Equation (C8)
f (x, z)	Function defining hull surface , Equation (B4)
g	Acceleration due to gravity
h	Submergence measured to propeller axis
i	Imaginary number = $\sqrt{-1}$
i_A	Induction factor for axial velocity , Equation (C5)
i_E	Angle of entrance of hull
i_R	Angle of run of hull
i_T	Induction factor for tangential velocity , Eqn. (C6)
k	Empirical factor defining propeller foil characteristics , Equation (C12)
k	Circular wave number (Appendix B)
k_w	Empirical wake corrector , Appendix C.3
k + 1	Viscous form factor , Equation (8)
ℓ	Half length of hull = L/2
m	Hull form parameter , Equation (3)
n	Hull form parameter , Equation (3)
n	Rate of revolutions of propeller
r_1	Distance between field point and source point Equation (B33)
r_2	Distance between field point and mirror image of source point , Equation (B33)
s	Function of u , $s = \sqrt{(1+v)/2}$
t	Thrust deduction fraction

t_p	Potential component of t
t_v	Viscous component of t
t_w	Wave component of t
u	Transverse wave number
u_A	Axial velocity induced at the lifting line by the vortex trail of the propeller
u_T	Tangential velocity induced at the lifting line by the vortex trail of the propeller
v	Function of u , $v = \sqrt{1+4u^2}$
w	Longitudinal wave number (only in Appendix B)
w	Wake fraction (Unless otherwise specified , the disk average of the nominal , axial wake is implied .)
w_f	Self-induced free-surface wake of propeller
w_p	Potential component of wake w
w_v	Viscous component of wake w
w_w	Wave component of wake w
w (R)	Circumferentially averaged value of w (R,Θ) Subscripts f , p ,v , w , apply as to w
w (R,Θ)	Local nominal wake fraction at point (R ,Θ) Subscripts f, p, v, w apply as to w
w_E	Effective wake fraction
w_M	Mean of w_Q and w_T
w_Q	Effective wake fraction from torque identity
w_T	Effective wake fraction from thrust identity
$\tilde{w}_T$	Simulated effective wake fraction , Equation (C18)
w_1, w_2	Weights in iteration formula , Equation (C11)
x	Longitudinal coordinate , positive forward
x_P	Longitudinal coordinate of center of propeller
x, y, z	Coordinates of field point
x', y', z'	Coordinates of hull source point
y	Transverse coordinate , positive to port

y_o	Transverse position of longitudinal wave profile
y_P	Transverse coordinate of center of propeller
z	Vertical coordinate , positive upward
z_P	Vertical coordinate of center of propeller
$\Gamma(R)$	Bound circulation along propeller blade
Φ	Geometric pitch angle , Equation (C3)
Δt	Step size in time t
Δu	Step size in wave number u
Δx	Step size in distance x
α	Angle of attack of blade section , Equation (C2)
α_D	Value of α at design point J_D
β_i	Hydrodynamic pitch angle , Equation (C4)
β_{iD}	Hydrodynamic pitch angle at design point J_D
γ_o	Nondimensional speed-length parameter = $gL/2V^2$
$\delta_H R_{WP}$	Increase in propeller wave resistance due to presence of hull
$\delta_p R_{WH}$	Increase in hull wave resistance due to presence of propeller = force of thrust deduction
ϵ	Hull form parameter in Appendix B, Equation (B5)
ϵ	Drag / lift ratio in Appendix C , Equation (C18)
$\zeta(x, y)$	Free-surface elevation at point (x, y)
η_D	Propulsive efficiency , Equation (15)
η_H	Hull efficiency , Equation (16) Additional subscripts M , Q , T defined in Eqn. (22)
η_0	Openwater propeller efficiency = $K_T J / 2\pi K_Q$ Additional subscripts M , Q , T , apply as to J
η_R	Relative rotative efficiency , Equation (15) Additional subscripts M , Q , T defined in Eqn. (23)
θ	Direction of wave propagation in Appendix B
θ, R	Polar coordinates in propeller plane , Equation (B9)

θ' , R'	Polar coordinates of propeller source point
λ	Scale ratio
ν	Kinematic viscosity of water
ν	Summation index , Equation (B50)
ξ, η, ζ	Relative field point coordinates , Equation (B36)
ξ' , ζ'	Relative source point coordinates , Equation (B36)
ρ	Density of water
σ	Source strength = Source output / 4π
$\sigma(x, z)$	Density of hull source distribution
$\sigma(R, \theta)$	Density of propeller source distribution
$\sigma(R)$	Circumferentially averaged value of $\sigma(R, \theta)$
τ	Draft/half-length ratio , Equation (B36)
φ	Velocity potential of perturbation flow
$\varphi_x, \varphi_y, \varphi_z$	Partial derivatives of φ
φ_x^H	Longitudinal flow induced by hull
φ_x^P	Axial flow induced by propeller
$\varphi_x^{(N)}$	N = 1, 2, 3, 4 ; Components of φ_x, Equation (B34)
ω	Angular velocity of propeller = $2\pi n$
∇	Displacement volume of hull

REFERENCES

Note : - The following is a fairly complete list of recent publications , not necessarily cited in our text , directly dealing with the subject of hull propeller interaction . References to older literature can be found in Dickmann's (1939) monograph . We hope that this list will serve as a useful handy reference to future workers in this field .

AMTSBERG , H.: Investigations with axisymmetric bodies into the interaction between hull and propeller (in German), Jahrbuch STG 54, 117 - 152 (1960)

AMTSBERG , H., and ARLT , W. : Thrust deduction studies of bodies with bluff ends (in German) . Schiff und Hafen 17 , 786-790 (1965) .

BASSIN , A. M. : Theory of interaction between the propeller and hull of a vessel in an infinite fluid (in Russian) . Bulletin of USSR Academy of Science , Division of Technical Sciences 12 , 1723 - (1946) .

BEVERIDGE , J.L. : Thrust deduction due to a propeller behind a hydrofoil . DTMB Report N° 1603 (1962) .

BEVERIDGE, J.L. : Effect of axial position of propeller on the propulsion characteristics of a submerged body of revolution. DTMB Report N° 1456 (1963).

BEVERIDGE , J.L. : Pressure distribution on towed and propelled streamline bodies of revolution . DTMB Report N° 1655 (1966) .

BEVERIDGE , J.L. : Analytical prediction of thrust deduction for submersibles and surface ships . Journal of Ship Research 13 , 258 - 271 (1969) = NSRDC Report N° 2713 (1968)

CHERTOCK , G. : Forces on a submarine hull induced by the propeller. Journal of Ship Research 9 , 122 - 130 (1965) .

DICKMANN , H.E. : Thrust deduction , wave resistance of a propeller , and interaction with ship waves (in German) . Ingenieur Archiv 9 , 452 - 486 (1938) .

DICKMANN , H.E. : Propeller and surface waves (in German) . Schiffbau 40 , 434 - 437 (1938) .

DICKMANN , H.E. : Wave resistance of a propeller and its interaction with ship waves . Proc. International Congress for Applied Mechanics 5 ,-(1938) .

DICKMANN , H.E.: Interaction between hull and propeller with special consideration to the influence of waves (in German) . Jahrbuch STG 40 , 234 - 291 (1939) .

DREGER , W. : A procedure for computing the potential thrust deduction (in German) . Schiffstechnik 6 , 175 - 187 (1959) .

FROUDE , R.E. : A description of a method of investigation of screw propeller efficiency . Transactions INA 24 , 231 -255 (1883) .

HORN , F. : Study on the subject of interaction between hull and propeller (in German) . Schiff und Hafen 7 , 601 - 604 (1955) .

HORN , F. : Relation between thrust deduction and wake in pure displacement flow (in German) . Schiff und Hafen 8 , 472-475 (1956) .

HUCHO , W.H. : On the influence of a stern propeller upon the pressure distribution and boundary layer of a body of revolution (in German) . Institute of Fluid Mechanics , Braunschweig , Germany , Report N° 64 / 65 (1965) .

HUCHO , W.H. : On the relation between pressure thrust deduction , frictional thrust deduction and wake in flow about bodies of revolution (in German) . Schiff und Hafen 20 , 689-693 (1968).

HUNZIKER , R.R. : Hydrodynamic influence of the propeller on a deeply submerged submarine . International Shipbuilding Progress 5 , 166 -177 (1958) .

ISAY , W.H. : Propeller Theory - Hydrodynamic Problems (in German) Springer Verlag , Berlin/Heidelberg/New York (1964) .

ISAY , W.H. : Modern Problems of Propeller Theory (in German) . Springer Verlag , Berlin/Heidelberg/New York (1970) .

KORVIN - KROUKOVSKY , B.V. : Stern propeller interaction with streamline body of revolution . International Shipbuilding Progress 3 , 3 -24 (1956) .

LEFOL , J. : The interaction between ship and propeller (in French). Bulletin ATMA 46 , 221 - 252 (1947) .

MARTINEK , J. , and YEH ,G.C.K. : On potential wake and thrust deduction . International Shipbuilding Progress 1 , 79-82 (1954) .

NAKATAKE , K. : On the interaction between the ship hull and the screw propeller (in Japanese) . Journal of Seibu Zosen Kai 34 , 25-36 (1967) .

NAKATAKE , K. : On the interaction between the ship hull and the screw propeller (in Japanese) , Journal of Seibu Zosen Kai 36 , 23 -48 (1968) .

NIEMANN , U. : Survey of investigations on the interaction between hull and propeller for partially submerged propellers (in German) . Forschungszentrum des Deutschen Schiffbaus , Hamburg , Germany , Report N° 5 (1968) .

NOWACKI , H. : Potential wake and thrust deduction calculations for shiplike bodies (in German) . Jahrbuch STG 57 , 330-373 (1963) .

POHL , K.H.: On the interaction between hull and propeller (in German) Jahrbuch STG 55 , 255-305 (1961) .

POHL, K.H.: Investigation of nominal and effective wake in the propeller plane of single-screw ships (in German). Schiffstechnik 10, 23 - 28 (1963).

St. DENIS , M. and CRAVEN , J.P. : Recent contributions under the Bureau of Ships Fundamental Hydromechanics Research Program . Journal of Ship Research 2 , 1 - 36 (1958) .

TSAKONAS , S. : Analytical expressions for the thrust deduction and wave fraction for potential flows . Journal of Ship Research 2 , 50 - 59 (1958) ..

TSAKONAS , S. and JACOBS , W.R. : Potential and viscous parts of the thrust deduction and wake fraction for an ellipsoid of revolution . Journal of Ship Research 4 , 1 - 16 (1960) .

TSAKONAS , S . , and JACOBS , W. : Analytical study of the thrust deduction of a single-screw thin ship . International Shipbuilding Progress 9 , 65 - 80 (1962) .

WALD , Q. : Performance of a propeller in a wake and the interaction of propeller and hull . Journal of Ship Research 9 , 1-8 (1965)

WEINBLUM , G.P. : The thrust deduction . Journal ASNE 63 , 363 - 380 (1951) .

YAMAZAKI , R. : Introduction to propulsion of ships in calm seas (in Japanese) . Journal of Seibu Zosen Kai 33 , 177 - 196 (1967) .

* * *

ADDITIONAL REFERENCES

Note : - References not belonging by virtue of their subject matter into the foregoing Bibliography but cited in our text for some specific reason are listed below .

BURRILL , L.C. : Propeller Cavitation Committee Report . Proceedings ITTC 13 , 353 -355 (1960) .

EGGERS, K.W.H., SHARMA , S.D. , and WARD , L.W. : An assessment of some experimental methods for determining the wavemaking characteristics of a ship form . Transactions SNAME 75 ,112 - 144 (1967) .

GRADSHTEYN , I.S., and RYZHIK , I.M. : Table of Integrals , Series and Products . Academic Press , New York and London (1965) .

HASKINS , E.W. : Calculation of design data for moderately loaded propellers by means of induction factors . NSRDC Report N° 2380 (1967) .

HAVELOCK , T.H. : The theory of wave resistance. Proceedings of Royal Society (A) 138 , 339-348 (1932)

HESS , J.L. , and SMITH , A.M.O. : Calculation of non-lifting potential flow about arbitrary three - dimensional bodies . Douglas Aircraft Co. Report E.S. 40622 (1962) .

HOUGH , G.R. , and ORDWAY, D.E.: The generalized actuator disk . Developments in Theoretical and Applied Mechanics 2 , 317-336 (1965) .

KÜCHEMANN , D. and WEBER , J. : Aerodynamics of Propulsion . Mc Graw-Hill Book Company , New York/Toronto/London (1953) .

LERBS , H. : Moderately loaded propellers with a finite number of blades and an arbitrary distribution of circulation . Transactions SNAME 60 , 73-123 (1952) .

LUFT , H. : Wave probes for model tanks . Hamburg Ship Model Basin Report N° F 46/67 , translated from German by W.H.Roth and S.D.Sharma , University of Michigan , Department of Naval Architecture and Marine Engineering (1968) .

LUNDE , J.K. : On the linearized theory of wave resistance for displacement ships in steady and accelerated motion . Transactions SNAME 59 , 25-85 (1951) .

MEYNE , K. : Experimental and theoretical considerations on scale effect in propeller model tests (in German) . Hamburg Ship Model Basin Report N° 1361 (1967) .

MICHELL , J.H.: The wave resi stance of a ship . Philosophical Magazine 45 , 106-123 (1898) .

ÖSTERGAARD , C. : On computer-aided propeller design . The University of Michigan , Department of Naval Architecture and Marine Engineering Report N° 88 (1970) .

ÖSTERGAARD , C. , KRUPPA , C., and LESSENICH , J. : Contribution to problems of propeller design (in German) . Schiff und Hafen 23 , 531-538 (1971) .

PROHASKA , C.W. : A simple method for the evaluation of the form factor and the low speed wave resistance . Proceedings ITTC 11 , 65-66 (1960) .

SHARMA , S.D.: An attempted application of wave analysis techniques to achieve bow-wave reduction . Proceedings of Symposium on Naval Hydrodynamics 6 , 731-773 (1966) .

SHARMA , S.D. : Some results concerning the wavemaking of a thin ship . Journal of Ship Research 13 , 72-81 (1969) .

SHIBA , H. : Air-drawing of marine propellers . Transportation Technical Research Institute of Japan , Report N° 9 (1953) . English translation published by Unyu-Gijutsu Kenyujo , Tokyo , Japan .

WEHAUSEN , J.V. , and LAITONE , E.V. : Surface Waves . Encyclopedia of Physics 9 , 446-814 (1960) Springer Verlag, Berlin/Göttingen/Heidelberg .

APPENDIX A

EXPERIMENTAL PROCEDURES

All hull and propeller model experiments were conducted in the towing tank of the Ship Hydrodynamics Laboratory of the University of Michigan following essentially standard test procedures. Some of the more interesting, but less obvious details are documented here for the sake of record.

A.1. Hull Resistance Test

The University of Michigan ship model No. UM 1201, built out of wood to the shape and size determined by Equations (3) through (5), without appendages was used for the hull resistance test. An unusually high freeboard (equal to full draft) was provided to enable testing at high Froude numbers up to $F_n = 0.5$. Circular cylindrical studs of 1/8 inch diameter and 1/8 inch height were fitted at 5/8 inch spacing center-to-center along the entire girth of station No. 1 (that is 0.05 L abaft of the vertical stem) to stimulate turbulence.

Departing from standard practice, the model was almost rigidly attached to the towing carriage by means of a three-point system of vertical supporting rods in addition to the usual grasshopper type anti-yaw guides at the two ends. This constraint was necessitated by the marginal transverse stability of the model and by the desire to preclude dynamic trim and sinkage for the ease of comparison with theory. The model was correctly weighted before making the connections, and static draft, heel and trim were verified before and after each test.

The resistance was measured by means of tare weights and a horizontal load cell built into a floating beam arrangement between the model and the carriage. Carriage speed was measured from wheel contacts and displayed on a calibrated digital counter. The speed range was extended up to $V_m = 9.75$ ft/sec (about $F_n = 0.45$), which was the highest attainable within the limitations imposed by tank length, model freeboard, and instrumentation.

A.2. Propeller Performance Test

The Hamburg Ship Model Basin model propeller No. HSVA 1222 with a standard nose fairing piece as shown in Fig. 2 was used for the propeller performance tests in open water. The propeller material is bronze.

The test procedure was to keep a constant rate of revolution and measure thrust and torque at various speeds of advance so as to cover the entire range of advance coefficient from the bollard condition ($J = 0$) up to the zero thrust condition ($J \approx P/D$). A standard Kempf & Remmers propeller dynamometer was used. The measured torque was corrected for bearing friction determined under identical test conditions with the propeller replaced by a dummy hub. No "dummy" hub correction" was applied to the measured thrust.

The Reynolds number for open water propeller test is conventionally defined as

$$(R_n)_{0.7R_P} = \frac{nD^2}{\nu} \left(\frac{c}{D}\right)_{0.7R_P} \sqrt{J_D^2 + (0.7\pi)^2}$$

with the design advance coefficient J_D usually approximated by $0.75\ P/D$. Given the propeller geometry

$$D = 0.2\ \text{m}, (c/D)_{0.7R_P} = 0.328\ , \quad P/D = 1$$

and our test conditions

$$n = 11\ \text{rps}^* \qquad t = 69°\text{F} \quad \nu = 0.9904 \cdot 10^{-6}\ \text{m}^2/\text{s}$$

it is seen that the Reynolds number was about $3.4 \cdot 10^5$. This might appear to be barely sufficient to avoid scale effects due to laminar flow. However, we obtained satisfactory agreement with previous tests run at the Hamburg Ship Model Basin at a Reynolds number of $3.6 \cdot 10^5$. By contrast, a test series run at the Institut für Schiffbau in Hamburg with the same propeller at a Reynolds number of $6.0 \cdot 10^4$ showed systematic scale effect at advance coefficients $J \leq 0.6$, cf. report by Meyne (1967).

A.3. Self-Propulsion Test

Special care was taken in the self-propulsion tests to ensure that test conditions were identical to those of hull resistance and propeller performance tests. The model was constrained in the same fashion as in the resistance test and the towing force was measured by the same instrumentation used for resistance measurements. The model propeller was driven by an electric motor at predetermined rate of revolutions and thrust and torque were measured by the same dynamometer used for the open water tests. A streamlined tail fairing

---

* This was the highest rate of revolutions possible without overloading the propeller dynamometer in the bollard condition.

piece (see Fig. 2) was fitted to the propeller hub. The measured torque was corrected for bearing friction determined by replacing the propeller temporarily by a dummy hub. No "dummy hub correction" was applied to the measured thrust.

The self-propulsion points were determined by the so-called British method, i. e. for each test run the towing speed and propeller rate of revolutions were preset while thrust, torque and residual towing force were the quantities to be measured when the steady state condition had been reached. For each Froude number investigated, five to eight test runs at the same towing speed but varying rates of revolution were conducted to cover a wide range of propeller loading around the ship self-propulsion point (and usually extending up to and beyond the model self-propulsion point).

There was some indication (a characteristic knocking sound familiar from the previous open water tests) of mild ventilation at the highest propeller loadings encountered in the self-propulsion tests. However, there was no visible effect on the measured thrust and torque values.

A. 4. Wake measurement

A set of standard Kempf & Remmers four-bladed wake wheels was used to measure the nominal wake in the propeller plane behind the hull in both forward and reverse motion. The diameters of the wheels available ranged from 40 to 220 mm in steps of 20 mm. The wheels were designed to yield directly the circumferential average of the axial flow velocity at the wheel radius. There was provision for turning the wheels around by 180 deg on their axis to ensure that the direction of flow relative to the blades was the same for both forward and reverse motions of the model (thus requiring only one set of calibrations).

The wheels were first calibrated in open water at a submergence of 150 mm (identical to that used for the model wake measurements) by means of a special towing device also supplied by the manufacturer. In principle, the calibration curves (i. e. wheel rate of revolution as a function of towing speed) should have been linear. In practice, a few wheels showed pronounced nonlinearities and even mild discontinuities at some speeds, presumably due to flow instabilities. However, all calibrations were highly repeatable.

For the actual wake measurements, the wheel towing device was mounted rigidly to the inside of the model with only its axis projecting out of the stern tube on to which each respective wake wheel

was mounted at the appropriate propeller clearance (45 mm from wheel center to the vertical stem profile). Every measurement was repeated at least once.

It has been noted elsewhere that the measured wake in both forward and reverse motion showed somewhat erratic undulations at the outer radii (see Fig. 6 and 7). This could possibly be blamed on the method of measurement. We had no way of establishing just how accurately the uniform flow calibrations could be relied upon for determining the circumferential averages of a varying axial velocity in a complex nonuniform flow involving significant circumferential and radial components.

A.5. Wave Measurement

A stationary wave probe was mounted at a point about midway along the length of the towing tank and at a fixed transverse distance y_o = 605 mm from the center plane of the model (which coincided nearly with the center plane of the tank itself). Hence, a time record of local wave height at the probe, while the model passed by, was obviously equivalent to a longitudinal cut $z = \zeta(x, y_o)$ through the steady wave pattern of the model in a coordinate system $Oxyz$ moving with the model.

A thin light beam was set up across the tank at a known fixed distance (x_1 = 336 mm) upstream of the probe. During the run a shutter affixed to the model at a known fixed distance (x_s = 2933 mm) forward of the midship section interrupted the light beam and generated an event signal marking the point $x = x_s - x_1$ on the wave record, thus defining the coordinate origin.

The wave probe itself was of the conductance wire type adapted from the HSVA design of Luft (1968) to match the available Sanborn carrier frequency preamplifiers. The circuit output was fed into one channel of a Sanborn strip chart recorder. The overall sensitivity was set at 6 to 9 mm deflection per inch of wave height so as to produce full scale deflection at the measured wave peaks. Wave height records were manually read off at about 350 points at equal time intervals Δt = 0.03 sec, that is at a step size $\Delta x = -V \Delta t$, and key-punched on IBM cards. All further analysis was done by computer programs.

It should be noted that at the highest Froude number investigated the length of useful record (taken before running into tank wall reflection) was not really adequate to establish with confidence the asymptotic character of the wave profile behind the model which is needed for the application of a truncation correction (see Fig. 16). However, this was due to a purely geometrical constraint resulting

from the given ratio of model length to tank width, so there was little we could do about it.

APPENDIX B

WAVEMAKING CALCULATIONS

All calculations concerning the wavemaking of the hull and the propeller were based on the strictly linearized theory and therefore involved the usual assumptions of irrotational flow, infinitesimal wave heights etc., see e.g. Lunde (1951) or Wehausen and Laitone (1960). The following is essentially a compilation of the important formulas used in the present study without attempting to give complete proofs o derivations.

B.1. Nondimensional Notation

Throughout this Appendix a special nomenclature particularly adapted to the analysis of steady-state gravity-wave problems will be used. This differs from the nomenclature in the rest of the report only in that all * dimensional variables have been consistently rendered dimensionless by reference to a set of three fundamental quantities, namely the acceleration due to gravity $\underline{g}$, water density $\underline{\rho}$, and ship speed $\underline{V}$. Thus if $\underline{Q}$ is any dimensional quantity involving only the units of mass, length and time, its nondimensional counterpart Q is defined simply as

$$Q = \underline{Q} \,/\, \underline{g}^{\alpha}\,\underline{\rho}^{\beta}\,\underline{V}^{\gamma} \tag{B1}$$

where the choice of α, β and γ is obviously unique. For instance,

$$\begin{aligned} x &= \underline{x} \,/\, \underline{g}^{-1}\,\underline{V}^{2}\,, \qquad \ell = \underline{\ell} \,/\, \underline{g}^{-1}\underline{V}^{2} \\ \sigma &= \underline{\sigma} \,/\, \underline{V} \\ R_W &= \underline{R_W} \,/\, \underline{g}^{-2}\,\underline{\rho}\,\underline{V}^{6} \end{aligned} \tag{B2}$$

where x is the longitudinal coordinate, ℓ the half-length of hull (now identical to the dimensionless speed-length parameter γ_o used elsewhere in the report), σ the density of a surface distribution of sources, R_W the wavemaking resistance etc. With this notation the quantities ρ, V and g can be formally eliminated from the analysis, thus leading to a considerable simplification of many formulas without any essential loss of generality.

---

* Where dimensional variables are nevertheless required, e.g. for purposes of definition, they are identified by underlining to avoid any possible ambiguity.

B.2. Source Representations

All wavemaking calculations were based on the Havelock (1932) theory of sources moving under a free surface . It was therefore necessary to first define mathematical representations of the hull and propeller by means of source distributions .

The standard first order (linearized) approximation in thin ship theory is to represent the hull by a center-plane source distribution of density

$$\sigma(x, z) = - (\partial f / \partial x) / 2\pi \tag{B3}$$

where

$$|y| = f(x, z) \geq 0 \tag{B4}$$

defines the hull surface (see Fig. 1) . The results obtained by Havelock's theory are then identical to those of Michell (1898) .

The family of hull forms considered in the present study is defined by

$$y = \pm b \left\{ 1 - (x/\ell)^{2m} \right\} \left\{ 1 - \epsilon (-z/T)^{n} \right\} \tag{B5}$$

where b , ℓ and T are half-beam , half-length and draft respectively, while ϵ is a flat-bottom parameter that can vary from $\epsilon = 0$ (wall sided hull with completely flat bottom) to $\epsilon = 1$ (sharp keeled hull with completely curved bottom) . By virtue of Equations (B3, B4) this form is represented by the polynomial source distribution

$$\sigma(x, z) = (m/\pi) (b/\ell) (x/\ell)^{2m-1} \left\{ 1 - \epsilon (-z/T)^{n} \right\} \tag{B6}$$

over the rectangular plane

$$-\ell \leq x \leq \ell , \quad y = 0 \quad -T \leq z \leq 0 \tag{B7}$$

Following Dickmann (1938) the propeller can be represented by a continuous distribution of sources of (negative) density $\sigma(R, \Theta)$ over the propeller disk

$$x = x_P , \quad R_H \leq R \leq R_P , \quad -\pi \leq \Theta \leq \pi \tag{B8}$$

where R, Θ are polar coordinates

$$y = R \cos \Theta , \quad z = z_P + R \sin \Theta \tag{B9}$$

the point $(x_p, 0, z_P)$ is the geometrical center of the propeller and

R_H , R_P are the hub and tip radius of the propeller respectively . There is no simple way of relating the source strength directly to propeller geometry , speed and rate of revolutions . However , using momentum theory , Dickmann derived two useful approximations connecting propeller source strength to thrust loading , one of which yields a uniform sink disk of source density

$$\sigma(R, \Theta) = -\left(\sqrt{1+C_{Th}} - 1\right)/4\pi$$

over

$$x = x_P, \quad R_H \leq R \leq R_P, \quad -\pi \leq \Theta \leq \pi \qquad \text{(B10)}$$

and the other a discrete point sink of source strength

$$-\left(\sqrt{1+C_{Th}} - 1\right)(R_P^2 - R_H^2)/4 \text{ at } (x_P, 0, z_P) \qquad \text{(B11)}$$

where

$$C_{Th} = 2\ \underline{T}\ /\ \underline{\rho}\ \underline{V}^2\ \pi\ (\underline{R}_P^2 - \underline{R}_H^2) \qquad \text{(B12)}$$

is the thrust loading coefficient based on disk area (excluding the hub).

In addition to the above we have also used the following alternative relation due to Hough and Ordway (1965) :

$$\sigma\ (R, \Theta) = -\ Z\ G\ /\ 4\ J \qquad \text{(B13)}$$

where

$$G(R) = \underline{\Gamma}(\underline{R})\ /\ 2\ \pi\ \underline{V}\ \underline{R}_P \qquad \text{(B14)}$$

is a non dimensional function representing the radial distribution of bound circulation $\underline{\Gamma}$ along each blade of a Z bladed propeller at advance coefficient $J = \underline{V}\ /\ 2\ \underline{n}\ \underline{R}_P$. Here the source density is a function of radius R , but still independent of angle Θ . Since the circulation is obtained numerically from a computer program at discrete radii , σ will generally be defined merely as a tabulated function. Unless analytical interpolation is used for further processing , it is tantamount to a radially stepped sink disk .

A certain ambiguity arises in interpreting the speed $\underline{V}$ in the above relations when the propeller is operating in a wake behind the hull . We believe that the physical sink strength of the propeller should be determined by the local speed of advance $\underline{V}_A$ while its wave pattern must be characterized by the speed $\underline{V}$ relative to the fluid at infinity . Hence the corresponding relations in the presence of an effective axial wake w_E become

$$\sigma\,(R\,,\,\Theta) \;=\; -\,\left(\sqrt{1 + C_{Th}} \;-\; 1\right)\left(1 \;-\; w_E\right)/\,4\pi$$

$$C_{Th} \;=\; 2\;\underline{T}\;/\;\underline{\rho}\;\underline{V}_A^{\,2}\;\pi\,(\underline{R}_P^{\,2} - \underline{R}_H^{\,2}) \qquad \text{(B15)}$$

in the Dickmann approximation , and

$$\sigma(R\;,\;\Theta) \;=\; -\;Z\;\underline{n}\;\underline{\Gamma}\,(R)\;/\;\underline{V}^2\;\left\{1 \;-\; w_E(R)\right\} \qquad \text{(B16)}$$

in the Hough and Ordway approximation . In either case , the left hand side is the appropriate dimensionless source density σ to be used in the subsequent calculations of wavemaking and thrust deduction .

It may be noted that source disk representations of the propeller are only useful for calculating the induced flow field (outside the slipstream) . For calculating propeller performance (thrust and torque) resort must be taken to the correct vortex model . In principle , it is possible to calculate also flow field and wavemaking directly from the vortex model , cf. e.g. Nakatake (1968) . However , the increased computational effort is hardly justified in view of the other approximations in the analysis.

B. 3. Free-Wave Spectrum

A useful description of the wavemaking characteristics of a ship is provided by its free-wave spectrum as defined for example in Eggers , Sharma and Ward (1967) . Given an arbitrary source distribution σ (x, y, z) over a domain D , its complex-valued free-wave spectrum (as a function of transverse wave number u) becomes

$$G\,(u) + iF(u) \;=\; 8\pi\left\{\frac{1+v}{v}\right\}\int_D \sigma(x,\;y,\;z)\;\exp\;\left\{s^2\,z + i(sx+uy)\right\}\,dD \qquad \text{(B17)}$$

where

$$v \;=\; \sqrt{1+4u^2} \qquad \text{and} \qquad s \;=\; \sqrt{(1+v)/2} \qquad \text{(B18)}$$

The significance of the free-wave spectrum lies in its ability to yield a simple description of the asymptotic wave pattern behind the ship .

For $x \to -\infty$;

$$\zeta(x, y) = \frac{1}{4\pi} \int_{-\infty}^{\infty} \left\{ F(u) \sin(sx+uy) + G(u) \cos(sx+uy) \right\} du \tag{B19}$$

Here s and u can be interpreted as the circular wave numbers induced by a free plane wave (moving with the ship) in the x and y direction respectively . Hence F(u) and G(u) are called the sine and cosine components of the spectrum and its amplitude is given by

$$E(u) = \sqrt{F^2(u) + G^2(u)} \tag{B20}$$

The phase of the free-wave spectrum depends on the choice of the coordinate origin but its amplitude does not . The associated wavemaking resistance

$$R_W = \frac{1}{16\pi} \int_{-\infty}^{\infty} E^2(u) \frac{v}{1+v} du \tag{B21}$$

is determined solely by the amplitude spectrum .

By virtue of formulas (B6) and (B17) the free-wave spectrum of the hull becomes

$$G_H(u) + iF_H(u) = 8\pi \left\{ \frac{1+v}{v} \right\} \int_{-\ell}^{\ell} dx \int_{-T}^{0} dz \left[\frac{m}{\pi} \left\{ \frac{b}{\ell} \right\} \left\{ \frac{x}{\ell} \right\}^{2m-1} \left\{ 1 - (-z/T)^n \right\} \cdot \exp(s^2 z + isx) \right] \tag{B22}$$

or after some simplification

$$G_H(u) = 0$$
$$F_H(u) = 16 \frac{b}{v} F^{(1)}(m, s\ell) F^{(2)}(n, \epsilon, Ts^2) \tag{B23}$$

with

$$F^{(1)}(m,p) = m\int_{-1}^{1} \xi^{2m-1}\sin(\xi p)\,d\xi$$

$$F^{(2)}(n,\epsilon,q) = F^{(3)}(0,q) - \epsilon F^{(3)}(n,q)$$

$$F^{(3)}(n,q) = q\int_{0}^{1} \zeta^{n}\exp(-\zeta q)\,d\zeta \qquad \text{(B24)}$$

The integrals $F^{(1)}$ and $F^{(3)}$ can be solved in closed form [see formulas 2.6334 and 2.3212 in Gradshteyn and Ryzhik (1965)] or evaluated by recurrence formulas :

$$F^{(1)}(0,p) = 0,$$

$$F^{(1)}(m,p) = 2m\left\{(2m-1)\left[\sin(p)-F^{(1)}(m-1,p)\right]/p-\cos(p)\right\}/p$$

$$F^{(3)}(0,q) = 1-\exp(-q),$$

$$F^{(3)}(n,q) = -\exp(-q) + nF^{(3)}(n-1,q)/q \qquad \text{(B25)}$$

Similarly , the free-wave spectrum of the propeller can be written as

$$G_P(u)+iF_P(u) = 8\pi\left\{\frac{1+v}{v}\right\}\int_{R_H}^{R_P} dR \int_{-\pi}^{\pi} R\,d\theta \left[\sigma(R,\theta)\exp\left\{s^2(z_P+R\sin\theta) + i(sx_P + uR\cos\theta)\right\}\right] \qquad \text{(B26)}$$

If the propeller source distribution σ is a function of radius only , then this simplifies by virtue of transverse symmetry to

$$G_P(u)+iF_P(u) = 8\pi\left\{\frac{1+v}{v}\right\}\exp(s^2z_P+isx_P)\int_{R_H}^{R_P} R\sigma(R)\,dR \int_{-\pi}^{\pi}\exp(s^2R\sin\theta)x \cos(uR\cos\theta)d\theta$$

$$= 16\pi^2\left\{\frac{1+v}{v}\right\}\exp(s^2z_P+isx_P)\int_{R_H}^{R_P} R\sigma(R)I_o(sR)\,dR \qquad \text{(B27)}$$

where I_o is the modified Bessel function of zero order [see Gradshteyn and Ryzhik (1965), formula 3.9372]. This last integral can be easily evaluated for any numerically defined function $\sigma(R)$.

B.4. Wavemaking Resistance

The individual wavemaking resistances of the bare hull R_{WH} and the free running propeller R_{WP} are found directly by substituting the appropriate free-wave spectra (B23) and (B27) into the general formula (B21).

$$R_{WH} = \frac{1}{8\pi} \int_0^\infty \left\{ \frac{16\,b}{v} F^{(1)}(m, s\ell) F^{(2)}(n, \epsilon, Ts^{(2)}) \right\}^2 \frac{v}{1+v}\, du \qquad (B28)$$

$$R_{WP} = \frac{1}{8\pi} \int_0^\infty \left[16\pi^2 \left\{ \frac{1+v}{v} \right\} \exp(s^2 z_P) \int_{R_H}^{R_P} R\,\sigma(R)\, I_o(sR)\, dR \right]^2 \frac{v}{1+v}\, du \qquad (B29)$$

To calculate the wavemaking resistance R_{WT} of the total system hull with propeller one can use the principle of linear superposition of free-wave spectra, that is

$$G_T(u) = G_H(u) + G_P(u)$$
$$F_T(u) = F_H(u) + F_P(u) \qquad (B30)$$

provided both spectra are expressed in the same coordinate system. The general formula (B21) can then be applied to the total spectrum

$$E_T(u) = \sqrt{\left\{ G_T^2(u) + F_T^2(u) \right\}}$$

Evidently, in general

$$R_{WT} \neq R_{WH} + R_{WP} \qquad (B31)$$

and the difference

$$R_{WT} - R_{WH} - R_{WP} = \frac{1}{8\pi} \int_0^\infty 2 \left\{ G_H(u) G_P(u) + F_H(u) F_P(u) \right\} \frac{v}{1+v} du \tag{B32}$$

is a measure of the interference between the wave patterns of the hull and the propeller . The interaction term can be positive or negative .

B. 5. Wave Flow due to Hull

The perturbation flow induced at the propeller plane by the motion of the hull under the free surface can also be calculated by thin ship theory . We start with the Green's function of the problem as defined by Equation (63) of Eggers , Sharma and Ward (1967) :

$$G(x, y, z, x', y', z') = -\frac{1}{r_1} + \frac{1}{r_2}$$

$$-\mathrm{Re}\frac{2}{\pi} \int_{-\infty}^{\infty} du \int_{|u|}^{\infty} \frac{\exp\left[-w|x-x'| + iu(y-y') + i\sqrt{w^2-u^2}(z+z')\right]}{\sqrt{w^2-u^2} - iw^2} dw$$

$$+\mathrm{Im}\frac{1}{2} \left\{ 1 - \mathrm{sgn}(x-x') \right\} \int_{-\infty}^{\infty} \frac{4s}{v} \exp\left\{ is(x-x') + iu(y-y') + s^2(z+z') \right\} du \tag{B33}$$

with

$$r_1^2 = (x-x')^2 + (y-y')^2 + (z-z')^2$$

$$r_2^2 = (x-x')^2 + (y-y')^2 + (z+z')^2$$

This is the velocity potential due to a point source of unit strength at (x', y', z') . Integration over the hull source distribution (B6) yields the velocity potential of the hull $\varphi(x, y, z)$, and subsequent differentiation with respect to x, y, z yields the components of perturbation velocity φ_x , φ_y , φ_z . It is convenient to break up each expression into four parts corresponding to the four terms of the Green's function (B33) . For instance

$$\varphi_x(x, y, z) = \varphi_x^{(1)} + \varphi_x^{(2)} + \varphi_x^{(3)} + \varphi_x^{(4)} \tag{B34}$$

with

$$\varphi_x^{(1)}(x,y,z) = \int_{-\ell}^{\ell} dx' \int_{-T}^{0} \frac{bm}{\pi \ell} \left\{\frac{x'}{\ell}\right\}^{2m-1} \left\{1 - \epsilon(-z'/T)^n\right\} \cdot \tag{B34}$$

$$\frac{(x-x')}{\left\{(x-x')^2 + (y-y',^2 + (z-z')^2\right\}^{3/2}} \, dz' \tag{B35}$$

etc . It turns out that in the resulting integrals the x' , z' integrations can be carried out in closed form , while the u , w integrations must be performed by numerical quadrature .

It takes some algebra to reduce the expressions to a form suitable for computer programming . We will show this for one example . Substitute in (B35)

$$\xi = x/\ell \ , \quad \xi' = x'/\ell \ , \quad \eta = y/\ell \ , \quad \zeta = z/\ell \ , \quad \zeta' = z'/\ell \ , \quad \tau = T/\ell \tag{B36}$$

Then

$$\varphi_x^{(1)} = \frac{b}{\ell}\frac{m}{\pi} \int_{-1}^{1} d\xi' \int_{-\tau}^{0} \frac{(\xi')^{2m-1}\left[1 - \epsilon(-\zeta'/\tau)^n\right](\xi - \xi')}{\left\{(\xi - \xi')^2 + \eta^2 + (\zeta - \zeta')^2\right\}^{3/2}} \, d\zeta' \tag{B37}$$

Now put

$$\bar{\xi} = \xi - \xi' \qquad \bar{\zeta} = \zeta - \zeta' \tag{B38}$$

Then

$$\varphi_x^{(1)} = \frac{b}{\ell}\frac{m}{\pi} \int_{\xi+1}^{\xi-1} d\bar{\xi} \int_{\zeta+\tau}^{\zeta} \frac{(\xi - \bar{\xi})^{2m-1}\left[1 - \epsilon(-1/\tau)^n(\zeta - \bar{\zeta})^n\right]}{\left\{\bar{\xi}^2 + \eta^2 + \bar{\zeta}^2\right\}^{3/2}} \, d\bar{\zeta}$$

Now factor out the constants and apply the binomial theorem to get

$$\varphi_x^{(1)} = \frac{b}{\ell}\frac{m}{\pi}\left[\left\{\sum_{i=0}^{2m-1} (-)^i \binom{2m-1}{i} \xi^{2m-1} E_{i+1,0}\right\}\right.$$

../..

$$-\epsilon \left\{ -\frac{1}{\tau} \right\}^{n} \sum_{i=0}^{2m-1} \sum_{j=0}^{n} (-)^{i+j} \binom{2m-1}{i} \binom{n}{j} \xi^{2m-1} \zeta^{n-j} E_{i+1,j} \Big]$$

where

$$E_{i,j}(\xi, \eta, \zeta, \tau) = \int_{\xi+1}^{\xi-1} d\bar{\xi} \int_{\zeta+\tau}^{\zeta} d\bar{\zeta} \frac{\bar{\xi}^{i} \bar{\zeta}^{j}}{\left\{ \bar{\xi}^2 + \eta^2 + \bar{\zeta}^2 \right\}^{3/2}} \tag{B39}$$

This double integral $E_{i,j}$ has a closed form solution (for constant limits of integration) amenable to numerical evaluation by a recurrence formula . (The authors are indebted to Drs K. Eggers and H. Kajitani for this suggestion) . Consider the indefinite integral

$$E_{i,j}(x, y, z) = \iint \frac{x^{i} z^{j}}{r^3} dx\, dz , \quad r = \sqrt{x^2 + y^2 + z^2} \tag{B40}$$

By repeated use of formula 2.2631 from Gradshteyn and Ryzhik (1965) it can be shown that

$$E_{i,j} = \frac{1}{i+j-1} \left\{ j x^{i-1} E_{1,j} - \left(i-1 \right) \left(z^{j+1} E_{i-2,1} + y^2 E_{i-2,j} \right) \right\}$$

$$= \frac{1}{i+j-1} \left\{ i z^{j-1} E_{i,1} - \left(j-1 \right) \left(x^{i+1} E_{1,j-2} + y^2 E_{i,j-2} \right) \right\} \tag{B41}$$

Hence, starting from the four fundamental solutions

$$E_{0,0} = -\frac{1}{y} \arctan (yr/xz)$$

$$E_{0,1} = -\ln (x+r)$$

$$E_{1,0} = -\ln (z+r)$$

$$E_{1,1} = -r \tag{B42}$$

any element $E_{i,j}$ can be constructed by recurrence , for example

$$E_{2,2} = -\frac{xzr}{3} + \frac{x^3}{3} \ln(z+r) + \frac{z^3}{3} \ln(x+r) + \frac{y^3}{3} \arctan(xz/yr)$$

$$E_{3,3} = \frac{r}{5}\left\{\frac{2}{3} y^2 (x^2+z^2-2y^2) + 2(x^4+z^4) - x^2 z^2\right\} \tag{B43}$$

For a computer algorithm , however , it is not necessary to develop the analytical expressions explicitly since the recurrence formula (B41) can be applied numerically to each of the four summands (corner values) of the definite integral (B39) .

A similar analysis can be applied to the second term of (B34) , but but the final result is obtained more easily by considerations of symmetry :

$$\varphi_x^{(2)}(x, y, z) = -\varphi_x^{(1)}(x, y, -z) \tag{B44}$$

Restricting our attention to field points behind the hull ($x < -1$) , the third and fourth terms of (B34) can be simplified as follows .

$$\varphi_x^{(3)} = -\mathrm{Re}\frac{2}{\pi}\int_{-\infty}^{\infty} du \int_{|u|}^{\infty} dw \int_{-1}^{1} dx' \int_{-T}^{0} dz' \left[\frac{b}{\ell}\frac{m}{\pi}\left\{\frac{x'}{\ell}\right\}^{2m-1}\left\{1-\epsilon(-z'/T)^n\right\}\cdot \frac{w \exp\left[w(x-x') + iuy + i\sqrt{w^2-u^2}\,(z+z')\right]}{\sqrt{w^2-u^2}\,\sqrt{-iw^2}}\right]$$

$$= -\frac{b}{\ell}\frac{4}{\pi}\int_0^{\infty} I(u, x, z, \ell, m, n, \epsilon, T)\cos(uy)\, du \tag{B45}$$

where

$$I = -\frac{\exp[u(x+\ell)]}{x+\ell}\int_0^{\infty} \frac{G^{(1)}(m, w\ell)}{\sqrt{w^2-u^2}}\,\mathrm{Re}\left\{\frac{\exp(iz\sqrt{w^2-u^2})\,G^{(2)}(n, \epsilon, T\sqrt{w^2-u^2})}{\sqrt{w^2-u^2}\,\sqrt{-iw^2}}\right\}\int \exp(-t)\, dt \tag{B46}$$

with $t = -(w-u)(x+\ell)$ and

$$G^{(1)}(m,p) = \frac{m}{\pi} p \exp(-p) \int_{-1}^{1} \xi^{2m-1} \exp(-p\xi)\, d\xi$$

$$G^{(2)}(n, \epsilon, q) = G^{(3)}(0,q) - \epsilon G^{(3)}(n,q)$$

$$G^{(3)}(n,q) = p \int_{0}^{1} \zeta^{n} \exp(-iq\zeta)\, d\zeta \qquad \text{(B47)}$$

The integrals $G^{(1)}$ and $G^{(3)}$ can be solved in closed form or evaluated by recurrence formulas :

$$G^{(1)}(0,p) = 0,$$

$$G^{(1)}(m,p) = m\left\{(2m-1)\left[(1-e^{-2p})/\pi + 2G^{(1)}(m-1,p)/p\right]/p - (1+e^{-2p})/\pi\right\}$$

$$G^{(3)}(0,q) = (1-e^{-iq})/i$$

$$G^{(3)}(n,q) = \left\{nG^{(3)}(n-1,q) - e^{-iq}\right\}/i \qquad \text{(B48)}$$

The integral I has an exponentially decaying factor in the integrand and is therefore suited to Gauss-Laguerre numerical quadrature . The real part in (B46) need not be evaluated analytically , if complex arithmetic may be used in the program .

Similarly , for $x < -\ell$:

$$\varphi_x^{(4)} = \mathrm{Im} \int_{-\infty}^{\infty} du \int_{-\ell}^{\ell} dx' \int_{-T}^{0} dz' \left[\frac{b}{\ell} \frac{m}{\pi} \left\{\frac{x'}{\ell}\right\}^{2m-1} \left\{1 - \epsilon(-z'/T)^{n}\right\} 4i \frac{s^2}{v} \cdot \exp\left\{is(x-x') + iuy + s^2(z+z')\right\}\right]$$

$$= \frac{8b}{\pi} \int_{0}^{\infty} \left\{\frac{\exp(s^2 z)}{v} \sin(sx)\, F^{(1)}(m, s\ell)\, F^{(2)}(n, \epsilon, s^2 T)\right\} \cos(uy)\, du \qquad \text{(B49)}$$

where $F^{(1)}$ and $F^{(2)}$ are the functions already defined in (B24) . The integrals (B45) and (B49) can be truncated at a sufficiently large value of u and approximated by the known recurrence formulas for Fourier series . Suppose

$$C + iS = \int_0^{\infty} I(u) \left\{ \cos(uy) + i \sin(uy) \right\} du$$

$$\approx \Delta u \sum_{\nu=0}^{N} I(u_\nu) \left\{ \cos(u_\nu y) + i \sin(u_\nu y) \right\} \epsilon_\nu \qquad \text{(B50)}$$

with

$$u_\nu = \nu \Delta u, \quad \epsilon_\nu = \frac{1}{2} \text{ for } \nu = 0 , \quad \epsilon_\nu = 1 \text{ for } \nu \neq 0$$

where Δu is a suitable step size and N is sufficiently large . Then

$$C = \frac{1}{2} (U_o - U_2) \Delta u$$

and

$$S = U_1 \sin(y \Delta u) \Delta u \qquad \text{(B51)}$$

where the U_ν are defined by the sequence

$$U_{N+1} = U_{N+2} = 0$$

$$\nu = N, \; N-1 \; , \; . \; . \; . \; , \; 0 :$$

$$U_\nu = I(u_\nu) + 2\cos(y \Delta u) \, U_{\nu+1} - U_{\nu+2} \qquad \text{(B52)}$$

This completes the wanted algorithm for all four terms of (B34) .

By our definition , φ_x evaluated in the propeller plane is identical to the total potential wake fraction , i.e. the sum of the so-called potential wake (zero Froude number effect) and the wave wake (finite Froude number effect) . Thus

$$w_p(R, \theta) + w_w(R, \theta) = \varphi_x(x, y, z) \qquad \text{(B53)}$$

if $x = x_P, \quad y = R \cos\theta , \quad z = z_P + R \sin\theta$

By evaluating φ_x at a sufficiently large number of field points the circumferential and disk averages of the theoretical wake can be estimated. Moreover, it can be shown that the zero Froude number wake, the infinite Froude number wake and the bow wake $(x > \ell)$ can also be derived from the four components of expression (B34)

$$F_n = 0: \quad w_w = 0, \quad w_p = \varphi_x^{(1)} - \varphi_x^{(2)} \tag{B54}$$

$$F_n = \infty: \quad w_p + w_w = \varphi_x^{(1)} + \varphi_x^{(2)} \tag{B55}$$

$$x > \ell: \quad \varphi_x(x,y,z) = \varphi_x^{(1)}(-x,y,z) + \varphi_x^{(2)}(-x,y,z) + \varphi_x^{(3)}(-x,y,z) \tag{B56}$$

This last quantity evaluated at $x = -x_p$ yields by virtue of longitudinal symmetry the desired theoretical wake in the propeller plane "behind" the hull in reverse motion.

B. 6. Wave Flow due to Propeller

In order to calculate the perturbation flow induced by the motion of the propeller under the free surface, we start with an alternative expression for the Green's function (B33), see formula (56) in Eggers, Sharma and Ward (1967):

$$G = -\frac{1}{r_1} + \frac{1}{r_2} + \mathrm{Re}\frac{2}{\pi}\int_{-\pi/2}^{\pi/2} \sec^2\theta \, d\theta \int_0^\infty \frac{\exp\left[k(z+z'+i\bar{\omega})\right]}{k-\sec^2\theta}\,dk + \mathrm{Im}\, 2\int_{-\pi/2}^{\pi/2} \sec^2\theta \exp\left[\sec^2\theta\,(z+z'+i\bar{\omega})\right] d\theta \tag{B57}$$

with $\bar{\omega} = (x-x')\cos\theta + (y-y')\sin\theta$ and r_1, r_2 as before. Differentiating with respect to x, and taking advantage of the symmetry in θ, we obtain

$$G_x(x-x', y-y', z, z') = \frac{x-x'}{r_1^3} - \frac{x-x'}{r_2^3} - \frac{4}{\pi}\int_0^{\pi/2} \sec\theta \, d\theta \cdot$$

$$\int_0^\infty \exp\left[k(z+z')\right] \sin\left[k(x-x')\cos\theta\right] \cos\left[k(y-y')\sin\theta\right] \frac{k\,dk}{k-\sec^2\theta}$$

(contd..)

$$+4\int_0^{\pi/2} \sec^3\theta \exp\left[(z+z')\sec^2\theta\right]\cos\left[(x-x')\sec\theta\right] \cos\left[(y-y')\tan\theta\sec\theta\right]d\theta \qquad (B58)$$

Since we are interested only in the flow induced by the propeller in its own plane (the so-called self-induced wake), we confine further analysis to the case $x = x' = x_P$. The first three terms of (B58) then vanish and in the last we substitute

$$u = \sec\theta\tan\theta, \quad v = \sqrt{1+4u^2}, \quad s = \sqrt{(1+v)/2}, \quad du/d\theta = sv \qquad (B59)$$

to get

$$G_x(0, y-y', z, z') = 2\int_0^{\infty} \exp\left[(z+z')s^2\right]\cos\left[(y-y')u\right]\frac{1+v}{v}\,du \qquad (B60)$$

Now integrating over the propeller source distribution σ (R) and taking advantage of its transverse symmetry, we get for the self-induced wake the following expression:

$$w_f(R,\theta) = \int_{R_H}^{R_P} dR' \int_{-\pi/2}^{\pi/2} G_x(0, y-y', z, z')\ \sigma(R')\,R'd\theta'$$

$$= 4\pi \int_0^{\infty}\left\{\frac{1+v}{v}\right\}\exp\left[(z+z_P)s^2\right]\left\{\int_{R_H}^{R_P} R'\sigma(R')\,I_o(sR')dR'\right\} \cos(uy)\,du \qquad (B61)$$

where the integral formula quoted after (B27) has been applied again. Since the function $\sigma(R')$ is in general not analytic, the R' integral must be evaluated by numerical quadrature (e.g. Simpson's rule) for suitable values $s(u_\nu)$ such that the u integral can be approximated by the recurrence formulas for Fourier series, see Equations (B50-B52).

By proper choice of the fields points $y = R\cos\theta$, $z = z_P + R\sin\theta$ the self-induced free-surface wake $w_f(R,\theta)$ can be calculated at suitable points (R_j, θ_k) on the disk, from which the circumferential average $w_f(R)$ and the disk average w_f can be obtained by numerical integration.

A useful check on the numerical accuracy of the calculated values of $w_f(R,\theta)$ is obtained by using them to determine the wave-making resistance of the propeller by virtue of Lagally's theorem [see Equation (11) of Eggers, Sharma and Ward (1967)]:

$$R_{WP} = 8\pi \int_{R_H}^{R_P} R \; \sigma(R) \int_{-\pi/2}^{\pi/2} w_f(R,\theta)\, d\theta \; dR \tag{B62}$$

Analytically, of course, this is identical to the more direct formula (B29) based on the free-wave spectrum. Numerically, we found that the differences were negigibly small for a reasonable step size $\Delta\theta \leq \pi/6$.

B.7. Thrust Deduction

We wish to calculate the force of thrust deduction, i.e. the augmentation of hull resistance due to propeller action. Let us call it $\delta_P R_{WH}$. Conceptually, the most direct approach would be to use Lagally's theorem, i.e.

$$\delta_P R_{WH} = 4\pi \int_{-\ell}^{\ell} dx \int_{-T}^{0} dz \; \left\{ \sigma(x,z)\, \varphi_x^P(x,0,z) \right\} \tag{B63}$$

This would seem to necessitate the explicit calculation of the longitudinal perturbation flow φ_x^P induced by the propeller on the center-plane of the hull $y = 0$, which is not quite easy due to the singular double integral in formula (B58). However, we will circumvent this difficulty by an indirect approach. Let us denote by $\delta_H R_{WP}$ the augmentation of propeller resistance due to hull action. Then again by Lagally's theorem

$$\delta_H R_{WP} = 8\pi \int_{R_H}^{R_P} dR \int_{-\pi/2}^{\pi/2} R \; d\theta \; \left\{ \sigma(R,\theta) \varphi_x^H(x_P, R, \theta) \right\} \tag{B64}$$

where φ_x^H now is the axial perturbation flow induced by the hull in the propeller plane, i.e. the wake as already defined by (B53). On the other hand, by virtue of previous definitions we have

$$R_{WT} = R_{WH} + R_{WP} + \delta_P R_{WH} + \delta_H R_{WP}$$

Hence,

$$\delta_P R_{WH} = R_{WT} - R_{WH} - R_{WP} - \delta_H R_{WP} \tag{B65}$$

where the sum of the first three terms as defined by (B32) is relatively easy to calculate . Thus we see that the calculation of thrust deduction requires no further effort beyond that already expended for the calculation of hull wake and the wavemaking resistance of hull alone , propeller alone and the total system hull with propeller . In particular, it is needless to calculate the flow induced by the propeller on the hull.

Note that $\delta_P R_{WH}$ is the total potential thrust deduction , i.e. the sum of the so-called "potential" component (zero Froude number effect) and the "wave" component (finite Froude number effect) . The thrust deduction fraction becomes

$$t_p + t_w = \delta_P R_{WH}/T_H$$

$$= (\delta_P R_{WH}/K_{TH})\ (V^2/gD)^2(V/nD)^2$$

$$= (\delta_P R_{WH}/K_{TH})\ (L/D)^2(F_n)^4(J_H)^2 \qquad \text{(B66)}$$

At zero Froude number , of course ,

$$R_{WT} = R_{WH} = R_{WP} = 0$$

and therefore

$$\delta_P R_{WH} = -\delta_H R_{WP} \qquad \text{(B67)}$$

Thus if we use the zero Froude number wake (B54) in (B64) to calculate $\delta_H R_{WP}$, we can determine the "potential" component of thrust deduction t_p from the simple principle of reprocity (B67) already exploited by Dickmann (1939)

It must be emphasized that the force $\delta_H R_{WP}$ apparently exerted on the propeller by the hull does not necessarily have a physical meaning since the source disk is an inappropriate model for calculating propeller forces . However , it is a perfectly valid mathematical artifice for a simple , although indirect , determination of the quantity $\delta_P R_{WH}$ which is a real force exerted on the hull due to propeller action, viz. the force of thrust deduction.

Incidentally, if the source strength is uniform over the disk, as in Equation (B15), the integral (B64) simplifies to

$$\delta_H R_{WP} = 4\pi^2 (R_P^2 - R_H^2)\, \sigma(R)\, (w_p + w_w) \tag{B68}$$

where w_p and w_w are the disk averages of the potential and wave wake respectively. Moreover, if only the potential component of thrust deduction is wanted, substituting from (B15) in (B68) and taking advantage of (B67) one obtains

$$t_p = -\delta_H \frac{R}{WP} / \frac{T}{H}$$

$$= \frac{2}{1 + \sqrt{1 + C_{Th}}} \left\{ \frac{w_p}{1 - w_T} \right\} \tag{B69}$$

This is slightly different from the classical result of Dickmann (1939), cf. his equation (15). However it agrees with Tsakonas' (1958) equation (12), except that he does not distinguish between the potential component w_p and the total wake w_T.

B.8. Wave Profile Analysis

The purpose of wave profile analysis was to establish the true or experimental free-wave spectrum (and associated wavemaking resistance) of the hull and propeller as opposed to the theoretical spectrum based on linearized source representations discussed in the previous sections. The longitudinal cut method of Sharma (1966) as described in Eggers, Sharma and Ward (1967) was used. The essential steps of the analysis are given below.

Let $z = \zeta(x, y_o)$ be a longitudinal cut through the wave pattern of the model as measured at a fixed transverse location $y = y_o$ in the coordinate system of Fig. 1. Define modified * Fourier transforms

$$C^*(s, y_o) + iS^*(s, y_o) = \int_{-\infty}^{\infty} \sqrt{s^2 - 1}\; \zeta(x, y_o) \exp(isx)\, dx \tag{B70}$$

---

* The asymptotic nature of the wave pattern behind a ship is such

$$x/|y| \longrightarrow -\infty \;:\quad \zeta(x, y) \simeq \exp(ix)/\sqrt{c - x}$$

that the modified Fourier transform remains finite for any s, while the ordinary Fourier transform becomes infinite at $s = 1$.

Then the free-wave spectrum of the model is given by

$$G(u) = \frac{4}{2s^2-1}\left\{C^*(s,y_o)\cos(uy_o) - S^*(s,y_o)\sin(uy_o)\right\}$$
$$F(u) = \frac{4}{2s^2-1}\left\{C^*(s,y_o)\sin(uy_o) + S^*(s,y_o)\cos(uy_o)\right\} \qquad \text{(B71)}$$

where $u = s\sqrt{s^2-1}$ in accordance with (B18). By applying this procedure separately to the model hull with and without propeller one can obtain the spectrum $G_T(u)$, $F_T(u)$ of the total system hull and propeller and the spectrum $G_H(u)$, $F_H(u)$ of the bare hull respectively. The spectrum of the propeller alone $G_P(u)$, $F_P(u)$ then follows from the principle of linear superposition.

$$G_P(u) = G_T(u) - G_H(u)$$
$$F_P(u) = F_T(u) - F_H(u) \qquad \text{(B72)}$$

For the ease of comparison with theory the propeller spectrum may be transformed to a new coordinate system $0\tilde{x}\tilde{y}\tilde{z}$ which has its origin in the propeller plane. If $\tilde{x} = x - x_P$, $\tilde{y} = y$, $\tilde{z} = z$, then

$$\tilde{G}_P(u) = G_P(u)\cos(sx_P) + F_P(u)\sin(sx_P)$$
$$\tilde{F}_P(u) = F_P(u)\cos(sx_P) - G_P(u)\sin(sx_P) \qquad \text{(B73)}$$

The associated wavemaking resistances of bare hull (R_{WH}), bare propeller (R_{WP}) and total system hull-propeller (R_{WT}) are obtained from the respective spectra by use of the general formula :

$$R_W = \frac{1}{8\pi}\int_0^\infty \left\{F^2(u) + G^2(u)\right\}\frac{\sqrt{1+4u^2}}{1+\sqrt{1+4u^2}}\,du \qquad \text{(B74)}$$

It is assumed here that the wave pattern has transverse symmetry.

* * *

APPENDIX C

LIFTING LINE CALCULATIONS

C. 1. Problem Formulation

The principal method for calculating thrust deduction and free-surface effects due to a propeller as described in Appendix B pre - supposes that a lifting line representation of the propeller , i. e. the distribution of bound circulation along the radius , is known . In order to be able to apply this method to a given propeller we need a scheme for determining the circulation distribution for any given operating condition of a propeller of predetermined geometry . This is essentially the classical "performance" problem in propeller theory (as opposed to the design problem , in which a certain performance criterion is prescribed and the optimum propeller geometry is sought for) .

Physically , the problem can be formulated as a set of rela - tions which must be satisfied at every propeller radius between the hub and the tip . Using standard symbols , these relations are :

$$C_L = C_L(\alpha) \tag{C 1}$$

$$\alpha = \Phi - \beta_i \tag{C 2}$$

$$\tan \Phi = P/2\pi R \tag{C 3}$$

$$\tan \beta_i = \left\{ (1-w)V + u_A \right\} / \left\{ \omega R - u_T \right\} \tag{C 4}$$

$$u_A = \frac{1}{4\pi} \int_{R_H}^{R_P} i_A (R/R_P, \beta_i, Z) \left\{ \frac{d\Gamma(R')}{dR'} \right\} \frac{dR'}{R-R'} \tag{C 5}$$

$$u_T = \frac{1}{4\pi} \int_{R_H}^{R_P} i_T (R/R_P, \beta_i, Z) \left\{ \frac{d\Gamma(R')}{dR'} \right\} \frac{dR'}{R-R} \tag{C 6}$$

$$\Gamma = C_L \, c \left\{ (1-w)V + u_A \right\} / (2 \sin \beta_i) \tag{C 7}$$

Here , Equation (C 1) represents the predetermined two-dimensional foil characteristics , i.e. the lift coefficient C_L as a function of angle of attack α . Equations (C2) to (C4) establish the local angle of attack α as the difference between the predetermined geometric pitch angle Φ and the unknown hydrodynamic pitch angle β_i . The velocities u_A and u_T induced by the free vortex trail of the propeller may be obtained from Biot-Savart's Law and are expressed in Equations (C5) and (C6) as integrals involving the slope of the bound circulation $\Gamma(R)$ and two special functions i_A and i_T (of three variables) , the so-called induction factors , see Lerbs (1952) . Equation (C7), finally , is the relation between lift and circulation in accordance with Kutta-Joukowsky's theorem . Mathematically , the problem is an integral equation for the unknown function $\beta_i (R/R_P)$, which can be solved by iteration if efficient algorithms are available for computing the induced velocities u_A and u_T .

The solution of the above problem yields the distribution of circulation , and hence lift , over the radius :

$$dL = \rho \left\{ (1-w) V + u_A \right\} \Gamma \, dR / (\sin \beta_i) \qquad (C\,8)$$

Now the drag can also be estimated from the known foil characteristics :

$$C_D = C_D (\alpha) \qquad (C\,9)$$

$$dD = \frac{c}{2} \rho \left\{ (1-w) V + u_A \right\}^2 C_D dR / (\sin \beta_i)^2 \qquad (C10)$$

Hence , by resolving lift and drag along the axial and circumferential directions and integrating over the radius , one can calculate the thrust and torque produced by the propeller .

C.2. Method of solution

Our method of solution was dictated by the computational tools and the information on propeller characteristics available to us . The principal computational tools at our disposal were two computer programs for propeller design , both based on the lifting line theory and incorporating efficient algorithms for numerical evaluation of induced velocities . One was obtained from the Naval Ship Research and Development Center and the other from the Technical University of Berlin by courtesy of Dr. Östergaard . They are well documented in the litterature , cf. Haskins (1967) and Östergaard (1970) , and therefore

need not be described here in detail . After several test runs had revealed that the two programs yielded practically identical solution of the design problem , we chose the Berlin program for further use and adapted it to a solution of the performance problem . The principal modification necessary was the following . In the design problem the hydrodynamic pitch angle $\beta_i (R/R_P)$ is generally prescribed to fulfil the optimum (minimum energy loss) condition thus eliminating the need to solve an integral equation . In the performance problem , however , the integral equation must be solved . This was done by the method of successive approximations to the unknown function $\beta_i(R/R_P)$. Starting with an initial guess $(\beta_i)_o$, say corresponding to the optimum condition , a better approximation was found by cycling through Equations (C1) to (C7) . In order to prevent the iteration from diverging it was found necessary to weight the successive approximations as follows :

$$(\beta_i)_{n+2} = w_1 (\beta_i)_n + w_2 (\beta_i)_{n+1} \qquad (C11)$$

With $w_1 = 0.9$ and $w_2 = 0.1$ the final error in $\beta_i(R/R_P)$ after ten iterations was found to be generally less than 1 % .

A major handicap in this algorithm was that the two-dimensional foil characteristics of our propeller (see Fig. 2) were not explicitly known to us . We therefore back-calculated the foil characteristics from the known measured performance (thrust and torque) of the propeller (in the deeply submerged open water condition) . This was done by treating any given operating condition as a small perturbation from an assumed design (optimum) condition , i.e.

$$C_L(\alpha) = C_{LD} + 2\pi(\alpha-\alpha_D)\, k \qquad (C12)$$

$$C_D(\alpha) = a_1 \left| C_L(\alpha) - C_{LD} \right|^{a_2} + C_{DD} \qquad (C13)$$

The design angles of attack α_D and the corresponding lift coefficients C_{LD} were specified indirectly by the choice of a design advance coefficient J_D. Let β_{iD} be the optimum hydrodynamic pitch angle at any radius at the design point J_D. Then for calculating the performance at any other advance coefficient J (and assumed pitch angle β_i) , it is only necessary to evaluate the differences (see next page)

.. / ..

$$(\alpha - \alpha_D)' = \beta i_D - \beta i \qquad (C14)$$

$$C_L(\alpha) - C_{LD} = 2\pi(\alpha - \alpha_D)k \qquad (C15)$$

$$C_D(\alpha) - C_{DD} = a_1 \left| C_L(\alpha) - C_{LD} \right|^{a_2} \qquad (C16)$$

It is thus seen that in all five arbitrary constants (J_D, C_{DD}, k, a_1, a_2) were used to match the calculated propeller performance to the actual measured performance . By trial and error the following best fit values were determined for our propeller :

$$J_D = 0.8, \quad C_{DD} = 0.01$$

$$k = 0.67$$

$$a_1 = 0.17, \quad a_2 = 6 \qquad (C17)$$

Note that the only critical parameter here is the factor k , which may be interpreted as an empirical catch-all to account for viscous losses and miscellaneous three-dimensional effects .

The degree of agreement finally achieved between the measured and calculated (more precisely , simulated) performance of the propeller is obvious from the following table and from Fig. 10 .

Further details of this method of calculating off-design performance and results obtained with other propellers are reported in a recent paper by Östergaard , Kruppa and Lessenich (1971) .

	Measured		Simulated	
J	K_T	$10K_Q$	K_T	$10K_Q$
0.6	0.223	0.355	0.223	0.353
0.7	0.179	0.300	0.178	0.296
0.8	0.135	0.242	0.135	0.242
0.9	0.087	0.182	0.088	0.179

C. 3. Applications

It should be obvious from the foregoing that as far as the deeply submerged open water condition is concerned , our computer program as described above did not really predict propeller performance analytically but rather simulated the known measured performance by means of a lifting line model . This was perfectly acceptable because our primary aim here was not to predict propeller performance , but to determine the equivalent lifting line for use in calculating thrust deduction and free-surface effects . However , in two subsequent applications this program was indeed used to obtain certain genuine predictions of propeller performance.

First , for estimating the effect of free-surface on propeller performance at shallow submergence the program was run with the calculated self-induced wake $w_f(R)$ of the propeller as an additional input (see Section B. 6) without any attempt to manipulate the foil characteristics fixed once for all on the basis of the deeply submerged condition , see Equation (C17) . Hence , the thrust and torque calculated for shallow submergence as plotted in Fig. 13 and reproduced in the following table are , in a certain sense , true predictions of the free-surface effect .

	$h/R_P = 3.47 \approx \infty$ Measured		$h/R_P = 1.00$ Measured		$h/R_P = 1.00$ Calculated	
J	K_T	$10K_Q$	K_T	$10K_Q$	K_T	$10K_Q$
0.6	0.223	0.355	0.194	0.313	0.198	0.324
0.7	0.179	0.300	0.163	0.275	0.165	0.280
0.8	0.135	0.242	0.124	0.226	0.126	0.229
0.9	0.087	0.182	0.079	0.170	0.084	0.170

It may be noted that the wake $w_f(R)$ input to the program was here calculated for the lifting line corresponding to the deeply submerged propeller . In principle, it would be possible to run a second iteration with the wake $w_f(R)$ recomputed for the new lifting line determined

by the program for the shallow submergence. However, this refinement is considered unnecessary.

Second, for evaluating the propeller performance in the behind hull condition again the same procedure was used, with the measured nominal wake $w(R)$ substituted in Equations (C4) and (C7). However, the calculated thrust and torque were found to deviate substantially from the measured values. Since the primary purpose of this calculation was to obtain a realistic simulation of actual propeller performance by a mathematical lifting line, it was decided to enforce a thrust identity. However, this was accomplished not by further manipulating the assumed foil characteristics but by multiplying the input wake $w(R)$ with a constant wake corrector k_w whose final value was determined by iteration. Thus the program was here used not only to determine the equivalent circulation distribution but also to simulate the physical difference between the nominal and effective wake through the factor k_w. Moreover, the program also calculated a mean effective wake $\tilde{w}_T$ which was based on a thrust average rather than a volume flux average. This was defined as

$$\tilde{w}_T = \frac{k_w \int_{R_H}^{R_P} w(R) \left\{\omega R - u_T\right\} \left\{1 - \epsilon \tan \beta_i\right\} \Gamma(R) dR}{\int_{R_H}^{R_P} \left\{\omega R - u_T\right\} \left\{1 - \epsilon \tan \beta_i\right\} \Gamma(R) dR} \qquad \text{(C18)}$$

where not only the nominal wake w and the circulation Γ but also the quantities u_T, β_i, and $\epsilon = C_D/C_L$ vary with radius, even though this has not been explicitly indicated in the formula. The numerical values obtained for k_w and $\tilde{w}_T$ and their practical significance have been discussed in Section 3.6.2.

* * *

APPENDIX D

DOUBLE BODY CALCULATIONS

D.1. Motivation

All calculations described in Appendix B are based on the first-order thin ship theory in which the hull is represented by a linearized (with respect to the beam) source distribution on the center plane, see Equation (B6). This has the great advantage that "potential" (i.e. zero Froude number) effects and wave (i.e. finite Froude number) effects can be calculated consistently using the same source distribution. However, the accuracy of the results depends in an uncontrolled manner on the "thinness" of the ship. In order to obtain a quantitative estimate of the error involved in the application of thin ship theory to our hull, a few wake calculations were also performed by the method of Hess and Smith (1962), which does not impose any restrictions on hull geometry. As is well known, the Hess and Smith algorithm provides a general solution of the Neumann problem of nonlifting potential flow about arbitrary bodies by means of a surface distribution of sources. Due to the enormous amount of numerical computation involved, however, the application of this method to the calculation of flow about ships is still limited to the so-called zero Froude number approximation, in which the ship (including the propeller) is conceptually replaced by a deeply submerged double body generated by reflecting the under water form about the static water plane. In our terminology, therefore, only the pure potential effects (as distinguished from the viscous and wave effects) can be evaluated by this method. An improved version of the original Hess and Smith computer program was made available to us by the Naval Ship Research and Development Center.

D.2. Results

Without going into the intricate details of the Hess and Smith method we report here only a few relevant results obtained by this program. First, a series of nominal wake calculations was performed with the propeller disk assumed in its proper transverse and vertical position ($y_P = 0$, $z_P = -0.5\ T$) but at five different longitudinal positions as shown in the following table. Since the accuracy and computing effort in this method depend critically on the number and size of the body surface elements, we tried four different arrangements involving N = 100, 125, 145 and 150 elements. As our double body had three planes of symmetry, the elements are understood to cover only one eighth of the total body surface. To ensure finer detail near the stern the element size was not uniform over the entire length of the hull but made increasingly smaller toward the ends.

The results showed that the arrangement with 125 elements yielded adequate accuracy for our purposes. Moreover, the average wake was practically identical to that calculated by thin ship theory. (This gave us, of course, more confidence in applying the thin ship theory also to the finite Froude number case where no such accuracy control was possible.)

Potential wake w_P averaged over the propeller disk					
$2x_P/L$	Hess and Smith Program				Thin Ship Theory
	N = 100	N = 125	N = 145	N = 150	
-1.01	0.1785	0.1769	0.1756	0.1769	0.1758
-1.02	0.1520	0.1502	0.1496	0.1506	0.1492
-1.03	0.1307	0.1295	0.1287	0.1296	0.1278
-1.04	0.1136	0.1127	0.1120	0.1127	0.1107
-1.05	0.0998	0.0990	O.0985	0.0991	0.0969

Next, a series of effective wake calculations was conducted with the propeller located in its proper position (x_P = -0.51 L) and assumed operating at the advance coefficients J_H = 0.733, 0.889 and 1.131 corresponding to the ship self-propulsion points at γ_0 = 4.0, 7.0 and 12.5 respectively, see Section 3.6. This involved two extra complications compared to the previous nominal wake calculations. One, the presence of the propeller destroyed the longitudinal symmetry of the flow so the number of significant hull surface elements had to be doubled from 125 to 250. Two, the flow induced by the propeller (and its mirror image about the plane z = 0) on the hull surface had to be given as an additional input to the Hess and Smith program. For this the Hough and Ordway source disk representation of the propeller (see Fig. 29) was used. The algorithm for computing the flow induced by source rings at arbitrary field points was taken from Küchemann and Weber (1953), pp. 310-316. The results are summarized in the following table.

Calculated effective wakes w_{Ep} versus nominal wakes w_p								
R/R_P	Hess and Smith Program							Thin Ship
	$\gamma_o = 4.0$		$\gamma_o = 7.0$		$\gamma_o = 12.5$		(σ=0)	(σ=0)
	$-\sigma$	w_{E_p}	$-\sigma$	w_{E_p}	$-\sigma$	w_{E_p}	w_p	w_p
0.2	0	.1924	0	.1908	0	.1874	.1822	.1838
0.3	.0573	.1866	.0609	.1850	.0482	.1819	.1770	.1778
0.4	.0669	.1795	.0640	.1781	.0452	.1753	.1708	.1711
0.5	.0700	.1719	.0616	.1706	.0395	.1680	.1641	.1637
0.6	.0688	.1640	.0582	.1629	.0359	.1606	.1571	.1560
0.7	.0653	.1562	.0506	.1552	.0290	.1531	.1501	.1484
0.8	.0561	.1486	.0382	.1477	.0206	.1459	.1433	.1411
0.9	.0415	.1413	.0310	.1405	.0122	.1389	.1366	.1341
1.0	0	.1344	0	.1337	0	.1323	.1303	.1275
Disk Avg.	.0533	.1573	.0439	.1562	.0260	.1541	.1510	.1495

It is seen that the calculated effective wake w_{Ep} is 2 to 4% higher than the calculated nominal wake w_p , depending upon propeller loading of which the source strength σ is a measure . This is exactly what one would expect from theoretical considerations , since the propeller sinks induce extra sink strength in the afterbody which in turn induces an additional positive wake in the propeller plane . However , the difference is too small to have a significant effect on the calculation of thrust deduction .

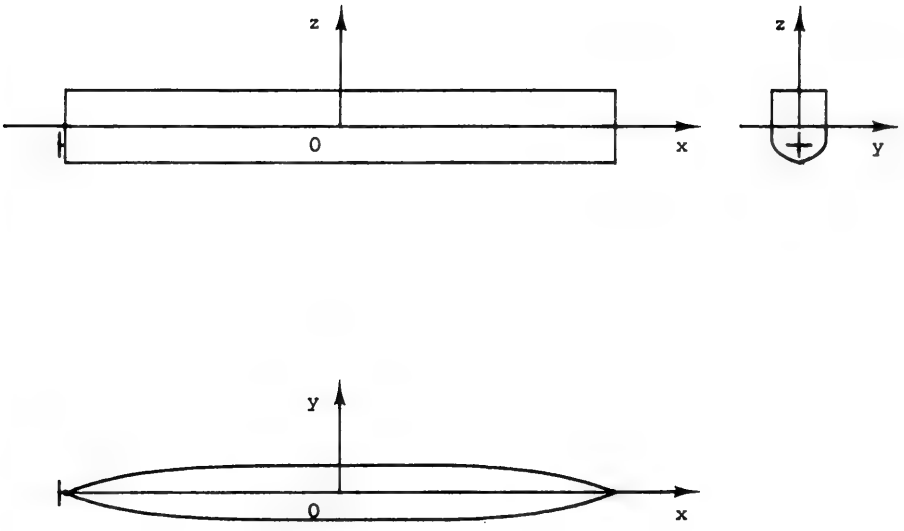

Figure 1 Hull propeller configuration and coordinate system

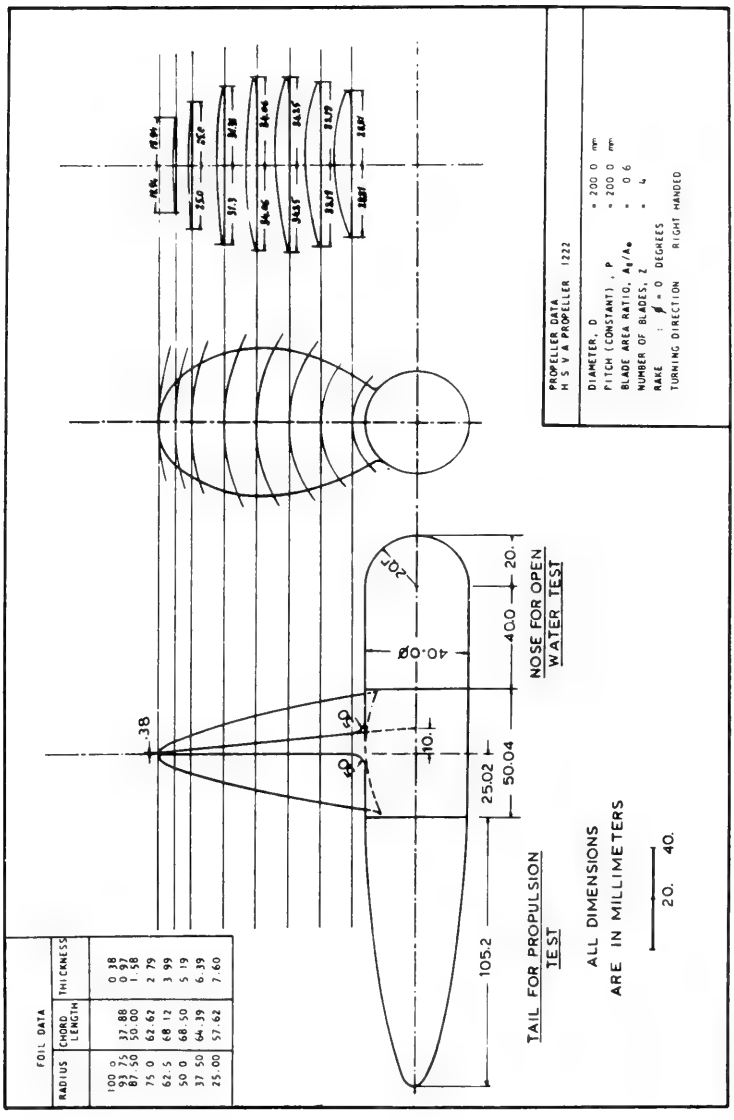

Figure 2 Propeller geometry

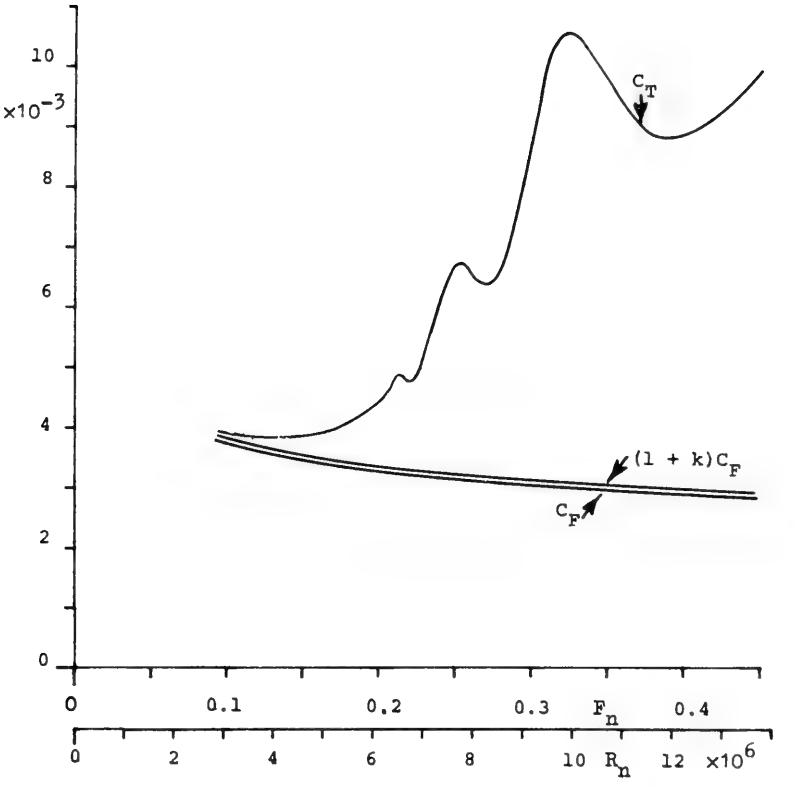

Figure 3 Measured total resistance

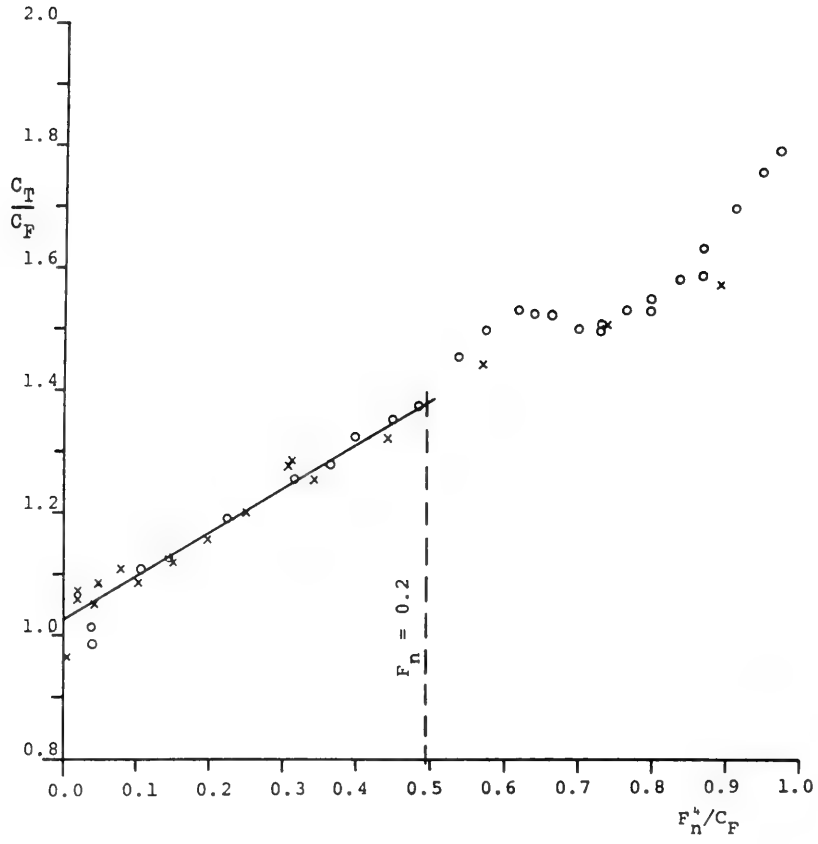

Figure 4 Measured total resistance at low Froude numbers. Determination of viscous form factor

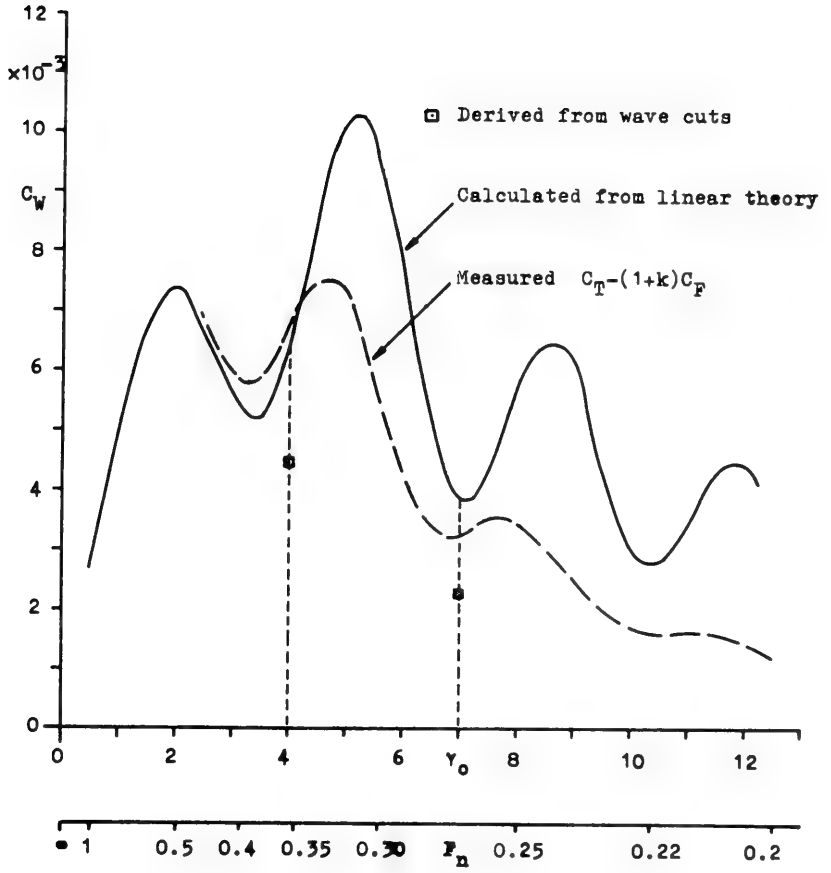

Figure 5 Calculated and measured wave resistance

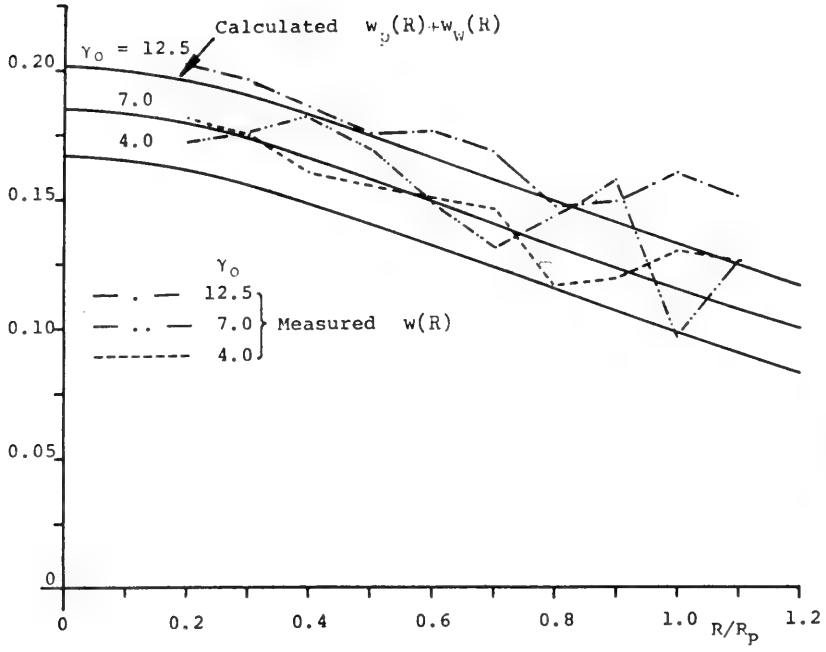

Figure 6 Calculated and measured wake in reverse motion

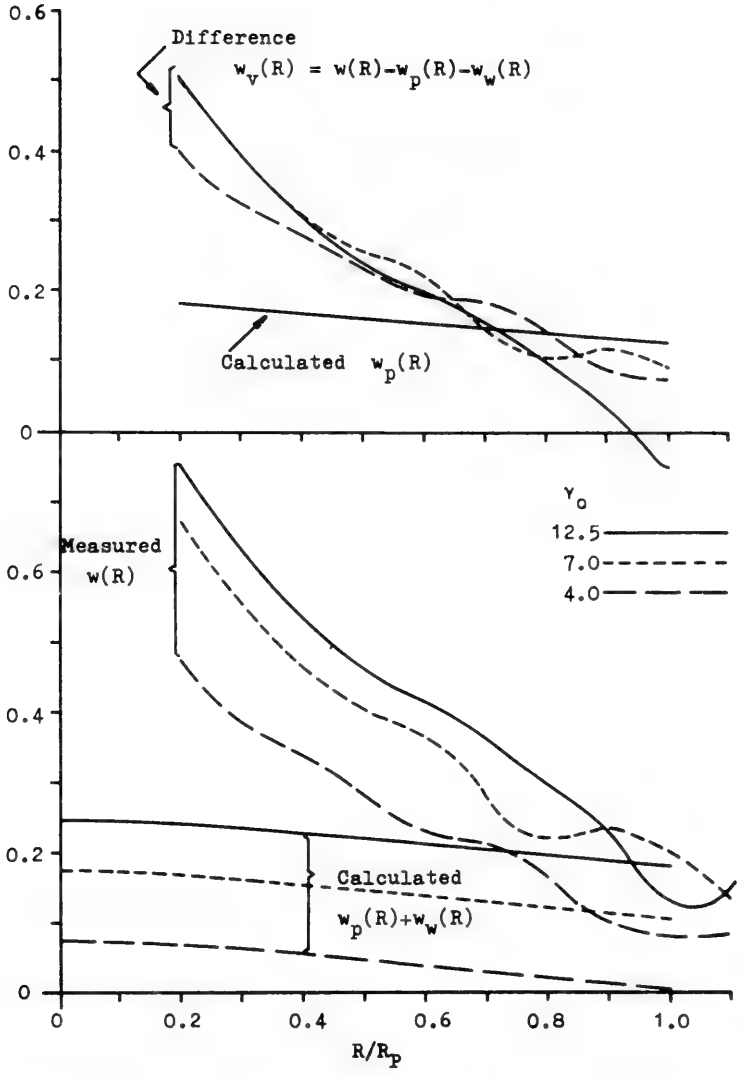

Figure 7 Calculated and measured wake components

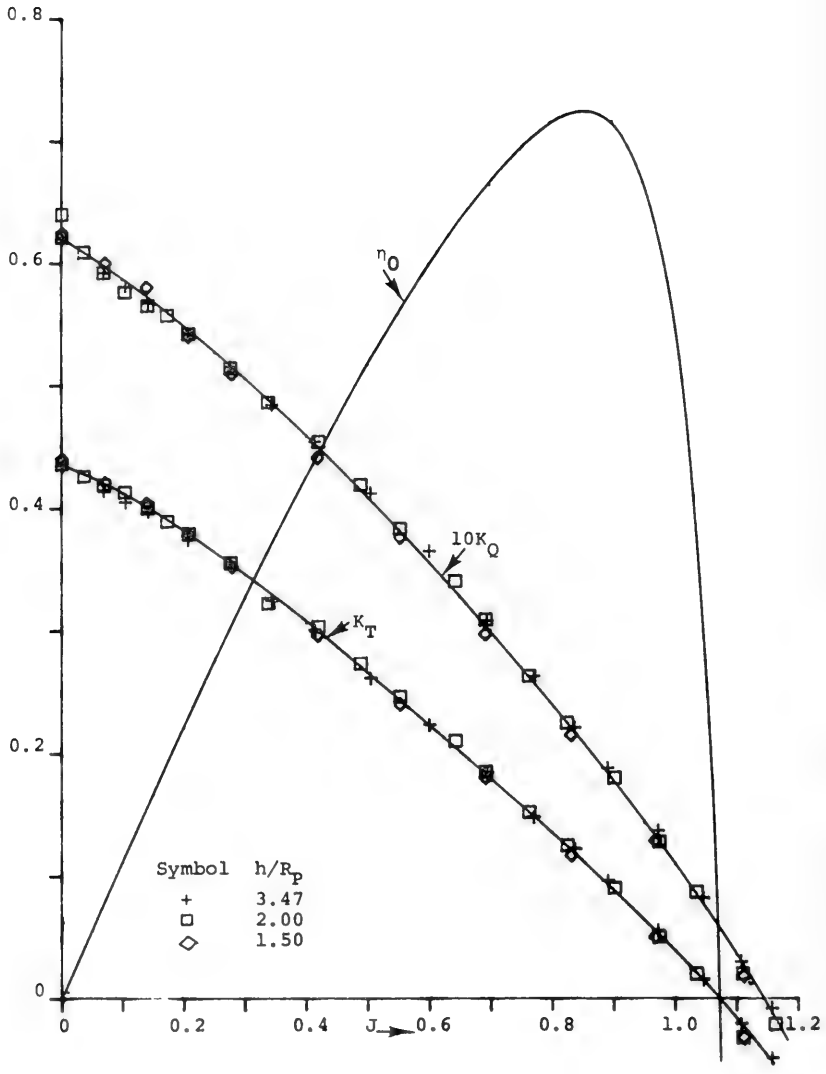

Figure 8 Propeller characteristics at deep submergence

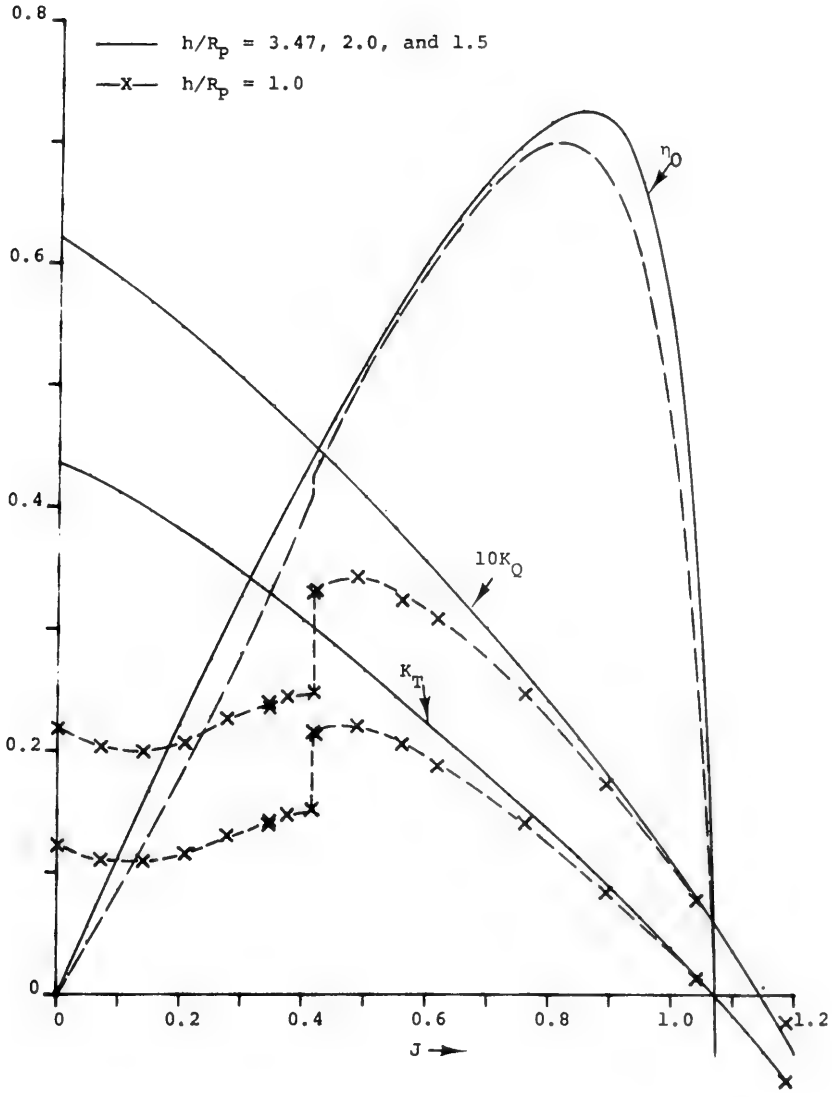

Figure 9 Effect of low submergence on measured free-running propeller characteristics

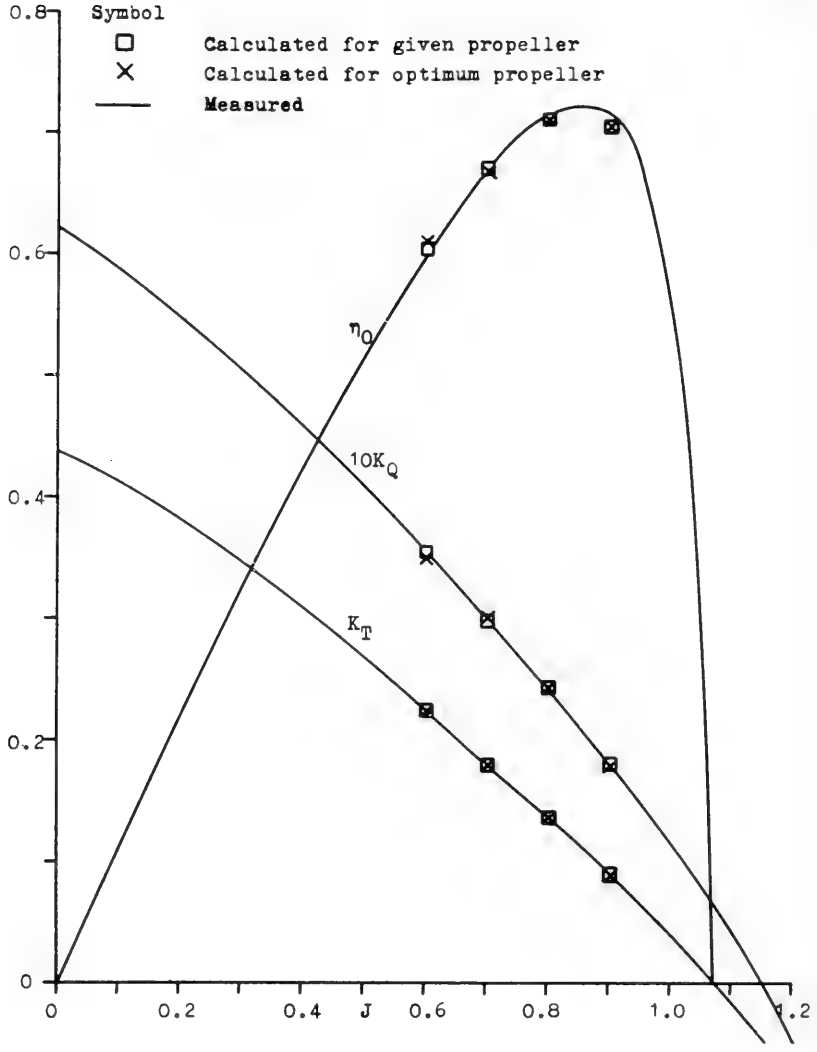

Figure 10 Calculated and measured propeller characteristics at deep submergence

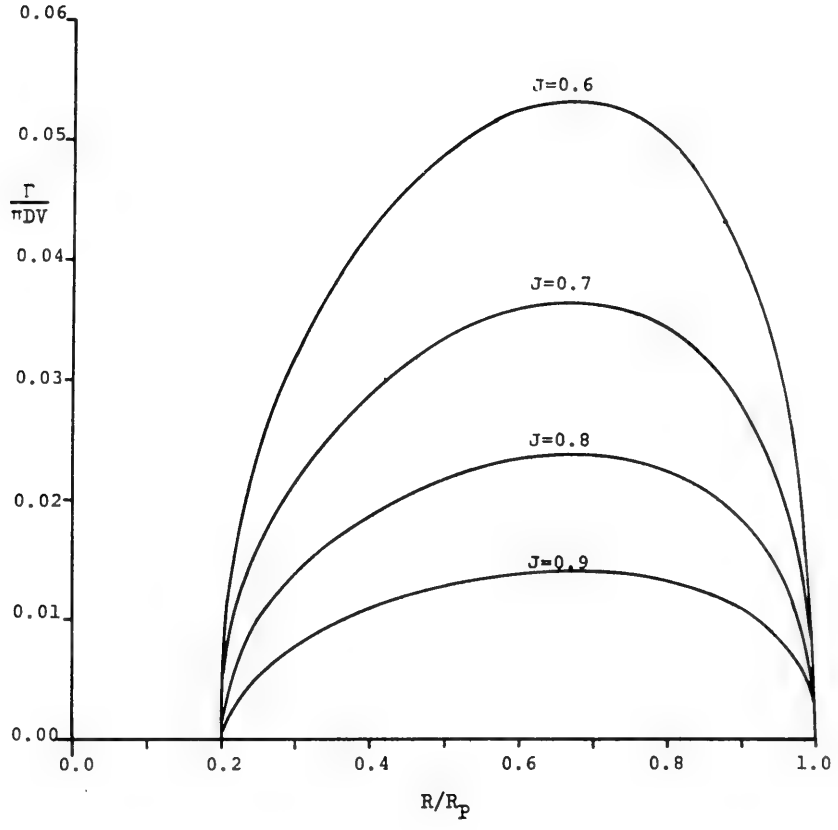

Figure 11 Calculated distribution of bound circulation for free-running propeller at deep submergence

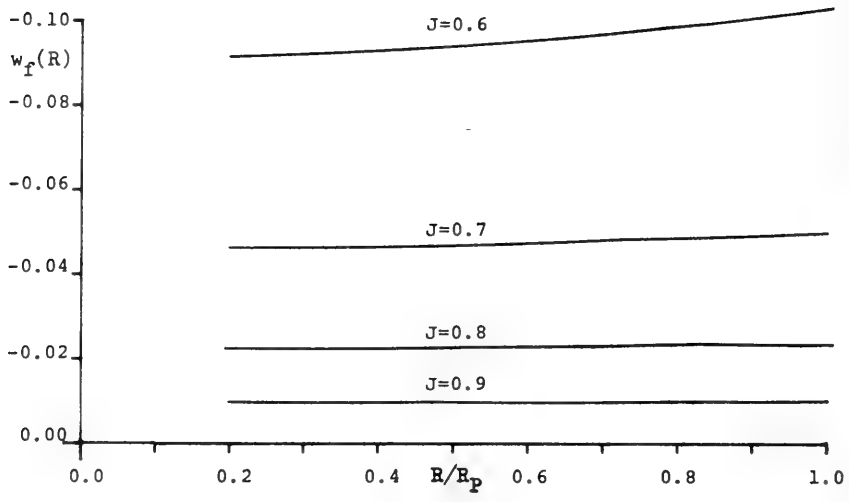

Figure 12 Calculated self-induced free-surface wake of free-running propeller at submergence $h = R_P$

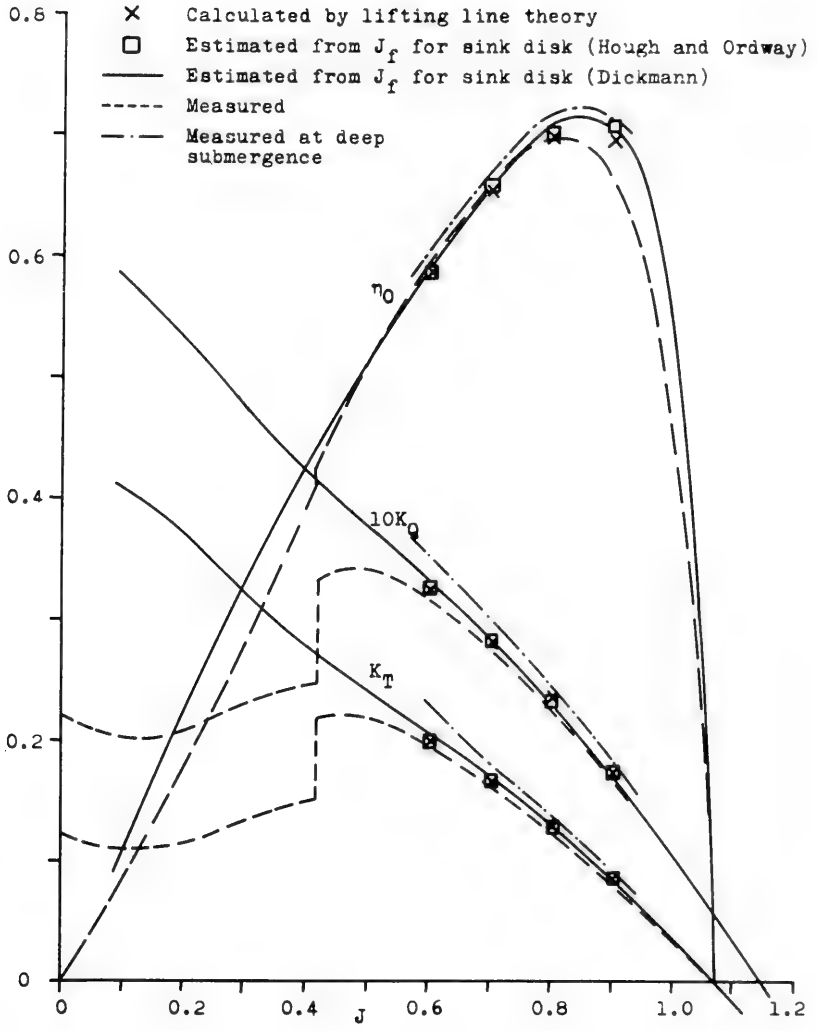

Figure 13 Calculated and measured propeller characteristics at shallow submergence

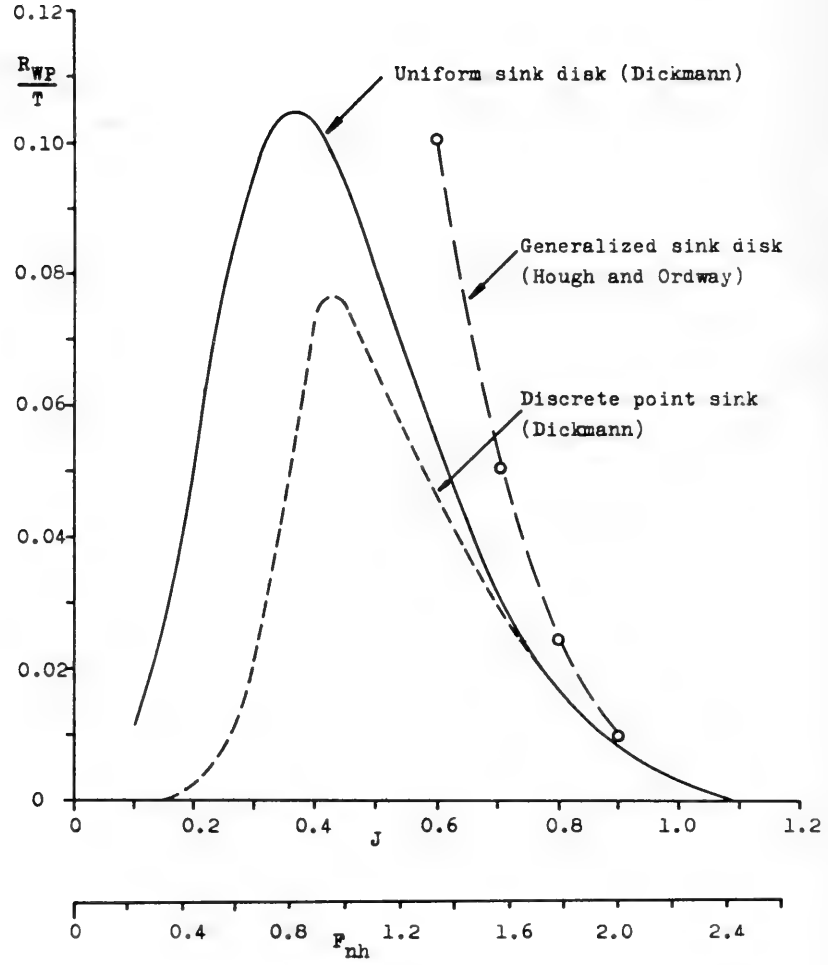

Figure 14 Calculated wave resistance of free-running propeller at shallow submergence $h = R_P$

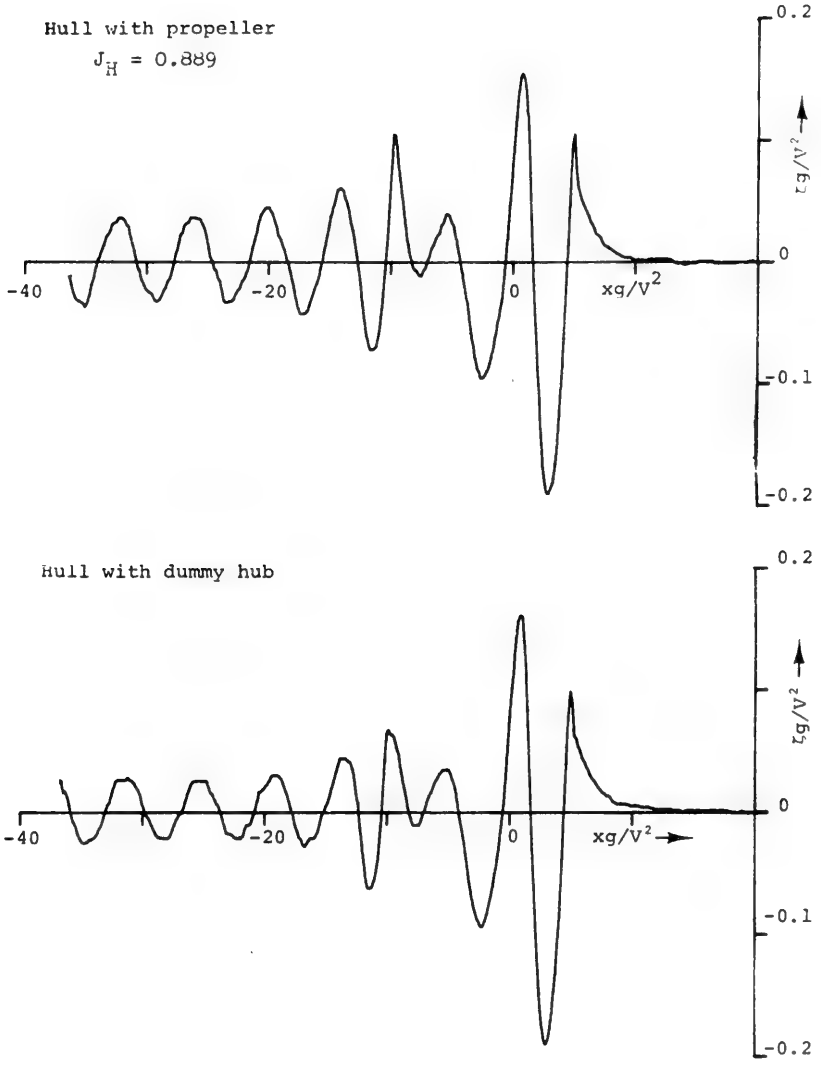

Figure 15 Measured wave profiles at $F_n = 0.267$

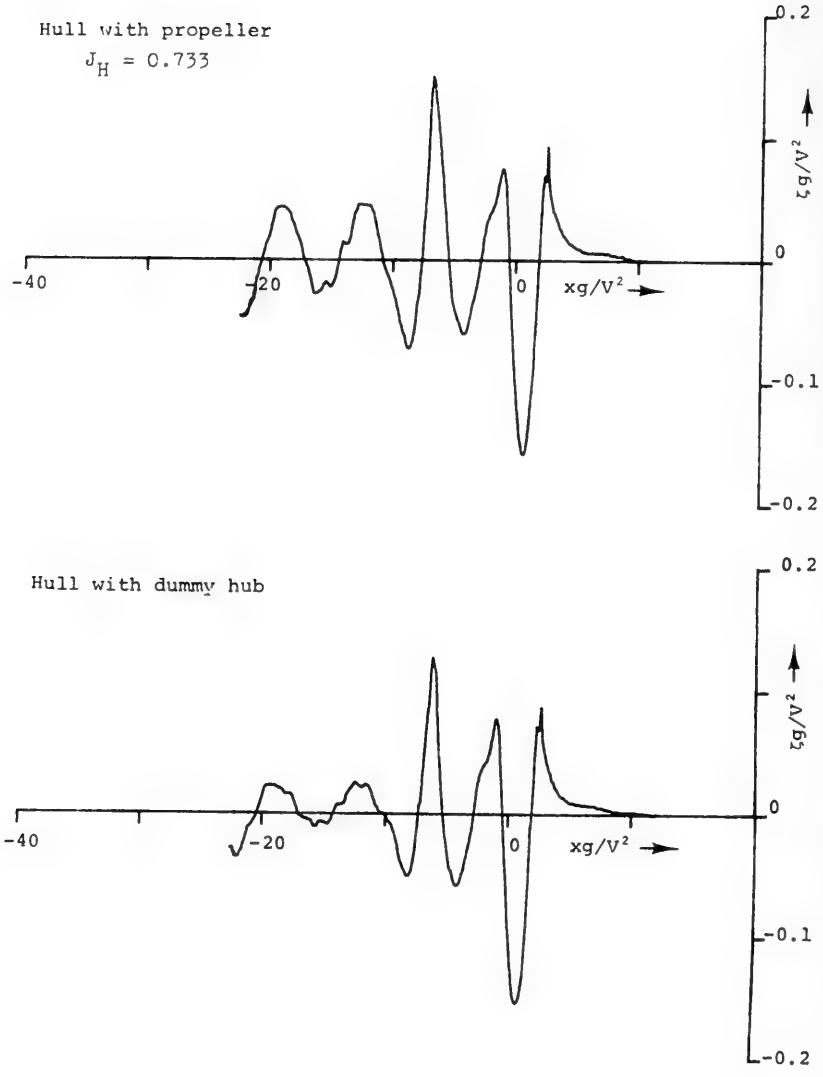

Figure 16 Measured wave profiles at $F_n = 0.354$

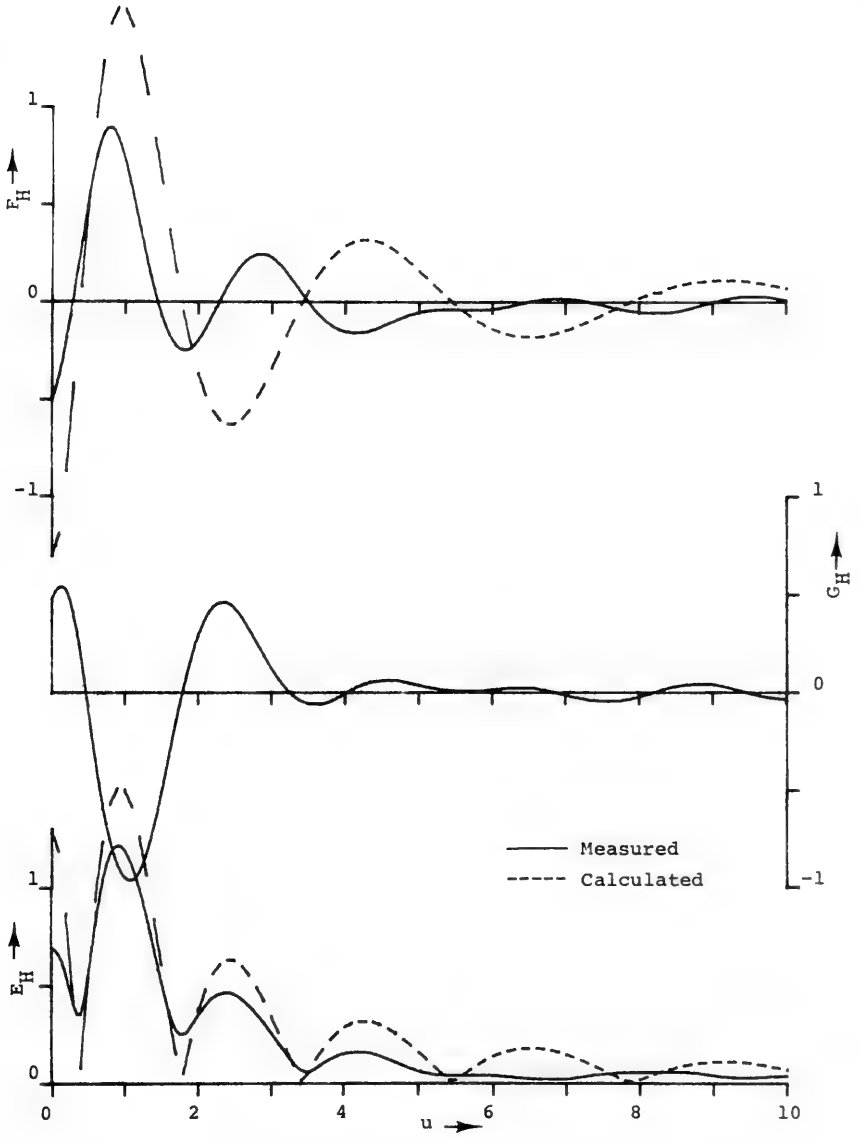

Figure 17 Free-wave spectrum of bare hull at $F_n = 0.267$

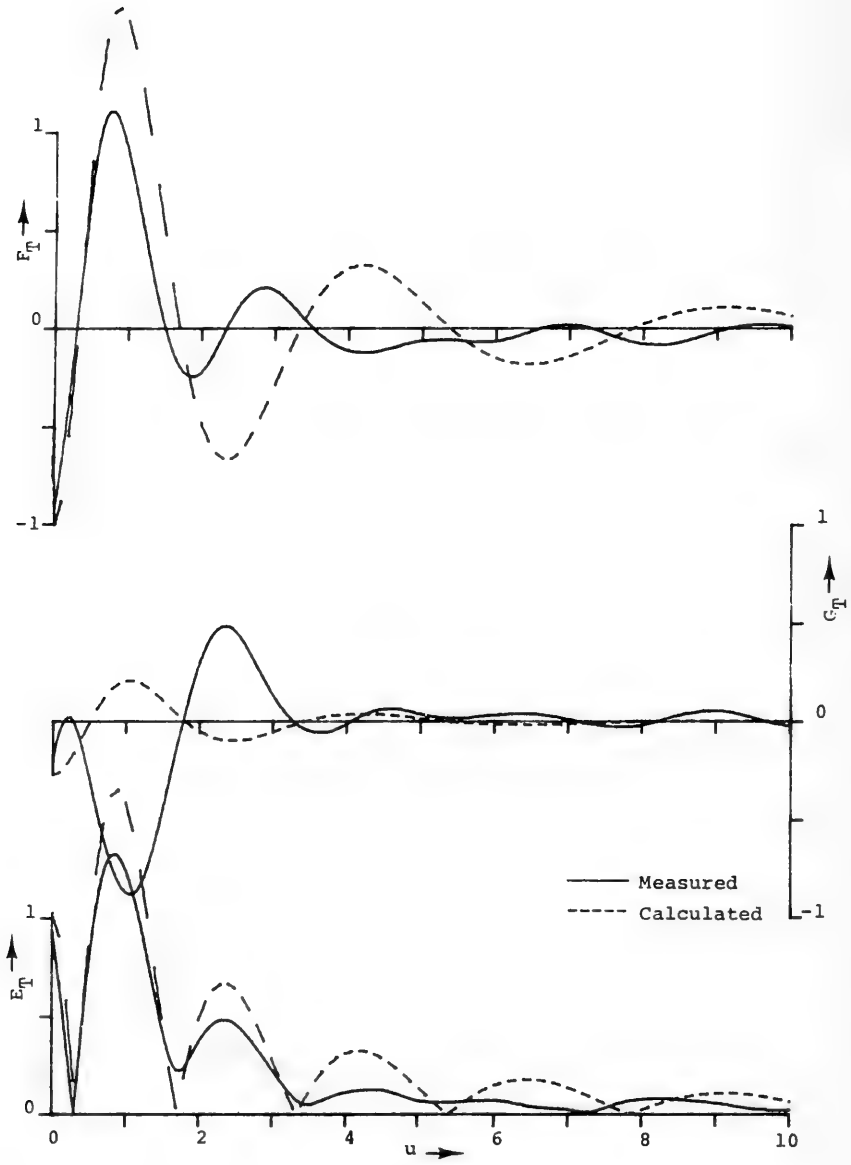

Figure 18 Free-wave spectrum of hull with propeller at $F_n = 0.267$

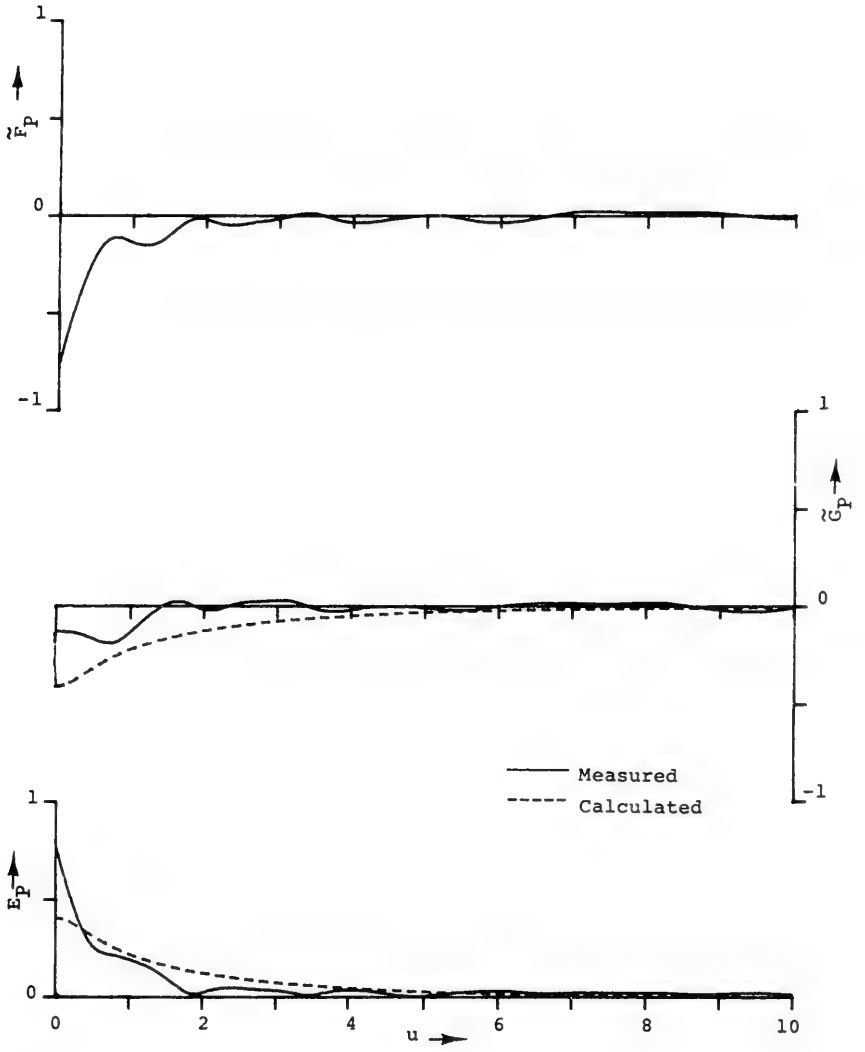

Figure 19 Free-wave spectrum of propeller at $F_n = 0.267$

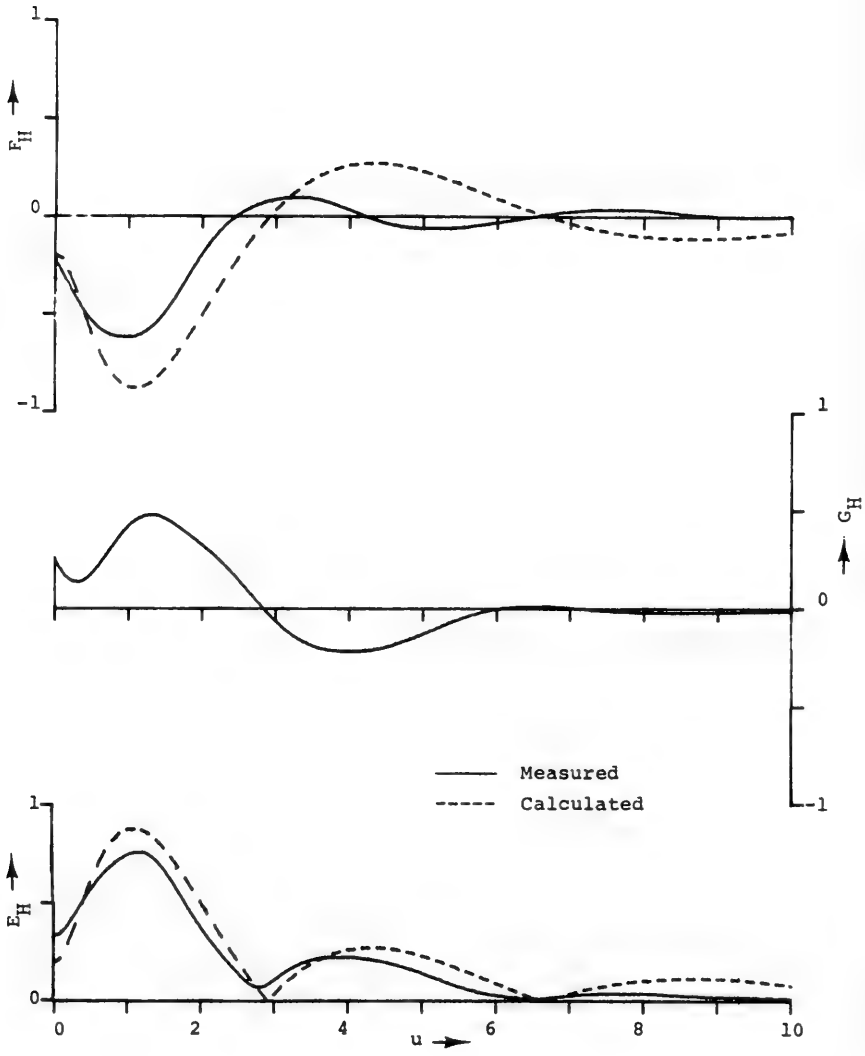

Figure 20 Free-wave spectrum of bare hull at $F_n = 0.354$

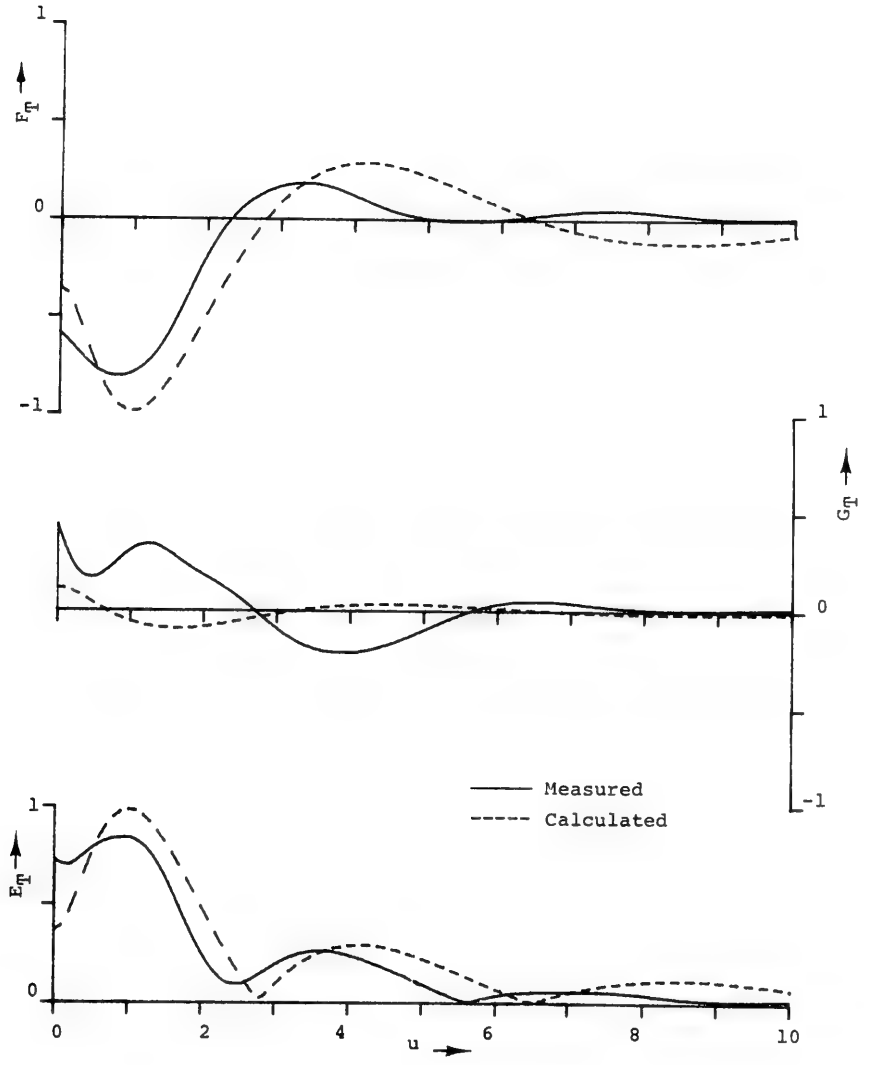

Figure 21 Free-wave spectrum of hull with propeller at $F_n = 0.354$

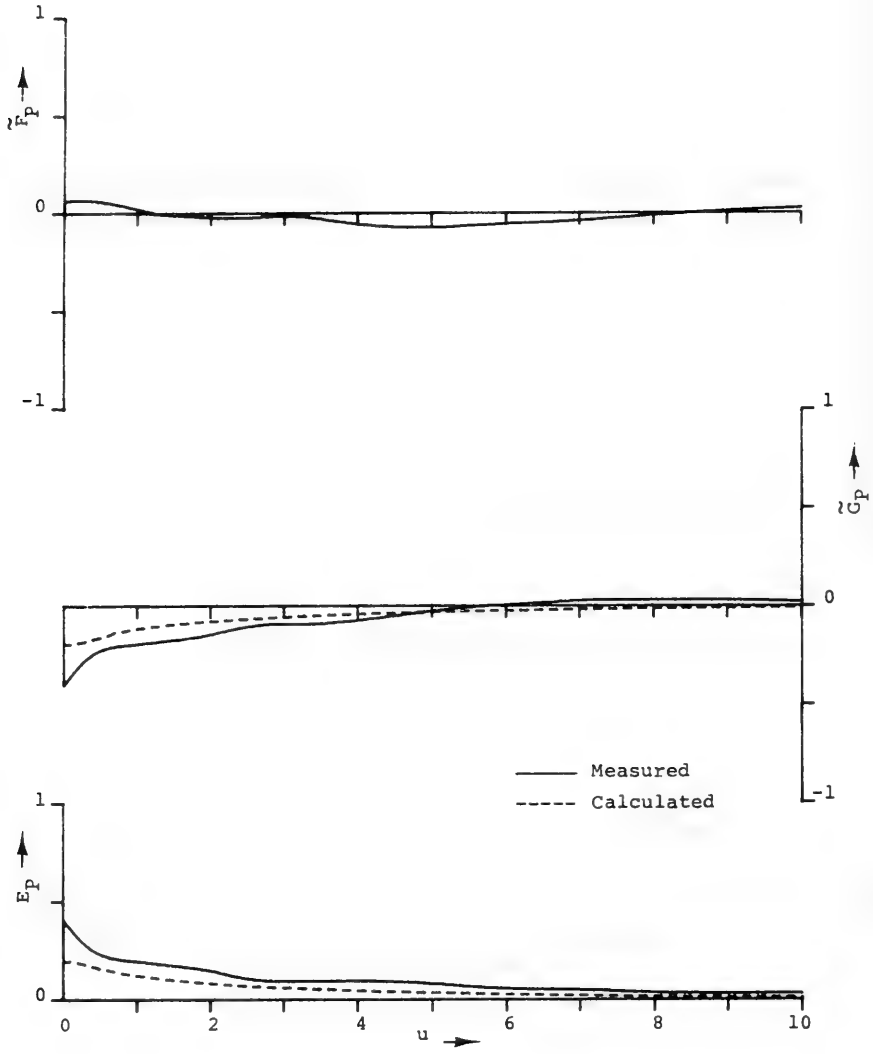

Figure 22 Free-wave spectrum of propeller at $F_n = 0.354$

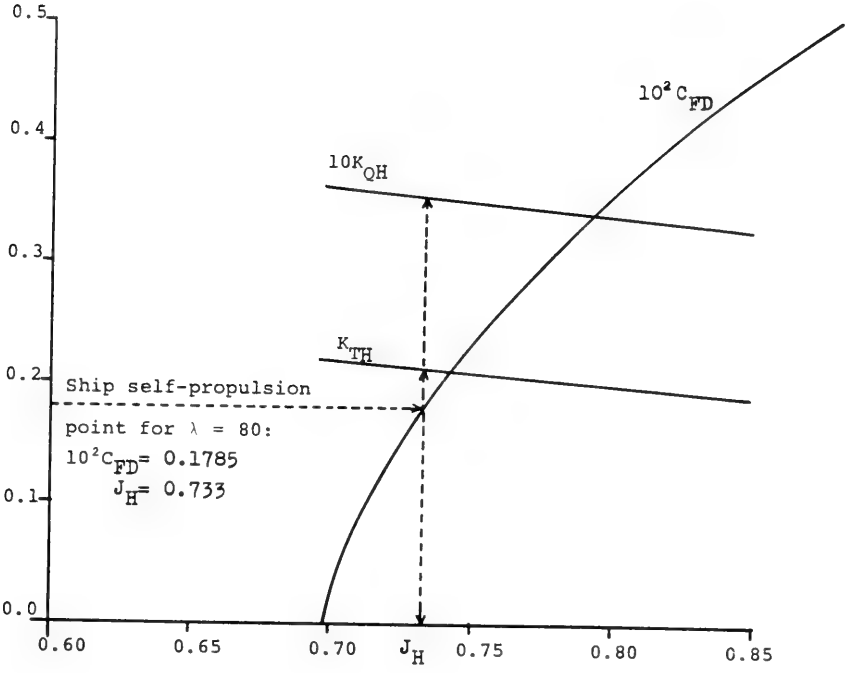

Figure 23 Typical result of a propulsion test and the determination of self-propulsion points, $\gamma_o = 4.0$

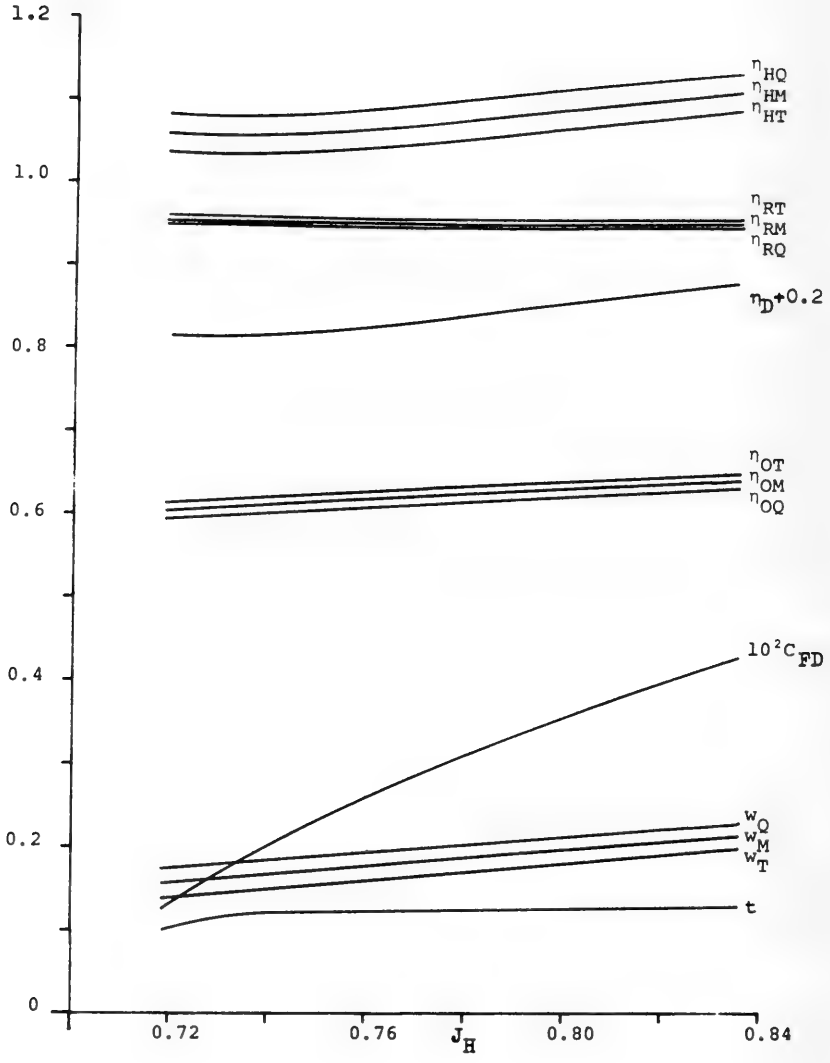

Figure 24 Variation of propulsion factors with loading for $\gamma_o = 4$

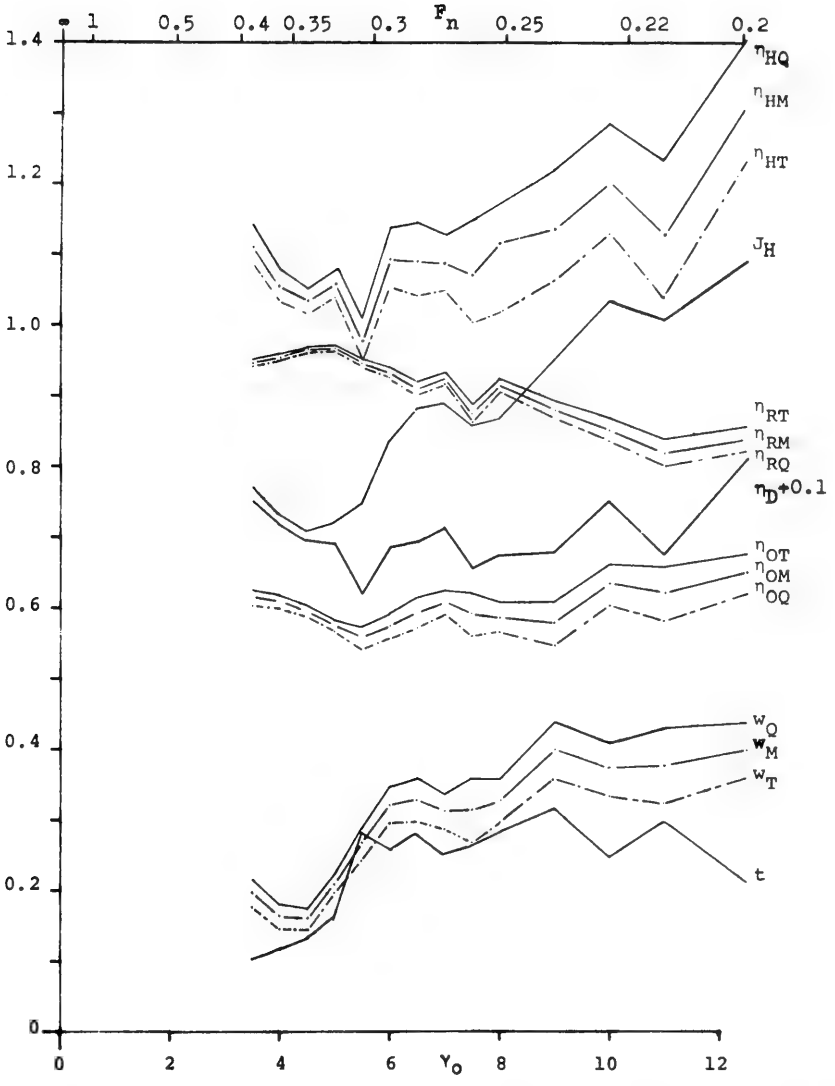

Figure 25 Variation of propulsive factors with Froude number at the ship self-propulsion point

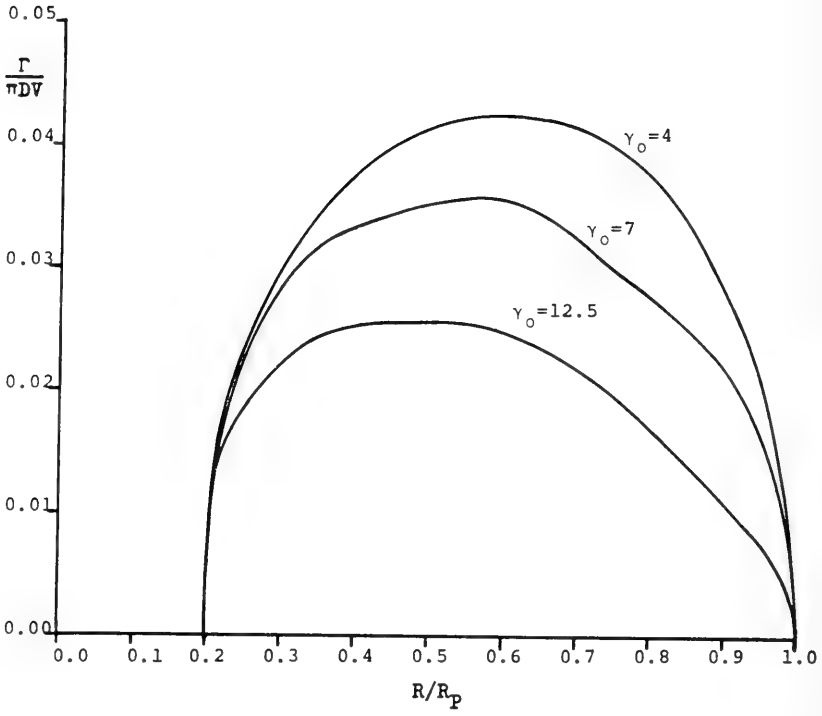

Figure 26 Calculated distribution of bound circulation for propeller behind hull at self-propulsion point

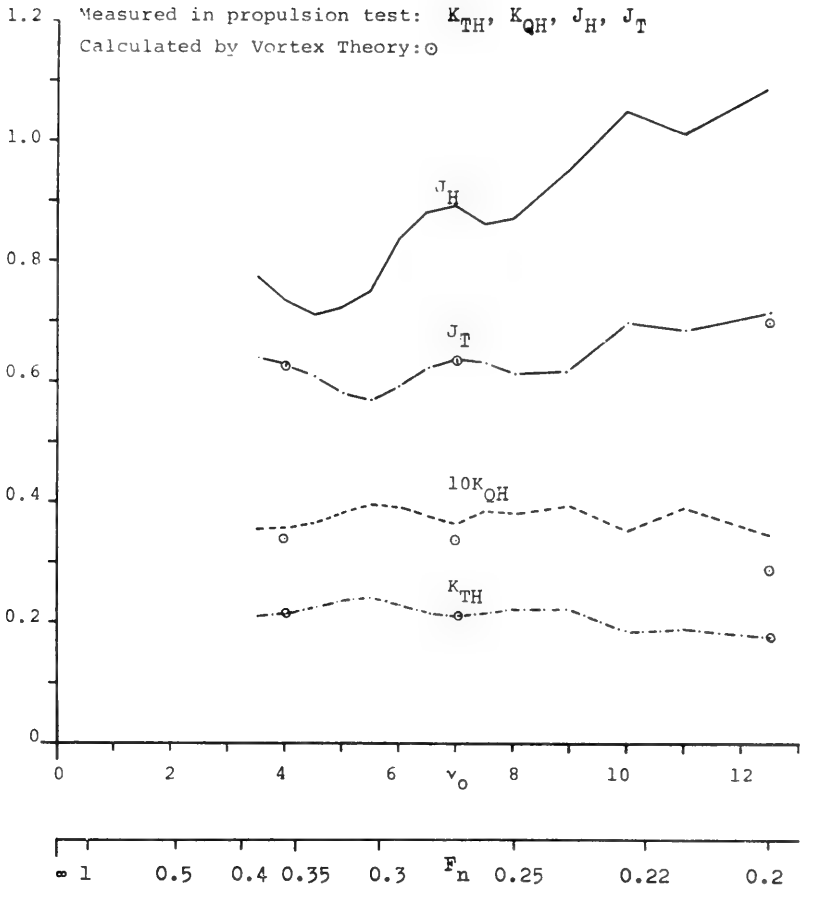

Figure 27 Calculated and measured characteristics of propeller operating behind hull at self-propulsion point

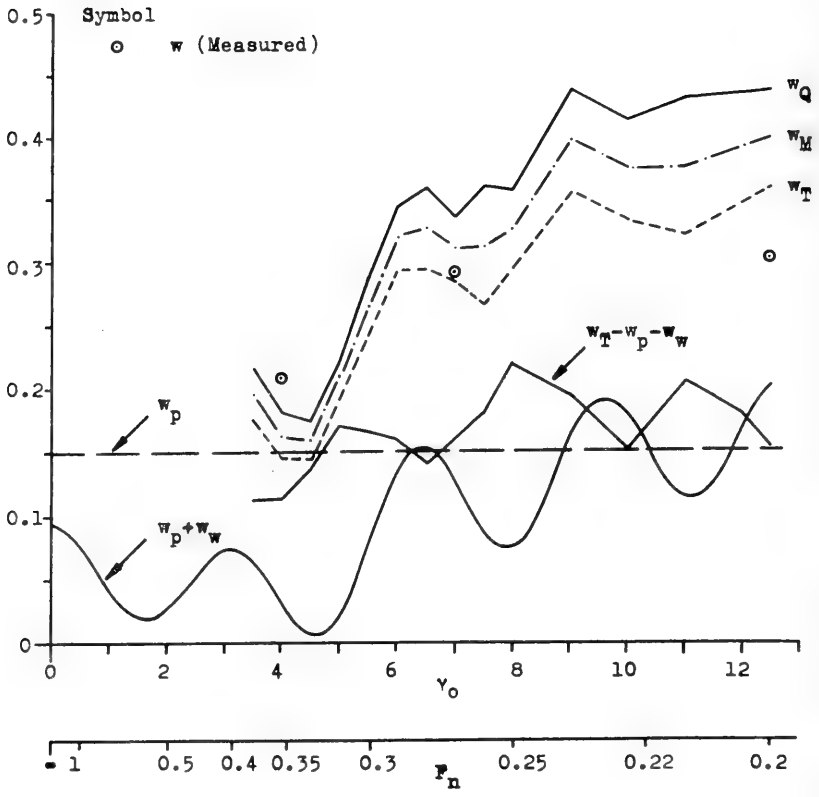

Figure 28 Calculated and measured wake fractions as functions of Froude number

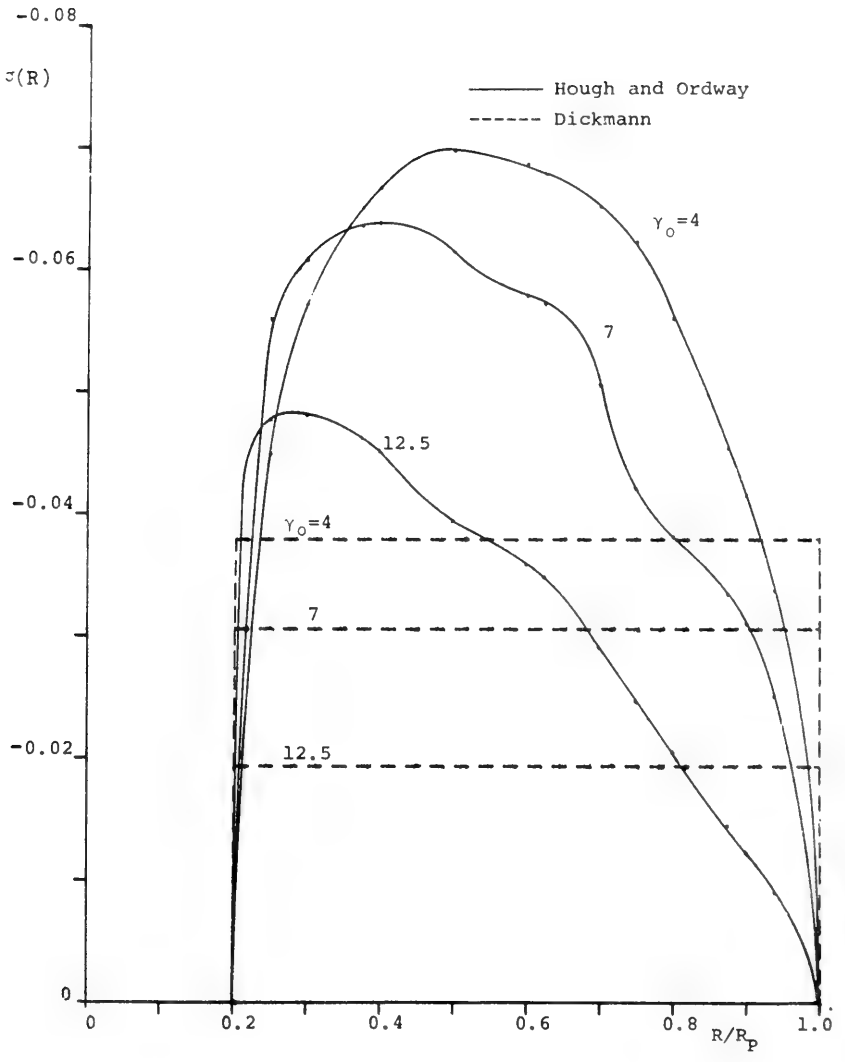

Figure 29 Calculated distribution of source strength for propeller behind hull at self-propulsion point

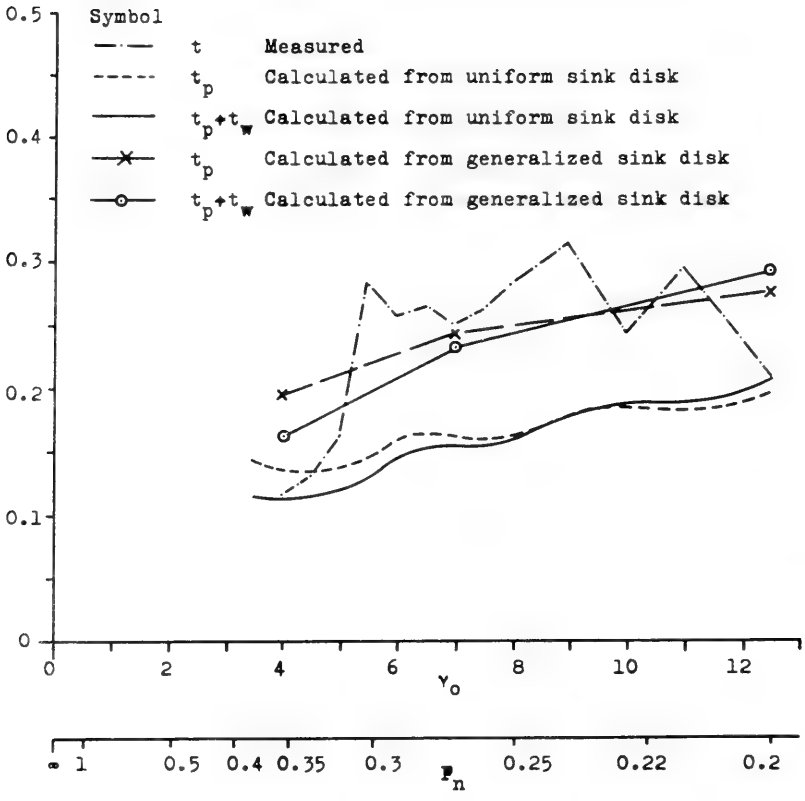

Figure 30 Calculated and measured thrust deduction fractions as functions of Froude number

DISCUSSION

Edmund V. Telfer
R.I.N.A.
Ewell, Surrey, U.K.

Anybody who has attempted to read this paper, as I have during the past two or three days and this morning at 2 o'clock after coming back from our delightful banquet, will appreciate that it contains a lot of matter for real thought. The first point I would like to deal with is the authors' attack on the subject of relative rotative efficiency and their quite innocent reference to relative rotative efficiency being an empirical "catch-all" for various unclarified effects of relatively insignificant magnitude. I am not sure whether that is fair. Undoubtedly during the thirties, a lot of attention was given to the subject. In 1951 I published a North East Coast Institution paper on various aspects of the propeller/hull interaction problem and I made a suggestion that the real meaning of relative rotative efficiency could be very simply understood by plotting K_T to a K_Q base so getting the well-known propeller polar. Suppose we have such a plot of all propeller polars over a range of pitch ratio, we will then have the higher pitch ratios on the right and the lower ones to the left. What then happens in self-propeller tests is that the measured K_T value does not locate on the correct pitch polar with the corresponding K_Q value. In most cases it will be found that the K_Q lies to the low pitch ratio side of the actual open polar and it is this that produces the phenomenon of relative rotative efficiency. Values of relative rotative efficiency exceeding unity are then obtained, which to the logical mind appears to be impossible, but if it is realised that what has really happened is that the actual correlation of the behind thrust and torque has left the open line and come to a smaller K_Q value or in other words the centroid of the thrust of the behind propeller has been moved radially inboard, as a consequence of the normal wake distribution in a single-screw ship, having the heavier wake towards the shaft centre. Thus when we see this taking place we realise that all that positive relative rotative efficiency is showing is that there has been a change in the wake distribution compared with the uniform distribution of the open condition. Therefore, really, relative rotative efficiency is merely a wake distribution factor and if one thinks of it in that way one can get a much clearer understanding of the problem.

R. E. Froude, when he first introduced the idea of rotative efficiency was then principally concerned with twin screw naval vessels, and there the erratic variation of rotative efficiency with opposite screws certainly puzzled him. Part of the trouble was due to the fact that the starboard and port propellers, being of opposite hands, were never made with identical accuracy ; and one frequently found different rotative efficiencies for the two screws, so offering some justification for the authors' own statement that rotative efficiency was earlier known as a "catch-all". Model manufacturing inaccuracy should no longer be allowed to occur and so cloud a fundamental issue.

The effect of a positive rotative thus indicates a change in the wake distribution and therefore a bigger wake towards the root. If one makes the thrust wake integration as the authors have done radially, it will be found to yield a correct rotative efficiency (in the real meaning of the word) which is actually less than unity. Thus if one does not presume the propeller to do the integration but if, as the authors did, one takes each radius separately, from such integration a lower rotative efficiency and a higher wake will be obtained. It is rather significant however that in the authors' tests the thrust wake is less than the torque wake. This is most unusual. Most single screw ships show the reverse, certainly with ordinary testing methods. When this is more deeply considered, as the authors have done, it becomes clear that the wake has actually increased, and one has then to recredit what was previously known as rotative efficiency to an increase in the wake due to the difference in the wake distribution.

I am extremely glad that the authors have brought out this particular point and I hope my remarks are understandable in the light of their own work. One is tempted to believe that the original description of the words "rotative efficiency" was a justifiable one, but we now see that there is no justification for thinking that the propeller normally can work with a higher efficiency behind the hull than in the open. Yet certainly in the thirties, Teddington was reporting rotative efficiencies of about 1.2 and even higher, and Dr. Baker himself expressed the view that these results were evidently "phoney" and there was some other explanation to be found for the meaning of rotative efficiency. I suggest that the wake distribution effect is the real interpretation.

The authors state that the wake is caused by the presence of the hull and the free surface. This is not quite correct. It is not caused by the presence of the free surface, but provided there are waves on the free surface then admittedly they may have some effect on the

wake. One could have, for example, a submarine generating waves on the surface when the submarine itself was totally submerged. There could then be a wake change depending upon the orbital motion of the waves passing the propeller. If there were no surface waves, however, there could not be any additional wake, at least not in my opinion.

Finally, I should like to refer to the authors' determination of the form effect of their model. They have used the ITTC line with its 75 numerical coefficient to determine the form effect deduced by the Prohaska method. If one allows for the fact that the low value they obtained of about 2 1/2 per cent, by using the 75 coefficient should be changed to refer to the Hughes' two-dimensional basis using a 66 coefficient, one will find a form effect of 16 1/2 per cent. On the other hand, when one investigates what the equivalent plank would be for the model - that is a plank having the same length as their model and the same measured surface as their model - one finds the minimum value to be some 22 1/2 per cent. This throws doubt on the Prohaska method which is insecurely based, in my opinion, on the unjustifiable assumption that the specific resistance initially varies as the fourth power of the Froude number. Older work, and certainly the very early work of Hovgaard, Taylor and others, appeared to produce a certain unanimity in the finding that the specific resistance initially varies as the square of the Froude number. One has just the choice between the fourth and the second power and if the Prohaska method is used with either of these assumptions one finds that using the square relation gives a much smaller form effect than using the fourth power of the Froude number. It is suggested therefore that the method is not sufficiently acceptable for determining form effect ; and when this is also associated with the basic defect of the ITTC line in its inability correctly to extrapolate to the ship, I think we have to fall back on the only alternative way of correctly determining a form effect, which is to have a geosim series for each particular ship. Against this it is always held that a geosim series is much too expensive, and this is certainly true. But I suggest that the cost of truth has to be faced and in the general euphoria is soon forgotten.

I would say, in conclusion, that I have greatly enjoyed this paper and strongly recommend it to all who are interested in the subject.

DISCUSSION

Georg P. Weinblum
Institut für Schiffbau der Universität Hamburg
Hamburg, Federal Republic Germany

There exists a small number of investigations on the interaction problem of the complete system hull-propeller-rudder. Herbert Voigt showed (JSTG 1932) that the thrust deduction t of a single screw ship with an old fashioned square rudder post and a plate rudder could be appreciably reduced by fitting a stream lined rudder. Results of a systematic investigation of the "complete" problem have been published by Ivchenko (publications of the Krylov Institute, Ship hydrodynamics II ; unfortunately, I was unable to obtain the report by the same author which show the pertinent proofs, Krylov Institute, No 146). Ivchenko's findings are supported by extended experimental work.

Most advanced ideas on the subject are due to Yamazaki ; the first of a general and therefore rather programmatic character, the second one presenting the application of theory to a thin ship, showing an unexpected increase of t due to a streamlined rudder.

Because of the complex character of our problem the authors justly restrict themselves to the classical hull-propeller system, emphasizing free surface effects while a recent paper by Dyne treats pertinent scale effects. It may be permitted to state, that the authors lived up to the high standard, set by Dickmann in his classical work on the subject. Especially they used all modern methods partially developed by them and were not anxious to perform tedious calculations to obtain quantitative results. The choice of a simplified mathematical model is justified by the fundamental character of the investigation leading to the conclusion (Fig. 30), following which the wave thrust deduction t_w contrary to Dickmann's conjecture becomes heavily dependent upon the Froude number for $F_n = 0.30$. Indications of this dependence $t_w(Fn)$ have been communicated by Pien (SNAME Jubilee meeting, 1968). Because of the extremely bad wave making properties of the model this speed limit may be higher and the effect much less pronounced with usual practical forms. I disagree with the authors statement in concluding remarks that "contrary to common belief the wave component can be dominant in the wake.... at $F_n \approx 0.3$" .

The dependency of the wake upon the Froude number was an important finding by F.Horn, several times published by him and his school, also in English, and recommended as design principle. The authors being thoroughly familiar with the German school, I would prefer a statement that their findings nicely support these well known results.

It is a matter of opinion and of considerable importance with regard to scale effects that the difference between measured and calculated t-values is due to an appreciable viscous component. Ivchenko corrected the disagreement by a factor caused by non uniformity and unsteadiness. As pointed out by the authors here much remains to be done.

DISCUSSION

Klaus W. Eggers
Institut für Schiffbau der Universität Hamburg
Hamburg, Federal Republic Germany

I have a short comment regarding the analytical method for determining the wave-thrust deduction, which was performed here following Eq. (B65) in order to avoid explicit calculation of the flow generated by the propeller singularity at the hull surface. I want to suggest a more elegant and direct method. As the wave flow generated by the hull within the propeller area is available through closed form integration over the hull, the wave induced drag on the hull due to the propeller field can easily be calculated as a Lagally-force on the propeller singularities induced by the inverse flow due to the hull. i. e. the flow for the case that the ship travels astern with the same speed. I wonder if such a calculation would confirm the numerical results obtained so far only indirectly through (B65).

DISCUSSION

Carl-Anders Johnsson
Statens Skeppsprovningsanstalt
Göteborg, Sweden

I should like to emphasise Professor Telfer's plea for taking the relative rotative efficiency seriously and draw the authors' attention to an earlier work by Yamazaki in 1966 which contains some interesting calculations of the relative rotative efficiency. I should also like to ask the authors why they use wheels for measuring the wake and not pitot tubes. Some years ago we used wheels at the Swedish tank but we had difficulties in getting consistent results.

DISCUSSION

Gilbert Dyne
Statens Skeppsprovningsanstalt
Göteborg, Sweden

The investigation presented in this paper is a valuable contribution to the understanding of the important hull propeller interaction problem. The paper illustrates clearly how fruitful a combination of theory and experiment can be when treating complicated flow phenomena.

The strength, σ, of the sinks representing the propeller is directly related to the propeller induced mean axial velocities at the disk. Following the definitions used by the authors, σ, is given by

$$\sigma(R,\theta) = -\frac{u_{A\infty}}{4\pi} = \frac{Z}{4}\int_x^1 \frac{dG}{dx}\cdot\frac{\frac{\pi x}{J}-\frac{u_{T\infty}}{V_A}}{\pi x\left(1+\frac{u_{A\infty}}{V_A}\right)}\,dx \qquad (1)$$

for a moderately loaded propeller, see [1]. In Eq. (1) $u_{A\infty}$ and $u_{T\infty}$

are propeller induced velocities in the ultimate wake.

If the rotation of the slipstream is ignored ($u_{T\infty} \ll \frac{\pi x}{J}$) and G is assumed to be independent of the radius x

$$\sigma(R,\theta) = -\frac{u_{A\infty}}{4\pi} = \frac{-Z}{4J} \cdot \frac{G}{1 + \frac{1}{2}\frac{u_{A\infty}}{V_A}}$$

Inserting

$$C_{Th} = \frac{2\pi}{J} \cdot Z \cdot G$$

see [1], and eliminating $\frac{u_{A\infty}}{V_A}$, the Dickmann formula

$$\sigma(R,\theta) = -\frac{\sqrt{1 + C_{Th}} - 1}{4\pi} \qquad (2)$$

is obtained.

If on the other hand G is assumed to vary along the radius, but both $\frac{u_{A\infty}}{V_A}$ and $\frac{u_{AT\infty}}{V_A}$ are ignored, the formula proposed by Hough and Ordway is obtained :

$$\sigma(R,\theta) = -\frac{ZG}{4J} \qquad (3)$$

This formula is strictly valid only for very lightly loaded propellers.

Fig. 1 illustrates the different values of σ obtained with the exact formula, Eq. (1) and the approximate ones, Eq. (2) and (3), for a propeller loading typical for the investigation in question. As seen the Dickman approximation agrees much better with the exact solution than the light load approximation of Hough and Ordway. Thus the reason for the higher σ values obtained with Eq. (3) is not the more realistic distribution of circulation but the erroneous ignoration of the propeller induced velocities. This means that the calculated

- self induced free surface wake of free-running propeller in Fig. 12,
- wave resistance of free-running propeller in Fig. 14,
- free-wave spectrum of propeller and hull with propeller in Figs 18, 19, 21 and 22 and
- thrust deduction fractions in Fig. 30 .

are overestimated in these cases where the Hough and Ordway approximation is used.

The authors have calculated the potential (or displacement) and wave wake fractions assuming ideal flow conditions. In real flow these fractions are, as pointed out by Dickmann, influenced by the viscous wake in a complicated way. This influence can, however, be calculated if experimental values of velocity and static pressure at the propeller disk are available, see [2]. Are there any plans to follow up the investigation with pitot tube measurings ?

The oscillations in the measured thrust deduction with Froude number were found to be much stronger than in the calculated. The reason for this is said to be that either the viscous thrust deduction oscillates appreciably or that the assumption of the hull sources being independent of Froude number is invalid. In my opinion a much more likely explanation can be the measuring errors. Everyone acquainted with towing tank experiments knows how difficult it is to determine the thrust deduction with good accuracy. No direct information on these errors is given in the paper, but the measuring points in Fig. 4 indicate that resistance is determined with an accuracy of $\pm$ 2 % . Assuming the same accuracy for the thrust measurements the error in thrust deduction will be $\Delta t = \pm 0.04$ - a value which is of the same order as the oscillations in t shown in Fig. 30.

The influence of the free water surface on the propulsive coefficients has been determined for the ideal flow case. As pointed out by the authors the viscous flow around the ship can make the stern less effective in wavemaking. This means that the presented calculation procedure instead of giving an exact measure gives almost equally important qualitative results and an upper limit of the wave influence.

REFERENCES

1 DYNE, G., "A Method for the Design of Ducted Propellers in a Uniform Flow", Publ. N° 62 of the Swedish State Shipbuilding Experimental Tank, 1967.

2 DYNE, G., "On the Scale Effect on Thrust Deduction", RINA 1972.

REPLY TO DISCUSSION

Som D. Sharma
Hamburgische Schiffbau Versuchsanstalt
Hamburg, Federal Republic Germany

To Professor Telfer

We agree with Professor Telfer that our treatment of relative rotative efficiency has been probably less than adequate. While we still regard it as an empirical catch-all for various unclarified effects, we must admit in the light of our own results that these effects are not necessarily of insignificant magnitude ! We are well aware of the historical reason why R. E. Froude (1898) first introduced the concept of relative rotative efficiency and of the fundamental research in the thirties, notably by Horn (1932), which led to the modern interpretation of relative rotative efficiency as representing the effects of dissimilarity in flow conditions on the propeller behind the hull and in open water, while still retaining the original, somewhat misleading name. The multifarious nature of this dissimilarity can be illustrated by enumerating some of its aspects :

1. Spatial nonuniformity of the incident flow, i. e. the variation of axial wake component w^x with the three space coordinates (x, R, Θ), and the very presence of any non-zero radial and circumferential wake components w^R, w^Θ as well as their local variation with the coordinates (x, R, Θ).

2. Temporal nonuniformity of the incident flow at any fixed point in space, e. g. due to unsteady boundary layer separation from the hull; including ambient turbulence in the hull wake.

3. Guide vane effect of hull and rudder.

4. Hub effect due to the opposite directions in which the propeller shaft generally extends in the behind-hull and open-water conditions.

5. Possible differences in the Reynolds (and Froude) numbers between the behind-hull and the open-water tests.

In the currently accepted method of propulsion factor analysis the relative rotative efficiency is indirectly determined as a derived quantity thereby lumping together all these effects into a single fudge factor. Despite some remarkable attempts in the thirties, such as by Lammeren (1938), to identify individual phenomena, it can

hardly be asserted that the effects involved have been really clarified.

The confusion and mystery still surrounding the relative rotative efficiency are best illustrated by the fact that values larger than unity are often observed on models of single screw ships while physical reasoning suggests that nonuniformities of flow would in general tend to lower propeller efficiency. The traditional explanation for this phenomenon used to be a favorable propulsive effect attributed to the rudder. However, it is doubtful whether this view can be sustained in view of recent rational calculations of propeller-rudder interaction such as by Isay (1965) and Brunnstein (1968). They have evaluated this interaction in three parts. First, it is found that a suitably profiled rudder does experience a thrust in the slip stream. However, a force acting on the rudder must by definition show up in the thrust deduction fraction and not in the relative rotative efficiency. Second, the displacement flow associated with a thick rudder tends to increase both propeller thrust and torque. This, however, is just a consequence of the increased mean effective wake. Third, what then remains as contribution of the rudder to relative rotative efficiency is a guide vane effect reflected in a nonuniform flow induced by the rudder singularities in way of the propeller. This effect, as Isay and Brunnstein conclude, actually tends to decrease propeller efficiency!

It is true that Professor Telfer in his (1951) paper had suggested a different explanation of relative rotative efficiency. His argument was based on the notion that the simple thrust identity principle yields a wrong value of mean effective wake since propeller performance behind the hull is affected in a peculiar way by the radial variation of the (circumferentially constant) axial wake. He proposed an alternative analysis in which the mean effective wake is determined from the K_T vs. J curve of a virtual propeller which is similar to the real propeller in all respects except pitch, such that the open-water K_T vs. K_Q polar of the virtual propeller matches the behind-hull K_{TH} vs. K_{QH} polar of the real propeller. It is easy to deduce from propeller series charts that Telfer's analysis would almost always lead to a value of relative rotative efficiency closer to unity than the conventional analysis. Suppose for instance that the conventional analysis produces $\eta_R > 1$. Then the behind-hull K_{TH} vs. K_{QH} polar will lie to the left of the open-water K_T vs. K_Q polar and hence a virtual propeller of lower pitch will have to be chosen. This would indicate a lower value of J , which in turn due to the convex shape of the η_0 vs. J curve would yield a higher value of $\eta_0/(1-w)$ for the real propeller. But since η_D and t are independent of the choice of wake, so is the quantity

$$\eta_R \, \eta_0/(1-w) = \eta_D/(1-t)$$

Consequently, the increased value of $\eta_0/(1-w)$ in Telfer's analysis would automatically lead to a lower value of η_R. If we had started out with the conventional analysis yielding $\eta_R<1$, an opposite effect would have been achieved. Thus Telfer's analysis simply transfers to wake a part of the effect manifested in conventional analysis as relative rotative efficiency, whether or not his argument is physically justified.

Professor Telfer seems to interpret our results as providing new evidence in favor of his hypothesis. This requires some clarification. First, it should be emphasized that our propulsion factors as depicted in Fig. 25 were derived by strictly conventional analysis and not by any special method as Professor Telfer seems to imply. Results for the three speeds chosen for detailed study are reproduced below :

Speed parameter		Measured behind hull			Measured in open-water at thrust identity				η_R
γ_0	F_n	J_H	K_{TH}	$10\,K_{QH}$	J_T	K_T	$10\,K_Q$	η_0	$\frac{K_Q}{K_{QH}}$
4.0	.354	.733	.210	.358	.627	.210	.341	.615	.95
7.0	.267	.889	.207	.361	.636	.207	.336	.624	.93
12.5	.200	1.131	.170	.341	.724	.170	.290	.675	.85

If nominal wakes indicated by wake wheels (see III.6.2) had been used instead of the thrust identity wakes, the following propulsion factors would have been obtained :

Speed	From open-water at mean nominal wake					From open-water at 0.7R nominal wake				
γ_0	J	K_T	$10\,K_Q$	η_0	η_R	J	K_T	$10\,K_Q$	η_0	η_R
4.0	.581	.228	.365	.578	.94	.564	.237	.375	.567	.93
7.0	.630	.209	.340	.616	.93	.603	.221	.354	.599	.92
12.5	.787	.140	.252	.696	.90	.713	.173	.294	.668	.85

It is seen that our relative rotative efficiencies always come out less than unity, irrespective of whether nominal or effective wakes are used for analysis. The above numbers cannot be used as evidence either for or against Telfer's hypothesis. However, our paper contains more specific information not explicitly pointed up in the text. Since our computer simulation of the propeller behind the hull included the radially varying circumferentially averaged axial wake component but none of the other nonuniformities, its results may be used to isolate what may be termed for brevity the "rvcaaw" factor from all the other influences responsible for relative rotative efficiency. This is done in the following table (see below). It is seen that the "rvcaaw" factor, represented by the ratio of open-water torque K_Q to the simulated torque $\tilde{K}_{QH}$ in a hypothetical flow in which only a radial variation of the axial wake is allowed, is here indeed slightly

Speed	Computer simulated behind-hull condition					Factors of η_R		
γ_0	J volume average	$\tilde{J}_T$	$\tilde{K}_{TH}$	$10\,\tilde{K}_{QH}$	$\tilde{\eta}_B$	$\frac{K_Q}{\tilde{K}_{QH}}$	$\frac{\tilde{K}_{QH}}{K_{QH}}$	$\frac{K_Q}{K_{QH}}$
4.0	.626	.621	.211	.336	.621	1.01	.94	.95
7.0	.659	.630	.207	.332	.625	1.01	.92	.93
12.5	.810	.705	.171	.284	.676	1.02	.83	.85

larger than unity, while the remaining factors nevertheless lead to an exceptionally low overall relative rotative efficiency of our model. However, we recall that Beveridge (1963a) by a different numerical procedure obtained values of 0.94 (in a submarine hull wake) and 1.01 (in a ship hull wake) for the "rvcaaw" factors of two wake-adapted propellers. Hence the question, whether or not a radially varying (but circumferentially uniform) axial wake can be blamed for spuriously large values of relative rotative efficiency as argued by Telfer (1951), must be regarded as still open.

In reply to Professor Telfer's next comment, we do not want to argue whether the wave component of wake should be attributed tc the presence of the free surface or to the waves on the free surface. The fact is that any finite disturbance moving at or near the free surface will cause waves and hence wave wake. In particular, a propeller moving near the otherwise undisturbed free surface will also cause waves even in the absence of a hull and thus experience a wave wake ;

this is what we have called the self-induced wave wake. Ambient waves caused by wind or moving objects other than the hull and propeller have not been considered in our paper.

Professor Telfer's final comment deals with the Hughes-Prohaska method of determining form factors and the value obtained for our model. Taking the value first, we agree with him that if the two-dimensional plane friction formula is assumed to be

$$C_{F0} = 0.067 (\log_{10} R_n - 2)^{-2} ,$$

then the "true" form factor for our model becomes $1.025 \cdot 75/67 = 1.15$. The length/breadth ratio of a flat plate equivalent to a submerged double model of our hull form would be $L^2/S = 5.79$. From Figure 10 of Hughes (1954) we find that the form factor of such a plate arising from three-dimensional edge effects would be about 1.11, which compares well with our value for the model. We do not know how Professor Telfer derived his minimum value of 1.225. Turning now to the method itself, we have followed the Hughes (1963) idea as reflected in our Equations (7) to (11) because it is consistent with our data (see Figure 4) and the linearized theory of the wave resistance of thin ships. In fact our Equation (B28) for the theoretical wave resistance can be shown to have the asymptotic representation :

$$F_n \longrightarrow 0 : \quad C_{WH} = \frac{2048}{3\pi} (b^2/S) F_n^4 + 0(F_n^5) \simeq 3.15 F_n^4 .$$

That the measured coefficient, see Equation (12), is only about 1/4 of the theoretical value may be explained by the fact that as $F_n \longrightarrow 0$ the stern becomes almost totally ineffective in wavemaking. - We agree with Professor Telfer that if extrapolation rather than analysis were our goal, the most direct and reliable method would have been to test geosims.

To Professor Weinblum

We are most grateful to Professor Weinblum for his kind remarks ; the comparison with Dickmann's legendary work is almost too much of a compliment. His reference to the work of Yamazaki, Nakatake and Ueda (1972) is very much to the point. This is evidently the most comprehensive theoretical study of the complete interaction problem of hull, propeller and rudder published to date. Due to the complexity of the problem we decided to restrict our study to the simpler hull-propeller system. The interaction between propeller and rudder has been theoretically calculated also by Isay (1965) and

Brunnstein (1968). They identify two counteracting forces on the rudder in the slipstream : a thrust resulting from virtual angles of attack induced by the rotation of the slipstream, and a frictional drag due to the increased axial velocity in the slipstream. Depending on the relative magnitudes of these two forces, the net effect might be a decrease or increase in the thrust deduction as compared to the no-rudder case.

We admit that our hull form has rather poor wavemaking properties so that the results may not be representative of ordinary ships. As explained in Section 3.1, an unusually high waterplane coefficient was necessary to produce appreciable thrust deduction effects without sacrificing thinness (L/B = 10), which seemed to be a prerequisite for the application of wavemaking theory.

Professor Weinblum caught us on a vulnerable formulation in Section 4 of our paper. Of course, it is a matter of opinion whether or not a dominant wave component in the wake runs contrary to "common belief" . However, we accept Professor Weinblum's better judgement on this point.

To Professor Eggers

Professor Eggers has hit upon the most intricate point in our theoretical analysis : the calculation of thrust deduction taking account of the wavemaking of the hull and the propeller. Despite its misleading name thrust deduction is actually a force physically acting on the hull. Therefore, the conceptually most direct approach would be to compute it by Lagally's theorem as an integral over the source distribution of the hull, see Equation (B63). However, as explained in Section B.7 we preferred an indirect but numerically more expedient approach involving the wave resistances of the hull and the propeller and a fictitious force $\delta_{H}R_{WP}$ induced by the hull on the propeller sources, see Equation (B65). Our method thus involved in some cases the evaluation of relatively small differences of large numbers. This made us a bit doubtful of our results, specially because the wave component t_w of the calculated thrust deduction fraction $(t_p + t_w)$ changed its sign at about $F_n = 0.23$, a feature we could not intuitively explain, see Figure 30.

Fortunately, Professor Eggers recently suggested to us an alternative and analytically equivalent but numerically even more expedient method based on the inverse flow principle. Since the longitudinal flow induced at the location (x, z) of a hull source by a unit propeller source at (x_P, R, θ) is numerically equal to the longitudinal flow induced at the location (x_P, R, θ) by a unit hull source at

(x, z) in reverse motion, our basic Equation (B63) can be written as

$$\delta_P R_{WH} = 8\pi \int_{R_H}^{R_P} dR \int_{-\pi/2}^{\pi/2} R \, d\theta \left\{ \sigma(R,\theta) \overleftarrow{\phi}^{H}_{x} (x_p, R, \theta) \right\}$$

where the arrow is supposed to indicate reverse motion of the hull. This formula is no more complex than our Equation (B64) for the fictitious force $\delta_H R_{WP}$ and yet elegantly obviates any need for calculating differences of wave resistances. Moreover, by virtue of the fore and aft symmetry of our hull form we have

$$\overleftarrow{\phi}^{H}_{x} (x_P, R, \theta) = - \phi^{H}_{x} (-x_P, R, \theta)$$

so that the required inverse flow in the propeller plane is simply the "bow wake" already computed by us for other purposes. Therefore, taking the circumferentially averaged propeller source strengths from Figure 29 and the circumferentially averaged bow wakes from Figure 6 we were easily able to recalculate our nondimensional thrust deduction $\delta_P R_{WH}$ and thence by Equation (B66) the thrust deduction fraction $(t_p + t_w)$ for the three cases $\gamma_o = 4.0$, 7.0 and 12.5. The results turned out to be identical with our original calculations, thus providing a useful crosscheck and enhancing our confidence in the numerical analysis.

To Dr. Johnsson

Our detailed discussion of relative rotative efficiency in reply to Professor Telfer will hopefully satisfy Dr. Johnsson. The reason we used wake wheels rather than Pitot tubes was simply that they happened to be available. Moreover, they provided an easy means of measuring both stern and bow wake. Our calibrations (revolutions versus speed) were sometimes highly nonlinear, specially for the larger diameters, but always perfectly consistent and repeatable.

To Dr. Dyne

Dr. Dyne's critical discussion is very welcome, specially in view of his own recent contributions to the subject referred to also by Professor Weinblum.

Although we have not been able to fully verify the details of Dr. Dyne's analysis, we basically agree with him that the Hough and Ordway (1965) analysis applies strictly to lightly loaded propellers

and that his formula is likely to yield a better approximation to the source density of a moderately loaded propeller. As we have provided two complete sets of calculations, one based on Dickmann's uniform sink disk and the other on the Hough and Ordway generalized sink disk, and since Dr. Dyne's approximation would lie between these two extremes, we do not consider it necessary to provide a third set of calculations at this time. However, it is interesting to observe that the reduced source strengths following Dr. Dyne would lead to calculated values of the thrust deduction fraction $(t_p + t_w)$ which are substantially lower than the measured value of t, as is also the case in Dr. Dyne's (1972) paper. It is unlikely that such large differences can be attributed soleley to the viscous component t_v. This suggests that it would probably be necessary to invoke a mathematical propeller model involving finite chord length and finite blade number even for calculating such "simple" time-averaged effects as the thrust deduction. Professor Weinblum's reference to Ivchenko's hypothesis that the discrepancy between calculated and measured thrust deduction might be due to unsteady effects is a valuable hint in this direction.

Dr. Dyne further suggests that the oscillations of the measured thrust deduction with respect to Froude number observed in our Figure 30 might simply reflect random measuring errors. We beg to disagree. As explained in the paper (see Figure 23) the propulsion factors at the ship self-propulsion point were not determined from single runs but by least squares polynomial interpolation between five or more measurements at different loadings. It is unlikely that such faired results would randomly produce oscillations with respect to Froude number in obvious correlation with the calculated wave resistance and wake.

We agree with Dr. Dyne that our theoretical wavemaking calculations probably represent upper bounds for the true magnitude of these effects in a real fluid. Finally, we regret that we are not contemplating a follow-up investigation of our wake by means of Pitot tubes as suggested by Dr. Dyne, but we would consider it a valuable extension if others working on this problem would care to do so.

REFERENCES

BEVERIDGE, J.L., "Performance of wake-adapted propellers in open-water and propulsion conditions as determined by theory and experiment", DTMB Report N° 1777 (1963a).

BRUNNSTEIN, K., "Wechselwirkung zwischen Nachstrom, Schraubenpropeller und Schiffsruder", Institut für Schiffbau Bericht Nr. 210, Hamburg (1968).

FROUDE, R.E., "Experiments on the effect of direction of rotation in twin screws", Transactions INA 40, 61-68 (1898).

HORN, F., "Ungleichförmigkeitseinflüsse bei Schiffsschrauben", Hydromechanische Probleme des Schiffsantriebs 1, 343-379, Hamburg (1932).

HUGHES, G., "Friction and form resistance in turbulent flow, and a proposed formulation for use in model and ship correlation", Transactions INA 96, 314-376 (1954).

HUGHES, G., "The influence of form and scale on model and ship resistance. Proceedings ITTC 10-2, 96-109, London (1963).

ISAY, W.H., "Über die Wechselwirkung zwischen Schiffsruder und Schraubenpropeller", Schiffstechnik 12, 65-76 (1965).

LAMMEREN, W.P.A., van, "Zerlegung der Antriebskomponenten in Abhängigkeit vom Maszstabseinfluss mit Hilfe von Schiffsmodellversuchen", Werft, Reederei, Hafen 19, 261-265 (1938).

TELFER, E.V., "Marine propeller and propulsion miscellany", Transactions NECIES 68, 107-132 (1951).

YAMAZAKI, R., NAKATAKE, K., UEDA, K., "On the propulsion theory of ships on still water", Memoirs of the Faculty of Engineering, Kyushu University 31, 132-229 (1972).

* * *

SHEAR STRESS AND PRESSURE DISTRIBUTION ON A SURFACE SHIP MODEL : THEORY AND EXPERIMENT

T. T. Huang and C. H. von Kerczek
Naval Ship Research and Development Center
Bethesda, Maryland, U.S.A.

ABSTRACT

This paper presents the results of an experimental and theoretical investigation of the distribution of shear stress and pressure on BRIAN BORU, a 20-foot model of a Series 60, Block 60, surface ship. Boundary layer calculations were carried out using the Cumpsty-Head-Smith momentum integral method under the small crossflow assumption; the potential flow was obtained from slender body theory for zero Froude number. Surface shear stress and pressure distribution were measured at sixty points on the hull ; the magnitude and direction of shear stress were determined from high-aspect ratio hot films and Preston tubes. Additional data on total resistance, sinkage, trim, and wave profiles on the hull are also presented.

The experimental and theoretical results are compared for a range of Froude numbers ($0.2<Fn\leq 0.35$) The present boundary layer computation is adequate for the ship model tested (moderate block coefficient) if the potential flow around the ship is accurately prescribed. The sinkage and trim, and wave profiles along the hull predicted by thin ship theory are not in good agreement with the measured values.

1963

INTRODUCTION

Since the contribution of Froude about a century ago, total ship resistance has been assumed to be composed of two separate and independent parts : (1) frictional resistance, equal to the resistance of an equivalent plank or flat plate of the same wetted area and length as the ship, and (2) the remainder, called "residual" resistance. It has been a practical engineering solution to extrapolate the resistance measured on a model to that of a full-scale ship either (1) by assuming that the frictional resistance follows a Reynolds-number scaling law and that the residual resistance follows a Froude-number scaling law, or (2) by using a form factor to distribute part of the residual resistance into viscous form drag. These phenomenological assumptions have never allowed one to predict by pure analytical means the resistance of a ship.

The prediction of total ship resistance depends on our ability to calculate the potential flow and turbulent boundary layer flow around ship hulls. The calculation of the potential flow not only provides the wave resistance, but also provides the "outer" flow for the boundary layer computation. At present, the potential flow about a given hull has been solved only approximately (e. g. , Michell thin ship theory and slender ship theory). It is well known that thin ship theory fails for the flow around the bilges and on flat bottoms of ships, Lunde[1] , and slender ship theory overpredicts the effect of the waves, Tuck[2] . More accurate methods for predicting the potential flow around surface ships are not available. We can, however, calculate the potential flow about deeply-submerged bodies and about ships at zero Froude number (e. g. , the submerged "double model"). This can be done accurately by the Douglas-Neumann[3] computer program, and approximately by the slender-body computer program of Tuck and von Kerczek[4] . As will be demonstrated, this program yields an adequate approximation of streamlines and pressure distributions on "slender" ships at very small Froude number for the boundary layer calculations. The calculation of the boundary-layer flow in the context of the submerged double model can serve to develop and to test the boundary layer calculation methods. Furthermore, this computation may provide a good approximation of the boundary layer flow around a ship hull at low Froude number, especially in the vicinity of the shoulder and bilge.

The present status of three-dimensional boundary layer calculation methods is somewhat better than the ship potential flow theory. Several computation methods have been developed recently :

(1) the "differential methods" of Bradshaw[5] and Nash[6] ; and (2) the momentum integral methods of Cumpsty and Head[7] , and Smith[8] . The differential methods use the Reynolds boundary layer equations and transport equations for the Reynolds stresses. These methods are numerically complex and have not yet been applied to fully three-dimensional flows such as over a ship hull. The momentum-integral methods are fairly simple extensions of two-dimendional momentum-integral methods. The extension is carried out in the natural setting of streamline coordinates. The main assumptions are : (1) skin-friction in the streamline direction is related to the streamwise boundary-layer velocity profile in exactly the same way as in a two-dimensional flow, (2) the crossflow velocity profile is simply related to the streamwise profile by an empirical formula, and (3) the auxilliary equation is the three-dimensional extension of the two-dimensional equation with exactly the same empirical auxilliary function as in two-dimensional flow. A straight forward computation scheme based on these assumptions has been developed [7,8,9] . Landweber[10] has criticized the use of momentum-integral methods for three-dimensional flows because of the assumptions made for the skin friction and crossflow velocity profile, especially when crossflow occurs along streamlines which have changes in the sign of geodesic curvature. For a ship of moderate block coefficient where the crossflow is generally small[11,12] , the usual momentum-integral methods can be expected to lead to useful results. A computation scheme proposed by Lanweber, using a differential method or integral-vorticity equations in principal-curvature coordinates, has yet to be developed.

A few previous attempts at ship boundary layer calculations invariably employed momentum-integral methods. The early attempts of Wu[13] and Uburoi[14], consisting simply of the application of strictly two-dimensional methods along waterlines, account only for pressure gradient effects and are not reliable since the equally important effect of streamline convergence and divergence is neglected. Gadd[12] used a modified form of the Cumpsty-Head-Smith method and included the effect of streamline convergence and divergence, but the method was applied along waterlines instead of the streamlines. The error incurred due to departure of streamline direction from waterline direction is difficult to assess, but may be significant in the bilge area. However, Gadd makes calculations for cases for which he has some experimental data and obtains fair agreement.

Webster and Huang[15] made calculations similar to Gadd's. They used Cooke's[16] method for three-dimensional boundary layers and Guilloton's[17] method for the potential flow. Their calculations

show mainly the effect of the wave-induced pressure gradients since Guilloton's potential flow method cannot be used to trace, accurately, the streamlines on the lower half of the hull surface. Thus, their results are restricted to boundary layer characteristics along streamlines on the hull near the free surface.

Finally, von Kerczek[18] has applied the Cumpsty-Head-Smith[7,8] method and the slender body potential flow program of Tuck and von Kerczek[4] to calculate the boundary layer on a double hull of the LUCY ASHTON corresponding to the experiments of Joubert and Matheson[19]. von Kerczek[18] found that the effect of streamline convergence and divergence is of overriding importance. Computed skin friction coefficients are in good agreement with the measured values. The present study uses von Kerczek's[18] computer program to compute the boundary layer for BRIAN BORU, the series 60 block 60 model at zero Froude number. The computed results are compared with experimental data at Froude numbers equal to 0.22, 0.28, and 0.32. These comparisons are a first step towards developing a boundary layer computation method for a ship at arbitrary Froude number.

Shear stress distributions on the ship hull at arbitrary Froude number has been measured by Steele[20] (Tanker Model), Steele and Pearce[21] (High Speed Linear), and Tzou[22] (Series 60 block 60 model). All of these shear stress measurements were along waterlines only and considerable oscillation of the shear stress along the waterlines was noted[20,21]. In none of these experiments was shear stress direction measured.

In the present study we use hot-film and Preston tubes located at sixty points on the hull to measure the shear stress distribution on BRIAN BORU at various Froude numbers. The probes were located along four zero Froude number streamlines and along one waterline (14% draft). The direction of shear stress was determined by the hot-film shear probe. In addition, pressure distribution, total resistance, trim, sinkage, and wave profiles were also measured for a range of Froude numbers. A completely-detailed set of experimental ship resistance data is collected and presented. Available theories are compared with the corresponding experimental data. Only the boundary layer computation method will be described briefly in the next section. The other theories will be used without derivation.

CALCULATION OF THE TURBULENT BOUNDARY LAYER

We calculate the turbulent boundary layer on the ship hull

by the method of Cumpsty and Head [7] and Smith [8] with the additional assumption of small crossflow. A complete description of the method is given in References (7) and (8) and a description of its application to ship hulls in Reference (18). We will only reproduce the final formulas here.

In the following we have non-dimensionalized with the following units : half the ship length, $L/2$, for length, the ship speed, V, for velocity, and $\rho U^2/2$ for stress, where U is the (dimensional) inviscid velocity at the edge of the boundary layer. Let θ_{11} and δ_1^*, be the momentum and displacement thickness of the streamline component of the boundary layer flow, where

$$\theta_{11} = \int_o^{\delta} \left(1 - \frac{u}{U_s}\right) \frac{u}{U_s}\, dN\,, \quad \delta_1^* = \int_o^{\delta} \left(1 - \frac{u}{U_s}\right) dN \qquad (1)$$

N is the coordinate normal to the body, U_s is the inviscid velocity at the edge of the boundary layer, u is the boundary-layer time-averaged velocity component in the streamline direction and δ is the nominal boundary layer thickness. The relationship between θ_{11}, δ_1^*, and $C_{f1} = \tau_{\omega 1}/(\rho U^2/2)$ where $\tau_{\omega 1}$ is the wall shear stress in the streamline direction is determined by assuming small crossflow and integrating the approximate momentum-integral equation

$$\frac{d\theta_{11}}{d\alpha} + \theta_{11}(2 + H)\frac{1}{U_s}\frac{dU_s}{d\alpha} - \theta_{11}K_1 = C_{f1}(\theta_{11}, H) \qquad (2)$$

and the auxilliary rate-of-entrainment equation

$$\frac{d(\theta_{11} G)}{d\alpha} + \theta_{11} G \left(\frac{1}{U_s}\frac{dU_s}{d\alpha} - K_1\right) = F(G) \qquad (3)$$

along the streamlines, where α is the arc length parameter along the streamlines. In equations (2) and (3) K_1 is the geodesic curvature of the equipotential line, $H = \theta_{11}/\delta_1^*$ is the shape factor and G is the parameter $(\delta - \delta_1^*)/\theta_{11}$ and F is the empirical rate-of-entrainment function. The empirical correlation of F to G to H is given by Standen [23] as

$$F(G) = 0.0306\,(G - 3.0)^{-0.653}$$

$$G = 1.535\,(H - 0.7)^{-2.715} + 3.3$$

The skin friction coefficient C_{f1} is given by the two-dimensional formula

$$\left.\begin{aligned} C_{f1} &= \frac{0.0146\,\left(\frac{Q}{Q_o}\right)^{\frac{4}{H_o+1}}}{\log_{10}(2R_{\theta_{11}})\left[\frac{1}{2}\log_{10}(2R_{\theta_{11}}) + 0.4343\right]} \\ H_o &= 1.475 \,/\, \log_{10} R_{\theta_{11}} + 0.9698 \\ Q &= 0.9058 - 1.818 \log_{10} H \\ Q_o &= Q(H_o) \end{aligned}\right\} \quad (4)$$

where $R_{\theta_{11}} = R_L U_s \theta_{11}$ and $R_L = VL/2\nu$ (recall U_s and θ_{11} are non-dimensional).

This is Granville's [24] formula and is an extension of the Von Karmann-Schoenherr flat-plate skin-friction formula to flows with a pressure gradient. This skin friction formula was chosen over others, for instance the Ludweig-Tillman formula, because it is more accurate at high Reynolds numbers. With the Mager [25] profile assumptions for the crossflow, the crossflow momentum integral equation is transformed into an equation for the angle β that the shear stress makes with the streamline direction. Then β is defined by

$$\tan\beta = \frac{C_{f2}}{C_{f1}}$$

where $C_{f2} = \tau_{w2}/(\rho U^2/2)$ and τ_{w2} is the wall shear stress in the crossflow (e. g. normal to the surface streamlines) direction.

The shear stress magnitude is then given by

$$C_{fm} = C_{f1}\sqrt{1 + \tan^2\beta}$$

β remained less than about 8.5° on all streamlines except in some local regions near the stern on the keel and waterline. Here the transverse section curvatures are very large and the boundary layer approximation is not valid anyway.

Note that equations (2) and (3) correspond to the axisymmetric boundary-layer momentum-integral equations for a body of revolution with local radius r if r is defined by

$$\frac{1}{r}\frac{dr}{d\alpha} = -K_1$$

The dominant three-dimensional effect on slender ships is simply the streamline convergence and divergence represented ty the equipotential line geodesic curvature K_1 [18]

Any potential flow that supplies the streamlines and inviscid velocity distribution thereon can be used with equations (3) and (4), but we have used the very simple zero Froude number, slender-body potential flow theory given by Tuck and von Kerczek[4] in conjunction with the surface equation for the hull described in von Kerczek and Tuck[26]. This combination seemed to give fairly good results for the LUCY ASHTON when compared to the double-model experiments of Joubert and Matheson.[19] We used exactly the same procedure for the Series 60 block 60 calculations and will compare the results to model experiments in a towing tank. The extension of the Tuck-von Kerczek[4] slender-body potential flow program to include free-surface effects is underway. We have used the zero Froude number potential flow because of its availability and the expectation that wave effects on the boundary-layer flow will be relatively minor on the lower portions of the hull. This calculation will serve mainly to illustrate the suitability of the Cumpsty-Head-Smith[7,8] boundary layer method for moderate block-coefficient hulls.

THE MODEL, EXPERIMENTAL SETUP, AND PROCEDURES

The ship model used was a 20-foot Series 60, block 60, wood model. The name "BRIAN BORU" was given to the model as a counterpart to the British research ship model "LUCY ASHTON". A photograph of the model is shown in Figure 1. The body plan is shown in Figure 2. A slight hull modification aft of station 18 (which preserved sectional areas) was made to accommodate a propeller shaft used earlier for propulsion and vibration experiments. This

model has been tested by many of the towing tanks in the world as a standard vibration model. The streamlines on the "double model" were computed by Douglas-Neuman[3] and slender-body[4] potential flow methods. In Figure 2 good agreement between the streamlines computed by each method is noted. The slight difference in streamlines plotted is due mainly to the fact that the starting points in the two computations are not exactly the same.

A coordinate system $0'x'y'$ with its origin in the undisturbed free surface and another coordinate system $o\ x\ y\ z$ fixed in the ship are used. Both are right handed coordinate systems moving with the steady velocity of the ship. The plane $o'x'z'$ is on the undisturbed free surface, $o'x'$ is in the direction of the ship motion and $o'z'$ is upward. The plane oyz contains the midship section, plane oxz the center plane section and the plane oxz the design water plane. The locations of the shear probes and pressure taps in the $oxyz$ coordinate system are tabulated in Table 1. The reference length used to non-dimensionalize all lengths is $L/2$ where L is the length between perpendiculars. When the model is tested in the free-to-trim condition, the two coordinate systems are no longer coincident. We denoted the vertical distance from the axes $o'x$ to ox by $h(x)$ (positive above the undisturbed free surface). The sinkage is defined as $-\left[h(-1) + h(1)\right]/2$, trim by bow by $-\left[(h(-1) - h(1)\right]$, and trim angle by $\tan^{-1}\left[(-h(-1) + h(1))/L\right]$.

Provisions were made for sixty interchangeable shear probes and pressure taps spaced evenly along a total of four zero Froude number streamlines, designated by A, B, C, and D, on the double model, and along a waterline E (14% draft). These probes have to be mounted flush to the hull surface. At each location a one-inch diameter teflon mounting plug was sunk into the hull with its axis parallel to the normal of the ship surface, and its face flush with the ship surface, the surface of the plug was carefully polished to follow the original contour of the hull. The hot-film shear probe penetrated the plug and was fastened by four screws. The depth and angle of the probe with respect to the hull were adjustable. A photograph of this arrangement is shown in Figure 3. The depth of the probe with respect to the surface was carefully set to protude less than 0.002 inches out of the hull surface by using a flat face pressure transducer as a probe-protuberance feeler. Preston tubes and static pressure taps were placed on the hull through the same mounting plugs. Dynasco pressure transducers were used to measure the pressure from the Preston tubes or the pressure taps. Seven-channel DISA (Franklin Lake, New Jersey) constant temperature anemometers were used for the hot-film shear probes which were manufactured by Lintronics

Laboratory (Silver Spring, Maryland). The use and calibration of the shear probes is given in the Appendix. The electrical output of the calibrated transducers was digitized, averaged for 100 seconds, and analyzed in various dimensionless forms using an Interdata computer. The results were printed out immediately after each experiment. At each Froude number the model was first run free to trim. This trim condition was then fixed for subsequent runs at the same F_n .

The total resistance was routinely measured by a floating girder and a block gage. The trim and sinkage were measured using two potentiometers located at FP and AP, and wave profiles were traced along the hull using a colored pencil and then measured. These provided a complete set of experimental data for BRIAN BORU.

RESULTS AND DISCUSSION

The experimentally measured wave profiles along the hull, sinkage and trim, total resistance, and pressure and shear stress distributions at various Froude numbers will be presented and compared with relevant theories and numerical results.

(1) Wave profiles along the hull. Photographs and a dimensionless plot of wave profiles along the hull at six different Froude numbers are shown in Figures 4 and 5, respectively. Figure 6 shows the measured profiles at Fn = 0.22 and 0.28 compared with the profiles predicted by Guilloton's method. Although the forward quarter of the predicted wave profiles on the model compare favorably with the measured profile, the agreement becomes poorer downstream. The prediction not only overestimates the magnitude of the last trough, but also misses the location (phase).

(2) Sinkage and trim. The measured sinkage and trim compared with the first-order thin ship theory computed by Yeung[27] are shown in Figure 7. The measured values of sinkage are all smaller than that predicted. However, the measured sinkage and trim coefficients agree rather well with the calculated values using the zero Froude number, slender body[4] or Douglas-Neuman[3] theoretical pressure distribution. It should be noted that the measured trim does not vary with Froude number as much as that predicted. Since the sinkage, and trim and the wave profiles predicted by the thin ship theory are not in good agreement with the measured values, the thin ship theory may not be suitable for this model which has a flat bottom and a moderate block coefficient. No further comparison of experimental data with thin ship theory is attempted.

(3) Total and residual resistance. The measured total resistance and the residual resistance, $C_R = C_T - C_F$, are shown in Figure 8, where the 1957 ITTC friction line was used to determine C_F for all of the data. The other data of the geosims by Todd [28], and by Tsai and Landweber [29] (parent hull without stern modification) are also shown. The 6-, 10-, and 14- foot models were tested in the Iowa Tank. The C_R of the 10- and 14- foot models is higher than that of 6- and 20- foot models. The 20 model was tested in NSRDC basin I and II. However, reasonable agreement for the 6- and 20-foot models is noted. The C_T of the present 20- foot model was measured in NSRDC basin I and II by a floating girder and a block gage. Turbulence stimulation, a row of studs, 1/8-inch in diameter, 0.1-inches in height, and 1-inch in spacing was used in one of the tests. No significant difference in C_T with the turbulence stimulator was found. The discrepancy in C_T's among the four present tests is less than 2%.

(4) Pressure distribution. If the flow is assumed irrotational, then the Bernoulli equation in the o'x'y'z' coordinate system is

$$\frac{P}{\rho} - V\varphi_{x'} - gz' + \frac{1}{2}\left[\varphi_{x'}^2 + \varphi_{y'}^2 + \varphi_{z'}^2\right] = \frac{P_a}{\rho}$$

where V is ship speed, P_a is the atmospheric pressure and φ the perturbation potential. We define the pressure coefficient by

$$C_p = \frac{P - (P_a - \gamma z')}{\rho V^2/2} = \frac{2V\varphi_{x'} - \left[\varphi_{x'}^2 + \varphi_{y'}^2 + \varphi_{z'}^2\right]}{V^2} \tag{6}$$

which yields $C_p = 1$ at the stagnation point where $\varphi_{x'} = V$ and $\varphi_{y'} = \varphi_{z'} = 0$. If the linearized free-surface boundary condition is used, at any waterline below the undisturbed water surface φ reduces to $\varphi(x', y', z') = \exp(gz'/V^2)\varphi(x', y', z' = 0)$. From Equation (6) we have

$$C_p = \frac{(\zeta + h)}{V^2/2g} \exp\left[\frac{(z+h)g}{V^2}\right] \tag{7}$$

where ζ is the wave height in the oxyz coordinate system and h is the distance between o'x' and ox.

The measured C_p along streamlines A, B, C, and D, and along waterline E and the corresponding approximate C_p computed from Equation (7) and for the double models are shown in Figure 9. As shown in Figure 9-e the wave approximation (Equation 7) is in good agreement with measured values near the free surface (14% draft) for the three Froude numbers tested. However, this approximation is not valid near or on the ship bottom. On the after half of the flat ship bottom the measured C_p is in general close to the C_p predicted by the double model (Figure 9-a through 9-c), and the effect of the surface wave (Froude number) there is small. However, some effect of waves (Froude number) on C_p on the forward half of the ship bottom is noted. It should also be noted that C_p near the keel (streamline A) at a $Fn = 0.22$ is very close to the C_p predicted by the double model. Figure 9-b shows the C_p of the double model model computed by the Douglas-Neuman theory [3] and slender body theory [4,18] Close agreement between the two computations in the middle of the ship is noted.

(5) Shear Stress Distribution. The local shear stress coefficient is defined as $\vec{C_f} = \vec{\tau_w} / (\rho V^2/2)$, a vector tangent to the hull surface. The shear stress magnitude and the angle of the probe relative to the waterline for points on the ship side and to the buttock lines for points on the ship's bottom were measured by rotating the probe to three angular positions $(0, \pm \theta)$. This can be used to compute the magnitude and angular position of shear stress vector on the hull. This information along with the direction cosines of the waterline or buttock line tangents and the surface normal calculated from the surface equation [26], were sufficient to decompose the shear stress vector into three components (C_{fx}, C_{fy}, C_{fz}) relative to the body axes (x, y, z,). The measured direction cosines of $\vec{C_f}$ relative to the (x, y, z) axes are shown in Figure 10 at the high and low Froude numbers of the experiments. Note that these direction cosines do not vary much with Froude number except near the station of maximum wave slope (i.e., between $x = -0.7$ and -0.5).

In Figure 11 we present the measured and calculated distributions of C_{fx} along various streamlines and on waterline E. Note that the agreement between experiment and calculation is better at low Froude numbers and is fairly good on streamline A for the entire range of Froude numbers of the experiment. In these cases, wave effects were at a minimum and this indicates that the Cumpsty-Head-Smith boundary layer calculation is adequate for moderate block-

block-coefficient hulls at small Froude numbers. Crossflow effects are very small throughout. The main discrepancy is near the stern and in the region of maximum wave slope. The discrepancy near the stern is due to a combination of inadequate boundary layer theory, poor pressure distribution prediction, and poor body-geometry fitting by the surface equations there. Improvement of prediction techniques for this region requires special attention. In the region of maximum wave slope, we find that the calculated shear stress magnitude and the measured shear-stress magnitude agree fairly well, so that the differences between C_{fx} measured and C_{fx} calculated shown in Figure 11 is mainly due to differences in streamline direction at zero and finite Froude number.

In the last graph of Figure 11 we have included the calculation of C_{fx} along waterline E of Webster and Huang[15]. Here the pressure gradient effects on the boundary layer due to body geometry and the waves are very small, and thus there is little difference from flat plate values except very near the stern and near the maximum wave slope. An interesting observation is that the Webster-Huang[15] calculation seems to have not predicted the effect of the wave satisfactorily. This effect is mainly due to change in the shear stress direction in accordance with the streamline direction. Webster and Huang[15] used Guilloton's[17] potential flow method to calculate the inviscid velocity on the ship surface. Due to the rather crude approximation of the body and the potential flow, accurate streamlines and consequently accurate values for streamline convergence and divergence are not obtained. The present calculation is also not expected to predict the shear stress near the free surface since the effect of the free surface is neglected in the potential flow computation. From these considerations it seems that it is very important to obtain an accurate discription of the potential flow streamline and pressure distribution in order to adequately calculate the proper magnitudes of the shear stress components (C_{fx} , C_{fy} , C_{fz}).

It also should be noted that both the present computation and the computation of Webster and Huang[15] overpredict C_{fx} near the stern. It is not possible to predict thick boundary layer characteristics near the stern by these methods.

CONCLUSION

Comparison of the measured pressure and shear stress distributions, trim and sinkage, and wave profiles along the hull of BRIAN BORU at various Froude numbers with various theories and boundary layer calculations allows the following conclusions to be

drawn :

1. The sinkage and trim, and the wave profiles along the hull predicted by thin ship theory are not in good agreement with the measured values. Thin ship theory is not satisfactory for ships having a flat bottom and a moderate block coefficient.

2. The measured pressure distributions on the after half of the ship bottom are rather close to those computed on a double-hull model and show little effects from waves (Froude number). Thin ship theory does not give a good approximation of the flow in this region. Near the free surface the pressure distributions behave like a linearized wave, which agrees with the thin ship approximation. The flows near and on the forward half of the ship bottom are affected by the combination of the free surface waves and the details of the ship geometry. A new physical model is needed in order to predict the flow over the after half of the hull.

3. The measured shear stress vectors at selected points on the model show that the shear stress vectors are oriented in nearly the same direction as the local streamlines indicating, as has been found previously, that boundary layer crossflow is small on moderate block coefficient hull forms. Although the local shear stress values depart little from equivalent flat plate values, the trend of the departure is fairly well predicted by the Cumpsty-Head-Smith boundary-layer calculation method with the small crossflow assumption, especially along streamlines where wave effects are negligible. This indicates that boundary layer calculations carried out along the streamlines, taking into account pressure gradients and streamline convergence or divergence, using momentum integral methods can be quite useful. It is important, however, to develop an accurate potential flow calculation methods and methods for calculating thick boundary-layer approaching separation.

ACKNOWLEDGMENT

The authors are indebted to J. H. McCarthy of the Naval Ship Research and Development Center for his stimulation and interest during the course of this work. The authors would also like to thank Messrs. N. Santelli, G. S. Belt, and L. B. Crook for their assistance during the experiment. Mr. C. W. Dawson is also thanked for performing the exact double hull potential flow computation. This work was authorized and funded by the Naval Ship Systems Command under its General Hydromechanics Research Program, Task SR0090103.

APPENDIX

EXPERIMENTAL TECHNIQUES FOR MEASURING MAGNITUDE AND DIRECTION OF SHEAR STRESS

In order to determine the shear stress vector distribution on the hull, it is necessary to measure the distribution of the magnitude of the shear stress vector $\vec{\tau}_w$ and its angle Ω with respect to a convenient direction on the ship hull. Two useful measuring devices are considered in this Appendix : the flush-mounted hot-film shear probe, and the Preston tube and the directional Preston probe.

(1) Hot-Film Shear Probes

The principle of the hot-film shear probe is that skin friction is a function of electrical current required to maintain a metal film at the constant temperature placed on the hull surface[31,32]. The output of the hot-film anemometer is a nonlinear power function of shear stress. The ideal response of the hot-film is that the output of the instrument is directly proportional to the shear stress measured. This ideal response can be accomplished by processing the nonlinear output from the anemometer through a linearizer which is commercially available (e.g. DISA type 55D15 linearizer). The functional relationship between the output of the linearizer and the shear stress is obtained through calibration, and slight nonlinear response is tolerable. Most commercial anemometers and linearizers can be adjusted to achieve almost perfect linearization.

Hot-film shear probes designed and built by Ling[31,32] were used in this study. A strip of platinum film about 0.1mm wide and 0.8 mm long is fused under high temperature to the polished end of a pyrex rod 0.1-inch in diameter and 1-inch long. Figure A1 shows the outputs of a hot-film anemometer and linearizer before and after the test versus the shear stresses measured by a Preston tube. A special wall-jet calibration facility, in which the wall shear stress on a flat wall two feet from a 1/2 inch jet can be varied from 0 to 0.5 psf, was built for this study. This facility using towing basin water (not to vary chemical properties and temperature), is essential for the proper calibration of the hot-film shear probes. The directional response of the hot-film shear probe is calibrated by rotating the hot-film element with respect to the flow direction. Typical results are shown in Figure A2. The directional response is proportional to cosine θ up to θ = 65 degrees. The difference between a

misaligned probe is also shown. Since the angular response is a cosine function, the angle between the maximum shear stress and a reference line, Ω can be obtained by rotating the probe $\pm\theta$ with respect to this line, i.e.,

$$\tan \Omega = \frac{(e)_{+\theta} - (e)_{-\theta}}{(e)_{+\theta} + (e)_{-\theta}} \tag{A1}$$

where $(e)_{\pm\theta}$ is the output when the probe is rotated at an angle equal to $\pm\theta$ respectively. The values of θ used in the study were 45 deg. and 30 deg. depending upon the angle of the shear stress vector with respect to the reference line. The film on the probe element was aligned parallel to the waterlines for points on the ship side and parallel to the buttock lines for points on the ship bottom. The angle between the maximum stress and the reference line is obtained through Equation (A1). The magnitude of the shear stress along the reference line and the angle Ω, along with the direction cosines of the waterline and buttock line tangents and the surface normals calculated from the surface equation[26] were sufficient to decompose the shear stress coefficient vector C_f into the components (C_{fx}, C_{fy}, C_{fz}), relative to the body axes (x, y, z).

One of the difficulties in using the hot-film shear probe is mounting the probe perfectly flush to the surface. As shown in Figure A3, the response is very sensitive to the probe protuberance. In order to keep the accuracy within 5%, the probe protuberance should be kept within 0.002 inches. This was accomplished by using a flat face pressure transducer as a probe feeler.

(2) Preston Tube and Directional Preston Probe

The Preston method of measuring skin friction in the turbulent boundary layer makes use of a circular pitot tube resting on the wall. The Preston tube pressure, together with the static pressure at the same point, permits the computation of the skin friction at that point. The use of the Preston tube is based on the assumption that the tube lies within the law-of-the-wall region of the boundary layer. In this study we limit the diameter of the Preston tube to less than 15% of the boundary layer thickness in order to satisfy this assumption. The calibration of a Preston tube reported by Landweber and Siao[33], by Patel[34], and many others is shown in Figure A4. The Preston tube used was also calibrated in a 1-inch pipe flow.

The present calibration is in good agreement with references (33 and 34).

Patel [34] also found that a Preston tube can be used with acceptable accuracy (maximum error of 3 percent) if the pressure gradient parameter is limited to the range $-0.005 < \nu/(\rho u_\tau^3)\, dp/dx < 0.01$ where dp/dx is the pressure gradient along the flow direction and $U_\tau = \sqrt{\tau w/\rho}$ is the shear velocity. The validity of using a Preston tube in boundary layers with large crossflows is not known. However, it is believed that the crossflow on the present ship model is rather small (the crossflow angles calculated are all less than 15 deg.).

The directional response of the Preston tube has been calibrated and is shown in Figure A5. It is not practical to rotate the Preston tube flush on the three-dimensional ship hull and therefore the Preston tube is not used for measuring the angular position of the shear stress vector. The three-tube directional Preston probe, as shown in Figure A6, has very good directional response. One drawback of the Preston tube and the directional Preston probe is that several of them can not be used close together because they will not only cause an increase in the ship model resistance but will also have an interference effect on the downstream probes (see Figure A7).

* * *

REFERENCES

[1] LUNDE, J.K., "On the Linearized Theory of Wave Resistance for Displacement Ships in Steady and Accelerated Motion", Transactions of Society of Naval Architects and Marine Engineers, Vol. 59, p. 25 (1951).

[2] TUCK, E.O., "A Systematic Asymptotic Expansion Procedure of Slender Ships", Journal of Ship Research, Vol. 8, No. 1, 1964.

[3] HESS, J.L. and SMITH, A.M.O., "Calculation of Potential Flow about Arbitrary Bodies", Progress in Aeronautical Sciences, Vol. 8, Pergamon Press, New York, 1966. See also, DAWSON, C.W. and DEAN, J.S., "The XYZ Potential Flow Program", Naval Ship Research and Development Center Report 3892, 1972.

[4] TUCK, E.O., and von KERCZEK, C., "Streamlines and Pressure Distribution on Arbitrary Ship Hulls at Zero Froude Number", Journal of Ship Research, Vol. 12, No. 3, Sep 1968.

[5] BRADSHAW, P., "Calculation of Three-Dimensional Turbulent Boundary Layers", Journal of Fluid Mechanics, Vol. 46, Part 3, 1971.

[6] NASH, J.F., "The Calculation of Three-Dimensional Turbulent Boundary Layers in Incompressible flow", Journal of Fluid Mechanics, Vol. 37, Part 4, p. 625, 1969.

[7] CUMPSTY, N.A. and HEAD, M.R., "The Calculation of Three-Dimensional Turbulent Boundary Layers, Par 1 : Flow Over the Rear of an Infinite Swept Wing", The Aeronautical Quaterly, Vol. 18, 1967.

[8] SMITH, P.D., "Calculation Methods for Three-Dimensional Turbulent Boundary Layers", Aeronautical Research Council, Report and Memorandum No. 3523, 1966.

[9] COOKE, J.C. and HALL, M.G., "Boundary Layers in Three Dimensions", Progress in Aeronautical Sciences, Vol. 2, Pergamon Press, New York, 1962.

[10] LANDWEBER, L., "Characteristics of Ship Boundary Layers", 8th Symposium on Naval Hydrodynamics, Office of Naval Research, Pasadena, California, 1968.

[11] NEWMAN, J.N., "Some Hydrodynamic Aspects of Ship Maneuverability", 6th Symposium on Naval Hydrodynamics, Washington, D.C., Office of Naval Research, 1966.

[12] GADD, G.E., "The Approximate Calculation of Turbulent Boundary Layer Development on Ship Hulls", Transactions of the Royal Institution of Naval Architects, Vol. 113, No. 1, 1971.

[13] WU, T.Y., "Interaction Between Ship Waves and Boundary Layers", International Symposium on Theoretical Wave Resistance, University of Michigan, 1963.

[14] UBUROI, S.B.S., "Viscous Resistance of Ships and Ship Models", Hydro-og Aerodynamisk Laboratorium Report No. Hy-13, Lyngby, Denmark, sep 1968.

[15] WEBSTER, W.C., and HUANG, T.T., "Study of the Boundary Layer on Ship Forms", Journal of Ship Research, Vol. 14, No. 3, sep 1970.

[16] COOKE, J.C., "A Calculation Method for Three-Dimensional Turbulent Boundary Layers", Aeronautical Research Council, Report and Memorandum, No. 3199, 1961.

[17] GUILLOTON, R., "Potential Theory of Wave Resistance of Ships with Tables for its Calculation", Transactions of Society of Naval Architects and Marine Engineers, Vol. 59, 1951; also KORVIN-KROUKOVSKY, B.V. and WINNIFRED, R.J., "Calculation of the Wave Profile and Wave Making Resistance of Ships of Normal Commercial Form by Guilloton's Method and Comparison with Experimental Data", SNAME Technical and Research Bulletin No. 1-16, dec 1954.

[18] von KERCZEK, C., "Calculation of the Turbulent Boundary Layer on a Ship Hull at Zero Froude Number", Journal of Ship Research, Vol. 17, No. 2, June 1973.

[19] JOUBERT, P.N., and MATHESON, M., "Wind Tunnel Tests of Two Lucy Ashton Reflex Geosims", Journal of Ship Research, Vol. 14, No. 4, dec 1970.

[20] STEELE, B.N., "Measurements of Components of Resistance on a Tanker Model", National Physical Laboratory Ship Division Report No. 106, 1967.

[21] STEELE, B.N., and PEARCE, G.B., "Experimental Determination of the Distribution of Skin Friction on a Model of a High Speed Linear", Transactions of Royal Institution of Naval Architects vol. 110, p. 79, 1968.

[22] TZOU, K.T.S., "An Experimental Study of Shear Stress Variation on Series-60 Ship Model", Iowa Institute of Hydraulic Research Report, No. 108, 1968.

[23] STANDEN, N.M., "A Concept of Mass Entrainment Applied to Compressible Turbulent Boundary Layers in Adverse Pressure Gradients", American Institute for Aeronautics and Astronautics No. 64-584, 1964.

[24] GRANVILLE, P.S., "Integral Methods for Turbulent Boundary Layers in Pressure Gradients", Naval Ship Research and Development Center Report 3308, apr 1970.

[25] MAGER, A., "Generalization of Boundary Layer Momentum-Integral Equations ot Three-Dimensional Flows Including Those of a Rotating System", National Advisory Committee for Aeronautics Report 1067, 1952.

[26] von KERCZEK, C., and TUCK, E.O., "The Representation of Ship Hulls by Conformal Mapping Function", Journal of Ship Research, Vol. 13, No. 4, dec 1969.

[27] YEUNG, R.W., "Sinkage and Trim in First-Order Thin-Ship Theory", Journal of Ship Research, Vol. 16, No. 1, 1972.

[28] TODD, F.H., "Series 60 - Methodical Experiments with Models of Single-Screw Merchant Ships", David Taylor Model Basin Research and Development Report 1712, 1963.

[29] TSAI, C.E., and LANDWEBER, L., "Total and Viscous Resistance of Four Series-60 Models", 13th International Towing Tank Conference, Berlin, Hamburg (Sep 1972).

[30] WEHAUSEN, J.V., and E.V. LAITONE, "Surface Waves", Encyclopedia of Physics, edited by S. Flugge, Vol. IX,

Fluid Dynamics III, Springer-Verlag, 1960.

[31] LING, S. C., "Heat Transfer Characteristics of Hot-Film Sensing Elements Used in Flow Measurement", Transactions of American Society of Mechanical Engineers, Journal of Basic Engineering, Vol. 82, p. 629, 1960.

[32] LING, S. C., et al., "Application of Heated-Film Velocity and Shear Probes to Hemodynamic Studies", Circulation Research, Vol. XXIII, No. 789, dec 1968.

[33] LANDWEBER, L. and SIAO, T. T., "Comparison of Two Analyses of Boundary-Layer Data on a Flat Plate", Journal of Ship Research, Vol. 1, No. 4, 1958.

[34] PATEL, V. C., "Calibration of the Preston Tube and Limitation on Its Use in Pressure Gradients", Journal of Fluid Mechanics, Vol. 23, pp. 185-208, 1965.

[35] RAJARATNAM, N., and MURALIDHAR, D., "Yaw Probe Used as Preston Tube", Royal Aeronautical Society Journal, Vol. 72, No. 1060, dec 1968.

[36] SIGALLA, A., "Experiments with Pitot Tubes Used for Skin Friction Measurement", British Iron and Steel Research Association Report, mar 1958.

* * *

TABLE I - PROBE LOCATIONS ON THE MODEL HULL

STREAMLINE A			
No.	X/L/2	Y/L/2	Z/L/2
1	-0.900	0.0109	-0.0798
2	-0.800	0.0167	-0.0952
3	-0.700	0.0085	-0.1056
4	-0.600	0.0039	-0.1067
5	-0.400	0.0022	-0.1067
6	-0.200	0.0020	-0.1067
7	-0.100	0.0019	-0.1067
8	0.100	0.0019	-0.1067
9	0.200	0.0019	-0.1067
10	0.400	0.0020	-0.1067
11	0.600	0.0024	-0.1067
12	0.800	0.0046	-0.1067
13	0.900	0.0087	-0.0881
STREAMLINE B			
14	-0.900	0.0118	-0.0491
15	-0.800	0.0270	-0.0573
16	-0.700	0.0422	-0.0730
17	-0.500	0.0361	-0.1053
18	-0.300	0.0260	-0.1067
19	0.000	0.0243	-0.1067
20	0.300	0.0246	-0.1067
21	0.500	0.0270	-0.1067
22	0.700	0.0377	-0.0896
23	0.900	0.0141	-0.0535
L = 20 feet			

STREAMLINE C			
No.	X/L/2	Y/L/2	Z/L/2
24	-0.900	0.0120	-0.0350
25	-0.700	0.0462	-0.0506
26	-0.600	0.0644	-0.0651
27	-0.500	0.0721	-0.0871
28	-0.400	0.0660	-0.1028
29	-0.300	0.0608	-0.1066
30	-0.200	0.0249	-0.1067
31	-0.100	0.0543	-0.1067
32	0.000	0.0689	-0.1067
33	0.100	0.0537	-0.1067
34	0.200	0.0542	-0.1067
35	0.300	0.0555	-0.1067
36	0.400	0.0585	-0.1067
37	0.500	0.0585	-0.1067
38	0.600	0.0641	-0.0792
39	0.800	0.0343	-0.0445
40	0.900	0.0145	-0.0326

STREAMLINE D			
No.	X/L/2	Y/L/2	Z/L/2
41	-0.800	0.0287	-0.0246
42	-0.600	0.0696	-0.0409
43	-0.400	0.1046	-0.0635
44	-0.200	0.1203	-0.0854
45	0.006	0.1241	-0.0939
46	-0.200	0.1204	-0.0888
47	-0.400	0.1078	-0.0733
48	-0.600	0.0816	-0.0495
49	-0.800	0.0439	-0.0277
WATERLINE E			
50	-0.900	0.0128	-0.0150
51	-0.800	0.0294	-0.0150
52	-0.500	0.0941	-0.0150
53	-0.300	0.1236	-0.0150
54	0.100	0.1338	-0.0150
55	0.500	0.1195	-0.0150
56	0.700	0.0836	-0.0150
57	0.800	0.0540	-0.0150
58	-0.950	0.0122	-0.0150
ADDITIONAL POINTS			
59	-0.600	0.1093	-0.0400
60	-0.100	0.1338	-0.0400
61	0.300	0.1308	-0.040
62	0.950	0.0090	-0.0752
63	0.950	0.0042	-0.0250

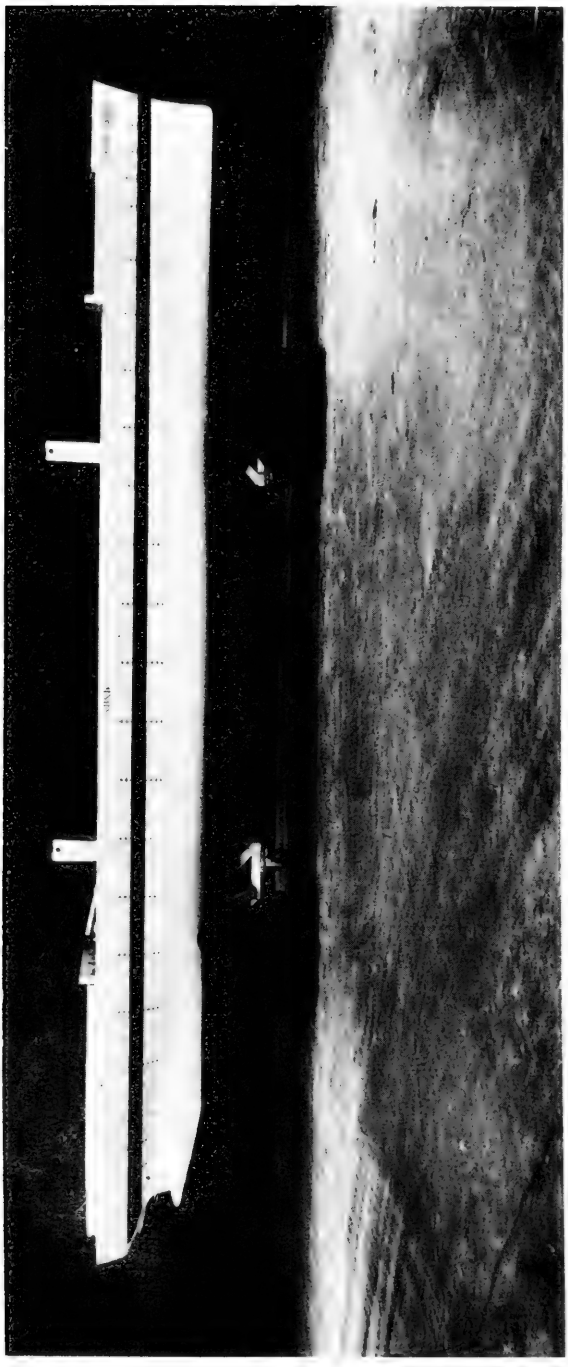

Figure 1. BRIAN BORU : 20-Foot Series 60 (C_B = 0.60) Model

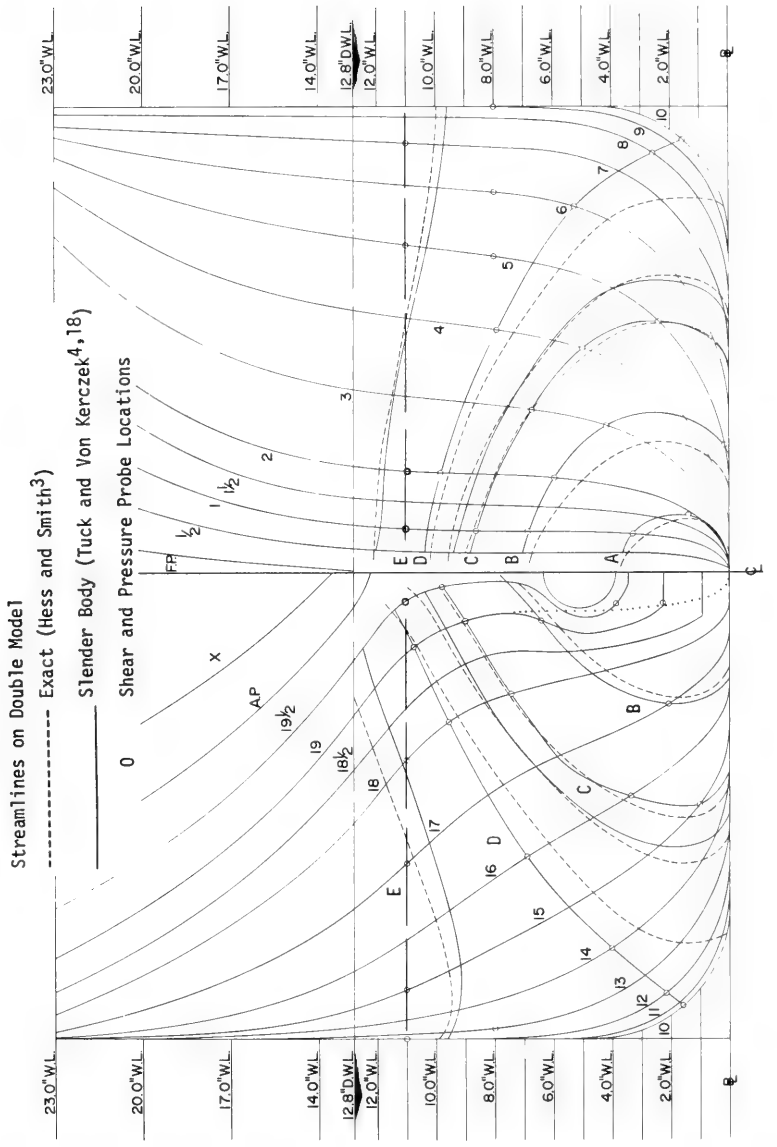

Figure 2. Body Plan, Streamlines, and Probe Locations

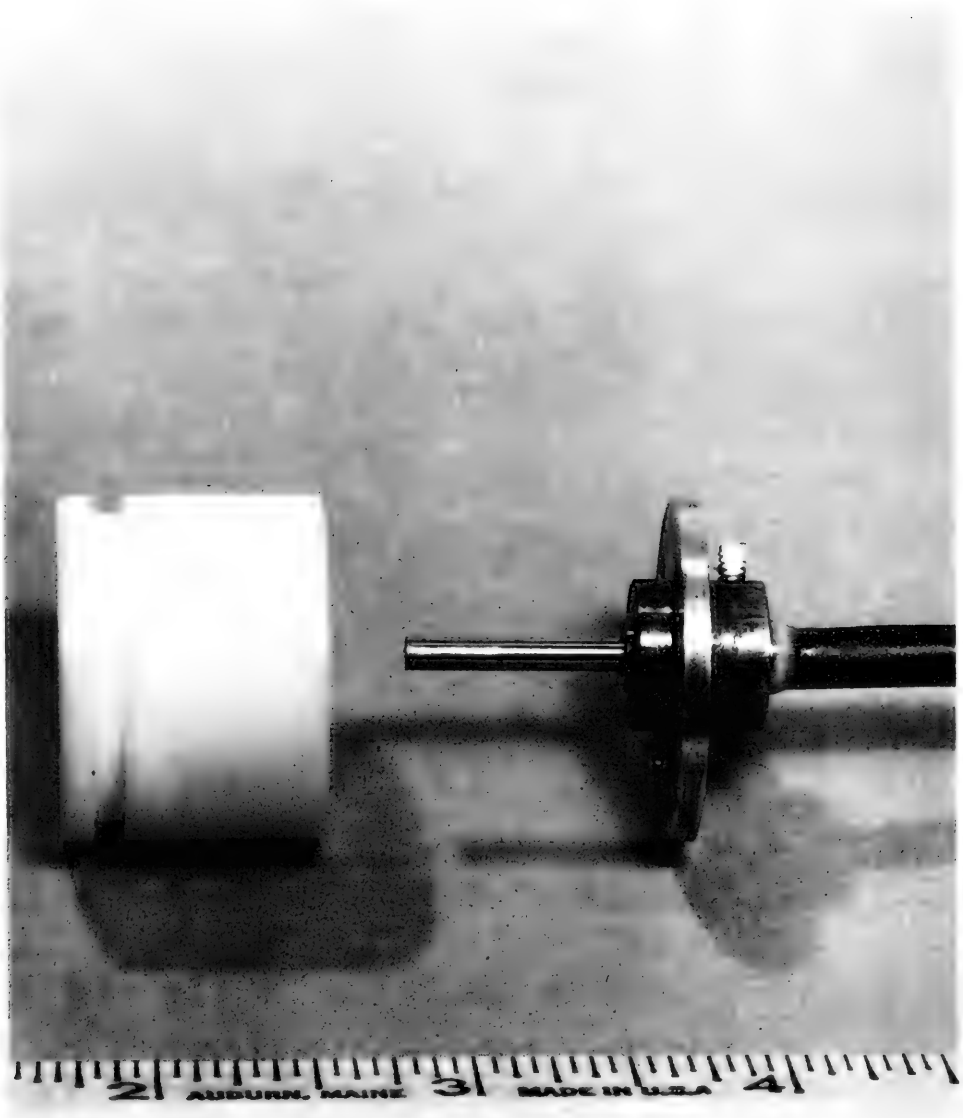

Figure 3. Photograph of Hot-Film Shear Probe and Mounting Plug

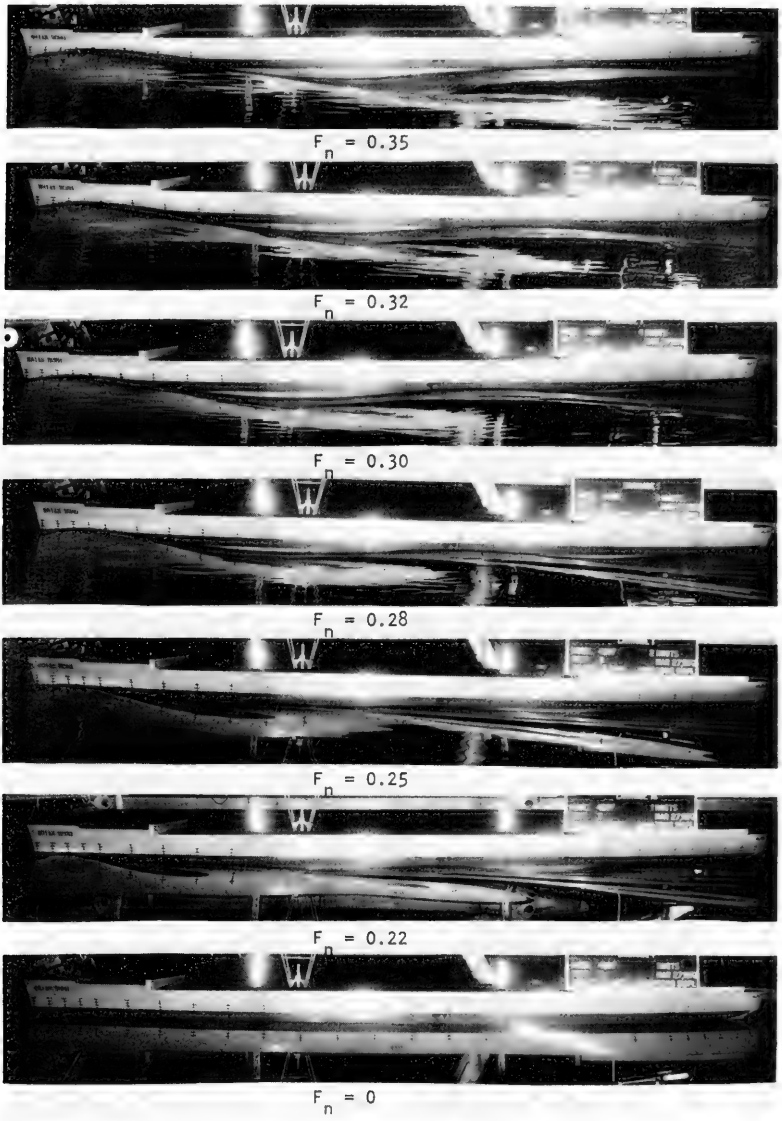

Figure 4. Wave Profiles at Various Froude Numbers

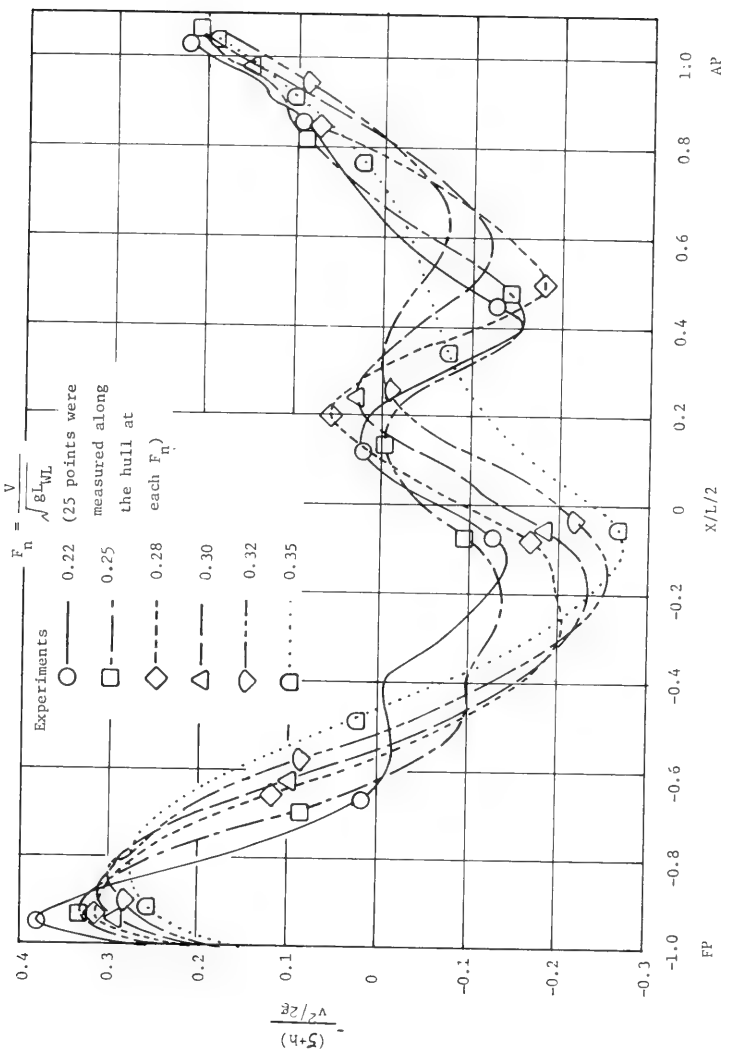

Figure 5. Dimensionless Wave Profiles Measured along the Hull at Various Froude Numbers

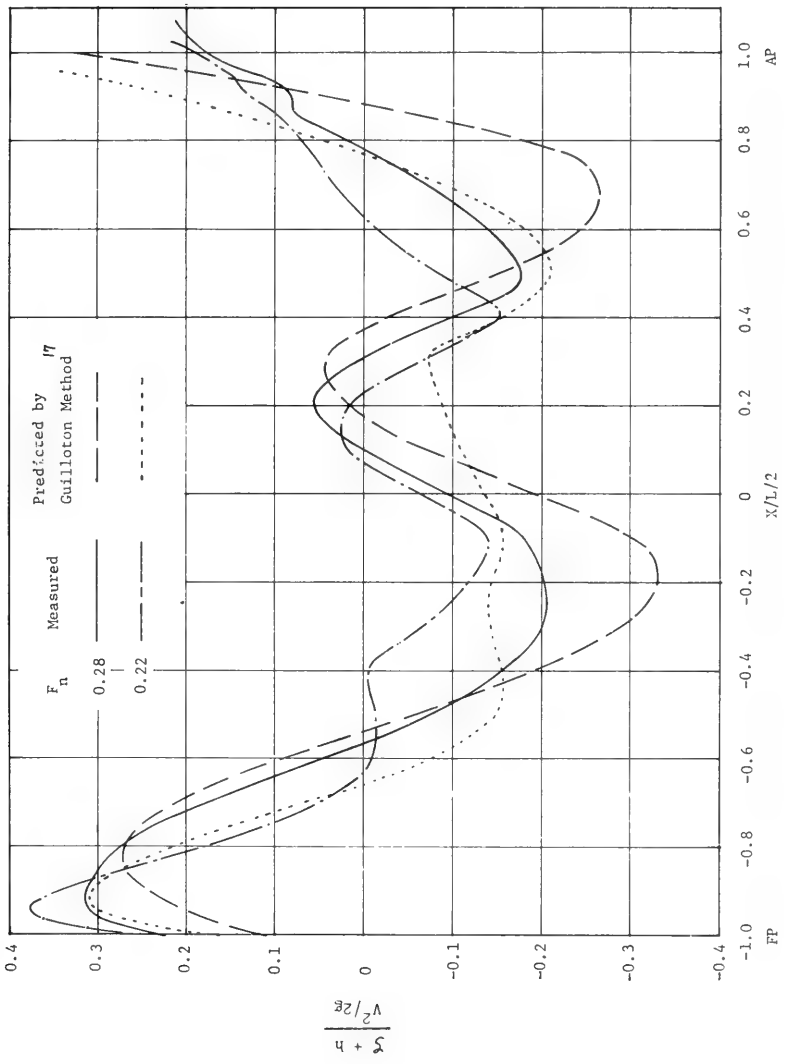

Figure 6. Comparison of Measured and Predicted Wave Profiles

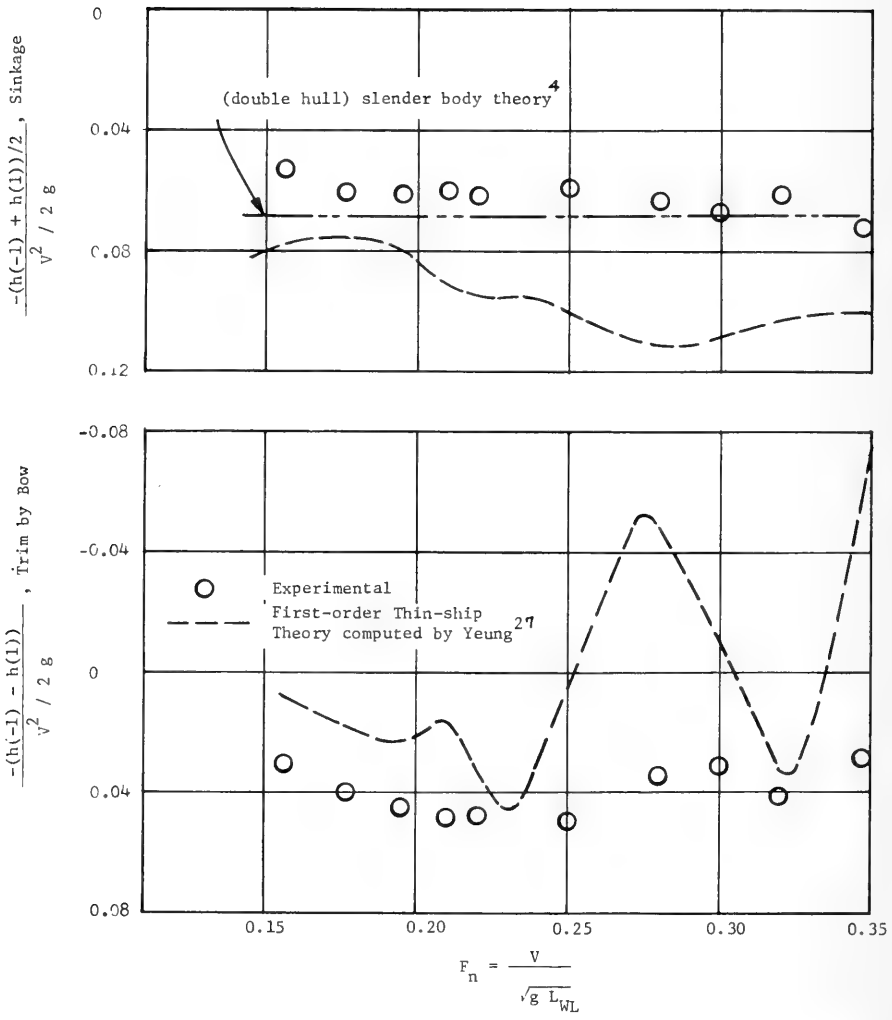

Figure 7. Dimensionless Sinkage and Trim

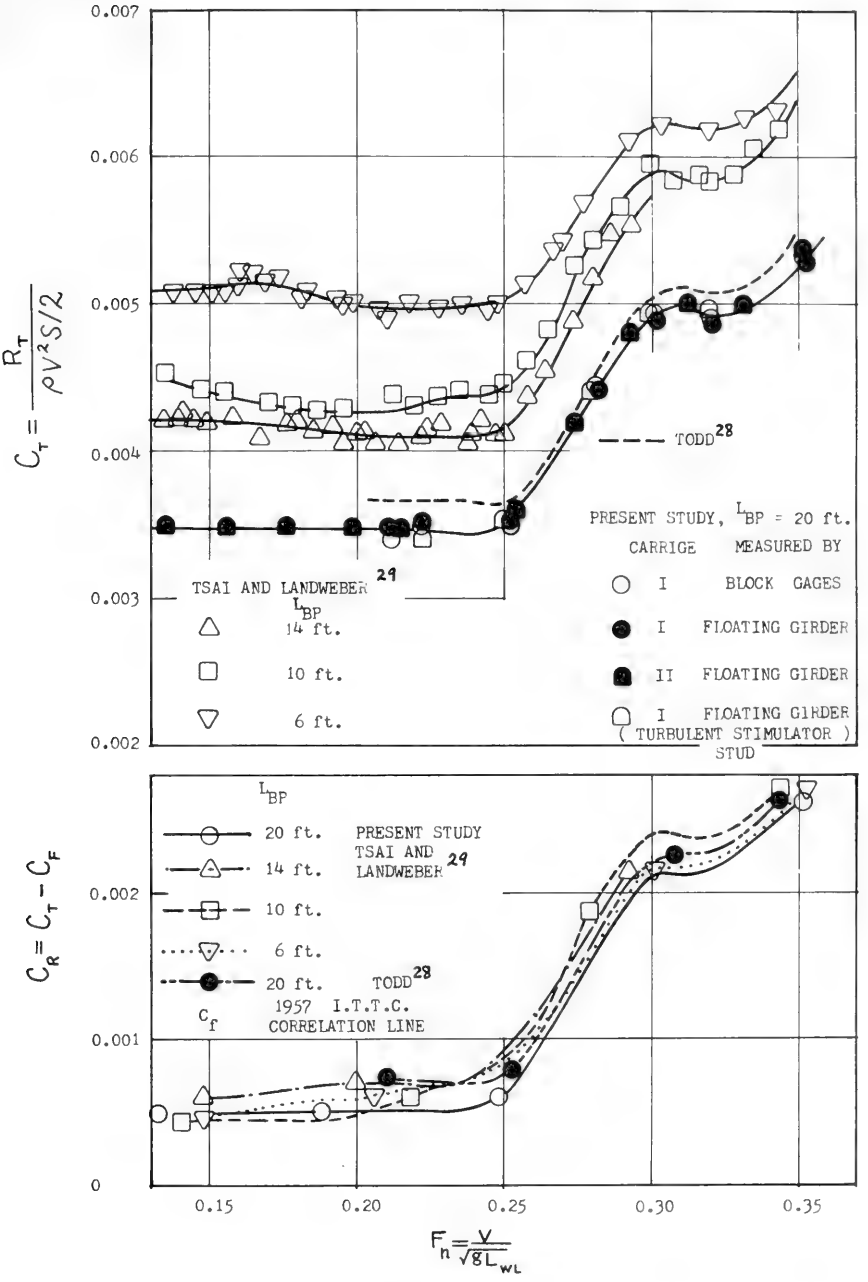

Figure 8. Total Resistance and Residual Resistance of the Various Length Models

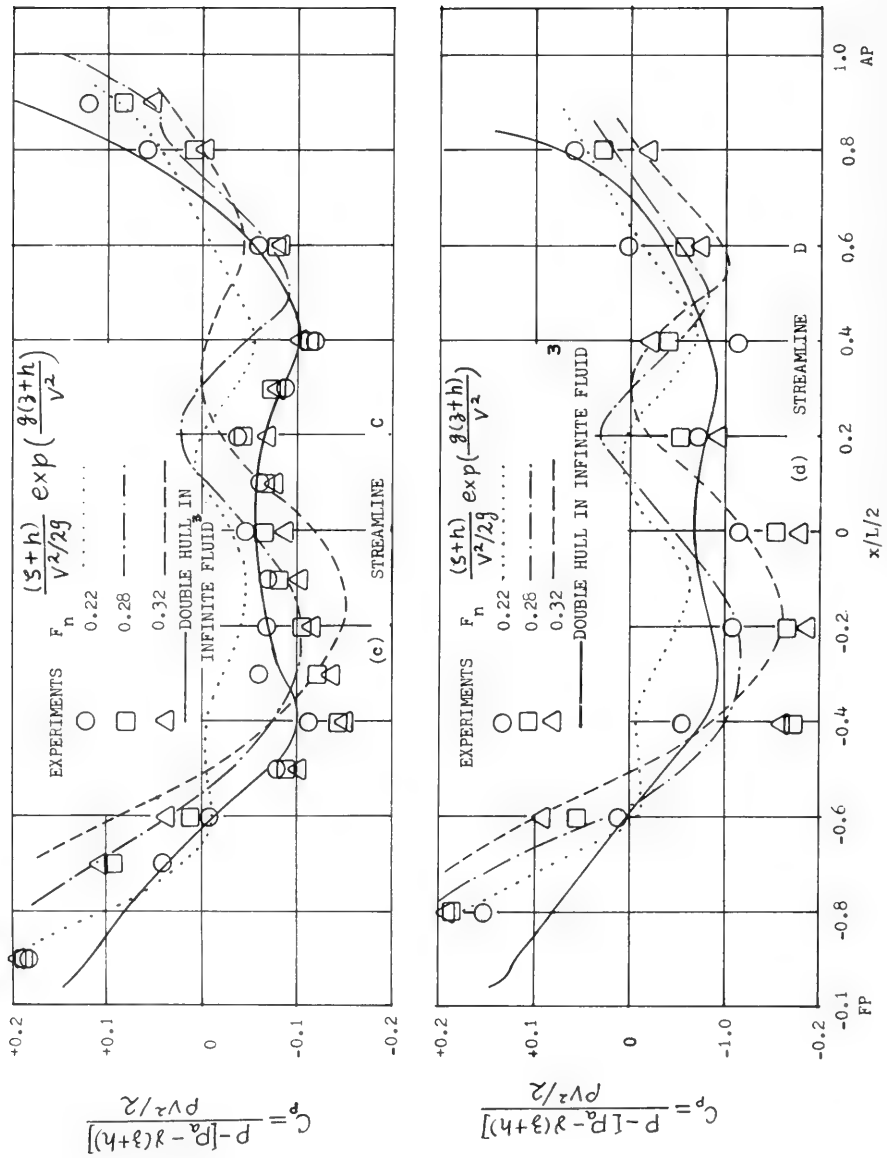

Figure 9. Measured and Calculated Pressure Distribution on the Hull

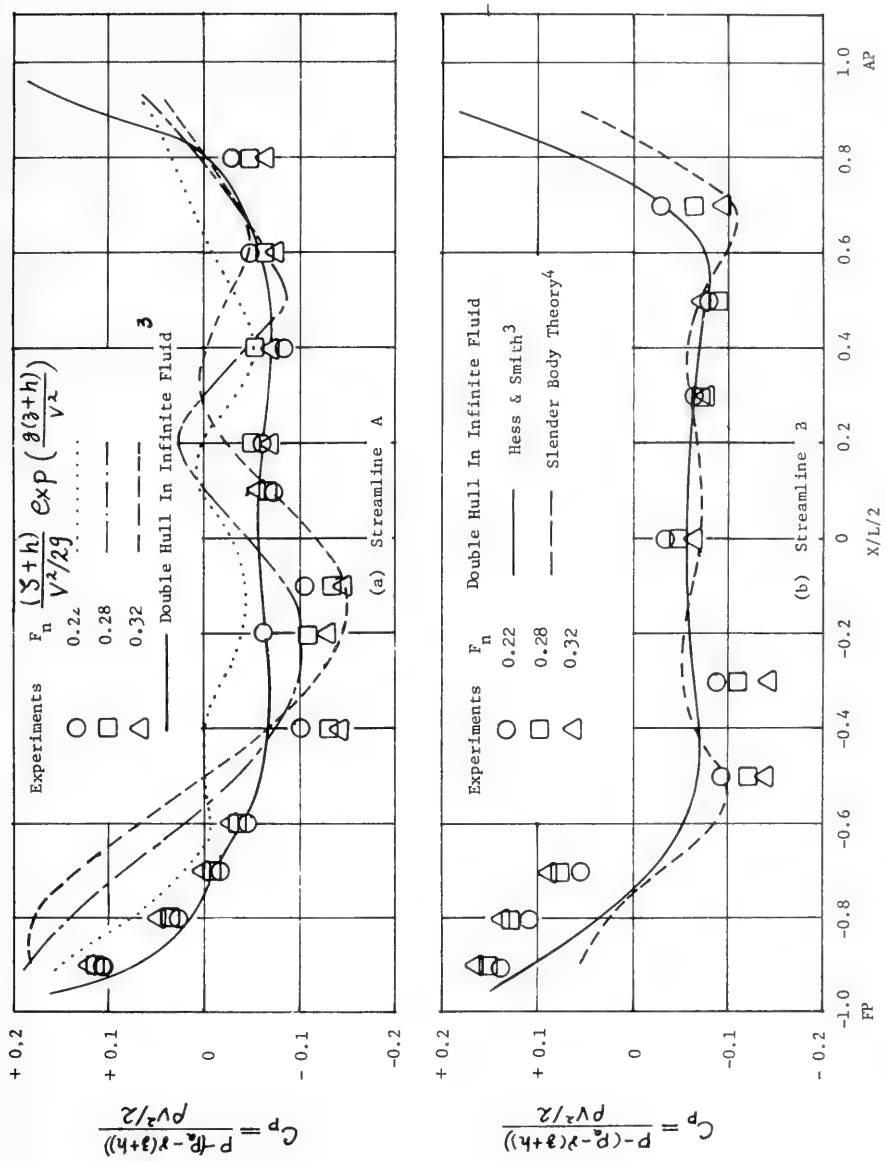

Figure 9. Measured and Calculated Pressure Distribution on the Hull (Continued)

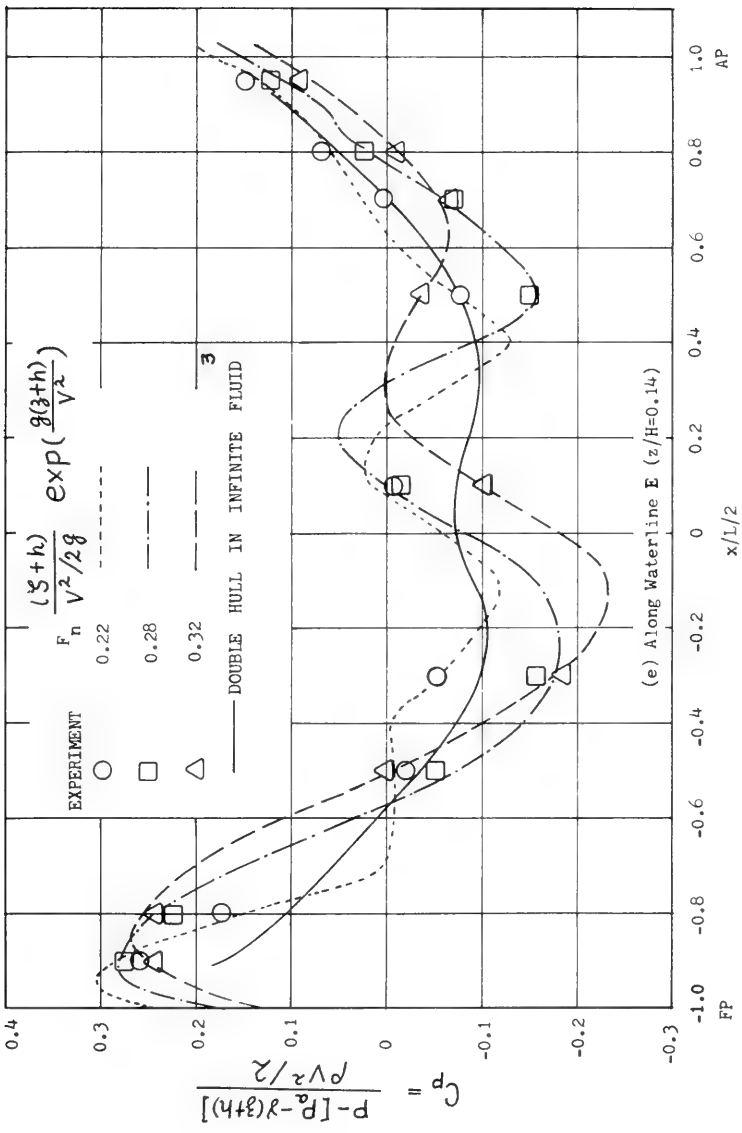

Figure 9. Measured and Calculated Pressure Distribution on the Hull (Continued)

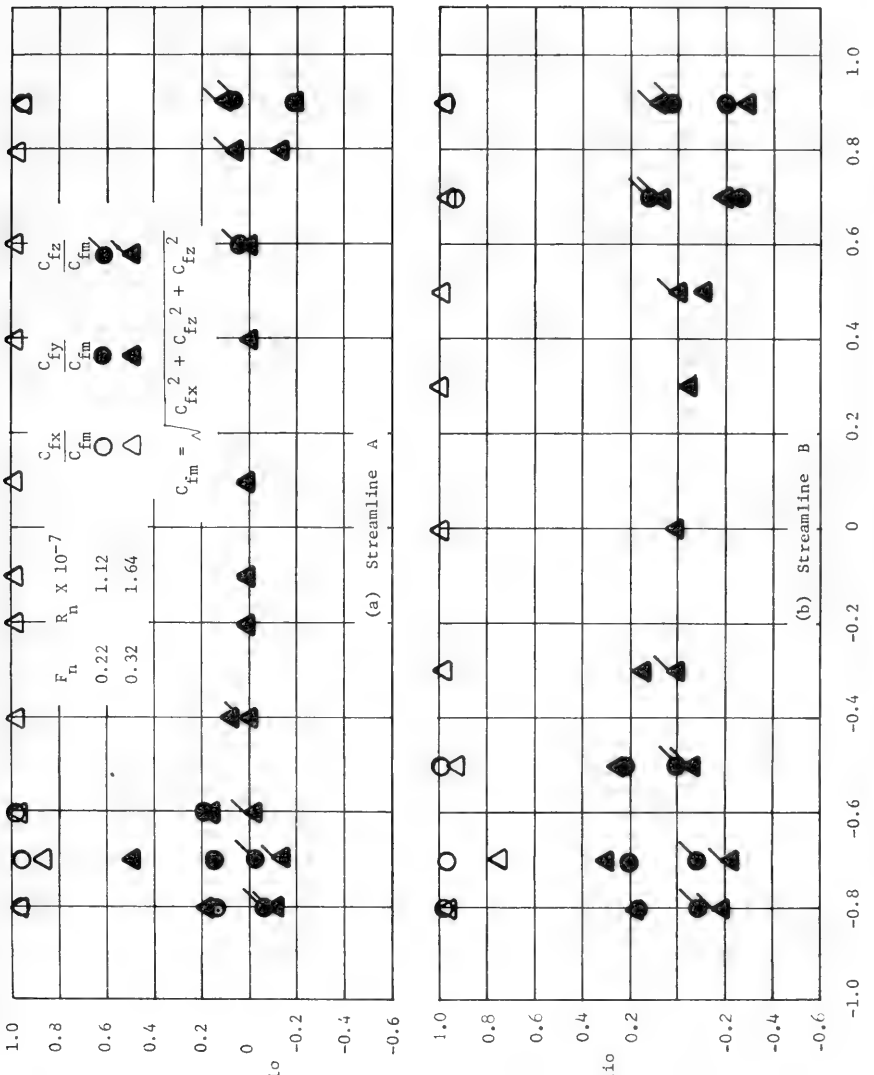

Figure 10. Measured Shear-Stress Components

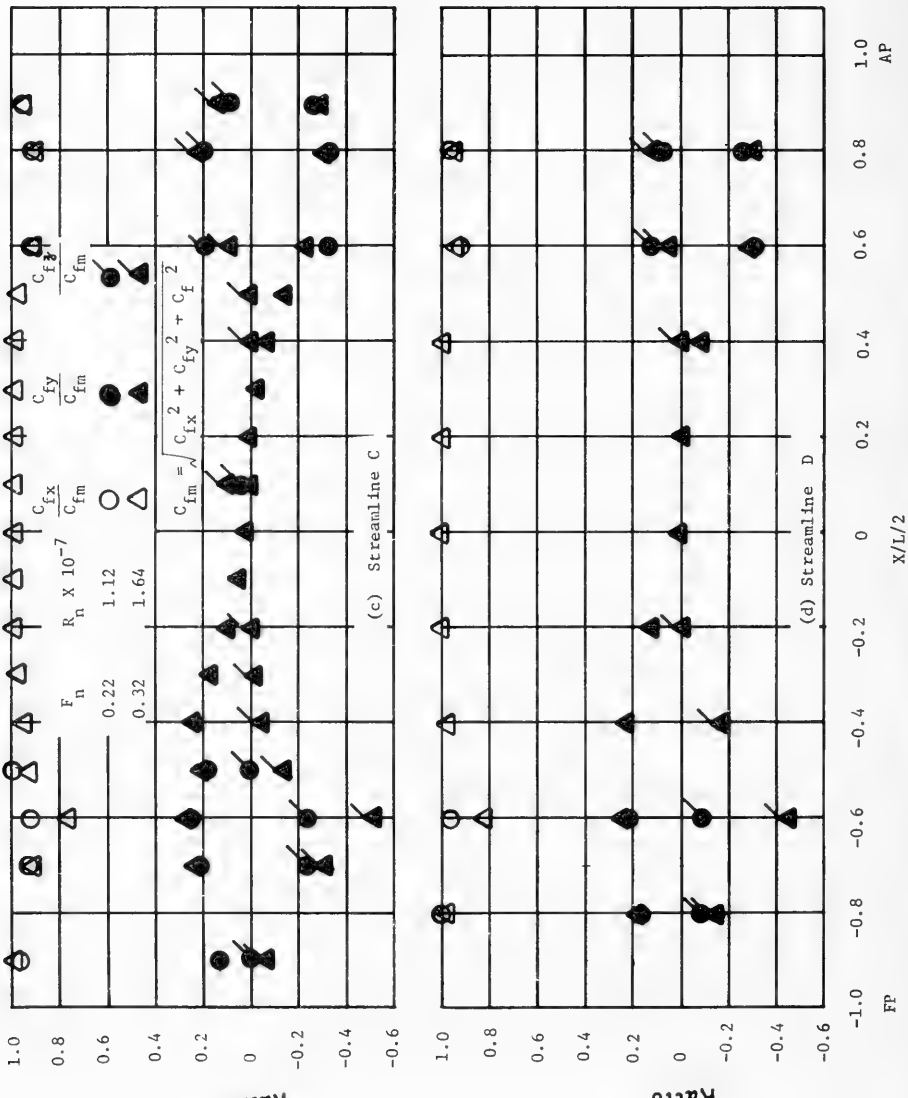

Figure 10. Measured Shear-Stress Components (Continued)

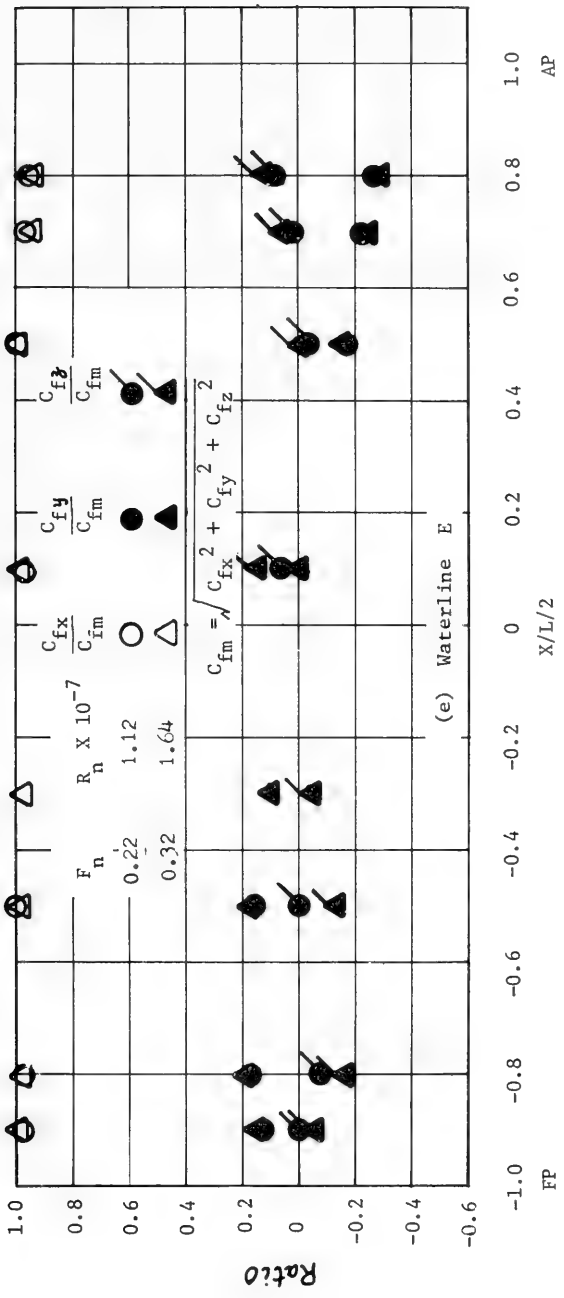

Figure 10. Measured Shear-Stress Components (Concluded)

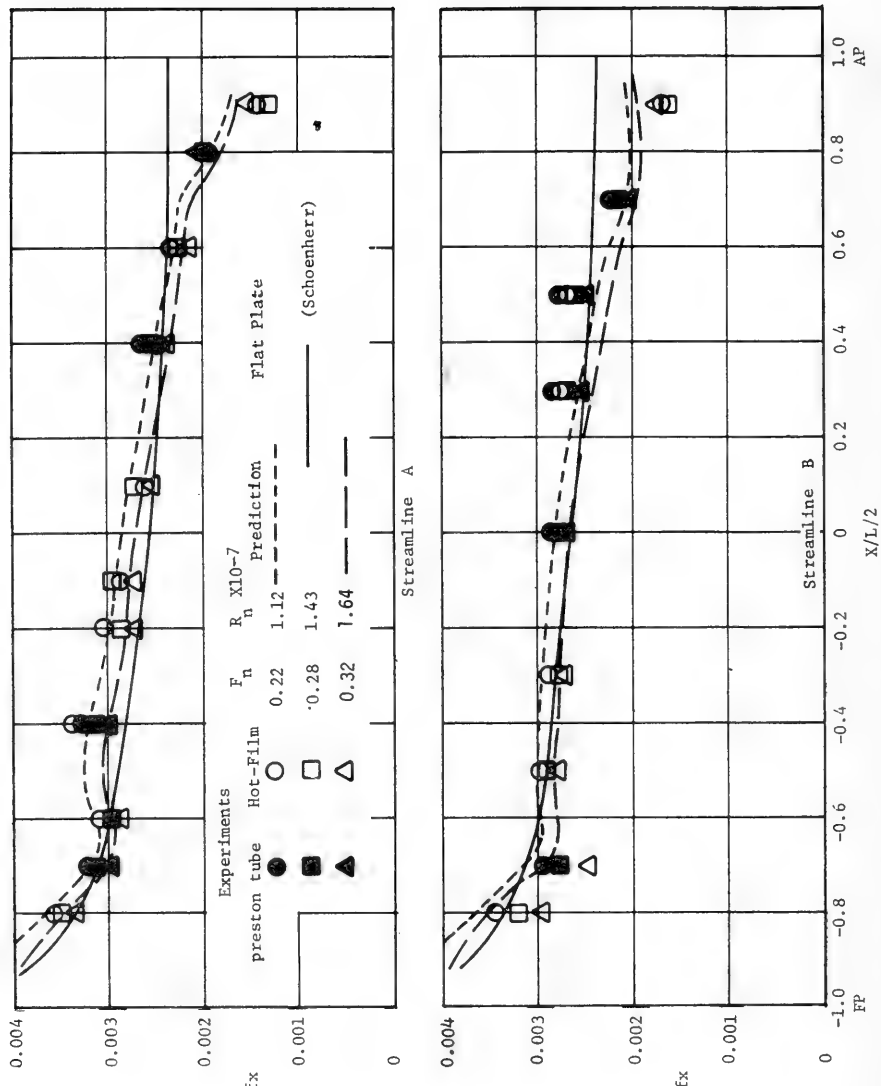

Figure 11. Measured and Calculated Shear Stress Distributions on the Hull

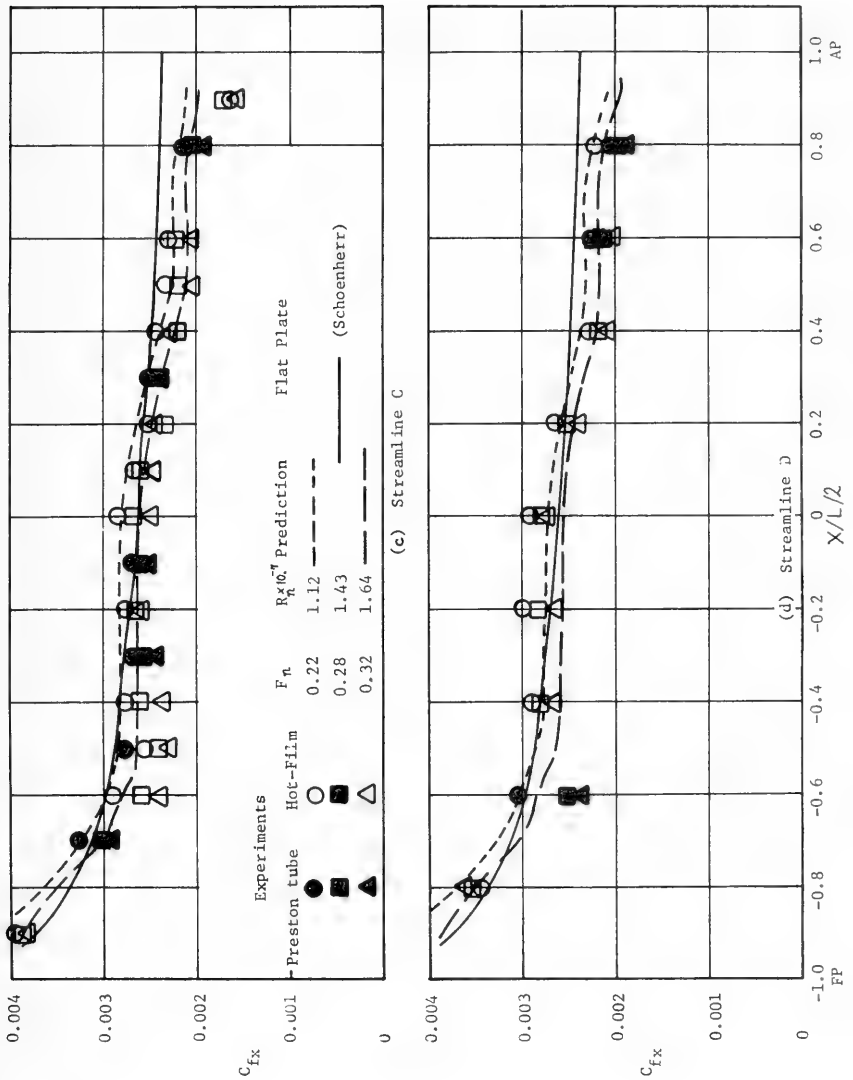

Figure 11. Measured and Calculated Shear Stress Distributions on the Hull (Continued)

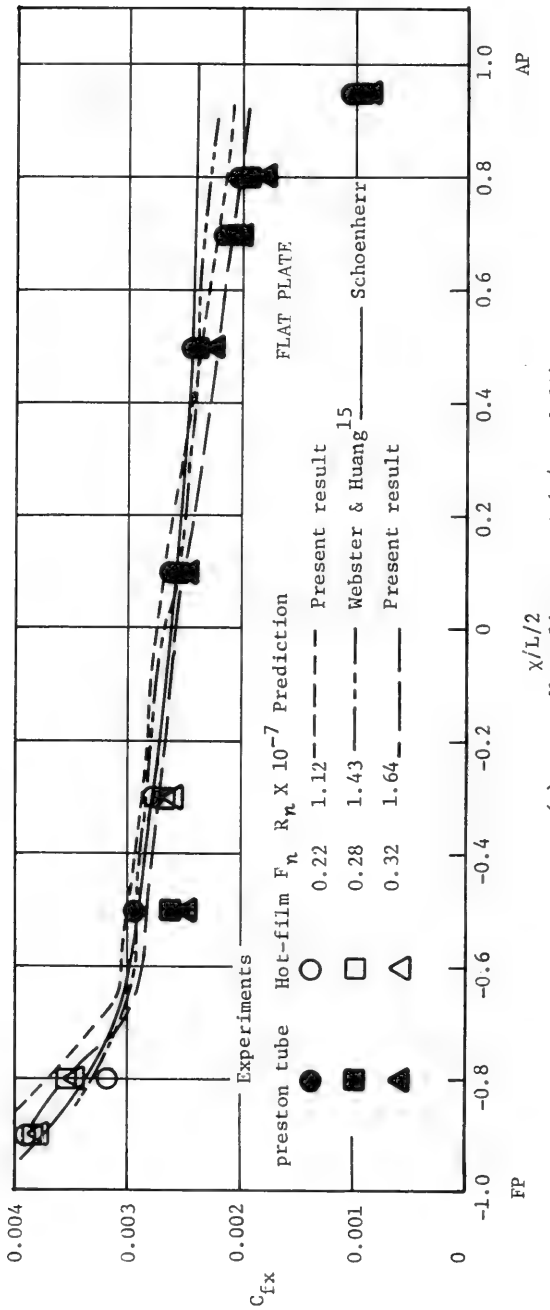

Figure 11. Measured and Calculated Shear Stress Distributions on the Hull (Concluded)

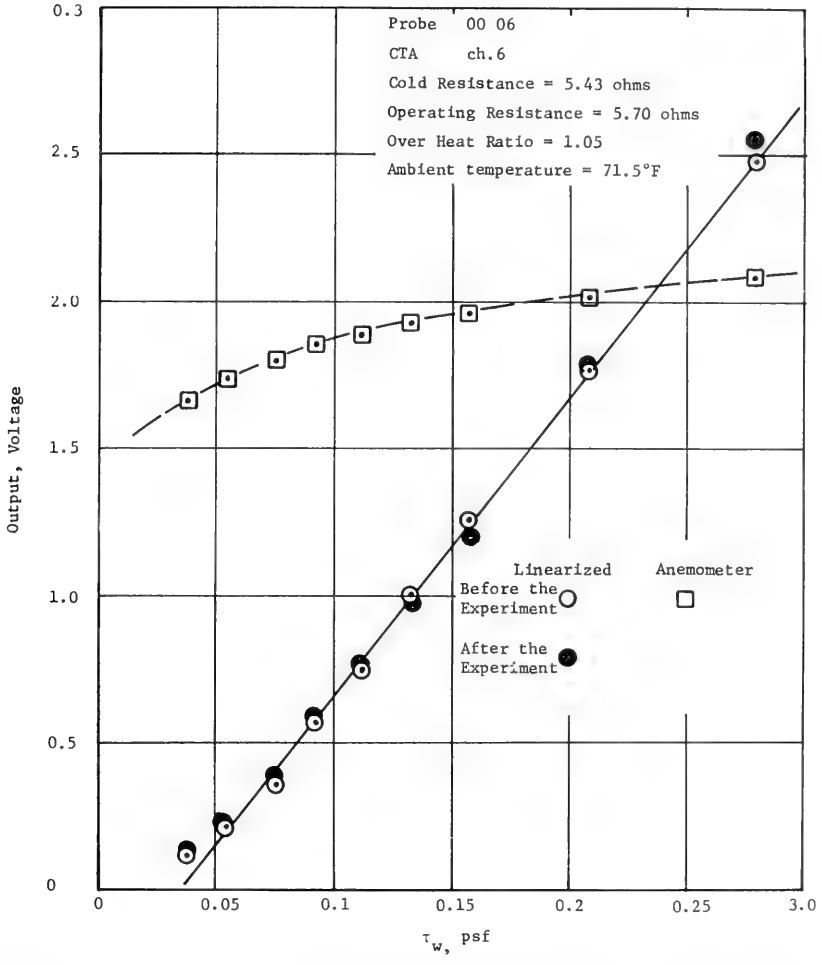

Figure A1. Typical Calibration Curve for a Hot-Film Shear Probe

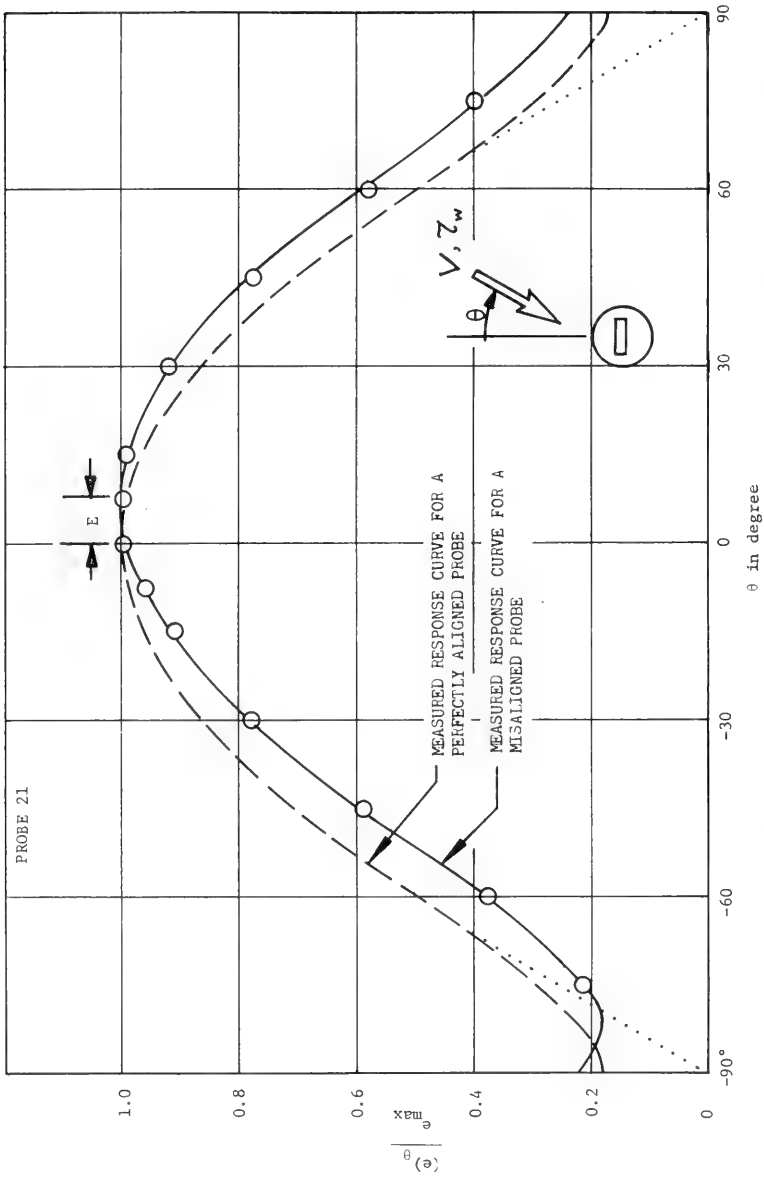

Figure A2. Typical Response of a Hot-Film Shear Probe as a Function of Angular Orientation

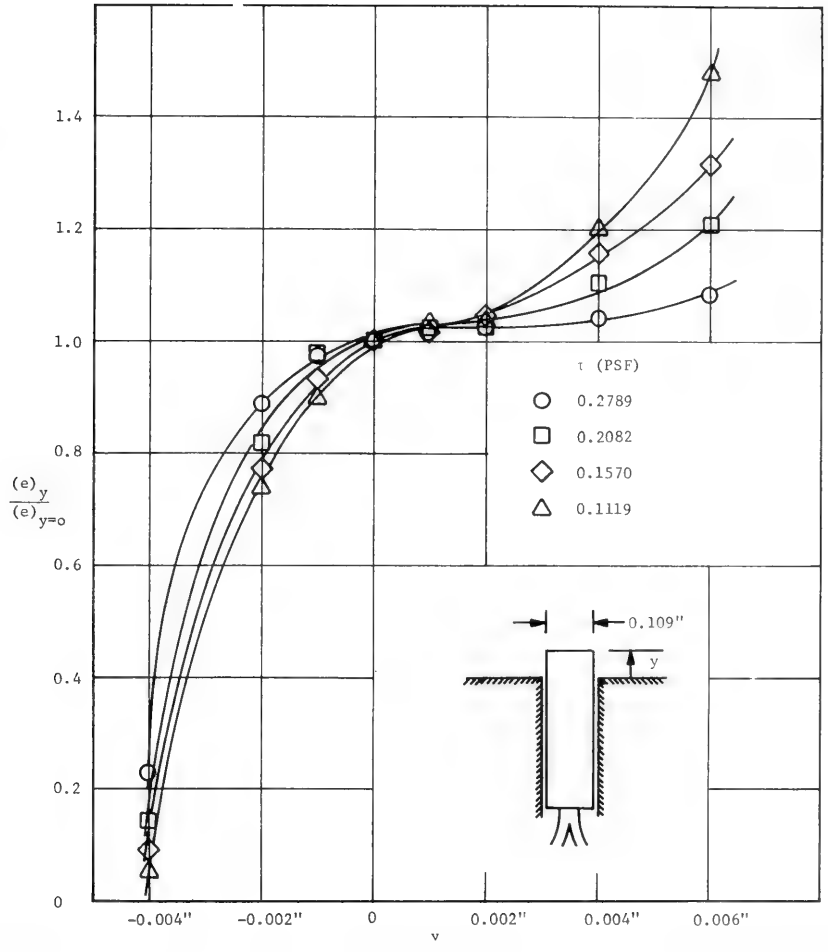

Figure A3. Effect of Probe Protuberance on Hot-Film Response

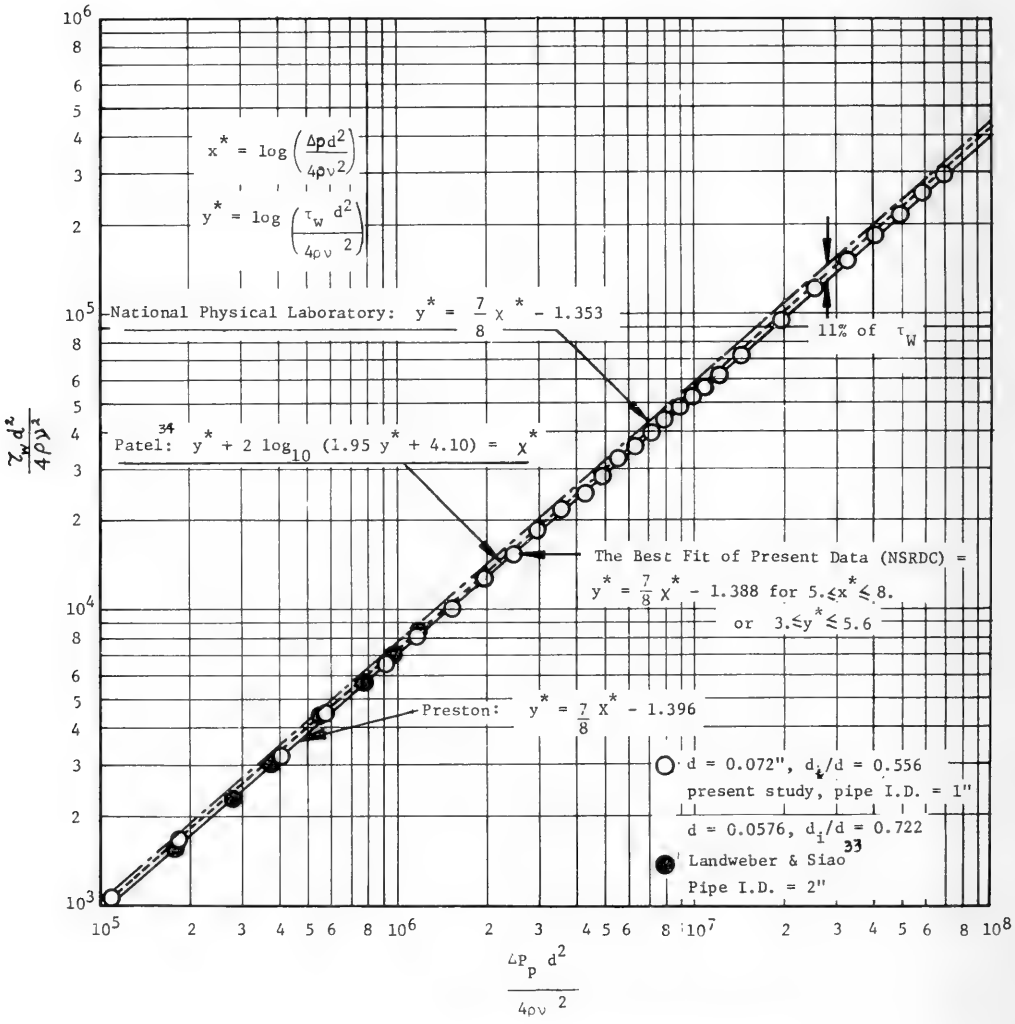

Figure A4. Calibration Curve for Preston Tube in a Pipe

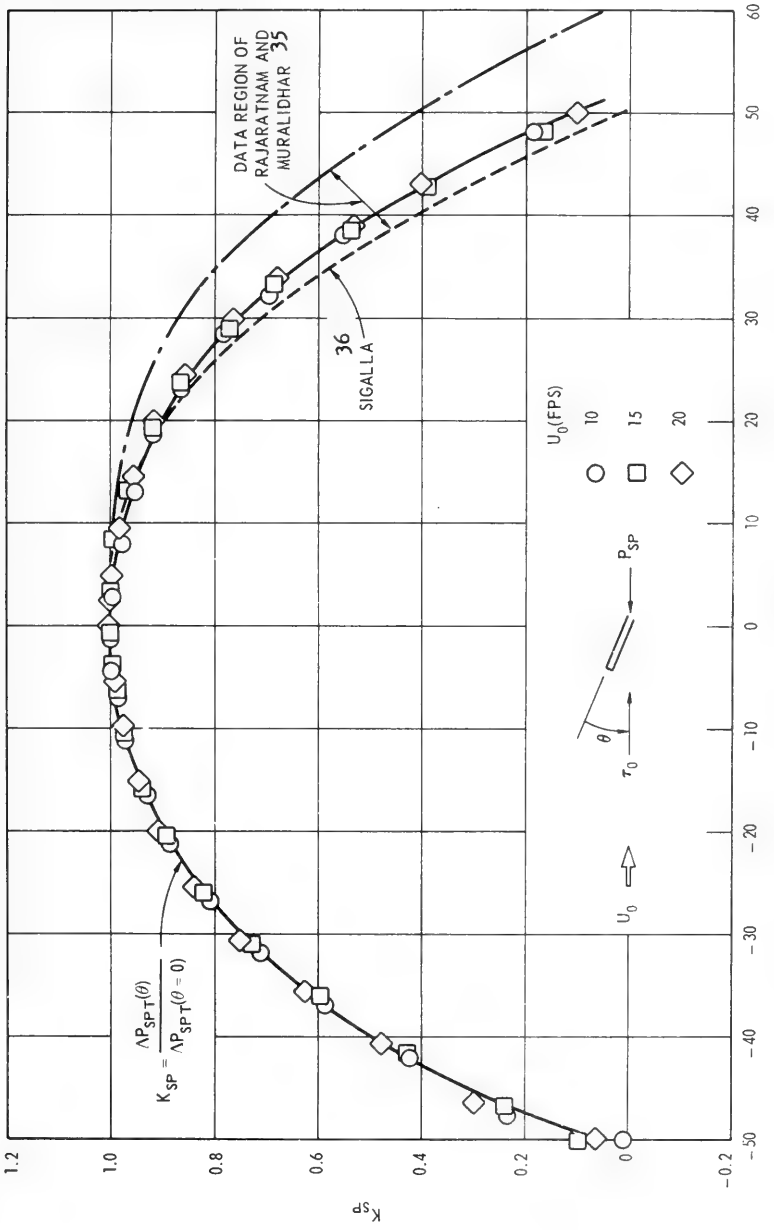

Figure A5. Directional Respose of Single Preston Tube

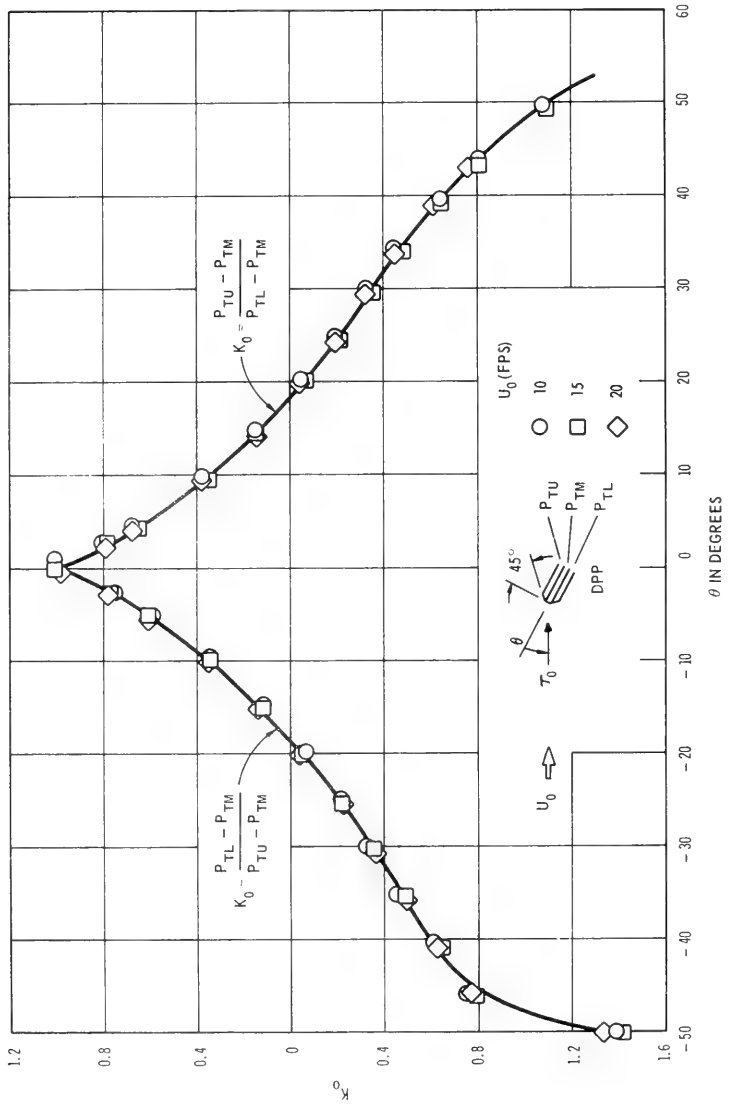

Figure A6. Respose of Directional Preston Tube (Nose Angle α = 45 Degrees)

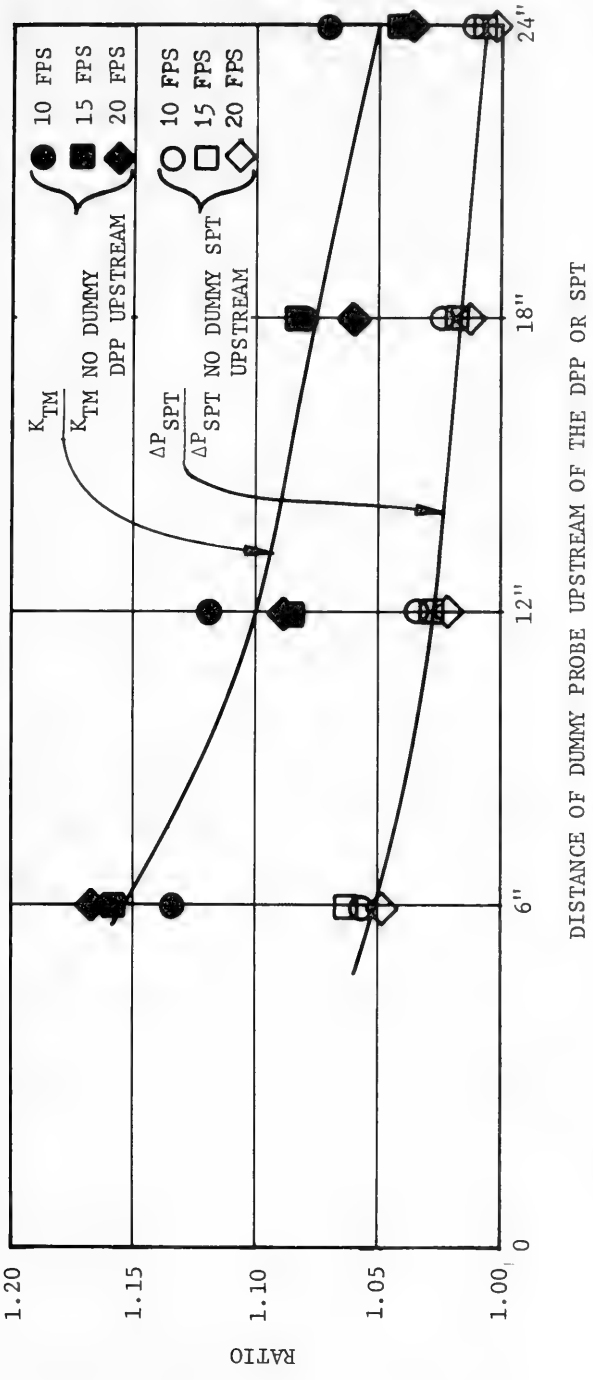

Figure A7. Interference Effect of DPP and SPT

DISCUSSION

L. Landweber
University of Iowa
Institute of Hydraulic Research
Iowa City, U.S.A.

I am very pleased to see such a basic study of viscous characteristics of flow about a ship at nonzero Froude number. There have been too few such studies. As the authors realise, the method that they used to calculate the three-dimensional boundary layer on the ship is suitable only for fine formes, free of the cross flows, bilge vortices, secondary flows and separation. I hope that, in the continuation of their work, they will use methods which are suitable for fuller forms, possibly with separation, extending even into the thick boundary layer zone near the stern.

I would like to call attention to a book on three-dimensional boundary layers, recently published by one of my colleagues at the University of Iowa, V. C. Patel. It is available only directly from him ; he is his own publisher.

Concerning the potential flow, we at the University of Iowa have tried the technique that is used in this paper, that of Tuck-Kerczek, and some of our work on this method was reported at the Seventh Symposium in Rome. The method is a very attractive one. It appears to enable one to obtain the parametric equations of a ship form in a very compact way. Our exprerience has been, however, that the method cannot give a sufficiently accurate representation of the hull at the bow and stern, so that it could not be useful for obtaining source distributions or for calculating wave resistance, especially since, for wave resistance, the result is very sensitive to small deviations from the original form. It appears, however, that the method is suitable for determining the streamlines at low Froude number and can serve as the basis for determining a streamline co-ordinate system for boundary-layer calculation, as the authors have shown.

One results in the paper is not clear to me, and may be incorrect. On page 10 the authors give a separable form for the potential function.

Their assumption is that the free-surface condition can be applied below the undisturbed water surface. I think that this result

is valid for two dimensions, not for three.

The authors have shown some of our data for a family of series 60 geosims ranging in length from 6 to 14 feet. The results for the 14 feet model should be corrected for blockage, as we plan to show at the forthcoming ITTC in Berlin.

The authors are to be congratulated on their very interesting and valuable paper.

DISCUSSION

John V. Wehausen
University of California
Berkeley, California, U.S.A.

Bruce Adee has recently made a computation which seems very similar to yours, except that instead of using the rigid free-surface boundary condition, he actually used the linearized free-surface boundary condition. I wonder if you have had a chance to compare your results with his, or if even he sent you a copy of his thesis ?

REPLY TO DISCUSSION

Thomas T. Huang
Naval Ship Research and Development Center
Bethesda, Maryland, U.S.A.

We have not yet received a copy of Dr. Adee's thesis for comparison.

I thank Professor Landweber for his kind suggestion. This is a complicated problem involving the free surface boundary condition and turbulent boundary layer. This topic would open many interesting investigations in the future. We shall take Dr. Landweber's suggestion very seriously.

Dr. Landweber's comment on page 10 is right, but the measurements show that the wave along the mid-ship is almost a two-dimensional wave. The blockage correction is a very interesting problem which has to be considered. The 14-ft and 10-ft models appeared to need some blockage correction in the Iowa tank. It is interesting that the 6-ft model and the 20-ft model agree very well.

DISCUSSION

Jean-François Roy
Bassin d'Essais des Carènes
Paris, France

(Translated from French)

All the results presented in this paper are very interesting. And especially, I think it is exceptional to know both distributions of pressure and shear stress on a hull. In such a case, I would have been tempted to check, by integration, the values of the total resistance and its two components that have been measured by other means. May I ask the authors whether they did make such a verification. Thank you.

REPLY TO DISCUSSION

Thomas T. Huang
Naval Ship Research and Development Center
Bethesda, Maryland, U.S.A.

Because of time, the actual integration of the pressure distribution and shear stress distribution has not been done. We want to improve our computation methods for the potential flow as well as boundary layer first and the actual integration can be done if we have time, and probably will be carried out in the near future. It is not a major point of our paper.

AUTHOR INDEX

☆ U.S. GOVERNMENT PRINTING OFFICE : 1975 O—565-527